ELSEVIER
PERGAMON

Comprehensive Coordination Chemistry II

FROM BIOLOGY TO NANOTECHNOLOGY

EDITORS-IN-CHIEF
Jon A McCleverty
Thomas J Meyer

Edited by
A.B.P. Lever

Volume 2
Fundamentals: Physical Methods, Theoretical Analysis and Case Studies

Introduction to Volumes 1 and 2

In this first two volumes of *Comprehensive Coordination Chemistry II* we have endeavored to lay down the fundamentals of coordination chemistry as it is understood in the early part of the twenty-first century. We hope to have provided all the necessary fundamental background information needed to prosecute coordination chemistry in the physical and theoretical laboratory and to appreciate fully the information provided in the remaining volumes of this treatise.

These volumes contain 112 contributions from some 130 outstanding, internationally known, contributors. They are subdivided into nine major sections whose content is described briefly below. The contributors were asked to emphasize developments in the field achieved since 1980 and since the publication of CCC (1987).

1. LIGANDS – a survey of the syntheses, characterization, and properties of many of the more commonly employed ligands.
2. SYNTHESIS, PURIFICATION AND CHARACTERIZATION OF COORDINATION COMPOUNDS – including a detailed survey of aqua metal ions, the use of solvents, chromatographic methods, and crystal growth techniques.
3. REACTIONS OF COORDINATED LIGANDS – dealing with the chemistry of molecules such as oxygen, nitric and nitrous oxide, carbon dioxide, oximes, and nitriles
4. STEREOCHEMISTRY, STRUCTURE, AND CRYSTAL ENGINEERING – structure and stereochemistry involving lone pair effects, outer sphere interactions, and hydrogen bonding.
5. NEW SYNTHETIC METHODS – nine contributions dealing with a wide range of newer methodologies from biphasic synthesis to sol–gel to genetic engineering.
6. PHYSICAL METHODS – a very extensive chapter incorporating 34 contributions detailing the enormous breadth of modern physical methods.
7. THEORETICAL MODELS, COMPUTATIONAL METHODS, AND SIMULATION – 17 contributions illustrating the wealth of information that can be extracted from a range of computational methods from semi-empirical to *ab initio*, and from ligand field theory to metal–metal exchange coupling to topology, etc.
8. SOFTWARE – a brief glimpse of some of the packages which are currently available.
9. CASE STUDIES – putting it all together – eight studies which reveal how the many physical and theoretical techniques presented earlier in the volume can be used to solve specific problems.

The creation of these volumes has been an exciting, challenging, time-consuming, and all-absorbing experience. The Editor hopes that it will also be a rewarding experience to the readership. Finally, the Editor is greatly indebted to Paola Panaro for her untiring assistance in the considerable secretarial work associated with these volumes – without her it would have been impossible. He is also much indebted to his wife Elaine Dodsworth for her emotional support!

A B P Lever
Toronto, Canada
March 2003

COMPREHENSIVE COORDINATION CHEMISTRY II

From Biology to Nanotechnology

Second Edition

Edited by
J.A. McCleverty, University of Bristol, UK
T.J. Meyer, Los Alamos National Laboratory, Los Alamos, USA

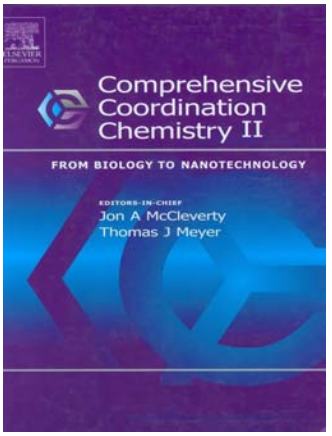

Description

This is the sequel of what has become a classic in the field, Comprehensive Coordination Chemistry. The first edition, CCC-I, appeared in 1987 under the editorship of Sir Geoffrey Wilkinson (Editor-in-Chief), Robert D. Gillard and Jon A. McCleverty (Executive Editors). It was intended to give a contemporary overview of the field, providing both a convenient first source of information and a vehicle to stimulate further advances in the field. The second edition, CCC-II, builds on the first and will survey developments since 1980 authoritatively and critically with a greater emphasis on current trends in biology, materials science and other areas of contemporary scientific interest. Since the 1980s, an astonishing growth and specialisation of knowledge within coordination chemistry, including the rapid development of interdisciplinary fields has made it impossible to provide a totally comprehensive review. CCC-II provides its readers with reliable and informative background information in particular areas based on key primary and secondary references. It gives a clear overview of the state-of-the-art research findings in those areas that the International Advisory Board, the Volume Editors, and the Editors-in-Chief believed to be especially important to the field. CCC-II will provide researchers at all levels of sophistication, from academia, industry and national labs, with an unparalleled depth of coverage.

Bibliographic Information

10-Volume Set - Comprehensive Coordination Chemistry II
Hardbound, ISBN: 0-08-043748-6, 9500 pages
Imprint: ELSEVIER
Price:
USD 5,975
EUR 6,274 Books and electronic products are priced in US dollars (USD) and euro (EUR). USD prices apply world-wide except in Europe and Japan.EUR prices apply in Europe and Japan. See also information about conditions of sale & ordering procedures -http://www.elsevier.com/wps/find/bookconditionsofsale.cws_home/622954/conditionsofsale, and links to our regional sales officeshttp://www.elsevier.com/wps/find/contact.cws_home/regional
GBP 4,182.50
030/301
Last update: 10 Sep 2005

Volumes

Volume 1: Fundamentals: Ligands, Complexes, Synthesis, Purification, and Structure
Volume 2: Fundamentals: Physical Methods, Theoretical Analysis, and Case Studies
Volume 3: Coordination Chemistry of the s, p, and f Metals
Volume 4: Transition Metal Groups 3 - 6
Volume 5: Transition Metal Groups 7 and 8
Volume 6: Transition Metal Groups 9 - 12
Volume 7: From the Molecular to the Nanoscale: Synthesis, Structure, and Properties
Volume 8: Bio-coordination Chemistry
Volume 9: Applications of Coordination Chemistry
Volume 10: Cumulative Subject Index

10-Volume Set: Comprehensive Coordination Chemistry II

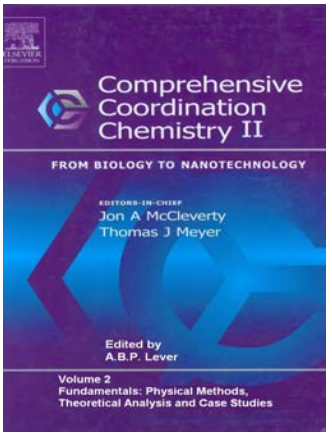

COMPREHENSIVE COORDINATION CHEMISTRY II

Volume 2:
Fundamentals: Physical Methods, Theoretical Analysis, and Case Studies

Edited by
A.B.P. Lever

Contents

Section I - Physical Methods

Nuclear Magnetic Resonance Spectroscopy (P. Pregosin, H. Rueegger).
Electron Paramagnetic Resonance Spectroscopy (S.S. Eaton, G.R. Eaton).
Electron-Nuclear Double Resonance Spectroscopy and Electron Spin Echo Envelope Modulation Spectroscopy (S.S. Eaton, G.R. Eaton).
X-ray Diffraction (W. Clegg).
Chiral Molecules Spectroscopy (R.D. Peacock, B. Stewart).
Neutron Diffraction (G.J. Long).
Time Resolved Infrared Spectroscopy (J.J. Turner et al.).
Raman and FT Raman Spectroscopy (I.S. Butler, S. Warner).
High Pressure Raman Techniques (I.S. Butler, S. Warner).
Resonance Raman: Coordination Compounds (J. Kincaid, K. Czarnecki).
Resonance Raman: Bioinorganic Applications (J. Kincaid, K. Czarnecki).
Gas Phase Coordination Chemistry (P.B. Armentrout, M. Rodgers).
X-Ray Absorption Spectroscopy (J. Penner-Hahn).
Photoelectron Spectroscopy (Dong-Sheng Yang).
Electrochemistry: General Introduction (A.M. Bond).
Electrochemistry: Proton Coupled Systems (K.A. Goldsby).
Electrochemistry: Mixed Valence Systems (R.J. Crutchley).
Electrochemistry: High Pressure (T.W. Swaddie).
Ligand Electrochemical Parameters and Electrochemical-Optical Relationships (B. Lever).
Mossbauer: Introduction (G.J. Long, F. Grandjean).
Mossbauer: Bioinorganic (E. Muenck et al.).
Optical (Electronic) Spectroscopy (C. Reber, R. Beaulac).
Stark Spectroscopy (K.A. Walters).
Electronic Emission Spectroscopy (J. Simon, R.H. Schmehl).

Magnetic Circular Dichroism (W.R. Mason).
Magnetic Circular Dichroism of Paramagnetic Species E.I. Soloman et al.).
Solvation and Solvatochromism (W. Linert et al.).
Mass Spectrometry
Neutralization-Reionization Mass Spectrometry
Electrospray Mass Spectroscopy
Magnetism: General Introduction
Electronic Spin Crossover
Excited Spin State Trapping (LIESST, NIESST)
Notes on Time Frames

Section II - Theoretical Models, Computational Methods and Simulation

Ligand Field Theory
Angular Overlap Model (AOM)
Molecular Mechanics
Semiempirical SCF MO Methods, Electronic Spectra and Configurational Interaction (INDO)
Density Functional Theory (DFT)
Time Dependent Density Functional Resonance Theory (DFRT)
Molecular Orbital Theory (SCF Methods and Active Space SCF)
Valence Bond Configuration Interaction Model (VBCI)
Time-dependent Theory of Electronic Spectroscopy
Electronic Coupling Elements and Electron Transfer Theory
Metal-metal Exchange Coupling
Solvation
Topology: General Theory
Topology: Assemblies
Electrode Potential Calculations
Comparison of DFT, AOM and Ligand Field Approaches
MO description of Transition Metal Complexes by DFT and INDO/S

Section III - Software

AOMX - Angular Overlap Model Computation
GAMESS and MACMOLPLT
CAMMAG
LIGFIELD
ADF
DeMON
Survey of Commercial Software Websites

Section IV - Case Studies

Spectroscopy and Electronic Structure of $[FeX_4]^n$ (X=CI,SR)(E.I. Soloman, P. Kennepohl).
Mixed Valence Dinuclear Species (J.T. Hupp).
Mixed Valence Clusters (Tasuku Ito et al.).
Non-biological Photochemistry Multiemission (A. Lees).
Nitrosyl and Oxo Complexes of Molybdenum (M. Ward, J. McCleverty).
Structure of Oxo Metallic Clusters (R.J. Errington).
Iron Centred Clusters (T. Hughbanks).
The Dicyanamide System (R.J. Crutchley).

2.1
Nuclear Magnetic Resonance Spectroscopy

P. S. PREGOSIN and H. RÜEGGER
ETH Hönggerberg, Zürich, Switzerland

2.1.1 INTRODUCTION 2
2.1.2 SOLUTION NMR 2
2.1.2.1 Detecting Less Sensitive X-nuclei 2
2.1.2.2 Chemical Shifts 3
2.1.2.3 Coupling Constants 6
2.1.2.4 Structural Applications 7
2.1.2.5 Dynamics 9
2.1.2.6 NOE and Exchange Spectroscopy 10
2.1.2.7 Special Topics 11
2.1.2.7.1 High-pressure studies 11
2.1.2.7.2 Molecular hydrogen and agostic complexes 13
2.1.2.8 Relaxation 13
2.1.3 NMR DIFFUSION MEASUREMENTS 15
2.1.3.1 Introduction 15
2.1.3.2 Methodology 15
2.1.3.2.1 Spin-echo method 15
2.1.3.2.2 Stimulated echo method 16
2.1.3.2.3 Derived sequences 16
2.1.3.3 Study of Complex Nuclearity 17
2.1.3.4 Study of Ion Pairing 18
2.1.3.5 Study of Hydrogen Bonding 19
2.1.3.6 Concluding Remarks 19
2.1.4 SOLID-STATE NMR SPECTROSCOPY 19
2.1.4.1 Introduction 19
2.1.4.2 Principles and Methodologies 20
2.1.4.3 Spin-1/2 Metal Nuclei 21
2.1.4.4 Quadrupolar Metal Nuclei 21
2.1.4.5 Ligand Nuclei 22
2.1.4.5.1 ^{1}H NMR 22
2.1.4.5.2 ^{2}H NMR 22
2.1.4.5.3 ^{13}C NMR 22
2.1.4.5.4 ^{15}N NMR 23
2.1.4.5.5 ^{17}O NMR 23
2.1.4.5.6 ^{19}F NMR 23
2.1.4.5.7 ^{31}P NMR 23
2.1.4.6 Applications of Two-dimensional NMR Spectroscopy 26
2.1.5 OUTLOOK 26
2.1.6 REFERENCES 26

2.1.1 INTRODUCTION

For more than 50 years, NMR spectroscopy has provided a major aid in solution structure analysis. Starting from modest, 40 MHz machines, one can now measure on instruments approaching the gigahertz range. Coordination chemists have been somewhat slow in profiting from this method, as many of the metal complexes of the first transition series are paramagnetic, and thus only sometimes suitable for this methodology. Further, sensitivity was initially a problem, i.e., many metal complexes are only sparingly soluble; however, the advent of polarization-transfer methods, high-field magnets, and improved probe-head technology have more or less eliminated this difficulty. Measurements of ^{1}H, ^{13}C, ^{19}F, and ^{31}P spins on ca. 1–2 mg of sample, with molecular weights in the range 500–1,000 Da, are now a fairly routine matter.

The spin $I = 1/2$ nuclei with the largest magnetic moments and natural abundance are still favored in the inorganic community, e.g., ^{1}H, ^{13}C, ^{19}F, ^{31}P, $^{111,113}Cd$, ^{195}Pt, and ^{199}Hg; however, ^{15}N, ^{29}Si, ^{77}Se, ^{103}Rh, $^{107,109}Ag$, and ^{183}W are now all fairly routine candidates.[1–4] The ^{103}Rh literature is expanding rapidly;[5–11] however, for other nuclei, e.g.,$^{107,109}Ag$, the results continue to develop slowly.[12–14] ^{57}Fe[15,16] and ^{187}Os[17–19] both represent examples of spins with considerable but not insurmountable difficulties, primarily due to their small magnetic moments (see Table 1). There are ongoing efforts on quadrupole nuclei,[20,21] e.g., ^{67}Zn,[22,23] ^{55}Mn,[24,25] ^{99}Ru,[26,27] and ^{95}Mo.[28]

Slowly, multidimensional methods are increasing in popularity within the inorganic community; however, while several of these may be necessary to properly characterize a specific complex, they are not all equally useful. COSY measurements connect coupled proton spins and are thus useful for assignments. However, NOESY data can provide three-dimensional structure features and also reveal exchange phenomena, thereby making these much more valuable for the coordination chemist.

The number of solid-state measurements has increased exponentially, due both to interests in heterogeneous catalysis and to the number of interesting complexes with very limited solubility. Further, relatively new NMR methods are finding application, e.g., PHIP and PGSE diffusion studies, so that the sections which follow cannot do justice to the individual topics, because of space restrictions.

We have tried to emphasize results since about 1990. This will undoubtedly have resulted in some unfortunate omissions.

2.1.2 SOLUTION NMR

2.1.2.1 Detecting Less Sensitive X-nuclei

The most sensitive and now routinely used method for obtaining spin $I = 1/2$ NMR signals for less sensitive nuclei involves double-polarization transfer ($I \rightarrow S \rightarrow I$), and uses one of the two-dimensional NMR sequences shown in Figures 1 and 2.[33–35]

Table 1 Relative sensitivities for selected nuclei of common interest.

Nucleus	*Abundance* (%)	*Rel. sensitivity*	*Comment*[a]
^{1}H	99.9	1	
^{29}Si	4.7	7.84×10^{-3}	Both[b]
^{57}Fe	2.2	3.37×10^{-5}	Indirect
^{59}Co	100	0.28	Direct[c]
^{95}Mo	15.7	3.23×10^{-3}	Direct[c]
^{103}Rh	100	3.11×10^{-5}	Indirect
^{109}Ag	48.2	1.01×10^{-4}	Indirect
^{119}Sn	8.58	5.18×10^{-2}	Both[b]
^{183}W	14.4	7.20×10^{-4}	Indirect
^{187}Os	1.6	1.22×10^{-5}	
^{195}Pt	33.7	9.94×10^{-3}	Both
^{199}Hg	16.8	5.67×10^{-3}	Both

[a] Both direct and indirect methods (INEPT, HMQC, ... , etc.) are in use. [b] Most efficient via indirect methods. [c] Lines can be broad due to the quadrupole moment of the metal.

The I-spins are assumed to be a high receptivity nucleus, most often ^{1}H, i.e., one needs a ^{n}J(X, ^{1}H) interaction, $n = 1$–4. The data are detected using the proton signals and the spectra are usually presented as contour plots, as shown in Figures 3 and 4. Occasionally, ^{31}P or ^{19}F are suitable alternatives to protons. Specifically, for metal complexes containing phosphorus ligands in which the ^{31}P is directly bound to the metal center, one occasionally has a relatively large ^{1}J(M,P) value of the order of 10^{2}–10^{3} Hz.[36–38] Consequently, one need not be restricted to molecules revealing suitably large proton–metal coupling constants. The time Δ is set to $\leq 1/(2\,J(S, I))$, and the time t_1 represents the time variable for the second dimension. These sequences provide a theoretical enhancement of $(\gamma_I/\gamma_S)^{5/2}$. For nuclei such as ^{57}Fe, ^{103}Rh, and ^{183}W this means factors of 5,328, 5,689, and 2,831, respectively.

2.1.2.2 Chemical Shifts

Once obtained, the signals need to be interpreted. The general subject[39] of metal and heavy-atom NMR chemical shifts is approached by noting that the magnetic field, B, experienced by nucleus X differs from that of the applied field, B_0, as shown in Equation (1):

$$B = B_0(1 - \sigma_t) \tag{1}$$

The screening constant, σ, is a scalar quantity which is the trace of a second-rank tensor, i.e.,

$$\sigma = 1/3(\sigma_{xx} + \sigma_{yy} + \sigma_{zz}) \tag{2}$$

In a high-resolution NMR solution experiment one normally measures the average, σ_{ii}, due to rapid molecular tumbling. The total screening constant consists of two components σ_d and σ_p, such that:

$$\sigma = \sigma_d + \sigma_p \tag{3}$$

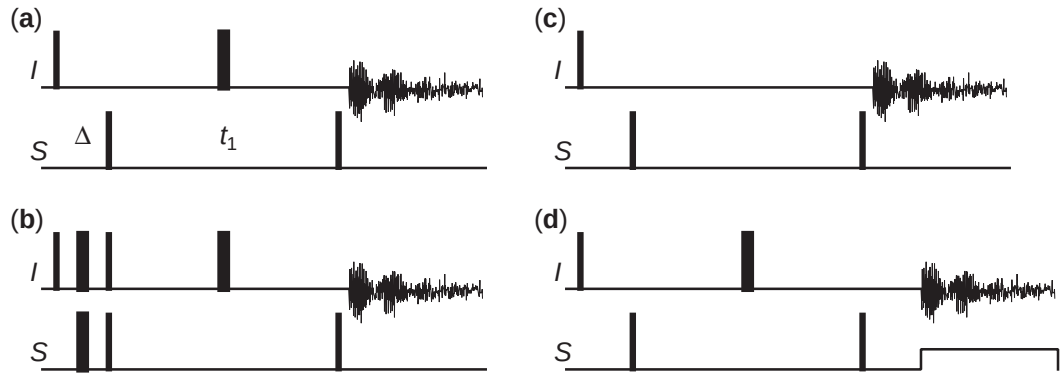

Figure 1 Heteronuclear multiple quantum correlation (HMQC) pulse sequences: (a) sequence for small $J(I, S)$ values; (b) for larger, resolved $J(I, S)$ values and phase-sensitive presentation; (c) zero or double quantum variant for the determination of the I-spin-multiplicity; (d) with refocusing and optional S-spin decoupling.

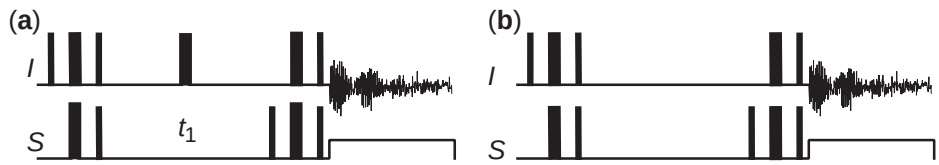

Figure 2 Heteronuclear single quantum correlation (HSQC) pulse sequences with optional decoupling of the S-spin: (a) standard sequence; (b) modified for the I-spin-multiplicity determination.

The diamagnetic screening constant, σ_d, involves the rotation of electrons around the nucleus and is important for proton NMR. These electrons may be immediately associated with the atom in question, or with circulating electrons associated with proximate functionalities, i.e., anisotropic effects. For the paramagnetic screening constant, σ_p (which makes the major contribution to the nuclei ^{13}C, ^{15}N, ^{31}P, ^{57}Fe, ^{103}Rh, ^{119}Sn, ^{195}Pt, ... etc.), the average energy approximation, for an atom A is often made, i.e.,

$$\sigma^{A}{}_{p} \propto - < r^{-3} > \Sigma_B Q_{A,B}/\Delta E \tag{4}$$

The term $Q_{A,B}$ represents the bond order charge-density terms, r is an average distance from nucleus A to the next atoms, and ΔE an averaged energy difference (between suitable filled and empty orbitals). Equation (4) indicates that energies, bond orders, and distances all contribute to $\sigma^{A}{}_{p}$. As ΔE can be relatively small (perhaps due to a small n–π^* or π–π^* separation), the observed range of chemical shifts is often hundreds of ppm for donor atoms, and thousands of ppm for transition metals. It is not unusual to find several terms in Equation (4) which change as a function of ligand complexation, so that a thorough understanding of heavy-atom shifts

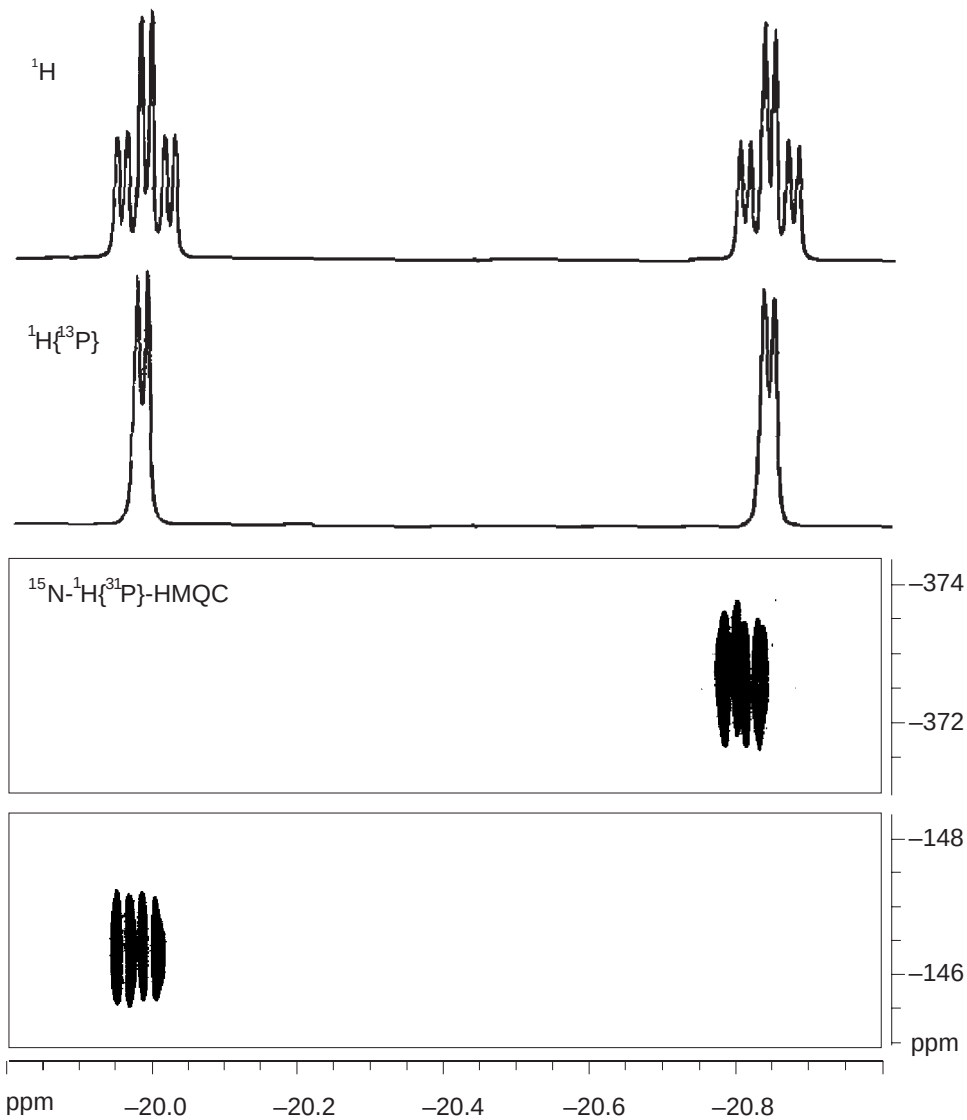

Figure 3 $^{15}N,^{1}H$ {^{31}P} HMQC for the $[IrH_2(8\text{-aminoquinoline})(PPh_3)_2]^+$cation. The two hydride ligands are *trans* to the two N-donors, thereby affording relatively large, selective $^{2}J(^{15}N,^{1}H^{hydride})$ values. The vertical scale shows the ^{15}N chemical shift.

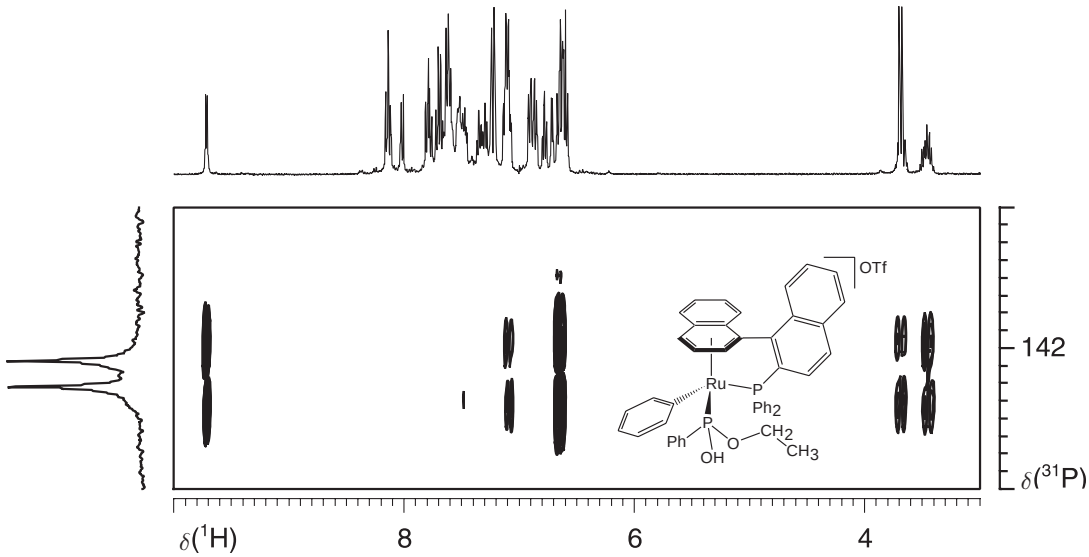

Figure 4 $^{31}P,^{1}H$ COSY for the complex shown. Note that the two $POCH_2$methylene protons are diastereotopic and that one of these happens to fall exactly under the solvent (THF) signal. However, the correlation readily reveals two types of cross-peaks and thus the chemical shift of the hidden proton. There are also correlations to POH, and *ortho* and *meta* protons of the P-phenyl.

requires a more detailed consideration of their source than for proton chemical shifts. It is insufficient to interpret metal chemical shifts using concepts such as "local electron density" at the atom in question, as this approach can be misleading; e.g., the ^{13}C chemical shift of the anionic carbon in $Li(CPh_3)$ is at a higher frequency than that for $CHPh_3$.[40] It is clear from the literature[41–49] that it is now possible to calculate screening constants (and thus chemical shifts, δ, of heavier atoms) fairly accurately.

Often, heavy-atom chemical shifts are considered empirically. The range of metal chemical shifts is usually of the order of thousands of ppm and is very sensitive to changes in, and close to, the local coordination sphere. Simple ligand-field-type considerations result in significant changes in energy levels at a metal center when the donor atoms are changed. This will clearly affect the ΔE term in Equation (4), e.g., the $Co(H_2O)_6^{3+}$ ^{59}Co resonance is found at ca. 15,000, whereas the $Co(CN)_6^{3-}$ ^{59}Co resonance is at "0" ppm. Further, the $Rh(H_2O)_6^{3+}$ ^{103}Rh resonance is at 9,924, whereas the $Rh(CN)_6^{3-}$ ^{103}Rh resonance is at 340. Crude correlations relating the metal chemical shift with oxidation state or stability[50] have been found, e.g., for $Pt(CN)_4^{2-}$ the ^{195}Pt resonance is at −4,746, whereas for $Pt(CN)_6^{2-}$ the ^{195}Pt resonance is at −3,866 (both vs. $PtCl_6^{2-}$); however, ambiguities exist, so that each case should be viewed on its own merits.

Solvent effects on metal resonances are routinely tens of ppm, and changes in temperature during a measurement result in large enough shifts (often in the range 0.1–0.5 ppm $°C^{-1}$) that fine structure on the resonance is readily lost. Isotope effects (e.g., ^{35}Cl vs. ^{37}Cl, ^{16}O vs. ^{18}O, or ^{1}H vs. ^{2}H) on metal resonance positions[51–55] are sufficiently large that the different chemical shifts from the individual isotopomers are often well resolved. These effects are not so marked in donor-atom NMR spectra, i.e., for ^{13}C, ^{15}N, or ^{31}P complexed to a metal center, solvent effects are normally a few ppm or less.

For the two donor atoms nitrogen and phosphorus, the normal chemical-shift range is of the order of hundreds of ppm. A change in hybridization from sp^3 to sp^2 will be associated with new orbitals. These represent orbitals, e.g., π and π^*, whose energy separation will strongly affect the chemical shift. As an example, the ^{15}N resonance for trialkyl amines, R_3N, is at −300 to −390, whereas the ^{15}N resonance for pyridines is found at +80 to −175, both classes relative to CH_3NO_2.[56] Moreover, complexation of a sigma donor, e.g., either an aliphatic nitrogen or a tertiary phosphine donor, simultaneously changes both the lone-pair energy and the local geometry at the donor atom, so that interpretation can be complicated. For pyridine (or related heterocyclic ligands with sp^2 donors[14]), complexation to a metal usually affords a shift to low frequency, whereas for triphenyl phosphine complexation there is normally a high frequency change. There exist compilations of both $^{14,15}N$[56] and ^{31}P[36–38] chemical shifts. Electronegative groups on these donors, and inclusion in various ring sizes, as well as the size of the substituent on

the donor atom, all play important roles in determining the chemical shift. As there are literally hundreds of reported nitrogen chemical shifts and thousands of measurements for the ^{31}P spin, the reader is advised to consult the reviews noted.

The special case of carbon as donor, i.e., alkyl, phenyl, alkynyl, allyl, CO, olefin (or arene or Cp, ... etc.), and carbene ligands, continues to attract significant attention and several articles[57–63] have been written on this subject. Nevertheless, Equation (4) is valid. CO derivatives are often found in the region $\delta = 150$–250. Carbene compounds have ^{13}C positions at relatively high frequency, usually >200 ppm, and this special position is often diagnostic. Aryl complexes reveal the coordinated ipso carbon at high frequency, with representative values between 130 ppm and 180 ppm. Complexed olefins show their ^{13}C positions over a wide range, with coordination chemical shifts as small as 10–15 ppm, but often 30–70 ppm or more. The oxidation state of the metal (and thus the d–π^* back bonding) is important in determining ^{13}C frequencies for these complexes.

Given that both the metal centers and parts of the ligands can contain strongly anisotropic regions, ligand complexation often has a significant effect on proton chemical shifts. Individual protons can be forced into environments which result in marked high- or low-frequency resonance positions. The axial positions in square-planar complexes often afford high-frequency proton shifts,[64,65] e.g., as in (**1**); and, of course, phenyl ligands (or aromatic substituents), as well as donors such as pyridine or triphenyl phosphine—which contain aromatic fragments—can strongly affect the local environments of proximate protons, e.g., as in (**2**).

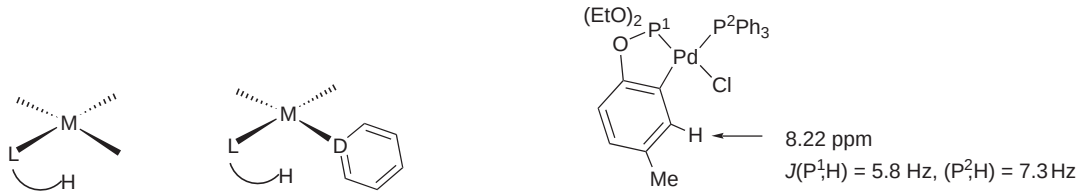

(**1**) (**2**) D = C or N (**3**)

Even simple ligands such as chloride can influence the position of proximate protons, e.g., in structure (**3**), the proton indicated might be expected at around 7 ppm, but it appears above 8 ppm.[66]

Metal–metal multiple bonds can also be strongly anisotropic with respect to protons.[67] In the quadruply bonded Cr and Mo complexes shown in (**4**), the NH protons appear at $\delta = 3.46$ and $\delta = 3.04$, instead of at $\delta = 8.04$ and $\delta = 6.44$ in the free ligand and Li salt, respectively.

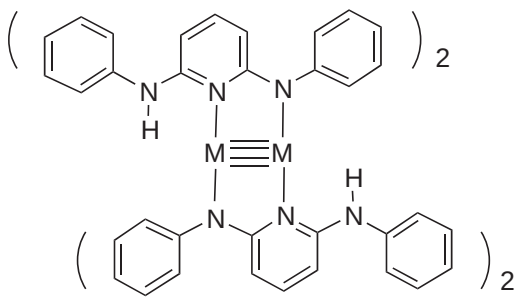

(**4**) M = Cr or Mo

Apart from transition-metal hydride compounds, which appear at very low frequency, most proton chemical shifts are relatively routine.

2.1.2.3 Coupling Constants

The theory for spin–spin interactions between a spin $I = 1/2$ metal and an appropriate ligand atom follows directly from the description developed by Pople and Santry. Currently a number of mathematical methods[68] are in use which allow the calculation of various J-values.

A modified form of the Pople and Santry expression is given in Equation (5) and

$$^{1}J(\mathrm{M,L}) \propto \gamma_{\mathrm{M}}\gamma_{\mathrm{L}}|\psi_{\mathrm{s}}(\mathrm{M})(0)|^{2}|\psi_{\mathrm{s}}(\mathrm{L})(0)|^{2} \sum_{\mathrm{j}}^{\mathrm{occ}} \sum_{\mathrm{k}}^{\mathrm{unocc}} (E_{\mathrm{k}} - E_{\mathrm{j}})^{-1} \mathrm{C(M)_k}^{\mathrm{s}}\mathrm{C(L)_k}^{\mathrm{s}}\mathrm{C(M)_j}^{\mathrm{s}}\mathrm{C(L)_j}^{\mathrm{s}} \quad (5)$$

reveals that the one-bond interaction depends on the metal and ligand atom magnetogyric ratios, γ, the s-expectation values, ψ, the occupied, j, and unoccupied, k, molecular orbital energies, and the s-coefficients of the atomic orbitals used in making up the molecular orbitals.

Given that the γ and s-expectation values, ψ, depend markedly on the individual metal and ligand atoms under consideration, the values of these spin–spin interactions vary over several orders of magnitude, e.g., $^{1}J(^{195}\mathrm{Pt}, ^{1}\mathrm{H})$ is often >1,000 Hz, but $^{1}J(^{103}\mathrm{Rh}, ^{1}\mathrm{H})$ is usually <30 Hz. $^{1}J(^{195}\mathrm{Pt}, ^{31}\mathrm{P})$ is often >2,000 Hz, but $^{1}J(^{103}\mathrm{Rh}, ^{31}\mathrm{P})$ is usually <300 Hz. Since both the γ and s-expectation values for the ^{31}P atom are relatively large, one finds spin–spin interactions of the order of 10^{2}–10^{4} Hz, depending upon the metal and the nature of the phosphorus ligand. There is an extensive literature on $^{1}J(\mathrm{M}, ^{31}\mathrm{P})$,[36–38] although much work has involved platinum and rhodium complexes. Metal–metal one-[69,70] and two-bond[71] coupling constants can be surprisingly large and, in some cases, are 20,000–40,000 Hz.[69–72] Complexes (**5**) and (**6**) are clear, albeit somewhat extreme, examples of this idea. With the possible exception of complexes containing ^{31}P, (e.g., see (**3**) above), long-range coupling constants such as $^{3}J(\mathrm{M}, (\mathrm{spin} = 1/2))$ have not received as much attention as $^{1}J(\mathrm{M, L})$. Nevertheless, spin $I = 1/2$ metals and ligands can easily couple to protons and other nuclei over three, four, and sometimes more bonds (and these interactions can be quite useful for determining metal chemical shifts of e.g., ^{119}Sn,[73] ^{109}Ag,[74] ^{183}W,[75–77] ^{195}Pt,[78,79] and ^{199}Hg.[80]

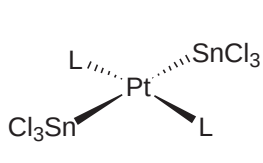

$^{1}J(\mathrm{Pt,Sn})$ = ca 20,000 Hz

L = $P(OEt)_3$

(**5**)

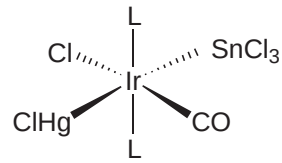

$^{2}J(\mathrm{Hg,Sn})$ = ca 40,000 Hz

L = PPh_3

(**6**)

2.1.2.4 Structural Applications

In terms of applications, the subjects of chemical equivalence and symmetry still deserve honorable mention in that one can use the relative number and NMR multiplicity to assign structure, e.g., trigonal bipyramidal, (**7**), vs. square pyramidal, (**8**), in "ML_5" complexes (especially where L is a spin $I = 1/2$ donor).

For ligands with suitable proton, fluorine, or phosphorus atoms, low-temperature NMR studies are informative and reveal either the 3:2 or 4:1 ratio.

A useful empiricism involves chemical shifts and/or one-bond coupling constants to spin $I = 1/2$ metal centers in square-planar, (**9**), or octahedral, (**10**), compounds.

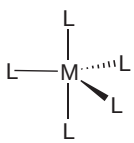

(**7**)

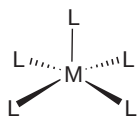

(**8**)

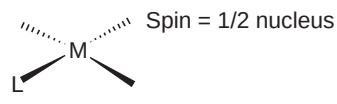

(**9**)

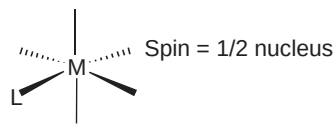

(**10**)

There is sometimes a dependence of either δ ^{13}C, ^{15}N, or ^{31}P, ... etc. and/or $^{1}J(\mathrm{M}, \mathrm{spin} = 1/2 \text{ nucleus})$ on the *trans* influence of L.[81,82] For stronger L-donors the chemical shift

moves to lower frequencies, whereas the value of ^{1}J(M, spin = 1/2 nucleus) can be markedly reduced. This is the case for NH_3 (or amine) complexes of Pt(II) and, specifically, for (**11**) and related amino-acid complexes. It has been suggested that O, N, and S donors, in the *trans* position, can be distinguished by the chemical shift of the $^{15}NH_3$ signal. Sadler and co-workers[83–89] have been very active in this area.

In general, ^{15}N chemical shifts in platinum complexes have received increasing attention and most reports use indirect methods of detection, even on enriched materials. The development of *cis*-$PtCl_2(NH_3)_2$, and related cancer drugs, has been accompanied by a renewed interest in $^{1}J(^{195}Pt, ^{15}N)$.[90–97] This parameter varies by ca. one order of magnitude between 80 Hz and about 800 Hz. ^{15}N data can also be used to recognise unique three-center interactions[98] in Pt chemistry, e.g., (**12**), or to identify an enol form of the amide, e.g., (**13**), an amino-quinoline Ir(III) derivative.

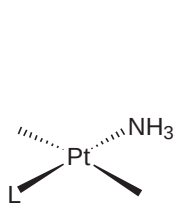

(**11**)

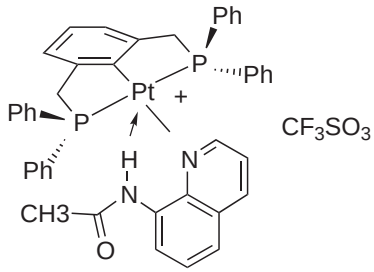

(**12**)

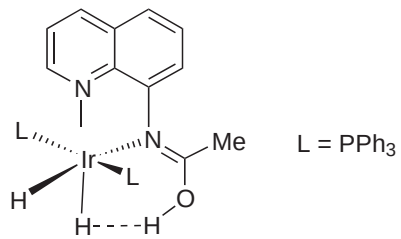

(**13**)

In the latter complex, the expected one-bond N—H interaction, found in acetamide complexes, is absent.[99] This type of complex shows a rarely observed $^{2}J(^{15}N,^{1}H)$ value. Given the interest in organometallic and catalytic chemistry, there are many reports on ^{1}J(M, ^{13}C)[100–103] and ^{1}J(M, ^{31}P).[104,105]

Many applications of spin–spin interactions through two bonds center on the empiricism that $^{2}J(X, Y)_{trans} \gg {}^{2}J(X, Y)_{cis}$, i.e., the *trans* coupling in (**14**) is greater than the *cis* coupling in (**15**). This is most likely to be valid only for the second- and third-row transition metals. Moreover, it is thought that the signs of these two ^{2}J interactions are different. $^{2}J(^{31}P, X)$, X = ^{1}H, ^{13}C, or ^{31}P represent the most abundant examples. There are relatively few modern, detailed studies on this subject, and Field and co-workers[106,107] have used 2-D methods to obtain some useful data on signs and values of $^{n}J(X, Y)$ in organometallic complexes of Ru^{II} and Rh^{I}.

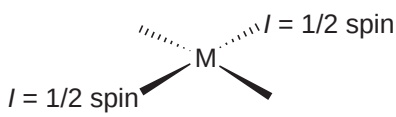

(**14**)

>>

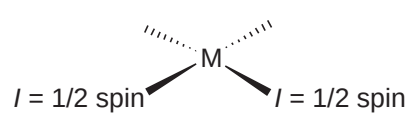

(**15**)

Inserting and/or exploiting specific NMR-active isotopes still attracts attention. In both mono- and polynuclear complexes, one can occasionally use the integrated intensities of e.g., ^{29}Si,[73] ^{117,119}Sn,[108–110] or ^{195}Pt,[111,112] satellites, arising from two- or three-bond interactions together with integrals relative to the center band, to obtain a quantitative determination of the number of metals in the cluster; see Figure 5. In all of these examples, the structural information derives from the integrals and/or the presence of coupling constants, and not from the positions of the signals.

Both chemical shifts and coupling constants have been used[113] to characterize the novel Pt–pyrazolyl borate formyl complex, (**16**). The observed coupling constant from the Pt atom to the formyl proton, 327 Hz, is relatively large.

The ^{13}C NMR parameters for the Pt–methyl group provide an interesting contrast when compared to those of the formyl group. The methyl carbon resonance is found at 0.48 ppm, with ^{1}J(Pt, C) expected to be in the range 620–710 Hz.

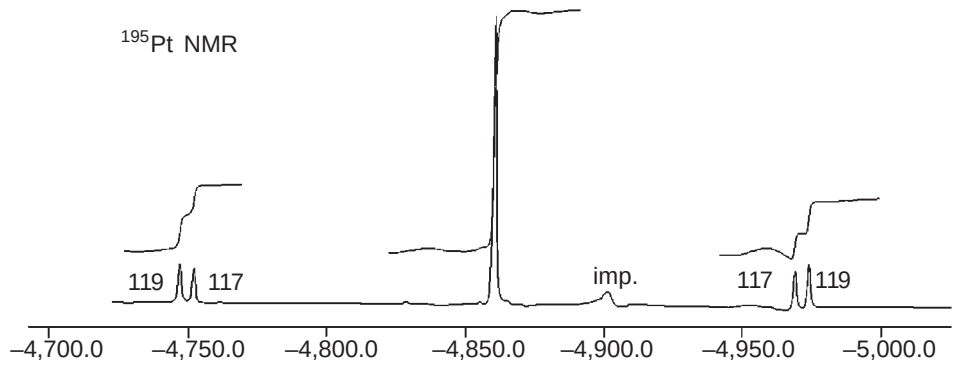

Figure 5 ^{195}Pt NMR spectrum of the $[Pt(SnCl_3)_3(2\text{-methylallyl})]^{2-}$dianion. The intensities of the ^{117,119}Sn satellites reflect the number of complexed tin ligands.

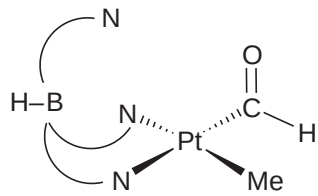

^{13}C CO = 237 ppm
^{1}J(Pt, C) = 1,260 Hz
^{1}H formyl = 12.66 ppm
^{2}J(Pt, H) = 327 Hz

(**16**)

2.1.2.5 Dynamics

NMR spectroscopy allows the coordination chemist access to a variety of dynamic phenomena via spin–lattice, T_1, and spin–spin, T_2, relaxation times, plus line-shape analyses and phase-sensitive exchange (NOE) spectroscopy. The spin–lattice relaxation time, T_1, can be correlated to molecular tumbling and rotations. Classical T_2 measurements, together with the Swift and Connick equations for paramagnetic metal systems, lead to ligand-exchange-rate information.[114–116] An example of the latter type of application concerns proton and phosphorus T_2 relaxation enhancement in several phosphite ester anions by manganese paramagnetic complexes. These compounds contain the fragment (**17**) shown, and analysis of the various relaxation data allows the determination of metal/ligand association rate constants without temperature studies.[117] The important subject of NMR studies on paramagnetic complexes in biological systems, i.e., the rather special consequences of porphyrin, phosphate, and amino-acid derived ligands, has been reviewed several times.[118,119]

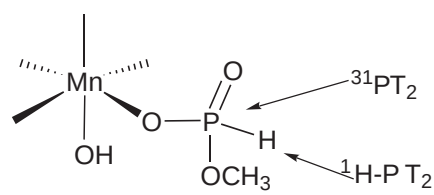

(**17**)

Since 1970 or before, chemists have relied on classical, detailed temperature-dependent line-shape analyses.[120,121] Indeed, fundamental contributions to our understanding of the dynamics of fluxional metal complexes with π-hydrocarbon ligands,[122] tertiary phosphorus donors,[123] as well as π-allyl anions,[124–126] all stem from these types of measurement. Their contributions to metal carbonyl dynamics and rearrangements in cluster compounds is even more pronounced, and we cite selected studies in this very large area of organometallic chemistry.[127–148] For slow exchange

between two sites and negligible overlap of the signals, expressions such as Equation (6)[120] (or more complicated versions[149]) have served well:

$$W = (1/\pi)(k + 1/T_2) \tag{6}$$

(W = bandwidth at half height, k = first-order rate constant)

In the early reports, line-shape studies predominated; however, many of the more recent reports use 2-D exchange spectroscopy.

2.1.2.6 NOE and Exchange Spectroscopy

Nuclear Overhauser effects, NOEs, involve dipole–dipole relaxation phenomena which result in signal enhancements.[150] For two interacting protons, the maximum NOE, η_{max} is:

$$\eta_{max} = (5 + \omega^2\tau_c^2 - 4\omega^4\tau_c^4)/(10 + 23\omega^2\tau_c^2 + 4\omega^4\tau_c^4) \tag{7}$$

(ω = frequency, τ_c = correlation time).

For small molecules with short τ_c values (extreme narrowing limit), this equation reduces to $\eta_{max} = +50\%$. This is rarely achieved for a single proton in coordination compounds, as there are often a number of spins contributing to the relaxation of an individual proton and the τ_c values are not always so short. Clearly, if the quantity $(5 + \omega^2\tau_c{}^2 - 4\omega^4\tau_c{}^4) = 0$, then there is no NOE. It is well known[150] that η_{max} can pass through zero and the limiting value is -100%. This can be the case for biological or other macromolecules. Further, a negative NOE is also possible for higher molecular weight metal complexes, e.g., MW > 1,000, and/or in viscous media (perhaps due to low-temperature studies). In these cases ROESY spectra[150,151] can be useful.

Although selective ^{1}H NOE studies and magnetization-transfer experiments are still frequently in use,[150] the simple three-pulse (phase-sensitive) 2-D NOESY sequence, given in Figure 6, is finding increasing popularity.[152–159] The mixing time should be chosen such that exchange can take place without losing too much signal intensity. Practically, this often means values in the range 0.4–1.0 seconds, although individual T_1 values and temperature will require that this parameter be constantly adjusted to suit the coordination compound in question.

Wherever coordination chemistry problems overlap with those of organic chemistry, e.g., conformational analysis, ^{1}H NOE studies will have their classical value. Chiral inorganic complexes have been studied with emphasis on inter- and not intra-ligand NOEs.[155,156,160–166] These results allow the determination of the 3-D structure of the complex and thus, for enantioselective catalysts, the shape of the chiral pocket offered by a chiral auxiliary to an incoming organic substrate. Since many such auxiliaries possess phenyl phosphine donors, the interactions between the *ortho* protons of the *P*-phenyl group and those from a second ligand make a decisive contribution to the structure determination. Structure (**18**) shows a hypothetical Pd(chiraphos)-(allyl) cation, and it is easy to see how NOEs, from the three allyl protons to the *P*-phenyl *ortho* protons, can provide useful structural data. The four phenyl groups, two pseudo-axial and two pseudo-equatorial, are all nonequivalent.

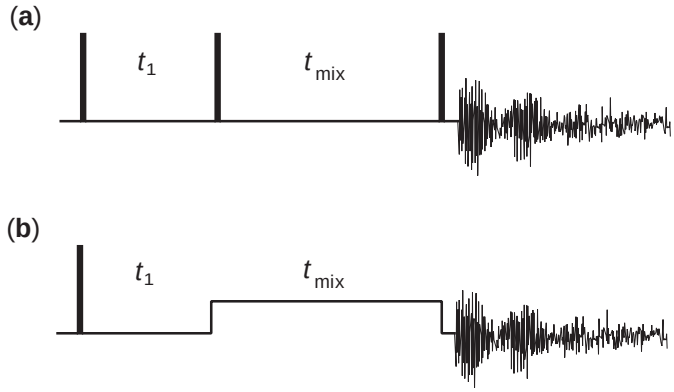

Figure 6 Pulse sequences for nuclear Overhauser and chemical exchange spectroscopy: (a) NOESY; (b) ROESY.

For complexes of modest size which tumble relatively rapidly, 2-D NOESY methods distinguish between NOE and exchange phenomena via the phases of the signals. The diagonal and exchange peaks have the same phase in contrast to those due to NOE. Since the 2-D methodology is not selective, i.e., all of the spins are excited simultaneously, the exchange map can reveal several species in exchange with each other as well as two or more different processes. A nice example is provided by the tetranuclear Ir-cluster anion (**19**).[167] The CO ligands are involved in several temperature-dependent exchange processes.

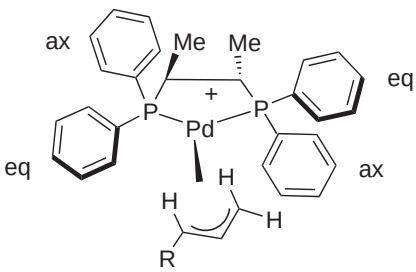

(**18**)

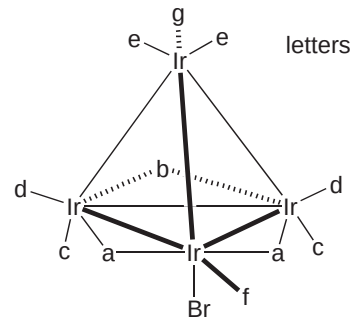

(**19**) $[Ir_4(CO)_{11}Br]^-$

letters = different CO ligands

"merry-go-round" =

a to d,
d to b,
b to d
d to a and
a to f

One of these, the so-called "merry-go-round," selectively exchanges the bridging and terminal CO ligands, a, d, b, and f, in the pseudo-equatorial direction. Since the various ^{13}CO signals can be assigned, 2-D ^{13}C NOESY spectroscopy reveals exchange cross-peaks connecting all four of these signals, thus identifying this selective process, as indicated in the drawing.

A unique aspect of this form of exchange spectroscopy concerns the ability to detect species whose concentration is so low that they escape detection in a conventional one-dimensional experiment. Figure 7 shows a section of the ^1H NOESY spectrum for a mixture of isomeric palladium phosphino–oxazoline, 1,3-diphenylallyl complexes.[168] One observes a major component in exchange with a visible minor component (ca. 10% of the more abundant isomer). However, there are additional, very broad, exchange cross-peaks from the main isomer to an "invisible" species, which would easily have gone undetected.

Interest in ^{19}F, ^1H NOEs in coordination chemistry is developing,[169,170] and several interesting examples of ^{31}P, ^{31}P exchange spectroscopy have been reported.[171–173]

2.1.2.7 Special Topics

2.1.2.7.1 High-pressure studies

NMR studies under high pressure have increased markedly in the last two decades. Technically, these measurements are most frequently carried out using sapphire NMR tubes, and this methodology has been modified over the years.[174–179] These pressure experiments are usually carried out with the joint aims both of determining activation volumes and of shifting chemical equilibria. Occasionally, details with respect to the pressure dependence of NMR parameters are published.[180]

Measuring rate constants vs. pressure allows the determination of activation volumes, and thus gives a hint as to whether the reaction mechanism is associative or dissociative.

$$\ln(k_I) = \ln(k_I, 0) - \Delta V_I^{\ddagger} P/RT \tag{8}$$

Much work has been done on solvated metal complexes by Merbach and co-workers.[178,181–189] These pressure studies have been extended to organometallic CO[190–192] and SO_2[193] complexes plus, interestingly, the first dihydrogen aqua-complex, $Ru(H_2)(H_2O)_5^{2+}$, (**20**),[194] produced as shown in Equation (9):

$$Ru(H_2O)_6^{2+} + H_2 \rightarrow Ru(H_2)(H_2O)_5^{2+} \tag{9}$$

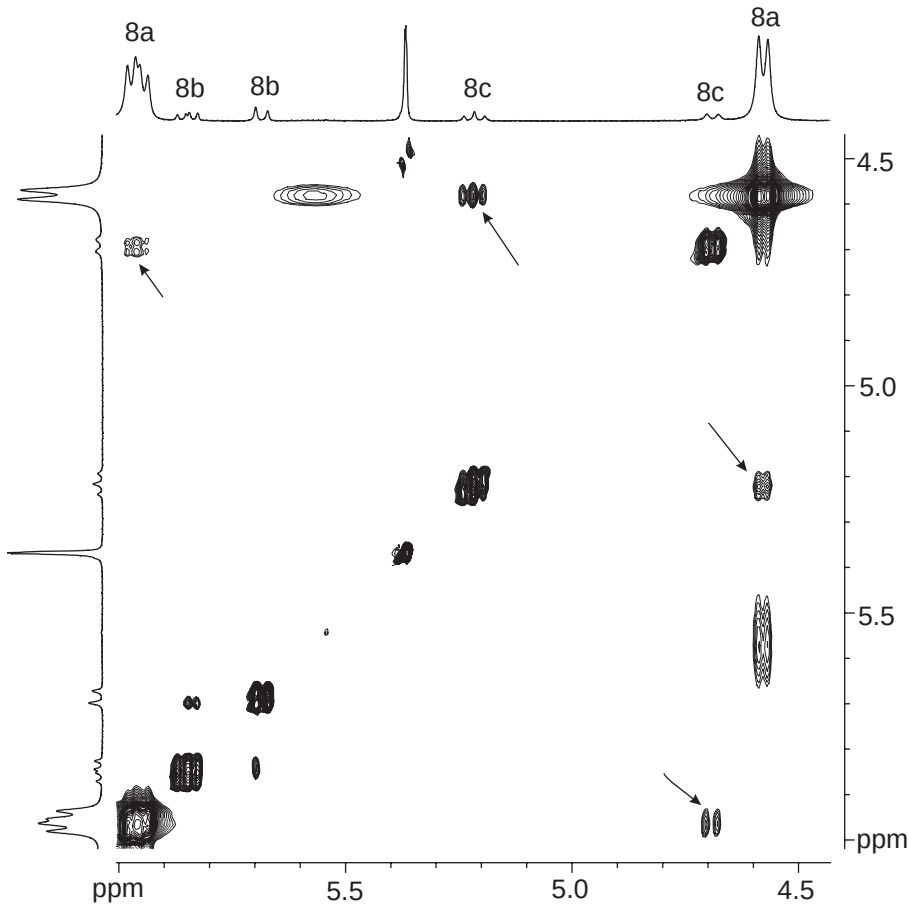

Figure 7 Section of the phase-sensitive 2-D NOESY for isomeric palladium phosphino-oxazoline, 1,3-diphenylallyl cationic complexes. The major isomer (**8a**) (which does not correspond to (**8**) in the text) is clearly exchanging with (**8c**). However, (**8a**) is also exchanging with an unknown compound (broad exchange peaks).

The ^{1}J(H, D) value of 31.2 Hz in the H_2 ligand allows an estimation of the H–D separation, ca. 0.90 Å, using the relationship:

$$d(H-D) \approx -0.0167\,{}^{1}J(H,D) + 1.42 \tag{10}$$

suggested by Maltby *et al.*[195] It is probably useful to remember[196] that correlations with activation volumes may not be straightforward. Elsevier and co-workers[27,170,197–199] have used high pressures in connection with supercritical fluids, and have studied effects on line widths and other NMR parameters.

Homogeneously catalyzed hydrogenation chemistry, often under an overpressure of gas, has been followed by proton NMR for decades, and frequently important intermediates go undetected due to their relatively low concentration. Since the para hydrogen induced polarization, (PHIP) signal magnification can be several orders of magnitude, Bargon,[200–207] and the Duckett and Eisenberg groups[208–222] plus others have studied *in situ* reactions using parahydrogen under mild hydrogen pressure. The major limitation arises from the necessity for the two parahydrogen atoms to be transferred pairwise. The PHIP effect has also been recently shown to be useful for ^{13}C, as well.[200]

The PHIP approach has been used to help identify the cationic Rh(I) dihydrido-bis-solvento complex shown, (**21**).[222]

This type of dihydrido-phosphine chelate complex is often mentioned in mechanistic discussions on enantioselective hydrogenation, but was previously thought to be not very stable.

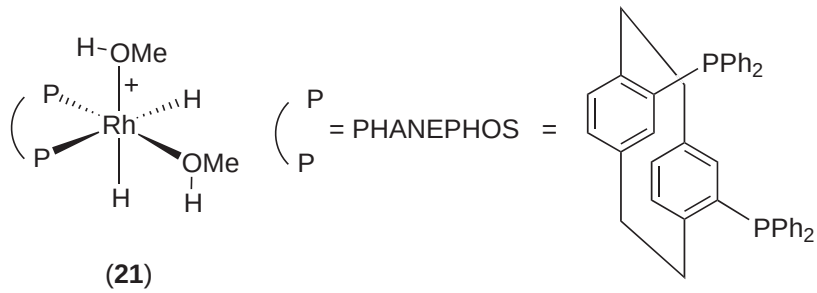

(**21**)

2.1.2.7.2 *Molecular hydrogen and agostic complexes*

Much effort has been invested in the use of NMR methods to study molecular hydrogen complexes.[223–241] The identification of an $L_mM(\eta^2\text{–}H_2)$ often requires variable temperature, deuterium enrichment, and T_1 studies. The deuterium incorporation is useful in that the value of $^1J(H, D)$ can be diagnostic, as noted above.

In polyhydride complexes, exchange between hydride and complexed molecular hydrogen often leads to observable dynamics in their ^1H NMR spectra. In many cases these processes are associated with relatively low activation-energy barriers.[242] In the complex $IrH_2X(H_2)(PR_3)_2$, (**22**), X = Cl, Br, or I, the exchange can proceed via either hydride/hydrogen exchange leading to (**23**), or oxidative addition leading to (**24**).

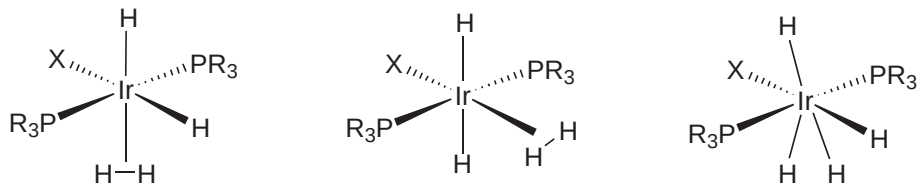

(**22**) (**23**) (**24**)

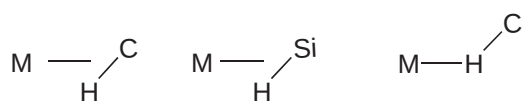

(**25**) (**26**) (**27**)

It is only a small extrapolation to move from side-on complexed H_2 to side-on complexed X—H, and Crabtree[243] has commented on how these interactions are related. The name "agostic" is often used[244–246] for the case of X = a suitably substituted carbon atom. There are also a number of examples of X = a suitably substituted silicon atom.[247–250] The agostic interaction of a C—H bond, (**25**), results in a low-frequency shift of the proton resonance (due to the development of "hydride-like" character) and substantial reduction in the one-bond coupling constant, $^1J(^{13}C, ^1H)$. This reduction can be 50% or more. Similarly, for $X = SiR_3$, the one-bond, $^1J(^{29}Si, ^1H)$ value decreases. In the solid state one finds the C—H bond as a donor to the metal. There are many examples of this type of interaction.[251–261]

2.1.2.8 Relaxation

Relaxation times can be useful for coordination chemists. For our discussion it is sufficient to express the longitudinal relaxation rate of a nucleus, R_1, $(= 1/T_1)$, as the sum shown in Equation (11):[262]

$$R_1 = R_1^{DD} + R_1^{CSA} + R_1^{SR} + R_1^{SC} + R_1^{Q} + R_1^{EN} + R_1^{other} \quad (11)$$

with the various contributions defined as follows: DD = dipole–dipole; CSA = chemical-shift anisotropy; SR = spin rotation; SC = scalar coupling; Q = quadrupole; and EN = electron–nuclear. It should be noted, however, that for coupled-spin systems, this simple sum is no longer valid.[263–265]

The measurement of the relaxation rate gives the coordination chemist access to parameters related to the anisotropic interactions described by the spin Hamiltonian which, in solution, are averaged to their isotropic values or even zero. In principle structural information can thus be retrieved, since R_1^{DD} and R_1^{E} render information with respect to the separation to other nuclei or unpaired electrons, respectively, e.g., via the $1/r^6$ distance dependence shown in Equation (12). Frequently, a number of dipoles contribute to relaxation, so that a sum is necessary:

$$R_1^{DD} \propto \tau_c/\Sigma r^6 \tag{12}$$

The R_1^{CSA} term describes the substitution pattern and the local stereochemistry. R_1^{SR} leads to moments of inertia, and the scalar and quadrupolar coupling constants are obtainable from R_1^{SC} and R_1^{Q}, respectively, with the latter describing the electric-field gradient at the site. Beside this wealth of structural information, each of the individually contributing rates correlates to molecular tumbling, via a correlation time, τ_c, plus global and local rotations and other dynamic phenomena.

In practice, however, it is often difficult to separate or exclude some of the contributing pathways unless one of the interactions is clearly dominating.

The R_1^{DD} term can usually be evaluated. Consequently, data from one- and two-dimensional nuclear Overhauser spectroscopy studies contribute to the coordination chemists understanding of three-dimensional solution structures[152–166] and molecular association phenomena such as ion pairs.[169,170,266–269] Distance constraints are usually qualitatively established, based on cross-peak intensities or volumes. Occasionally monitoring the build-up rates is preferred, in order to quantify internuclear distances.[266,268]

The determination of R_1^{DD}, and in particular the maximum rate, i.e., the T_1 minimum, is popular for the determination of the H—H distance in molecular hydrogen complexes, as the intraligand H—H separation is much shorter than other interproton distances.[270] The H—H distances are calculated from the T_1 minima according to two models involving static[271] or fast-rotating hydrogen ligands,[272] respectively. Distances thus derived should be considered as semiquantitative, as additional spins (e.g., other hydride ligands in polyhydrides) or dipolar coupling to NMR active metal centers may shorten T_1.[273] Other relaxation contributions, such as the spin-rotation mechanism, may not be ruled out. Moreover, the exact nature of ligand dynamics (classical vs. quantum-mechanical rotation and tunneling of hydrogen) is not settled.[270]

R_1^{CSA} is an important contributor to the relaxation of heavy nuclei, particularly for the transition metals, and can be separated from the other contributions due

$$R_1^{CSA} \propto B_0^2 \tau_c \tag{13}$$

to its unique B_0^2 dependence (see Equation (13)). Structural conclusions have been derived from this parameter, e.g., linear, trigonal, and tetrahedral $Pt(PR_3)_n$ complexes can easily be distinguished from their ^{195}Pt T_1^{CSA} values.[29]

R_1^{Q} is normally the dominating relaxation pathway for quadrupolar nuclei. For a series of metal deuterides, quadrupole coupling constants have been determined using this method, thus shedding light on the size of the electric-field gradient at the D nucleus. These results reflect the characteristics of the M—D bond, in particular ionic vs. covalent contributions.[274–276]

R_1^{EN} is responsible for relaxation of the nuclei in a paramagnetic complex and depends strongly on the relaxation rate of the unpaired electrons, correlation times for molecular reorientation, ligand-exchange rates, the bonding situation, and the electron–nucleus distance. The study of various enzymes containing paramagnetic metal centers,[118,119,277–283] and the use of complexes of rare-earth metal ions as contrast agents in magnetic resonance imaging,[284–287] represent two important applications of this methodology.

The term R_1^{other} summarizes other possible contributions to spin–lattice relaxation, e.g., a spin–photon Raman scattering mechanism has been proposed for relaxation of the ^{205}Pb nucleus in lead nitrate and other heavy spin-1/2 nuclei in solids.[288]

2.1.3 NMR DIFFUSION MEASUREMENTS

2.1.3.1 Introduction

The determination of relative molecular size in solution remains a subject of considerable interest to the coordination chemistry community, in particular with respect to the formation of polynuclear complexes, ion pairs, and otherwise aggregrated species. Apart from classical methods such as mass spectrometry[289] (see Chapter 2.28) and those based on colligative properties[290] — boiling-point elevation, freezing-point depression, vapor and osmotic pressure—the Pulsed Field Gradient Spin-Echo (PGSE) methodology[291,292] has recently resurged as a promising technique. PGSE measurements make use of the translational properties, i.e., diffusion, of molecules and ions in solution, and thus are directly responsive to molecular size and shape. Since one can measure several components of a mixture simultaneously,[293,294] PGSE methods are particularly valuable where the material in question is not readily isolable and/or the mixture is of especial interest.

PGSE methods were introduced in 1965 by Stejskal and Tanner[295] and, since then, have been widely used. In the 1970s this approach was used to determine diffusion coefficients of organic molecules.[296] In the following decade, variants of the technique were applied to problems in polymer chemistry.[297–300] Since then, diffusion data on dendrimers[301–306] and peptides,[307–310] as well as on molecules in various environments, e.g., in porous silica[311] and zeolites,[312] have been obtained. Recent applications of PGSE methods in coordination and/or organometallic chemistry have emerged.[169,313–326]

2.1.3.2 Methodology

The basic element of an NMR diffusion measurement consists of a spin-echo sequence,[327] in combination with the application of static or pulsed field gradients.[295,328] Several common sequences are shown inFigure 8, and we discuss these only briefly as the subject is covered in several reviews.[291,292,329–334]

2.1.3.2.1 Spin-echo method

In the Stejskal–Tanner experiment,[295] Figure 8a, transverse magnetization is generated by the initial $\pi/2$ pulse which, in the absence of the static or pulsed field gradients, dephases due to chemical shift, hetero- and homonuclear coupling evolution, and spin–spin (T_2) relaxation. After application of an intermediate π pulse, the magnetization refocuses, generating an echo. At this point the sampling (signal intensity measurement) of the echo decay starts. Fourier transformation of these data results in a conventional NMR spectrum, in which the signal amplitudes are weighted by their individual T_2 values and the signal phases of the multiplets due to homonuclear coupling are distorted. Both effects are present in the diffusion experiment; however, due to the fixed timing, these are kept constant within the experiment.

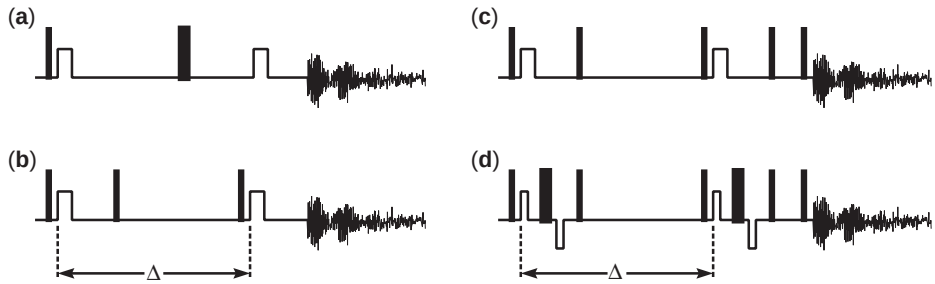

Figure 8 Pulse sequences commonly used for PGSE measurements: sequences with (a) spin-echo; (b) stimulated echo; (c) stimulated echo and longitudinal eddy-current delay (LED); (d) stimulated echo with bipolar pulsed field gradients and LED. Narrow and wide black rectangles represent $\pi/2$ and π radio-frequency pulses, respectively. Narrow and wide open rectangles are field-gradient pulses of duration $\delta/2$ and δ, respectively, and strength G.

The application of the first pulsed linear field gradient results in an additional (strong) dephasing of the magnetization, with a phase angle proportional to the length (δ) and the amplitude (G) of the gradient. Because the strength of the gradient varies linearly along, e.g., the z-axis, only spins contained within a narrow slice of the sample acquire the same phase angle. In other words, the spins (and therefore the molecules in which they reside) are phase encoded in one-dimensional space. The second gradient pulse, which must be exactly equal to the first, reverses the respective phases and the echo forms in the usual way. If, however, spins move out of their slice into neighbouring slices via Brownian motion, the phase they acquire in the refocusing gradient will not be the one they experienced in the preparation step. This leads to incomplete refocusing, as in the T_2 dephasing, and thus to an attenuation of the echo amplitude. As smaller molecules move faster, they translate during the time interval Δ into slices further apart from their origin, thus giving rise to smaller echo intensities for a given product of length and strength of the gradient.

2.1.3.2.2 *Stimulated echo method*

The second experiment, shown in Figure 8b,[328] works in quite the same way, with the difference that the phase angles which encode the position of the spins are stored along the z-axis in the rotating frame of reference by the action of the second $\pi/2$ pulse. Transverse magnetization and the respective phases are restored by the third $\pi/2$ pulse. This method is advantageous in that during time Δ, T_1 as opposed to T_2 is the effective relaxation path. Since T_1 is often longer than T_2, a better signal/noise ratio is obtained. Furthermore, phase distortion in multiplets due to homonuclear coupling is attenuated.

2.1.3.2.3 *Derived sequences*

The accurate determination of diffusion coefficients for large, slow-moving species requires strong gradient amplitudes. The resulting eddy-current fields can cause severe errors in the spatial phase encoding. The sequence shown in Figures 8c[335,336] and 8d[337,338] contains an additional, so-called longitudinal eddy-current delay (LED) element, i.e., magnetization is again stored along the z-axis during the decay time of the eddy currents. Disturbance of the field-frequency lock system can be minimized by the use of bipolar field-gradient pulses, Figure 8d.

Technically, all of the above experiments are performed by repeating the sequence while systematically changing the time allowed for diffusion (Δ), or the length (δ) or the strength (G) of the gradient. Mathematically, the diffusion part of the echo amplitude can be expressed by Equation (14):

$$\ln\left(\frac{I}{I_0}\right) = -(\gamma\delta)^2 G^2 \left(\Delta - \frac{\delta}{3}\right) D \tag{14}$$

(G = gradient strength, Δ = delay between the midpoints of the gradients, D = diffusion coefficient, δ = gradient length).

The diffusion coefficient D is obtained from the slope of the regression line by plotting $\ln(I/I_0)$ (I/I_0 = observed spin-echo intensity/intensity without gradients) vs. either $\Delta - \delta/3$, $\delta^2(\Delta - \delta/3)$, or G^2, depending on the parameter varied in the course of the experiment. Although slopes and diffusion coefficients differ by a proportionality factor depending on the experimental parameters, it is often convenient (for visualization) to group several measurements recorded under identical settings in one figure. Compounds which possess smaller hydrodynamic radii move faster, show larger diffusion coefficients, and reveal steeper slopes: see Figure 9.

The diffusion constant D can be related to the hydrodynamic radii of the molecules via the Stokes–Einstein Equation (15):

$$D = \frac{kT}{6\pi\eta r_{\mathrm{H}}} \tag{15}$$

(k = Boltzmann constant, T = absolute temperature, η = viscosity, r_{H} = hydrodynamic radius).

The validity of hydrodynamic radii obtained from NMR diffusion measurements was demonstrated by comparison with radii calculated from either crystallographically determined

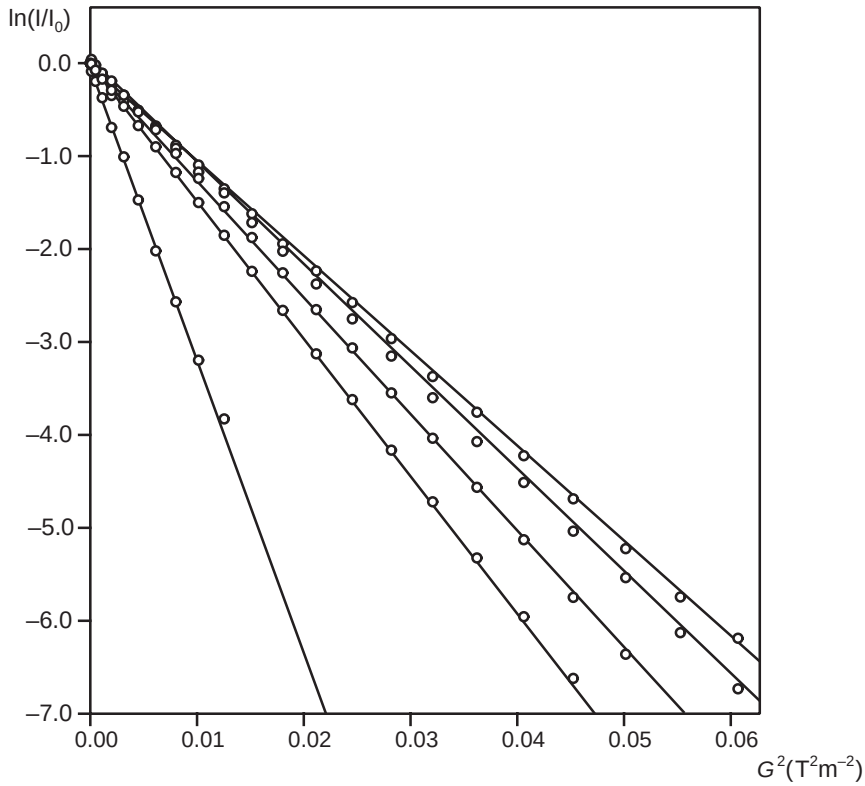

Figure 9 Plot of $\ln(I/I_0)$ vs. the square of the gradient amplitude. The slopes of the lines are related to the diffusion coefficients, D. The five lines stem from $CHCl_3$ and the four Pd–arsine complexes $PdCl_2L_2$, $L = AsMe_xPh_{3-x}$, $x = 3, 2, 1, 0$ (increasing molecular volume from left to right). The absolute value of the slope decreases with increasing molecular volume.

volumes,[322,324,325] analogous complexes, or from calculated structures.[324] The agreement between the two parameters—see Figure 10 and Table 2—is generally acceptable: perhaps even too good, given the assumption that all of the complexes have spherical shapes.

Given favorable receptivity and T_1 and/or T_2 relaxation times, one is not limited in the choice of the nucleus measured. Although most studies in coordination and organometallic chemistry involved the observation of ^1H, the use of alternative or additional nuclei often gives a complementary view. Studies based on ^7Li,[325] ^{13}C,[324] and ^{19}F[169,316,322,326] have appeared.

2.1.3.3 Study of Complex Nuclearity

The determination of molecular size in solution is a frequent problem for coordination compounds; e.g., in lithium and copper, as well as in transition-metal carbonyl and hydroxo/oxo chemistry, one finds numerous examples of polynuclear species. Increasingly, use is made of NMR diffusion measurements to directly assess molecular volumes in solution.

Venanzi and co-workers[320] characterized the equilibrium between the monomeric $RuCl_2$-(mesetph)—mesetph = $(C_6Me_3H_2)P\{CH_2CH_2PPh_2\}_2$—and the dinuclear $[Ru_2(\mu\text{-}Cl_3)(mesetph)_2]Cl$ complexes, based on the 1.23 ratio of their diffusion coefficients indicating a doubling of the volume for the latter. The structures of the mixed-ligand dinuclear complexes (MeOBiphep)-$RuCl(\mu\text{-}Cl_2)RuCl(\eta^6\text{-}p\text{-cymene})$[316] and $[(Duphos)(\eta^6\text{-}p\text{-cymene})Ru(\mu\text{-Cl})RuCl(\eta^6\text{-}p\text{-cymene})]Cl$[326] were postulated from identical diffusion rates for both subunits and their larger volumes compared to, e.g., [(Duphos)(η^6-*p*-cymene) RuCl]Cl and $Ru_2(\mu\text{-}Cl)_2(Cl)_2(\eta^6\text{-}p\text{-cymene})_2$. Interesting applications in zirconocene chemistry involved (i) the characterization of the dinuclear intermediate $[\{Cp_2ZrCl\}_2(\mu\text{-}O_2CH_2)]$ in the course of the CO_2 reduction with $Cp_2Zr(H)Cl$[324]; and (ii) the observation of ion quadruples for $Cp_2Zr(Me)_2$ in the presence of a Lewis acid like $B(C_6F_5)_3$.[313] Diffusion measurements also showed that addition of isonitrile to coordinatively unsaturated tetrameric copper(I) complexes proceeds with the retention of the square Cu_4S_4 core.[321]

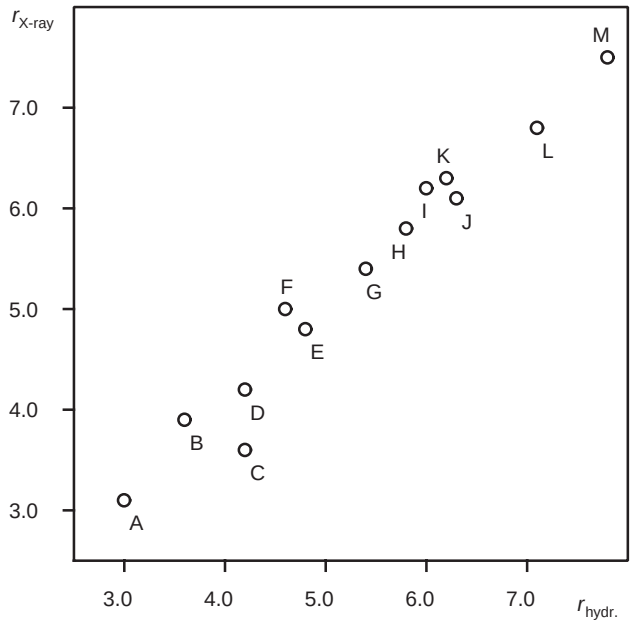

Figure 10 Plot of hydrodynamic radii obtained from PGSE experiments vs. the radii calculated from crystallographic data. For compounds D, E, G, and H, the radii in the solid state were estimated using reported structures for analogous phosphine, instead of arsine. For C and J the value was calculated from minimized gas-phase structures (PM3).

Experimental diffusion coefficients for the dimeric and tetrameric THF solvated *n*-butyllithium aggregates, [*n*-BuLi]$_2$·THF$_4$ and [*n*-BuLi]$_4$·THF$_4$, respectively, agree well with those calculated from X-ray or PM3 structures.[325] In terms of larger species, Valentini *et al.*[317] investigated dendrimeric ferrocenylphosphine ligands, while in a bioinorganic application, Gorman *et al.*[301] estimated the hydrodynamic radii of iron–sulphur-cluster-based dendrimers with the cube Fe_4S_4 core. The largest examined particles containing coordination compounds result from the self-assembly of 30 $\{R_3P\}_2\{CF_3SO_3\}Pt$–$(C_6H_4)_n$–$Pt\{CF_3SO_3\}\{R_3P\}_2$, $n = 1$ and R = Et, or $n = 2$ and R = Ph; and 20 tri(4′-pyridyl)methanol into dodecahedra with 55 Å and 75 Å diameter.[314]

2.1.3.4 Study of Ion Pairing

Occasionally one can determine the diffusion coefficients for cations and anions separately, and thus determine whether they move together as ion pairs or separately as free ions. Frequently, coordination compounds in use in homogeneous catalysis possess anions such as PF_6^-, BF_4^-, $CF_3SO_3^-$, or $BArF^-$, and ^{19}F PGSE experiments represent an alternative and complement.

Table 2 Hydrodynamic and crystallographic radii.

	Compound	r_H	$r_{X\text{-ray}}$
A	$ZrCl_2(Cp)_2$	3.0[324]	3.1[339]
B	$\{Cp_2ZrCl\}_2(\mu\text{-O})$	3.7[324]	3.9[340]
C	$ZrCl(OMe)(Cp)_2$	4.2[324]	3.6[324]
D	$PdCl_2(AsMe_3)_2$	4.2[317]	4.1[342]
E	$PdCl_2(AsMe_2Ph)_2$	4.8[317]	4.8[342]
F	$Tp^{Me2}W(CO)_3H$	4.6[317]	5.0[343]
G	$PdCl_2(AsMePh_2)_2$	5.4[317]	5.4[344]
H	$PdCl_2(AsPh_3)_2$	5.8[317]	5.8[345]
I	PdBr(C_6F_5)(MeOBiphep)	6.0[317]	6.2[322]
J	$\{Cp_2ZrCl\}_2(\mu\text{-}O_2CH_2)$	6.3[324]	6.1[324]
K	$Pd_2(dba)_3$	6.2[317]	6.3[346]
L	PdBr(C_6H_4CN)(Binap)	7.1[317]	6.8[347]
M	$[Ru_2(\mu\text{-}Cl_3)(mesetph)_2]Cl$	7.8[320]	7.5[348]

Macchioni and co-workers,[315] in pioneering work, measured diffusion coefficients of the structurally closely related complexes *trans*-[Ru(PMe_3)$_2$(CO)(COMe)(pz_2CH_2)]BPh_4 and *trans*-[Ru(PMe_3)$_2$(CO)-(COMe)(pz_2BH_2)], and found clear evidence for ions in nitromethane, ion pairs in chloroform at low concentrations, and ion quadruples in the latter solvent at high concentration. Ion quadruples were also mentioned by Beck *et al.*[313] for zirconocene compounds in benzene solution. An interesting solvent dependence was noted for the complexes [RuCl(η^6-benzene)(PBu_3)$_2$]PF_6 and [Pd(diphenylallyl)(Duphos)](CF_3SO_3).[322,326] In CD_2Cl_2 the diffusion coefficients are quite different, with the anions moving much faster, whereas in $CDCl_3$ they are the same within experimental error, suggesting that free ions and ion pairs are present in the two solvents, respectively. Effective doubling of the volume was observed when replacing the chloride anion in [(Duphos)RuCl(η^6-*p*-cymene)]Cl with BArF, a fluorine-containing derivative of tretraphenylborate.[322] The conclusion that the BArF analog is present as a relatively tight ion pair is supported by the ^{19}F diffusion measurement on the anion giving almost the same diffusion coefficient derived from the ^1H study.[322] Ion pairing with the BArF anion has also been reported for a series of iridium complexes, whereas analogs with PF_6^- are separated.[169]

Given that there are several known examples of anions that affect results from homogeneously catalyzed reactions,[349–351] studies of ion-pairing effects assume new significance.

2.1.3.5 Study of Hydrogen Bonding

Yet another promising area concerns hydrogen bonding in metal complexes.

The two triflates in complex (**28**), were found to move at almost the same rate.[322] Although tight ion pairing could be an explanation, it was concluded that hydrogen bonding to the P–OH fragment carries the noncoordinated triflate effectively along with the cation.[322]

2.1.3.6 Concluding Remarks

Conventional NMR methods depend on the interpretation of interactions explicitly included in the spin Hamiltonians, i.e., chemical shifts, scalar, dipolar, and quadrupolar coupling constants. An empirically well-established parameter-to-structure relationship is generally essential for elucidating complex molecular structures. As the spin interactions tend to be rather local, it is often tedious to describe overall molecular properties such as size, shape, mass, and charge. In this respect, the size- and shape-sensitive NMR techniques based on pulsed field-gradient spin-echo methods add an invaluable tool to the coordination chemist's armory. With (i) the widespread availability of self-shielded gradient equiment, (ii) the proven reproducibility of results, and (iii) the straightforward interpretation of "size," PGSE methods will find frequent application in solving problems in coordination chemistry.

2.1.4 SOLID-STATE NMR SPECTROSCOPY

2.1.4.1 Introduction

Since about 1980, NMR spectroscopy of coordination compounds in solution has been increasingly used on a routine basis to address a multitude of new and older chemical problems. The introduction of two-dimensional correlation methods afforded quick access to parameters for relatively rare spin-1/2 nuclei. Further, three-dimensional solution structures can now routinely be solved, including not only their constitution but also all aspects of configuration, conformation, and intra- and intermolecular dynamics.

Although there are now hundreds of publications on the applications of solid-state NMR spectroscopy in coordination chemistry, this technique has not yet made a similar transition. It still remains mostly in the realm of "specialists," often more interested in the physical properties itself than in their chemical significance. This is certainly partly due to the additional equipment and knowledge required, but also due to the neglect of chemists who define structural chemistry as X-ray crystallography. At the moment, solid-state NMR exists only as a tool for bridging the gap to solution studies, thereby overlooking the inherent wealth of information available.

Naturally, but certainly not exclusively, solid-state NMR spectroscopy is the method of choice for all those materials that are neither crystalline nor soluble, e.g., coordination complexes

adsorbed or covalently linked to organic or inorganic polymer supports, and compounds in amorphous or glass phases.

2.1.4.2 Principles and Methodologies

Comprehensive treatments of solid-state NMR spectroscopy are available elsewhere.[352–358] For this discussion, it is sufficient to express the principal spin interactions as the following sum:

$$H = H_Z + H_{CS} + H_Q + H_D^{IS} + H_J^{IS} \quad (17)$$

where the subscripts in the Hamiltonians denote the following relevant interactions: Z, Zeeman; CS, chemical shift;[359–361] Q, quadrupolar;[362,363] D, direct dipolar coupling; and J, indirect or scalar spin–spin coupling.[364,365] As NMR measurements are usually carried out in strong magnetic fields, the Zeeman interaction is dominant and the other terms represent only modest perturbations. Only in cases where a quadrupolar nucleus is involved will the magnitude of the quadrupolar coupling constant, χ, be comparable to, or greater than, its Larmor frequency, ν_L. All of the above interactions transform as tensors under rotation, and thus their magnitudes depend on molecular orientation.[355] The values of the familiar chemical shifts are determined not only by the position of the nucleus within the molecule, but also by the orientation of each molecule or crystallite with respect to the external magnetic field. In solution, where molecules are tumbling fast with respect to the Larmor frequency, thus sampling all possible orientations on a short timescale, chemical shifts and scalar coupling constants average to their isotropic values, and to zero for the traceless quadrupolar and dipolar interactions.

Given the angular dependence mentioned, it is obvious that the anisotropic spectra obtained from the condensed phase must be much richer in information, if more complicated. They contain all the essential geometrical information describing a molecule in terms of angles between the chemical shift, electric-field gradient, direct and indirect dipolar tensors. The angular dependence of the resonance frequencies can be separated from the molecular contribution by monitoring line positions as a function of a systematic rotation of the sample in the three orthogonal directions. Because of resolution restrictions, this can generally be realized only with single crystals, and the most accurate results are still obtained using this method.

In a powder sample, the orientations of the molecules are fixed within the rigid lattice but the crystallites are randomly distributed. Their resonance frequencies generally sum to form a broad "powder line," representing the sum of their individual contributions. The frequency span encountered for such lines is often larger by orders of magnitude than the differences based on the position within the molecule itself, and the limited resolution is of general concern. Two different approaches to address this problem have been proposed: (i) line-narrowing techniques which simulate the tumbling of molecules either in the spin space using elaborate multipulse sequences,[366–368] or in real space with macroscopic rotation of the sample around specific, so-called "magic," angles[369–372] with the aim of observing an isotropic spectrum; (ii) application of additional frequency dimensions in two- and multidimensional experiments which correlate or separate the different anisotropic spin interactions.[373] A combination is also possible, i.e., correlating an anisotropic spectrum with one of its isotropic counterparts, thus retaining the geometric information while benefitting from the high resolution of the latter.[373]

The first approach is well established and experiments employing magic-angle spinning (MAS) constitute the bulk of all reported studies. Fast rotation, relative to their frequency span, around an angle of 54° 44′ reduces the chemical shift and scalar coupling interactions to their isotropic averages and the dipolar interaction to zero. Averaging of the quadrupolar interaction, described by a rank 4 tensor, to zero requires an additional simultaneous rotation around the angle of 30° 34′ which is achieved in the double-rotation (DOR) experiment.[370,374,375] Alternatively, in the dynamic angle-spinning (DAS) 2D experiment, the rotor hops sequentially between the angles 37° 23′ and 79° 11′.[376–378] Anisotropies at one angle cancel those at the other.

A potential problem in obtaining solid-state NMR spectra involves the longitudinal relaxation times which tend to be long, thus compromising sensitivity. To overcome this, cross-polarization from abundant nuclei, such as ^{1}H, to the dilute spin, S, under observation may be employed.[379–383] Recycle delays are then determined by the T_1 of ^{1}H rather than of S. In addition, the magnetization of S can be increased up to a maximum of γ_H/γ_S.

The quadrupolar-echo experiment represents the most widely used experiment for the observation of quadrupolar nuclei.[384] For half-integer nuclei, it may be tuned to observe only the central transition (1/2–1/2), which is perturbed by the quadrupolar interaction only to second order, thus allowing the observation of less dominant anisotropic interactions. A significant improvement in sensitivity can be obtained by ncorporating a spin-echo method such as the Carr–Purcell–Meiboom–Gill sequence into the detection period.[385–388] The powder line-shape splits into a manifold of sidebands, from which information on the homogeneous and inhomogeneous interactions can be extracted from the line-shape of the sidebands and their envelope, respectively.

One- and two-dimensional multiple-quantum techniques have been introduced for the observation of quadrupolar nuclei with half-integer spin. These methods have proven powerful in resolving overlapping resonances of multiple sites.[389–395]

2.1.4.3 Spin-1/2 Metal Nuclei

The importance of NMR for molecular structure determination rests primarily on the phenomenon of chemical shielding effects, which are particularly large for the heavy atoms. Isotropic metal chemical shifts obtained from MAS studies are often sufficient to solve most chemical problems, as there is now a large empirical body of data derived from solution NMR. However, taking the orientation dependence of the chemical shielding into account provides considerably more insight into the bonding at the metal center. Studies concerned with establishing the span of the metal chemical-shift anisotropy and its relation to coordination geometries and oxidation states have been reported.[396–419] The topic was reviewed in the 1990s for the *d*- and *p*-block elements,[396,397] and in particular also for mercury compounds.[398] Procedures for intrumental set-up have been suggested.[399]

The span,[420] $\Omega = \delta_{11} - \delta_{33}$, of the ^{199}Hg chemical shift tensors in [Hg(S-2,4,6-$^{i}Pr_3C_6H_2)_2$], [PPh_4][Hg(S-2,4,6-$^{i}Pr_3C_6H_2)_3$], and [NMe_4]$_2$[$Hg(SC_6H_4Cl)_4$] are found to be 4479, 1548, and 178 ppm, respectively.[398] This decrease, which follows the sequence linear ML_2 > trigonal ML_3 > tetrahedral ML_4, was also established for ^{195}Pt shielding, based on the CSA contribution to T_1 relaxation in Pt^0 phosphine complexes.[29] Interestingly, the sequence found for *sp*, sp^2, and sp^3 hybridized carbon is similar.[421–423] Octahedral coordination environments generally show smaller spans, e.g., <120 ppm for M_2PtCl_6, M = Na, K, NH_4 complexes,[409–412] whereas those associated with square-planar geometries can be very large,[409,413–415] e.g., 10,414 ppm in K_2PtCl_4.[409] Large shielding anisotropies were also observed for 2-coordinate tin(II) compounds,[406–408] as opposed to moderate ones in tin(IV) complexes.[404–406]

In bioinorganic applications, ^{113}Cd has attracted considerable interest,[400–402] due to its function as an effective spin-spy in monitoring the active site in metalloproteins where the native metals have poor spectroscopic properties. The elements of the shielding tensors as a function of the donor atoms, N, O, and S, and the coordination number have been determined, and empirical correlations to structure deduced.[401–403]

2.1.4.4 Quadrupolar Metal Nuclei

NMR spectra of quadrupolar nuclei are of particular interest, because they offer a unique opportunity to investigate both the electric-field gradient and the chemical-shift tensors at a common nuclear site simultaneously. Furthermore, many of the biologically relevant nuclei, e.g., ^{23}Na, ^{25}Mg, ^{39,41}K, ^{55}Mn, ^{59}Co,[424–427] ^{61}Ni, ^{63,65}Cu,[428] ^{67}Zn,[22,429,430] ^{95,97}Mo,[431,432] are quadrupolar. The measurement and interpretation of solid-state NMR spectra of these nuclei obtained on powders is still a challenge. New spectroscopic techniques[385–395] and especially the impressive advances in computational chemistry, which make possible the calculation of both electric-field gradient and chemical-shift tensors, provide much-needed assistance. Solid-state NMR on quadrupolar *d*- and *p*-metals was reviewed in the early 1990s.[396]

The Euler angles relating the electric-field gradient and chemical shielding tensors in the acetylacetonato complexes of beryllium,[433] aluminum,[434] and cobalt[424,427] have been determined. In the case of ^{59}Co the results arise from single-crystal NMR.[427] Euler angles relating the two interactions have also been retrieved from the manifolds of the spinning sidebands of the central and satellite transitions, observed in ^{51}V MAS spectra of a series of *ortho*- and *meta*-vanadates.[434,436] Reports on the chemical shielding anisotropies for quadrupolar nuclei are becoming more frequent in the early 2000s.[424–428,432–439]

2.1.4.5 Ligand Nuclei

2.1.4.5.1 ^{1}H *NMR*

The concentrated presence, high abundance, high gyromagnetic ratio, and low chemical-shift dispersion of the proton make this nucleus a difficult one: homogeneous broadening due to strong homonuclear dipole–dipole couplings lead to featureless absorptions much broader than its chemical-shift range. As a consequence of the homogeneous nature of the broadening, slow-spinning MAS only scales the interaction and does not resolve the spectrum into an isotropic part and a spinning side-band manifold. Ultrafast spinning is mandatory; otherwise homonuclear decoupling sequences—either alone[368] or in combination[366,368] with magic-angle spinning—would have to be employed. Fortunate cases exist where one particular interaction dominates the dipolar Hamiltonian.

Molecular hydrogen complexes are again special, since the strong dipolar coupling due to the short H—H distance dominates all other interactions. Zilm *et al.*[270,440] reported the solid-state ^{1}H NMR spectrum of $W(H_2)(CO)_3(PCy_3)_2$ showing a distorted Pake-pattern, from which information on the H—H separation and the chemical-shift anisotropy of the hydrogen atoms could be obtained. The temperature dependence indicated an in-plane motion of $\pm 16°$.[440] Similar results were also obtained for Mo,[270] Mn[441], and Ru[270] hydrogen complexes.

2.1.4.5.2 ^{2}H *NMR*

The deuterium quadrupolar coupling constant is a sensitive measure of the magnitude of the electric-field gradient at the nucleus, and is therefore affected by the bonding situation. The deviation from axial symmetry sheds light on the bonding mode, e.g., in distinguishing molecular hydrogen complexes from classical hydrides. The facile isotope substitution for hydride and hydrogen ligands renders the observation of deuterium an alternative to ^{1}H. In general, motional properties of ligands are easily assessed with the ^{2}H NMR method.

A highly asymmetric quadrupolar tensor has been found for $OsCl_2(D_2)(CO)(P^iPr_3)_2$, together with characteristic line-shapes in the MAS side-bands, originating from interference of dipolar and quadrupolar interactions.[442] From the strength of the dipolar interaction, D—D distances could be obtained as well as the relative orientations of the tensors.[442] Solid-state ^{2}H NMR data have also been reported for $W(D_2)(CO)_3(P^iPr^3)_2$ and interpreted as a motionally averaged quadrupolar tensor of axial symmetry due to significant molecular motion.[443] Coherent D_2 rotational tunneling and incoherent D_2 dynamics were shown to affect the ^{2}H NMR lineshapes of nonclassical $Ru(D_2)$ complexes.[444,445]

Studies on Zeise's salt and the complex $Pt(\eta^2\text{-}C_2D_4)(PPh_3)_2$ ruled out rotation of the ethylene ligand based on the observed ^{2}H quadrupole coupling constants, which are comparable in magnitude to those found in rigid olefins.[446]

2.1.4.5.3 ^{13}C *NMR*

Structural data on coordination compounds can be gathered from ^{13}C CP–MAS spectra of the carbon nuclei in the backbone of ligands.[447] Here, however, we restrict the discussion to carbon nuclei directly bound to the metal center, i.e., σ-bonded CO,[448–459] CN^-,[428,429,460–465] acetylide,[414,415] alkyl[466,467] and aryl ligands,[447,466] and the π-bonded alkenes, alkynes,[446,466–469] cyclopentadienyls, and arenes.[470–474]

Metal carbonyl complexes are at the center of many areas of chemistry. Interest has focussed on their dynamic processes,[447,449] but also on the shielding tensor itself.[454–458] With respect to the latter, the three modes (μ_1 to μ_3) of CO bonding have been investigated;[455] CO coordination is characterized by ^{13}C tensors spanning ca. 400 ppm and 200 ppm for terminal and bridging COs, respectively. A large deviation from axial symmetry is observed for the μ_2-mode, and it is interesting to note that in $Fe(CO)_5$ the shielding of the equatorial ligands deviates slightly from axial symmetry.[455]

Copper(I) cyanides have been extensively studied by ^{13}C solid-state NMR, and reveal axial chemical-shift tensors plus the novel coupling constants $^{1}J(^{63,65}Cu, ^{13}C)$ and Cu–C separations from the dipolar coupling.[428,460] CuCN has a linear polymeric structure $[–Cu–CN–]_n$, with the cyanides subject to "head–tail" disorder.[460]

The low-frequency isotropic chemical shift normally observed for σ-bonded alkyl organometallic carbon is due to one particularly shielded component, whose orientation with respect to the carbon–metal bond could not be determined.[466] For methyl groups, the span, Ω of the shielding tensor is larger than for organic compounds and depends strongly on the other ligands present in the complex.[466]

Powder as well as MAS studies are available for several η^2-bonded olefins.[446,466–469] The spans of the chemical-shift tensors are reduced with respect to the free olefins, which is discussed in terms of the Dewar–Chatt–Duncanson model of σ-donation and π-back-bonding.[446,468] The C—C bond lengths and the orientations of the shielding tensor elements are available from dipolar-chemical shift methods and 2-D spin-echo experiments on the doubly ^{13}C labelled olefins.[445,469]

η^5-cyclopentadienyl and η^6-benzene ligands of transition-metal complexes,[466,470–473] but also some derivatives of alkali or main-group elements,[474] exhibit single ^{13}C resonances and shielding tensors of axial symmetry at room temperature. Both observations point to relatively fast rotations around the respective 5- and 6-fold local rotor axis.[470,471]

2.1.4.5.4 ^{15}N NMR

The question of nitrogen vs. carbon in cyanides as a donor atom has been investigated by ^{15}N solid-state NMR.[428,460,461] This problem could also be addressed from the metal side, given that a suitable spin-1/2 metal is involved.[475] Interest in the antitumor reagent *cis*-$[PtCl_2(NH_3)_2]$ prompted studies on the ^{15}N characteristics of this and related types of platinum complexes.[476–478] Cobaloximes with aniline and pyridine ligands have been investigated, yielding the orientations of the nitrogen shift and the cobalt electric-field gradient tensors with respect to the molecular frame, plus the signs and magnitudes of $^1J(^{59}Co, ^{15}N)$ scalar and the ^{59}Co quadrupole coupling constants.[479] Nitroso and aryl-nitroso metalloporphyrins have been studied with interest towards O_2 binding.[480,481]

2.1.4.5.5 ^{17}O NMR

Oxygen has been studied in conjunction with ^{13}C in transition-metal carbonyls and is often found to be more sensitive to structural changes than the latter.[450,455–458]

2.1.4.5.6 ^{19}F NMR

After some initial MAS studies of tin fluorides,[405] this nucleus seems to have attained "sleeping beauty" status. New interest in fluorination catalysis may awaken some interest. Potential exists for crystal structure refinements, where often F^- and OH^- are indistinguishable.[482]

2.1.4.5.7 ^{31}P NMR

^{31}P in phosphines, phosphates, and their metal complexes remains the most studied ligand nucleus. Developments up to 1992 have been summarized by Davies and Dutremez.[483] MAS studies often show isotropic chemical shifts and isotropic scalar coupling constants very similar to those derived from solution studies.[484–488]

The problem of η^1 vs. η^2-coordination in phosphaalkene platinum chemistry has been solved by ^{31}P MAS NMR.[489,490] Whereas the solution $\delta(^{31}P)$ value and the smallish $J(^{195}Pt,^{31}P)$ coupling constant were consistent with the η^2 bonding mode, (**29**), η^1-coordination, (**30**), was unambigously assigned in the solid from the high-frequency chemical shift and the large one-bond coupling to platinum, in agreement with an X-ray crystal structure determination.[491]

Static disorder in crystals represents a problem which can lead to a crystallographic symmetry higher than its molecular symmetry, thus hiding important structural features. In this respect the presence of a P—H—Pd agostic interaction in the dinuclear Pd(I) complex (**31**) was established[492] in solution and shown to remain intact in the solid phase, as evidenced from the four quite different ^{31}P parameters of the four P ligands, which were in good agreement with their solution values.[493] The centrosymmetrical crystal structure suggested that only half of the molecule would be independent.[493]

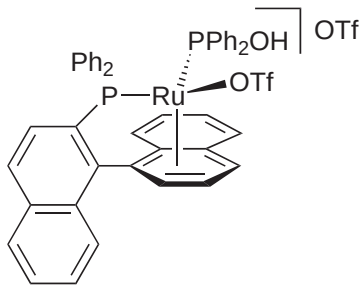

(**28**)

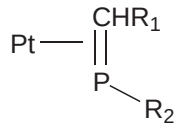

(**29**)

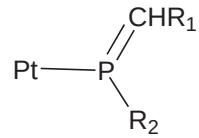

(**30**)

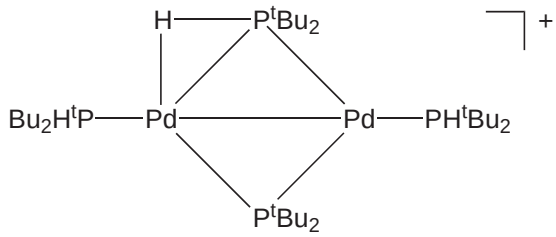

(**31**)

Due to packing effects, molecules in the solid state generally reveal lower symmetry relative to the solution phase, and often there are as many resonances resolved as there are sites in the coordination complex.[484–487] Spin–spin coupling, unobservable in solution, can be employed for structural assignments. Unless they are related by an inversion center, spins are magnetically inequivalent even if they are related by symmetry planes or axes. Although they have the same isotropic chemical shifts, they do have different orientations of their chemical-shift tensor. In cases where such spins show dipolar interactions (direct and/or indirect), a spinning-frequency-dependent splitting of resonances is observed in their MAS spectra, thus offering insight into their molecular structure.[494–496]

The magnitudes of the one-bond metal–phosphorus coupling constants represent a rich source of structural information.[483–490,495–498] The anisotropy of the indirect ^{199}Hg–^{31}P spin–spin coupling constant has been determined.[497–499] Additional information on metal-ligand one-bond coupling constants can be gained from MAS spectra of phosphorus ligands coordinated to quadrupolar metal nuclei. In solution, T_1 values for the latter nuclei are extremely short, unless they are in a cubic environment, leading to "self-decoupling" effects. In the solid phase, these T_1

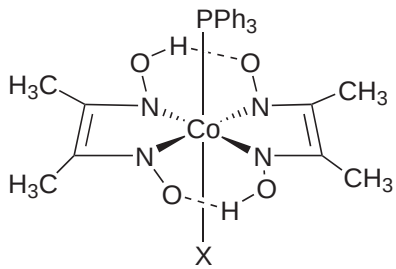

(**32**)

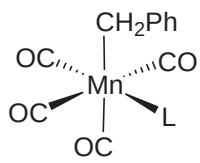

(**33**)

X = CH_3	^1J(Co,P) = 225 (2) Hz	L = PPh_3	^1J(Mn,P) = 216 (4) Hz
X = Cl	^1J(Co,P) = 371 (2) Hz	L = PCy_3	^1J(Mn,P) = 220 (2) Hz
		L = P(p-Tol)$_3$	^1J(Mn,P) = 196 (3) Hz

values are long, even for quadrupolar nuclei, and coupling to phosphorus ligands is observed. One-bond scalar couplings have been reported for the following spin $>1/2$ nuclei: ^{55}Mn,[500–502] ^{59}Co,[500,502] ^{63,65}Cu,[504–511] ^{93}Nb,[500,512] ^{95,97}Mo,[501,513] ^{99}Ru,[514] ^{105}Pd,[515] ^{115}In.[517] Within the limits of the high-field approximation, i.e., $\nu_L > \nu_Q$, the observed ^1J values are readily interpreted. Occasionally, first-order perturbation theory or even a full treatment of the Hamiltonians is necessary.[500,504,517–520] It is worth emphasizing that, given the utility of ^1J(M,L), such information is otherwise not available.

Two nice examples are shown in (**32**) and (**33**). The cobaloxime complexes of the type (**32**) are especially informative,[503] as they reveal the expected change in $^1J(^{59}\text{Co},^{31}\text{P})$ as a function of the *trans* influence of the ligand X.[81,82]

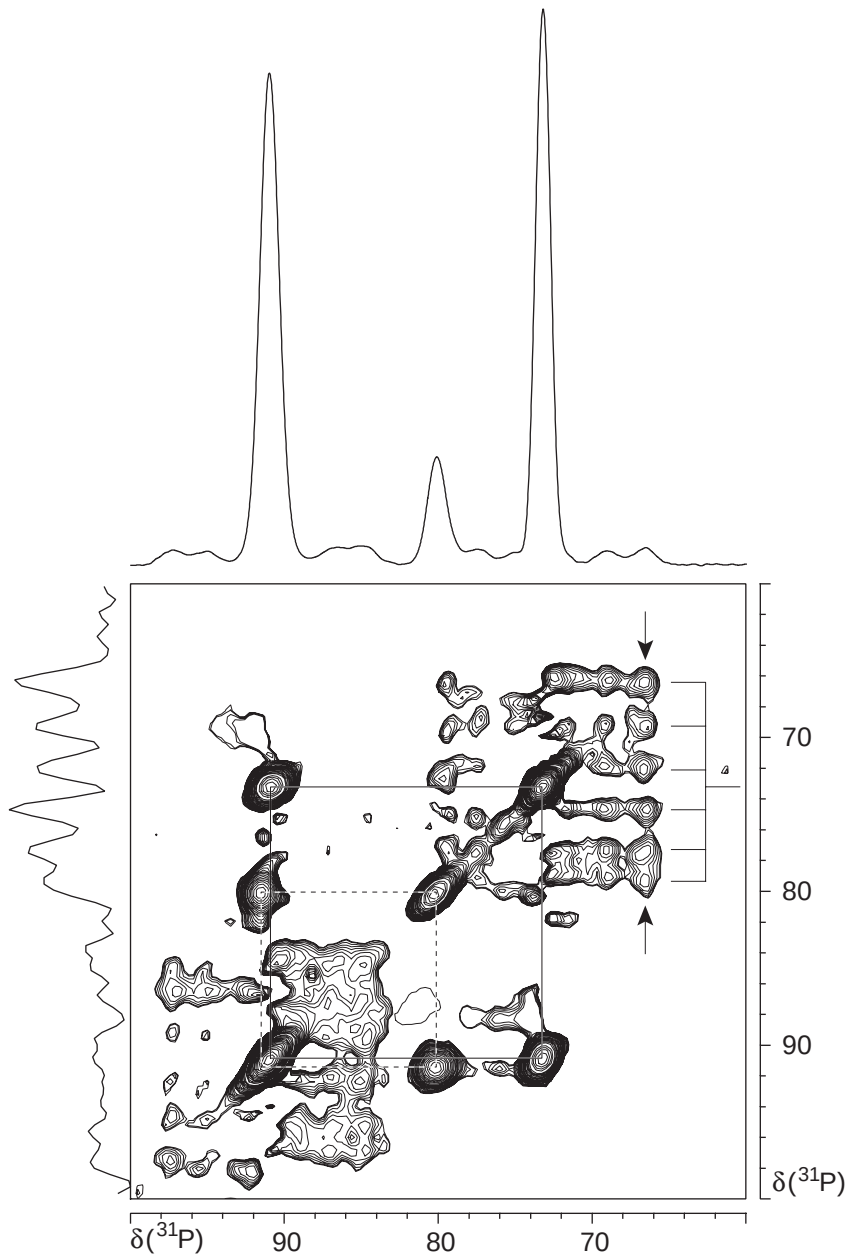

Figure 11 Contour plot showing the isotropic part of the 162.0 MHz 2D ^{31}P CP/MAS exchange spectrum ($\tau_{mix} = 1$s) recorded for *cis*-[$PdCl_2${$P(OC_6H_4$-*o*-Me)$}_2$]. Two crystalline modifications of this complex are indicated by full and dotted lines, respectively. The corresponding part of the conventional ^{31}P CP/MAS spectrum is plotted above. A column taken at the position indicated by the arrows and shown to the left, exhibits the complete set of six ^{105}Pd(I = 5/2, 22.2%) satellites associated with the lowest frequency resonance with $^1J(^{105}\text{Pd},^{31}\text{P}) = 420$ (**3**) Hz.

Phosphine ligands and their transition-metal complexes immobilized on inorganic or organic supports have also been the subject of MAS studies.[521–527]

2.1.4.6 Applications of Two-dimensional NMR Spectroscopy

Examples of solid-state, two-dimensional NMR spectroscopy in the field of coordination chemistry are still relatively rare. The incorporation of the cross-polarization scheme into the preparation period of the INADEQUATE,[528] COSY,[74,528–531] SECSY,[531] and NOESY[74,531–533] sequences leads to three different types of chemical-shift correlation methods, based on double-quantum, single-quantum, and spin-diffusion interactions, respectively. The former three methods rely on the presence of scalar spin–spin coupling constants of suitable size, a restriction not encountered in the spin-diffusion experiment. Overlapping resonances may be resolved with two-dimensional methods, e.g., the ^{105}Pd satellites in ^{31}P NMR spectra of palladium phosphine or phosphite complexes: see Figure 11.

The two-dimensional spin-echo experiment has found applications for static samples of compounds containing homonuclear spin pairs, where dipolar and chemical shift interactions could be separated allowing the determination of internuclear distances.[446,534] It was also shown that a considerable improvement in resolution could be obtained for samples rotated in the magic angle, thus allowing the determination of the magnitude of relatively small homonuclear scalar coupling constants,[535–537] e.g., $^{2}J(^{31}\mathrm{P}, ^{31}\mathrm{P})_{\mathrm{cis}}$ in Wilkinson's-type rhodium complexes.[535]

2.1.5 OUTLOOK

NMR still represents the most varied and flexible analytical method for coordination chemists. Access to difficult metal spins such as ^{57}Fe, hydride signal enhancement via PHIP, 3-D solution structures using NOESY, ion pairing through PGSE techniques, recognizing molecular hydrogen complexes by measuring T_1, fluctionality in the solid state, and new bonding probes via ^{1}J with quadrupolar nuclei represent only some of the opportunities offered. NMR will not replace X-ray crystallography, but its breadth of applications makes it extremely attractive.

2.1.6 REFERENCES

1. von Philipsborn, W. *Chem. Soc. Rev.* **1999**, *28*, 95–105.
2. Granger, P. In *Advanced Applications of NMR to Organometallic Chemistry*; Gielen, M., Willem, R., Wrackmeyer, B., Eds.; Wiley: Chichester, UK 1996; 313–357.
3. Mann, B. E. In *Annual Reports on NMR Spectroscopy*; Academic Press: London, 1991; Vol. 23, pp 141–207.
4. Pregosin, P. S.*Transition Metal NMR Spectroscopy* **1991**, Elsevier: Amsterdam.
5. Tedesco, V.; von Philipsborn, W. *Magn. Reson. Chem.* **1996**, *34*, 373–376.
6. Bender, B. R.; Koller, M.; Nanz, D.; von Philipsborn, W. *J. Am. Chem. Soc.* **1993**, *115*, 5889–5890.
7. Koller, M.; von Philipsborn, W. *Organometallics* **1992**, *11*, 467–469.
8. Graham, P. B.; Rausch, M. D.; Taschler, K.; von Philipsborn, W. *Organometallics* **1991**, *10*, 3049–3052.
9. Ernsting, J. M.; Elsevier, C. J.; Delange, W. G. J.; Timmer, K. *Magn. Reson. Chem.* **1991**, *29*, S118–S124.
10. Aizenberg, M.; Ott, J.; Elsevier, C. J.; Milstein, D. *J. Organomet. Chem.* **1998**, *551*, 81–92.
11. Bregman, F. R.; Ernsting, J. M.; Muller, F.; Boele, M. D. K.; van der Veen, L. A.; Elsevier, C. J. *J. Organomet. Chem.* **1999**, *592*, 306–311.
12. Eujen, R; Hoge, B.; Brauer, D. J. *Inorg. Chem.* **1997**, *36*, 1464–1475.
13. Lianza, F.; Macchioni, A.; Pregosin, P.; Rüegger, H. *Inorg. Chem.* **1994**, *33*, 4999–5002.
14. Carmona, D.; Oro, L. A.; Lamata, M. P.; Jimeno, M. L.; Elguero, J.; Belguise, A.; Lux, P. *Inorg. Chem.* **1994**, *33*, 2196–2203.
15. Gisler, A.; Schaade, M.; Meier, E. J. M.; Linden, A.; von Philipsborn, W. *J. Organomet. Chem.* **1997**, *546*, 315–326.
16. Bell, A. G.; Kozminski, W.; Linden, A.; von Philipsborn, W. *Organometallics* **1996**, *15*, 3124–3135.
17. Wrackmeyer, B.; Tok, O. L.; Herberhold, M. *Organometallics* **2001**, *20*, 5774–5776.
18. Wrackmeyer, B.; Ayazi, A.; Maisel, H. E.; Herberhold, M. *J. Organomet. Chem.* **2001**, *630*, 263–265.
19. Wrackmeyer, B.; Seidel, G.; Koster, R. *Magn. Reson. Chem.* **2000**, *38*, 520–524.
20. Rehder, D.; Rodewald, D. In *Advanced Applications of NMR to Organometallic Chemistry*; Gielen, M., Willem, R., Wrackmeyer, B., Eds.; Wiley: Chichester, UK, 1996; pp 291–313.
21. Rehder, D. *Chimia* **1986**, *40*, 186–199.
22. Lipton, A. S.; Smith, M. D.; Adams, R. D.; Ellis, P. D. *J. Am. Chem. Soc.* **2002**, *124*, 410–414.
23. Lipton, A. S.; Buchko, G. W.; Sears, J. A.; Kennedy, M. A.; Ellis, P. D. *J. Am. Chem. Soc.* **2001**, *123*, 992–993.
24. Rentsch, D.; Nill, L.; von Philipsborn, W.; Sidler, D. R.; Rybczynski, P. J.; DeShong, P. *Magn. Reson. Chem.* **1998**, *36*, S54–S60.
25. Rentsch, D.; Hany, R.; von Philipsborn, W. *Magn. Reson. Chem.* **1997**, *35*, 832–838.

26. Gaemers, S.; van Slageren, J.; O'Connor, C. M.; Vos, J. G.; Hage, R.; Elsevier, C. J. *Organometallics* **1999**, *18*, 5238–5244.
27. Gaemers, S.; Groenevelt, J.; Elsevier, C. J. *Eur. J. Inorg. Chem.* **2001**, 829–835.
28. Minelli, M.; Enemark, J. H. *Coord. Chem. Rev.* **1985**, *68*, 169–278.
29. Benn, R.; Büch, H. M.; Reinhardt, R. D. *Magn. Reson. Chem.* **1985**, *23*, 559–564.
30. Benn, R.; Brenneke, H.; Heck, J.; Rufinska, A. *Inorg. Chem.* **1987**, *27*, 2826–2829.
31. Benn, R.; Brenneke, H.; Joussen, E.; Lehmkuhl, H.; Ortiz, F. L. *Organometallics* **1990**, *9*, 756–761.
32. Benn, R.; Brenneke, H.; Frings, A.; Lehmkuhl, H.; Mehler, G.; Rufinska, A.; Wildt, T. *J. Am. Chem. Soc.* **1988**, *110*, 5661–5668.
33. Pregosin, P. S. *Inorganic Nuclei: Low Sensitivity Transition Metals* 1996, Wiley: Chichester, UK.
34. Gielen, M.; Willem, R.; Wrackmeyer, B., Eds. *Advanced Applications of NMR to Organometallic Chemistry*; Wiley: Chichester, UK, 1996.
35. Nanz, D.; von Philipsborn, W. *J. Magn. Reson.* **1991**, *92*, 560–571.
36. Quin, L. D.; Verkade, J. G., Eds. *Phosphorus-31 NMR Spectral Properties in Compound Characterization and Structural Analysis*; VCH: New York, 1994.
37. Pregosin, P. S. In Verkade, J. G., Quin, L. D., Eds. *Phosphorus-31 NMR Spectral Properties in Compound Characterization and Structural Analysis*; VCH: Deerfield Beach, FL, 1987; Vol. 8, p 465.
38. Pregosin, P. S.; Kunz, R. W. *^{31}P and ^{13}C NMR of Transition Metal Phosphine Complexes* 1979, Springer: Berlin.
39. Harris, R. K.; Mann, B. E., Ed., *NMR and the Periodic Table* 1978, Academic Press: London.
40. Kalinowski, H. O.; Berger, S.; Braun, S. *^{13}C-NMR Spektroskopie* 1984, Thieme: Stuttgart, Germany.
41. Buhl, M.; Parrinello, M. *Chem. Eur. J.* **2001**, *7*, 4487–4494.
42. Buhl, M.; Gaemers, S.; Elsevier, C. J. *Chem. Eur. J.* **2000**, *6*, 3272–3280.
43. Donkervoort, J. G.; Buhl, M.; Ernsting, J. M.; Elsevier, C. J. *Eur. J. Inorg. Chem.* **1999**, 27–33.
44. Czech, P. T.; Ye, X. Q.; Fenske, R. F. *Organometallics* **1990**, *9*, 2016–2022.
45. Ehlers, A. W.; Ruiz-Morales, Y.; Baerends, E. J.; Ziegler, T. *Inorg. Chem.* **1997**, *36*, 5031–5036.
46. Tschoerner, M.; Kunz, R. W.; Pregosin, P. S. *Magn. Reson. Chem* **1999**, *37*, 91–97.
47. Buhl, M. *Chem. Phys. Lett.* **1997**, *267*, 251–257.
48. Buhl, M. *Angew. Chem. Int. Ed. Engl.* **1998**, *37*, 142–144 and references therein.
49. Chesnut, D. B.; Rusiloski, B. E. In *Phosphorus-31 NMR Spectral Properties in Compound Characterization and Structural Analysis*; Quin, L. D., Verkade, J. G., Eds.; VCH: New York, 1994.
50. Öhrström, L. *Comments Inorganic Chem.* **1996**, *18*, 305–323.
51. Groning, O.; Elding, L. I. *Inorg. Chem.* **1989**, *28*, 3366–3372.
52. Dunham, S. O.; Larsen, R. D.; Abbott, E. H. *Inorg. Chem.* **1993**, *32*, 2049–2055.
53. Boardman, L. D.; Newmark, R. A. *Magn. Reson. Chem.* **1992**, *30*, 481–489.
54. Carr, C.; Glaser, J.; Sandstrom, M. *Inorg. Chim. Acta* **1987**, *131*, 153–156.
55. Ismail, F. M.; Kerrison, S. J. S.; Sadler, P. J. *J. Chem. Soc., Chem Comm.* **1980**, 1175–1176.
56. Webb, G., Ed., *Ann. Rep. NMR Spectrosc.* **1981**, *11b*Academic Press: London.
57. Mann, B. E.; Taylor, B. F. *^{13}C NMR Data for Organometallic Compounds* **1981**, Academic Press: London.
58. Åkermark, B.; Krakenberger, B.; Hanson, S.; Vitagliano, A. *Organometallics* **1987**, *6*, 620–628.
59. Alt, H. G.; Jung, M.; Kehr, G. *J. Organomet. Chem.* **1998**, *562*, 153–181.
60. Lee, L. W. M.; Piers, W. E.; Parvez, M.; Rettig, S. J.; Koung, V. G. *Organometallics* **1999**, *18*, 3904–3912.
61. Tschoerner, M.; Pregosin, P. S. *Inorg. Chim. Acta* **1999**, *290*, 95–99.
62. Granell, J.; Muller, G.; Rocamora, M.; Vilarrasa, J. *Magn. Reson. Chem.* **1986**, *24*, 243–246.
63. Bodmer, G. M.; May, M. P.; McKinney, L. E. *Inorg. Chem.* **1980**, *19*, 1951–1958.
64. Pregosin, P. S.; Wombacher, F. *Magn. Reson. Chem.* **1991**, *29*, S106–S117.
65. Anklin, C. G.; Pregosin, P. S.; Wombacher, F. J.; Rüegg, H. J. *Organometallics* **1990**, *9*, 1953–1958.
66. Albinati, A.; Affolter, S.; Pregosin, P. S. *Organometallics* **1990**, *9*, 379–387.
67. Cotton, F. A.; Daniels, L. M.; Lei, P.; Murillo, C. A.; Wang, X. P. *Inorg. Chem.* **2001**, *40*, 2778–2784.
68. Autschbach, J. Ziegler, T. *J. Am. Chem Soc.* **2001**, *123*, 3341–3349 and references therein.
69. Ostoja-Starzewski, K. H. A.; Pregosin, P. S.; Rüegger, H. *Helv. Chim. Acta* **1982**, *65*, 785–797.
70. Albinati, A.; NägeliR.; Rüegger, H; Pregosin, P. S. *Angew. Chem. Int. Edit.* **1982**, *21*, 284–285.
71. Kretschmer, M.; Pregosin, P. S; Favre, P.; Schlaepfer, C. W. *J. Organomet. Chem.* **1983**, *253*, 17–30.
72. Albinati, A.; Pregosin, P. S.; Rüegger, H. *Inorg. Chem.* **1984**, *23*, 3223–3229 and references therein.
73. Wrackmeyer, B. In *Advanced Applications of NMR to Organometallic Chemistry*; Gielen, M., Willem, R., Wrackmeyer, B., Eds.; Wiley: Chichester, UK, 1996; pp 87–117.
74. Blumer, R.; Lianza, F.; Pregosin, P. S.; Rüegger, H.; Togni, A. *Inorg. Chem.* **1993**, *32*, 2663–2669.
75. Pregosin, P. S.; Macchioni, A.; Templeton, J. L.; White, P. S.; Feng, S. G. *Magn. Reson. Chem.* **1994**, *32*, 415–421.
76. Macchioni, A.; Pregosin, P. S.; Rüegger, H.; Vankoten, G.; Vanderschaaf, P. A.; Abbenhuis, R. *Magn. Reson. Chem.* **1994**, *32*, 235–241.
77. Macchioni, A.; Pregosin, P. S.; Engel, P. F.; Mecking, S.; Pfeffer, M.; Daran, J. C.; Vaissermann, *J. Organometallics* **1995**, *14*, 1637–1645.
78. Hintermann, S.; Pregosin, P. S.; Rüegger, H.; Clark, H. C. *J. Organomet. Chem.* **1992**, *435*, 225–234.
79. Pregosin, P. S. In *Encyclopedia of Nuclear Magnetic Resonance*; Grant, D. M., Harris, R. K., Eds.; Wiley: Chichester, UK, 1996; Vol. 4, pp 2549–2557.
80. Robert, J. M.; Rabenstein, D. L. *Anal. Chem.* **1991**, *63*, 2674–2679.
81. Wendt, O. F.; Elding, L. I. *J. Chem. Soc., Dalton Trans.* **1997**, 4725–4731 and references therein.
82. Appleton, T. G.; Clark, H. C.; Manzer, L. E. *Coord. Chem. Rev.* **1973**, *10*, 335–422.
83. Barnham, K. J.; Djuran, M. J.; Murdoch, P.; Ranford, J. D.; Sadler, P. J. *Inorg. Chem.* **1996**, *35*, 1065–1072.
84. Berners-Price, S. J.; Sadler, P. J. *Coord. Chem. Rev.* **1996**, *151*, 1–40.
85. Guo, Z.; Sadler, P. J.; Zang, E. *Chem. Comm.* **1997**, 27–28.
86. Barnham, K. J.; Berners-Price, S. J.; Frienkel, T. A.; Frey, U.; Sadler, P. J. *Angew. Chem.* **1995**, *107*, 2040–2043.
87. Kratochwil, N. A.; Parkinson, J. A.; Sacht, C.; Murdoch, P. D.; Brown, T.; Sadler, P. J. *Eur. J. Inorg. Chem.* **2001**, 2743–2746.

88. Murdoch, P. D.; Kratochwil, N. A.; Parkinson, J. A.; Patriarca, M.; Sadler, P. J. *Angew. Chem. Int. Edn. Engl.* **1999**, *38*, 2949–2951.
89. Kratochwil, N. A.; Ivanov, A. I.; Patriarca, M.; Parkinson, J. A.; Gouldsworthy, A. M.; Murdoch, P. D.; Sadler, P. J. *J. Am. Chem. Soc.* **1999**, *121*, 8193–8203.
90. El-Khateeb, M.; Appleton, T. G.; Gahan, L. R.; Charles, B. G.; Berners-Price, S. J.; Bolton, A. M. *J. Inorg. Biochem.* **1999**, *77*, 13–21.
91. Appleton, T. G. *Coord. Chem. Rev.* **1997**, *166*, 313–359.
92. Appleton, T. G.; Barnham, K. J.; Byriel, K. A.; Hall, J. R.; Kennard, C. H. L.; Mathieson, M. T.; Penman, K. G. *Inorg. Chem.* **1995**, *34*, 6040–6052.
93. Appleton, T. G.; Bedgood, D. R.; Hall, J. R. *Inorg. Chem.* **1994**, *33*, 3834–3841.
94. Appleton, T. G.; Byriel, K. A.; Hall, J. R.; Kennard, C. H. L.; Lynch, D. E.; Sinkinson, J. A.; Smith, G. *Inorg. Chem.* **1994**, *33*, 444–455.
95. Qu, Y.; Farrell, N.; Valsecchi, M.; de Greco, L.; Spinelli, S. *Magn. Reson. Chem.* **1993**, *31*, 920–924.
96. Lippert, B. *Coord. Chem. Rev.* **2000**, *200*, 487–516.
97. Reedijk, J. *Chem. Rev.* **1999**, *99*, 2499–2510.
98. Albinati, A.; Lianza, F.; Pregosin, P. S.; Müller, B. *Inorg. Chem.* **1994**, *33*, 2522–2526.
99. Lee, D. H.; Müller, B.; Pregosin, P. S.; Yap, G. P. A.; Rheingold, A. L.; Crabtree, R. H. *Inorg. Chem.* **1995**, *34*, 6295–6301.
100. Mann, B. E. *^{13}C NMR Chemical Shifts and Coupling Constants in Organometallic Compounds: Advances in Organometallic Chemistry*; Academic Press: London, 1974; Vol. 12, p 135.
101. Hung, A. Y. C.; Woolcock, J. C.; Rettig, M. F.; Wing, R. M. *Inorg. Chem.* **1992**, *31*, 810–812.
102. Haynes, A.; Mann, B. E.; Morris, G. E.; Maitlis, P. M. *J. Am. Chem. Soc.* **1993**, *115*, 4093–4100.
103. Roe, C. D.; Sheridan, R. E.; Bunel, E. E. *J. Am. Chem. Soc.* **1994**, *116*, 1163–1164.
104. Pregosin, P. S. In *Annual Reports on NMR Spectroscopy*; Academic Press: London, 1986; Vol. 17, pp 285–349.
105. Pregosin, P. S.; Kunz, R. W. *^{31}P and ^{13}C NMR of Transition Metal Phosphine Complexes*; Springer: Berlin, 1979; Vol. 16.
106. Partridge, M. G.; Messerle, B. A.; Field, L. D. *Organometallics* **1995**, *14*, 3527–3530.
107. Bampos, N.; Messerle, B. A.; Field, L. D. *Organometallics* **1993**, *12*, 2529–2535.
108. Ammann, C.; Pregosin, P. S.; Rüegger, H.; Grassi, M.; Musco, A. *Magn. Reson. Chem.* **1989**, *27*, 355–359.
109. Moriyama, H.; Pregosin, P. S.; Saito, Y.; Yamakawa, T. *J. Chem. Soc., Dalton Trans.* **1984**, 2329–2332.
110. Farkas, E.; Kollar, L.; Moret, M.; Sironi, A. *Organometallics* **1996**, *15*, 1345–1350.
111. Moor, A.; Pregosin, P. S.; Venanzi, L. M. *Inorg. Chim. Acta* **1982**, *61*, 135–140.
112. Moor, A.; Pregosin, P. S.; Venanzi, L. M.; Welch, A *Inorg. Chim. Acta* **1984**, *85*, 103–110.
113. Reinartz, S.; Brookhart, M.; Templeton, J. L. *Organometallics* **2002**, *21*, 247–249.
114. Stengle, T. R.; Langford, C. *Coord. Chem. Rev.* **1967**, *2*, 349–370.
115. Hunt, J. P. *Chem. Rev.* **1971**, *71*, 1–10.
116. Duccomon, Y.; Newman, K. E.; Merbach, A. E. *Inorg. Chem.* **1980**, *19*, 3696–3703.
117. Summers, J. S.; Hoogstraten, C. G.; Britt, D.; Base, K.; Shaw, B. R.; Ribeiro, A. A.; Crumbliss, A. I. *Inorg. Chem.* **2001**, *40*, 6547–6554.
118. Bertini, I.; Luchinat, C. *NMR of Paramagnetic Molecules in Biological Systems* 1986, Benajamin/Cummings: Menlo Park, CA.
119. Bertini, I.; Luchinat, C. *Coord. Chem. Rev.* **1996**, *150*.
120. Sandström, J. *Dynamic NMR Spectroscopy* 1982, Academic Press: London.
121. Jackman, L. M.; Cotton, F. A. *Dynamic Nuclear Magnetic Resonance Spectroscopy* 1975, Academic Press: New York.
122. Cotton, F. A. In *Dynamic Nuclear Magnetic Resonance Spectroscopy*; Jackman, L. M., Cotton, F. A., Eds.; Academic Press: New York, 1975.
123. Jesson, J. P.; Muetterties, E. L. In *Dynamic Nuclear Magnetic Resonance Spectroscopy*; Jackman, L. M., Cotton, F. A., Eds.; Academic Press: New York, 1975.
124. Vrieze, K. In *Dynamic Nuclear Magnetic Resonance Spectroscopy*; Jackman, L. M., Cotton, F. A., Eds.; Academic Press: New York, 1975; pp , 441–488.
125. Faller, J. W. *Determination of Organic Structures by Physical Methods* 1973, *5*, Academic Press: New York.
126. Faller, J. W.; Stokes-Huby, H. L.; Albrizzio, M. A. *Helv. Chim. Acta* **2001**, *84*, 3031–3042.
127. Adams, H.; Agustinho, S. C. M.; Mann, B. E.; Smith, S. *J. Organomet. Chem.* **2000**, *607*, 175–181.
128. Chen, X. T.; Mann, B. E. *J. Chem. Soc., Dalton Trans.* **2000**, 2259–2266.
129. Mann, B. E. *J. Chem. Soc., Dalton Trans.* **1997**, 1457–1471.
130. Chen, X. T.; Mann, B. E. *Organometallics* **1996**, *15*, 3703–3707.
131. Adams, H.; Carr, A. G.; Mann, B. E.; Melling, R. *Polyhedron* **1995**, *14*, 2771–2785.
132. Mann, B. E.; Vargas, M. D.; Khattar, R. *J. Chem. Soc., Dalton Trans.* **1993**, 203–203.
133. Mann, B. E.; Vargas, M. D.; Khadar, R. *J. Chem. Soc., Dalton Trans.* **1992**, 1725–1728.
134. Guillevic, M. A.; Hancox, E. L.; Mann, B. E. *J. Chem. Soc., Dalton Trans.* **1992**, 1729–1733.
135. Ball, G. E.; Mann, B. E. *J. Chem. Soc., Chem. Commun.* **1992**, 561–563.
136. Blazina, D.; Duckett, S. B.; Dyson, P. J.; Johnson, B. F. G.; Lohman, J. A. B.; Sleigh, C. J. *J. Am. Chem. Soc.* **2001**, *123*, 9760–9768.
137. Johnson, B. F. G.; Quadrelli, E. A.; Ferrand, V.; Bott, A. W. *J. Chem. Soc., Dalton Trans.* **2001**, 1063–1068.
138. Johnson, B. F. G. *Coord. Chem. Rev.* **1999**, *192*, 1269–1285 and references therein.
139. Dyson, P. J.; Johnson, B. F. G.; Martin, C. M. *Coord. Chem. Rev.* **1998**, *175*, 59–89 and references therein.
140. Ros, R.; Tassan, A.; Laurenczy, G.; Roulet, R. *Inorg. Chim. Acta* **2000**, *303*, 94–99.
141. Laurenczy, G.; Dellavia, I.; Roulet, R. *ACH-Models Chem.* **1999**, *136*, 317–324.
142. Besancon, K.; Laurenczy, G.; Lumini, T.; Roulet, R.; Bruyndonckx, R.; Daul, C. *Inorg. Chem.* **1998**, *37*, 5634–5640.
143. Lumini, T.; Laurenczy, G.; Roulet, R.; Tassan, A.; Ros, R.; Schenk, K.; Gervasio, G. *Helv. Chim. Acta* **1998**, *81*, 781–791.
144. Laurenczy, G.; Bondietti, G.; Ros, R.; Roulet, R. *Inorg. Chim. Acta* **1996**, *247*, 65–70.
145. Beguin, A.; Dai, M. C.; Laurenczy, G.; Rheinwald, G.; Roulet, R.; Stoeckli-Evans, H.; Suss-Fink, G.; Tabacchi, R. *J. Organomet. Chem.* **1997**, *527*, 167–172.

146. van der Slot, S. C.; Kamer, P. C. J.; van Leeuwen, P. W. N. M.; Heaton, B. T.; Iggo, J. A. *Organometallics* **2001**, *20*, 430–441.
147. Egushi, T.; Heaton, B. T. *J. Chem. Soc., Dalton Trans* **1999**, 3523–3529.
148. Sabounchei, J. S. Z.; Heaton, B. T.; Iggo, J. A.; Jacob, C.; Podkorytov, I. S. *J. Cluster Sci.* **2001**, *12*, 339–349.
149. Takeda, M.; Stejskal, E. O. *J. Am. Chem. Soc.* **1960**, *82*, 25.
150. Neuhaus, D.; Williamson, M. P. *The Nuclear Overhauser Effect in Structural and Conformational Analysis,* 2, 2000, Wiley-VCH, New York.
151. Alessio, E.; Calligaris, M.; Iwamoto, M.; Marzilli, L. G. *Inorg. Chem.* **1996**, *35*, 2538–2545.
152. Pregosin, P. S.; Rüegger, H.; Salzmann, R.; Albinati, A.; Lianza, F.; Kunz, R. W. *Organometallics* **1994**, *13*, 83–90.
153. Pregosin, P. S.; Rüegger, H. *Magn. Reson. Chem.* **1994**, *32*, 297–302.
154. Pregosin, P. S.; Rüegger, H.; Salzmann, R.; Albinati, A.; Lianza, F.; Kunz, R. W. *Organometallics* **1994**, *13*, 5040–5048.
155. Pregosin, P. S.; Salzmann, R. *Coord. Chem. Rev.* **1996**, *155*, 35–68.
156. Pregosin, P. S.; Trabesinger, G. *J. Chem. Soc., Dalton Trans.* **1998**, 727–734.
157. Pregosin, P. S. In *Advances in BioChirality*; Palyi, G., Zucchi, C., Caglioti, L., Eds.; Elsevier: Amsterdam, 1999; pp 335–345.
158. Drago, D.; Pregosin, P. S. *J. Chem. Soc., Dalton Trans.* **2000**, 3191–3196.
159. Geldbach, T. J.; Pregosin, P. S.; Bassetti, M. *Organometallics* **2001**, *20*, 2990–2997.
160. Valentini, M.; Selvakumar, K.; Wörle, M.; Pregosin, P. S. *J. Organomet. Chem.* **1999**, *587*, 244–251.
161. Selvakumar, K.; Valentini, M.; Pregosin, P. S.; Albinati, A. *Organometallics* **1999**, *18*, 4591–4597.
162. Kimmich, B. F. M.; Somsook, E.; Landis, C. R. *J. Am. Chem. Soc.* **1998**, *120*, 10115–10125.
163. Giovanetti, J. S.; Kelly, C. M.; Landis, C. R. *J. Am. Chem. Soc.* **1993**, *115*, 4040–4057.
164. Albinati, A.; Eckert, J.; Pregosin, P.; Rüegger, H.; Salzmann, R.; Stossel, C. *Organometallics* **1997**, *16*, 579–590.
165. Drommi, D.; Nesper, R.; Pregosin, P. S.; Trabesinger, G.; Zurcher, F. *Organometallics* **1997**, *16*, 4268–4275.
166. Albinati, A.; Kunz, R. W.; Ammann, C. J.; Pregosin, P. S. *Organometallics* **1991**, *10*, 1800–1806.
167. Strawcznski, A.; Ros, R.; Roulet, R. *Helv. Chim. Acta* **1988**, *71*, 867–871.
168. Dotta, P.; Anil Kumar, P. G.; Pregosin, P. S. *Magn. Reson. Chem.* **2002**, *40*, 653–658.
169. Romeo, R.; Fenech, L.; Scolaro, L. M.; Albinati, A.; Macchioni, A.; Zuccaccia, C. *Inorg. Chem.* **2001**, *40*, 3293–3302.
170. Drago, D.; Pregosin, P. S.; Pfaltz, A. *Chem. Commun* **2002**, 286–287.
171. Kesanli, B.; Charles, S.; Lam, Y. F.; Bott, S. G.; Fettinger, J.; Eichhorn, B. *J. Am. Chem. Soc.* **2000**, *122*, 11101–11107.
172. Heise, J. D.; Raftery, D.; Breedlove, B. K.; Washington, J.; Kubiak, C. P. *Organometallics* **1998**, *17*, 4461–4468.
173. Bender, B. R.; Koller, M.; Nanz, D.; von Philipsborn, W. *J. Am. Chem. Soc.* **1993**, *115*, 5889–5890.
174. Roe, D. C. *J. Magn. Res.* **1985**, *63*, 388–391.
175. Roe, D. C. *Organometallics* **1987**, *6*, 942–946.
176. Horvath, I. T.; Ponce, E. C. *Rev. Sci. Instrum.* **1991**, *62*, 1104–1105.
177. Helm, L.; Merbach, A. E. *J. Chem. Soc., Dalton Trans.* **2002**, *5*, 633–641.
178. Cusanelli, A.; Frey, U.; Richens, D. T.; Merbach, A. E. *J. Am. Chem. Soc.* **1996**, *118*, 5265–5271.
179. Gaemers, S.; Luyten, H.; Ernsting, J. M.; Elsevier, C. J. *Magn. Reson. Chem.* **1999**, *37*, 25–30.
180. Gillies, D. G.; Sutcliffe, L. H.; Williams, A. J. *Magn. Reson. Chem.* **2002**, *40*, 57–64.
181. Grundler, P. V.; Laurenczy, G.; Merbach, A. E. *Helv. Chim. Acta* **2001**, *84*, 2854–2867.
182. Burai, L.; Toth, E.; Seibig, S.; Scopelliti, R.; Merbach, A. E. *Chem. Eur. J.* **2000**, *6*, 3761–3770.
183. Bugnon, P.; Laurenczy, G.; Ducommun, Y.; Sauvageat, P. Y.; Merbach, A. E.; Ith, R.; Tschanz, R.; Doludda, M.; Bergbauer, R.; Grell, E. *Anal. Chem.* **1996**, *68*, 3045–3049.
184. Toth, E.; Vanthey, S.; Pubanz, D.; Merbach, A. E. *Inorg. Chem.* **1996**, *35*, 3375–3379.
185. Kowall, T.; Foglia, F.; Helm, L.; Merbach, A. E. *Chem. Eur. J.* **1996**, *2*, 285–294.
186. Powell, D. H.; Furrer, P.; Pittet, P. A.; Merbach, A. E. *J. Phys. Chem.* **1995**, *99*, 16622–16629.
187. Dadci, L.; Elias, H.; Frey, U.; Hornig, A.; Koelle, U.; Merbach, A. E.; Paulus, H.; Schneider, J. S. *Inorg. Chem.* **1995**, *34*, 306–315.
188. Gonzalez, G.; Moullet, B.; Martinez, M.; Merbach, A. E. *Inorg. Chem.* **1994**, *33*, 2330–2333.
189. Laurenczy, G.; Bondietti, G.; Merbach, A. E.; Moullet, B.; Roulet, R. *Helv. Chim. Acta* **1994**, *77*, 547–553.
190. Churlaud, R.; Frey, U.; Metz, F.; Merbach, A. E. *Inorg. Chem.* **2000**, *39*, 304–307.
191. Churlaud, R.; Frey, U.; Metz, F.; Merbach, A. E. *Inorg. Chem.* **2000**, *39*, 4137–4142.
192. Olsson, A.; Roodt, A.; Bojczuk, M.; Heaton, B. T.; Elding, L. I. *J. Chem. Soc., Dalton Trans.* **1994**, 3723–3726.
193. Albrecht, M.; Gossage, R. A.; Frey, U.; Ehlers, A. W.; Baerends, E. J.; Merbach, A. E.; van Koten, G. *Inorg. Chem.* **2001**, *40*, 850–855.
194. Aebischer, N.; Frey, U.; Merbach, A. E. *Chem. Commun.* **1998**, 2303–2304.
195. Maltby, P. A.; Schlaf, M.; Steinbeck, M.; Lough, A. J.; Morris, R. H.; Klooster, W. T.; Koetzle, T. F.; Srivastava, R. C. *J. Am. Chem. Soc.* **1996**, *118*, 5396–5407.
196. Shi, T. S.; Elding, L. I. *Inorg. Chem.* **1997**, *36*, 528–536.
197. Gaemers, S.; Elsevier, C. J. *Magn. Reson. Chem.* **2000**, *38*, 650–654.
198. Gaemers, S.; Elsevier, C. J. *Chem. Soc. Rev.* **1999**, *28*, 135–141.
199. Gaemers, S.; Elsevier, C. J.; Bax, A. *Chem. Phys. Lett.* **1999**, *301*, 138–144.
200. Stephan, M.; Kohlmann, O.; Niessen, H. G.; Eichhorn, A.; Bargon, J. *Magn. Reson. Chem.* **2002**, *40*, 157–160.
201. Eichhorn, A.; Koch, A.; Bargon, J. *J. Mol. Catal. A-Chem.* **2001**, *174*, 293–295.
202. Wildschutz, S.; Hubler, P.; Bargon, J. *Chem Phys* **2001**, *2*, 328–331.
203. Heinrich, H.; John, B. D.; Maeda, K. *Pure Appl. Chem.* **2001**, *73*, 343–346.
204. Schleyer, D.; Niessen, H. G.; Bargon, J. *New J. Chem.* **2001**, *25*, 423–426.
205. Koch, A.; Bargon, J. *Inorg. Chem.* **2001**, *40*, 533–539.
206. Giemoth, R.; Heinrich, H.; Adams, N. J.; Deeth, R. J.; Bargon, J.; Brown, J. M. *J. Am. Chem. Soc.* **2000**, *122*, 12381–12382.
207. Hubler, P.; Bargon, J. *Angew. Chem., Int. Ed. Engl.* **2000**, *39*, 3701–3703.
208. Blazina, D.; Duckett, S. B.; Dyson, P. J.; Lohman, J. A. B. *Angew. Chem., Int. Ed. Engl.* **2001**, *40*, 3874.

209. Blazina, D.; Duckett, S. B.; Dyson, P. J.; Johnson, B. F. G.; Lohman, J. A. B.; Sleigh, C. J. *J. Am. Chem. Soc.* **2001**, *123*, 9760–9768.
210. Oldham, S. M.; Houlis, J. F.; Sleigh, C. J.; Duckett, S. B.; Eisenberg, R. *Organometallics* **2000**, *19*, 2985–2993.
211. Colebrooke, S. A.; Duckett, S. B.; Lohman, J. A. B. *Chem. Commun.* **2000**, 685–686.
212. Duckett, S. B.; Kuzmina, L. G.; Nikonov, G. I. *Inorg. Chem. Commun.* **2000**, *3*, 126–128.
213. Morran, P. D.; Duckett, S. B.; Howe, P. R.; McGrady, J. E.; Colebrooke, S. A.; Eisenberg, R.; Partridge, M. G.; Lohman, J. A. B. *J. Chem. Soc., Dalton Trans.* **1999**, 3949–3960.
214. Hasnip, S. K.; Duckett, S. B.; Sleigh, C. J.; Taylor, D. R.; Barlow, G. K.; Taylor, M. J. *Chem. Commun.* **1999**, 1717–1718.
215. Sleigh, C. J.; Duckett, S. B.; Mawby, R. J.; Lowe, J. P. *Chem. Commun.* **1999**, 1223–1224.
216. Hasnip, S. K.; Duckett, S. B.; Taylor, D. R.; Barlow, G. K.; Taylor, M. J. *Chem. Commun.* **1999**, 889–890.
217. Messerle, B. A.; Sleigh, C. J.; Partridge, M. G.; Duckett, S. B. *J. Chem. Soc., Dalton Trans.* **1999**, 1429–1435.
218. Morran, P. D.; Colebrooke, S. A.; Duckett, S. B.; Lohman, J. A. B.; Eisenberg, R. *J. Chem. Soc.-Dalton Trans.* **1998**, 3363–3365.
219. Hasnip, S.; Duckett, S. B.; Taylor, D. R.; Taylor, M. J. *Chem. Commun.* **1998**, 923–924.
220. Duckett, S. B.; Newell, C. L.; Eisenberg, R. *J. Am. Chem. Soc.* **1997**, *119*, 2068–2068.
221. Sleigh, C. J.; Duckett, S. B.; Messerle, B. A. *Chem. Commun.* **1996**, 2395–2396.
222. Heinrich, H.; Giernoth, R.; Bargon, J.; Brown, J. M. *Chem. Commun.* **2001**, 1296–1297.
223. Hinman, J. G.; Abdur-Rashid, K.; Lough, A. J.; Morris, R. H. *Inorg. Chem.* **2001**, *40*, 2480–2481.
224. Rocchini, E.; Rigo, P.; Mezzetti, A.; Stephan, T.; Morris, R. H.; Lough, A. J.; Forde, C. E.; Fong, T. P.; Drouin, S. D. *J. Chem. Soc., Dalton Trans.* **2000**, 3591–3602.
225. Abdur-Rashid, K.; Gusev, D. G.; Lough, A. J.; Morris, R. H. *Organometallics* **2000**, *19*, 1652–1660.
226. Landau, S. E.; Morris, R. H.; Lough, A. J. *Inorg. Chem.* **1999**, *38*, 6060–6068.
227. Fong, T. P.; Forde, C. E.; Lough, A. J.; Morris, R. H.; Rigo, P.; Rocchini, E.; Stephan, T. *J. Chem. Soc.-Dalton Trans.* **1999**, 4475–4486.
228. Bartucz, T. Y.; Golombek, A.; Lough, A. J.; Maltby, P. A.; Morris, R. H.; Ramachandran, R.; Schlaf, M. *Inorg. Chem.* **1998**, *37*, 1555–1562.
229. Forde, C. E.; Landau, S. E.; Morris, R. H. *J. Chem. Soc., Dalton Trans.* **1997**, 1663–1664.
230. Schlaf, M.; Lough, A. J.; Morris, R. H. *Organometallics* **1997**, *16*, 1253–1259.
231. Morris, R. H. *Can. J. Chem.* **1996**, *74*, 1907–1915.
232. Law, J. K.; Mellows, H.; Heinekey, D. M. *J. Am. Chem. Soc.* **2001**, *123*, 2085–2086.
233. Heinekey, D. M.; Mellows, H.; Pratum, T. *J. Am. Chem. Soc.* **2000**, *122*, 6498–6499.
234. Toner, A. J.; Donnadieu, B.; Sabo-Etienne, S.; Chaudret, B.; Sava, X.; Mathey, F.; Floch, P. L. *Inorg. Chem.* **2001**, *40*, 3034–3038.
235. Sabo-Etienne, S.; Rodriguez, V.; Donnadieu, B.; Chaudret, B.; el Makarim, H. A.; Barthelat, J. C.; Ulrich, S.; Limbach, H. H.; Moise, C. *New J. Chem.* **2001**, *25*, 55–62.
236. Atheaux, I.; Donnadieu, B.; Rodriguez, V.; Sabo-Etienne, S.; Chaudret, B.; Hussein, K.; Barthelat, J. C. *J. Am. Chem. Soc.* **2000**, *122*, 5664–5665.
237. Borowski, A. F.; Donnadieu, B.; Daran, J. C.; Sabo-Etienne, S.; Chaudret, B. *Chem. Commun.* **2000**, 543–544.
238. Grundemann, S.; Ulrich, S.; Limbach, H. H.; Golubev, N. S.; Denisov, G. S.; Epstein, L. M.; Sabo-Etienne, S.; Chaudret, B. *Inorg. Chem.* **1999**, *38*, 2550–2551.
239. Sabo-Etienne, S.; Chaudret, B. *Coord. Chem. Rev.* **1998**, *180*, 381–407.
240. Sabo-Etienne, S.; Chaudret, B. *Chem. Rev.* **1998**, *98*, 2077–2091.
241. Peruzzini, M.; Poli, R., Eds. *Recent Advances in Hydride Chemistry* 2001, Elsevier: Amsterdam.
242. Li, S.; Hall, M. B.; Eckert, J.; Jensen, C. M.; Albinati, A. *J. Am. Chem. Soc.* **2000**, *122*, 2903–2910 and references therein.
243. Crabtree, R. H. *Angew. Chem., Int. Ed. Engl.* **1993**, *32*, 789–805.
244. Brookhart, M.; Green, M. L. H. *Progress in Inorganic Chemistry*; Lippard, S. J., Ed.; Wiley Interscience: New York, 1988, Vol. 36, p 1.
245. Carr, N.; Dunne, B. J.; Orpen, A. G.; Spencer, J. L. *J. Chem. Soc, Chem. Commun.* **1988**, 926–928.
246. Bullock, R. M.; Lemke, F. R.; Szalda, D. J. *J. Am. Chem. Soc.* **1990**, *112*, 3244.
247. Kalt, D.; Schubert, U. *Inorg. Chim. Acta* **2000**, *306*, 211–214.
248. Pfeiffer, J.; Kickelbick, G.; Schubert, U. *Organometallics* **2000**, *19*, 62–71 and references therein.
249. Hussein, K.; Marsden, C. J.; Barthelat, J.; Rodriguez, V.; Conejero, S.; Sabo-Etienne, S.; Donnadieu, B.; Chaudret, B. *Chem Comm.* **1999**, 1315–1316.
250. Butts, M.; Bryan, J. C.; Luo, X.; Kubas, G. J. *Inorg. Chem.* **1997**, *36*, 3341–3353.
251. Ledford, J.; Shultz, C. S.; Gates, D. P.; White, P. S.; DeSimone, J. M.; Brookhart, M. *Organometallics* **2001**, *20*, 5266–5276.
252. Shultz, L. H.; Tempel, D. J.; Brookhart, M. *J. Am. Chem. Soc.* **2001**, *123*, 11539–11555.
253. Hii, K. K.; Claridge, T. D. W.; Brown, J. M.; Smith, A.; Deeth, R. J. *Helv. Chim. Acta* **2001**, *84*, 3043–3056.
254. Bau, R.; Mason, S. A.; Patrick, B. O.; Adams, C. S.; Sharp, W. B.; Legzdins, P. *Organometallics* **2001**, *20*, 4492–4501.
255. Nikonov, G. L.; Mountford, P.; Ignatov, S. K.; Green, J. C.; Leech, M. A.; Kuzmina, L. G.; Razuvaev, A. G.; Rees, N. H.; Blake, A. J.; Howard, J. A. K.; Lemenovskii, D. A. *J. Chem. Soc., Dalton Trans.* **2001**, 2903–2915.
256. Shultz, L. H.; Brookhart, M. *Organometallics* **2001**, *20*, 3975–3982.
257. Dias, A. R.; Galvao, A. M.; Galvao, A. C. *J. Organomet. Chem.* **2001**, *632*, 157–163.
258. Gusev, D. G.; Madott, M.; Dolgushin, F. M.; Lyssenko, K. A.; Antipin, M. Y. *Organometallics* **2000**, *19*, 1734–1739.
259. Eppinger, J.; Spiegler, M.; Hieringer, W.; Herrmann, W. A.; Anwander, R. *J. Am. Chem. Soc.* **2000**, *122*, 3080–3096.
260. Schneider, J. J.; Hagen, J.; Czap, N.; Kruger, C.; Mason, S. A.; Bau, R.; Ensling, J.; Gutlich, P.; Wrackmeyer, B. *Chem.-Eur. J.* **2000**, *6*, 625–635.
261. Haaland, A.; Scherer, W.; Volden, H. V.; Verne, H. P.; Gropen, O.; McGrady, G. S.; Downs, A. J.; Dierker, G.; Herrmann, W. A.; Roesky, P. W.; Geisberger, M. R. *Organometallics* **2000**, *19*, 22–29.
262. Traficante, D. D. In *Encyclopedia of Nuclear Magnetic Resonance*; Grant, D. M., Harris, R. K. Eds.; Wiley: Chichester, UK, 1996; pp 3988–4003.

263. Mayne, C. L.; Smith, S. A. In *Encyclopedia of Nuclear Magnetic Resonance*; Grant, D. M., Harris, R. K., Eds.; Wiley: Chichester, UK, 1996; pp 4053–4071.
264. Werbelow, L. G. In *Encyclopedia of Nuclear Magnetic Resonance*; Grant, D. M., Harris, R. K., Eds.; Wiley: Chichester, UK, 1996; pp 4072–4078.
265. Farrar, T. C.; Jablonsky, M. J. *J. Phys. Chem.* **1991**, *95*, 9159–9166.
266. Zuccaccia, C.; Bellachioma, G.; Cardaci, G.; Macchioni, A. *J. Am. Chem. Soc.* **2001**, *123*, 11020–11028.
267. Macchioni, A.; Zuccaccia, C.; Clot, E.; Gruet, K.; Crabtree, R. H. *Organometallics* **2001**, *20*, 2367–2373.
268. Zuccaccia, C.; Bellachioma, G.; Cardaci, G.; Macchioni, A. *Organometallics* **1999**, *18*, 1–3.
269. Macchioni, A.; Bellachioma, G.; Cardaci, G.; Gramlich, V.; Rüegger, H.; Terenzi, S.; Venanzi, L. M. *Organometallics* **1997**, *16*, 2139–2145.
270. Zilm, K. W.; Millar, J. M. *Adv. Magn. Opt. Reson.* **1990**, *15*, 163–200.
271. Hamilton, D. G.; Crabtree, R. H. *J. Am. Chem. Soc.* **1988**, *110*, 4126–4133.
272. Bautista, M. T.; Earl, K. A.; Maltby, P. A.; Morris, R. H.; Schweitzer, C. T.; Sella, A. *J. Am. Chem. Soc.* **1988**, *110*, 7031–7036.
273. Luo, X. L.; Howards, J. A. K.; Crabtree, R. H. *Magn. Reson. Chem.* **1991**, *29*, S89–S93.
274. Nietlisbach, D.; Bakhmutov, V. I.; Berke, H. *J. Am. Chem. Soc.* **1993**, *115*, 9191–9195.
275. Bakhmutov, V. I.; Bertrán, J.; Esteruelas, M. A.; Lledós, A.; Maseras, F.; Modrego, J.; Oro, L. A.; Sola, E. *Chem. Eur. J.* **1996**, *2*, 815–825.
276. Bakhmutov, V. I.; Bianchini, C.; Maseras, F.; Lledos, A.; Peruzzini, M.; Vorontsov, E. V. *Chem. Eur. J.* **1999**, *5*, 3318–3325.
277. Bertini, I.; Luchinat, C.; Parigi, G. In *Current Methods in Inorganic Chemistry*; Vol. 2; Elsevier: Amsterdam, 2001.
278. Belle, C.; Bougault, C.; Averbuch, M. T.; Durif, A.; Pierre, J. L.; Latour, J. M.; Le Pape, L. *J. Am. Chem. Soc.* **2001**, *123*, 8053–8066.
279. Kingry, K. F.; Royer, A. C.; Vincent, J. B. *J. Inorg. Biochem.* **1998**, *72*, 79–88.
280. Ciringh, Y.; Gordon-Wylie, S. W.; Norman, R. E.; Clark, G. R.; Weintraub, S. T.; Horwitz, C. P. *Inorg. Chem.* **1997**, *36*, 4968–4982.
281. Lin, S. K.; Jaun, B. *Helv. Chim. Acta* **1991**, *74*, 1725–1738.
282. Dennison, C.; Berg, A.; de Vries, S.; Canters, G. W. *FEBS Letters* **1996**, *394*, 340–344.
283. Aime, S.; Canton, S.; Geninati Crich, S.; Terreno, E. *Magn. Reson. Chem.* **2002**, *40*, 41–48.
284. Tóth, É.; Burai, L.; Merbach, A. E. *Coord. Chem. Rev.* **2001**, *216–217*, 363–382.
285. Aime, S.; Botta, M.; Geninatti Crich, S.; Giovenzana, G.; Pagliarin, R.; Sisti, M.; Terreno, E. *Magn. Reson. Chem.* **1998**, *36*, S200–S208.
286. Doble, D. M. J.; Botta, M.; Wang, J.; Aime, S.; Barge, A.; Raymond, K. N. *J. Am. Chem. Soc.* **2001**, *123*, 10758–10759.
287. Aime, S.; Botta, M.; Fedeli, F.; Gianolio, E.; Terreno, E.; Anelli, P. *Chem. Eur. J.* **2001**, *7*, 5262–5269.
288. Grutzner, J. B.; Stewart, K. W.; Wasylishen, R. E.; Lumsden, M. D.; Dybowski, C.; Beckmann, P. A. *J. Am. Chem. Soc.* **2001**, *123*, 7094–7100.
289. Colton, R.; D'Agostino, A.; Traeger, J. C. *Mass Spectrom. Rev.* **1995**, *14*, 79–106.
290. Beyer, G. L. In *Physical Methods of Chemistry*; Weissberger, A., Rossiter, B. W., Eds. Wiley: New York, 1971; Vol. 1, p 126.
291. Johnson, C. S., Jr. *Prog. NMR Spectrosc.* **1999**, *34*, 203–256.
292. Stilbs, P. *Prog. NMR Spectrosc.* **1987**, *19*, 1–45.
293. Morris, K. F.; Johnson, C. S., Jr. *J. Am. Chem. Soc.* **1992**, *114*, 3139–3141.
294. Pelta, M. D.; Barjat, H.; Morris, G. A.; Davis, A. L.; Hammond, S. J. *Magn. Reson. Chem.* **1998**, *36*, 706–714.
295. Stejskal, E. O.; Tanner, J. E. *J. Chem. Phys.* **1965**, *42*, 288–292.
296. Stilbs, P. *Anal. Chem.* **1981**, *53*, 2135–2137.
297. van Meerwal, E. E. *Adv. Polym. Sci.* **1984**, *54*, 1–29.
298. Nystrom, B.; Mosley, M. E.; Stilbs, P.; Roots, J. *Polymer* **1981**, *22*, 218–220.
299. Brown, W.; Stilbs, P. *Polymer* **1982**, *23*, 1780–1789.
300. Brown, W.; Stilbs, P. *Polymer* **1982**, *24*, 188–192.
301. Gorman, C. B.; Smith, J. C.; Hager, M. W.; Parkhurst, B. L.; Sierzputowska-Gracz, H.; Haney, C. A. *J. Am. Chem. Soc.* **1999**, *121*, 9958–9966.
302. Ihre, H.; Hult, A.; Soderlind, E. *J. Am. Chem. Soc.* **1996**, *118*, 6388–6395.
303. Newkome, G. R.; Young, J. K.; Baker, G. R.; Potter, R. L.; Audoly, L.; Cooper, D.; Weis, C. D.; Morris, K.; Johnson, C. S. *Macromolecules* **1993**, *26*, 2394–2396.
304. Rietveld, I. B.; Bedeaux, D. *Macromolecules* **2000**, *33*, 7912–7917.
305. van Duijvenbode, R. C.; Rietveld, I. B.; Koper, G. J. M. *Langmuir* **2000**, *16*, 7720–7725.
306. Young, J. K.; Baker, G. R.; Newkome, G. R.; Morris, K. F.; Johnson, C. S. *Macromolecules* **1994**, *27*, 3464–3471.
307. Chien, W. J.; Cheng, S. F.; Chang, D. K. *Anal. Biochem.* **1998**, *264*, 211–215.
308. Liu, M. L.; Toms, H. C.; Hawkes, G. E.; Nicholson, J. K.; Lindon, J. C. *J. Biomol. NMR* **1999**, *13*, 25–30.
309. Park, S.; Johnson, M. E.; Fung, L. W. M. *FEBS Lett.* **2000**, *485*, 81–86.
310. Yao, S. G.; Howlett, G. J.; Norton, R. S. *J. Biomol. NMR* **2000**, *16*, 109–119.
311. Förste, C.; Heink, W.; Kärger, J.; Pfeifer, H.; Feokistova, N. N.; Zhdanov, S. P. *Zeolites* **1989**, *9*, 299–302.
312. Sørland, G. H.; Aksnes, D.; Gjerdåker, L. *J. Magn. Reson.* **1999**, *137*, 397–401.
313. Beck, S.; Geyer, A.; Brintzinger, H. H. *Chem. Commun.* **1999**, 2477–2478.
314. Olenyuk, B.; Levin, M. D.; Whiteford, J. A.; Shield, J. E.; Stang, P. J. *J. Am. Chem. Soc.* **1999**, *121*, 10434–10435.
315. Zuccaccia, C.; Bellachioma, G.; Cardaci, G.; Macchioni, A. *Organometallics* **2000**, *19*, 4663–4665.
316. Valentini, M.; Pregosin, P. S.; Rüegger, H. *J. Chem. Soc., Dalton Trans.* **2000**, 4507–4510.
317. Valentini, M.; Pregosin, P. S.; Rüegger, H. *Organometallics* **2000**, *19*, 2551–2555.
318. Mayzel, O.; Cohen, Y. *J. Chem. Soc., Chem. Commun.* **1994**, 1901–1902.
319. Hoffman, R. E.; Shabtai, E.; Rabinovitz, M.; Iyer, V. S.; Müllen, K.; Rai, A. K.; Bayrd, E.; Scott, L. T. *J. Chem. Soc., Perkin Trans* **1998**, *2*, 1659–1664.
320. Jiang, Q.; Rüegger, H.; Venanzi, M. L. *Inorg. Chim. Acta* **1999**, *290*, 64–79.

321. Pichota, A.; Pregosin, P. S.; Valentini, M.; Wörle, M.; Seebach, D. *Angew. Chem., Int. Ed. Engl.* **2000**, *39*, 153–156.
322. Valentini, M.; Rüegger, H.; Pregosin, P. S. *Helv. Chim. Acta* **2001**, *84*, 2833–2853.
323. Stoop, R. M.; Bachmann, S.; Valentini, M.; Mezzetti, A. *Organometallics* **2000**, *19*, 4117–4126.
324. Schlörer, N. E.; Cabrita, E. J.; Berger, S. *Angew. Chem. Int. Ed.* **2002**, *41*, 107–109.
325. Keresztes, I.; Williard, P. G. *J. Am. Chem. Soc.* **2000**, *122*, 10228–10229.
326. Chen, Y.; Valentini, M.; Pregosin, P. S.; Albinati, A. *Inorg. Chim. Acta* **2002**, *327*, 4–14.
327. Hahn, E. L. *Phys. Rev.* **1950**, *80*, 580–594.
328. Tanner, J. E. *J. Chem. Phys.* **1970**, *52*, 2523.
329. Johnson, C. S.; Jr. In *Nuclear Magnetic Resonance Probes of Molecular Dynamics*; Tycko, R., Ed.; Kluwer Academic: Dordrecht, Netherlands, 1994, p 445.
330. Johnson, C. S.; Jr. In *Encyclopedia of Nuclear Magnetic Resonance*; Grant, D. M., Harris, R. K., Eds.; Wiley: Chichester, UK, 1996; pp 1626–1644.
331. Callaghan, P. T. *Principles of Nuclear Magnetic Resonance Microscopy* 1991, Oxford University Press: Oxford, UK.
332. Kärger, J.; Pfeifer, H.; Heink, W. *Adv. Magn. Reson.* **1988**, *12*, 1–89.
333. Price, W. S. *Concepts Magn. Reson.* **1997**, *9*, 299–336.
334. Price, W. S. *Concepts Magn. Reson.* **1998**, *10*, 197–237.
335. Gibbs, S. J.; Johnson, C. S., Jr. *J. Magn. Reson.* **1991**, *93*, 395–402.
336. Altieri, A. S.; Hinton, D. P.; Byrd, R. A. *J. Am. Chem. Soc.* **1995**, *117*, 7566–7567.
337. Wu, D.; Chen, A.; Johnson, C. S., Jr. *J. Magn. Reson.A* **1995**, *115*, 260–264.
338. Jerschow, A.; Müller, N. *J. Magn. Reson.* **1997**, *125*, 372–375.
339. Schultz, G.; Subbotina, N. Y.; Jensen, C. M.; Golen, J. A.; Hargittai, I. *Inorg. Chim. Acta* **1992**, *191*, 85–90.
340. Bradley, H. B.; Dowell, L. G. *Anal. Chem.* **1958**, *30*, 548–550.
341. Reid, A. F.; Shannon, J. S.; Swan, J. M.; Wailes, P. C. *Aust. J. Chem.* **1965**, *18*, 173–181.
342. Martin, L. L.; Jacobsen, R. A. *Inorg. Chem.* **1971**, *10*, 1795.
343. Caffyn, A. J. M.; Feng, S. G.; Dierdorf, A.; Gamble, A. S.; Eldredge, P. A.; Vossen, M. R.; White, P. S.; Templeton, J. L. *Organometallics* **1991**, *10*, 2842–2848.
344. Guzman-Jimenez, I. Y.; Whitmire, K. H. *Acta Crystallogr.* **1999**, *C55*, IUC9900028.
345. Ferguson, G.; McCrindle, R.; McAlees, A. J.; Perez, M. *Organometallics* **1999**, *18*, 1207–1215.
346. Selvakumar, K.; Valentini, M.; Wörle, M.; Pregosin, P. S. *Organometallics* **1999**, *18*, 1207–1215.
347. Drago, D.; Pregosin, P. S.; Tschoerner, M.; Albinati, A. *J. Chem. Soc., Dalton Trans.* **1999**, 2279–2280.
348. Albinati, A.; Jiang, Q.; Rüegger, H.; Venanzi, L. M. *Inorg. Chem.* **1993**, *32*, 4940–4950.
349. Evans, D. A.; Murry, J. A.; von Matt, P.; Norcross, R. D.; Miller, S. J. *Angew. Chem., Intl. Edn.* **1995**, *34*, 798–800.
350. Lightfoot, A.; Schnider, P.; Pflaltz, A. *Angew. Chem., Intl. Edn.* **1998**, *37*, 2897–2899.
351. Trost, B. M.; Bunt, R. C. *J. Am. Chem. Soc.* **1998**, *120*, 70–79.
352. Ernst, R. R.; Bodenhausen, G.; Wokaun, A. *Principles of Nuclear Magnetic Resonance in One and Two Dimensions* 1987, Clarendon Press: Oxford, UK.
353. Fyfe, C. A. *Solid State NMR for Chemists*; CFC Press, Guelph, ON, Canada 1983.
354. Slichter, C. P. *Principles of Magnetic Resonance*, 2nd edn.; Springer: Berlin, 1978.
355. Mehring, M. *NMR Basic Principles and Progress: High Resolution NMR Spectroscopy in Solids*; Diehl, P., Fluck, E., Kosfeld, R., Eds.; Springer: Berlin, 1983; Vol. 11.
356. Spiess, H. W. *NMR Basic Principles and Progress: Rotation of Molecules and Nuclear Spin Relaxation*; Diehl, P., Fluck, E., Kosfeld, R., Eds.; Springer: Berlin, 1983; Vol. 15, pp 55–214.
357. Vaughan, R. W. *Ann. Rev. Phys. Chem.* **1978**, *29*, 297–419.
358. Mehring, M. In *Encyclopedia of Nuclear Magnetic Resonance*; Grant, D. M., Harris, R. K., Eds.; Wiley: Chichester, UK, 1996; pp 2585–2603.
359. Grant, D. M. In *Encyclopedia of Nuclear Magnetic Resonance*; Grant, D. M., Harris, R. K., Eds.; Wiley: Chichester, UK, 1996; pp 1298–1321.
360. Sherwood, M. H. In *Encyclopedia of Nuclear Magnetic Resonance*; Grant, D. M., Harris, R. K., Eds.; Wiley: Chichester, UK, 1996; pp 1322–1330.
361. Orendt, A. M. In *Encyclopedia of Nuclear Magnetic Resonance*; Grant, D. M., Harris, R. K., Eds.; Wiley: Chichester, UK, 1996; pp 1282–1297.
362. Man, P. P. In *Encyclopedia of Nuclear Magnetic Resonance*; Grant, D. M., Harris, R. K., Eds.; Wiley: Chichester, UK, 1996; pp 3838–3848.
363. Vega, A. J. In *Encyclopedia of Nuclear Magnetic Resonance*; Grant, D. M., Harris, R. K., Eds.; Wiley: Chichester, UK, 1996; pp 3869–3889.
364. Wasylishen, R. E. In *Encyclopedia of Nuclear Magnetic Resonance*; Grant, D. M., Harris, R. K., Eds.; Wiley: Chichester, UK, 1996; pp 1685–1695.
365. Power, W. P.; Wasylishen, R. E. *Ann. Rep. NMR Spectrosc.* **1991**, *23*, 1–84.
366. Gerstein, B. C. In *Encyclopedia of Nuclear Magnetic Resonance*; Grant, D. M., Harris, R. K., Eds.; Wiley: Chichester, UK, 1996; pp 1501–1509.
367. Waugh, J. S.; Huber, L. M.; Haeberlen, U. *Phys. Rev. Lett.* **1968**, *20*, 180–182.
368. Gerstein, B. C.; Pembleton, R. G.; Wilson, R. C.; Ryan, L. M. *J. Chem. Phys.* **1977**, *66*, 361–362.
369. Andrew, E. R. In *Encyclopedia of Nuclear Magnetic Resonance*; Grant, D. M., Harris, R. K., Eds.; Wiley: Chichester, UK, 1996; pp 2891–2901.
370. Wooten, E. W.; Mueller, K. T.; Pines, A. *Acc. Chem. Res.* **1992**, *25*, 209–215.
371. Andrew, E. R.; Bradbury, A.; Eades, R. G. *Nature* **1958**, *182*, 1659.
372. Lowe, I. J. *Phys. Rev. Lett.* **1959**, *2*, 285–287.
373. Blümich, B.; Spiess, H. W. *Angew. Chem., Int.Ed.Engl.* **1988**, *27*, 1655–1672.
374. Wu, Y. In *Encyclopedia of Nuclear Magnetic Resonance*; Grant, D. M., Harris, R. K., Eds.; Wiley: Chichester, UK, 1996; pp 1749–1758.
375. Samoson, A.; Pines, A. *Rev. Sci. Instrum.* **1989**, *60*, 3239–3241.
376. Grandinetti, P. J. In *Encyclopedia of Nuclear Magnetic Resonance*; Grant, D. M., Harris, R. K., Eds.; Wiley: Chichester, UK, 1996; pp 1768–1776.

377. Llor, A.; Virlet, J. *Chem. Phys. Lett.* **1988**, *152*, 248–253.
378. Mueller, K. T.; Sun, B. Q.; Chingas, G. C.; Zwanziger, J. W.; Terao, T.; Pines, A. *J. Magn. Reson.* **1990**, *86*, 470–487.
379. Engelke, F. In *Encyclopedia of Nuclear Magnetic Resonance*; Grant, D. M., Harris, R. K., Eds.; Wiley: Chichester, UK, 1996; pp 1529–1535.
380. Burum, D. P. In *Encyclopedia of Nuclear Magnetic Resonance*; Grant, D. M., Harris, R. K., Eds.; Wiley: Chichester, UK, 1996; pp 1535–1543.
381. Hartmann, S. R.; Hahn, E. L. *Phys. Rev.* **1962**, *128*, 2042–2053.
382. Pines, A.; Gibby, M. G.; Waugh, J. S. *J. Chem. Phys.* **1972**, *56*, 1176.
383. Pines, A.; Gibby, M. G.; Waugh, J. S. *J. Chem. Phys.* **1973**, *59*, 569–590.
384. Davis, J. H.; Jeffrey, K. R.; Bloom, M.; Valic, M. I.; Higgs, T. P. *Chem. Phys. Lett.* **1976**, *42*, 390–394.
385. Larsen, F. H.; Jakobsen, H. J.; Ellis, P. D.; Nielsen, N. C. *Chem. Phys. Lett.* **1998**, *292*, 467–473.
386. Larsen, F. H.; Nielsen, N. C. *J. Phys. Chem. A* **1999**, *103*, 10825–10832.
387. Larsen, F. H.; Skibsted, J.; Jakobsen, H. J.; Nielsen, N. C. *J. Am. Chem. Soc.* **2000**, *122*, 7080–7086.
388. Lefort, R.; Wiench, J. W.; Pruski, M.; Amoureux, J. P. *J. Chem. Phys.* **2002**, *116*, 2493–2501.
389. Frydman, L.; Harwood, J. S. *J. Am. Chem. Soc.* **1995**, *117*, 5367–5368.
390. Baltisberger, J. H.; Xu, Z.; Stebbins, J. F.; Wang, S. H.; Pines, A. *J. Am. Chem. Soc.* **1996**, *118*, 7209–7214.
391. Amoureux, J. P.; Fernandez, C.; Frydman, L. *Chem. Phys. Lett.* **1996**, *259*, 347–355.
392. Amoureux, J. P.; Fernandez, C. *Solid State Nucl. Magn. Reson.* **1998**, *10*, 211–223.
393. Vosegaard, T.; Larsen, F. H.; Jakobsen, H. J.; Ellis, P. D.; Nielsen, N. C. *J. Am. Chem. Soc.* **1997**, *119*, 9055–9056.
394. Hanaya, M.; Harris, R. K. *J. Phys. Chem. A* **1997**, *101*, 6903–6910.
395. Wu, G.; Kroeker, S.; Wasylishen, R. E.; Griffin, R. G. *J. Magn. Reson.* **1997**, *124*, 237–239.
396. Davies, J. A.; Dutremez, S. *Coord. Chem. Rev.* **1992**, *114*, 201–247.
397. Yamasaki, A. *Coord. Chem. Rev.* **1991**, *109*, 107–123.
398. Bowmaker, G. A.; Harris, R. K.; Oh, S. W. *Coord. Chem. Rev.* **1997**, *167*, 49–94.
399. Harris, R. K.; Sebald, A. *Magn. Reson. Chem.* **1987**, *25*, 1058–1062.
400. Darensbourg, D. J.; Wildeson, J. R.; Yarbrough, J. C.; Taylor, R. E. *Inorg. Chem.* **2001**, *40*, 3639–3642.
401. Lipton, A. S.; Mason, S. S.; Myers, S. M.; Reger, D. L.; Ellis, P. D. *Inorg. Chem.* **1996**, *35*, 7111–7117.
402. Reger, D. L.; Myers, S. M.; Mason, S. S.; Darensbourg, D. J.; Holtcamp, M. W.; Reibenspies, J. H.; Lipton, A. S.; Ellis, P. D. *J. Am. Chem. Soc.* **1995**, *117*, 10998–11005.
403. Lipton, A. S.; Mason, S. S.; Reger, D. L.; Ellis, P. D. *J. Am. Chem. Soc.* **1994**, *116*, 10182–10187.
404. Bai, H.; Harris, R. K.; Reuter, H. *J. Organomet. Chem.* **1991**, *408*, 167–172.
405. Cherryman, J. C.; Harris, R. K. *J. Magn. Reson.* **1997**, *128*, 21–29.
406. Harris, R. K.; Lawrence, S. E.; Oh, S. W.; Das, V. G. K. *J. Mol. Struct.* **1995**, *347*, 309–320.
407. Eichler, B. E.; Phillips, B. L.; Power, P. P.; Augustine, M. P. *Inorg. Chem.* **2000**, *39*, 5450–5453.
408. Zilm, K. W.; Lawless, G. A.; Merrill, R. M.; Millar, J. M.; Webb, G. G. *J. Am. Chem. Soc.* **1987**, *109*, 7236–7238.
409. Sparks, S. W.; Ellis, P. D. *J. Am. Chem. Soc.* **1986**, *108*, 3215–3218.
410. Harris, R. K.; Reams, P.; Packer, K. J. *J. Chem. Soc., Dalton Trans.* **1986**, 1015–1020.
411. Hayashi, S.; Hayamizu, K. *Magn. Reson. Chem.* **1992**, *30*, 658–661.
412. Heard, P. J.; Kite, K.; Aliev, A. E. *Polyhedron* **1998**, *17*, 2543–2554.
413. Harris, R. K.; McNaught, I. J.; Reams, P.; Packer, K. J. *Magn. Reson. Chem.* **1991**, *29*, S60–S72.
414. Challoner, R.; Sebald, A. *Solid State Nucl. Magn. Reson.* **1995**, *4*, 39–45.
415. Duer, M. J.; Khan, M. S.; Kakkar, A. K. *Solid State Nucl. Magn. Reson.* **1992**, *1*, 13–16.
416. Bowmaker, G. A.; Harris, R. K.; Apperley, D. C. *Inorg. Chem.* **1999**, *38*, 4956–4962.
417. Bowmaker, G. A.; Churakov, A. V.; Harris, R. K.; Howard, J. A. K.; Apperley, D. C. *Inorg. Chem.* **1998**, *37*, 1734–1743.
418. Bowmaker, G. A.; Churakov, A. V.; Harris, R. K.; Oh, S. W. *J. Organomet. Chem.* **1998**, *550*, 89–99.
419. Santos, R. A. ;. Harbison, G. S. *J. Am. Chem. Soc.* **1994**, *116*, 3075–3077.
420. Harris, R. K.; Kowalewski, J.; Cabral de Menezes, S. *Magn. Reson. Chem.* **1998**, *36*, 145–149.
421. Zilm, K. W.; Conlin, R. T.; Grant, D. M.; Michl, J. *J. Am. Chem. Soc.* **1978**, *100*, 8038–8039.
422. Zilm, K. W.; Conlin, R. T.; Grant, D. M.; Michl, J. *J. Am. Chem. Soc.* **1980**, *102*, 6672–6676.
423. Zilm, K. W.; Beeler, A. J.; Grant, D. M.; Michl, J.; Chou, T. C.; Allred, E. L. *J. Am. Chem. Soc.* **1981**, *103*, 2120–2121.
424. Wi, S.; Frydman, L. *J. Chem. Phys.* **2002**, *116*, 1551–1561.
425. Power, W. P.; Kirby, C. W.; Taylor, N. J. *J. Am. Chem. Soc.* **1998**, *120*, 9428–9434.
426. Larsen, F. H.; Jakobsen, H. J.; Ellis, P. D.; Nielsen, N. C. *J. Phys. Chem. A* **1997**, *101*, 8597–8606.
427. Eichele, K.; Chan, J. C. C.; Wasylishen, R. E.; Britten, J. F. *J. Phys. Chem. A* **1997**, *101*, 5423–5430.
428. Kroeker, S.; Wasylishen, R. E. *Can. J. Chem.* **1999**, *77*, 1962–1972.
429. Wu, G.; Kroeker, S.; Wasylishen, R. E. *Inorg. Chem.* **1995**, 34, 1595–1598.
430. Larsen, F. H.; Lipton, A. S.; Jakobsen, H. J.; Nielsen, N. C.; Ellis, P. D. *J. Am. Chem. Soc.* **1999**, *121*, 3783–3784.
431. Eichele, K.; Wasylishen, R. E.; Nelson, J. H. *J. Phys. Chem. A* **1997**, *101*, 5463–5468.
432. Vosegaard, T.; Skibsted, J.; Jakobsen, H. J. *J. Phys. Chem. A* **1999**, *103*, 9144–9149.
433. Bryce, D. L.; Wasylishen, R. E. *J. Phys. Chem. A* **1999**, *103*, 7364–7372.
434. Schurko, R. W.; Wasylishen, R. E.; Foerster, H. *J. Phys. Chem. A* **1998**, *102*, 9750–9760.
435. Nielsen, U. G.; Jakobsen, H. J.; Skibsted, J. *Inorg. Chem.* **2000**, *39*, 2135–2145.
436. Skibsted, J.; Jacobsen, C. J. H.; Jakobsen, H. J. *Inorg. Chem.* **1998**, *37*, 3083–3092.
437. Schurko, R. W.; Wasylishen, R. E.; Phillips, A. D. *J. Magn. Reson.* **1998**, *133*, 338–394.
438. Kroeker, S.; Eichele, K.; Wasylishen, R. E.; Britten, J. F. *J. Phys. Chem. B* **1997**, *101*, 3727–3733.
439. Bryce, D. L.; Wasylishen, R. E.; Gee, M. *J. Phys. Chem. A* **2001**, *105*, 3633–3640.
440. Zilm, K. W.; Merrill, R. A.; Kummer, M. W.; Kubas, G. J. *J. Am. Chem. Soc.* **1986**, *108*, 7837–7839.
441. King, W. A.; Luo, X. L.; Scott, B. L.; Kubas, G. J.; Zilm, K. W. *J. Am. Chem. Soc.* **1996**, *118*, 6782–6783.
442. Facey, G.; Gusev, D.; Morris, R. H.; Macholl, S.; Buntkowsky, G. *Phys. Chem. Chem. Phys.* **2000**, *2*, 935–941.
443. Kubas, G. J.; Unkefer, C. J.; Swanson, B. I.; Fukushima, E. *J. Am. Chem. Soc.* **1986**, *108*, 7000–7009.
444. Wehrmann, F.; Fong, T. P.; Morrism, R. H.; Limbach, H. H.; Buntkowsky, G. *Phys. Chem. Chem. Phys.* **1999**, *1*, 4033–4041.

445. Buntkowsky, G.; Limbach, H. H.; Wehrmann, F.; Sack, I.; Vieth, H. M.; Morris, R. H. *J. Phys. Chem. A* **1997**, *101*, 4679–4689.
446. Bernard, G. M.; Wasylishen, R. E.; Phillips, A. D. *J. Phys. Chem. A* **2000**, *104*, 8131–8141.
447. Ritleng, V.; Bertani, P.; Pfeffer, M.; Sirlin, C.; Hirschinger, J. *Inorg. Chem.* **2001**, 40 5117–5122.
448. Aime, S.; Botta, M.; Gobetto, R.; Osella, D.; Milone, L. *Inorg. Chim. Acta* **1988**, *146*, 151–152.
449. Hanson, B. E.; Lisic, E. C.; Petty, J. T.; Iannacone, G. I. *Inorg. Chem.* **1986**, *25*, 4062–4064.
450. Oldfield, E.; Keniry, M. A.; Shinoda, S.; Schramm, S.; Brown, T. L.; Gutowsky, H. S. *J. Chem. Soc., Chem. Commun.* **1985**, 791–793.
451. Bodenbinder, M.; Balzer-Jöllenbeck, G.; Willner, H.; Batchelor, R. J.; Einstein, F. W. B.; Wang, C.; Aubke, F. *Inorg. Chem.* **1996**, *35*, 82–92.
452. Bernhardt, E.; Willner, H.; Jonas, V.; Thiel, W.; Aubke, F. *Angew. Chem. Intl. Edn. Engl.* **2000**, *39*, 168–171.
453. Willner, H.; Bodenbinder, M.; Bröchler, R.; Hwang, G.; Rettig, S. J.; Trotter, J.; von Ahsen, B.; Westphal, U.; Jonas, V.; Thiel, W.; Aubke, F. *J. Am. Chem. Soc.* **2001**, *123*, 588–602.
454. Walter, T. H.; Reven, L.; Oldfield, E. *J. Phys. Chem.* **1989**, *93*, 1320–1326.
455. Salzmann, R.; Kaupp, M.; McMahon, M. T.; Oldfield, E. *J. Am. Chem. Soc.* **1998**, *120*, 4771–4783.
456. McMahon, M. T.; deDios, A. C.; Godbout, N.; Salzmann, R.; Laws, D. D.; Le, H.; Havlin, R. H.; Oldfield, E. *J. Am. Chem. Soc.* **1998**, *120*, 4784–4797.
457. Salzmann, R.; Ziegler, C. J.; Godbout, N.; McMahon, M. T.; Suslick, K. S.; Oldfield, E. *J. Am. Chem. Soc.* **1998**, *120*, 11323–11334.
458. Salzmann, R.; McMahon, M. T.; Godbout, N.; Sanders, L. K.; Wojdelski, M.; Oldfield, E. *J. Am. Chem. Soc.* **1999**, *121*, 3818–3828.
459. Gerothanassis, I. P.; Momenteau, M.; Barrie, P. J.; Kalodimos, C.; Hawkes, G. E. *Inorg. Chem.* **1996**, *35*, 2674–2679.
460. Kroeker, S.; Wasylishen, R. E.; Hanna, J. V. *J. Am. Chem. Soc.* **1999**, *121*, 1582–1590.
461. Curtis, R. D.; Ratcliffe, C. I.; Ripmeester, J. A. *J. Chem. Soc., Chem. Commun.* **1992**, 1800–1802.
462. Schütze, J. U.; Eckhardt, R.; Fischer, R. D.; Apperley, D. C.; Davies, N. A.; Harris, R. K. *J. Organomet. Chem.* **1997**, *534*, 187–194.
463. Brimah, A. K.; Siebel, E.; Fischer, R. D.; Davies, N. A.; Apperley, D. C.; Harris, R. K. *J. Organomet. Chem.* **1994**, *475*, 85–94.
464. Kim, A. J.; Butler, L. G. *Inorg. Chem.* **1993**, 32, 178–181.
465. Ding, S.; Jones, N. D.; McDowell, C. A. *Solid State Nucl. Magn. Reson.* **1998**, *10*, 205–210.
466. Gay, I. D.; Young, C. B. *Organometallics* **1996**, *15*, 2264–2269.
467. Benn, R.; Grondey, H.; Lehmkuhl, H.; Nehl, H.; Agermund, K.; Krüger, C. *Angew. Chem. Intl. Edn. Engl.* **1987**, *26*, 1279–1280.
468. Havlin, R.; McMahon, M.; Srinivasan, R.; Le, H.; Oldfield, E. *J. Phys. Chem. A* **1997**, *101*, 8908–8913.
469. Bernard, G. M.; Wu, G.; Wasylishen, R. E. *J. Phys. Chem. A* **1998**, *102*, 3184–3192.
470. Wemmer, D. E.; Pines, A. *J. Am. Chem. Soc.* **1981**, *103*, 34–36.
471. Wemmer, D. E.; Ruben, D. J.; Pines, A. *J. Am. Chem. Soc.* **1981**, *103*, 28–33.
472. Heise, H.; Köhler, F. H.; Brouwer, E. B.; Harris, R. K.; Steuernagel, S. *Magn. Reson. Chem.* **1999**, *37*, 573–578.
473. Blümel, J.; Herker, M.; Hiller, W.; Köhler, F. H. *Organometallics* **1996**, *15*, 3474–3476.
474. Pietrass, T. ;.Burkert, P. K. *Inorg. Chim. Acta* **1993**, *207*, 253–254.
475. Nishikiori, S.; Ratcliffe, C. I.; Ripmeester, J. A. *J. Chem. Soc., Chem. Commun.* **1991**, 735–736.
476. Santos, R. A.; Chien, W. J.; Harbison, G. S.; McCurry, J. D.; Roberts, J. E. *J. Magn. Reson.* **1989**, *84*, 357–360.
477. Austin, E. J. W.; Barrie, P. J.; Clark, R. J. H. *Inorg. Chem.* **1992**, *31*, 4281–4285.
478. Barrie, P. J.; Austin, E. J. W.; Barbieri, A.; Clark, R. J. H. *Inorg. Chim. Acta* **1997**, *264*, 81–88.
479. Schurko, R. W.; Wasylishen, R. E. *J. Phys. Chem. A* **2000**, *104*, 3410–3420.
480. Salzmann, R.; Wojdelski, M.; McMahon, M.; Havlin, R. H.; Oldfield, E. *J. Am. Chem. Soc.* **1998**, *120*, 1349–1356.
481. Godbout, N.; Sanders, L. K.; Salzmann, R.; Havlin, R. H.; Wojdelski, M.; Oldfield, E. *J. Am. Chem. Soc.* **1999**, *121*, 3829–3844.
482. Riou, D.; Taulelle, F.; Férey, G. *Inorg. Chem.* **1996**, *35*, 6392–6395.
483. Davies, J. A.; Dutremez, S. *Coord. Chem. Rev.* **1992**, *114*, 61–103.
484. Nelson, J. H.; Rahn, J. A.; Bearden, W. H. *Inorg. Chem.* **1987**, *26*, 2192–2193.
485. Rahn, J. A.; O'Donnell, D. J.; Palmer, A. R.; Nelson, J. H. *Inorg. Chem.* **1989**, *28*, 2631–2635.
486. Rahn, J. A.; Baltusis, L.; Nelson, J. H. *Inorg. Chem.* **1990**, *29*, 750–755.
487. Bowmaker, G. A.; Clase, H. J.; Alcock, N. W.; Kessler, J. M.; Nelson, J. H.; Frye, J. S. *Inorg. Chim. Acta* **1993**, *210*, 107–124.
488. Thomaier, J.; Boulmaâz, S.; Schönberg, H.; Rüegger, H.; Currao, A.; Grützmacher, H.; Hillebrecht, H.; Pritzkow, H. *New J. Chem.* **1998**, 947–958.
489. van der Knaap, T. A.; Bickelhaupt, F.; Kraaykamp, J. G.; van Koten, G.; Bernards, J. P. C.; Edzes, H. T.; Veeman, W. S.; de Boer, E.; Baerends, E. J. *Organometallics* **1984**, *3*, 1804–1811.
490. Kroto, H. W.; Klein, S. I.; Meidine, M. F.; Nixon, J. F.; Harris, R. K.; Packer, K. J.; Reams, P. *J. Organomet. Chem.* **1985**, *280*, 281–287.
491. van der Knaap, T. A.; Bickelhaupt, F.; van der Poel, H.; van Koten, G.; Stam, C. H. *J. Am. Chem. Soc.* **1982**, *104*, 1756–1757.
492. Leoni, P.; Pasquali, M.; Sommovigo, M.; Laschi, F.; Zanello, P.; Albinati, A.; Lianza, F.; Pregosin, P. S.; Rüegger, H. *Organometallics* **1993**, *12*, 1702–1713.
493. Albinati, A.; Lianza, F.; Pasquali, M.; Sommovigo, M.; Leoni, P.; Pregosin, P. S.; Rüegger, H. *Inorg. Chem.* **1991**, *30*, 4690–4692.
494. Challoner, R.; Nakai, T.; McDowell, C. A. *J. Chem. Phys.* **1991**, *94*, 7038–7045.
495. Klaus, E.; Sebald, A. *Angew. Chem. Int. Edn. Engl.* **1995**, *34*, 667–669.
496. Lindner, E.; Fawzi, R.; Mayer, H. A.; Eichele, K.; Hiller, W. *Organometallics* **1992**, *11*, 1033–1043.
497. Lumsden, M. D.; Eichele, K.; Wasylishen, R. E.; Cameron, T. S.; Britten, J. F. *J. Am. Chem. Soc.* **1994**, *116*, 11129–11136.
498. Power, W. P.; Lumsden, M. D.; Wasylishen, R. E. *Inorg. Chem.* **1991**, *30*, 2997–3002.

499. Power, W. P.; Lumsden, M. D.; Wasylishen, R. E. *J. Am. Chem. Soc.* **1991**, *113*, 8257–8262.
500. Gobetto, R.; Harris, R. K.; Apperley, D. C. *J. Magn. Reson.* **1992**, *96*, 119–130.
501. Lindner, E.; Fawzi, R.; Mayer, H. A.; Eichele, K.; Pohmer, K. *Inorg. Chem.* **1991**, *30*, 1102–1107.
502. Christendat, D.; Markwell, R. D.; Gilson, D. F. R.; Butler, I. S.; Cotton, J. D. *Inorg. Chem.* **1997**, *36*, 230–235.
503. Schurko, R. W.; Wasylishen, R. E.; Moore, S. J.; Marzilli, L. G.; Nelson, J. H. *Can. J. Chem.* **1999**, *77*, 1973–1983.
504. Menger, E. M.; Veeman, W. S. *J. Magn. Reson.* **1982**, *46*, 257–268.
505. Diesveld, J. W.; Menger, E. M.; Edzes, H. T.; Veeman, W. S. *J. Am. Chem. Soc.* **1980**, *102*, 7936–7937.
506. Barron, P. E.; Dyason, J. C.; Engelhardt, L. M.; Healy, P. C.; White, A. H. *Inorg. Chem.* **1984**, *23*, 3766–3769.
507. Bowmaker, G. A.; Cotton, J. D.; Healy, P. C.; Kildea, J. D.; Silong, S. B.; Skelton, B. W.; White, A. H. *Inorg. Chem.* **1989**, *28*, 1462–1466.
508. Attar, S.; Bowmaker, G. A.; Alcock, N. W.; Frye, J. S.; Bearden, W. H.; Nelson, J. H. *Inorg. Chem.* **1991**, *30*, 4743–4753.
509. Olivieri, A. *J. Am. Chem. Soc.* **1992**, *114*, 5758–5763.
510. Asaro, F.; Camus, A.; Gobetto, R.; Olivieri, A. C.; Pellizer, G. *Solid State Nucl. Magn. Reson.* **1997**, *8*, 81–88.
511. Kroeker, S.; Hanna, J. V.; Wasylishen, R. E.; Ainscough, E. W.; M. Brodie, A. *J. Magn. Reson.* **1998**, *135*, 208–215.
512. Gibson, V. C.; Gobetto, R.; Harris, R. K.; Langdale-Brown, C.; Siemeling, U. *J. Organomet. Chem.* **1994**, *479*, 207–211.
513. Eichele, K.; Wasylishen, R. E.; Maitra, K.; Nelson, J. H.; Britten, J. F. *Inorg. Chem.* **1997**, *36*, 3539–3544.
514. Eichele, K.; Wasylishen, R. E.; Corrigan, J. F.; Doherty, S.; Sun, Y.; Carty, A. J. *Inorg. Chem.* **1993**, *32*, 121–123.
515. Rüegger, H. unpublished results.
516. Wasylishen, R. E.; Wright, K. C.; Eichele, K.; Cameron, T. S. *Inorg. Chem.* **1994**, *33*, 407–408.
517. Harris, R. K.; Olivieri, A. C. *Prog. Nucl. Magn. Reson. Spectrosc.* **1992**, *24*, 435–456.
518. Olivieri, A. C. *J. Magn. Reson.* **1989**, *81*, 201–205.
519. Alarcón, S. H.; Olivieri, A. C.; Harris, R. K. *Solid State Nucl. Magn. Reson.* **1993**, *2*, 325–334.
520. Ding, S.; McDowell, C. A. *J. Chem. Phys.* **1997**, *107*, 7762–7772.
521. Bemi, L.; Clark, H. C.; Davies, J. A.; Fyfe, C. A.; Wasylishen, R. E. *J. Am. Chem. Soc.* **1982**, *104*, 438–445.
522. Bemi, L.; Clark, H. C.; Davies, J. A.; Drexler, D.; Fyfe, C. A.; Wasylishen, R. E. *J. Organomet. Chem.* **1982**, *224*, C5–C9.
523. Clark, H. C.; Davies, J. A.; Fyfe, C. A.; Hayes, P. J.; Wasylishen, R. E. *Organometallics* **1983**, *2*, 177–180.
524. Fyfe, C. A.; Clark, H. C.; Davies, J. A.; Hayes, P. J.; Wasylishen, R. E. *J. Am. Chem. Soc.* **1983**, *105*, 6577–6584.
525. Blümel, J. *Inorg. Chem.* **1994**, *33*, 5050–5056.
526. Behringer, K. D.; Blümel, J. *Inorg. Chem.* **1996**, *35*, 1814–1819.
527. Lindner, E.; Jäger, A.; Kemmler, M.; Auer, F.; Wegner, P.; Mayer, H. A.; Benez, A.; Plies, E. *Inorg. Chem.* **1997**, *36*, 862–866.
528. Benn, R.; Grondey, H.; Brevard, C.; Pagelot, A. *J. Chem. Soc., Chem.Commun.* **1988**, 102–103.
529. Allman, T. *J. Magn. Reson.* **1989**, *83*, 637–642.
530. Han, X.; Rüegger, H.; Sonderegger, J. *Chin. Sci. Bull.* **1991**, *36*, 382–386.
531. Wu, G.; Wasylishen, R. E. *Organometallics* **1992**, *11*, 3242–3248.
532. Albinati, A.; Jiang, Q.; Rüegger, H.; Venanzi, L. M. *Inorg. Chem.* **1993**, *32*, 4940–4950.
533. Rocchini, E.; Mezzetti, A.; Rüegger, H.; Burckhardt, U.; Gramlich, V.; del Zotto, A.; Martinuzzi, P.; Rigo, P. *Inorg. Chem.* **1997**, *36*, 711–720.
534. Eichele, K.; Ossenkamp, G. C.; Wasylishen, R. E.; Cameron, T. S. *Inorg. Chem.* **1999**, *38*, 639–651.
535. Wu, G.; Wasylishen, R. E. *Inorg. Chem.* **1992**, *31*, 145–148.
536. Wu, G.; Wasylishen, R. E. *Inorg. Chem.* **1996**, *35*, 3113–3116.
537. Schlager, F.; Haack, K. J.; Mynott, R.; Rufinska, A.; Pörschke, K. R. *Organometallics* **1998**, *17*, 807–814.

Comprehensive Coordination Chemistry II
ISBN (set): 0-08-0437486

Volume 2, (ISBN 0-08-0443249); pp 1–35

2.2
Electron Paramagnetic Resonance Spectroscopy

G. R. EATON and S. S. EATON
University of Denver, Colorado, USA

2.2.1 INTRODUCTION 37
2.2.2 EPR PARAMETERS AND THEIR INTERPRETATION 38
2.2.2.1 g Values 38
2.2.2.2 A Values 39
2.2.2.3 Temperature Dependence 39
2.2.2.4 Electron Spin Relaxation Times 39
2.2.2.5 Phase of Sample 39
2.2.3 SELECTION OF MICROWAVE FREQUENCY 40
2.2.4 CONTINUOUS WAVE VS. PULSED EXPERIMENTS 40
2.2.5 SPECTRA OF $Cu(DTC)_2$ 40
2.2.5.1 Single Crystal 40
2.2.5.2 Powder Spectra 42
2.2.5.3 Line Widths 42
2.2.5.4 Fluid Solution 43
2.2.5.5 Electron Spin Relaxation Times 44
2.2.6 BIOINORGANIC EXAMPLES 46
2.2.6.1 Blue Copper Model Complexes for Cu^{II}-thiolate Complexes and Fungal Laccase 46
2.2.6.2 Dinuclear Cu_A Site in Cytochrome C Oxidase and Nitrous Oxide Reductase 46
2.2.6.3 Oxygen-evolving Complex in Photosystem II 47
2.2.7 SUMMARY 47
2.2.8 REFERENCES 47

2.2.1 INTRODUCTION

Electron paramagnetic resonance (EPR) spectroscopy, also called electron spin resonance (ESR) or electron magnetic resonance (EMR) measures the absorption of microwaves by paramagnetic centers with one or more unpaired electrons.[1–5] A single unpaired electron ($S = 1/2$) can have two possible spin states, $m_s = \pm 1/2$, that are degenerate in the absence of an external magnetic field. In the presence of a magnetic field the degeneracy is lifted, and transitions can be caused to occur by supplying energy. When the energy of the microwave photons equals the separation between the spin energy levels, the system is said to be at "resonance," and there is absorption of energy by the sample. The energies for the transitions are determined by the type of paramagnetic center and are influenced by interactions with neighboring nuclei with $I > 0$ and with other unpaired electrons. The focus of this section is on samples in which the distance between paramagnetic centers is long enough that the sample can be regarded as magnetically dilute, i.e., the spectra are dominated by features of the individual centers or pairs of centers, rather than the interaction between large numbers of paramagnetic centers. In magnetically concentrated samples information can be obtained about the spin state of the metal ion, and about the strength of magnetic

interaction between the centers, but little information usually can be obtained about the g and A values that are described in the following paragraphs.

EPR spectra of magnetically dilute samples are described by a phenomenological spin Hamiltonian:

$$\hat{H} = \beta_e g \cdot B \cdot \hat{S} + \sum_i A_i \cdot \hat{I} \cdot \hat{S} \quad (1)$$

where β_e is the electron Bohr magneton, $\hat{S}$ and $\hat{I}$ are the electron and nuclear spin operators, respectively, and g and A are 3×3 matrices that define the anisotropic (orientation-dependent) interaction of the unpaired electron with the external magnetic field, B, and with nuclear spins, respectively. The g values determine the magnetic field for the center of the spectrum at a particular orientation of the molecule with respect to the magnetic field. The interaction with nuclear spins is called hyperfine interaction and causes splittings of the EPR signal. The summation in Equation (1) reflects the fact that there is a hyperfine term for each set of inequivalent nuclear spins. For some spectra it is possible to estimate g and A values by inspection, but computer simulation of the spectra usually is required to obtain precise values. When an axis system is selected in which the g and A matrices are diagonal, the elements of the g and A matrices are called the principal values. These axes are the magnetic axes for the paramagnetic center, and may not coincide with bond axes of the molecule. For metal ions with more than one unpaired electron there is an additional term in the Hamiltonian, $\hat{S} \cdot D \cdot \hat{S}$, where D is the zero-field splitting matrix, which describes the electron–electron interaction.

2.2.2 EPR PARAMETERS AND THEIR INTERPRETATION

The observation of an EPR signal can be an important test of the oxidation state of a metal ion because no signal is observed for diamagnetic metal ions. Thus, for example, there is no EPR signal for Cu^{I} or for low-spin Fe^{II}. For metals with $S = 1/2$, such as Cu^{II}, Cr^{V}, or vanadyl ion, EPR spectra can be seen at room temperature for many geometries and coordination environments. For some electron configurations (such a low-spin Fe^{III}) or geometries, relaxation times are shorter and lower temperatures are required for detection of the EPR signal. For metals with $S > 1/2$, the EPR signal is strongly dependent on the magnitude of the zero-field splitting relative to the EPR quantum, $h\nu$. For metals with $S = 3/2$ or 5/2, transitions between levels with $m_s = \pm 1/2$ can be observed even if the zero-field splitting is large, although cryogenic temperatures may be required because of faster spin lattice relaxation for these metal ions than for ones with $S = 1/2$. For metal ions with an even number of unpaired electrons and large zero-field splittings, many or all of the transition energies may be too large or too orientation dependent to observe a spectrum in powder samples, although signals may be observed for selected orientations of single crystals. As discussed in Section 2.2.3, higher microwave frequencies and magnetic fields make it possible to study spectra from metals with larger zero-field splitting than can be observed at X-band (ca. 9.5 GHz).

Spin quantitation is a key part of the EPR signal characterization.[3] EPR spectroscopy is sufficiently sensitive that signals can sometimes be observed from species that constitute only a small fraction of the potentially paramagnetic centers. For an $S = 1/2$ metal ion the double integral of the first-derivative EPR signal is proportional to the number of spins in the sample. Comparison with a spin standard can then be used to determine the spin concentration for the species of interest. Quantitation is more difficult for metal ions with $S > 1/2$ and zero-field splitting greater than the EPR quantum, because only some of the transitions may be observable for a particular microwave frequency.[6]

2.2.2.1 g Values

The g value for the free electron is 2.0023. Spin–orbit coupling results in g values for metal ions that are substantially different from the free electron value. The g values are characteristic of the electronic structure, local symmetry, and often the coordination environment. Thus, g values are powerful tools for characterization of metal complexes.[2,4,5]

2.2.2.2 A Values

The hyperfine splitting pattern in an EPR spectrum reflects the interaction of the unpaired electron with nuclear spins. The number of hyperfine lines equals $2nI+1$, where n is the number of equivalent nuclei and I is the nuclear spin. Spectra due to certain metal ions are readily recognized because of characteristic numbers of lines that arise from coupling to the metal nuclear spin: for example, vanadium (99.75% $I=7/2$), chromium (9.5% $I=3/2$, other isotopes have $I=0$), manganese (100% $I=5/2$), cobalt (100% $I=7/2$), copper (69.2% ^{63}Cu $I=3/2$ and 30.8% ^{65}Cu $I=3/2$), and molybdenum (15.9% ^{95}Mo $I=3/2$, 9.6% ^{97}Mo $I=3/2$, other isotopes have $I=0$). The magnitude of the hyperfine coupling to the metal nuclear spin is proportional to the electron spin density on the metal.

Hyperfine splitting due to interaction with ligand nuclei with $I>0$ reflects the extent of spin delocalization onto neighboring atoms and can be used to characterize the types and numbers of such nuclei. In cases where these couplings are too small to be resolved in the EPR spectra, electron nuclear double resonance (ENDOR) or electron spin echo envelope modulation (ESEEM) can be used to measure the couplings as discussed in Chapter 2.3. Modern calculational tools are approaching the capabilities required to calculate g and A values from electronic wave functions.[7,8] However, much of the spectroscopy that has been performed to date has used empirical correlations to interpret g and A values.

2.2.2.3 Temperature Dependence

For some metal ions, such as high-spin Co^{II} ($S=3/2$)[9] or iron–sulfur clusters,[10] the electron spin relaxation time is strongly temperature dependent. If the relaxation time becomes too short, then the signal becomes so broad that the signal is essentially undetectable. For many high-spin Co^{II} complexes and iron–sulfur clusters, detection of an EPR signal requires temperatures in the liquid helium range.

For spin-coupled systems the EPR spectrum may be temperature dependent due to temperature-dependent populations of excited states. For example, in strongly antiferromagnetically coupled copper(II) dimers, there is no EPR signal at low temperatures, but a characteristic triplet ($S=1$) signal grows in as the temperature is increased due to thermal population of the excited state.[11]

Dynamic processes that interconvert conformations of a metal complex can be detected by EPR if the rate of the process is comparable to separations between peaks in the EPR spectrum.[12] For splittings on the order of a few milliteslas (tens of MHz) that timescale corresponds to rates on the order of 10^7 to $10^8\,s^{-1}$, which is significantly faster than the NMR timescale.

2.2.2.4 Electron Spin Relaxation Times

Electron spin relaxation times reflect both intramolecular and intermolecular dynamic processes. In favorable cases relaxation times can be estimated from progressive power-saturation measurements, but more accurate values can be obtained by pulsed time domain techniques.[13] For metal ions with low-lying excited states the temperature dependence of relaxation times can be used to determine the energy of the excited state.[9]

2.2.2.5 Phase of Sample

EPR spectra can be observed in gas, liquid, or solid phases. Interpretation of gas-phase EPR spectra is complicated by coupling between the spin angular momentum and rotational angular momentum and has not been used for transition metal complexes. For small metal complexes in fluid solution, the rate of tumbling typically is fast enough to largely average the g and A anisotropy, and the spectra are described by the isotropic averages of the g and A values: $g_{iso}=(g_x+g_y+g_z)/3$ and $A_{iso}=(A_x+A_y+A_z)/3$. For metal ions with significant g and/or A anisotropy, line shapes in fluid solution often are strongly dependent on the rate of tumbling. When a metal complex is immobilized, either by freezing a solution or by doping into a diamagnetic host, the resulting sample contains a random distribution of orientations of the metal ion with respect to the external magnetic field. Analysis of the spectra usually can provide the three principal components of the g matrix and the principal components of resolved

hyperfine splittings. To fully characterize g and A matrices and the orientations of the principal axes of the matrices with respect to the molecular axes requires spectra from a doped single crystal as a function of orientation of the crystal with respect to the magnetic field.[1]

2.2.3 SELECTION OF MICROWAVE FREQUENCY

Historically, the vast majority of EPR experiments have been performed at a microwave frequency between about 9 and 9.5 GHz, which falls in the range that is called X-band. At this microwave frequency the free electron g value corresponds to a resonant field of about 3,300 G (330 mT). Relatively recently, commercially available spectrometers have become available over a widening range of frequencies: currently about 1 GHz (L-band) to 95 GHz (W-band). It now becomes important to consider what EPR frequency is optimum to answer a particular question. For some questions, the clearest answers are obtained by comparing spectra as a function of microwave frequency.[14]

As the magnetic field is increased, the separation of features in the spectra that arise from g value differences becomes larger.[15] For example, the 10-fold increase in microwave frequency from 9.5 to 95 GHz results in a 10-fold increase in separations of features in the spectra that arise from g anisotropy. Resolution of these features may be key to determining whether the effective symmetry at a metal site is axial or rhombic. When the zero-field splitting for metal ions with $S > 1/2$ is greater than the EPR quantum ($h\nu$) the energies for some transitions may be too large to detect. By increasing the microwave frequency, higher energy transitions become accessible, so higher microwave frequencies and the corresponding high magnetic field strengths are particularly useful for metal ions with $S > 1/2$ and large zero-field splittings.[16] Higher magnetic fields also sometimes make it possible to obtain EPR signals for complexes with an even number of unpaired electrons such as Ni^{II} ($S = 1$)[17] and Mn^{III} ($S = 2$).[18]

However, for other problems, microwave frequencies lower than 9.5 GHz can be advantageous. At lower microwave frequencies the relative importance of g anisotropy is decreased relative to hyperfine interaction. A particularly dramatic example is the improved resolution of nitrogen hyperfine structure in Cu^{II} complexes that can be achieved with spectra at about 2 GHz (S-band).[19]

2.2.4 CONTINUOUS WAVE VS. PULSED EXPERIMENTS

The EPR spectra for most transition metal complexes in rigid lattices extend over hundreds to thousands of gauss. With current pulsed microwave technology it is only possible to excite bandwidths of about 50 gauss, so Fourier transform EPR is limited to relatively narrow spectra. Most pulsed EPR experiments examine only a limited segment of a spectrum. This permits sequential examination of sets of spins for which there is a small distribution of orientations of the magnetic axes with respect to the external magnetic field, which is called orientation selection (see Chapter 2.3, Section 2.3.4). Pulsed experiments also require relaxation times longer than about 0.1 μs, which means that for most metal ions experiments must be performed at cryogenic temperatures. Within these limitations, there is a wide range of pulsed experiments that have been designed to obtain specific information about relaxation times (Section 2.2.5.5) and nuclear hyperfine interactions (Chapter 2.3).[20]

2.2.5 SPECTRA OF $Cu(DTC)_2$

The preceding generalizations concerning information content from various types of EPR experiments can be made more concrete by considering the series of spectra for $Cu(dtc)_2$ shown in Figures 1–5. The spectra for this complex are better resolved than for most transition metal complexes, which makes them well suited to be a tutorial example.

2.2.5.1 Single Crystal

$Ni(dtc)_2$ is square–planar and diamagnetic which makes it a convenient host for examining square–planar $Cu(dtc)_2$. The CW spectrum for one orientation of a single crystal of $Ni(dtc)_2$

doped with $Cu(dtc)_2$ is shown in Figure 1. Continuous wave EPR spectra routinely are detected by magnetic field modulation with phase-sensitive detection which gives the first derivative of the microwave absorption as shown in Figure 1a. The corresponding absorption spectrum, obtained by integration of the spectrum in Figure 1a is shown in Figure 1b. In the single-crystal spectrum there are distinct peaks in the absorption spectrum with negligible intensity between the peaks. There are two inequivalent sites of substitution in this oriented crystal, so there are two distinct orientations of the magnetic axes of the Cu^{II} center with respect to the external magnetic field (Figure 1). The ratio of populations of the two copper isotopes (^{63}Cu and ^{65}Cu) at natural abundance is approximately 2:1. Due to difference in the magnetogyric ratios for the two isotopes, the hyperfine coupling to ^{65}Cu is 1.07 times larger than for ^{63}Cu so there are separate lines for the two isotopes as marked for the low-field lines of site 1. For each isotope, at each site, the spectrum is split into four lines because of hyperfine coupling to the copper nuclear spin ($I = 3/2$), which can have $m_I = -3/2$, $-1/2$, $1/2$, or $3/2$. Thus, there is a total of 16 lines in the single-crystal spectrum, all of which are resolved in the first derivative display. The decreased resolution in the absorption spectrum compared to that of the first derivative is one of the main reasons why EPR spectra are usually displayed as first derivatives.

The spacing between adjacent hyperfine lines (Figure 1) is approximately equal to the copper hyperfine coupling for that orientation of the molecule in the magnetic field. The discrepancy between the true value of A and the value estimated by measuring the splitting is due to terms that arise from solving the Hamiltonian (Equation (1)).[1] In a second-order perturbation analysis these terms are proportional to m_I^2 times A^2/B_{res} where A is the hyperfine coupling constant and B_{res} is the resonant field.[1,4,5] These terms, which commonly are called "second order corrections," become more significant as A increases and B_{res} decreases, so they are of particular concern for large metal hyperfine couplings. For each Cu isotope at each of the sites, the copper hyperfine

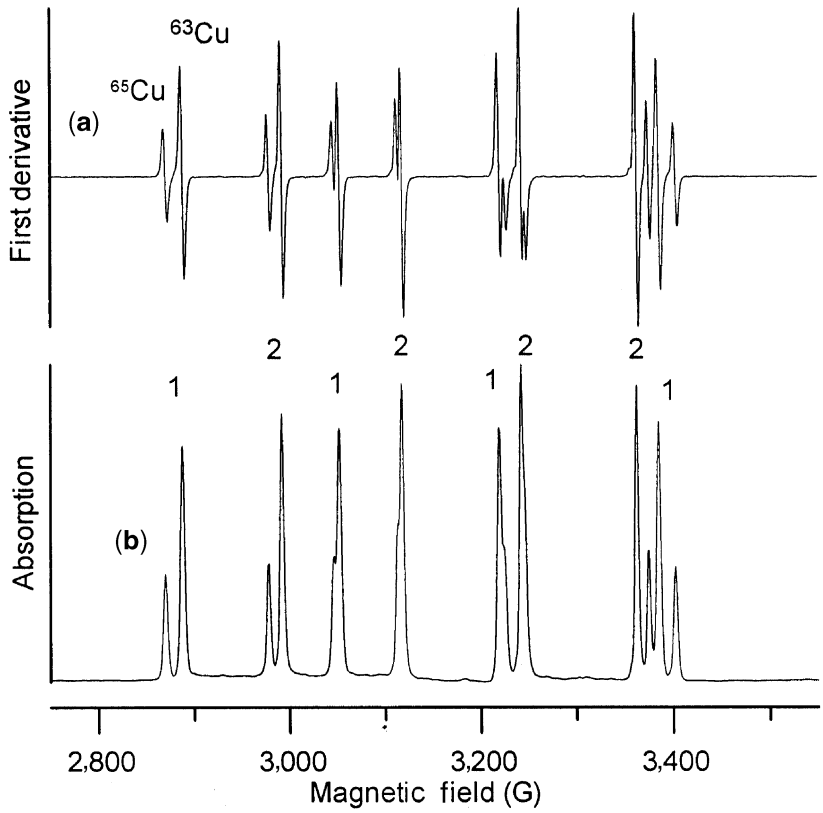

Figure 1 X-band (9.119 GHz) CW spectrum of a single crystal of $Ni(dtc)_2$ doped 1:500 with $Cu(dtc)_2$ obtained at 100 K with 0.04 mW microwave power and 1.0 G modulation amplitude displayed as the traditional first derivative (a). Computer integration of the spectrum in A gave the absorption spectrum (b). The lines for the two inequivalent sites in the crystal are marked with the numbers "1" and "2." The four hyperfine lines for each isotope at each site are due to copper nuclear spin states with $m_I = -3/2$, $-1/2$, $1/2$, and $3/2$. Computer simulations showed that the angle between the external magnetic field and the magnetic z-axis is 20° for site 1 and 49° for site 2.

interaction can be estimated by measuring the spacing between the corresponding lowest-field line and the highest-field line (the $m_I = \pm 3/2$ lines) and dividing by three. This measurement is more precise than the spacing between adjacent hyperfine lines because the second order corrections contribute equally to the low-field and high-field lines. The g value can be estimated from the field that is half-way between the two middle hyperfine lines ($m_I = \pm 1/2$ lines), using the expression $g = h\nu/\beta B$. The use of the two $m_I = \pm 1/2$ lines is better for the calculation of the g value than the $m_I = \pm 3/2$ lines because the second order corrections are smaller for the $m_I = \pm 1/2$ lines. It must be stressed, however, that parameters estimated from the spectra in this fashion are not accurate and to obtain accurate values it is important to use computer simulations that are based on diagonalization of the Hamilton matrix or a perturbation calculation to at least second order. The orientation of the crystal for which spectra are shown in Figure 1a resulted in an angle of 20° between the external magnetic field and the z-axis for site 1 and an angle of 49° for site 2. As is characteristic of square-planar Cu^{II},[21] the g and A values are larger along the z-axis (perpendicular to the molecular plane) and smaller in the x,y plane. Since $h\nu = g\beta B$, a decrease in g value results in resonance at higher magnetic field (B) so the center of the spectrum is at higher field for site 2 than for site 1.

2.2.5.2 Powder Spectra

The term "powder" EPR spectrum implies that there is a random distribution of orientations of the molecules with respect to the external magnetic field. This random distribution can be achieved by rapidly cooling a solution to form a glass or with a large number of tiny crystallites. The X-band (9.107 GHz) spectrum of a powdered sample of $Ni(dtc)_2$ doped with $Cu(dtc)_2$ is shown as the first-derivative and absorption displays in Figures 2a and 2b, respectively. The dominant features of the first-derivative spectrum occur at magnetic fields where there is an abrupt change in the absorption spectrum. These positions correspond to extrema in the orientation dependence of the transitions, although the terminology peak or line is commonly used in describing the spectra. The four extrema marked as "z" in Figure 2a correspond to the four copper hyperfine lines for molecules aligned with the magnetic field along the magnetic z-axis. For the low-field and high-field extrema, the ^{63}Cu and ^{65}Cu contributions are resolved. The four extrema marked as "$\perp$" correspond to the four copper hyperfine lines for molecules oriented with the magnetic field in the molecular plane. At X-band the g values for $Cu(dtc)_2$ along the x and y axes are so similar that the spectrum appears to be axial. It is important to remember that for each hyperfine line (each value of m_I), the spectrum actually extends from the parallel (z-axis) to the perpendicular extrema. Intermediate orientations of the molecule are at resonance at magnetic fields intermediate between the corresponding extrema, but the absorption spectrum changes relatively slowly with magnetic field in these intermediate regions, so the slope is small, and the first derivative signal is close to baseline. This orientation dependence is more clearly seen in the absorption display (Figure 2b) than in the first derivative display of the spectrum. The spectrum of $Cu(dtc)_2$ in glassy toluene solution at 100 K is very similar to that shown for the doped solid in Figure 2, because it, too, represents a random distribution of molecular orientations, and the g and A values in toluene solution are similar to those in the doped solid.

The W-band (ca. 95 GHz) spectrum of $Ni(dtc)_2$ doped with $Cu(dtc)_2$ is shown in Figure 3. To achieve resonance at the higher microwave frequency requires a correspondingly higher magnetic field, which at 95 GHz requires a superconducting magnet. The hyperfine interaction is independent of field, but the separation between extrema due to inequivalent g values increases proportional to magnetic field. Thus, at W-band the separation between g_z and g_x or g_y is much larger than the hyperfine splitting for either extrema. In addition, at W-band, the perpendicular region of the spectrum is resolved into two sets of four extrema due to observable inequivalence between g_x and g_y.

2.2.5.3 Line Widths

For $Cu(dtc)_2$ the line widths of the peaks in the single-crystal spectra and of the extrema in the powder spectra are a few gauss. These line widths are unusually small for a metal complex in a solid sample, which is due to a combination of several factors. (i) Unresolved nuclear hyperfine splitting can be a major contributor to line widths for many complexes. However, for $Cu(dtc)_2$ the directly coordinated ligand atoms are sulfur, for which only 0.75% has a nuclear spin. The nearest nuclei with a high abundance of nuclear spin are the nitrogens that are three bonds removed from

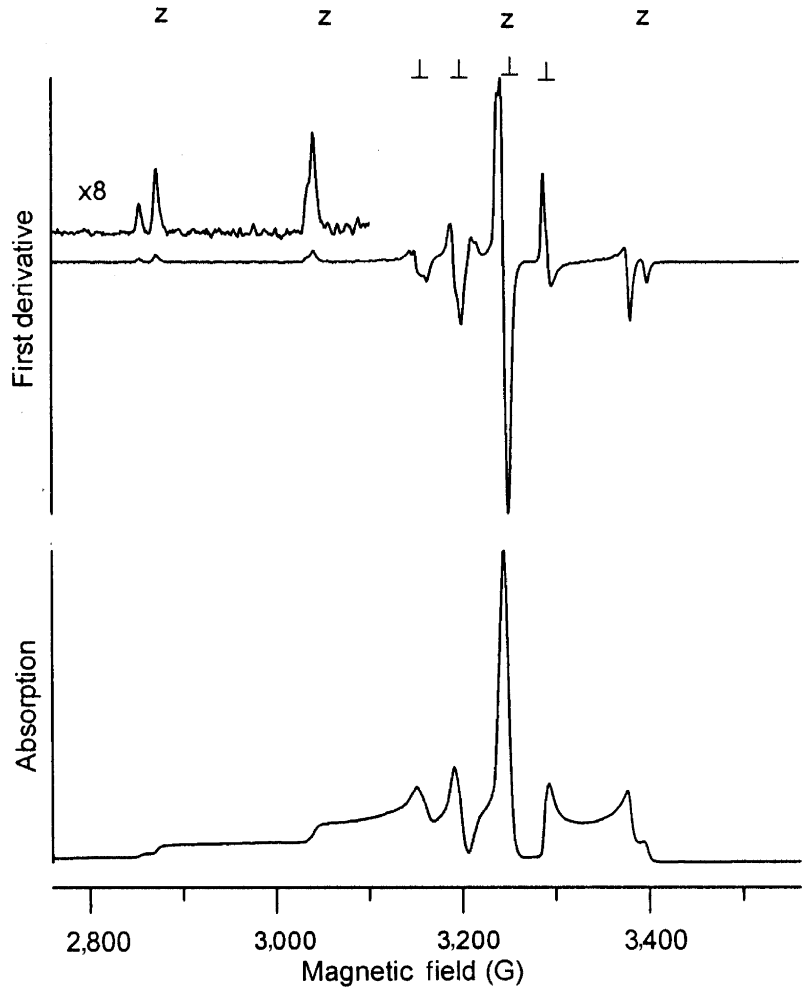

Figure 2 X-band (9.107 GHz) CW spectrum of a powdered sample of $Ni(dtc)_2$ doped 1:500 with $Cu(dtc)_2$ obtained at 150 K with 1.0 mW microwave power and 1.0 G modulation amplitude and displayed as the traditional first derivative (a). Computer integration of the spectrum in *A* gives the absorption spectrum (b). The turning points in the powder pattern that correspond to the four copper hyperfine lines for molecules aligned with the magnetic field along the magnetic *z*-axis or in the perpendicular plane are marked as "z" or "⊥", respectively.

the Cu. The couplings to these nuclei are so small that measurement of the hyperfine interaction requires either ENDOR or ESEEM as described in Chapter 2.3. (ii) As discussed earlier, the electron spin relaxation times for square–planar Cu^{II} in this ligand environment are long enough that relaxation does not make a significant contribution to the line widths at the temperatures for which the spectra in Figures 1–3 were obtained. (iii) If the molecule is relatively flexible or the host environment forces a range of distortions, there can be a distribution of values for the principal components of the g and A matrices, which is known as "*g* strain" and "*A* strain," and results in broadening of the lines in the spectra.[22,23] For $Cu(dtc)_2$ in glassy toluene solution or doped into $Ni(dtc)_2$ the geometry is relatively well defined so *g* and *A* strain are relatively small.

2.2.5.4 Fluid Solution

The X-band CW spectrum of $Cu(dtc)_2$ in toluene solution (Figure 4) consists of four lines with a splitting of $A_{iso} = 78$ G. The tumbling of the molecule is fast enough to largely average the anisotropy of the *g* and *A* matrices. The lines are narrow enough that the contributions from the ^{63}Cu and ^{65}Cu isotopes are resolved on the high-field line and partially resolved on the low-field

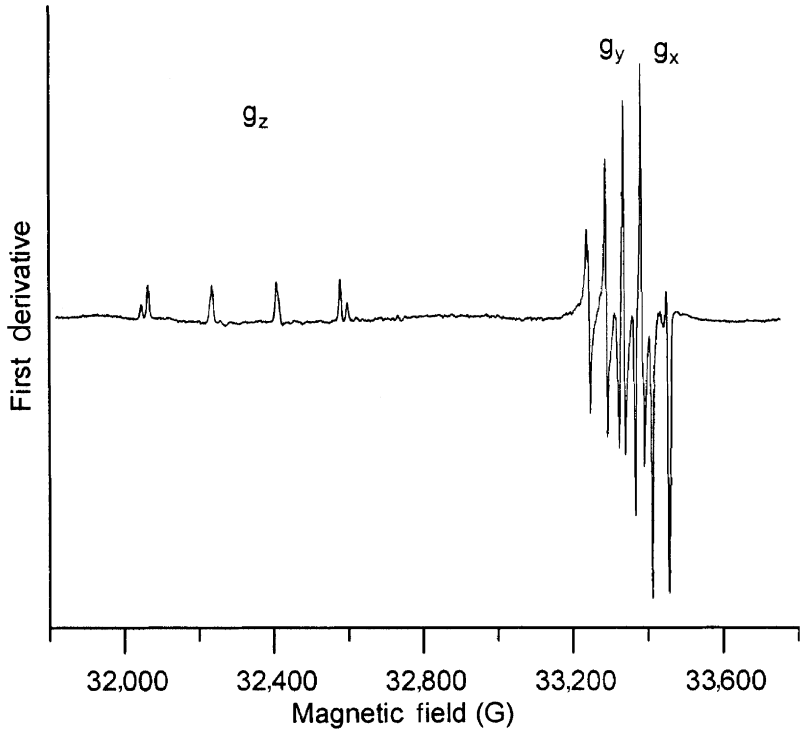

Figure 3 W-band (94.19 GHz) CW spectrum of a powdered sample of $Ni(dtc)_2$ doped 1:500 with $Cu(dtc)_2$ obtained at 50 K with 60 nW of microwave power and 4 G modulation amplitude, and displayed as the first derivative of the microwave absorption. The turning points in the powder pattern that correspond to g_z, g_y, and g_x are marked. Copper hyperfine coupling is resolved along each of the principal axes. Spectrum was obtained by Dr. Ralph Weber, Bruker Instruments.

line. The amplitudes of the four lines are different because of differences in the line widths. These line width differences can be analyzed to determine the tumbling correlation time,[24,25] which depends upon microscopic viscosity, and can be very different from macroscopic viscosity due to specific interactions between solute and solvent. For $Cu(dtc)_2$ in toluene at room temperature the tumbling correlation time is about 4×10^{-11} sec/rad.[26]

2.2.5.5 Electron Spin Relaxation Times

Although power saturation curves can be used as a monitor of changes in relaxation times, for most samples pulsed measurements are required to accurately define the relaxation times and to characterize contributions from other competing processes that take spins off resonance.[13] Long-pulse CW saturation recovery measurements for $Cu(dtc)_2$ doped into $Ni(dtc)_2$ found that T_{1e} decreased from 180 μs at 26 K to 0.6 μs at 298 K, and the temperature dependence could be modeled with a Raman process and a local vibrational mode.[27] The relaxation times for $Cu(dtc)_2$ between 30 and 160 K were very similar for the doped $Ni(dtc)_2$ solid and for glassy toluene solution, which showed that the surrounding environment had little impact on the relaxation. However, the relaxation times for $Cu(dtc)_2$ are much longer than for a less rigid Cu^{II} complex, which highlights the important role of molecular rigidity in relaxation processes in the solid state.[28]

A two-pulse spin echo experiment consists of a 90°-τ-180°-τ-echo pulse sequence (see Chapter 2.3, Section 2.3.2). The amplitude of the echo is monitored as a function of the time τ between the echoes, and the decay time constant is denoted as T_m, the phase memory decay time.[20] T_m is strongly dependent upon dynamic processes that result in echo dephasing on the time scale of the experiment. In $Cu(dtc)_2$ the coupling of the unpaired electron to the spins of the protons of the ethyl groups is too small to be resolved in the CW spectra. However, when the rate of rotation of the

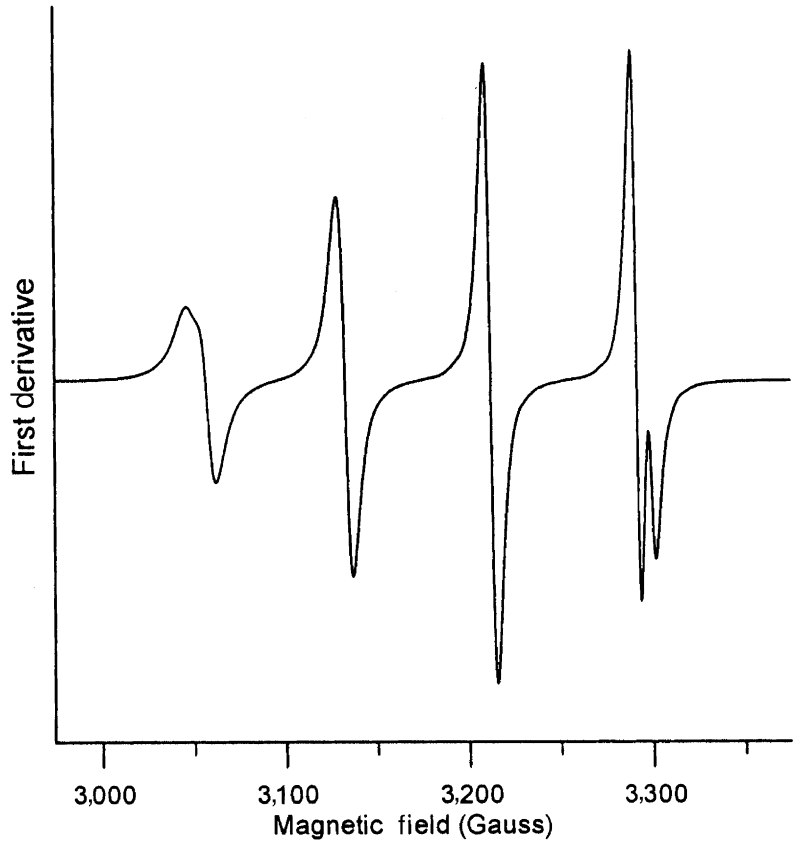

Figure 4 X-band (9.099 GHz) CW spectrum of 1.0 mM $Cu(dtc)_2$ in toluene solution at 294 K obtained with 50 mW microwave power and 0.5 G modulation amplitude, and displayed as the first derivative of the microwave absorption.

methyl groups is comparable to the inequivalence between couplings to individual methyl protons, the rotation results in substantial decreases in T_m. The temperature dependence of T_m has been analyzed to determine the barrier to methyl group rotation in $Cu(dtc)_2$ and in Cr^V complexes of ligands that contain methyl groups.[29,30]

Figure 5 shows the field-swept echo-detected spectrum of $Cu(dtc)_2$ in glassy toluene solution at 30 K. The spectrum was recorded by setting the τ value for the two-pulse spin echo sequence to 1 μs and recording the echo amplitude as a function of magnetic field. If T_m were uniform through the spectrum, the echo-detected spectrum (Figure 5) should match the absorption spectrum (Figure 2b). However, there are substantial differences that are particularly conspicuous in the regions highlighted by the vertical arrows. In the absorption spectrum the signal amplitude increases abruptly near the low-field extrema for the $m_I = -3/2$ ^{65}Cu and ^{63}Cu lines at about 2,850 G then slowly increases between about 2,900 and 3,000 G. Another abrupt increase in signal intensity occurs at the low-field extrema for the parallel orientation of the $m_I = -1/2$ transition at about 3,040 G. By contrast, in the echo-detected spectrum the amplitude of the spectrum is much lower between 2,900 and 3,000 G than at 2,850 G. This dramatic difference between the CW absorption spectrum and the echo-detected spectrum occurs because T_m is much shorter between 2,900 G and 3,000 G than near the extrema. This behavior arises from low-amplitude vibrations (librations) on the timescale of the spin echo experiment that move spins off resonance. The effects of librations on T_m are particularly evident in this region of the spectrum because the transition energy is so orientation dependent that reorientation by a few degrees is sufficient to move spins that were excited by the first pulse out of the range of detection for the second pulse.[31] In the doped solid sample at the same temperature (30 K), variation of T_m through the spectrum is much less than for the glassy solution, which highlights the lower mobility of the $Cu(dtc)_2$ in the doped solid than in glassy solution.

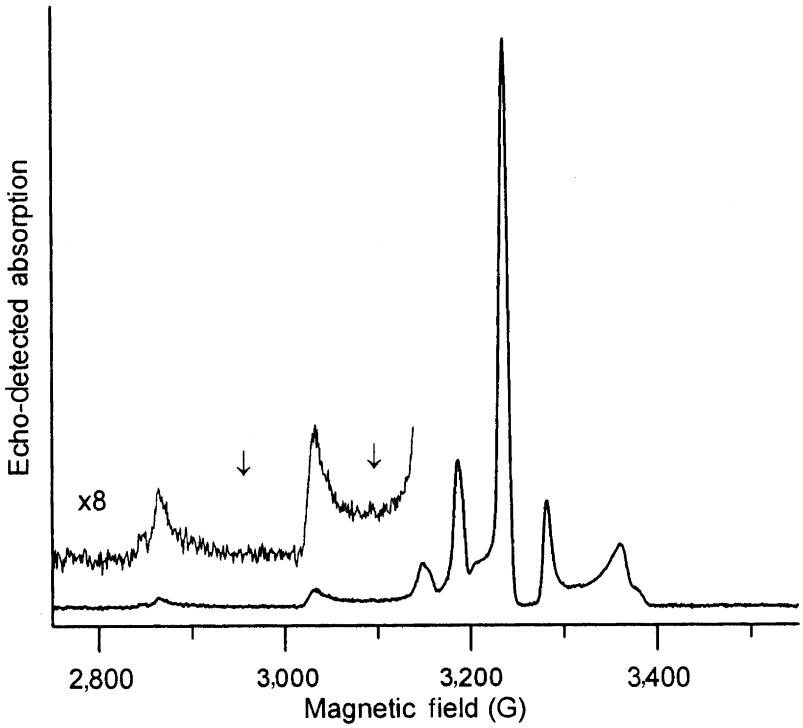

Figure 5 X-band (9.101 GHz) two-pulse spin-echo detected absorption spectrum of 2.0 mM $Cu(dtc)_2$ in glassy toluene solution at 30 K, obtained with 20 and 40 ns pulses and a fixed time between the pulses of 1 μs.

2.2.6 BIOINORGANIC EXAMPLES

Many examples of applications of EPR can be found in the discussions of individual classes of compounds in this compendium. Here we present a few examples of types of problems to which EPR has been recently applied, with an emphasis on the strategies that were used to obtain electronic and structural information.

2.2.6.1 Blue Copper Model Complexes for Cu^{II}-thiolate Complexes and Fungal Laccase

The EPR spectrum of a 3-coordinate [2N + S] model complex exhibited nitrogen hyperfine splitting of about 30 MHz in the perpendicular region of the spectrum, which was not observed in fungal laccase.[7] Analysis of the isotropic and anisotropic components of the nitrogen hyperfine interaction showed that the HOMO of the complex had ~25% nitrogen covalency. The EPR results, together with S and Cu XAS experiments, made it possible to account for essentially all of the covalency in the HOMO of the model complex. The nitrogen covalency is substantially smaller for the blue copper centers in fungal laccase or plastocyanin than for the model complex. The covalency of the Cu center in the model complex could be reproduced by DFT calculations.[7]

2.2.6.2 Dinuclear Cu_A Site in Cytochrome C Oxidase and Nitrous Oxide Reductase

EPR spectra at multiple microwave frequencies permitted identification of the Cu_A site in these proteins as dinuclear well before this geometry was characterized crystallographically.[32,33] The comparison of spectra at several frequencies (L-band (1.2 GHz), S-band (4 GHz), C-band (6 GHz), X-band (9 GHz), and Q-band (35 GHz)) coupled with computer simulations was key to the characterization because different portions of the spectra are better resolved at different

microwave frequencies. A distinctive feature of the EPR spectra of this center is the small copper hyperfine splitting (38 G) on the g-parallel lines. Also, comparison of the spectra at multiple microwave frequencies provided convincing evidence that the hyperfine splitting pattern was seven lines, not four lines. Based on spectra at a single microwave frequency it would be very difficult to unambiguously eliminate the possibility that the seven lines arose from overlapping hyperfine splittings along inequivalent hyperfine axes. Isotopically enriched ^{63}Cu or ^{65}Cu was used to decrease the complexity of the spectra and to improve the resolution of the copper hyperfine splitting. In addition, the increase in the hyperfine coupling by a factor of 1.07 between ^{63}Cu and ^{65}Cu for nitrous oxide reductase demonstrated that the hyperfine splitting was due to copper and not some other nucleus. The data all point to a binuclear center with one unpaired electron delocalized over two copper nuclei, i.e., a formal oxidation state of 1.5 for each copper atom. The electron spin relaxation times for the Cu_A signal are substantially shorter than for type I or type II monomeric copper, which also pointed to a dinuclear center.

2.2.6.3 Oxygen-evolving Complex in Photosystem II

The manganese cluster in the oxygen-evolving complex of Photosystem II presents a challenge for EPR because of the complexity of the spin system. The Mn $I = 5/2$ results in six hyperfine lines. Additional splittings result from electron spin $S > 1/2$, which is further complicated by electron spin–spin coupling within the cluster. Despite the name "multiline" signal, the spectra of the manganese cluster at X-band are deceptively simple, and there are many more transitions than give resolved lines.[34,35] Spectra at multiple frequencies and careful computer simulations with attention to relative intensities of features have been crucial to showing that there is a cluster of four Mn atoms. Even so, the parameters obtained by simulations for the Mn centers are not unique. For these membrane-bound proteins an additional useful tool is one-dimensional ordering of the molecules on a mylar film. Orientation of the mylar film in the EPR resonator and subsequent rotation of the film provides orientation-dependent spectra that provide key insights. This technique has been used to determine the distance between the manganese cluster and the neighboring tyrosyl radical, and the orientation of the interspin vector relative to the plane of the membrane.[36] EPR has been extensively used to define distances between other pairs of paramagnetic centers in photosynthetic systems.[37]

2.2.7 SUMMARY

EPR encompasses a wide range of powerful methods to probe the geometry and electronic structure of paramagnetic metal complexes. Techniques that were until recently available only in a few specialized laboratories are becoming more widely available in commercial spectrometers. The challenge to the experimentalist is to select the set of experiments that will most directly address the particular question of interest.

2.2.8 REFERENCES

1. Weil, J. A.; Bolton, J. R.; Wertz, J. E. *Electron Paramagnetic Resonance: Elementary Theory and Practical Applications* Wiley-Interscience: New York, 1994.
2. Pilbrow, J. R. *Transition Ion Electron Paramagnetic Resonance* 1990, Oxford University Press, New York.
3. Eaton, S. S.; Eaton, G. R. Electron Paramagnetic Resonance. In *Analytical Instrumentation Handbook*, 2nd Ed.; Ewing, G. W., Ed.; Dekker: New York, 1997, pp 767–862.
4. Kuska, H. A.; Rogers, M. T. Electron Spin Resonance of Transition Metal Complex Ions. In *Coordination Chemistry*, ACS Symposium Series. No. 168, Martell, A. E., Ed. Van Nostrand: New York, 1971, 186–263.
5. McGarvey, B. R. *Trans. Met. Chem. Ser. Adv.* **1966**, *3*, 89–201.
6. Silverstone, H. J.; Gaffney, B. J. *Biol. Magn. Reson.* **1993**, *13*, 1–57.
7. Randall, D. W.; George, S. D.; Holland, P. L.; Hedman, B.; Hodgson, K. O.; Tolman, W. B.; Solomon, E. I. *J. Am. Chem. Soc.* **2000**, *122*, 11632–11648.
8. Larsen, S. C. *J. Phys. Chem.* **2001**, *105*, 8333–8338.
9. Makinen, M. W.; Wells, G. B. *Metal Ions in Biological Systems* **1987**, *22*, 129–206.
10. Beinert, H.; Sands, R. H. Biological Applications of EPR Involving Iron. In *Foundations of Modern EPR*, Eaton, G. R.; Eaton, S. S.; Salikov, K. M. Eds., World Scientific: Singapore, 1998, pp 379–409.
11. Wasson, J. R.; Shyr, C.-I.; Trapp, C. *Inorg. Chem.* **1968**, *7*, 469–475.
12. Folgado, J. V.; Henke, W.; Allman, R.; Stratemeier, H.; Beltran-Porter, D.; Rojo, T.; Reinen, D. *Inorg. Chem.* **1990**, *29*, 2035–2042.

13. Eaton, S. S.; Eaton, G. R. *Biol. Magn. Reson.* **2000**, *19*, 29–154.
14. Basosi, R.; Antholine, W. E.; Hyde, J. S. *Biol. Magn. Reson.* **1993**, *13*, 103–150.
15. Eaton, S. S.; Eaton, G. R. EPR at High Magnetic Fields and High Frequencies. In *Handbook of Electron Spin Resonance*, Poole, C. P. Jr.; Farach, H. A., Eds, AIP Press, 1999, Vol. 2, pp 345–370.
16. Wood, R. M.; Stucker, D. M.; Jones, L. M.; Lynch, W. B.; Misra, S. K.; Freed, J. H. *Inorg. Chem.* **1999**, *38*, 5384–5388.
17. van Dam, P. J.; Klaasen, A. A. K.; Reijerse, E. J.; Hagen, W. R. *J. Magn. Reson.* **1998**, *130*, 140–144.
18. Barra, A.-L.; Gatteschi, D.; Sessoli, R.; Abbati, G. L.; Cornia, A.; Fabretti, A. C.; Uytterhoeven, M. G. *Angew. Chem. Int. Ed. Engl.* **1997**, *36*, 3239–2331.
19. Hyde, J. S.; Froncisz, W. *Ann. Rev. Biophys. Bioeng.* **1982**, *11*, 391–417.
20. Schweiger, A.; Jeschke, G. *Principles of Pulse Electron Paramagnetic Resonance* 2001, Oxford University Press, Oxford, UK.
21. Hathaway, B. J.; Billing, D. E. *Coord. Chem. Rev.* **1970**, *5*, 143–207.
22. Froncisz, W.; Hyde, J. S. *J. Chem. Phys.* **1980**, *73*, 3123–3131.
23. Hagen, W. R. g-Strain: Inhomogeneous Broadening in Metalloprotein EPR. In *Advanced EPR: Applications in Biology and Biochemistry*, Hoff, A. J., Ed., Elsevier: Amsterdam, 1989, Chapter 2.
24. Wilson, R.; Kivelson, D. *J. Chem. Phys.* **1966**, *44*, 154–161.
25. Chasteen, N. D.; Hanna, M. W. *J. Phys. Chem.* **1972**, *76*, 3951–3956.
26. Heinig, M. J.; Ph.D. Thesis, University of Denver, 1979.
27. Zhou, Y.; Bowler, B.; Eaton, S. S.; Eaton, G. R. *J. Magn. Reson.* **1999**, *139*, 165–174.
28. Du, J.-L.; Eaton, G. R.; Eaton, S. S. *J. Magn. Reson. A* **1995**, *117*, 67–72.
29. Nakagawa, K.; Candelaria, M. B.; Chik, W. W. C.; Eaton, S. S.; Eaton, G. R. *J. Magn. Reson.* **1992**, *98*, 81–91.
30. Du, J.-L.; Eaton, G. R.; Eaton, S. S. *Appl. Magn. Reson.* **1994**, *6*, 373–8.
31. Du, J.-L.; More, K. M.; Eaton, S. S.; Eaton, G. R. *Israel J. Chem.* **1992**, *32*, 351–355.
32. Antholine, W. E.; Kastrau, D. H. W.; Steffens, C. M.; Buse, G.; Zumft, W. G.; Kroneck, P. M. H. *Eur. J. Biochem.* **1992**, *209*, 875–881.
33. Antholine, W. E. *Adv. Biophys. Chem.* **1997**, *6*, 217–246.
34. Zheng, M.; Dismukes, G. C. *Inorg. Chem.* **1996**, *35*, 3307–3319.
35. Lakshmi, K. V.; Eaton, S. S.; Eaton, G. R.; Frank, H. A.; Brudvig, G. W. *J. Phys. Chem. B* **1998**, *102*, 8327–8335.
36. Lakshmi, K. V.; Eaton, S. S.; Eaton, G. R.; Brudvig, G. W. *Biochemistry* **1999**, *38*, 12758–12767.
37. Lakshmi, K. V.; Brudvig, G. W. *Biol. Magn. Reson.* **2001**, *19*, 513–567.

Comprehensive Coordination Chemistry II
ISBN (set): 0-08-0437486

Volume 2, (ISBN 0-08-0443249); pp 37–48

2.3 Electron–Nuclear Double Resonance Spectroscopy and Electron Spin Echo Envelope Modulation Spectroscopy

G. R. EATON and S. S. EATON
University of Denver, CO, USA

2.3.1 INTRODUCTION 49
2.3.2 ELECTRON SPIN ECHO ENVELOPE MODULATION 49
2.3.3 ELECTRON–NUCLEAR DOUBLE RESONANCE 50
2.3.4 ORIENTATION SELECTION 51
2.3.5 EXAMPLES OF APPLICATIONS 51
2.3.5.1 Hyperfine Coupling to Ligand Nitrogens in $Cu(dtc)_2$ Measured by ENDOR and ESEEM 52
2.3.5.2 ESEEM of Cu^{II} Exchanged into Synthetic Gallosilicate 52
2.3.5.3 Two-dimensional ESEEM (HYSCORE) of Rieske-type Fe–S Clusters 53
2.3.5.4 Determination of the Structure of VO^{2+} in Frozen Solution by ENDOR 54
2.3.5.5 ENDOR of the OH_x Bridge in Hydrogenase from *Desulfovibrio gigas* 55
2.3.6 REFERENCES 55

2.3.1 INTRODUCTION

The linewidths in continuous wave (CW) EPR spectra (see Chapter 2.2) of transition metal complexes typically are many gauss wide due to unresolved hyperfine couplings to neighboring nuclei. These unresolved hyperfine couplings are of substantial interest because they contain information concerning the types of nuclei in the vicinity of the metal ion, electron spin delocalization on to neighboring nuclei, and, in an immobilized sample, the distance from the metal to a nucleus. Two EPR techniques can be used to measure coupling constants that are too small to be resolved in the CW spectra–electron spin echo envelope modulation (ESEEM) and electron–nuclear double resonance (ENDOR). Although both techniques measure electron–nuclear hyperfine couplings, the experimental approaches are quite different. Detailed discussions of these techniques can be found in the literature.[1–6] In this chapter we provide brief overviews of the techniques and discuss some examples that illustrate the power of these techniques to elucidate the nuclear structure around paramagnetic metal ions.

2.3.2 ELECTRON SPIN ECHO ENVELOPE MODULATION

The basic principle involved in electron spin echo spectroscopy is the formation of an echo.[3] The simplest spin echo experiment uses two microwave pulses to form an echo, which is also

known as a Hahn echo. The experiment can be described in terms of a vector model in the rotating reference frame. At equilibrium, in the presence of an external magnetic field, the net magnetization can be viewed as a vector precessing about the direction of the external magnetic field. The Larmor precession frequency is characteristic of the environment of the unpaired electron. When a short (tens of nanoseconds) pulse of microwaves is applied along an axis perpendicular to the external field (the z-axis), the microwave magnetic field exerts a torque on the net magnetization. The length of the pulse and magnitude of the microwave magnetic field are selected to cause the magnetization to rotate into the x–y plane. This is called a 90° pulse. Due to small differences in the Larmor frequency for different spins in the sample, the spins precess at slightly different frequencies and diverge from the average. After a variable time interval, τ, a 180° pulse is applied that flips the average magnetization vector from, for example, the $+x$ direction to the $-x$ direction and interchanges the roles of faster and slower precessing spins. After a second interval τ, the vectors reconverge to form the echo. In a two-pulse ESEEM experiment the time interval τ is varied and the echo intensity is recorded as a function of τ. In the absence of specific electron–nuclear hyperfine coupling the echo decays monotonically with a time constant T_m, the phase memory time constant. T_m reflects the effects of stochastic processes that occur on the time scale of the experiment and are not refocused by the 180° pulse. These processes include electron–electron T_2 as well as spin diffusion of nuclei that are dipolar coupled to the unpaired electron.[7] For samples with specific electron–nuclear hyperfine interactions characteristic modulation frequencies are superimposed on the monotonic T_m decay. Fourier transformation of the modulated echo decay curve gives the spectrum of the nuclear modulation frequencies. Even at liquid helium temperatures the value of T_m for metal ions in proton-containing molecules in proton-containing solvents or lattices usually does not exceed about 5 μs,[8] which limits the number of modulation cycles that can be observed in a two-pulse experiment. For a three-pulse experiment the decay constant may be as long as T_{1e}.[9] At low temperatures, T_{1e} for metal ions typically is much longer that T_m,[8] which permits observation of many additional modulation cycles. Resolution of the nuclear frequencies in the three-pulse experiment then is limited by the inherent "beating" down of the multiple modulation frequencies in a sample. Among other requirements, the observation of a nuclear hyperfine frequency by ESEEM requires that both the upper and lower level of the transition be encompassed by the microwave magnetic field, B_1, of the pulse.[5] The finite microwave B_1 available in the pulse experiments limits ESEEM experiments to smaller hyperfine couplings than can be observed by ENDOR.

More elaborate pulse sequences have been designed to selectively extract specific information about a spin system.[9] A particularly useful experiment for structural studies of metal complexes is the two-dimensional four-pulse experiment called HYSCORE, hyperfine sublevel correlation spectroscopy. The resulting two-dimensional plot reveals the correlation between different modulation frequencies arising from the same nucleus, which greatly facilitates assignment of frequencies in complicated spin systems.[5]

For nuclei with $I=\frac{1}{2}$ such as ^{1}H, ^{13}C, ^{31}P, and ^{15}N the depth of the modulation increases as the external magnetic field is decreased, so it is possible to see weaker interactions by operating at microwave frequencies lower than X-band (9 GHz). For nuclei with $I>\frac{1}{2}$ and substantial quadrupole interactions such as ^{14}N the nuclear modulation is deepest when the condition known as "exact cancellation" is satisfied.[10] This condition occurs when the hyperfine coupling constant, a_n, is approximately equal to $2\nu_n$ where ν_n is the nuclear Larmor frequency. Thus for these nuclei there is an optimum microwave frequency for observing the nuclear modulation.

2.3.3 ELECTRON–NUCLEAR DOUBLE RESONANCE

The name ENDOR encompasses several types of experiments.[1] The common feature in all ENDOR experiments is the simultaneous use of a microwave frequency to excite electron spin transitions and a RF to excite NMR transitions, hence the use of the term "double resonance." ENDOR can be viewed as NMR spectroscopy detected via the electron spins. Smaller hyperfine couplings can be observed by ENDOR than by CW EPR because the linewidths of the ENDOR signals are orders of magnitude smaller than the widths of the EPR signals.

The original ENDOR experiments were CW.[2] In the CW experiments an EPR transition is saturated with high microwave power and the RF frequency is swept. When the RF frequency

matches a NMR transition, the saturation of the EPR transition is relieved. The increase in the intensity of the EPR signal due to partial relief of saturation is the ENDOR response. A disadvantage of CW ENDOR is that it relies upon a delicate balance of relaxation times, which may be difficult to achieve for some samples.[2]

More recently, pulsed ENDOR methods have been introduced.[1] There are two commonly used ENDOR pulse sequences, both of which are based on the impact of RF pulses on the intensity of a spin echo that is formed from a series of three pulses at the microwave frequency. These techniques are sometimes called ESE-ENDOR. In Mims ENDOR the pulse at the RF frequency is applied between the second and third microwave pulses whereas in Davies ENDOR the RF pulse is applied between the first and second microwave pulses. The Mims ENDOR experiment is particularly effective for weakly coupled nuclei, but has some "blind" spots (frequencies that cannot be observed).[11] It is often advantageous to combine data from both ENDOR methods.

For nuclei with large magnetic moments such as ^{1}H or ^{19}F the effect of the external magnetic field at X-band typically is larger than the hyperfine field and so the ENDOR response is centered at the Larmor frequency, ν_n, of the nucleus and is split by the hyperfine coupling, A_n, and by quadrupole interactions. However, for nuclei with smaller magnetic moments such as ^{2}H or ^{14}N the ENDOR response is centered at the frequency that corresponds to the hyperfine coupling and is split into two lines that are separated by the Larmor frequency. At X-band the proton Larmor frequency is about 14 MHz, which is comparable to the magnitude of many nuclear hyperfine couplings. This frequently results in substantial overlap of the proton ENDOR signals with signals from other nuclei. Since ν_n increases proportional to external magnetic field and A_n is independent of field, the overlap of proton ENDOR signals with signals from other nuclei can be decreased by going to higher magnetic field. This improvement in resolution is a major incentive for performing ENDOR at microwave frequencies of 35 (Q-band)[1] or 95 (W-band) GHz.[12]

2.3.4 ORIENTATION SELECTION

If sufficient information can be obtained concerning the orientation dependence of a nuclear hyperfine coupling, the coupling can be separated into its isotropic and anisotropic components. The anisotropic component arises from dipolar interaction that varies as r^{-3} and, therefore, can be used to determine the distance between the metal ion and the interacting nucleus. The anisotropic contribution can be determined in a straightforward fashion from the orientation dependence of the ENDOR splittings in a single crystal.[2] However, many samples, particularly of metalloproteins, are not readily obtained as single crystals. The anisotropy of the EPR spectra of most transition metal ions provides the possibility to extract the orientation dependence of the ENDOR splittings even from spectra of a randomly oriented rigid-lattice sample because of orientation selection.[13] Each ENDOR experiment is performed at a particular position in the CW spectrum. At each point in the CW spectrum from a frozen-solution or powder sample with anisotropic g and A values, only a limited number of orientations of the molecule with respect to the external magnetic field contribute to the EPR or ENDOR signal, although this selectivity may be blurred by distributions in g and/or A values or by spin diffusion. At the magnetic fields that correspond to the low-field and high-field extremes of the CW spectrum, the ENDOR spectrum is single-crystal-like. At each intermediate position in the CW spectrum there is a limited range of orientations of the molecule with respect to the external magnetic field that result in resonance at a particular combination of field and microwave frequency. By careful selection of the field positions at which the ENDOR experiment is performed and by analysis of the orientations of the molecule that contribute to the signal at that magnetic field, it is possible to extract the orientation dependence of the hyperfine interaction. The greater dispersion of the CW spectrum that arises at higher magnetic field (and microwave frequency) gives increased orientation selectivity and is an incentive for performing ENDOR at microwave frequencies higher than 9 GHz.[1]

2.3.5 EXAMPLES OF APPLICATIONS

The following examples were selected to show the types of information that can be obtained by ENDOR and ESEEM studies of metal ions in randomly oriented (powder) samples.

2.3.5.1 Hyperfine Coupling to Ligand Nitrogens in $Cu(dtc)_2$ Measured by ENDOR and ESEEM

EPR spectra obtained by various experiments for Cu(diethyldithiocarbamate)$_2$ samples are shown in Chapter 2.2. Although the splitting due to copper hyperfine interaction is well resolved, there is no hint in these spectra of hyperfine coupling to the nitrogens in the diethyldithiocarbamate ligands. Because of the anisotropy of g and of copper hyperfine for $Cu(dtc)_2$, the full orientation dependence from parallel to perpendicular of the highest-field hyperfine line ($m_I = \frac{3}{2}$) does not overlap with other copper hyperfine lines (see Figure 2 of Chapter 2.2). This region of the spectrum is then a prime target for orientation-selected ENDOR or ESEEM. ESEEM, Mims ESE-ENDOR, and CW-ENDOR at X-band have been compared for a powder sample of $Cu(dtc)_2$ doped into $Ni(dtc)_2$.[14,15] CW-ENDOR was performed at 27 K. ESEEM and Mims ESE-ENDOR were performed at 20 K. These low temperatures are required to achieve sufficiently slow relaxation rates for the Cu^{II}. Spectra were recorded at 7–15 magnetic fields that correspond to orientations ranging from the magnetic field along the magnetic z-axis to the magnetic field in the perpendicular plane, which is the plane of the molecule.

Due to nitrogen nuclear hyperfine ($I = 0$) and quadrupole coupling, the electron spin $m_s = \pm\frac{1}{2}$ energy levels are each split into three levels. The spacings between levels are not equal because of the quadrupole contribution to the coupling. There are five transitions between these levels that might potentially be observed by ESEEM or ENDOR, with frequencies up to 5 MHz. For $Cu(dtc)_2$ calculation of the nuclear frequencies as a function of orientation requires matrix diagonalization, because the quadrupole and hyperfine couplings are of approximately the same magnitude as the nuclear Zeeman interaction. Nuclear interaction frequencies for $Cu(dtc)_2$ were clearly resolved and orientation dependent for each experimental technique; however, no one technique permitted observation of all five frequencies at all orientations (i.e., positions in the CW spectrum).[14,15] In the CW-ENDOR spectra the more strongly angularly dependent features were not detectable at orientations where the angular dependence was largest, but three transitions could be observed over the full range of orientations. Spectral features that were not observed in the ESE-ENDOR spectra were observed by ESEEM, which demonstrates the complementary nature of the two techniques. The effects of spectral diffusion were larger in the ESEEM experiment. The finite dead-time in the pulsed experiments limited the ability to observe broader transitions. For this sample the maximum information from the powder sample was obtained by combining ESEEM and either of the ENDOR measurements.[14,15] The hyperfine and quadrupole parameters obtained by analysis of the ENDOR and ESEEM spectra of the powder sample were consistent with the values that had been obtained previously by analysis of single-crystal data.

The ability to detect interaction with nitrogens that are three bonds away from the Cu^{II} in $Cu(dtc)_2$ is a demonstration of the power of ENDOR and ESEEM to characterize weak nuclear interactions. The long-range interaction is particularly large in these complexes because about 50% of the unpaired electron spin density from the copper is delocalized on to the sulfur atoms in the first coordination sphere.[16]

2.3.5.2 ESEEM of Cu^{II} Exchanged into Synthetic Gallosilicate

Isomorphous substitution of Al by Ga in zeolite frameworks is a route to modifying the characteristics of the framework. Copper adsorbed in the framework has potential as a catalyst and it is anticipated that modification of the framework will modify the catalytic properties.[17] CW EPR plus ESEEM is a powerful combination for characterizing the coordination environment for the Cu^{II} as a function of hydration and in the presence of adsorbed alcohols. Based on the ESEEM data it was possible to determine the number of coordinated water and/or alcohol molecules. The curves shown in Figure 1 are typical three-pulse ESEEM data, recorded at 4.5 K. The modulation frequency is characteristic of deuterium at the magnetic field (~3,200 G) that corresponds to electron spin resonance at ~9 GHz. The depth of the modulation increases with increasing number of interacting nuclei and decreases as the distance between the unpaired electron and the nucleus increases. The decrease in the depth of modulation from Figures 1a to 1b is due to the decrease in the number of deuterons from six (2 mol of CD_3OH) to two (2 mol of MeOD), even though the distance decreased from 0.40 nm to 0.29 nm. The decrease in the modulation depth from Figures 1b to 1c is due to the decrease in the number of deuterons from two (2 mol of MeOD) to one (1 mol of EtOD) at approximately constant electron–nuclear

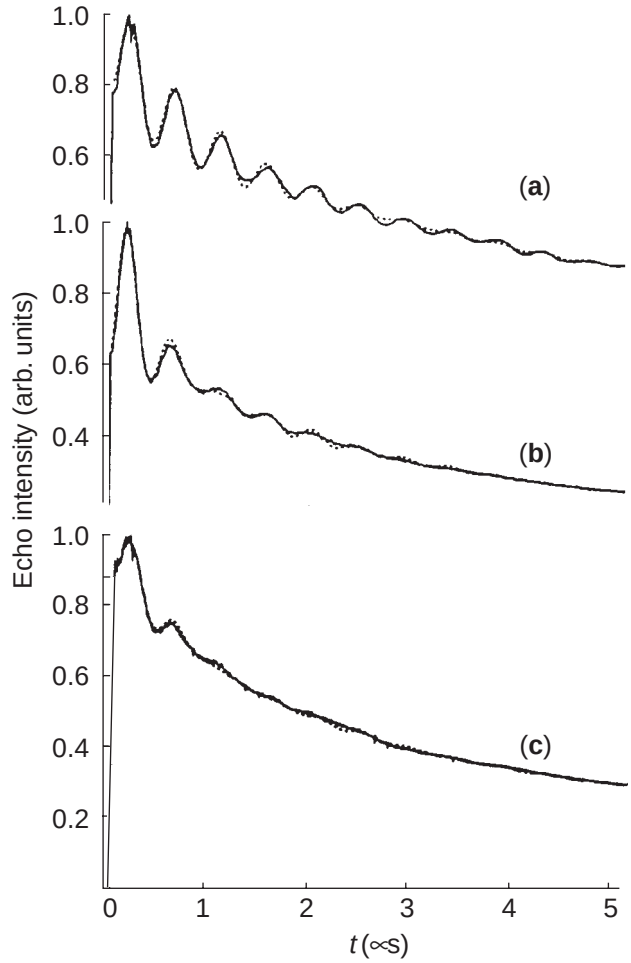

Figure 1 Experimental (——) and simulated (···) three-pulses ESEEM data for Cu^{II} in gallosilicate with adsorbed (a) CD_3OH, (b) MeOD, and (c) EtOD. The simulated curves were obtained with (a) six deuterons at 0.40 nm with $A_{iso} = 0.10$ MHz, (b) two deuterons at 0.29 nm with $A_{iso} = 0.29$ MHz; (c) one deuteron at 0.30 nm with $A_{iso} = 0.29$ MHz (reproduced by permission of The Royal Society of Chemistry from *J. Chem. Soc., Faraday Trans.* **1997**, *93*, 4211–4219).

distance. In these experiments the key observable was the depth of the modulation, which was analyzed in the time domain. The nuclear frequency could have been obtained by Fourier transformation of the time domain signals.

2.3.5.3 Two-dimensional ESEEM (HYSCORE) of Rieske-type Fe–S Clusters

ENDOR and three-pulse ESEEM studies of the Rieske-type cluster in 2,4,5-trichlorophenoxyacetate monooxygenase from *Burkholderia cepiacia* showed the coordination of two nitrogens to one of the irons of the ferredoxin replacing two of the cysteines that are coordinated in plant ferredoxins.[18] For each interacting ^{14}N nucleus there are several nuclear modulation frequencies because of the nitrogen quadrupole moment as well as the nuclear spin. HYSCORE data exhibit off-diagonal correlation peaks between modulation frequencies that arise from the same nucleus, which is very helpful in assigning the sets of frequencies arising from each nucleus. Comparison of the X-band HYSCORE spectra for Rieske centers for this monooxygenase with data for related benzene and phthalate diooxygenases demonstrated systematic differences in the nitrogen hyperfine coupling parameters, which may reflect functional differences in histidine ligation or interaction with nearby amino acids.[18]

2.3.5.4 Determination of the Structure of VO^{2+} in Frozen Solution by ENDOR

CW ^{1}H ENDOR spectra of VO^{2+} in methanol solutions at 5 K are shown in Figure 2. These single-crystal-like spectra were obtained with the magnetic field set to the lowest field turning point in the powder spectrum, which is the $m_I = \frac{7}{2}$ line for molecules with the magnetic field along the principal (z) axis. The frequency that is labeled as "0" on the x-axis in Figure 2 corresponds to the free proton frequency (11.88 MHz) at the magnetic field (~2,800 G) for the experiment. The pairs of lines that are marked with the letters A to J correspond to distinguishable proton environments and the frequency separation for each pair of lines is the proton hyperfine coupling for this orientation of the molecule. Pairs of lines that are present in both CD_3OH and MeOH solution are from hydroxy protons and pairs of lines that are present in both MeOH and MeOD are from methyl protons. Comparison with ENDOR spectra obtained along a well-isolated perpendicular turning point of the spectrum defined the orientation dependence of the hyperfine splittings. Comparison of data in methanol and water–methanol mixtures permitted the determination of the distances to protons in axially coordinated water molecules, water molecules hydrogen-bonded to the vanadyl oxygen, water molecules coordinated in the equatorial plane, and water molecules hydrogen-bonded in the equatorial plane. Distances were in the range of 2.6–4.8 Å.[19] Similarly, in pure methanol there are inner-sphere and outer-sphere methanols in axial and equatorial positions. This study demonstrates the structural detail that can be obtained by ENDOR.

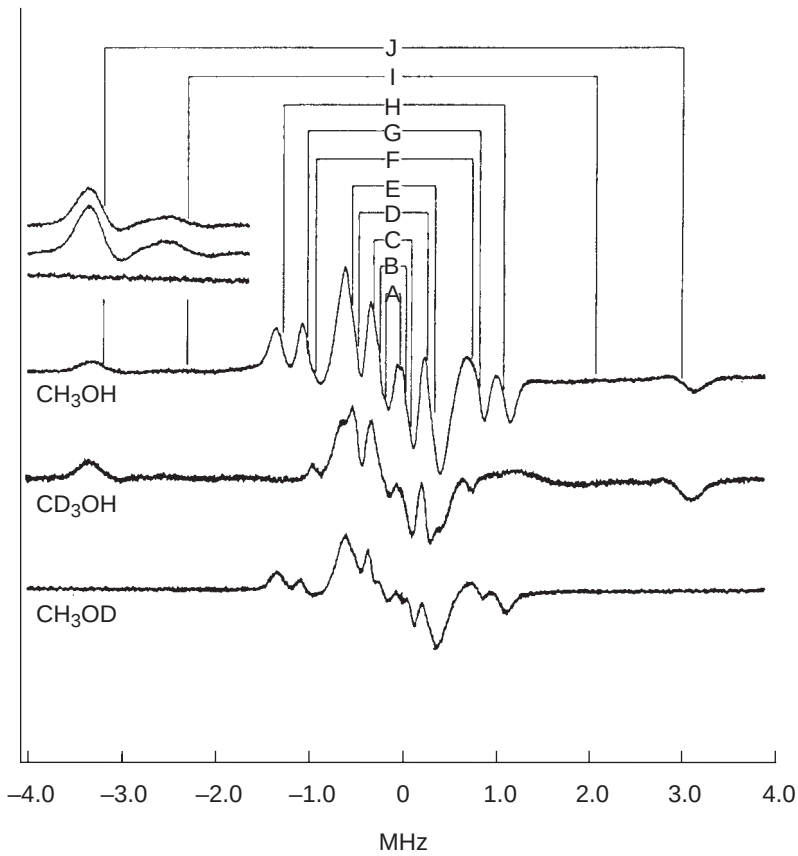

Figure 2 Proton ENDOR spectra of the VO^{2+} ion in methanol. The external magnetic field was set at the $m_I = \frac{7}{2}$ parallel turning point in the CW spectrum. The samples were prepared in MeOH, CD_3OH, and CD_3OD solvents. The ENDOR absorption features are equally spaced about the free-proton frequency of 11.88 MHz (reproduced by permission of the American Chemical Society from *Inorg. Chem.* **1988**, *27*, 3360–3368).

2.3.5.5 ENDOR of the OH_x Bridge in Hydrogenase from *Desulfovibrio gigas*

X-ray crystal structures of hydrogenase from *Desulfovibrio gigas* have shown that that there is a heteronuclear iron–nickel active site. EPR signals have been observed for three forms of the protein: Ni-A which is the as-isolated "unready" state, Ni-B which is the "ready" state, and Ni-C which is the active form and can be prepared by reduction of Ni-A with hydrogen gas. The X-ray structure of the Ni-A form indicated a nonprotein ligand, X, bridging between the Ni and Fe in the cluster and X was proposed to be O^{2-} or OH^{-}. ENDOR studies at 35 GHz were used to characterize the bridging ligand.[20] CW ^{17}O ENDOR studies at 2 K of the Ni-A form exchanged with $H_2{}^{17}O$ showed no ^{17}O ENDOR signal, which could indicate that the bridging ligand does not involve oxygen or that the bridging ligand cannot be exchanged with water. The latter suggestion is supported by ENDOR studies that showed no H/D exchange at the active site in Ni-A. When the Ni-A sample in $H_2{}^{17}O$ was reduced with hydrogen to form Ni-C, no ^{17}O ENDOR was observed. However, when the Ni-C form in $H_2{}^{17}O$ was reoxidized to Ni-A, ENDOR signals were observed that were not present in the starting Ni-A and were assigned to ^{17}O. The orientation dependence of the ^{17}O hyperfine interaction was mapped by recording the ENDOR signal as a function of position in the CW spectrum. The hyperfine tensor is approximately axial and the orientation of the axes of the hyperfine tensor relative to the magnetic axes of the Ni-center was determined. The substantial isotropic component of the hyperfine interaction ($\sim$11 MHz) indicates that the solvent-derived oxygen is a ligand to the Ni of Ni-A. Pulsed (Mims)^{57}Fe ESE-ENDOR at 2 K for an isotopically enriched sample found an ^{57}Fe coupling of 1.0 MHz in Ni-A and 0.8 MHz in Ni-C. The ^{17}O coupling is lost upon reduction of Ni-A to Ni-C. These observations suggest that reductive activation opens up a coordination site on the Ni–Fe cluster, which may play a key role in the mechanism of the protein.[20] These experiments demonstrate the power of CW and pulsed ENDOR, combined with isotopic substitution, to characterize the coordination environment of a metal site in a protein.

2.3.6 REFERENCES

1. Hoffman, B. M.; DeRose, V. J.; Doan, P. E.; Gurbiel, R. J.; Houseman, A. L. P.; Telser, J. *Biol. Magn. Reson.* **1993**, *13*, 151–218.
2. Kevan, L.; Kispert, L. D. *Electron Spin Double Resonance*. Wiley Interscience: New York, 1976, Chapter 1.
3. Mims, W. B. Electron Spin Echoes. In *Electron Paramagnetic Resonance*; Geschwind, S., Ed.; Plenum Press: New York, 1972, pp 263–351.
4. Norris, J. R.; Thurnauer, M. C.; Bowman, M. K. *Adv. Biol. Med. Phys.* **1980**, *17*, 365–416.
5. Dikanov, S. A.; Tsvetkov, Yu. D. *Electron Spin Echo Envelope Modulation (ESEEM) Spectroscopy*. CRC Press, Boca Raton, FL, 1992.
6. Chasteen, N. D.; Snetsinger, P. A. ESEEM and ENDOR Spectroscopy. In *Physical Methods in Bioinorganic Chemistry: Spectroscopy and Magnetism*; Que, L. J., Ed.; University Science Books, Sausalito, CA, 2000, Chapter 4.
7. Zecevic, A.; Eaton, G. R.; Eaton, S. S.; Lindgren, M. *Mol. Phys.* **1998**, *95*, 1255–1263.
8. Eaton, S. S.; Eaton, G. R. *Biol. Magn. Reson.* **2000**, *19*, 29–154.
9. Schweiger, A.; Jeschke, G. *Principles of Pulse Electron Magnetic Resonance*. Oxford University Press: Oxford, 2001.
10. Flanagan, H. L.; Singel, D. J. *J. Chem. Phys.* **1987**, *87*, 5606–5616.
11. Thomann, H.; Bernardo, M. *Biol. Magn. Reson.* **1993**, *13*, 275–322.
12. Slutter, C. E.; Gromov, I.; Epel, B.; Pecht, I.; Richards, J. H.; Goldfarb, D. *J. Am. Chem. Soc.* **2001**, *123*, 5325–5336.
13. Rist, G. H.; Hyde, J. S. *J. Chem. Phys.* **1968**, *49*, 2449–2451.
14. Reijerse, E. J.; Van Aerle, N. A. J. M.; Keijzers, C. P.; Boettcher, R.; Kirmse, R.; Stach, J. *J. Magn. Reson.* **1986**, 67, 114–124.
15. Reijerse, E. J.; Keijzers, C. P. *In Pulsed EPR: A New Field of Applications*; Keijzers, C. P.; Reijerse, E. J.; Schmidt, J. Eds.; North-Holland: Amsterdam, 1989.
16. Keijzers, C. P.; DeVries, H. J. M.; Van der Avoird, A. *Inorg. Chem.* **1972**, *11*, 1338–1343.
17. Yu, J.-S.; Kim, J. Y.; Lee, C. W.; Kim, S. J.; Hong, S. B.; Kevan, L. *J. Chem. Soc., Faraday Trans.* **1997**, *93*, 4211–4219.
18. Dikanov, S. A.; Xun, L.; Karpiel, A. B.; Tyryshkin, A. M.; Bowman, M. K. *J. Am. Chem. Soc.* **1996**, *118*, 8408–8416.
19. Mustafi, D.; Makinen, M. W. *Inorg. Chem.* **1988**, *27*, 3360–3368.
20. Carepo, M.; Tierney, D. L.; Brondino, C. D.; Yang, T. C.; Pampiona, A.; Telser, J.; Moura, I.; Moura, J. J. G.; Hoffman, B. *J. Am. Chem. Soc.* **2002**, *124*, 281–286.

Comprehensive Coordination Chemistry II
ISBN (set): 0-08-0437486
Volume 2, (ISBN 0-08-0443249); pp 49–55

2.4
X-ray Diffraction

W. CLEGG
University of Newcastle upon Tyne, UK

2.4.1 INTRODUCTION 57
2.4.2 X-RAY DIFFRACTION 57
2.4.2.1 Introduction 57
2.4.2.2 X-ray Detector Developments 58
2.4.2.3 X-ray Sources 59
2.4.2.4 Low-temperature Data Collection 60
2.4.2.5 Advances in Computing 61
2.4.2.6 Disorder, Twinning, and other Structural Problems 61
2.4.2.7 Anomalous Scattering and Absolute Configuration 62
2.4.2.8 X-ray Powder Diffraction 63
2.4.2.9 Publication and Crystallographic Databases 63
2.4.3 REFERENCES 64

2.4.1 INTRODUCTION

Detailed structural characterization of coordination compounds is usually carried out by diffraction methods, which can provide not only information on composition and molecular connectivity, but also full geometrical parameters. The most widely used technique is X-ray diffraction by single crystals. Neutron diffraction offers advantages in some cases, especially where the location of hydrogen atoms is important, and electron diffraction can be used to investigate gas-phase structures of compounds with sufficient volatility and molecular simplicity. These X-ray techniques are described in this section, together with related topics; other methods for analysis of chiral compounds using spectroscopy, and other methods for investigating solid-state materials, are described elsewhere.

2.4.2 X-RAY DIFFRACTION

2.4.2.1 Introduction

Single-crystal X-ray diffraction is the most powerful technique for the detailed structural analysis of crystalline solid materials, and so it finds widespread use in coordination chemistry. It is a mature experimental technique, and the basic principles have been well known for almost a century. Nevertheless, the subject has constantly developed throughout its history, and there have been very significant advances in the last decade or two of the twentieth century. These developments and their exploitation will be the main focus of this section. Background theory and its application in general is described in many standard texts, including some relatively simple treatments.[1–5]

X-ray crystallography may be regarded as essentially an extremely high-powered microscope, in which X-rays are used instead of visible light in order to view molecules; the wavelengths of

X-rays are comparable to the dimensions of atoms and molecules. Single crystals are used because the component molecules (or atoms, or ions) are regularly arranged in three dimensions and hence give cooperative scattering to generate a diffraction pattern with discrete "reflections," having a range of intensities, in well defined directions. The observed directions of diffraction are related to the repeat geometry (lattice and unit cell) of the sample crystal, and the reflection intensities are related to the distribution of electron density within the unit cell, i.e., to the nature, positions, and vibrations of atoms. Unlike optical microscopy, the diffracted X-rays can not be directly recombined by physical lenses to obtain an immediate image of the crystal structure, and the diffraction pattern must instead be recorded and the recombination carried out by subsequent mathematical calculation with computers (Fourier transformation). Recombination requires both diffracted amplitudes (derived from measured intensities) and relative phases of the individual reflections, but these phases are not available from the recorded pattern, and so the whole process is not fully automatic or instantaneous.

When the method is successful, the primary results are the unit cell geometry and the space group; positions of atoms within the "asymmetric unit" (the symmetry-unique fraction of the unit cell); "anisotropic displacement parameters" describing mainly the vibrational motion of atoms in different directions, but covering also some aspects of structural disorder and other imperfections; and a few other parameters of more or less interest, some of which will be described later. From these, detailed geometrical parameters are calculated; these include not only intramolecular, but also intermolecular geometry. By the application of standard statistical procedures, every derived numerical parameter has an associated "standard uncertainty" (also known as "estimated standard deviation"), which indicates its precision or reliability.

The precision and quality of the crystal structure depends on a number of factors. These include the precision (affected mainly by random errors) and accuracy (affected by systematic errors) of the measured diffraction pattern intensities, the number of measured data (fewer data lead to reduced precision), and the appropriateness of the structural model used in the refinement (correct atom types, treatment of hydrogen atoms, disorder, and other features). The major contributory factor is the quality of the single-crystal sample, since this directly affects the quality and quantity of the diffraction data. Samples with poor crystallinity, containing significant disorder, or of inadequate size lead to weak diffraction; intensities have greater uncertainties, and those at higher angles of diffraction are of insignificant intensity, so they contain no useful information. By rearrangement of the Bragg equation $\lambda = 2d \sin \theta$, we see that

$$d_{\min} = \frac{\lambda}{2} \frac{1}{\sin \theta_{\max}} \tag{1}$$

so that a lack of data at higher angles means features close together in the structure can not be resolved; the effective resolution of the structure is determined by the maximum Bragg angle to which significant data can be measured. This is a well-known problem in protein crystallography, where large structures, high thermal motion, and extensive disorder of solvent of crystallization can severely curtail the high-angle data, and structures are usually described as being at "2 Å resolution," for example. For a reliable geometry of a coordination compound, a resolution markedly smaller than atomic separations (bond lengths) is required, and the desirable value is commonly taken to be around 0.8 Å. Problems similar to those of protein crystallography can afflict other large structures, such as polynuclear coordination compounds, especially when many counter-ions and/or solvent molecules are also present and there is scope for substantial disorder. Some of these can be obviated by use of special techniques for crystal growth, as described in Chapter 1.28.

2.4.2.2 X-ray Detector Developments

For about 30 years from the 1960s, most single-crystal X-ray diffraction made use of computer-controlled diffractometers. Detectors were small scintillators coupled to photomultipliers, and measured one reflection at a time, providing information on both the direction and the intensity. For a given overall level of diffracted intensity, the time needed to collect a full data set was proportional to the size of the asymmetric unit of the structure: a structure twice the size gave twice as many unique reflections. The most productive systems measured a few thousand reflections per day, and up to about an hour was required for the initial determination of the unit cell and crystal orientation, without which further measurements could not proceed since the correct

diffractometer angles had to be calculated for each individual reflection. Any serious error in the unit cell determination (such as a unit cell axis half its correct length, resulting from overlooking a systematically weak subset of the data) meant the data set was unusable. Such effects are by no means uncommon in coordination chemistry, especially when heavy-metal atoms lie on crystallographic symmetry elements in certain space groups and make no contribution to an entire class of reflections.

Area detectors are larger and can record many reflections simultaneously. In order to be useful, they must record not only the arrival of X-ray photons, but also their position on the face of the detector. Although electronic detectors of this type came into use in protein crystallography soon after their development for other purposes (mainly medical imaging), they were not widely used in chemical crystallography for a number of reasons, until the particular technology of charge-coupled devices (CCDs) was introduced and incorporated into fully featured commercial instruments in the mid-1990s. A decade or more later, they are now the standard method of choice.

The most obvious advantage of an area detector is its ability to record many reflections at the same time, thus reducing the time required for a full data collection. A larger structure needs no more time than a smaller one, because it gives a higher density of reflections on the detector. A further advantage is that many symmetry-equivalent data are usually measured, and these provide an indication of the data quality as well as being a basis for various methods of correcting systematic errors such as absorption.

In addition, an area detector records the whole of the diffraction pattern, not just the expected Bragg reflection positions. This ensures that no data are overlooked, and means that the unit cell and crystal orientation do not actually have to be determined before the full data collection begins; this can be done afterwards. With an area detector, it is much easier to detect the presence of crystal twinning or other effects that lead to two or more superimposed diffraction patterns from a sample that is not, in fact, a single crystal after all. With rapid recording of the diffraction pattern, unit cell determination is very quickly achieved, and samples can be screened in a short time. The sensitivity of modern CCD detectors permits the collection of data from poorer and more weakly scattering crystals than can be tolerated with a four-circle diffractometer, thus extending the range of application of the technique. Finally, the pedagogical advantage of an area detector should not be overlooked; it makes the teaching of crystallography and training of researchers easier, because of the clearer visualization of diffraction patterns.

2.4.2.3 X-ray Sources

The standard source of X-rays in a crystallography research laboratory is a sealed X-ray tube, in which a small fraction of electron kinetic energy is converted into X-rays on impact on a metal target, the majority being lost as heat; of the generated X-rays, a small proportion leaves the evacuated apparatus through a thin window and is collimated to a narrow beam after removal of unwanted wavelengths by diffraction through a monochromator crystal. The whole process is extremely inefficient. One obvious approach to the problem of weak diffraction from small crystals and other difficult samples is to increase the intensity of the incident X-rays. The basic X-ray tube can be modified to achieve a modest increase, by keeping the target moving in its own plane, thus reducing the heat loading and enabling a higher electron beam current. These rotating anode sources are considerably more expensive to buy and to maintain than conventional X-ray tubes, and the intensity increase is usually less than an order of magnitude, so the advantages are limited.

A more recent development is the collection and concentration of more of the X-rays generated instead of just the narrow beam taken from a standard tube. This depends on modern technological advances to produce extremely well polished mirrors giving glancing-angle reflection of X-rays, the use of devices consisting of variable-thickness layers of materials with different crystal lattice spacings to give a focusing effect through diffraction effects, and total internal reflection of X-rays in glass capillaries. Each of these can give about an order of magnitude increase in intensity delivered from an X-ray tube to a crystalline sample for study. Some of them can be combined with microfocus X-ray tubes, in which magnetic focusing of the electron beam gives a very small target spot, reducing heat loading.[6]

Very much higher intensities are derived from synchrotron storage rings. These are major national or international facilities that generate intense radiation extending from the infrared through the X-ray region of the electromagnetic spectrum, by constraining a beam of relativistic

electrons to a polygon circuit by means of strong magnetic fields. Each deflection of the electron beam from a straight line, whether by the main bending magnets of the storage ring or by further magnetic devices inserted between them (known as wigglers and undulators), produces a highly collimated beam of so-called synchrotron radiation with an intensity-wavelength spectrum depending on the magnetic device and other operating parameters of the storage ring. The relativistic nature of the electrons leads to a number of unusual properties of the radiation, including its high degree of collimation and almost complete polarization in the horizontal plane, and any wavelength can be selected from the total output, focused and deflected by various X-ray optic devices such as crystal monochromators and glancing-angle mirrors.

For chemical crystallography, the most important features of synchrotron radiation X-rays are their enormous intensity and the wavelength selectability.[7] The intensity is several orders of magnitude greater than any laboratory X-rays, and it can also be focused to a very narrow beam to match the dimensions of microcrystals. Crystals as small as a few microns can be routinely examined on suitable diffraction facilities at synchrotron sources, though few such facilities are available for general public use, others being restricted to commercial concerns. In order to maximize the benefit of the high intensities and make cost-effective use of these expensive central facilities, area detectors are used, and the combination means that very fast data collection can be achieved, even from tiny crystals, with several full data sets in a single day. Crystals may be effectively single grains from coarse powder samples, or they may be very fine needles or thin plates having a vanishingly small total volume. Even larger crystals may give weak diffraction, because of disorder or other structural problems, and synchrotron radiation can help in such situations. The high intensity is also an advantage in the study of superstructure problems, where small but systematic differences in atomic arrangements in a regular pattern lead to very weak subsets of reflections in an otherwise normal diffraction pattern.

The possibility of choosing a particular wavelength, rather than taking the output of one of the standard laboratory X-ray tubes, provides opportunities for special types of experiment beyond the scope of this discussion. Among the possible advantages are the avoidance or reduction of some systematic errors such as X-ray absorption or extinction, which may severely affect measured intensities and hence the precision and accuracy of crystal structures, and the exploitation of effects such as anomalous scattering for the determination of absolute configuration of chiral structures, as described in Section 2.4.2.7.

2.4.2.4 Low-temperature Data Collection

One of the most effective ways of improving the quality of a crystal structure is to collect the diffraction data from a crystal maintained at a reduced temperature. A couple of decades ago, low-temperature crystallography was a major undertaking, with unreliable and cumbersome cooling devices, and it was not widely practiced. These days the equipment is easy to use, very reliable and stable, and inexpensive compared with other components of a crystallography facility. Its use is essentially routine, and low-temperature data collection should be considered the norm rather than a special experiment. The most widely used devices operate by converting liquid nitrogen to a constant-flow stream of gas and heating it to the desired temperature, with monitoring and feedback control of the temperature. Formation of ice on the sample by condensation from the atmosphere is avoided by a room-temperature sheath of dry air or nitrogen surrounding the cold stream. With such an apparatus, temperatures down to about 100 K are readily achieved, and in some cases the boiling point of nitrogen, 77 K, can be more closely approached. Some cooling systems use liquid helium, and these allow very much lower temperatures to be reached for special purposes.

The main advantage of low-temperature data collection is the reduced atomic vibration in the sample. This concentrates the average electron density distribution more closely around the atomic nuclei and reduces destructive interference effects in the X-ray scattering. As a result, reflection intensities are higher, especially at higher Bragg angles, and the data can be measured more precisely. This leads to greater precision in the final crystal structure. The effect is particularly marked for peripheral atoms in a molecule, including the terminal atoms of ligands and substituents, hydrogen atoms, counter-ions, and uncoordinated solvent molecules. For atoms with high displacement parameters at room temperature, the reduction of movement on cooling also improves the fit of the usual mathematical model for anisotropic vibration, further improving the precision and reducing systematic errors that often make bond lengths appear too short

(libration effects). In many cases, disorder is substantially reduced or eliminated on cooling and, even where it remains, it is usually easier to model because of less severe overlap of the separate electron density distributions of the disorder components.

Cooling may also reduce any decomposition of the sample in the X-ray beam, which imposes some thermal loading on the crystal through absorption effects. Furthermore, it is far easier to handle air-sensitive materials in this way than for room-temperature data collection. Instead of having to provide such crystals with a stable and robust protective shield (either a coating such as epoxy resin, or a sealed thin-walled capillary tube), they can simply be handled under an inert viscous oil into which they are introduced from a Schlenk tube. The oil serves as an adhesive for mounting the crystal on the diffractometer and forms a thin protective film that vitrifies by shock-cooling in the cold gas stream.[8] Air-stable and air-sensitive samples can be handled in virtually the same way.

The only serious problem with low-temperature data collection comes when a sample undergoes a major structural change on cooling, as it passes through a phase transition. Small changes may leave the single crystal intact; indeed, the incidence of an order–disorder transition can be an advantage. Large changes, however, probably lead to degradation of crystal quality and the loss of single-crystal character; some samples disintegrate in a spectacular way. It may be possible to determine the temperature at which the change occurs by monitoring the crystal optically and with X-rays as it is cooled slowly, and then collecting data from a fresh crystal at a slightly higher temperature.

2.4.2.5 Advances in Computing

Throughout its history, significant advances in crystallography have gone hand-in-hand with developments in computing resources and power, and the subject relies heavily on computers. The availability of low-cost, high-power computing has been important for recent advances in crystallography. The real-time control of modern diffractometers, and the measurement, storage, and processing of huge quantities of raw data from area detectors are heavily dependent on sufficient computing speed and data capacity. Fortunately, present-day personal computers are adequate for these purposes, and most crystallographic work does not require special high-performance workstations or supercomputers. Inexpensive high-capacity data storage in the form of compact disks and magnetic tapes of various formats is invaluable for the reliable archiving of diffraction data and crystal structure results.

Adequate computing hardware is essential, but so is good-quality software. Crystallographers are relatively well served, both by integrated commercial systems available from a number of firms and by individual programs or suites of software in the public domain. Commercial software covering all aspects from data collection to the analysis of geometrical results and molecular graphics is usually provided as part of an overall package with diffractometer systems. Widely used free and inexpensive shareware public-domain software, together with many specialized programs, is available conveniently through the British public-funded Collaborative Computational Project CCP14 and its mirror sites;[9] some programs can be downloaded directly, while contact information is provided for others. The collection includes a wide range of software for "small molecule" crystallography and related topics.

2.4.2.6 Disorder, Twinning, and other Structural Problems

For an ideal crystal structure, all unit cells are identical, and all asymmetric units are exactly equivalent by operation of space group symmetry. Atomic vibrations mean that this is not true instantaneously, but these are catered for in the atomic displacement parameters on the assumption that the movements are not correlated throughout the structure, and the equivalence applies to the time-averaged structure.

Disorder is a random variation in the detailed contents of the asymmetric unit, such that not all units are truly equivalent; for some atoms or groups of atoms, there are alternative positions, with no regular pattern in their adoption; such a regular pattern would lead to a larger true repeat in the structure, and the observation of a superstructure. X-ray diffraction sees the average asymmetric unit when the variation is random, and this manifests itself in the structural model as partially occupied atom sites. Examples include: the disorder of bridging cyano ligands over

M—C—N—M and M—N—C—M configurations; disorder over two orientations of a methyl group bonded to an aromatic ring; a toluene solvent molecule with two opposite possible orientations, such that the average conforms to an inversion center at this site; an almost spherical anion such as PF_6^- with no significant interactions other than normal ionic forces, which may adopt two or more different orientations; a flexible ring such as a tetrahydrofuran ligand adopting alternative conformations; and a weakly held solvent molecule that is present in some asymmetric units but not in others, leading to a non-stoichiometric solvate formula.

The presence of disorder generally reduces diffraction intensities and hence affects the precision of the crystal structure; the largest effect is on the disordered part of the structure itself, but the nature of the Fourier transform relationship is such that precision overall is affected, albeit not significantly in many cases. The problem is compounded if the disorder is difficult to model with partial atoms, and this is especially the case when the two or more components do not have resolved electron density distributions.

Disorder is best avoided if possible. The most common contributing factors are pseudo-spherical weakly interacting counter-ions and conformationally flexible groups. This has a bearing on the choice of substituents, counter-ions, and solvents in the preparation and crystallization of samples. Unfortunately, disorder can affect such important features as chelate rings in complexes of multidentate ligands.

If it can not be avoided, disorder may be reduced or its effects ameliorated by low-temperature data collection, which is almost always to be recommended. Modern crystallographic software provides many effective and powerful methods for modeling disorder, even in quite complex manifestations, and the judicious application of refinement techniques such as sensible geometrical constraints and restraints, and an appropriate treatment of atomic displacement parameters, can often salvage what would otherwise be a structural mess.

Crystal twinning has come into greater prominence with the advent of area detectors, since its incidence is now more often noted and it can be successfully dealt with in many cases. The term is, however, more widely used than it should be, as a general description of any situation in which a sample gives a superposition of more than one diffraction pattern. Samples consisting of split crystals or polycrystalline aggregates are not usually twins. A twinned crystal is one in which there are two (or more) different orientations or mirror images of the same structure within one crystal, with a well-defined relationship to each other often based on fortuitous rational relationships among the unit cell parameters. It results from putting together blocks of unit cells in different but related orientations during the formation of the crystal. One type of twinning, for example, is a result of a unit cell with a metric symmetry (geometrical shape) higher than the actual symmetry of its contents, such as a monoclinic unit cell with a β angle close to 90°, or an orthorhombic crystal with two axes almost equal in length; in these cases, unit cells can be put together the wrong way round, leading to regions of the complete structure that are rotated relative to each other, and the resulting diffraction pattern consists of two different orientations of the same pattern occurring simultaneously, with superposition of reflections that are not actually symmetry-equivalent. Some other forms of twinning lead to only partial overlap of the diffraction patterns. Twinning is characterized by two properties: the twin law, which is the mathematical relationship between the two orientations of the structure in the sample; and the twin fraction, which gives the relative amounts of the components present.

The subject is quite complex and beyond the scope of this discussion. For our purposes here, we note only that twinning is far more easily recognized with an area detector, and the complete diffraction pattern is measured, covering the contributions from both (or more) components. Computer programs have been developed that can extract the twin law from a multiple diffraction pattern, and the twin fraction is usually refined as a parameter in the crystal structure model. The incidence of twinning may or may not have an adverse effect on the quality of a crystal structure, depending on the exact nature of the twinning and the success with which it can be modeled.

2.4.2.7 Anomalous Scattering and Absolute Configuration

Simple diffraction theory indicates that diffraction patterns are always centrosymmetric, even when the corresponding crystal structure is not; this is known as Friedel's law. It is not, however, true under certain circumstances. The simple theory assumes that all atoms scatter any X-rays with a constant fixed phase relationship between the incident and scattered rays (a phase shift of exactly 180°). If the X-ray photon energy is close to a difference in atomic orbital energies,

however, there is an additional phase shift that depends on the atom and on the X-ray wavelength; it is usually small, but it can be significant. This is known as anomalous scattering. For a centrosymmetric crystal structure, the effects from symmetry-related atoms cancel out, so Friedel's law still applies. For structures without inversion symmetry, the effect is that reflections having equal but opposite indices do not have exactly the same intensity. The small differences, if they are not too small, can be used to distinguish between a structure and its inverse, since these give opposite effects. The most important application is to structures of enantiomerically pure chiral molecules, which must form non-centrosymmetric crystal structures. If anomalous scattering effects are significant, the absolute configuration can be determined with confidence. This is often the case for coordination compounds, since anomalous scattering effects tend to be larger for heavier atoms, though this is not a steady trend across the periodic table.

2.4.2.8 X-ray Powder Diffraction

A single crystal gives a single diffraction pattern with no overlapping reflections. Twinned and multiple crystals correspondingly generate superimposed multiple diffraction patterns, in which there may be some overlap. A microcrystalline powder consists of very many tiny single crystals, each giving its own diffraction pattern. This produces essentially all possible orientations of the pattern superimposed. Each reflection is now a cone of radiation rather than lying in a unique direction, and the three-dimensional single diffraction pattern has been collapsed into a one-dimensional set of data, the only geometrical variable being the Bragg angle. Reflection overlap is severe except for the simplest and smallest crystal structures.

Nevertheless, powder diffraction patterns are used for crystal structure determination, simply because some samples can never be obtained as single crystals. The underlying principles are the same as for single-crystal diffraction, but their implementation is rather different, as a result of the severe overlap of the powder diffraction patterns and the loss of three-dimensional information. Structure refinement based on matching observed and calculated total diffraction profiles (Rietveld refinement) is now well established, and considerable progress is currently being made in developing *ab initio* methods for solving the crystallographic phase problem, but there will always be a limit on the size and complexity of structures that can be determined in this way.[10] The method is more widely employed with neutrons instead of X-rays, and is generally more successful with synchrotron radiation than with laboratory X-ray sources, because of the better angular resolution available in the powder diffraction pattern. For discussion of neutron powder diffraction, see Chapter 2.6.

2.4.2.9 Publication and Crystallographic Databases

The nature of crystal structures and the methods of determining them lend themselves very well to procedures of standardization in the format, archiving and retrieval, exchange, and publication of data and results. The scope of the results of a crystal structure determination is well defined, with a set of parameters of certain kinds that are generally expected to be present. It is not surprising, therefore, that standard forms of crystallographic data exchange and publication have been developed. Of various attempts that have been made, the Crystallographic Information File (CIF) format has been essentially universally adopted,[11] with the promotion of the International Union of Crystallography.[12] It serves as a widely accepted medium for the transmission of crystal structure results to journals publishers as supplementary material, and is even the sole format permitted for the submission of complete manuscripts to some sections of *Acta Crystallographica*; the CIF contents (including sections such as abstract and discussion, supplied by the author as raw text) are converted by automatic routines into a formatted manuscript.

In a similar way, crystal structure results are ideal candidates for computer-searchable databases, and several such exist for the subject of crystallography as a whole. The vast majority of coordination compounds contain organic groups as ligands or counter-ions, and so are included in the Cambridge Structural Database,[13,14] developed and maintained by the Cambridge Crystallographic Data Centre.[15] Others may be found in the Inorganic Crystal Structure Database, supplied by the Fachinformationszentrum Karlsruhe.[16] These large and comprehensive repositories of crystal structures contain primary crystallographic data derived from published sources and from personal depositions by researchers of otherwise unpublished work. They are subjected

to extensive consistency tests and are sometimes more reliable than the original primary publication since errors are corrected wherever possible. Most important, they can be searched by powerful and easily used software to extract information based on many different criteria, including the matching of a desired fragment with a particular chemical connectivity. They are most widely used for making comparisons between new results and those previously published, and for checking for duplication of crystal structure determinations, but they also provide vast quantities of data for statistical analysis, leading to research projects probing structural trends and geometrical patterns.[17] It is a reflection of the importance of X-ray crystallography in chemical structure determination, and in coordination chemistry in particular, that these two databases contain over 300,000 entries; over half of the 250,000 entries in the Cambridge Structural Database are for metal-containing compounds.

2.4.3 REFERENCES

1. Giacovazzo, C.; Monaco, H. L.; Viterbo, D.; Scordari, F.; Gilli, G.; Zanotti, G.; Catti, M. *Fundamentals of Crystallography* 1992, Oxford University Press: Oxford, UK.
2. Glusker, J. P.; Lewis, M.; Rossi, M. *Crystal Structure Analysis for Chemists and Biologists* 1994, Wiley-VCH: Weinheim, Germany.
3. Dunitz, J. D. *X-ray Analysis and the Structure of Organic Molecules* 1995, Wiley-VCH: Weinheim, Germany.
4. Clegg, W. *Crystal Structure Determination* 1998, Oxford University Press: Oxford.
5. Clegg, W.; Blake, A. J.; Gould, R. O.; Main, P. *Crystal Structure Analysis: Principles and Practice* 2001, Oxford University Press: Oxford, UK.
6. Arndt, U. W.; Duncumb, P.; Long, J. V. P.; Pina, L.; Inneman, A. *J. Appl. Crystallogr.* **1998**, *31*, 733–741.
7. Clegg, W. *J. Chem. Soc., Dalton Trans.* **2000**, 3223–3232.
8. Köttke, T.; Stalke, D. *J. Appl. Crystallogr.* **1993**, *26*, 615–619.
9. http://www.ccp14.ac.uk/
10. Louër, D. *Acta Crystallogr., Sect. A* **1998**, *54*, 922–933.
11. Hall, S. R. *Acta Crystallogr., Sect. A* **1998**, *54*, 820–832.
12. http://www.iucr.org/iucr-top/cif/index.html.
13. Allen, F. H. *Acta Crystallogr., Sect. A* **1998**, *54*, 758–771.
14. Allen, F. H. *Acta Crystallogr., Sect. B* **2002**, *58*, 380–388.
15. http://www.ccdc.cam.ac.uk/
16. http://crystal.fiz-karlsruhe.de/
17. Bürgi, H. B. *Acta Crystallogr., Sect. A* **1998**, *54*, 873–888.

Comprehensive Coordination Chemistry II
ISBN (set): 0-08-0437486

Volume 2, (ISBN 0-08-0443249); pp 57–64

2.5
Chiral Molecules Spectroscopy

R. D. PEACOCK
University of Glasgow, UK
and
B. STEWART
University of Paisley, UK

2.5.1 INTRODUCTION 65
2.5.2 THEORY 66
2.5.2.1 Absorption 66
2.5.2.2 Circular Dichroism 67
2.5.2.3 E1–M1 Mechanism 67
2.5.2.4 E1–E2 Mechanism 67
2.5.3 CIRCULAR DICHROISM OF *d–d* AND *f–f* TRANSITIONS 68
2.5.3.1 Introduction 68
2.5.3.2 Trigonal Complexes 68
2.5.3.3 Complexes of Lower Symmetry 71
2.5.3.4 Lanthanide Circular Dichroism and Circularly Polarized Luminescence 72
2.5.4 CIRCULAR DICHROISM OF INTERNAL LIGAND TRANSITIONS—EXCITON COUPLING 72
2.5.5 CIRCULAR DICHROISM OF CHARGE-TRANSFER TRANSITIONS 73
2.5.6 CIRCULAR DICHROISM OF CHIRAL METAL–METAL-BONDED SPECIES 74
2.5.7 X-RAY NATURAL CIRCULAR DICHROISM 75
2.5.7.1 Introduction 75
2.5.7.2 Theoretical Background 76
2.5.7.3 Measurements 77
2.5.8 SUMMARY 78
2.5.9 REFERENCES 80

2.5.1 INTRODUCTION

The origin of optical activity in molecules often reduces to the question of how the molecule acquires the electronic properties expected of a chiral object when it is formed from an achiral object. Most often an achiral molecule becomes chiral by chemical substitution. In coordination compounds, chirality commonly arises by the assembly of achiral units. So it is natural to develop ideas on the origins of chiral spectroscopic properties from the interactions of chirally disposed, but intrinsically achiral, units. Where this approach, an example of the "independent systems" model, can be used, it has obvious economic benefits. Exceptions will occur with strongly interacting subunits, e.g., twisted metal–metal-bonded systems, and in these cases the system must be treated as a whole—as an "intrinsically chiral chromophore."

This subsystem approach is familiar in the crystal field model where the effects of the ligand environment on a coordinated metal are treated using perturbation theory. In dealing with the optical activity of a metal center, we simply need to extend this approach to discover the extra perturbation terms that become switched on when the metal finds itself in a chiral environment.

In this chapter we begin by describing a general theory of circular dichroism (CD). In subsequent sections we deal with the CD of metal localized (*d–d* and *f–f*) transitions, internal ligand transitions, and charge-transfer transitions. Next we describe the CD spectra of twisted compounds with metal–metal multiple bonds and conclude with an account of a new form of CD spectroscopy, X-ray natural CD (XNCD), which has been pioneered using coordination compounds.

2.5.2 THEORY

2.5.2.1 Absorption

The quantum mechanical approach to light absorption[1] involves evaluating matrix elements of a radiation-molecule interaction operator between initial and final states, subject to the conservation of energy. The cross-section for a photon absorption process in which there is an electronic transition from an initial state $\langle i|$ to a final state $|f\rangle$ is given by

$$\sigma = 4\pi^2\alpha_o\hbar\omega|\langle i|\boldsymbol{H}_{int}|f\rangle|^2\delta(E_f - E_i - \hbar\omega) \tag{1}$$

for radiation of angular frequency ω where α_o is the fine structure constant and the δ-function takes care of energy conservation. The interaction operator is essentially the scalar product of the electron momentum $\mathbf{p}$ and the vector potential $\mathbf{A}$ of the radiation field:

$$\boldsymbol{H}_{int} = (e/mc)\ \mathbf{p}\cdot\mathbf{A},\ \mathbf{A} = \boldsymbol{\varepsilon}e^{i\,\mathbf{k}\cdot\mathbf{r}} \tag{2}$$

for photons of wavelength λ with wave vector $\mathbf{k}$ $(=2\pi/\lambda)$ and polarization vector $\boldsymbol{\varepsilon}$ interacting with an electron at position $\mathbf{r}$.

The vector potential may be expanded in a truncated Taylor series,

$$e^{i\,\mathbf{k}\cdot\mathbf{r}} = 1 + i\,\mathbf{k}\cdot\mathbf{r}(\text{provided that } \mathbf{k}\cdot\mathbf{r} \ll 1) \tag{3}$$

which, when substituted into the cross-section expression, gives:

$$\sigma = 4\pi^2\alpha_o\hbar\omega|\langle i|\boldsymbol{\varepsilon}\cdot\mathbf{p} + i(\boldsymbol{\varepsilon}\cdot\mathbf{p})(\mathbf{k}\cdot\mathbf{r})|f\rangle|^2\delta(E_f - E_i - \hbar\omega) \tag{4}$$

The $|\langle i|\ \boldsymbol{\varepsilon}\cdot\mathbf{p}\ |f\rangle|^2$ contribution gives rise to the familiar electric dipole absorption responsible for a large part of electronic spectroscopy. The second term in the matrix element may be divided into a symmetric part, identifiable with the electric quadrupole interaction, and an antisymmetric part which is the magnetic dipole operator:

$$\begin{aligned}(\boldsymbol{\varepsilon}\cdot\mathbf{p})(\mathbf{k}\cdot\mathbf{r}) &= \tfrac{1}{2}[(\boldsymbol{\varepsilon}\cdot\mathbf{p})(\mathbf{k}\cdot\mathbf{r}) + (\boldsymbol{\varepsilon}\cdot\mathbf{r})(\mathbf{k}\cdot\mathbf{p})] + \tfrac{1}{2}[(\boldsymbol{\varepsilon}\cdot\mathbf{p})(\mathbf{k}\cdot\mathbf{r}) - (\boldsymbol{\varepsilon}\cdot\mathbf{r})(\mathbf{k}\cdot\mathbf{p})] \\ &= \text{electric quadrupole} + \text{magnetic dipole}\end{aligned} \tag{5}$$

The presence of these higher-order terms in the expansion of the transition operator results in further contributions to the absorption cross-section. Due to their dependence on powers of $\mathbf{k}\cdot\mathbf{r}$, these are expected to be smaller than the electric dipole contribution in many circumstances. For example, consider visible light for which $|\mathbf{k}| = 2\pi/\lambda \sim 2\times10^6\,m^{-1}$. Since $|\mathbf{r}| \approx 10^{-10}$ m for a valence electron, $\mathbf{k}\cdot\mathbf{r} \approx 2\times10^{-4}$.

At X-ray wavelengths, however, $|\mathbf{k}| \sim 5\times10^9\,m^{-1}$ and $\mathbf{k}\cdot\mathbf{r} \approx 5\times10^{-1}$. Quadrupole activity is thus expected to be considerably enhanced in the X-ray compared with the visible region. It has been found that quadrupole transitions play a key role in natural CD in the X-ray region.

2.5.2.2 Circular Dichroism

As seen above, the general treatment of the photon-molecule interaction[2] expands the transition operator as a series with electric and magnetic multipole contributions:

$$\begin{aligned} T &= \mathrm{E1} + \mathrm{E2} + \mathrm{E3} + \cdots + \mathrm{M1} + \mathrm{M2} + \mathrm{M3} + \cdots \\ &= \text{electric dipole} + \text{electric quadrupole} + \text{electric octupole} + \cdots + \text{magnetic dipole} \\ &\quad + \text{magnetic quadrupole} + \text{magnetic octupole} + \cdots \end{aligned} \tag{5}$$

These multipoles behave as tensors of increasing rank (k) and alternating parity given by $(-1)^k$ for electric moments and $(-1)^{k-1}$ for magnetic moments.

The total transition probability will, therefore, contain contributions from each of these transition probability amplitudes (channels). There will also be contributions from cross-terms between the different channels. When the cross-terms involve transition moment operators of opposite parity this gives rise to the differential absorption of circularly polarized light and this is the origin of CD.

2.5.2.3 E1–M1 Mechanism

Of particular interest here is the leading cross-term (E1–M1) which provides the pseudoscalar product between the electric ($\boldsymbol{\mu}$) and the magnetic ($\mathbf{m}$) dipole operators occurring in the famous Rosenfeld–Condon equation for the rotational strength of a transition $i \rightarrow f$ in an isotropic system:

$$R_{\mathrm{if}} = Im\{\langle i|\boldsymbol{\mu}|f\rangle \cdot \langle f|\mathbf{m}|i\rangle\} = Im\{\langle i|\mu_{\mathbf{x}}|f\rangle\langle f|m_{\mathbf{x}}|i\rangle + \langle i|\mu_{\mathbf{y}}|f\rangle\langle f|m_{\mathbf{y}}|i\rangle + \langle i|\mu_{\mathbf{z}}|f\rangle\langle f|m_{\mathbf{z}}|i\rangle \tag{6}$$

This will be referred to as the E1–M1 mechanism and is the most important one for the majority of chiral systems. The importance of other terms, notably E1–E2 will be discussed later but for the moment it will be assumed that the E1–M1 mechanism is sufficient. A pseudoscalar quantity is a rotational invariant but, unlike a true scalar, it has odd parity and, therefore, inverts its sign between enantiomeric systems and vanishes in achiral systems. This is what we expect of a quantity related to CD.

The integrated area under a CD curve is directly related to the rotational strength in Debye–Bohr magneton units:

$$R = 0.248 \int (\Delta\varepsilon/\tilde{\nu})\ \mathrm{d}\tilde{\nu} \tag{7}$$

An important experimental quantity is the Kuhn dissymmetry factor g defined as the ratio of the rotational strength to the dipole strength for a given transition, or practically as the ratio of absorbances or molar absorptivities: $g = (A_{\mathrm{L}} - A_{\mathrm{R}})/(A_{\mathrm{L}} + A_{\mathrm{R}}) = \Delta\varepsilon/\varepsilon$, usually at the wavelength of a CD maximum. The magnitude of the g factor gives a measure of the magnetic dipole character of the transition. Typically, $g \sim 10^{-2}$ for a magnetic dipole allowed transition and 10^{-3}–10^{-4} for a magnetic dipole forbidden transition. The dissymmetry factor is also related to the practical limitation on the instrumental measurement of CD; currently commercial CD spectrometers can measure g factors of around 10^{-6}.

2.5.2.4 E1–E2 Mechanism

In the optical activity arising from higher-order cross-terms, the effects are in most cases expected to be orientation-dependent. Pseudoscalar terms are the only ones which survive in random orientation (molecules in solution or liquid phase). At the same order of perturbation as E1–M1 there is a product of the electric dipole and electric quadrupole transition operators (E1–E2). Since the latter product involves tensors of unequal rank, the result cannot be a pseudoscalar and this term would not, therefore, contribute in random orientation but can be significant for oriented systems with quadrupole-allowed transitions. The E1–E2 mechanism was developed by Buckingham and Dunn[3] and recognized by Barron[4] as a potential contribution to the visible CD in oriented crystals containing the $[\mathrm{Co(en)_3}]^{3+}$ ion.

Recent work on the XNCD of coordination compounds[5–7] has found that the predominant contribution to X-ray optical activity is from the E1–E2 mechanism. The simplest case is that of a rotational symmetry axis of order $n \geq 3$. The expression for the rotational strength observed with radiation propagating along the n-fold axis (z-axis) is then:

$$R_{if} = -\omega_{if} Re\{\langle i|\mu_x|f\rangle\langle f|Q_{yz}|i\rangle - \langle i|\mu_y|f\rangle\langle f|Q_{xz}|i\rangle\} \tag{8}$$

This rotational strength behaves as a second-rank odd-parity irreducible tensor with cylindrical symmetry, displaying the following angular dependence,

$$R_{if} \sim \tfrac{1}{2}(3\cos^2\theta - 1)$$

where θ is the angle between the propagation direction and the rotational symmetry axis. It follows that the orientational average vanishes and that the rotational strengths for propagation parallel and perpendicular to the symmetry axis should be in the ratio $+1{:}-1/2$ respectively. Thus the observation of E1–E2 optical activity requires an oriented system such as a single crystal. Note the frequency factor in Equation (8), which does not appear in the E1–M1 rotational strength (Rosenfeld–Condon equation, Equation (6)).

2.5.3 CIRCULAR DICHROISM OF *d–d* AND *f–f* TRANSITIONS

2.5.3.1 Introduction

In 1895 Cotton coined the term *circular dichroism*[8] to describe the differential absorption of right and left circularly polarized light by a solution of basic copper *d*-tartarate. Thus the *d–d* transitions of a coordination compound were the first electronic transitions to be found to exhibit CD. Since *d–d* and *f–f* transitions are magnetic dipole allowed at the atomic orbital level, the dominant mechanism is E1–M1 for these transitions in the vast majority of coordination compounds. In lower symmetries, there is always at least one transition which can act as a magnetic dipole source and in chiral symmetries this source is mixed with electric-dipole allowed transitions to produce a nonvanishing pseudoscalar product and hence CD. Except in certain high symmetries, this mixing distributes magnetic dipole activity over all of the *d–d* or *f–f* transitions of a given metal.

The development of the theory of *d–d* and *f–f* CD has largely revolved around the origin of the electric dipole transition probability in these formally Laporte-forbidden transitions.[9] The most successful approach recognizes the role of transient ligand excitations of dipole character. In this "ligand polarizability" model,[10] the ligand excitations are induced by the (nonresonant) radiation field and Coulombically correlated with (resonant) even-order allowed electric multipole transition moments of the metal. This contrasts with the earlier crystal field approach in which the ligands provided only a static potential to mix higher energy metal-based or charge-transfer electric dipole activity into the *d–d* or *f–f* excitations.

2.5.3.2 Trigonal Complexes

The CD spectrum of the Λ–$[Co(en)_3]^{3+}$ (where en = 1,2-diaminoethane) ion will be used to exemplify the various aspects of *d–d* CD. The solution and uniaxial single crystal CD spectra of $\{\Lambda\text{-}[Co(en)_3]Cl_3\}_2NaCl{\cdot}6H_2O$ are shown in Figure 1. The lowest energy transition $^1A_{1g} \rightarrow {}^1T_{1g}$ is magnetic dipole allowed and electric dipole forbidden in the parent O_h symmetry, the next transition ($^1A_{1g} \rightarrow {}^1T_{2g}$) is electric quadrupole allowed and both magnetic dipole and electric dipole forbidden. In D_3 symmetry the $^1T_{1g}$ state splits into $^1A_2$ and ^1E states and the $^1T_{2g}$ state into $^1A_1$ and ^1E states. The E symmetry states may mix and thus the $^1A_1 \rightarrow {}^1E(^1T_{2g})$ transition acquires some magnetic dipole activity. In the uniaxial crystal spectrum only the E-polarized transitions are active; in solution, or random dispersal in an alkali halide disk, both E and A_2 polarized transitions can be detected. The restricted sum rule for the trigonal components leads to considerable cancellation of CD in the $^1A_{1g} \rightarrow {}^1T_{1g}$ transition since the trigonal splitting is quite small in this complex.

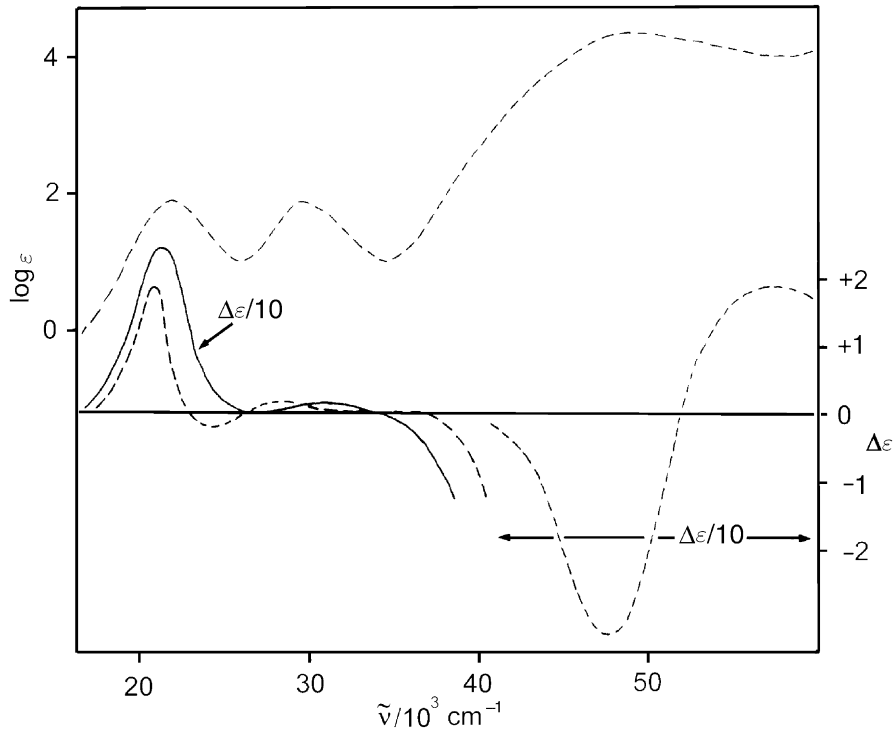

Figure 1 The axial single crystal spectrum of $\{\Lambda\text{-}[Co(en)_3]Cl_3\}_2 \cdot NaCl \cdot 6H_2O$ (solid line) and the absorption and CD spectra of $\Lambda\text{-}[Co(en)_3][ClO_4]_3$ in water (upper and lower dashed curves, respectively).

By combining uniaxial crystal and random orientation measurements the rotational strengths of both the E and A_2 components may be obtained.[11] Table 1 lists the rotational strengths of the $^1A_1 \rightarrow {}^1E(^1T_{1g})$ and $^1A_1 \rightarrow {}^1A_2(^1T_{1g})$ transitions for all the pseudo-octahedral Co^{III} complexes which have been measured, along with the angle of twist (ω) as defined in Figure 2. From Table 1 it can be seen that there is an empirical correlation between the sign of the CD and the sense of twist about the C_3 axis: an anticlockwise twist gives rise to a positive CD for the $^1A_1 \rightarrow {}^1E(^1T_{1g})$ transition.[17] Note that there is no correlation between the sign of the CD and the conventional definition of absolute configuration, Λ or Δ, based on the ligand connections. The angle ω is a measure of the *ligator* chirality and so the observed correlation is indicative of the dominant contribution of the ligator chirality to the CD of the lowest *d–d* excitations in these complexes. The sense of chirality of the saturated chelate rings (Λ or Δ), although contributing to the intensity of the CD, does not control it.[17] The sole exceptions to the sign/twist correlation[16] are $[M(pd)_3]$, (where pd = 2,4-pentanedionato; M = Co, Cr) complexes which have an *unsaturated* chelate ring backbone.

The principal problem in explaining the CD in these (and indeed all) *d–d* transitions is to explain the source of electric dipole intensity. Before the advent of accessible *ab initio* methods of

Table 1 Rotational strengths ($\times 10^{40}$ cgs units) of trigonal Co^{III} complexes.

Crystal	$R(E)$	$R(A_2)$	ω (°)	*References*
$\{\Lambda\text{-}[Co(en)_3]Cl_3\}_2 \cdot NaCl \cdot 6H_2O$	+62.9	−58.6	−54.9	12
$\Lambda\text{-}[Co(S\text{-pn})_3]Br_3$	+38.1	−36.6	−55	11
$\Lambda\text{-}[Co(S,S\text{-chxn})_3]Cl_3 \cdot 5H_2O$	+56.5	−51.1	−55	11
$\Lambda\text{-}[Co(S,S\text{-cptn})_3]Cl_3 \cdot 4H_2O$	+57.3	−54.5	−54.5	11
$\Lambda\text{-}[Co(S,S\text{-ptn})_3]Cl_3 \cdot 2H_2O$	+12.5	−14.4	−57	11
$\Lambda\text{-}[Co(tmd)_3]Br_3$	+31.1	−38.7	−55.7	11
$\Lambda\text{-}[Co(tn)_3]Cl_3 \cdot 4H_2O$	−10.5	+10.2	+53	13
$[Co(2R\text{-Me-tacn})_2]Cl_3$	−14.8	+29.7	+52.4	14
$\Lambda\text{-}NaMg[Co(ox)_3] \cdot 9H_2O$	+114	−101	−54	15
$\Lambda\text{-}[Co(pd)_3]$	+54.7	−39.0	+52.7	16

chxn = *trans*-1,2-diaminocyclohexane; cptn = *trans*-1,2-diaminocyclopentane; ptn = 2,4-diaminopentane; tmd = 1,4-diaminobutane; tn = 1,3-diaminopropane; Me-tacn = *N*-methyl-1,4,7-triazacyclononane.

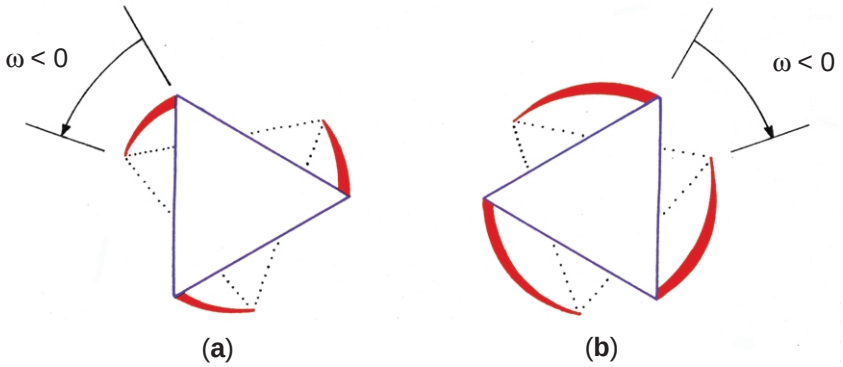

Figure 2 The angle, ω, characterizing the ligator twist of trisbidentate chelate complex of D_3 symmetry. The diagram shows how ω can be positive or negative for the same absolute configuration of the chelate rings. (a) and (b) show the situation in, for example, Λ-$[Co(en)_3]^{3+}$ and Λ-$[Co(tn)_3]^{3+}$, respectively.

calculation the emphasis was on acquisition of electric dipole intensity by mixing from a single identifiable source of electric dipole transition intensity (independent systems). In historical order[18,19] these sources were: perturbational *d–p* metal-based transitions, charge-transfer transitions and internal ligand transitions (ligand polarizability theory). It is generally agreed that only the last source is significant for pseudo-octahedral complexes although the other two sources may be of comparable importance in lower symmetry (e.g., pseudotetrahedral) species. According to the ligand polarizability theory the electric dipole intensity at the metal center arises from the allowed electric dipole transitions on the ligands correlated by the allowed higher multipole transition (hexadecapole in the case of the $^1A_1 \rightarrow {}^1E(^1T_{1g})$ transition of $[Co(en)_3]^{3+}$) of the metal ion. The theory can account[10] for the signs and magnitudes of the E and A_2 components of the $^1A_1 \rightarrow {}^1E(^1T_{1g})$ transition of $[Co(en)_3]^{3+}$ and for the conformational CD of a variety of Co^{III} trisdiamines.[19]

There have been two *ab initio* calculations (Table 2) of the CD of $[Co(en)_3]^{3+}$; both reproduce the CD of the $^1A_1 \rightarrow {}^1A_2, {}^1E(^1T_{1g})$ transitions reasonably well while one also accounts for the rotational strength of the $^1A_1 \rightarrow {}^1E(^1T_{2g})$ transition (*vide infra*). In each case an analysis of the wave functions confirmed that the principal source of the electric dipole intensity was internal ligand transitions (particularly the N–H and N–C $\sigma \rightarrow \sigma^*$ transitions). The CD in this case is, therefore, dominated by the position of the nitrogen ligators, and not by the position of the CH_2 groups of the ligand backbone. This finding helps to rationalize the empirical sign/twist correlation noted above. The position of the N—H bonds are expected to have a particularly large effect on the CD, thus explaining the well known sensitivity of the CD spectra of Co^{III} trisdiamine complexes to H-bonding interactions involving the N–H protons[21] (gegenion effect). For unsaturated ligands such as 2,4-pentanedione, however, the ligand is not readily separated into ligators and backbone and all the bonds in the ligand are expected to contribute to the electric dipole intensity and thus the CD.[16,17]

The CD of the $^1A_1 \rightarrow {}^1E(^1T_{2g})$ transition has been the subject of debate for some time. The $^1A_1 \rightarrow {}^1T_{2g}$ transition splits into $^1A_1 \rightarrow {}^1E(^1T_{2g})$ and $^1A_1 \rightarrow {}^1A_1(^1T_{2g})$ components in D_3 symmetry. The latter transition is both electric and magnetic dipole forbidden and cannot acquire intensity by mixing with any other metal-based transitions. Thus the solution and uniaxial single crystal CD spectra of the $^1A_1 \rightarrow {}^1E(^1T_{2g})$ transition should be identical. This is not the case; the CD is both stronger and at a slightly different energy in the single crystal. Barron suggested[4] that the explanation was that the CD in the oriented crystal arose not from the "normal" electric dipole–magnetic dipole (E1–M1) mechanism but from the interference between the borrowed electric dipole transition and the allowed electric quadrupole transition (E1–E2 mechanism). Since the

Table 2 Experimental and calculated rotational strength ($\times 10^{40}$ cgs units) of the $^1A_1 \rightarrow {}^1A_2(^1T_{1g})$, $^1A_1 \rightarrow {}^1E(^1T_{1g})$, and $^1A_1 \rightarrow {}^1E(^1T_{2g})$ transitions of the $[Co(en)_3]^{3+}$ ion.

	Experimental	*Calculated*[20]	*Calculated*[6]
$^1A_1 \rightarrow {}^1A_2(^1T_{1g})$	+62.9	+19.0	+41.2
$^1A_1 \rightarrow {}^1E(^1T_{1g})$	−58.6	−11.9	−42.9
$^1A_1 \rightarrow {}^1E(^1T_{2g})$	+2.0		+1.22

CD intensity from this source vanishes in random orientation leaving only that from the E1–M1 mechanism, the anomaly is explained. Some evidence in support of this explanation came from the phase modulated orthoaxial spectrum reported by Jensen and Galsbøl.[22] Final confirmation came from the recent *ab initio* calculation[6] where both the E1–M1 and E1–E2 contributions to the CD were calculated and found to be of the same sign and comparable magnitudes.

Other reported single crystal CD spectra include those of Λ-$[Cr(en)_3]^{3+}$,[23] Λ-$[Cr(ox)_3]^{3-}$ (where ox = oxalato),[15] Λ-$[Cr(pd)_3]$,[16] $M(en)_3(NO_3)_2$ (M = Co^{2+}, Ni^{2+}, Mn^{2+}, Cu^{2+}, and Ru^{2+}),[24] $[Rh(en)_3]^{3+}$,[15] and $[Rh(ox)_3]^{3-}$.[15]

2.5.3.3 Complexes of Lower Symmetry

The CD of species with symmetry lower than D_3 are more difficult to interpret. The effect of introducing axial asymmetry ($D_3 \rightarrow C_3$) is shown in Figure 3, using $[Ni(en)_3]^{2+}$ (6N ligators) and $[NiLH_3]^{2+}$ (LH_3 = *N,N′N″*-tris[(2*R*)-2-hydroxy-3-methylbutyl]-1,4,7-triazacyclononane)[25] (3N and 3O ligators) as examples. The spin-allowed transitions are, in octahedral parentage, from lowest to highest energy $^3A_{2g} \rightarrow {}^3T_{2g}$, $^3T_{1g}$(F), and $^3T_{1g}$(P) with the lowest energy transition being magnetic dipole allowed. In C_3 all states now have either *A* or *E* symmetry. It can be seen that while the intensity of the magnetic dipole allowed $^3A_{2g} \rightarrow {}^3T_{2g}$ transition is considerably larger in the C_3 complex, the dissymmetry factors of the $^3A_{2g} \rightarrow {}^3T_{2g}$ transitions are essentially the same. This reflects the mixing of electric dipole intensity into a magnetic dipole allowed transition. In contrast the magnetic dipole forbidden $^3A_{2g} \rightarrow {}^3T_{1g}$(F) and $^3T_{1g}$(P) transitions have much the same intensity in both complexes but much larger CD in the lower symmetry complex, reflecting the increased mixing of magnetic dipole intensity.

A second type of low symmetry complex is that with pseudotetrahedral symmetry. These are exemplified by $[Co(Me_4pn)Cl_2]$ (where Me_4pn = (*R*)-*N,N,N′N′*-tetramethyl-1,2-diaminopropane) where the ligators have effectively C_{2v} symmetry and the chirality comes from the conformation of the chelate ring and $[Co(sp)Cl_2]$[26] (where sp = (–)spartein) where there is a substantial twist of the ligators about the C_2 axis. The two complexes show very different CD. Firstly the dissymmetry factors for the twisted complex are substantially larger than those for $[Co(Me_4pn)Cl_2]$. Secondly $[Co(Me_4pn)Cl_2]$ reflects its C_{2v} ligator symmetry in showing no detectable CD under the $^4A_2 \rightarrow {}^4A_2(\,{}^4T_1)$ transition,

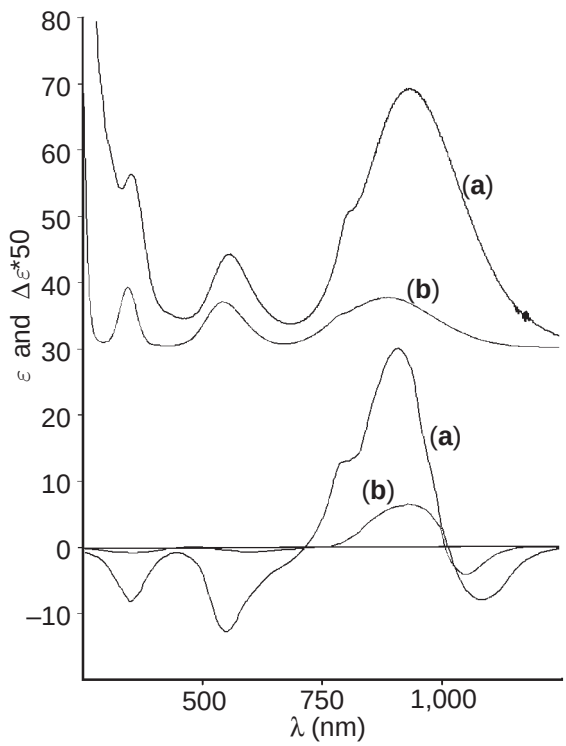

Figure 3 The absorption (upper curves) and CD (lower curves) spectra of (a) $[NiLH_3]^{2+}$ (LH_3 = *N,N′N″*-tris[(2*R*)-2-hydroxy-3-methylbutyl]-1,4,7-triazacyclononane) and (b) $[Ni(en)_3]^{2+}$ in aqueous solution.

which is both magnetic and electric dipole forbidden in C_{2v}. In $[Co(sp)Cl_2]$ the C_2 symmetry allows this transition to mix with neighboring electric and magnetic dipole transitions of A symmetry and results in a dissymmetry factor of $\sim 5 \times 10^{-3}$. These complexes have been discussed in detail.[17]

2.5.3.4 Lanthanide Circular Dichroism and Circularly Polarized Luminescence

Lanthanide *f–f* transitions are, in principal, more useful than their transition metal counterparts in probing the geometry round the metal ion. In particular the circularly polarized luminescence (CPL) spectra of Eu^{3+} and Tb^{3+} has been extensively used for this purpose.[27] However, our understanding of *f–f* CD/CPL is less than that of *d–d* transitions. In both the lanthanide ions mentioned above there are sources of both magnetic and electric dipole intensity. The problem is that the transitions belong to different J states and J is, to a first approximation, a good quantum number. To exemplify: the $^7F_0 \rightarrow {}^5D_1$ transition of Eu^{3+} is magnetic dipole allowed, the $^7F_0 \rightarrow {}^5D_2$, $^5D_4$, and $^5D_6$ transitions can acquire electric dipole intensity via both the static field and ligand polarization mechanisms. However, in order to produce a rotational strength, the magnetic and electric dipole transitions must mix and this requires J mixing, which has proved extremely difficult to calculate. Richardson and co-workers have measured both the CPL and CD of the single crystals of $Na_3[Eu(digly)_3]\cdot 2NaClO_4 \cdot 6H_2O$ (where digly = 2,2′-oxydiacetate) and have calculated[28,29] the chiroptical spectra including all possible sources of electric and magnetic dipole intensity. Unfortunately the CD/CPL of the important $^7F_0 \rightarrow {}^5D_2$ and $^5D_0 \rightarrow {}^7F_2$ transitions are not well reproduced.

Lanthanide (especially Eu^{3+} and Tb^{3+}) CPL has undergone somewhat of a renaissance recently. For example, the CPL of Eu^{3+} with chiral septadentate ligands related to 1,4,7,10-tetraazocyclododecane tetra-acetic acid (DOTA) has been used to monitor bicarbonate binding under physiological conditions (Figure 4).[30]

2.5.4 CIRCULAR DICHROISM OF INTERNAL LIGAND TRANSITIONS—EXCITON COUPLING

If the ligands attached to a trisbidentate transition metal complex of D_3 symmetry have long-axis polarized electric dipole transitions then these may couple together (exciton coupling) to give a pair of transitions which are both electric and magnetic dipole allowed and thus show CD (Figure 5).

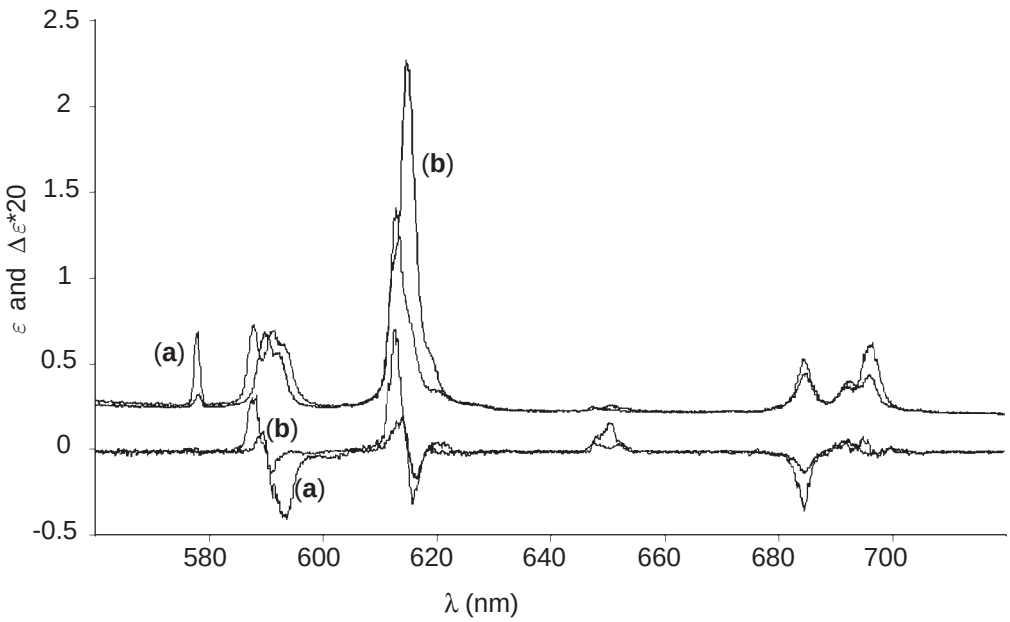

Figure 4 The total luminescence (upper curves) and circularly polarized luminescence (lower curves) of a 1 mM aqueous solution of [Eu(*S,S,S*-1,4,7-tris[1-(1-phenyl)-ethylcarbamoylmethyl]-1,4,7,10-tetraazacyclodecane)]$^{3+}$ in the absence (a) and presence (b) of 10 mM $[HCO_3]^-$.

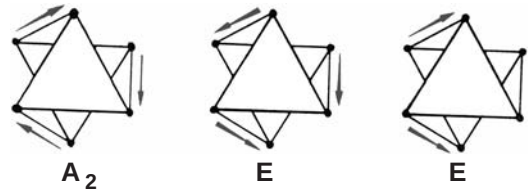

Figure 5 The coupling modes of the long-axis polarized ligand transitions of a trisbidentate metal complex.

The pair of exciton-coupled transitions show (in the absence of other interactions) equal and opposite CD and the sign of this pair of transitions may be used to establish the absolute configuration of the metal complex. Indeed measurement of the exciton-coupled CD of internal ligand transitions is the most reliable method, apart from X-ray crystallography, of determining the absolute configuration of a trischelated metal complex.

The theory of this method has been detailed and extensively reviewed.[31,32] The most common ligands to which the method is applicable are unsaturated chelating ligands with low lying $\pi \rightarrow \pi^*$ transitions such as 1,10-phenanthroline (phen), 2,2′-bipyridyl (bipy), oxalate (ox), and 2,4-pentandionate (pd). For trischelates (D_3 symmetry) the transitions have E (lower energy) and A_2 (higher energy) symmetry and the absolute configuration of the trischelate is Δ if the A_2 transition has a positive sign and *vice versa*. This is illustrated in Figure 5 where the Λ configuration of a trischelate is shown to lead to a left-handed helical charge distribution around the C_3 axis for the higher energy (head-to-head dipoles) charge distribution of A_2 symmetry. Quantitatively, the rotational strengths are given by:

$$R(A_2) = -R(\mathrm{E}) = \sqrt{2/3}\pi\tilde{\nu}_0 \mathrm{r}_{12}|\mu_0|^2 \tag{9}$$

where $\tilde{\nu}_0$ and μ_0 are the wave number and electric dipole transition moment of the single ligand excitation, respectively, and r_{12} is the distance between the point transition dipoles of two of the ligands.

A recent application of the method is to the chromatographically resolved enantiomers of $[Si(phen)_3]^{4+}$ and $[Si(bipy)_3]^{4+}$.[33] Exciton coupling has also been observed in the spectra of tetrakis complexes of the lanthanide elements.[34]

The method is applicable to *cis*-bis complexes and to mixed ligand complexes[35] such as $[Ru(bipy)_2(phen)]^{2+}$. In the case of a *cis*-bis (C_2 symmetry) chelate of the type MX_2Y, three exciton-coupled CD bands are seen, one of A and two of B symmetry. For the Δ absolute configuration the A-polarized transition has negative CD and the B-polarized transitions have positive and negative CD; again, in the absence of other interactions, the overall CD should sum to zero. The magnitudes of the three CD bands depend, as in the trischelate case above, on the magnitudes of the two electric dipole transitions in the X and Y ligands and the distances between them; in addition, in the *cis*-bis case, there is a dependence on the magnitude of the exciton coupling between the X and Y ligands and within the pair of X ligands. A novel use of the technique was to help establish the correct formulation of the partially reduced species $[Ru(bipy)_2(bipy^-)]^+$ and $[Ru(bipy)(bipy^-)_2]$ and their Os^{2+} analogues; the exciton CD spectra unambiguously proved[36] that the added electron(s) were localized on individual bipy ligands and not delocalized over all three.

Exciton CD has been used in a number of cases to monitor binding and complexation. The exciton CD spectra of a Co(salen) complex in which the ligand has been functionalized with boronic acid groups has been used to detect binding by sugar molecules.[37] Exciton CD has been used to monitor the binding, as a function of the H-bonding capacity of the solvent, of Fe^{3+} to a novel tripod ligand based on cyclodextrin which was synthesized as a model for ferrichrome.[38]

2.5.5 CIRCULAR DICHROISM OF CHARGE-TRANSFER TRANSITIONS

CD of charge-transfer transitions is still a topic of some debate in which, as noted previously, simple "independent system" models tend to break down. The term "charge-transfer" covers a

range of excitations with varying "transfer" character. Charge-transfer CD has been reviewed by Ziegler and von Zelewsky.[39]

The most extensively studied systems are complexes with planar aromatic ligands, such as low-spin d^6 $[Ru(bipy)_3]^{2+}$ and its analogues, having low-lying empty π^*-orbitals acting as receptors for metal to ligand charge-transfer excitations. The exciton-coupled, ligand-based CD of these systems was discussed in the previous section. Single crystal CD data were obtained by Ferguson *et al.*[40] for $[M(bipy)_3]^{2+}$ (where M = Fe, Ru, or Os) in the uniaxial host $Zn(bipy)_3(BF_4)_2$. These were interpreted in terms of the theoretical model of Ceulemans and Vanquickenborne.[41] Ferguson *et al.* attributed the magnetic transition moment to metal *d*-orbital rearrangements.

Due to the common coupling symmetries of the π^* target orbitals a simple relation is expected between the CD of $\pi \rightarrow \pi^*$ and metal $\rightarrow \pi^*$(ligand) transitions, at least in the case of closed-shell ground states: The correspondingly polarized charge-transfer and $\pi \rightarrow \pi^*$ transitions are expected to have the same sign of CD. Thus for Δ-$[Ru(bipy)_3]^{2+}$ the lower energy, *E* polarized, ligand and charge-transfer transitions have the same negative sign. This relationship has been confirmed by the measurement of CD and linear dichroism (LD) on $Ru[(phen)_2dppz]^{2+}$ (where dppz = dipyrido [3,2-a:2′,3′-c] phenazine) oriented in a liquid crystal film.[42] One *ab initio* calculation of charge-transfer CD has been reported [39] and shows extremely good agreement with experiment.

2.5.6 CIRCULAR DICHROISM OF CHIRAL METAL–METAL-BONDED SPECIES

In a recent review on "predetermined chirality at metal centers," Khof and von Zelewsky described the chiral quadruply bonded species Δ and Λ-$[Mo_2Cl_4(S,S\text{-dppb})_2]$ (where dppb = 2,3-bis(diphenylphosphino)butane) as *M*-configurational double helices.[43] Such twisted multiply bonded complexes are paradigm examples of intrinsically chiral chromophores where the "chiral center" is not located at the metal atom but embraces the whole twisted $Mo_2X_4P_4$ unit. The CD spectra of a range of chiral quadruply bonded compounds, with a variety of bidentate and monodentate chiral ligands (phosphines and amines) have been reported and can be explained by a simple metal localized theory.[44,45]

Figure 6 shows the absorption and CD spectra of Δ-$[Mo_2Cl_4(S,S\text{-dppb})_2]$. The electronic transitions are assigned (from longer to shorter wavelength) as $\delta_{xy} \rightarrow \delta_{xy}^*$, $\delta_{xy} \rightarrow \delta_{x^2-y^2}$, and charge transfer. In the eclipsed untwisted chromophore, the $\delta_{xy} \rightarrow \delta_{xy}^*$ transition is electric dipole allowed along the Mo—Mo bond and the $\delta_{xy} \rightarrow \delta_{x^2-y^2}$ transition is magnetic dipole allowed along the Mo—Mo bond. Upon twisting, both transitions become electric and magnetic dipole allowed along the Mo—Mo bond thus creating for both transitions a transient helical charge displacement along and about the Mo—Mo bond. This helical charge displacement, and thus the CD spectrum, can be correlated with the absolute chirality of the $Mo_2X_4P_4$ unit, the $\delta_{xy} \rightarrow \delta_{xy}^*$ transition having a negative and the $\delta_{xy} \rightarrow \delta_{x^2-y^2}$ a positive CD for a Λ absolute configuration. There is one slight complication; because of the nodal structure of the *d*-orbitals, the sign of the CD obeys a quadrant rule, i.e., the sign is opposite for a twist of 0–45° and 45–90° for the same sense of twist and so the same absolute configuration (Figure 7).

Most molecules which have been structurally characterized have twists in the 0–45° range, but Λ and Δ-$[Mo_2Cl_4(R,R\text{-DIOP})_2]$ have twists of −78° and +87° respectively and positive and negative CD as predicted.[46] The CD spectrum of $[Mo_2(R\text{-pn})_4]^{4+}$ (where pn = 1,2-diaminopropane, which has not been structurally characterized) has been interpreted as implying a twist of 45–90°.[47] Table 3 shows the dissymmetry factors for both the $\delta_{xy} \rightarrow \delta_{xy}^*$ and $\delta_{xy} \rightarrow \delta_{x^2-y^2}$ transitions for a range of twisted Mo_2 complexes.

There is a second type of chiral quadruple-bonded species in which the twist is zero or close to zero.[52–54] In these cases the Mo_2 unit must be treated as an achiral chromophore and the CD (which is weak) can be explained by one electron static coupling. This theory has also been used to explain the CD of singly bonded $Rh_2(S\text{-mandelate})_4(EtOH)_2$.[55]

When flexible or monodentate ligands are the cause of the twist the same hand of ligand may induce twists of opposite chirality. Thus *R,R*-DIOP forms both Λ(89%) and Δ(11%)-$[Mo_2Cl_4(R,R\text{-DIOP})_2]$ in the same crystal.[46] In the case of the monodentate ligand *S*-chea, the complex $Mo_2Cl_4(S\text{-chea})_4$ (where chea = 1-cyclohexylethylamine) has the Λ conformation predominant in the crystal but in solution isomerizes to an equilibrium mixture of Λ and Δ species with the Δ configuration predominating.[56] The CD spectrum of the complex has been used to study the rate and measure the activation energy for this "twisting" isomerization.

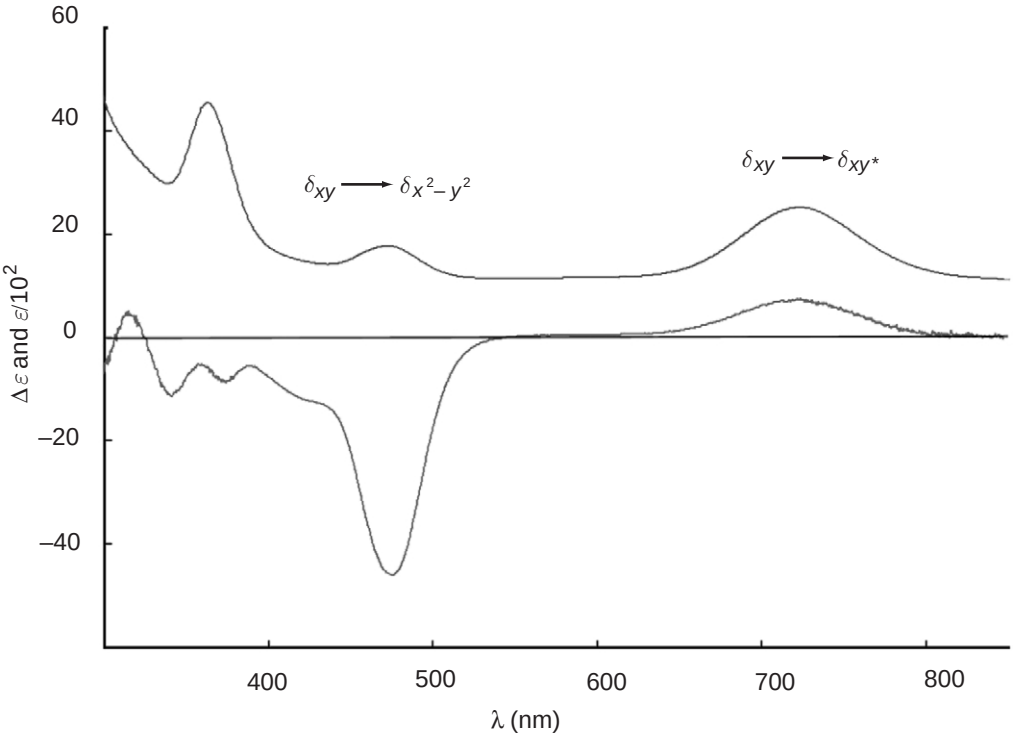

Figure 6 The absorption (upper curve) and CD (lower curve) spectra of Δ-$[Mo_2Cl_4(R,R\text{-dppb})_2]$ in MeCN solution.

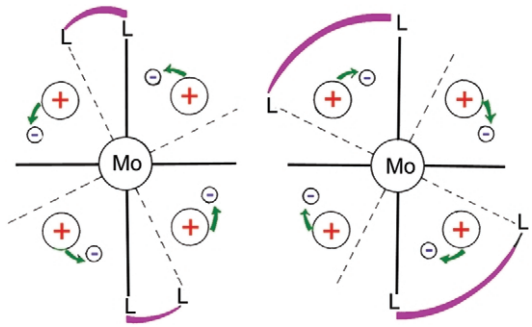

Figure 7 The transient charge distributions for the $\delta_{xy} \rightarrow \delta_{xy}^*$ transition of a twisted $Mo_2L_4L'_4$ chromophore. On rotating the rear set of ligators through an angle of between 0° and 45° in the counterclockwise direction, the charge distribution is that of a left-handed helix. When the rotation is between 45° and 90°, the transition gives rise to a right-handed helical charge displacement.

The signs of the CD spectra obtained when $Rh_2(CF_3CO_2)_4$,[57] is reacted in DMSO with a chiral diol have been proposed as a method of determining the absolute configuration of the diol. This method has recently been reinvestigated using $Mo_2(MeCO_2)_4$.[58] At present the sign/structure relationship is empirical, but clearly if the nature of the diol complex can be elucidated, this potentially useful method of absolute configuration determination could be put on a sound theoretical footing.

2.5.7 X-RAY NATURAL CIRCULAR DICHROISM

2.5.7.1 Introduction

The measurement of natural CD[7] in the X-ray region (XNCD) has developed as a result of the availability of third generation synchrotron sources with insertion devices (helical undulators and

Table 3 Wave numbers and dissymmetry factors for the $\delta_{xy} \rightarrow \delta_{xy}$ and $\delta_{xy} \rightarrow \delta_{x^2-y^2}$ transitions of quadruple-bonded dimolybdenum complexes.

Compound	$\tilde{\nu}$ ($\delta_{xy} \rightarrow \delta_{xy}$) ($10^3\,cm^{-1}$)	$(\Delta\varepsilon/\varepsilon) \times 10^3$	$\tilde{\nu}$ ($\delta_{xy} \rightarrow \delta_{x^2-y^2}$) ($10^3\,cm^{-1}$)	$(\Delta\varepsilon/\varepsilon) \times 10^3$	*Twist angle* (°)	*References*
Λ-[Mo_2Cl_4(*S*,*S*-dppb)$_2$]	13.7	−5.8	21.1	+7.3	23	48
Λ-[Mo_2Br_4(*S*,*S*-dppb)$_2$]	13.2	−3.2	20.7	+8.5	22	48
Δ-[Mo_2Cl_4(*R*-dppp)$_2$]	13.3	+7.5	21.7	−6.7	0–45	48
Δ-[Mo_2Br_4(*R*-dppp)$_2$]	12.8	+3.0	20.8	−4.5	0–45	48
Δ-[Mo_2Cl_4(*R*-phenphos)$_2$]	13.2	+6.0	21.5	−6.2	0–45	49
Λ-[Mo_2Cl_4(*S*,*S*-skewphos)$_2$]	13.9	−10.8	20.8	+3.7	0–45	49
Λ-[Mo_2Cl_4(*S*-chairphos)$_2$]	14.3	−2.0	21.3	+1.1	0–45	49
[Mo_2Cl_4(*R*,*R*-dach)$_2$]	18.0	+ve	22.2	−ve		50
Λ-[Mo_2Cl_4(*R*,*R*-DIOP)$_2$]		+ve			−78	46
Δ-[Mo_2Cl_4(*R*,*R*-DIOP)$_2$]		−ve			+84	46
Δ-[$Mo_2(MeCO_2)_2$ (*S*,*S*-dppb)$_2$]	19.2	+0.35	25.6	−0.32	1–2	51
Δ-[Mo_2Cl_4(*R*-pn)$_2$]	21.0	−9.1	27.8	+17	45–90	47

dppb = 2,3-bis(diphenylphosphino)butane; dppp = 1,2-bis(diphenylphosphino)propane; phenphos = 1-phenyl-1,2-bis(diphenylphosphino) ethane; skewphos = 2,4-bis(diphenylphosphino)pentane; chairphos = 1,3-bis(diphenylphosphino)butane; dach = 1,2-diaminocyclohexane; −ve = negative; +ve = positive.

wigglers) capable of delivering reproducible, high brilliance, photon fluxes with controlled helicity. The X-ray region, with both element specific absorption and the established methods of obtaining structural information from EXAFS and XANES, is clearly an area where the extension of CD spectroscopy provides a new technique for the study of both molecular and crystal structural enantiomorphism. XNCD has been measured in the core excitations of first-row transition metal and lanthanide complexes as well as some main group materials.

2.5.7.2 Theoretical Background

The differences between the origins of CD in core–valence excitations and in valence–valence excitations will now be discussed. The Condon–Eyring sum rule implies that optical activity vanishes at very low and very high energies *relative to the excitation energies* of an electronic system. However, this does not mean that CD is necessarily small at the extremes of the electromagnetic spectrum. In particular, in the X-ray region the interaction with quadrupole transition moments is enhanced when the dimensions of the electronic displacement are comparable to the wavelength of the radiation (breakdown of the dipole approximation). This allows substantial CD to be derived from the E1–E2 mechanism. This situation pertains in the so-called near-edge absorption (XANES) where multiple scattering of the photoelectron by near neighbor atoms is largely responsible for the structure of the absorption profile, and to preedge excitations with effectively pure quadrupole character (e.g., $1s \rightarrow 3d$, $2p \rightarrow 4f$).

An important basic feature of X-ray absorption spectroscopy (XAS) is the core nature of the one-electron initial state. Consequently, the transition matrix elements involve integrals which are dominated by the region close to the photo-absorbing atom. The major part of an X-ray edge absorption is, therefore, atomic in nature and contains no chemical structural information. It is the analysis of the small modulations of the edge absorption due to the presence of neighboring atoms that provides structural information (EXAFS). Scattering theoretical methods are commonly used to describe the propagation of the photo-electron in the neighborhood of the absorber. Conventional EXAFS analysis is applied to energies above ~100 eV from the ionization threshold where the de Broglie wavelength of the photo-electron is short in comparison to interatomic spacings and the effect of neighbor atoms is largely accounted for by single-scattering events. Below ~100 eV (the XANES region), the photo-electron wavelength is comparable to the near-neighbor distances and multiple scattering processes are of significant importance. The analysis of multiple scattering is complicated but it can provide 3D structural information about the neighborhood of a photo-absorber. This contrasts with the single scattering interpretation of EXAFS which gives only a radial distribution function. It is for this last reason that multiple scattering analysis is essential to account for the effects of chirality in XAS.

The optical activity in *valence* excitations of chiral metal complexes has been effectively treated using the model of an achiral chromophore (metal ion) in a chiral environment (ligands) and this model appears also appropriate for XAS in view of the core nature of the initial orbital state. The zero-order electric and magnetic transition moments arise from different transitions and must be mixed by some chiral environmental potential ($\mathbf{V}^*$). Considering the case of a lanthanide ion, and taking the electric dipole transitions for the $L_{2,3}$ edge as $2p \rightarrow \phi_d$, a first-order perturbation expression for the rotational strength looks like:

$$R \approx Im\langle 2p|\boldsymbol{\mu}|\boldsymbol{\phi}_d\rangle\langle\boldsymbol{\phi}_d|\mathrm{V}^*|\boldsymbol{\phi}_{p'}\rangle\langle\boldsymbol{\phi}_{p'}|\mathbf{m}|2p\rangle \tag{10}$$

The problem is with the magnetic dipole transition moment, $\langle\phi_{p'}|\mathbf{m}|2p\rangle$, which vanishes in the zeroth approximation. The magnetic dipole selection rule $|\Delta l| = 0$, allows the transition from $2p$ to the np and continuum εp states but, since $\mathbf{m}$ is a pure angular operator it cannot connect states which are radially orthogonal. This results in the $|\Delta n| = 0$ selection rule for bound states and also clearly forbids $2p \rightarrow \varepsilon p$ except via core-hole relaxation.

The E1–M1 mechanism is even more restrictive for K-edge or L_1-edge spectra. Magnetic dipole transitions are forbidden from s-orbitals so the only possible source of magnetic dipole intensity involves $1s$–$2p$-orbital mixing in addition to core-hole relaxation. This may account for XNCD in light atom systems but is unlikely to be significant for transition metals or lanthanides.

In all XNCD measured so far, it has been found that the predominant contribution to X-ray optical activity is from the E1–E2 mechanism. The reason for this is that the E1–M1 contribution depends on the possibility of a significant magnetic dipole transition probability and this is strongly forbidden in core excitations due to the radial orthogonality of core with valence and continuum states. This orthogonality is partially removed due to relaxation of the core-hole excited state, but this is not very effective and in the cases studied so far there is no definite evidence of pseudoscalar XNCD.

The appearance of E1–E2 optical activity is restricted to those symmetry groups in which the components of a second rank odd-parity tensor are totally symmetric.[5] As pointed out by Jerphagnon and Chemla,[59] optical activity may be observed even in nonenantiomorphous systems due to the nonpseudoscalar parts of the optical activity tensor—only enantiomorphous crystal classes having a nonvanishing pseudoscalar part.

Table 4 shows the occurrence of the pseudoscalar, vector, and second rank odd-parity (pseudodeviator) parts of the optical activity tensor in the noncentrosymmetric crystallographic point groups.

2.5.7.3 Measurements

XNCD spectra were first measured for uniaxial single crystals of $Na_3Nd(digly)_3{\cdot}2NaBF_4{\cdot}6H_2O$ (digly = 2,2′-oxydiacetate) (Nd L_2, L_3 edges)[5] (Figure 8) and $\{Co(en)_3Cl_3\}_2{\cdot}NaCl{\cdot}6H_2O$ (Co K edge)[6] (Figure 9) where the lanthanide and the transition metal occupy chiral coordination sites, and for the ionic crystal $LiIO_3$ (I L_1, L_2, L_3 edges)[60] in which the achiral iodate anions are helically arranged. The XANES part of the XNCD shows CD corresponding to chiral multiple scattering paths of the photoelectron. In addition, both the Nd^{III} (Figure 8) and Co^{III} (Figure 9)

Table 4 Irreducible components of the optical activity tensor for the noncentrosymmetric crystallographic point groups.

Crystal class	*Pseudoscalar*	*Vector*	*Pseudodeviator*
O, T	✓	0	0
D_3, D_4, D_6	✓	0	✓
C_1, C_2, C_3, C_4, C_6	✓	✓	✓
D_2	✓	0	✓
S_4, D_{2d}	0	0	✓
C_s, C_{2v}	0	✓	✓
C_{3v}, C_{4v}, C_{6v}	0	✓	0
T_d, D_{3h}, C_{3h}	0	0	0

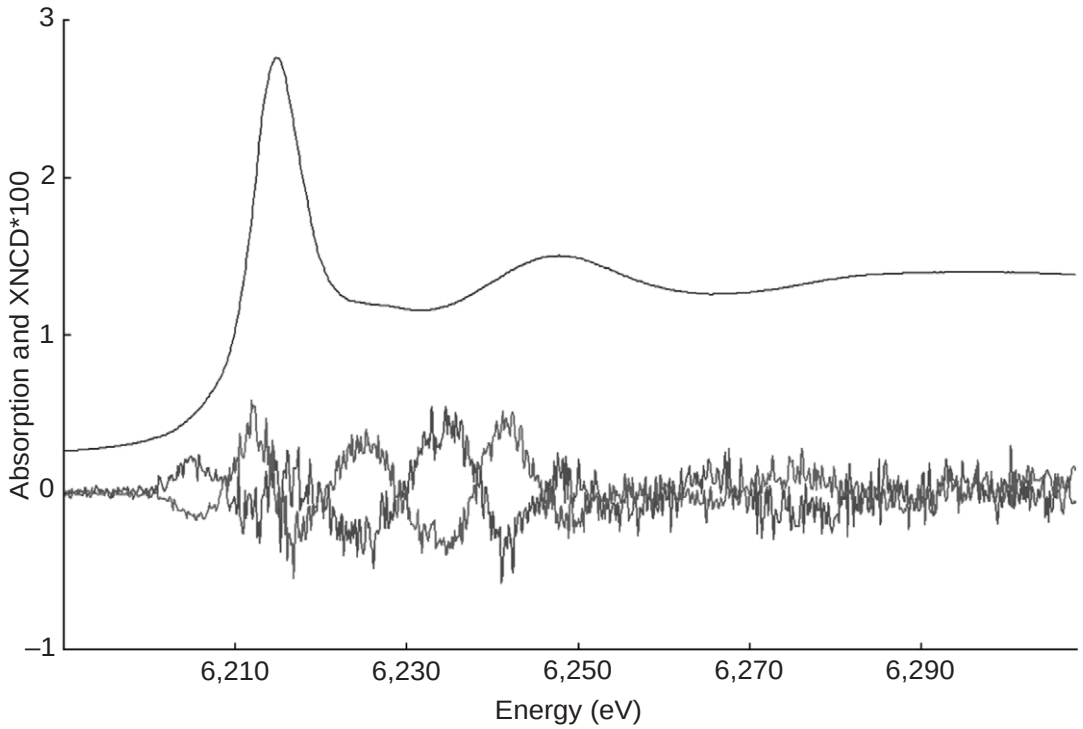

Figure 8 Axial absorption (upper curve) and X-ray CD (lower curves) of Λ and Δ-$Na_3[Nd(digly)_3]\cdot 2NaBF_4\cdot 6H_2O$ at the Nd L_2 edge.

compounds show quadrupole-allowed preedge features ($2p \rightarrow 4f$ for Nd and $1s \rightarrow 3d$ for Co) which have exceptionally large Kuhn dissymmetry factors. The theory of XNCD shows that the CD is due to the interference between allowed electric dipole and electric quadrupole transition moments (E1–E2 mechanism).

Subsequent to the first measurements, $KTiOPO_4$, a gyrotropic crystal of the nonenantiomorphous *mm*2 crystal class, has been studied[61] and the predictions of Jerphagnon and Chemla[59] have been confirmed. Tellurium L_1-edge XNCD[61] in α-TeO_2 is dominated by chiral multiple scattering paths of the type $Te\cdots O_1\cdots O_2\cdots Te$ involving the nearest oxygen neighbors. A range of trigonal complexes of the first transition series have been studied in uniaxial crystals, with measurements on biaxial faces confirming the expectations of the E1–E2 mechanism.[62]

2.5.8 SUMMARY

Whereas conventional XAS is dominated by the atomic contribution of the photo-absorber and by single scattering contributions from the near neighbors, neither of these make any contribution to XNCD. The XNCD spectrum extracts the multiple-scattering contributions, specifically those involving chiral photo-electron paths (Figure 10). As expected, XNCD is especially sensitive to chiral angular structure and the absolute chirality at individual atomic sites may be determined. The technique is useful for identifying preedge features that are not resolved from the tail of the white-line in ordinary absorption. Theoretical analysis has shown that XNCD depends on the mixing of odd and even parity orbital character in the photo-electron wave function (e.g., p–d mixing) and this mixing can be mapped as a function of energy and atomic species. The E1–E2 mechanism is more restrictive than E1–M1, requiring oriented systems and ideally uniaxial single crystals. However, experimental and theoretical studies have shown that with the use of fluorescence detection, birefringence effects in biaxial systems are less problematic than at first expected.[63] Orientational averaging around the beam transmission direction can be used to extract the true XNCD where linear dichroism is also present. The orientational sensitivity of the E1–E2 mechanism has yet to be exploited in the study of chiral molecules on surfaces.

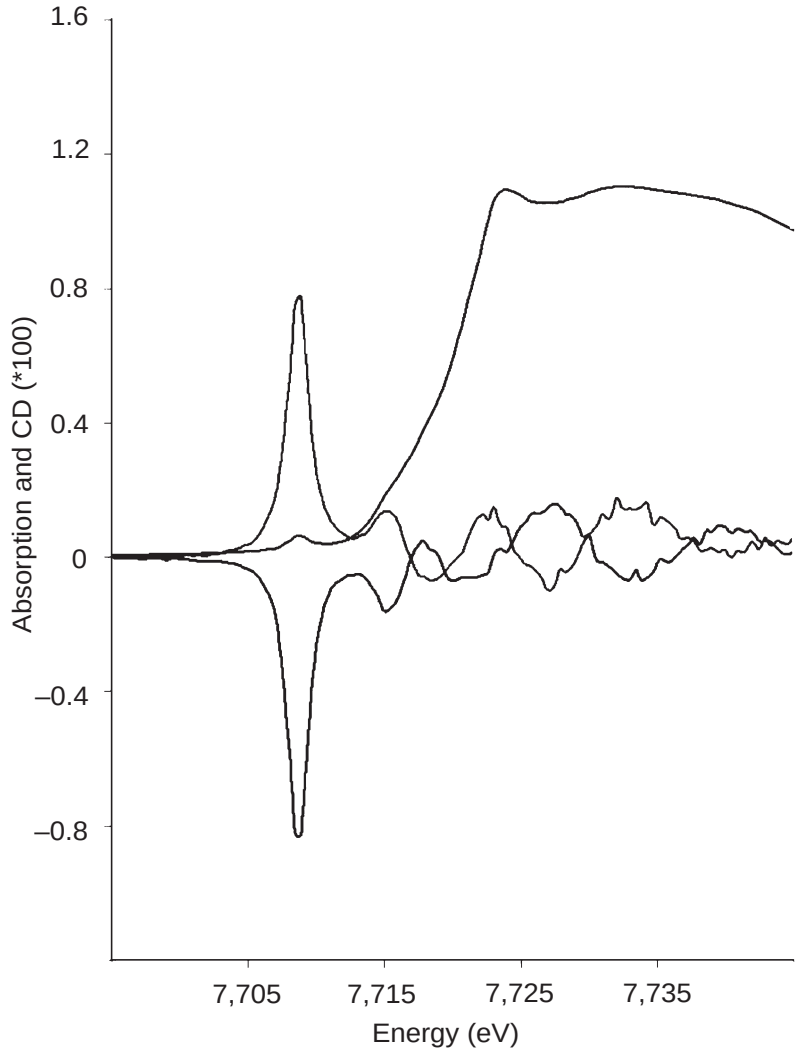

Figure 9 Axial absorption (upper curve) and X-ray CD (lower curves) of $\{\Lambda\text{-}[Co(en)_3]Cl_3\}_2 \cdot NaCl \cdot 6H_2O$ and $\{\Delta\text{-}[Co(en)_3]Cl_3\}_2 \cdot NaCl \cdot 6H_2O$ at the Co *K* edge.

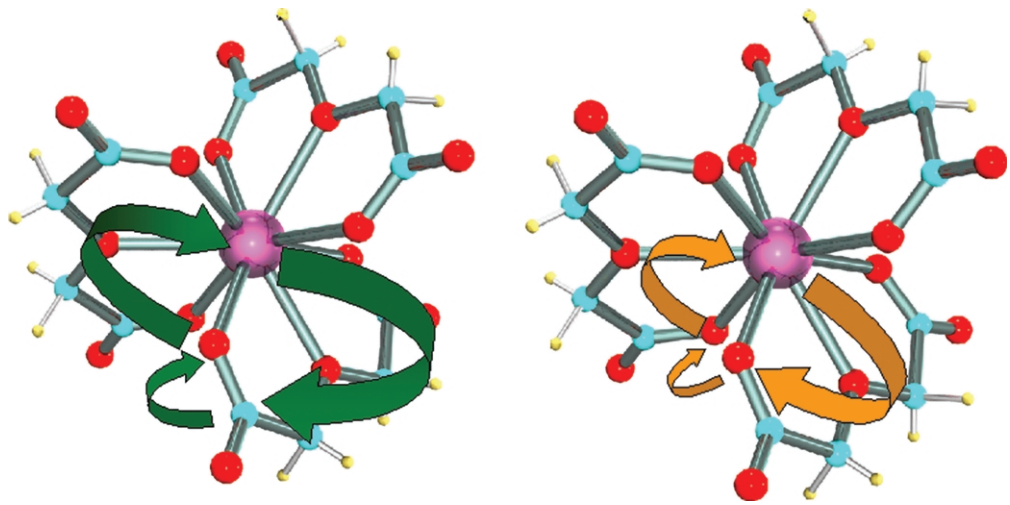

Figure 10 The two main multiple scattering chiral paths contributing to the XANES X-ray CD in the $[Nd(digly)_3]$ cluster.

2.5.9 REFERENCES

1. Weissbluth, M. *Atoms and Molecules*, Academic Press: New York, 1978.
2. Chiu, Y. N. *J. Chem. Phys.* **1970**, *52*, 1042–1053.
3. Buckingham, A. D.; Dunn, M. B. *J. Chem. Soc.* **1971**, 1988–1991.
4. Barron, L. D. *Mol. Phys.* **1971**, *21*, 241–246.
5. Alagna, L.; Prosperi, T.; Turchini, S.; Goulon, J.; Rogalev, A.; Goulon-Ginet, C; Natoli, C. R.; Peacock, R. D.; Stewart, B. *Phys. Rev. Lett.* **1998**, *80*, 4799–4802.
6. Stewart, B.; Peacock, R. D.; Alagna, L.; Prosperi, T.; Turchini, S.; Goulon, J.; Rogalev, A.; Goulon-Ginet, C. *J. Am. Chem. Soc.* **1999**, *121*, 10233–10234.
7. Peacock, R. D.; Stewart, B. *J. Phys. Chem.* **2001**, *105*, 351–360.
8. Cotton, A. *C. R. Hebd. Acad. Sci.* **1895**, *120*, 989–991.
9. Stewart, B. The Ligand Polarisation Model for *d–d* and *f–f* Intensities. In *Vibronic Processes in Inorganic Chemistry*; Flint, C. D.; Ed.; Kluwer Academic Publishers: Dordrecht, 1989, pp 327–345.
10. Mason, S. F.; Seal, R. H. *Mol. Phys.* **1976**, *31*, 755–775.
11. Kuroda, R.; Saito, Y. *Bull. Chem. Soc. Jpn.* **1976**, *49*, 433–436.
12. McCaffery, A. J.; Mason, S. F. *Mol. Phys.* **1963**, *6*, 359–371.
13. Judkins, R. R.; Royer, D. J. *Inorg. Chem.* **1974**, *13*, 945–950.
14. Drake, A. F.; Kuroda, R.; Mason, S. F. *J. Chem. Soc., Dalton Trans.* **1979**, 1095–1100.
15. Mason, S. F. Optical Activity and Molecular Dissymmetry in Coordination Compounds. In *Fundamental Aspects and Recent Developments in Optical Rotatory Dispersion and Circular Dichroism;* Ciardelli, F.; Salvadori, P., Eds.; Heyden: London, 1973, 196–239.
16. Peacock, R. D. *J. Chem. Soc., Dalton Trans.* **1983**, 291–294.
17. Peacock, R. D.; Stewart, B. *Coord. Chem. Rev* **1982**, *46*, 129–157.
18. Mason, S. F. *Molecular Optical Activity and the Chiral Discriminations* 1982, Cambridge University Press: London.
19. Richardson, F. S. *Chem. Rev.* **1979**, *79*, 17–36.
20. Ernst, M. C.; Royer, D. J. *Inorg. Chem.* **1993**, *32*, 1226–1232.
21. Mason, S. F.; Norman, B. *J. Chem. Soc.* **1966**, 307–312.
22. Jensen, H.-P.; Galsbøl, F. *Inorg. Chem.* **1977**, *16*, 1294–1297.
23. Geiser, U.; Gudel, H. U. *Inorg. Chem.* **1981**, *20*, 3013–3019.
24. Palmer, R. A.; Chin-Lan Yang, M. *Chem. Phys. Lett.* **1975**, *31*, 492–497.
25. Fallis, I. A.; Farrugia, L. J.; Macdonald, N. M.; Peacock, R. D. *J Chem. Soc., Dalton Trans.* **1993**, 2759–2763.
26. Drake, A. F.; Kuroda, R.; Mason, S. F.; Peacock, R. D.; Stewart, B. *J. Chem. Soc., Dalton Trans.* **1981**, 976–980.
27. Reil, J. P.; Richardson, F. S. *Chem. Revs.* **1986**, *86*, 1–16.
28. Morley, J. P.; Saxe, J. D.; Richardson, F. S. *Mol. Phys.* **1982**, *47*, 379–406.
29. Richardson, F. S.; Berry, M. T.; Reid, M. F. *Mol. Phys.* **1986**, *58*, 929–945.
30. Bruce, J. I.; Dickins, R. S.; Govenlock, L. J.; Gunnlaugsson, T.; Lopinski, S.; Lowe, M. P.; Parker, D.; Peacock, R. D.; Perry, J. J. P.; Aime, S.; Botta, M. *J. Am. Chem. Soc.* **2000**, *112*, 9574–9684.
31. Mason, S. F. *Inorg. Chim. Acta Rev.* **1968**, *2*, 89–109.
32. Bosnich, B. Exciton Circular Dichroism in Metal Complexes. In Ciardelli, F.; Salvadori, P.; Eds.; *Fundamental Aspects and Recent Developments in Optical Rotatory Dispersion and Circular Dichroism;* Heyden: London, 1973, 240–253.
33. Ohmori, Y.; Namba, M.; Kuroda, Y.; Kojima, M.; Yoshikawa, Y. *Inorg. Chem.* **1992**, *31*, 2299–2300.
34. Dickens, R. S.; Howard, J. A. K.; Moloney, J. M.; Parker, D.; Peacock, R. D. Siligardi, G. *Chem. Commun.* **1997**, 1747–1748.
35. Bosnich, B. *Inorg. Chem.* **1968**, *7*, 2379–2386.
36. Noble, B.; Peacock, R. D. *Inorg. Chem.* **1996**, *35*, 1616–1620.
37. Mizuno, T.; Masashi, Y.; Takeuchi, M.; Shinkai, S. *Tetrahedron* **2000**, 6193–6198.
38. Matsuda, T.; Hayashi, J.; Tanagaki, S. *J. Chem. Soc., Perkin Trans.* **2000**, *2*, 161–167.
39. Ziegler, M.; von Zelewsky, A. *Chem. Revs.* **1998**, *177*, 257–300.
40. Ferguson, J.; Herren, F.; McLaughlin, G. N. *Chem. Phys. Lett.* **1982**, *89*, 376–380.
41. Ceulemans, A.; Vanquickenborne, L. G. *J. Am. Chem. Soc.* **1981**, *103*, 2238–2241.
42. Ardhammer, M.; Lincoln, P.; Rodger, A.; Nordén, B. *Chem. Phys. Lett.* **2002**, *354*, 44–50.
43. Knof, U; von Zelewsky, A. *Angew. Chem., Int. Ed. Engl.* **1999**, *38*, 302–322.
44. Agaskar, P. A.; Cotton, F. A.; Fraser, I. F.; Peacock, R. D. *J. Am. Chem. Soc.* **1984**, *106*, 1851–1853.
45. Peacock, R. D. *Polyhedron* **1987**, *6*, 715–721.
46. Chen, J.-D; Cotton, F. A.; Falvello, R. L. *J. Am. Chem. Soc.* **1990**, *112*, 1076–1082.
47. Fraser, I. F.; Peacock, R. D. *Inorg. Chem.* **1985**, *24*, 989–990.
48. Agaskar, P. A.; Cotton, F. A.; Fraser, I. F.; Manojlovic-Muir, L.; Muir, K.; Peacock, R. D. *Inorg. Chem.* **1986**, *25*, 2511–2519.
49. Fraser, I. F.; Peacock, R. D.; McVitie, A. *Polyhedron* **1986**, *5*, 39–45.
50. Gerards, M. *Inorg. Chim. Acta* **1995**, *229*, 101–103.
51. Farrugia, L. J.; McVitie, A.; Peacock, R. D. *Inorg. Chem.* **1988**, *27*, 1257–1260.
52. Chen, J.-D.; Cotton, F. A. *Inorg. Chem.* **1990**, *29*, 1797–1802.
53. Chen, J.-D.; Cotton, F. A. *J. Am. Chem. Soc.* **1991**, *113*, 2509–2512.
54. Lee, C.-T.; Chen, J.-D.; Chen-Yang, Y. W.; Liou, L.-S.; Wang, J.-C. *Polyhedron* **1997**, *16*, 473–479.
55. Agaskar, P. A.; Cotton, F. A.; Falvello, L. R.; Han, S. *J. Am. Chem. Soc.* **1986**, *108*, 1214–1223.
56. Chen, H.-L.; Lee, C.-T.; Chen, C.-T.; Chen, J.-D.; Liou, L.-S.; Wang, J.-C. *J. Chem. Soc., Dalton Trans.* **1998**, 31–35.
57. Gerard, M; Snatzke, G. *Tetrahedron: Asymmetry* **1990**, *1*, 221–236.
58. Di Bari, L.; Pescitelli, G.; Pratelli, C.; Pini, D; Salvadori, P. *J. Org. Chem.* **2001**, *66*, 4819–4825.
59. Jerphagnon, J.; Chemla, D. S. *J. Chem. Phys.* **1976**, *65*, 1522–1529.
60. Goulon, J.; Goulon-Ginet, C.; Rogalev, A.; Gotte, V.; Malgrange, C.; Brouder, C.; Natoli, C. R. *J. Chem. Phys.* **1998**, *108*, 6394–6403.

61. Goulon, J.; Goulon-Ginet, C.; Rogalev, A.; Benayoun, G.; Brouder, C.; Natoli, C. R. *J. Synchrotron Radiat*. **2000**, *7*, 182–188.
62. Peacock, R.D.; Stewart, B. in preparation.
63. Goulon, J.; Goulon-Ginet, C.; Rogalev, A.; Gotte, V.; Brouder, C.; Malgrange, C. *Eur. Phys. J.* **1999**, *B12*, 373–385.

Comprehensive Coordination Chemistry II
ISBN (set): 0-08-0437486

Volume 2, (ISBN 0-08-0443249); pp 65–81

2.6
Neutron Diffraction

G. J. LONG
University of Missouri-Rolla, Rolla, MO, USA

2.6.1 INTRODUCTION 83
2.6.2 NEUTRON INTERACTIONS WITH MATTER 83
2.6.3 ADVANTAGES AND DISADVANTAGES OF NEUTRON DIFFRACTION 86
2.6.4 APPLICATIONS TO COORDINATION CHEMISTRY 87
2.6.4.1 Single Crystal Neutron Diffraction in Coordination Chemistry 87
2.6.4.2 Powder Neutron Diffraction in Coordination Chemistry 88
2.6.5 REFERENCES 89

2.6.1 INTRODUCTION

Although the neutron is stable when incorporated into a nuclide, a free neutron is unstable and decays into an electron, a proton, and an antineutrino with a half-life of 13 minutes. As a consequence, neutron diffraction experiments must be carried out with neutrons from either a nuclear reactor or a spallation source. In either case the high kinetic energy of the neutrons that result from the nuclear fission or spallation must be reduced, i.e., the neutrons must be thermalized, through collisions with a moderator such as light or heavy water. The resulting thermal neutrons have an energy of ca. 10^{-1} to 10^{-3} eV or a wavelength, as derived from the de Broglie equivalence, of ca. 1–5 Å. Thus thermal neutrons have wavelengths appropriate for diffraction by an atomic or molecular lattice. As a consequence, neutron diffraction is closely related to X-ray diffraction, and typically neutron diffraction studies are preceded by X-ray diffraction structural studies. Neutron diffraction does, however, have certain advantages over X-ray diffraction, advantages which will be discussed herein.

The neutron is a neutral particle that has a nuclear spin of $1/2$ and hence a magnetic moment, μ, of $-1.913\ \mu_N$, where $\mu_N = eh/2m_p = 5.051 \times 10^{-27}\,\mathrm{J\,T^{-1}}$ is the nuclear Bohr magneton. A comparison of the fundamental properties of neutrons and X-rays is given in Table 1.

2.6.2 NEUTRON INTERACTIONS WITH MATTER

The fundamental aspects of neutron diffraction and its use in the study of materials has been covered in detail in several excellent books which should be consulted for details.[1–8] Neutrons interact with matter in a variety of ways which make neutron diffraction both similar to and yet different from X-ray diffraction.

First, because the neutron is uncharged it can easily approach the point-like atomic nuclei found in a material and *nuclear* scattering occurs at very short distances of ca. 10^{-14} to 10^{-15} m. It is this scattering from an ordered crystalline material that produces coherent Bragg scattering and yields either the intensity of the various *hkl* reflections from a single crystal or the powder diffraction pattern; results that are familiar from X-ray diffraction and provide essentially the same structural information. However, there is a distinct difference in the scattering lengths for

Table 1 Fundamental properties of X-rays and neutrons.

	X-rays	*Neutrons*
Nature	Electromagnetic	Particle wave
Mass (10^{-27} kg)	0	1.6749286(10)
Charge	0	0
Spin	1	1/2
Magnetic moment (μ_N)	0	−1.91304275(45)
Typical energy (eV)	8042	0.036
Typical wavelength (Å)	1.5418	1.50
Velocity ($m\,s^{-1}$)	3.0×10^8	2.6×10^3

X-ray and neutron scattering. Because X-ray diffraction results from scattering by the electrons, atoms of similar atomic number exhibit very similar scattering and it is hard to distinguish between them by X-ray diffraction. In contrast, neutron scattering depends upon the nature of the scattering nuclide and, as a consequence, atoms of similar atomic number often have quite different neutron scattering lengths[9] (see Figure 1). This difference[8] is also apparent in Table 2 for the first row transition metals. Further, in contrast to X-ray scattering, which is highly dependent upon the scattering angle, neutron scattering by a nuclide is virtually independent of scattering angle, θ, a difference which is easily observed in the angular dependence of the form factor for the different scattering processes (see Figure 2).

Second, because the neutron has a magnetic moment, it also is scattered by interaction with any magnetic moments found within a material; the resulting coherent scattering, the *magnetic* scattering, is superimposed upon the nuclear scattering in any magnetic material. This magnetic scattering may or may not result in a reorientation of the neutron spin. Because the magnetic neutron scattering results from an interaction with both the spin and orbital components of the magnetic moments, moments that result from the unpaired valence electrons, magnetic scattering has an angular dependence that is similar to that of X-ray scattering by electrons (see Figure 2). Thus, in contrast to the nuclear scattering, the magnetic scattering of neutrons is highly dependent upon the scattering angle as is apparent in Figure 2 which shows the typical angular dependence of the spin, orbital, and nuclear form factors for neutron scattering by chromium as well as, for comparison, the form factor for X-ray scattering. The difference in the angular dependence is one way in which the magnetic and nuclear neutron scattering can be distinguished. Other possible

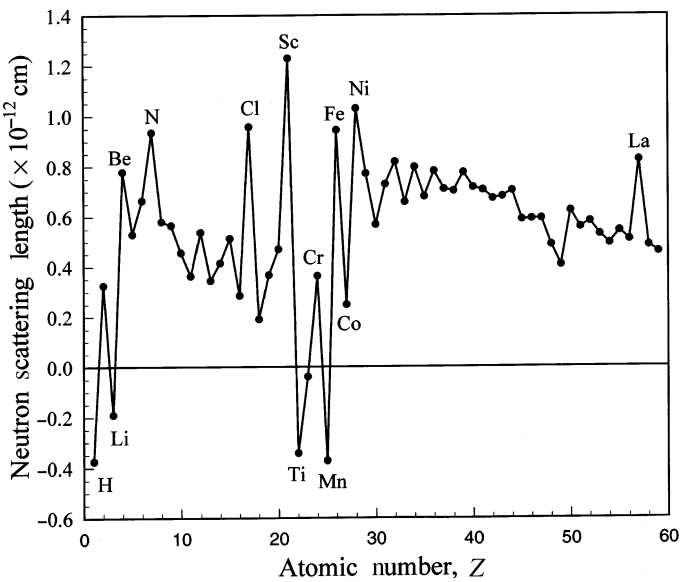

Figure 1 The scattering length of thermal neutrons as a function of atomic number for the natural abundance elements.

Table 2 Selected elastic scattering lengths and cross-sections.

Atom	b_{coh} (10^{-12} cm)	σ_{coh} (10^{-24} cm^2)	σ_{incoh} (10^{-24} cm^2)	σ_{abs} (10^{-24} cm^2)
Hydrogen	−0.3739	1.7568	80.26	0.3326
Deuterium	0.6671	5.592	2.05	0.000519
Boron-10	−0.01	0.144	3	3835
Boron	0.530	3.54	1.7	767
Carbon	0.6646	5.551	0.001	0.0035
Titanium	−0.3438	1.485	2.87	6.09
Vanadium	−0.03824	0.0184	5.08	5.08
Chromium	0.3635	1.66	1.83	3.05
Manganese	−0.373	1.75	0.4	13.3
Iron	0.945	11.22	0.4	2.56
Cobalt	0.249	0.779	4.8	37.18
Nickel	1.03	13.3	5.2	4.49
Copper	0.7718	7.485	0.55	3.78
Zinc	0.5680	4.054	0.077	1.11
Cadmium	0.487	3.04	3.46	2 520
Gadolinium	0.65	29.3	151	49 700

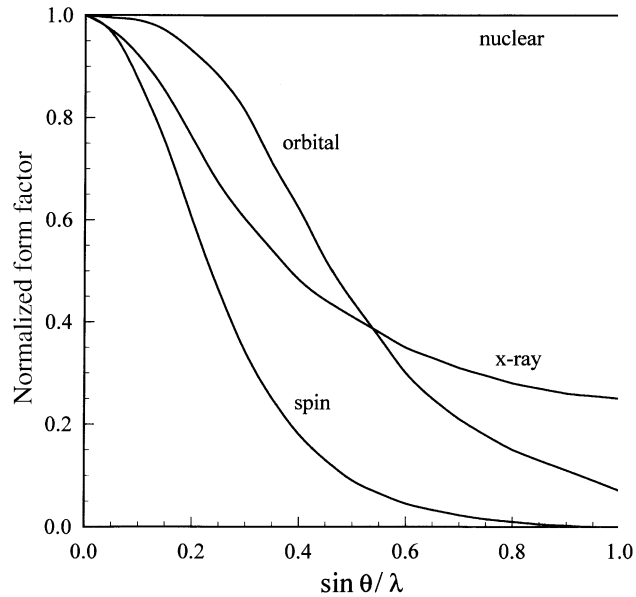

Figure 2 The angular dependence of the normalized form factor for nuclear, and spin and orbital magnetic scattering for chromium metal. The comparable values for X-ray scattering are given for comparison.

methods would be a study of the temperature dependence of the magnetic scattering or the use of polarized neutron scattering.

Third, for some nuclei the neutron will actually interact with the nuclide to form a short-lived compound nucleus, a process that often results in isotropic incoherent scattering with a negative scattering length; this interaction may also be associated with a neutron spin reorientation. Neutron scattering by hydrogen is a special case in which the incoherent scattering is especially strong because the scattering proton may have either the same or the opposite spin to that of the scattered neutron.[9] These two different types of scattering, singlet or triplet scattering, lead to strong incoherent scattering by hydrogen. Fortunately, this does not apply to neutron scattering

Table 3 Coherent elastic scattering lengths of the isotopes of nickel.

Isotope	*Natural abundance* (%)	*Nuclear spin*	*Scattering length,* b_{coh} (10^{-12} cm)
Nickel-58	68.27	0	1.44(1)
Nickel-60	26.10	0	0.28(1)
Nickel-61	1.13	3/2	0.760(6)
Nickel-62	3.59	0	−0.87(2)
Nickel-64	0.91	0	−0.037(7)
Nickel-na			1.03(1)

by deuterium and many neutron diffraction studies require the replacement of hydrogen by deuterium.

Fourth, most atoms have nuclei which consist of several isotopes, isotopes that usually have different neutron scattering lengths and cross-sections.[10] As a result, unless a material is made with a single isotope of a given atom, neutron scattering from the various isotopes results, in part, in isotropic incoherent nuclear scattering. The values for the different isotopes of nickel are given in Table 3 along with that of natural abundance nickel. The differences in scattering lengths for nickel isotopes given in Table 3 show that different but pure isotopes can be used to provide contrast with other elements in a compound, a contrast that is impossible to obtain with X-ray diffraction.

2.6.3 ADVANTAGES AND DISADVANTAGES OF NEUTRON DIFFRACTION

As a consequence of the above interactions of neutrons with matter, neutron diffraction has both advantages and disadvantages as compared to X-ray diffraction.

The advantages of neutron diffraction include the magnetic scattering which can be very useful, particularly in conjunction with polarized neutron scattering studies, in determining the magnetic structure of a magnetically ordered material. Further, because of the very different neutron scattering lengths, it is usually possible to both accurately locate light atoms, such as hydrogen, deuterium, or lithium, even in the presence of heavy atoms, and to distinguish between atoms with similar atomic numbers, such as nitrogen and oxygen or manganese and iron. In both cases the analogous X-ray studies are either impossible or very difficult. Finally, because spallation sources of neutrons operate in a pulsed mode,[10] the time dependence of neutron scattering can be studied by neutron time of flight experiments.

As may be seen in Table 2, the vanadium nuclide produces virtually no neutron scattering, which may seem unfortunate. But this lack of scattering does mean that thin-walled vanadium containers may be used to hold the samples used in neutron diffraction studies. These containers both facilitate neutron diffraction studies of air-sensitive materials and permit very low-temperature studies, i.e., studies to as low as a few millikelvin. In contrast similar X-ray diffraction studies are often very difficult.

Unfortunately, there are some serious disadvantages for neutron diffraction studies. First and most obviously, neutron diffraction must be carried out at large and expensive to operate reactor or spallation facilities, such as at the high-flux reactor at the Institut Laue-Langevin in Grenoble, France, or at the high-intensity spallation neutron source, ISIS, at the Rutherford Laboratory in Chilton, U.K. Beam time at these facilities requires advance application and is in very high demand. Further, because of the cost of neutron diffraction studies, it is usually imperative to have determined the crystal structure, or at least the structure type, of any material to be studied through earlier X-ray diffraction studies. Unfortunately, because of the incoherent scattering by hydrogen, the neutron diffraction study of material containing extensive amounts of hydrogen is either impossible or very difficult. As a consequence, neutron diffraction studies of biologically based materials are often quite difficult but sometimes more accurate in the location of light atoms.

Because some isotopes, such as boron-10, cadmium-113, gadolinium-155, and samarium-149, have large neutron capture cross-sections[9] (see Table 2), it is often almost impossible to carry out neutron diffraction studies of compounds which contain these isotopes. In some cases this

problem can be overcome by using selected pure isotopes, such as boron-11 or samarium-154, but this is sometimes prohibitively expensive. Finally, neutron diffraction studies require far larger samples than do X-ray diffraction studies. Typically single crystal neutron diffraction studies require crystal volumes of one to several cubic millimeters and powder neutron diffraction studies require at least 100 mg and usually 500 mg to several grams of sample.

2.6.4 APPLICATIONS TO COORDINATION CHEMISTRY

The applications of neutron diffraction in coordination chemistry may be divided into two categories, single crystal and polycrystalline studies. This distinction arises because of the very different methods required in each case for both the data acquisition and its subsequent analysis.

2.6.4.1 Single Crystal Neutron Diffraction in Coordination Chemistry

There is a tendency to accept the results of a single crystal structural study as correct and only occasionally does a scientist question such structural results. But is this a good idea? Indeed a single crystal neutron diffraction study has been used to show[11] that a seemingly perfectly well-refined single crystal X-ray diffraction structure was wrong. The complex studied was $WPMe_3H_2Cl_2$, one in the series $WPMe_3H_2X_2$, in which X is F, Cl, Br, or I. The X-ray structures of all these compounds refined to give seemingly correct well-behaved structures in the polar $Cmc2_1$ space group. However, although perfectly refined and structurally reasonable, the X-ray structure of $WPMe_3H_2Cl_2$ was, for no apparent reason, different from the remaining complexes. Because it is known[11] that complexes that crystallize in a polar space group may refine to a false minimum, and because the structural refinement can be heavily influenced by the presence of a heavy X-ray scattering atom such as tungsten, a neutron diffraction study of $WPMe_3H_2Cl_2$ was carried out. Fortunately, unlike for X-ray scattering, the neutron scattering length for tungsten, 0.486×10^{-24} cm, is similar to that of the other atoms in $WPMe_3H_2Cl_2$. Neutron diffraction did indeed reveal a different structure, a structure which was quite analogous to those of the remaining three complexes. Thus, neutron diffraction has been used to show that the single crystal X-ray structure of a coordination complex had been refined to a false minimum and was incorrect. The reader should refer to reference 11 for more details and for a discussion of some of the various reasons why a single crystal structure may be wrong.

In a continuation of their extensive earlier studies[12–16] of hydride coordination complexes, Bau and co-workers[16] have determined by neutron diffraction the single crystal structure of $[(\eta^5\text{-Cp*})Co]_2H_3$. An earlier single crystal X-ray diffraction study[17,18] had failed to locate the three hydride ions and, as a consequence, Schneider has proposed that the short Co—Co bond distance of 2.253(1) Å corresponded to a double bond. However, further theoretical and structural studies[19–22] indicated the presence of three bridging μ_2-hydride ions in $[(\eta^5\text{-Cp*})Co]_2H_3$ which is thus better formulated as $Co_2(\mu_2\text{-H})_3(\eta^5\text{-Cp*})_2$. Indeed, a subsequent neutron diffraction study of a 3.6 mm^3 single crystal of $Co_2(\mu_2\text{-H})_3(\eta^5\text{-Cp*})_2$ revealed that the two cobalt atoms are symmetrically bridged by three μ_2-hydride ions with a Co—H distance of 1.641(6) Å, a distance that is substantially longer than the 1.47(5) Å value obtained[21,22] by X-ray diffraction. The nonbonded H—H distance was found to be 2.068(7) Å, a distance which is somewhat shorter but similar to the nonbonding distances of 2.22(2) and 2.30(4) Å observed by single crystal neutron diffraction studies[23,24] of $[Ir_2(\mu_2\text{-H})_3(\eta^5\text{-Cp*})_2][ClO_4]\cdot 2C_6H_6$ and $[Re(\mu_2\text{-H})_3H_6(\text{triphos})][N(C_2H_5)_4]$ (where triphos = 1,1,1-tris(diphenylphosphinomethyl)ethane), respectively. By combining their work on $Co_2(\mu_2\text{-H})_3(\eta^5\text{-Cp*})_2$ with neutron diffraction studies of related cobalt complexes, Bau and co-workers[16] have shown that the Co—H bond distance increases uniformly with increasing coordination number from 1.558(18) Å in $CoH(CO)_4$, in which the hydride is terminal, to 1.641(6) Å in $Co_2(\mu_2\text{-H})_3(\eta^5\text{-Cp*})_2$, to 1.734(4) Å in $CoFe_3(\mu_3\text{-H})(CO)_9[PO(Me)_3]_3$, and to 1.823(13) Å in $[Co_6(\mu_6\text{-H})(CO)_{15}]^-$. This study demonstrates nicely the importance of neutron diffraction in accurately locating hydrogen in the coordination environment of a metal complex.

Recently, Bau *et al.*[25] have determined the neutron diffraction single crystal structure of $[N(CH_3)_4]_3[(\mu_5\text{-H})_2Rh_{13}(CO)_{24}]$ and found that five-coordinate hydrogen atoms are located in the square pyramidal cavities on the surface of the Rh_{13} cluster in positions that are almost coplanar with the Rh_4 faces of the cluster. Again, through a comparison with neutron diffraction studies of related rhodium complexes, Bau *et al.*[25] have shown a correlation between the Rh—H

bond distance and the hydrogen coordination number. Indeed, as the hydrogen coordination number increases from 1 to 2 to 3, and to 5, the Rh—H bond distance increases from 1.55 to 1.76 to 1.86, and to 1.95 Å.

In a totally different type of study, through a novel use of the $[AuCl_4]^-$ salt, (2*R*,3*R*)-L-(−)-[2-D]carnitine tetrachloroaurate, Bau *et al.*[26] have used single crystal neutron diffraction to determine the absolute stereochemistry of the crotonobetaine to carnitine transformation as it is catalyzed by L-carnitine dehydratase from *Escherichia coli*.

The importance of both neutron diffraction and inelastic neutron scattering in the study of coordination complexes with dinitrogen and dihydrogen ligands is illustrated by work on dinuclear zirconium complexes, complexes of potential importance in the functionalization of dinitrogen. Fryzuk *et al.*[27] have studied the reaction with dihydrogen of $[P_2N_2]Zr(\mu\text{-}\eta^2\text{-}N_2)\text{-}Zr[P_2N_2]$ (where $[P_2N_2] = PhP(CH_2NSiMe_2NSiMe_2CH_2)_2PPh$), a compound which contains a side-on bridging dinitrogen ligand. They reported,[28] on the basis of NMR and X-ray diffraction studies, the formation of $[P_2N_2]Zr(\mu\text{-}\eta^2\text{-}N_2)(\mu\text{-}\eta^2\text{-}H_2)Zr[P_2N_2]$, i.e., a dinuclear complex with separate dihydrogen and dinitrogen bridging ligands. However, a subsequent single crystal neutron diffraction study[28] at 25 K of an ca. 1.4 mm^3 single crystal of this complex revealed that the bridging ligands were not dihydrogen and dinitrogen but rather a bridging hydride and a bridging N_2H group. The complex is thus better formulated as $[P_2N_2]Zr(\mu\text{-}\eta^2\text{-}N_2H)(\mu\text{-}H)\text{-}Zr[P_2N_2]$. The Zr—H bridging bond distances are 1.95(6) and 1.98(6) Å and thus the hydride acts as an essentially symmetric bridging ligand. In contrast, the dinitrogen in the N_2H moiety serves as a side-on bridging ligand with a N—N distance of 1.39(2) Å and a $N—H_{terminal}$ bond distance of 0.93(6) Å. The neutron diffraction results indicate that even at 25 K, the bridging hydride ion has very large atomic displacement parameters, so large that X-ray diffraction results were consistent with its being a dihydrogen bridging ligand. The presence of the two different bridging modes in this complex has also been confirmed by inelastic neutron scattering, a technique which is especially useful for hydride studies because the incoherent neutron scattering cross-section of hydrogen, see Table 2, is huge and thus its scattering dominates the observed inelastic neutron scattering.[29] Further, the inelastic neutron scattering is enhanced by the large atomic displacement observed for the bridging hydride ligand. Both neutron diffraction and inelastic neutron scattering have also been used in the study[30] of dihydrogen as a ligand in *trans*-$[Ru(\eta^2\text{-}H_2)H(dppe)_2][BPh_4]$; dppe is $PPh_2CH_2CH_2PPh_2$.

In another neutron diffraction study of dinitrogen complexes, Fryzuk *et al.*[31] have shown that dinitrogen can serve as both an end-on and side-on bridging ligand in $\{[NPN]Ta(\mu\text{-}H)\}_2(\mu\text{-}\eta^1\text{:}\eta^2\text{-}N_2)$ (where $NPN = PhP(CH_2SiMe_2NPh)_2$).

2.6.4.2 Powder Neutron Diffraction in Coordination Chemistry

The applications of powder neutron diffraction have been expanded greatly by the use of the Rietveld line profile analysis technique,[32–35] a technique which permits a detailed analysis of the intensity of the individual powder diffraction lines in terms of a refinement from a proposed structure. Unfortunately, this technique usually requires a previous knowledge of the space group and structure type for the material under study. In many cases this information is available and the Rietveld method will, for instance, permit the determination of the occupancy of a given metal crystallographic site by, for example, manganese and/or iron. Powder neutron diffraction structural and magnetic studies are often facilitated by time of flight studies[36] with spallation neutron sources and through the application of a magnetic field.[37]

There have of course been a large number of powder neutron diffraction studies of copper oxide complexes related to the high T_c superconducting compounds. These studies will not be discussed herein and the reader should refer to the powder neutron diffraction studies of Day and colleagues[38–40] for examples of such work.

There have been many powder neutron diffraction structural studies of coordination compounds and only a few will be mentioned here. Because of the presence of an unrefinable preferred orientation, it was not possible to solve the structure of the polymeric coordination complex, $Ni(1,3\text{-thiazole})_2Br_2$, by powder X-ray diffraction.[41] In contrast, a Rietveld refinement of powder neutron diffraction data did yield a pseudooctahedral structure doubly linked by bridging bromide ions into infinite linear chains.

At 295 K the $[N(CD_3)_4]^+$ cations in the infinite linear chain complex, $[N(CD_3)_4]MnCl_3$, are disordered.[42] However, upon cooling $[N(CD_3)_4]MnCl_3$ to 126 K it undergoes a first-order phase

transition. A powder neutron diffraction study of $[N(CD_3)_4]MnCl_3$ at 8 K indicates that the phase transition occurs because of an orientational ordering of the $[N(CD_3)_4]^+$ cations.

The cubic to orthorhombic phase transition which occurs at ca. 12 K in $CsTi(SO_4)_2 \cdot 12H_2O$, a β-alum, has been shown[43] through high-resolution powder neutron diffraction, to arise from a long-range interaction between the Jahn-Teller titanium ions, an interaction which gives rise to a cooperative Jahn-Teller effect.

The structure of ReF_7 was long a subject of speculation until in 1994 Vogt *et al.*[44] showed, through powder neutron diffraction studies that, at least at 1.5 K, ReF_7 has a very slightly distorted pentagonal bipyramidal structure.

Long-range magnetic interactions sometimes occur in coordination complexes that contain magnetic ions, and the determination of these magnetic structures in terms of their crystallographic Shubnikov groups is an important application of powder neutron diffraction. Indeed, Figgis and co-workers[45] have shown that powder neutron diffraction profiles obtained in varying external magnetic fields are useful in determining the magnetic structure, i.e., the magnitude, direction, and location within the lattice of the differing magnetic moments found in complex magnetic clusters, such as $[Mn_{12}O_{12}(CD_3COO)_{16}(D_2O)_4] \cdot 2CD_3COOD \cdot 4D_2O$, in which the magnetic ground state is Ising-like with opposed Mn^{II} and Mn^{IV} magnetic moments.

Reynolds and co-workers[46–51] have also used powder neutron diffraction, sometimes in conjunction with low-temperature single crystal X-ray diffraction, to determine the long range magnetic interactions in several ruthenium(III), rhenium(IV), and technetate(VI) complexes. A specific example [51] is the study of metamagnetism in *cis*$[Re(NH{=}CMeNPh)_2Cl_4]$ which contains rhenium(IV) with the expected paramagnetic magnetic moment of 3.6 μ_B above its Neel temperature of 9.7 K. At lower temperatures polarized neutron diffraction studies[51] indicate that the magnetic structure depends upon the absence or presence and the orientation of an applied field, i.e., the complex is metamagnetic, with a tricritical point at $T_c = 5.8$ K and $H_c = 4.4$ T. The observed two-dimensionality of the exchange interactions is correlated with the presence of the $[ReCl_4]^{-4}$ moieties in the *ab*-crystallographic planes, planes which are well separated by intervening phenyl groups.

A polarized powder neutron diffraction study of $(d_{20}\text{-}PPh_4)[Fe^{II}Fe^{III}(ox)_3]$ (where ox = oxalate), a potential molecular magnet, by Day and co-workers[52] has indicated that there is *no* long-range three-dimensional magnetic order in this honeycomb layered oxalate coordination complex, but that there is short-range antiferromagnetic exchange within the layers over a distance of ca. 65 Å at 5 K. In a subsequent study of $(d_{20}\text{-}PPh_4)[Fe^{II}Fe^{III}(ox)_3]$ between 1.9 K and 50 K by both polarized neutron diffraction and Mössbauer spectroscopy, Day and co-workers[53] have been able to determine both the spatial and temporal dependence of the short-range antiferromagnetic exchange as a function of temperature.

2.6.5 REFERENCES

1. Bacon, G. E. *Neutron Diffraction*, 2nd ed. Clarendon Press: Oxford, U.K., 1962.
2. Bacon, G. E., Ed., *Fifty Years of Neutron Diffraction: the Advent of Neutron Scattering*; Adam Hilger: Bristol, U.K., 1987.
3. Lovesey, S. W.; Springer, T., Eds. *Dynamics of Solids and Liquids by Neutron Scattering*, Topics in Current Physics, Vol. 3, Springer-Verlag: Berlin, 1977.
4. Squires, G. L. *Introduction to the Theory of Thermal Neutron Scattering*; Cambridge University Press: Cambridge, U.K., 1978.
5. Williams, W. G. *Polarized Neutrons*; Clarendon Press: Oxford, U.K., 1988.
6. Willis, B. T., Ed., *Chemical Applications of Thermal Neutron Scattering*; Oxford University Press: Oxford, U.K., 1973.
7. Baruchel, J.; Hodeau, J. L.; Lehmann, M. S.; Regnard, J. R.; Schlenker, C., Eds. *Neutron and Synchrotron Radiation for Condensed Matter Studies, Volume I: Theory, Instruments and Methods, Vol. II: Applications to Solid State Physics and Chemistry*, Springer-Verlag: Berlin, 1993, and 1994.
8. Brückel, T.; Heger, G.; Richter, D.; Zorn, R., Eds. *Fifth Laboratory Course on Neutron Scattering*, Vol. 9, Schriften des Forschungszentrums: Jülich 2001.
9. Sears, V. T. *Neutron News* **1992**, *3*, 26–37. The scattering lengths and cross sections are also available at the website: http://www.ncnr.nist.gov/resources/n-length/list.html.
10. Windsor, C. G. *Pulsed Neutron Scattering*; Taylor & Francis: London, U.K., 1981.
11. Murphy, V. J.; Rabinovich, D.; Hascall, T.; Klooster, W. T.; Koetzle, T. F.; Parkin, G. *J. Am. Chem. Soc.* **1998**, *120*, 4372–4387.
12. Bau, R.; Teller, R. G.; Kirtley, S. W.; Koetzle, T. F. *Acc. Chem. Res.* **1979**, *12*, 176–183.
13. Bau, R.; Drabnis, M. H. *Inorg. Chim. Acta* **1997**, *259*, 27–50.
14. Teller, R. G.; Wilson, R. D.; McMullan, R. K.; Koetzle, T. F.; Bau, R. *J. Am. Chem. Soc.* **1978**, *100*, 3071–3077.
15. Hart, D. W.; Teller, R. G.; Wei, C.-Y.; Bau, R.; Longoni, G.; Campanella, S.; Chini, P.; Koetzle, T. F. *J. Am. Chem. Soc.* **1981**, *103*, 1458–1466.

16. Lutz, F.; Bau, R.; Wu, P.; Koetzle, T. F.; Krüger, C.; Schneider, J. J. *Inorg. Chem.* **1996**, *35*, 2698–2700.
17. Schneider, J. J. *Angew. Chem.* **1992**, *104*, 1422–1424.
18. Schneider, J. J. *Angew. Chem., Int. Ed. Engl.* **1992**, *31*, 1392–1394.
19. Abrahamson, H. B.; Niccolai, G. P.; Heinekey, D. M.; Casey, C. P.; Bursten, B. E. *Angew. Chem.* **1992**, *104*, 464–466.
20. Abrahamson, H. B.; Niccolai, G. P.; Heinekey, D. M.; Casey, C. P.; Bursten, B. E. *Angew. Chem., Int. Ed. Engl.* **1992**, *31*, 471–473.
21. Kersten, J. L.; Rheingold, A. L.; Theopold, K. H.; Casey, C. P.; Widenhoefer, R. A.; Hop, C. E. C. A. *Angew. Chem.* **1992**, *104*, 1364–1366.
22. Kersten, J. L.; Rheingold, A. L.; Theopold, K. H.; Casey, C. P.; Widenhoefer, R. A.; Hop, C. E. C. A. *Angew. Chem., Int. Ed. Engl.* **1992**, *31*, 1341–1343.
23. Stevens, R. C.; McLean, M. R.; Wen, T.; Carpenter, J. D.; Bau, R.; Koetzle, T. F. *Inorg. Chim. Acta* **1989**, *161*, 223–231.
24. Abrahams, S. C.; Ginsberg, A. P.; Koetzle, T. F.; Marsh, S. P.; Sprinkle, C. R. *Inorg. Chem.* **1986**, *25*, 2500–2510.
25. Bau, R.; Drabnis, M. H.; Garlaschelli, L.; Klooster, W. T.; Xie, Z.; Koetzle, T. F.; Martinengo, S. *Science* **1997**, *275*, 1099–1102.
26. Bau, R.; Schreiber, A.; Metzenthin, T.; Lu, R. S.; Lutz, F.; Klooster, W. T.; Koetzle, T. F.; Seim, H.; Kleber, H.-P.; Brewer, F.; Englard, S. *J. Am. Chem. Soc.* **1997**, *119*, 12055–12060.
27. Fryzuk, M. D.; Love, J. B.; Rettig, S. J.; Young, V. G. *Science* **1997**, *275*, 1445–1447.
28. Basch, H.; Musaev, D. G.; Morokuma, K.; Fryzuk, M. D.; Love, J. B.; Seidel, W. W.; Albinati, A.; Koetzle, T. F.; Klooster, W. T.; Mason, S. A.; Eckert, J. *J. Am. Chem. Soc.* **1999**, *121*, 523–528.
29. Archer, J.; Lehmann, M. S. *J. Appl. Crystallogr.* **1986**, *19*, 456–458.
30. Albinati, A.; Klooster, W. T.; Koetzle, T. F.; Fortin, J. B.; Ricci, J. S.; Eckert, J.; Fong, T. P.; Lough, A. J.; Morris, R. H.; Golombek, A. P. *Inorg. Chim. Acta* **1997**, *259*, 351–357.
31. Fryzuk, M. D.; Johnson, S. A.; Patrick, B. O.; Albinati, A.; Mason, S. A.; Koetzle, T. F. *J. Am. Chem. Soc.* **2001**, *123*, 3960–3973.
32. Young, R. A., Ed., *The Rietveld Method*; Oxford University Press: Oxford, U.K., 1993.
33. Rietveld, H. M. *Acta Cryst.* **1967**, *22*, 151–152.
34. Rietveld, H. M. *J. Appl. Cryst.* **1969**, *2*, 65–71.
35. Rodriguez-Carvajal, J. *Appl. Cryst.* **2001**, *18*, 30–36.
36. Cheetham, A. K.; David, W. I. F.; Eddy, M. M.; Jakeman, R. J. B.; Johnson, M. W.; Torardi, C. C. *Nature* **1986**, *320*, 46–48.
37. Reynolds, P. A.; Gilbert, E. P.; Figgis, B. N. *Inorg. Chem.* **1996**, *35*, 545–546.
38. Rosseinsky, M. J.; Prassides, K.; Day, P. *Physica C* **1989**, *161*, 21–33.
39. Day, P.; Rosseinsky, M. J.; Prassides, K.; David, W. I. F.; Moze, O.; Soper, A. *J. Phys. C: Solid State Phys.* **1987**, *20*, L429–L434.
40. Rosseinsky, M. J.; Prassides, K.; Day, P. *Inorg. Chem.* **1991**, *30*, 2680–2687.
41. James, M. *J. Chem. Soc., Dalton Trans.* **1998**, 2757–2760.
42. Rodriguez, V.; Aguirre-Zamalloa, G.; Couzi, M.; Roisnel, T. *J. Phys.: Cond. Matter* **1996**, *8*, 969–981.
43. Tregenna-Piggott, P. L. W.; Best, S. P.; O'Brien, M. C. M.; Knight, K. S.; Forsyth, J. B.; Pilbrow, J. R. *J. Am. Chem. Soc.* **1997**, *119*, 3324–3332.
44. Vogt, T.; Fitch, A. N.; Cockcroft, J. K. *Science* **1994**, *263*, 1265–1267.
45. Reynolds, P. A.; Gilbert, E. P.; Figgis, B. N. *Inorg. Chem.* **1996**, *35*, 545–546.
46. Figgis, B. N.; Reynolds, P.A.; Murry, K. S.; Moubaraki, B. *Aust. J. Chem.* **1998**, *51*, 229–234.
47. Reynolds, P. A.; Figgis, B. N.; Martin, M. D. *J. Chem. Soc., Dalton Trans.* **1999**, 945–950.
48. Reynolds, P. A.; Cable, J. W.; Sobolev, A. N.; Figgis, B. N. *J. Chem. Soc., Dalton Trans.* **1998**, 559–569.
49. Reynolds, P. A.; Figgis, B. N.; Forsyth, J. B.; Tasset, F. *J. Chem. Soc., Dalton Trans.* **1997**, 1447–1453.
50. Reynolds, P. A.; Moubaraki, B.; Murry, K. S.; Cable, J. W.; Engelhardt, L. M.; Figgis, B. N. *J. Chem. Soc., Dalton Trans.* **1997**, 263–267.
51. Reynolds, P. A.; Figgis, B. N.; Forsyth, J. B.; Tasset, F. *J. Chem. Soc., Dalton Trans.* **1997**, 1447–1453.
52. Visser, D.; Carling, S. G.; Watts, I. D.; Day, P.; Andersen, K. H. *Physica B* **1999**, *267–268*, 266–269.
53. Carling, S. G.; Visser, D.; Hautot, D.; Watts, I. D.; Day, P.; Ensling, J.; Gütlich, P.; Long, G. J.; Grandjean, F. *Phys. Rev. B* **2002**, *66*, 104407 (12 pages).

Comprehensive Coordination Chemistry II
ISBN (set): 0-08-0437486

Volume 2, (ISBN 0-08-0443249); pp 83–90

2.7 Time-resolved Infrared Spectroscopy

D. C. GRILLS, J. J. TURNER, and M. W. GEORGE
University of Nottingham, UK

2.7.1 INTRODUCTION 91
2.7.1.1 The Modern Fourier Transform IR (FTIR) Instrument 92
2.7.1.2 Continuous Scan FTIR 92
2.7.1.3 Step Scan FTIR 92
2.7.1.4 Curve Fitting and Resolution Enhancement 93
2.7.2 NOVEL APPLICATIONS OF IR SPECTROSCOPY 93
2.7.2.1 Matrix Isolation and Liquid Noble Gas Solvents 93
2.7.2.2 Time-resolved IR (TRIR) 94
2.7.2.2.1 Reactive intermediates generated by photolysis of coordination compounds 95
2.7.2.2.2 Excited states of coordination compounds 95
2.7.2.3 Dynamics From Band Shapes and Coalescence 97
2.7.3 THE FUTURE 99
2.7.4 REFERENCES 100

2.7.1 INTRODUCTION

In these days of the availability to coordination chemists of very sophisticated instrumentation, why should we do infrared spectroscopy, one of the classical "sporting" methods? The short answer is when it provides information that would not otherwise be readily obtainable. For example, X-ray crystallography, which is now such a rapid technique, gives very limited information on solutions. IR spectroscopy is often used as a rapid analytical tool for the characterization of coordination complexes. Some of the more common uses of IR spectroscopy in coordination chemistry include: (i) detecting the presence of particular ligands (e.g., CO, CN, etc.) and their mode of binding, e.g., whether they are terminal or bridging; (ii) determining the mode of coordination of some ligands (e.g., NO_2,[1] N_2,[2] or H_2)[3]; or some further structural information, using new subtle approaches;[4,5] (iii) providing some information on bonding (electron distribution, oxidation state, etc.); and (iv) monitoring equilibria and following the progress of reactions, for which IR spectroelectrochemistry[6] is a particularly good example.

However, IR becomes a particularly powerful structural probe when it is used to monitor kinetic processes, from the very slow to the extraordinarily fast, in the latter case particularly for electron-transfer processes. As we shall see, this can refer either to direct, time-resolved experiments or to band width/coalescence behavior, which is very useful for mixed valence compounds.

All this requires some understanding about the principles of vibrational spectroscopy, force constants, the use of symmetry, and knowledge of the frequencies (and intensities) of a wide range of functional groups. Fortunately this has all been done superbly by Nakamoto,[7,8] and every coordination chemist who makes any use of vibrational spectroscopy should have easy access to these publications. In this chapter we have no intention of repeating this work. Rather, we intend

to describe some novel features or methods of IR spectroscopy that are not described by Nakamoto (except occasionally briefly) and that have been shown to be particularly valuable for coordination chemistry. We also mention some very new techniques that we believe have great potential for the future. It should be noted at this stage that since many of the exciting advances in the use of IR rely on monitoring the behavior of strong diagnostic bands (CO ligands in particular, but also others such as CN ligands), some of the examples we shall describe involve complexes that would strictly be defined as organometallic.

2.7.1.1 The Modern Fourier Transform IR (FTIR) Instrument

Since almost all conventional IR spectra are currently recorded on an FTIR instrument, we shall briefly describe the two different types of FTIR: "continuous scan" and "step scan." This is partly because it is possible with some step scan instruments to record spectra on very fast (ca. 10 ns) timescales, an important topic that we shall return to later. This is not the place to describe the usual advantages of FTIR over dispersive grating instruments,[9] but it is worth a reminder of the principle of an FTIR instrument. Figure 1 shows a schematic diagram of a Michelson interferometer. The spectrum is "scanned" by moving the mirror, M_m. As the distance traveled by the light beams A and B changes, this produces an interferogram, a plot of intensity vs. light beam path difference (δ). This signal is digitized and, following a Fourier Transform (FT), it can be ratioed against a previously measured background file to give the IR spectrum.

2.7.1.2 Continuous Scan FTIR

In routine FTIR spectroscopy the spectrometer is operated in continuous scan mode. In this mode of operation, the moving mirror is scanned at a constant velocity, ν ($cm\,s^{-1}$), with the light beam path difference at any time, t being given by $\delta = 2\nu t$ (cm). An internal HeNe laser beam is also passed through the interferometer and, since it is essentially monochromatic ($15{,}798\,cm^{-1}$), it is used to accurately calibrate the positions of M_m for data sampling. Continuous scan FTIR is most commonly used to monitor stable samples, but can also be used in rapid-scan mode to monitor time-dependent processes on timescales down to ca. 20 ms.

2.7.1.3 Step Scan FTIR

In step scan FTIR[10,11] the moving mirror, M_m, is moved incrementally in discrete steps. There are two main types of step scan experiment: (i) time-domain step scan; and (ii) frequency-domain or

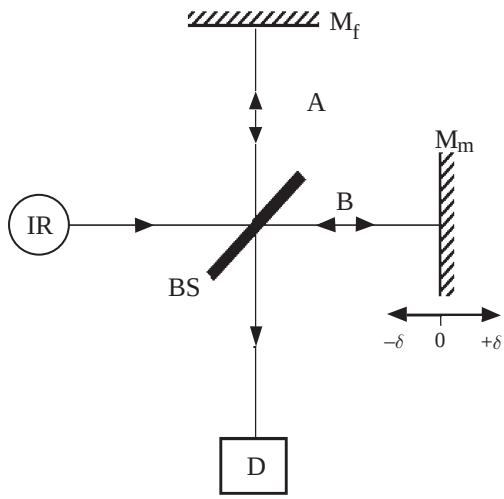

Figure 1 Schematic diagram of a Michelson interferometer in a typical FTIR spectrometer. BS = beamsplitter; D = IR detector; IR = IR source; M_f = fixed mirror; M_m = moving mirror.

phase modulation (PM) step scan. This chapter will concentrate on the former, since this has more applications to coordination compounds. In time-domain step scan, at each position of M_m both mirrors are held completely stationary whilst data are collected as a function of time. This is repeated at all positions of M_m, and then the data are sorted into individual interferograms by time and are subjected to FT to obtain the IR spectra at different times. A time resolution of 10 ns can now routinely be achieved in such experiments.

2.7.1.4 Curve Fitting and Resolution Enhancement

Modern FTIR instruments often have facilities for "curve fitting" and "resolution enhancement" built into the instrument control software, or at least these facilities are readily available "off line" by exporting the data to suitable software packages. Curve fitting of spectra that contain overlapping bands, using a series of peak shapes such as Lorentzian or Gaussian, is often a powerful method of extracting accurate values for the individual peak parameters.[12] Resolution enhancement methods, such as Fourier self-deconvolution and Fourier derivation,[13] are less subjective and can often be used to narrow broad bands that cannot be instrumentally resolved due to their intrinsic linewidth. Thus the individual components under a broad overlapping band contour can be visually separated to aid spectral interpretation. These facilities have featured more in biological applications, but we expect coordination chemists, including bioinorganic chemists, may make increasing use of them in the future.

2.7.2 NOVEL APPLICATIONS OF IR SPECTROSCOPY

We now consider some novel applications of IR spectroscopy, in some cases involving sophisticated instrument development not available at the time of *Comprehensive Coordination Chemistry* (*CCC*, 1987). Most of these come from examining the spectra of the simple ligands CO, N_2, CN, and a few others, such as H_2, RCN, RNC, CO_2, and NO.

2.7.2.1 Matrix Isolation and Liquid Noble Gas Solvents

There are many occasions when it is desirable to study highly reactive, short-lived coordination compounds such as radical species, unsaturated compounds, excited states, and the reactive intermediates involved in catalytic mechanisms. Low temperature is a convenient method of stabilizing highly reactive species. One method for observing these species is to generate them (generally by UV photolysis of some precursor) within a cryogenically cooled (typically 4–77 K) solid matrix.[14,15] Typical matrices include frozen inert gases, such as argon, xenon, methane, or nitrogen; organic glasses such as methylcyclohexane or 2-methyltetrahydrofuran; and polymer films. The photogenerated species are isolated from one another, and the extremely low temperatures prevent their diffusion. This means that even the most highly reactive molecules are sufficiently stabilized so that they can be examined at leisure, using conventional techniques such as FTIR spectroscopy. Early matrix-isolation IR experiments allowed the characterization of transition-metal alkane and noble gas complexes. For example, IR spectroscopy was used to identify $M(CO)_5L$ (M = Cr, Mo, or W; L = Ar, Kr, Xe, or CH_4) in either noble gas or CH_4 matrices following UV photolysis of the precursor metal hexacarbonyl in the matrix.[16] Co-condensation of metal atoms and substrates in the matrix, either by simple heating or more recently, for instance, by laser ablation,[14] is another method for generating and stabilizing reactive fragments. Matrix-isolation infrared spectroscopy has been used to study a wide range of species, such as metal oxides and halides, dinitrogen and dihydrogen complexes, and many others. Many of these experiments have relied on using FTIR with isotopic substitution, e.g., $^{12}C/^{13}C$, $^{16}O/^{18}O$, and $^{14}N/^{15}N$ for the structural identification of the species of interest. For example, the IR spectra of a series of M–CO_2 (M = Ti, V, Cr, Fe, Co, Ni, and Cu) complexes in CO_2 matrices were obtained by co-condensing the metal atoms with CO_2.[17] Isotopic substitution revealed a correlation between the mode of CO_2 coordination and the isotopic frequency shifts in ^{13}C- and ^{18}O-labelled CO_2 complexes. A recent example of the use of laser ablation with matrix-isolation IR spectroscopy was the characterization of the first actinide–noble gas complexes,

CUOL (L = Ar, Kr, or Xe) in noble gas matrices.[18] Laser-ablated U atoms reacted with CO during condensation in a noble gas at 4 K to form CUO molecules. Shifts in the IR bands of CUO when the experiment was performed in different noble gas matrices showed that the resulting CUO molecules had a significant interaction with the noble gas atoms. Another important area that has been studied by matrix-isolation infrared spectroscopy is the identification of key intermediates in important catalytic cycles, such as the carbonylation of methanol and the hydroformylation and hydrogenation of olefins. Such experiments have recently been performed in polymer film matrices,[19] which are particularly suitable[20,21] since they can be used over a large temperature range—from 4 K to above room temperature—and reactant gases can be added to and removed from the matrix during an experiment. Recent advances in computational chemistry have also meant that theoretical methods, particularly density functional theory (DFT), have been used to interpret spectroscopic results.

The use of liquefied noble gases as solvents has allowed unstable coordination compounds to be studied in an inert solution at low temperature. Advantages of liquefied noble gas solvents are their complete IR and UV transparency and the fact that long pathlengths can be used, permitting weak features, e.g., the ν(H—H) bands of dihydrogen complexes,[22] to be detected in the infrared. Furthermore, the band splitting that is sometimes observed in solid matrices does not occur, making spectra easier to interpret.

2.7.2.2 Time-resolved IR (TRIR)

Another method, which allows the structural characterization and elucidation of the reactivity of transient species using infrared spectroscopy, is to observe them in real time, using fast time-resolved infrared (TRIR) spectroscopy. In this section we shall focus on the application of fast (submillisecond) and ultrafast (subnanosecond) TRIR spectroscopy to coordination compounds, and describe experiments that cannot be performed using conventional infrared spectrometers.

TRIR spectroscopy has a long history and there are a variety of different methods for obtaining TRIR spectra, depending on the timescales involved.[23–25] On timescales of 10 ns and longer, the sample is probed using a continuous wave IR source, which is then detected using a fast rise-time IR detector. This allows temporal changes in the IR transmittance of the sample to be monitored in real time following initiation of the process of interest (usually with a short UV/visible laser pulse). A variety of IR sources and experimental approaches are available for TRIR on this timescale.[23] A commonly used IR source is the tunable IR diode laser.[23] This is a narrowband technique, in which the sample is probed with an essentially monochromatic IR beam. The experiment is then repeated in a "point-by-point" fashion at many different IR frequencies across the desired spectral region. Another approach is that of step scan FTIR spectroscopy (see above),[10] which has the inherent advantages that all IR frequencies are probed simultaneously and it is fully computer controlled. However, step scan FTIR requires many thousands of laser pulses during a single experiment, and exactly the same process must be monitored at each mirror position. This means that the sample must either be completely photo-reversible or must be refreshed between laser pulses.

On timescales ranging from femtoseconds up to a few nanoseconds, an entirely different approach is used.[25,26] The sample is pumped *and* probed, using femto- or picosecond laser pulses, and the timing of the experiment is controlled by spatially delaying the infrared probe pulse with respect to the UV/visible pump pulse using an optical delay line (1 ps $\equiv$ 0.3 mm). Kinetic processes are monitored by repeating the experiment at a series of time delays. Originally, these ultrafast TRIR experiments were performed using narrowband IR pulses in a "point-by-point" fashion, similar to that used in nanosecond[23] TRIR studies. However, it is becoming more common to use broadband (ca. 100–500 cm^{-1} FWHM) IR probe pulses. These are dispersed, using IR spectrographs, across multichannel IR array detectors, which probe the component IR frequencies simultaneously. This has improved the sensitivity and capability of such experiments, and advances in laser and detector technology are constantly improving the technique.[26]

One of the earliest condensed-phase TRIR measurements monitored the recombination of photodissociated CO from carboxymyoglobin on the millisecond timescale.[27] Since then TRIR has frequently been applied to coordination compounds, to characterize reactive intermediates for the elucidation of reaction mechanisms and to study their excited states and electron/energy transfer processes.

2.7.2.2.1 Reactive intermediates generated by photolysis of coordination compounds

TRIR has a long history of probing the reaction mechanisms of organometallic carbonyl species. This is largely because the intense ν(CO) bands can be used to easily characterize the different reactive intermediate species. Subsequent to the early carboxymyoglobin TRIR experiments, rapid advances in TRIR spectroscopy were made by studying the reactive intermediates formed upon photolysis of various transition-metal carbonyls, such as $Cr(CO)_6$, $Mn_2(CO)_{10}$, $CpM(CO)_3$ (M = Mn or Re), and $[CpFe(CO)_2]_2$, both in the gas phase and in alkane solution.[28] In the latter case, photolysis induced either the dissociation of a CO ligand to give the long-lived intermediate $CpFe(\mu\text{-}CO)_3FeCp$, or the splitting of the metal–metal bond, to generate the short-lived radical, $CpFe(CO)_2$.[29] TRIR has since been applied to a wide array of samples on timescales ranging from milliseconds down to femtoseconds.[30]

However, TRIR has also been applied to more classical coordination compounds. Ford and co-workers have used a combination of ns-TRIR and time-resolved UV/vis spectroscopy to investigate the mechanism of hydrocarbon C—H bond activation with the rhodium complex, *trans*-$RhCl(CO)(PR_3)_2$ (R = Ph, *p*-tolyl, or Me).[31] Upon photoexcitation, each of these species was found to undergo CO dissociation to form the transient solvated complex, *trans*-$RhCl(Sol)(PR_3)_2$ (Sol = solvent). The solvated complexes reacted with added CO to regenerate the parent complex, and also underwent competitive unimolecular C–H activation to form the Rh^{III} products of hydrocarbon oxidative addition. These were identified from the step scan FTIR spectra, which showed a positive shift in ν(CO) relative to the parent complex, which is consistent with oxidation of the metal center.

Other C–H-activating coordination compounds have been studied using TRIR spectroscopy. For example, the activation of cyclohexane by $Tp^*Rh(CO)_2$ (Tp^* = hydrotris(3,5-dimethylpyrazolyl)borate) was monitored using fast and ultrafast TRIR.[32] It was found that UV excitation resulted in dissociation of a CO ligand and solvation of cyclohexane within a few picoseconds, to form the alkane complex, $Tp^*Rh(CO)$(cyclohexane). The Tp^* ligand then underwent $\eta^3 \rightarrow \eta^2$ dechelation on the 200 ps timescale, with the resulting complex activating a C—H bond of the cyclohexane ligand on the 230 ns timescale. Rechelation of Tp^* yielded the long-lived alkyl hydride, $Tp^*Rh(CO)(H)(C_6H_{11})$.

Nitric oxide serves important roles in mammalian bioregulation and immunology. This has prompted research into metal nitrosyl complexes, which display low thermal reactivity but which are photochemically active to release NO and potentially deliver it to biological targets. One such complex that has been studied with ns-TRIR in the ν(NO) region and also conventional flash photolysis is Roussin's black salt anion, $[Fe_4S_3(NO)_7]^-$.[33] The TRIR experiments identified an intermediate species with a ν(NO) that was shifted to lower frequency, relative to the parent complex. This was identified as the product of NO photodissociation from one of the $Fe(NO)_2$ units.

Two Pt^{II}azido complexes, *cis*-$Pt^{II}(PPh_3)_2(N_3)_2$ and $Pt^{II}(dppp)(N_3)_2$ (dppp = 1,3-bis(diphenylphosphino)propane) have been studied with a combination of flash photolysis and μs-TRIR.[34] UV excitation was found to cause photoinduced electron transfer and loss of an azidyl radical ($^{\bullet}N_3$) to form $Pt^{I}(PPh_3)_2(N_3)$ and $Pt^{I}(dppp)(N_3)$, identified by their IR azido absorptions at ca. 2050 cm^{-1}. For the PPh_3 complex, photoisomerization to *trans*-$Pt^{II}(PPh_3)_2(N_3)_2$ was a competitive pathway. Both Pt^{I} complexes were found to decay via intramolecular electron transfer to the coordinatively unsaturated products, $Pt^0(PPh_3)_2$ and $Pt^0(dppp)$.

2.7.2.2.2 Excited states of coordination compounds

An understanding of the structure and properties of excited states in the photochemistry of coordination compounds is of fundamental importance.[35] Furthermore, monitoring electron and energy transfer is vital for a wide range of applications. TRIR spectroscopy often provides key information on the excited states of coordination compounds,[36,37] in particular those containing CO or CN ligands, since these groups act as direct probes of the electron density at the metal center.

The first application of TRIR to the excited state of a transition-metal coordination compound was the detection of the ^{3}MLCT (metal-to-ligand charge transfer) state of $Re(CO)_3Cl(4,4'\text{-bpy})_2$ (4,4′-bpy = 4,4′-bipyridine).[38] In these and subsequent[39] experiments, it was shown that the ν(CO) bands of the complex in the excited state were shifted to higher frequency (ca. +55–65 cm^{-1}) relative to the ground state. This is expected for a MLCT excited state in which there is a formal oxidation of the Re^{I} metal center to Re^{II}, causing a reduction in the back-bonding from the Re $d\pi$

orbitals to the π^* antibonding orbitals of the CO ligands. Applying an energy-factored force-field (EFFF) analysis to the TRIR spectra, it was possible to show that there was an approximately equal increase in the EFFF force constants (k_{CO}) for each bond, compared to the ground state, and that the three C—O bonds shorten by equal amounts in the excited state.[39,40] Step scan FTIR has become a commonly used technique for studying the excited states of these systems,[41] which has made the determination of the IR spectra of ^{3}MLCT excited states a more routine measurement. Shifts of ν(CO) to higher frequency are now a diagnostic probe for ^{3}MLCT states of transition-metal carbonyls.[36,37] We illustrate this, and demonstrate the increasing time resolution of modern instrumentation, with the TRIR measurement of $Re(CO)_3Cl(bpy)$ (bpy = 2,2′-bipyridine) on the picosecond timescale (see Figure 2). This clearly shows the positive shift of the ν(CO) bands in the excited state.

Relative shifts in the ν(CO) bands of coordination compounds have been used to characterize many other different types of excited states, e.g., ligand-centered $\pi\pi^*$ states, XLCT (X = halide) states, $\sigma\pi^*$ states, and ligand field states. Furthermore, the precise band positions, and hence force field, can be used to probe the mixing between different states.[36,37]

A powerful application of TRIR has been to use the ν(CO) and ν(CN) vibrations of supramolecular coordination compounds to monitor electron- and energy-transfer processes in solution. For example, a combination of fast and ultrafast TRIR was used to show that excitation into the Re-MLCT transition of $[(phen)(CO)_3Re^{I}(NC)Ru^{II}(CN)(bpy)_2]^+$ (phen = 1,10-phenanthroline) produces the Re-MLCT state, followed by energy transfer to the Ru-based MLCT state.[42] For the related complex, $(CO)_5W(4,4'\text{-bpy})W(CO)_5$ ns-TRIR was used to confirm that, on the IR

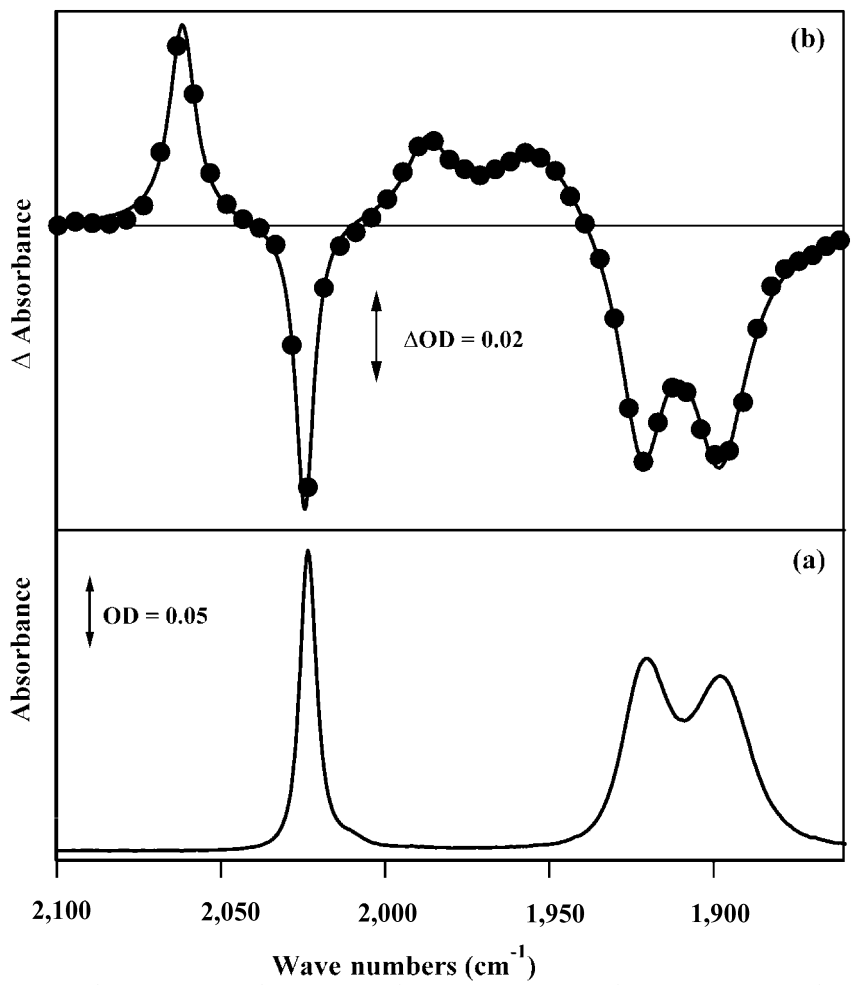

Figure 2 (a) Ground state FTIR of $Re(CO)_3Cl(bpy)$ in CH_2Cl_2 in the ν(CO) region; (b) the ps-TRIR spectrum obtained 100 ps after 400 nm excitation of this solution. Circles represent data points and the solid line is a multi-Lorentzian curve fit of the data. Negative bands indicate depletion of the ground state and the positive bands show the characteristic positive shift of ν(CO) in the ^{3}MLCT excited state.

timescale, the electron involved in the W → bpy charge transfer excited state is localized, i.e., W^{+}(4,4′-bpy)$^{-}$W, as opposed to $W^{0.5+}$(4,4′-bpy)$^{-}W^{0.5+}$.[43,44] This was confirmed by the presence of two CO environments identified in the TRIR spectrum. A similar approach was used on the picosecond timescale to show that the short-lived ^{3}MLCT state of $Cl(CO)_3Re(BL)Re(CO)_3Cl$ (BL = a substituted bridging quinoxaline or pyrazine ligand) is a localized mixed valence state, $Re^{+}(BL)^{-}Re$.[45] Step scan FTIR has also been used to probe electron-transfer processes in these types of dinuclear system.[46] For $[(dmb)(CO)_3Re(4,4'\text{-bpy})Re(CO)_3(dmb)]^{2+}$, the MLCT electron was shown to be localized on the bpy ligand, whereas in $[(bpy)(CO)_3Re(4,4'\text{-bpy})Re(CO)_3(bpy)]^{2+}$ there was an equilibrium between the bpy and 4,4′-bpy ligands. However, for both complexes the TRIR spectra indicated a localized description for the excited state, i.e., $Re^{II}-Re^{I}$. Picosecond TRIR was used to study the photoinduced electron transfer in the cyano-bridged mixed valence dimer, $[(NC)_5Ru^{II}(CN)Ru^{III}(NH_3)_5]^{-}$.[47] It was shown that, following excitation into the metal–metal charge transfer (MMCT) band, the back-electron transfer occurs on the femtosecond timescale ($\tau < 0.5$ ps). More recently, the related complex $[(NC)_5Fe^{II}(CN)Ru^{III}(NH_3)_5]^{-}$ was studied using broadband femtosecond TRIR.[48] The lifetime of back-electron transfer was found to be <0.3 ps.

The excited states of coordination compounds that do not contain CO or CN ligands have also been investigated using TRIR by probing peripheral organic ν(CO) reporter groups, such as carboxylic acids, esters, and amides, on substituted diimine ligands. For example, step scan FTIR was used to probe the ester ν(CO) bands in the ^{3}MLCT states of $[Ru(bpy)_2(4,4'\text{-}(COOEt)_2\text{-bpy})]^{2+}$ and $[Ru(bpy)_2(4\text{-}COOEt\text{-}4'\text{-}CH_3\text{-bpy})]^{2+}$.[49] Such an approach has been used with ps-TRIR spectroscopy to probe the excited state dynamics in the Pt^{II} chromophore, $Pt(4,4'\text{-}(COOEt)_2\text{-bpy})Cl_2$. The lifetime of the MLCT excited state was found to be 8.7 ps.[50]

Improvements in the sensitivity of the step scan FTIR approach have led to its being applied to the ^{3}MLCT states of several Ru and Os polypyridyl complexes, probing the ring vibrations in the "fingerprint" region. Examples include the step scan FTIR of the excited states of $[Ru(bpy)_3]^{2+}$,[51] $[Ru(phen)_3]^{2+}$,[52] $[Ru(dmb)_x(dea)_{3-x}]^{2+}$ ($x = 0$, 1, 2, 3),[53] (dmb = 4,4′-dimethyl-2,2′-bipyridine; dea = 4,4′-bis(diethylamino)-2,2′-bipyridine), $[Os(phen)(DAS)_2]^{2+}$ (DAS = 1,2-bis-(diphenylarsino)ethane)[52] and $[Re(bpy)(CO)_3(4\text{-Etpy})]^{+}$.[51] These experiments complement previous TR^3 studies and confirm the localized nature of the MLCT excited state on the nanosecond timescale, with the electron residing on one of the diimine ligands. To illustrate the power of this technique, Figure 3 shows an example in which we have repeated the step scan FTIR measurement of the ^{3}MLCT excited state of $[Ru(bpy)_3]^{2+}$ in CD_3CN.

2.7.2.3 Dynamics From Band Shapes and Coalescence

Vibrational band shapes, although often ignored, contain a wealth of information about the dynamics of a system.[54] The application of dynamic NMR to the rates of rapid chemical processes is now well established.[55] Therefore, in principle, one should be able to conduct similar experiments on the much faster vibrational timescale (10^{-12} s), using conventional FTIR or Raman spectroscopy. This would be useful for examining ultrafast phenomena, such as electron-transfer processes in mixed-valence compounds, and would provide an alternative to the direct observation method of ultrafast TRIR spectroscopy. In fact, due to its extremely short timescale, IR is often considered to be one of the most reliable methods of distinguishing between trapped (or localized) class II and detrapped (or delocalized) class III mixed-valence systems. A large number of studies have been performed on this type of system, in which the sample is electrochemically oxidized or reduced through its various oxidation states. IR spectra are recorded during this process and the IR bands monitored. The appearance of separated IR bands, or at least broadened features, indicates localization of the electrons. However, if the IR bands appear averaged with respect to the neighboring oxidation states, this suggests electron delocalization on the IR timescale. For example, IR spectroelectrochemistry was performed on the Creutz–Taube ion, $[(NH_3)_5Ru(\mu\text{-pyrazine})Ru(NH_3)_5]^{n+}$ ($n = 4$, 5, or 6).[56] The results indicated that on the vibrational time scale the odd electron is fully delocalized between the two Ru centers. In another study, the related complex $[(NC)_5Fe(\mu\text{-pyrazine})Fe(CN)_5]^{n-}$ ($n = 4$, 5, or 6) was studied by IR spectroelectrochemistry in the ν(CN) and aromatic ring vibration regions.[57] The results suggested a borderline localized/delocalized situation for the complex with a 5^{-} charge.

It would be extremely desirable to expand these experiments to a wide range of systems and use IR spectroscopy in the same way as dynamic NMR, to extract detailed parameters such as the kinetics and activation energies of exchange. However, dynamic NMR relies on the application of

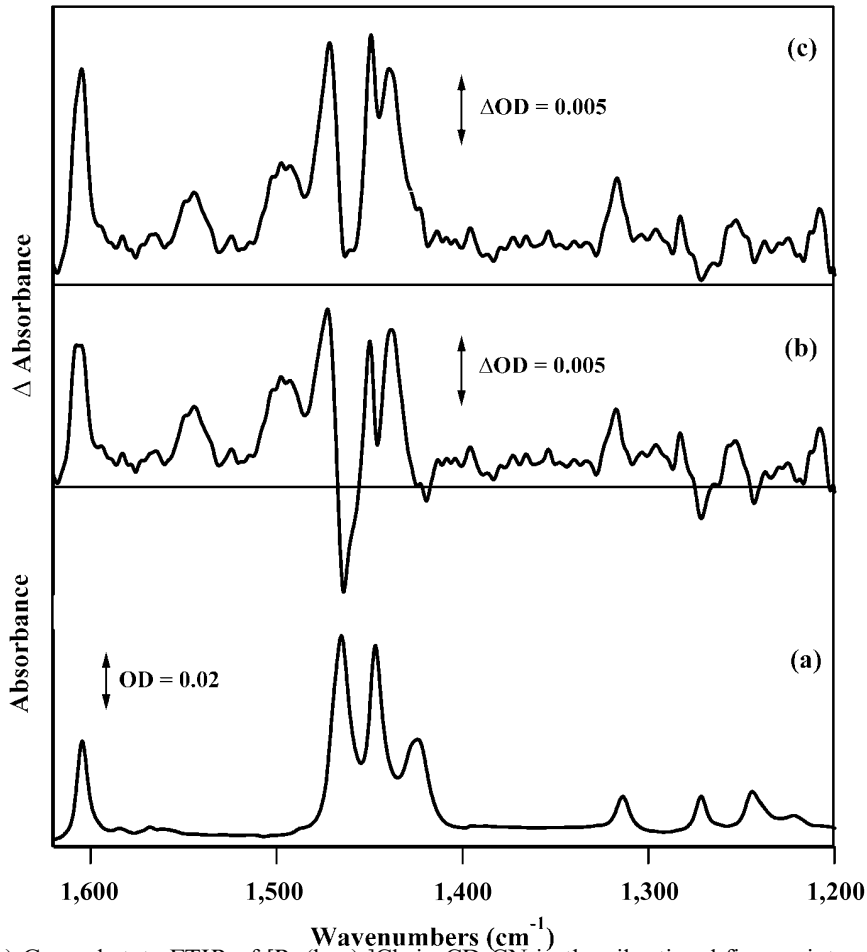

Figure 3 (a) Ground state FTIR of $[Ru(bpy)_3]Cl_2$ in CD_3CN in the vibrational fingerprint region; (b) the step scan FTIR spectrum obtained 200 ns after 355 nm excitation of this solution; (c) a scaled addition of the ground state and step scan FTIR spectra. Thus (c) reveals the IR spectrum of the ^{3}MLCT excited state of $[Ru(bpy)_3]^{2+}$. (These spectra were recorded by Mr. Jixin Yang in the authors' laboratory.)

the Bloch equations modified for exchange.[58,59] It has been argued that for ordinary chemical exchange processes on the IR timescale (ca. 10^{-12} s), the Bloch equations cannot be applied.[60] Others have disagreed with this conclusion.[54,61] Fortunately, for electron-transfer processes the Bloch equations will apply, and we now concentrate on some elegant examples of this application.

The first is a variable temperature IR study of $Fe^{III}{}_2Fe^{II}O(OOCCMe_3)_6(pyridine\text{-}d_5)_3$ between 80 K and 410 K.[62] The core of this compound consists of a central O atom surrounded by three Fe atoms, with oxidation states (III), (III), and (II). The IR bands assigned to in-plane vibration of the central O atom showed temperature dependence and, although the temperature range was too small to observe actual band coalescence, the Bloch model was applied to the increase in breadth of one of the bands. This gave a rate constant for electron transfer between the Fe atoms of the cluster of 5×10^{11} s^{-1}. In another example,[63] Ito and co-workers synthesized some complicated Ru complexes whose core features consisted of a (OC)$[Ru_3]$L$[Ru_3]$(CO) unit (L = pyrazine or bipyridine). $[Ru_3]$ is a core structure with a central O atom surrounded by three Ru atoms, with different O donors bridging the Ru atoms; each $[Ru_3]$ group also has one CO group attached to a particular Ru atom, and L is a bridging pyrazine or bipyridine. For the $[Ru_3]/[Ru_3]$ and the electrochemically reduced $[Ru_3]^-/[Ru_3]^-$ species, the ν(CO) IR bands of each of the two CO groups occurred at the same frequency. For example they appeared at 1,938 cm^{-1} and 1,889 cm^{-1} for one of the compounds. However, for some of the mixed complexes, $[Ru_3]^-/[Ru_3]$, there was a single ν(CO) band at the midpoint, due to very rapid electron transfer $[Ru_3]^-/[Ru_3] \rightarrow [Ru_3]/[Ru_3]^-$. The Bloch analysis was applied and gave electron-transfer rate constants, for the series of complexes, ranging from 10^{11} s^{-1} to 10^{12} s^{-1}. We expect that in the future increasing use

will be made of the Bloch equation analysis to extract detailed information about electron-transfer processes, and possibly other exchange processes in coordination compounds.

2.7.3 THE FUTURE

Most of the recent advances in the use of IR have followed on from new instrumentation techniques. We believe that emerging technology will make increasing use, particularly in bio-inorganic chemistry, of femtosecond IR laser pulses for multidimensional (mostly 2D) IR,[64] in a manner that is analogous to the multiple-pulse techniques now ubiquitous in NMR.[65] Conventional 2D IR spectroscopy, based on the generalized correlation approach, has become an important technique in polymer and biological chemistry since its introduction in the late 1980s.[66–68] In these experiments, which are performed using conventional IR spectrometers, some external perturbation, e.g., optical, mechanical, electrical, thermal, etc. is applied to a sample, which is probed with IR. A series of perturbation-induced dynamic spectra are collected and then transformed into a set of 2D correlation spectra by a cross-correlation analysis. In 2D spectra, the spectral intensity is plotted as a function of two independent spectral variables. Some advantages of 2D IR spectroscopy include: the simplification of complex overlapping spectra; an enhancement of spectral resolution by spreading peaks along the second dimension; and the ability to unambiguously assign vibrations through the correlation of coupled bands. However, these conventional 2D IR experiments are not really equivalent to modern pulsed NMR experiments. Performing 2D IR experiments that are exact equivalents of the NMR measurements requires the use of a train of femtosecond IR pulses having well-defined bandwidth, phase, and amplitude.[69] This is because vibrational relaxation lifetimes occur on the picosecond timescale. These experiments allow the couplings between molecular vibrations to be determined, which could then be used to calculate the 3D structure. The beauty of femtosecond 2D IR is its intrinsically high time resolution, giving access to timescales that are inaccessible to 2D NMR. Therefore the structural dynamics of molecules can potentially be followed on timescales ranging from femtoseconds to milliseconds. These techniques are still developing, but have already been applied to a series of biological molecules such as peptides and small proteins, using the IR equivalents of NMR experiments such as COSY and NOESY.[70–73] As a simple illustration of these complex experiments, Figure 4 shows the femtosecond 2D IR vibrational echo spectrum of (acac)$Rh(CO)_2$ (acac = acetylacetonate) in hexane.[74] This involves the fundamental ν(CO)

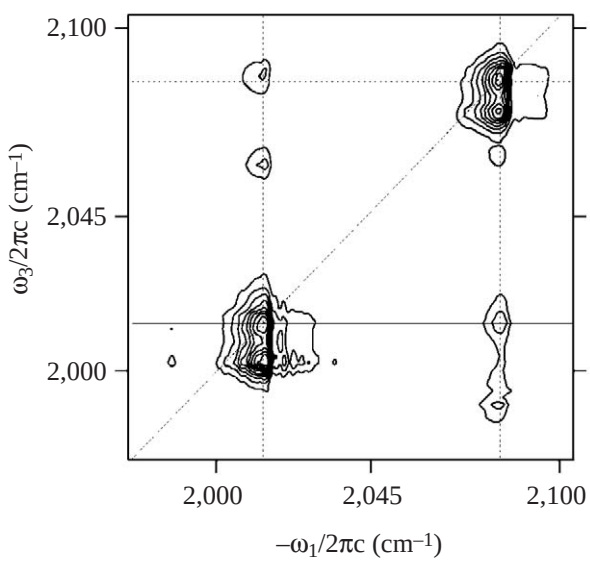

Figure 4 Femtosecond 2D-IR vibrational echo spectrum of (acac)$Rh(CO)_2$ in hexane in the ν(CO) region. This is the spectrum obtained when the train of four IR pulses used in the experiment had parallel polarizations. It displays a correlation of vibrational frequencies during two experimentally controlled time periods and the data are plotted as a function of frequencies excited during the evolution (ω_1) and detection (ω_3) periods. Off-diagonal peaks represent anharmonic coupling between the ν(CO) modes. (Adapted by permission of the American Institute of Physics from *J. Chem. Phys.* **2001**, *115*, 10814–10828.)

vibrations, ν_s and ν_{as}, which occur at 2,084 cm^{-1} and 2,015 cm^{-1} respectively. The off-diagonal peaks show anharmonic coupling between the two modes. This allowed the transient molecular structure to be characterized with a time window of ca. 20 ps. With the increasing availability of ultrafast laser systems, we expect that the potential applications of femtosecond 2D IR will expand rapidly in the coming years to encompass a broader array of samples.

2.7.4 REFERENCES

1. Nakamoto, K. *Infrared and Raman Spectra of Inorganic and Coordination Compounds*, 5th ed.; Wiley: New York, 1997; Vol. B, pp 48–53.
2. Huber, H.; Kündig, E. P.; Moskovits, M.; Ozin, G. A. *J. Am. Chem. Soc.* **1973**, *95*, 332.
3. Upmacis, R. K.; Poliakoff, M.; Turner, J. J. *J. Am. Chem. Soc.* **1986**, *108*, 3645–3651.
4. Kettle, S. F. A.; Diana, E.; Rossetti, R.; Stanghellini, P. L. *J. Am. Chem. Soc.* **1997**, *119*, 8228–8231.
5. Kettle, S. F. A.; Diana, E.; Rossetti, R.; Stanghellini, P. L. *Inorg. Chem.* **1998**, *37*, 6502–6510.
6. Hartl, F.; Luyten, H.; Nieuwenhuis, H. A.; Schoemaker, G. C. *Appl. Spectrosc.* **1994**, *48*, 1522–1528.
7. Nakamoto, K. *Infrared and Raman Spectra of Inorganic and Coordination Compounds*, 5th ed.; Wiley: New York, 1997; Vols. A & B.
8. Nakamoto, K. Infrared and Raman spectra of inorganic and coordination compounds. In *Handbook of Vibrational Spectroscopy*; Chalmers, J. M.; Griffiths, P. R., Eds.; Wiley: Chichester, UK, 2002; Vol. 3, pp 1872–1892.
9. Smith, B. C. *Fundamentals of Fourier Transform Infrared Spectroscopy*; CRC Press: Boca Raton, FL, 1996.
10. Smith, G. D.; Palmer, R. A. Fast time-resolved mid-infrared spectroscopy using an interferometer. In *Handbook of Vibrational Spectroscopy*; Chalmers, J. M.; Griffiths, P. R., Eds.; Wiley: Chichester, UK, 2002; Vol. 1, pp 625–640.
11. Sun, X. Z.; Nikiforov, S. M.; Yang, J.; Colley, C. S.; George, M. W. *Appl. Spectrosc.* **2002**, *56*, 31–39.
12. Dodd, J. G.; DeNoyer, L. K. Curve-fitting: modeling spectra. In *Handbook of Vibrational Spectroscopy*; Chalmers, J. M.; Griffiths, P. R., Eds.; Wiley: Chichester, UK, 2002; Vol. 3, pp 2215–2223.
13. Mantsch, H. H.; Moffatt, D. J.; Casal, H. L. *J. Mol. Struct.* **1988**, *173*, 285–298.
14. Willson, S. P.; Andrews, L. Matrix isolation infrared spectroscopy. In *Handbook of Vibrational Spectroscopy*; Chalmers, J. M.; Griffiths, P. R., Eds.; Wiley: Chichester, UK, 2002, Vol. 2, pp 1342–1351.
15. Bitterwolf, T. E. Photochemistry of inorganic molecules in hydrocarbon matrices. In *Handbook of Vibrational Spectroscopy*; Chalmers, J. M.; Griffiths, P. R., Eds.; Wiley: Chichester, UK, 2002, Vol. 4, pp 3137–3151.
16. Perutz, R. N.; Turner, J. J. *J. Am. Chem. Soc.* **1975**, *97*, 4791–4800.
17. Mascetti, J.; Tranquille, M. *J. Phys. Chem.* **1988**, *92*, 2177–2184.
18. Li, J.; Bursten, B. E.; Liang, B. Y.; Andrews, L. *Science* **2002**, *295*, 2242–2245.
19. Childs, G. I.; Cooper, A. I.; Nolan, T. F.; Carrott, M. J.; George, M. W.; Poliakoff, M. *J. Am. Chem. Soc.* **2001**, *123*, 6857–6866.
20. Hooker, R. H.; Rest, A. J. *J. Organomet. Chem.* **1983**, *249*, 137–147.
21. Cooper, A. I.; Poliakoff, M. *Chem. Phys. Lett.* **1993**, *212*, 611–616.
22. Upmacis, R. K.; Gadd, G. E.; Poliakoff, M.; Simpson, M. B.; Turner, J. J.; Whyman, R.; Simpson, A. F. *J. Chem. Soc., Chem. Commun.* **1985**, 27–30.
23. George, M. W.; Poliakoff, M.; Turner, J. J. *Analyst* **1994**, *119*, 551–560.
24. McFarlane, K.; Lee, B.; Bridgewater, J.; Ford, P. C. *J. Organomet. Chem.* **1998**, *554*, 49–61.
25. Grills, D. C.; George, M. W. Fast and ultrafast time-resolved mid-infrared spectrometry using lasers. In *Handbook of Vibrational Spectroscopy*; Chalmers, J. M.; Griffiths, P. R., Eds.; Wiley: Chichester, UK, 2002, Vol. 1, pp 677–692.
26. Heilweil, E. J. Applications of broadband transient infrared spectroscopy. In *Ultrafast Infrared and Raman Spectroscopy*; Fayer, M. D., Ed.; Marcel Dekker: New York, 2001; pp 117–147.
27. Siebert, F.; Mäntele, W.; Kreutz, W. *Biophys. Struct. Mech.* **1980**, *6*, 139–146.
28. See Poliakoff, M.; Weitz, E. *Adv. Organomet. Chem.* **1986**, *25*, 277–316 for a review of these early experiments and the key advances made by different research groups.
29. Moore, B. D.; Simpson, M. B.; Poliakoff, M.; Turner, J. J. *J. Chem. Soc., Chem. Commun.* **1984**, 972–974.
30. See ref. 25 for a full discussion of the advances made by a wide range of workers.
31. Bridgewater, J. S.; Netzel, T. L.; Schoonover, J. R.; Massick, S. M.; Ford, P. C. *Inorg. Chem.* **2001**, *40*, 1466–1476.
32. Bromberg, S. E.; Yang, H.; Asplund, M. C.; Lian, T.; McNamara, B. K.; Kotz, K. T.; Yeston, J. S.; Wilkens, M.; Frei, H.; Bergman, R. G.; Harris, C. B. *Science* **1997**, *278*, 260–263.
33. Bourassa, J.; Lee, B.; Bernard, S.; Schoonover, J.; Ford, P. C. *Inorg. Chem.* **1999**, *38*, 2947–2952.
34. Hennig, H.; Ritter, K.; Chibisov, A. K.; Gorner, H.; Grevels, F. W.; Kerpen, K.; Schaffner, K. *Inorg. Chim. Acta* **1998**, *271*, 160–166.
35. Meyer, T. J. *Pure Appl. Chem.* **1986**, *58*, 1193–1206.
36. George, M. W.; Turner, J. J. *Coord. Chem. Rev.* **1998**, *177*, 201–217.
37. Schoonover, J. R.; Strouse, G. F. *Chem. Rev.* **1998**, *98*, 1335–1355.
38. Glyn, P.; George, M. W.; Hodges, P. M.; Turner, J. J. *J. Chem. Soc., Chem. Commun.* **1989**, 1655–1657.
39. Gamelin, D. R.; George, M. W.; Glyn, P.; Grevels, F. W.; Johnson, F. P. A.; Klotzbücher, W.; Morrison, S. L.; Russell, G.; Schaffner, K.; Turner, J. J. *Inorg. Chem.* **1994**, *33*, 3246–3250.
40. Morrison, S. L.; Turner, J. J. *J. Mol. Struct.* **1994**, *317*, 39–47.
41. Schoonover, J. R.; Strouse, G. F.; Omberg, K. M.; Dyer, R. B. *Comments Inorg. Chem.* **1996**, *18*, 165–188.
42. Schoonover, J. R.; Gordon, K. C.; Argazzi, R.; Woodruff, W. H.; Peterson, K. A.; Bignozzi, C. A.; Dyer, R. B.; Meyer, T. J. *J. Am. Chem. Soc.* **1993**, *115*, 10996–10997.
43. George, M. W.; Turner, J. J.; Westwell, J. R. *J. Chem. Soc., Dalton Trans.* **1994**, 2217–2219.
44. George, M. W.; Johnson, F. P. A.; Turner, J. J.; Westwell, J. R. *J. Chem. Soc., Dalton Trans.* **1995**, 2711–2718.
45. Abbott, L. C.; Arnold, C. J.; Ye, T. Q.; Gordon, K. C.; Perutz, R. N.; Hester, R. E.; Moore, J. N. *J. Phys. Chem. A* **1998**, *102*, 1252–1260.

46. Omberg, K. M.; Schoonover, J. R.; Meyer, T. J. *J. Phys. Chem. A* **1997**, *101*, 9531–9536.
47. Doorn, S. K.; Dyer, R. B.; Stoutland, P. O.; Woodruff, W. H. *J. Am. Chem. Soc.* **1993**, *115*, 6398–6405.
48. Wang, C. F.; Mohney, B. K.; Akhremitchev, B. B.; Walker, G. C. *J. Phys. Chem. A* **2000**, *104*, 4314–4320.
49. Chen, P. Y.; Omberg, K. M.; Kavaliunas, D. A.; Treadway, J. A.; Palmer, R. A.; Meyer, T. J. *Inorg. Chem.* **1997**, *36*, 954–955.
50. Weinstein, J. A.; Grills, D. C.; Towrie, M.; Matousek, P.; Parker, A. W.; George, M. W. *Chem. Commun.* **2002**, 382–383.
51. Omberg, K. M.; Schoonover, J. R.; Treadway, J. A.; Leasure, R. M.; Dyer, R. B.; Meyer, T. J. *J. Am. Chem. Soc.* **1997**, *119*, 7013–7018.
52. Omberg, K. M.; Schoonover, J. R.; Bernhard, S.; Moss, J. A.; Treadway, J. A.; Kober, E. M.; Dyer, R. B.; Meyer, T. J. *Inorg. Chem.* **1998**, *37*, 3505–3508.
53. Curtright, A. E.; McCusker, J. K. *J. Phys. Chem. A* **1999**, *103*, 7032–7041.
54. Turner, J. J. Bandwidths. In *Handbook of Vibrational Spectroscopy*; Chalmers, J. M.; Griffiths, P. R., Eds.; Wiley: Chichester, UK, 2002; Vol. 1, pp 101–127.
55. Sandström, J. *Dynamic NMR Spectroscopy* **1982**, Academic Press: London.
56. Best, S. P.; Clark, R. J. H.; McQueen, R. C. S.; Joss, S. *J. Am. Chem. Soc.* **1989**, *111*, 548–550.
57. Ketterle, M.; Kaim, W.; Olabe, J. A.; Parise, A. R.; Fiedler, J. *Inorg. Chim. Acta* **1999**, *291*, 66–73.
58. Gutowsky, H. S.; McCall, D. W.; Slichter, C. P. *J. Chem. Phys.* **1953**, *21*, 279–292.
59. McConnell, H. M. *J. Chem. Phys.* **1957**, *28*, 430–431.
60. MacPhail, R. A.; Strauss, H. L. *J. Chem. Phys.* **1985**, *82*, 1156–1166.
61. Grevels, F. W.; Kerpen, K.; Klotzbücher, W.; McClung, R. E. D.; Russell, G.; Viotte, M.; Schaffner, K. *J. Am. Chem. Soc.* **1998**, *120*, 10423–10433.
62. Wu, R.; Arap Koske, S. K.; White, R. P.; Anson, C. E.; Jayasooriya, U. A.; Cannon, R. D. *J. Chem. Soc., Chem. Commun.* **1994**, 1657–1658.
63. Ito, T.; Hamaguchi, T.; Nagino, H.; Yamaguchi, T.; Kido, H.; Zavarine, I. S.; Richmond, T.; Washington, J.; Kubiak, C. P. *J. Am. Chem. Soc.* **1999**, *121*, 4625–4632.
64. Mukamel, S. *Annu. Rev. Phys. Chem.* **2000**, *51*, 691–729.
65. Sanders, J. K. M.; Hunter, B. H. *Modern NMR Spectroscopy*; Oxford University Press: Oxford, UK, 1993.
66. Noda, I. *J. Am. Chem. Soc.* **1989**, *111*, 8116–8118.
67. Noda, I. General theory of two-dimensional (2D) analysis. In *Handbook of Vibrational Spectroscopy*; Chalmers, J. M.; Griffiths, P. R., Eds.; Wiley: Chichester, UK, 2002; Vol. 3, pp 2123–2134.
68. Ozaki, Y. 2D correlation spectroscopy in vibrational spectroscopy. In *Handbook of Vibrational Spectroscopy*; Chalmers, J. M.; Griffiths, P. R., Eds.; Wiley: Chichester, UK, 2002; Vol. 3, pp 2135–2172.
69. Zanni, M. T.; Hochstrasser, R. M. *Curr. Opin. Struct. Biol.* **2001**, *11*, 516–522.
70. Hamm, P.; Lim, M.; DeGrado, W. F.; Hochstrasser, R. M. *Proc. Natl. Acad. Sci. U. S. A.* **1999**, *96*, 2036–2041.
71. Asplund, M. C.; Zanni, M. T.; Hochstrasser, R. M. *Proc. Natl. Acad. Sci. U. S. A.* **2000**, *97*, 8219–8224.
72. Zanni, M. T.; Gnanakaran, S.; Stenger, J.; Hochstrasser, R. M. *J. Phys. Chem. B* **2001**, *105*, 6520–6535.
73. Ge, N.-H.; Hochstrasser, R. M. *Phys Chem Comm.* **2002**, *5*, 17–26.
74. Golonzka, O.; Khalil, M.; Demirdöven, N.; Tokmakoff, A. *J. Chem. Phys.* **2001**, *115*, 10814–10828.

Comprehensive Coordination Chemistry II
ISBN (set): 0-08-0437486

Volume 2, (ISBN 0-08-0443249); pp 91–101

2.8 Raman and FT-Raman Spectroscopy

S. D. WARNER and I. S. BUTLER
McGill University, Montreal, PQ, Canada

2.8.1 INTRODUCTION 103
2.8.2 THEORETICAL BACKGROUND 104
2.8.3 SELECTED APPLICATIONS OF FT-RAMAN SPECTROSCOPY 106
2.8.3.1 Introduction 106
2.8.3.2 Active Homogeneous Catalysis Identification 106
2.8.3.3 Metal–Ligand Bond Strengths in Tellurium(II) Thiourea Complexes 108
2.8.3.4 Metal–Carbon Bond Strengths in Metal–Alkene Complexes 110
2.8.4 CONCLUSIONS 111
2.8.5 REFERENCES 111

2.8.1 INTRODUCTION

Raman spectroscopy is another spectroscopic method commonly used by inorganic chemists today to help in establishing the structures of the new molecules that have been synthesized. It is a complementary technique to infrared (IR) spectroscopy in that it also provides important information about the vibrations of the molecules in the gaseous, liquid, and solid states. The origins of these two molecular spectroscopic methods are, however, quite different. Infrared spectroscopy involves the absorption of electromagnetic (IR) radiation, while Raman spectroscopy is based on the scattering of electromagnetic radiation, usually in the visible region. Raman spectroscopy is named after the famous Indian physicist, Chandrasekhara Venkata Raman, who became particularly interested in the scattering of light by molecules during the 1920s, following a return voyage from Great Britain to India on passing through the Mediterranean Sea, where he became fascinated with the effect of sunlight being scattered from the surface of the water. Raman's academic brilliance was recognized early on—he graduated with a B.A. (Hons.) degree in Physics and English at the age of 15 and had completed his M.A. degree in Physics by the time he was 17 years old. Professor C. V. Raman, as he later became, was knighted by King George V of England in 1929 and was awarded the Nobel Prize in Physics in 1930 for his discovery of what has become known as the "Raman Effect." Following an outstanding research career as Director of the Indian Institute of Physics in Bangalore and the first National Professor of India, Raman retired in 1948 and then founded the world-renowned Raman Research Institute in Bangalore, where he remained until his death in 1970 at the age of 82 years. Throughout his lifetime, Sir C. V. Raman received many honors, including the Government of India's highest award, the "Bharat Ratna" (Jewel of India). There is a really interesting biography by Bhatt in which many fascinating stories about C. V. Raman are related.[1] There is also a fascinating account by Fabelinskii[2] in which he explains that the Raman effect was actually first observed by Landsberg and Mandel'shtam, in Moscow, for crystals[3] on February 21, 1928, a week before Raman and Krishnan, in Calcutta, observed the same effect for liquids.[4] However, the Indian physicists

published their observations on April 21, 1928, while the Russians results appeared a few weeks later on July 13, 1928. With this information in mind, it is clear why the subsequent award of the Nobel Prize in Physics, in 1930, to only Raman has been a contentious issue for over 70 years.

Raman scattering measurements were quite popular in the 10-year period before World War II, primarily for colorless liquids, such as CCl_4 and CH_3Cl, but, eventually, the technique fell into disfavor because of the ready decomposition of many colored materials, such as transition-metal complexes, upon the long exposures to the intense light sources that were necessary to detect the Raman signals on photographic plates. The advent of high-power, visible gas lasers in the 1960s and, more recently, the introduction of near-IR, solid-state lasers, have led to a renaissance in the Raman field that has continued unabated to the present day. Also, the ability to perform measurements over a wide range of temperatures and pressures has made Raman spectroscopy a powerful analytical technique in materials science. There is a wide range of commercial instrumentation available and the sensitivity of the technique has been greatly enhanced by the introduction of charge-coupled detectors and Fourier transform mathematical manipulations. In recent years, through the application of a specialized technique known as surface-enhanced Raman scattering (SERS), it has even been demonstrated that it is possible to detect single molecules on metallic silver surfaces. The Raman spectroscopy field has grown so much that the biannual *International Conference on Raman Spectroscopy (ICORS)* is approaching its twentieth meeting and normally has well over 500 participants from all over the world. In addition, there is a well-established international, *Journal of Raman Spectroscopy*, that is dedicated solely to new research in this area. Finally, there are numerous textbooks dealing with the theory and applications of Raman spectroscopy, but excellent introductions to the field are provided by the two books entitled *Introductory Raman Spectroscopy* by J. R. Ferraro and K. Nakamoto[5] and *Infrared and Raman Spectra of Inorganic and Coordination Compounds* by K. Nakamoto.[6]

2.8.2 THEORETICAL BACKGROUND[7]

When a monochromatic beam of light from a laser is focused on to a vibrating molecule, the majority of the incident radiation is scattered *elastically*, i.e., with the same frequency as the incident radiation. This process is referred to as Rayleigh scattering and accounts, for example, for why our sky appears blue—the water molecules in the upper atmosphere scatter radiation from the sun predominantly in the blue region. The remainder of the incident laser radiation is scattered *inelastically*, with frequencies either more or less than the frequency of the incident radiation. A useful diagram illustrating both Rayleigh and Raman scattering for a typical heteronuclear diatomic molecule, such as HCl, is shown in Figure 1.

Since electromagnetic radiation is quantized, the energy of the fundamental transition ($v = 0 \rightarrow v = 1$) of HCl is given by $h\nu_1$. In the IR, this would be the energy absorbed by the vibrating HCl molecule. Exactly the same vibrational information is obtained from the Raman effect, but by a totally different process. You should note that in Figure 1, the elastic Rayleigh

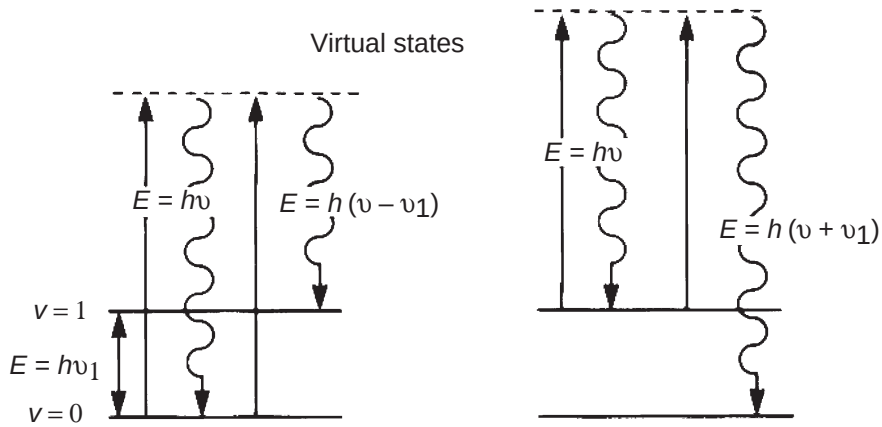

Figure 1 Qualititative picture of Rayleigh and Raman scattering for a simple heteronuclear diatomic molecule.

scattering can originate from both the $v=0$ and $v=1$ levels. The inelastic Raman scattering processes that are illustrated, however, result in either an energy loss [$E=h(v_0-v_1)$] or an energy gain [$E=h(v_0+v_1)$]. As mentioned above, Raman used photographic plates to detect the scattered radiation from vibrating molecules and the signals appeared as a series of lines of varying intensities on the photographic plates. The signals appearing at lower energies than does the central Rayleigh line are referred to as *Stokes lines*, while the signals appearing at higher energies are known as *anti-Stokes lines*. Rayleigh scattering is a much more favorable process than is Raman scattering by a factor of about 10^4. Moreover, because of the Boltzmann distribution, most molecules are in the $v=0$ state at room temperature, so that the Stokes signals are usually more intense than are the anti-Stokes signals. Consequently, a Raman spectrum is normally scanned towards lower energies (decreasing wavenumber, cm^{-1}) from that of the incident laser line. The Raman signals are actually reported as Raman shifts (Δv, in cm^{-1}) from the Rayleigh line. In the case of the HCl vibration, it is detected as an IR absorption and a Raman shift at 2,886 cm^{-1}.

There are several benefits of the Raman technique over IR spectroscopy for inorganic chemists, including the fact that the low-energy ($<400\,cm^{-1}$) region, where most of the important metal–ligand vibrations occur, is routinely available in the Raman. The cut-off for most mid-IR instruments is $\sim 650\,cm^{-1}$ and usually to access the lower energies a special far-IR spectrometer is required. In addition, water is an extremely weak Raman scatterer and a very strong IR absorber. Therefore, while aqueous IR spectroscopy is really difficult to do, the Raman spectra of inorganic compounds dissolved in water are relatively easy to measure.

The theoretical basis for the Raman effect was developed originally by Professor A. G. Smekal in 1923,[8] five years before Professor C. V. Raman actually demonstrated the effect experimentally.[4] Because Smekal's classical theory is reproduced in many textbooks, including refs. 5 and 7, it will not be presented here. The key point is that the Raman effect depends on the changes that occur in the *polarizability* (α) of a molecule during a vibration. Polarizability can be defined as "the ease with which the electron clouds associated with atoms in a molecule can be distorted". Since heavier atoms have larger electron clouds than do lighter ones, the heavier atoms should also have larger polarizabilities and therefore give rise to stronger Raman scattering, which is indeed the case.

Raman intensities are directly proportional to the fourth power of the excitation frequency (v^4) and so the choice of the incident laser beam plays a significant role in the resulting intensities of the observed Raman signals. All things being equal, the Raman signals should be more intense when excited by a high frequency (i.e., shorter wavelength) laser than when a lower frequency (i.e., longer wavelength) laser is used. For inorganic compounds, visible noble-gas lasers have been normally used to excite the Raman spectra, e.g., an argon-ion laser (488.0 nm, blue; 514.5 nm, green) or a krypton-ion laser (647.1 nm, red). Therefore, higher Raman intensities would be expected when using the blue laser line than for the red one. More recently, attention has been turned to Fourier transform Raman (FT-Raman) spectroscopy for which longer wavelength, near-infrared lasers are commonly employed, e.g., 1,032 nm and 780 nm. The lower-intensity signals produced are offset by the rapid data collection abilities of the FT-Raman systems. Usually, a visible laser line is chosen for conventional Raman spectroscopy that most closely matches the actual color of the compound. If any other laser excitation is used, the possibility of the laser energy being absorbed by the compound is increased dramatically and there is a strong chance of a so-called resonance Raman spectrum being produced, e.g., the resonance spectrum of TiI_4 in Figure 2, in which several overtones of the symmetric Ti–I stretching vibration are induced when 514.5 nm laser excitation is used. (For further information on resonance Raman spectroscopy, see refs. 5 and 7.) Finally, a really important feature of Raman spectroscopy is that it is quite easy to examine the polarization of the scattered radiation and thus obtain more information about the nature of the vibrations of molecules than can usually be obtained from IR spectroscopy.

Raman spectra can now be routinely obtained for all types of materials. It is particularly useful for centrosymmetric species, such as octahedral SF_6 or $Cr(CO)_6$, for which the *rule of mutual exclusion* applies. This rule states that "vibrations which are Raman-active are IR-inactive, and vice versa". This means that a centrosymmetric species can be readily identified from the non-coincidence of the peaks appearing in its IR and Raman spectra.

We will now consider a few selected examples of some recent inorganic chemistry research that has benefited immensely from the ready availability of commercial Raman spectrometers. We will focus particularly on FT-Raman spectroscopy because this technique is fast becoming the method of choice owing to the speed of spectral measurement and manipulation, and the fact that the full spectrum can be obtained as opposed to usually only specific spectral regions, even when rapid, charged-couple detection (CCD) devices are used. An excellent summary of FT-Raman

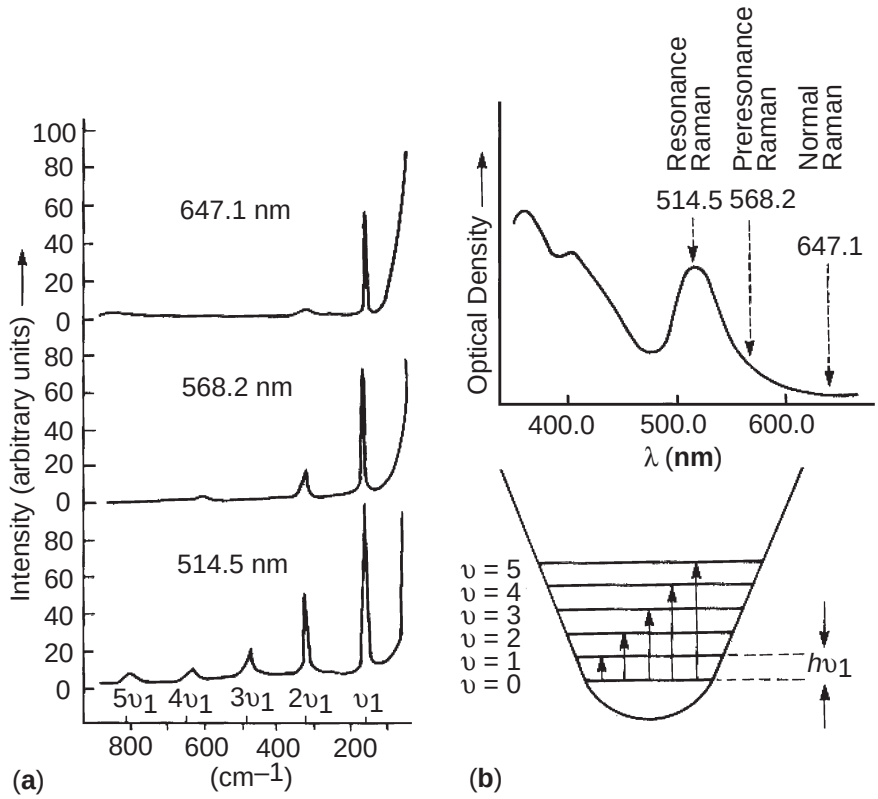

Figure 2 Raman spectra of TiI_4 in cyclohexane solution excited with different laser lines. Adapted from Butler, I. S.; Harrod, J. F. *Inorganic Chemistry: Principals and Applications*, Figure 6.15 (reproduced by permission of The American Chemical Society from Clark, R. J. H.; Mitchell, R. D. *J. Am. Chem. Soc.* **1973**, *95*, 8300).

spectroscopy is given in ref. 5, pp 179–188 and the seminal work on the new spectroscopic technique is presented in a book by Chase and Rabolt,[9] two of the original discovers of the technique.

2.8.3 SELECTED APPLICATIONS OF FT-RAMAN SPECTROSCOPY

2.8.3.1 Introduction

During the past decade, Raman spectroscopy has moved out of the shadow of IR spectroscopy and has become a routine tool for characterization. The cost of the instrumentation is decreasing rapidly. With its ease of operation, lack of sample preparation, and rapid analysis time, high-quality FT-Raman spectra have been reported for many colored, main-group metal, transition-metal coordination, and organometallic complexes. Air-sensitive compounds can easily be analyzed in sealed ampoules, because as mentioned earlier, glass is a weak Raman scatter and so does not interfere with the resulting spectra. As the field of inorganic chemistry continues to grow, so do the uses of FT-Raman spectroscopy for analysis. Below are three examples of current uses of the FT-Raman technique in inorganic field in inorganic chemistry.

2.8.3.2 Active Homogeneous Catalysis Identification

Heterogeneous catalysis is an important area, both in academic and industrial settings, with the characterization of the catalytic process continuing to be a subject of considerable interest. Often these catalysts are metals, such as palladium or rhodium, or metal oxides, such as vanadium oxide. Vibrational spectroscopy, and in particular FT-Raman spectroscopy, has emerged as a powerful tool for the identification and characterization of the active catalyst. And, in cases where the catalyst is adsorbed on a heterogeneous substance, the effect that this solid phase has

on the active catalyst and the catalytic cycle can be determined. The feasibility of FT-Raman spectroscopy for this purpose was recently demonstrated by van der Pol *et al.*[10] who characterized the 2,2′-bis-(inden-2-yl)-biphenyl-zirconium dichloride catalyst (**A**), supported on silica, and in the presence of a co-catalyst, methylaluminoxane (MAO). Metallocenes are particularly useful in the industrial-scale polymerization of alkenes and are unique in this application because the active catalyst is comprised of only one metal atom. In the catalysis of olefin polymerization by the simpler system, Cp_2ZrCl_2/MAO ($Cp = \eta^5$-C_5H_5), the co-catalyst activates the metal center of the precatalyst by methylation, yielding the dimethyl metal fragment **C**, followed by further reaction with MAO to give the cationic monomethyl complex **D** (Scheme 1).

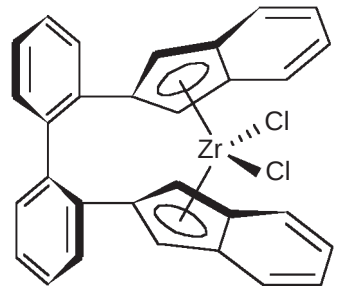

(**A**)

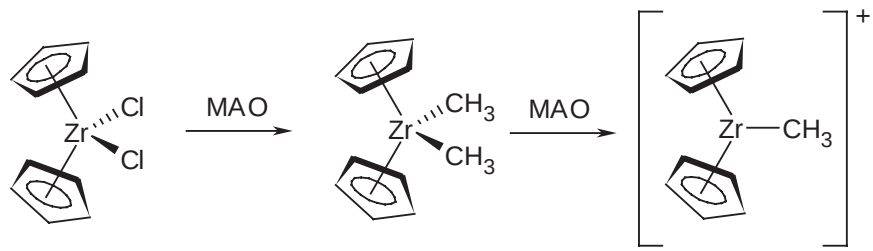

(**B**) (**C**) (**D**)

Scheme 1

In characterizing the mechanistic intermediates involving complex **A**, peak assignments for the Zr—Cl, Zr—CH_3 (neutral dimethyl metal fragment), and Zr—CH_3 (cationic monomethyl metal fragment) stretching vibrations were made by analogy to those involving complex **B** using a combination of FT-Raman spectroscopy and *ab initio* quantum mechanics calculations. After assignment of these vibrations, which occur in the spectroscopic region below 500 cm^{-1}, the calculated stretching frequencies were compared with the experimental values for the pure complexes **B** and **C** in order to validate this method. When the spectra of complex **A** adsorbed onto the MAO/silica support were collected, useful data on the vibrations of the active site of the metallocene (i.e., Zr—Cl and/or Zr—CH_3 vibrations) were obtained even though the transition metal was only present at a concentration of about 0.12–0.40 wt.% (Table 1). To ease the analysis of the spectrum of the supported catalyst system, individual spectra of MAO, MAO on silica, the unsupported catalyst, the supported catalyst, and biph[2-Ind]$_2ZrCH_3$ were recorded (Figure 3). Two key results were obtained using FT-Raman spectroscopy to characterize this system. The first was that the catalyst loading on the solid could be quantitated because the ratio of the peak integration for the Zr complexes (spectral region 1,517–1,489 cm^{-1}) to the integration of the peaks representing total MAO loading (spectral region 3,021–2,746 cm^{-1}) correlated very well to the actual ratio loading of the Zr and MAO loading ($R^2 = 0.9991$). Finally, the catalytic yield of the catalyst in the olefin polymerization correlated very well with the intensity of the Zr—CH_3 stretching frequency at 454 cm^{-1}. Thus, the quality of the catalyst in terms of the catalytic yield can be determined using FT-Raman spectroscopy.

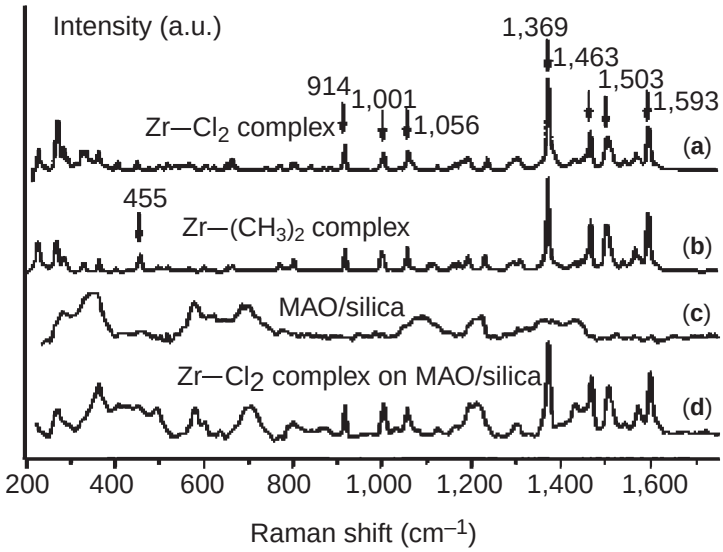

Figure 3 FT-Raman spectra of biph[2-Ind]$_2$ZrCl$_2$ (a) biph[2-Ind]$_2$Zr(CH$_3$)$_2$, (b) MAO/silica, (c) and of biph[2-Ind]$_2$ZrCl$_2$ on MAO/silica (12.8 wt.% Al and 0.4 wt.% Zr) (d). Many peaks due to the indenyl ligand are insensitive to the silica support; the strongest peaks of the indenyl ligand have been labeled in trace a. In the spectrum of the Zr—(CH$_3$)$_2$ complex (b) the peak due to the symmetric Zr—CH$_3$ stretching vibration has been labeled (455 cm^{-1}) (reproduced by permission of Elsevier from *J. Organomet. Chem.* **2002**, *651*, 80–89).

Table 1 Assignment of M—Cl and M—CH$_3$ vibrations.

Wavenumber (cm^{-1})	*Assignment*
1,105	CH$_3$ specific, 'umbrella mode'
794	Cl specific
454	ν(Zr—CH$_3$)
321	ν_{asym}(Zr—Cl)
308	ν_{sym}(Zr—Cl)

2.8.3.3 Metal–Ligand Bond Strengths in Tellurium(II) Thiourea Complexes

Structural information, such as bond strength and intermolecular bonding, can be obtained with the aid of vibrational spectroscopy. Many compounds, which have been thoroughly studied by IR spectroscopy, are being now examined by the FT-Raman technique. Remaining ambiguous or uncertain assignments from the IR experiments can be elucidated with the use of FT-Raman spectroscopy. An interesting example of this application is the recent FT-Raman spectroscopic investigation of a series of *cis*-bis(thiourea)tellerium(II) halide and thiocyanate compounds (**E**) by Alía *et al.*[11] These compounds have a distorted square–planar configuration with identical ligands in a *cis* configuration.[12,13] At first glance, the analysis of these compounds by FT-Raman spectroscopy would seem to be a routine task. For example, analogous to the IR studies, the 3,500–3,000 cm^{-1} region of the spectra is dominated by the thiourea NH stretching vibrations. However, the power of FT-Raman spectroscopy as an analytical tool for characterization lies in the analysis of the low-frequency region of the spectra (i.e., <400 cm^{-1}). This region is relatively simple and consists mainly of the Te–S, Te–X, and lattice mode vibrations (Figure 4 and Table 2).

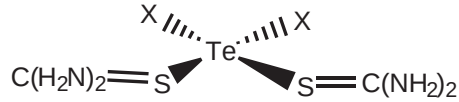

(**E**) X = Cl, Br, I or SCN

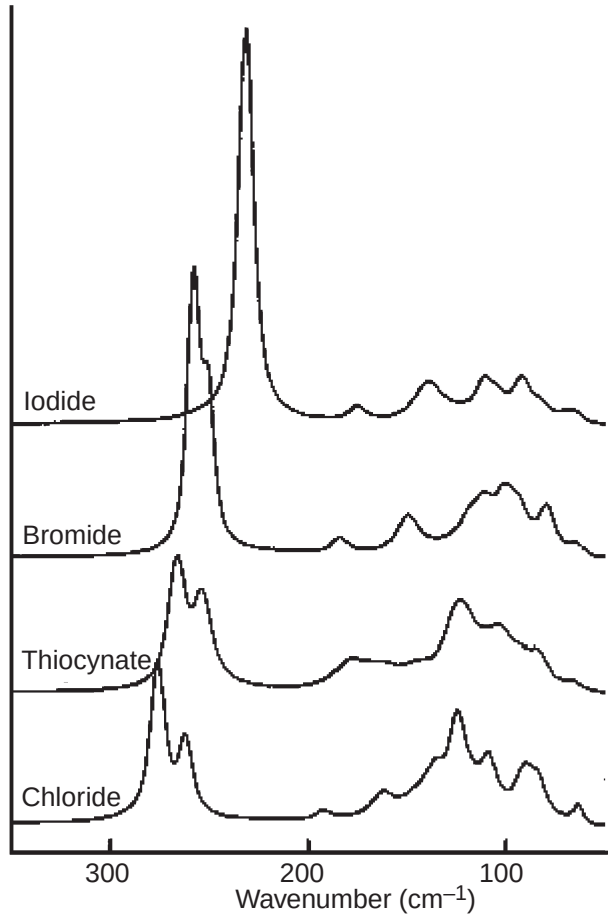

Figure 4 FT-Raman spectra of thiourea and its complexes with tellurium(II) in the 350–60 cm^{-1} region.

Table 2 FT-Raman spectral assignments of tellurium(II)–thiourea complexes in the 350–60 cm^{-1} region.

Thiourea	*Assignment*	*Thiocyanate*	*Chloride*	*Bromide*	*Iodide*
	ν(Te—S)	266	276	258	232
	ν(Te—S)	253	262	250	
	δ(S—Te—S)	178	192	184	175
	ν(Te—X)	162	162	150	139
	δ(X—Te—X)	143	144	137	
	Lattice Mode	124	124	127	124
117	Lattice Mode		117	118	
	Lattice Mode	111	109	111	111
101	Lattice Mode	103	98	101	103
	Lattice Mode	92	91	93	92
84(sh)	Lattice Mode	83	84	79	83

The assignments reported in this study for the Te–S and Te–X stretching vibrations are the reverse of those published earlier for the chloride compound, where the higher frequency vibration was assigned as the Te–X stretching vibration and the Te–S stretching vibration was attributed to the lower frequency vibration.[14] In the compounds examined in this study, the Te—X bonds are considerably longer than are the Te—S bonds (Table 3). This observation led the authors to assign the higher frequency vibration to the symmetric Te–S stretching mode in the decreasing order Cl > SCN > Br > I, corresponding to the increasing Te—X bond lengths from X-ray crystallographic data. A comparison of the FT-Raman spectrum of thiourea with those of

Table 3 Te—S and Te—X (X = Cl, Br, I, or SCN) bond lengths obtained from X-ray crystallographic data (from refs. 12 and 13).

Bond Type	*Bond Length* (Å)			
	$Te(tu)_2Cl_2$[a]	$Te(tu)_2Br_2$	$Te(tu)_2I_2$	$Te(tu)_2SCN_2$
Te—S	2.457	2.476	2.521	2.458
Te—X	2.936	3.038	3.162	3.039

[a] tu = thiourea

the complexes facilitated the assignment of the lattice modes. In this work, the use of FT-Raman spectroscopy has greatly complemented the existing IR data, but it also has provided new insight into the metal–ligand vibrational modes. As mentioned earlier, the low-frequency vibrational region is of particular interest to the synthetic inorganic chemist.

2.8.3.4 Metal–Carbon Bond Strengths in Metal–Alkene Complexes

The *v*(CO) stretching modes of metal carbonyls have often been used to compare the donor strengths of ligands coordinated to the metal center in such complexes. However, little effort has been made to examine, by FT-Raman spectroscopy, the effect of donor ligands on the strengths of the corresponding M—C bonds. This dearth of data has prompted Moigno and co-workers[15] to investigate the *trans* effect observed for a series of rhodium halide complexes, where a potentially labile ligand is located *trans* to the halide, which is varied in the series. The *trans* effect is defined as "the effect of a coordinated ligand on a metal center upon the rate of ligand substitution involving ligands positioned *trans* to the first ligand". As part of this study, a comparison of the FT-Raman spectra of *trans*-[RhF(C═CH_2)($PiPr_3$)$_2$] and *trans*-[RhF(^{13}C═$^{13}CH_2$)($PiPr_3$)$_2$] was undertaken, which resulted in the assignment of the *v*(Rh═C) and *v*(Rh═^{13}C) vibrations and showed that *v*(Rh═^{13}C) is of higher intensity and isolated from other vibrations in complexes of this type, whereas the *v*(Rh═C) frequency is overlapped with vibrations of the tertiary phosphine ligand.[15] Therefore, Moigno and co-workers measured the FT-Raman spectra of a series of ^{13}C-labeled complexes of the general formula, *trans*-[RhX(^{13}C═$^{13}CH_2$)($PiPr_3$)$_2$], where X = F, Cl, Br, and I.[16] This particular series of complexes facilitated an investigation of the electronic influence of the ligand X *trans*-disposed to the ^{13}C═$^{13}CH_2$ ligand on the strength of the Rh═^{13}C bond, since the vibrational mode for a bond is related to its force constant, which is in turn closely related to its bond strength. The corresponding phenyl-substituted vinylidene and carbonyl rhodium(I) complexes were also examined

Table 4 *v*(Rh═^{13}C) or *v*(Rh═C) frequencies for complexes 1–12.

	v(Rh═^{13}C) (cm^{-1})	*v(Rh═C)* (cm^{-1})
trans-[RhF(^{13}C═$^{13}CH_2$)($PiPr_3$)$_2$] **(1)**	559	
trans-[RhCl(^{13}C═$^{13}CH_2$)($PiPr_3$)$_2$] **(2)**	551	
trans-[RhBr(^{13}C═$^{13}CH_2$)($PiPr_3$)$_2$] **(3)**	548	
trans-[RhI(^{13}C═$^{13}CH_2$)($PiPr_3$)$_2$] **(4)**	540	
trans-[RhF(═C═CHPh)($PiPr_3$)$_2$] **(5)**		579
trans-[RhCl(═C═CHPh)($PiPr_3$)$_2$] **(6)**		574
trans-[RhBr(═C═CHPh)($PiPr_3$)$_2$] **(7)**		573
trans-[RhI(═C═CHPh)($PiPr_3$)$_2$] **(8)**		572
trans-[RhF(CO)($PiPr_3$)$_2$] **(9)**		573
trans-[RhCl(CO)($PiPr_3$)$_2$] **(10)**		559
trans-[RhBr(CO)($PiPr_3$)$_2$] **(11)**		555
trans-[RhI(CO)($PiPr_3$)$_2$] **(12)**		546

to explore the *trans* effect on other potentially labile ligands. The $\nu(Rh{=}{}^{13}C)$ or $\nu(Rh{=}C)$ frequencies are listed in Table 4. A number of interesting conclusions can be drawn from the trends observed in the FT-Raman data. First, for the vinylidine complexes (**1–4**), the frequency of the $\nu(Rh{=}{}^{13}C)$ vibration increases as the ligand is varied in the order $F > Cl \geq Br \geq I$, which implies that the bond strength increases in the same direction. Throughout this study, the experimental results and the conclusions drawn were also supported by density functional theory (DFT) calculations. The data derived from the calculations showed that the trends observed were primarily due to the change in the $Rh{=}{}^{13}C$ bond lengths and not due to a mass effect or to coupling of the Rh–X and $Rh{=}{}^{13}C$ modes. In the related phenyl-substituted vinylidine complexes (**5–8**), the trend in bond strength as X is varied is essentially the same. Thus, it was concluded from the FT-Raman data for complexes (**1–8**) that the order of increasing *trans* effect of the coordinating ligand followed the sequence $I > Br > Cl > F$. Interestingly, when the CO complexes (**9–12**) were compared with the isoelectronic complexes (**1–4**) and also complexes (**5–8**), an unexpected observation was made. While the ν(Rh-C) frequencies in the series (**9–12**) increased in the same manner as for compounds (**1–8**), when the *trans* ligand was varied, the ν(CO) frequency increased in compounds (**9–12**), while that of $\nu({}^{13}C{=}{}^{13}C)$ in compounds (**1–4**) (or the $\nu(C{=}C)$ vibration in complexes (**5–8**)) decreased as the *trans* ligand was varied in the order $F \rightarrow Cl \rightarrow Br \rightarrow I$. These results are explained by an increased π-donor capability of X as one goes up the periodic table in group 17, and support a push–pull π-interaction as an explanation for why the strongest Rh—C bond is formed with fluorine, the most electronegative substituent. Taken together with the DFT calculations, which are not discussed here, the work conducted by Moigno and co-workers is an excellent example of just how FT-Raman spectroscopy can be an invaluable source of experimental physical data to help explain chemical phenomena.

2.8.4 CONCLUSIONS

Raman spectroscopy continues to develop as an important weapon in the structural armory of the modern inorganic chemist. One of the most promising areas is bioinorganic chemistry. The metal–ligand vibrations in bioinorganic molecules can be readily detected in the low-frequency region by Raman spectroscopy and these vibrations are free from interference from the higher-frequency vibrations associated with the backbones of the proteins and other related species, such as hemoglobin derivatives. Most inorganic research laboratories are now equipped with Raman and/or FT-Raman spectrometers since the prices are becoming competitive with IR instruments. These Raman spectrometers are often equipped with microscopes so that Raman imaging is also a rapidly emerging technique for today's chemists, physicists, geologists, and materials scientists. The future of Raman spectroscopy seems assured for some time to come.

2.8.5 REFERENCES

1. See the article by A. K. Bhatt on C. V. Raman on the following Hindunet website http://www.freeindia.org/biographies/greatscientists/drcvraman/index.htm.
2. Fabelinskii, I. L. *Physics-Uspekhi* **1998**, *41*, 1229–1247.
3. Landsberg, G. S.; Mandelstam, L. I. *Naturwissenschaften* **1928**, *16*, 557–558.
4. Raman, C. V.; Krishnan, K. S. *Nature (London)* **1928**, *121*, 501–502.
5. Ferraro, J. R.; Nakamoto, K. *Introductory Raman Spectroscopy*. **1994**, Academic Press: San Diego, CA, and references therein.
6. Nakamoto, K. *Infrared and Raman Spectra of Inorganic and Coordination Compounds: Parts A and B*, 5th. ed., Wiley Interscience: New York, 1997.
7. Butler, I. S.; Harrod, J. F. *Inorganic Chemistry: Principles and Applications*. Benjamin/Cummings: Redwood City, CA, 1989, Chapter 6.
8. Smekal, A. G. *Naturwissenschaften* **1923**, *11*, 873–875.
9. Chase, D. B.; Rabolt, J. F. *Fourier Transform Spectroscopy from Concept to Experiment*. **1994**, Academic Press: Cambridge, MA.
10. van der Pol, A.; van Heel, J. P. C.; Meijers, R. H. A. M.; Meier, R. J.; Kranenburg, M. *J. Organomet. Chem.* **2002**, *651*, 80–89.
11. Alía, J. M.; Edwards, H. G. M.; García-Navarro, F. J. *J. Mol. Struct.* **1999**, *508*, 51–58.
12. Foss, O.; Maartmann-Moe, K. *Acta. Chem. Scand.* **1987**, *A41*, 121–129.

13. Foss, O.; Henjum, J.; Maartmann-Moe, K.; Maroy, K. *Acta. Chem. Scand.* **1987**, *A41*, 77–86.
14. Hendra, P. J.; Jovic, Z. *J. Chem. Soc.(A)* **1967**, 735–736.
15. Moigno, D.; Kiefer, W.; Callejas-Gaspar, B.; Gil-Rubio, J.; Werner, H. *New J. Chem.* **2001**, *25*, 1389–1397.
16. Moigno, D.; Kiefer, W.; Gil-Rubio, J.; Werner, H. *J. Organomet. Chem.* **2000**, *612*, 125–132.

Comprehensive Coordination Chemistry II
ISBN (set): 0-08-0437486

Volume 2, (ISBN 0-08-0443249); pp 103–112

2.9
High-pressure Raman Techniques

I. S. BUTLER
McGill University, Montreal, PQ, Canada

2.9.1 INTRODUCTION 113
2.9.2 DIAMOND-ANVIL CELL 113
2.9.3 SELECTED EXAMPLES OF HIGH-PRESSURE VIBRATIONAL SPECTROSCOPY OF ORGANOMETALLIC AND COORDINATION COMPOUNDS 115
2.9.3.1 Pentacarbonyl(methyl)manganese(I) 115
2.9.3.2 *cis*-Dithiolatobis(triphenylphosphine)platinum(II) 115
2.9.3.3 Pressure-induced Disproportionation 118
2.9.3.4 Decarbonyldimanganese(0) 118
2.9.3.5 Mercuric(II) Cyanide 118
2.9.4 CONCLUSIONS 120
2.9.5 REFERENCES 120

2.9.1 INTRODUCTION

By comparison with low- and high-temperature studies, the effects of high pressures on the spectroscopic properties of solid organometallic and coordination compounds have been relatively little explored. The application of high pressures can lead to significant and sometimes drastic perturbations in the molecular and crystal structures of solid materials, e.g., phase transitions, such as the conversion of graphite into diamond. The information obtained from studies of the changes in the electronic (UV–visible) and vibrational spectra of inorganic materials can lead to valuable information about the nature of metal–ligand and inter- and intramolecular interactions. This spectroscopic information can sometimes be useful in designing pressure sensors and other electronic devices, and in detecting the conversion of semiconductors into metallic-like species under the influence of high pressures. Both the experimental techniques and applications of high-pressure electronic and vibrational spectroscopy with respect to organometallic and coordination compounds have been thoroughly reviewed recently.[1,2] An excellent introduction to high-pressure Raman spectroscopy and its applications can be found in ref. 3, pp 153–160. In this section, we describe the results of some high-pressure vibrational spectroscopic studies of organometallic and coordination compounds to illustrate the growing importance of this field of research.

2.9.2 DIAMOND-ANVIL CELL

High pressures can be readily applied to inorganic materials with the aid of commercial or home-built diamond-anvil cells (DACs). The original DAC was developed at the National Bureau of Standards just after World War II[4] and one of the co-inventors, A. Van Valkenburg, founded *High-pressure Diamond Optics*, a small, family-run, specialist optical company in Tucson, Arizona, which is still in existence today. A schematic drawing of the so-called Weir–Van Valkenburg DAC is shown in Figure 1.

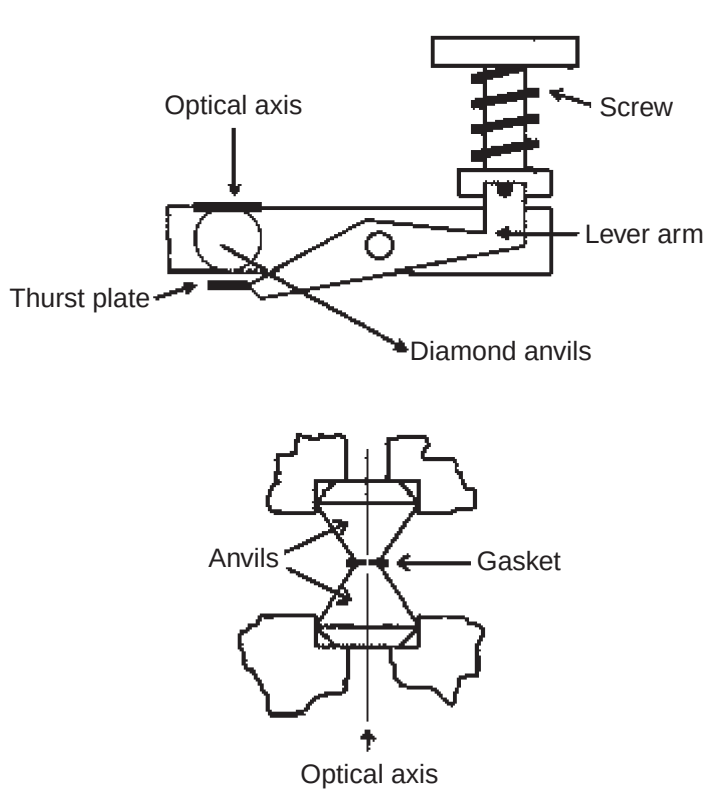

Figure 1 Weir–Van Valkenburg DAC: (a) side view and (b) view of the gasketed diamond anvils (reproduced by permission of Elsevier from *Coord. Chem. Rev.* **2001**, *219–221*, 713–759).

The operation of the DAC is quite simple—the opposing faces of two type-IIA, gem-quality diamonds (1–2 mm in size) are mechanically forced together by means of the screw–lever–thrust plate mechanism. To achieve a uniform pressure gradient across the diamond faces, a 100–300 μm stainless-steel gasket is located between the parallel faces of the two diamonds. The sample is placed, with the aid of an optical microscope, into an approximately 300 μm diameter hole drilled in the center of the stainless-steel gasket. Sometimes, a pressure-transmitting fluid, such as Nujol, is added to the sample in order to ensure a uniform pressure gradient across the sample. For crystalline powders and modest pressures of up to 50 kbar (~50,000 atm), however, a pressure-transmitting fluid is not normally necessary. The DAC is about the size of one's hand and can be easily mounted into a modern IR or Raman spectrometer equipped with a microscope. In fact, it is also possible to focus a color TV camera down the optical axis of the DAC and monitor precisely what is happening to the sample in the gasket as pressure is being applied. For certain samples, dramatic color changes may sometimes occur as the pressure is changed, i.e., these materials are said to be *piezochromic*. (Extensive work on piezochromism has been performed by Professor Dickamer's research group at the University of Illinois, Urbana-Champaign, Illinois, USA. See, for example,[5]). The spectroscopic regions around 2,000 cm^{-1} in the IR and 1,350 cm^{-1} in the Raman are not useful regions in which to work because of interfering vibrations from the diamonds.

How is the pressure inside the DAC determined? Usually, this is achieved by adding to the sample a small amount of a pressure calibrant with a known vibrational or electronic spectroscopic response to changes in pressure.[6] For the infrared, a material such as powdered $NaNO_3$ is normally used—the symmetric N—O stretching mode of the NO_3^- group is located at 1,401.3 cm^{-1} at ambient pressure[7] and moves steadily to higher wavenumbers with increasing pressure. For the Raman, the most common pressure calibrant is a ruby chip—the R_1 fluorescence of ruby at 694.2 nm has a well-established pressure dependence up to ~160 kbar.[8] More recently, it has been shown that the t_{2g} phonon mode of the diamonds in the DAC itself, located at 1,332.5 cm^{-1}, at ambient pressure, can be used as an *in situ* calibrant for pressures up to ~50 kbar.[9]

2.9.3 SELECTED EXAMPLES OF HIGH-PRESSURE VIBRATIONAL SPECTROSCOPY OF ORGANOMETALLIC AND COORDINATION COMPOUNDS

A typical pressure-tuning experiment involves loading the sample and appropriate pressure calibrant in the DAC with the aid of an optical microscope and, after bolting the cell onto a plate in the IR or Raman spectrometer, gradually increasing the pressure by tightening the mechanical screw (turning clockwise) on the cell. Practice reveals just how many turns are necessary to bring about small incremental steps in pressure. At the same time as the pressure is being increased, the infrared and/or Raman spectra of the sample and the calibrant are being monitored. From the data obtained, the wavenumber (ν) vs. pressure (P) results are then plotted for selected vibrational modes and the pressure dependences ($d\nu/dP$) are determined from the slopes of the resulting lines. Stretching modes are usually more pressure sensitive ($\sim$0.3–1.0 cm^{-1}/kbar) than are bending and deformation modes ($<$0.1–0.3 cm^{-1}/kbar).[6] External (i.e., lattice) modes are particularly sensitive to pressure (1–3 cm^{-1}/kbar). The vibrational modes normally increase in energy with increasing pressure because compression results in increased force constants. In certain cases, there are spectacular changes in the pressure dependences due to major structural modifications such as phase transitions, changes in intermolecular interactions (e.g., H-bonding), or changes in the π-backbonding in organometallic ligands (e.g., CO, CS, CNPh, NO, alkene, etc.).[1,2] A few examples of these effects for organometallic and coordination compounds will now be given.

2.9.3.1 Pentacarbonyl(methyl)manganese(I)

An excellent prototype molecule for elucidating the effects of high pressures on the molecular structures of organometallic compounds is $CH_3Mn(CO)_5$, which has a simple metal–carbon σ bond. Under pressure, the axial a_1 ν(CO) mode (*trans* to the CH_3 group), at 1,975 cm^{-1} at ambient pressure, initially decreases in wavenumber with the application of pressure until $\sim$10 kbar (Figure 2).[10] At this point, the $d\nu/dP$ value changes from being negative (-0.82 cm^{-1}/kbar) to positive (0.30 cm^{-1}/kbar).

Similar results are obtained for the axial a_1 ν(CO) modes of several other pentacarbonylmetal species, such as $CH_3Re(CO)_5$,[10] $Cr(CO)_5(CS)$,[11] and $Mn(CO)_5Br$.[12,13] This interesting observation is explained by a competition between two opposing effects: (i) the effect of pressure to compress the axial metal–CO bond, thereby increasing the metal–carbon force constant and increasing the metal–CO π^* overlap, resulting in a decrease in wavenumber of the axial a_1 ν(CO) mode; and (ii) the effect of pressure to compress the axial CO bonds, thereby increasing the CO force constants resulting in increases in wavenumber of the axial a_1 ν(CO) modes. Initially, the π-backbonding effect dominates but, eventually, the second effect comes into prominence.

2.9.3.2 *cis*-Dithiolatobis(triphenylphosphine)platinum(II)

The petrochemical industry continues to focus much of its research effort on hydrodesulfurization and the Claus Process for the elimination and recovery of sulfur from fossil fuels. This research will become even more important in the future with the worldwide emphasis on the emission controls projected in the Kyoto Protocol. The Claus Process results in the conversion of toxic H_2S gas, emitted by hydrodesulfurization of fossil fuels, into sulfur and water. In order to better understand the mechanism of the Claus Process, some research has been directed at model intermediate compounds, such as *cis*-$(Ph_3P)_2Pt(SH)_2$. This compound reacts with SO_2 to produce the catenated sulfur species, $(Ph_3P)_2PtS_3O$, and water, mimicking the kind of chemistry that occurs in the Claus Process.[14] While the S—H stretching modes of *cis*-$(Ph_3P)_2Pt(SH)_2$ are too weak to be detected in the infrared, they are clearly present at $\sim$2,500 cm^{-1} in the Raman spectrum. The pressure sensitivities of the S—H stretching modes of *cis*-$(Ph_3P)_2Pt(SH)_2$ have recently been investigated.[15]

The wavenumber (ν) vs. pressure (P) plots for the ν_{asym}(S—H) and ν_{sym}(S—H) vibrations of *cis*-$(Ph_3P)_2Pt(SH)_2$, at $\sim$2,552 cm^{-1} and $\sim$2,540 cm^{-1}, respectively, at ambient pressure, are shown in Figure 3. Initially, the two peaks are not particularly pressure sensitive. At $\sim$15 kbar, however, the ν_{asym}(S—H) vibration suddenly splits into two and the pressure dependence of the ν_{sym}(S—H) vibration increases dramatically. Similarly, the C—H stretching vibrations show a marked increase in $d\nu/dP$ at around 15 kbar (Figure 4). There is clear evidence of a phase transition occurring in this compound at $\sim$15 kbar.

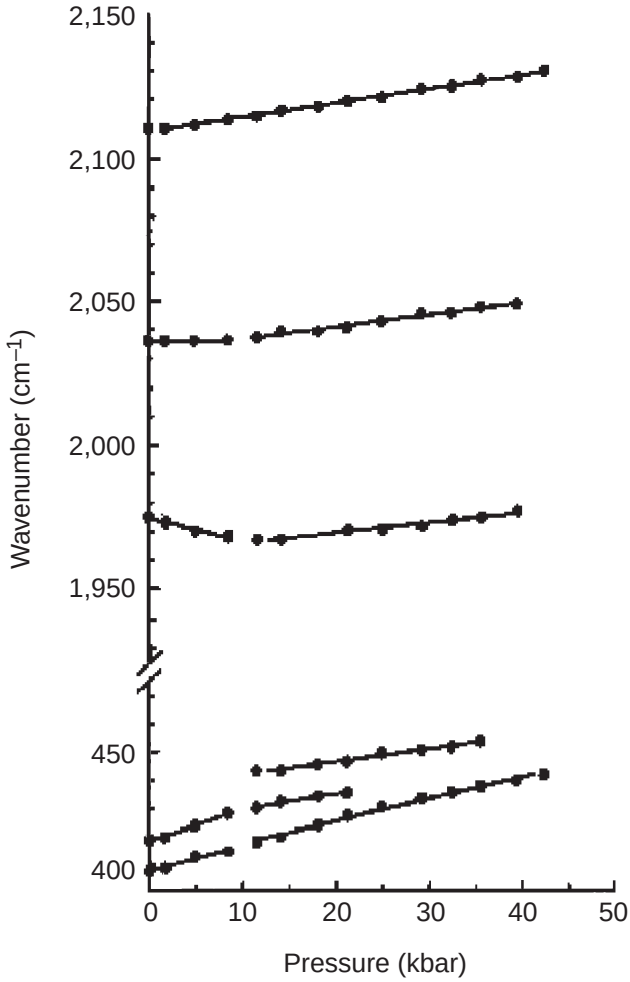

Figure 2 Pressure dependence of selected Raman bands of $CH_3Mn(CO)_5$ (reproduced by permission of The American Chemical Society from *Inorg. Chem.* **1991**, *30*, 117–120).

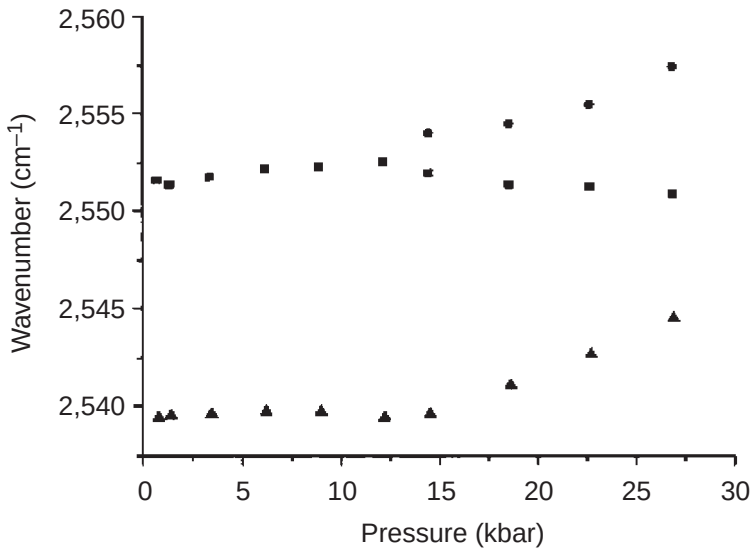

Figure 3 Wavenumber (ν) vs. pressure (P) plots for S—H stretching modes of *cis*-$[(Ph_3P)_2Pt(SH)_2]$ (reproduced by permission of Elsevier from *Spectrochim. Acta.* **2002**, *A58*, 2581–2587).

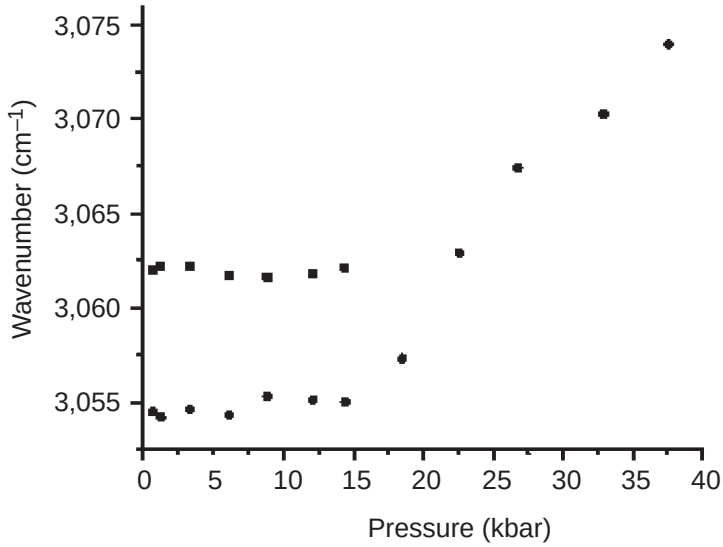

Figure 4 Wavenumber (ν) vs. pressure (P) plots for C—H stretching modes of *cis*-[$(Ph_3P)_2Pt(SH)_2$] (reproduced by permission of Elsevier from *Spectrochim. Acta*. **2002**, *A58*, 2581–2587).

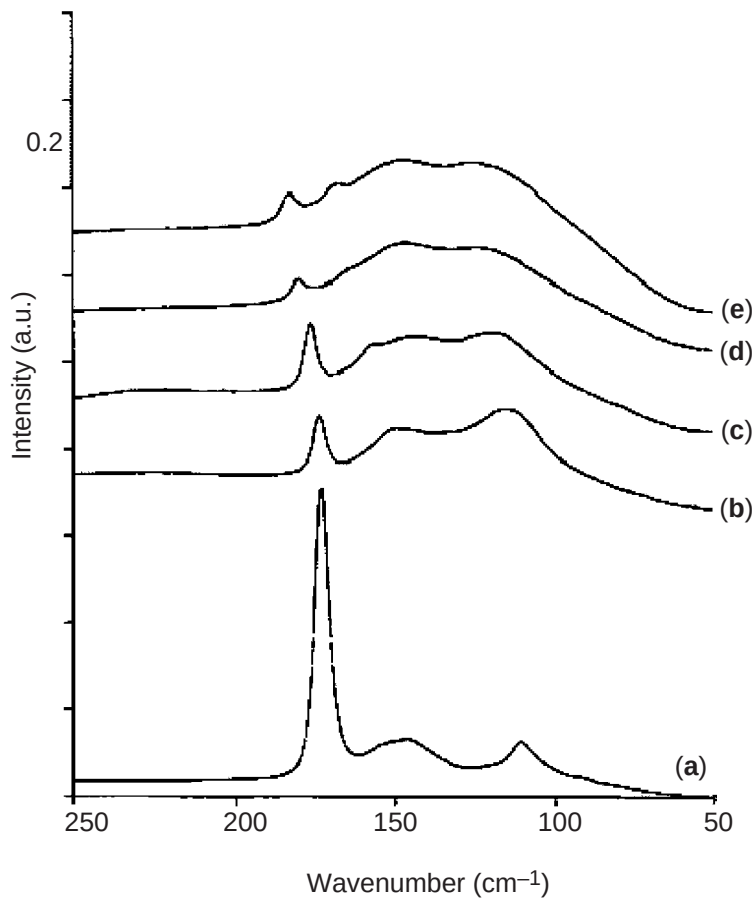

Figure 5 FT-Raman spectra of $[(bztzdtH)I_2]{\cdot}I_2$ in the 250−50 cm^{-1} region at different compression pressures: (a) 12.8, (b) 26.9, (c) 32.2, (d) 46.7 kbar (reproduced by permission of Elsevier from *Spectrochim. Acta*. **2002**, *A58*, 2725–2735).

2.9.3.3 Pressure-induced Disproportionation

Sometimes, solid-state chemistry can be initiated under pressure. One interesting example is the pressure-induced disproportionation of the solid, heterocyclic, thioamide–diiodine adduct $[(bztzdtH)I_2]^{\cdot}I_2$ (bztzdtH = benzothiazole-2-thione).[16] The effect of high pressures (approaching 47 kbar) on the Raman spectrum of this thioamide adduct is shown in Figure 5. The peaks at $\sim$110 cm^{-1} and $\sim$148 cm^{-1} are growing in relative intensity with increasing pressure and are attributed to the presence of the triiodide I_3^- ion being formed by disproportionation of the thioamide–diiodine adduct.

2.9.3.4 Decarbonyldimanganese(0)

Another interesting example is that of the $M_2(CO)_{10}$ complexes, where M = Mn, Re.[17,18] In the solid state, both complexes adopt a staggered D_{4d}-symmetry conformation, at ambient state, with a single M—M bond between the two $M(CO)_5$ fragments. When pressure is applied, there are marked changes occurring in the IR spectra in the ν(CO) region (Figure 6), which have been attributed to rotation about the M—M bond of the two $M(CO)_5$ fragments in the staggered D_{4d} conformation into the eclipsed D_{4h} conformation under pressure.

2.9.3.5 Mercuric(II) Cyanide

Mercuric(II) cyanide, $Hg(CN)_2$, affords an excellent example of a pressure-induced phase transition.[19] The CN stretching modes are detected in the Raman at $\sim$2,200 cm^{-1}. As the pressure is increased, the single band becomes two and eventually becomes a single band again (Figure 7). The pressure dependences of the CN stretching modes are plotted in Figure 8. There is clear evidence of the occurrence of a pressure-induced phase transition.

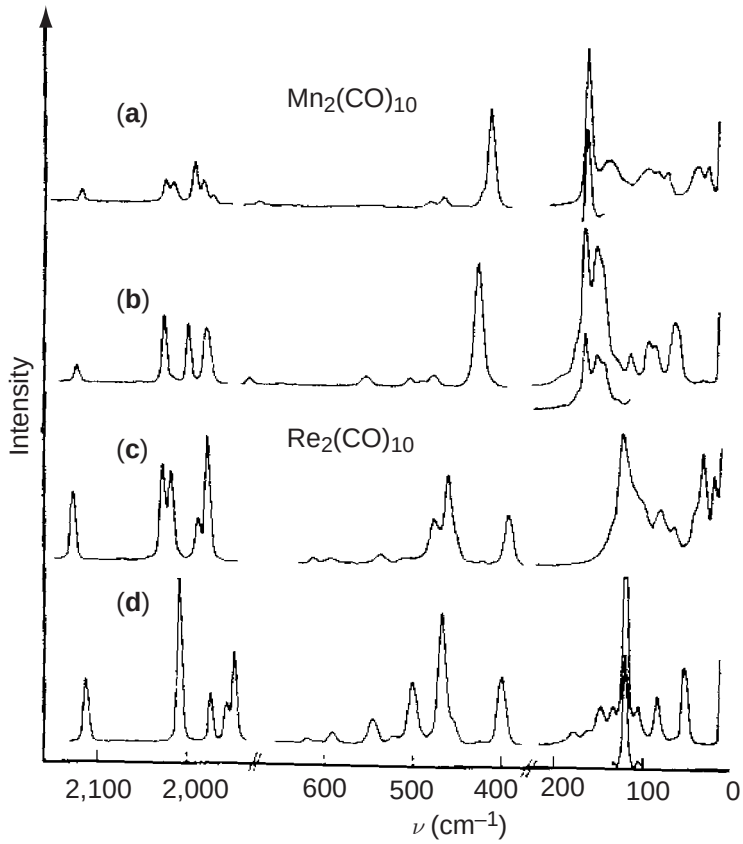

Figure 6 Raman spectrum of $M_2(CO)_{10}$ (M = Mn, Re) at (a) ambient and (b) 16 kbar pressure. (Reprinted with permission from Ref. 19.)

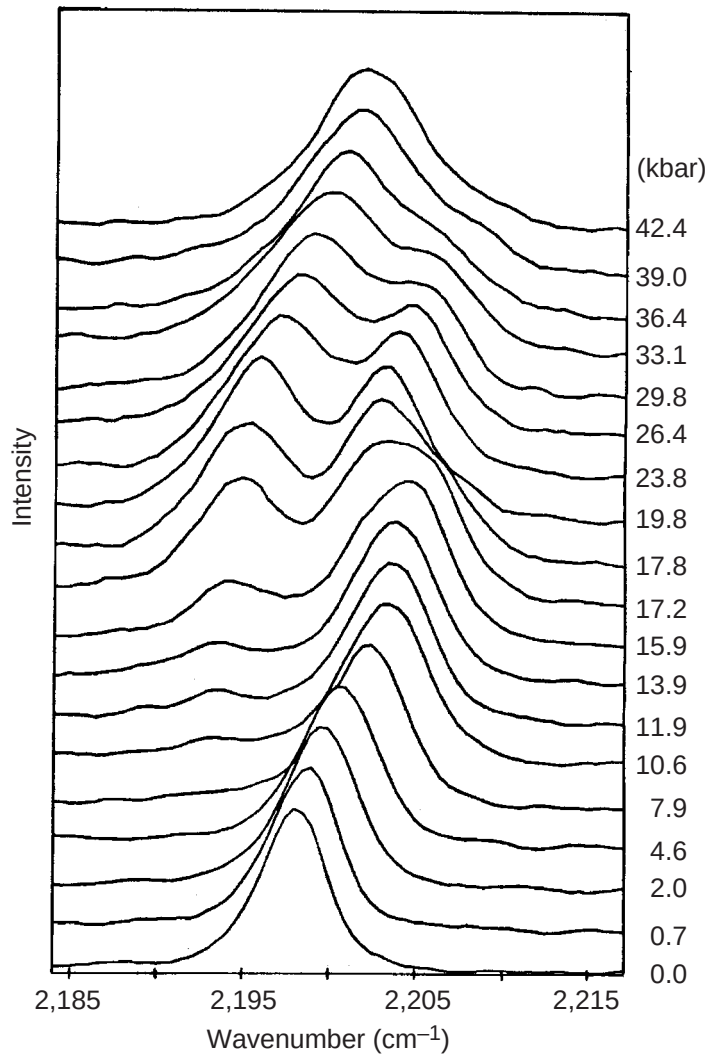

Figure 7 Effect of pressure on the CN stretching modes of $Hg(CN)_2$. (reproduced by permission of The Society for Applied Spectroscopy from *Appl. Spectrosc.* **1987**, *41*, 915–917.)

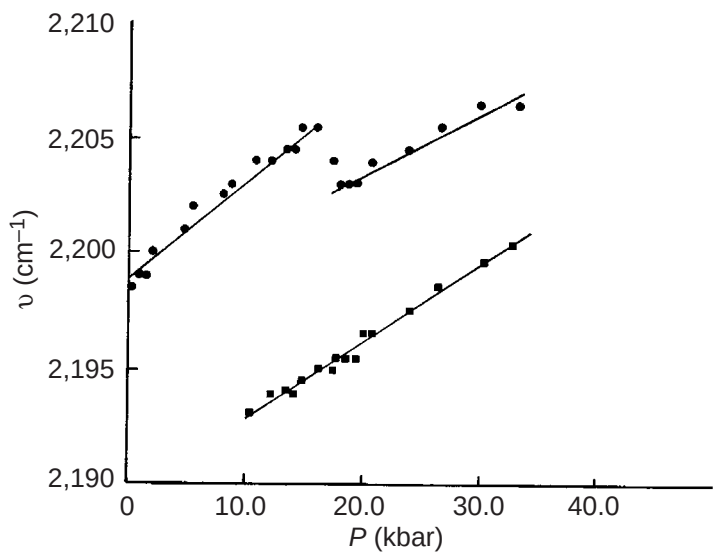

Figure 8 Pressure dependences of the CN stretching modes of $Hg(CN)_2$. (reproduced by permission of The Society for Applied Spectroscopy from *Appl. Spectrosc.* **1987**, *41*, 915–917.)

2.9.4 CONCLUSIONS

In conclusion, it is possible to adapt DACs for both low- and high-temperature studies, as well as for conductivity measurements. Coupled with high-pressure X-ray powder diffraction DAC studies, these instrumental modifications are enabling today's chemists and geochemists to mimic the chemical processes that are thought to occur at great depths in the earth's crust and thus provide a greater understanding of the mysteries of our planet. Apart from the growing amount of pressure-tuning vibrational work that is appearing in the research literature, there is now interest in the effect of pressure on resonance-Raman active species, e.g., $KMnO_4$,[20] and in continued studies of piezochromism in inorganic materials, such as in the pressure-induced conversion of the yellow cobalt dihydride species, $[(PP_3)Co(H)_2]BPh_4$ $[PP_3 = P(C_2H_4)PPh_2)_3]$, into the closely structurally related, red molecular dihydrogen complex, $(PP_3)Co(\eta^2\text{-}H_2)]BPh_4$. This pressure-induced conversion can be conveniently monitored by UV–visible spectroscopy.[21] High-pressure vibrational spectroscopy will continue to attract the attention of scientists, especially following the remarkable discovery that bacteria such as *E. coli* can withstand high pressures in DACs and still retain their biological activity.[22] Such examples of "extreme chemistry" have led some microbiologists to suggest that similar bacteria might survive the high-pressure conditions on other planets.

2.9.5 REFERENCES

1. Grey, J. K.; Butler, I. S. *Coord. Chem. Rev.* **2001**, *219–221*, 713–759 and references therein.
2. Edwards, C. M.; Butler, I. S. *Coord. Chem. Rev.* **2000**, *199*, 1–53 and references therein.
3. Ferraro, J. R.; Nakamoto, K. *Introductory Raman Spectroscopy* **1994**, Academic Press: San Diego, CA.
4. Weir, C. E.; Lippincott, E. R.; Van Valkenburg, A.; Bunting, E. N. *J. Natl. Bur. Stand. Sec.* **1959**, *A63*, 55–62.
5. Bray, K. L.; Drickamer, H. G. *J. Phys. Chem.* **1990**, *94*, 2154–2159.
6. Ferraro, J. R. *Vibrational Spectroscopy at High External Pressures. The Diamond Anvil Cell* **1984**, Academic Press: New York.
7. Klug, D. D.; Whalley, E. *Rev. Sci. Instrum.* **1983**, *54*, 1205–1208.
8. Forman, R. A.; Piermarini, G. J.; Barnett, J. D. *Science* **1972**, *176*, 284.
9. Markwell, R. D.; Butler, I. S. *Can. J. Chem.* **1995**, *73*, 1019–1022.
10. Huang, Y.; Butler, I. S.; Gilson, D. F. R.; Lafleur, D. *Inorg. Chem.* **1991**, *30*, 117–120.
11. Huang, Y.; Butler, I. S.; Gilson, D. F. R. *Inorg. Chem.* **1992**, *31*, 4762–4765.
12. Adams, D. M.; Ekejuiba, I. O. C. *J. Chem. Phys.* **1982**, *77*, 4793–4795.
13. Adams, D. M.; Davey, L. M.; Hatton, P. D.; Shaw, A. C. *J. Mol. Struct.* **1982**, *79*, 415–418.
14. Shaver, A.; Boily, H.; Lebuis, A. *Inorg. Chem.* **1996**, *35*, 6356–6357 and references therein.
15. Song, Y.; Butler, I. S.; Shaver, A. *Spectrochim. Acta* **2002**, *A58*, 2581–2587.
16. dos Santos, J. H. Z.; Butler, I. S.; Daga, V.; Hadjikakou, S.; Hajiliadis, N. *Spectrochim. Acta.* **2002**, *A58*, 2725–2735.
17. Adams, D. M.; Hatton, P. D.; Shaw, A. C.; Tan, T.-K. *J. Chem. Soc., Chem. Comm.* **1981**, 226–227.
18. Adams, D. M.; Hatton, P. D.; Shaw, A. C. *J. Phys. Condens. Matter* **1991**, *3*, 6145–6158.
19. Benham, V.; Lord, G.; Butler, I. S.; Gilson, D. F. R. *Appl. Spectrosc.* **1987**, *41*, 915–917.
20. Gilson, D. F. R. personal communication.
21. Edwards, C. M. Ph.D. Thesis, McGill University, 1998.
22. Sharma, A.; Scott, J. H.; Cody, G. D.; Fogel, M. L.; Hazen, R. M.; Hemley, R. J.; Huntress, W. T. *Science* **2002**, *295*, 1514–1516.

Comprehensive Coordination Chemistry II
ISBN (set): 0-08-0437486
Volume 2, (ISBN 0-08-0443249); pp 113–120

2.10 Resonance Raman: Coordination Compounds

J. R. KINCAID and K. CZARNECKI
Marquette University, Milwaukee, WI, USA

2.10.1 INTRODUCTION 121
2.10.2 THE RESONANCE EFFECT 121
2.10.3 PROBING SPECIFIC MOLECULAR FRAGMENTS 123
2.10.4 RR SPECTROSCOPY OF TRANSIENT SPECIES 125
2.10.4.1 Characterization of Excited States 125
2.10.4.2 Deducing Excited-state Structural Changes 127
2.10.5 REFERENCES 129

2.10.1 INTRODUCTION

The resonance Raman (RR) and time-resolved RR (TR^3) techniques have emerged over the past two decades as superb structural probes of transition-metal complexes in both their ground and electronic excited states, overcoming the low sensitivity of conventional Raman spectroscopy by exploiting the phenomenon whereby the intensities of certain vibrational modes are dramatically enhanced using laser excitation lines in resonance with allowed electronic transitions of the target chromophoric complex. The present work attempts to provide a concise summary of the essential utility of these methods through consideration of several especially illustrative applications; no preference has been given to recent work, the essential goal being to select particularly straightforward examples. Given the enormous impact the RR and TR^3 techniques have had in advancing our understanding of transition-metal polypyridine complexes and their photochemically important excited states, attention is focused on these applications. However, it is expected that this somewhat focused summary will provide an adequate background for appreciating the specific applications of these techniques to various species encountered in other volumes of this work and elsewhere. Finally, the reader is referred to several excellent reviews and monographs which provide comprehensive formal treatments of the theory and fundamentals of the techniques.[1–7]

2.10.2 THE RESONANCE EFFECT

A clear illustration of the resonance enhancement effect is shown in Figure 1 which depicts the spectra acquired for a 0.50×10^{-3} M solution of the familiar tris-phenanthroline (phen) complex of divalent ion plus 0.50 M sulfate ion as a nonenhanced internal standard.[8] The complex possesses an intense metal-to-ligand charge transfer (MLCT) transition, centered near 510 nm. With 647.1 nm excitation, far to the red of the MLCT maximum, the acquired Raman spectrum is dominated by scattering from the sulfate ion, SO_4^{2-}, whose symmetric ν(S—O) mode occurs at

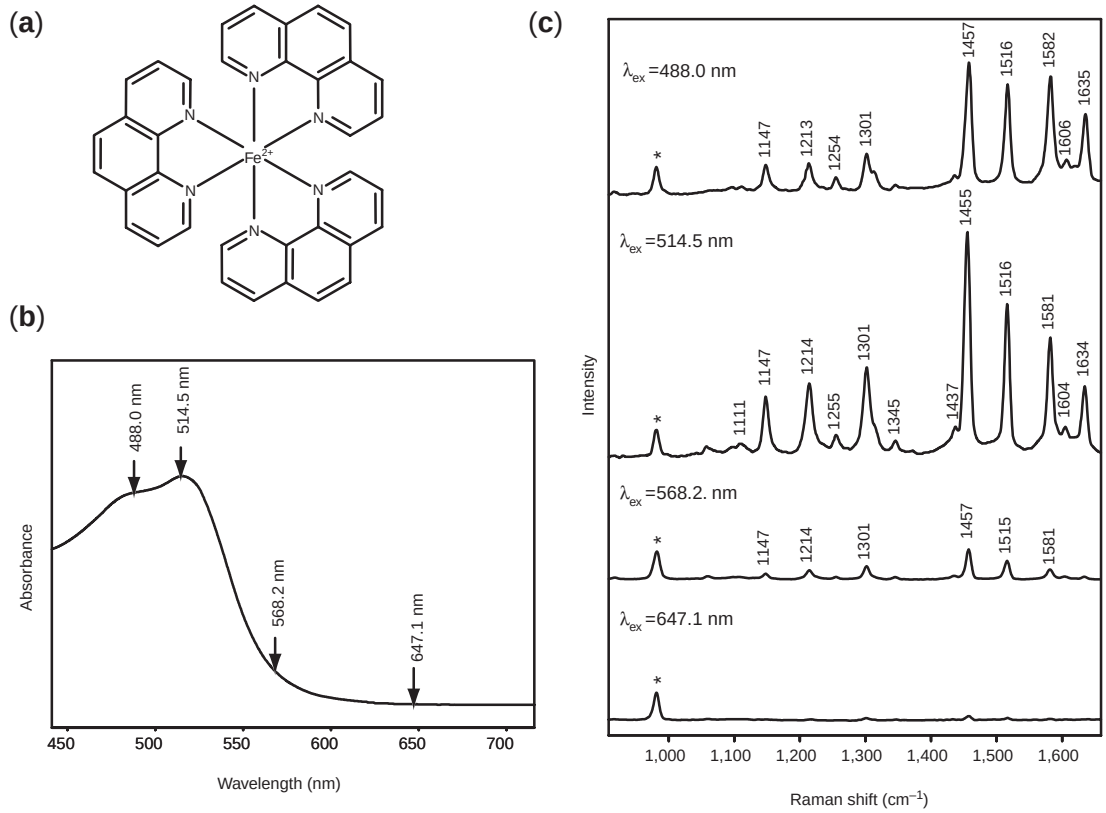

Figure 1 (a) Schematic structure of $Fe^{2+}(phen)_3$; (b) Electronic absorption spectrum of $Fe^{2+}(phen)_3$; arrows indicate laser excitation line wavelengths used for acquiring resonance Raman spectra of $Fe^{2+}(phen)_3$ depicted in part; (c) the asterisk indicates the 981 cm^{-1} reference band of the sulfate ion (adapted from ref. 8).

981 cm^{-1}. Inspection of the spectra acquired with the other three excitation lines clearly demonstrates that, as the energy of the excitation line approaches that of the MLCT maximum of the $Fe(phen)_3^{2+}$ complex, the characteristic modes of the coordinated ligand are dramatically enhanced, relative to that of the internal standard at 981 cm^{-1}; i.e., the modes of the complex dominate the spectrum, even though the concentration of the sulfate is 1,000 times greater than that of the complex.

This beneficial sensitivity improvement afforded by the RR effect carries with it a remarkable selectivity advantage in probing systems with multiple chromophores, because only those modes coupled to a given electronic transition are effectively enhanced.[1–3,5–7] This concept is clearly illustrated by the spectra depicted in Figure 2,[9] acquired for a divalent ruthenium complex bearing two 2,2′-bipyridine (bpy) ligands and one 2,2′-bipyrazine ligand (bpz), i.e., $Ru(bpy)_2(bpz)^{2+}$. Figure 2a depicts the electronic absorption spectrum of the complex, which exhibits two relatively strong bands, one presumably assignable to a Ru-bpy MLCT and the other associated with a bpz-localized MLCT. From comparison of the three RR spectra (Figure 2b), it is immediately obvious that different sets of bands are observed with the 407.6 nm and 476.5 nm excitation lines. In fact, the features observed with the former excitation line, designated ν_i , are characteristic of those of a coordinated bpy ligand, as had been previously documented for $Ru(bpy)_3^{2+}$.[10] Use of the 476.5 nm excitation line, however, reveals an entirely different set of modes, designated ω_i, ascribable to those of a coordinated bpz ligand; i.e., these modes are observable in the RR spectrum of $Ru(bpz)_3^{2+}$. Not surprisingly, the use of an excitation line which falls between the two absorption bands, such as the 441.8 nm line, gives rise to a RR spectrum which exhibits both sets of bands. What is important to note here is the high degree of selectivity provided by variation of the excitation wavelength. Such information permits definitive assignment of the higher-energy band to the Ru-bpy MLCT transition, and that occurring near 485 nm to the Ru-bpz transition. This selective enhancement feature not only aids assignment of a particular electronic absorption band to a given chromophore in a multichromophoric molecule, but also allows one to effectively probe specific fragments of large, multicomponent samples; an

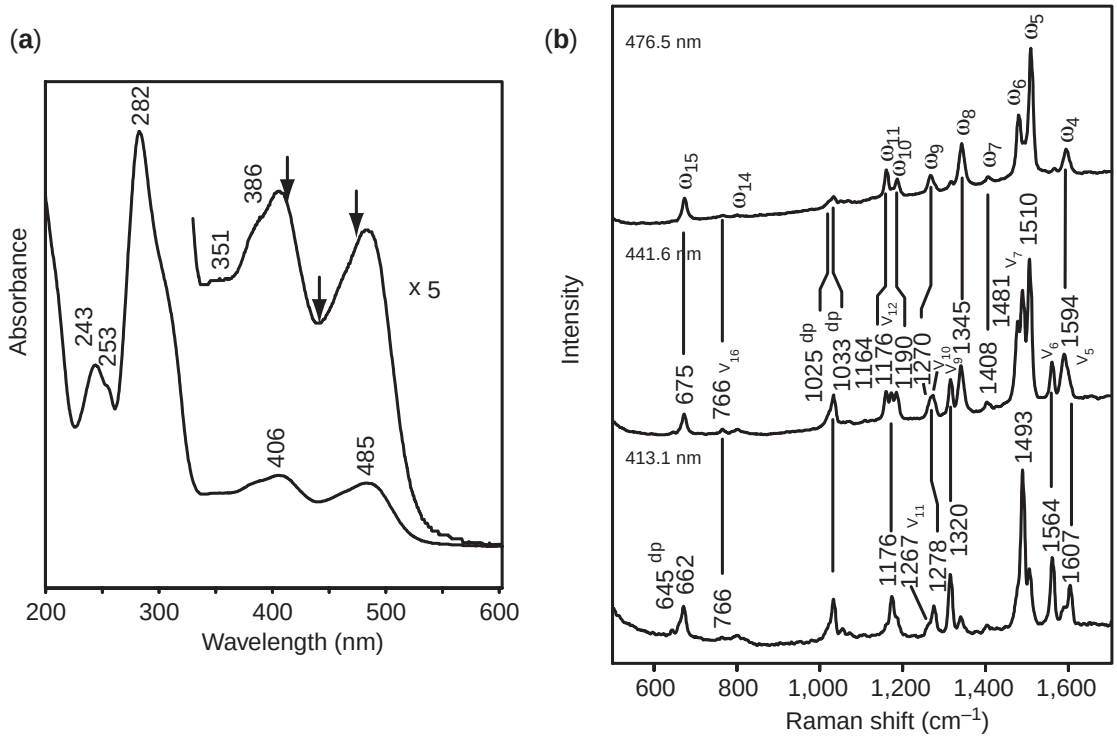

Figure 2 (a) Electronic absorption spectrum of $Ru(bpy)_2bpz^{2+}$ in H_2O; arrows indicate laser excitation line wavelengths used for acquiring resonance Raman spectra of $Ru(bpy)_2bpz^{2+}$ depicted in part (b) (adapted from ref. 9).

advantage which is especially important in biological applications of the RR and TR^3 techniques, as will be seen in a later section.

2.10.3 PROBING SPECIFIC MOLECULAR FRAGMENTS

In many cases it is possible to associate a given RR spectral feature with a specific bond or fragment within a large molecule, permitting one to probe bond strength changes under different conditions. In order to do so, it is imperative that the assignment of a given spectral feature to a particular molecular fragment be firmly established; a task which is readily accomplished, in general, by employing isotopically labeled analogues.

This strategy is effectively illustrated by considering a number of elegant RR studies of the dimeric water oxidation catalyst shown in Figure 3. This is one member of a class of complexes of

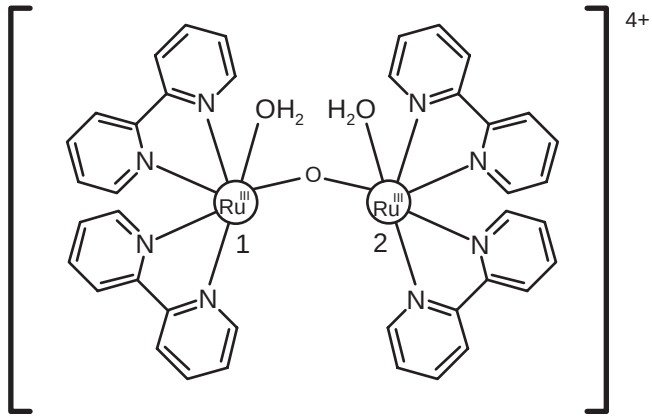

Figure 3 Structure of the water oxidation catalyst $[(bpy)_2H_2ORu^{III}ORu^{III}OH_2(bpy)_2](ClO_4)_4$.

general formula, *cis,cis*-$[L_2Ru(OH_2)]_2O^{n+}$ (where L is 2,2′-bipyridine or other diimine ligand), originally reported by Meyer and co-workers,[11] which are capable of catalyzing the oxidation of water to molecular oxygen. Starting from the $[L_2Ru(OH_2)]_2O^{4+}$ form, which is designated (3,3) to represent the formal oxidation states of the two ruthenium ions, the molecular ion undergoes a series of one-electron oxidations to generate the (5,5) species that is chemically competent to produce molecular oxygen; it is noted, however, that there is extensive delocalization over the Ru—O—Ru fragment, and that designations such as (3,4) do not imply the existence of discrete, valence-localized Ru^{3+} and Ru^{4+} ions. While the details of the reaction mechanism and the nature of various catalytic intermediates are still being debated,[12,13] RR spectroscopy has been exploited to probe the structure of several species encountered during the successive oxidation steps.[14–16]

Considering the RR data illustrated in Figure 4, which presents the spectra of species produced by electrochemical oxidation of a flowing solution of the (3,3) ion at various applied potentials to generate several oxidized intermediates, it is noted that the relatively strong polarized bands appearing at 389 cm^{-1}, 356 cm^{-1}, and 369 cm^{-1} in the species studied exhibit only slight shifts to lower energy (i.e., to 382 cm^{-1}, 356 cm^{-1}, and 364 cm^{-1}, respectively) upon replacement of ^{16}O with ^{18}O in the bridging oxygen atom (by preparing the initial (3,3) ion in $H_2{}^{18}O$), and are attributable to the ν_{sym}(Ru—O—Ru) stretching mode of the Ru—O—Ru fragment. By comparison with corresponding isotopic shift data acquired for other (structurally well-defined) species containing the M—O—M fragment, the magnitudes of these shifts imply a nearly linear Ru—O—Ru fragment in all of the observed intermediates; it is further noted that the results of crystallographic data for the perchlorate salt of the (3,4) ion yield a Ru—O—Ru bond angle of 170°.[15]

The RR spectrum of the most highly oxidized intermediate (bottom trace of Figure 4) reveals a very intense band at 818 cm^{-1}, which has been reasonably attributed to the presence of a Ru═O, ruthenyl, fragment owing to its shift to 780 cm^{-1} in $H_2{}^{18}O$, an assignment that is justified, in part, by acquiring spectra in solutions containing mixtures of both $H_2{}^{16}O$ and $H_2{}^{18}O$. Thus, observation of a large shift upon ^{18}O substitution is also consistent with the possible presence of a peroxo fragment. However, in solutions containing equal parts of $H_2{}^{16}O$ and $H_2{}^{18}O$, a peroxo fragment would produce a band of intermediate frequency (attributable to ^{16}O–^{18}O) in addition to the 818 and 780 cm^{-1} features, an expectation not realized in the cited experiments.

Finally, in the most recently reported work from Hurst's group, the sensitivity of vibrational frequencies to isotopic substitution has been elegantly exploited to conveniently monitor the progress of reactions which are otherwise quite difficult to probe.[16] Thus, as shown in Figure 5, the rates of water exchange in the (3,3) ion are monitored by analysis of the changes observed in

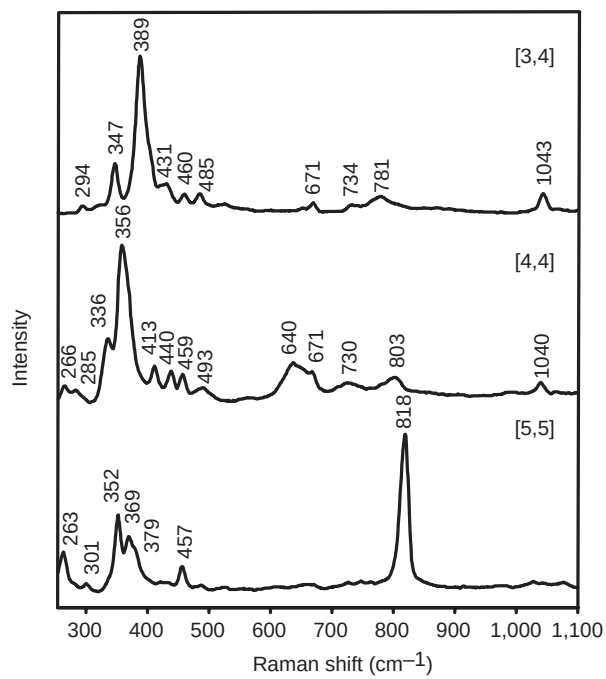

Figure 4 Resonance Raman spectra of the ruthenium dimer in various oxidation states; numbers in parentheses indicate the oxidation states on the ruthenium ions of the dimer (adapted from ref. 13).

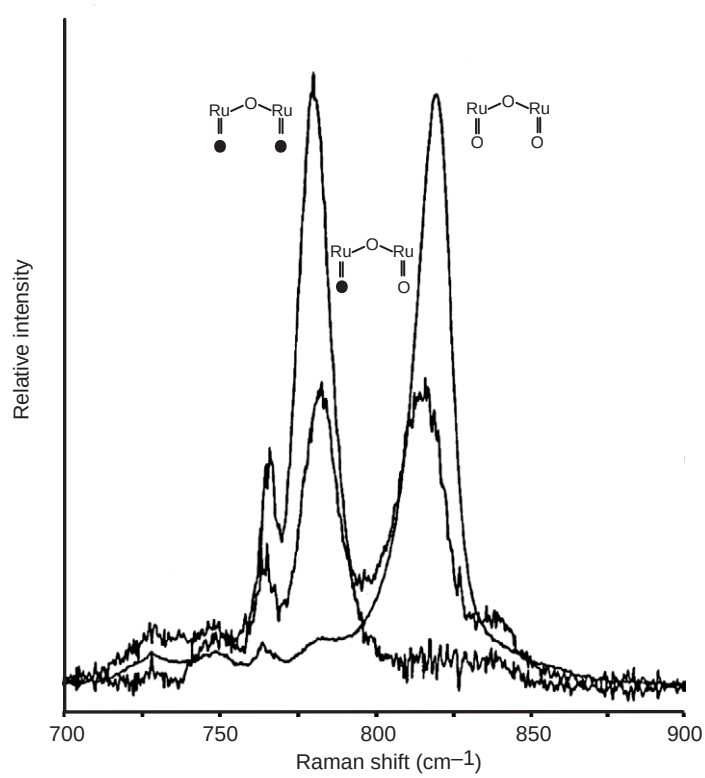

Figure 5 Resonance Raman spectra of the ruthenyl fragments for various O isotopes of $[(bpy)_2(^{X}O)\text{-}Ru^{V}]_2{}^{16}O^{4+}$, where X indicates ^{18}O or ^{16}O atoms (the filled circles in the drawings labeling the spectra indicate the positions of ^{18}O atoms, adapted from ref. 16).

the RR spectra of the (5,5) ion, generated by chemical oxidation of the $[L_2Ru(^{18}OH_2)]_2{}^{16}O^{n+}$ precursor, following incubation in $H_2{}^{16}O$ for various lengths of time. The strong $\nu(Ru{=}{}^{18}O)$ stretch near 780 cm^{-1} diminishes, and is replaced by the strong $\nu(Ru{=}{}^{16}O)$ mode as the incubation time is increased. Analysis of the data for both the (3,3) and the (3,4) precursor complexes revealed that the (3,3), but not the (3,4), ion undergoes the exchange. Such examples clearly illustrate the unique potential of isotopic labeling, in combination with RR and TR^3 methods, to address mechanistic problems.

2.10.4 RR SPECTROSCOPY OF TRANSIENT SPECIES

2.10.4.1 Characterization of Excited States

Recognizing the fact the scattering process occurs on a very short timescale of $\sim 10^{-13}$ s, it becomes evident that short-pulse-width lasers can be used to acquire RR spectra of transient species that can be generated by a photolysis pulse. In favorable cases the species of interest can be "prepared" and interrogated within the same laser pulse, whereas in other situations a short probe pulse is temporally delayed relative to an initial "pump" pulse, the latter protocol properly being called time-resolved resonance Raman or TR^3 spectroscopy.

In one of the first important applications of transient RR spectroscopy to coordination compounds, Dallinger, Woodruff, and co-workers,[17,18] used 10 ns, 355 nm pulses from a Nd:YAG laser to study the ^{3}MLCT state of $Ru(bpy)_3{}^{2+}$, which has a lifetime (at room temperature in aqueous solution) of ~600 ns. The ground state of the complex exhibits relatively weak absorption near 350 nm. However, the high photon fluxes available are sufficient to saturate the irradiated volume in excited state within a few picoseconds, so that scattering occurs from the ^{3}MLCT excited state. Fortuitously, in this case and many others, the ^{3}MLCT state possesses a ligand centered π–π^* absorption band near 350 nm, so that the 355 nm laser wavelength is in resonance with the ^{3}MLCT excited-state species.

The top spectrum in Figure 6[19] is that of the ground state of $Ru(bpy)_3^{2+}$, acquired with the 350.7 nm line from a continuous-wave argon-ion laser; i.e., at this low photon flux there is an insignificant population of the ^{3}MLCT state. Indeed, the observed frequencies are attributable to a 2,2′-bipyridine ligand coordinated to a transition-metal ion.[8–10] The transient RR spectrum shown in Figure 6 (middle trace), is comprised of two sets of features. One set exhibits frequencies that are quite similar to those of the ground state and are reasonably attributed to the two coordinated "neutral" bpy ligands. The other set of features exhibit frequencies and approximate relative intensities that are very similar to those observed in the RR spectrum of a solution of the lithium salt of 2,2′-bipyridine anion radical, the latter spectrum being shown in the bottom trace of Figure 6.

The most reasonable interpretation of the RR spectrum of the ^{3}MLCT of the $Ru(bpy)_3^{2+}$ complex is that it provides direct evidence for localization of excited-state electron density on a single coordinated bpy ligand, rather than for delocalization over all three coordinated ligands; i.e., the proper formulation for the ^{3}MLCT state is $[Ru^{III}(bpy)_2(bpy^{-\bullet})^{2+}]$. The studies reported by Dallinger, Woodruff, and their co-workers,[17,18] summarized above, were important in providing direct experimental evidence for a localized formulation of the ^{3}MLCT state, at least under the conditions investigated (i.e., room temperature in aqueous solution). The debate over whether the initially populated excited state is inherently localized or delocalized continues with results of some recent and elegant experiments being interpreted as evidence for an inherently delocalized initial excited state; the reader is referred to a representative, though not comprehensive, list of more recent articles.[20–23]

The impressive capability of transient RR for probing short-lived excited states led to its widespread use to characterize the nature of the lowest energy ^{3}MLCT states of metal complexes bearing two or more different chelating polypyridine ligands.[9,24–26] The spectra shown in Figure 7, depicting the transient RR spectra of several complexes comprised of both bpy and bpz ligands, clearly illustrate the unique power of the technique. The top trace again shows the RR spectrum of the $Ru(bpy)_3^{2+}$ excited state, while the bottom trace displays that of the corresponding ^{3}MLCT state of $Ru(bpz)_3^{2+\bullet}$. Continuing with the labeling convention introduced earlier, the bpy and bpy^- modes are designated with the symbols ν_i and ν_i', respectively, while the corresponding symbols used for the modes of the coordinated bpz and $bpz^{-\bullet}$ ligands are designated ω_i and ω_i'.

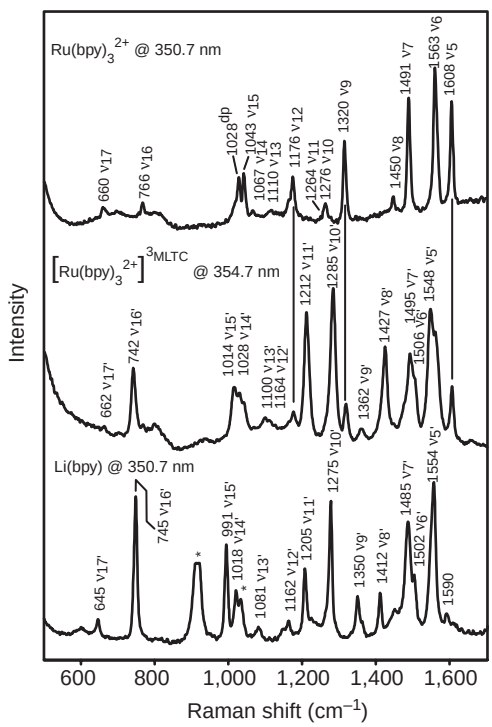

Figure 6 Resonance Raman and time-resolved resonance Raman spectra of the ground and ^{3}MLCT excited states of $Ru(bpy)_3^{2+}$, and the lithium salt of bipyridine anion radical (adapted from ref. 19).

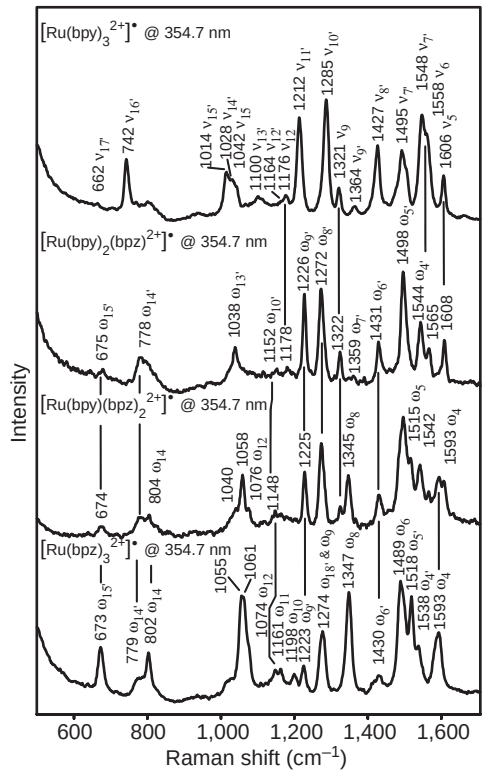

Figure 7 Transient resonance Raman spectra of homoleptic and heteroleptic complexes of ruthenium(II) with bipyridine and bipyrazine (adapted from ref. 9).

Inspection of the spectra shown in the two middle traces of Figure 7, those of the ^{3}MLCT states of $Ru(bpy)_2(bpz)^{2+}$ and $Ru(bpy)(bpz)_2{}^{2+}$, reveals directly the proper formulation of the lowest-energy excited state of each of these two complexes. In the spectrum of the $Ru(bpy)_2(bpz)^{2+}$ complex it is noted that there is no evidence of features that could be attributable to a coordinated $bpy^{-\bullet}$, i.e., those designated as ν_i' in the top trace. In fact, the only "radical-like" features observed in the spectrum of the ^{3}MLCT state of $Ru(bpy)_2(bpz)^{2+}$ are characteristic of those of the bpz^- ligand, i.e., those labeled ω_i' in the bottom trace. Furthermore, it is clear that features characteristic of a coordinated neutral bpz ligand are conspicuously absent, the only "ground-state-like" features present being those of a bpy ligand. Obviously, this is precisely the RR spectrum one would expect for a ^{3}MLCT state with the formulation $[Ru^{III}(bpy)_2(bpz^{-\bullet})]^{2+}$. Similar reasoning can be used to deduce the proper formulation of the ^{3}MLCT of the second heteroleptic complex as $[Ru^{III}(bpy)(bpz)(bpz^{-\bullet})]^{2+}$; i.e., now features are observed which are characteristic of both bpy and bpz "neutral" ligands, along with the $bpz^{-\bullet}$ characteristic modes, and again no modes are observed which are characteristic of a coordinated $bpy^{-\bullet}$. Clearly, the availability of these techniques presents a relatively convenient and direct method for obtaining structural information on otherwise elusive intermediates. An excellent summary of TR^3 applications to a large number of complexes of this type is provided in a review article by Schoonover, Meyer and co-workers.[27]

2.10.4.2 Deducing Excited-state Structural Changes

While transient RR and TR^3 techniques can certainly be used to detect "fingerprints" of various types of molecular fragments in excited states, a higher-level interpretation presents itself when it is recognized that, in favorable cases, relatively reliable relationships exist between vibrational frequencies and bond lengths.[1–3] Again, a particularly straightforward example of such an application of transient RR is provided by a study of $Re_2Cl_8{}^{2-}$ and $Re_2Br_8{}^{2-}$, reported by Woodruff and co-workers.[28] These extensively studied M_2X_8 complexes continue to serve as paradigms of a large class of multiply metal–metal-bonded dimers. Crystallographic analysis of each of these two halide complexes reveals a ground-state symmetry of D_{4h}, with two nearly square-planar ReX_4

units held together in an eclipsed orientation by a quadruple bond, resulting in a short metal–metal bond distance (Figure 8a). The lowest energy excited state in such complexes is the $^1(\delta–\delta^*)$ ($^1A_{2u}$) state, involving promotion of an electron from the δ to the antibonding δ^* orbital, with an associated reduction to a metal–metal bond order of 3. As is seen below, TR^3 spectroscopy provides direct evidence for reduction of metal–metal bond strength in the excited state.

The electronic absorption spectrum of the ground-state $Re_2Br_8^{2-}$ complex, along with the transient absorption spectrum of the corresponding $\delta–\delta^*$ excited state, whose lifetime is approximately 90 ns, are given in Figure 8b. The low-energy (715 nm) absorption band observed in the spectrum of the ground state is assigned to the $\delta–\delta^*$ transition, while those at higher energy, near 400 nm, are associated with $Br^-Re(\delta^*)$ ligand-to-metal charge-transfer (LMCT) transitions. The peaks occurring near 500 nm in the transient absorption spectrum of the $\delta–\delta^*$ excited state are reasonably attributed to (red-shifted) $Br^-Re(\delta^*)$ transitions. To acquire the TR^3 spectrum of the excited state, the 1,064 nm fundamental output from a pulsed Nd:YAG laser was frequency-doubled and -tripled to generate the second (532 nm) and third (355 nm) harmonics. The intense second harmonic was used to pump a dye laser, producing 680 nm excitation pulses, falling within the 715 nm ground-state absorption band, generating the $(\delta–\delta^*)$ excited state within the irradiated volume of the spinning sample. A collinear (503 nm) probe pulse, in resonance with the ~500 nm excited-state absorption band, was generated from the (355 nm) third harmonic by passing the beam through a so-called Raman Shifter—a stainless steel tube with quartz windows filled with H_2 gas which, via stimulated Raman scattering, gives rise to a series of secondary lines shifted to higher and lower frequencies from the primary wavelength by the vibrational frequency of the gaseous H_2 molecules. Given the fact that the lifetime of the excited state is ~90 ns, the probe beam can be temporally delayed relative to the pump beam, in order to facilitate detection of the Raman scattered light without the interference of high background scattering from the intense pump beam; although in this particular case, this problem is partially alleviated by the fact that the monochromator is capable of isolating the (~500 nm) probe beam Raman scattered light from the relatively far-removed (~680 nm) pump-beam scatter.

The useful information directly available from such studies is illustrated in Figure 8c. The top spectrum, showing the RR spectrum of the $Re_2Br_8^{2-}$ ion, obtained with a (low photon flux) CW laser, exhibits features at 275 cm^{-1} and 209 cm^{-1}, attributable to the ground state ν(Re—Re) and ν_{sym}(Re—Br) stretching modes, respectively. In addition to a strong solvent mode observed at 282 cm^{-1} the RR spectrum of the $(\delta–\delta^*)$ excited state, shown in the bottom trace, reveals a

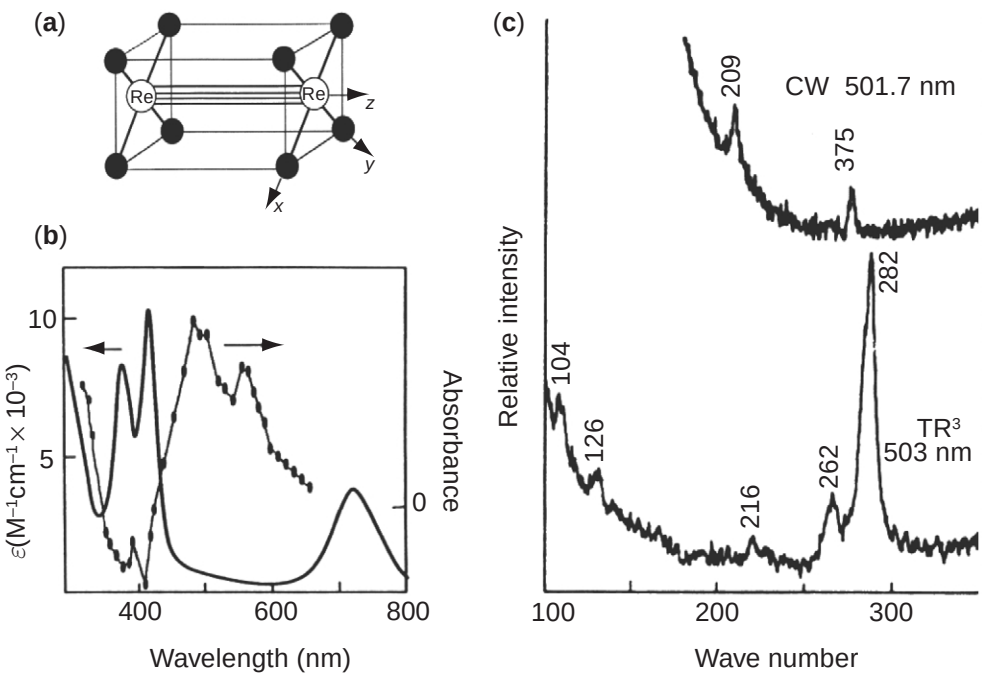

Figure 8 (a) Schematic structure of the $Re_2Br_8^{2-}$ ion; (b) ground-state absorption and transient difference spectra of $Re_2Br_8^{2-}$ in CH_3CN; (c) resonance Raman spectra of the ground (upper trace) and $(\delta–\delta^*)$ -excited states of $Re_2Br_8^{2-}$ (reproduced by permission of the American Chemical Society from *Inorg. Chem.* **1991**, *30*, 1093–1098).

ν(Re—Re) stretching mode at 262 cm^{-1} shifted down by 13 cm^{-1}, relative to its frequency in the ground state; an observation entirely consistent with the expected weakening of this bond in the δ–δ^* excited state. Corresponding experiments conducted for $Re_2Cl_8^{2-}$ reveal a similar lowering of the frequency of the ν(Re—Re) stretching mode (by 12 cm^{-1}) upon formation of the (δ–δ*) excited state. Applying equations relating stretching frequencies to bond lengths,[29] these data imply a lengthening of the Re—Re bond by 0.037 Å in the excited state.

An especially noteworthy aspect of the above study is that the excited-state frequencies observed by TR^3 spectroscopy in fluid solution are significantly higher than those extracted from vibronic analysis of single-crystal absorption spectra; i.e., the TR^3 data indicate a slightly shorter bond length than that deduced from data acquired for the crystal. The authors of the TR^3 work reasonably attribute this difference to the restricted environment of the crystal, arguing that elimination of the δ bond in the (δ–δ*) excited state eliminates the barrier to rotation about the Re—Re axis, permitting relaxation to a staggered orientation of the two square-planar ReX_4^{2-} fragments. To the extent that such relaxation yields a stronger Re—Re bond, the slightly higher frequency of the ν(Re—Re) stretch observed in the solution phase TR^3 measurement, compared with that extracted from the vibronic analysis of the crystal spectra, is expected. The reader is referred to the original work for a more detailed discussion of these issues.[28] However, the important point to be made here is that transient RR and TR^3 methods provide a relatively convenient and effective approach for detailed structural characterization of electronic excited states under chemically relevant conditions.

2.10.5 REFERENCES

1. Nakamoto, K. *Infrared and Raman Spectra of Inorganic and Coordination Compounds: Theory and Applications in Inorganic Chemistry*, 5th ed.; Wiley: New York, 1997.
2. Ferraro, J. R.; Nakamoto, K. *Introductory Raman Spectroscopy*; Academic Press: San Diego, CA, 1994; pp 1–298.
3. Tang, J. J. J.; Albrecht, A. C. Developments in the Theories of Vibrational Raman Intensities. In *Raman Spectroscopy*; Szymanski, H. A., Ed.; Plenum Press: New York, 1970; Vol. 2, pp 33–68.
4. Alden, R. G.; Ondrias, M. R. *Adv. Multi-Photon Processes Spectrosc.* **1990**, *6*, 1–60.
5. McHale, J. L. *Acc. Chem. Res.* **2001**, *34*, 265–272.
6. Myers, A. B. *Adv. Multi-Photon Processes Spectrosc.* **1998**, *11*, 3–50.
7. Lyon, L. A.; Keating, C. D.; Fox, A. P.; Baker, B. E.; He, L.; Nicewarner, S. R.; Mulvaney, S. P.; Natan, M. *J. Anal. Chem.* **1998**, *70*, 341R–361R.
8. Clark, R. J. H.; Turtle, P.; Strommen, D.; Streusand, B.; Kincaid, J. R.; Nakamoto, K. *Inorg. Chem.* **1977**, *16*, 84–89.
9. Danzer, G. D.; Kincaid, J. R. *J. Phys. Chem.* **1990**, *94*, 3976–1380.
10. McClanahan, S. F.; Kincaid, J. R. J. *Raman Spectrosc.* **1984**, *15*, 173–178.
11. Gersten, S. W.; Samuels, G. J.; Meyer, T. J. *J. Am. Chem. Soc.* **1982**, *104*, 4029–4030.
12. Binstead, R. A.; Chronister, C. W.; Ni, J.; Hartshorn, C. M.; Meyer, T. J. J. *Am. Chem. Soc.* **2000**, *122*, 8464–8473.
13. Yamada, H.; Hurst, J. K. *J. Am. Chem. Soc.* **2000**, *122*, 5303–5311.
14. Lei, Y.; Hurst, J. K. *Inorg. Chem.* **1994**, *33*, 4460–4467.
15. Schoonover, J. R.; Ni, J.; Roecker, L.; White, P. S.; Meyer, T. J. *Inorg. Chem.* **1996**, *35*, 5885–5892.
16. Yamada, H.; Koike, T.; Hurst, J. K. *J. Am. Chem. Soc.* **2001**, *123*, 12775–12780.
17. Dallinger, R. F.; Woodruff, W. H. *J. Am. Chem. Soc.* **1979**, *101*, 4391–4393.
18. Bradley, P. G.; Kress, N.; Hornberger, B. A.; Dallinger, R. F.; Woodruff, W. H. *J. Am. Chem. Soc.* **1981**, *103*, 7441–7446.
19. Strommen, D. P.; Mallick, P. K.; Danzer, G. D.; Lumpkin, R. S.; Kincaid, J. R. *J. Phys. Chem.* **1990**, *94*, 1357–1366.
20. Yersin, H.; Donges, D. *Top. Curr. Chem.* **2001**, *214*, 81–186.
21. Breu, J.; Kratzer, C.; Yersin, H. *J. Am. Chem. Soc.* **2000**, *122*, 2548–2555.
22. Yersin, H.; Humbs, W.; Strasser, *J. Coord. Chem. Rev.* **1997**, *159*, 325–358.
23. Damrauer, N. H.; Cerullo, G.; Yeh, A.; Boussie, T. R.; Shank, C. V.; McCusker J. K. *Science* **1997**, *275*, 54–57.
24. McClanahan, S. F.; Dallinger, R. F.; Holler, F. J.; Kincaid, J. R. *J. Am. Chem. Soc.* **1984**, *107*, 4853–4860.
25. Mabrouk, P. A.; Wrighton, M. S. *Inorg. Chem.* **1986**, *25*, 526–531.
26. Chung, Y. C.; Leventis, N.; Wagner, P. J.; Leroi, G. E. *J. Am. Chem. Soc.* **1985**, *107*, 1414–1416.
27. Schoonover, J. R.; Bignozzi, C. A.; Meyer, T. J. *Coord. Chem. Rev.* **1997**, *165*, 239–266.
28. Schoonover, J. R.; Dallinger, R. F.; Killough, P. M.; Sattelberger, A. P.; Woodruff, W. H. *Inorg. Chem.* **1991**, *30*, 1093–1098.
29. Conradson, S. D.; Sattelberger, A. P.; Woodruff, W. H. *J. Am. Chem. Soc.* **1988**, *110*, 1309–1311.

Comprehensive Coordination Chemistry II
ISBN (set): 0-08-0437486
Volume 2, (ISBN 0-08-0443249); pp 121–129

2.11 Resonance Raman: Bioinorganic Applications

J. R. KINCAID and K. CZARNECKI
Marquette University, Milwaukee, WI, USA

2.11.1 INTRODUCTION 131
2.11.2 HEME PROTEINS 131
2.11.2.1 The Origins of Functional Diversity 131
2.11.2.2 Vibrational Modes of the Heme Macrocycle 131
2.11.2.3 Axial Ligand and Heme Substituent Modes 132
2.11.3 RR AND TR^3 STUDIES OF SELECTED HEME PROTEINS 133
2.11.3.1 Myoglobin and Hemoglobin 133
2.11.3.2 Plant Peroxidases 136
2.11.3.3 Cytochromes P450 137
2.11.4 REFERENCES 139

2.11.1 INTRODUCTION

The ability to selectively enhance the modes of the resonant chromophore has fueled the steady development of RR spectroscopy and its transient RR and TR^3 variants as exquisite probes of active site structure and dynamics in a wide range of metalloproteins and enzymes. Inasmuch as this remarkable potential has been more fully realized in the study of heme proteins than for any other class of metalloproteins, it is natural that the illustrative applications presented here be focused on these systems. However, excellent summaries of applications to other metalloproteins and their model compounds are available, including copper proteins,[1–3] iron–sulfur proteins,[4–6] and non-heme oxo–iron clusters.[7–9]

2.11.2 HEME PROTEINS

2.11.2.1 The Origins of Functional Diversity

Proteins containing the protoheme prosthetic group, or closely related structural analogues, are widely distributed in nature and exhibit remarkable functional diversity, as a consequence of the manipulation of inherent reactivity patterns of the heme macrocycle by the associated polypeptides of the different proteins. Thus, the oxygen-storage protein, myoglobin (Mb), possesses an active site comprised of a ferrous protoheme axially coordinated by an imidazole fragment of a proximal histidine residue, with the distal side of the macrocycle consisting mainly of hydrophobic residues with one histidine residue, providing an imidazole hydrogen-bond donor group capable of stabilizing the resultant Fe–O_2 fragment; Figure 1. In contrast, the polypeptides of many electron-transport proteins, such as cytochrome b_5, present two endogenous axial ligands

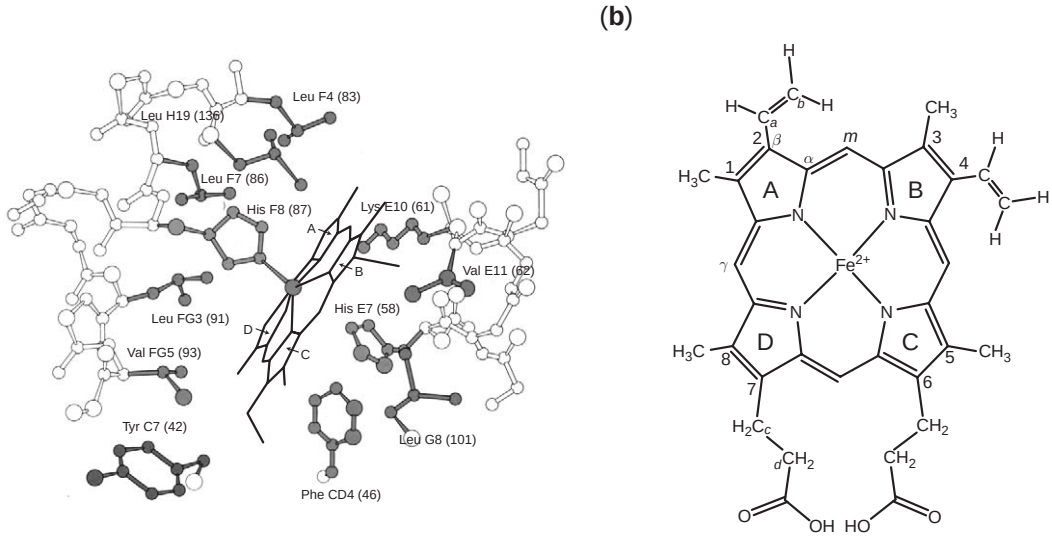

Figure 1 (a) Myoglobin active site (adapted from ref. 10); (b) molecular structure and atom labeling scheme of protoporphyrin IX.

to the protoheme prosthetic group, effectively preventing it from binding exogenous ligands. In addition to differences in the nature and number of axial ligands presented to the heme prosthetic group, its reactivity is sensitively controlled by more subtle variations of the active site environment, as will become apparent in considering several illustrative examples of RR and TR^3 studies of specific heme proteins.

2.11.2.2 Vibrational Modes of the Heme Macrocycle

The ability to extract useful structural information from the rich RR spectral data requires a sound knowledge of the nature of the vibrational modes of the heme macrocycle. This basic interpretational framework was established by studies of structurally well-defined model compounds and their isotopically labeled analogues.[11–13] One of the most useful and extensively studied models is the nickel complex of octaethylporphyrin (NiOEP), whose RR spectra are depicted in Figure 2, along with the electronic absorption spectrum (inset).[12] Employing an excitation line in resonance with the so-called Soret band (or B band), appearing near 400 nm, gives rise to strongly enhanced, totally symmetric modes (A_{1g} assuming D_{4h} symmetry), $\nu_2 - \nu_9$. Use of a line in resonance with the Q_{0-0} band enhances the depolarized modes, B_{1g} ($\nu_{10} - \nu_{18}$) and B_{2g} ($\nu_{27} - \nu_{35}$), while excitation within the Q_{0-1} vibronic side band enhances the A_{2g} modes ($\nu_{19} - \nu_{26}$), which exhibit unusual "anomalous" depolarization ratios of greater than $\frac{3}{4}$. Detailed explanations of this behavior, as well as the precise formulations of the various modes in terms of stretching and bending internal coordinates, are provided elsewhere.[11–15] It is also noted here that a discussion of the specific values of depolarization ratios expected for resonance enhanced modes of different symmetries, using NiOEP as an example, is very clearly presented in an excellent tutorial article.[16]

Many RR studies of heme proteins and heme model compounds have resulted in the identification of so-called marker modes, which are sensitive to spin- or oxidation-state and coordination number of the central iron ion.[17–19] In addition, the frequencies of various marker modes observed for structurally well-defined metalloporphyrins have been shown to vary in a systematic way as a function of the core size of the macrocycle,[14,15] distortions of the macrocycle from planarity,[20] and to oxidation of the macrocycle to form π-cation radicals[19] (species believed to arise in the enzymatic cycles of several oxidative heme enzymes, *vide infra*).

2.11.2.3 Axial Ligand and Heme Substituent Modes

Under certain conditions, internal modes of the various peripheral substituents, as well as those associated with coordinated axial ligands, are also observable in the RR and TR^3 spectra of heme

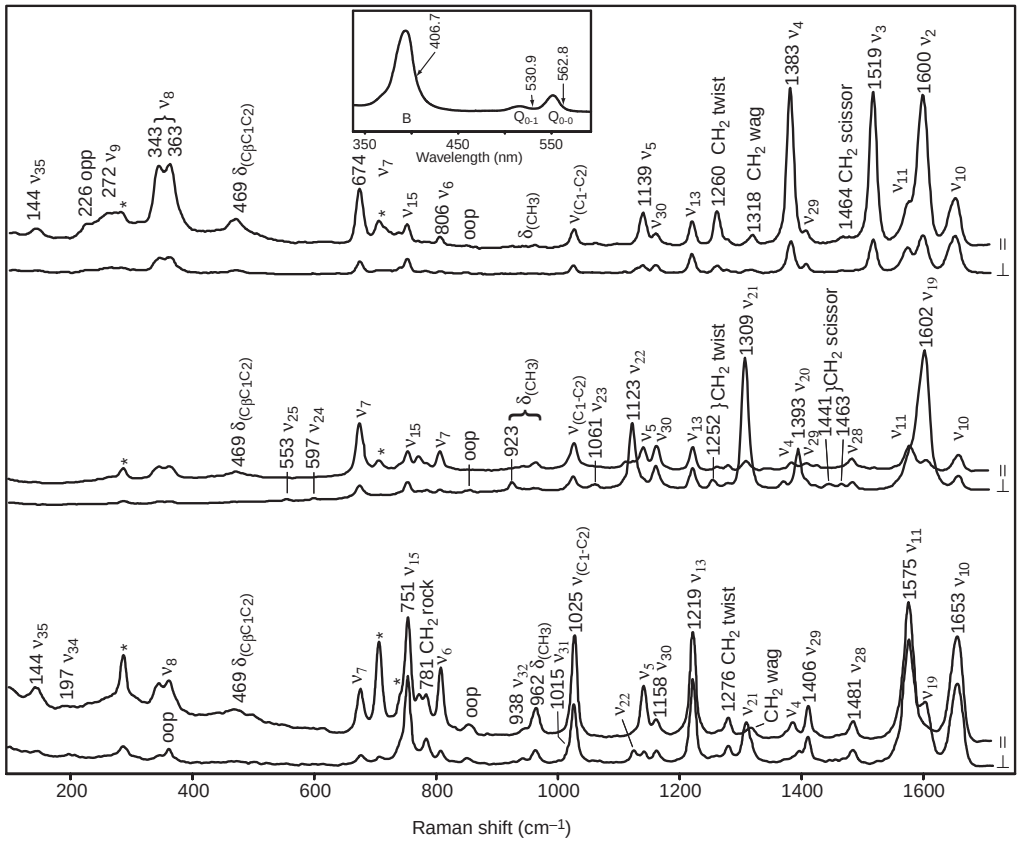

Figure 2 Resonance Raman spectra (|| parallel and ⊥ perpendicular polarization) of NiOEP. Inset depicts the electronic absorption spectrum of NiOEP (adapted from ref. 12).

proteins. For example, unsaturated groups, such as the vinyl substituents of the common protoheme prosthetic group and substituted formyl fragments of the prosthetic groups of cytochrome oxidase, may conjugate with the aromatic macrocycle, leading to enhancement of internal modes of the unsaturated fragments, such as the ν(C=C) vinyl stretching and deformation modes.[14–19,21] In addition to the direct contributions such groups make to the observed RR spectra, their presence lowers the effective symmetry of the heme macrocycle, activating otherwise RR-silent, nontotally symmetric modes, including some of the nominally IR-active E_u modes.[17–19] Modes associated with coordinated axial ligands can be enhanced by resonance with various MLCT or LMCT transitions, or by excitation within the strong Soret π–π^* transition,[22] permitting RR monitoring of the key linkages between the heme prosthetic group and exogenous ligands or the endogenous ligands provided by the associated protein.[23,24]

2.11.3 RR AND TR^3 STUDIES OF SELECTED HEME PROTEINS

2.11.3.1 Myoglobin and Hemoglobin

Hemoglobin, Hb, is the tetrameric oxygen transport protein consisting of two pairs of heme-containing polypeptides, $\alpha_2\beta_2$, each with tertiary and active site structures generally similar to those of myoglobin. However, owing to the existence of two distinct quaternary structures, labeled T and R, characteristic of the unligated and fully ligated forms, respectively, the affinity of the Hb tetramer for exogenous ligands, including O_2, changes dramatically as a function of ligand concentration.[25,26] Thus, binding of a dioxygen ligand to the lower affinity T-state induces changes in the heme structure—including its conversion from a high-spin ferrous form to a species best formulated as a low-spin ferric superoxide adduct—which consequently lead to changes in the surrounding active site polypeptide structure. The accumulation of forces resulting from these active site structural changes eventually, after two or three sites are ligated, triggers a global

structural transition, involving specific intra- and inter-subunit contacts, to the R-state quaternary conformation, wherein the remaining unligated sites possess an increased affinity for an exogenous ligand. Conversely, dissociation of two or three ligands from the fully ligated tetramer induces a corresponding transition to the lower-affinity T-state structure, from which release of the remaining ligands is facilitated. It is through this cooperative ligand binding process that the O_2 transport function of Hb is made so efficient, loading up all four binding sites in a region of high oxygen concentrations—the lungs—while more easily releasing the transported O_2 in regions of low concentrations of dioxygen. The interesting analogy has been made of Hb as a molecular lung, "inhaling" dioxygen in the lungs as it undergoes the T–R transition, while "exhaling" its cargo of dioxygen molecules, via the R–T transition, in the oxygen-poor tissues.[26] As will be seen below, RR and TR^3 spectroscopic techniques have proven to be truly exquisite probes of the structure and dynamics of this fascinating allosteric protein.

The heme group structural alterations associated with oxygenation are clearly reflected in the observed RR spectra shown in Figure 3. The oxidation state marker band, ν_4, shifts from its ferrous-state value of 1,358–1,376 cm^{-1} upon ligation, while shifts of several of the spin-state marker modes, including ν_3 and ν_{10}, are indicative of a high-spin to low-spin conversion. In the low-frequency region, not shown here, the ν(Fe–O) stretching mode of the Fe–O_2 fragment is clearly identified near 570 cm^{-1}, as confirmed by its shift to 548 cm^{-1} upon replacement of $^{16}O_2$ with $^{18}O_2$.[27]

Based on the X-ray crystal structures of deoxy and ligated hemoglobins, Perutz formulated a molecular stereochemical mechanism for hemoglobin, a key tenet of which is a strained linkage between the heme iron and the proximal histidyl imidazole bond in the "tense" T-state.[28] In an effective demonstration of the power of the technique, RR spectral data acquired for deoxy Mb, Hb, and chemical constructs of hemoglobin that exist in either quaternary state provide direct evidence for the suggested changes in this key linkage. Thus, Kitagawa and co-workers[29] employed $^{54/57}$Fe-labeled hemes to show that the ν(Fe–N_{his}) stretching mode occurs at 223 cm^{-1} in deoxy Mb, while the corresponding modes of deoxy Hb are manifested as a rather asymmetric envelope of bands centered near 216 cm^{-1}; Figure 4. Later studies on Mb, employing ^{15}N-labeling, confirmed the essential validity of the assignment and helped to further clarify its precise nature.[30,31] An important and elegant experiment, first reported by Kitagawa and co-workers[32] and later confirmed by others,[33] employed so-called met-hemoglobin hybrids, $(\alpha^{CN}\beta)_2$ and $(\alpha\beta^{CN})_2$,

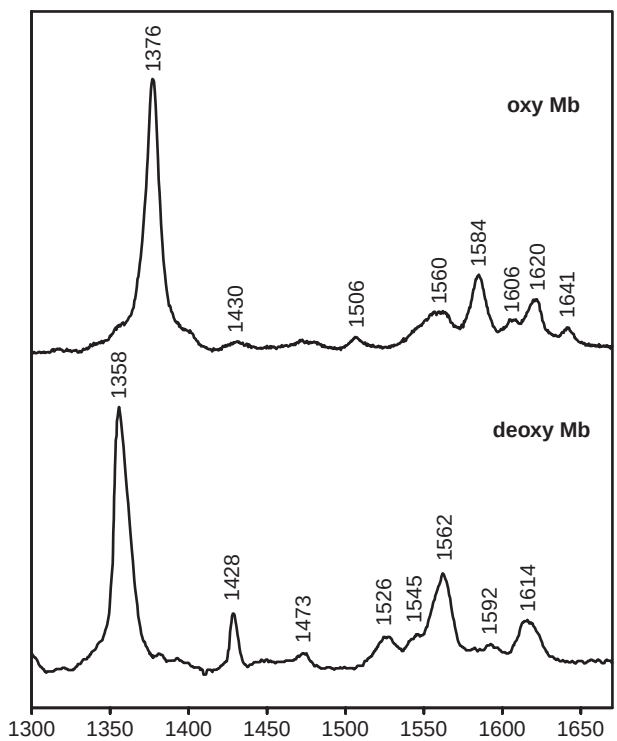

Figure 3 High-frequency resonance Raman spectra of deoxy Mb and oxy Mb.

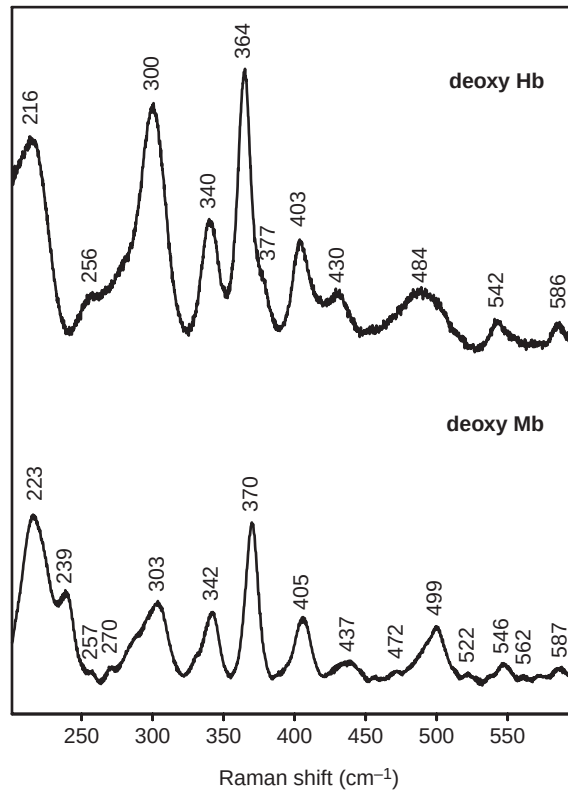

Figure 4 Low-frequency resonance Raman spectra of deoxy Mb and deoxy Hb.

containing low-spin ferric cyanide adducts in only one type of subunit; the hybrids are converted from an "R-like" quaternary state to one closely resembling the T-state upon the addition of allosteric effectors, such as inositol hexaphosphate, IHP. As shown in Figure 5, the RR spectra of such species, acquired with an excitation line that enhances only the ferrous subunits, document a significant shift to a lower frequency for the $\nu(\text{Fe–N}_{\text{his}})$ of the α subunits in the T-state, while a much smaller R/T difference is observed for the β subunits, implying that the hemes of the α subunits of the intact T-state tetramer experience the greater strain in the iron–histidine linkages.

The most attractive approach for characterization of fleeting allosteric intermediates is to exploit the efficient photo-dissociation of CO from the fully ligated adduct, Hb(CO)_4 , to facilitate transient RR and TR^3 studies which permit direct interrogation of the structure of these species. Pioneering studies by Friedman, Rousseau, and others have been concisely summarized in several review articles,[34–37] with the following examples providing convincing illustrations of the remarkable potential of these methods.

With a sufficiently intense laser pulse, all of the bound CO ligands of the Hb(CO)_4 precursor are rapidly photolyzed, with the collected scattered light revealing the RR spectrum of the initial photoproduct, a species possessing deligated hemes trapped in an R-state quaternary conformation.[34] While the high-frequency region of the RR spectra provides evidence for small changes in heme macrocycle structure compared with that of equilibrium deoxy Hb,[38] more substantial changes are seen in the low-frequency region, including a shift of the $\nu(\text{Fe–N}_{\text{his}})$ envelope, which now appears as a nearly symmetric band near $228\,\text{cm}^{-1}$, as can be seen by inspection of Figure 6; i.e., direct evidence for weakening of the Fe–N_{his} linkage in the T-state conformation.[34–37] Subsequent (pump/probe) TR^3 studies document the temporal evolution of this key $\nu(\text{Fe–N}_{\text{his}})$ stretching mode through various intermediates, terminating in a frequency quite similar to that of genuine deoxy Hb as the system relaxes (tens of microseconds) to a "T-like" state; the actual terminal state in this experiment, referred to as T′, is a diligated species, Hb(CO)_2, owing to relatively rapid (~50 ns) geminate recombination of two CO ligands.[39] In a recent comprehensive application of these methods, Jayaraman *et al.* have used visible excitation lines to probe heme prosthetic group structure and ultraviolet lines to monitor the status of key aromatic residues within various intermediates encountered throughout the R to T′ transition.[40]

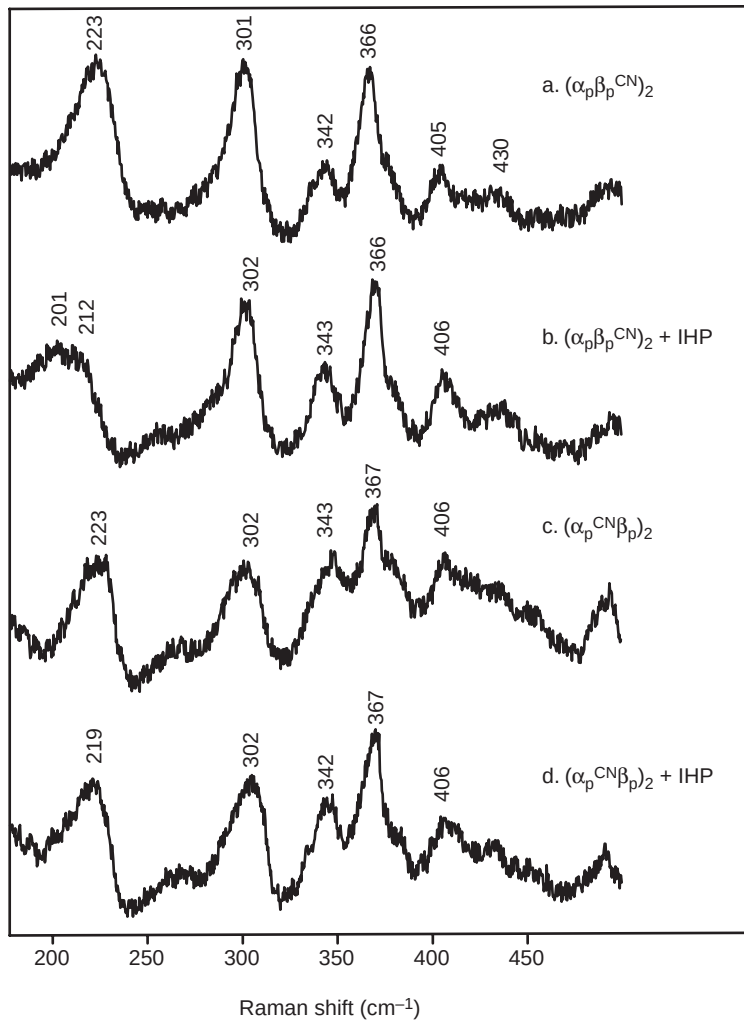

Figure 5 Low frequency resonance Raman spectra of deoxy Hb hybrids (adapted from ref. 33).

2.11.3.2 Plant Peroxidases

An illustration of the utility of RR for characterizing reactive heme enzymatic intermediates is provided by studies of the plant peroxidases, which contain the same protoheme prosthetic group as Mb, as well as a similar histidine axial ligand, but which present an otherwise different active site environment around the heme, dramatically altering its properties.[41,42] Thus, in these peroxidases, which catalyze the oxidation of various substrates via heterolytic cleavage of an initial, very short-lived ferric-hydroperoxo intermediate, the proximal histidyl ligand is strongly H-bonded to nearby acceptor groups, rendering a distinct imidazolate character to the coordinated fragment; while the distal pocket contains more hydrophilic residues than that of Mb, including distal histidine and arginine residues. This active site environment stabilizes the ferric form of the heme in the resting state of the enzyme, and also promotes heterolytic cleavage of the peroxo O—O bond; the basic proximal imidazole ligand stabilizes a resulting oxo-iron(IV), ferryl fragment and the positively charged distal arginine helps to stabilize the developing negative charge on the terminal oxo atom. The immediate product of the heterolytic cleavage, called Compound I, which is two oxidation equivalents above the ferric resting state and is usually formulated as a ferryl heme π-cation radical, O=Fe(protoporphyrin$^+$), undergoes successive one-electron reductions by oxidation of substrates to first form so-called Compound II, a ferryl heme, O=Fe(protoporphyrin), and then to regenerate the ferric resting state.

Resonance Raman spectroscopy has proven itself as an effective probe in revealing the nature of all of these enzymatic species.[19,42,43] The increased donor strength of the H-bonded proximal histidylimidazole is evidenced by the observation of a $\nu(Fe–N_{his})$ stretching frequency of 244 cm^{-1}

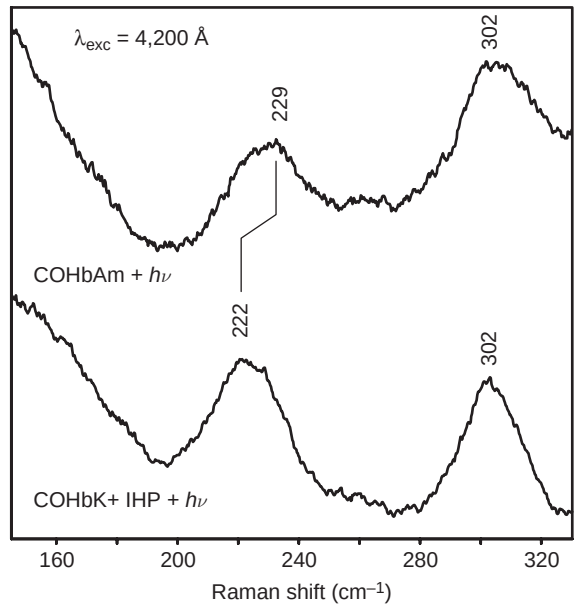

Figure 6 Low-frequency resonance Raman spectra of the transient deoxy Hb species occurring within 10 ns of photo-dissociating of the carboxyhemoglobin (adapted from ref. 37).

in the spectrum of the ferrous form of horseradish peroxidase, HRP, a value significantly higher than that observed for Mb.[44] The first intermediate to be studied by RR was the more stable Compound II, which exhibited marker-mode frequencies consistent with the expected low-spin Fe^{IV} formulation. In addition, direct evidence was obtained for the presence of an Fe=O fragment from the observation of a band at 776 cm^{-1} which shifted to 745 cm^{-1} when $H_2{}^{18}O_2$ was employed, a shift consistent with that expected for the ferryl fragment.[45,46] Problems initially encountered in acquiring the spectrum of Compound I, including its efficient photo-degradation in the laser beam,[19] were eventually overcome by Palaniappan and Terner, who employed excitation near 350 nm, where the modes of this intermediate are selectively enhanced, relative to those of the photo-product, Figure 7.[47] The RR spectra of HRP Compound I, later reproduced by other workers,[48] not only provide direct evidence for the presence of a ferryl fragment (using $H_2{}^{18}O_2$), but also reveal shifts of key marker modes, such as ν_2, ν_3, and ν_4, relative to Compound II, which are consistent with its formulation as a ferryl heme π-cation radical. This latter conclusion is supported by studies of model compounds, such as $Ni(OEP^{+\cdot})$ and others, which exhibit comparable core-mode shifts relative to their neutral parents.[19]

2.11.3.3 Cytochromes P450

Members of this widely distributed class of heme proteins contain the same protoheme prosthetic group common to the systems described above, but are able to efficiently catalyze some of the most difficult reactions known to occur in biological systems; i.e., the hydroxylation or epoxidation of relatively inert hydrocarbon fragments of various substrates, utilizing molecular oxygen as the ultimate source of oxidizing equivalents.[49] The active site environment in all of these enzymes presents an electron-rich cysteine thiolate axial ligand to the heme and a relatively hydrophobic distal side, possessing only a weak H-bond donor, e.g., a threonine hydroxyl group. Binding of substrate to the low-spin ferric resting state generates a higher potential high-spin ferric species, triggering a reduction by an associated redox partner. The resulting high-spin ferrous protoheme binds dioxygen to form an adduct best formulated as a ferric-superoxide complex, which is presumably stabilized by a weak H-bonding interaction with the distal side donor. This is the last intermediate sufficiently stable to be definitively characterized by crystallographic or spectroscopic methods. Delivery of a second electron and a proton apparently facilitates heterolytic cleavage of the putative ferric hydroperoxo species, to generate a remarkably potent hydroxylating intermediate; a reactivity which has earned this species the nickname of "biological blowtorch."[50]

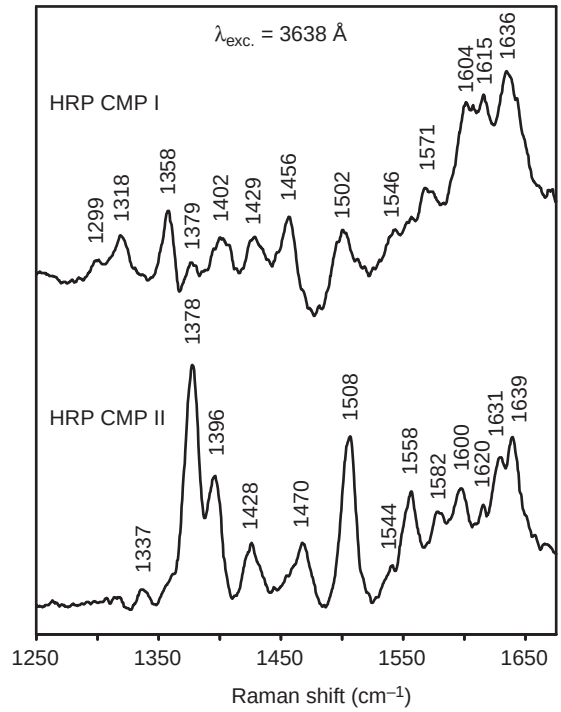

Figure 7 High-frequency resonance Raman spectra of horseradish peroxidase compound I-HRP CMP I and compound II-HRP CMP II (adapted from ref. 47).

It has been only in the 1990s and early 2000s that high-resolution crystal structures have become available for cytochromes P450 and their substrate-bound analogues.[49] Prior to this impressive accomplishment, RR techniques, conducted mainly by Champion and co-workers,[51] were quite valuable in providing definitive structural data for various species involved in these systems.[19,51] Thus, RR studies of the resting state provided direct evidence for its formulation as a low-spin ferriheme, and confirmed its conversion to a high-spin configuration upon binding of substrate, e.g., the ν_3 spin-state marker band shifts to lower frequencies in the substrate-bound form. Evidence for the presence of the electron-rich thiolate axial ligand was provided indirectly by the observation of anomalously low values for the ν_4 oxidation-state marker mode, especially in the ferrous form, where it occurs near 1,346 cm^{-1}, approximately 10 cm^{-1} below its value for histidine-ligated ferroheme proteins. More importantly, direct confirmation of this linkage was provided by an impressive RR study, employing both ^{54}Fe-labeled protoheme and ^{34}S-labeled protein,[24] documenting the existence of a ν(Fe–S) stretching mode in the ferric high-spin, substrate-bound form, which is sensitive to both isotopic labels. In fact, in an elegant study in 2002, Champion and co-workers have used RR spectroscopy to monitor changes in the ν(Fe–S) mode which reflect perturbations in this key Fe–S linkage brought about by interactions with native and modified redox partners.[52]

Early RR studies of the O_2 adduct, also reported by Champion and co-workers,[51] established its proper formulation as a ferriheme-superoxo species by observation of a strongly enhanced $\nu(^{16}O–^{16}O)$ stretching mode occurring at 1,140 cm^{-1} (1,074 cm^{-1} for the corresponding $^{18}O_2$ adduct), a value typical of superoxo complexes. Later studies, reported by the Champion research group[53] and others,[54] identify the ν(Fe–O) stretching mode as a relatively weak $^{16}O/^{18}O$-sensitive band occurring near 540 cm^{-1}, a value also consistent with the suggested ferric superoxo formulation.

Given the impressively demonstrated utility of the RR technique as an exquisite probe of the active site structures of these cytochrome P450 species, it is anticipated that it will play a major role in defining the structure of subsequent intermediates in the enzymatic cycle of this class of proteins. However, for such expectations to be realized, it will be necessary to devise effective strategies to trap these highly reactive species, or to prolong their lifetime to an extent sufficient to permit acquisition of their RR spectra.

2.11.4 REFERENCES

1. Messerschmidt, A. *Struct. Bonding (Berlin)* **1998**, *90*, 37–68.
2. Loehr, T. M.; Sanders-Loehr, J. *Copper Proteins Copper Enzymes*, **1984**, *1*, 115–155.
3. Andrew, C. R.; Sanders-Loehr, J. *Acc. Chem. Res.* **1996**, *29*, 365–372.
4. Staples, C. R.; Duin, E. C.; Lafferty, M. E.; Duderstadt, R. E. *Pure Appl. Chem.* **1998**, *70*, 939–946.
5. Sanders-Loehr, J. *Met. Clusters Proteins: ACS Symp. Ser.* **1987**, *372*, 49–67.
6. Meyer, J.; Moulis, J. M.; Lutz, M. Resonance Raman Spectroscopy of Iron–Sulfur Proteins. In *Frontiers of Bioinorganic Chemistry*; Lecture, International Conference on Bioinorganic Chemistry, Algarve, Portugal, April 15–19, 1985; Xavier, A. V., Ed.; VCH: Weinheim, Germany, 1986, pp 537–546.
7. Arendsen, A. F.; Hadden, J.; Card, G.; McAlpine, A. S.; Bailey, S.; Zaitsev, V.; Duke, E. H. M.; Lindley, P. F.; Kröckel, M.; Trautwein, A. X.; Feiters, M. C.; Charnock, J. M.; Garner, C. D.; Marritt, S. J.; Thomson, A. J.; Kooter, I. M.; Johnson, M. K.; Hagen, W. R. *J. Biol. Inorg. Chem.* **1998**, *3*, 81–95.
8. Solomon, E. I.; Brunold, T. C.; Davis, M. I.; Kemsley, J. N.; Lee, S. K.; Lehnert, N.; Neese, F.; Skulan, A. J.; Yang, Y. S.; Zhou, J. *Chem. Rev.* **2000**, *100*, 235–349.
9. Que, L., Jr. *J. Chem. Educ.* **1985**, *62*, 938–943.
10. Voet, D.; Voet, J. G. *Biochemistry*, 2nd ed.; Wiley: New York, 1995, pp 215–250.
11. Abe, M.; Kitagawa, T.; Kyogoku, Y. *J. Chem. Phys.* **1978**, *69*, 4526–4534.
12. Li, X. Y.; Czernuszewicz, R. S.; Kincaid, J. R.; Stein, P. B.; Spiro, T. G. *J. Phys. Chem.* **1990**, *94*, 47–61.
13. Stoll, L. K.; Zgierski, M. Z.; Kozlowski, P. M. *J. Phys. Chem. A.* **2002**, *106*, 170–175.
14. Spiro, T. G.; Czernuszewicz, R. S.; Li, X. Y. *Coord. Chem. Rev.* **1990**, *100*, 541–571.
15. Czernuszewicz, R. S. Resonance Raman Spectroscopy of Petroporphyrins. In *The Porphyrin Handbook*; Kadish, K. M.; Smith, K. M.; Guillard, R., Eds.; Academic Press: New York, 1999; Vol. 7, pp 292–337.
16. Strommen, D. P. *J. Chem. Educ.* **1992**, *69*, 803–807.
17. Spiro, T. G.; Czernuszewicz, R. S. Resonance Raman spectroscopy of metalloproteins. *Method Enzymol* **1995**, *246*, 416–460.
18. Spiro, T. G.; Czernuszewicz, R. S. Resonance Raman spectroscopy. In *Physical Methods in Bioinorganic Chemistry*; Que, L., Jr., Ed.; University Science Books: Sausalito, CA, 2000, pp 59–119.
19. Kincaid, J. R. Resonance Raman Spectroscopy of Heme Proteins and Model Compounds. In *The Porphyrin Handbook*; Kadish, K. M.; Smith, K. M.; Guillard, R., Eds.; Academic Press: New York, 1999; Vol. 7, pp 225–291.
20. Shelnutt, J. A. Molecular Simulation and Normal-coordinate Structural Analysis of Porphyrins and Heme Proteins. In *The Porphyrin Handbook*; Kadish, K. M.; Smith, K. M.; Guillard, R., Eds.; Academic Press: New York, 1999; Vol. 7, pp 167–224.
21. Kalsbeck, W. A.; Ghosh, A.; Pandey, R. K.; Smith, K. M.; Bocian, D. F. *J. Am. Chem. Soc.* **1995**, *117*, 10959–10968.
22. Kerr, E. A.; Yu, N. T. Vibratonal Modes of Coordinated CO, CN^-, O_2 and NO. In *Biological Applications of Raman Spectroscopy*; Spiro, T. G., Ed.; Wiley: New York, 1988; Vol. 3, pp 39–96.
23. Kitagawa, T. Heme Protein Structure and The Iron–Histidine Stretching Mode. In *Biological Applications of Raman Spectroscopy*; Spiro, T. G., Ed.; Wiley: New York 1988, Vol. 3, pp 97–132.
24. Champion, P. M.; Stallard, B. R.; Wagner, G. C.; Gunsalus, I. C. *J. Am. Chem. Soc.* **1982**, *104*, 5469–5472.
25. Antonini, E.; Rossi, F.; Maria, R. Immobilized Hemoproteins, *Methods Enzymol.* **1976**, *44*, 538–46.
26. Dickerson, R. E.; Geis, I. *Hemoglobin: Structure, Function, Evolution, and Pathology*, Benjamin/Cummings: Menlo Park, CA, 1983.
27. Walters, M. A.; Spiro, T. G. *Biochemistry*. **1982**, *21*, 6989–6995.
28. Perutz, M. F. *Nature* **1970**, *228*, 726–734.
29. Kitagawa, T.; Nagai, K.; Tsubaki, M. *FEBS Lett.* **1979**, *104*, 376–378.
30. Argade, P.; Sassaroli, M.; Rousseau, D. L.; Inubushi, T.; Ikeda-Saito, M.; Lapidot, A. *J. Am. Chem. Soc.* **1984**, *106*, 6593.
31. Wells, A. W.; Sage, J. T.; Morikis, D.; Champion, P. M.; Chiu, M. L.; Sligar, S. G. *J. Am. Chem. Soc.* **1991**, *113*, 9655–9660.
32. Nagai, K.; Kitagawa, T.; Morimoto, H. *J. Mol. Biol.* **1980**, *136*, 271–289.
33. Jeyarajah, S.; Kincaid, J. R. *Biochemistry* **1990**, *29*, 5087–5094.
34. Rousseau, D. L.; Friedman, J. M. Transient and Cryogenic Studies of Photodissociated Hemoglobin and Myoglobin. In *Biological Applications of Raman Spectroscopy*, Spiro, T. G., Ed.; Wiley: New York, 1988, Vol. 3, pp 133–216.
35. Spiro, T. G.; Rodgers, K.; Su, C. *Springer Proc. Phys.* **1992**, *68*, 3–5.
36. Kincaid, J. R. *Methods Enzymol.* **1995**, *246*, 460–501.
37. Friedman, J. M. *Methods Enzymol.* **1994**, *232*, 205–231.
38. Dasgupta, S.; Spiro, Thomas G. *Biochemistry* **1986**, *25*, 5941–5948.
39. Scott, T. W.; Friedman, J. M. *J. Am. Chem. Soc.* **1984**, *106*, 5677–5687.
40. Jayaraman, V.; Rodgers, K. R.; Mukerji, I.; Spiro, T. G. *Science* **1995**, *269*, 1843–1848.
41. Everse, J.; Everse, K. E.; Grisham, M. B., Eds. *Peroxidases in Chemistry and Biology*; CRC Press: Boca Raton, FL, 1990; Vol. 2.
42. Smulevich, G. *Biospectroscopy* **1998**, *4*, *Suppl.*, S3–S17.
43. Kitagawa, T.; Mizutani, Y. *Coord. Chem. Rev.* **1994**, *135/136*, 685.
44. Kitagawa, T.; Hashimoto, S.; Teraoka, J.; Nakamura, S.; Yajima, H.; Hosoya, T. *Biochemistry* **1983**, *22*, 2788–2792.
45. Hashimoto, S.; Tatsuno, Y.; Kitagawa, T. *Proc. Natl. Acad. Sci. USA* **1986**, 83, 2417–2421.
46. Sitter, A. J.; Reczek, C. M.; Terner, J. *J. Biol. Chem.* **1985**, *260*, 7515–7522.
47. Palaniappan, V.; Terner, J. *J. Biol. Chem.* **1989**, *264*, 16046–16053.
48. Kincaid, J. R.; Zheng, Y.; Al-Mustafa, J.; Czarnecki, K. *J. Biol. Chem.* **1996**, *271*, 28805–28811.
49. Ortiz de Montellano, P. R., Ed. *Cytochrome P450: Structure, Mechanism, and Biochemistry*, *2nd ed.*; Plenum: New York, 1995.
50. Schlichting, I.; Berendzen, J.; Chu, K.; Stock, A. M.; Maves, S. A.; Benson, D. E.; Sweet, R. M.; Ringe, D.; Petsko, G. A.; Sligar, S. G. *Science* **2000**, *287*, 1615–1622.

51. Champion, P. M. Cytochrome P450 and the Transform Analysis of Heme Protein Raman Spectra. In *Biological Applications of Raman Spectroscopy*; Spiro, T. G., Ed.; Wiley: New York, 1988, Vol. 3, pp 249–292.
52. Unno, M.; Christian, J. F.; Sjodin, T.; Benson, D. E.; Macdonald, I. D. G.; Sligar, S. G.; Champion, P. M. *J. Biol. Chem.* **2002**, *277*, 2547–2553.
53. Macdonald, I. D. G.; Sligar, S. G.; Christian, J. F.; Unno, M.; Champion, P. M. *J. Am. Chem. Soc.* **1999**, *121*, 376–380.
54. Hu, S.; Schneider, A.; Kincaid, J. R. *J. Am. Chem. Soc.* **1991**, *113*, 4815–4822.

Comprehensive Coordination Chemistry II
ISBN (set): 0-08-0437486

Volume 2, (ISBN 0-08-0443249); pp 131–140

2.12
Gas Phase Coordination Chemistry

M. T. RODGERS
Wayne State University, Detroit, MI, USA
and
P. B. ARMENTROUT
University of Utah, Salt Lake City, UT, USA

2.12.1 INTRODUCTION 141
2.12.2 GROUP 1 142
2.12.2.1 Metal Dependence 142
2.12.2.2 Dipole Alignment Effects 142
2.12.2.3 Ligand Polarizability Effects 143
2.12.2.4 Chelation 143
2.12.2.5 Conformers and Tautomers 143
2.12.2.6 Saturating the First Coordination Sphere 144
2.12.3 GROUPS 2 AND 3 144
2.12.3.1 Comparison to Alkali Metal Ions 144
2.12.3.2 Coordination to Doubly Charged Ions 145
2.12.4 TRANSITION METALS 145
2.12.4.1 Periodic Trends 145
2.12.4.2 Ligand Effects: Sequential Bonds to Fe^+ 146
2.12.4.3 Ligand Effects: Periodic Trends and π-Backbonding 148
2.12.4.4 π-Bonding (C_2H_4 and C_6H_6) 149
2.12.4.5 Anionic Systems 150
2.12.5 THRESHOLD COLLISION-INDUCED DISSOCIATION 150
2.12.5.1 Introduction 150
2.12.5.2 Instrumentation 152
2.12.5.3 Data Analysis 152
2.12.5.4 Collision Gas 153
2.12.5.5 Energy Deposition Distributions 153
2.12.5.6 Kinetic Shifts 153
2.12.5.7 Competitive Shifts 155
2.12.6 REFERENCES 156

2.12.1 INTRODUCTION

Studies of coordination chemistry in the gas phase include spectroscopic and structural characterizations, similar to information gleaned in condensed phase work. Somewhat uniquely, the gas phase also allows the characterization of unsaturated coordination complexes and the measurement of the thermochemistry of metal–ligand bonds. This latter topic will be the focus of the present article. In particular, trends in the thermochemistry will be discussed, including comparisons among the bond dissociation energies (BDEs) for a variety of metals, ligands, and numbers of coordinated ligands. Most of the work discussed here involves the +1 oxidation state of all metals, an unusual oxidation state for many metals in the condensed phase except for

the alkalis and coinage metals. Much less data are available in the gas phase for more highly oxidized metal ions[1–5] and for reduced metals (anions in the gas phase),[6] so these topics are only touched upon here. For more detailed compilations of most of the thermochemistry discussed here, the interested reader is referred to other reviews.[7–10]

2.12.2 GROUP 1

2.12.2.1 Metal Dependence

We start our discussion of metal–ligand bonds by considering the alkali ions, Li^+, Na^+, K^+, Rb^+, and Cs^+. The key trend, illustrated in Figure 1 for water ligands, is that the bond energies for a specific ligand fall from Li^+ to Cs^+. This trend is explained by the relative sizes of the metal ions, which have radii of 0.68 Å, 0.97 Å, 1.33 Å, 1.47 Å, and 1.67 Å, respectively.[11] This determines how close a specific ligand can approach the metal and charge center, thereby controlling the electrostatic interaction with an electron-donating ligand.

For fairly obvious electrostatic reasons, the strength of the metal–ligand interaction increases as the polarizability of the ligand increases, as the size of the ligand dipole increases, and as the number of electrons that the ligand can donate increases. Further, it can be shown that σ-donors, e.g., pyridine (or any of the azines, 6-membered nitrogen heterocycles, c-$C_xH_xN_{6-x}$),[12] bind more strongly than comparable π-donors, e.g., benzene.[13] Indeed, the localized lone pairs of electrons on the nitrogen atoms in the azines bind ions much more tightly than the diffuse π clouds on any of the six-membered rings, even though the π interaction involves 6 electrons rather than just two. A similar conclusion can be drawn for the azoles (5-membered nitrogen heterocycles, c-$C_xH_xN_{5-x}$),[14,15] with a single exception: the σ-donor, 2*H*-1,2,3-triazole, binds more weakly than either benzene or pyrrole, both π-donors.[13–15] In addition, molecules containing a carbonyl group (e.g., ketones, aldehydes, formamides, as well as carbon monoxide itself) also prefer σ interactions over π complexation.[16,17]

More subtle variations in the strengths of the metal–ligand bonds can be attributed to misalignment of the ligand dipole, chelating effects, different conformations, and steric effects. Illustrative examples of these effects are included below, although they cannot be isolated completely.

2.12.2.2 Dipole Alignment Effects

When the ligand has a permanent dipole, the strongest long-range interaction with an ionic metal center is the ion–dipole interaction. This potential has the form, $V(r) = (-\mu e/4\pi\varepsilon_0 r^2)\cos\theta$, where μ is the dipole moment of the ligand, e is the charge on the electron, ε_0 is the vacuum permittivity, r is the distance between the charge and the dipole, and θ is the angle between the dipole and a vector along r. Clearly, the strength of the metal–ligand bond is greatest when the dipole moment is aligned with the metal ion ($\theta = 0°$). In some cases, however, the lone pair of electrons forming the preferred binding site does not lie along the dipole moment of the molecule, such as

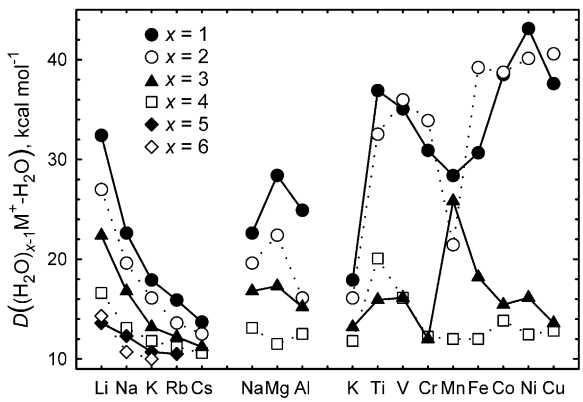

Figure 1 Bond dissociation energies (kcal mol^{-1}) of the first (●), second (○), third (▲), fourth (□), fifth (◆), and sixth (◇) water ligands bound to monovalent metal ions. All values are at 0 K.

in pyrimidine (1,3-c-$C_4H_4N_2$)[12] and 2*H*-1,2,3-triazole (c-$C_2H_3N_3$).[14] Binding at the lone pair of electrons on one of the equivalent nitrogen atoms in either of these molecules leads to substantially weaker binding than comparable molecules such as pyridazine (1,2-c-$C_4H_4N_2$) and 1*H*-1,2,4-triazole systems, respectively, where binding nearly along the dipole is favorable, although other effects are also operative.

2.12.2.3 Ligand Polarizability Effects

Ion-induced dipole interactions, $V(r) = -\alpha e^2/8\pi\varepsilon_0 r^4$, where α is the polarizability of the ligand, also contribute significantly to the overall potential for ligands with a permanent dipole and dominate the interaction for molecules with no dipole. The strength of the ion-induced dipole interactions scale with α, a trend that can be observed for alcohols of differing chain length. The metal ion binding in all these systems occurs primarily with the lone pair of electrons on the oxygen atom. However, as the number of carbon atoms increases, the polarizability increases, leading to enhanced binding.[18,19] Such trends are also evident in an examination of the various azines, where the CH units are more polarizable than N atoms.[12]

2.12.2.4 Chelation

Chelation is clearly one important factor influencing the strength of metal–ligand interactions. One clear-cut example of chelation involves comparisons of monodentate dimethyl ether (dme), bidentate dimethoxyethane (dxe, $CH_3OCH_2CH_2OCH_3$), the tetradentate 12-crown-4 molecule (12c4, c-$(OC_2H_4)_4$), and the hexadentate 18-crown-6 molecule (18c6, c-$(OC_2H_4)_6$).[20–25] Here, the BDEs to these various ligands increase as the number of binding sites increases, namely, as 1:2:4:6; however, the BDEs are *not* directly proportional to these numbers. This disproportionality occurs because the strength of the chelating effect is modified by the strain in the ligand induced by metal ion binding, variations in dipole alignment, and solvation effects. The trends illustrate that when the ligands are independent, the dipole moment of the ligand can align with the metal and the metal–ligand distance can be optimized. However, chelating ligands are constrained and cannot simultaneously optimize bond distance and local dipole orientation. For example, a dxe ligand binds to alkali ions with only about 85% of the bond strength of two dme ligands, and a second dxe ligand binds with about 85% of the bond strength of the third and fourth dme ligands.[25] Likewise, 12c4, which has the same number of heavy atoms and oxygen binding sites as 4 dmes or 2 dxes, binds with about 80% of the strength of 4 dme ligands. These data demonstrate that the macrocyclic effect in the condensed phase is driven by favorable entropic, rather than enthalpic, effects.

Another simple example of chelation is observed for the diazines, c-$C_4H_4N_2$: pyridazine (1,2), pyrimidine (1,3), and pyrazine (1,4). The BDEs of pyrimidine and pyrazine bound to Li^+, Na^+, or K^+ are nearly equivalent, whereas those for pyridazine are higher.[12] This difference indicates that the metal ion interacts strongly with both nitrogen atoms in pyridazine, whereas only one nitrogen is involved in the other two diazines, a conclusion confirmed by theoretical calculations. Further, Li^+ and Na^+ bind pyridazine more strongly than pyrimidine and pyrazine by about $53 \pm 4\%$, whereas the enhancement for K^+ is $90 \pm 4\%$. This result indicates that the larger ion is able to overlap more effectively with both nitrogen lone pairs. Similar observations hold for chelation with 2*H*-tetrazole, c-CH_2N_4, which forms stronger bonds than 2*H*-1,2,3-triazole, c-$C_2H_3N_3$, by 10%, 20%, and 60% for Li^+, Na^+, and K^+, respectively.[14] In this case, the enhancement in the BDE resulting from chelation is partially offset by the decrease in the polarizability of the tetrazole as compared to the 1,2,3-triazole.

2.12.2.5 Conformers and Tautomers

Two tautomeric forms are possible for 1,2,3-triazole (1*H* and 2*H*), 1,2,4-triazole (1*H* and 4*H*), and tetrazole (1*H* and 2*H*) and are distinguished by the position of the N—H bond. In all three cases, the tautomer most stable in the gas phase has a smaller dipole moment than the alternate tautomer, which therefore should form more stable metal–ligand complexes with alkali metal ions. Experimentally, the BDEs measured for Li^+, Na^+, and K^+ bound to these three azoles can

all be assigned to complexes with the most stable gas phase tautomer with no apparent tautomerization occurring upon complex formation or dissociation.[14] This finding can be explained by a large barrier to gas-phase tautomerization.

2.12.2.6 Saturating the First Coordination Sphere

One of the strengths of examining metal ion coordination in the gas phase is the ability to examine individual metal–ligand interactions. However, to relate these data to condensed phase coordination chemistry, it is clearly of interest to examine how BDEs between metal ions and ligands vary as the number of ligands reaches saturation. For the alkali ions, multiple ligation has been examined for water, dimethyl ether, dimethyoxyethane, and carbon monoxide. The results for water are summarized in Figure 1. For all five metal ions, the bond energies are observed to decline as the ligation increases. This simple trend in the relative BDEs is a reflection of the increasing electron density on the metal ion as ligands are added, effectively decreasing the charge on the metal center. Ligand–ligand repulsions also increase as more ligands are packed around the metal center. Steric interactions among the ligands can be seen by comparing BDEs for ligands like water and dimethylether, where the latter shows a more rapid decline with increasing ligand number because of the greater repulsions between the larger ligands.[8] The strength of such ligand–ligand steric interactions is metal dependent and most severe for the smallest ion, Li^+.

Once the inner coordination sphere is saturated, additional ligands can still be added, especially if the ligand–ligand bonds are enhanced by hydrogen bonding. For example, theory[26] indicates that the first solvent shell of Li^+ involves four water molecules occupying equivalent tetrahedral sites with the fifth and sixth water ligands hydrogen-bound to separate pairs of water ligands in the first solvent shell. This geometry rationalizes why the fifth and sixth bond energies are comparable to one another (Figure 1).

2.12.3 GROUPS 2 AND 3

2.12.3.1 Comparison to Alkali Metal Ions

We continue our discussion of metal–ligand bonds by considering the Mg^+ and Al^+ ions, unusual oxidation states for these two metals. However, the valence electron configurations of Na^+ (s^0), Mg^+ (s^1), and Al^+ (s^2) allow a systematic evaluation of how the electronic structure can influence metal–ligand bond energies. As shown in Figure 1 for water ligands, BDEs for the first ligand increase from Na^+ to Mg^+, and from Na^+ to Al^+,[27] even though occupation of the s orbital might have been anticipated to decrease the strength of the interaction. As additional ligands are added, BDEs for Mg^+ and Al^+ decrease more rapidly than for Na^+ such that the BDEs for all three metal ions are comparable for the fourth water ligand. The explanation for these trends involves hybridization of the valence s electrons with unoccupied p orbitals on Mg^+ and Al^+.[28–30] Although there is an energetic cost associated with such hybridization, it allows the electron density to polarize away from the ligand, exposing a higher nuclear charge to the ligand and thereby enhancing the BDE. *sp*-Hybridization is more costly for Al than for Mg, explaining why the enhancement for the former metal is smaller.

As additional ligands coordinate the metal ion, the hybridized valence electron(s) on Mg^+ and Al^+ strongly influence the geometry of the complex. Alkali metal cation complexes have geometries that minimize ligand–ligand repulsion, essentially the ideal structures predicted by the simple valence shell electron pair repulsion (VSEPR) model: 2 ligands are on opposite sides of the metal ion, 3 ligands are trigonal planar, and 4 ligands are tetrahedral.[28] For complexes of Mg^+ and Al^+, the polarized valence electron(s) occupy one of the binding sites. Hence, $Mg^+(H_2O)_2$ and $Al^+(H_2O)_2$ have bent geometries (part of a near-trigonal planar complex) and $Mg^+(H_2O)_3$ and $Al^+(H_2O)_3$ have pyramidal geometries (part of a near-tetrahedral ligand arrangement).[29,30] Thus, ligand–ligand interactions grow more rapidly for Mg^+ and Al^+ such that the BDEs decrease more quickly than for Na^+.

sp-Hybridization is the dominant effect differentiating the metal–ligand BDEs of Mg^+ and Na^+ and yields a relatively uniform enhancement of 30–50% for the first ligand over a substantial range of interactions (BDEs of 7–40 kcal mol^{-1}).[8,31] Thus, as for the alkalis, the bond strengths to Mg^+ increase for polar molecules and for molecules donating more electrons. On the basis of the

results from the water system, this enhancement should decrease upon subsequent ligation. The decrease will be ligand dependent because of differing metal–ligand bond strengths, ligand–ligand repulsions, and steric effects.

2.12.3.2 Coordination to Doubly Charged Ions

Experimental gas-phase studies of the thermochemistry of complexes of multiply charged metal cations have largely focused on the alkaline earths with water as a ligand, $M^{2+}(H_2O)_x$ complexes,[1–5] although some transition metals (TMs) have also been studied.[2] As for the alkali cations, the alkaline earth dications exhibit BDEs to water that decrease monotonically with increasing ligation,[1] as expected for ions with closed-shell electronic configurations. As for the alkali cations, smaller ions bind more tightly than larger ions. Comparisons with theoretical calculations suggest that the first solvent shell is complete for $x = 6$ with Mg^{2+}, Ca^{2+}, and Sr^{2+}, whereas the larger Ba^{2+} may accommodate as many as eight or nine ligands in the first shell.[1] However, experimental evidence exists for higher-energy isomers (but still accessible at temperatures below 200 °C) of $Mg^{2+}(H_2O)_5$ and $Mg^{2+}(H_2O)_6$, likely to be geometries with only four water molecules in the first solvent shell.[4,5]

2.12.4 TRANSITION METALS

2.12.4.1 Periodic Trends

Periodic trends in metal–ligand bonding for the first-row TM monocations are illustrated in Figure 1 for the water ligand.[32–35] Notably, the BDEs of the first and second water ligands are much stronger for the TMs than for the alkali cation of the same row, K^+. Oddly, the second ligand is *more* strongly bound than the first for several TMs, in contrast to expectations from the electrostatic considerations discussed above. For the third and fourth water ligands, the BDEs for many TM ions are comparable to K^+. In addition, there are also some striking variations, such as the $Mn^+(H_2O)_x$ complexes. Although the detailed explanation of these periodic variations involves explicit consideration of the varying electronic configurations of the metal ions,[9,35–39] to first order, these observations can be explained by *sd*-hybridization along with promotion to favorable electronic states for ligand binding.

sd-Hybridization is a more effective way to reduce metal–ligand repulsion than the *sp*-hybridization invoked for Mg^+ and Al^+ because p orbitals are higher lying than the *s* and *d*-orbitals.[28] Both *sp*- and *sd*-hybridization remove electron density from the metal–ligand bonding axis, allowing the ligand to approach the metal more closely and to see a higher effective nuclear charge, and thereby increasing the BDE. This explains why the bonds to TM ions are much stronger than those to K^+. Because of the symmetry of *d*-orbitals, *sd*-hybridization places the electron density in a direction perpendicular to the bonding axis, rather than along the axis in the opposite direction as in *sp*-hybridization. Therefore, a ligand approaching the metal from the opposite side as the first ligand sees the same enhanced electrostatic potential and simultaneously minimizes ligand–ligand interactions. Now, the energetic cost of the *sd*-hybridization is divided between both ligands rather than just one, such that the second metal–ligand BDE can be greater than the first BDE.

Figure 1 shows that the second BDEs of water to the TM ions are much more constant than the BDE of the first water ligand. This indicates that the energetic costs of hybridization have been incorporated largely in the first BDE. Comparison of the BDEs of the second ligand make it clear that the early TM ions bind somewhat less strongly than the late TM ions. This is because the ionic radius of the TM decreases as the nuclear charge increases, a simple electrostatic consideration.

The BDEs of the third and fourth water ligands are much smaller than those of the first two ligands for all TM ions but Mn^+. Increased ligand–ligand repulsion accounts for part of this, but the dominant factor is a loss of the sd-hybridization mechanism. As noted above, the symmetry of the sd hybrid orbitals is effective for only two ligands on opposite sides of the metal, and a third ligand is forced to interact with this hybridized electron density. By the fourth ligand, the BDEs for the TM ions have generally returned to values comparable to those of the alkali and alkaline earth metal ions (Figure 1).

Clearly, the BDEs to Mn^+ do not follow the same trends as the other TM ions. Fundamentally, this is because all valence orbitals are occupied in the ground state of Mn^+ (^7S, $4s^13d^5$), such that *sd*-hybridization cannot remove electron density from the bonding axis. Thus, the first and second BDEs to Mn^+ are very similar to those for Mg^+ a result consistent with both metal, ions having a singly occupied valence *s*-orbital and the utilization of *sp*-hybridization to enhance the bonding. The BDE of the third water ligand to Mn^+ is actually stronger than the second, a unique result among all the metal ions studied thus far. The only conceivable way to increase the bonding is to remove the Pauli repulsion between the incoming ligands and the occupied s orbital of this metal ion. Removal of this repulsion can be achieved by promoting the electronic state of Mn^+ (^7S, $4s^13d^5$) to Mn^+ (^5D, $3d^6$). However, such electronic promotion is sufficiently costly (41 kcal mol^{-1})[40] that it is not energetically favorable until there are three water ligands. Mg^+ has no such low-lying electronic states, such that this type of bond-enhancing mechanism is unavailable.

Such promotions to electronically excited states of different spin are possible for any of the TM ions. When they occur depends upon the degree of ligation and the identity of the ligand and metal.[9] As ligands are placed around the metal, the ligand field splits the degeneracy of the d orbitals. The addition of more ligands increases the strength of the field and the splitting between orbitals. Strong field ligands effect this change with fewer ligands than weak field ligands. Eventually, the difference in orbital energies becomes greater than the stabilization derived from the electron exchange interactions that keep the ion in a high-spin state. By removing electrons from high-lying orbitals with antibonding character and putting them into orbitals with bonding character, the spin state of the complex decreases and the BDE increases. The experimental observation of such changes in BDEs, e.g., in the $Mn^+(H_2O)_3$ and the FeL_4^+ complexes discussed below, serve as a qualitative diagnostic for such spin changes.

2.12.4.2 Ligand Effects: Sequential Bonds to Fe^+

Changes in BDEs as ligands are varied can be examined by looking at results for Fe^+, one of the most comprehensively studied TM ions both in terms of the variety of ligands and the extent of ligation. The trends in the BDEs for several ligands, all of which are nominally 2-electron σ-donors, are shown in Figure 2. In all cases shown, the second ligand is more strongly bound than the first by an average of 7 ± 3 kcal mol^{-1}. The weak BDE of the first ligand can be explained as for the weak $Mn^+(H_2O)$ bond discussed above, namely ground state Fe^+ (^6D, $4s^13d^6$) has an occupied 4*s*-orbital. For some ligands, the potential well evolving from this state of Fe^+ is sufficiently shallow that the ground state of the FeL^+ complex actually corresponds to the Fe^+ (^4F, $3d^7$) excited-state asymptote, lying 5.3 kcal mol^{-1} above the ground state.[40] This state binds more efficiently because it can engage in *sd*-hybridization, as discussed above. With two ligands sharing the cost of this sextet–quartet promotion and 4*s*–3*d*

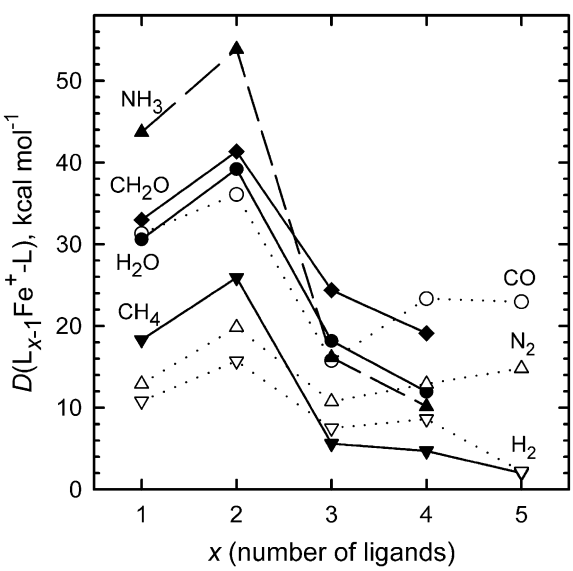

Figure 2 Bond dissociation energies (kcal mol^{-1}) of $L_{x-1}Fe^+-L$, where L = NH_3 (▲), CH_2O (◆), H_2O (●), CH_4 (▼), CO (○), N_2 (△), and H_2 (▽), plotted versus *x*. All values are at 0 K.

hybridization, bis-ligated Fe^+ complexes are generally expected to have quartet ground states with linear L–Fe^+–L geometries. Thus, the BDE of the second ligand is larger than that of the first by approximately the promotion energy of 5.3 kcal mol^{-1}. Differences in the first and second BDEs can deviate from this value depending on ligand–ligand interactions and the interplay between the quartet and sextet surfaces. In contrast to the behavior shown in Figure 2 for Fe^+, complexes with Co^+ and Ni^+ have first and second ligand BDEs that are more similar, for example, the water ligand shown in Figure 1. This is because the ground state electron configurations of Co^+ and Ni^+ are both $3d^n$ configurations such that no spin changes are expected upon complexation. The small differences in BDEs can be attributed to the energetic costs of *sd*-hybridization.

For more extensive ligation, it can be seen that the trends in the iron formaldehyde BDEs are comparable to those for water (Figure 2), which is reasonable because the molecular orbitals of H_2O and CH_2O are similar.[41] The BDEs to formaldehyde are larger than those towater because the dipole moment (2.31 D) and polarizability (2.81 $Å^3$) of CH_2O are larger than those of H_2O (1.84 D and 1.45 $Å^3$).[42] The difference in the CH_2O and H_2O BDEs is greater for the third and fourth ligands, as a result of greater ligand–ligand steric repulsion in the latter case.[43]

Ammonia also shows a similar trend in the sequential BDEs,[44] however, the first two NH_3 BDEs are larger than those for H_2O and CH_2O. This is at first surprising because NH_3 has a smaller dipole moment (1.47 D) than either water or formaldehyde, and a polarizability between the two (2.16 $Å^3$). Theoretical calculations[45] indicate that the magnitude of the ligand dipole moment and its proximity to the TM center must both be considered in quantitatively understanding metal–ligand BDEs. Here, theory finds that the effective position of the NH_3 dipole in a $M^+(NH_3)_x$ complex is 0.48 Å closer to the TM than the effective position of the H_2O dipole in a $M^+(H_2O)_x$ molecule, thereby leading to larger electrostatic interactions. In contrast to the first two NH_3 ligands, the third and fourth NH_3 ligands have weaker bonds than the comparable H_2O complexes (Figure 2). Presumably, this is because there are stronger ligand–ligand interactions in the ammonia complexes as a result of the shorter metal–ligand bond lengths, precisely for the same reason that the first two NH_3 ligands bind strongly.

$Fe^+(CH_4)_x$ complexes also show a similar trend to these other complexes,[46] with decreasing BDEs for $x = 2-5$. Overall, the BDEs are quite weak, as befits a ligand having no lone pair of electrons for donation to the metal ion. Here the relative decrease in the bond energies from $x = 3$ to 4 is not as large as for the other ligands, but the BDEs to methane are already quite weak. Calculations indicate that methane is a weak σ- and π-donor.[46]

Figure 2 also shows that BDEs for $Fe(CO)_x^+$ and $Fe(N_2)_x^+$ have similar trends to one another,[43,47] consistent with the formally isoelectronic character of the CO and N_2 ligands. N_2 has bond strengths averaging only $57 \pm 10\%$ of the carbonyl species, indicating that it is a weaker σ-donor and π-acceptor. Likewise, the trends for the $Fe(H_2)_x^+$ complexes follow the same pattern through $x = 4$.[48] This observation indicates that H_2, like CO and N_2, is a π-accepting ligand.

For all ligands shown in Figure 2, the BDE of the third ligand is substantially weaker than that of the second. As noted above, this results from the loss of sd-hybridization. For the BDE of the fourth ligand, there are interesting variations as a function of the ligand. The π-accepting ligands, CO, N_2, and H_2, have stronger bonds for the fourth ligand compared to the third, whereas the opposite result is exhibited by the π-donating ligands, CH_2O, H_2O, and CH_4, as well as by NH_3, which has no appreciable metal–ligand π interactions. This observation can be rationalized by considering the two fundamental geometries for a four-coordinate system: tetrahedral and square planar.[43] In a tetrahedral geometry, the d-orbitals break into two degenerate groups: the z^2 and x^2-y^2 orbitals are lower in energy with the xy, xz, and yz orbitals higher in energy. For Fe^+ in a quartet state, the electronic configuration would be $(z^2)^2(x^2-y^2)^2(xy)^1(xz)^1(yz)^1$. All three singly occupied orbitals have the right symmetry to act as π-acceptors, thereby favoring π-donating ligands. No obvious energy advantage is gained by putting Fe^+ in a doublet state for a tetrahedral structure. Therefore, π-donating ligands should favor quartet ground states with near-tetrahedral geometries. Because the spin state does not change from the second to the fourth ligand, the additional steric interactions among the ligands should decrease the BDE of the fourth ligand, the trend seen for the alkali cations.

The *d*-orbitals in a square–planar geometry (where the ligands lie in the xy plane) have the xz, yz, and xy orbitals lowest in energy, with the z^2 orbital higher, and the x^2-y^2 orbital very high because it points directly at the ligands. Therefore, in a quartet state, the seven electrons on Fe^+ would have a $(xz)^2(yz)^2(xy)^1(z^2)^1(x^2-y^2)^1$ configuration. The strongly antibonding character of the x^2-y^2 orbital makes it energetically favorable to change to a $(xz)^2(yz)^2(xy)^2(z^2)^1$ configuration having doublet spin. Because the xz, yz, and xy orbitals are π-like and all doubly

occupied, this configuration strongly favors π-accepting ligands, such as CO, N_2, and H_2. Thus, tetracoordinate complexes of these ligands are expected to form low-lying doublet states with square–planar geometries. The change to doublet spin removes electrons from antibonding orbitals, such that the BDE of the fourth ligand can increase compared to the third BDE. These ideas are qualitatively consistent with the results of high level *ab initio* calculations on $Fe(CO)_4^+$,[49] $Fe(H_2)_4^+$,[48] and $Fe(H_2O)_4^+$,[50] although the detailed calculations provide geometries for the FeL_4^+ complexes that are more complicated than the simple ligand field ideas allow. (For $Fe^+(CH_4)_4$, calculations find a square–planar ground state, but the near-tetrahedral geometry is only 0.2 kcal mol^{-1} higher in energy.[46])

2.12.4.3 Ligand Effects: Periodic Trends and π-Backbonding

As noted above, the ability of ligands to interact with metals using π-orbitals can be observed in the sequential BDEs of Fe^+. An examination of the periodic trends in the first-row TM ion–ligand BDEs also reveals the thermodynamic consequences of these interactions. These are shown in Figure 3 for the first bond to several ligands: carbonyl,[47,51–55] ethene,[56] water,[35] ammonia,[44] pyrimidine (pym, 1,2-c-$C_4H_4N_2$),[57] pyridine (pyr, c-C_5H_5N),[58] benzene,[59] and adenine (ade, $C_5H_5N_5$).[60]

We start this discussion with ammonia, a ligand that does not engage in substantial π interactions with the metal. In $M^+(NH_3)_x$ ($x = 1$, 2) complexes, the BDEs for the early-first-row TMs (Ti−Cr) are about 14 kcal mol^{-1} weaker than for the late-first-row TMs (Co−Cu). This 32% difference is largely a result of electrostatics, i.e., the late TM ions are smaller than the early TM ions.[35,45] In $M^+(CO)_x$ complexes, the BDEs for the early-first-row TM ions are also weaker than those for the late metal ions, again by about 14 kcal mol^{-1}, but this is a 60% difference in BDEs. The larger relative enhancement for the carbonyl complexes is attributed to π-backdonation from the doubly occupied orbitals of the late-first-row TM ions, whereas the early TM ions have only singly occupied π orbitals available for π-backdonation.

In $M^+(H_2O)$ complexes, the BDEs of the early- and late-first-row TM ions are more similar, with an increase of only 5 kcal mol^{-1} or about 16%. Water is a weak π-donor such that it prefers empty or singly occupied $d\pi$-orbitals on the metal, thereby the bond strengths of the early TM ions are enhanced compared to those of the late TM ions, which have doubly occupied $d\pi$ orbitals. Here, the decreased π bonding of the early TM ions is largely compensated for by the increased electrostatic contribution to the bonding for the smaller, late TM ions.

Manganese provides an interesting data point for the periodic trends of the BDEs of water, ammonia, and CO. In all cases, the BDEs to Mn^+ are the weakest of the TMs, but the bond to CO is exceptionally weak. As noted above, the polar water and ammonia ligands are able to induce *sp*-hybridization to remove 4s electron density from the ligand binding site, whereas the nonpolar CO molecule cannot do this efficiently. As more ligands are added, the patterns in the

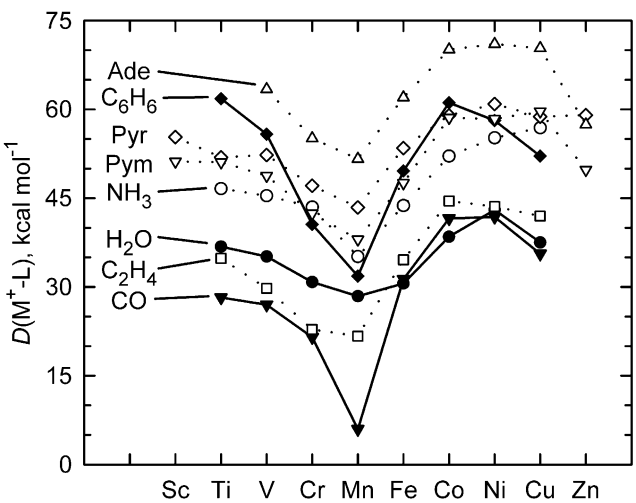

Figure 3 Bond dissociation energies (kcal mol^{-1}) of M^+−L to first row transition metal monocations, where L = adenine (Ade, △), C_6H_6 (◆), pyridine (Pyr, ◇), pyrimidine (Pym, ▽), NH_3 (○), H_2O (●), C_2H_4 (□), and CO (▼). All values are at 0 K.

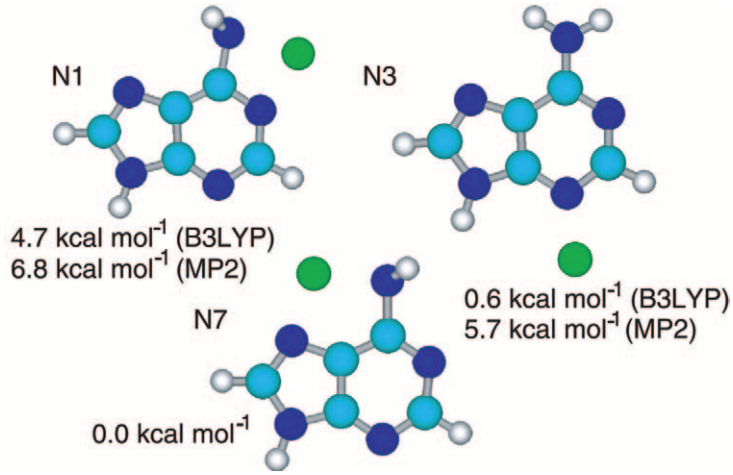

Figure 4 Stable geometries of Cu^+(adenine) complexes bound at the N1, N3, and N7 sites, optimized at the B3LYP/6-31G(d) level of theory. Relative energies of these stable conformers at the B3LYP/6-311+G(2*d*,2*p*) and MP2(full)/6-311+G(2*d*,2*p*) levels of theory are provided.

BDEs differ for each type of ligand. For water, it was suggested above that the BDE of the third ligand was stronger than that of the second because the complex changes spin from a septet state evolving from ground state Mn^+ (^7S, $4s^1 3d^5$) to a quintet state evolving from Mn^+ (^5D, $3d^6$). In contrast, it has been suggested that a comparable spin change occurs for only two CO or NH_3 ligands, which are stronger field ligands than H_2O, thereby leading to the distinct patterns in bonding for these three ligands bound to Mn^+.

The larger ligands included in Figure 3, pyr, pym, and ade, are all nitrogen heterocycles in which the metal ion binds to a nitrogen lone pair in the plane of the ring.[57,58,60] Calculations indicate that interactions with the π-cloud are much weaker. It can be seen that these BDEs largely parallel those of NH_3 across the periodic table. Compared to ammonia, pyridine binds metal ions more strongly because it is more polarizable (9.51 Å^3) and has a bigger dipole (2.2 D). Pyridine is found to be a π-donor comparable to water on the basis of an 18% increase in BDEs for late TM ions compared to early TM ions. BDEs to pyrimidine fall in between those to ammonia and pyridine, consistent with an intermediate polarizability (8.6 Å^3) and similar π-donor capability (22% increase from early to late metal ions). Pyrimidine has a substantial dipole moment, 2.3 D, but it is oriented between the two nitrogen binding sites, and therefore is not as influential as in ammonia or pyridine where the dipole is aligned with the binding site.

The bicyclic adenine ligand forms the strongest bonds with M^+ among the ligands shown in Figure 3. This is partially because adenine has a larger polarizability than the other ligands (13.1 Å^3), but other interesting effects are also operative. Theory on the Cu^+(ade) complex finds two comparable low-energy structures,[60] shown in Figure 4. The lowest-energy structure has the primary binding site as the N7 nitrogen of the five-membered ring, with the bonding enhanced by chelation to the amino group. Another low-lying structure has the metal ion located at N3 with no chelation, and a higher-energy conformer has an N1 binding site augmented by chelation. The relative energies of these different structures can be rationalized by realizing that in the absence of the metal ion, the amino group lies in the plane of the molecule to allow π-resonance delocalization of the lone pair of electrons on the amino group with the aromatic ring system. Thus, the N7 conformer benefits from chelation but not as much as might be expected because of the energy lost by the disruption of the delocalization—about 16 kcal mol^{-1}.[60] Hence, the N7 and N3 structures end up having comparable BDEs. The same loss of delocalization affects the N1 conformer, but here the chelation is not as effective because of the angle of the chelating sites. Specifically, as discussed above, *sd*-hybridization favors chelating sites at angles close to 180°. Therefore, chelation at the N7 site where the N–Cu^+–N angle is 102° is much more favorable than at the N1 site where the angle is smaller at 73°.

2.12.4.4 π-Bonding (C_2H_4 and C_6H_6)

The BDEs of ethene are similar to those of CO across the periodic table (Figure 3) as might be expected for ligands that are both π-acceptors. Consistent with this assignment is the observation that the early TM ions have BDEs with ethene that are about 53% weaker than the late TMs,

comparable to the 60% difference seen for CO. In most cases, the ethene BDEs are slightly greater than those for CO, a result that can be attributed to the larger polarizability of C_2H_4 (4.10 Å^3) compared to CO (1.94 Å^3).[42]

Benzene shows a different periodic trend in its bonding to the first-row TM ions[59] (Figure 3). The bonds to benzene are fairly strong because benzene is a 6-electron donor compared to the other ligands, which are 2-electron donors except for the chelating adenine. Theory finds that the metal–ligand bonds are primarily electrostatic augmented by additional metal π-backdonation.[61,62] The complexes have C_{6v} symmetry and the 3*d*-orbitals split into $3de_2(\delta) < 3da_1(\sigma) < 3de_1(\pi)$ molecular orbitals. The $3de_1(\pi)$ orbitals are antibonding and become progressively occupied across the sequence of Ti^+ to V^+ to Cr^+ (with 3–5 *d* electrons) and of Co^+ to Ni^+ to Cu^+ (with 8–10 *d* electrons). This explains the strong decrease in BDEs observed for the first BDE to benzene compared with the other ligands. To rationalize why the BDE for Fe^+ is greater than that for Cr^+, the $Fe^+(C_6H_6)$ complex is suggested to have a quartet ground state ($\delta^4\sigma^1\pi^2$), such that there are two additional electrons in the bonding $3de_2(\delta)$ molecular orbitals compared with $Cr^+(C_6H_6)$, ($\delta^2\sigma^1\pi^2$). $Mn^+(C_6H_6)$ has a weak bond because of the occupied 4*s*-orbital on Mn^+.

As discussed elsewhere,[8,59] BDEs for a second benzene ligand show a completely different pattern compared to the other ligands. For example, the $(C_6H_6)Fe^+-(C_6H_6)$ BDE is weaker than the $Fe^+-(C_6H_6)$ BDE, in striking contrast to the trends of Figure 2. These results are understood by appealing to the 18-electron rule and presuming that two benzenes form a sufficiently strong ligand field that all $M^+(C_6H_6)_2$ complexes have low spin. This assignment is confirmed by other experiments for the Ti^+, V^+, and Cr^+ complexes, which are 15, 16, and 17 electron complexes, respectively, with doublet, singlet, and doublet ground states, respectively.[63–65] Thus, the bis-benzene complexes reach an 18-electron configuration at $Mn^+(C_6H_6)_2$, which has a singlet $\delta^4\sigma^2$ configuration. The sum of the BDEs for this complex combined with the promotion energy necessary to place atomic Mn^+ in its singlet state[59] are greater than comparable quantities for any of the other bis-benzene complexes, a result of the closed-shell 18-electron character of the complex. Indeed, this sum is about twice those calculated for the complexes of Co^+, Ni^+, and Cu^+. In these complexes, 2, 3, and 4 electrons, respectively, must occupy the antibonding $3de_1(\pi)$ orbitals, thereby decreasing the BDEs. Alternatively, the ligands can reduce the number of electrons donated (thereby staying 18-electron complexes) by slipping from the normal η^6-bonding mode to η^4 or η^2. This also leads to a decrease in the BDE.

2.12.4.5 Anionic Systems

Gas-phase studies of ligand coordination to anionic metals are much less extensive than for cationic complexes. One comprehensive study was conducted by Sunderlin, Wang, and Squires who examined the anionic TM carbonyl complexes for V, Cr, Mn, Fe, Co, and Ni.[6] BDEs for sequential addition of CO to M^- were measured using threshold collision-induced dissociation (TCID) methods described below. Comparison of TM carbonyl BDEs among isoelectronic species showed that the ordering was usually $D[(CO)_xM^--CO] > D[(CO)_xM-CO] > D[(CO)_xM^+-CO]$, a trend easily rationalized on the basis of π-backdonation. Cases where a different order was observed could be understood as metals having different electronic states, e.g., Ni^+ ($3d^9$, ^2D) vs. Fe^- ($4s^23d^7$, ^4F).

2.12.5 THRESHOLD COLLISION-INDUCED DISSOCIATION

Gas-phase metal–ligand bond energies can be measured by a variety of experimental techniques. Measurements of absolute values can be made by temperature-dependent equilibrium methods,[1,2,16,46,48,66–69] blackbody infrared radiative dissociation (BIRD),[2–5,70–72] radiative association,[73–75] and the TCID method discussed in detail here. Measurements of relative thermochemistry can be accomplished using equilibrium methods,[76,77] the kinetic method,[78–81] and competitive CID[82] (see Section 2.12.5.7). This review cannot include the details of all such measurements.

2.12.5.1 Introduction

Collision-induced dissociation (CID) as employed by mass spectrometrists is a powerful tool for structural elucidation.[83] Although the possibility that the energy onset of CID could be a

useful means of ascertaining thermodynamic information was recognized early on, the ability to determine accurate thermochemistry is a recent development dating back to the early 1980s. Extensive refinements allowing applications to larger molecules have been developed only since the early 1990s. TCID emerges from a simple concept involving the study of the reaction of a metal–ligand complex with a collision gas (Equation1) as a function of the kinetic energy available to the reactants.

$$ML_x^+ + Rg \rightarrow ML_{x-1}^+ + L + Rg \quad (1)$$

Although Equation (1) refers to a cationic coordination complex, the concept also holds for anionic reactions. Neutrals could also be studied in this fashion, but the ease with which ions are accelerated to energies capable of breaking chemical bonds makes them the systems of choice for TCID work. Here we identify the collision partner as a rare gas atom (Rg), a choice discussed further below, but any species (including a surface) can be used. A broad range of metals, ligands, extent of coordination, and bond energy magnitudes (2–100 kcal mol^{-1}) have been studied using TCID experiments as illustrated in the remainder of this section. The type of TCID experiment now being performed routinely is illustrated in Figure 5 for copper bis-acetone cations colliding with Xe.[84] This shows the reaction cross-section as a function of energy in the center-of-mass frame, the energy available to induce chemical processes. The reaction cross-section, σ, describes the probability that an ion and a neutral collide and proceed to products. Cross-sections can be converted to rate constants simply by multiplying by the relative velocity of the reactants, v, such that $k(E) = \sigma v$, which can then be averaged over a Maxwell–Boltzmann distribution to give $k(T)$. Thus, a cross-section is a microscopic reaction probability directly related to the rate constant for reaction at a specific kinetic energy. In Figure 5, it can be seen that collisions of $Cu^+(acetone)_2$ with Xe yield no products at low energies, below those needed to cleave the metal–ligand bond. As the energy is increased, intact acetone molecules are lost from the complex progressively to form Cu^+(acetone) and Cu^+, with more extensive decomposition occurring at higher energies. In competition with these simple CID processes are ligand exchange reactions that form $XeCu^+(acetone)_x$, $x = 0$ and 1.

By measuring the threshold for a CID process, the BDE between ML_{x-1}^+ and L can be measured, subject to several constraints. One of these is another key reason to use ions in TCID studies: the long-range attractive forces between a charged species and the ligand generally overcome barriers to dissociation typically observed in neutral systems. For coordination complexes, it is also useful to note that the bonds are generally cleaved heterolytically, i.e., with

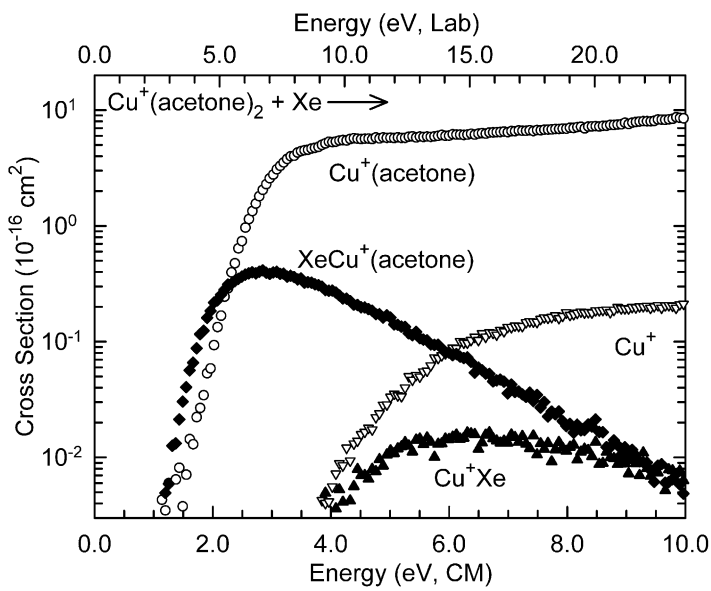

Figure 5 Cross-sections for collision-induced dissociation of $Cu^+(acetone)_2$ with Xe as a function of kinetic energy in the center-of-mass frame (lower x-axis) and the laboratory frame (upper x-axis). Primary and secondary product CID cross-sections are shown as ○ and ▽, respectively. Primary and secondary ligand exchange product cross-sections are shown as ◆ and ▲, respectively.

different numbers of the bonding electrons attached to the two fragments. For such dissociations, qualitative quantum mechanical arguments show that there are no barriers in excess of the BDE along the potential energy surface.[85]

2.12.5.2 Instrumentation

To measure the threshold for a CID reaction, the reactant ion must be isolated and accelerated to a specific kinetic energy, undergo a collision, and the resulting products analyzed. Such studies are carried out using tandem mass spectrometers such as a guided ion beam tandem mass spectrometer (GIBMS), an instrument designed expressly for TCID studies.[86–90] In our laboratories, this instrument utilizes a versatile source region that is capable of generating a wide variety of ions and thermalizing them so that their internal energies are known. The latter characteristic is vital to threshold studies as the energy available for dissociation must be fully characterized. An initial mass analysis device follows to select particular ions for interaction with neutral reagents in a collision cell. The use of an rf trapping field in this interaction region provides several benefits, as outlined elsewhere.[91,92] Chief among these is the ability to efficiently collect product ions and to carefully define the kinetic energy of the ions. Product ions are identified using a second mass analyzer followed by a sensitive ion detector. Thus, the raw data of a reaction threshold measurement are reactant and product ion intensities as a function of the ion kinetic energy. These are converted to cross-sections as a function of the energy in the center-of-mass frame, like the data shown in Figure 5, as detailed elsewhere.[86,91]

Other types of tandem mass spectrometers can also be used for such experiments, e.g., commercial triple quadrupoles (QQQ) have been used occasionally, but such instruments are not designed specifically for threshold studies. The disadvantages of such instrumentation include perturbations of the ion kinetic energy induced by the quadrupole field and an ill-defined collision region.[91] Likewise, ion cyclotron resonance (ICR) mass spectrometers[93–96] and, conceivably, ion trap mass spectrometers can be used,[97,98] but specification of the kinetic energy and incomplete isolation of the acceleration and reaction steps are problematic.

2.12.5.3 Data Analysis

The kinetic energy dependence of CID reactions is often modeled using a simple empirical formula (Equation (2)) for reasons reviewed recently:[92]

$$\sigma(E) = \sigma_0 \Sigma\, g_i\,(E + E_i - E_0)^n/E \tag{2}$$

Here σ_0 is an energy-independent scaling factor, E is the center-of-mass kinetic energy, E_0 is the reaction threshold, and n describes the shape of the energy dependence. When $E < E_0$, the model predicts that $\sigma(E) = 0$. The sum is over all rovibrational and electronic states i of the reactants with energies E_i and populations g_i, where $\Sigma g_i = 1$. This requires molecular parameters (electronic, vibrational, and rotational constants) of both reactants (obtained from experimental or theoretical sources) along with information regarding the populations of these states. As noted above, a key requirement of ion sources used in TCID measurements is that the internal energy content of the reactant ions must be well characterized, so that the populations g_i are known. To accurately reproduce experimental TCID data, this model must also be convoluted with the kinetic energy distributions of the reactants, using formulae found elsewhere.[86,99,100]

In TCID, multiple collisions between the ionic and neutral reactants lead to the same overall products but with a lowered threshold energy, because additional collisions deposit additional energy. When the dissociation kinetics are particularly slow (see Section 2.12.5.6), this extra energy can increase the probability of observing dissociation by orders of magnitude, such that TCID cross-sections are very sensitive to multiple collisions. Even at low neutral pressures, the probability of secondary collisions is finite; therefore, the acquisition of true single-collision cross-sections is achieved by measuring the pressure dependence of the cross-section and extrapolating to zero pressure.[101]

2.12.5.4 Collision Gas

The neutral reagent in TCID experiments, Rg in Equation (1), is optimally chosen to provide efficient kinetic-to-internal energy transfer during the collision. In addition, this species should not carry away extensive amounts of energy either in internal or translational modes. Translational-to-internal energy transfer occurs most efficiently when there are long-lived collisions in which the transient $(ML_x^+)(Rg)$ collision complex dissociates statistically. If ML_{x-1}^+ or L is modestly complex, there are many more internal modes than translational modes such that statistical behavior puts most of the reactant kinetic energy into internal energy of the reactant complex. The amount of energy removed from the complex by Rg can be minimized by the use of monatomic gases, most conveniently, the stable rare gases, which have no internal modes. Of these, Xe is preferred as it has the highest polarizability, meaning that it has the strongest interaction with the ML_x^+ reactant. This maximizes the probability of forming a long-lived $(ML_x^+)(Rg)$ complex. Indeed, a number of studies have demonstrated that Xe is a more efficient energy transfer reagent than the lighter rare gases.[35,102–104] In some cases, however, reactions such as charge transfer (Equation (3))[102] or ligand exchange (Equation (4)) (such as the minor products shown in Figure 5),[31,105] can compete strongly with the desired CID process, thereby adversely affecting the ability to measure the CID threshold. In such cases, a lighter rare gas may be a better choice as a collision gas because it has a higher ionization energy and lower polarizability than Xe. In the case shown in Figure 5, the magnitude of the ligand exchange cross-sections is sufficiently small that such competition is minimal:

$$ML_x^+ + Rg \rightarrow ML_x + Rg^+ \tag{3}$$

$$ML_x^+ + Rg \rightarrow RgML_{x-1}^+ + L \tag{4}$$

2.12.5.5 Energy Deposition Distributions

Collisions between ML_x^+ and Rg can be head on (allowing the possibility that all of the kinetic energy can be transferred into internal degrees of freedom of the ML_x^+ complex), grazing (such that almost no energy is transferred), and everywhere in between, resulting in a broad distribution of energies transferred. For CID processes, the parameter n in Equation (2) empirically describes the distribution of energies deposited in the ML_x^+ reactant by the collision with Rg. A recent direct measurement found that the distribution of energy deposited, ε, can be described by Equation (5)

$$P(\varepsilon) = \sigma_0 n(E-\varepsilon)^{n-1}/E \tag{5}$$

Importantly, the values of n used in Equation (2) to describe the cross-section for CID and in Equation (5) to describe the energy deposition distribution are found to be equivalent. Thus, modeling TCID cross-sections with Equation (2) and the extensions described below is physically reasonable.

2.12.5.6 Kinetic Shifts

The CID process can be viewed as two separate steps: an energy-deposition step (Equation (6)) and a unimolecular dissociation step (Equation (7))

$$ML_x^+ + Rg \rightarrow [ML_x^+]^* + Rg \tag{6}$$

$$[ML_x^+]^* \rightarrow ML_{x-1}^+ + L \tag{7}$$

In this picture, the energized complex, $[ML_x^+]^*$, will have a lifetime that depends on its internal energy, E^*, and the number of degrees of freedom it possesses. If ML_x^+ is a small molecule, the dissociation rate is generally rapid, such that dissociation will be observed as long as the internal energy of $[ML_x^+]^*$ exceeds its bond energy. However, for larger molecules, the lifetime of the complex can increase to the point that it exceeds the timescale that a particular instrument has available to observe the dissociation, τ, which is typically in the microsecond time regime. This

produces what is known as a kinetic shift, i.e., the lowest energy observation of the dissociation products (as limited by deviations in product signal from background noise levels) moves to energies higher than the thermodynamic threshold.

When kinetic shifts occur, the dissociation kinetics must be included in the analysis in order to acquire accurate thermochemistry. This is achieved by explicitly including the unimolecular dissociation probability,[106–108] thereby modifying Equation (2) to yield Equation (8)

$$\sigma(E) = (n\sigma_0/E)\sum_i g_i \int_{E_0-E_i}^{E} [1 - e^{-k(\varepsilon+E_i)\tau}](E-\varepsilon)^{n-1} d(\varepsilon) \quad (8)$$

Here, most quantities are defined above and $k(\varepsilon + E_i) = k(E^*)$ is the unimolecular dissociation rate constant, evaluated using modern statistical theories, such as Rice–Ramsperger–Kassel–Marcus (RRKM) theory.[109] Note that Equation (8) combines the distribution of deposited energies (Equation (5)) with the probability that the complex dissociates in time τ (term in square brackets), and a summation over the internal energy available to the reactants. Importantly, the integration recovers Equation (2) when the dissociation rate, $k(E^*)$, is faster than the experimental time scale, such that the term in brackets is unity.

Vibrational and rotational constants for the energized molecule, $[ML_x^+]^*$, and for the transition state (TS) leading to products are needed to evaluate kinetic shifts using RRKM theory. For the simple bond cleavages appropriate for coordination complexes, it is a good approximation to treat the TS as loose and located at the centrifugal barrier for product formation.[108] This makes the choice of the vibrational and rotational constants of the TS particularly simple as they equal those of the products.

A striking example of a large kinetic shift that has been accurately modeled involves the dissociation of a complex of Na^+ with the multidentate 18-crown-6 cyclic polyether (18c6) (Figure 6).[24,25] When these data are analyzed using Equation (2), a threshold of 7.37 ± 0.24 eV is obtained. In contrast, when the data are analyzed using Equation (8), the threshold obtained is 3.07 ± 0.20 eV, as indicated by the arrow in Figure 6. This large kinetic shift, 4.3 eV, results from the large number of internal states available in the large and floppy 18c6 ligand combined with the strong Na^+—18c6 bond. In the region above the background noise, the model of Equation (8) reproduces the data very well. The threshold obtained including the kinetic shift agrees well with a value of 3.44 eV calculated using high-level quantum theory.[110] (Indeed, the agreement between

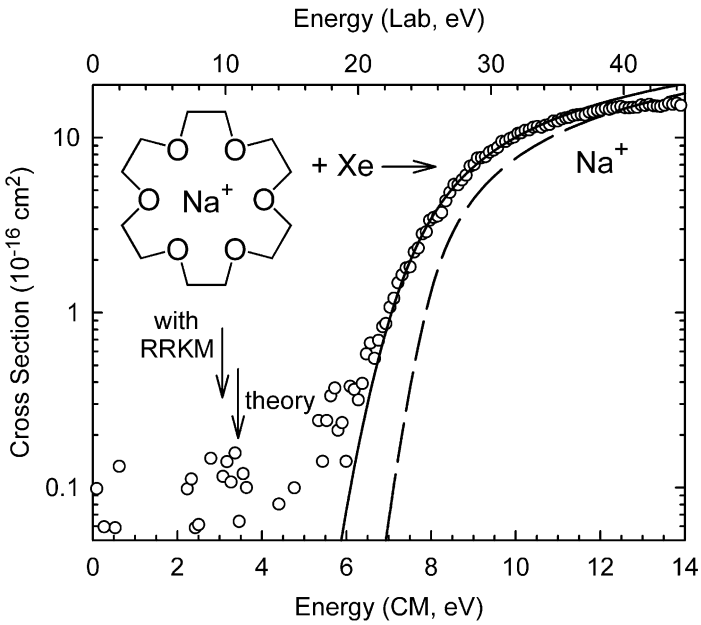

Figure 6 Zero-pressure extrapolated cross-sections for the primary collision-induced dissociation product of the Na^+(18c6) complex with Xe in the threshold region as a function of kinetic energy in the center-of mass frame (lower x-axis) and the laboratory frame (upper x-axis). The solid line shows the best fit to the data using the model of Equation (6) convoluted over the neutral and ion kinetic and internal energy broadening for reactants with an internal energy of 0 K. Arrows indicate the threshold values derived from this analysis and from theory (see text).

experiment and theory is better than it first appears as this level of theory systematically overestimates, by $12 \pm 8\%$, experimental BDEs of Na^+ to one to four dimethylethers, systems that exhibit minimal kinetic shifts. For the 18c6 system, this overestimate corresponds to an increase of 0.37 ± 0.25 eV in the calculated bond energy, in good agreement with the difference observed.[25]).

Many such studies demonstrate that kinetic shifts must be included in the threshold analysis of CID reactions. The accuracy of the correction for the kinetic shift is limited by the models used for the kinetics, by the assumptions made regarding the TS, and by the sensitivity of the experiment. The magnitude of kinetic shifts depends on the size of the system being considered and the bond energy. Typically, systems containing fewer than about six heavy atoms dissociate rapidly enough so that kinetic shifts are minimal.

2.12.5.7 Competitive Shifts

If the ML_x^+ complex can dissociate by two independent pathways (for example, when two of the ligands differ from one another), competition between these channels can influence the shapes of the cross-sections and consequently the ability to accurately model the kinetic energy dependence of both channels. This is illustrated in Figure 7 for a bis-ligated Li^+ complex.[82] The kinetic energy dependence of the total cross-section is typical of simple TCID processes, but the two product cross-sections have distinct shapes. As the collision energy of the $(H_2O)Li^+(C_2H_5OH)$ complex increases, it first dissociates exclusively to the lowest energy channel, $Li^+(C_2H_5OH) + H_2O$, yielding a rapidly rising cross-section. As the threshold for the $Li^+(H_2O) + C_2H_5OH$ channel is exceeded, the cross-section for the dominant channel begins to decline as some of the energized complexes now decompose to the high-energy channel.

Statistically, most complexes still dissociate to the lower-energy channel such that the cross-section for $Li^+(H_2O)$ rises more slowly but continuously as the energy is increased. This slow rise in the cross-section generally leads to a threshold (when analyzed using Equations (2) or (8)) that is higher than the thermodynamic threshold for this channel. Further increases in the energy reduce the statistical difference between the two channels such that the magnitudes of the two cross-sections approach one another. In general, such competition leads to differences in the thresholds being overestimated when the cross-sections are analyzed independently.

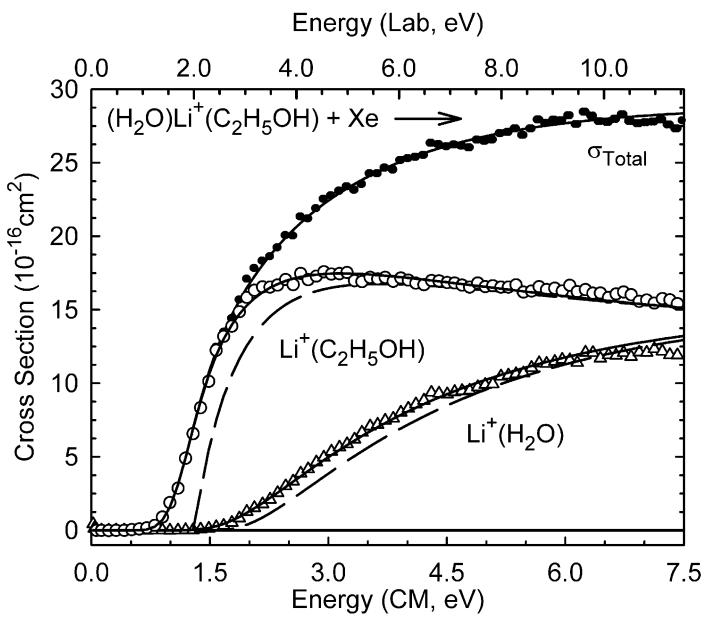

Figure 7 Zero-pressure extrapolated cross-sections for the collision-induced dissociation of the $(H_2O)Li^+(C_2H_5OH)$ complex with Xe in the threshold region as a function of kinetic energy in the center-of mass frame (lower x-axis) and the laboratory frame (upper x-axis). Solid lines show the best fits to the data using the model of Equation (9) convoluted over the neutral and ion kinetic and internal energy distributions. Dashed lines show the model cross-sections in the absence of experimental kinetic energy broadening for reactants with an internal energy of 0 K.

For systems that behave statistically, it is straightforward to include the effects of competition in the threshold analysis. This is achieved by modifying Equation (8) to include multiple channels,[82] indexed by j.

$$\sigma_j(E) = \frac{n\sigma_{0,j}}{E}\sum_i g_i \int_{E_{0,j}-E_i}^{E} \frac{k_j(E*)}{k_{tot}(E*)}[1 - e^{-k_{tot}(E*)\tau}](E-\varepsilon)^{n-1}d(\varepsilon) \quad (9)$$

In this equation, $k_{tot} = \Sigma k_j$ and all rate constants are again calculated using RRKM theory. This equation introduces the competition between product channels as the ratio of dissociation rates k_j/k_{tot}.[82,111,112] The analysis of the data for the $(H_2O)Li^+(C_2H_5OH)$ complex is typical and illustrates the power of the statistical analysis. If the two product cross-sections are analyzed independently using Equation (8), the difference in the two thresholds is found to be 0.60 ± 0.10 eV. In contrast, a difference of 0.29 ± 0.01 eV is obtained from an analysis of the same data using Equation (9) in which both channels are simultaneously reproduced.[82] This latter analysis, shown in Figure 7, reproduces both channels and the total cross-section extremely well over an extended range of energies. Because two cross-sections must be reproduced simultaneously, the precision in the relative thresholds from this competitive analysis is very high. To verify which interpretation of the data is more accurate, we compare these values to those obtained from direct CID measurements, 0.31 ± 0.16 eV,[18] and from equilibrium measurements, 0.29 eV.[77] Clearly, analysis of the data without consideration of the competition does not yield accurate thermochemistry and overestimates the difference between the thresholds, whereas the statistical analysis using Equation (9) and explicit consideration of the competition provides excellent results. Recent studies show that all statistical factors, such as symmetry numbers for internal rotors, need to be included in competitive analyses in order to maintain accuracy and precision.[111]

2.12.6 REFERENCES

1. Peschke, M.; Blades, A. T.; Kebarle, P. *J. Phys. Chem. A* **1998**, *102*, 9978–9985.
2. Peschke, M.; Blades, A. T.; Kebarle, P. *J. Am. Chem. Soc.* **2000**, *122*, 10440–10449.
3. Rodriguez, S. E.; Jockusch, R. A.; Williams, E. R. *J. Am. Chem. Soc.* **1998**, *120*, 5842–5843.
4. Rodriguez, S. E.; Jockusch, R. A.; Williams, E. R. *J. Am. Chem. Soc.* **1999**, *121*, 1986–1987.
5. Rodriguez, S. E.; Jockusch, R. A.; Williams, E. R. *J. Am. Chem. Soc.* **1999**, *121*, 8898–8906.
6. Sunderlin, L. S.; Wang, D.; Squires, R. R. *J. Am. Chem. Soc.* **1993**, *115*, 12060–12070.
7. Freiser, B. S., Ed. *Organometallic Ion Chemistry*; Kluwer: Dordrecht, The Netherlands, 1996.
8. Rodgers, M. T.; Armentrout, P. B. *Mass Spectrom. Rev.*, **2000**, *19*, 215–247.
9. Armentrout, P. B. *Acc. Chem. Res.* **1995**, *28*, 430–436.
10. Armentrout, P. B.; Kickel, B. L. In *Organometallic Ion Chemistry*; Freiser, B. S., Ed. Kluwer: Dordrecht, The Netherlands, 1996, pp 1–45.
11. Weast, R. C., Ed. *CRC Handbook of Chemistry and Physics*, 63rd ed., CRC Press: Boca Raton, Fl, 1982.
12. Amunugama, R.; Rodgers, M. T. *Int. J. Mass Spectrom.* **2000**, *195/196*, 439–457.
13. Amicangelo, J. C.; Armentrout, P. B. *J. Phys. Chem. A* **2000**, *104*, 11420–11432.
14. Rodgers, M. T.; Armentrout, P. B. *Int. J. Mass Spectrom.* **1999**, *185–187*, 359–380.
15. Huang, H.; Rodgers, M. T. *J. Phys. Chem. A* **2002**, *106*, 4277–4287.
16. Hoyau, S.; Norrman, K.; McMahon, T. B.; Ohanessian, G. *J. Am. Chem. Soc.* **1999**, *121*, 8864–8875.
17. Armentrout, P. B.; Rodgers, M. T. *J. Phys. Chem. A* **2000**, *104*, 2238–2247.
18. Rodgers, M. T.; Armentrout, P. B. *J. Phys. Chem. A* **1997**, *101*, 2614–2625.
19. Rodgers, M. T.; Armentrout, P. B. *J. Phys. Chem. A* **1999**, *103*, 4955–4963.
20. More, M. B.; Glendening, E. D.; Ray, D.; Feller, D.; Armentrout, P. B. *J. Phys. Chem.* **1996**, *100*, 1605–1614.
21. More, M. B.; Ray, D.; Armentrout, P. B. *J. Phys. Chem. A* **1997**, *101*, 831–839.
22. More, M. B.; Ray, D.; Armentrout, P. B. *J. Phys. Chem. A* **1997**, *101*, 4254–4262.
23. More, M. B.; Ray, D.; Armentrout, P. B. *J. Phys. Chem. A* **1997**, *101*, 7007–7017.
24. More, M. B.; Ray, D.; Armentrout, P. B. *J. Am. Chem. Soc.* **1999**, *121*, 417–423.
25. Armentrout, P. B. *Int. J. Mass Spectrom.* **1999**, *193*, 227–240.
26. Feller, D.; Glendening, E. D.; Kendall, R. A.; Peterson, K. A. *J. Chem. Phys.* **1994**, *100*, 4981–4997.
27. Dalleska, N. F.; Tjelta, B. L.; Armentrout, P. B. *J. Phys. Chem.* **1994**, *98*, 4191–4195.
28. Bauschlicher, C. W.; Langhoff, S. R.; Partridge, H.; Rice, J. E.; Komornicki, A. *J. Chem. Phys.* **1991**, *95*, 5142–5148.
29. Bauschlicher, C. W.; Partridge, H. *J. Phys. Chem.* **1991**, *95*, 9694–9698.
30. Bauschlicher, C. W.; Sodupe, M.; Partridge, H. *J. Chem. Phys.* **1992**, *96*, 4453–4463.
31. Andersen, A.; Muntean, F.; Walter, D.; Rue, C.; Armentrout, P. B. *J. Phys. Chem. A* **2000**, *104*, 692–705.
32. Holland, P. M.; Castleman, A. W. *J. Am. Chem. Soc.* **1980**, *102*, 6174–6175.
33. Magnera, T. F.; David, D. E.; Michl, J. *J. Am. Chem. Soc.* **1989**, *111*, 4100–4101.
34. Marinelli, P. J.; Squires, R. R. *J. Am. Chem. Soc.* **1989**, *111*, 4101–4103.
35. Dalleska, N. F.; Honma, K.; Sunderlin, L. S.; Armentrout, P. B. *J. Am. Chem. Soc.* **1994**, *116*, 3519–3528.
36. Rosi, M.; Bauschlicher, C. W. *J. Chem. Phys.* **1989**, *90*, 7264–7272.

37. Rosi, M.; Bauschlicher, C. W. *J. Chem. Phys.* **1990**, *92*, 1876–1878.
38. Irigoras, A.; Ugalde, J. M.; Lopez, X.; Sarasola, C. *Can. J. Chem.* **1996**, *74*, 1824–1829.
39. Irigoras, A.; Elizalde, O.; Silanes, I.; Fowler, J. E.; Ugalde, J. M. *J. Am. Chem. Soc.* **2000**, *122*, 114–122.
40. Sugar, J.; Corliss, C. *J. Phys. Chem. Ref. Data, Suppl. No. 2* **1985**, *14*, 1.
41. Jorgensen, W. L.; Salem, L. *The Organic Chemist's Book of Orbitals*; Academic Press: New York, 1973.
42. Rothe, E. W.; Bernstein, R. B. *J. Chem. Phys.* **1959**, *31*, 1619–1627.
43. Tjelta, B. L.; Armentrout, P. B. *J. Phys. Chem. A* **1997**, *101*, 2064–2073.
44. Walter, D.; Armentrout, P. B. *J. Am. Chem. Soc.* **1998**, *120*, 3176–3187.
45. Langhoff, S. R. Bauschlicher, C. W.; Partridge, H.; Sodupe, M. *J. Phys. Chem.* **1991**, *95*, 10677–10681.
46. Zhang, Q.; Kemper, P. R.; Bowers, M. T. *Int. J. Mass Spectrom.* **2001**, *210/211*, 265–281.
47. Schultz, R. H.; Crellin, K.; Armentrout, P. B. *J. Am. Chem. Soc.* **1991**, *113*, 8590–8601.
48. Bushnell, J. E.; Kemper, P. R.; Bowers, M. T. *J. Phys. Chem.* **1995**, *99*, 15602–15607.
49. Ricca, A.; Bauschlicher, C. W. *J. Phys. Chem.* **1994**, *98*, 12899–12903.
50. Ricca, A.; Bauschlicher, C. W. *J. Phys. Chem.* **1995**, *99*, 9003–9007.
51. Meyer, F.; Chen, Y.-M.; Armentrout, P. B. *J. Am. Chem. Soc.* **1995**, *117*, 4071–4081.
52. Goebel, S.; Haynes, C. L.; Khan, F. A.; Armentrout, P. B. *J. Am. Chem. Soc.* **1995**, *117*, 6994–7002.
53. Sievers, M. R.; Armentrout, P. B. *J. Phys. Chem.* **1995**, *99*, 8135–8141.
54. Khan, F. A.; Steele, D. L.; Armentrout, P. B. *J. Phys. Chem.* **1995**, *99*, 7819–7828.
55. Meyer, F.; Armentrout, P. B. *Molec. Phys.* **1996**, *88*, 187–197.
56. Sievers, M. R.; Jarvis, L. M.; Armentrout, P. B. *J. Am. Chem. Soc.* **1998**, *120*, 1891–1899.
57. Amunugama, R.; Rodgers, M. T. *J. Phys. Chem. A* **2001**, *105*, 9883–9892.
58. Rodgers, M. T.; Stanley, J. R.; Amunugama, R. *J. Am. Chem. Soc.* **2000**, *122*, 10969–10978.
59. Meyer, F.; Khan, F. A.; Armentrout, P. B. *J. Am. Chem. Soc.* **1995**, *117*, 9740–9748.
60. Rodgers, M. T.; Armentrout, P. B. *J. Am. Chem. Soc.* **2002**, *124*, 2678–2691.
61. Bauschlicher, C. W.; Partridge, H.; Langhoff, S. R. *J. Phys. Chem.* **1992**, *96*, 3273–3278.
62. Yang, C.-N.; Klippenstein, S. J. *J. Phys. Chem. A* **1999**, *103*, 1094–1103.
63. Prins, R.; Reinders, F. J. *Chem. Phys. Lett.* **1969**, *3*, 45–48.
64. Cabelli, D. E.; Cowley, A. H.; Lagowski, J. J. *Inorg. Chim. Acta.* **1982**, *57*, 195–198.
65. Andrews, M. P.; Mattar, S. M.; Ozin, G. A. *J. Phys. Chem.* **1986**, *90*, 1037–1043.
66. Dzidic, I.; Kebarle, P. *J. Phys. Chem.* **1970**, *74*, 1466–1474.
67. Davidson, W. R.; Kebarle, P. *J. Am. Chem. Soc.* **1976**, *98*, 6133–6138.
68. Kemper, P. R.; Bushnell, J.; van Koppen, P.; Bowers, M. T. *J. Phys. Chem.* **1993**, *97*, 1810–1817.
69. Bouchard, F.; Hepburn, J. W.; McMahon, T. B. *J. Am. Chem. Soc.* **1990**, *111*, 8934–8935.
70. Dunbar, R. C.; McMahon, T. B. *Science* **1998**, *279*, 194–197.
71. Schnier, P. D.; Price, W. D.; Jockusch, R. A.; Williams, E. R. *J. Am. Chem. Soc.* **1996**, *118*, 7178–7189.
72. Schnier, P. D.; Klassen, J. S.; Strittmatter, E. F.; Williams, E. R. *J. Am. Chem. Soc.* **1998**, *120*, 9605–9613.
73. Pozniak, B. P.; Dunbar, R. C. *J. Am. Chem. Soc.* **1997**, *119*, 10439–10445.
74. Ho, Y.-P.; Yang, Y.-C.; Klippenstein, S. J.; Dunbar, R. C. *J. Phys. Chem. A* **1997**, *101*, 3338–3347.
75. Ryzhov, V.; Dunbar, R. C. *J. Am. Chem. Soc.* **1999**, *121*, 2259–2268.
76. Woodin, R. L.; Beauchamp, J. L. *J. Am. Chem. Soc.* **1978**, *100*, 501–508.
77. Taft, R. W.; Anvia, F.; Gal, J. F.; Walsh, S.; Capon, M.; Holmes, M. C.; Hosn, K.; Oloumi, G.; Vasamwala, R.; Yazdani, S. *Pure Appl. Chem.* **1990**, *62*, 17–23.
78. Cooks, R. G.; Wong, P. S. H. *Acc. Chem. Res.* **1998**, *31*, 379–386.
79. Cooks, R. G.; Koskinen, J. T.; Thomas, P. D. *J. Mass Spectrom.* **1999**, *34*, 85–92.
80. Armentrout, P. B. *J. Mass Spectrom.* **1999**, *34*, 74–78.
81. Armentrout, P. B. *J. Am. Soc. Mass Spectrom.* **2000**, *11*, 371–379.
82. Rodgers, M. T.; Armentrout, P. B. *J. Chem. Phys.* **1998**, *109*, 1787–1800.
83. Cooks, R. G., Ed., *Collision Spectroscopy*; Plenum: New York, 1978.
84. Chu, Y.; Yang, Z.; Rodgers, M. T. *J. Am. Soc. Mass Spectrom.* **2002**, *13*, 453–468.
85. Ervin, K. M.; Armentrout, P. B. *J. Chem. Phys.* **1985**, *83*, 166–189.
86. Armentrout, P. B.; Simons, J. *J. Am. Chem. Soc.* **1992**, *114*, 8627–8633.
87. Muntean, F.; Armentrout, P. B. *J. Chem. Phys.* **2001**, *115*, 1213–1228.
88. Rodgers, M. T. *J. Phys. Chem. A* **2001**, *105*, 2374–2383.
89. DeTuri, V. F.; Hintz, P. A.; Ervin, K. M. *J. Phys. Chem. A*, **1997**, *101*, 5969–5986.
90. Chiu, Y.-H.; Fu, H.; Huang, J.-T.; Anderson, S. L. *J. Chem. Phys.* **1995**, *102*, 1199–1216.
91. Armentrout, P. B. *J. Am. Soc. Mass Spectrom.* **2002**, *13*, 419–434.
92. Armentrout, P. B. *Int. J. Mass Spectrom.* **2000**, *200*, 219–241.
93. Forbes, R. A.; Lech, L. M.; Freiser, B. S. *Int. J. Mass Spectrom. Ion Processes* **1987**, *77*, 107–121.
94. Hop, C. E. C. A.; McMahon, T. B.; Willett, G. D. *Int. J. Mass Spectrom. Ion Processes* **1990**, *101*, 191–208.
95. Beyer, M.; Bondybey, V. E. *Rapid Comm. Mass Spectrom.* **1997**, *11*, 1588–1591.
96. Kruckeberg, S.; Dietrich, G.; Lutzenkirchen, K.; Schweikhard, L.; Walther, C.; Ziegler, J. *J. Chem. Phys.* **1999**, *110*, 7216–7227.
97. Hart, K. J.; McLuckey, S. A. *J. Am. Soc. Mass Spectrom.* **1994**, *5*, 250–259.
98. Satterfield, M.; Brodbelt, J. S. *Inorg. Chem.* **2001**, *40*, 5393–5400.
99. Chantry, P. J. *J. Chem. Phys.* **1971**, *55*, 2746–2759.
100. Lifshitz, C.; Wu, R. L. C.; Tiernan, T. O.; Terwilliger, D. T. *J. Chem. Phys.* **1978**, *68*, 247–260.
101. Hales, D. A.; Lian, L.; Armentrout, P. B. *Int. J. Mass Spectrom. Ion Processes* **1990**, *102*, 269–301.
102. Armentrout, P. B. In *Advances in Gas Phase Ion Chemistry*, *1*; Adams, N. G., Babcock, L. M., Eds.; JAI: Greenwich, 1992; pp 83–119.
103. Aristov, N.; Armentrout, P. B. *J. Phys. Chem.* **1986**, *90*, 5135–5140.
104. Rodgers, M. T.; Armentrout, P. B. *J. Phys. Chem. A* **1997**, *101*, 1238–1249.
105. Tjelta, B. L.; Walter, D.; Armentrout, P. B. *Int. J. Mass Spectrom.* **2001**, *204*, 7–21.
106. Loh, S. K.; Hales, D. A.; Lian, L.; Armentrout, P. B. *J. Chem. Phys.* **1989**, *90*, 5466–5485.

107. Khan, F. A.; Clemmer, D. E.; Schultz, R. H.; Armentrout, P. B. *J. Phys. Chem.* **1993**, *97*, 7978–7987.
108. Rodgers, M. T.; Ervin, K. M.; Armentrout, P. B. *J. Chem. Phys.* **1997**, *106*, 4499–4508.
109. Gilbert, R. G.; Smith, S. C. *Theory of Unimolecular and Recombination Reactions*. Blackwell Scientific Publications: Oxford, 1990.
110. Glendening, E. D.; Feller, D.; Thompson, M. A. *J. Am. Chem. Soc.* **1994**, *116*, 10657–10669.
111. Amicangelo, J. C.; Armentrout, P. B. *Int. J. Mass Spectrom.* **2001**, *212*, 301–325.
112. DeTuri, V. F.; Ervin, K. M. *J. Phys. Chem. A* **1999**, *103*, 6911–6920.

Comprehensive Coordination Chemistry II
ISBN (set): 0-08-0437486

Volume 2, (ISBN 0-08-0443249); pp 141–158

2.13
X-ray Absorption Spectroscopy

J. E. PENNER-HAHN
The University of Michigan, Ann Arbor, MI, USA

2.13.1 PHYSICS OF X-RAY ABSORPTION 159
2.13.1.1 X-ray Absorption Edges 160
2.13.1.2 X-ray Fluorescence 161
2.13.1.3 Measurement of X-ray Absorption Spectra 161
2.13.2 EXTENDED X-RAY ABSORPTION FINE STRUCTURE 164
2.13.2.1 Theoretical Description of EXAFS Spectra 164
2.13.2.1.1 Single scattering 164
2.13.2.1.2 Multiple scattering 166
2.13.2.1.3 Other corrections to the EXAFS equation 167
2.13.2.2 Programs for Calculating and Analyzing EXAFS 167
2.13.2.2.1 Fourier transforms 168
2.13.2.2.2 Curve fitting 169
2.13.2.3 Limitations of EXAFS 170
2.13.2.4 Applications of EXAFS to Coordination Chemistry 172
2.13.2.4.1 De novo structure determination 172
2.13.2.4.2 Solution structure determination 173
2.13.2.4.3 Resolution of crystallographic disorder 173
2.13.2.4.4 Time-dependent structural evolution 174
2.13.3 X-RAY ABSORPTION NEAR EDGE STRUCTURE 174
2.13.3.1 Sensitivity of XANES to Oxidation State 175
2.13.3.2 Multiple Scattering and XANES 176
2.13.3.3 Bound State Transitions in XANES 176
2.13.3.4 Multi-electron Transitions in XANES 177
2.13.3.5 Applications of XANES to Coordination Chemistry 178
2.13.4 HIGHER RESOLUTION XAS 178
2.13.4.1 Polarization-dependent Measurements 179
2.13.4.1.1 Linearly polarized measurements 179
2.13.4.1.2 X-ray MCD 179
2.13.4.1.3 Natural circular dichroism 179
2.13.4.2 High-resolution X-ray Fluorescence 180
2.13.4.2.1 Elimination of lifetime broadening in XANES 180
2.13.4.2.2 Site-selective XAS 180
2.13.4.3 Spatially Resolved Measurements 181
2.13.4.3.1 Methods for focusing X-rays 181
2.13.4.3.2 Applications of X-ray microprobes 181
2.13.5 REFERENCES 182

2.13.1 PHYSICS OF X-RAY ABSORPTION

X-rays are ionizing radiation and thus, by definition, have sufficient energy to eject a core election from an atom. Each core shell has a distinct binding energy, and thus if one plots X-ray absorption as a function of energy, the spectrum for any atom resembles the X-ray absorption spectrum for Pb, shown in Figure 1.[1–4] When the X-ray energy is scanned through the binding energy of a core shell, there is an abrupt increase in absorption cross-section. This gives rise to a

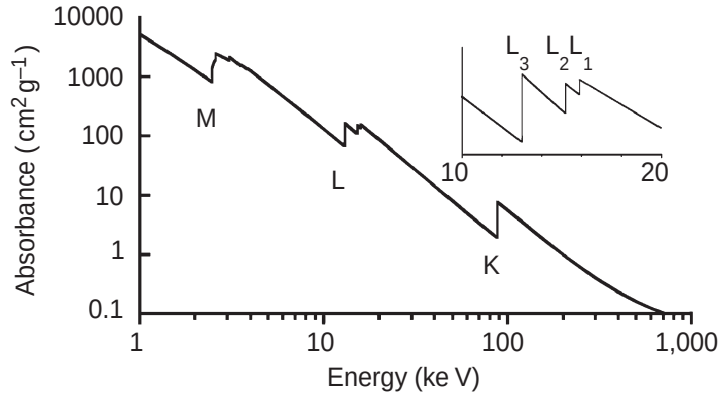

Figure 1 Low-resolution X-ray absorption spectrum for Pb. Three major transitions are seen (K, L, and M edges), corresponding to excitation of an electron from $n = 1$, 2, and 3 shells, respectively. At higher resolution (inset) both the L and the M edges are split (see text for details).

so-called absorption edge, with each edge representing a different core–electron binding energy. The edges are named according to the principle quantum number of the electron that is excited: K for $n = 1$, L for $n = 2$, M for $n = 3$, etc. The core–electron binding energy increases with increasing atomic number, ranging from 284 eV for the C K edge to 115,606 eV for the U K edge, with the L edges at significantly lower energies than the corresponding K edge (e.g., 270 eV for the Cl L_1 edge, 20,948 eV and 17,166 eV for the U L_2 and L_3 edges).

Closer examination of Figure 1 (see inset) shows that the L edge is in fact three distinct L edges, named L_1, L_2, and L_3 in order of decreasing energy. L_1 corresponds to excitation of a $2s$ electron. The $2p$ excitation is split into two edges, L_2 and L_3, as a consequence of the spin–orbit coupling energy of the $2p^5$ configuration that is created when a $2p$ electron is excited. The higher energy of the $2p^5$ excited states is the $^2P_{1/2}$ term; This gives rise to the L_2 edge. At lower energy is the L_3 edge, corresponding to the $^2P_{3/2}$ excited state. Due to degeneracy, the L_3 edge has twice the edge jump of the L_2 and L_1 edges. In contrast with valence electron shells where spin–orbit coupling energies are relatively small, the spin–orbit coupling for core shells can be quite large. For Pb, the L_2–L_3 splitting is 2,165 eV (1 eV = 8,066 cm^{-1}). Analogous, albeit smaller, splitting occurs for the lower-energy edges, with 5 M edges, 7 N edges, etc. X-ray absorption spectroscopy (XAS) refers to the measurement of X-ray absorption cross-section in the vicinity of one or more absorbing edges.

2.13.1.1 X-ray Absorption Edges

An absorption edge by itself is of little value beyond elemental identification.[5,6] However, if one examines any of the edges in Figure 1 in more detail, they are found to contain a wealth of information. This is illustrated by the schematic absorption edge shown in Figure 2. The absorption edge is not simply a discontinuous increase in absorption, as suggested by Figure 1, but in

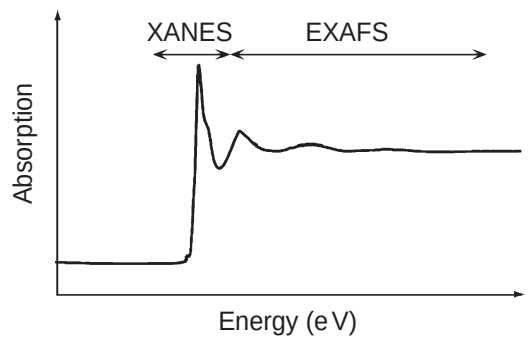

Figure 2 Schematic illustration of an X-ray absorption spectrum, showing the structured absorption that is seen both within ca. 50 eV of the edge (the XANES) and for several hundred to >1,000 eV above the edge (the EXAFS).

fact shows significant structure both in the immediate vicinity of the edge jump and well above the edge. The structure in the vicinity of the edge is sometimes referred to as X-ray absorption near-edge structure (XANES). The oscillations above the edge, which can extend for 1,000 eV or more, are often referred to as extended X-ray absorption fine structure (EXAFS). The distinction between XANES and EXAFS is arbitrary, since the same fundamental physical principles govern photoabsorption over the entire XAS region and there is no unambiguous definition that distinguishes between "near-edge" and "extended" structure. In an attempt to emphasize the essential similarity of these regions, the term XAFS (X-ray absorption fine structure) has gained some currency as a reference to the entire structured absorption region. Nevertheless, the terms EXAFS and XANES remain the most widely used, with some justification, since the XANES and EXAFS regions are generally analyzed differently. As described in detail below, the XANES region is sensitive to oxidation state and geometry, but is not, in most cases, analyzed quantitatively. The EXAFS region is sensitive to the radial distribution of electron density around the absorbing atom and is used for quantitative determination of bond length and coordination number. A fourth acronym, which is popular in the soft X-ray and surface science communities, is NEXAFS, standing for near-edge X-ray absorption fine structure. This acronym is redundant, since NEXAFS and XANES are used to refer to the same features, and is potentially confusing, given its similarity to EXAFS.

2.13.1.2 X-ray Fluorescence

Absorption of an ionizing X-ray results in photoelectron ejection, leaving behind a highly excited core-hole state. This can relax by a variety of mechanisms, with the two most important being emission of an Auger electron and X-ray fluorescence. For lower-energy excitation, Auger emission can be the dominant relaxation process. For higher-energy excitation (e.g., for the K edges of elements with atomic numbers greater than 40), X-ray fluorescence is the primary relaxation process, with X-ray fluorescence yields approaching 1. For light elements, the X-ray fluorescence spectrum is quite simple. However, for heavy elements, a large number of X-ray emission lines are observed. The nomenclature associated with X-ray fluorescence lines predates a modern, quantum understanding of the origins of X-ray fluorescence and consequently there is not a simple relationship between the names of different emission lines and the origin of the line.[7] Some of the possible emission lines[7–9] are shown in Figure 3. Like all emission spectroscopy, X-ray fluorescence is governed by a series of selection rules. Consequently, only certain transitions, referred to as "diagram lines," are allowed. As with other spectroscopies, a variety of forbidden transitions (nondiagram lines) are also observed, and can yield important information (see discussion of high-resolution X-ray fluorescence, Section 2.13.4.2). Each element has unique "characteristic" X-ray emission energies which are, in most cases, well resolved from neighboring emission lines.[4,10,11]

2.13.1.3 Measurement of X-ray Absorption Spectra

In the simplest case, measurement of an X-ray absorption spectrum involves only measurement of the incident and the transmitted X-ray flux. This can be accomplished, for example, with an

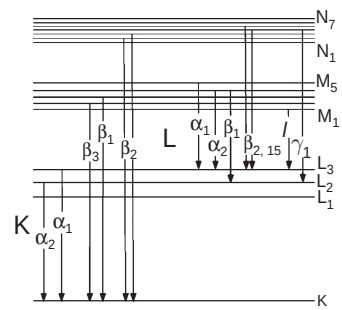

Figure 3 Nomenclature for selected X-ray emission lines. Excitation of a K shell results in K_α and K_β emission lines (originating from $n = 2$ and $n = 3$, respectively). At higher resolution, these can be resolved into $K\alpha_1$, $K\alpha_2$, with the splitting due to spin–orbit coupling. A similar pattern,with much greater complexity, is seen for L edge excitation. Redrawn from data in.[9] For a more complete list of emission lines, see.[7]

ionization chamber[12] in front of and behind the sample, using Beer's law to convert to absorption coefficient. This approach is limited to moderately concentrated samples (greater than ca. 10 mM or 500 ppm) and, depending on the energy of the absorption edge, even these concentrations may not be accessible. For example, sulfur or chlorine containing solvents are nearly opaque to lower-energy X-rays and thus interfere with XAS measurements.

To avoid the limitations of absorption, XAS spectra are frequently measured as fluorescence excitation spectra.[13] This is particularly important for dilute samples such as catalysts, biological samples, or environmental samples. The basic experimental geometry is illustrated in Figure 4. Providing the sample is dilute (absorbance due to the element of interest is much smaller than the background absorbance) or thin (total absorbance $\ll 1$), the intensity of the fluorescence X-rays is proportional to the X-ray absorption cross-section (see Figure 4).[14] In most cases, the sample will emit a variety of X-rays, both the fluorescence X-rays of interest and a background of scattered X-rays. In order to have good sensitivity, the fluorescence detector needs some kind of energy resolution to distinguish between the signal and background X-rays. In some cases, energy resolution can be provided by a simple low-pass filter[15,16] although for the ultimate sensitivity it is necessary to use higher resolution in order to more effectively exclude background radiation. This is typically an energy-resolving solid-state fluorescence detector,[17–19] although recent advances with wavelength-resolving detectors (i.e., multilayer diffraction gratings) may be important in special cases.[20,21]

In principle, any physical property that changes in proportion to X-ray absorption could be used to measure XAS spectra. In addition to X-ray fluorescence, properties that have been used include photoconductivity,[22] optical luminescence,[22–24] and electron yield,[25,26] although only the latter is widely used. Electron yield detection of XAS is particularly important for studies of surfaces. Since the penetration depth of an electron through matter is quite small, electron yield can be used to make XAS measurements surface sensitive.[27,28]

Although XAS can be studied for virtually any X-ray absorption edge, experiments are simplest when they can be performed at atmospheric pressure. This limits the accessible X-ray energies to those greater than approximately 5 keV (for air) or 2 keV (for a He atmosphere). Lower energy measurements (i.e., measurements of the K edges for elements lighter than phosphorus) require that the sample be in vacuum in order to avoid excessive attenuation of the incident X-ray beam. Similarly, it is difficult, although not impossible, to make XAS measurements at energies above approximately 30 keV (K edge energy for Sn = 30.5 keV). However, this does not limit XAS significantly, since elements that are heavy enough to have K edge energies >30 keV have readily accessible L edge energies (the L_3 edge for Sn is at 4 keV). This means that XAS spectra can be measured for virtually every element, although measurements for elements lighter than phosphorus generally require that the sample be made vacuum compatible. X-ray absorption spectra can be measured for solids, liquids, or gases and do not require that samples have long-range order (i.e., be crystalline) or that samples possess particular magnetic properties (e.g., nonzero electron spin or specific isotopes). Measurements can be made at low temperature for studies of unstable samples, or at high temperature and/or pressure, for example for studies of catalysts under reaction conditions or of geochemical samples under conditions that approximate the inner mantle. This flexibility, combined with near universality, has made XAS a widely utilized technique in all areas of coordination chemistry.

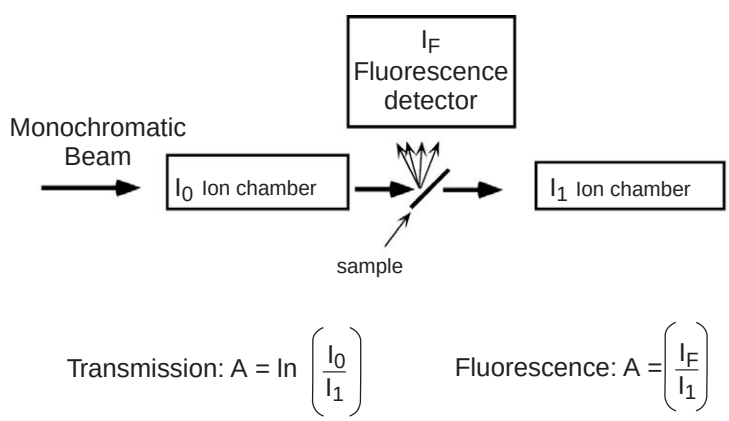

Figure 4 Typical experimental apparatus for XAS measurements. Incident and transmitted intensities are typically measured using an ion chamber; a variety of detectors can be used to measure X-ray fluorescence intensity for dilute samples (see text).

The critical experimental detail that limits the utility of XAS, and that accounts for XAS having been an obscure technique prior to about 1975, is the need for an intense, tunable X-ray source. Conventional X-ray sources work much the same as the X-ray tube that was invented by Röntgen:[29] an electron beam strikes a target which emits both "characteristic" radiation (X-ray fluorescence lines) and a broad continuous background of bremsstrahlung radiation. Only the latter is useful for XAS, since XAS measurements require a broad band of X-ray energies. The intensity of monochromatic radiation that can be obtained from the bremsstrahlung radiation is too low for most XAS measurements.

The development that allowed XAS to become a routine analytical tool was the recognition that the electron storage rings that are used in high-energy physics can serve as an extremely intense X-ray source. When an electron beam is accelerated, for example by using a magnetic field to cause the beam to follow the curvature of a storage ring, the electron beam radiates a broad spectrum of "synchrotron" radiation. From modest beginnings in the early 1970s, synchrotron radiation laboratories have grown enormously to the point that there are now over 75 laboratories, either planned, under construction, or in operation, devoted to the production of synchrotron radiation in one form or another, located in 23 countries.[30] A selection of some of the more important sources for XAS is given in Table 1. Other countries that will soon join this list include Armenia, Canada, Jordan, Spain, Thailand, and the Ukraine. Each of these laboratories is based around an electron (or positron) storage ring. Ring sizes vary, but modern synchrotrons typically have a circumference of approximately one kilometer. This size is large enough to accommodate anywhere from 10 to perhaps 100 independent "beamlines" (the hardware that transports the X-rays from the synchrotron source to the experimental apparatus) at each synchrotron laboratory.

The importance of synchrotron radiation can be seen by comparing the X-ray flux that is available from X-ray tubes with that available from synchrotron sources (Figure 5). The spectral brightness (X-ray flux normalized by area that is irradiated and divergence of the beam) of the most powerful sources is more than 10 orders of magnitude greater than that available from X-ray tubes. Another advantage of synchrotron sources is that the synchrotron X-ray beam is polarized, thus permitting orientation-dependent measurements for ordered samples. In addition,

Table 1 Major synchrotron sources for XAS.

Country	*Location*	*Synchrotron source*
Brazil	Campinas	LNLS
China (PRC)	Beijing	BSRF
	Hefei	NSRL
China (ROC-Taiwan)	Hsinchu	SRRC
Denmark	Aarhus	ASTRID
France	Grenoble	ESRF
	Orsay	LURE
Germany	Berlin	BESSY
	Hamburg	HASYLAB/DESY
India	Indore	INDUS
Italy	Trieste	ELETTRA
Japan	Nishi Harima	Spring-8
	Tsukuba	Photon Factory
Korea	Pohang	Pohang Light Source
Russia	Moscow	Siberia 1
	Novosibirsk	VEPP
Singapore	Singapore	SSLS
Sweden	Lund	MAX
Switzerland	Villigen	SLS
UK	Daresbury	SRS
USA	Argonne, IL	APS
	Baton Rouge, LA	CAMD
	Berkeley, CA	ALS
	Ithaca, NY	CHESS
	Stanford, CA	SSRL
	Stoughton, WI	Aladdin
	Upton, NY	NSLS

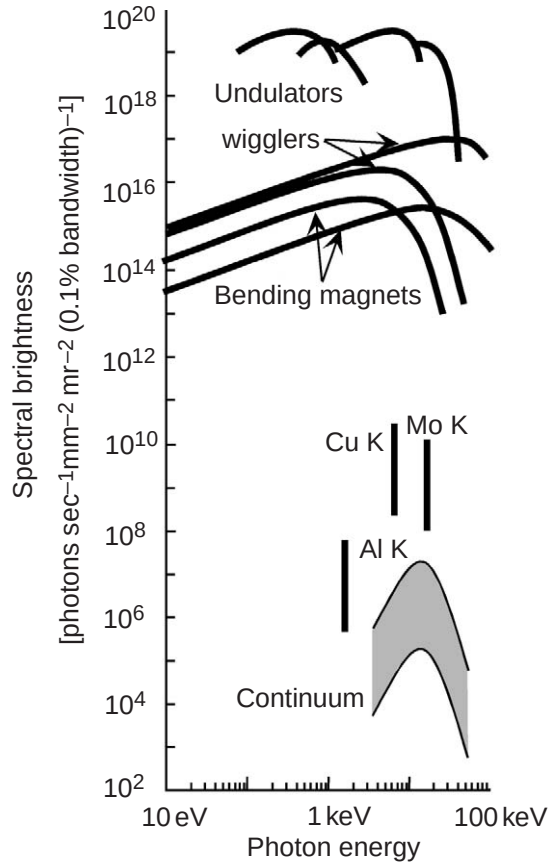

Figure 5 Typical spectral brightness of different X-ray sources (details will vary depending on the properties of the source). X-ray tube spectra, shown in gray (bremsstrahlung) and vertical bars (characteristic lines), can vary by two orders of magnitude depending on whether fixed or rotating anodes are used. Synchrotron sources vary depending on the details of the storage ring and on the energy of the electron beam. Representative data are shown for electron beam energies of 2 GeV and 7 GeV. In addition to the bending magnets, which cause the electron beam to curve around the storage ring, more recent synchrotrons use "insertion devices" to alter the orbit of the electron beam. These can produce broad-band spectra ("wigglers") or relatively narrow spectra ("undulators") depending on the details of the insertion device design. Redrawn from data in.[9]

with appropriate design, beamline can be made to produce circularly polarized X-rays, thus permitting magnetic circular dichroism (MCD) studies in the X-ray region.

This increase in X-ray intensity, together with the development of synchrotron laboratories with facilities dedicated to measurement of XAS, has allowed XAS to develop into a relatively routine analytical tool. It is straightforward to measure XAS spectra for transition metal solutions with concentrations greater than 1 mM (ca. 50 ppm) and it is possible, using the most intense synchrotron sources and the most sensitive detectors, to measure high-quality XAS spectra for samples containing less than 1 ng of the metal of interest. Typical sample volumes range from one mL to one μL and with microfocused X-ray beams (see below) even smaller volumes can be studied.

2.13.2 EXTENDED X-RAY ABSORPTION FINE STRUCTURE

2.13.2.1 Theoretical Description of EXAFS Spectra

2.13.2.1.1 Single scattering

The EXAFS region is typically taken as starting 20–30 eV above the edge jump. At these energies, the X-ray excited photoelectron has significant energy, and thus has a de Broglie wavelength that

is comparable to the interatomic distances. The EXAFS photoexcitation cross-section is modulated by the interference between the outgoing and the back-scattered photoelectron waves as illustrated schematically in Figure 6. At energy E_1, the outgoing and the back-scattered X-rays are in phase, resulting in constructive interference and a local maximum in the X-ray photoabsorption cross-section. At higher X-ray energy, the photoelectron has greater kinetic energy and thus a shorter wavelength, resulting in destructive interference and a local minimum in photoabsorption cross-section (energy E_2). The physical origin of EXAFS is thus electron scattering, and EXAFS can be thought of as a spectroscopically detected scattering method, rather than as a more conventional spectroscopy.

For a single absorber–scatterer pair (for example, in a diatomic gas) this alternating interference will give rise to sinusoidal oscillations in the absorption coefficient if the energy is given in units proportional to the inverse photoelectron wavelength (the photoelectron wavevector, or k, defined as in Equation (1)). In Equation (1), the threshold energy, E_0, is the binding energy of the photoelectron:

$$k = \sqrt{2m_e(E - E_0)/h^2} \tag{1}$$

In XAS analyses, it is typical to define the EXAFS, $\chi(k)$, as the fractional modulation in the X-ray absorption coefficient as in Equation (2), where μ is the observed absorption coefficient and μ_0 is the absorption that would be observed in the absence of EXAFS effects. Since μ_0 cannot be directly measured, it is approximated, typically by fitting a smooth spline function through the data. Division by μ_0 normalizes the EXAFS oscillations "per atom," and thus the EXAFS represents the average structure around the absorbing atoms:

$$\chi(k) = \frac{\mu - \mu_0}{\mu_0} \tag{2}$$

When plotted as $\chi(k)$, EXAFS oscillations have an appearance similar to that shown in Figure 7. The amplitude of the EXAFS oscillations is proportional to the number of scattering atoms, the frequency of the oscillations is inversely proportional to the absorber–scatterer distance, and the shape of the oscillations is determined by the energy dependence of the photoelectron scattering, which depends on the identity of the scattering atom. For quantitative analyses, the EXAFS can be described[31–33] by an equation such as Equation (3), with the summation taken over all of the scattering atoms near the absorber:

$$\chi(k) = \sum_s \frac{N_s A_s(k) S_0^2}{k R_{as}^2} \exp(-2R_{as}/\lambda(k)) \exp(-2k^2\sigma_{as}^2) \cdot \sin(2kR_{as} + \phi_{as}(k)) \tag{3}$$

In Equation (3), the parameters that are of principal interest for coordination chemistry are the number of scattering atoms, N_s and the absorber–scatterer distance, R_{as}. However, there are a variety of other parameters that must either be determined or be defined in order to extract the chemically relevant information. Chief among these are $A_s(k)$ and $\phi_{as}(k)$. These represent, respectively, the energy dependence of the photoelectron scattering, and the phase shift that the photoelectron wave undergoes when passing through the potential of the absorbing and scattering atoms. These amplitude and phase parameters contain the information necessary to identify the scattering atom. Thus, for example, sulfur and oxygen introduce phase shifts, $\phi_{as}(k)$, that differ by approximately π. Unfortunately, both $A_s(k)$ and $\phi_{as}(k)$ depend only weakly on scatterer identity, and thus it is difficult to identify the scatterer with precision. This means that O and N, or S and Cl, typically cannot be distinguished, while O and S can.

The EXAFS amplitude falls off as $1/R^2$. This reflects the decrease in photoelectron amplitude per unit area as one moves further from the photoelectron source (i.e., from the absorbing atom). The main consequence of this damping is that the EXAFS information is limited to atoms in the near vicinity of the absorber. There are three additional damping terms in Equation (2). The S_0^2 term is introduced to allow for inelastic loss processes and is typically not refined in EXAFS analyses. The first exponential term is a damping factor that arises from the mean free path of the photoelectron ($\lambda(k)$). This serves to limit further the distance range that can be sampled by EXAFS. The second exponential term is the so-called "Debye–Waller" factor. This damping reflects the fact that if there is more than one absorber–scatterer distance, each distance will contribute EXAFS oscillations of a

slightly different frequency. The destructive interference between these different frequencies leads to damping in the EXAFS amplitude. The Debye–Waller factor, σ_{as}, is the root-mean-square deviation in absorber–scatterer distance. This damping is always present due to zero-point thermal motion, and may, for polyatomic systems, also occur as a consequence of structural disorder. As a consequence of the damping terms in Equation (3), EXAFS oscillations are typically only observed for atoms within approximately 5 Å of the absorbing atom.

In Equation (3) the backscattering amplitude and phase are assumed to depend only on the identity of the absorber and the scatterer. This derives from the so-called plane wave approximation, in which the curvature in the photoelectron wave is neglected and the photoelectron is treated as a plane wave.[34–36] For energies well above the X-ray edge (high k, short photoelectron wavelength) or for long absorber–scatterer distances this is a fairly reasonable assumption. It is not, however, a good assumption for most of the useful EXAFS region. Modern approaches to calculating amplitude and phase parameters (see Section 2.13.2.2) include spherical wave corrections to the amplitude and phase, thus introducing a distance dependence to A_s and ϕ_{as}.

2.13.2.1.2 *Multiple scattering*

The discussion above assumed that the X-ray excited photoelectron was scattered only by a single scattering atom before returning to the absorbing atom (e.g., Figure 6). In fact, the X-ray excited photoelectron can be scattered by two (or more) atoms prior to returning to the absorbing atom. Multiple scattering is particularly important at low k where the photoelectron has a very low energy and consequently a long mean-free path, allowing it to undergo extensive multiple scattering. Multiple scattering is particularly strong if the two scattering atoms are nearly collinear since the photoelectron is strongly scattered in the forward direction. In this case, the EXAFS oscillations due to the multiple scattering pathway (absorber → scatterer 1 → scatterer 2 → scatterer 1 → absorber in Figure 8) can be as much as an order of magnitude stronger than that due to the single scattering pathway (absorber → scatterer 2 → absorber).[37–39] Failure to account for multiple scattering can lead to serious errors in both EXAFS amplitude and phase, with consequent errors in the apparent coordination number and bond length.

Multiple scattering is extremely angle dependent. For scattering angles less than ca. 150° (the angle A–S_1–S_2 in the example above), multiple scattering is weak and can often be neglected. However, for angles between 150° and 180°, multiple scattering must be considered. The angle dependence of multiple scattering means that EXAFS can, at least in principle, provide direct information about bond angles. Even when accurate angular information cannot be obtained (see below), multiple scattering is still important because it gives certain coordinating groups unique EXAFS signatures. These include both linear ligands such as CO and CN^-, as well as rigid cyclic ligands such as pyridine or imidazole. This can, in some cases, improve the limited sensitivity of EXAFS to scatterer identity. For example, in biological systems water and the imidazole group of

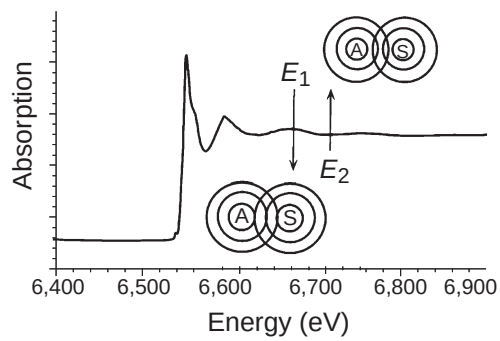

Figure 6 Schematic illustration of the physical basis of EXAFS oscillations. The X-ray excited photoelectron is represented by concentric circles around the absorbing atom (A), with the spacing between circles representing the de Broglie wavelength of the photoelectron. The photoelectron is scattered by surrounding atoms (indicated by a single atom S in the figure). At energy E_1, the out-going and back-scattered waves are in phase, resulting in constructive interference and a local maximum in photoabsorption cross-section. At a slightly higher energy E_2 (shorter photoelectron wavelength) the absorber–scatterer distance gives destructive interference and a local minimum in absorbance.

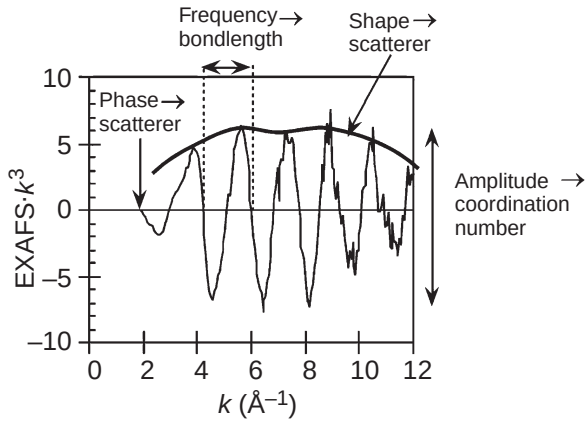

Figure 7 EXAFS spectrum calculated as in Equation (2). The structural information is encoded in the amplitude, the shape, the phase, and the frequency of the oscillations. Data have been multiplied by k^3 to enhance the oscillations at high k. These data (the Fe EXAFS for a di-μ-sulfido bridged Fe dimer) show a characteristic "beat" in amplitude at $k = 7\,\text{Å}^{-1}$, due to the presence of both Fe—S and Fe—Fe scattering). Note the noise at high k. For dilute samples, noise often limits the data to $k = 12\,\text{Å}^{-1}$ or less.

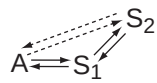

Figure 8 Illustration of single scattering (dashed line) and multiple scattering (solid lines) pathways. The absorbing atom is A, which is surrounded in this example by two scattering atoms, S_1 and S_2.

a histidine amino acid have nearest-neighbor EXAFS that is virtually indistinguishable (O vs. N). However, the imidazole group can be identified by its unique multiple-scattering signature.[37,40–42]

2.13.2.1.3 Other corrections to the EXAFS equation

There are a variety of additional correction factors that are not included in Equation (3). These are not widely used and can often be ignored in data analysis. However, for the most accurate description of the EXAFS, it is necessary to include several other effects. The discussion thus far has assumed that there is only a single core electron that is excited by the incident X-ray. However, the incident X-ray has sufficient energy to eject more than one electron, and this can give rise to additional small edge jumps above the main edge due to the opening of absorption channels creating double-hole configurations such as [1*s*4*p*], [1*s*3*d*], and [1*s*3*p*].[43–45] Multielectron excitations will take place whenever the incident X-ray energy equals the sum of two core-electron excitations. In practice, multielectron excitations are most important near the edge and are often detectable only for samples that have very weak EXAFS signals (for example, for ionic solutions, which have only weak cation-solvent interactions).[46–48] A second complication is that the photoelectron wave can be scattered not only by atoms but also by the potential barrier that develops when a free atom is embedded into a condensed phase. In this case, the free-atom potential is modified and the resulting scattering of the outcoming photoelectron produces weak oscillations in the absorption cross-section.[49,50] This can be treated as a variation in the atomic background,[51,52] and is sometimes referred to as "atomic" EXAFS. As with multielectron features, atomic EXAFS features are quite weak and are typically seen only near the absorption edge. Since this is a region that is very sensitive to background subtraction (the μ_0 in Equation (2)) it is not always clear what physical phenomenon is responsible for the observed spectral anomalies,[53] particularly in view of the similar appearance of multielectron excitations and atomic EXAFS.[54,55]

2.13.2.2 Programs for Calculating and Analyzing EXAFS

The analysis of EXAFS data can be divided into two stages: reduction of the measured absorption spectra to EXAFS (i.e., application of Equation (2)) and analysis of the $\chi(k)$ data to obtain structural parameters (N_s, σ_{as}, and R_{as}). Data reduction involves both normalization (Equation (2))

and conversion to k space (Equation (1)). Data analysis is, at least in principle, a relatively straightforward problem of optimizing the variable parameters in Equation (3) so as to give the best fit to the observed data using some sort of nonlinear least-squares fitting procedure. Over 20 programs are available to accomplish the data reduction and analysis.[56] Most are quite similar in their functionality.

In order to fit EXAFS data, it is first necessary to determine the parameters that define the scattering ($A_s(k)$, S_0^2, $\phi_{as}(k)$, and $\lambda(k)$). This can be done using *ab initio* calculations or from model compounds of known structure. In recent years, the available theoretical methods for quickly and accurately calculating these parameters have improved dramatically. *Ab initio* calculations are now relatively straightforward, with three main programs that are in wide use: FEFF,[39,57,58] EXCURVE,[41,59] and GNXAS.[60–62] Although these differ in the particulars of their approach to EXAFS, all give approximately the same structural parameters.[63] In contrast, older approaches, particularly those using the earliest plane-wave parameters[34–36] often fail to give accurate structural results. Despite these well-known errors,[64] publications using these parameters continue to appear occasionally in the literature. Regardless of what theoretical parameters are used, careful comparison with model compounds remains important for proper calibration of the calculated parameters.[65]

Using carefully calibrated parameters to determine S_0^2 and E_0, it is possible to obtain excellent accuracy for EXAFS bond length determinations. Typical values, determined by measuring data for structurally defined complexes, are 0.01–0.02 Å for nearest-neighbor distances and somewhat worse for longer distance interactions. The precision of bond-length determinations is even better, with experimentally determined reproducibilities as good as 0.004 Å.[66] Coordination number is less well defined, due in part to correlation between N and σ^2 (see Equation (3)). In many cases, EXAFS coordination numbers cannot be determined to better than ±1. As noted above, EXAFS has only weak sensitivity to atomic type. Typically it is only possible to determine the atomic number of the scattering atom to ±10. Despite these limitations, the ability to provide structural information, particularly highly accurate bond lengths, for noncrystalline systems, has made EXAFS an extremely important tool in coordination chemistry.

2.13.2.2.1 Fourier transforms

Although Equation (3) provides a complete description of the EXAFS oscillations, it is not a particularly convenient form for visualizing the information content of an EXAFS spectrum. As with NMR spectroscopy, Fourier transformation can be used to decompose a k-space signal into its different constituent frequencies.[67] This is illustrated using the EXAFS data[68] for a THF solution of CuCN·2LiCl. The EXAFS spectrum (Figure 9) clearly contains more than one frequency, based on the complex variation in amplitude. For EXAFS, the canonical variables are k (in Å^{-1}) and R (in Å), and the Fourier transform (FT) of an EXAFS spectrum gives a

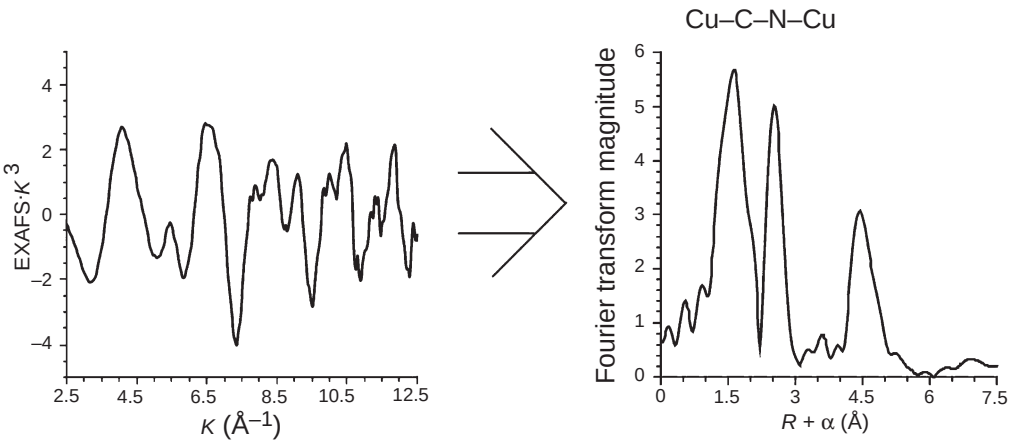

Figure 9 EXAFS data (left) and its Fourier transform (right) for a THF solution of CuCN·2LiCl.[68] The Fourier transform clearly shows three distinct peaks, reflecting the presence of three distinct absorber–scatterer interactions, as indicated above the Fourier transform.

pseudo-radial distribution function. The FT of the data in Figure 9 shows that there are three principal frequencies that contribute to this spectrum. These are due to scattering from the Cu nearest neighbors (C from the cyanide), the next-nearest neighbors (N from the cyanide), and the next-next-nearest neighbors (an additional Cu coordinated to the distal end of the cyanide). The third peak thus clearly shows formation of a $(CuCN)_n$ oligomer under these conditions. The FT amplitude is not a true radial distribution function since the amplitude cannot be related directly to electron density around the absorber due to the $A_s(k)$ factor and the damping factors in Equation (3), and the apparent distances in the FT are shifted by about -0.5 Å due to the phase shift $\phi_{as}(k)$. The unusually high intensity of the second and third peaks in Figure 9 is due to the near linearity of the Cu—C—N—Cu unit, which leads to intense multiple scattering.

The FT is useful for obtaining a qualitative understanding of a system. However, FTs are subject to several potential artifacts and cannot be used for quantitative data analysis. Depending on the resolution of the data (see below), multiple shells of scatterers do not necessarily give rise to multiple peaks in the FT.[69] Perhaps more important, two peaks may appear to be well resolved despite the fact that they have substantial overlap. This is illustrated in Figure 10, where the top FT is for the sum of two EXAFS spectra (simulated for Mn—O distances of 1.9 Å and 2.1 Å) while the bottom shows the FTs of the two individual components. Although the two peaks appear to be well resolved, each peak, in fact, contains significant contributions from the other scatterer. This phenomenon is due to the fact that the FT is a complex function, including both real and imaginary components. Typically (e.g., Figure 10) what is plotted is the modulus of the FT, thus losing all phase information. In Figure 10, the Fourier components from the two different scatterers interfere destructively, leading to the minimum in the modulus.

Interference such as that in Figure 10 is particularly important if the data are Fourier filtered. Fourier filtering involves selecting certain frequencies in R space to use for a back FT (back into k space). Filtering can greatly simplify the curve-fitting problem, since the filtered data contains only a single shell of scatterers (this amounts to dropping the summation in Equation (3)). However, as illustrated by Figure 10, filtering can have unexpected consequences. Neither of the peaks in the top panel actually represents the scattering from a single atom, despite the apparent resolution of the data; attempts to fit these as though they represent single shells leads to erroneous conclusions.[69]

2.13.2.2.2 Curve fitting

A typical coordination complex might have six different nearest-neighbor distances, together with a larger number of longer distance interactions. Although each of these contributes a slightly different signal to the overall EXAFS, it is not realistic to refine all of the different absorber–scatterer

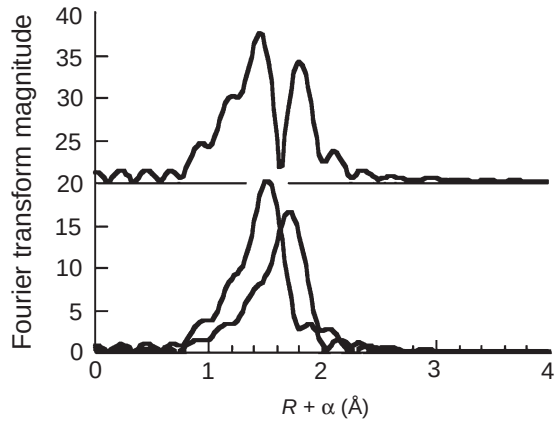

Figure 10 Fourier transform of the simulated EXAFS for two shells of scatterers. Data calculated for Mn—O distances of 1.9 Å and 2.1 Å. (top) FT of the sum of the EXAFS signals of each shell. (bottom) FTs of the two individual components. Although there is significant overlap in the two shells, the FT of the sum appears to show baseline separation as a consequence of phase differences in the Fourier terms.

interactions. Typically, absorber–scatterer interactions are grouped into "shells." A shell is a group of similar scatterers at approximately the same distance from the absorber. A non-linear least-squares fitting algorithm is then used to model the observed data using Equation (3). A frequent problem is to determine whether the inclusion of an additional shell (i.e., an additional sum in Equation (3)) is justified. Since data are available only over a finite k range and since there is always some noise, particularly at high k, it can be difficult to distinguish genuine improvements in the fit from the inevitable improvement that occurs when a least-squares fitting engine is provided with more variable parameters. One solution is to not use a simple mean-square deviation (Equation (4)) as the measure of fit quality, but to replace this with a reduced chi-squared statistic, ξ^2 (Equation (5)).[64]

$$F = \sqrt{\frac{\sum_{i=1}^{N}(\chi_{\text{obs}}(k_i) - \chi_{\text{calc}}(k_i))^2}{N}} \tag{4}$$

$$\xi^2 = \frac{(N_{\text{idp}}/\nu)\cdot\sum_{i=1}^{N}(\chi_{\text{obs}}(k_i) - \chi_{\text{calc}}(k_1))^2/\varepsilon_i^2}{N} \tag{5}$$

In Equation (5), ν is the number of degrees of freedom, calculated from Equation (6), where N_{idp} is the number of independent data points and N_{var} is the number of variables that are refined.

$$\nu = N_{\text{idp}} - N_{\text{var}} \tag{6}$$

The sum in Equation (5) is calculated over all of the measured data points, N, and the deviation at each point is weighted by $1/\varepsilon_i^2$, where ε_i is the root-mean-square uncertainty in χ_{obs}. The $1/\nu$ weighting introduces a penalty for adding additional, unnecessary, shells of scatterers.

The number of independent data points in an EXAFS spectrum is not equal to the number of measured data points.[64,70] In most cases, EXAFS spectra are significantly oversampled, so that $N_{\text{idp}} \ll N$. The limitation in N_{idp} results from the fact that EXAFS spectra are "band-limited" and thus do not contain contributions from all possible frequencies. N_{idp} can be estimated as in Equation (7).

$$N_{\text{idp}} = \frac{2\Delta k \Delta R}{\pi} \tag{7}$$

Since k_{min} is approximately 2 Å, k_{max} is often 12–14 Å^{-1} or less, and the R range over which EXAFS signals are seen is approximately 1−4 Å, N_{idp} can be 20 or less, although larger values are possible. For filtered data, N_{idp} is often much smaller; For $\Delta R \leq 0.8$ Å, N_{idp} may be as small as 6–8. In such cases, it may be impossible to obtain meaningful fits using two shells of scatterers. If three parameters (R, σ^2, and N) are refined per shell, then for two shells there may be no free parameters. Although the fit may reproduce the data perfectly, the refined structural parameters need not be physically meaningful.[71]

The number of degrees of freedom increases linearly with R, therefore if data can be detected to high R, for example by making measurements at very low temperatures, it should be possible to obtain sufficient data to permit a detailed description of the structure. Outer shell data is particularly interesting because it is sensitive to multiple scattering, and thus can provide information about the three-dimensional geometry of the complex. Unfortunately, the number of multiple-scattering atoms and the number of possible multiple-scattering paths (e.g., Figure 8), increases approximately as R^2. This makes it unlikely that EXAFS alone will ever be able to provide reliable structural information for atoms beyond the third, or perhaps the fourth coordination shell.[69,72]

2.13.2.3 Limitations of EXAFS

The ability to determine accurate structures for noncrystalline samples has made EXAFS extremely useful in coordination chemistry. However, there are several practical limitations to the

ability of EXAFS to probe structure. One involves the ability of EXAFS to resolve contributions from two different scatterers. The best resolution that can be achieved[73] is given in Equation (8).

$$\Delta R \geq \pi/2\Delta k \tag{8}$$

This gives $\Delta R \geq 0.13$ Å for data to $k_{max} = 12$ Å^{-1}. However, this estimate is generally too optimistic as illustrated by Figure 11, which shows pairs of simulated EXAFS spectra for one shell (dashed lines) and two shells (solid lines).[69] The top trace shows the simulation for a pair of scatterers separated by 0.25 Å ($R_1 = 1.75$ Å, $R_2 = 2.00$ Å). There is an obvious "beat" in the EXAFS amplitude at $k \approx 8$ Å^{-1} which distinguishes these data from the EXAFS for a single shell at the same average distance (1.875 Å). The middle simulation shows that there is still a beat when ΔR decreases to 0.15 Å, although the beat has moved close to k_{max}. It is straightforward to distinguish between two shells and a single shell at the average distance (1.925 Å, dashed line). However, if the single-shell simulation is damped with an exponential damping factor (lower traces) it is now nearly impossible to distinguish between one shell (dashed line) and two shells (solid line). It is only at high k, where the noise in an experimental spectrum is the largest, that the one- and two-shell simulations are distinguishable. It is unlikely that these spectra could be distinguished for

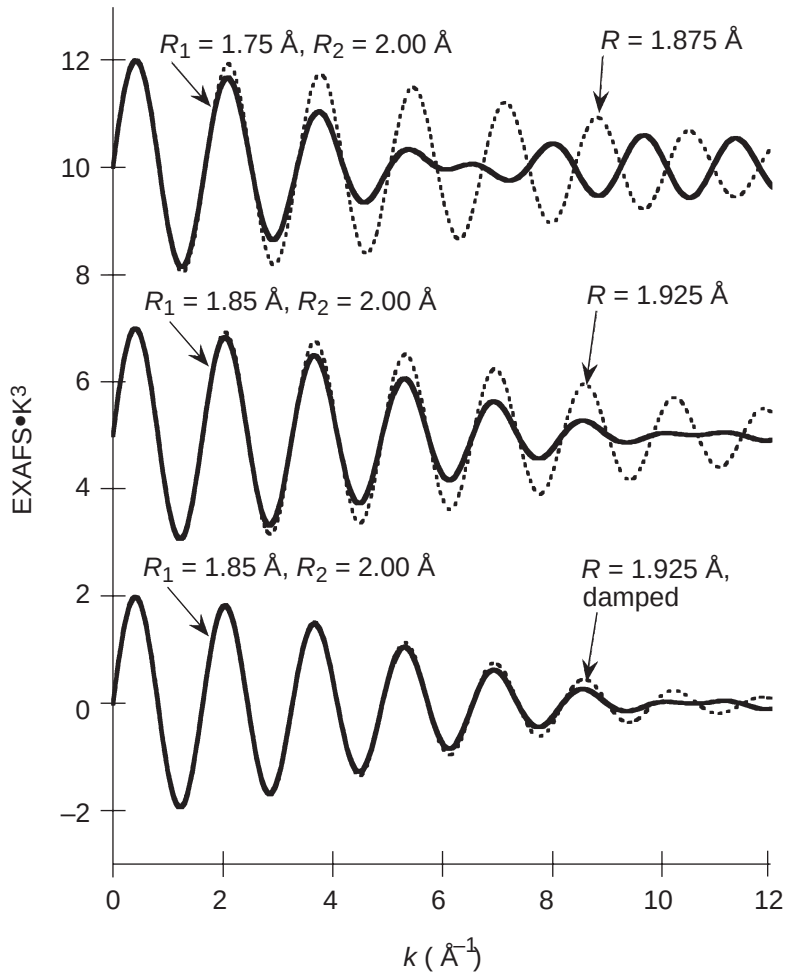

Figure 11 Simulated EXAFS data for one-shell (dashed line) and two-shell (solid line) models. In each case, the one-shell simulation has a distance equal to the average of the two-shell simulation. For the top and middle simulations, both one-shell and two-shell data use the same Debye–Waller factor. For the bottom simulation, the one-shell Debye–Waller factor has been increased to give the best agreement with the two-shell data. Two shells with a small Debye–Waller factor are, for any realistic noise level, indistinguishable from a single shell with a large Debye–Waller factor.

real (i.e., noisy) data, even though $\Delta R > \pi/2\Delta k$. This is because the Debye–Waller factor (σ^2 in Equation (3)) can mimic the damping that is caused by the presence of two shells of scatterers. This illustrates the fact that although the resolution limit of EXAFS is much better than those of most crystallography, it is nevertheless sufficiently poor that it is often not possible to resolve the contributions from different nearest neighbors, even when they are known chemically to be present at different distances.

The definition of resolution is more complicated if there is more than one type of scattering atom. The presence of two different kinds of scattering atoms may increase the effective resolution. For example, the EXAFS signals for F and Cl have quite different $A_s(k)$ and $\phi_{as}(k)$. This means that F and Cl EXAFS signals *can* be resolved even if the distances are identical, although this can be complicated by destructive interference between the O and Cl signals.[65] Conversely, the presence of several different scatterers at about the same distance can change the apparent amplitude of an EXAFS feature, thus leading to misassignment of the chemical identity of the scatterer. For example, a Cu–Cu shell in the CuA site of cytochrome oxidase[74] was initially assigned as a Cu–S interaction[75–77] due to interference and the limited k range of the data.

2.13.2.4 Applications of EXAFS to Coordination Chemistry

There are over 15,000 papers dealing with the application of X-ray absorption spectroscopy. Since the development of intense, readily accessible synchrotron sources in about 1980, there has been a steady growth in the applications of EXAFS (see Figure 12). Although the applications cover all areas of science, a significant fraction of these address questions of interest to coordination chemistry. Given the size of this literature, it is not realistic to report on all of the applications of EXAFS. In selecting the examples below, no attempt has been made to provide a comprehensive survey of the literature; a number of excellent reviews exist that survey different field-specific applications of EXAFS[27,78–91] together with several monographs on the subject.[86,92–94] Rather, the examples below have been selected to illustrate important types of applications.

2.13.2.4.1 De novo structure determination

For de novo structure determination, one measures the EXAFS spectra for one or more of the atoms in a sample and uses this information to determine the structure around the absorbing atom. In principle this is straightforward, although in practice the analysis is often complicated by the limitations discussed above. It is seldom the case that EXAFS can provide reliable information for scatterers that are more than 5 Å from the absorbing atom and in most cases EXAFS provides little or no angular information. Despite these limitations, de novo structure determination remains one of the most important applications for EXAFS. The areas in which de novo structure determination are most important are those in which crystallography cannot be used. One key area is bioinorganic chemistry. It has been estimated that one-third of all proteins bind

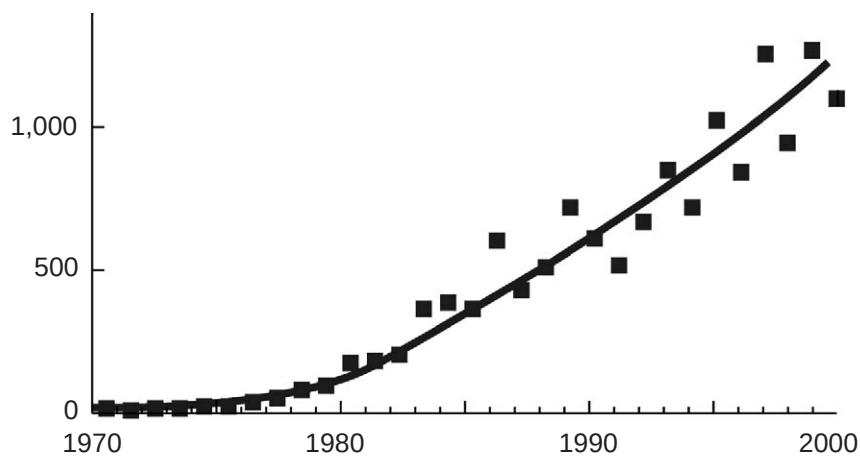

Figure 12 Number of XAS papers published per year. Solid line is a polynomial fit to the data.

metals. In many cases, the metal is at the active site, and thus structural characterization of the metal site is critical to a detailed understanding of the protein. Unfortunately, many proteins are difficult to crystallize, particularly when the form of interest is an unstable intermediate. Even when a protein *can* be crystallized, many protein crystal structures lack sufficient resolution to define the metal site accurately, and in some cases the metal site may be completely disordered. In these cases, EXAFS is the only technique that can provide direct structural information for the active site metal, and there are hundreds of examples of EXAFS being used to provide structural insight.[83,84,91,95]

Exactly the same arguments make EXAFS a useful tool for materials chemistry, where many of the samples of interest are amorphous. Examples include studies of glasses,[96,97] of catalysts,[80,98–100] of liquids,[82,101–103] and of surfaces.[27,104–109] The limitations for amorphous samples are similar to those for biological samples, with the important additional complication that the metal of interest is typically not present in a single site but rather in an ensemble of sites. The EXAFS thus represents only the average structure and need not reflect the structure of any one of the individual absorbing sites.

2.13.2.4.2 Solution structure determination

Although X-ray crystallography is extremely powerful as a structural probe, it only provides a description of the structure in the solid state. Since most chemical reactions take place in solution, determination of the solution structure is important for understanding reactivity. In some cases, for example in studies of transition metal cations dissolved in aqueous solution,[110–112] or for organometallics dissolved in solution,[68,113] EXAFS offers the only direct route for structure determination. In other cases, it is possible to crystallize the solute, but solution EXAFS is still important to determine if the crystallographic structure accurately represents the molecule of interest when it is dissolved in solution. The latter is particularly important for multinuclear aggregates, which might be expected to dissociate into smaller units when dissolved.[114] There have, to date, been relative few examples of EXAFS being used to determine solute structure, or to compare solute and crystalline structure. However, with the increased availability of synchrotron radiation, this is an area that is likely to grow in importance.

2.13.2.4.3 Resolution of crystallographic disorder

Although most applications are to noncrystalline materials, EXAFS is also useful for characterizing the structure of metal ions in crystals. This is because crystallographic structure determination can suffer from resolution limitations analogous to those in EXAFS. In particular, the crystallographically determined structure for a metal ion that occupies a high symmetry site in a crystalline lattice is necessarily high symmetry, even though individual ions may have much lower symmetry. In such cases both X-ray diffraction, which gives the structure averaged over all unit cells, and XAS, which gives the structure averaged over all metal sites, may be necessary for a complete description of the structure. For example, the Jahn–Teller active Cu^{2+} may crystallize in a high symmetry site with six crystallographically identical bond lengths, in apparent violation of the Jahn–Teller theorem. EXAFS has been used to show[115] that the Cu site in bis[tris (2-pyridyl)methane]Cu^{2+} nitrate has the expected tetragonal distortion, with four short (2.04 Å) and two long (2.25 Å) Cu–N distances, despite the $\bar{3}$ symmetry of the crystallographic site, and to show[116] that $CuCl_6^{4-}$ ion in (3-chloroanilinium)$_8(CuCl_6)Cl_4$ has a conventional tetragonally elongated structure rather than the tetragonally compressed structure that had been suggested from the crystallography.[117]

Similar concerns apply in studies of variable-composition crystals such as doped samples (e.g., high-T_c superconductors)[118–121] and ceramics.[122–126] Often, these samples are crystalline and have well-defined three-dimensional structures. However, the crystallographic structure gives only the average location of the major components of the crystal, and is insensitive to the location of the dopant ions. Moreover, crystallography, which reflects the structure averaged over all unit cells, may not give an accurate description of the local structure of the individual ions. For example, Vegard's law predicts a linear variation in lattice constant on going between composition extremes in a solid solution. EXAFS can be used to determine whether this variation is reproduced in the bond lengths around the individual components of the solid solution.[127,128] The combination of

EXAFS with crystallography thus provides a more detailed structural characterization than would be possible from either measurement alone.

2.13.2.4.4 Time-dependent structural evolution

An exciting new development in XAS is the ability to measure time-resolved spectra. This provides a powerful tool for investigating the reactivity of solids in catalysis and solid-state chemistry.[129,130] To date, most studies have been limited to a time resolution of seconds although this can, in principle, extend into the femtosecond regime.[130,131] The latter offers the possibility of probing directly the structure of photoexcited states, thus following directly the structural changes that accompany a chemical.[132,133] Before this can be widely applied, more intense femtosecond X-ray sources are needed.[134] At present, time-resolved studies in the second to millisecond times are becoming relatively straightforward, and are providing important new chemical information.

Although other probes may be substantially easier to use, XAS is sometimes the only method that is sensitive to the structures of interest, particularly for solid-state samples and *in situ* studies of catalysts.[135–138] For example, in a study of the reduction of NiO, time-resolved X-ray diffraction had shown that the catalyst went directly from $NiO \rightarrow Ni$ without a well-ordered intermediate phase,[137] but could not rule out the existence of an amorphous NiO_x phase, since the diffraction was not sensitive to disordered phases. However, the formation of an intermediate phase could be ruled out by time-resolved EXAFS. A similar situation exists for spectroscopically "silent" metals (d^{10} systems), which are difficult to probe with methods other than XAS. Examples that are important in bioinorganic chemistry include Cu^{+1} and Zn^{2+}. For carboxypeptidase, time-resolved XAS could be used to determine the rate of change of the native Zn^{2+} site, while conventional UV–visible methods could only be used on the Co^{2+} substituted enzyme.[139] The importance of XAS in both of these examples is as a tool for measuring rate constants.

A second area where time-resolved EXAFS is important is for structural characterization of reactive intermediates. Reactive intermediates are difficult or impossible to crystallize. They may, however, be accessible to structural characterization by EXAFS. The difficulty is that a bulk technique such as EXAFS cannot easily be used to measure structure for minor components in a complex mixture. However, mathematical approaches such as principal component analysis[140–142] can be used to extract information about relatively minor components if a large enough number of individual spectra are measured. For example, in a study of the oxidation of *n*-butane over a V_2O_5 catalyst, hundreds of XAS spectra were measured with 1 second time resolution.[143] No single spectrum gave sufficient information that could be used to distinguish the different species that were present. However, by using principal component analysis, it was possible to identify contributions from three different species (one present at only ca. 20 mol.%) that contributed to the overall data variation. From comparison with standards, these components could be assigned to V^{5+}, V^{4+}, and V^{3+}.

Time-resolved studies frequently make use of a dispersive geometry in which the synchrotron beam is focused onto the sample using a curved crystal,[144] as shown in Figure 13. In this geometry, the sample is illuminated with all X-ray energies simultaneously. The transmitted X-rays are dispersed onto a position-sensitive detector, allowing much more rapid measurement of the spectrum. However, because this is a transmission geometry, dispersive measurements are limited to relatively concentrated samples; dilute samples require the fluorescence geometry shown in Figure 4. For fluorescence, the time resolution is limited to the speed with which the monochromator can be scanned. This is typically several seconds per scan, although there are recent advances in rapid-scanning monochromators that can extend this to the millisecond regime.[145,146] Extremely fast time resolution (nanosecond to femtosecond) requires a pump-probe experiment with a pulsed X-ray source.[130,131,133]

2.13.3 X-RAY ABSORPTION NEAR EDGE STRUCTURE

A typical XANES spectrum is shown in Figure 14 (this is an expansion of the edge shown in Figure 2). It is clear that the XANES region is more complex than simply an abrupt increase in absorption cross-section. There are several weak transitions below the edge (pre-edge transitions) together with structured absorption on the high energy side of the edge. Some XANES spectra show intense narrow transitions on the rising edge (these can be much more intense than the transition at the edge in Figure 14). These are often referred to as "white lines" in reference to the fact that when film was used to record X-ray absorption spectra, an intense transition would

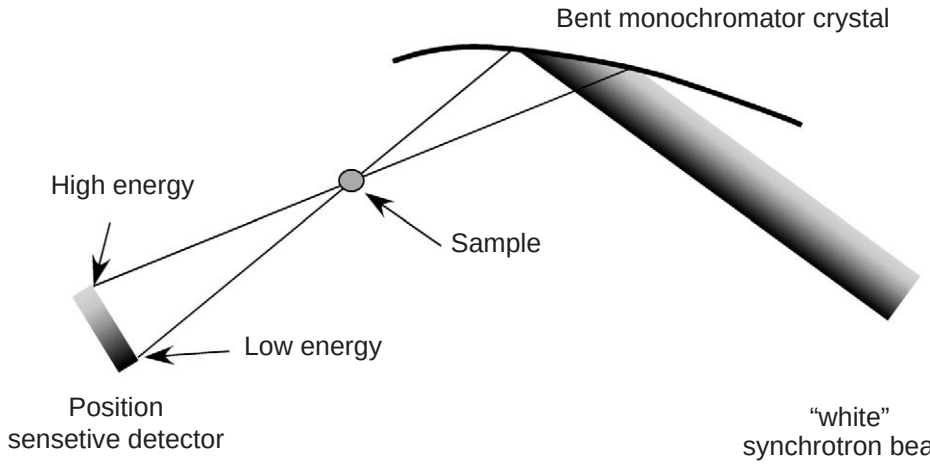

Figure 13 Dispersive XAS geometry. A broad band of X-ray energies is focused onto the sample using a curved crystal and detected using a position-sensitive detector. Time resolution is limited only by the readout time of the detector (microseconds in principle) but samples are limited to those accessible by transmission.

absorb all of the incident X-rays, thus preventing the film from being exposed and leaving a white line on the film. Above the edge, there are a variety of structures that show generally oscillatory behavior, ultimately becoming the EXAFS oscillations.

The same physical principles govern both the EXAFS region and the XANES region. However, in the near edge region the photoelectron has low kinetic energy, giving it a long mean-free path. In addition, the $\exp(-k^2)$ dependence of the Debye–Waller factor means that this damping factor is negligible in the XANES region. These effects combine to make the XANES region sensitive to longer distance absorber–scatterer interactions than are typically sampled by EXAFS. This greatly complicates simulation of XANES structure, since many interactions and a large number of multiple scattering pathways need to be included.[147–149] However, the sensitivity to multiple scattering is, at least in principle, an advantage since it provides the possibility of extracting information about the three-dimensional structure from XANES spectra. Although much progress has been made recently in the theoretical modeling of XANES,[111,112,147–150] most simulations of XANES structure remain qualitative. Nevertheless, the ability to make even qualitative fingerprint-like comparisons of XANES spectra can be important. If a representative library of reference spectra is available, spectral matching can be used to identify an unknown. Beyond this qualitative application, there are three main ways in which XANES spectra are used: to determine oxidation state, to deduce three-dimensional structure, and as a probe of electronic structure.

2.13.3.1 Sensitivity of XANES to Oxidation State

The energy of an absorption edge is not well defined. It can be taken as the energy at half-height or, more commonly, as the maximum in the first derivative with respect to energy. However, as

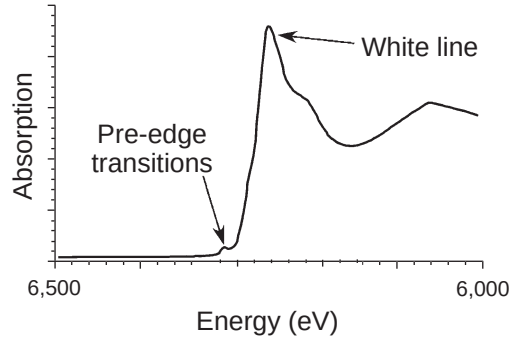

Figure 14 Expansion of the XANES region for the data shown in Figure 2, showing different features within the XANES region.

shown by Figure 14, edge spectra frequently have unresolved transitions superimposed on the rising edge. These will affect any attempt to define a unique "edge energy." Despite this ambiguity, edge energies have proven extremely useful in determining the oxidation state of the absorber. It has been known for many years that the energy of an edge increases as the oxidation state of the absorber increases.[151] This can be explained using an electrostatic model, since atoms with a higher oxidation state should have a higher charge, thus requiring more energetic X-ray to eject a core electron. An alternative interpretation of edge energies treats the edge features as "continuum resonances."[152] A continuum resonance involves excitation of a core electron into a high-energy state (above the continuum) that has a finite lifetime. An example is the potential well created by the absorbing and scattering (nearest neighbor) atoms. As the absorber–scatterer distance gets shorter, the energy of the continuum state increases as $1/R^2$. Since higher-oxidation-state metals have shorter bond lengths, both models predict an increase in edge energetic with increasing oxidation state. Regardless of which explanation is most appropriate, the phenomenological correlation between edge energy and oxidation state is well established, and is widely used in coordination chemistry.

2.13.3.2 Multiple Scattering and XANES

As noted above, multiple scattering is particularly important in the XANES region. In principle, this means that it should be possible to determine the three-dimensional structure of the absorbing atom from analysis of the XANES features. Empirically, this is certainly the case; the XANES region is quite sensitive to small variations in structure, to the extent that two sites having identical EXAFS spectra can nevertheless have distinct XANES spectra.[65] This sensitivity is, at least in part, due to the fact that geometrical differences between sites alter the multiple scattering pathways, and thus the detailed structure in the immediate vicinity of the absorption edge. Although there has been progress in the interpretation of XANES spectra,[111,149] the agreement between calculated and observed spectra remains relatively poor in most cases. The development of theoretical and computational methods that will permit detailed interpretation of XANES spectra is one of the outstanding problems in the field.[153]

2.13.3.3 Bound State Transitions in XANES

The weak pre-edge transitions (Figure 14) arise from bound state transitions. For the K edge of a first row transition metal, these arise from $1s \rightarrow 3d$ transitions, and are observed for every metal that has an open $3d$ shell.[154] Although the $1s \rightarrow 3d$ transition is forbidden by dipole selection rules, it is nevertheless observed due both to $3d + 4p$ mixing and to direct quadrupolar coupling.[155] The sensitivity to $3d + 4p$ mixing means that the intensity of the $1s \rightarrow 3d$ transition can be used as a probe of geometry, with the intensity increasing as the site is progressively distorted from a centrosymmetric environment (i.e., octahedral < square–pyramidal < tetrahedral)[156] or to distinguish between square–planar (i.e., centrosymmetric) and tetrahedral sites.[157] With careful analysis, the details of the $1s \rightarrow 3d$ transitions can be used to explore the electronic structure of the absorbing atom.[158]

The analogous $1s \rightarrow 4d$ transition for second transition series metals is generally not observed. These edges occur at higher energy, where monochromator resolution is worse and core-hole lifetimes, which determine the intrinsic line width of a transition, are much shorter.[11] This results in broad edges for which the weak $1s \rightarrow 4d$ transitions are undetectable. However, for second row transition metals, it is still possible to obtain information about the empty bound states by measuring data at the L_3 and L_2 edges, which have $2p \rightarrow 4d$ transitions.[159] The low energy of these edges makes the transitions relatively sharp, and the $2p \rightarrow 4d$ transition is allowed, thus making these transitions intense. Similar spectroscopic advantages (narrow lines, allowed transitions) are found for L edge studies of the first transition series metals.[160,161] However, in this case the very low edge energy is experimentally challenging, requiring the use of ultra-high vacuum for the sample.

In addition to excitations into the $3d$ (or $4d$) shells, XANES can also be used to probe higher-lying excited states. For atomic spectra, a complete series of "Rydberg" transitions can be seen.[162,163] For first transition series metals, the allowed $1s \rightarrow 4p$ transition is sometimes observed. This is the assignment given to the intense transition observed on the rising edge for Cu^{I} and for some square–planar Cu^{II} and Ni^{II} complexes. From studies of model compounds, it is found that the "$1s \rightarrow 4p$" transition is intense for square–planar complexes but weak for tetrahedral

complexes, as shown in Figure 15.[164,165] and thus can be used to deduce geometry. The greater intensity for square–planar complexes may be due to decreased mixing between the empty $4p$ orbital ($4p_z$) and the ligand orbitals. This intensity of the $1s \rightarrow 4p$ transition is even more dramatic for 2-coordinate Cu^{I}.[166]

An alternative, complementary, approach to electronic structure information is to use ligand XANES rather than metal XANES. This is particularly promising as a tool for investigating sulfur or chlorine ligands[167–169] and has been used to quantitate the amount of metal–ligand orbital mixing (i.e., the covalency) of different complexes.[170] For example, excitation at the Cl K edge gives rise to an allowed $1s \rightarrow 3p$ transition. Since the Cl $3p$ orbitals are bonding orbitals in metal chlorides, the lowest energy transition at the Cl edge is actually a $1s$(Cl) $\rightarrow$ HOMO transition, where the HOMO has both metal $3d$ and Cl $3p$ character. The intensity of this transition is a direct measure of the percent $3p$ character of this orbital (i.e., the covalency of the complex). Ligand XANES can be more useful than metal XANES due to the fact that the transitions of interest from a bonding perspective are $1s \rightarrow 3p$ for S or Cl ligands and $1s \rightarrow 3d$ for a metal from the first transition series. The former is an allowed transition while the latter is forbidden by dipole selection rules, and consequently much weaker and harder to detect.

2.13.3.4 Multi-electron Transitions in XANES

The single-electron bound-state transitions described above can be written as $\underline{1s}\ (V^*)^1$, where the underline in $\underline{1s}$ refers to a hole in the $1s$ orbital, and V* is a valence orbital. At higher photon energies, the X-ray has sufficient energy to excite an extra electron into the valence band (e.g., $V \rightarrow V^*$) resulting in double excitations such as $\underline{1s}\ \underline{V}\ V^{*2}$. In this notation, excitation of the core electron to the continuum is described as $\underline{1s}\ \varepsilon_p$, where ε_p indicates a p-symmetry photoelectron, with variable energy ε. The continuum states also have the possibility of multi-electron excitations, giving final states such as $\underline{1s}\ \underline{V}\ V^{*1}\ \varepsilon_p$. This class of multi-electron transition is sometimes referred to as shake-up transitions, to reflect the description of the excess energy as "shaking" a second electron into a higher-lying state.[171,172]

In addition to shake-up transition, a second class of multi-electron transition is possible, as illustrated in Figure 16. Excitation of a core electron has the effect of converting an atom with atomic number Z into an atom with an apparent atomic number of $Z+1$. This means that, for example, in the $\underline{1s}4p^1$ state of Cu^{II}, the valence electrons experience the effective nuclear charge of Zn^{II}. The increased nuclear charge lowers the energy of the Cu^{II} $3d$ orbitals so that they are now lower than the ligand orbitals (Figure 16b and c). Two transitions are now possible: the direct $\underline{1s}3d^9 4p^1$ transition (Figure 16b) and the multielectron transition to $\underline{1s}3d^{10}4p^1\underline{L}$, in which a ligand electron has been transferred to the lower-energy Cu $3d$ orbital. The latter gives a lower-energy excited state, and is often referred to as a shake-down transition. Shake-down transitions are seen frequently in photoelectron spectroscopy but have not been invoked often in XANES. One prominent exception is Cu^{II}, where polarized XANES spectra and theoretical calculations provide good evidence for shake-down transitions.[157,173–175] The large covalency of many Cu^{II} complexes

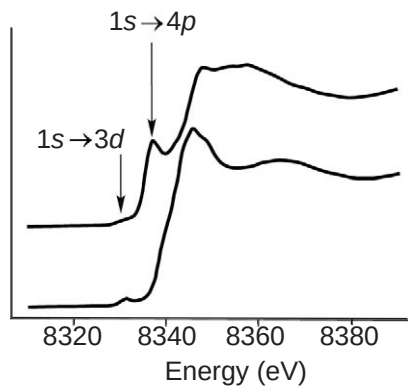

Figure 15 XANES spectra for 4-coordinate Ni^{II}, redrawn from data in Ref. 164. (top) Ni(cyclam) $(ClO_4)_2$ (square–planar) ; (bottom) $(Me_4N)_2NiCl_4$ (tetrahedral). Note the weaker $1s \rightarrow 3d$ transition and stronger $1s \rightarrow 4p$ transition for the square–planar site.

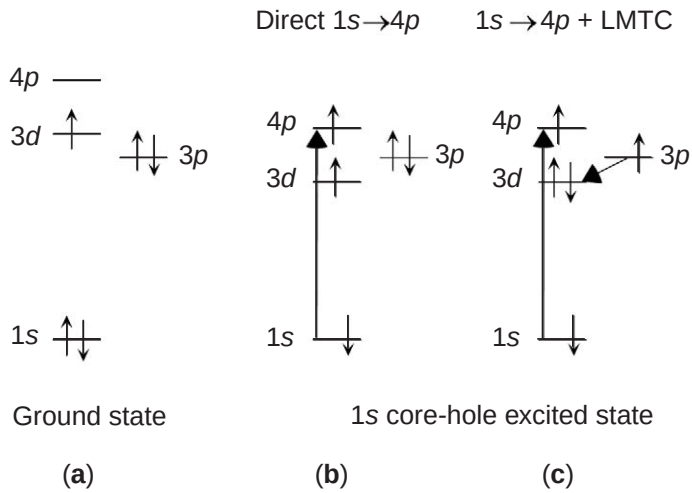

Figure 16 Schematic illustration of the energy levels involved in bound-state XANES features for 3*d* transition metals. For each diagram, metal orbitals (1*s*, 3*d*, 4*p*) are on the left and ligand orbitals (3*p*) are on the right. (a) Ground state; (b) 1*s* core-hole excited state showing direct $1s \rightarrow 4p$ transition; (c) 1*s* core-hole excited state showing multielectron $1s \rightarrow 4p$ plus ligand-to-metal charge transfer shake-down transition. Due to the higher effective charge of the core-hole excited state, the multielectron transition is at lower energy than the direct transition. The intensity of the shake-down transition is a measure of the covalency of the site (i.e., the metal $3d+$ ligand $3p$ mixing).

makes shake-down transitions more important here, but it seems likely that shake-down and other multielectron transtions[176] contribute to many XANES spectra.

2.13.3.5 Applications of XANES to Coordination Chemistry

XANES spectra are much easier to measure than EXAFS spectra since even weak transitions are considerably more intense than EXAFS oscillations at high k. A second advantage of XANES spectra is that they can often be treated spectroscopically—that is, that individual spectral features can be attributed to specific features in the electronic structure. In contrast, EXAFS spectra are spectroscopically detected scattering patterns; it is not possible to attribute a specific EXAFS oscillation to a specific structural feature. Despite these advantages, and the fact that the XANES region is inevitably scanned during the process of measuring EXAFS spectra, relatively little use has been made of XANES beyond qualitative comparisons of an unknown spectrum to reference spectra. The most common qualitative use is for oxidation state assignment, although near-edge features have also been used to distinguish metal-site geometry (e.g., Figure 15).

The complexity of XANES spectra, and in particular their sensitivity to multiple scattering from distant atoms, is largely responsible for the relatively limited attention that XANES spectra have received for quantitative analyses. With the development of new theoretical and computational approaches to XANES,[148,149,158,169,177] the utility of XANES for investigating coordination complexes is likely to increase.

2.13.4 HIGHER RESOLUTION XAS

Despite the numerous applications of XAS, XAS spectra have, in general, quite limited resolution. For XANES, resolution limits are the consequence of relatively broad spectral lines and severe spectral overlap. Resolution can be improved, in some cases quite dramatically, by using polarization-dependent measurements to reduce spectral overlap (Section 2.13.4.1) or by using inelastic scattering (high-resolution fluorescence) to reduce line widths (Section 2.13.4.2). For EXAFS, one of the most serious resolution limitations results from the fact that EXAFS is sensitive to all of the absorber in a sample; if two different metal sites are present, EXAFS will give only the average structure. This can be addressed, in some cases, by using high-resolution fluorescence to

measure site-specific EXAFS spectra (Section 2.13.4.2), and in other cases by using spatially resolved EXAFS to resolve the EXAFS spectra from different absorbers (Section 2.13.4.3).

2.13.4.1 Polarization-dependent Measurements

Synchrotron radiation is naturally polarized in the plane of the electron orbit. This can be used with oriented (typically single crystal) samples to make polarization-dependent measurements. In addition, it is possible to prepare circularly polarized X-ray beams, either by manipulating the properties of the electron orbit in the synchrotron[178,179] or by using the X-ray analog of a quarter-wave plate.[180,181]

2.13.4.1.1 Linearly polarized measurements

Linear dichroism can be used to extract additional information from both EXAFS and XANES spectra.[182,183] For EXAFS, polarization-dependent measurements can add angular resolution to the normal EXAFS structural information,[184] allowing, for example, distinction between in-plane and axial bond lengths.[185,186] or detection of weak signals in the presence of strong signals by orienting the sample to minimize contributions from the strong signals.[187] Although often used with single crystals, polarized EXAFS can be used to determine the orientation dependence of the structure for any oriented sample. Examples of noncrystalline orientation include studies probing the structure of substrates adsorbed on surfaces,[188] the orientation of dye molecules in Langmuir–Blodgett films,[189] and the orientation of metal active sites in protein multilayers[190,191] and monolayers.[192]

Polarized XANES measurements have similar advantages to polarized EXAFS, and have been widely used to determine the orientation of the absorber. A second use of polarized XANES is to determine the symmetry properties of particular edge features, and thus to limit the possible interpretation of particular transitions.[165,175,193,194] For example, the observation of fourfold periodicity was used to prove that the $1s \rightarrow 3d$ transitions in first row transition metals arise from direct quadrupolar coupling.[155,195]

2.13.4.1.2 X-ray MCD

If a circularly polarized X-ray beam is used, it is possible to measure the circular dichroism (CD) of a sample. By far the most important use is to study the circular dichroism that is induced by application of a magnetic field, i.e., MCD. Just as in the UV–visible region, X-ray MCD makes use of the fact that the energy of an orbital will vary depending on relative orientation of the local and the applied magnetic field. This allows one to measure element-selective magnetic properties of a sample, since each element can be probed independently. X-ray MCD spectra can be used to deduce the local spin and orbital moments of an atom.[196–198]

Although most widely used for studies of magnetic materials, it is also possible to use X-ray MCD to study metal sites in proteins.[199] Although X-ray MCD is most often used to study XANES features, it can also be used to probe EXAFS. In this case, the dichroic signal is limited to scattering atoms that are affected by the magnetic field. This can be used to enhance the detectability of the EXAFS signal from a small number of magnetic neighbors in the presence of a large EXAFS signal from nonmagnetic scatterers.[200–202]

2.13.4.1.3 Natural circular dichroism

Very recently, it has been shown that it is also possible to measure natural (i.e., nonmagnetic) circular dichroism for X-ray absorption.[203] For crystals of $Na_3Nd(digly)_3 \cdot 2NaBF_4 \cdot 6H_2O$, the dissymmetry, $(A_L - A_R)/(A_L + A_R)$, is approximately 10^{-3}, comparable to dissymmetries seen in UV–visible CD spectra. However, for crystals of $2[Co(en)_3Cl_3] \cdot NaCl \cdot 6H_2O$ there is an amazing dissymmetry of 12.5% in the vicinity of the $1s \rightarrow 3d$ pre-edge transition.[204] This can be understood by considering the origin of circular dichroism. Differential absorption of left and right circularly polarized light is due to odd-parity interference between different photon–molecule interaction

operators. In the UV–visible region, CD is dominated by the interference between the electric and magnetic dipole transition moments. However, CD can also arise from interference between electric dipole and electric quadrupole terms, and this is the dominant source of CD in the X-ray region. For transitions such as $1s \rightarrow 3d$, which are quadrupole allowed and dipole forbidden, the X-ray CD is extremely large. X-ray CD thus provides a unique tool for investigating the origin of specific edge features. In addition, X-ray CD can significantly enhance the resolution of edge features. For example, the dipole-forbidden $2p \rightarrow 4f$ transition at the NdL_3 edge of $Na_3Nd(digly)_3$ appears only as an extremely weak shoulder on the low-energy side of the allowed white-line transitions ($2p \rightarrow nd$). However, in the CD spectrum of $Na_3Nd(digly)_3$, only the $2p \rightarrow 4f$ transition is seen, allowing this feature to be readily distinguished from the white line.

In addition to core $\rightarrow$ valence transitions, it is also possible to observe X-ray CD at higher energy, in the XANES and EXAFS regions. Single-scattering terms, which dominate the X-ray photoabsorption cross-section, cannot give rise to circular dichroism. Consequently, X-ray CD spectra are sensitive only to multiple scattering and not to single scattering.[205,206] This dramatically simplifies interpretation of the spectra and has the added benefit that simulations of X-ray CD are often better than the corresponding simulations of X-ray absorption, since the inelastic effects that complicate interpretation of the absorption do not survive in the CD.[203,207] Since multiple-scattering terms are sensitive to geometry, X-ray CD is a very sensitive probe of three-dimensional structure. In addition, from the sign of the CD, it is possible to distinguish between enantiomers.

2.13.4.2 High-resolution X-ray Fluorescence

As discussed above, XAS is frequently measured as fluorescence excitation spectra. Typically, this involves collecting all of the X-ray fluorescence, with little or no energy discrimination, and the discussion thus far has ignored the structure that is observed in emission spectra. However, it is possible to use a high-resolution fluorescence monochromator to give energy resolution <1 eV. Such measurements, which can be described as X-ray inelastic scattering, reveal a wealth of structural detail in the emission spectra. Detailed discussion of emission spectra is beyond the scope of this review, but has been treated elsewhere.[208] For the present discussion, there are two important consequences of high-resolution measurements; these can be used to enhance the resolution of absorption edges and to give site-selective XAS data.

2.13.4.2.1 Elimination of lifetime broadening in XANES

XANES spectra frequently have very broad features due to the intrinsic broadening from the core-hole lifetime, which may be as much as 5–10 eV for L edges. By monitoring emission with high resolution, one samples only a small subset of the excited states and thus effectively eliminates broadening from the core-hole. For $Dy(NO_3)_3$, the L_3 lifetime broadening is ca. 5 eV and the $L_{\alpha 1}$ (L_3M_5) emission line has a width of nearly 10 eV. By monitoring a narrow band (ca. 0.3 eV) from within $L_{\alpha 1}$ emission band, the resolution of the excitation spectrum was dramatically enhanced.[209] In the sharpened spectrum, the resolution is effectively governed by the lifetime of the M_5 state that gives rise to the emission rather than by the much shorter lifetime of the excited L_3 state.[208] Measurements using high-resolution emission are much more challenging than conventional X-ray absorption, since the high-resolution of the fluorescence monochromator results in a much weaker signal. This requires an extremely intense X-ray beam and consequently high-resolution measurements are more sensitive to radiation damage. Nevertheless, for certain samples, the experimental difficulties are more than compensated for by the ability to resolve transitions that would be otherwise unresolvable.

2.13.4.2.2 Site-selective XAS

If emission spectra are measured with sufficiently high resolution, it is found that emission energies correlate both with oxidation state and with spin state.[208] Consequently, high-resolution emission offers the possibility of distinguishing the XAS spectra for different absorbing sites. For example, Fe^{2+} and Fe^{3+} have slightly different emission spectra. By tuning the fluorescence

analyzer to energies dominated by one or the other oxidation state, it was possible to measure valence-selective EXAFS spectra for Prussian Blue, $Fe^{3+}{}_4(Fe^{2+}(CN)_6)_3$.[210] This possibility of measuring site-selective EXAFS has the potential to significantly simplify the interpretation of EXAFS data for complex mixtures.[211] In a related experiment, it was possible to measure spin-selective XANES spectra for MnF_2 by monitoring a satellite on the low-energy side of the K_β emission line.[212] The satellite arises because of the fact that the K_β ($3p \rightarrow 1s$) energy varies depending on whether the spin of the $3p^5$ shell (created by the K_β emission) is parallel or anti-parallel to the spin of the $3d^5$ shell. This makes it possible to distinguish spin-up excitations (photoelectron has spin parallel to the $3d^5$ shell) from spin-down excitations and thus to obtain magnetic information similar to that obtained by X-ray MCD, but without the need for an applied magnetic field.

2.13.4.3 Spatially Resolved Measurements

Another way to improve the resolution of XAS is to add spatial resolution.[213] With modern synchrotron facilities, it is relatively straightforward to record XAS spectra using a 1 μm × 1 μm beam.[214,215] These so-called X-ray microprobe beams can be used for all of the XANES and EXAFS experiments discussed above, but with the added benefit of permitting spatially resolved measurements. In addition, it is possible to construct a true soft X-ray microscope with spatial resolution (30–50 nm) close to the diffraction limit of light.[216] X-ray microscopy provides many of the benefits of electron microscopy, with the advantage of lower sample damage and greater tolerance of wet samples but does not usually involve spectroscopic measurements. The emphasis here is on X-ray spectroscopy using X-ray microprobe beams.

2.13.4.3.1 Methods for focusing X-rays

In the simplest X-ray microprobe implementation, slits or a pinhole can be used to limit the size of the beam. Although easy to implement and widely used, this approach greatly reduces the available photon flux and is thus limited to concentrated samples and relatively poor spatial resolution.[213] A variety of schemes can be used to focus the X-ray beam prior to (or in place of) beam-defining slits.[217]

Conventional focusing optics require a material that is both transparent and significantly refractive. This is difficult to accomplish in the X-ray region since the refractive index of most materials is extremely close to 1 in the X-ray region. There has been recent progress in designing compound refractive X-ray lenses, in which multiple lenses are used to compensate for the small focusing power of each lens.[218] However, most X-ray microprobes rely on reflective or diffractive optics. Although X-rays are not reflected at normal incidence, they do undergo total external reflection at a sufficiently grazing angle of incidence. The widely used Kirkpatrick–Baez geometry uses a pair of curved mirrors set perpendicular to one another in order to minimize the astigmatism of a single curved mirror. This can provide spot sizes of a few μm when used with modern synchrotron sources. Capillary optics rely on total external reflection of an X-ray beam propagating inside of a capillary. These can give spatial resolutions as small as 50 nm, but suffer from extremely high divergence, necessitating that the sample be placed very close (<100 μm) to the capillary. Bragg diffraction, which is used for X-ray monochromators, can also be used to focus an X-ray beam by using a curved crystal. Fresnel zone plates are a diffractive optical element, made up of alternating concentric circular zones. With modern microfabrication, the minimum attainable zone width (which determines the spatial resolution) is approximately 20 nm in the soft X-ray region and closer to 100 nm in the hard X-ray region (due to the need for thicker zones in order to have sufficient contrast in the hard X-ray regime). Unfortunately, zone plates are a chromatic optical element and must be refocused if the energy is changed, thus limiting their use for spectroscopic measurements.

2.13.4.3.2 Applications of X-ray microprobes

X-ray microprobe studies to date have concentrated mostly on geological and environmental samples. If the sample of interest is very small, for example because it is contained in a diamond

anvil cell, the X-ray microprobe may be required to obtain high-quality data.[219] More frequently, the microprobe is required because the sample is heterogeneous. In these cases, the X-ray microprobe can be used to measure XAS spectra selectively for different parts of the sample. This was used, for example, to study the different types of Au present in arsenopyrite ore[220] and to define the U oxidation state associated with spatially resolved uranium precipitates in U-contaminated soils.[221] In these examples, the microprobe beam simplifies interpretation of the spectra by permitting measurements on a distance scale at which the sample is homogeneous. Alternatively, known spectral differences, for example between chromate and Cr^{3+},[222] or between Se^{6+} and elemental Se[215] can be used in conjunction with microprobe imaging to follow the evolution of a sample, for example during the course of a reaction.

2.13.5 REFERENCES

1. Bearden, J. A.; Burr, A. F. *Rev. Mod. Phys.* **1967**, *39*, 125–142.
2. James, R. W. *The Optical Principles of the Diffraction of X-ray*; Ox Bow Press, 1982.
3. X-ray optical constants, Center for X-ray Optics, Lawrence Berkeley Laboratory. http://www-cxro.lbl.gov/optical_constants/web.html.
4. NIST Physical Reference Data. http://physics.nist.gov/PhysRefData/XrayMassCoef/cover.html.
5. Moseley, H. G. J. *Phil. Mag.* **1914**, *27*, 703–714.
6. Moseley, H. G. J. *Phil. Mag.* **1913**, *26*, 1024–1034.
7. Markowicz, A. A. In *Handbook of X-ray Spectrometry*; 2nd ed.; Van Grieken, R. E., Markowicz, A. A., Eds.; Marcel Dekker: New York, 2002.
8. Compton, A. H.; Allison, S. K. *X-rays in Theory and Experiment*; 2nd ed.; D. Van Nostrand Company: Princeton, 1935.
9. *X-ray Data Booklet*, 2nd ed.; Thompson, A. C.; Vaughan, D. Eds.; Lawrence Berkeley National Laboratory: Berkeley, 2001.
10. Bearden, J. A. *Rev. Mod. Phys.* **1967**, *39*, 78.
11. Krause, M. O.; Oliver, J. H. *J. Phys. Chem. Ref. Data* **1979**, *8*, 329.
12. Pettifer, R. F.; Borowski, M.; Loeffen, P. W. *J. Synchrot. Radiat.* **1999**, *6*, 217–219.
13. Jaklevic, J.; Kirby, J. A.; Klein, M. P.; Robertson, A. S.; Brown, G. S.; Eisenberger, P. *Solid State Commun.* **1977**, *23*, 679–682.
14. Goulon, J.; Goulonginet, C.; Cortes, R.; Dubois, J. M. *J. Physique* **1982**, *43*, 539–548.
15. Stern, E. A.; Elam, W. T.; Bunker, B. A.; Lu, K.; Heald, S. M. *Nucl. Instrum. Methods Phys. Res.* **1982**, *195*, 345–346.
16. Stern, E. A.; Heald, S. M. *Rev. Sci. Instrum.* **1979**, *50*, 1579–1582.
17. Cramer, S. P.; Tench, O.; Yocum, M.; George, G. N. *Nucl. Instrum. Methods Phys. Res. Sect. A-Accel. Spectrom. Dect. Assoc. Equip.* **1988**, *266*, 586–591.
18. Furenlid, L. R.; Kraner, H. W.; Rogers, L. C.; Cramer, S. P.; Stephani, D.; Beuttenmuller, R. H.; Beren, J. *Nucl. Instrum. Methods Phys. Res. Sect. A-Accel. Spectrom. Dect. Assoc. Equip.* **1992**, *319*, 408–413.
19. Ellis, A. T. In *Handbook of X-ray Spectrometry*; 2nd ed.; Van Grieken, R. E., Markowicz, A. A., Eds.; Marcel Dekker: New York, 2002.
20. Zhang, K.; Rosenbaum, G.; Bunker, G. *J. Synchrot. Radiat.* **1998**, *5*, 1227–1234.
21. Helsen, J. A.; Kuczumow, A. In *Handbook of X-ray Spectrometry*; 2nd ed.; Van Grieken, R. E., Markowicz, A. A., Eds.; Marcel Dekker: New York 2002.
22. Emura, S.; Moriga, T.; Takizawa, J.; Nomura, M.; Bauchspiess, K. R.; Murata, T.; Harada, K.; Maeda, H. *Phys. Rev. B* **1993**, *47*, 6918–6930.
23. Goulon, J.; Tola, P.; Brochon, J. C.; Lemonnier, M. *Acta Crystallogr. Sect. A* **1984**, *40*, C394–C394.
24. Tola, P.; Retournard, A.; Dexpertghys, J.; Lemonnier, M.; Pagel, M.; Goulon, J. *Chem. Phys.* **1983**, *78*, 339–345.
25. Stohr, J.; Jaeger, R.; Brennan, S. *Surf. Sci.* **1982**, *117*, 503–524.
26. Stohr, J. *Jpn J Appl Phys* **1978**, *17*, 217–220.
27. Haase, J. *J. Chem. Soc.-Faraday Trans.* **1996**, *92*, 1653–1667.
28. Schroeder, S. L. M.; Moggridge, G. D.; Ormerod, R. M.; Rayment, T.; Lambert, R. M. *Surf. Sci.* **1995**, *324*, L371–L377.
29. Röntgen, W. C. *Nature* **1896**, *53*, 274.
30. Storage Ring Synchrotron Radiation Sources. www-ssrl.slac.stanford.edu/sr-source.html.
31. Stern, E. A.; Sayers, D. E.; Lytle, F. W. *Phys. Rev. B* **1975**, *11*, 4836–4846.
32. Lee, P. A.; Pendry, J. B. *Phys. Rev. B* **1975**, *11*, 2795–2811.
33. Ashley, C. A.; Doniach, S. *Phys. Rev. B* **1975**, *11*, 1279–1288.
34. Teo, B. K.; Lee, P. A.; Simons, A. L.; Eisenberger, P.; Kincaid, B. M. *J. Am. Chem. Soc.* **1977**, *99*, 3854–3856.
35. Lee, P. A.; Teo, B. K.; Simons, A. L. *J. Am. Chem. Soc.* **1977**, *99*, 3856–3859.
36. Lee, P. A.; Teo, B. K.; Simons, A. L. *Bull. Am. Phys. Soc.* **1977**, *22*, 319–319.
37. Strange, R. W.; Blackburn, N. J.; Knowles, P. F.; Hasnain, S. S. *J. Am. Chem. Soc.* **1987**, *109*, 7157–7162.
38. Teo, B. K. *J. Am. Chem. Soc.* **1981**, *103*, 3990–4001.
39. Rehr, J. J.; Albers, R. C.; Zabinsky, S. I. *Phys. Rev. Lett.* **1992**, *69*, 3397–400.
40. Wang, S.; Lee, M. H.; Hausinger, R. P.; Clark, P. A.; Wilcox, D. E.; Scott, R. A. *Inorg. Chem.* **1994**, *33*, 1589–1593.
41. Binsted, N.; Strange, R. W.; Hasnain, S. S. *Biochemistry* **1992**, *31*, 12117–12125.
42. Boswell, J. S.; Reedy, B. J.; Kulathila, R.; Merkler, D.; Blackburn, N. J. *Biochemistry* **1996**, *35*, 12241–12250.
43. Chaboy, J.; Marcelli, A.; Tyson, T. A. *Phys. Rev. B* **1994**, *49*, 11652–11661.
44. Dangelo, P.; Nolting, H. F.; Pavel, N. V. *Phys. Rev. A* **1996**, *53*, 798–805.
45. Filipponi, A.; Dicicco, A. *Phys. Rev. A* **1995**, *52*, 1072–1078.

46. Dangelo, P.; Pavel, N. V.; Roccatano, D.; Nolting, H. F. *Phys. Rev. B* **1996**, *54*, 12129–12138.
47. D'Angelo, P.; Pavel, N. V.; Borowski, M. *J. Synchrot. Radiat.* **2001**, *8*, 666–668.
48. Dubiel, M.; Brunsch, S.; Arcon, I.; Frahm, R. *J. Physique* **1997**, *7*, 1169–1170.
49. Wende, H.; Baberschke, K. *J. Electron Spectrosc. Relat. Phenom.* **1999**, *103*, 821–826.
50. Wende, H.; Srivastava, P.; Chauvistre, R.; May, F.; Baberschke, K.; Arvanitis, D.; Rehr, J. J. *J. Phys.-Condes. Matter* **1997**, *9*, L427–L433.
51. Ankudinov, A. L.; Conradson, S. D.; de Leon, J. M.; Rehr, J. J. *Phys. Rev. B* **1998**, *57*, 7518–7525.
52. Ankudinov, A. L.; Rehr, J. J.; Low, J.; Bare, S. R. *Phys. Rev. Lett.* **2001**, *86*, 1642–1645.
53. Michalowicz, A.; Vlaic, G. *J. Synchrot. Radiat.* **1998**, *5*, 1317–1320.
54. Rehr, J. J.; Booth, C. H.; Bridges, F.; Zabinsky, S. I. *Phys. Rev. B.* **1996**, *53*, 9468–9470.
55. Filipponi, A.; DiCicco, A. *Phys. Rev. B* **1996**, *53*, 9466–9467.
56. Sanchez del Rio, M.; San Miguel, A. ESRF XAFS Software database. http://www.esrf.fr/computing/scientific/exafs/intro.html.
57. Rehr, J. J.; Mustre, d. L. J.; Zabinsky, S. I.; Albers, R. C. *J. Am. Chem. Soc.* **1991**, *113*, 5135–5140.
58. Rehr, J. J.; Albers, R. C. *Rev. Mod. Phys.* **2000**, *72*, 621–654.
59. Gurman, S. J.; Binsted, N.; Ross, I. *J. Phys. C.* **1986**, *19*, 1845–1861.
60. Filipponi, A.; DiCicco, A.; Natoli, C. R. *Phys. Rev. B* **1995**, *52*, 15122–15134.
61. Filipponi, A.; DiCicco, A. *Phys. Rev. B* **1995**, *52*, 15135–15149.
62. Dicicco, A. *Physica B* **1995**, *209*, 125–128.
63. Vaarkamp, M.; Dring, I.; Oldman, R. J.; Stern, E. A.; Koningsberger, D. C. *Phys. Rev. B.* **1994**, *50*, 7872–7883.
64. Bunker, G.; Hasnain, S.; Ayers, D. In *X-ray Absorption Fine Structure*; Hasnain, S. S., Ed., Ellis Horwood: New York, 1991.
65. Clark-Baldwin, K.; Tierney, D. L.; Govindaswamy, N.; Gruff, E. S.; Kim, C.; Berg, J.; Koch, S. A.; Penner-Hahn, J. E. *J. Am. Chem. Soc.* **1998**, *120*, 8401–8409.
66. Riggs-Gelasco, P. J.; Mei, R.; Yocum, C. F.; Penner-Hahn, J. E. *J. Am. Chem. Soc.* **1996**, *118*, 2387–2399.
67. Sayers, D. E.; Stern, E. A.; Lytle, F. W. *Phys. Rev. Lett.* **1971**, *27*, 1204.
68. Stemmler, T. L.; Barnhart, T.; Penner-Hahn, J. E.; Tucker, C. E.; Knochel, P.; Böhme, M.; Frenking, G. *J. Am. Chem. Soc.* **1995**, *117*, 12489–12497.
69. Riggs-Gelasco, P. J.; Stemmler, T. L.; Penner-Hahn, J. E. *Coord. Chem. Rev.* **1995**, *144*, 245–286.
70. Stern, E. A. *Phys. Rev. B.* **1993**, *48*, 9825–9827.
71. Michalowicz, A.; Provost, K.; Laruelle, S.; Mimouni, A.; Vlaic, G. *J. Synchrot. Radiat.* **1999**, *6*, 233–235.
72. Stern, E. A. *Jpn. J. Appl. Phys.* **1993**, *1*, 851–855.
73. Lee, P. A.; Citrin, P. H.; Eisenberger, P.; Kincaid, B. M. *Rev. Mod. Phys* **1981**, *53*, 769–806.
74. Blackburn, N. J.; Barr, M. E.; Woodruff, W. H.; van der Ooost, J.; de Vries, S. *Biochemistry* **1994**, *33*, 10401–10407.
75. Scott, R. A.; Zumft, W. G.; Coyle, C. L.; Dooley, D. M. *Proc. Natl. Acad. Sci. USA* **1989**, *86*, 4082–4086.
76. Dooley, D. M.; McGuirl, M. A.; Rosenzweig, A. C.; Landin, J. A.; Scott, R. A.; Zumft, W. G.; Devlin, F.; Stephens, P. J. *Inorg. Chem.* **1991**, *30*, 3006–3011.
77. George, G. N.; Cramer, S. P.; Frey, T. G.; Prince, R. C. *Biochim. Biophys. Acta* **1993**, *1142*, 240–252.
78. Penner-Hahn, J. E. *Coord. Chem. Rev.* **1999**, *192*, 1101–1123.
79. Bertagnolli, H.; Ertel, T. S. *Angew. Chem.-Int. Edit. Engl.* **1994**, *33*, 45–66.
80. Alexeev, O.; Gates, B. C. *Top. Catal.* **2000**, *10*, 273–293.
81. Bazin, D.; Guczi, L. *Appl. Catal. A-Gen.* **2001**, *213*, 147–162.
82. Filipponi, A. *J. Phys.-Condes. Matter* **2001**, *13*, R23–R60.
83. Garner, C. D. *Adv. Inorg. Chem.* **1991**, *36*, 303–339.
84. Scott, R. A. *Methods Enzymol.* **1985**, *117*, 414–459.
85. Sharpe, L. R.; Heineman, W. R.; Elder, R. C. *Chem. Rev.* **1990**, *90*, 705–722.
86. Teo, B. K. *EXAFS: Basic Principles and Data Analysis*; Springer-Verlag: New York, 1986.
87. Grady, B. P. *Microchem J.* **2002**, *71*, 267–279.
88. Johnston, P.; Wells, P. B. *Radiat. Phys. Chem.* **1995**, *45*, 393–412.
89. Linford, R. G. *Chem. Soc. Rev.* **1995**, *24*, 267.
90. Parsons, J. G.; Aldrich, M. V.; Gardea-Torresdey, J. L. *Appl. Spectrosc. Rev.* **2002**, *37*, 187–222.
91. Penner-Hahn, J. E. *ACS Symposium Series* 1988, *372*, 28–48.
92. Stöhr, J. *NEXAFS Spectroscopy*; Springer: Berlin, 1992.
93. Koningsberger, D. C.; Prins, R. Eds.; *X-ray Absorption: Principles, Applications, Techniques of EXAFS SEXAFS, and XANES*; John Wiley & Sons: New York, 1988; Vol. 91.
94. Teo, B. K.; Joy, D. C. Eds.; *EXAFS [Extended X-Ray Absorption Fine Structure] Spectroscopy: Techniques and Applications*; Plenum Press: New York, 1981.
95. Cramer, S. P. *Chem. Anal.* **1988**, *92*, 257–320.
96. Yamanaka, T.; Nagai, T.; Tsuchiya, T. *Z. Kristall.* **1997**, *212*, 401–410.
97. Gleiter, H. *Adv. Mater.* **1992**, *4*, 474–481.
98. Shido, T.; Prins, R. *Curr. Opin. Solid State Mat. Sci.* **1998**, *3*, 330–335.
99. Evans, J. *Chem. Soc. Rev.* **1997**, *26*, 11–19.
100. Thomas, J. M.; Sankar, G. *Acc. Chem. Res.* **2001**, *34*, 571–581.
101. Minicucci, M.; DiCicco, A. *J. Physique* **1997**, *7*, 1027–1028.
102. DiCicco, A.; Minicucci, M.; Filipponi, A. *Phys. Rev. Lett.* **1997**, *78*, 460–463.
103. DiCicco, A. *Phys. Rev. B* **1996**, *53*, 6174–6185.
104. Sinfelt, J. H. *Surf. Sci.* **2002**, *500*, 923–946.
105. Scheidegger, A. M.; Sparks, D. L. *Soil Sci.* **1996**, *161*, 813–831.
106. Randall, S. R.; Sherman, D. M.; Ragnarsdottir, K. V.; Collins, C. R. *Geochim. Cosmochim. Acta* **1999**, *63*, 2971–2987.
107. Ohta, T.; Yokoyama, T.; Terada, S.; Imanishi, A.; Kitajima, Y. *Res. Chem. Intermed.* **2000**, *26*, 29–43.
108. Stohr, J. *Bull. Am. Phys. Soc.* **1980**, *25*, 323–323.
109. Hubbard, A. T. *Heterogeneous Chem. Rev.* **1994**, *1*, 3–39.

110. D'Angelo, P.; Barone, V.; Chillemi, G.; Sanna, N.; Meyer-Klaucke, W.; Pavel, N. V. *J. Am. Chem. Soc.* **2002**, *124*, 1958–1967.
111. D'Angelo, P.; Benfatto, M.; Della Longa, S.; Pavel, N. V. *Phys. Rev. B* **2002**, *66*, art. no.-064209.
112. Benfatto, M.; D'Angelo, P.; Della Longa, S.; Pavel, N. V. *Phys. Rev. B* **2002**, *65*, art. no.-174205.
113. Barnhart, T. M.; Huang, H.; Penner-Hahn, J. E. *J. Org. Chem* **1995**, *60*, 4310–4311.
114. Lah, M. S.; Gibney, B. R.; Tierney, D. L.; Penner-Hahn, J. E.; Pecoraro, V. L. *J. Am. Chem. Soc.* **1993**, *115*, 5857–5858.
115. Astkey, T.; Ellis, P. J.; Freeman, H. C.; Hitchman, M. A.; Keene, F. R.; Tiekink, E. R. T. *J. Chem. Soc., Dalton Trans.* **1995**, 595–601.
116. Ellis, P. J.; Freeman, H. C.; Hitchman, M. A.; Reinen, D.; Wagner, B. *Inorg. Chem.* **1994**, *33*, 1249–1250.
117. Tucker, D.; White, P. S.; Trojan, K. L.; Kirk, M. L.; Hatfield, W. E. *Inorg. Chem.* **1991**, *30*, 823.
118. Wu, Z. Y.; Saini, N. L.; Bianconi, A. *Phys. Rev. B* **2001**, *6409*, art. no.-092507.
119. Oyanagi, H.; Saini, N. L.; Bianconi, A. *Int. J. Mod. Phys. B* **2000**, *14*, 3623–3631.
120. Dimitrov, D. A.; Ankudinov, A. L.; Bishop, A. R.; Conradson, S. D. *Phys. Rev. B* **1998**, *58*, 14227–14237.
121. Conradson, S. D. *Appl. Spectrosc.* **1998**, *52*, 252A–279A.
122. Mastelaro, V. R.; Briois, V.; de Souza, D. P. F.; Silva, C. L. *J. European Ceram. Soc.* **2003**, *23*, 273–282.
123. Winterer, M.; Delaplane, R.; McGreevy, R. *J. Appl. Crystallogr.* **2002**, *35*, 434–442.
124. Li, P.; Chen, I. W.; Pennerhahn, J. E. *Phys. Rev. B* **1993**, *48*, 10063–10073.
125. Li, P.; Chen, I. W.; Pennerhahn, J. E. *Phys. Rev. B* **1993**, *48*, 10074–10081.
126. Li, P.; Chen, I. W.; Pennerhahn, J. E. *Phys. Rev. B* **1993**, *48*, 10082–10089.
127. Scheinost, A. C.; Stanjek, H.; Schulze, D. G.; Gasser, U.; Sparks, D. L. *Am. Miner.* **2001**, *86*, 139–146.
128. Lebedev, A. I.; Sluchinskaya, I. A.; Demin, V. N.; Munro, I. *Phys. Solid State* **1999**, *41*, 1275–1282.
129. Ressler, T.; Wienold, J.; Jentoft, R. E.; Neisius, T.; Gunter, M. M. *Top. Catal.* **2002**, *18*, 45–52.
130. Coppens, P.; Novozhilova, I. V. *Faraday Discuss.* **2003**, *122*, 1–11.
131. Bressler, C.; Saes, M.; Chergui, M.; Grolimund, D.; Abela, R.; Pattison, P. *J. Chem. Phys.* **2002**, *116*, 2955–2966.
132. Chen, L. X. *J. Electron Spectrosc. Relat. Phenom.* **2001**, *119*, 161–174.
133. Oulianov, D. A.; Tornov, I. V.; Dvornikov, A. S.; Rentzepis, P. M. *Proc. Natl. Acad. Sci. USA.* **2002**, *99*, 12556–12561.
134. Norman, D. *J. Synchrot. Radiat.* **2001**, *8*, 72–75.
135. Lamberti, C.; Prestipino, C.; Bonino, F.; Capello, L.; Bordiga, S.; Spoto, G.; Zecchina, A.; Moreno, S. D.; Cremaschi, B.; Garilli, M.; Marsella, A.; Carmello, D.; Vidotto, S.; Leofanti, G. *Angew. Chem.-Int. Edit.* **2002**, *41*, 2341–2344.
136. Ressler, T.; Wienold, J.; Jentoft, R. E.; Timpe, O.; Neisius, T. *Solid State Commun.* **2001**, *119*, 169–174.
137. Rodriguez, J. A.; Hanson, J. C.; Frenkel, A. I.; Kim, J. Y.; Perez, M. *J. Am. Chem. Soc.* **2002**, *124*, 346–354.
138. Yamaguchi, A.; Suzuki, A.; Shido, T.; Inada, Y.; Asakura, K.; Nomura, M.; Iwasawa, Y. *J. Phys. Chem. B* **2002**, *106*, 2415–2422.
139. Zhang, K.; Dong, J.; Auld, D. S. *Physica B* **1995**, *209*, 719–721.
140. Wasserman, S. R. *J. Physique* **1997**, *7*, 203–205.
141. Wasserman, S. R.; Allen, P. G.; Shuh, D. K.; Bucher, J. J.; Edelstein, N. M. *J. Synchrot. Radiat.* **1999**, *6*, 284–286.
142. Frenkel, A.; Kleifeld, O.; Wasserman, S. R.; Sagi, I. *J. Chem. Phys.* **2002**, *116*, 9449–9456.
143. Coulston, G. W.; Bare, S. R.; Kung, H.; Birkeland, K.; Bethke, G. K.; Harlow, R.; Nerron, N.; Lee, P. L. *Science* **1997**, *275*, 191–193.
144. Dent, A. J. *Top. Catal.* **2002**, *18*, 27–35.
145. Lutzenkirchen-Hecht, D.; Grundmann, S.; Frahm, R. *J. Synchrot. Radiat.* **2001**, *8*, 6–9.
146. Richwin, M.; Zaeper, R.; Lutzenkirchen-Hecht, D.; Frahm, R. *Rev. Sci. Instrum.* **2002**, *73*, 1668–1670.
147. Briois, V.; Moulin, C. C.; Verdaguer, M. *Actual Chim.* **2000**, 31–40.
148. Rehr, J. J.; Schattke, W.; de Abajo, F. J. G.; Muino, R. D.; Van Hove, M. A. *J. Electron Spectrosc. Relat. Phenom.* **2002**, *126*, 67–76.
149. Benfatto, M.; Della Longa, S. *J. Synchrot. Radiat.* **2001**, *8*, 1087–1094.
150. Sipr, O. *Phys. Rev. B* **2002**, *65*, art. no.-205115.
151. Kirby, J. A.; Goodin, D. B.; Wydrzynski, T.; Robertson, A. S.; Klein, M. P. *J. Am. Chem. Soc.* **1981**, *103*, 5537–5542.
152. Natoli, C. R. In *Springer Series in Chemical Physics*; Bianconi, A.; Incoccia, L., Stipcich, S., Eds.; Springer-Verlag: Berlin, 1983; Vol. 27.
153. Rehr, J. J.; Ankudinov, A. L. *J. Synchrot. Radiat.* **2001**, *8*, 61–65.
154. Shulman, R. G.; Yafet, Y.; Eisenberger, P.; Blumberg, W. E. *Proc. Natl. Acad. Sci. USA* **1976**, *73*, 1384–1388.
155. Hahn, J. E.; Scott, R. A.; Hodgson, K. O.; Doniach, S.; Desjardins, S. R.; Solomon, E. I. *Chem. Phys. Lett.* **1982**, *88*, 595–598.
156. Roe, A. L.; Schneider, D. J.; Mayer, R. J.; Pyrz, J. W.; Widom, J.; Que, L. *J. Am. Chem. Soc.* **1984**, *106*, 1676–1681.
157. Shadle, S. E.; Penner-Hahn, J. E.; Schugar, H. J.; Hedman, B.; Hodgson, K. O.; Solomon, E. I. *J. Am. Chem. Soc.* **1993**, *115*, 767–776.
158. Westre, T. E.; Kennepohl, P.; DeWitt, J. G.; Hedman, B.; Hodgson, K. O.; Solomon, E. I. *J. Am. Chem. Soc.* **1997**, *119*, 6297–6314.
159. George, G. N.; Cleland, W. E. J.; Enemark, J. H.; Smith, B. E.; Kipke, C. A.; Roberts, S. A.; Cramer, S. P. *J. Am. Chem. Soc.* **1990**, *112*, 2541–2548.
160. Cramer, S. P.; Ralston, C. Y.; Wang, H.; Bryant, C. *J. Electron Spectrosc. Relat. Phenom.* **1997**, *86*, 175–183.
161. George, S. J.; Lowery, M. D.; Solomon, E. I.; Cramer, S. P. *J. Am. Chem. Soc.* **1993**, *115*, 2968–2969.
162. Steinberger, I. T.; Teodorescu, C. M.; Gravel, D.; Flesch, R.; Wassermann, B.; Reichardt, G.; Hutchings, C. W.; Hitchcock, A. P.; Ruhl, E. *Phys. Rev. B* **1999**, *60*, 3995–4004.
163. Federmann, F.; Bjorneholm, O.; Beutler, A.; Moller, T. *Phys. Rev. Lett.* **1994**, *73*, 1549–1552.
164. Colpas, G. J.; Maroney, M. J.; Bagyinka, C.; Kumar, M.; Willis, W. S.; Suib, S. L.; Baidya, N.; Mascharak, P. K. *Inorg. Chem.* **1991**, *30*, 920–928.
165. Smith, T. A.; Penner-Hahn, J. E.; Berding, M. A.; Doniach, S.; Hodgson, K. O. *J. Am. Chem. Soc.* **1985**, *107*, 5945–5955.

166. Kau, L. S.; Spira-Solomon, D. J.; Penner-Hahn, J. E.; Hodgson, K. O.; Solomon, E. I. *J. Am. Chem. Soc.* **1987**, *109*, 6433–6442.
167. Pickering, I. J.; George, G. N. *Inorg. Chem.* **1995**, *34*, 3142–3152.
168. Shadle, S. E.; Hedman, B.; Hodgson, K. O.; Solomon, E. I. *J. Am. Chem. Soc.* **1995**, *117*, 2259–2272.
169. Glaser, T.; Hedman, B.; Hodgson, K. O.; Solomon, E. I. *Acc. Chem. Res.* **2000**, *33*, 859–868.
170. Neese, F.; Hedman, B.; Hodgson, K. O.; Solomon, E. I. *Inorg. Chem.* **1999**, *38*, 4854–4860.
171. Bianconi, A.; Li, C.; Campanella, F.; Della Longa, S.; Pettiti, I.; Pompa, M.; Turtu, S.; Udron, D. *Phys. Rev. B: Condens. Matter* **1991**, *44*, 4560–4569.
172. Li, C.; Pompa, M.; Castellano, A. C.; Della Longa, S.; Bianconi, A. *Physica C (Amsterdam)* **1991**, *175*, 369–80.
173. Yokoyama, T.; Kosugi, N.; Kuroda, H. *Chem. Phys.* **1986**, *103*, 101–109.
174. Kosugi, N.; Yokoyama, T.; Kuroda, H. *Springer Proc. Phys.* **1984**, *2*, 55–57.
175. Kosugi, N.; Yokoyama, T.; Asakura, K.; Kuroda, H. *Chem. Phys.* **1984**, *91*, 249–256.
176. Sipr, O.; Simunek, A. *J. Phys.-Condes. Matter* **2001**, *13*, 8519–8525.
177. Solomon, E. I.; Randall, D. W.; Glaser, T. *Coord. Chem. Rev.* **2000**, *200*, 595–632.
178. Elleaume, P. *J. Synchrot. Radiat.* **1994**, *1*, 19–26.
179. Elleaume, P.; Chavanne, J.; Marechal, X.; Goulon, J.; Braicovich, L.; Malgrange, C.; Emerich, H.; Marot, G.; Susini, J. *Nucl. Instrum. Methods Phys. Res. Sect. A-Accel. Spectrom. Dect. Assoc. Equip.* **1991**, *308*, 382–389.
180. Varga, L.; Giles, C.; Zheng, Y. L.; Pizzini, S.; de Bergevin, F.; Fontaine, A.; Malgrange, C. *J. Synchrot. Radiat.* **1999**, *6*, 1125–1132.
181. Hirano, K.; Ishikawa, T.; Kikuta, S. *Nucl. Instrum. Methods Phys. Res. Sect. A-Accel. Spectrom. Dect. Assoc. Equip.* **1993**, *336*, 343–353.
182. Hahn, J. E.; Hodgson, K. O. *ACS Symposium Series* 1983, *211*, 431–444.
183. de Groot, F. M. F. *J. Electron Spectrosc. Relat. Phenom.* **1994**, *67*, 529–622.
184. Beni, G.; Platzman, P. M. *Phys. Rev. B* **1976**, *14*, 1514–1518.
185. Pellicer-Porres, J.; Segura, A.; Munoz, V.; San Miguel, A. *Phys. Rev. B: Condens. Matter Mater. Phys.* **2000**, *61*, 125–131.
186. Mustre de Leon, J.; Conradson, S. D.; Batistic, I.; Bishop, A. R.; Raistrick, I. D.; Aronson, M. C.; Garzon, F. H. *Phys. Rev. B: Condens. Matter* **1992**, *45*, 2447–2457.
187. Scott, R. A.; Hahn, J. E.; Doniach, S.; Freeman, H. C.; Hodgson, K. O. *J. Am. Chem. Soc.* **1982**, *104*, 5364–5369.
188. Schlegel, M. L.; Manceau, A.; Chateigner, D.; Charlet, L. *J. Colloid Interface Sci.* **1999**, *215*, 140–158.
189. Oyanagi, H.; Sugi, M.; Kuroda, S.; Iizima, S.; Ishiguro, T.; Matsushita, T. *Thin Solid Films* **1985**, *133*, 181–188.
190. Dau, H.; Andrews, J. C.; Roelofs, T. A.; Latimer, M. J.; Liang, W. C.; Yachandra, V. K.; Sauer, K.; Klein, M. P. *Biochemistry* **1995**, *34*, 5274–5287.
191. Schiller, H.; Dittmer, J.; Iuzzolino, L.; Dorner, W.; Meyer-Klaucke, W.; Sole, V. A.; Nolting, H. F.; Dau, H. *Biochemistry* **1998**, *37*, 7340–7350.
192. Edwards, A. M.; Zhang, K.; Nordgren, C. E.; Blasie, J. K. *Biophys. J.* **2000**, *79*, 3105–3117.
193. Uozumi, T.; Okada, K.; Kotani, A.; Durmeyer, O.; Kappler, J. P.; Beaurepaire, E.; Parlebas, J. C. *Europhys. Lett.* **1992**, *18*, 85–90.
194. Cabaret, D.; Joly, Y.; Renevier, H.; Natoli, C. R. *J. Synchrotron Radiat.* **1999**, *6*, 258–260.
195. Kosugi, N.; Yokoyama, T.; Kuroda, H. *Chem. Phys.* **1986**, *104*, 449–453.
196. van Elp, J.; Searle, B. G. *J. Electron Spectrosc. Relat. Phenom.* **1997**, *86*, 93–106.
197. Chakarian, V.; Idzerda, Y. U.; Meigs, G.; Chen, C. T. *IEEE Trans. Magn.* **1995**, *31*, 3307–3312.
198. Schuetz, G.; Knuelle, M.; Ebert, H. *Phys. Scr., T* **1993**, *T49A*, 302–306.
199. van Elp, J.; George, S. J.; Chen, J.; Peng, G.; Chen, C. T.; Tjeng, L. H.; Meigs, G.; Lin, H. J.; Zhou, Z. H.; Adams, M. W. W.; Searle, B. G.; Cramer, S. P. *Proc. Natl. Acad. Sci. USA* **1993**, *90*, 9664–9667.
200. Popescu, V.; Ebert, H.; Ahlers, D. *J. Magn. Magn. Mater.* **1999**, *191*, 368–372.
201. Schutz, G.; Ahlers, D. *J. Physique* **1997**, *7*, 59–65.
202. Isnard, O.; Miraglia, S.; Fruchart, D.; Giorgetti, C.; Dartyge, E.; Krill, G. *J. Phys.-Condes. Matter* **1996**, *8*, 2437–2446.
203. Alagna, L.; Prosperi, T.; Turchini, S.; Goulon, J.; Rogalev, A.; Goulon-Ginet, C.; Natoli, C. R.; Peacock, R. D.; Stewart, B. *Phys. Rev. Lett.* **1998**, *80*, 4799–4802.
204. Stewart, B.; Peacock, R. D.; Alagna, L.; Prosperi, T.; Turchini, S.; Goulon, J.; Rogalev, A.; Goulon-Ginet, C. *J. Am. Chem. Soc.* **1999**, *121*, 10233–10234.
205. Natoli, C. R.; Brouder, C.; Sainctavit, P.; Goulon, J.; Goulon-Ginet, C.; Rogalev, A. *Eur. Phys. J. B* **1998**, *4*, 1–11.
206. Brouder, C.; Natoli, C. R.; Sainctavit, P.; Goulon, J.; Goulon-Ginet, C.; Rogalev, A. *J. Synchrot. Radiat.* **1999**, *6*, 261–263.
207. Goulon, J.; Goulon-Ginet, C.; Rogalev, A.; Benayoun, G.; Brouder, C.; Natoli, C. R. *J. Synchrotron Radiat.* **2000**, *7*, 182–188.
208. de Groot, F. *Chem. Rev.* **2001**, *101*, 1779–1808.
209. Hamalainen, K.; Siddons, D. P.; Hastings, J. B.; Berman, L. E. *Phys. Rev. Lett* **1991**, *67*, 2850–2853.
210. Glatzel, P.; Jacquamet, L.; Bergmann, U.; de Groot, F. M. F.; Cramer, S. P. *Inorg. Chem.* **2002**, *41*, 3121–3127.
211. de Groot, F. M. F. *Top. Catal.* **2000**, *10*, 179–186.
212. Hamalainen, K.; Kao, C. C.; Hastings, J. B.; Siddons, D. P.; Berman, L. E.; Stojanoff, V.; Cramer, S. P. *Phys. Rev. B: Condens. Matter* **1992**, *46*, 14274–14277.
213. Bertsch, P. M.; Hunter, D. B. *Chem. Rev.* **2001**, *101*, 1809–1842.
214. Sutton, S. R.; Rivers, M. L.; Bajt, S.; Jones, K.; Smith, J. V. *Nucl. Instrum. Methods Phys. Res., Sect. A* **1994**, *347*, 412–416.
215. Sutton, R. S.; Bajt, S.; Delaney, J.; Schulze, D.; Tokunaga, T. *Rev. Sci. Instrum* **1995**, *66*, 1464–1467.
216. Kirz, J.; Jacobsen, C.; Howells, M. *Q. Rev. Biophys.* **1995**, *28*, 33–130.
217. Dhez, P.; Chevallier, P.; Lucatorto, T. B.; Tarrio, C. *Rev. Sci. Instrum.* **1999**, *70*, 1907–1920.
218. Snigirev, A.; Kohn, V.; Snigireva, I.; Lengeler, B. *Nature* **1996**, *384*, 49–51.
219. Anderson, A. J.; Jayanetti, S.; Mayanovic, R. A.; Bassett, W. A.; Chou, I. M. *Am. Miner.* **2002**, *87*, 262–268.

220. Cabri, L. J.; Newville, M.; Gordon, R. A.; Crozier, E. D.; Sutton, S. R.; McMahon, G.; Jiang, D. T. *Can. Mineral.* **2000**, *38*, 1265–1281.
221. Bertsch, P. M.; Hunter, D. B.; Sutton, S. R.; Bajt, S.; Rivers, M. L. *Environ. Sci. Technol.* **1994**, *28*, 980–984.
222. Hunter, D. B.; Bertsch, P. M.; Kemner, K. M.; Clark, S. B. *J. Physique* **1997**, *7*, 767–771.

Comprehensive Coordination Chemistry II
ISBN (set): 0-08-0437486

Volume 2, (ISBN 0-08-0443249); pp 159–186

2.14 Photoelectron Spectroscopy

D.-S. YANG
University of Kentucky, Lexington, KY, USA

2.14.1 BASIC CONCEPTS 187
2.14.2 SPECTRAL FEATURES 188
2.14.3 SPECTRAL ASSIGNMENTS 189
2.14.3.1 Electronic Structure Methods 189
2.14.3.2 Franck–Condon Principle 189
2.14.3.3 Photon Energy Dependence of Band Intensities 189
2.14.3.4 Ionization Energy Trends and Resolved Fine Structures 190
2.14.4 He^{I}, He^{II}, AND X-RAY PHOTOELECTRON SPECTROSCOPY 190
2.14.5 SYNCHROTRON RADIATION PHOTOELECTRON SPECTROSCOPY 190
2.14.6 LASER-BASED PULSED FIELD IONIZATION-ZERO ELECTRON KINETIC ENERGY PHOTOELECTRON SPECTROSCOPY 191
2.14.7 LASER-BASED NEGATIVE ION PHOTOELECTRON SPECTROSCOPY 194
2.14.8 OTHER PHOTOELECTRON TECHNIQUES 194
2.14.9 REFERENCES 195

2.14.1 BASIC CONCEPTS

Molecular photoelectron spectroscopy (PES) involves the application of the photoelectric effect to the study of electronic states and geometric structures.[1–3] Electrons are ejected from molecules by irradiation of monochromatic photons with energy $h\nu$,

$$M + h\nu \longrightarrow M^+ + e^- \tag{1}$$

The energy difference ΔE between a final ion state and an initial neutral state equals the incident photon energy minus the kinetic energy KE of the ejected electron,

$$\Delta E = h\nu - KE \tag{2}$$

By defining adiabatic ionization energy (IE) as the minimum energy required to remove an electron from the ground electronic state of the neutral,

$$\Delta E = IE + E_i - E_n \tag{3}$$

where E_i and E_n are the internal energies of the ion and neutral states, which include excited electronic, vibrational, and rotational energies. If the initial neutral molecules are in their ground states ($E_n = 0$), the PES of neutral molecules provides information about the corresponding cations; if some of the initial neutral molecules are in their excited states, information about the neutral excited states may also be obtained.

Photoelectron spectroscopy can also be used to study negative ions. In this case, the technique is termed negative ion (anion) PES or photodetachment PES.

$$M^{n-} + h\nu \longrightarrow M^{(n-1)-} + e^- \tag{4}$$

and

$$\Delta E = EA + E_{(n-1)-} - E_{n-} \tag{5}$$

where EA is the electron affinity of M^{n-} that is the minimum energy to eject en electron from the ground state of M^{n-} to the ground state of the $M^{(n-1)-}$ and E_{n-} and $E_{(n-1)-}$ are the internal energies of M^{n-} and $M^{(n-1)-}$.

2.14.2 SPECTRAL FEATURES

A photoelectron spectrum is a record of the electron signal as a function of the electron kinetic energies at fixed photon energy or as a function of photon wavelengths at specific electron kinetic energy. Because molecular energy states are quantized, a photoelectron spectrum will consist of a series of discrete bands at various energy positions. Because photoelectron transition probabilities are proportional to transition dipole moments, the intensity of each ionization band will reflect the difference of the potential energy surfaces in the initial and final states. Thus, the characteristic features of an ionization band involve its energy, intensity, shape, and resolved fine structures (vibrational, rotational, vibronic, spin-orbit, etc). Each of these features is sensitive to the electronic state and geometry of the molecule. Figure 1 shows a textbook example of the N_2 photoelectron spectrum taken at the He^I photon energy (21.2 eV).[4] The spectrum consists of three band systems, originating from transitions of the electronic ground state $^1\Sigma_g^+$ of N_2 to the $^2\Sigma_g^+$, $^2\Pi_u$, and $^2\Sigma_u^+$ states of N_2^+. The $^2\Sigma_g^+ \leftarrow {}^1\Sigma_g^+$ and $^2\Sigma_u^+ \leftarrow {}^1\Sigma_g^+$ transitions consist of two peaks, separated by 2,150 and 2,390 cm^{-1}, respectively, whereas the $^2\Pi_u \leftarrow {}^1\Sigma_g^+$ transition has six peaks with a spacing of 1,810 cm^{-1}. These energy intervals correspond to the vibrational frequencies in the three ionic states, which are significantly different from the frequency of 2,345 cm^{-1} in the neutral ground state. The measured vibrational frequencies infer that the strength of the N_2^+ bonding follows the trend of $^2\Sigma_u^+ > {}^2\Sigma_g^{+2} > \Pi_u$. The number of the observed vibrational quanta indicates a larger change of bond distance with the $^2\Pi_u \leftarrow {}^1\Sigma_g^+$ transition than the $^2\Sigma_{g,u}^+ \leftarrow {}^1\Sigma_g^+$ transitions. The bond

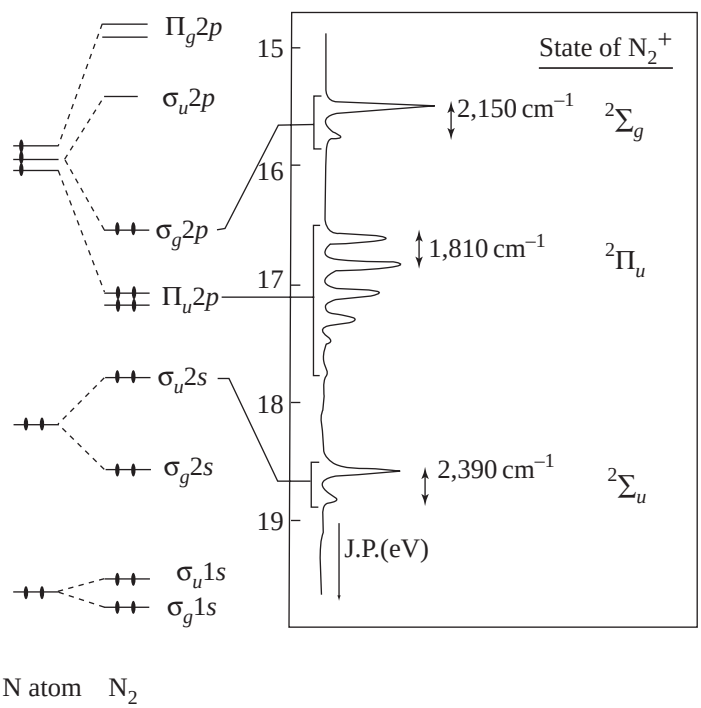

Figure 1 Left: the MO diagram of N_2; middle: the PE spectrum of N_2; right: the ion states of N_2^+ (reproduced by permission of Bancroft and Hu, 1999;[4] © 1999, Wiley).

lengths of the $^2\Sigma_g$, $^2\Pi_u$ and $^2\Sigma_u$ states of N_2^+ are 1.11642, 1.1749, and 1.074 Å, respectively, compared to 1.09769 Å in the $^1\Sigma_g^+$ ground state of N_2.

The energy of an ion state may be related to the energy of a molecular orbital (MO) from which an electron is ejected by photoionization. In N_2, the $^1\Sigma_g^+$ ground state has an electron configuration of $1\sigma_g^2(1s^2)1\sigma_u^2(1s^2)2\sigma_g^2(2s^2)2\sigma_u^2(2s^2)1\pi_u^4(2p^4)3\sigma_g^2(2p^2)$. The removal of an electron from the $2\sigma_u^2$, $1\pi_u^4$, and $3\sigma_g^2$ orbitals forms the electronic states $^2\Sigma_u^+$, $^2\Pi_u$, and $^2\Sigma_g^+$ of N_2^+, respectively. In a zero-order approximation or Koopmans theorem, the experimental energy of an ionic state equals the negative value of the theoretical one-electron orbital energy. Though rarely accurate in practice (because electron relaxation, correlation, and relativistic effect are ignored), Koopmans theorem has proven molecular orbitals to be more than a product of the quantum chemist's imagination and has contributed to the understanding of photoelectron spectra and thus, the bonding and structure of molecules. For example, the reduced vibrational frequencies and increased bond lengths of the $^2\Sigma_g^+$ and $^2\Pi_u$ states of N_2^+ (with respect to those of N_2) can be viewed as the result of removing the bonding electrons from the σ_g and π_u orbitals in the $^1\Sigma_g^+$ ground state of N_2. The increased vibrational frequency and shortened bond distance of the $^2\Sigma_u^+$ state are due to the ejection of an antibonding electron from the neutral σ_u orbital (Figure 1). Moreover, the smaller vibrational frequency, longer vibrational progression, and larger bond distance of the $^2\Pi_u$ state (with respect to that of the $^2\Sigma_g^+$ state) reflect a stronger electron binding in the π_u orbital than in the σ_g orbital of the neutral $^1\Sigma_g^+$ state. Thus, the spectral information about a molecular ion can be related to the MO picture of the corresponding neutral.

2.14.3 SPECTRAL ASSIGNMENTS

2.14.3.1 Electronic Structure Methods

Because PES is an experimental version of quantum chemistry, quantum chemical calculations play a powerful role in the interpretation of PE spectra. Such calculations provide electronic transition energies, vibrational frequencies, and rotational constants to compare with PE band positions. Theoretical electron configurations and geometries of the initial and final states can be used to correlate with spectral intensity profiles. In the 1970s and 1980s, most computations were carried at semiempirical and non-correlation *ab initio* levels of theory. Since the 1990s, higher levels of computational methods are increasingly employed, which include density functional theory, configuration interaction, many-body perturbation theory, and coupled cluster methods.[5] Density functional theory has been the most popular choice because of its efficiency and reasonable accuracy.

2.14.3.2 Franck–Condon Principle

For vibrationally resolved PE spectra, comparing Franck–Condon factors and PE peak intensities helps identify the geometric conformation and electronic state of the photoelectron carrier. According to the Franck–Condon principle, the intensity of a vibrational peak in an electronically allowed transition is proportional to the absolute square of the overlap integral of the vibrational wave functions of the initial and final states. This overlap integral is known as the Franck–Condon factor. To calculate such factors, potential functions must be known for both the initial and final states and can be obtained by *ab initio* calculations. In many cases, a harmonic approximation has yielded adequate descriptions for low vibrational levels of potential wells.[6,7]

2.14.3.3 Photon Energy Dependence of Band Intensities

For PE spectra of metal compounds where vibrational fine structures are not resolved, the identification of the nature of the ionized MOs is often aided by taking the advantage of the photon energy dependence of molecular ionization cross sections. It has been shown early that the intensities of the metal *d* orbital ionization bands increase dramatically from He^I to He^{II} (40.8 eV) radiation, compared to those of ligand-based *s* and *p* ionization bands.[8–11] This is known as the He^I/He^{II} intensity rule. More recently, synchrotron radiation has been employed to measure relative band intensities at different photon wavelengths.[4,12,13] The synchrotron radiation has

the advantage of the extensive wavelength tunability over the He^{I}/He^{II} radiations, allowing for detailed studies of photon energy dependence of ionization band intensities.

2.14.3.4 Ionization Energy Trends and Resolved Fine Structures

In some cases, ionization bands may be assigned by comparing the spectra of electronically and chemically related molecules. For example, ionization bands from highly localized metal orbitals are expected to show little energy shifts in a series of molecules consisting of a certain metal atom, whereas those from ligand-based orbitals should exhibit small energy changes for molecules containing the same ligand. In addition, resolved spin–orbit, Jahn–Teller, ligand-field, and vibrational splittings provide fingerprints about the nature of MO ionizations.[4]

2.14.4 He^{I}, He^{II}, AND X-RAY PHOTOELECTRON SPECTROSCOPY

He^{I}/He^{II} PES has greatly contributed to the understanding of electronic structures of coordinately saturated stable metal compounds. The technique has been widely used since the 1960s and is still being applied to new molecular systems.[8–11,14–24] The He^{I} radiation, combined with a hemispheric electron analyzer, gives a total instrumental resolution of about 20 meV.[21,22] This level of resolution is sufficient to resolve vibrational energy levels for simple and light molecules, but it is not enough to resolve low-frequency modes of metal compounds. Recently, a newly designed PE spectrometer consisting of a hemispherical analyzer and an electron cyclotron resonance He discharge lamp has improved the resolution to ~3 meV,[25] though the instrument has not been used on metal-containing molecules. He^{II} PES measurements are mainly used to aid spectral assignments according to the He^{I}/He^{II} intensity rule. Because the He^{I}/He^{II} radiation is in the UV region, the He^{I}/He^{II} PES is also known as UPS (ultraviolet photoelectron spectroscopy).

X-ray PES or XPS has been used to study molecular core levels, and information from the core electron ionization can be used to evaluate orbital overlap and charge potential contributions to electron binding energies of valence orbitals.[26] XPS resolution is lower than that of UPS due to broader X-ray photon line widths and shorter lifetimes of core electrons. The most commonly used X-ray sources involve Mg$K\alpha$ (1,253.6 eV) and Al$K\alpha$ (1,486.6 eV). In XPS, a monochromator is used to remove the background continua and unwanted lines from the X-ray sources to increase the X-ray purity and reduce the X-ray line width. A line width of about 0.2 eV has been achieved for the Mg$K\alpha$ and Al$K\alpha$ sources.[27] The electron analyzer of an XPS spectrometer can be similar to that in a UPS spectrometer. Therefore, UPS and XPS spectra can be taken on the same instrument if both sources are available.

2.14.5 SYNCHROTRON RADIATION PHOTOELECTRON SPECTROSCOPY

Synchrotron radiation is produced by electrons circulating in a storage ring at nearly the speed of light and deflected in their trajectories by magnets.[28] The major advantage of the synchrotron radiation is its wavelength tunability from UV to X-ray region. It can be used to study valence and core electrons and allows the investigation of photoionization cross sections as a function of photon energies. Since its application to metal carbonyls in 1987, synchrotron PES has been established as a powerful tool in elucidating molecular electronic structures.[4,12,13,29] In studying core levels, synchrotron PE measurements have resolved ligand field splitting, vibrational splitting, and other fine structures of many molecular systems for the first time. For valence levels, it has provided unequivocal settlements for some controversies in PE spectral assignments.

For example, $TiCl_4$ was investigated by several He^{I}, He^{II}, and theoretical studies, however, the assignment of its PE spectrum has only been resolved by a combined synchrotron PE and theoretical study.[30] The valence electron configuration of $TiCl_4$ is predicted by theory to be either the form of $2a_1^2 2t_2^6 1e^4\ 3t_2^6 1t_1^6$ or $2t_2^6 2a_1^2 1e^4\ 3t_2^6 1t_1^6$, where the Cl 3*s* orbitals are not included. The $2a_1$ and $3t_2$ orbitals are predominantly Cl 3*p*, mixed with a small amount of Ti 4*s* in the $2a_1$ orbitals and Ti 3*d* in the $3t_2$ orbitals, the $2t_2$ and $1e$ are bonding orbitals between Cl 3*p* and Ti 3*d*, and the highest occupied orbital $1t_1$ is a non-bonding orbital of Cl 3*p*. The discrepancy between the two electron configurations lies in the energy ordering of the $2a_1$ and $2t_2$ orbitals. Figure 2 presents the PE spectra of the molecule recorded at photon energies (a) 24 and (b) 40 eV, which

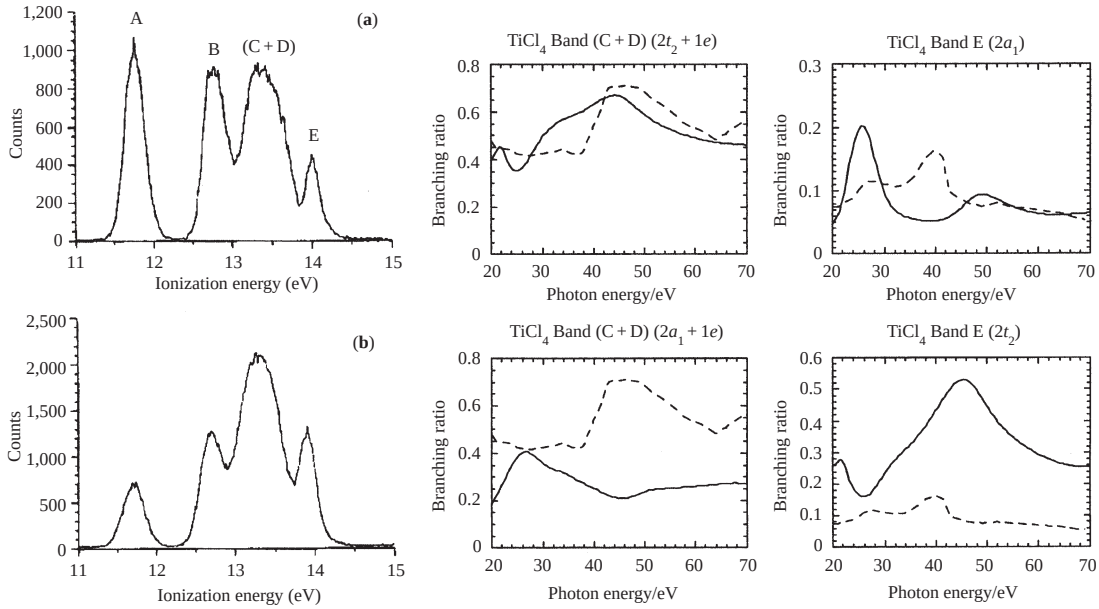

Figure 2 Left: PE spectra of $TiCl_4$ recorded with photon energies at (a) 24 and (b) 40 eV; right: comparison of experimental (dashed line) and theoretical (solid line) branching ratios for the PE bands (C + D) and E with two possible assignments (see text) (reproduced by permission of the American Chemical Society from *Inorg. chem.* **1994**, *33*, 5086–5093).

reproduce the band intensity profiles of He^{I}/He^{II} spectra. The spectra display four bands, labeled A, B, (C + D), and E. The relative intensities of bands A and B decrease, whereas the intensity of band E increases from ~20 to 40 eV. According to the He^{I}/He^{II} rule, bands A and B are expected to be the ionization of the ligand-based orbitals, which is consistent with the theoretical predictions of the Cl 3*p*-based $1t_1$ and $3t_2$ orbitals. Band (C + D) is about twice as broad as any of the other bands and may be viewed as the ionization of the two closely lying $1e$ and $2t_2$ orbitals. However, the intensity increase for band E is not expected on the basis of the He^{I}/He^{II} intensity rule if the electron is ejected from the Cl 3*p*-based $2a_1$ orbital. Therefore, an alternative spectral assignment attributed band (C + D) to the $1e$ and $2a_1$ orbitals and band E to the $2t_2$ orbitals.

The disagreement between these two assignments is settled by synchrotron PE measurements and ionization cross section calculations in the photon energy range of 20–70 eV.

Figure 2 presents theoretical (solid line) and experimental (dashed line) branching ratios (i.e., ratio of the intensity of a photoelectron band versus the sum of the intensities of the all bands in a spectrum) for the PE bands (C + D) and E. The agreement between the experimental values for band (C + D) and the theoretical values for the $(2t_2 + 1e)$ orbitals is far superior to that from the alternative assignment. A branching ratio maximum is observed at 46 eV, in agreement with the calculated result if the band is from the ionization of the $2t_2$ and $1e$ orbitals, whereas the experimental and theoretical ratio profiles are completely different if the band is assigned to the $2a_1$ and $1e$ ionizations. For band E, the experimental branching ratio shows two peaks at 26 and 42 eV, which may be correlated with the calculated peaks at 26 and 48 eV from the $2a_1$ ionization and 22 and 46 eV from the $2t_2$ ionization. However, the experiment branching ratios exhibit no significant photon energy dependence of the band E intensity above 46 eV, whereas the calculation predicts a sharp decrease of the branching ratio for the $2t_2$ ionization. Therefore, band (C + D) is assigned to the $2t_2 + 1e$ ionization and band E to the ionization of $2a_1$ orbital.

2.14.6 LASER-BASED PULSED FIELD IONIZATION-ZERO ELECTRON KINETIC ENERGY PHOTOELECTRON SPECTROSCOPY

Perhaps, the most important PES development over the past two decades is the introduction of pulsed field ionization-zero electron kinetic energy (PFI-ZEKE) technique.[31–34] Other names in use for this technique include ZEKE-PFI, PFI-PE, or simply ZEKE. PFI-ZEKE involves the detection of electrons produced by delayed, pulsed, electric field ionization of very high-lying

Rydberg states with a principle quantum number $n > 100$. These Rydberg states are formed by laser excitation and are located a few cm^{-1} (or a fraction of meV) below the ionization threshold. Because the electrons ejected from these Rydberg states carry near zero electron kinetic energy, these states are known as ZEKE states and the ejected electrons are named as ZEKEs. The measured electron peak position is lower than that without the presence of the field by the Stark shift (δ)

$$\delta = CE^{1/2}\,\mathrm{cm}^{-1} \tag{6}$$

where E is the magnitude of the pulsed electric field in the unit of V/cm^{-1} and C is a proportional constant that can be determined experimentally. Experiments at various electric fields show that the value of C is ~4 for metal-containing molecules.[35] On the basis of the continuity of ionization oscillator strengths, the relative intensities of the photoelectron bands in a PFI-ZEKE spectrum are expected to be identical to those in a direct threshold photoionization PE spectrum, provided that perturbations by nearby autoionizing states are small. Indeed, PFI-ZEKE spectra of many metal compounds have shown Franck–Condon intensity profiles.[6,7,36,37] The delay of pulsed field ionization from laser excitation is typically a few microseconds, which allows the ZEKE detection to be free from background electrons produced by direct photoionization and autoionization. Because of the pulsed nature of the experiment, a time-of-flight electron analyzer is used for the ZEKE detection. The longevity of the ZEKE states is currently contributed to the angular moment l mixing due to the presence of the weak d.c. field in the excitation volume and to the magnetic momentum m_l mixing due to the inhomogeneous electric field formed by nearby prompt ions.

The major advantage of PFI-ZEKE is its energy resolution, which allows the resolution of rotational and vibrational structures of metal compounds.[6,7,34–51] For example, the ZEKE spectra of vanadium dimers (V_2) have a line width of $1.5\,cm^{-1}$ (0.19 meV), from which the rotational

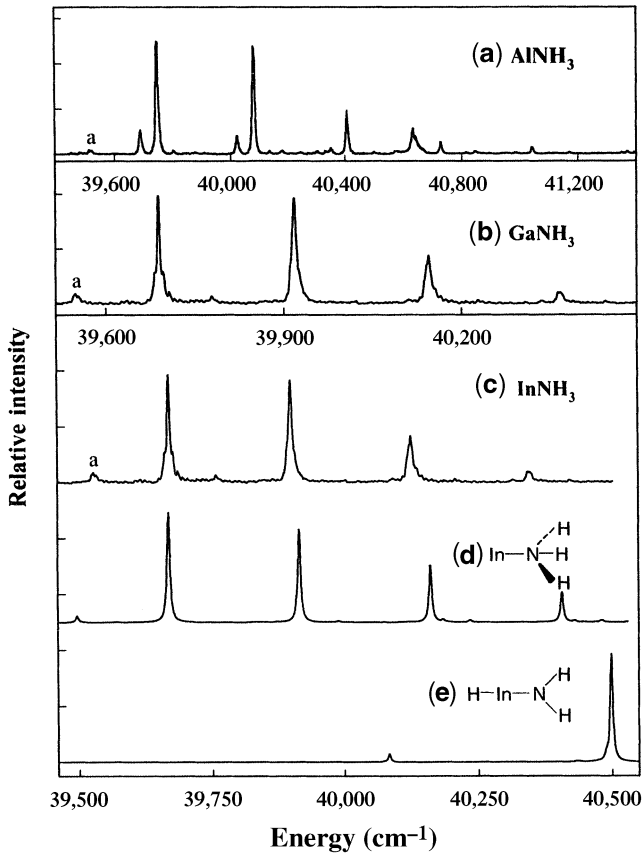

Figure 3 ZEKE spectra of MNH_3 (M = Al, Ga, In) and spectral simulations for indium adduct and insertion isomers (reproduced by permission of the American Chemical Society from *J. Phys. Chem. A* **2000**, *104*, 8178–8182).

constant and bond length of the corresponding cation have been accurately determined for the first time.[51] Figure 3 shows the vibrationally resolved PFI-ZEKE spectra of MNH_3 (M = Al, Ga, In), with spectral line widths of $\sim 5.0\,cm^{-1}$.[42–44] Each of the spectra displays a short vibrational progression and a small peak (a) at the left side of the strongest peak. Additionally, the $AlNH_3$ spectrum exhibits a doublet in the first three strong bands. The doublet is separated by $58\,cm^{-1}$ and is due to the spin–orbit interaction in $AlNH_3$. The splitting is not observed for the Ga and In species due to large energy separations between the two spin components of the heavy metal atoms, which prevent a significant population of the upper spin level. The vibrational progressions yield the M^+-N stretching frequencies of 339 (Al^+-N), 270 (Ga^+-N), and 234 (In^+-N) cm^{-1}. The strongest peaks determine adiabatic IEs, 39,746, 40,135, and 39,689 cm^{-1}, for the Al, Ga, and In complexes, respectively. The small peaks (a) arise from the transitions of the first vibrational levels of MNH_3 to the vibrational ground states of MNH_3 and yield the M–N stretching frequencies of 227, 161, and 141 cm^{-1} for the three neutral radicals. Converting the frequencies into stretching force constants shows the strength of the metal–nitrogen bonding in the order of Al > Ga > In, and the trend is explained by involving electrostatic and orbital interactions. To determine the geometric conformations of the complexes, density functional calculations were used to obtain the minimum energy structures and harmonic vibrational analyses for both the neutral and the ion; Franck–Condon factors were calculated using the theoretical geometries and vibrational analysis, and spectral simulations were performed with the experimental line widths and at various temperatures to obtain the best fit. A comparison of the 100 K simulations from the two indium isomers (Figures 4d and 4e) and the experimental spectrum of $InNH_3$ (Figure 3(c)) clearly identifies that the electron carrier is a simple adduct rather than an insertion compound.

An alternative to PFI-ZEKE would be mass-analyzed threshold ionization (MATI), where cations rather than ZEKE electrons are detected.[52] In principle, MATI is attractive because of the inherent mass selection. However, MATI experiments are difficult to implement because of ion separation fields affecting the high Rydberg levels required for delayed pulsed field ionizations. The technique has so far only been used for the smallest metal molecules.[53]

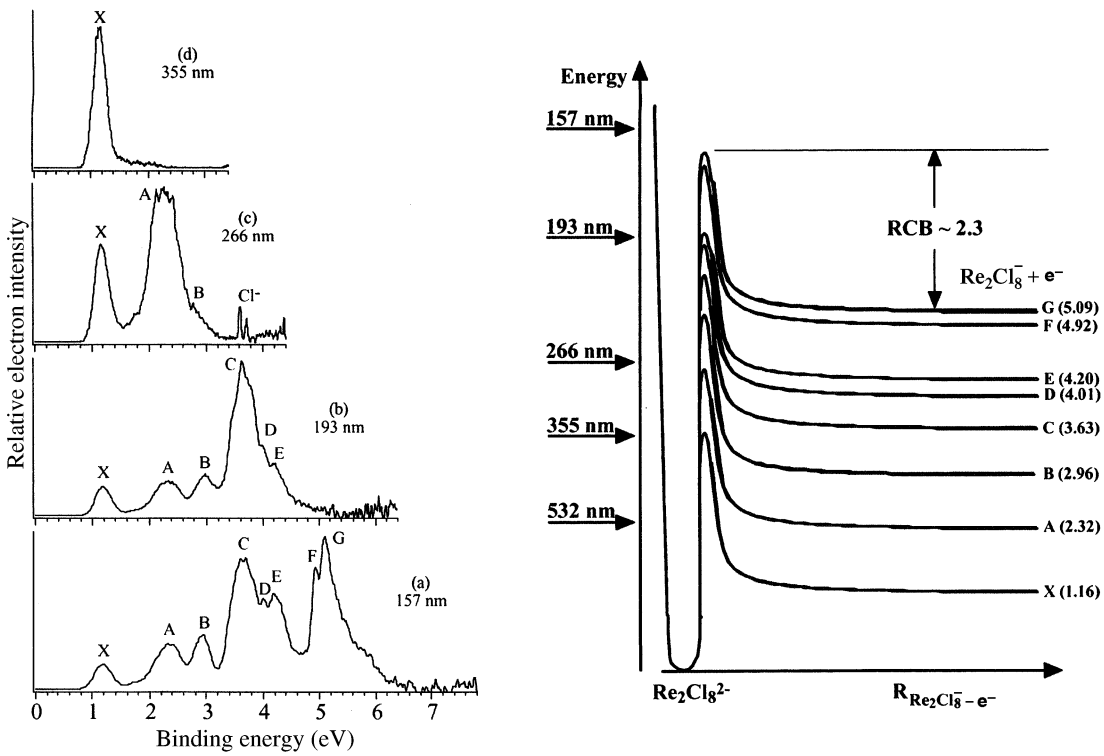

Figure 4 Left: PE spectra of $Re_2Cl_8^{2-}$ taken with 157, 193, 266, and 355 nm lasers; right: schematic drawing of potential energy curves showing the repulsive Coulomb barriers (RCB, eV) and vertical detachment energies (eV) of PE bands. The relative positions of the five laser wavelengths are also indicated (reproduced by permission of the American Chemical Society from *J. Am. Chem. Soc.* **2000**, *122*, 2096–2100).

2.14.7 LASER-BASED NEGATIVE ION PHOTOELECTRON SPECTROSCOPY

Although the principle is the same for photoionization of neutrals and photodetachment of anions, their description differs in detail. First, negative ion PES has the advantage of species selectivity when combined with mass spectrometry. Second, all neutrals have positive IEs, whereas EAs of some anions may be negative. If a singly charged anion has a negative EA, the ion is energetically unstable. Third, an electron ejected from a neutral experiences an attractive Coulomb field of the positively charged core, an electron detached from a singly charged anion is subject to a angular momentum interaction with the residual neutral core, and photodetachment of a multiply charged anion results in Coulomb repulsion between two negatively charged particles (an anion and a free electron). Anions do not possess Rydberg-analogous states that converge to neutral states; thus, PFI technique does not apply to these species. For multiply charged anions, threshold photodetachment is not feasible because Coulomb repulsion barriers are often higher than the EAs of anions.

Similar to neutral PES, negative ion PES can use a fixed-frequency light source and measure the energies of detached electrons, or scan photon wavelengths and detect ZEKE electrons. Most studies have been reported on singly charged anions and at fixed photon energies,[54–64] although anion ZEKE experiments have also been reported.[34,65–71] More recently, studies have also been carried out for multiply charged negative ions.[72–76] An anion PES instrument consists of a photodetachment laser, an anion source, a mass selector, and an electron analyzer. Singly charged metal-containing anions are often prepared by pulsed laser vaporization in supersonic jets,[54–61] or in electric discharge-flowing afterglow reactors,[63,64] whereas multiply charged anions are produced by electrospray.[73–76] Ions with a specific mass are selected by magnetic, electrostatic, or time-of-flight mass spectrometers. There are basically three widely used types of electron analyzers. The simplest one is a time-of-flight spectrometer. Its disadvantage is the small acceptance angle and thus, a small collection efficiency for photoelectrons. This problem is avoided in a magnetic bottle electron spectrometer that has high collection efficiency.[57,61] The high efficiency is achieved by magnetic fields which guide the ejected electrons into the detector. However, the collection of electrons with relatively large velocity differences results in a reduced spectral resolution. For experiments with a continuous ion source (e.g., flowing afterglow), a hemispherical analyzer can be used to provide a better energy resolution, but a lower collection efficiency, than that of the magnetic bottle spectrometer.[63,64]

Combining an electrospray ion source with anion PES has opened up a new avenue for studying multiply charged anions in the gas phase. It provides information about the repulsive Coulomb barrier produced by the superposition of a long-range Coulomb repulsion between two negatively charged photoproducts and a short-range electron binding. Because of the presence of this barrier, electron detachment requires the incident photon energy to be greater than the Coulomb potential if electron tunneling is ignored. Figure 4 shows the PE spectra (left) and band positions (right) of $Re_2Cl_8^{2-}$ at 157 nm (7.866 eV), 193 nm (6.424 eV), 266 nm (4.661 eV), and 355 nm (3.496 eV).[75] The 157 nm spectrum exhibits eight bands labeled X—G. Bands X, A, and B are attributed to three Re—Re bonding orbitals (δ, π, and σ), whereas features C—F are assigned to Re—Cl bonding and Cl non-bonding orbitals. The analysis of the PE spectrum confirms a $(\ldots\sigma^2\pi^4\delta_2)$ electron configuration and a formal quadruple Re—Re bond of the dianion. As photon wavelengths increase, the number of PE bands decrease. Because the Coulomb barrier should not be larger than the energy difference between the incident photon and the electron binding (if the binding energy is positive), the Coulomb barrier can be estimated to be <2.77 eV ($h\nu - E_G$) from the 157 nm spectrum, <2.79 eV ($h\nu - E_C$) from the 193 nm spectrum, <2.34 eV ($h\nu - E_A$) from the 266 nm spectrum, and <2.34 eV ($h\nu - E_X$) from the 355 nm spectrum. Moreover, a measurement at 532 nm (2.331 eV) shows no photoelectron signal, indicating that the Coulomb barrier is at least 2.33 eV. Therefore, the repulsion potential between $Re_2Cl_8^{2-}$ and the free electron should be $\sim$2.3 eV at its ground state. If the two negative charges of $Re_2Cl_8^{2-}$ are localized on the Cl atoms, the intramolecular Coulomb repulsion may be calculated according to Coulomb's law, $e^2/4\pi\varepsilon_0 r$. The calculated value is 2.5 eV, fairly close to the experimental value of $\sim$2.3 eV.

If the Coulomb repulsion is stronger than the electron binding, the anion shall have a negative electron binding energy. For example, the binding energy of a quadruply charged anion, copper phthalocyanine, 3,4′,4″,4‴-tetrasulfonate $[CuPc(SO_3)_4]^{4-}$, is measured to be -0.9 eV.[76]

2.14.8 OTHER PHOTOELECTRON TECHNIQUES

Other PES methods have also been developed and may be of potential uses for metal compounds. These techniques include, among others, vacuum ultraviolet (VUV) laser-based PFI,[77]

synchrotron-based PFI,[78] photoelectron–photoion coincidence,[79–83] two-dimensional imaging,[84,85] and femtosecond time-resolved experiments.[86,87] The VUV laser and synchrotron PFI may be used for high-resolution PES studies of metal compounds with higher IE (>6 eV). However, at the present time neither VUV lasers nor synchrotron radiations can provide photon intensities as high as UV lasers. The photoelectron–photoion coincidence technique correlates the electron signal to its carrier, but it often operates at relatively low particle counting rates. The two-dimensional PES, which measures photoelectron yields as a function of electron and photon energies, can provide new opportunities to study photoexcitation and photoionization processes. The femtosecond time-resolved technique is emerging as a new means for the study of ultrafast excited state dynamics.

2.14.9 REFERENCES

1. Turner, D. W.; Baker, C.; Baker, A. D.; Brundle, C. R. *Molecular Photoelectron Spectroscopy*; Wiley: London, 1970.
2. Eland, J. H. D. *Photoelectron Spectroscopy*; Butterworths: London, 1974.
3. Rabalais, J. W. *Principle of Ultraviolet Photoelectron Spectroscopy*; Wiley: New York, 1977.
4. Bancroft, G. M.; Hu, Y. F. In *Inorganic Electronic Structure and Spectroscopy, Volume 1: Methodology*. Solomon, E. I., Lever, A. B. P., Eds.; Wiley: New York, 1999, pp 443–512.
5. Jensen, F. *Introduction to Computational Chemistry*; Wiley: Chichester, 1999.
6. Yang, D. S. *Coord. Chem. Rev.* **2001**, *214*, 187–213.
7. Bérces, A.; Zgierski, M. Z.; Yang, D. S. In *Computational Molecular Spectroscopy*; Jensen, P., Bunker, P. R., Eds.; Wiley: New York, 2000, pp 109–134.
8. Cowley, A. H. *Prog. Inorg. Chem.* **1979**, *26*, 45–160.
9. Green, J. C. *Struct. Bonding (Berlin)* **1981**, *43*, 37–112.
10. Solomon, E. I. *Comm. Inorg. Chem.* **1984**, *3*, 227–320.
11. Lichtenberger, D. L.; Kellogg, G. E. *Acc. Chem. Res.* **1987**, *20*, 379–387.
12. Green, J. C. *Acc. Chem. Res.* **1994**, *27*, 131–137.
13. Li, X.; Bancroft, G. M.; Puddephatt, R. J. *Acc. Chem. Res.* **1997**, *30*, 213–218.
14. Oskam, A. In *Spectroscopy of Inorganic-based Materials*; Clark, R. J. H., Hester, R. E., Eds.; Wiley: New York, 1987, pp 429–461.
15. Yang, D. S.; Bancroft, G. M.; Puddephatt, R. J.; Bursten, B. E.; McKee, S. D. *Inorg. Chem.* **1989**, *28*, 872–877.
16. Yang, D. S.; Bancroft, G. M.; Dignard-Bailey, L.; Puddephatt, R. J.; Tse, J. S. *Inorg. Chem.* **1990**, *29*, 2118–2122, 2496–2501.
17. Yang, D. S.; Bancroft, G. M.; L. Puddephatt, R. J.; Tse, J. S. *Inorg. Chem.* **1990**, *29*, 2487–2495.
18. Lichtenberger, D.; Rai-Chaudhuri, A.; Hogan, R. H. In *Organometallic Chemistry*; Fehlner, P., Ed.; Plenum: New York, 1992, pp 223–251.
19. Lichtenberger, D. L.; Lynn, M. A.; Chisholm, M. H. *J. Am. Chem. Soc.* **1999**, *121*, 12167–12176.
20. Westcott, B. L.; Gruhn, N. E.; Michelsen, L. J.; Lichtenberger, D. L. *J. Am. Chem. Soc.* **2000**, *122*, 8083–8084.
21. Lichtenberger, D. L.; Gruhn, N.; Rai-Chaudhuri, A.; Renshaw, S. K.; Gladysz, J. A.; Jiao, H.; Seyler, J.; Igau, A. *J. Am. Chem. Soc.* **2002**, *124*, 1417–1423.
22. Westcott, B. L.; Gruhn, N. E.; Enemark, J. H. *J. Am. Chem. Soc.* **1998**, *120*, 3382–3386.
23. Downs, A. J.; Green, J. C.; McGrady, G. S.; Munkman, N.; Parkin, R. P. G. *Dalton* **2000**, 21–27.
24. Al-Ktaifani, M.; Green, J. C.; Hitchcock, P. B.; Nixon, J. F. *J. Chem. Soc., Dalton Trans.* **2001**, 1726–1731.
25. Baltzer, P.; Karlsson, L.; Lundqvist, M.; Wannberg, B. *Rev. Sci. Instrum.* **1993**, *64*, 2179–2189.
26. Jolly, W. L. *Acc. Chem. Res.* **1983**, *16*, 370–376.
27. Hollas, J. M. *High Resolution Spectroscopy*, Butterworths: London; 1982, pp 435–480.
28. Margaritondo, G. *Introduction to Synchrotron Radiation*, Oxford University Press: New York, 1988.
29. Hu, Y. F.; Bancroft, G. M.; Tan, K. H. *J. Electron. Spectrosc. Relat. Phenom.* **2001**, *114–116*, 147–151.
30. Bursten, B. E.; Green, J. C.; Kaltsoyannis, N.; MacDonald, M. A.; Sze, K. H.; Tse, J. S. *Inorg. Chem.* **1994**, *33*, 5086–5093.
31. Müller-Dethlefs, K.; Schlag, E. W. *Ann. Rev. Phys. Chem.* **1991**, *42*, 109–136.
32. Müller-Dethlefs, K.; Schlag, E. W.; Grant, E. R.; Wang, K.; McKoy, B. V. In *Advances in Chemistry and Physics, Volume XC*.; Rice, S. A., Prigogine, I., Eds.; Wiley: New York, 1995, pp 1–103.
33. Schlag, E. W. *ZEKE Spectroscopy*; Cambridge University Press: Cambridge, 1998.
34. Müller-Dethlefs, K.; Schlag, E. W. *Angew. Chem., Int. Ed. Engl.* **1998**, *37*, 1346–1373.
35. Yang, D. S.; James, A. M.; Rayner, D. M.; Hackett, P. A. *Chem. Phys. Lett.* **1994**, *231*, 177–182.
36. Yang, D. S.; Hackett, P. A. *J. Electron. Spectrosc. Relat. Phenom.* **2000**, *106*, 153–169.
37. Yang, D. S. In *Advances in Metal and Semiconductor Clusters, Volume 5: Metal Ion Solvation and Metal–Ligand Interactions*. Duncan, M. A., Ed.; Elsevier: Amsterdam, 2001, pp 187–226.
38. Rodham, D. A.; Black, G. A. *Chem. Phys. Lett.* **1997**, *264*, 522–530.
39. Panov, S. I.; Powers, D. E.; Miller, T. A. *J. Chem. Phys.* **1997**, *108*, 1335–1346.
40. Barckholtz, T. A.; Powers, D. E.; Miller, T. A.; Bursten, B. E. *J. Am. Chem. Soc.* **1999**, *121*, 2576–2584.
41. Agreiter, J. K.; Knight, A. M.; Duncan, M. A. *Chem. Phys. Lett.* **1999**, *313*, 162–170.
42. Yang, D. S.; Miyawaki, J. *Chem. Phys. Lett.* **1999**, *313*, 514–518.
43. Rothschopf, G. K.; Perkins, J. S.; Li, S.; Yang, D. S. *J. Phys. Chem. A* **2000**, *104*, 8178–8182.
44. Li, S.; Rothschopf, G. K.; Pillai, D.; Sohnlein, B. R.; Wilson, B. M.; Yang, D. S. *J. Chem. Phys.* **2001**, *115*, 7968–7974.
45. Rothschopf, G. K.; Li, S.; Perkins, J. S.; Yang, D. S. *J. Chem. Phys.* **2001**, *115*, 4565–4572.
46. Pedersen, D. B.; Zgierski, M. Z.; Anderson, S.; Rayner, D. M.; Simard, B.; Li, S.; Yang, D. S. *J. Phys. Chem. A* **2001**, *105*, 11462–11469.

47. Li, S.; Rothschipf, G. K.; Yang, D. S. *J. Chem. Phys.* **2002**, *116*, 6589–6594.
48. Harrington, J.; Weisshaar, J. C. *J. Chem. Phys.* **1992**, *97*, 2809–2812.
49. Németh, G. I.; Ungar, H. Yeretzian, C.; Selzle, H. L.; Schlag, E. W. *Chem. Phys. Lett.* **1994**, *228*, 1–8.
50. Linton, C.; Simard, B.; Peter-Look, H.; Wallin, S.; Rothschopf, G. K.; Gunion, R. F.; Morse, M. D. *J. Chem. Phys.* **1999**, *111*, 5017–5026.
51. Yang, D. S.; James, A. M.; Rayner, D. M.; Hackett, P. A. *J. Chem. Phys.* **1995**, *102*, 3129–3134.
52. Zhu, L.; Johnson, P.; *J. Chem. Phys.* **1991**, *94*, 5679–5681.
53. Wiley, K. F.; Yeh, C. S.; Duncan, M. A. *Chem. Phys. Lett.* **1993**, *211*, 156–160.
54. Kaya, K.; Nakajima, A. In *Adv. Met. Semicond. Clusters, Volume 2*; Duncan, M. A., Ed.; JIA: Greenwich, 1995, pp 87–114.
55. Arnold, C. C.; Neumark, D. M. In *Adv. Met. Semicond. Clusters*; Duncan, M. A., Ed.; JIA: Greenwich, 1995, pp 113–148.
56. Hendricks, J. H.; De Clercq, H. L.; Lyapustina, S. A.; Fancher, C. A.; Lippa, T. P.; Collins, J. M.; Arnold, S. T.; Lee, G. H.; Bowen, K. H. *Front. Sci. Ser.* **1996**, *16*, 321–328.
57. Wang, L. S.; Wu, H. In *Adv. Met. Semicond. Clusters, Volume 4*; Duncan, M. A., Ed.; JIA: Greenwich, 1998, pp 299–343.
58. Boesl, U.; Knott, W. J. *Mass Spectrom. Rev.* **1999**, *17*, 275–305.
59. Fuke, K.; Hashimoto, K.; Takasu, R. In *Adv. Met. Semicond. Clusters, Volume 4*; Duncan, M. A., Ed.; Elsevier: Amsterdam, 2001, pp 299–343.
60. Conceicao, J.; Laaksonen, R. T.; Wang, L. S.; Guo, T.; Nordlander, P.; Smalley, R. E. *Phys. Rev. B* **1995**, *51*, 4668–4671.
61. Kietzmann, H.; Morenzin, J.; Bechthold, P. S.; Gantefor, G.; Eberhardt, W. *J. Chem. Phys.* **1998**, *109*, 2275–2278.
62. Dessent, C. E. Johnson, M. A. In *Fundamentals and Applications of Gas Phase Ion Chemistry*; Jennings, K. R., Ed.; Kluwer: Netherlands, 1999, pp 287–306.
63. Ervin, K. M.; Lineberger, W. C. In *Adv. Gas Phase Ion Chem. Volume 1*; Adams, N. G., Babcock, L. M., Eds.; JAI: Greenwich, 1992, pp 121–166.
64. Green, S. M. E.; Alex, S.; Fleischer, N. L.; Millam, E. L.; March, T. P.; Leopold, D. G. *J. Chem. Phys.* **2001**, *114*, 2653–2668.
65. Gantefor, G. F.; Cox, D. M.; Kaldor, A. *Z. Phys. D Atoms Mol. Clusters* **1991**, *19*, 59–61.
66. Gantefor, G. F.; Cox, D. M.; Kaldor, A. *Z. J. Chem. Phys.* **1990**, *93*, 8395–8396.
67. Gantefor, G. F.; Cox, D. M.; Kaldor, A. *Z. J. Chem. Phys.* **1992**, *96*, 4102–4105.
68. Arnold, C. C.; Neumark, D. M. *J. Chem. Phys.* **1993**, *99*, 3353–3362.
69. Arnold, C. C.; Neumark, D. M. *J. Chem. Phys.* **1993**, *100*, 1797–1804.
70. Arnold, C. C.; Xu, C.; Burton, G. R.; Neumark, D. M. *J. Chem. Phys.* **1995**, *102*, 6982–6989.
71. Drechsler, G.; Bëßmann, C.; Bosel, U.; Schlag, E. W. *J. Mol. Struct.* **1995**, *348*, 337–340.
72. Compton, R. N. In *Advances in Gas Phase Ion Chemistry*; Adams, N. G., Babcock, L. M., Eds.; JAI: Greenwich, 1992, pp 257–305.
73. Wang, L. S.; Wang, X. B. *J. Phys. Chem. A* **2000**, *104*, 1978–1990.
74. Wang, L. S. *Comm. Mod. Phys.* **2001**, *2*, D207–221.
75. Wang, X. B.; Wang, L. S. *J. Am. Chem. Soc.* **2000**, *122*, 2096–2100.
76. Wang, X. B.; Wang, L. S. *Nature* **1999**, *400*, 2096–2100.
77. Ng, C. Y. *Int. J. Mass Spectrom* **2000**, *200*, 357–386.
78. Ng, C. Y. *J. Electron. Spectrosc. Relat. Phenom.* **2000**, *108*, 41–45.
79. Baer, T. *Int. J. Mass Spectrom.* **2000**, *200*, 443–457.
80. Continetti, R. E. *Annu. Rev. Phys. Chem.* **2001**, *52*, 165–192.
81. Eland, J. H. D. *J. Electron. Spectrosc. Relat. Phenom.* **2000**, *112*, 1–8.
82. Becker, U. *J. Electron. Spectrosc. Relat. Phenom.* **2000**, *112*, 47–65.
83. Hall, R. I.; McConkey, A.; Ellis, K.; Dawber, G.; Avaldi, L.; MacDonald, M. A.; King, G. C. *Meas. Sci. Technol.* **1992**, *3*, 316–324.
84. Sokell, E.; Wills, A. A.; Cubric, D.; Currell, F. J.; Comer, J.; Hammond, P. *J. Electron. Spectrosc. Relat. Phenom.* **1998**, *94*, 107–125.
85. Berrah, N.; Langer, B.; Wills, A. A.; Kukk, E.; Bozek, J. D.; Farhat, A.; Gorczyca, T. W. *J. Electron. Spectrosc. Relat. Phenom.* **1999**, *101–103*, 1–11.
86. Lochbrunner, S.; Larsen, J. J.; Shaffer, J. P.; Schmitt, M.; Schultz, T.; Underwood, J. G.; Stolow, A. *J. Electron. Spectrosc. Relat. Phenom.* **2000**, *112*, 183–198.
87. Neumark, D. M. *Annu. Rev. Phys. Chem.* **2001**, *52*, 255–277.

Comprehensive Coordination Chemistry II
ISBN (set): 0-08-0437486

Volume 2, (ISBN 0-08-0443249); pp 187–196

2.15 Electrochemistry: General Introduction

A. M. BOND
Monash University, Clayton, Vic., Australia

2.15.1 INTRODUCTION 197
2.15.2 A SURVEY OF ELECTROCHEMICAL TECHNIQUES COMMONLY USED BY COORDINATION CHEMISTS 198
2.15.2.1 Basic Definitions of Voltammetry 199
2.15.2.1.1 Transient voltammetry 199
2.15.2.1.2 Steady state voltammetry 201
2.15.2.2 A Reversible Electrode Process 202
2.15.2.2.1 Electrochemical reversibility and irreversibility 206
2.15.2.2.2 Chemical reversibility and irreversibility 207
2.15.2.3 Bulk Electrolysis 208
2.15.2.3.1 Theory of bulk electrolysis 210
2.15.2.4 Spectroelectrochemistry 212
2.15.2.4.1 ESR spectroelectrochemistry 213
2.15.2.4.2 IR spectroelectrochemistry 214
2.15.2.4.3 UV–visible spectroelectrochemistry 215
2.15.2.4.4 NMR spectroelectrochemistry 215
2.15.2.4.5 Other forms of spectroelectrochemistry 216
2.15.2.4.6 Combining mass spectrometry and electrochemistry 216
2.15.2.4.7 Examples of electrode mechanisms elucidated by combined voltammetric and spectroelectrochemical studies 217
2.15.2.4.8 Concluding remarks—broadening electrochemical and coordination chemistry horizons 220
2.15.3 REFERENCES 221

2.15.1 INTRODUCTION

The coordination chemist may be interested in employing electrochemical techniques for a wide range of reasons which could include: defining the redox chemistry of coordination compounds; understanding the redox chemistry of metal centers of compounds of biological significance; electrosynthesis of compounds; electrochemical generation of unstable species in unusual oxidation states and the study of their reaction pathways or spectroelectrochemical attainment of their spectroscopic properties; obtaining thermodynamic or kinetic data. Data relevant to these and other subjects ranging from catalysis of a reaction achieved by modifying the properties of an electrode surface by adsorption of a coordination compound to the establishment of fundamental aspects of electron transfer kinetics are all obtainable by the application of modern electrochemical techniques.[1–5]

The above brief survey implies that uses of electrochemistry are extremely broad ranging. Given that the application of coordination chemistry also is extremely diverse, it therefore logically follows that electrochemistry and coordination chemistry overlap in many areas of applied science.[1,2] For example, a detailed understanding of the photoredox chemistry of

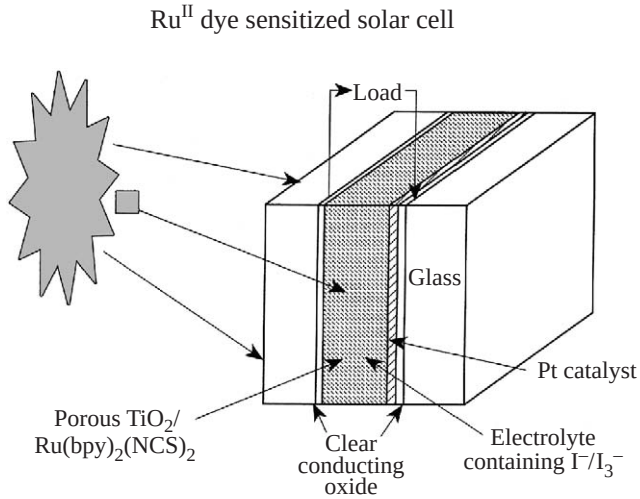

Figure 1 Schematic diagram of a ruthenium dye-sensitized photoelectrochemical cell. Provided courtesy of Leone Spiccia and Douglas MacFarlane.

compounds of the type $Ru(bpy)_2(NCS)_2$ (bpy = bypyridine or a derivative; NCS = N-bonded thiocyanate) has been integral to the success in the development of Grätzel-type photoelectrochemical solar cells[6,7] that have achieved photon-to-electric current conversion consistently in excess of 10%. Figure 1 represents a schematic diagram of such a cell, whilst Reaction Scheme 1 summarizes the relevant reactions when the cell is based on the use of the *cis*-$Ru(bpy)_2(NCS)_2$ dye, titania semiconductor and platinum electrodes, and acetonitrile containing I^- and I_3^-. The iodine components act as the electrolyte and also contribute the chemical components in the $2I_3^- + 2e^- \rightleftharpoons 3I_2$ "dark" half-cell reaction.

$$\text{excitation: } Ru^{II}(bpy)_2(NCS)_2 \xrightleftharpoons{h\nu} [Ru^{III}(bpy^{\bullet-})(bpy)(NCS)_2]^*$$

$$e^- \text{ injection: } [Ru^{III}(bpy^{\bullet-})(bpy)(NCS)_2]^* \xrightarrow{TiO_2} [Ru^{III}(bpy)_2(NCS)_2]^+ + e^-$$

$$\text{dye regeneration: } [Ru^{III}(bpy)_2(NCS)_2]^+ + El^- \longrightarrow Ru^{II}(bpy)_2(NCS)_2 + El$$

$$\text{electrolyte regeneration: } El + e^- \xrightleftharpoons{Pt} El$$

Scheme 1

2.15.2 A SURVEY OF ELECTROCHEMICAL TECHNIQUES COMMONLY USED BY COORDINATION CHEMISTS

The most commonly employed techniques used by coordination chemists undertaking electrochemical experiments are:

Voltammetry under transient (e.g., cyclic voltammetry) or steady-state (e.g., rotated disk or microelectrode) conditions[2–5] which requires the interpretation of current–potential–time (*I–E–t*) curves.

Spectroelectrochemical measurements[9,10] in which a spectroscopic or other (e.g., mass spectrometric) method of measurement is used in conjunction with electrochemistry to characterize intermediates or products of electrode processes.

Bulk electrolysis[2] for the purpose of electrosynthesis or for a coulometric determination of the number of electrons (n) associated with a half-cell reaction of the kind $A \rightarrow B + ne^-$ (A is the compound being oxidized and B is product, with charges being omitted for simplicity, and n is the overall number of electrons transferred per molecule of A oxidized as determined by coulometry and application of Faraday's Law of electrolysis).

The basic concept of the most common form of electrochemical investigation of the redox chemistry of a coordination compound is that voltammetric data are initially collected and a mechanism for the half-cell reaction that occurs at the working electrode is postulated. A simple process, often used as a voltammetric reference potential standard,[2] would be (Equation (1)) oxidation of ferrocene (Fc) to the ferrocenium cation (Fc^+) in an organic solvent (acetonitrile, dichloromethane, etc.) containing 0.1 M of an electrolyte such as Bu_4NPF_6 (added to lower the resistance):

$$Fc \rightleftharpoons Fc^+ + e^- \tag{1}$$

The reduction of potassium ferricyanide in water (0.1 M KCl) as summarized in Equation (2),

$$[Fe(CN)_6]^{3-} + e^- \rightleftharpoons [Fe(CN)_6]^{4-} \tag{2}$$

and the reduction of cytochrome *c* in its oxidized form (Fe^{III}cyt *c*) to the reduced (Fe^{II}cyt *c*) form in a buffered aqueous environment (Equation (3))

$$Fe^{III}\text{cyt } c + e^- \rightleftharpoons Fe^{II}\text{cyt } c \tag{3}$$

represent other very well known redox systems that have been widely studied by voltammetric techniques.

Ideally, the proposed mechanism may be theoretically simulated by solving the appropriate mathematical problem.[2,11–13] Satisfactory agreement between experiment and theory is used to provide a quantitative description for the postulated mechanism, but as with any kinetic study, ideally the identity of proposed reaction intermediates and the final product will be confirmed by an independent technique (e.g., a spectroscopic method). It is inherently dangerous to assume the structure of a reaction intermediate or product solely on the basis of a voltammetric response. A general procedure for obtaining quantitative data related to an electrode mechanism using a voltammetric technique is summarized in Figure 2.

2.15.2.1 Basic Definitions of Voltammetry

Voltammetric techniques involve monitoring the current when a time-dependent potential is applied to an electrochemical cell. Even in a simple process, in which the oxidized and reduced forms of the electrode process are soluble in solution, the measured current frequently results from a complex combination of heterogeneous electron charge transfer processes that occur across the solution–electrode interface and homogeneous processes which occur in the solution phase. If a redox active solid is adhered to the electrode surface, then significantly greater complexity is introduced.[2] Comprehensive information concerning a particular electrode reaction mechanism can be obtained from examining how the current varies as a function of time (or frequency) and the applied electrode potential. It is the variation of this current–potential–time relationship that is commonly crucial for the quantitative determination of the mechanistic details of an electrochemical reaction.

A typical electrochemical cell for a voltammetric experiment is illustrated in Figure 3. The processes that are probed in a voltammetric experiment occur at or in the region of the working electrode, which is the electrode of critical interest. The reference electrode merely provides a fixed reference potential and the counter electrode, present when a potentiostatted form of apparatus is used, completes the electrical circuit.[2,6–8,13,14] Other noteworthy features of the cell depicted in Figure 3 are that N_2 or Ar gas is introduced into the cell to remove oxygen, and a Luggin capillary is present in order to minimize the distance between working and reference electrode, thereby also minimizing the influence of uncompensated resistance.

The importance of the time element may be understood by briefly considering the commonly used transient and steady-state voltammetric methods.

2.15.2.1.1 Transient voltammetry

In these experiments, a potential perturbation to the working electrode is applied to the system of interest and the resulting current response is measured as a function of potential (time). Transient

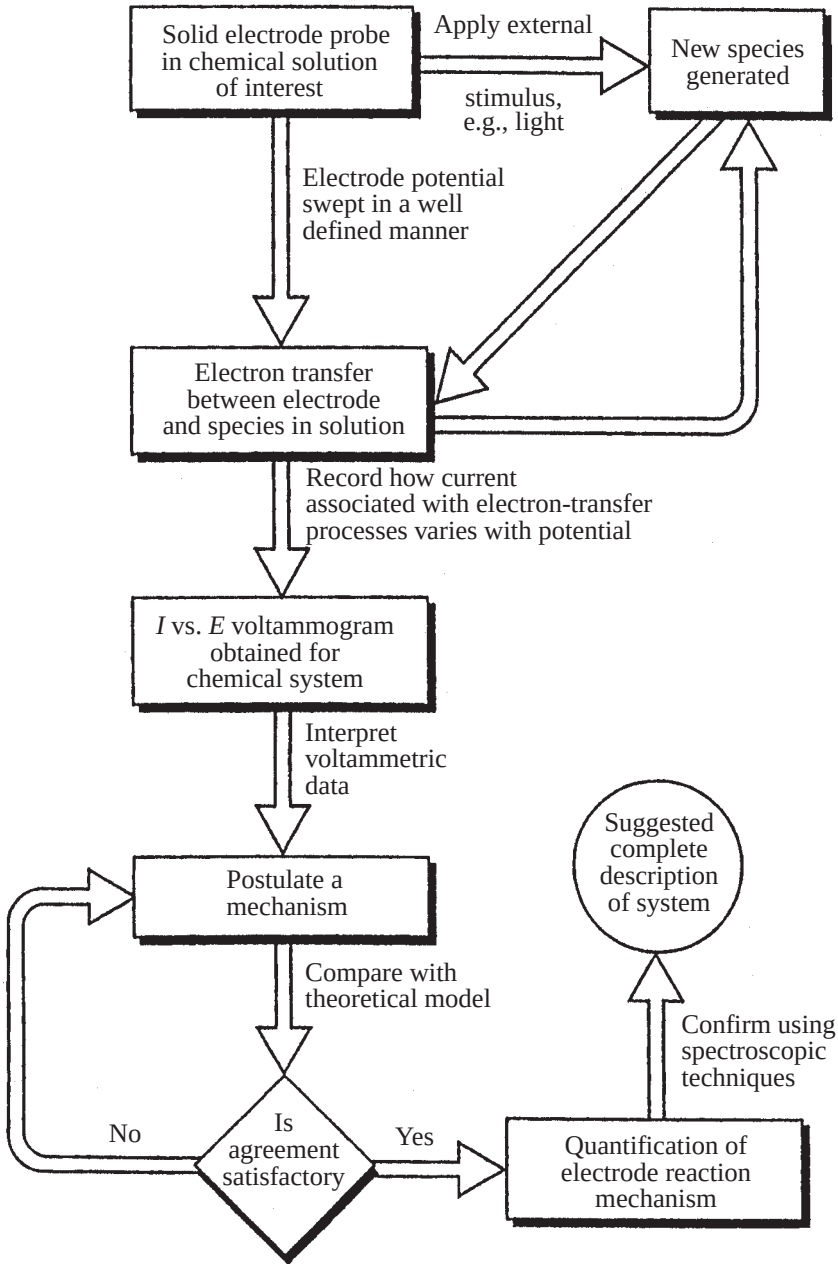

Figure 2 Schematic diagram of a systematic procedure recommended for the elucidation of the details of an electrode reaction mechanism; (reproduced by courtesy: *Adv. Phys. Org. Chem.* **1999**, *32*, 1; © Academic Press).

techniques include cyclic, linear sweep, staircase, square wave, pulsed, alternating current, etc. voltammetries.[2–5,13] In the former two cases, and in the traditional format (analog instrumentation), the potential at the working electrode is scanned in a linear fashion with time with the current being continuously monitored. The temporal aspect arises from the rate at which the potential is ramped, known as the scan rate, ν. When the potential is swept in only one direction the technique is known as linear sweep voltammetry. If the potential is swept in one direction and then reversed, this technique is known as cyclic voltammetry (Figure 4). (It should be noted that the International Union of Pure and Applied Chemistry (IUPAC) recommended convention of positive potential to the right and oxidation current being positive is indicated in Figure 4. Unfortunately, even present-day literature all too often fails to comply with this official convention. Until uniformity is achieved via widespread use of IUPAC recommendations, confusion that presently exists with respect to the format used to present voltammetric data will remain.) With

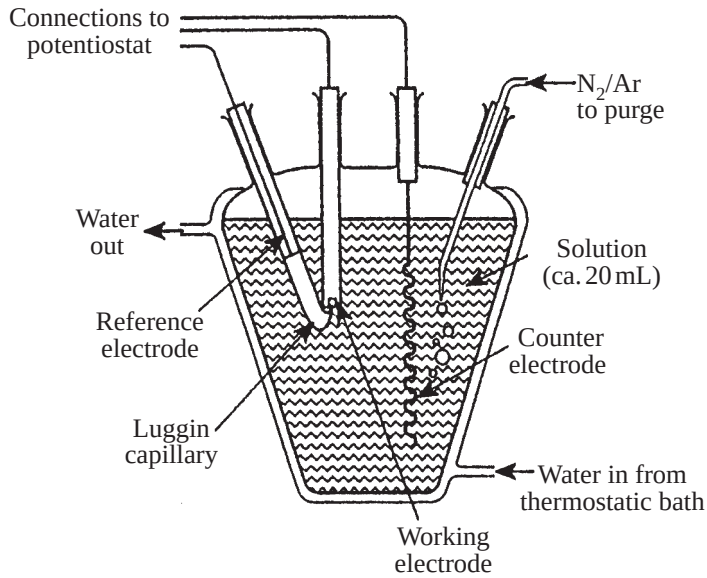

Figure 3 Schematic representation of a typical electrochemical cell employed in a voltammetric experiment (reproduced by courtesy: *Adv. Phys. Org. Chem.* **1999**, *32*, 1; © Academic Press).

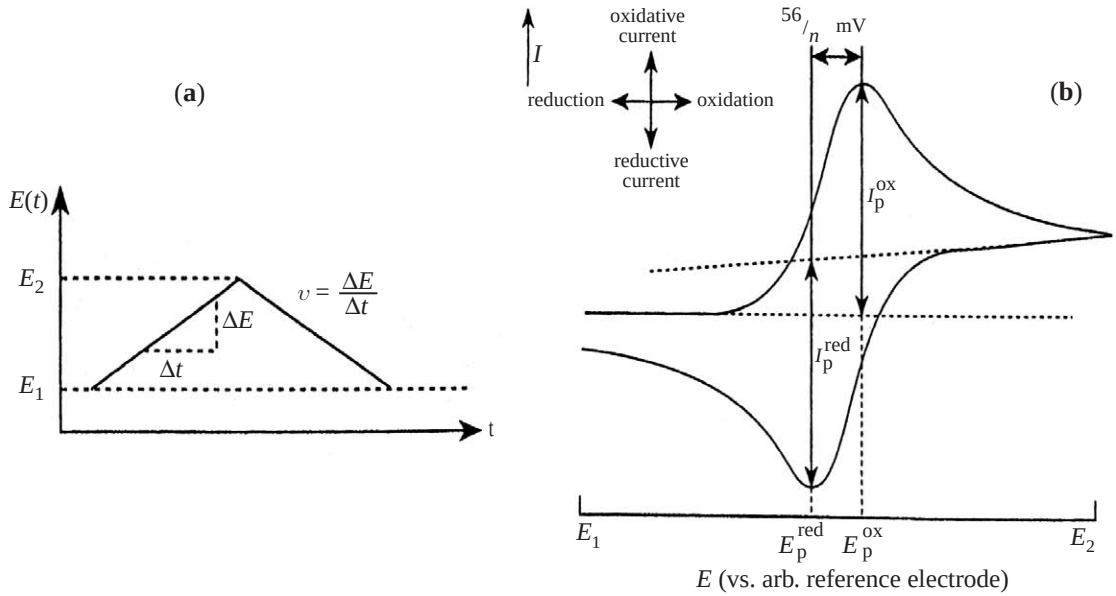

Figure 4 (a) Waveform used in cyclic voltammetry and (b) the readout obtained with this technique for a reversible oxidation process of the type $A_{(solution)} \rightleftharpoons B_{(solution)} + e^-$.

digital instrumentation, the linear ramp is often replaced by a staircase waveform, which mimics a linear ramp if the potential steps in the staircase waveform are sufficiently small. In the other techniques, a time- (square wave or pulse) or frequency- (alternating current) dependent perturbation usually is superimposed onto the linear or staircase waveforms and the current measured as a function of time or frequency. Cyclic voltammetry is the prime transient technique used by coordination chemists.

2.15.2.1.2 Steady state voltammetry

In this form of voltammetry, the concentration distributions of each species in the electrode reaction mechanism are temporally invariant at each applied potential. This condition applies to a

good approximation, despite various processes still occurring such as mass transport (e.g., diffusion), heterogeneous electron transfer, and homogeneous chemical processes. Theoretically, it takes an infinite time to reach the steady state. Thus, in a practical sense, steady state voltammetric experiments are conducted under conditions that approach sufficiently close to the true steady state that the experimental uncertainty of the steady state value of the parameter being probed (e.g., current) is greater than that associated with not fully reaching the steady state. The time scale of a near steady state process is determined by the rate at which material reaches the electrode surface.[11] This time scale may be varied in a number of ways:

Altering the convective rate of transport, e.g., by changing the rotation frequency of a rotating disk electrode or the flow rate in a channel electrode. Experiments in which the convective rate of transport can be altered are known as hydrodynamic techniques.

Decreasing the size of the electrode so that the rate of radial diffusion of material to the electrode surface is enhanced. This is a key component in many important applications of microelectrode voltammetry.[11]

2.15.2.2 A Reversible Electrode Process

Almost all publications containing descriptions of cyclic voltammetric experiments related to coordination compounds introduce concepts of "reversible" or "irreversible" when summarizing the nature of the measured electrode process. Figure 4b illustrates the asymmetrical peak shaped curve obtained under conditions of cyclic voltammetry for the "reversible" process,

$$A_{(solution)} \overset{E_f^o}{\rightleftharpoons} B_{(solution)} + ne^- \tag{4}$$

when both A and B are solution soluble and E_f^o is the reversible formal potential. For this process, the average of the oxidation (E_p^{ox}) and reduction (E_p^{red}) peak potentials, or $(E_p^{ox} + E_p^{red})/2$, is equal to E_f^o (assuming the diffusion coefficients of A and B are equal). Furthermore, the magnitude of corresponding peak currents, I_p^{ox} and I_p^{red} is unity and I_p^{ox} is given by the Randles–Sevcik equation[2–5,13] which realizes a square root dependence on scan rate. To obtain the cyclic voltammogram depicted in Figure 4b, the potential was scanned at a rate ν (V s^{-1}) from an initial potential (E_1), which is considerable less positive than E_f^o, to a value E_2, which is considerably more positive than E_f^o, and then back to E_1 (Figure 4a).

The equivalent reversible voltammogram obtained under steady state conditions is shown in Figure 5, where the half-wave potential or $E_{1/2}$-value obtained at half the limiting current (I_{lim}) is equal to E_f^o. In this case the wave shape is readily defined by the equation

$$E = E_f^o + \frac{RT}{nF} \ln \frac{I_{lim} - I}{I} \tag{5}$$

where I_{lim} is a linear function of concentration and electrode radius for a microdisk electrode or square root of rotation rate for a rotated disk electrode. Use of the "log plot" in Equation (5) enables the values of both E_f^o and n to be calculated from the intercept and slope respectively. The theory for the different steady state techniques is available in the following references.[2–5,11] Both the cyclic and steady state voltammograms depicted in Figures 4 and 5 assume perfect Ohmic compensation and correction for background current, which is rarely achieved.[14] Distortions introduced by the presence of uncompensated resistance and background current are explained in Eklund *et al.*[11]

(1)

Voltammetric measurement of E_f^o has been widely employed by coordination chemists. Commonly, these reversible potentials are compared for a series of compounds and the systematics of the redox chemistry of a particular class of compound are established in this manner. For

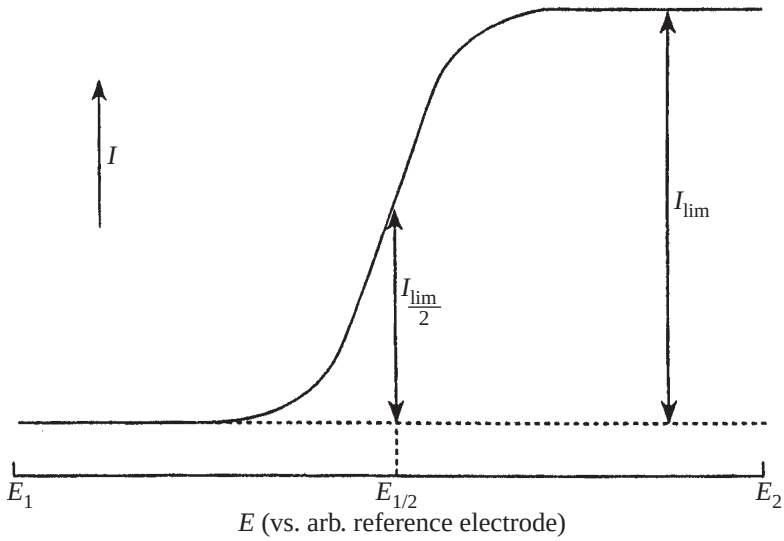

Figure 5 Sigmoidal-shaped, steady state voltammogram obtained at a microdisk or hydrodynamic electrode for a simple process of the type $A_{(solution)} \rightleftharpoons B_{(solution)} + e^-$.

example, Chant *et al.*[15] have studied the voltammetric reduction and oxidation of a very extensive series of iron(III) dithiocarbamate ($Fe(R_2dtc)_3$ or $Fe(R,R'dtc)_3$) complexes (R_2dtc^- is the dithiocarbamate ligand (1)) and examined the redox chemistry as a function of substituent, R, R′. Reversible potentials for the

$$Fe^{III}(R_2dtc)_3 \rightleftharpoons [Fe^{IV}(R_2dtc)_2]^+ + e^- \quad (6)$$

and

$$Fe^{III}(R_2dtc)_3 + e^- \rightleftharpoons [Fe^{II}(R_2dtc)_3]^- \quad (7)$$

processes have been obtained. Figure 6 shows that a linear relationship is obtained between the reversible potentials for these oxidation and reduction processes. Analogous ligand substituent effects are observed with other metal dithiocarbamate complexes.[16] A plot of reversible potential for a series of compounds having the same central metal atom with the substituent on the ligand being varied also often may be correlated with Taft, Hammett or other substituent parameters. These linear free energy vs. substituent parameters of the kind illustrated in Figure 7 are widely encountered in both organic[17] and coordination chemistry.[18–20]

The role of the central metal ion also is important as indicated by the voltammetrically determined reversible potentials of 4*d* and 5*d* hexafluoro and hexachlorometallate complexes in acetonitrile.[21,22] Thus, as shown in Figure 8a, E_f^o-values ($E_{1/2}$) for the $[MF_6]^{n/(n-1)}$ couples ($n = 0$, -1, -2; M = Ta, W, Ro, Os, Nb, Mo, Tc, Rh) 4*d* and 5*d* complexes follow linear progressions related to central ion nuclear and electronic structures for $d^0 \rightarrow d^1$, $d^1 \rightarrow d^2$, and $d^2 \rightarrow d^3$. Deviations observed for the $d^3 \rightarrow d^4$ and subsequent effects are attributable to spin-pairing effects.[21] It can also be noted from data in Figure 8 that the corresponding 4*d* and 5*d* couples are almost uniformly separated by 1 V. The even more extreme data set for the $[MCl_6]^{n/(n-1)}$ couples ($n = 0$, -1, -2, -3; M = Zr–Pd for 4*d* metals, and Ta–Pt, excluding Tc for 5*d* metals) also reveal orderly trends (Figure 8b) that have been interpreted in terms of core charge and inter-electronic correlations.[22] Links to data obtained by electronic spectroscopy have also been reported in many studies[20] and, for example, a linear correlation of $h\nu_{max}$ (ligand to metal charge transfer) and E_f^o has emerged with a gradient of 1.35 eV V^{-1} for the above mentioned $[MCl_6]^{n/n^{-1}}$ systems.[23]

Extensive data are now available to quantify ligand additivity effects on E_f^o values. In a detailed study by Lever,[24] ligand electrochemical parameters for over 200 ligands are presented and the model proposed has been tested with a wide range of coordination complexes (see Section 2.15.2.4). In the more sophisticated models, the E_f^o value is described in terms of the sum of factors involving the ligand electrochemical parameter and the metal. As expected, E_f^o depends on the

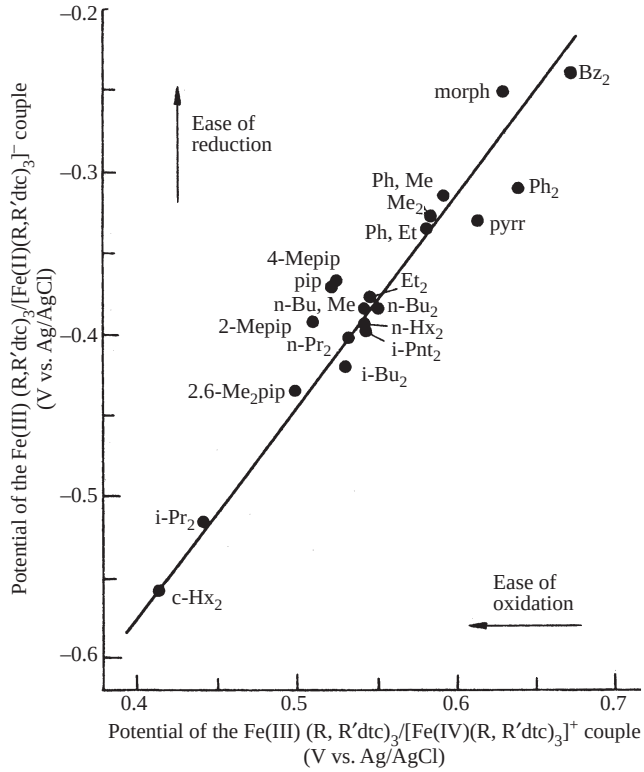

Figure 6 Relation between the reversible potentials for oxidation and reduction of $Fe(R,R'dtc)_3$ complexes (reproduced by courtesy: *Inorg. Chem.* **1975**, *14*, 1894; © American Chemical Society).

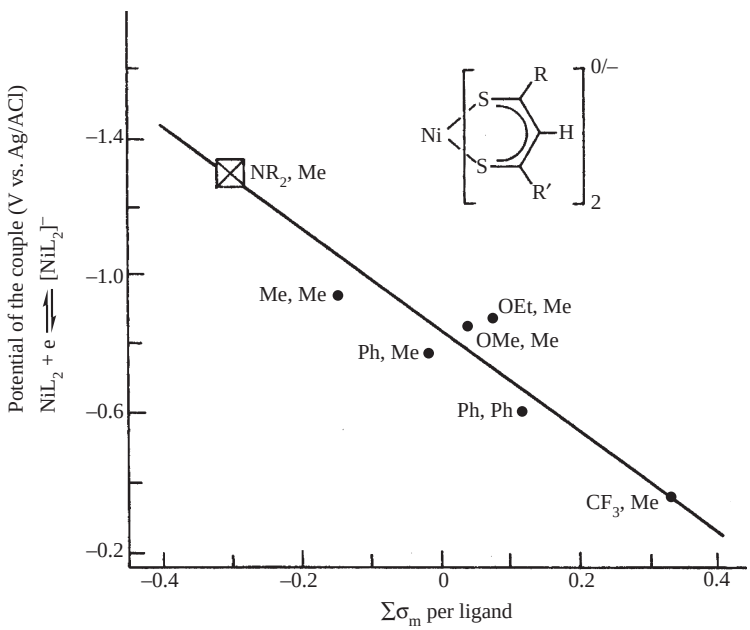

Figure 7 Correlation between substituent effects (approximated by the Taft parameter $\varepsilon\sigma_m$ and the reversible potentials for reduction of nickel(II) dithioacetylacetonate complexes $Ni(R\text{-}Sac\ R'\text{-}Sac)_2$ (reproduced by courtesy: *Inorg. Chem.* **1976**, *15*, 1118; © American Chemical Society).

metal, ligand, redox couple, spin state, and stereochemistry, but is generally insensitive to the net charge or the species involved in the redox process. A recent review of different ligand additivity models has been reported by Lever and Dodsworth.[20] Ligand electrochemical parameters perform a similar role to that of the *Dq* parameter in electronic spectroscopy.

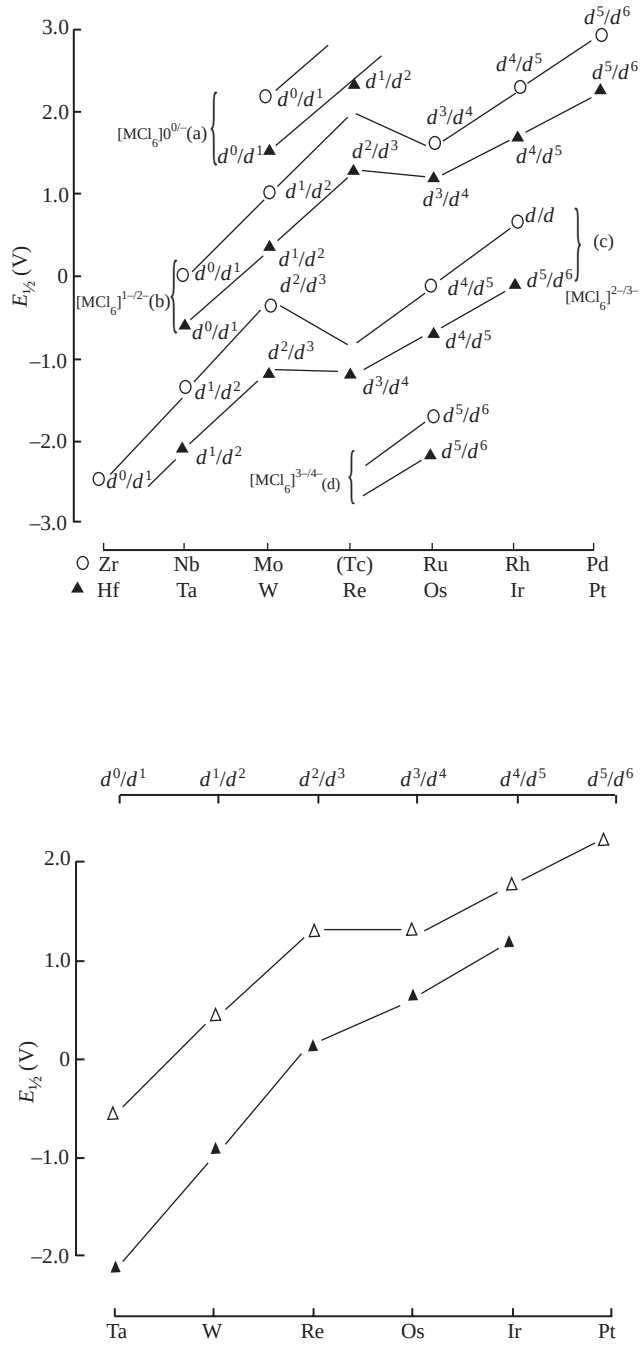

Figure 8 Dependence of reversible potential on metal ion. (Upper curves): trends in half-wave potentials, $E_{1/2}$ in V vs. SCE of $[MCl_6]^{n/n-1}$ couples in CH_2Cl_2; O: 4*d*-hexachlorometallates; ▲: 5*d*-hexachlorometallates. (a) $n=0$; (b) $n=-1$; (c) $n=-2$; (d) $n=-3$. (Lower curves): comparison of half-wave potentials for $[MX_6]^{-1/-2}$ couples of 5d-hexafluorometallates (▲; X = F) and hexachlorometallates (Δ; X = Cl) (reproduced by courtesy: *J. Chem. Soc. Chem. Commun.* **1985**, 1503; © Royal Society of Chemistry).

In a reduction process, an electron is usually added to the LUMO, whereas in an oxidation process, an electron usually is removed from the HOMO. This is the reason why it is commonly assumed that E_f^o values for oxidation and reduction processes correlate with HOMO and LUMO energies respectively. However, the redox potential reflects the relative free energies of both the oxidized and reduced forms of a redox couple, whilst the HOMO and LUMO energies belong to only one species. Thus, it is only in the absence of nuclear and electronic rearrangement and change in solvation energy that E_f^o values of a series of related molecules would correlate linearly

with HOMO or LUMO orbitals as appropriate. It is this linear relationship approximation which forms the basis of many ligand additivity or substituent models. Clearly, the concept works in many cases, but caution should be maintained as the models contain approximations. The concept that the energy difference between the HOMO and LUMO corresponds with the optical energy of the HOMO → LUMO electronic transition has a similar basis. However, again this widely used concept is also not strictly correct.[20] The origin of these and other energy relationships, such as those associated with metal-to-ligand and ligand-to-metal charge transfer electronic transitions (see above), and their limitations, have all been discussed in detail by Lever and Dodsworth.[20] Consequently, readers wishing to employ these relationships in experimental studies are urged to carefully consult this article.

2.15.2.2.1 Electrochemical reversibility and irreversibility

Despite the fact that thermodynamic E_f^o values may be calculated under some conditions, an understanding of the basics of the technique of voltammetry actually requires a kinetic rather than thermodynamic theoretical treatment. In a voltammetric experiment, current flows in response to the reaction in Equation (8), being driven in either the forward or

$$A_{(solution)} \underset{k_b}{\overset{k_f}{\rightleftharpoons}} B_{(solution)} + ne^- \tag{8}$$

reverse directions at a rate which is governed by the forward (k_f) and back (k_b) rate constants as well as by the value of the potential, E, relative to E_f^o. Consequently, whenever current flows, the half-cell reaction can never be genuinely in equilibrium, since this requires that no net reaction takes place (zero current) or that the rate of the forward reaction equals the rate of the back reaction. However, if the rate of the forward and backward reactions in Equation (8) are both sufficiently fast relative to the voltammetric timescale, then the electrode process can readjust to equilibrium conditions, within experimental error, as the potential is varied. This is equivalent to being able to provide a theoretical description of the cyclic voltammogram or other technique by assuming that the Nernst relationship (Equation (9)) is valid at the electrode surface,

$$E = E_f^o - \frac{RT}{nF} \ln \frac{[A]_{(x=0)}}{[B]_{(x=0)}} \tag{9}$$

where x is the distance from the electrode surface.

The terminology of "reversible" and "irreversible" is therefore clearly an operational one which must be defined in terms of the timescale (e.g., scan rate in cyclic voltammetry). To provide a full theoretical description, the electrode process in Equation (8) can be rewritten in terms of parameters contained in Equation (10)

$$A_{(solution)} \underset{}{\overset{E_f^o, k_s, \alpha}{\rightleftharpoons}} B_{(solution)} + ne^- \tag{10}$$

where k_s (cm s^{-1}) is the heterogeneous charge transfer rate constant at potential E_f^o, α is the charge transfer process (usually 0.5) and where the rate constant k_f and k_b contained in Equation (8) are related to potential and k_s via the Butler–Volmer or other relationship.[2,3] Reversibility requires that the electron transfer kinetics (k_s) are fast enough to maintain the surface concentrations $[A]_{x=0}$ and $[B]_{x=0}$ at the values required by the Nernst equation. Thus, reversibility depends on the relative values of k_s and the rate of change of potential or scan rate, ν, in a cyclic voltammetric experiment. If the ratio of k_s/ν is sufficiently small that Nernstian surface concentrations cannot be maintained as the potential is swept, then the process is said to be nonreversible. Terms widely used in the literature to cover this case are quasi-reversible (some back reaction) or irreversible (no back reaction). Unlike a reversible process (Figure 4b), a quasi-reversible process is characterized by $\Delta E_p > 57/n$ mV at 25 °C, with the value becoming larger with increasing ν. The effect of decreasing k_s from a value where reversibility is achieved (k_s large), to where nonreversibility is exhibited (k_s small) is illustrated by the cyclic voltammograms displayed in Figure 9 (upper part) (note that the magnitude of I_p^{ox}/I_p^{red} only remains unity if $\alpha = 0.5$ when the process is quasi-reversible).

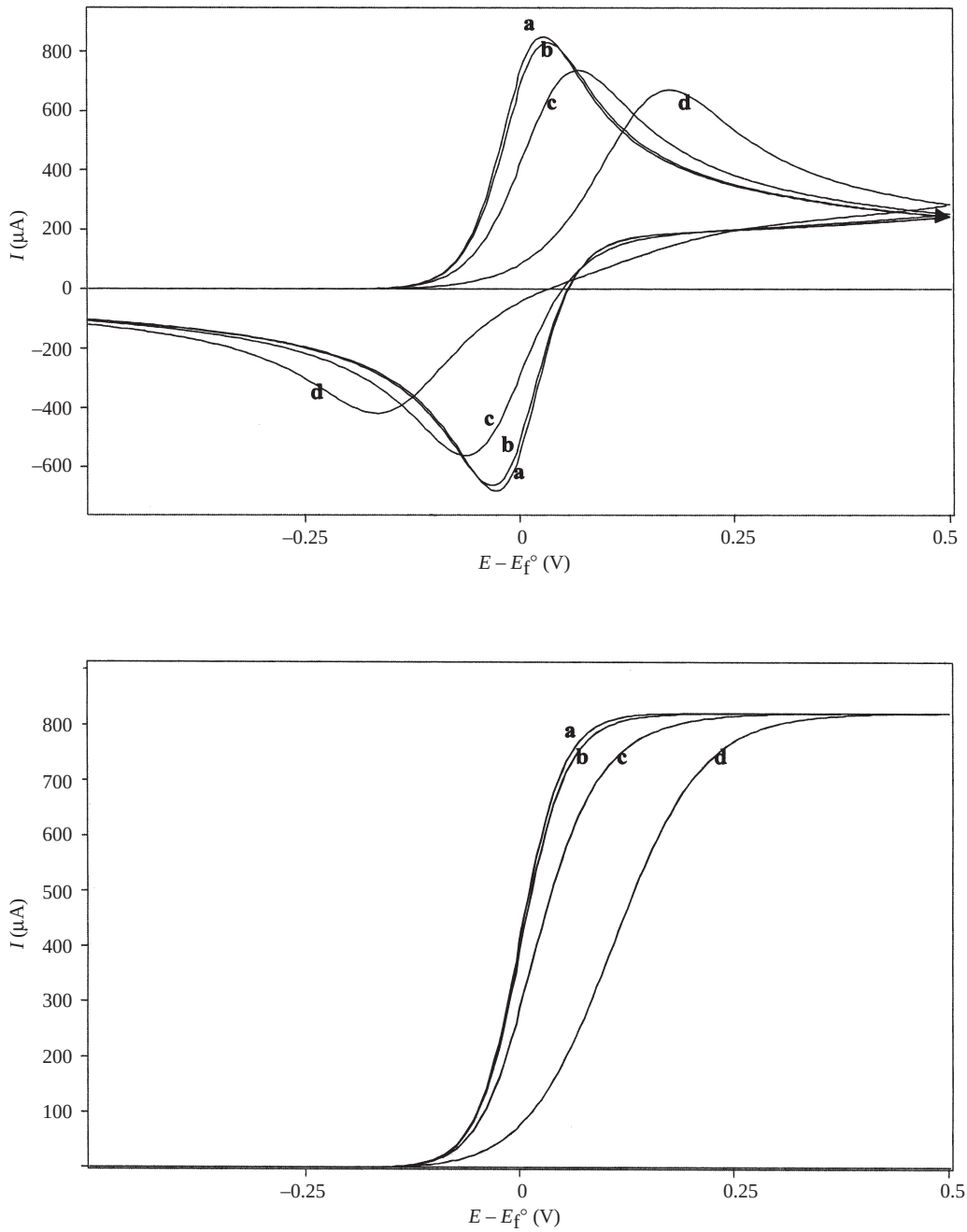

Figure 9 (Upper curves) cyclic (scan rate = 1.0 V s^{-1}) and (lower curves) rotated disk electrode (rotation rate = 200 rad s^{-1}; scan rate = 5 mV s^{-1}; kinematic viscosity = 1×10^{-2} cm^2 s^{-1}) voltammograms at 25 °C for the electrode process $A_{(solution)} \rightleftharpoons B_{(solution)} + e^-$ where bulk concentration of A = 10^{-3} M, diffusion coefficients of A and B = 1×10^{-5} cm^2 s^{-1}, electrode area = 1.0 cm^2, $E_f^o = 0.000$ V, k_s = (a) ∞, (b) 0.1, (c) 0.01, (d) 0.001 cm s^{-1}. Simulations undertaken with Bioanalytical Systems DigiSim software, version 3.03.

2.15.2.2.2 Chemical reversibility and irreversibility

Irreversibility of an electrode process also may arise if either A or B are chemically unstable on the voltammetric timescale. For example, the electrode process,

$$\begin{array}{lll} A_{(solution)} & \overset{E_f^o}{\rightleftharpoons} & B_{(solution)} + e^- \\ & & \downarrow k_1 \\ & & C_{(solution)} \end{array} \qquad (11)$$

where oxidation of A to B is followed by the conversion of B to electroreactive C (usually referred to as an **EC** mechanism), requires that additional concentrations of A are converted to B to compensate for loss of B caused by the influence of the homogeneous chemical reaction $B \xrightarrow{k_1} C$ which has a rate constant k_1. Under conditions of cyclic voltammetry the net effect is that the rate of oxidation increases and E_p^{ox} becomes less positive. In addition, the ratio I_p^{ox}/I_p^{red} is no longer unity because only a fraction of the materials oxidized to B on the forward scan are available for reduction back to A on the reverse scan.

Figure 10 (upper part) shows that the effect of a chemical reaction for an **EC** process depends on the value of k_1. The effect is actually a function of k_1/ν. If this ratio is large, then the chemical reaction has a significant effect, but it also follows therefore that it may be possible to outrun the chemical reaction and achieve redox reversibility by increasing ν so that the ratio k_1/ν becomes small. That is, a process can be chemically irreversible or reversible depending on the scan rate and as is the case with electrochemical reversibility or irreversibility, an operational definition is applied to this terminology. The closely related reaction scheme in Equation (12) can be chemically and electrochemically reversible if the rate constants k_1 and k_{-1} for the forward and backward homogeneous chemical reactions respectively are both very fast. Note that $K_{eq} = k_1/k_{-1}$ in the simulated voltammograms in Figure 10 was set at a value of 1×10^6 so that $k_1 \gg k_{-1}$ in order that k_{-1} has a negligible influence on the voltammogram:

$$\begin{array}{ccc} A_{(solution)} & \overset{E_f^o}{\rightleftharpoons} & B_{(solution)} + e^- \\ & k_{-1} \Big\| \Big\downarrow k_1 & \\ & C_{(solution)} & \end{array} \qquad (12)$$

The dependence of the **CE** reaction scheme (Equation (13)) on k_2 is illustrated

$$D_{(solution)} \underset{k_{-2}}{\overset{k_2}{\rightleftharpoons}} A_{(solution)} \overset{E_f^o}{\rightleftharpoons} B_{(solution)} + e^- \qquad (13)$$

in Figure 11 for the case where K_{eq} the equilibrium constant ($K_{eq} = k_2/k_{-2}$) is 1×10^{-4} and k_2 is varied. The apparent reversibility and even the current magnitude with this scheme is a function of the rate constants k_2 and k_{-2} and the scan rate.

Equivalent voltammograms to the transient cyclic voltammograms described above, but obtained under rotated disk electrode steady state conditions, are contained in the lower curves presented in Figures 9–11 and illustrate that whilst the terms reversible and irreversible are generally associated with cyclic voltammetry in the coordination chemistry literature, the same concepts apply to steady state methods. A useful feature of the steady state method is that the limiting current (unlike the peak current in cyclic voltammetry) is insensitive to the value of k_s for the **E** and k_s or k_1 for the **EC** processes. This means that mass transport terms (diffusion coefficients) are readily extracted from these steady state limiting current measurements, because these and heterogeneous and homogeneous kinetic terms are separated in this potential regime for many mechanisms (not **CE** curve). Thus, whilst the cyclic voltammetric method contains a vast amount of information, the simplification that may be achieved with steady state methods for some mechanisms also may often be attractive. Consequently, the combined use of both transient and steady state methods is highly recommended in voltammetric studies of coordination compounds.

2.15.2.3 Bulk Electrolysis

Electrochemical synthesis and subsequent isolation of gram or greater amounts of a pure sample of product B, via the electrode process $A \rightarrow B + ne^-$, requires exhaustive or bulk electrolysis of electroactive material A at a large-size working electrode, although, of course, exhaustive electrolysis of A frequently is achieved on the microscale (mg to μg) level in mechanistic studies at smaller-sized electrodes. Thus, bulk electrolysis can be a useful large-scale synthetic tool and, indeed, is widely used for commercial production of metals such as Cu, Zn, and Al. Bulk electrolysis experiments, when the data are analyzed in a coulometric form, also enable the n value in a voltammetric electrode process to be determined, provided no additional reactions occur on the longer time scale (typically minutes to tens of minutes) associated with such experiments.

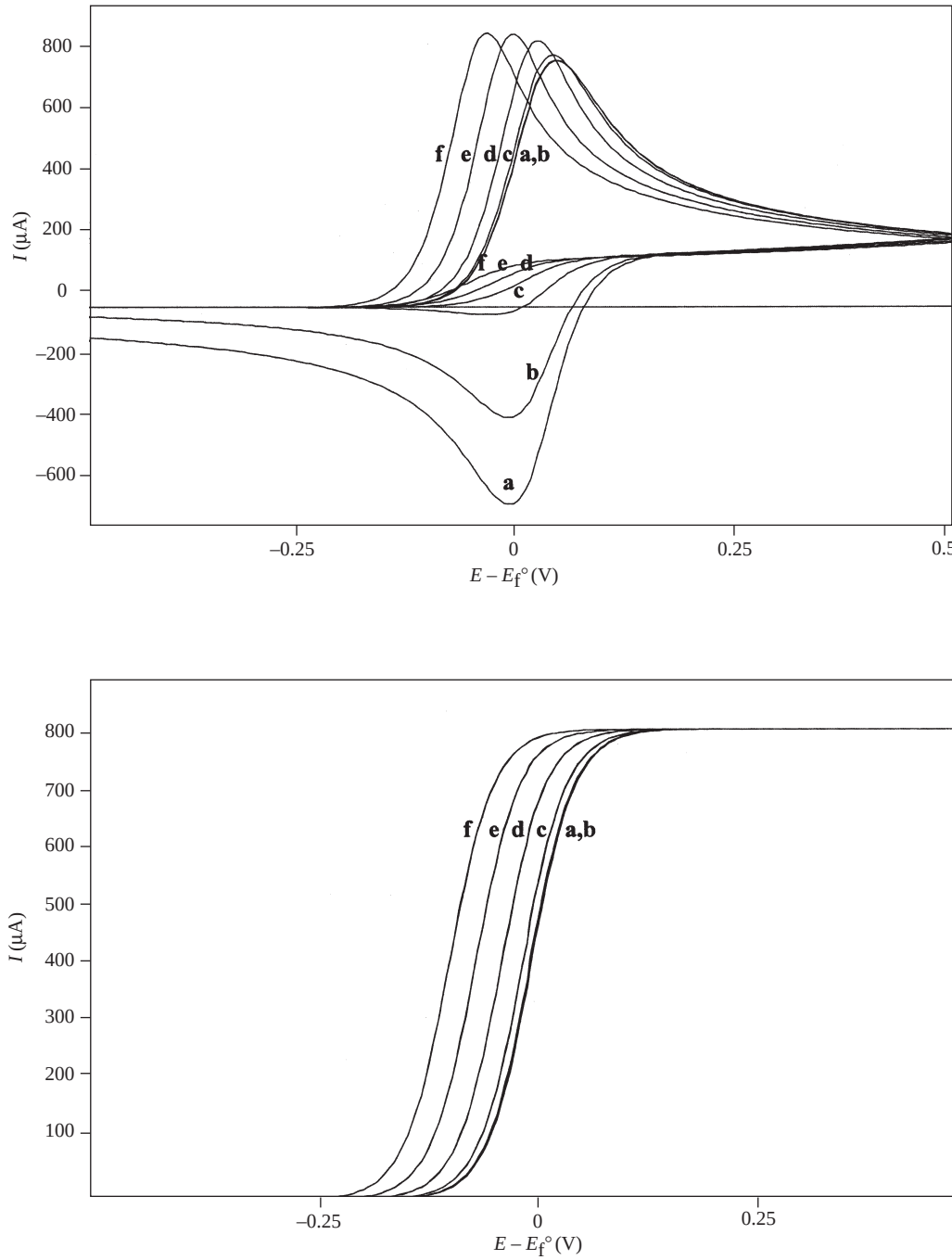

Figure 10 (Upper curves) cyclic (scan rate = $1.0\,V\,s^{-1}$) and (lower curves) rotated disk electrode (rotation rate = 200 rad s^{-1}, scan rate = $5\,mV\,s^{-1}$, kinematic viscosity = $1 \times 10^{-2}\,cm^2\ s^{-1}$) voltammograms at 25 °C for the electrode process

$$A_{(solution)} \overset{E_f^o}{\rightleftharpoons} B_{(solution)} + e^-$$

$$k_{-1} \Big\Uparrow \Big\Downarrow k_1$$

$$C_{(solution)}$$

where bulk concentration of A = 10^{-3} M, diffusion coefficients of A, B, and C = $1 \times 10^{-5}\,cm^2\ s^{-1}$, $K_{eq} = k_1/k_1 = 1 \times 10^{-6}$, electrode area = $1.0\,cm^2$, $k_s = \infty$, $E_f^o = 0.000$ V and k_1 = (a) 0, (b) 1.0, (c) 10.0, (d) 100, (e) 1,000, (f) 10,000 s^{-1}. Simulations undertaken with Bioanalytical Systems DigiSim software, version 3.03.

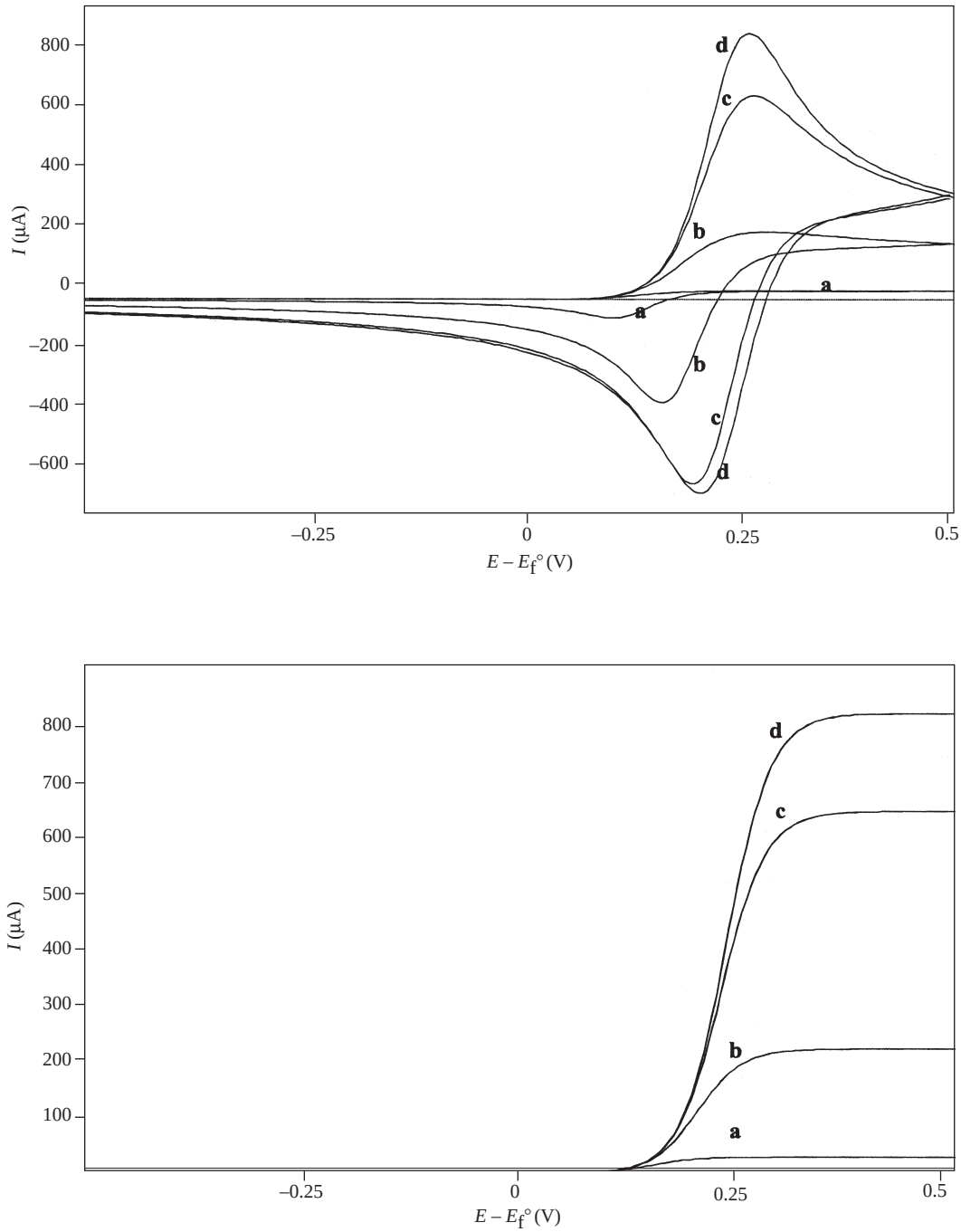

Figure 11 (Upper curves) cyclic (scan rate $= 1.0\,\mathrm{V\,s^{-1}}$) and (lower curves) rotated disk electrode (rotation rate $= 200\,\mathrm{rad\ s^{-1}}$, scan rate $= 5\,\mathrm{mV\,s^{-1}}$, kinematic viscosity $= 1 \times 10^{-2}\,\mathrm{cm^2\ s^{-1}}$) voltammograms for the process $\mathrm{D_{(solution)} \overset{k_2}{\underset{k_{-2}}{\rightleftharpoons}} A_{(solution)} \overset{E_f^o}{\rightleftharpoons} B_{(solution)} + e^-}$ where bulk concentration of $\mathrm{D} = 1 \times 10^{-3}\,\mathrm{M}$, diffusion coefficients of D, A, and $\mathrm{B} = 1 \times 10^{-5}\,\mathrm{cm^2\ s^{-1}}$, $K_{eq} = k_2/k_{-2} = 1 \times 10^{-4}$, electrode area $= 1.0\,\mathrm{cm^2}$, $k_s = \infty$, $E_f^o = 0.000\,\mathrm{V}$ and $k_2 =$ (a) 1×10^2, (b) 1×10^4, (c) 1×10^6, (d) $\infty\ \mathrm{s^{-1}}$. Simulations undertaken with Bioanalytical Systems DigiSim software, version 3.03.

2.15.2.3.1 Theory of bulk electrolysis

The bulk electrolysis method may be applied in a constant potential (potentiostatic) or constant current (galvanostatic) modes. In a controlled potential electrolysis (CPE) experiment, the working electrode is held at a constant potential until the solution is exhaustively electrolyzed. The

electrolysis potentially usually is chosen, for example, to be slightly more positive than the $E_{1/2}$ value of a species being oxidized or slightly more negative than the $E_{1/2}$ value of a species being reduced, and hence just into the limiting current region of a steady state voltammogram. In a constant current or galvonstatic experiment, as the name implies, the current is maintained at a constant value for the desired period of time. In a coulometry experiment, commonly undertaken during the course of bulk electrolysis, the current passed as a function of time is integrated by means of an electronic integrator or coulometer to give the charge. Faraday's law of electrolysis requires that the quantity of electricity passed or charge (coulombs) is directly proportional to the amount of chemical reaction (*equivalents*) that has taken place at an electrode. Thus,[25]

$$Q = \int_0^t I \, \mathrm{d}t = (F)(\text{equivalents}) \tag{14}$$

where I is the current at time t and Q is the charge or number of coulombs passed during the course of the electrolysis experiment. Alternatively, this equation may be expressed as

$$N = Q/nF \tag{15}$$

where N is the number of moles of electroactive material oxidized or reduced, F is Faraday's constant and n is the equivalents per mole, i.e., the number of electrons transferred per molecule or ion that has undergone electrolysis. It can be seen from Equation (15) that coulometric monitoring of the bulk electrolysis experiment involving the reaction $\mathrm{A} \rightarrow \mathrm{B} + n\mathrm{e}^-$ can be used to calculate n, if the number of moles of A initially present in the bulk solution is known. Conversely, the equation may be used to calculate the number of moles of species A initially present, and hence the concentration of A in solution (provided the solution volume and n are known).

Provided there is only a negligibly small background current present and uniform mass transport conditions operate throughout the course of the electrolysis experiment, the current is proportional to the concentration of electroactive species for the process $\mathrm{A} \rightarrow \mathrm{B} + n\mathrm{e}^-$. Due to the exponential relationship of the decay of the current with time in a bulk electrolysis experiment, the rate of the electrolysis decays with time as illustrated in Figure 12. If mechanistic nuances involving electron transfer and coupled chemical reactions are present, the current–time and current–charge curves may of course become much more complex but in principle may be analyzed to enable the rates of homogenous reactions coupled with the electron transfer reaction to be calculated.[25] Figure 13 provides an example of a commercially available cell for bulk electrolysis.

There are three main differences between a cell designed for bulk electrolysis and a voltammetric cell which are related to electrode surface area, stirring, and electrode separation. In voltammetric experiments only a small fraction of the redox active species needs to be electrolyzed. Therefore, the area of the working electrode does not need to be large (e.g., the diameters of disk electrodes range from micrometers to a few millimeters). In addition, the solution need not be stirred. In contrast, in bulk electrolysis experiments, the emphasis is on rapid electrolysis, so a large-surface-area working electrode is used and the solution is stirred. Typically, the working electrode is platinum gauze, glassy carbon, or other form of carbon or a mercury pool. Since large currents are generated, a large-surface-area auxiliary electrode (typically a coil of platinum wire) or platinum gauze also is required. The relative positions of the auxiliary and working electrodes need to be carefully considered since efficient electrolysis requires uniform current density at all points on the working electrode.

During any electrochemical experiment, electrolysis occurs at the auxiliary electrode. In voltammetry experiments, the length of the experiment is typically short enough that the products from electrolysis at

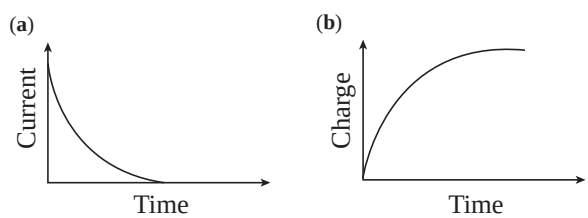

Figure 12 (a) Faradaic current and (b) charge vs. time plots obtained for controlled potential electrolysis experiments when constant convection conditions are maintained for the duration of the experiment.

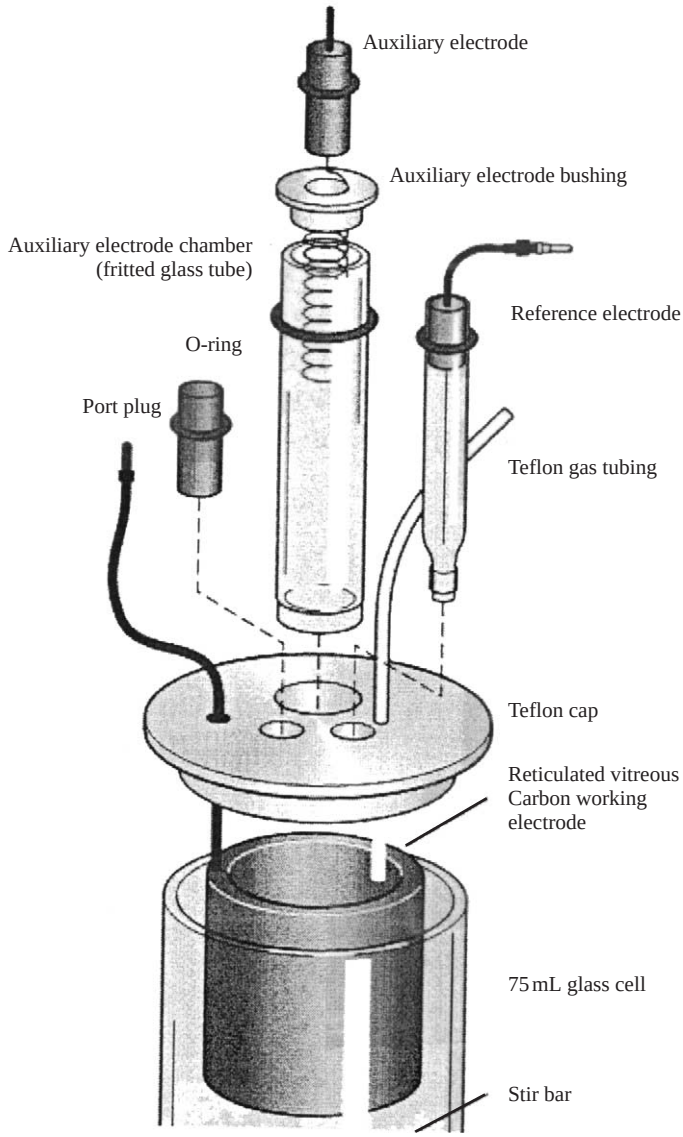

Figure 13 Schematic diagram of Bioanalytical Systems F3 glassy carbon bulk electrolysis cell. Provided courtesy of Bioanalytical Systems.

the auxiliary electrode do not have time to diffuse to the working electrode and in any case are very dilute. However, electrosynthetic experiments typically are stirred and require many minutes, so the auxiliary electrode must be separated from the working electrode in such a way that current can pass between the two electrodes without any significant product convection or diffusion between the two. Typically, a glass frit or an ion-conducting membrane is used to isolate the auxiliary electrode.

2.15.2.4 Spectroelectrochemistry

Comparisons of voltammetric experiment and theory frequently provide significant clues to the mechanisms of an electrode process, but only rarely can the identity of intermediates and products be deduced solely from voltammetric data. Consequently, the characterization of intermediates and final products proposed in a mechanism, whenever possible, should be confirmed by spectroscopic identification (Figure 2). *Ex situ* spectroscopic measurements made after bulk electrolysis experiments obviously can be used to identify stable products. However, because *in situ* spectroelectrochemical measurements apply to much shorter time domains, they provide

a powerful method of identifying the nature and even structures of intermediates involved in reaction mechanisms. The nature of the spectroelectrochemical technique should be appropriate to the problem.[9,10] Thus, for example, ESR (electron spin resonance—also called electron paramagnetic resonance (EPR)) spectroelectrochemical techniques are likely to be ideal for identifying paramagnetic complexes or radicals that are formed by one-electron oxidation or reduction of a diamagnetic complex.

A detailed review of the subject of spectroelectrochemistry containing many examples relevant to coordination chemistry is available in Chapter 1.45.

2.15.2.4.1 ESR spectroelectrochemistry

Undertaking an electrolysis experiment on a flowing solution which moves over an electrode surface and then passing the electrolyzed solution into an ESR spectrometer, or, indeed, a Raman, infrared, UV–visible, or other kind of spectrometer (including an electrospray mass spectrometer), represents an ideal method of detecting and identifying moderately stable species generated upstream at the electrode surface. Figure 14 depicts an *in situ* channel electrode cell design that has been used in the ESR and other forms of spectroelectrochemistry. Alternatively, designs can be achieved in which the entire electrochemical cell may be placed inside the cavity of the ESR spectrometer.

The effect of convection on the intensity, S, of the ESR signals generated in a channel electrode is demonstrated in Figure 15, which shows signal (S)/flow rate (V_f)/current (I) data. Clearly, mechanistic information is accessible via channel electrode measurements in which the ESR signal is monitored as a function of the flow rate and electrode current. Product instability is revealed by curvature in plots of the type displayed in Figure 15. Such plots can be analyzed to provide information concerning the mechanism and the associated kinetics. Clearly, bulk electrolysis experiments followed by transferal of solution to an ESR instrument in an *ex situ* mode of operation are also commonly employed in coordination chemistry redox studies. Useful overviews of the subject of ESR-spectroelectrochemistry can be found in the references.[26,27]

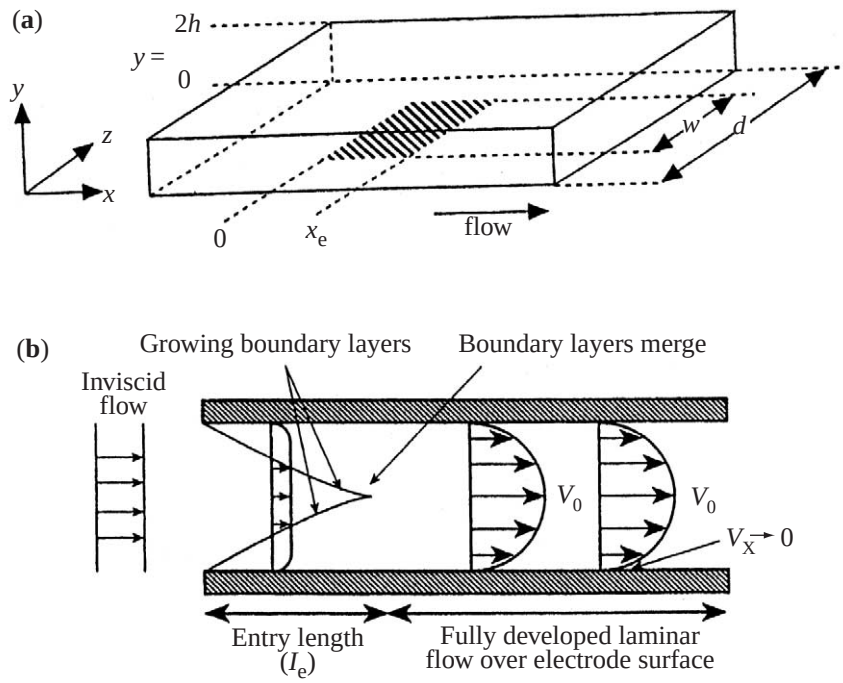

Figure 14 (a) Schematic representation of a channel electrode, and (b) convective flow profile associated with a channel electrode having a maximum flow velocity, V_0, at the center of the channel (adapted from *Adv. Phys. Org. Chem.* **1999**, *32*, 1; this reference should be consulted for further details).

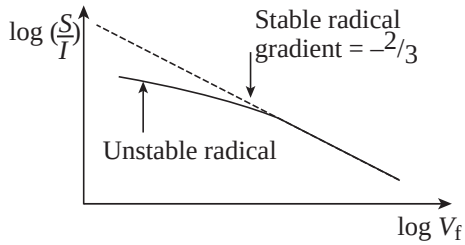

Figure 15 ESR-signal vs. flow rate data for stable and unstable paramagnetic ESR-active complexes or radicals (adapted from *J. Electroanal. Chem.* **1996**, *404*, 303).

2.15.2.4.2 IR spectroelectrochemistry

Clearly, infrared spectroelectrochemical monitoring is likely to be excellent for electrochemical studies on compounds where intermediates and/or final products exhibit strong infrared bands. Figure 16 illustrates what effectively acts as a very small volume thin-layer cell design in order to achieve very efficient electrolysis at a platinum macrodisk electrode.[28,29] With this design,

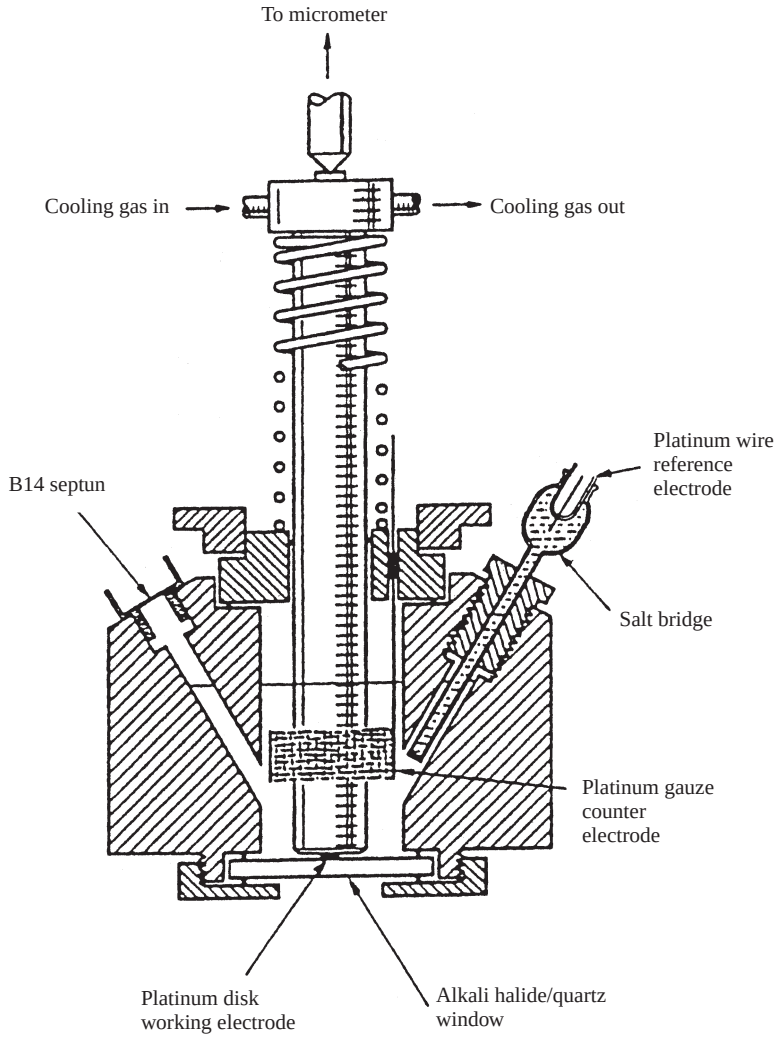

Figure 16 Example of a cell used for IR-spectroelectrochemical experiments. A flow of cold nitrogen gas is maintained for low-temperature experiments (reproduced by courtesy: *J. Chem. Soc., Dalton Trans.* **1996**, 2945; © Royal Society of Chemistry).

infrared radiation only has to pass through a very thin layer of solution and after being absorbed by the species of interest can be reflected off the platinum electrode and then detected by the IR spectrometer. The method is based on the use of a modified infrared reflection-absorption spectroscopy (IRRAS) cell which is mounted on a specular reflectance accessory located in the sample of a Fourier transform infrared (FTIR) spectrometer.[28,29]

As an alternative to the use of a thin layer electrolysis method, systems based on the use of fiber optic cable for transmission of infrared radiation may be used in an *in situ* dip probe made for monitoring the course of conventional bulk electrolysis experiments.[30] Unlike thin layer cell methods, this spectroelectrochemical technique requires no cell design compromises which diminish the accuracy of the voltammetric data that also may be obtained during the course of the electrolysis.

2.15.2.4.3 UV–visible spectroelectrochemistry

UV–visible spectroelectrochemical monitoring of the course of electrolysis has been widespread for many years. Thus, optically transparent gauze minigrid gold or platinum (Figure 17) or optically transparent tin or iridium oxide semiconductor electrodes have been commonly used[9,10] for *in situ* UV–visible spectroelectrochemical measurements over very wide temperature ranges. Alternatively, flowing solution channel electrode techniques can be used conveniently with detection by UV–visible spectrophotometry in manners akin to their ESR spectroelectrochemical analogs described in Section 2.15.2.4.1.

2.15.2.4.4 NMR spectroelectrochemistry

Provided a suitable electrolyte is used that does not contain the nuclei of interest, then NMR is a very valuable tool widely used to identify products formed after bulk electrolysis experiments. Thus, 0.1 M Bu_4NBF_4 would be a suitable electrolyte for obtaining ^{31}P NMR spectra, whilst 0.1 M Bu_4NPF_6 probably would not be appropriate. However, *in situ* coupling of solution phase electrochemistry and NMR spectroscopy has proved difficult even though the great value of NMR as a structural tool is well recognized. The desirability of spinning the NMR tube whilst simultaneously undertaking an electrolysis experiment represents a far more difficult technical

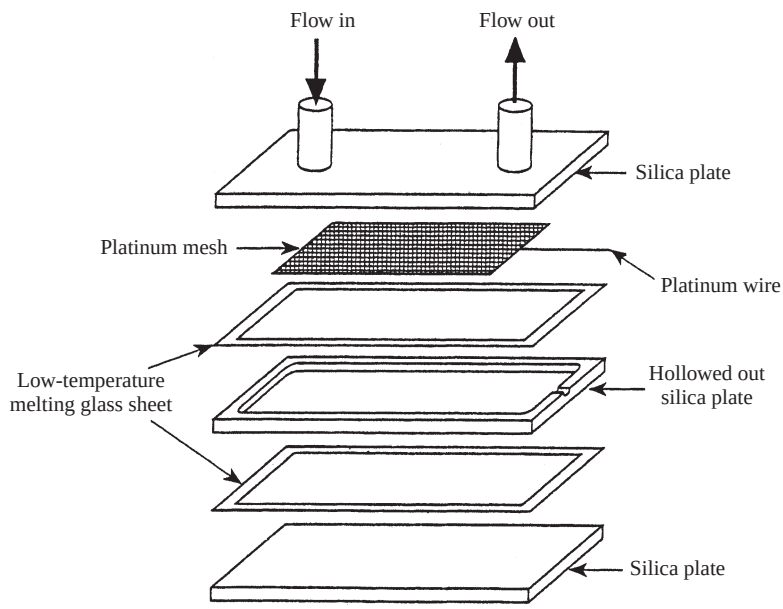

Figure 17 Schematic diagram of an optically transparent platinum mesh electrode–thin layer cell which in UV/visible spectroelectrochemical experiments is placed in the sample holder of the spectrophotometer and electronic spectra are then recorded during the course of electrolysis. Provided by courtesy of G. A. Heath, Australian National University.

problem than encountered in the ESR, IR, and UV/visible *in situ* spectroelectrochemical techniques. A solution phase NMR spectroelectrochemical technique has been described by Prenzler *et al.*,[31] which allows solution electrolysis to occur in the receiving coil region of a superconducting, high-field NMR spectrometer. Although the idea of coupling electrochemical generation with NMR detection is not new,[31] this cell is unique in that: the NMR spectra may be accumulated as the electrolytic current is flowing; the electrolysis products are generated directly at the receiver coil; the outer tube spins keeping the inner tube strictly centered and the sample mixed as electrolysis occurs; and finally, the unit is designed to work in a commercial probe—i.e., no custom-built probe is necessary.

2.15.2.4.5 Other forms of spectroelectrochemistry

Almost every other form of spectroscopy has been combined with electrochemistry including the Mössbauer and Raman techniques.[9] In the situation where solids are adhered to electrode surfaces, almost every conceivable surface science techniques such as X-ray diffraction, surface analysis, and scanning microscopy have been coupled with electrochemistry to provide a powerful adjunct to solid state electrochemical investigations.[2,9]

2.15.2.4.6 Combining mass spectrometry and electrochemistry

As noted above, an almost unlimited range of *in situ* and *ex situ* spectroelectrochemical techniques have been reported in the literature and have become an essential tool for electrochemical studies involving redox studies on coordination compounds. Obviously, products obtained during or after completion of an electrolysis experiment also may be examined by mass spectrometry.

The advantages of mass spectrometry (MS) as an analytical technique have long been recognized. Until quite recently, a limitation of the technique was the inability to routinely determine nonvolatile species present in solution as is required for identification of products formed by electrolysis in the solution phase. However, following its initial development in the late 1970s, electrospray mass spectrometry (ESMS) has been widely used for the identification of solution-based species.[32] Not surprisingly, therefore, the on-line coupling of ESMS for monitoring of electrochemically generated species is becoming more and more common.

ESMS is the "softest" method for transfer of ions from solution to the gas phase and has the advantage of minimal decomposition and fragmentation of ions. Thus, it is ideally suited for the determination of charged solution species which are frequently generated in electrochemical experiments. The ability to identify the charged products of electrolysis reactions in solution by ESMS is very desirable, in both off-line and on-line modes. However, a basic incompatibility exists between the two techniques which has to be solved. Electrolysis reactions are normally carried out with high concentrations of supporting electrolyte (typically about 0.1 M) and with an approximately 100-fold excess of electrolyte over electroactive compound, whereas in ESMS, high concentrations of ions are very undesirable, causing problems of peak suppression[33] and fouling of the interface plates and lenses. This problem has limited the coupling of electrochemistry and ESMS. For example, Dupont and co-workers describe the ESMS of products produced with off-line electrolysis of fullerenes.[34] Using 10 mM Bu_4NPF_6 as electrolyte and 100 μM fullerene, optimized conditions gave ESMS signals with the loss of signal intensity relative to that expected under other conditions being attributed to the high concentration of supporting electrolyte.

Despite problems with the electrolyte, several groups have reported the use of electrochemical cells on-line with ESMS.[35–39] In one study[35] the problems of high electrolyte concentrations were minimized by use of an electrolyte incorporating a small metal ion and a relatively volatile anion (for example, 20 mM lithium triflate). In another study[39] it has been shown that on-line ESMS–electrochemical methods can be used with low concentrations of supporting electrolytes using very simple flow cells which, for example, afford electrolysis of 0.2 mM $Ni(Et_2dtc)_2$ in acetonitrile (0.2 mM Bu_4NPF_6). Prior to electrolysis, the positive ion mass spectrum in Figure 18a was recorded, and clearly verifies the presence of the Bu_4N^+ electrolyte cation. After oxidative electrolysis and after allowing time for the electrolyzed solution to reach the mass spectrometer detector, the spectrum shown in Figure 18b was obtained. Clearly, the product, $[Ni(Et_2dtc)_3]^+$, is readily detected via its m/z value (mass/charge anion) and the comparison of experimental and predicted isotopic patterns. Thus, the ESMS data support previous proposals that the

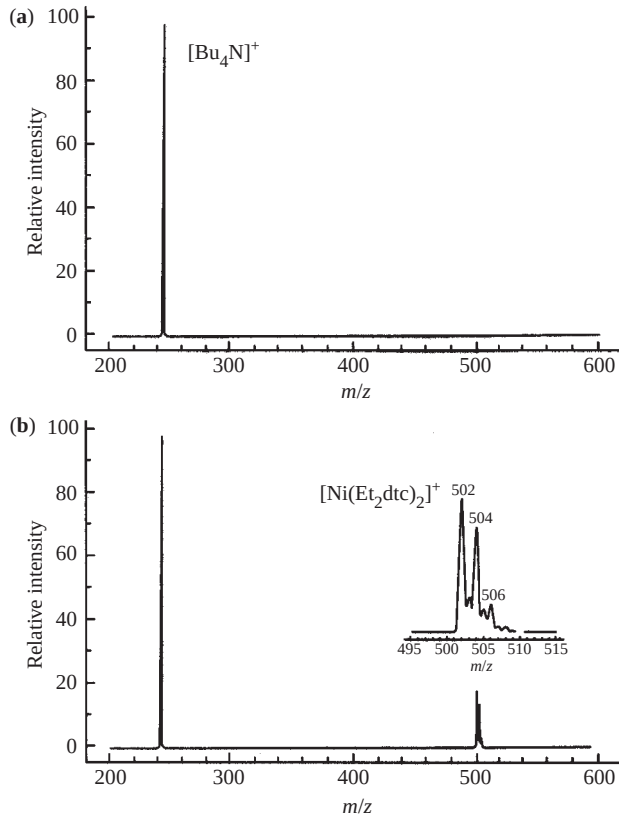

Figure 18 Positive ion mass spectra obtained with an on-line electrochemical–electrospray mass spectrometry flow cell containing equimolar 0.02 mM acetonitrile solutions of $Ni(Et_2dtc)_2$ and Bu_4NPF_6 (a) before and (b) during oxidative electrolysis (adapted from *Anal. Chem.* **1995**, *67*, 1699).

electrochemical oxidation of $Ni(Et_2dtc)_2$ occurs[16] via the overall reaction $3Ni(Et_2dtc)_2 \rightarrow 2[Ni(Et_2dtc)_3]^+ + Ni^{2+} + 4e^-$. The advantage of the on-line technique is obvious: the flow line can be introduced to the mass spectrometer without modification of the instrument; for air-sensitive species, the solution can be degassed prior to being introduced into the syringe; and the required sample volume is small. In contrast, in the off-line method, larger volumes of solution are required, products must be stable on longer time domains, and prevention of reaction with adventitious oxygen is difficult.

2.15.2.4.7 Examples of electrode mechanisms elucidated by combined voltammetric and spectroelectrochemical studies

Stable and isolable compounds containing cobalt in oxidation state IV are rare, with a well-known example[40] being octahedral $[CoF_6]^{2-}$. However, a larger number of examples of reactive formally cobalt(IV) species have been proposed to be generated by one-electron electrochemical oxidation of their parent cobalt(III) complexes. One important, but contentious, case detailed in the literature for over 25 years involves[41] the one-electron oxidation of $Co^{III}(R_2dtc)_3$. A combination of voltammetric and spectroelectrochemical studies confirms that at low temperatures in non-coordinating solvents and even at room temperature with some substituents that the process

$$Co^{III}(R_2dtc)_3 \rightleftharpoons [Co^{IV}(R_2dtc)_3]^+ + e^- \tag{16}$$

does occur whereas in other cases the overall process is

$$2Co^{III}(R_2dtc)_3 \rightleftharpoons [Co_2^{III}(R_2dtc)5]^+ + [\text{oxidized ligand}]^+ + 2e^- \tag{17}$$

In the case of the cyclohexyl derivative in CH_2Cl_2, the simple translation of voltammograms from a reversible oxidation to a reversible one-electron reduction process[42] is consistent with formation of $[Co(R_2dtc)_3]^+$. The low-temperature electronic spectra[41,42] obtained in an optically transparent thin layer spectroelectrochemical cell (Figure 17) and ESR spectra[41] coupled with the electrochemical data confirm that the one-electron oxidation of ethyl (low temperature) and cyclohexyl (room temperature) generates a low-spin cobalt(IV) complex. The approximately axial ESR spectra suggest a distorted octahedral structure, whilst the UV–vis–NIR data are consistent with low-spin $d^5(t_{2g}{}^5)$ complexes displaying a series of transitions to t_{2g} and e_g levels. In contrast, room-temperature bulk electrolysis of $Co(Et_2dtc)_3$ produces voltammograms which are the same[41] as those observed for $[Co^{III}{}_2(Et_2dtc)_5]^+$. Cobalt NMR spectra clearly reveals this product is a diamagnetic cobalt(III) complex with two nonequivalent centers.[43] Whilst all the details related to the formation of $[Co_2(R_2dtc)_5]^+$ are unknown, the basic reaction scheme is given in Equations (18a)–(18c):

$$Co^{III}(R_2dtc)_3 \rightleftharpoons [Co^{IV}(R_2dtc)_3]^+ + e^- \tag{18a}$$

$$2[Co^{IV}(R_2dtc)_3]^+ \rightarrow [Co^{IV}_2(R_2dtc)_6]^{2+} \tag{18b}$$

$$[Co^{IV}{}_2(R_2dtc)_6]^{2+} \rightarrow [Co^{III}{}_2(R_2dtc)_5]^+ + [\text{oxidized ligand}]^+ \tag{18c}$$

Very clear evidence for this reaction scheme is obtained from concentration and scan- and flow-rate-dependent voltammetric studies on the oxidation of $Co(R_2dtc)_3$ and analogous $Rh(R_2dtc)_3$ complexes.[44,45]

A second example that illustrates the outcome of careful voltammetric and spectroelectrochemical studies is provided by the studies of Clark *et al.*[46,47] on the oxidation and reduction of *trans*-$[RuBr_4(CNBu^t)_2]^-$ and the chloride analog in the coordinating acetonitrile solvent. Figure 19 shows a cyclic voltammogram for both the reduction and oxidation of the bromide complex along with the IR spectroelectrochemical experiment which corresponds to formation of *mer,trans*-$[RuBr_3(CNBu^t)_2(NCCH_3)]^-$ and *mer,trans*-$[RuBr_3(CNBu^t)_2(NCCH_3)]$ respectively. Consequently, a fascinating result is achieved where the product formed in both the oxidation and reduction processes is part of the same reversible *mer,trans*-$[RuBr_3(CN\ Bu^t)_2(NCCH_3)]^{0/-}$ couple as seen in Figure 20. The **ECE** mechanism for reduction is

$$\mathbf{E}\ \textit{trans}\text{-}[RuBr_4(CNBu^t)_2]^- + e^- \rightleftharpoons \textit{trans}\text{-}[RuBr_4(CNBu^t)_2]^{2-} \tag{19}$$

$$\mathbf{C}\ \textit{trans}\text{-}[RuBr_4(CNBu^t)_2]^{2-} + CH_3CN \rightarrow \textit{mer,trans}\text{-}[RuBr_3(CNBu^t)_2(NCCH_3)]^- + Br^- \tag{20}$$

$$\mathbf{E}\ \textit{mer,trans}\text{-}[RuBr_3(CNBu^t)_2(NCCH_3)]^- \rightleftharpoons \textit{mer,trans}\text{-}[RuBr_3(CNBu^t)_2(NCCH_3)] + e^- \tag{21}$$

whilst for oxidation it is

$$\mathbf{E}\ \textit{trans}\text{-}[RuBr_4(CNBu^t)_2]^- \rightleftharpoons \textit{trans}\text{-}[RuBr_4(CNBu^t)_2] + e^- \tag{22}$$

$$\mathbf{C}\ \textit{trans}\text{-}[RuBr_4(CNBu^t)_2] + CH_3CN \longrightarrow \textit{mer,trans}\text{-}[RuBr_3(CNBu^t)_2(NCCH_3)] + 1/2\ Br_2 \tag{23}$$

$$\mathbf{E}\ \textit{mer,trans}\text{-}[RuBr_3(CNBu^t)_2(NCCH_3)] + e^- \rightleftharpoons \textit{mer,trans}\text{-}[RuBr_3(CNBu^t)_2(NCCH_3)]^- \tag{24}$$

Voltammetric, IR, and spectroelectrochemical experiments on the chloride analog show that the reduction process follows the same pathway. However, analogous oxidation of *trans*-$[RuCl_4(CNBu^t)_2]^-$ under low-temperature conditions is a simple one-electron oxidation process

$$\mathbf{E}\ \textit{trans}\text{-}[RuCl_4(CNBu^t)_2]^- \rightleftharpoons \textit{trans}\text{-}[RuCl_4(CNBu^t)_2] + e^- \tag{25}$$

The cyclic voltammogram of *trans*-$[NBu_4][RuCl_4(CNBu^t)_2]$ in acetonitrile–dichloromethane (1:1) containing 0.25 M $[NBu_4][PF_6]$ is shown in Figure 20 (upper curves). A chemically reversible oxidation process is observed at $E_{1/2} = +1.57$ V vs. Ag/AgCl, indicating that the tetravalent *trans*-$[Ru^{IV}Cl_4(CN\text{-}Bu^t)_2]$ species is stable on the timescale of the voltammetric experiment. Oxidation of

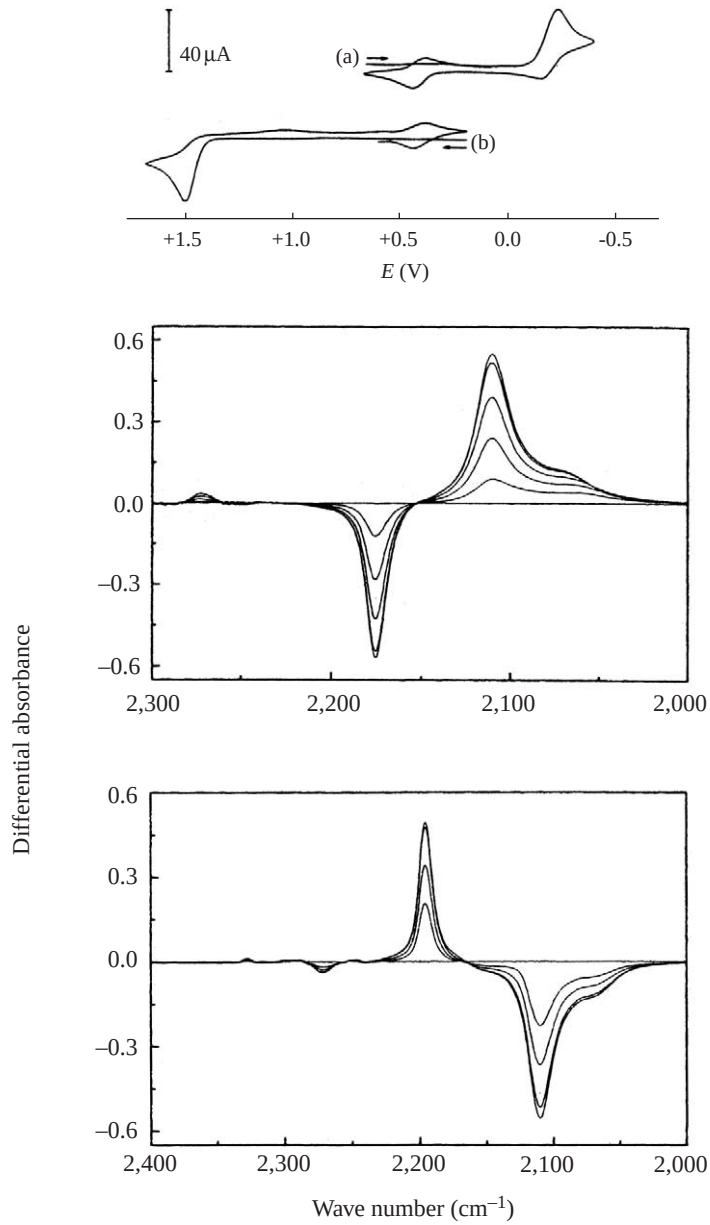

Figure 19 Voltammetry and spectroelectrochemistry for reduction and oxidation of *trans*-$[RuBr_4(CNBu^t)_2]^-$. (Upper curve): cyclic voltammograms for reduction (a) and oxidation (b) of *trans*-$[NBu_4][RuBr_4(CNBu^t)_2]$ in an acetonitrile–dichloromethane (1:1) solution containing 0.25 M $[NBu_4][PF_6]$ at ≈290 K. Scan rate = 100 mV s^{-1} in each case. Potentials are quoted vs. Ag/AgCl which has a potential of +0.55 V vs. Fc/Fc^+. (Middle curve): changes in IR difference absorption spectra accompanying reduction of *trans*-$[RuBr_4(CNBu^t)_2]^-$ in 0.25 M $[NBu_4][PF_6]$ in acetonitrile–dichloromethane (1:1) in the IR spectroelectrochemical cell shown in Figure 16 at ≈290 K. The horizontal line at zero absorbance corresponds to the initial spectrum, i.e., that of *trans*-$[RuBr_4(CNBu^t)_2]^-$, prior to electrolysis. The potential of the working electrode is stepped to $E_{app} = -0.4$ V, and single scan IR spectra collected as a function of time. Consumption of *trans*-$[RuBr_4(CNBu^t)_2]^-$ upon reduction is indicated by increasing negative absorbance at 2,170 cm^{-1}, whilst increasing positive absorbance at 2,272 cm^{-1} and 2,109 cm^{-1} corresponds to the formation of *mer,trans*-$[RuBr_3(CNBu^t)_2(NCMe)]^-$. (Lower curve): oxidation of *mer,trans*-$[RuBr_3(CNBu^t)_2(NCMe)]^-$ to *mer,trans*-$[RuBr_3(CNBu^t)_2(NCMe)]$ at $E_{app} = +0.6$ V (reproduced by courtesy: *J. Chem. Soc., Dalton Trans.* 1997, 2535; © Royal Society of Chemistry).

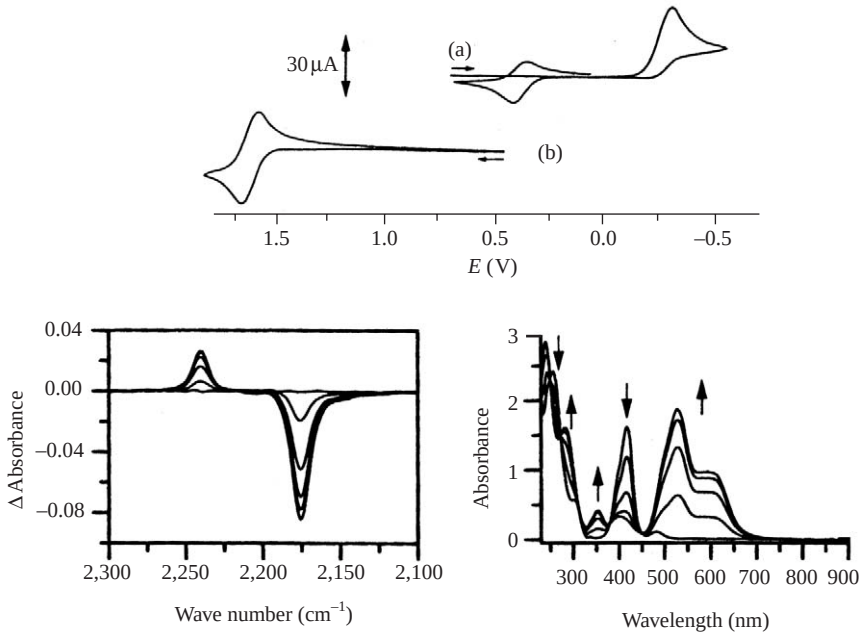

Figure 20 (Upper curve): cyclic voltammograms for reduction (a) and oxidation (b) of *trans*-$[NBu_4][RuCl_4(CNBu^t)_2]$ in acetonitrile–dichloromethane (1:1) solution containing 0.25 M $[NBu_4][PF_6]$ at ≈290 K. Scan rate = 100 mV s^{-1} in each case. (Middle curve): changes in the IR difference absorption spectra (see Figure 16 for description of cell) accompanying oxidation of *trans*-$[NBu_4][RuCl_4(CNBu^t)_2]$ in acetonitrile–dichloromethane (1:1) containing 0.25 M $[NBu_4][PF_6]$ at 233 K. (Lower curve): the UV–vis spectral changes accompanying oxidation of *trans*-$[NBu_4][RuCl_4(CNBu^t)_2]$ in a cell of the kind shown in Figure 17 in acetonitrile–dichloromethane (1:1) containing 0.25 M $[NBu_4][PF_6]$ at 233 K (reproduced by courtesy: *J. Chem. Soc., Dalton Trans.* **2000**, 933; © Royal Society of Chemistry).

trans-$[RuCl_4(CNBu^t)_2]^-$ in an IRRAS cell (Figure 16) at $E_{app} = +1.70$ V is accompanied by the loss of the parent ν_{NC} band at 2,176 cm^{-1}, and simultaneous growth of a single band at 2,240 cm^{-1}, as also shown in Figure 20 (middle curve). The single ν_{NC} band indicates retention of the *trans* geometry. At low temperature, the spectral changes are fully reversible, in that re-reduction at $E_{app} = +1.40$ V regenerates the starting spectrum, and isosbestic points are observed with each series of spectral changes. The tetravalent chloride species is evidently quite stable at low temperatures ($T \leq 228$ K), since it is also possible to electrogenerate *trans*-$[RuCl_4(CNBu^t)_2]$ reversibly in an OTTLE cell (Figure 17) to give the electronic spectra shown in Figure 20 (lower curve). The principal band in the spectrum of *trans*-$[RuCl_4(CNBu^t)_2]^-$ is shifted to lower wavelength (418–528 nm) upon oxidation, as anticipated for a ligand-to-metal charge transfer transition of the type $Cl(p\pi) \rightarrow Ru(d\pi)$.

2.15.2.4.8 *Concluding remarks—broadening electrochemical and coordination chemistry horizons*

The above material focuses on the conventional electrochemical methods, which typically means studies employing conventional-sized electrodes, DC waveforms, and solution phase redox chemistry in organic solvents containing electrolyte to provide adequate conductivity. With modern forms of electrochemistry, each of these parameters may be altered to facilitate studies in non-conventional media with respect to usual conditions employed in studies of coordination compounds. Examples of variations of methodology that broaden the scope of redox studies of coordination compounds include:

Use of microelectrodes under steady state conditions, where radial rather than linear diffusion is dominant,[2,48] minimizes the influence of uncompensated resistance and enables studies to be routinely undertaken in toluene, conducting polymers, solids, gas phase, critical fluids, as well as without deliberately added supporting electrolyte.[48]

Use of AC, square wave, pulse methods, and impedance methods as well as very fast scan rate methods with microelectrodes enhances the accuracy and/or scope of measurement of E_f^o values, provides greater kinetic sensitivity, and allows superior methods of quantifying the details of electrode processes to be introduced.[2–5,13]

Solids may be adhered to electrode surfaces as thin films and then electrochemically oxidized or reduced in the absence of diffusion.[49,50] Work by Armstrong *et al.* on metalloproteins illustrates advantages relative to conventional solution phase studies.[50] Thick-film formats also may be used, but the theoretical principles may differ from the thin-film case.[2]

Use of ionic liquids as an alternative to conventional solvents containing deliberately added supporting electrolyte is emerging as a medium that may be ideal for electrochemical studies of coordination compounds.[51,52]

2.15.3 REFERENCES

1. Pickett, C. J. In *Comprehensive Coordination Chemistry*; Wilkinson, G.; Gillard, R. D.; McCleverty, J. A., Eds.; Pergamon Oxford, 1987, Vol. 1, Chapter 8.1, pp 475–501.
2. Bond, A. M. *Broadening Electrochemical Horizons*; Oxford University Press: Oxford, 2002.
3. Bard, A. J.; Faulkner, L. R. *Electrochemical Methods: Fundamentals and Applications*, 2nd edition, Wiley New York, 2001.
4. Oldham, K. B.; Myland, J. C. *Fundamentals of Electrochemical Science*, Academic Press, San Diego, 1994.
5. Rieger, P. H. *Electrochemistry*, 2nd Ed., Chapman and Hall, New York, 1994.
6. Hagfeldt, A.; Grätzel, M. *Chem. Rev.* **1995**, *95*, 49–68, and references cited therein.
7. Bach, U.; Lupo, D.; Comte, P.; Moser, J. E.; Wilssörtel, F.; Salbeck, J.; Spreitzer, H.; Grätzel, M. *Nature* **1998**, *395*, 583–585.
8. Argazzi, R.; Bignozzi, C. A.; Heimer, T. A.; Castellano, F. N.; Meyer, G. J. *Inorg. Chem.* **1994**, *33*, 5741–5749.
9. Gale, R. J., Ed., *Spectroelectrochemistry: Theory and Practice*, Plenum Press: New York, 1988, and references cited therein.
10. Crayston, J. A. *In Encyclopedia of Electrochemistry*, Bard, A. J.; Stratman, M., Eds.; Wiley-VCH: Weinheim, 2002; Chapter 20.
11. Eklund, J. C.; Bond, A. M.; Alden, J. A.; Compton, R. G. *Adv. Phys. Org. Chem.* **1999**, *32*, 1–120.
12. Rudolph, M.; Reddy, D. P.; Feldberg, S. W. *Anal. Chem.* **1994**, *66*, 589A–600A.
13. Scholz, F., Ed., *Electroanalytical Methods: Guide to Experiments and Applications*, Springer-Verlag, Heidelberg, 2002.
14. Roe, D. K. Overcoming Solution Resistance with Stability and Grace in Potentiostatic Circuits. In *Laboratory Techniques in Electroanalytical Chemistry*, Kissinger, P. T.; Heineman, W. R., Eds.; Marcel Dekker, New York, 1984, Chapter 7, pp 193–234.
15. Chant, R.; Hendrikson, A. R.; Martin, R. L.; Rohde, N. M. *Inorg. Chem.* **1975**, *14*, 1894–1902.
16. Bond, A. M.; Martin, R. L. *Coord. Chem. Rev.* **1984**, *54*, 23–98, and references cited therein.
17. Zuman, P. *Substituent Effects in Organic Polarography*, Plenum Press, New York, 1967.
18. Lever, A. B. P. *Inorg. Chim. Acta* **1993**, *203*, 171–174.
19. Lever, A. B. P.; Milaeva, E. R.; Speier, G. The Redox Chemistry of Metallophthalocyanines in Solution. In *The Phthalocyanines, Properties and Applications*, Leznoff, C. C.; Lever, A. B. P., Eds.; VCH, New York, 1993, Vol. 3, pp 1–69.
20. Lever, A. B. P.; Dodsworth, E. S. Electrochemistry, Charge Transfer Spectroscopy and Electronic Structure. In *Inorganic Electronic Structure and Spectroscopy*, Solomon, E. I.; Lever, A. B. P., Eds.; John Wiley, New York, 1999, pp 227–287.
21. Brownstein, S.; Heath, G. A.; Sengupta, A.; Sharp, D. W. A. *J. Chem. Soc. Chem. Commun.* **1983**, 669–670.
22. Heath, G. A.; Moock, K. A.; Sharp, D. W. A.; Yellowlees, L. J. *J. Chem. Soc. Chem. Commun.* **1985**, 1503–1505.
23. Heath, G. A. Spectroelectrochemistry and Electrochemical Spectroscopy. In *Molecular Electrochemistry of Inorganic, Bioinorganic and Organometallic Compounds*; Pombeiro, A. J. L.; McCleverty, J. A., Eds.; NATO ASI Series, Series C; Kluwer Academic, Dordrecht 1993, pp 533–547.
24. Lever, A. B. P. *Inorg. Chem.* **1990**, *29*, 1271–1285.
25. Harrar, J. E. *Electroanalytical Chemistry* **1975**, *8*, 1–167.
26. Bagchi, R. N.; Bond, A. M.; Scholz, F. *Electroanalysis* **1989**, *1*, 1–11.
27. Goldberg, I. B.; McKinney, T. M. Principles and Techniques of Electrochemical–Electron Spin Resonance Experiments. In *Laboratory Techniques in Electroanalytical Chemistry*, Kissinger, P. T.; Heineman, W. R., Eds.; Marcel Dekker, New York, 1984, Chapter 24, pp 675–728.
28. Best, S. P.; Clark, R. J. H.; McQueen, R. C. S.; Cooney, R. P. *Rev. Sci. Instrument* **1987**, *58*, 2071–2074.
29. Best, S. P.; Ciniawsky, S. A.; Humphrey, D. G. *J. Chem. Soc. Dalton Trans.* **1996**, 2945–2949.
30. Shaw, M. J.; Geiger, W. E. *Organometallics* **1996**, *15*, 13–15.
31. Prenzler, P. D.; Bramley, R.; Downing, S. R.; Heath, G. A. *Electrochem. Commun.* **2000**, *2*, 516–521.
32. Volk, K. J.; Yost, R. A.; Brajter-Toth, A. *Anal. Chem.* **1992**, *64*, 21A–33A.
33. Tang, L.; Kebarle, P. *Anal. Chem.* **1993**, *65*, 3654–3668.
34. Dupont, A.; Gisselbrecht, J.-P.; Leize, E.; Wagner, L.; Van Dorssellaer, A. *Tetrahedron Lett.* **1994**, *35*, 6083–6086.
35. Zhou, F.; Van Berkel, G. J. *Anal. Chem.* **1995**, *67*, 3643–3649.
36. Deng, H.; Van Berkel, G. J. *Anal Chem.* **1999**, *71*, 4284–4293.
37. Xu, X.; Lu, W.; Cole, R. B. *Anal Chem.* **1996**, *68*, 4244–4253.
38. Lu, W.; Xu, X.; Cole, R. B. *Anal. Chem.* **1997**, *69*, 2478–2484.
39. Bond, A. M.; Colton, R.; D'Agostino, A.; Downard, A. J.; Traeger, J. C. *Anal Chem.* **1995**, 67, 1691–1695.
40. Allen, G. C.; Warren, K. D. *Inorg. Chem.* **1969**, *8*, 1902–1904.
41. Webster, R. D.; Heath, G. A.; Bond, A. M. *J. Chem. Soc. Dalton Trans.* **2001**, 3189–3195, and references cited therein.
42. Bond, A. M.; Hendrickson, A. R.; Martin, R. L.; Moir, J. E.; Page, D. R. *Inorg. Chem.* **1983**, *22*, 3440–3446.
43. Bond, A. M.; Colton, R.; Ho, Y.; Moir, J. E.; Mann, D. R.; Stott, R. *Inorg. Chem.* **1985**, *24*, 4402–4407.
44. Alden, J. A.; Bond, A. M.; Colton, R.; Compton, R. G.; Eklund, J. C.; Mah, Y. A.; Mahon, P. J.; Tedesco, V. *J. Electroanal. Chem.* **1998**, *447*, 155–171.

45. Bond, A. M.; Colton, R.; Mann, D. R. *Inorg. Chem.* **1989**, *28*, 54–59.
46. al Dulaimi, J. P.; Clark, R. J. H.; Humphrey, D. G. *J. Chem. Soc. Dalton Trans.* **1997**, 2535–2536.
47. al Dulaimi, J. P.; Clark, R. J. H.; Humphrey, D. G. *J. Chem. Soc. Dalton Trans.* **2000**, 933–939.
48. Bond, A. M. *Analyst* **1994**, *119*, R1–R21.
49. Scholz, F.; Meyer, B. *Electroanal. Chem.* **1998**, *20*, 1–86.
50. Armstrong, F. A.; Heering, H. A.; Hirst, J. *Chem. Soc. Rev.* **1997**, *26*, 169–179, and references cited therein.
51. Hultgren, V. M.; Mariotti, A. W. A.; Bond, A. M.; Wedd, A. G. *Anal. Chem.* **2002**, *74*, 3151–3156, and references cited therein.
52. Boxall, D. L.; Osteryoung, R. A. *J. Electrochem. Soc.* **2002**, *149*, E185–E188, and references cited therein.

Comprehensive Coordination Chemistry II
ISBN (set): 0-08-0437486

Volume 2, (ISBN 0-08-0443249); pp 197–222

2.16 Electrochemistry: Proton Coupled Systems

J. M. LEHNES
Wilson Greatbatch Technologies, Clarence, NY, USA
and
A. R. NORTHROP and K. A. GOLDSBY
Florida State University, Tallahassee, FL, USA

2.16.1 pH-DEPENDENT REDUCTION POTENTIALS 223
2.16.2 APPLICATION OF pH-DEPENDENT ELECTROCHEMISTRY TO COORDINATION COMPLEXES 225
2.16.3 EXPERIMENTAL CONSIDERATIONS 226
2.16.3.1 Chemical Reversibility 226
2.16.3.2 Electrochemical Reversibility 226
2.16.3.3 pH-dependence of Irreversible Couples 227
2.16.4 COORDINATION COMPLEXES EXHIBITING pH-DEPENDENT REDUCTION POTENTIALS 227
2.16.4.1 Metal-aquo/Hydroxide/Oxo Systems 227
2.16.4.2 Oxo-bridged Metal Systems 228
2.16.4.3 Metal–Oxime Systems 229
2.16.4.4 Metal–Amine Systems 230
2.16.4.5 Metal *N*-heterocycle Systems 230
2.16.5 pH-DEPENDENT REDUCTION POTENTIALS IN BIOLOGICAL SYSTEMS 231
2.16.6 REFERENCES 232

Electrochemistry provides a powerful tool for elucidating the pH-dependent redox mechanisms of coordination complexes. In principle, any electrochemically active chemical (or biological) system may exhibit pH-dependent reduction potentials, if the concomitant pH-dependent process occurs on the same timescale as electron transfer. While the pH-dependent process is ultimately chemical in nature (i.e., involves bond breaking and/or bond making), the phenomenon that perturbs the redox center and alters the reduction potential may be electronic, structural (e.g., a conformational change), or environmental (e.g., changes in solvation), and often will be some ill-defined combination of these factors.[1]

In the limit of fast, reversible redox processes (i.e., thermodynamic equilibrium is maintained throughout the electrochemical process), the pH-dependence is given by the Nernst equation. The basic theory has received thorough treatment, and only a brief overview is given here.

2.16.1 pH-DEPENDENT REDUCTION POTENTIALS

A general chemical equation for a pH-dependent redox couple is given in Equation (1) (note: generalized redox reactions in this section are written as reductions to follow the convention that

couples are reported as reduction potentials; however, the specific examples given later are written as oxidations or reductions, depending on the original oxidation state of the complex prior to measurement of the potential), where Ox is the oxidized species and Red is the reduced species, and overall charges are omitted except for the proton (or hydroxide) transferred in the process.

$$\mathrm{Ox} + n(\mathrm{e}^-) + m(\mathrm{H}^+) \rightarrow \mathrm{Red}(\mathrm{H}^+)_m \tag{1}$$

This reaction could just as well be some type of hydrolysis reaction (for example, Equation (2))

$$\mathrm{Ox}(\mathrm{OH}^-)_\mathrm{m} + n(\mathrm{e}^-) + m(\mathrm{H}^+) \rightarrow \mathrm{Red} + m(\mathrm{H_2O}) \tag{2}$$

or any other redox process involving the uptake of protons from (or release of protons to) the surrounding medium. The pH-dependence of the reduction potential is given by Equation (3),[2] where D_o and D_r are the respective diffusion coefficients of the oxidized and reduced species, m is the number of protons, n is the number of electrons, $E^{\mathrm{o}'}$ is the hypothetical formal potential in volts (assumes that the n-electron/m-proton process occurs at pH = 0), and $E_{1/2}$ is the measured half-wave potential in volts (the potential at which [Ox] = [Red$(\mathrm{H}^+)_m$] for Equation (1)).

$$E_{1/2} = E^{\mathrm{o}'} - [0.059/n]\log(D_\mathrm{o}/D_\mathrm{r})^{1/2} - 0.059(m/n)\mathrm{pH} \tag{3}$$

The diffusion coefficients are generally assumed to be roughly equal, removing the middle term in Equation (3) to give

$$E_{1/2} = E^{\mathrm{o}'} - 0.059(m/n)\mathrm{pH} \tag{4}$$

The pH dependence of redox potentials can be expressed graphically as a pH-potential diagram, also referred to as a predominance area diagram or a Pourbaix diagram,[3–7] although in the strictest sense a Pourbaix diagram includes activity as a third dimension.[8] Such diagrams have found wide use in many fields, including corrosion science,[9] geochemistry,[10] and materials processing.[11] While often complex, pH-potential diagrams are simply the superposition of multiple line segments separating the predominant regions of the various chemical species, as illustrated in Figure 1 for the simple system represented by Equation (1).

The horizontal lines correspond to the pH-independent reduction potentials for the redox processes where both the reduced and oxidized species are protonated (low pH side, Equation (5))

$$\mathrm{Ox}(\mathrm{H}^+)_m + n(\mathrm{e}^-) \rightarrow \mathrm{Red}(\mathrm{H}^+)_m \tag{5}$$

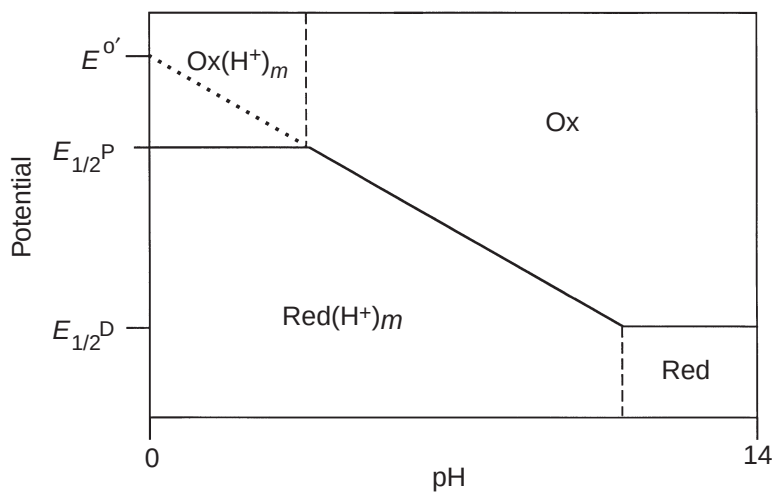

Figure 1 A pH-potential diagram showing the pH-dependence of a generalized n-electron, m-proton Ox/Red$(\mathrm{H}^+)_m$ couple. $E^{\mathrm{o}'}$ is the formal potential of the Ox/Red$(\mathrm{H}^+)_m$ couple that would occur hypothetically at pH = 0. $E_{1/2}{}^\mathrm{D}$ is the formal potential of the fully deprotonated Ox/Red couple; $E_{1/2}{}^\mathrm{P}$ is the formal potential of the fully protonated Ox$(\mathrm{H}^+)_m$/Red$(\mathrm{H}^+)_m$ couple.

or deprotonated (high pH side, Equation (6)).

$$\mathrm{Ox} + n(\mathrm{e}^-) \rightarrow \mathrm{Red} \tag{6}$$

The diagonal line connecting these segments corresponds to the pH-dependent potentials for the redox process where reduction/oxidation is coupled to protonation/deprotonation (Equation (1)). The intersection points connecting horizontal and diagonal lines represent a juncture for the change in the redox mechanism of that couple, and the vertical lines at these junctures indicate the boundaries between the protonated and deprotonated species of a particular redox state. Note that these results are consistent with Equation (4), which predicts a slope of $-0.059(m/n)$ V/pH-unit for a n-electron/m-proton reaction: a redox reaction that does not involve the transfer of protons ($m = 0$) will be a horizontal line, and an acid/base equilibrium that does not involve the transfer of electrons ($n = 0$) will be a vertical line.

2.16.2 APPLICATION OF pH-DEPENDENT ELECTROCHEMISTRY TO COORDINATION COMPLEXES

As noted above, the pH-dependent reduction potentials for a coordination complex may result from any pH-dependent process that sufficiently perturbs the metal center (e.g., hydrolysis of a coordinated aldehyde, Equation (7));[12] however, most examples in the literature are associated with protonation and deprotonation of one or more coordinated ligands. Depending on the ligands involved and the accessible oxidation states of the metal, the redox mechanisms can be quite complex, involving the transfer of multiple protons from one or more ligands. The resulting complexity can be seen in the pH-potential diagrams of many aqueous transition metal ions.[3–5]

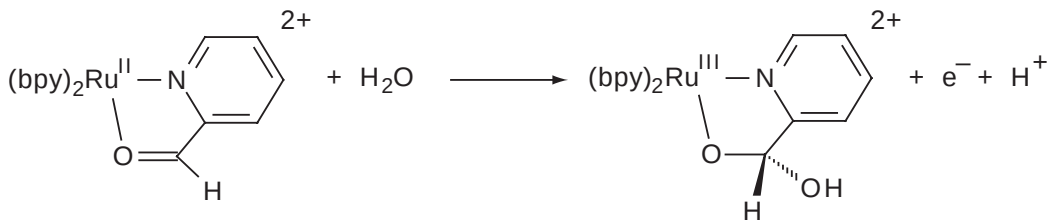

(7)

This situation can be simplified considerably by limiting the coordination sphere to a single ionizable proton within the pH range considered, as in Equation (8) where bimH is benzimidazole.[13]

$$[(\mathrm{H_3N})_5\mathrm{Ru^{II}(bimH)}]^{2+} \rightarrow [(\mathrm{H_3N})_5\mathrm{Ru^{III}(bim)}]^{2+} + \mathrm{e}^- + \mathrm{H}^+ \tag{8}$$

The pH-potential diagram for a generalized one-proton/one-electron couple is shown in Figure 2. Because only a single proton is involved in the chemical equilibrium, the intersection points will be determined by the acid dissociation constants for specific oxidation states of the metal complex. The ability to interrelate reduction potentials and acid/base equilibria constants is one of the most powerful aspects of pH-potential diagrams in terms of their ability to set the boundary conditions for redox mechanisms. For example, the horizontal line in the acidic region of Figure 2 corresponds to the potential at which $[\mathrm{M^{III}LH}] = [\mathrm{M^{II}LH}]$, and the diagonal line corresponds to the potential at which $[\mathrm{M^{III}L}] = [\mathrm{M^{II}LH}]$. At the intersection point, $[\mathrm{M^{III}LH}] = [\mathrm{M^{II}LH}] = [\mathrm{M^{III}L}]$ and hence $\mathrm{pH} = \mathrm{p}K_\mathrm{a}{}^{\mathrm{III}}$. By a similar argument, the intersection point in the basic region occurs at $\mathrm{pH} = \mathrm{p}K_\mathrm{a}{}^{\mathrm{II}}$. The more complicated pH-potential diagrams can be conceptionalized as a superposition of multiple redox processes.[7]

The range of pH-dependent behavior for a redox couple will therefore be defined by the $\mathrm{p}K_\mathrm{a}$ values of the complex for the two oxidation states involved in that couple, e.g., the generalized $\mathrm{M^{III/II}LH}$ couple will be pH-dependent between $\mathrm{p}K_\mathrm{a}{}^{\mathrm{III}}$ and $\mathrm{p}K_\mathrm{a}{}^{\mathrm{II}}$. As Figure 2 graphically illustrates, it is equivalent to say that the pH-dependent range is defined by $E_{1/2}{}^{\mathrm{P}}$ and $E_{1/2}{}^{\mathrm{D}}$, the respective potentials for the protonated and deprotonated couples, since $E_{1/2}{}^{\mathrm{P}} - E_{1/2}{}^{\mathrm{D}} = \Delta E_{1/2} = (59\,\mathrm{mV})\Delta\mathrm{p}K_\mathrm{a}$ for a one-electron/one-proton couple, where $\Delta\mathrm{p}K_\mathrm{a} = \mathrm{p}K_\mathrm{a}{}^{\mathrm{II}} - \mathrm{p}K_\mathrm{a}{}^{\mathrm{III}}$. Therefore, the extent of this reciprocal and mutual influence between electron transfer and proton transfer is reflected equally in the differences between the individual $\mathrm{p}K_\mathrm{a}$ values and redox potentials. The relationship between $\mathrm{p}K_\mathrm{a}$ and oxidation state of the complex will depend on a number of factors,

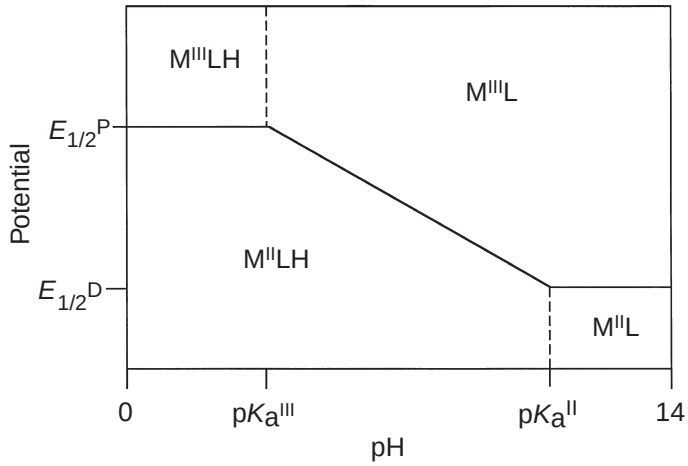

Figure 2 A generalized pH-potential diagram for a $M^{II}LH$ complex exhibiting a pH-dependent $M^{III/II}$ couple. $E_{1/2}{}^{D}$ is the formal potential of the $[M^{III}L]/[M^{II}L]$ couple, deprotonated in both oxidation states; $E_{1/2}{}^{P}$ is the formal potential of the $[M^{III}LH]/[M^{II}LH]$ couple, protonated in both oxidation states. $pK_a{}^{II}$ and $pK_a{}^{III}$ are pK_a values for the M^{II} and M^{III} species, respectively.

including sigma and pi bonding effects, distance between the metal and protonation site on the ligand, and the nature of the ancillary ligands on the complex.[1]

2.16.3 EXPERIMENTAL CONSIDERATIONS

The above treatment assumes that the measured reduction potentials are thermodynamically meaningful. Although redox potentials can be measured by a variety of electrochemical techniques, cyclic voltammetry, differential pulse polarography, and more recently, square wave voltammetry have found the greatest use because of the ability of these techniques to reveal the dynamics of the associated chemical processes, and hence access the chemical and electrochemical reversibility of the couple. Chemical and electrochemical reversibility have been defined and problems associated with the distinction between these terms have been covered in Chapter 2.15 (2.15.2.2.1), however, for the purpose of this discussion it is useful to treat these behaviors separately.

2.16.3.1 Chemical Reversibility

Chemical reversibility occurs when both oxidation states of a redox couple are stable within the timescale of the electrochemical measurement. This condition is rare among one-electron couples for main group compounds, since the resulting odd-electron species tend to be quite reactive. Redox processes involving *d* and *f* electrons can give relatively stable consecutive oxidation states that provide for one-electron couples well suited for electrochemical measurement, and the preponderance of pH-potential diagrams have been generated for transition metal, lanthanide, and actinide complexes.[3–5] In the case of cyclic voltammetry, the formed oxidation state should be stable on the timescale defined by the scan rate of the measurement. Fast scan rates can be achieved to instrumental limits by the use of electrodes with small surface areas[14] and/or cell configurations designed to minimize IR drop (e.g., use of Luggin probes).[15] To avoid physisorption to the electrode, complexes should be water soluble within the pH range of interest for the oxidation states to be studied. In some cases, the use of mixed solvents, such as acetonitrile/water[16,17] or dioxane/water[18] offer practical, if not ideal, solutions to this problem.

2.16.3.2 Electrochemical Reversibility

Electrochemical irreversibility caused by slow heterogeneous electron-transfer kinetics at the electrode surface can limit the ability of the measurement to yield thermodynamically meaningful potentials. While proton transfer in aqueous solutions is generally very fast,[19] heterogeneous

electron-transfer rates can be quite sensitive to the nature of the electrode surface. These rates can be optimized by techniques such as polishing, or chemical and/or electrochemical pretreatment. Carbon is generally the electrode material of choice for electrochemical measurements in water, and carbon electrodes are particularly susceptible to surface effects. A variety of electrode materials have been used, including glassy carbon, pyrolytic graphite, and carbon paste, and these surfaces are very sensitive to pretreatment procedures.[20,21] Oxidative activation of glassy-carbon electrodes has been shown to significantly enhance the electrode response for ruthenium–aquo/hydroxo/oxo couples, some other positively charged ions, and some organic processes (e.g., *o*-quinone/hydroquinone). It is generally believed that oxidative activation creates functionalities on the carbon surface (e.g., phenolic and carboxylic groups) that facilitate the heterogeneous electron-transfer reaction via specific interactions with the solution species.[22] Electrostatic factors also affect the response a molecule gives at an activated surface. Negatively charged complexes such as $[Fe^{III}(CN)_6]^{3-}$ and $[Fe^{II}(CN)_6]^{4-}$ showed improved reversibility at a reductively activated glassy carbon electrode as the pH was varied from 8 to 3.[23] The opposite effect was observed for the positively charged complex, $[Ru^{III}(NH_3)_6]^{3+}$; the reversibility of the $Ru^{III/II}$ couple decreased with decreasing pH. This difference in the behavior for negative and positive complexes as pH is decreased was attributed to the protonation of surface groups (e.g., carbonyl functionalities) which tends to attract negative ions and repel positive ions, accounting for the increased reversibility of the $[Fe(CN)_6]^{3-/4-}$ couple while the reversibility of the $[Ru(NH_3)_6]^{3+/2+}$ couple decreased.

2.16.3.3 pH-dependence of Irreversible Couples

Irreversible couples exhibit one or more of the following characteristics: reduced current intensity, broad voltammetric waves, and in the case of cyclic voltammetry, large peak-to-peak splittings, relative to rigorously reversible couples. While less reliable than reversible couples, the pH-dependence of irreversible couples may follow Nernstian behavior over limited pH ranges. For example, peak cathodic or peak anodic potentials will vary by $0.059(m/n)$ V/pH-unit for an *n*-electron/*m*-proton redox process, if the peak potentials remain proportional to the thermodynamic potentials. When using peak potentials to study pH-dependent redox processes, it is important to monitor the shape of the voltammetric wave, as reflected in the peak-to-peak splittings and/or peak widths. If the shape of the voltammogram changes as a function of pH, the varying differences between the measured peak potentials and underlying thermodynamic potentials will be manifested in the slope of the pH-potential diagram. For this reason, peak potentials should only be used if meaningful half-wave potentials cannot be measured over the pH range of interest, and their pH-dependence should be interpreted with great caution.

2.16.4 COORDINATION COMPLEXES EXHIBITING pH-DEPENDENT REDUCTION POTENTIALS

2.16.4.1 Metal-aquo/Hydroxide/Oxo Systems

While pH-potential diagrams have been used for decades to describe the complex redox chemistry of the transition metals, lanthanides, and actinides,[3,13] Meyer's seminal work on the catalytic oxidation of organic compounds by polypyridyl ruthenium-oxo complexes drew considerable attention to the use of pH-dependent redox potentials to elucidate the oxidation-reduction mechanisms of simple metal–aquo complexes.[24–27] The ruthenium(II)–aquo complexes undergo reversible two-electron/two-proton oxidations to give ruthenium(IV)–oxo complexes capable of a variety of oxidative transformations, regenerating the ruthenium(II)–aquo complex. Using cyclic voltammetry to measure half-wave potentials as a function of pH, Meyer showed that even simple monoaquo ruthenium complexes undergo a range of redox processes. For example, the complex $[(tpy)(bpy)Ru^{II}(OH_2)]^{2+}$ exhibits four distinct mechanisms depending on the pH region:[28]

(i) at low pH, a pH-independent $Ru^{III/II}$ couple was followed by a 2-proton/1-electron couple;

$$[(tpy)(bpy)Ru^{II}OH_2]^{2+} \rightarrow [(tpy)(bpy)Ru^{III}OH_2]^{3+} + e^- \quad (9)$$

$$[(tpy)(bpy)Ru^{III}OH_2]^{3+} \rightarrow [(tpy)(bpy)Ru^{IV}O]^{2+} + 2H^+ + e^- \quad (10)$$

(ii) at intermediate pH, two closely spaced 1-proton/1-electron couples;

$$[(tpy)(bpy)Ru^{II}OH_2]^{2+} \rightarrow [(tpy)(bpy)Ru^{III}OH]^{2+} + H^+ + e^- \quad (11)$$

$$[(tpy)(bpy)Ru^{III}OH]^{2+} \rightarrow [(tpy)(bpy)Ru^{IV}O]^{2+} + H^+ + e^- \quad (12)$$

(iii) at somewhat higher pH, a pH-independent $Ru^{III/II}$ couple was followed by a 1-proton/1-electron couple;

$$[(tpy)(bpy)Ru^{II}OH]^{+} \rightarrow [(tpy)(bpy)Ru^{III}OH]^{2+} + e^- \quad (13)$$

$$[(tpy)(bpy)Ru^{III}OH]^{2+} \rightarrow [(tpy)(bpy)Ru^{IV}O]^{2+} + H^+ + e^- \quad (14)$$

(iv) at high pH, a single 1-proton/2-electron couple;

$$[(tpy)(bpy)Ru^{II}OH]^{+} \rightarrow [(tpy)(bpy)Ru^{IV}O]^{2+} + H^+ + 2e^- \quad (15)$$

These mechanisms are reflected in the pH-dependence of the redox potentials in Figure 3. This approach has been used to elucidate the redox mechanisms of a wide variety of ruthenium–aquo complexes,[29–34] as well as aquo complexes of other metals.[35,36]

2.16.4.2 Oxo-bridged Metal Systems

Oxo-bridged metal complexes can be considered an extension of metal–aquo/hydroxo/oxo systems, and in fact these species often interconvert in the redox reactions of aqueous metal ions; however, the pH-dependent reduction potentials of oxo-bridged complexes have enjoyed a special distinction because of their relevance to the proposed mechanisms for the oxidation of water by a tetramanganese oxo cluster in photosystem II.[37] Thorp and co-workers[38–40] characterized the pH-dependent redox mechanisms of mixed-valence manganese oxo-bridged complexes such as $[(NN)_2Mn^{III}(O)_2Mn^{IV}(NN)_2]^{3+}$, where NN represents bpy[38] or phen.[39] This family of complexes

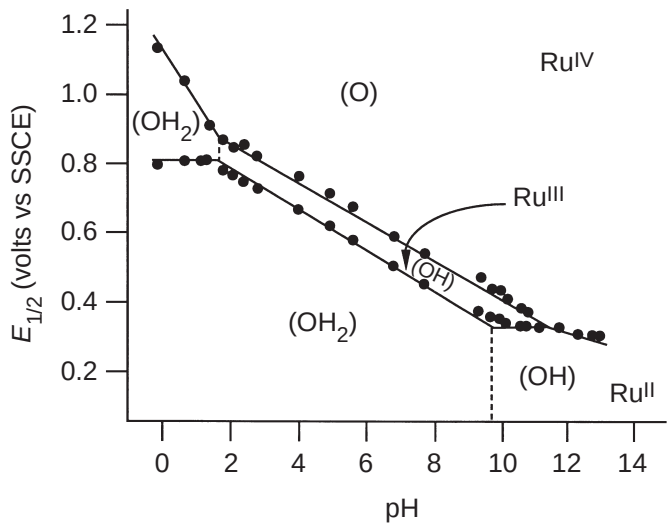

Figure 3 A pH-potential diagram for $[(tpy)(bpy)Ru^{II}(OH_2)]^{2+}$ (adapted from reference 28).

exhibits a one-electron/one-proton couple involving the $(Mn^{III})_2$ complex with a bridging oxo and bridging hydroxo (Equation (16)).

$$[(NN)_2Mn^{III}(O)_2Mn^{IV}(NN)_2]^{3+} + H^+ + e^- \rightarrow [(NN)_2Mn^{III}(O)(OH)Mn^{III}(NN)_2]^{3+} \quad (16)$$

A second reversible one-electron/one-proton couple was reported for the phen complex (Equation (17)).

$$[(phen)_2Mn^{III}(O)(OH)Mn^{III}(phen)_2]^{3+} + H^+ + e^- \rightarrow [(phen)_2Mn^{III}(OH)_2Mn^{II}(phen)_2]^{3+} \quad (17)$$

Analogous complexes involving other ancillary ligand systems have also been investigated.[40,41]

2.16.4.3 Metal–Oxime Systems

Oxime–metal complexes may show pH-dependent redox potentials as indicated in Equation (18). Chakravorty extensively investigated the redox reactions of nickel(II) and iron(II) complexes of linear hexadentate ligands with terminal oxime groups, with the majority of this work focusing on the complex $[Ni^{II}(Me_2LH_2)]^{2+}$ shown in Figure 4.[42–46] At $pH < 5$, a single reversible wave is observed by cyclic voltammetry, assigned as the two-electron/two-proton $Ni^{VI/II}$ couple based on the small peak-to-peak splitting of the wave ($\Delta E_p = 30$–40 mV) and constant-potential coulometry (Equation (19)).

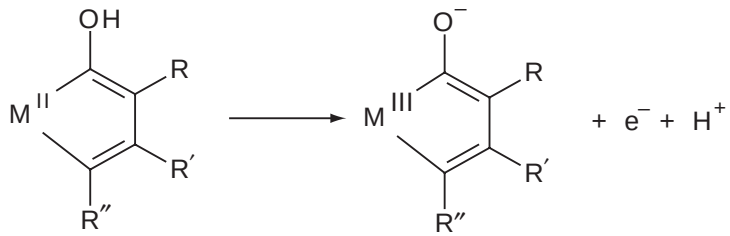

(18)

$$[Ni^{II}(Me_2LH_2)]^{2+} \rightarrow [Ni^{IV}(Me_2L)]^{2+} + 2H^+ + 2e^- \quad (19)$$

As the pH is increased beyond 5, ΔE_p increases, and by pH 6 two distinct couples are observed. The first couple is pH dependent up to pH 8.5, and the second couple is pH independent, consistent with Equations (20) and (21), respectively.

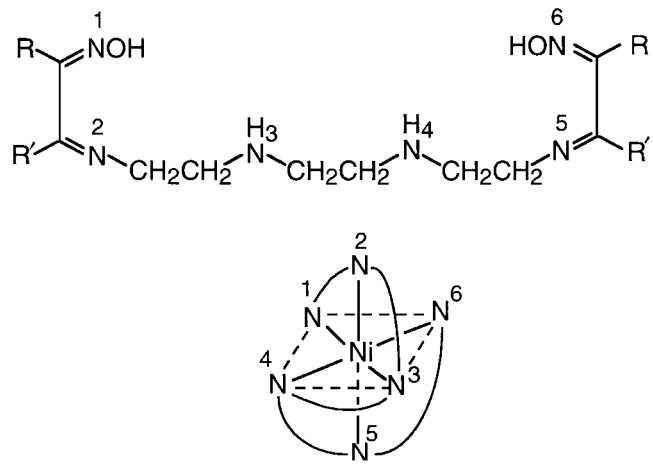

Figure 4 Structure of H_2Me_2L and its Ni^{II} complex (adapted from reference 42).

$$[Ni^{II}(Me_2LH_2)]^{2+} \rightarrow [Ni^{III}(Me_2L)]^{+} + 2H^{+} + e^{-} \quad (20)$$

$$[Ni^{III}(Me_2L)]^{+} \rightarrow [Ni^{VI}(Me_2L)]^{2+} + e^{-} \quad (21)$$

Above pH 8.5 the first couple also becomes pH independent (Equation (22)) due to deprotonation of the initial Ni^{II} complex at high pH.

$$Ni^{II}(Me_2L) \rightarrow [Ni^{III}(Me_2L)]^{+} + e^{-} \quad (22)$$

The redox behavior is simplified for the iron(II) complexes since the iron(IV) state is not accessible in these complexes; however, the presence of two ionizable protons leads to different mechanisms in different pH regions.[44] Other linear multi-dentate oxime ligand systems have been investigated, exhibiting analogous pH-dependence for the accessible potentials.[47,48]

Ruthenium complexes based on simple oxime ligands such as hydroxamates[49] and dimethylglyoxime[50] also give pH-dependent $Ru^{III/II}$ and $Ru^{IV/III}$ couples consistent with different combinations of coupled electron and proton transfers, depending on the pH region. Cyclic voltammetry of bis(dimethylglyoxime)copper(II), $Cu^{II}(DMGH)_2$, was also reported to exhibit a $Cu^{III/II}$ couple, which varies with pH by 59 mV/pH unit, in the range pH 4.1–8.5; however, it is not clear if the pH-dependence arises from deprotonation of an oxime group, or deprotonation of an axial H_2O which coordinates in aqueous solution (i.e., from $Cu^{II}(DMGH)_2(H_2O)$).[51]

2.16.4.4 Metal–Amine Systems

It is conceivable that metal–amine complexes would exhibit chemically and electrochemically reversible pH-dependent couples analogous to those observed for metal–aquo systems, such as the generalized one-electron/one-proton couples shown in Equations (23)–(25).

$$[M^{n+}NH_3]^{n+} \rightarrow [M^{(n+1)+}NH_2]^{n+} + H^{+} + e^{-} \quad (23)$$

$$[M^{(n+1)+}NH_2]^{n+} \rightarrow [M^{(n+2)+}{=}NH]^{n+} + H^{+} + e^{-} \quad (24)$$

$$[M^{(n+2)+}{=}NH]^{n+} \rightarrow [M^{(n+3)+}{\equiv}N]^{n+} + H^{+} + e^{-} \quad (25)$$

In practice, however, reversible pH-dependent couples based on metal–amine complexes are rare. For example, cyclic voltammograms of the complexes $[(tpy)(bpy)M(NH_3)]^{2+}$ (M = Ru, Os) show reversible $M^{III/II}$ couples at low pH, but as the pH is increased, multiple irreversible pH-dependent oxidations occur in which the coordinated ammine is oxidized, ultimately to nitrite or nitrate.[52–54] This behavior is in stark contrast to the analogous aquo complexes discussed earlier, where no such ligand-localized oxidations are possible.

$[Cl_2Os^{III}(NH_2CMe_2CMe_2NH_2)_2]^{+}$ does exhibit a reversible pH-dependent $Os^{IV/III}$ couple over the pH range of 1–5 with a slope of −60 mV/pH, consistent with a one-electron/one-proton process involving deprotonation of the coordinated ammine upon oxidation of osmium(III).[55] In contrast, *trans*-$[Cl_2Os^{III}(NH_3)_4]^{+}$ does not display pH-dependent potentials. The authors suggest that the bidentate 2,3-diamino-2,3-dimethylbutane ligand stabilizes the high-valent osmium(IV) center relative to simple amine ligands due to the chelate effect and/or better π donation, but apparently no effort was made to relate this explanation to the pK_a values for the coordinated ligands. The complex $[(bpy)_2Ru^{II}(NH_2CMe_2CMe_2NH_2)]^{2+}$ undergoes a reversible three-electron/three-proton oxidation, followed by an irreversible one-electron/one-proton oxidation.[56] The reversible couple shifts cathodically by ~60 mV/pH unit over the pH range 1–3 (as does the irreversible peak potential from pH 1 to 2), consistent with redox couples involving equal numbers of protons and electrons.

2.16.4.5 Metal *N*-heterocycle Systems

There are numerous examples of electrochemically reversible pH-dependent couples based on metal complexes of aromatic *N*-heterocycles.[13,17,57–61] Haga has extensively investigated the redox reactions of $[(bpy)_2M^{II}(bibzimH_2)]^{2+}$,[17] (M = Ru, Os; $bibzimH_2$ is 2,2′-bibenzimidazole) in 1:1

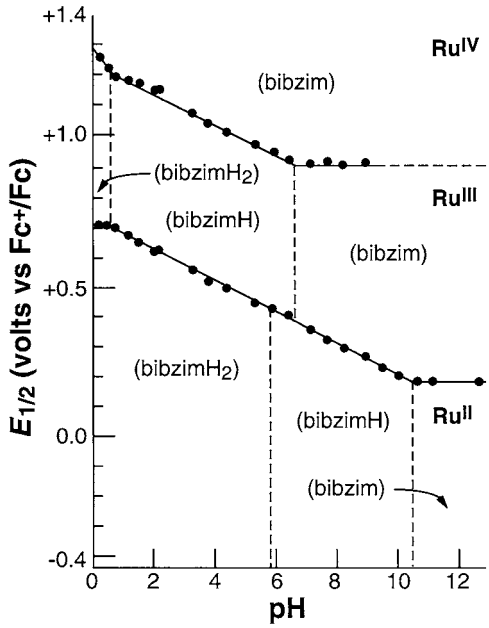

Figure 5 A pH-potential diagram for $[(bpy)_2Ru^{II}(bibzimH_2)]^{2+}$ in 1:1 v/v CH_3CN/buffer (adapted from reference 17).

acetonitrile/water over the effective pH range 0–11. The $M^{IV/III}$ couple is irreversible; however, it becomes reversible at fast scan rates ($5\,V\,s^{-1}$). The pH-potential diagram for $[(bpy)_2Ru^{II}(bibzimH_2)]^{2+}$ obtained from these data (Figure 5) is qualitatively very similar to the pH-potential diagrams for Ru^{II}–monoaquo complexes (Figure 3) which is understandable given that both complexes contain two ionizable protons.

The redox reactions of metal-phthalocyanines, [M{Pc(2-)}], illustrate the difficulty in assigning pH-dependent potentials when the complex contains multiple acid/base sites.[62–64] The phthalocyanine ligand contains four basic sp^2 nitrogen sites on the macrocycle, in addition to the four pyrolic nitrogens that coordinate to the metal, plus water molecules may coordinate at the axial positions on the metal. The low solubility of most metal-phthalocyanines in aqueous media requires that the pH-dependent electrochemical measurements be carried out on complexes immobilized on pyrolytic graphite electrodes, which may occupy one of the axial sites, depending on the mode of adsorption. The metal-localized and ligand-localized pH-dependent couples (roughly 60 mV/pH unit) observed for cobalt- and iron-phthalocyanines were tentatively assigned as electron transfer coupled to interconversion of coordinated aquo/hydroxide ligands (Equation (26)) and protonation of the phthalocyanine ligand (Equation (27)), respectively.

$$[(HO)M^{III}\{Pc(2-)\}] + H_2O + e^- \rightarrow [(H_2O)M^{II}\{Pc(2-)\}] + OH^- \quad (26)$$

$$[M^{I}\{Pc(2-)\}]^- + H_2O + e^- \rightarrow [M^{I}\{Pc(3-)H^+\}]^- + OH^- \quad (27)$$

The above reactions are written assuming basic conditions, since the surface-immobilized metal-phthalocyanines exhibited the best pH-dependent electrochemical behavior at high pH. These studies were further complicated by the irreversibility of some of the couples and the narrow voltammetric waves associated with surface-bound redox species.[65]

2.16.5 pH-DEPENDENT REDUCTION POTENTIALS IN BIOLOGICAL SYSTEMS

Proton-coupled electron transfer (PCET)[1,37,66] is known to play an important role in a variety of biological processes, including microbial iron transport by ferric enterobactin,[67] enzyme catalysis in systems such as fumarate reductase[68] and nitrate reducatase,[69] and dioxygen binding by the non-heme iron protein hemerythrin.[70] As such, pH-dependent electrochemical studies can play an important role in unraveling these mechanisms. The most heavily studied biological system known to involve PCET is cytochrome *c* oxidase, the terminal electron-transfer complex of the mitochondrial respiratory chain, which catalyzes the reduction of molecular oxygen to water.[71–78]

By consuming four protons from the interior of the mitochondrion and four electrons from the exterior, a proton–electrochemical potential gradient is formed across the membrane, providing fuel for ATP synthesis and other processes. This process is commonly referred to as proton pumping.

The earliest electrochemical studies of biological systems conducted with simple metal electrodes were not especially meaningful, yielding only irreversible behavior due to poor electron transfer between the metal center and the electrode, and passivation of the electrode caused by aggregation or denaturation of the biological species. Thus, early studies made use of indirect methods involving mediators to aid in electron transfer between the electrode and redox species. Kuwana and Hawkridge utilized potassium ferricyanide in coulometric titration of heme proteins as illustrated in Equations (28) and (29).[79]

$$[Fe^{II}(CN)_6]^{4-} \rightarrow [Fe^{III}(CN)_6]^{3-} + e^- \tag{28}$$

$$[Fe^{III}(CN)_6]^{3-} + \text{Cyto } c_{(Red)} \rightarrow [Fe^{II}(CN)_6]^{4-} + \text{Cyto } c_{(Ox)} \tag{29}$$

These methods allowed extraction of thermodynamic information but were only mildly useful in acquisition of kinetic data. Since the early 1970s, advances in the application of dynamic electrochemistry, also known as direct electrochemistry or bioelectrochemistry, have provided a simple yet powerful tool to aid in the elucidation of mechanisms involving electron transfer in biological systems.[80]

The work of Hill[81] and of Kuwana[82] and their co-workers in the late 1970s provided the first examples of reversible behavior for a heme protein. Kuwana achieved this behavior using a tin-doped indium oxide electrode, while Hill utilized gold electrodes modified with 4,4′-bipyridine, a strategy analogous to activation of a carbon surface to create functionalized sites for interaction with solution couples. Studies such as these created the groundwork for rapid advances in the application of direct electrochemical techniques towards understanding biological mechanisms.

Most recent work in this field has involved immobilization of the protein or enzyme species near the electrode surface.[83,84] Often referred to as protein-film voltammetry (PFV), this method achieves up to monolayer coverage on an electrode surface, which is usually modified to optimize interaction and stability. The three commonly used techniques for protein immobilization are: (i) adsorption at self-assembled monolayers (SAMs) prepared on gold surfaces using functionalized alkane thiolates;[85] (ii) integration into lipid bilayer membranes;[86,87] and (iii) adsorption onto pyrolytic graphite edge electrodes.[88] Monolayers are prepared by both self-assembly and LB techniques.[89] Armstrong and co-workers used PFV to probe interfacial electron-transfer kinetics, coupled chemical equilibria in labile centers, kinetics of gated electron transfer reactions, and the organization of catalytic electron transfer in iron–sulfur clusters found in various ferredoxins.[88]

Of the advantages protein-film voltammetry holds over static electrochemistry and conventional voltammetry applied to biological systems, preservation of the native structure is perhaps the most important. Additionally, at a monolayer coverage of between 10^{-11} and 10^{-12} mol cm^{-2}, only minute amounts of the commonly scarce samples are required. The resulting low Faradaic currents are easily viewed due to the excellent voltammetric response observed for surface-confined redox couples. By minimizing the distance between the electrode and redox-active species and by eliminating slow diffusion control, PFV achieves extremely facile electron exchange at the electrode. Rapid electron transfer at the electrode, in turn, allows for the use of very fast scan rates in the region of 500–1,000 Vs^{-1}, which reduces the time resolution to below 1 ms. This resolution enables the detection of transient species and measurement of coupled kinetics for the determination of rate limiting (gating) reactions.

Perhaps the greatest obstacle impeding the advancement of PFV revolves around the ability to construct and understand the monolayer films. Further development of techniques involving protein or enzyme immobilization at the electrode might be greatly assisted by insight into the nature of how the molecules are adsorbed and arranged onto the surface. Applications of techniques such as scanning probe microscopy and optical spectroscopy have already been used to assist in the interpretation of these films.[89,90]

2.16.6 REFERENCES

1. Slattery, S. J.; Blaho, J. K.; Lehnes, J.; Goldsby, K. A. *Coord. Chem. Rev.* **1998**, *174*, 391–416.
2. Stumm, W.; Morgan, J. J. *Aquatic Chemistry*, 2nd ed.; **1981**, Wiley: New York, Chapter 7.

3. Pourbaix, M. *Atlas of Electrochemical Equilibria in Aqueous Solution*, 2nd ed.; (English translation by J. A. Franklin); National Association of Corrosion Engineers: Houston, 1974.
4. Campbell, J. A.; Whitaker, R. A. *J. Chem. Ed.* **1969**, *46*, 90–92.
5. Wulfsberg, G. *Principles of Descriptive Inorganic Chemistry* **1987**, 146–153. Brooks/Cole Publishing: Monterey, CA.
6. Barnum, D. W. *J. Chem. Ed.* **1982**, *59*, 809–812 and references cited therein.
7. Douglas, B.; McDaniel, D. H.; Alexander, J. J. *Concepts and Models of Inorganic Chemistry*, 3rd ed.; Wiley: New York, 1994; pp 363–366.
8. Angus, J. C.; Lu, B.; Zappia, M. J. *J. Appl. Electrochem.* **1987**, *17*, 1–21.
9. Inaba, H.; Kimura, M.; Yokokawa, H. *Corros. Sci.* **1996**, *38*, 1449–1461 and references cited therein.
10. Brookins, D. G. *Eh-pH Diagrams for Geochemistry* **1988**, Springer-Verlag: New York.
11. Tamilmani, S.; Huang, W.; Raghavan, S.; Small, R. *J. Electrochem. Soc.* **2002**, *149*, G638–G642.
12. Blaho, J. K.; Goldsby, K. A. *J. Am. Chem. Soc.* **1990**, *112*, 6132–6133.
13. Rocha, R. C.; Rein, F. N.; Toma, H. E. *J. Braz. Chem. Soc.* **2001**, *12*, 234–242.
14. Gosser, D. K., Jr. *Cyclic Voltammetry Simulation and Analysis of Reaction Mechanisms* **1993**, 59–60. VCH: New York.
15. Bard, A. J.; Faulkner, L. R. *Electrochemical Methods: Fundamentals and Applications* **1980**, 24. Wiley: New York.
16. Perrin, D. D.; Dempsey, B. *Buffers for pH and Metal Ion Control* **1974**, Wiley: New York.
17. Bond, A.; Haga, M. *Inorg. Chem.* **1986**, *25*, 4507–4514.
18. Ghosh, P.; Chakravorty, A. *J. Chem. Soc., Dalton Trans.* **1985**, 361–367.
19. Eyring, E. M.; Marshall, D. B.; Strohbusch, F.; Suttinger, R. In *Mechanistic Aspects of Inorganic Reations*; Rorabacher, D. B.; Endicott, J. F., Eds.; American Chemical Society: Washington, DC, 1982; ACS Symposium Series 198, pp 63–80.
20. Engstrom, R. C. *Anal. Chem.* **1982**, *54*, 2310–2314.
21. Cabaniss, G. E.; Diamantis, A. A.; Murphy, W. R., Jr.; Linton, R. W.; Meyer, T. J. *J. Am. Chem. Soc.* **1985**, *107*, 1845–1853.
22. Thorp, H. H.; Brudvig, G. W.; Bowden, E. F. *J. Electroanal. Chem.* **1990**, *290*, 293–301.
23. Deakin, M. R.; Stutts, K. J.; Wightman, R. M. *J. Electroanal. Chem.* **1985**, *182*, 113–122.
24. Moyer, B. A.; Meyer, T. J. *Inorg. Chem.* **1981**, *20*, 436–444.
25. Moyer, B. A.; Meyer, T. J. *J. Am. Chem. Soc.* **1978**, *100*, 3601–3603.
26. Moyer, B. A.; Thompson, M. S.; Meyer, T. J. *J. Am. Chem. Soc.* **1980**, *102*, 2310–2312.
27. Meyer, Thomas, J. *J. Electrochem. Soc.* **1984**, *131*, 221C–227C and references cited therein.
28. Takeuchi, K. J.; Thompson, M. S.; Pipes, D. W.; Meyer, T. J. *Inorg. Chem.* **1984**, *23*, 1845–1851.
29. Dobson, J. C.; Meyer, T. J. *Inorg. Chem.* **1988**, *27*, 3283–3291.
30. Adeyemi, S. A.; Dovletoglou, A.; Guadalupe, A. R.; Meyer, T. J. *Inorg. Chem.* **1992**, *31*, 1375–1383.
31. Llobet, A.; Doppelt, P.; Meyer, T. J. *Inorg. Chem.* **1988**, *27*, 514–520.
32. Marmion, M. E.; Takeuchi, K. J. *J. Am. Chem. Soc.* **1988**, *110*, 1472–1480.
33. Ho, C.; Che, C.-M.; Lay, T.-C. *J. Chem. Soc., Dalton Trans.* **1990**, 967–970.
34. Che, C.-M.; Lau, K.; Lau, T.-C.; Poon, C.-K. *J. Am. Chem. Soc.* **1990**, *112*, 5176–5181.
35. Ram, M. S.; Skeens-Jones, L. M.; Johnson, C. S.; Zhang, X. L.; Stern, C.; Yoon, D. I.; Selmarten, D.; Hupp, J. T. *J. Am. Chem. Soc.* **1995**, *117*, 1411–1421, and references cited therein.
36. Allan, A. E.; Lappin, A. G.; Laranjeira, M. C. M. *Inorg. Chem.* **1984**, *23*, 477–482.
37. Manchanda, R.; Brudvig, G. W.; Crabtree, R. H. *Coord. Chem. Rev.* **1995**, *144*, 1–38.
38. Thorp, H. H.; Sarneski, J. E.; Brudvig, G. W.; Crabtree, R. H. *J. Am. Chem. Soc.* **1989**, *111*, 9249–9250.
39. Manchanda, R.; Thorp, H. H.; Brudvig, G. W.; Crabtree, R. H. *Inorg. Chem.* **1992**, *31*, 4040–4041.
40. Manchanda, R.; Thorp, H. H.; Brudvig, G. W.; Crabtree, R. H. *Inorg. Chem.* **1991**, *30*, 494–497.
41. Hage, R.; Krijnen, B.; Warnaar, J. B.; Hartl, F. Stufkens D. J.; Snoeck, T. L. *Inorg. Chem.* **1995**, *34*, 4973–4978.
42. Mohanty, J. G.; Chakravorty, A. *Inorg. Chem.* **1976**, *15*, 2912–2916.
43. Mohanty, J. G.; Singh, R. P.; Singh, A. N.; Chakravorty, A. *J. Indian Chem. Soc.* **1977**, *LIV*, 219–224.
44. Mohanty, J. G.; Chakravorty, A. *Inorg. Chem.* **1977**, *16*, 1561–1563.
45. Singh, A. N.; Singh, R. P.; Mohanty, J. G.; Chakravorty, A. *Inorg. Chem.* **1977**, *16*, 2597–2601.
46. Singh, A. N.; Chakravorty, A. *Inorg. Chem.* **1980**, *19*, 969–971.
47. Lappin, A. G.; Laranjeira, M. C. M. *J. Chem. Soc., Dalton Trans* **1982**, 1861–1865.
48. Levy, N. M.; Laranjeira, M. C.; Neves, A.; Franco, C. V. *J. Coord. Chem.* **1996**, *38*, 259–270.
49. Ghosh, P.; Chakravorty, A. *Inorg. Chem.* **1984**, *23*, 2242–2248.
50. Bell-Loncella, E. T.; Bessel, C. A. *Inorg. Chem. Acta* **2000**, *303*, 199–205.
51. Sulfab, Y. *Polyhedron* **1989**, *8*, 2409–2413.
52. Thompson, M. S.; Meyer, T. J. *J. Am. Chem. Soc.* **1981**, *103*, 5577–5579.
53. Murphy, W. R., Jr.; Takeuchi, K. J.; Meyer, T. J. *J. Am. Chem. Soc.* **1982**, *104*, 5817–5819.
54. Murphy, W. R., Jr.; Takeuchi, K.; Barley, M. H.; Meyer, T. J. *Inorg. Chem.* **1986**, *25*, 1041–1053.
55. Chin, K.-F.; Wong, K.-Y.; Che, C.-M. *J. Chem. Soc., Dalton Trans.* **1993**, 197–198.
56. Wong, K.-Y.; Che, C.-M.; Li, C.-K.; Chiu, W.-H.; Zhou, Z.-Y.; Mak, T. C. W. *J. Chem. Soc., Chem Commun.* **1992**, 754–756.
57. Rillema, D. P.; Sahai, R.; Matthews, P.; Edwards, A. K.; Shaver, R. J. *Inorg. Chem.* **1990**, *29*, 167–175.
58. Haga, M.; Ano, T.; Kano, K.; Yamabe, S. *Inorg. Chem.* **1991**, *30*, 3843–3849.
59. Haga, M.; Ali, M.; Maegawa, H.; Nozaki, K.; Yoshimura, A.; Ohno, T. *Coord. Chem. Rev.* **1994**, *132*, 99–104.
60. Xiaoming, X.; Haga, M.; Matsumura-Inoue, T.; Ru, T.; Addison, A. W.; Kano, K. *J. Chem. Soc., Dalton Trans.* **1993**, 2477–2484.
61. Ayers, T.; Caylor, N.; Ayers, G.; Godwin, C.; Hathcock, D. J.; Stuman, V.; Slattery, S. J. *Inorg. Chem. Acta* **2002**, 33–38.
62. Zecevic, S.; Simic-Glavaski, B.; Yeager, E.; Lever, A. B. P.; Minor, P. C. *J. Electroanal. Chem.* **1985**, *196*, 339–358.
63. Golovin, M. N.; Seymour, P.; Jayaraj, K.; Fu, Y.; Lever, A. B. P. *Inorg. Chem.* **1990**, *29*, 1719–1727, and references cited therein.
64. Lever, A. B. P. *J. Porphyrins Phthalocyanines* **1999**, *3*, 488–499.
65. Finklea, H. O. In *Electroanalytical Chemistry: A Series of Advances*; Bard, A. J.; Rubenstein, I., Eds.; Marcel Dekker: New York, 1996; Vol. 19, pp 109–335.

66. Thorp, H. H. *Chemtracts – Inorganic Chemistry* **1991**, *3*, 171–184.
67. Lee, C.-W.; Ecker, D. J.; Raymond, K. N. *J. Am. Chem. Soc.* **1985**, *107*, 6920–6923.
68. Kinnaer, K. T.; Monbouquette, H. G. *Langmuir* **1993**, *9*, 2255–2257.
69. De Vries, W.; Niekus, H. G. D.; Van Berchum, H.; Stouthamer, A. H. *Arch. Microbiol.* **1982**, *131*, 132–139.
70. Brunold, T. C.; Solomon, E. I. *J. Am. Chem. Soc.* **1999**, *121*, 8288–8295.
71. Gelles, J.; Blair, D. F.; Chan, S. I. *Biochim. Biophys. Acta* **1986**, *853*, 205–236.
72. Blair, D. F.; Gelles, J.; Chan, S. I. *Biophys. J.* **1986**, *50*, 713–733.
73. Thornstrom, P.-E.; Brzezinski, P.; Fredriksson, P.-O.; Malmstrom, B. G. *Biochemistry* **1988**, *27*, 5441–5447.
74. Malmstrom, B. G. *Chem. Scr.* **1987**, *27B*, 67–72.
75. Nilsson, T.; Gelles, J.; Li, P. M.; Chan, S. I. *Biochemistry* **1988**, *27*, 296–301.
76. Ellis, W. R., Jr.; Wang, H.; Blair, D. F.; Gray, H. B.; Chan, S. I. *Biochemistry* **1986**, *25*, 161–167.
77. Moroney, P. M.; Scholes, T. A.; Hinkle, P. C. *Biochemistry* **1984**, *23*, 4991–4997.
78. Zaslavsky, D.; Gennis, R. B. *Biochim. Biophys. Acta* **2000**, *1458*, 164–179.
79. Hawkridge, F. M.; Kuwana, T. *Anal. Chem.* **1973**, *45*, 1021–1027.
80. Kievit, O.; Grudvig, G. W. *J. Electroanal. Chem.* **2001**, *497*, 139–149 and references cited therein.
81. Eddowes, M. J.; Hill, H. A. O. *J. Am. Chem. Soc.* **1979**, *101*, 4461–4464.
82. Yeh, P.; Kuwana, T. *Chem. Lett.* **1977**, 1145–1148.
83. Armstrong, F. A. *Biochem. Soc. Trans.* **1999**, *27*, 206–210.
84. Hill, H. A. O. *Coord. Chem. Rev.* **1996**, *151*, 115–123.
85. El Kasmi, A.; Wallace, J. M.; Bowden, E. F.; Binet, S. M.; Linderman, R. J. *J. Am. Chem. Soc.* **1998**, *120*, 225–226.
86. Kong, J.; Lu, Z.; Lvov, Y. M.; Desamero, R. Z. B.; Frank, H. A.; Rusling, J. F. *J. Am Chem. Soc.* **1998**, *120*, 7371–7372.
87. Burgess, J. D.; Rhoten, M. C.; Hawkridge, F. M. *Langmuir* **1998**, *14*, 2467–2475.
88. Armstrong, F. A.; Heering, H. A.; Hirst, J. *Chem. Soc. Rev.* **1997**, *26*, 169–179.
89. Haas, A. S.; Pilloud, D. L.; Reddy, K. S.; Babcock, G. T.; Moser, C. C.; Blasie, J. K.; Dutton, P. L. *J. Phys. Chem. B* **2001**, *105*, 11351–11362.
90. Davis, J. J.; Hill, H. A. O.; Bond, A. M. *Coord. Chem. Rev.* **2000**, *200*, 411–442.

Comprehensive Coordination Chemistry II
ISBN (set): 0-08-0437486

Volume 2, (ISBN 0-08-0443249); pp 223–234

2.17 Electrochemistry: Mixed Valence Systems

R. J. CRUTCHLEY
Carleton University, Ottawa, ON, Canada

2.17.1 INTRODUCTION 235
2.17.2 THE COMPROPORTIONATION EQUILIBRIUM AND METAL–METAL COUPLING 237
2.17.3 EVALUATION OF REDOX COUPLES IN THE WEAK COUPLING CASE 238
2.17.4 REDOX COUPLES OF MIXED-VALENCE METALLO–OLIGOMERS AND DENDRIMERS 239
2.17.5 SPECTROELECTROCHEMISTRY 240
2.17.6 SELECTED STUDIES 241
2.17.7 REFERENCES 243

2.17.1 INTRODUCTION

Electrochemistry plays a key role in evaluating the properties of mixed-valence complexes. Not only can information concerning the resonance stabilization of the mixed-valence state be derived but intervalence transitions IT (or metal–metal charge transfer bands) can be identified through spectroelectrochemical methods. In addition, the extent of delocalization in a mixed-valence complex can be ascertained from a comparison of spectra in oxidized and reduced forms. While a detailed discussion of mixed-valence complexes appears in Chapter 2.61, an introduction with an emphasis on those parameters that can be probed by electrochemical methods is appropriate here.

A mixed-valence complex will fall into one of three categories, as proposed by Robin and Day,[1] depending upon the degree of coupling between the metal centers. Completely valence-trapped complexes (no coupling between the metal centers) are termed class I while complexes in which the valence electrons are fully delocalized (very strong coupling between the metal centers) are termed class III. All complexes whose behavior falls between these extremes constitute class II. The potential energy curves in Figure 1 illustrate the symmetric class I, class II and class III cases where E_{IT}, H, and ΔG_{th} are the intervalence band energy, metal–metal coupling element and the class I thermal electron transfer barrier, respectively.

Hush[2] applied Mulliken's theories[3] of the transition dipole moment of charge transfer bands to the specific question of IT bands in mixed-valence complexes. By equating theoretical and experimental expressions for f, where f is the oscillator strength of the intervalence band, it is possible to derive an expression for metal–metal coupling (H_{ad}),

$$H_{ad} = \frac{2.06 \times 10^{-2}}{r}\left(\varepsilon_{max}\Delta\nu_{1/2}E_{IT}\right)^{1/2} \quad (1)$$

In Equation (1), H_{ad} is the donor–acceptor coupling element, r the transition moment length (typically taken as the donor–acceptor separation in Å), and ε_{max}, $\Delta\nu_{1/2}$, and E_{IT}, are the molar absorptivity ($M^{-1}cm^{-1}$), bandwidth at half height (cm^{-1}), and energy at band maximum (cm^{-1}),

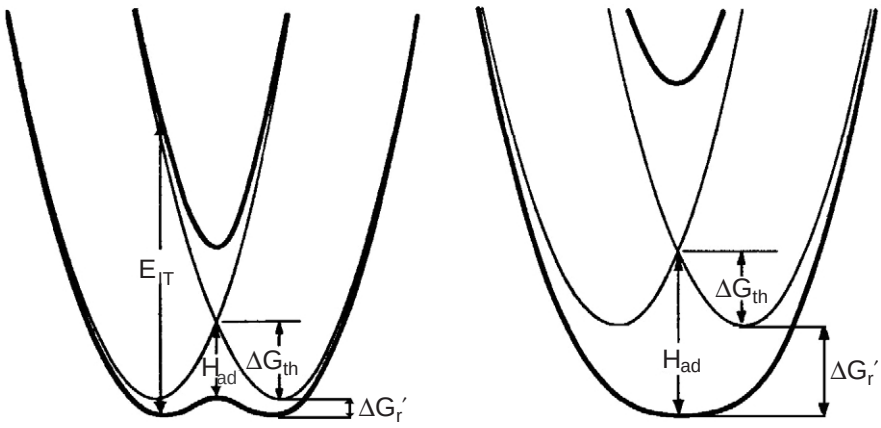

(a) (b)

Figure 1 Potential energy curves for class I (light line in both (a) and (b)), class II (a) and class III (b) symmetric mixed-valence complexes.

respectively, of the IT band. In addition, the bandwidth may be predicted by $\Delta\nu_{1/2} = (2310E_{IT})^{1/2}$. Creutz, Newton, and Sutin (CNS) have shown[4] that Equation 1 can be used to calculate metal–ligand coupling elements for any donor–acceptor system provided overlap may be neglected and the charge transfer transition dipole moment lies along the donor–acceptor bonding axis:

For a class III system (Figure 1b), the value of H_{ad} is given simply by

$$H_{ad} = \frac{E_{IT}}{2} \tag{2}$$

The intervalence transition for a class III complex involves a ground state in which the electron is delocalized and an excited state which is valence trapped.

For class II and III, metal–metal coupling causes stabilization of the mixed-valence complex relative to the uncoupled (or class I) case. This stabilization is termed the free energy of resonance exchange, $\Delta G_r'$. In the weak coupling case for symmetric systems (Figure 1a), it has been shown[5] that,

$$\Delta G_r' = \frac{H_{ad}{}^2}{E_{IT}} \tag{3}$$

whereas, for the strongly coupled class III systems (Figure 1b),

$$\Delta G_r' = H_{ad} - \Delta G_{th} \tag{4}$$

The thermal electron transfer barrier ΔG^* in class II cases depends upon the magnitude of metal–metal coupling and is given by[5]

$$\Delta G^* = \frac{\lambda}{4}\left(1 - \frac{2H_{ad}}{\lambda}\right)^2 \tag{5}$$

It should be clear that under conditions of very weak coupling, where $2H \ll \lambda$, $\Delta G^* \approx \Delta G_{th}$ and $E_{IT} \approx \lambda$. Thus, estimates of ΔG_{th} for a given metal ion and coordination sphere can be derived from the intervalence band energies. Equation (5) also gives the conditions for the boundary between class II and class III behavior, $2H_{ad} = \lambda$.

From Equations (3) and (4), it is possible to calculate the free energy of resonance exchange from intervalence band data. This value of $\Delta G_r'$ can be compared to an experimental value that is derived from electrochemical data and knowledge of the free energy factors that contribute to

the magnitude of the free energy of comproportionation. For moderate and strongly coupled systems a determination of the comproportionation equilibrium constant through electrochemical methods is straightforward. However, for weakly coupled systems or for overlapping couples in a mixed-valence oligomer, exact determination of redox couples poses significant challenges. These concerns and spectroelectrochemical methods will be discussed in the following sections.

2.17.2 THE COMPROPORTIONATION EQUILIBRIUM AND METAL–METAL COUPLING

Ruthenium mixed-valence complexes are ubiquitous in coordination chemistry. For this reason, the common oxidation states of ruthenium will be adopted in the following discussion of comproportionation constants.

The stability of a mixed-valence complex [III,II] relative to its oxidized and reduced forms can be quantified by the comproportionation equilibrium,

$$\left[Ru^{III}-Ru^{III}\right]+\left[Ru^{II}-Ru^{II}\right]\Leftrightarrow\left[Ru^{II}-Ru^{III}\right] \tag{6}$$

Equation (6) is simply the sum of the reduction and oxidation half-reactions of the oxidized and reduced forms of the complex and, thus, the comproportionation constant, K_c, may be determined from the difference between metal-centered redox couples, $\Delta E = E^{\circ}_{M2} - E^{\circ}_{M1}$, in volts, according to

$$K_c = 10^{16.91\Delta E} \tag{7}$$

Knowledge of K_c permits the calculation of the free energy of comproportionation ($\Delta G_c = -RT\ln(K_c)$), which is made up of the following free energy terms,[5]

$$\Delta G_c = \Delta G_s + \Delta G_e + \Delta G_i + \Delta G_r + \Delta G_{af} \tag{8}$$

where ΔG_s reflects the statistical distribution of the comproportionation equilibrium, ΔG_e accounts for the electrostatic repulsion of the two like-charged metal centers, ΔG_i is an inductive factor dealing with competitive coordination of the bridging ligand by the metal ions, ΔG_r is the free energy of resonance exchange, and ΔG_{af} is the free energy of antiferromagnetic exchange. Antiferromagnetic exchange stabilizes the [III,III] complex over its mixed-valence form and so ΔG_{af} has opposite sign compared to the other terms in Equation (8). A sixth term, ΔG_{st}, takes into account the possibility of structural factors that may increase the comproportionation equilibrium constant. It is not included in Equation (6) as it is rarely observed.[6] $\Delta G_r = 2\Delta G_r'$ (see Figure 1) because it is a measure of the resonance stabilization of two mixed-valence complexes (Equation (6)).

In systems where mixed-valence metal–metal coupling occurs through a superexchange pathway involving the bridging ligand's lowest unoccupied molecular orbital (LUMO), energetic mismatch of the ligand LUMO and the metal ion *d*-orbitals of the [III,III] complex should lead to a small or insignificant magnitude of ΔG_{af}. In systems involving superexchange via the bridging ligand's highest occupied molecular orbital (HOMO), the magnitude of ΔG_{af} may be such that ignoring this term would lead to misleadingly low estimates of free energy of resonance exchange. The comproportionation constant is sometimes taken as a measure of metal–metal coupling but as can be seen in Equation (3), resonance exchange in weakly coupled systems actually makes a very minor contribution to ΔG_c and hence K_c. However, when metal–metal coupling is very strong, the resonance exchange term ΔG_r largely determines the magnitude of ΔG_c.[7]

In a recent study, Evans *et al.* showed that it was possible to factor out ΔG_r from the comproportionation data of three families of similar mixed-valence complexes.[7] The value of ΔG_s may be calculated by recognizing that it stems directly from the statistical distribution of the comproportionation equilibrium, which implies $K_c = 4$ for a symmetrical system, and which relates to $\Delta G_s \approx 290\,cm^{-1}$. ΔG_e may be evaluated according to Equation (9) which assumes the medium in which the ionic metal centers are found can be treated as a dielectric continuum, and that there is a unit difference in ionic charge between the two centers.[8]

$$\Delta G_e = \frac{1.17\times10^{-5}}{\varepsilon R}(\text{in cm}^{-1}) \tag{9}$$

Here R is in angstroms and represents the separation of the metal centers and ε the solvent's static dielectric. The antiferromagnetic exchange term ΔG_{ex} may be estimated from room-temperature magnetic moments (Evans' method NMR experiments)[9] and the Van Vleck expression for magnetic susceptibility.[10] The inductive term ΔG_i was not calculated directly but estimated from the comproportionation constant of the mostly weakly coupled system where the resonance exchange and antiferromagnetic exchange terms are negligible. When the factored values of $\Delta G_r'$ were compared against those theoretically derived (Equation (3)), an excellent correlation was observed.

In an earlier study, Salaymeh *et al.*[11] suggested an electrochemical approach to assessing the degree of metal–metal coupling in mixed-valence complexes. The method follows a Mulliken formalism and suggests that there is a link between electrochemical potential shift data and the quantity $\rho = a/b$, the ratio of mixing coefficients of the ground and excited states resulting from the coupling of donor and acceptor wavefunctions,

$$\Psi_g = a\Psi_1^0(D, A) + b\Psi_2^0(D^+, A^-) \tag{10}$$

$$\Psi_e = a^*\Psi_2^0(D^+, A^-) + b^*\Psi_1^0(D, A) \tag{11}$$

The idea rests upon the assumption that the energy of either donor and acceptor wavefunction can be obtained independently by perturbing one end of a mixed-valence dimer through ligand substitution. In the limit of small overlap between donor and acceptor, the expression for ρ becomes,

$$\rho = \sqrt{n} \tag{12}$$

where n is related to the ratio of electrochemical shifts of perturbed and unperturbed metal centers. Once values of ρ are determined, it is possible to calculate the mixing coefficients a and b and the transition dipole moment. Overall, the relative ordering of coupling between pyrazine and 4-cyanopyridine complexes are in good qualitative agreement. The study also suggested that the degree of metal–metal coupling in these systems was at least three times that which would be predicted based solely on spectroscopic measurements. Finally, the thermodynamic resonance stabilization energies χ_g ($\Delta G_r'$) were derived from the difference in electrochemical couples between *trans*-$[\{LRu(NH_3)_4\}_2(\mu\text{–}BL)]^{5+/6+}$ and *trans*-$[\{Rh(NH_3)_5\}(LRu(NH_3)_5(\mu\text{–}BL)]^{5+/6+}$, where BL is either pyrazine or 4-cyanopyridine and L is NH_3, pyridine, 3-chloropyridine or 3-fluoropyridine. However, the values of χ_g derived in this way do not show the expected trend in metal–metal coupling.

2.17.3 EVALUATION OF REDOX COUPLES IN THE WEAK COUPLING CASE

If the metal sites are essentially non-interacting, the current–potential response for a given electrochemical method will have the same form as a single-step charge transfer for a monomeric center. The difference in standard potentials is given by $(RT/nF)ln4$, or $35.61/n$ mV at 298 K.[12] Thus, when the difference in metal-centered redox potentials is $35.61/n$ for a two-step charge transfer involving n electrons per step, the cyclic or differential pulse voltammogram will have the shape and current of a single-step charge transfer of $2n$ electrons.

Richardson and Taube[12] extended an analysis of overlapping charge transfer steps by Myers and Shain[13] and treated both differential pulse and cyclic voltammetry methods. As cyclic voltammetry is commonly used, the solution for this method will be presented.

Ruzic[14,15] has derived a general theory of multistep electron transfer for cases in which electron transfer is reversible and the rate of electron transfer is sufficient to maintain Nernstian conditions. This theory was derived for dc polarography, but it is applicable to normal-pulse polarography.[12] The current–potential relationship is

$$\frac{i}{i_d} = \frac{[n_1/(n_1 + n_2)](K_c P^{n_2})^{1/(n_1+n_2)} + 1}{P + (K_c P^{n_2})^{1/(n_1+n_2)} + 1} \tag{13}$$

where

$$P = \exp\left[\frac{(n_1 + n_2)F}{RT}\left(\frac{E_1 + E_2}{2} - \frac{n_1}{n_1 + n_2}E^1_{1/2} - \frac{n_1}{n_1 + n_2}E^2_{1/2}\right)\right] \quad (14)$$

and i_d is given by the Cottrel expression: $nFA(D/\pi t)^{1/2}$.[12]

By using Equation (13), Richardson and Taube[12] provided graphical solutions, which allow calculation of individual charge transfer steps $E_{1/2}{}^1$ and $E_{1/2}{}^2$ from the difference between anodic and cathode peaks $\Delta E_p = |E_p(\text{cathodic}) - E_p(\text{anodic})|$, when the charge transfer steps are not cleanly resolved ($|E_{1/2}{}^1 - E_{1/2}{}^2| = \Delta E_{1/2} < 200\,\text{mV}$). An important consideration is that the switching potential be extended by at least 250 mV beyond an anodic or cathodic peak in order to minimize distortion of the peak.

Figures 2 and 3 are used in the following manner. Consider $E_p(\text{cathodic}) = -100\,\text{mV}$ and $\Delta E_p = 72.4\,\text{mV}$. On Figure 2, at $\Delta E_p = 72.4\,\text{mV}$, $\Delta E_{1/2} = 50\,\text{mV}$. Going now to Figure 3, at $\Delta E_{1/2} = 50\,\text{mV}$, $E_p(\text{cathodic}) - E_{1/2} = -61.1\,\text{mV}$. Therefore, $E_{1/2}{}^1 = -100 + 61.1 = -38.9\,\text{mV}$ and $E_{1/2}{}^2 = -38.9 + 50 = 11.1\,\text{mV}$.

2.17.4 REDOX COUPLES OF MIXED-VALENCE METALLO–OLIGOMERS AND DENDRIMERS

Aoki and Chen[16] examined the statistical thermodynamics of polynuclear linear complexes with mixed-valence states by means of the theory of correlated walk. Expressions for the equilibrium electrode potential of linear N-nuclear complexes with homoredox centers were derived as a function of the molar fraction of the oxidized moiety, the nearest-neighbor interactions and N. Under conditions of large interaction energy, two-, three- and four-nuclear complexes were predicted to have two, three, and four voltammetric peaks, respectively. For odd number of $N > 3$, only three peaks are predicted while for even number $N > 4$, only four peaks are predicted. In cases where $N \to \infty$, the number of peaks reduces to two.

Soon after the above study was published, research by Rulkens *et al.*[17] on linear oligo(ferrocenyldimethylsilanes) gave a somewhat different experimental result. Odd-number N oligo(ferrocenyldimethylsilanes) showed only two peaks while even-numbered $N > 2$ showed three peaks. The redox behavior of these oligo(ferrocenyldimethylsilanes) is illustrated in Figure 4.

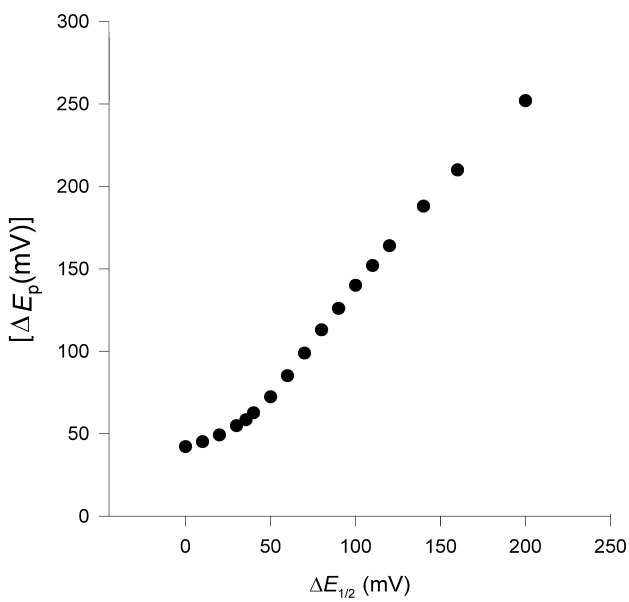

Figure 2 Plot of the difference between anodic and cathodic peaks ΔE_p and the difference between half-potentials $\Delta E_{1/2}$.

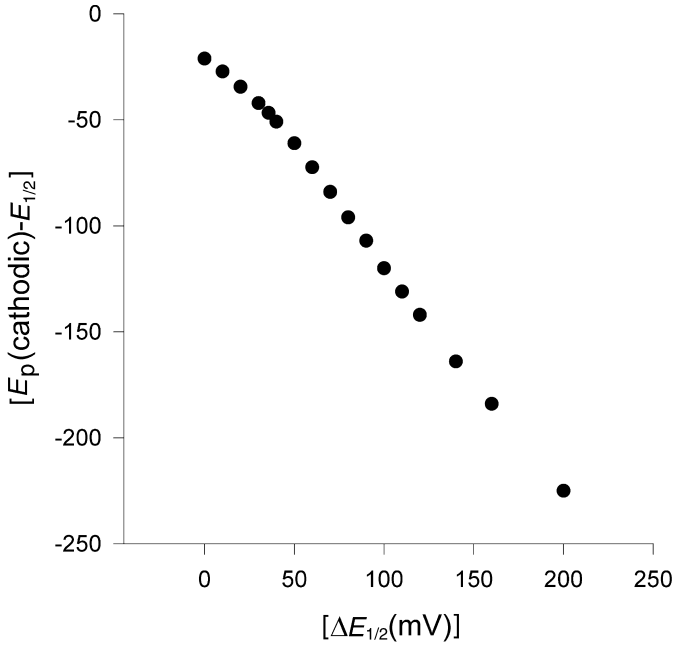

Figure 3 Plot of the difference cathodic peak and $E_{1/2}$ and the difference between half-potentials $\Delta E_{1/2}$.

It seems reasonable to suggest that the main difference between the theory of Aoki and Chen and that experimentally observed by Rulkens *et al.* is the magnitude of the interaction energy. As shown in Figure 4, the initial step is the addition of $(x+1)$ electrons at the same potential. If the interaction energy is large, this step must occur at two different potentials in which case the predictions of Aoki and Chen will hold. The prediction, that only two peaks will be seen at $N \rightarrow \infty$, was supported by the data of Rulkens *et al.*[17]

Haga *et al.*[18] developed a method to analyze the spectroelectrochemistry of tetranuclear dendrimer complexes, based on a combination of cyclic voltammetry simulation and flow through electrolysis. Using their method, the authors were able to predict and reconstruct the absorption spectra of the intermediate redox species with an estimated experimental error of 10%.

2.17.5 SPECTROELECTROCHEMISTRY

One of the most powerful methods of evaluating the properties of mixed-valence complexes is spectroelectrochemistry. A key experiment is to reversibly cycle a dinuclear complex through fully oxidized, mixed-valence and fully reduced states. A near IR absorption band that appears only in the electronic spectrum of the mixed-valence state is strong evidence for an intervalence transition. Determination of the nature of the mixed-valence state can also be achieved by spectroelectrochemical methods.

Infrared spectroscopy permits an evaluation of the extent of delocalization in a mixed-valence complex, as its time scale (10^{-13} s) gives an almost instantaneous view of the state. Previous infrared spectroscopic studies[19–32] have shown that for a valence-trapped complex (class II), the two different metal centers have distinguishable spectral features that will slowly coalesce as coupling between metal centers increases. For most mixed-valence systems, the infrared spectrum of a class III complex will resemble that of its fully reduced and fully oxidized states, but with an important difference: the energy of a given IR band in the mixed-valence complex will be the average of that found for the analogous band in the complex's fully oxidized and fully reduced states. A spectroelectrochemical analysis of pyrazine bridged mixed-valence ruthenium clusters is the subject of a case study (see Chapter 2.61).

The above general observation has exceptions. For mixed-valence complexes bridged by 1,4-dicyanamidebenzene dianion and its derivatives, it has been shown by infrared spectroelectrochemistry that polarization of the cyanamide bridging ligand has a significant effect on the cyanamide stretching frequency ν(NCN).[33] Because of this, it is more appropriate to state for

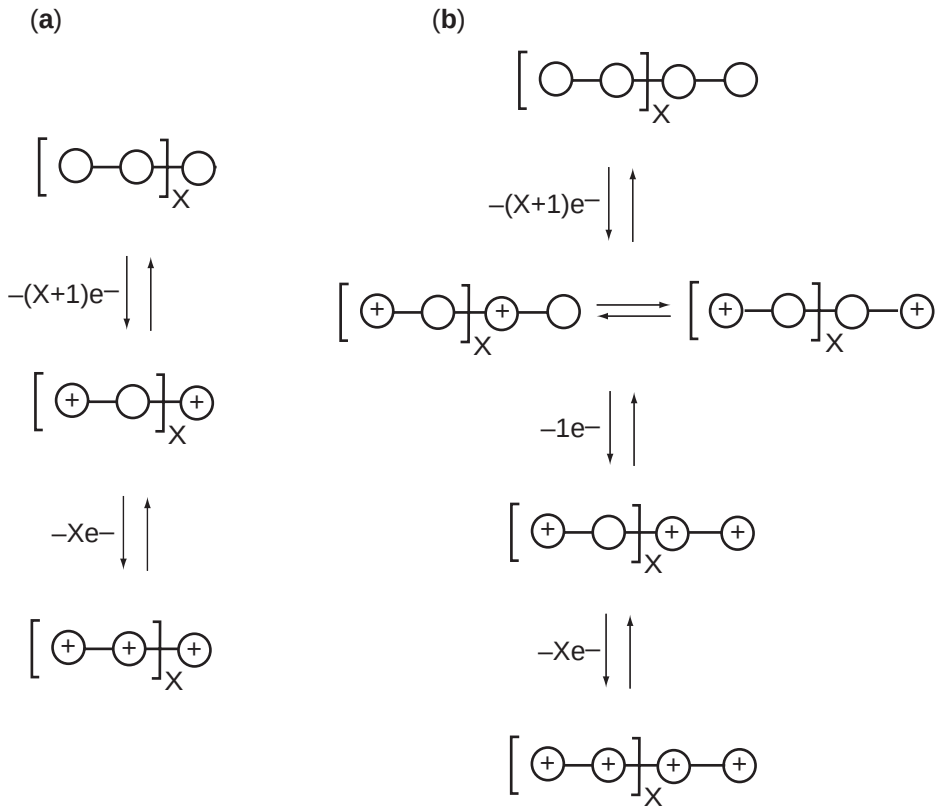

Figure 4 (a) Redox behavior of odd N oligo(ferrocenylsilanes), ($N = 3$, 5, 7 and 9). (b) Redox behavior of even N oligo(ferrocenylsilanes), ($N = 4$, 6 and 8).

mixed-valence complexes of dicyanamide bridging ligands that the frequency of the ν(NCN) of a class III complex is the average of the ν(NCN) bands of a similar class II complex. For mixed-valence complexes bridged by cyanide, the cyanide stretching frequency is shifted to lower energies compared to that expected for the mechanical coupling of C–N, metal–carbon and metal–nitrogen oscillators. A vibronic model has been proposed to describe metal–metal coupling as a function of nuclear coordinates of the bridging system.[34]

In infrared spectroelectrochemical studies of dinuclear ruthenium complexes bridged by 1.4-dicyanamidobenzene and its derivatives, the transformation from class II to class III behavior was observed as a function of both inner and outersphere perturbations.[33] For the complex, $[\{Ru(NH_3)_5\}_2(\mu-(1))]^{3+}$, where (1) is the 2,5-dimethyl-1,4-dicyanamidobenzene dianion, changing the solvent from nitromethane, to acetonitrile to dimethylsulfoxide changed the mixed-valence state from borderline class III to class II properties. This outer-sphere perturbation of the mixed-valence state occurs because of a donor–acceptor interaction between the solvent lone pairs and the protons of the ammine ligands.[7] In addition, the IR spectrum of *trans*, *trans*-$[\{Ru(NH_3)_4(pyridine)\}_2(\mu-(1))]^{3+}$, in acetonitrile, was shown to be consistent with class III properties in that this complex obeys the general condition for delocalization in symmetric mixed-valence complexes, $2H = \lambda$ (see Equation (5)), and possesses an experimental free energy of resonance exchange $\Delta G_r' = 1250\,cm^{-1}$ and resonance exchange integral $H = 3740\,cm^{-1}$. These properties were suggested to represent a benchmark for the transition between class II and class III behavior for these complexes.[33]

2.17.6 SELECTED STUDIES

As first shown by Boxer *et al.*[35] electroabsorption (or Stark effect) spectroscopy provides an experimental method to determine the extent of delocalization in mixed-valence complexes. Unfortunately, the technique is experimentally very difficult and this has limited its application. Nevertheless, Stark effect measurements of parallel and orthogonal intervalence transitions in

$[(CN)_5Os–CN–Ru(NH_3)_5]^{5-}$ have shown remarkable differences in the transition dipole moments lengths that are significantly shorter than simple geometric estimates.[36]

The distance dependence of donor–acceptor coupling is greatly dependent upon the nature of the bridging medium, as quantified by the decay exponential β[37] and the relationship,

$$H_{ad} \propto e^{-\beta r/2} \tag{16}$$

where r is the separation between donor and acceptor wavefunctions. Launay and other researchers[38–40] have estimated β to vary from 0.07 $Å^{-1}$ to 0.12 $Å^{-1}$ in valence-trapped mixed-valence systems incorporating polyene and polyphenylene spacers in which the metal ions were separated by as much as 25 Å. For a delocalized mixed-valence system, $\beta = 0$ and no distance dependence is predicted by Equation 16. Thus, the mixed-valence complex, $[\{Ru(trpy)(bpy)\}_2(adpc)]^{3+}$, where bpy = 2,2′-bipyridine, trpy = 2,2′:6′,2″-terpyridine, and $adpc^{2-}$ = 4,4′-azodi(phenylcyanamido), has been shown to possess a delocalized mixed-valence state despite a metal ion separation of over 18 Å.[41] The authors suggested that the bridging ligand can mediate metal–metal coupling by both hole transfer and electron transfer superexchange mechanisms.

Wolf *et al.*[42] studied mixed-valence complexes in which ferrocenyl groups were linked by an acetylene–ruthenium–acetylene spacer. The authors found that the nature of the ancillary ligands bound to ruthenium had a significant effect on coupling between mixed-valent ferrocenyl moieties. These results have implications in moderating the electronic properties of conducting polymers.[43] Similarly, bridging *trans*-$Ru(pyridine)_4(CN)_2$ or *trans*-$Os(bipyridine)_2(CN)_2$ in mixed-valence $Ru(NH_3)_5^{2+,3+}$ complexes were found to mediate superexchange coupling.[34] These authors noted that when metal-to-ligand or ligand-to-metal charge transfer energies are close in energy to metal–metal charge transfer energies, significant mixing of charge transfer excited states can be expected. Kaim *et al.*[44] examined a number of related mixed-valence complexes in which the metal, the auxiliary ligands, the molecular bridge, the *d*-electron configuration, the medium, the charge, the coordination mode, or the nuclearity were modified. The influence of these modifications on the extent of metal–metal coupling was discussed in terms of the superexchange mechanism involving the bridging ligand orbitals.

Ward *et al.*[45] prepared the complexes (**1**) and (**2**).

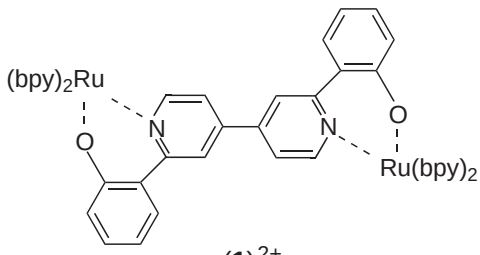

$(\mathbf{1})^{2+}$

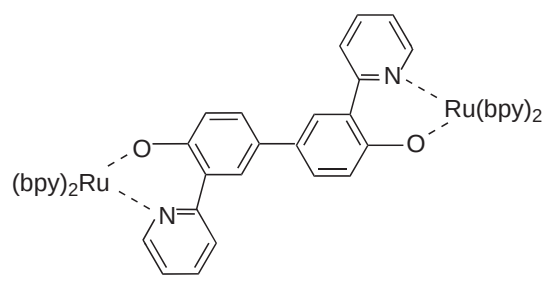

$(\mathbf{2})^{2+}$

These complexes are isomeric but possess different superexchange pathways for metal–metal coupling in their mixed-valence states. The authors[45] found that despite the longer pathway in $(2)^{3+}$, coupling is significantly greater for this complex than that observed for $(2)^{3+}$ and they ascribed this to the greater effectiveness of the hole-transfer superexchange mechanism in $(2)^{3+}$. An unusual pathway for metal–metal coupling is that seen in dicobalta–superphane complexes, in which transannular π/π interactions provide a pathway for donor–acceptor interactions.[46] By varying the fixed π/π distance in various complexes, the extent of delocalization in the mixed-valence state could be controlled. In this regard, Meyer[47] has published a comprehensive review of the localized-to-delocalized transition in mixed-valence chemistry in which he proposes a new mixed-valence classification between localized and delocalized cases, where the oxidation states are localized but the solvent is averaged. An analysis of optical transitions of symmetrical mixed-valence systems in this transition regime (i.e., almost delocalized) has been the subject of a recent review in which spectral band shapes and intensities are calculated utilizing increasingly complex models including two to four states.[48] For asymmetric mixed-valence complexes with small differences in energy between donor and acceptor wavefunctions, studies have shown that electron

transfer can be induced by changing the donor properties of the solvent.[49] Further discussions of mixed-valence complexes can be found in Chapters 2.60, 2.61, and 2.65.

An extended Mulliken–Hush treatment of mixed-valence complexes can be found in Chapter 2.45. In other studies, the effect of bridging ligand topology on metal–metal coupling was analyzed in terms of quantum interference.[50] Ferretti *et al.*[51] have proposed a model for the study of the optical properties of mixed-valence complexes, and Coronado *et al.*[52,53] have developed a general vibronic model in which both the electronic and magnetic properties of mixed-valence complexes are considered. Finally, the physical factors governing the amplitude of the electron transfer integral in mixed-valence complexes has been examined.[54]

2.17.7 REFERENCES

1. Robin, M. B.; Day, P. *Adv. Inorg. Chem. Radiochem.* **1967**, *10*, 247–422.
2. Hush, N. S. *Prog. Inorg. Chem.* **1967**, *8*, 391–444.
3. Mulliken, R. S.; Person, W. B. *Molecular Complexes*; **1969**, Wiley: New York.
4. Creutz, C.; Newton, M. D.; Sutin, N. *J. Photochem. Photobiol. A: Chem.* **1994**, *82*, 47–59.
5. Brunschwig, B. S.; Sutin, N. *Coord. Chem. Rev.* **1999**, *187*, 233–254.
6. D'Alessandro, D. M.; Kelso, L. S.; Keene, F. R. *Inorg. Chem.* **2001**, *40*, 6841–6844.
7. Evans, C. E. B.; Naklicki, M. L.; Rezvani, A. R.; White, C. A.; Kondratiev, V. V.; Crutchley, R. J. *J. Am. Chem. Soc.* **1998**, *120*, 13096–13103.
8. Ferrere, S.; Elliott, C. M. *Inorg. Chem.* **1995**, *34*, 5818–5824.
9. Evans, D. F. *J. Chem. Soc.* **1959**, 2003–2005.
10. Naklicki, M. L.; White, C. A.; Plante, L. L.; Evans, C. E. B.; Crutchley, R. J. *Inorg. Chem.* **1998**, *37*, 1880–1885.
11. Salaymeh, F.; Berhane, S.; Yusof, R.; de la Rosa, R.; Fung, E. Y.; Matamoros, R.; Lau, K. W.; Zheng, Q.; Kober, E. M.; Curtis, J. C. *Inorg. Chem.* **1993**, *32*, 3895–3908.
12. Richardson, D. E.; Taube, H. *Inorg. Chem.* **1981**, *20*, 1278–1285.
13. Myers, R. L.; Shain, I. *Anal. Chem.* **1969**, *41*, 980–981.
14. Ruzic, I. *J. Electroanal. Chem.* **1970**, *25*, 144–147.
15. Ruzic, I. *J. Electroanal. Chem.* **1974**, *52*, 331–354.
16. Aoki, K.; Chen, J. *J. Electroanal. Chem.* **1995**, *380*, 33–45.
17. Rulkens, R.; Lough, A. J.; Manners, I.; Lovelace, S. R.; Grant, C.; Geiger, W. E. *J. Am. Chem. Soc.* **1996**, *118*, 12683–12695.
18. Haga, M.; Ali, M. M.; Sato, H.; Monjushiro, H.; Nozaki, K.; Kano, K. *Inorg. Chem.* **1998**, *37*, 2320–2324.
19. Ito, T.; Hamaguchi, T.; Nagino, H.; Yamaguchi, T.; Kido, H.; Zavarine, I. S.; Richmond, T.; Washington, J.; Kubiak, C. P. *J. Am. Chem. Soc.* **1999**, *121*, 4625–4632.
20. Ito, T.; Hamaguchi, T.; Nagino, H.; Yamaguchi, T.; Washington, J.; Kubiak, C. P. *Science* **1997**, *277*, 660–663.
21. Ketterle, M.; Kaim, W.; Olabe, J. A.; Parise, A. R.; Fiedler, J. *Inorg. Chim. Acta* **1999**, *291*, 66–73.
22. Demadis, K. D.; Neyhart, G. A.; Kober, E. M.; Meyer, T. J. *J. Am. Chem. Soc.* **1998**, *120*, 7121–7122.
23. Wu, R.; Koske, S. K.; White, R. P.; Anson, C. E.; Jayasooriya, U. A.; Cannon, R. D.; Nakamoto, T.; Katada, M.; Sano, H. *Inorg. Chem.* **1998**, *37*, 1913–1922.
24. Omberg, K. M.; Schoonover, J. R.; Meyer, T. J. *J. Phys. Chem.* **1997**, *101*, 9531–9536.
25. Kaim, W.; Bruns, W.; Kohlmann, S.; Krejcik, M. *Inorg. Chim. Acta* **1995**, *229*, 143–151.
26. Chin, T. T.; Lovelace, S. R.; Geiger, W. E.; Davis, C. M.; Grimes, R. N. *J. Am. Chem. Soc.* **1994**, *116*, 9359–9360.
27. Geiger, W. E.; Pierce, D. T. *Inorg. Chem.* **1994**, *33*, 373–381.
28. Wu, R.; Poyraz, M.; Sowrey, F.; Anson, C. E.; Wocadlo, S.; Powell, A. K.; Jayasooriya, U. A.; Cannon, R. D. *J. Chem. Soc. Chem. Commun.* **1994**, 1657–1658.
29. Atwood, C. G.; Geiger, W. E.; Rheingold, A. L. *J. Am. Chem. Soc.* **1993**, *115*, 5310–5311.
30. Bruns, W.; Kaim, W.; Waldhor, E.; Krejcik, M. *J. Chem. Soc., Chem. Commun.* **1993**, 1868–1869.
31. Ketterle, M.; Fielder, J.; Kaim, Wolfgang. *J. Chem. Soc., Chem. Commun.* **1998**, 1701–1702.
32. Delville, M.-H.; Rittinger, S.; Astruc, D. *J. Chem. Soc., Chem. Commun* **1992**, 519–520.
33. DeRosa, M. C.; White, C. A.; Evans, C. E. B.; Crutchley, R. J. *J. Am. Chem. Soc.* **2001**, *123*, 1396–1402.
34. Macatangay, A. V.; Endicott, J. F. *Inorg. Chem.* **2000**, *39*, 437–446.
35. Oh, D. H.; Sano, M.; Boxer, S. G. *J. Am. Chem. Soc.* **1991**, *113*, 6880–6890.
36. Karki, L.; Hupp, T. J. *J. Am. Chem. Soc.* **1997**, *119*, 4070–4073.
37. Sachs, S. B.; Dudek, S. P.; Hsung, R. P.; Sita, L. R.; Smalley, J. F.; Newton, M. D.; Feldberg, S. W.; Chidsey, C. E. D. *J. Am. Chem. Soc.* **1997**, *119*, 10563–10564.
38. Launay, J.-P. *Chem. Soc. Rev.* **2001**, *30*, 386–397.
39. Ribou, A.-C.; Launay, J.-P.; Sachtleben, M. L.; Li, H.; Spangler, C. W. *Inorg. Chem.* **1998**, *35*, 3735–3740.
40. Patoux, C.; Launay, J.-P.; Beley, M.; Chodorowski-Kimmes, S.; Collin, J.-P.; James, S.; Sauvage, J.-P. *J. Am. Chem. Soc.* **1996**, *120*, 3717–3725.
41. Mosher, P. J.; Yap, G. P. A.; Crutchley, R. J. *Inorg. Chem.* **2001**, *40*, 1189–1195.
42. Zhu, Y.; Clot, O.; Wolf, M. O.; Yap, G. P. A. *J. Am. Chem. Soc.* **1998**, *120*, 1812–1821.
43. Zhu, Y. B.; Wolf, M. O. *J. Am. Chem. Soc.* **2000**, *122*, 10121–10125.
44. Kaim, W.; Klein, A.; Glöckle, M. *Acc. Chem. Res.* **2000**, *33*, 755–763.
45. Laye, R. H.; Couchman, S. M.; Ward, M. D. *Inorg. Chem.* **2001**, *40*, 4089–4091.
46. Stoll, M. E.; Lovelace, S. R.; Geiger, W. E.; Schimanke, H.; Hyla-Kryspin, I.; Gleiter, R. *J. Am. Chem. Soc.* **1999**, *121*, 9343–9351.
47. Meyer, T. J. *Chem. Rev.* **2001**, *101*, 2655–2685.
48. Brunschwig, B. S.; Creutz, C.; Sutin, N. *Chem. Soc. Rev.* **2002**, *31*, 168–184.

49. Neyhart, G. A.; Hupp, J. T.; Curtis, J. C.; Timpson, C. J.; Meyer, T. J. *J. Am. Chem. Soc.* **1996**, *118*, 3724–3729.
50. Patoux, C.; Coudret, C.; Launay, J.-P.; Joachim, C.; Gourdon, A. *Inorg. Chem.* **1997**, *36*, 5037–5049.
51. Ferretti, A.; Lami, A.; Villani, G. *Inorg. Chem.* **1998**, *37*, 2799–2805.
52. Borras-Almenar, J. J.; Clemente, J. M.; Coronado, E.; Palii, A. V.; Tsukerblat, B. S.; Georges, R. *J. Chem. Phys.* **1996**, *105*, 6892–6909.
53. Borras-Almenar, J. J.; Coronado, E.; Ostrovsky, S. M.; Palii, A. V.; Tsukerblat, B. S. *Chem. Phys.* **1999**, *240*, 149–161.
54. Calzado, C. J.; Malrieu, J.-P.; Sanz, J. F. *J. Phys. Chem. A* **1998**, *102*, 3659–3667.

Comprehensive Coordination Chemistry II
ISBN (set): 0-08-0437486

Volume 2, (ISBN 0-08-0443249); pp 235–244

2.18
Electrochemistry: High Pressure

T. W. SWADDLE
University of Calgary, AB, Canada

2.18.1 INTRODUCTION 245
2.18.2 TECHNIQUES 246
2.18.3 THERMODYNAMIC ASPECTS 246
2.18.4 KINETICS AND REACTION MECHANISMS 248
2.18.4.1 Aqueous Media 248
2.18.4.2 Nonaqueous Media 250
2.18.5 REFERENCES 250

2.18.1 INTRODUCTION

The effects of pressure on the electrode reactions of coordination compounds in solution can give many unique mechanistic insights,[1] but relatively little work has been done on this topic as a consequence of the need for special equipment and of the susceptibility of electrochemical measurements to the effects of contaminants. Furthermore, because compression of a fluid causes heating, a cycle of measurements over a range of pressures (typically 0–200 MPa) may take 5–10 hours because of slow thermal re-equilibration after each pressure change. Thus, slow degeneration of the reactants or the electrode surfaces may become prohibitive over a cycle of measurements (particularly in electrode kinetics). For example, the ferrocene–ferricenium couple in acetonitrile, though traditionally a reference couple for nonaqueous electrode reactions, exhibits excessive drift in the electrode reaction rate constant k_{el} in high-pressure studies, probably because of polymerization of ferrocene on the electrode surfaces.[2] Consequently, a key requirement of high-pressure electrochemical studies is that a final reading, taken at the same pressure as the first in the cycle, must agree with the first within the experimental uncertainty.

The effect of pressure P on equilibrium constant K^0 is given by

$$\left(\frac{\partial \ln K^0}{\partial P}\right)_T = -\frac{\Delta V^0}{RT} \tag{1}$$

where ΔV^0 is the *volume of reaction*, R is the gas constant, and T is temperature. For electrochemical reactions,

$$\ln K^0 = \frac{nF\Delta E^0}{RT} \tag{2}$$

$$\Delta V^0 = -nF\left(\frac{\partial \Delta E^0}{\partial P}\right)_T \tag{3}$$

where ΔE^0 is the standard electrode potential change (the standard potential of the oxidant half-reaction minus that of the reductant half-reaction), n is the number of moles of electrons transferred (normally 1), and F is the faraday (96,485 A s mol^{-1}). For a half-reaction $ML_x^{(z+1)/z}$ relative to a specific reference electrode (e.g., Ag/AgCl), we will write ΔE^0 and ΔV^0 as ΔE_{cell} and ΔV_{cell} (e.g., $\Delta E_{Ag/AgCl}$ and $\Delta V_{Ag/AgCl}$), respectively. Although it is possible in principle to calculate ΔV^0 from the algebraic sums of the molar volumes V^0 of the reactants, such V^0 values are not always available and besides are usually applicable only to infinite dilution. For the standard (i.e., zero overpotential) electrode reaction rate constants k_{el}, the *electrochemical volume of activation* $\Delta V_{el}^{\ddagger}$ is given by

$$\left(\frac{\partial \ln k_{el}}{\partial P}\right)_T = -\frac{\Delta V_{el}^{\ddagger}}{RT} \tag{4}$$

Theoretically, $\Delta V_{el}^{\ddagger}$ for an electrode reaction $ML_x^{(z+1)/z}$, like its counterpart $\Delta V_{ex}^{\ddagger}$ for the $ML_x^{(z+1)/z}$ *self-exchange* reaction in homogeneous solution,[3] should become numerically smaller with increasing pressure, but in practice ln k_{el} and ΔE_{cell} are usually linear functions of P over a 0–200 MPa range, within the experimental uncertainty, so that $\Delta V_{el}^{\ddagger}$ and ΔV_{cell} values obtained from linear plots should be regarded as average values valid at the mid-range pressure.

2.18.2 TECHNIQUES

The techniques of high-pressure liquid-phase chemistry have been described in two monographs,[4,5] one of which[5] contains a protocol for conducting high-pressure electrochemical measurements. A recent review[1] covers historical and current aspects of high-pressure electrochemistry. In essence, three electrodes (working, auxiliary, and reference) and the solution sample are contained in a small cell immersed in a stainless steel pressure vessel filled with an electrically insulating pressurizing fluid such as hexane. If the pressurizing pump delivers hydraulic oil, this should be isolated with a floating-piston separator from the pressurizing fluid. Electrical feedthroughs, tapered to resist extrusion and sheathed in an insulating material of suitable mechanical properties such as Vespel polyimide resin (DuPont), provide connections through the pressure vessel walls externally to a potentiostat and internally to extensions of the electrodes through the cell cap. The cell is built to contract freely under compression using either a syringe-like construction or a free piston as the cell base.[1] Reference electrodes are typically Ag wire/AgCl/KCl(aq) for aqueous samples, or Ag wire/$AgClO_4$(MeCN) for nonaqueous systems. To accommodate compression of the fluid in the reference electrode compartment, the porous glass (Vycor) frit that provides electrolyte contact is mounted in a free piston. The cell body is usually made of Teflon or Kel-F, although these materials retard thermal equilibration, machine poorly, and wear quickly. For service with nonaqueous solvents, AISI 316 stainless steel may be used, but requires electrically insulating seals around the electrode connections, and all seals should be of silicone rubber.

2.18.3 THERMODYNAMIC ASPECTS

The pressure dependence of ΔE_{cell} can be measured through half-wave potentials from cyclic voltammetry (CV),[1,6] cyclic staircase voltammetry,[7] or differential pulse voltammetry (DPV).[8] Since ΔE_{cell} and ΔV_{cell} include a contribution from the reference electrode, these values should be given relative to a common reference electrode, usually Ag/AgCl/KCl(aq, 4 mol L^{-1}) (although a discontinuity in the response of Ag/AgCl electrodes may occur at ~300 MPa[9]) or Ag/Ag^+(0.01 mol L^{-1})—for aqueous systems, the latter gives ΔV_{cell} values 2.9 cm^3 mol^{-1} more negative than the former at 25 °C.[8] For a particular redox reaction, ΔV^0 can then be obtained from the difference in ΔV_{cell} values for the constituent half-reactions.

ΔV_{cell} comprises contributions from the intrinsic volume change of the reactants, the change in solvation, and the reference half-cell. In principle, the contribution of the reference half-cell can be calculated from the molar volumes of its components, but these data refer unrealistically to infinite dilution. Tregloan *et al.*[7] however, showed that, for the series of low-spin/low-spin couples $Fe(CN)_{6-2x}L_x^{(z+1)/z}$ (L = 1,10-phenanthroline [phen] or 2,2′-bipyridine [bpy], $0 \le x \le 3$, charge number $z = 2x - 4$) in aqueous KNO_3, ΔV_{cell} relative to Ag/$AgNO_3$(aq) is a linear

Table 1 Volumes of reaction for selected couples in water relative to Ag/AgCl/KCl (4.0 mol L^{-1}) at 25.0 °C.

Couple	*Medium* (mol L^{-1})	$\Delta V_{Ag/AgCl}$ (cm^3 mol^{-1})
$Co(phen)_3^{3+/2+}$	NaCl (0.1)	27
$Co(en)_3^{3+/2+}$	KCl (0.5)	27
$Co(sepulchrate)^{3+/2+}$	KCl (0.5)	16
$Ru(NH_3)_6^{3+/2+}$	KNO_3 (0.1)	20
$Ru(en)_3^{3+/2+}$	KNO_3 (0.1)	17
$Ru(H_2O)_6^{3+/2+}$	$HClO_4$ (0.1)	3
$Fe(H_2O)_6^{3+/2+}$	$HClO_4$ (1.0)	5
$Fe(phen)_3^{3+/2+}$	KNO_3 (1.0)	10
$Fe(phen)_2(CN)_2^{+/0}$	KNO_3 (1.0)	−4
$Fe(phen)(CN)_4^{-/2-}$	KNO_3 (1.0)	−23
$Fe(CN)_6^{3-/4-}$	KNO_3 (1.0)	−35
$Os(CN)_6^{3-/4-}$	KCl (0.6)	−33
$Mo(CN)_8^{3-/4-}$	$NaClO_4$ (0.5)	−30
$W(CN)_8^{3-/4-}$	KCl (0.5)	−28

Source: Swaddle and Tregloan, 1999.[1] phen = 1,10-phenanthroline, en = ethylene 1,2 diamine.

function of $(z+1)^2 - z^2$. For this series, the effective radii r of the reactants change very little during redox, so the variation in ΔV_{cell} is attributable to solvational change, which, according to the Drude–Nernst theory, is proportional to the change in (ionic charge)$^2/r$. Thus, the correlation not only validates Drude–Nernst theory for fairly large complex ions, but also, because the intercept corresponds to the hypothetical case of no change in ionic charge (i.e., in solvation), reveals the contribution of the $Ag/Ag^+(aq)$ reference electrode to ΔV_{cell} ($-11.9\,cm^3\,mol^{-1}$; for the Ag/AgCl/KCl(4.0 mol L^{-1}) electrode, this contribution is $-9.0\,cm^3\,mol^{-1}$). Selected values of ΔV_{cell} for aqueous systems are given in Table 1, and for nonaqueous systems[1,2,10,11] in Table 2. The diversity of media precludes a comprehensive interpretation of ΔV_{cell} values, but generally they range from strongly negative for 3−/4− couples to moderately positive for most 3+/2+ (relative to Ag/AgCl or Ag/Ag^+), revealing the importance of Drude–Nernst solvational changes in electrode reactions.

The adaptation of the familiar "cross relation" of Marcus to high-pressure kinetics provides an example of the utility of ΔV_{cell} data.[3] The cross-relation connects the rate constant k_{AB} of a redox reaction ($A^+ + B \rightarrow$ products) in homogeneous solution to those (k_{AA}, k_{BB}) for the related self-exchange reactions ($A^+ + A \rightarrow A + A^+$, etc.) and the equilibrium constant K_{AB}:

$$k_{AB} = \sqrt{k_{AA} k_{BB} K_{AB} f} \tag{5}$$

where the factor f can be set to 1 for small ΔE_{AB}. Ignoring the pressure dependence of f, the corresponding relation in volume parameters

$$\Delta V_{AB}^{\ddagger} = \tfrac{1}{2}(\Delta V_{AA}^{\ddagger} + \Delta V_{BB}^{\ddagger} + \Delta V_{AB}^{0}) \tag{6}$$

allows for significant mechanistic information to be drawn from measurements of $\Delta V_{AB}^{\ddagger}$ and (via ΔV_{cell}) ΔV_{AB}^{0}, since $\Delta V_{AA}^{\ddagger}$ and $\Delta V_{BB}^{\ddagger}$ can be predicted by theory for simple outer-sphere mechanisms.[3] Experience to date[10] indicates that Equation (6) is valid for small ΔE^0, but fails for $\Delta E^0 > 500$ mV even if the pressure dependence of f is taken into account.

Electrochemical studies of bioinorganic redox reagents are complicated by the tendency of metalloproteins to adsorb irreversibly on electrode surfaces, but this can be countered by first coating the electrode with a promoter such as dipyridyl disulfide[8] or L-cysteine.[12] Conflicting negative $\Delta V_{Ag/AgCl}$ values have been reported[1,8,12] for the reduction of cytochrome c^{III}, but it appears that the absolute volume of cytochrome c^{III} *exceeds* that of cytochrome c^{II} by a small amount ($\sim 5\,cm^3\,mol^{-1}$), despite lengthening of the Fe−ligand bonds on reduction, probably because the concomitant opening of the heme cleft allows ingress of solvent water. For *intramolecular* electron transfer in cytochromes c^{II} to *trans*-$L(NH_3)_4Ru^{III}$ substituents ($L = NH_3$,

Table 2 Volumes of reaction and of activation for couples of various charge-types in organic solvents at 25 °C.

Couple/solvent/electrolyte (mol L^{-1})	ΔV_{cell}[a] ($cm^3\,mol^{-1}$)	$\Delta V_{diff}^{\ddagger}$ ($cm^3\,mol^{-1}$)	$\Delta V_{el}^{\ddagger}$ ($cm^3\,mol^{-1}$)	$\Delta V_{ex}^{\ddagger}$ ($cm^3\,mol^{-1}$)
$Ru(hfac)_3^{0/-}/MeCN/Bu_4NClO_4$ (0.2)	−25	12	8	−6
$Ru(hfac)_3^{0/-}/Me_2CO/Bu_4NPF_6$ (0.2)	−20	15	12	−6
$Ru(hfac)_3^{0/-}/MeOH/Bu_4NClO_4$ (0.5)	−18	15	10	−6
$Ru(hfac)_3^{0/-}/PC/Bu_4NPF_6$ (0.5)	−13	19	11	
$Mn(CNchx)_6^{2+/+}/MeCN/Bu_4NClO_4$ (0.5)	−18	9	8	−19
$Mn(CNchx)_6^{2+/+}/Me_2CO/Bu_4NClO_4$ (0.5)	−19	11	10	−20
$Mn(CNchx)_6^{2+/+}/MeOH/Bu_4NClO_4$ (0.5)	−13	8	6	−16
$Mn(CNchx)_6^{2+/+}/PC/Bu_4NClO_4$ (0.5)	−19	17	20	
$Fe(phen)_3^{3+/2+}/MeCN/Bu_4NClO_4$ (0.5)	3	8	14	−6
$Co(phen)_3^{3+/2+}/MeCN/Bu_4NClO_4$ (0.2)	16	9	9	
$Co(phen)_3^{3+/2+}/Me_2CO/Bu_4NClO_4$ (0.2)	12	11	10	
$Co(phen)_3^{3+/2+}/PC/Bu_4NClO_4$ (0.2)	14	16	12	

Source: Matsumoto *et al.* 2001;[2] Fu *et al.* 1999;[10] Zhou and Swaddle, 2001.[11] [a] Reference electrode $Ag/AgClO_4$(0.01 mol L^{-1} in MeCN). hfac = Hexafluoroacetylacetonato, PC = propylene carbonate, chx = cyclohexyl, en = 1,2-diaminoethane.

pyridine, isonicotinamide, 3,5-lutidine) at histidine-33, strongly positive $\Delta V_{Ag/AgCl}$ values clearly indicate a major change (evidently desolvation) associated with the reduction of the Ru ammine groups.[8]

2.18.4 KINETICS AND REACTION MECHANISMS

Although standard electrode reaction rate constants k_{el} are in principle obtainable from peak-to-peak separations in CVs or from extrapolations of Tafel plots to zero overpotential, the precision needed for measurement of $\Delta V_{el}^{\ddagger}$ demands alternating current voltammetry (ACV), in which a small AC potential of angular frequency ω is superimposed upon a DC potential ramp and the phase angle φ is extracted from measurements of the maximum in-phase and 90° out-of-phase currents.[1,6,10] If the diffusion coefficients of the oxidized and reduced species are taken to be the same (D),

$$\cot \varphi = 1 + (2D\omega)^{1/2}/\alpha^{-\alpha}(1-\alpha)^{-(1-\alpha)}k_{el} \tag{7}$$

in which α is the transfer coefficient (normally ~0.50).[10] To calculate k_{el} reliably, the uncompensated resistance R_u of the system should be measured directly for maximum accuracy (e.g., from impedance measurements at high frequency).[10] Values of D can be obtained from the maximum currents of CVs (calibrated against a standard such as $Fe(CN)_6^{3-/4-}$ for aqueous or Fe $(\eta^5\text{-}C_5H_5)_2^{+/0}$ for nonaqueous systems),[10] and the volume of activation $\Delta V_{diff}^{\ddagger}$ for diffusion of the reactants is given by $-RT(\partial \ln D/\partial P)_T$.

2.18.4.1 Aqueous Media

For the electrodeposition of Co, Ni, and Ag from solutions of Co^{2+}(aq), Ni^{2+}(aq), and Ag^{+}(aq), the respective volumes of activation are 13, 13, and 10 $cm^3\,mol^{-1}$ at low concentrations of supporting electrolytes.[13] These data strongly suggest that the rate determining step involves removal of one coordinated water molecule from the aqua cation.[1] Additives such as high concentrations of KCl or organic sulfonates decreased the volumes of activation for Co and Ni deposition significantly, probably by providing a bridging mechanism for electron transfer, while ammonia increased that for Ag.[13]

Pressure effects have helped clarify the relationship between the kinetics of self-exchange reactions of metal complexes in homogeneous solution (rate constants k_{ex}, volumes of activation $\Delta V_{ex}^{\ddagger}$) and of the same couples at electrodes (k_{el}, $\Delta V_{el}^{\ddagger}$). Marcus[14] proposed that the free energy of activation $\Delta G_{el}^{\ddagger}$ for an electrode reaction should be *one-half* of that ($\Delta G_{ex}^{\ddagger}$) for the corresponding self-exchange reaction. Simply put, this is because in self-exchange *two* reactants have to

undergo internal and solvational reorganization to reach a common intermediate configuration to permit electron transfer, whereas for the electrode reaction only *one* reactant has to be reorganized to the intermediate configuration. This proposal, however, is difficult to test by comparing k_{el} with k_{ex} values because, although the frequency factor Z_{ex} for self-exchange is expected from transition-state theory to be fairly constant for a series of couples under similar conditions, Z_{el} often depends upon the nature and history of the electrode surface:

$$k_{el} = Z_{el}\exp(-\Delta G_{el}^{\ddagger}/RT) \tag{8}$$

$$k_{ex} = Z_{ex}\exp(-\Delta G_{ex}^{\ddagger}/RT) \tag{9}$$

Neither Z_{ex} nor Z_{el}, however, is expected to be significantly pressure-dependent (an electrode surface is normally unchanged over pressure ranges of a few hundred MPa), so that, if transition-state theory is applicable,

$$\Delta V_{el}^{\ddagger} = \tfrac{1}{2}\Delta V_{ex}^{\ddagger} \tag{10}$$

In fact, Equation (10) holds for a variety of aqueous systems, regardless of charge type (Figure 1; the $Fe(CN)_6^{3-/4-}$ couple has been excluded because of wide discrepancies in the values reported for both $\Delta V_{el}^{\ddagger}$ and $\Delta V_{ex}^{\ddagger}$[15–19]). It is not obvious why this "50% rule" should hold for electron transfer between cyanometalate anions, for which the self-exchange reaction is strongly cation-catalyzed;[1,15,16,19] however, the strong dependence of the magnitude and even the *sign* of both $\Delta V_{el}^{\ddagger}$ and $\Delta V_{ex}^{\ddagger}$ on the nature of the counterion suggests that catalysis requires a *dehydrated* cation.[19] In the absence of counterion catalysis, $\Delta V_{el}^{\ddagger}$ and $\Delta V_{ex}^{\ddagger}$ are invariably negative for outer-sphere electron transfer in water at 25 °C, and can be accounted for quantitatively.[3,19]

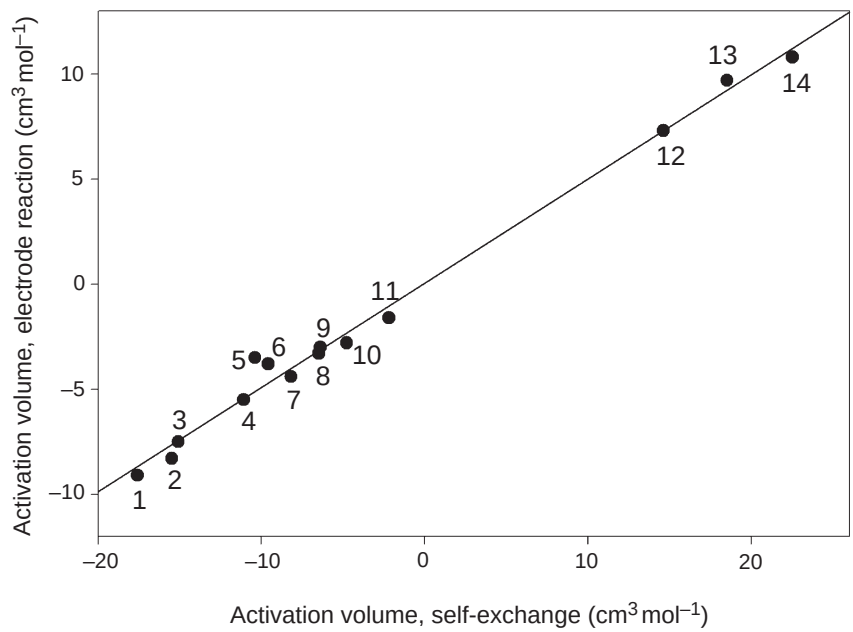

Figure 1 Relationship between $\Delta V_{el}^{\ddagger}$ and $\Delta V_{ex}^{\ddagger}$ in aqueous systems at 25 °C. Slope is 0.50 ± 0.02. 1: $Co(phen)_3^{3+/2+}$. 2: $Co(en)_3^{3+/2+}$. 3: $Ru(en)_3^{3+/2+}$. 4: $Fe(H_2O)_6^{3+/2+}$. 5: $Co(diaminosarcophagine)^{3+/2+}$. 6: $Co(diaminosarcophagineH_2)^{5+/4+}$. 7: $Mo(CN)_8^{3-/4-}/Et_4N^+$. 8: $Co(azacapten)^{3+/2+}$. 9: $Co(sepulchrate)^{3+/2+}$. 10: $Co(1,4,7\text{-trithiacyclononane})_2^{3+/2+}$. 11: $Fe(phen)_3^{3+/2+}$. 12: $Mo(CN)_8^{3-/4-}/K^+$. 13: $Os(CN)_6^{3-/4-}/K^+$. 14: $W(CN)_8^{3-/4-}/K^+$. Sources: Fu and Swaddle, 1997, 1999;[15,16] Metelski *et al.*, 1999.[20]

2.18.4.2 Nonaqueous Media

In striking contrast to the results for aqueous systems, $\Delta V_{el}^{\ddagger}$ for electrode reactions in organic solvents is invariably *positive*, even though $\Delta V_{ex}^{\ddagger}$ for the corresponding bimolecular self-exchange reactions is typically *negative* (Table 2) as expected from theory.[3] There is, however, a broad correlation between $\Delta V_{el}^{\ddagger}$ and $\Delta V_{diff}^{\ddagger}$, which, through the Stokes-Einstein relationship, implies an inverse dependence of k_{el} on solvent viscosity η.[10] In the absence of diffusion control of the reaction rate (as is almost certainly the case here), such a dependence is the signature of the predominance of *solvent dynamics* (solvent "friction")—in effect, the solvent coupling that enables the reactant(s) to climb the activation barrier can also hinder barrier crossing, resulting in an inverse dependence of the frequency factor Z_{el} (Equation (8)) on the longitudinal relaxation time τ_L of the solvent; for ideal (Debye) solvents, τ_L is proportional to η. Murray *et al.*[21] obtained evidence for the incursion of solvent dynamics into the $Co(bpy)_3^{3+/2+}$ electrode kinetics by changing solvents to vary η, while Bard *et al.*[22] reached a similar conclusion concerning the reduction of *aqueous* $Cr(EDTA)^-$ at a mercury electrode by adding sucrose to increase η. Variable pressure studies, however, allow η to be "tuned" without changing the solvent chemically.

For *water* near 25 °C, pressure-induced breakup of hydrogen bonding compensates almost exactly for the exponential rise of viscosity with pressure typical of normal liquids, so that η is fortuitously almost independent of pressure up to 200 MPa. Consequently, for aqueous systems, varying pressure exposes the 50% rule (Equation (11)) regardless of whether solvent dynamics are important, whereas for organic solvents the viscosity effect swamps the transition-state-theory component completely, resulting in large, positive $\Delta V_{el}^{\ddagger}$ values that are comparable to $\Delta V_{diff}^{\ddagger}$. At present, it is unclear whether solvent dynamics are also dominant in aqueous electrode reactions, as the results of Bard *et al.*[22] suggest; water, however, is an anomalous (nonDebye) solvent because of local hydrogen-bonding in three dimensions. Overall, pressure effects do show that, whereas the kinetics of redox reactions of metal complexes in homogeneous solution conform to transition-state theory, the corresponding electrode processes (in nonaqueous solvents at least) are subject to solvent-dynamical control.

2.18.5 REFERENCES

1. Swaddle, T. W.; Tregloan, P. A. *Coord. Chem. Rev.* **1999**, *187*, 255–289.
2. Matsumoto, M.; Lamprecht, D.; North, M. R.; Swaddle, T. W. *Can. J. Chem.* **2001**, *79*, 1864–1869.
3. Swaddle, T. W. *Can. J. Chem.* **1996**, *74*, 631–638.
4. Isaacs, N. S. *Liquid Phase High Pressure Chemistry*; Wiley: New York, 1981.
5. Swaddle, T. W. Electrochemical measurements at elevated pressures. In *High-Pressure Techniques in Chemistry and Physics*; Holzapfel, W. B.; Isaacs, N. S., Eds.; Oxford University Press: Oxford, 1997; pp 343–351.
6. Fu, Y.; Swaddle, T. W. *J. Am. Chem. Soc.* **1997**, *119*, 7137–7144.
7. Sachinidis, J. I.; Shalders, R. D.; Tregloan, P. A. *Inorg. Chem.* **1994**, *33*, 6180–6186.
8. Sun, J.; Wishart, J. F.; van Eldik, R.; Shalders, R. D.; Swaddle, T. W. *J. Am. Chem. Soc.* **1995**, *117*, 2600–2605.
9. Cruañes, M. T.; Drickamer, H. G.; Faulkner, L. R. *J. Phys. Chem.* **1992**, *96*, 9888–9892.
10. Fu, Y.; Cole, A. S.; Swaddle, T. W. *J. Am. Chem. Soc.* **1999**, *121*, 10410–10415.
11. Zhou, J.; Swaddle, T. W. *Can. J. Chem.* **2001**, *79*, 841–847.
12. Cruañes, M. T.; Rogers, K. K.; Sligar, S. G. *J. Am. Chem. Soc.* **1992**, *114*, 9660–9661.
13. Franklin, T. C.; Mathew, S. A. *J. Electrochem. Soc.* **1989**, *136*, 3627–3630.
14. Marcus, R. A. *Electrochim. Acta* **1968**, *13*, 995–1004.
15. Fu, Y.; Swaddle, T. W. *J. Am. Chem. Soc.* **1997**, *119*, 7137–7144.
16. Fu, Y.; Swaddle, T. W. *Inorg. Chem.* **1999**, *38*, 876–880.
17. Conway, B. E.; Currie, J. C. *J. Electrochem. Soc.* **1978**, *125*, 257–264.
18. Sato, M.; Yamada, T. Effect of high pressure on the rate of electrode reaction of metal complex. In *High Pressure Science and Technology*; Vol. 2; Vodar, B.; Marteau, P., Eds.; Pergamon: Oxford, 1980; pp 812–814.
19. Zahl, A.; van Eldik, R.; Swaddle, T. W. *Inorg. Chem.* **2002**, *41*, 757–764.
20. Metelski, P. D.; Fu, Y.; Khan, K.; Swaddle, T. W. *Inorg. Chem.* **1999**, *39*, 3103–3109.
21. Williams, M. E.; Crooker, J. C.; Pyati, R.; Lyons, L. J.; Murray, R. W. A. *J. Am. Chem. Soc.* **1997**, *119*, 10249–10250.
22. Zhang, X.; Yang, H.; Bard, A. J. *J. Am. Chem. Soc.* **1987**, *109*, 1916–1920.

Comprehensive Coordination Chemistry II
ISBN (set): 0-08-0437486
Volume 2, (ISBN 0-08-0443249); pp 245–250

2.19 Ligand Electrochemical Parameters and Electrochemical–Optical Relationships

A. B. P. LEVER
York University, Toronto, ON, Canada

2.19.1 INTRODUCTION 251
2.19.2 BURSTEN'S MODEL 252
2.19.3 THE P_L MODEL 253
2.19.4 LIGAND ELECTROCHEMICAL PARAMETERS—(LEVER PARAMETERS) 254
2.19.4.1 Relationship Between $E_L(L)$ and P_L 258
2.19.4.2 $E_L(L)$ Parameters and Reduction Potentials 258
2.19.4.3 Reduction Potentials Vs. Oxidation Potentials 259
2.19.4.4 Redox Processes of Homologous Series of Ligand Fragments 259
2.19.4.4.1 Reduction 259
2.19.4.4.2 Oxidation 260
2.19.4.5 $E_L(L)$ Relationships with Non-electrochemical Parameters 260
2.19.5 LIGAND ELECTROCHEMICAL PARAMETER THEORY APPLIED TO CLUSTERS 261
2.19.6 CHARGE TRANSFER SPECTROSCOPY 261
2.19.6.1 Other Correlations Between Electrochemical Potentials and Optical Transition Energies 263
2.19.6.1.1 $h\nu$(MLCT) *vs.* E_{ox} or $\Sigma E_L(L)$ 264
2.19.6.1.2 $h\nu$(MLCT) *vs.* E_{ox} *or* $\Sigma E_L(L)$ *in* $M(R\text{-}L)X_5$ *species* 264
2.19.6.1.3 $h\nu$(MLCT) *vs.* E_{red} *in* $[M(LL)(WXYZ)]^{n+}$ *type complexes* 265
2.19.6.1.4 $h\nu$(LMCT) *vs.* $E[M^{n+/n}(L)]$ *and* ΔE(Redox) 265
2.19.7 EMISSION DATA 265
2.19.8 CONCLUSIONS 265
2.19.9 REFERENCES 266

2.19.1 INTRODUCTION

The ability to assign an electrochemical parameter to a ligand provides a means to predict the potentials of a range of redox processes and also to predict some charge transfer spectroscopic energies. The general theoretical approach allows one to predict the potential of a particular redox process and compare this with experiment. If there is very poor agreement then, probably, the assignment is incorrect. Small deviations from the predicted value may provide insight into unusual electronic features. The same comments may be applied to the prediction of the energy of a charge transfer process. This cross-checking capability is a powerful tool to avoid errors in assignment.

At a more fundamental level, the parameters provide information about the intrinsic properties of the ligand themselves since they reflect the σ- and π-bonding properties of the ligand. Several different sets of parameters exist in the literature. We discuss them here but note that they have been extensively reviewed in the recent past[1] to which reference the reader is directed for greater

detail. There are three principal methods described in the literature, those of Bursten,[2] those of Chatt *et al.* (PPC)[3–5] and those of Lever *et al.*[6–8] All rely on the idea of "ligand additivity"; namely, that the effects of several ligands are obtained by summing the effect of each individual ligand. Synergistic effects, where the presence of one particular ligand influences the properties of another, i.e., change its effective parameter value, should reveal themselves in deviations between the predicted and experimental potentials. Examples will be presented.

An obvious problem with simple additivity is the fact that, in a few cases, different isomers of the same species have markedly different redox potentials; simple additivity cannot explain this. This is accommodated in the Bursten and in the PPC models and in the Lever model by adopting the Bursten procedure.

2.19.2 BURSTEN'S MODEL

Bursten and co-workers[2,9–11] correlated a wide range of experimental data including not only electrochemical potentials but molecular orbital energies, photoelectron spectroscopy, and ionization energies; however, these were focused specifically on metal carbonyls.

The model relies on the assumption that the HOMO energy of a complex is linearly related to its redox potential. This has been extensively investigated in the past and shown often to be true for homologous series of complexes. Thus, Sarapu and Fenske[12] illustrated such a relationship between the HOMO energy calculated by the Hartree–Fock method, and the observed metal-centered oxidation potential in the series $[Mn(CO)_{6-n}(CNMe)_n]^+$:

$$E_{1/2} = k\varepsilon(\text{HOMO}) + C \tag{1}$$

Redox potentials are thermodynamic properties which depend on the binding energies of both oxidized and reduced species. It is therefore somewhat surprising that they would correlate with the HOMO energy of one component alone. The inference is that in a homologous series, the relative binding energies in both oxidation states with change of ligand are also linearly related. Thus, a correlation between the HOMO (or LUMO) energies with the oxidation potential (or reduction potential) can be rationalized provided that there are no major nuclear rearrangements occurring subsequent to oxidation or reduction. These relationships (Equation (1)) have been demonstrated for many organic systems, e.g., see refs.13–17 or in many inorganic or organometallic species such as, for example, cited in refs. 2, 10–12, 18–23.

The energy, ε_i, of the ith $d\pi$-orbital of a substituted carbonyl species, $M(CO)_{6-n}L_n$, was defined by:

$$\varepsilon_i = a + bn + cx \tag{2}$$

where x is the number of CO π*-orbitals with which this ith $d\pi$-orbital specifically interacts; and a, b and c are empirically derived parameters which will vary with the particular metal carbonyl species concerned. Stereoisomers may be distinguished as follows. For example, in a *trans*-$ML_4(CO)_2$ species (CO groups aligned on the z-axis), the Angular Overlap model theory[24,25] predicts the energy order $(xz,yz) < xy$ (HOMO), assuming that ligand L is a poorer π acceptor than CO. In this situation, the (xz,yz)-orbitals each overlap a π-orbital on two CO groups (hence $x = 2$), while the xy-orbital does not interact with any CO π-orbitals. Thus, x is zero for this stereochemistry in Equation (1) for the HOMO. There is an implied assumption in this model that the $d\pi$-orbitals can each be recognized and behave independently, though mixing between these d-orbitals will occur in some point group symmetries. For a general complex $ML_nL'_{6-n}$ it is possible to rewrite Equation (2) as:[9]

$$\varepsilon_i = a_M{}^o + nb_M{}^L + (6-n)b_M{}^{L'} + x_i c_M{}^L + (4-x_i)c_M{}^{L'} \tag{3}$$

which is equivalent to Equation (2) when:

$$a = a_M{}^o + 6b_M{}^{L'} + x_i c_M{}^L + 4c_M{}^{L'},\ b = b_M{}^L - b_M{}^{L'},\ c = c_M{}^L - c_M{}^{L'} \tag{4}$$

where $a_M{}^o$ is a variable depending on the metal ion concerned, $b_M{}^L$ and $b_M{}^{L'}$ refer to the overall metal–ligand interaction with the ligands L and L′ and are reminiscent of the spherical term in

crystal field theory in affecting *d*-orbital energies. The differential π interaction of the ligands on the $d\pi$-orbitals is handled through the ${c_M}^L - {c_M}^{L'}$ term. The term in x_i distinguishes the energies of each $d\pi$-orbital with respect to the stereochemistry of the species using the number of interacting L and L′ π-orbitals in a manner described above (also see Table XI of ref. 2)

Since, at least for homologous series, $E_{1/2}$ and ε_i are related via Equation (1), it is feasible to rewrite Equation (2) for a metal-centered oxidation potential of a general $ML_nL'_{6-n}$ complex as:[2]

$$E_{1/2} = A + Bn + Cx_{\text{homo}} \tag{5}$$

where:

$$A = {A_M}^O + 6{B_M}^{L'} + 4{C_M}^{L'},\ B = {B_M}^L - {B_M}^{L'},\ C = {C_M}^L - {C_M}^{L'} \tag{5a}$$

These equations have been used to analyze a range of substituted organometallic species[2,10,11,18] but they are insufficiently general for practical use with newly described compounds and they are rarely utilized now.

2.19.3 THE P_L MODEL

The P_L model was introduced in a series of papers detailing ligand additivity behavior[26] by Chatt, Leigh, Pickett and co-workers.[4,5] The P_L parameter is defined using the $Cr^{I/O}$ redox potential via:

$$P_L = {E_{1/2}}^{ox}[Cr(CO)_5L] - {E_{1/2}}^{ox}[Cr(CO)_6] \tag{6}$$

i.e., it is defined as the change in redox potential when the ligand L replaces a carbonyl group in $Cr(CO)_6$. The more electron-releasing the ligand (or a substituent thereof) the more negative is P_L. It also measures the net electron π-donor minus π-acceptor ability of the ligand L. Although this seems like a highly specific parameter, it can be generalized, in principle, to any species. Consider a series of different complexes $E_{1/2}$[M(UVWXY)L] (where ligands UVWXY are fixed, such that the fragment M(UVWXY) represents a fixed core often called M_s).[5] If one plots the metal-centered oxidation potential of such a series with varying L against ${E_{1/2}}^{ox}[Cr(CO)_5L]$, a series of parallel lines is obtained, requiring that the metal-centered oxidation potential for a general complex M_sL is given by:

$${E_{1/2}}^{ox}[M_sL] = E_s + \beta P_L \tag{7}$$

Since $P_L(CO) = 0$, it is evident that E_s is, in fact, nominally equal to ${E_{1/2}}^{ox}$ for the species $[M_s(CO)]^{n+}$. Of course, one may observe several successive metal-centered oxidations of a species, e.g., $[Fe^{II}L_5(CO)]^{n+}$ to $[Fe^{III}L_5(CO)]^{n+1+}$ to $[Fe^{IV}L_5(CO)]^{n+2+}$ yielding, in this example, E_s values for both the $[Fe^{II}L_5]^{n+}$ and $[Fe^{III}L_5]^{n+1+}$ cores being equal to the $Fe^{III/II}$ and $Fe^{IV/III}$ potentials of these species. If the corresponding oxidation potentials for a series of different complexes $[FeL_5L']^{n+}$ are then plotted against $P_L(L')$ then the slope of the resulting line is β. The parameter E_s is obviously a characteristic of the core and how tightly bound are the electrons, or its "electron richness," while β must reflect the extent to which the core can be perturbed by the binding of L′, a measure of the polarizability of the site. While the basic theory is referenced to the $Cr(CO)_5L$ complex, a general set of P_L values for any ligands can be obtained by measuring the redox potentials of a series of M_sL species and extracting P_L parameters from Equation (7) when E_s and β are known. Table 1 contains a representative P_L data set and Table 2 a selection of E_s and β_L values. These fairly extensive tabulations are provided here because, aside from ref.1 they do not appear extensively tabulated elsewhere in the literature. However, see.[27]

P_L values have also been shown to correlate with other properties which relate to electron richness, principally infrared stretching frequencies such as $\nu(N_2)$ and $\nu(NO)$ in species such as $M(Y)(L)X_4$ with $Y = N_2$ or NO (e.g.,[27–29]). In an early paper, Chatt discussed[5] how the variation in E_s and β values might identify sites which would preferentially bind dinitrogen, N_2, or hydride ion, predicting binding behavior from a combination of electron richness and polarizability. This early work greatly predated the demonstration of the use of Lever parameters (vide infra) for this specific purpose by Morris.[30] Subsequently, Pombeiro has discussed the electroactivation of metal–hydrogen bonds using the P_L model.[27,31,32]

Table 1 A collection of P_L values.[5,27,33,35–38]

Ligand	P_L[a]	*Ligand*	P_L
NO^+	+1.40	Py	−0.59
≡C—CH_2—Ph	+0.27	NH_3	−0.77
≡C—NH_2	+0.09	$CF_3CO_2^-$	−0.78
CO	0	*o*-CN(H)C_6H_4C(PR_3)	−0.83
N_2	−0.07	$NCNH_2$	−0.85
$P(OPh)_3$	−0.18	$NCNC(NH_2)_2$	−0.86
Vinylidenes	−0.25 – −0.28	NCNHCN	−0.88
o-$_3PCH_2C_6H_4NC$	−0.32	NCS^-	−0.88
2,6-Cl_2PhNC	−0.33	*o*-N=C(H)C(PR_3)(C_6H_4)	−0.96
PPh_3	−0.35	CN^-	−1.00
4-ClPhNC	−0.37 (−0.11)	NCO^-	−1.16
PhNC	−0.38 (−0.12)	C≡CPh$^-$	−1.22
2-MePhNC	−0.38	$NCNC(NH)NH_2^-$	−1.22
4-MePhNC	−0.39 (−0.13)	H^-	−1.22
PhCN	−0.40	$NCNCN^-$	−1.14
4-MeOPhNC	−0.40 (−0.14)	I^-	−1.15
CH_3NC	−0.43 (−0.17)	Br^-	−1.17
^{t}BuNC	−0.44 (−0.18)	Cl^-	−1.19
Protonated indoles	−0.53	N_3^-	−1.26
Protonated carbenes	−0.55	OH^-	−1.55
CH_3CN	−0.58	carbynes	ca 0.27

[a] Quoted values for isocyanides are for linear MCNR bonding. Values for bent MCNR are given in parentheses.

Table 2 Core E_s and polarizability β_L values for a selection of species.[1,5,27,28,33,39–43]

M_s[a] *[MYX$_4$]*	E_s(*V*) *vs. SCE*	β_L
$Mo(CO)_5$	1.44	0.86
$W(CO)_5$	1.52	0.90
Tc(^{t}Bu-NC)$(dppe)_2$	1.34	0.99
$Re(N_2)(dppe)_2$	1.20	0.74
Re(CNMe)$(dppe)_2$	1.19	0.93
Fe(H)$(dppe)_2$	1.04	1.0
Mo(NO)$(dppe)_2$	0.91	0.51
TcH$(dppe)_2$	0.34	4.0
Mo(CO)$(dppe)_2$	−0.11	0.72
$Mo(N_2)(dppe)_2$	−0.13	0.84
Mo(PhCN)$(dppe)_2$	−0.40	0.82
$Mo(N_3)(dppe)_2$	−1.00	1.0
Re(Cl)$(dppe)_2$	0.41[b]	1.88[b]
[Re(Cl)$(dppe)_2$]$^+$	1.42	1.30
Trans-[FeBr(depe)$_2$]$^+$	1.32	1.10
Trans-[FeBr(depe)$_2$]$^{2+}$	1.98	1.30

[a] dppe = 1,2-diphenylphosphinoethane, depe = 1,2-diethylphosphinoethane.

Although the P_L model was initially proposed for a series of closed-shell, 18-electron, octahedral complexes with a single varying ligand coordinated to a 16-electron metal center, its extension to systems with two or three varying ligands, at 14 or 12 metal binding centers,[33] or to square–planar 16-electron complexes[34] has been proposed.

2.19.4 LIGAND ELECTROCHEMICAL PARAMETERS—(LEVER PARAMETERS)

The ligand electrochemical parameter E_L(L) introduced in 1990[6] has proven to be the most popular methodology for handling problems in electrochemistry as indicated by a very much higher citation rate for E_L(L) than for P_L or the Bursten model. A recent review[1] provides an in-depth assessment of the model.

The $E_L(L)$ parameters are defined via the reversible $E_{1/2}[Ru^{III}/Ru^{II}]$ couple such that for a general complex Ru(UVWXYZ) the observed $E_{1/2}[Ru^{III}/Ru^{II}]$ potential versus NHE is given by

$$E_{1/2}[Ru^{III}/Ru^{II}] = E_L(U) + E_L(V) + E_L(W) + E_L(X) + E_L(Y) + E_L(Z) = \Sigma E_L(L) \quad (8)$$

Through a statistical analysis of the very large number of $E_{1/2}[Ru^{III}/Ru^{II}]$ redox couples which have been reported in the literature, and making use of Hammett relationships, vide infra, $E_L(L)$ values for many hundreds of ligands are available. $E_L(L)$ parameter value ranges are shown in Table 3 and detailed data are shown in[1,44] and on the Lever website.[46] Several authors have published tables of additional $E_L(L)$ data, including[45,47]. Relationships have been developed between Hammett substituent constants ($\sigma(R)$) and the E_L parameters such that $E_L(L)$ parameters for substituted ligands can be extrapolated from the $E_L(L)$ value of the parent ligand via application of Hammett relationships, namely:[48] (Table 4), viz: (R_p is the so-called reaction parameter) (Equation (9)):

$$E_L(RL) = 2.303(RT \ln F)R_p\sigma(R) + E_L(HL) = f'\sigma(R) + E_L(HL) \quad (9)$$

Table 3 Ligand electrochemical parameters for typical ligands, V. vs. NHE.[1,27,39,41,44,45]

Alkyls, aryls, methyl, phenyl, NO^-, etc.
−0.90 to −0.70
Most anions, including organic carboxylates, SiH_3^-, MeO^-, MeS^-, etc.
−0.70 to 0
Saturated amines and weakly π-accepting amines, carbenes
0 to + 0.25
Unsaturated amines, pyridines, bipyridines, pyrazines, etc.
+0.1 to +0.4
Hard thioethers, softer phosphines, nitriles
+0.35 to +0.5
Isocyanides,[a] softer phosphites, harder phosphines, arsines, stibines, vinylidenes[a]
+0.4 to +0.65
Harder phosphites
+0.65 to +0.75
Dinitrogen, organic nitrites, PCl_3, PF_3, etc.
+0.7 to +0.95
Positively charged ligands, π-acid olefins, carbon monoxide[a]
>+0.9
Carbynes
ca +1.2
Nitrosonium[a]
>+1.5

[a] Generally non-innocent and subject to some variation depending on the π-donicity of the central metal ion.

Table 4 Ligand electrochemical parameters, $E_L(RL)$ and Hammett, $\sigma\rho$, relationships.[49]

Ligand Group	*Reaction parameter, S'_M*	*Parent $E_L(LH)$*	R^a
R-BQDI[b]	0.17	0.26	0.98
R-Phosphines, σ^*	0.17	0.35	0.95
R-Pyridines, $\Sigma\sigma$[c]	0.13	0.24	0.95
R-Bipyridines, $\Sigma\sigma$	0.07	0.25	0.99
R-Diketones, σ^+	0.12	0.01	0.98
R-Salen[d]	0.21	−0.14	1.00
Direct, σ_p[e]	0.62	−0.37	0.95

[a] Regression coefficient [b] *o*-benzoquinonediimine [c] $\sum\sigma = \sigma_p + \sigma_m$ as necessary [d] Based on a limited data set in ref. 50 [e] for substituents acting directly as ligands, e.g., Cl^-, H^-, etc.

The Lever ligand electrochemical parameter theory can be applied to any metal couple via the following expression (10):

$$E_{1/2}[M^{n+1}/M^{n+}] = S_M \Sigma E_L(L) + I_M \quad (10)$$

Redox potentials are related to the ratio of the stability constants for binding of the ligands to the metal ions in the two oxidation states. The S_M for a given couple then reflects how the ratio for that couple compares with the ratio for the $E_{1/2}[Ru^{III}/Ru^{II}]$ couple. As a consequence the S_M value depends on the spin states associated with each oxidation state, and will also depend on the stereochemistry. Thus the S_M value for $E_{1/2}[Fe^{III}(hs)/Fe^{II}(hs)]$ is different from that for $E_{1/2}[Fe^{III}(ls)/Fe^{II}(ls)]$ or for $E_{1/2}[Fe^{III}(hs)/Fe^{II}(ls)]$, etc. (hs = high spin, ls = low spin) and will differ for four- or five-coordinate versus six-coordinate species. The I_M parameter is a function of the difference in free energy of solvation for the pair of ions concerned (differential solvation energy), of the gas phase redox potential for the free ions involved, and trivially from the reference electrode used. The differential solvation energy term also influences S_M since, for example, the slopes for the $Ru^{III/II}$ couples in organic solvents and in water differ appreciably.

The net charge on the complexes, e.g., $[Os(en)_3]^{2+}$ versus $Os(en)_2Cl_2$ versus $[Os(CN)_6]^{4-}$ appears not to be a factor when the reversible potentials are recorded in an organic solvent, i.e., all these species would have the same S_M and I_M values for a given couple. However, there are some exceptions where solvation effects are more important, e.g.,[51–57] In general, solvatochromic species (see Chapter 2.27) may show deviations whereby the redox potential will be dependent on the solvent employed.[58–60]

Solvation effects are crucially important for data recorded in water phase wherein we can certainly expect different S_M, I_M values for different net charges for the same metal redox couple. Thus, systems of different net charge, when studied in water, should be independently analyzed.

This model has proven very effective for a wide range of Werner-type classical and organometallic species.[44] Some problems arise in the latter class where stereochemistry can be a factor, i.e., isomers of different stereochemistry having rather different redox potentials. This appears to be particularly troublesome with certain strongly π-bonding ligands such as carbonyls, isonitriles, carbenes, vinylidenes, etc.[33,35,41,44] In these cases it is preferable to adopt a correction following the methodology of Bursten described above (Equation (5)).[2,61]

Thus, for a carbonyl species, one may write Equation (11):

$$E_{1/2}[M^{n+1/n}] = S_M \Sigma E_L(L) + I_M + cx \quad (11)$$

where cx is as in Equation (2). (Unfortunately, this correction was termed "mx" in ref. 44 but with m being what is defined as "x" here and "x" being defined as c here. We have changed to the terminology used by Bursten to be consistent with Equation (2)). If a complex contains two (or more) types of strongly π-accepting ligand, such as isonitrile and carbonyl, then further corrections, $m'x'$ can be added to Equation (11). The value of "x" (and x', etc.) follows directly from the stereochemistry (see[1,2,44]) while the value of "c" was determined empirically as a best fit to sets of data for various $M^{n+1/n}$ potentials. Typically, such corrections are of the order of 0–0.3 V so that they can be significant (see footnote to Table 3[44]).

Most studies have involved six-coordinate species where the electron being removed during oxidation has originated from the t_{2g} (in O_h) non-bonding or pi-bonding set. There is no reason to suppose that the model would not also apply to complexes with other coordination numbers and indeed has been demonstrated to be valid for 4- and 5-coordinate rhodium(I) species.[34]

The model has also been extended to sandwich organometallic species[1,47,62] $M(\pi\text{-L})_2$ (e.g., π-L = arenes, cyclopentadienyls, etc.), however with the difference that the scale is based on the Fe^{III}/Fe^{II} couple due to the lack of a sufficient number of ruthenium sandwich species with reversible redox couples. The magnitudes of the $E_L(\pi\text{-L})$ values cover a wide range (Table 5) and depend critically on a simple net charge/atom calculation, i.e., (charge on π-L)/(no. of coordinating atoms) (Figure 1[1,63]). An extensive range of substituted cyclopentadienes and arenes, etc. can be analyzed by adding a Hammett parameter correction (vide infra). Regression lines for a range of redox couples have been reported.[1,62,63] For clarity in the discussion below, the slopes and intercepts of these correlations are defined as S_M^{Fe} and I_M^{Fe} because they are based on a $Fe^{III/II}$ standard and not a $Ru^{III/II}$ standard.

The redox potentials of half-sandwich species,[62,64] e.g., $M(\pi\text{-L})X_n$, can be rationalized using a combination of $E_L(L)$ and $E_L(\pi\text{-L})$ values.

Table 5 Ranges of sandwich ligand $E_L(\pi\text{-L})$ values, V vs. NHE.

η^4-$C_4Ph_4^{2-}$	−1.59
Substituted Cyclopentadienes	−0.04 to +0.75
Substituted Arenes	+1.6 to +2.6
η^7-$C_7H_7^+$	+3.62

[a] For full listing see.[1,62,63] Useful additional values can be derived from the data reported in.[65,66]

Thus, a large number of half-sandwich species can be written generally as $(\pi\text{-L})MX_n$, e.g., CpFe(dppe)Br or $(\eta^6\text{-}C_6H_6)Cr(CO)_2(PPh_3)$, etc. If one treats π-LM as a "common core" for a series of species of the same metal center and oxidation state, e.g., $(\pi\text{-L})M(XYZ)$ (vary X, Y, Z) then the ligand parameter model can be used in the classical fashion, plotting the redox potentials against $\Sigma E_L(XYZ)$, generating a slope $S_{ML}{}^{Ru}$ and an intercept $I_{ML}{}^{Ru}$. Since the stereochemistry differs from regular octahedral, the slopes and intercepts of these correlations will not be the same as those for the same redox process in an octahedral environment. Conversely one may have a series $(\pi\text{-L})$ MX_n in which MX_n is the common constant core and the π ligand is varied. In this case good linear correlations are obtained when plotting the redox energy against $E_L(\pi\text{-L})$ with slope $S_{MX}{}^{Fe}$ and intercept $I_{MX}{}^{Fe}$ [62] (but differing in value from those obtained for $M(\pi\text{-L})_2$ sandwich species).

Combining these two observations, it is evident that a set of redox data for a general half-sandwich $(\pi\text{-L})M(XYZ)$ species will obey:[62]

$$E_{1/2}[M^{n+1/n}] = S_{ML}{}^{Ru}\Sigma E_L(XYZ) + S_{MX}{}^{Fe}\Sigma E_L(\pi\text{-L}) + I_{MLX} \tag{12}$$

A dataset for $E_{1/2}[Cr^{1/0}]$ potentials exhibited by $(\pi\text{-L})Cr(XYZ)$ species is shown in Figure 2.

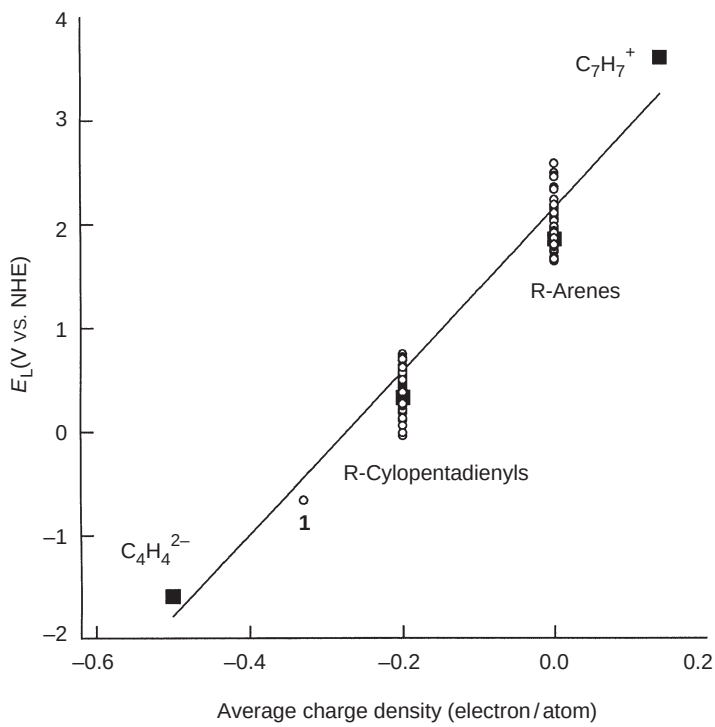

Figure 1 $E_L(\pi\text{-L})$ plotted against average charge density being defined as formal charge divided by number of coordinating atoms. The numbered ligand 1 is a carborane $[1,2\text{-}C_2(Et)_2B_4H_4]^{2-}$.

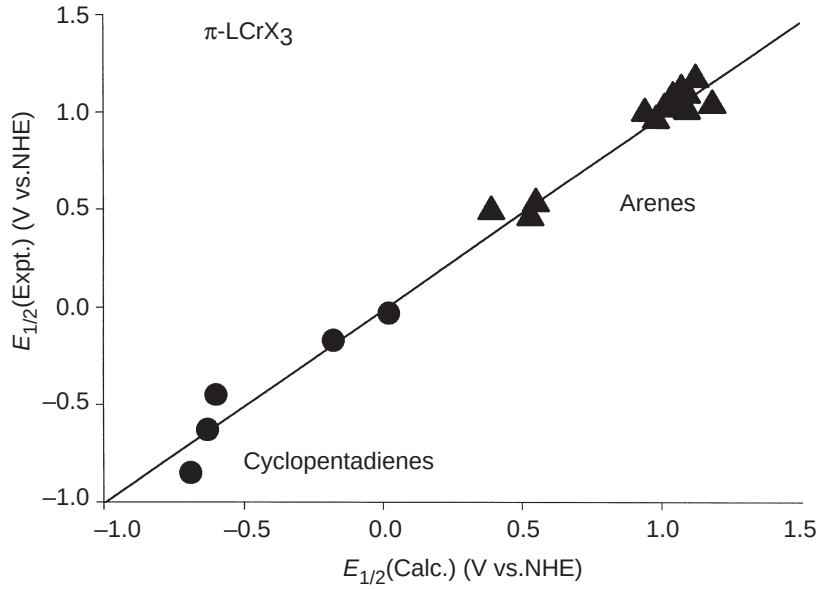

Figure 2 Observed $Cr^{III/II}$ potentials for some chromium half-sandwich species plotted versus the value calculated using Equation (12).

2.19.4.1 Relationship Between $E_L(L)$ and P_L

Since the P_L parameter is based on the potential changes when a carbonyl ligand is replaced by another ligand L, it should be linearly related to the $E_L(L)$ parameter; indeed, the appropriate expression is found, *experimentally*, to be (but vide infra):[1]

$$P_L = 1.17\ E_L(L) - 0.86\ (V)\ [24\ \text{species}, R = 0.996] \tag{13}$$

Equation (13) has been used fairly extensively[27,34,39,41] as a means to derive $E_L(L)$ values of ligands in somewhat esoteric organometallic species where only the P_L values can be directly derived. However, the relationship should be used with caution since a few ligands are known apparently to be ill-behaved in this correlation, carbonyl being one of them. Further, P_L values tend to be quite small and the relative error in using Equation (13) can be fairly high. It should also be evident that the E_s values of a core $[M_s]$ (e.g., $Mo(CO)_4Py$) as described in Section 2.19.3 can, in principle, be obtained by calculating the appropriate $M^{n+1/n}$ oxidation potential in $[M_s(CO)]$ (e.g., $Mo(CO)_5Py$)) using the available $E_L(L)$ parameters (plus appropriate corrections factors following Equation (11)). However, the $P_L = 0$ "point" (for L = CO) in a graph of $E[M_s^{n+1/n}]$ vs. P_L for a series $[M_sL]$ does not always lie on the best line through the other points (see, for example,[34,67]), possibly because of a need for the type of stabilization correction indicated in Equation (11). Thus, the E_s value (at $P_L = 0$) may not correspond precisely with $E_{1/2}[M_s(CO)]$. Because of these uncertainties, neither E_s nor β_L can be derived reliably from $E_L(L)$. Indeed the modus operandi of the P_L methodology is that it is extracting information out of more restricted sets of data than the usual $E_L(L)$ approach in order to look for more subtle variations in electronic structure. Thus, there should be no analytical relationship between E_L and P_L and Equation (13) is an approximation.

2.19.4.2 $E_L(L)$ Parameters and Reduction Potentials

Many ligands such as the polypyridines, quinones and quinonediimines, porphyrins and phthalocyanines, etc. can be reduced sequentially. Often, other ligands are attached to the metal center. These additional ligands influence the reduction potential at the reducible ligand in a systematic way that can be rationalized via the $E_L(L)$ parameter. For a reducible fragment $M^n(LL)$ in a complex, M(LL)WXYZ: we can write

$$E_{1/2}[LL^{0/-}(M^{n+})] = S_L \Sigma E_L(WXYZ) + I_L \tag{14}$$

where $E_{1/2}[LL^{0/-}(M^{n+})]$ is the reduction potential of LL^0 to LL^- when bound to M^{n+}. Note that we refer to a specific oxidation state, n^+, and that the behavior of LL bound to say, M^{n+1+}, will be different. S_L is an important parameter.[8] For example, if S_L is ca. 0, the reduction potential at the M(LL) site is independent of the other ligands WXYZ, i.e., there is no net transfer of electron density from these ligands to the M(LL) site—an improbable event, it would seem, but one which is approximately true for the $Mo(bpy)_2XY$ series where S_L is very small (0.06).[68] If S_L is large, then one may suppose that the M(LL) site is very polarizable and susceptible to the influence of the other ligands. Thus, S_L conveys information about coupling of the WXYZ ligands to the LL ligand via the metal center, or more precisely, the *relative* binding of the WXYZ ligands to LL in the LL and LL^- oxidation states.

I_L is also an interesting parameter. If binding of LL to the metal center has no effect upon its energy levels, $S_L = 0$, and I_L is the reduction potential of the free ligand. Thus, both S_L and I_L provide information about the extent of mixing between metal orbitals and the ligand reduction orbital. We may question whether Equation (14) is truly linear over a very wide range of $\Sigma E_L(L)$ values; data available suggest that it is, but a more detailed analysis could be profitable. One may wish to write a corresponding equation for ligand oxidation, $E_{1/2}[L^{+/0}]$, but this is trivial, because it is equivalent to using Equation (14) for a complex of the oxidized ligand.

2.19.4.3 Reduction Potentials Vs. Oxidation Potentials

Given that both the oxidation and reduction potentials can be written in terms of $\Sigma E_L(L)$ it should be true that within homologous series of complexes, E_{ox} and E_{red} must linearly correlate. This relationship has indeed been known experimentally for quite some time.[58,69–72] The equation for this linear correlation can be written:

$$E_{1/2}[LL^{0/-}(M^n)] = (S_L/S_M)E_{1/2}[M^{n+1/n}(LL)] + [I_L - (S_L/S_M)I_M - S_L d\Sigma E_L(LL)] \quad (15)$$

In Equation (15), LL is the ligand being reduced, d is the denticity of that ligand, and the term in square brackets is a constant for the given reducible ligand, LL. A table of these data is presented elsewhere.[1] The slopes do indeed equal (S_L/S_M) to within experimental error.

2.19.4.4 Redox Processes of Homologous Series of Ligand Fragments

Studies with substituted ligands (homologous series of ligands) can be very useful to reveal subtle changes in electrochemical behavior as a function of substituent. Coupled with computational techniques, such studies can yield detailed insight into metal–ligand interactions.

2.19.4.4.1 Reduction

In a homologous series of complexes such as $M^n(RL)X_5$ and $M^n(RLL)X_4$ maintaining X constant and varying R, and taking account of Equations (9), (10), and (14) it is clear that we can write Equation (15):

$$E_{1/2}[RL^{0/-}(M^n)] = df\sigma(R) + E_{1/2}[HL^{0/-}(M^n)] \quad (16)$$

which may be recast as Equation (17):

$$E_{1/2}[RL^{0/-}(M^n)] = (df/f')E_L(RL) + C \quad (17)$$

where $E_{1/2}[HL^{0/-}(M^n)]$ is the reduction potential of the parent ligand metal complex, in these examples, $[M(HL)X_5]^{n-}$ or $[M(HLL)X_4]^{n-}$ and will be a constant here, f and f' are reaction parameters indicating the sensitivity of the function to the variation in Hammett substituent parameter, and $\sigma(R)$ is an appropriate set of Hammett substituent constants.

There is an extensive literature pertaining to the observation that redox potentials in homologous series of complexes are linearly dependent upon a Hammett parameter $\sigma(R)$[36,50,73–95] (also see Table 2).[1]

Species of the type $[M(RLL)_2X_2]^{n+}$ and $[M(RLL)_3]^{n+}$ also generally obey Equations (15) and (16) which is rather surprising on reflection. Arguments can be made as to whether reduction

occurs at one RLL ligand site in a multi-RLL complex or whether the reduction process is delocalized over several RLL ligands. But the fact remains that the constant terms in Equations (15) and (16) should not be precisely constant in these multi-RLL (or multi-RL) species. With data currently available, they do appear to be essentially constant within the error of the experiment.

Similar correlations exist with metal-centered reduction processes as a function of ligand substituent.[96,97]

Compounds such as $[M(LL)X_4(RL)]^{n+}$ are interesting because they raise the issue of how 'tuning' the RL ligand will affect reduction at another ligand (LL), i.e., tuning the intra-ligand interactions in the molecule, Few investigations of M(LL) reduction potentials as a function of RL and X have been reported. The relevant equation (from Equations (9) and (14)) would simply be: [for given X]

$$E_{1/2}[LL^{0/-}(M)] = S_L f'\sigma(R) + C(\text{vary RL}) \tag{18}$$

$$= S_L f'' E_L(RL) + C'' \tag{19}$$

At first sight Equations (18) and (19) are independent of the X ligand provided X is kept constant. However, one might expect S_L to vary with X, in practice, if X does mediate and modify the coupling between RL and LL. Systematic studies of this type are virtually unknown but the complexes $[Re(bpy)(CO)_3(R\text{-}Py)]^+$ fall into this class.[66]

2.19.4.4.2 Oxidation

Tuning the metal-centered oxidation potentials of $M(RL)_xX_y$ species is essentially trivial since $E_L(RL)$ can be varied through Equation (10).

2.19.4.5 $E_L(L)$ Relationships with Non-electrochemical Parameters

Clot and co-workers[45] have explored relationships connecting the Tolman electronic parameters (TEP)[98] with other kinds of parameters. Like the ligand electrochemical parameters, the TEP values are believed to be a measure of the net donor power, σ and π, of the ligand. The Tolman parameters for a ligand L are based on the observed A_1 ν(CO) stretching frequency of the species $LNi(CO)_3$. These researchers also used density functional theory to computationally obtain A_1 ν(CO) values of $LNi(CO)_3$ species as means to determine if these parameters could be obtained by calculation instead of experiment, thereby expanding the range of possible structures to species not yet available in the laboratory. These computed electronic parameters (CEP) correlated extremely well with the experimental TEP values with the regression relationship:

$$\text{TEP} = 0.9572\ \text{CEP} + 4.081\ (\text{cm}^{-1}) \tag{20}$$

These authors then demonstrated a 'full transferability' between CEP/TEP and $E_L(L)$ through the relationships (21): ($E_L(L)$ in V vs. NHE, CEP/TEP in cm^{-1})

$$\begin{aligned} E_L(L) &= 0.01302\ \text{TEP} - 26.67 \\ &= 0.01246\ \text{CEP} - 26.62 \end{aligned} \tag{21}$$

As shown in Table 5[45] these relationships provide a very useful means to extend further the database of $E_L(L)$ values especially to ligands less commonly used in classical coordination chemistry, e.g., *t*-butyl ($E_L(L) = -0.90$ V), H_2S (0.43 V), SiH_3^- (−0.56 V) and a series of carbenes with $E_L(L)$ ca 0 − +0.2 V, etc.

However, these equations involve subtracting two relatively large numbers to obtain, in most cases, a rather small number for $E_L(L)$. Small errors are likely here but the final calculated redox potential may be seriously in error due to the need to multiply by 6 for an ML_6 species (see Figure 2[45]).

These authors also show how the Hammett parameter σ_m can be linked to $E_L(L)$ via Equation (22):

$$\sigma_m = 0.82\ E_L(L) + 0.60\ (E_L(L) \text{ in V vs. NHE}) \tag{22}$$

expanding on an earlier relationship with σ_p[49]

$$\sigma_p = 1.61\ E_L(L) + 0.60\ (E_L(L) \text{ in V vs. NHE}) \tag{23}$$

These equations should be used with caution as the regression coefficients are not sufficiently close to unity for high accuracy.

2.19.5 LIGAND ELECTROCHEMICAL PARAMETER THEORY APPLIED TO CLUSTERS

Several groups have explored whether the ligand electrochemical parameter model can be applied to clusters of ruthenium complexes, and by extension, to clusters of any metal ion. Toma first demonstrated that appropriate linear regressions could be obtained with a common cluster core to which various ligands could be substituted, i.e., $[Ru_3O(OAc)_6L_3]^{n+}$ [99,100] where, assuming three identical L ligands, the three ruthenium atoms are equivalent. Toma observed linear regressions for four successive oxidation processes beginning with the $Ru^{III,II,II}$ member of the redox series. The $E_{1/2}[Ru^{III,III,II/III,II,II}]$ regression exhibited a slope of 1.03 and therefore entirely equivalent to the monomeric $Ru^{III/II}$ process. However, significantly smaller slopes were observed with the higher oxidation state processes.[100]

An initial study of the electrochemistry of $(\mu\text{-H})_3Ru_3(\mu_3\text{-CX})(CO)_6L_3$ as a function of X and L[23,101] showed good agreement with the expression (a modification of Equations (9) and (10)):

$$E_{1/2}[M_3^{n+1/n}] = S_{M3}\Sigma E_L(L) + f''\sigma_p(X) + I_{M3} \tag{24}$$

with an observed S_{M3} of 0.37 consistent with the ligand effects being "equally" distributed over the three Ru atoms, i.e., the HOMO is delocalized over all three ruthenium atoms. The three Ru atoms are equivalent in most, though not all, of the species investigated.

Keister and colleagues[102] also explored the cluster $(\mu\text{-H})Ru_3(\mu_3\text{-}\eta^3\text{-XCCRCR}')(CO)_{9-n}(PPh_3)_n$ where the three ruthenium atoms are not equivalent and where one might be able to discern rather different behavior depending upon the regiochemistry of ligand substitution and also the percentage contribution of each Ru atom to the HOMO. Thus, more subtle behavior could be anticipated. The HOMO in this last case does involve metal–metal bonding while it does not in the Toma cluster.

2.19.6 CHARGE TRANSFER SPECTROSCOPY

Charge transfer spectra involve an electron being excited from an orbital mainly localized on the metal to one mainly localized on the ligand, so-called metal to ligand charge transfer (MLCT) or vice versa, ligand to metal charge transfer (LMCT).[103,104]

Since an MLCT excitation effectively involves oxidation of the metal and reduction of the ligand (or vice versa for LMCT), i.e., for example, a formal ground state $M^{II}L$ generates an MLCT excited state $M^{III}L^-$, it has long been known that these charge transfer energies should correlate with electrochemical potentials.[105,106]

Consider an excitation to an MLCT excited spin singlet state which can be formally described as $[M^{III}L^-]^*$ where the asterisk indicates a Franck–Condon (FC) state, i.e., a vibrationally excited electronic state having the same nuclear coordinates as the ground state species:

$$M^{II}L \rightarrow [M^{III}L^-]^* = h\nu(\text{MLCT}) \tag{25}$$

This FC state can relax to the vibrationally equilibrated (relaxed) excited state, $[M^{III}L^-]$. These two energy states are related, written as free energies via:

$$\Delta G^o[M^{III}L^-]^* = \Delta G^o[M^{III}L^-] + \chi_i + \chi_o \tag{26}$$

where χ_i is the inner-sphere reorganization energy, i.e., the FC vibrational excitation of the excited electronic state, and χ_o is the outer-sphere or solvent reorganization energy.[25] The term χ_o arises because the solvent environment around the excited state at the moment of electronic excitation corresponds to the equilibrium solvent environment of the ground state.

Consider the difference between two related half-cell redox potentials,

$$M^{II}L \rightarrow M^{III}L + e^- \qquad -E_{1/2}[M^{III/II}(L)] \tag{27}$$

$$M^{III}L + e^- \rightarrow M^{III}L^- \qquad E_{1/2}[L^{0/-}(M^{III})] \tag{28}$$

or an alternative pair:

$$M^{II}L + e^- \rightarrow [M^{II}L]^- \qquad E_{1/2}[L^{0/-}(M^{II})] \tag{29}$$

$$M^{II}L^- \rightarrow [M^{III}L^-]^- + e^- \qquad -E_{1/2}[M^{III/II}(L^-)] \tag{30}$$

Adding Equations (27) and (28) (or (29) and (30) yields the energy of the transition to the vibrationally relaxed excited state, in terms of half-cell potentials as:

$$M^{II}L \rightarrow M^{III}L^- \qquad h\nu[MLCT]$$

$$E_{1/2}[L^{0/-}(M^{III})] - E_{1/2}[M^{III/II}(L)] = E_{1/2}[L^{0/-}(M^{II})] - E_{1/2}[M^{III/II}(L^-)] = -\Delta E'(\text{Redox}) \tag{31}$$

Since the free energy is related to an electrochemical potential via $\Delta G^0 = -nFE$ the several equations can be combined to write (all data in eV):[107]

$$h\nu(MLCT) = \Delta E'(\text{Redox}) + \chi_o + \chi_I \tag{32}$$

We should write $nF\Delta E'$(redox) but writing it in eV, it is usually simplified to $\Delta E'$(Redox). Obviously, the orbitals involved in the optical process must be the same as those in the redox process. The charge transfer energy is an enthalpy whereas the redox potentials are Gibbs free energies, thus there is an implicit assumption that there is no significant entropy difference between the ground and excited state species.[108] Further, the optical transition should have a Gaussian band shape.[51] The solvation energies of the equilibrated ground and excited electronic state are included in both the optical and redox expressions, and so do not appear explicitly.

However, there is a serious practical problem involved in using these half cells. In each pair there is one that usually cannot be observed in a practical electrochemical experiment, i.e., Equations (28) and (30). For example, the electrochemical reduction of $M^{III}L$ to $[M^{III}L^-]^-$ cannot usually be observed because in most situations the metal would be reduced first to $[M^{II}L]^-$ with subsequent reduction of the ligand to form $[M^{II}L^-]^{2-}$ not $[M^{III}L]^-$.

Thus, it is very much more common to report correlation between hν(CT) and the *electrochemically observable* ΔE*(redox)*, i.e., in our example:

$$\Delta E(\text{Redox}) = E_{1/2}[M^{III/II}(L)] - E_{1/2}[L^{o/-}(M^{II})] \tag{33}$$

where the second term on the right refers to ligand reduction/oxidation attached to $M^{II}L$, not $M^{III}L$ as in Equation (28). In this situation the various solvation energies do *not* cancel from the optical and redox terms and must be explicitly considered. However, their total sum is frequently quite small so that the measured ΔE(Redox) often gives a good approximation of the CT band energy, typically to within about 0.3 eV.

The explicit relationship linking the measurable ΔE(Redox) to $h\nu$(CT) was developed by Dodsworth and Lever[58] (data in eV): (e.g., for an MLCT band)

$$h\nu(MLCT) = [\chi_i + \Delta E(\text{Redox}) + \Delta\Delta G_s + Q] + \chi_o + \Delta_{sol} \tag{34}$$

where Q is discussed below, Δ_{sol} is the difference in solvation free energy between the relaxed excited state and the ground state, and $\Delta\Delta G_s = [2\ \Delta G^0{}_s - \Delta G^0{}_s{}^+ - \Delta G^0{}_s{}^-]$ (difference between

twice the ground state and oxidized and reduced species free energies of solvation).[1,58] The term in brackets is solvent independent because of cancellation within ΔE(Redox). This expression (34) refers to a transition to the spin singlet state, and assumes the HOMO and LUMO of the complex are involved in both the optical transition and the redox process. In some cases, the actual intense optical CT transition may actually be HOMO-1 or HOMO-2 → LUMO, but if the (HOMO)-(HOMO-2) splitting is small, as it usually is, the system may still appear well-behaved. This analysis also assumes that the optical transition is pure, i.e., that there is no significant configuration interaction between the CT excited state and other states of the same symmetry, nor should there be mixing with other states due to spin–orbit coupling. The entropy difference between the ground and excited states is also assumed to be negligible in the MLCT transition.

Written in a simplified form:

$$h\nu(\mathrm{CT}) = \Delta E(\mathrm{Redox}) + C \tag{35}$$

This equation is by far the most commonly used expression almost invariably relating the lowest-energy intense visible region charge transfer transitions to differences in the first oxidation and reduction electrochemical potentials.[1,53,58,71,109,110] It has been used, for example, for a very large number of ruthenium(II), osmium(II), and rhenium(I) complexes where the terms collected in C sum approximately to $+0.2$ V.[1,6] Spin–orbit coupling can play a significant role in the energetics of osmium and rhenium species, but Equation (35) appears to remain generally valid. It is most useful in analyzing new data where one has tentatively assigned the redox processes and optical charge transfer transitions, to provide numerical evidence that the various assignments are correct.

However, there can be deviations from this simple situation, especially cases where C is substantially larger than $+0.2$ V or, conversely, can even be negative such that the charge transfer band lies at a lower energy than the value of ΔE(Redox). Excluding special cases such as solvatochromic species, the reason for this appears to involve the term Q in Equation (34). Q has been discussed by several authors.[53,111] We express Q in the form:[1]

$$Q = 2\ K_{\mathrm{d,L}} - J_{\mathrm{d,L}} + \Sigma E \tag{36}$$

where $K_{\mathrm{d,L}}$ and $J_{\mathrm{d,L}}$ are the exchange and Coulomb terms involved in the excitation and ΣE is net change in energies of all the orbitals in the ground and excited states.

A larger value of C been shown to be the case, for example, when the states involved in the excitations are heavily mixed, i.e., when instead of a 'simple' MLCT charge transfer band which may be described by $\Psi_{\mathrm{d}} \rightarrow \Psi_{\mathrm{L}\pi^*}$, extensive mixing between the specific *d*-orbital involved in the transition and the terminating ligand π^*-orbital leads to a transition which can be better described as $\Psi_{\mathrm{d+L}\pi^*} \rightarrow \Psi_{\mathrm{L}\pi^*-\mathrm{d}}$. This transition, while generally called charge transfer, in fact will involve relatively little actual net transfer of charge and therefore the excited electron remains relatively close to the metal center. The smaller net charge transfer distance of similar strongly coupled species has been directly measured via electroabsorption (Stark) measurements[57,112] (and see Chapter 2.23). This situation can lead to an exceptionally large value of $K_{\mathrm{d,L}}$[48,72] and hence to a larger value of Q leading to an increased value of the constant C in Equation (34).

It has not been common practice in the past to use Equation (34) to describe the properties of spin or orbitally forbidden charge transfer bands primarily because most researchers do not bother to search for, or record, such transitions which will be very weak and difficult to observe. Nevertheless there is useful information to be derived from such studies. With *o*-benzoquinonediimine-type ligands such forbidden and very weak transitions have been observed substantially to the red of the intense visible region CT absorption.[48,113,114] Unlike the previous example, these transitions involve a *d*-orbital which is *not* coupled to the terminating Lπ^*, they will have significantly more charge transfer character, and a relatively much smaller value for $K_{\mathrm{d,L}}$.[48,115] This small value of K contributes to a relatively smaller value of Q and can generate a negative value of C in Equation (35).

2.19.6.1 Other Correlations Between Electrochemical Potentials and Optical Transition Energies

Since ΔE(Redox) is a difference in metal oxidation and ligand reduction (or vice versa) and since both the potentials can be written in terms of ΣE_{L}(L), there must also be linear correlations between $h\nu$(CT) and metal oxidation or ligand reduction potentials (or vice versa) and also

between $h\nu$(CT) and a suitable function of E_L(L). Correlations of this nature are discussed in depth elsewhere[1] with extensive tables of data. Only a brief summary is presented here. These correlations may not always be valid, e.g., with solvatochromic species, or where different geometric isomers exist with significantly different E_{ox} data.

2.19.6.1.1 $h\nu$(MLCT) *vs.* E_{ox} or ΣE_L(L)

In a series of complexes M^n(LL)WXYZ, the energy of the lowest energy intense MLCT band associated with the M–LL fragment can be written as a function of varying WXYZ versus $E_{1/2}$ [$M^{n+1/n+}$] or ΔE_L(L) as:

$$h\nu(\text{MLCT}) = (S_M - S_L)\Sigma E_L(\text{WXYZ}) + C \tag{37}$$

$$= (S_M - S_L)E_{1/2}M^{n+1/n+} + C' \tag{38}$$

where S_L applies to the specific M^n(LL) fragment (see Equation (14)) and S_M to the specific M^{n+1}/M^n process. For $Ru^{III/II}$, ($S_M = 1$, in organic phase) the equation simplifies to:

$$h\nu(\text{MLCT}) = (1 - S_L)\Sigma E_L(\text{WXYZ}) + C = (1 - S_L)E_{1/2}M^{n+1/n+} + C' \tag{39}$$

A significant body of data exists showing the validity of this analysis.[1] Indeed, the correlation is generally excellent. For example, a very extensive early analysis of Ru^{II} bipyridine complexes[58] revealed that the $Ru^{II} \rightarrow \pi^*$ bpy MLCT band energy follows: (data in eV)

$$h\nu(\text{Ru} \rightarrow \pi^* \text{ bpy}) = 0.65E_{1/2}[Ru^{III/II}] + 2.0 \tag{40}$$

which is a very useful relationship. Obviously the analysis could be used to derive S_L if not otherwise available but since this is usually a fairly small number (ca. 0.25), a relatively large dataset is required for reasonable accuracy. For example, data reported for a series of Fe^{II} complexes[1] reveal rather higher slopes ($= S_M - S_L$) suggesting values of S_L smaller than those associated with Ru^{II} or Os^{II} which would be consistent with lesser covalency in the Fe^{II} systems, i.e., less coupling between reducible ligands and spectator ligands. Second order effects such as, for example, significant mixing of orbitals on WXYZ with LL π^*-orbitals, may be expected to cause deviations from linearity in this expression especially if the metal center is very strongly coupled to the LL reducible ligand. Thus, future studies should focus on systems where deviations can be expected.

An interesting series of complexes to study intra-ligand coupling mediated by the metal ion would be species of the general class $[M(LL)X_4(R\text{–}L)]^{n+}$ where the M → LL charge transfer band could be monitored as a function of R–L. Such series are very rare (e.g., $[Re(bpy)(CO)_3(R\text{-}Py)]^{+}$[116]). As anticipated, the $h\nu(\text{Re} \rightarrow \pi^* \text{ bpy})$ transition is linearly dependent on σ_p(R) (Table 2[1]).

2.19.6.1.2 $h\nu$(MLCT) *vs.* E_{ox} *or* ΣE_L(L) *in* M(R-L)X_5 *species*

There are fairly extensive data for $[MX_5(R\text{–}L)]^{n-}$ species where M is commonly Fe^{II}, Ru^{II}, and Os^{II}, X is commonly NH_3 or CN^-, and R–L is a reducible pyridine, pyrazine, or related species. Reduction potentials localized at the R–L ligand are rarely reported, but plots of $E_{1/2}[M^{n+1/n}(RL)]$ versus the M d → π^* R–L MLCT band are frequently linear. The required equation is:

$$h\nu(\text{MLCT}) = (1 - (f/(S_M df')))E_{1/2}[M^{n+1/n}(RL)] + C \tag{41}$$

where d is the denticity of the acceptor ligand (1 in this specific case), and the f, f' parameters are from Equations (9) and (16). The factor $f/(S_M xf')$ usually exceeds 1 so that the slope of this correlation will usually be negative. Thus, we have the counter-intuitive observation that as the oxidation potential at the metal site increases, the MLCT transition red shifts. This is readily explained through the slope factors in Equation (41).

A problem with this analysis is that the spread in E_L(R–L) values with R, and hence the range of $E_{1/2}[M^{n+1/n}(RL)]$, is rather limited. The differential solvation contributions are subsumed into

the constant C, and, for linearity, must remain essentially constant for all the members of the series. In practice, plots with these kinds of system tend to be rather scattered over a narrow potential range.[74,76,117,118]

2.19.6.1.3 $h\nu$(MLCT) *vs.* E_{red} *in* $[M(LL)(WXYZ)]^{n+}$ *type complexes*

Clearly, in view of the previous analyses, $h\nu$(MLCT) will correlate with E_{red}. However, the range of variation of $E_{1/2}(bpy^{0/1-})$ with XY in a series such as $M(bpy)_2XY$ is much smaller than the corresponding range in $E_{1/2}(Ru^{III/II})$, so that the statistics are poorer. This correlation should only be used where E_{ox} data are unavailable. However, since E_{ox} can usually be calculated via $E_L(L)$, there is little more understanding to gain by pursuing the E_{red} analysis. A negative slope is anticipated.[1]

2.19.6.1.4 $h\nu$(LMCT) *vs.* $E[M^{n+/n}(L)]$ *and* ΔE(Redox)

In species in which the central metal ion is in a higher oxidation state, LMCT transitions are anticipated. It would be the case here that electrochemical oxidation primarily involves the ligand and reduction involves the metal. A correlation essentially identical to Equation (35) is therefore expected. However, the observation of reversible ligand electrochemical oxidation is not very common. A few examples[119,120] confirm our expectation though in the case of the zirconium metallocenes[121] the slope is 1.39, implying that the situation is rather more complicated than indicated by Equation (35) (however, the oxidation process is irreversible).

The reduction potential of the metal is usually available, or may be calculated and the relevant equation is:[1]

$$h\nu(\text{LMCT}) = ((S_L/S_M) - 1)E_{1/2}[M^{n+1/n}(L)] + C \tag{42}$$

and which, in principle, allows estimation of the value of S_L for the oxidized ligand (see Section 2.19.4.2). Since it is very likely that S_L/S_M is less than unity, $h\nu$(LMCT) should shift to the red with increasing positive $E_{1/2}(M^{n+1/n})$, which is what one intuitively expects for an LMCT transition and is observed in the few examples listed in Table 13[1] (e.g., $Ir^{IV}-Cl$)[121,122]. Slopes are negative as anticipated by this analysis. Equation (42) leads one to suppose that a situation may arise where $S_L > S_M$ and hence the slope is positive even though the process is LMCT. The ramifications of such an observation are interesting but premature in the absence of appropriate experimental data.

2.19.7 EMISSION DATA

Literature examples of correlations between emission energies and electrochemical potentials are rare and such correlations are often scattered.[123] The emission CT band often displays vibrational components, and frequently shows marked medium and certainly temperature dependence. Ideally one requires the E_{00} transition, i.e., radiative relaxation from the relaxed excited state to the ground state $v = 0$ level, but this is often not identified or reported or is assumed as a high-energy shoulder without proof.

2.19.8 CONCLUSIONS

The ligand electrochemical parameters provide a powerful arsenal to coordination chemists. They have the mundane though still important use that one can 'double check' that one has correctly assigned a voltammogram, i.e., have properly identified the redox processes by seeing if their locations agree with the predictions of the model. Clearly the cross-checking can also be extended to the major low-energy charge transfer transitions using the relationships described above.

A second major application is in design – the ability to synthesize a molecule with predetermined redox potentials or spectroscopic absorption. For example, by using a selection of different ligands attached to the central ion, fine tuning of the electrochemical potentials and optical spectrum can be achieved.[124–126]

A third application lies in assessing the σ- and π-bonding characteristics of the ligands themselves. The numerical value of $E_L(L)$ is a property of the ligand and, for "innocent" ligands, is independent of the metal to which the ligand is bound. The more positive the value, the greater is the π-accepting property and the less the σ-donating ability of the ligand. However, for so-called "non-innocent" ligands such as nitrosyl(1+) and quinonoid ligands, the value of $E_L(L)$ can change according to the degree of electronic coupling with the central metal ion.[8,127] Isonitrile ligands can bind in a "non-innocent" manner such that the M—N—C—R bond may be linear or bent and give rise to different effective $E_L(L)$ values.[1,27,36,44] Carbon monoxide can effectively change its $E_L(L)$ value in the sense that corrections of the type illustrated in Equation (11) may have to be employed for strongly π-donating metal centers.

There are "gaps" in the $E_L(L)$ literature which need to be filled in the future. Relatively little attention has been paid to asymmetric polydentate ligands, i.e., ligands with different coordinating sites, e.g., Schiff bases (for example[50] but see[47]). Further, most of the $E_L(L)$ data involves redox processes where oxidation or reduction involves a change in the number of π-bonding, π-anti-bonding, or non-bonding *d*-electrons rather than σ–anti-bonding electrons[34] due to the absence of systematic datasets of reversible processes.

2.19.9 REFERENCES

1. Lever, A. B. P.; Dodsworth, E. S. *Inorganic Electronic Structure and Spectroscopy*; John Wiley & Sons: New York, 1999, pp 227–290.
2. Bursten, B. E.; Green, M. R. *Progr. Inorg.Chem.* **1988**, *36*, 393–485.
3. Pickett, C. J.; Pletcher, D. *J. Organomet. Chem.* **1975**, *102*, 327–333.
4. Chatt, J.; Kan, C. T.; Leigh, G. J.; Pickett, C. J.; Stanley, D. R. *J. Chem. Soc. Dalton* **1980**, 2032–2038.
5. Chatt, J. *Coord. Chem. Rev.* **1982**, *43*, 337–348.
6. Lever, A. B. P.; Gorelsky, S. I. *Coord. Chem. Rev.* **2000**, *208*, 153–168.
7. Lever, A. B. P. *Inorg. Chem.* **1991**, *30*, 1980–1985.
8. Gorelsky, S. I.; Lever, A. B. P.; Ebadi, M. *Coord. Chem. Rev.* **2002**, *230*, 97–105.
9. Bursten, B. E. *J. Am. Chem. Soc.* **1982**, *104*, 1299–1304.
10. Bursten, B. E.; Green, M. R.; Katovic, V.; Lightner, D. Jr. *Inorg. Chem.* **1986**, *25*, 831–834.
11. Treichel, P. M.; Mueh, H. J.; Bursten, B. E. *Isr. J. Chem.* **1977**, *15*, 253–257.
12. Sarapu, A. C.; Fenske, R. F. *Inorg. Chem.* **1975**, *14*, 247–253.
13. Gassman, P. G.; Mullins, M. J.; Richtsmeier, S.; Dixon, D. A. *J. Am. Chem. Soc.* **1979**, *101*, 5793–5797.
14. Tsai, E. W.; Throckmorton, L.; McKellar, R.; Baar, M.; Marynick, D. S.; Rajeshwar, K.; Ternay, A. L., Jr. *J. Electroanal. Chem. Interfacial Electrochem.* **1986**, *210*, 45–67.
15. Hoijtink, G. J. *Rec. Trav. Chim. Pays-Bas.* **1958**, *77*, 555.
16. Zweig, A.; Hodgson, W. G.; Jura, W. H. *J. Am. Chem. Soc.* **1964**, *86*, 4124–4129.
17. Zweig, A.; Lancaster, J. E.; Neglia, M. T.; Jura, W. H. *J. Am. Chem. Soc.* **1964**, *86*, 4130–4136.
18. Lyons, L. J.; Pitz, S. L.; Boyd, D. C. *Inorg. Chem.* **1995**, *34*, 316–322.
19. Gorelsky, S. I.; Lever, A. B. P. unpublished observations.
20. Yang, Y. F.; Arias, F.; Echegoyen, L.; Chibante, L. P. F.; Flanagan, S.; Robertson, A.; Wilson, L. J. *J. Am. Chem. Soc.* **1995**, *117*, 7801–7804.
21. Barigelletti, F.; Juris, A.; Balzani, V.; von Zelewsky, A. V. *Inorg. Chem.* **1987**, *26*, 4115–4119.
22. Baik, M. H.; Ziegler, T.; Schauer, C. K. *J. Am. Chem. Soc.* **2000**, *122*, 9143–9154.
23. Bierdeman, D. J.; Keister, J. B.; Jelski, D. A. *J. Organomet. Chem.* **2001**, *633*, 51–65.
24. Schaeffer, C. E.; Jorgensen, C. K. *Molec. Phys.* **1965**, *9*, 401–415.
25. Lever, A. B. P.; Solomon, E. I. *Inorganic Electronic Structure and Spectroscopy*, Solomon, E. I.; Lever, A. B. P., Eds.; John Wiley & Sons: New York, 1999, p 1–92.
26. Butler, G.; Chatt, J.; Leigh, G. J.; Pickett, C. J. *J. Chem. Soc. Dalton* **1979**, 113–116.
27. Pombeiro, A. J. L. *New J. Chem.* **1997**, *21*, 649–660.
28. Wang, Y.; Pombeiro, A. J. L.; Kaden, L.; Wahren, M. *Molecular Electrochemistry of Inorganic, Bioinorganic and Organometallic Compounds*; Kluwer Academic Publishers: Dordrecht, 1993.
29. Lopes, L. G. F.; Gomes, M. G.; Borges, S. S. S.; Franco, D. W. *Aust. J. Chem.* **1998**, *51*, 865–866.
30. Morris, R. H. *Inorg. Chem.* **1992**, *31*, 1471–1478.
31. Venancio, A. I. F.; Kuznetsov, M. L.; Guedes da Silva, M. F. C.; Martins, L. M. D. R. S.; Frausto da Silva, J. J. R.; Pombeiro, A. J. L. *Inorg. Chem.* **2002**, *41*, 6456–6467.
32. Lemos, M. A. N. D. A.; Pombeiro, A. J. L. *J. Organometal. Chem* **1992**, *438*, 159–165.
33. Pombeiro, A. J. L. *Inorg. Chim. Acta* **1985**, *103*, 95–103.
34. Guedes Da Silva, M. F. C.; Trzeciak, A. M.; Ziolkowski, J. J.; Pombeiro, A. J. L. *J. Organomet. Chem.* **2001**, *620*, 174–181.
35. Ribeiro, M. T. A.; Pombeiro, A. J. L.; Facchin, G.; Mozzon, M.; Michelin, R. A. *Molecular Electrochemistry of Inorganic, Bioinorganic and Organometallic Compounds*; Kluwer Academic Publishers: Dordrecht, 1992.
36. Pombeiro, A. J. L.; Pickett, C. J.; Richards, R. L. *J. Organomet. Chem.* **1982**, *224*, 285–294.
37. Carvalho, M. F. N. N.; Pombeiro, A. J. L.; Hills, A.; Hughes, D. L.; Richards, R. L. *J. Orgmet. Chem.* **1994**, *469*, 179–187.
38. Carvalho, M. F. N. N.; Pombeiro, A. J. L. *J. Chem. Soc., Dalton* **1989**, 1209–1216.
39. Guedes da Silva, M. F. C.; Martins, L. M. D. R. S.; Da Silva, J. J. R. F.; Pombeiro, A. J. L. *Coll. Czech. Chem. Comm.* **2001**, *66*, 139–154.

40. Carvalho, M. F. N. N.; Pombeiro, A. J. L. *J. Organomet. Chem.* **1991**, *410*, 347–355.
41. Almeida, S. S. P. R.; Pombeiro, A. J. L. *Organometallics* **1997**, *16*, 4469–4478.
42. Facchin, G.; Mozzon, M.; Michelin, R. A.; Ribeiro, M. T. A.; Pombeiro, A. J. L. *J. Chem. Soc.–Dalton Transactions* **1992**, 2827–2835.
43. Kaden, L.; Pombeiro, A. J. L.; Wang, Y.; Abram, U. *Inorg. Chim. Acta* **1995**, *230*, 189–192.
44. Lever, A. B. P. *Inorg. Chem.* **1990**, *29*, 1271–1285.
45. Perrin, L.; Clot, E.; Eisenstein, O.; Loch, J.; Crabtree, R. H. *Inorg. Chem.* **2001**, *40*, 5806–5811.
46. Lever Web *http://www.chem.yorku.ca/profs/lever*.
47. Rocha, R. C.; Rein, F. N.; Toma, H. E. *Inorg. Chem. Commun.* **2002**, *5*, 891–896.
48. Gorelsky, S. I.; Lever, A. B. P. *Can. J. Appl. Spectry* **2003**, *48*, 93–105.
49. Masui, H.; Lever, A. B. P. *Inorg. Chem.* **1993**, *32*, 2199–2201.
50. Pal, S.; Pal, S. *Zeitschrift Fur Anorg. Allgem. Chemie* **2002**, *628*, 2091–2098.
51. Timpson, C. J.; Bignozzi, C. A.; Sullivan, B. P.; Kober, E. M.; Meyer, T. J. *J. Phys. Chem.* **1996**, *100*, 2915–2925.
52. Junghae P. Chang, Fung E. Y.; Curtis, J. C. *Inorg. Chem.* **1986**, *25*, 4233–4241.
53. Curtis, J. C.; Sullivan, B. P.; Meyer T.J. *Inorg. Chem.* **1983**, *22*, 224.
54. Gritzner, G.; Danksagmuller, K.; Gutmann, V. *J. Electroanal. Chem.* **1976**, *72*, 177–185.
55. Mayer, U.; Katocova, A.; Gutmann, V.; Gerger, W. *J. Electroanal. Chem.* **1979**, *100*, 875–883.
56. Kadish, K. M.; Das, K.; Schaeper, D.; Merrill, C.; Welch, B. R.; Wilson, L. J. *Inorg. Chem.* **1980**, *19*, 2816–2821.
57. Shin, Y.-G.; Brunschwig, S. S.; Creutz, C.; Sutin, N. *J. Phys. Chem.* **1996**, *100*, 8157–8169.
58. Dodsworth, E. S.; Lever, A. B. P. *Chem. Phys. Lett.* **1986**, *124*, 152–158.
59. Fukuda, Y.; Hirota, M.; Kon-no, M.; Nakao, A.; Umezawa, K. *Inorg. Chim. Acta* **2002**, *339*, 322–326.
60. Kaim, W. *J. Organomet. Chem.* **1996**, *511*, 273–280.
61. Treichel, P. M.; Mueh, H. J.; Bursten, B. E. *J. Organomet. Chem.* **1976**, *110*, C49–C52.
62. Lu, S. X. 1999. M.Sc. Thesis. York University, Toronto, Canada.
63. Lu, S. X.; Strelets, V. V.; Ryan, M. F.; Pietro, W. J.; Lever, A. B. P. *Inorg. Chem.* **1996**, *35*, 1013–1023.
64. Lu, S. X.; Lever, A. B. P. **2003**, Submitted for publication.
65. Thornberry, M.; Slebodnick, C.; Deck, P. A.; Fronczek, F. R. *Organometallics* **2000**, *19*, 5352–5369.
66. Stepnicka, P.; Trojan, L.; Kubista, J.; Ludvik, J. *J. Orgmet. Chem.* **2001**, *637-639*, 291–299.
67. Zhang, L.; De Silva, M. F. C. G.; Kuznetsov, M. L.; Gamasa, M. P.; Gimeno, J.; Da Silva, J. J. R. F.; Pombeiro, A. J. L. *Organometallics* **2001**, *20*, 2782–2793.
68. Dodsworth, E. S.; Vlcek, A. A.; Lever, A. B. P. *Inorg. Chem.* **1994**, *33*, 1045–1049.
69. Hupp, J. P.; Meyer T. J. *Inorg. Chem.* **1987**, *26*, 2332–2334.
70. Rillema, D. P.; Allen, G.; Meyer, T. J.; Conrad, D. *Inorg. Chem* **1983**, *22*, 1617–1622.
71. Ross, H. B.; Boldajii, M.; Rillema, D. P.; Blanton, C. B.; White, R. P. *Inorg. Chem.* **1989**, *28*, 1013–1021.
72. Gorelsky, S. I.; Dodsworth, E. S.; Vlcek, A. A.; Lever, A. B. P. *Coord. Chem. Rev* **1998**, *174*, 269–296.
73. Vos, J. G.; Hage, R.; Reedijk, J. *Inorg. Chim. Acta* **1996**, *245*, 237–242.
74. Koba, I.; Toma, H. E.; Iha, N. Y. M. *IV Simp. Bras. Eletroquim. Eletroanal.; Anais* **1984**, 455–461.
75. Johnson, C. R.; Shepherd, R. E. *Inorg. Chem.* **1983**, *22*, 2439–2444.
76. Brisset, J. L.; Biquard, M. *Inorg. Chim. Acta* **1981**, *53*, L125–L128.
77. Johnson, C. R.; Shepherd, R. E. *Inorg. Chem.* **1983**, *22*, 2439–2444.
78. Slep, L.; Baraldo, L. M.; Olabe, J. *Inorg. Chem.* **1996**, *35*, 6327–6333.
79. Soe, K. N.; Ichimura, A.; Kitagawa, T. *Inorg. Chim. Acta* **1993**, *207*, 21–25.
80. Brisset, J. L.; Ilimbi, V. *Can. J. Chem.* **1980**, *58*, 1250–1252.
81. Moore, K. J.; Lee, L.; Mabbott, G. A.; Petersen, J. D. *Inorg. Chem.* **1983**, *22*, 1108–1112.
82. Ford, P. C. *J. Am. Chem. Soc.* **1968**, *90*, 1187–1194.
83. Della Ciana, L.; Dressick, W. J.; Sandrini, D.; Maestri, M.; Ciano, M. *Inorg. Chem.* **1990**, *29*, 2792–2798.
84. Nurhadi, A.; Graf, E.; Gross, M. *Electrochim. Acta* **1995**, *40*, 1939–1954.
85. Handy, R. F.; Lintvedt, R. L. *Inorg. Chem.* **1974**, *13*, 893–896.
86. Mukherjee, R. N.; Rajan, A. O.; Chakravorty, A. *Inorg. Chem.* **1982**, *21*, 785–790.
87. Mukherjee, R. N.; Chakravorty, A. *J. Chem. Soc. Dalton* **1983**, 955–959.
88. Jain, A. K.; Goyal, R. N.; Agarwal, D. D. *J. Electroanal. Chem.* **1978**, *93*, 145–149.
89. Giraudeau, A.; Callott, H. J.; Jordan, J.; Ezhar, I.; Gross, M. *J. Am. Chem. Soc.* **1979**, *101*, 3857–3862.
90. Goswami, S.; Mukherjee, R.; Chakravorty, A. *Inorg. Chem.* **1983**, *22*, 2825–2832.
91. Rillema, D. P.; Nagle, J. K.; Barringer, L. F. Jr.; Meyer, *J. Am. Chem. Soc.* **1981**, *103*, 56–62.
92. Skarda, V.; Cook, M. J.; Lewis, A. P.; McAuliffe, G. S. G.; Thomson, A. J.; Robbins, D. J. *J. Chem. Soc. Perkin, II* **1984**, 1309–1311.
93. Patterson, G. S.; Holm, R. H. *Inorg. Chem.* **1972**, *11*, 2285–2288.
94. Tse, Y. H.; Lam, H.; Zhang, J. J.; Pietro, W. J.; Lever, A. B. P. *J. Porph. Phthaloc. Chem.* **1997**, *1*, 3–15.
95. da Silva, M. F. C. G.; da Silva, J. J. R. F.; Pombeiro, A. J. L. *J. Chem. Soc.–Dalton Transactions* **1994**, 3299–3304.
96. Tsiamis, C.; Karageorgiou, S.; Lalia-Kantouri, M.; Manoussakis, G. *Gazz. Chim. Ital.* **1987**, *117*, 317–323.
97. Mukherjee, R. N.; Rajan, A. O.; Chakravorty, A. *Inorg. Chem.* **1982**, *21*, 785–790.
98. Tolman, C. A. *Chem. Rev.* **1977**, *77*, 313–348.
99. Alexiou, A. D. P.; Toma, H. E. *J. Chem. Res. S* **1993**, 464–465.
100. Toma, H. E.; Araki, K.; Alexiou, A. D. P.; Nikolaou, S.; Dovidauskas, S. *Coord. Chem. Rev.* **2001**, *219*, 187–234.
101. Feighery, W. G.; Yao, H.; Hollenkamp, A. F.; Allendoerfer, R. D.; Keister, J. B. *Organometallics* **1998**, *17*, 872–886.
102. Yao, H. R.; Mccargar, R. D.; Allendoerfer, R. D.; Keister, J. B.; Low, A. A. *J. Organomet. Chem.* **1998**, *568*, 63–76.
103. Lever, A. B. P. *Inorganic Electronic Spectroscopy*, 1st Edn.; Elsevier Science: Amsterdam, 1968.
104. Lever, A. B. P. *Inorganic Electronic Spectroscopy,* 2nd Edn.; Elsevier Science: Amsterdam, 1984.
105. Vlcek, A. A. *Electrochim. Acta* **1968**, *13*, 1063–1078.
106. Dodsworth, E. S.; Lever, A. B. P. *Chem. Phys. Lett.* **1984**, *112*, 567–570.; *Erratum. Chem. Phys. Lett.* **1985**, *116*, 245.
107. Lever, A. B. P.; Pickens, S. R.; Minor, P.; Licoccia, S.; Ramaswamy, B. S.; Magnell, K. *J. Amer. Chem. Soc.;* **1981**, *103*, 6800–6806.
108. Sahami, S.; Weaver, M. J. *J. Electroanal. Chem.* **1981**, *122*, 171–181.

109. Johnson, S. R.; Westmoreland, T. D.; Caspar, J. V.; Barqawi, K. R.; Meyer, T. J. *Inorg. Chem.* **1988**, *27*, 3195–3200.
110. Furue, M.; Naiki, M.; Kanematsu, Y.; Kushida, T.; Kamachi, M. *Coord. Chem. Rev.* **1991**, *111*, 221–226.
111. Ohsawa, Y.; Hanck, K. W.; DeArmond, M. K. *J. Electroanal. Chem.* **1984**, *175*, 229–240.
112. Shin, Y.; Brunsschwig, B. S.; Creutz, C.; Newton, M. D.; Sutin, N. *J. Phys. Chem.* **1996**, *100*, 1104–1110.
113. da Cunha, C. J.; Fielder, S. S.; Stynes, D. V.; Masui, H.; Auburn P. R.; Lever, A. B. P. *Inorg. Chim. Acta* **1996**, *242*, 293–302.
114. Das, C.; Kamar, K. K.; Ghosh, A. K.; a Majumdar, P.; Hung, C.-H.; Goswami, S. *New J. Chemistry* **2002**, 1409–1414.
115. Gorelsky, S. I.; Dodsworth, E. S.; Lever, A. B. P.; Vlcek, A. A. *Coord. Chem. Rev.* **1998**, *174*, 469–494.
116. Sacksteder, L.; Zipp, A. P.; Brown, E. A.; Julie, Demas J. N.; DeGraff, B. A. *Inorg. Chem.* **1990**, *29*, 4335–4340.
117. Toma, H. E.; Creutz, C. *Inorg.Chem.* **1977**, *16*, 545–550.
118. Estrin, D. A.; Hamra, O. Y.; Paglieri, L.; Slep, L. D.; Olabe, J. A. *Inorg. Chem.* **1996**, *35*, 6832–6837.
119. Loukova, V. G.; Strelets, V. V. *J. Orgmet. Chem.* **2000**, *606*, 203–206.
120. Crutchley, R. J.; McCaw, K.; Lee, F. L.; Gabe, E. J. *Inorg. Chem.* **1990**, *29*, 2576–2581.
121. Cipriano, R. A.; Levason, W.; Pletcher, D.; Powell, N. A.; Webster, M. *J. Chem. Soc. Dalton* **1987**, 1901–1910.
122. Duff, C. M.; Heath, G. A. *Inorg. Chem.* **1991**, *30*, 2528–2535.
123. Vogler, L. M.; Jones, S. W.; Jensen, G. E.; Brewer, B. K. J. *Inorg. Chim. Acta* **1996**, *250*, 155–162.
124. Anderson, P. A.; Keene, F. R.; Meyer, T. J.; Moss, J. A.; Strouse, G. F.; Treadway, J. A. *J. Chem. Soc.–Dalton Transactions* **2002**, 3820–3831.
125. Anderson, P. A.; Deacon, G. B.; Haarmann, K. H.; Keene, F. R.; Meyer, T. J.; Reitsma, D. A.; Skelton, B. W.; Strouse, G. F.; Thomas, N. C.; Treadway, J. A.; White, A. H. *Inorg. Chem.* **1995**, *34*, 6145–6157.
126. Anderson, P. A.; Strouse, G. F.; Treadway, J. A.; Keene, F. R.; Meyer, T. J. *Inorg. Chem.* **1994**, *33*, 3863–3864.
127. Metcalfe, R. A.; Lever, A. B. P. *Inorg. Chem.* **1997**, *36*, 4762–4771.

Comprehensive Coordination Chemistry II
ISBN (set): 0-08-0437486

Volume 2, (ISBN 0-08-0443249); pp 251–268

2.20 Mössbauer Spectroscopy: Introduction

G. J. LONG
University of Missouri-Rolla, MO, USA
and
F. GRANDJEAN
University of Liège, Belgium

2.20.1 INTRODUCTION 269
2.20.1.1 Fundamental Concepts of Recoil-free Absorption 269
2.20.1.2 Advantages and Disadvantages of the Effect 270
2.20.2 THE ISOMER SHIFT 271
2.20.3 THE QUADRUPOLE INTERACTION 272
2.20.4 ELECTRONIC SPIN-STATE STUDIES 272
2.20.5 MAGNETIC HYPERFINE FIELD 274
2.20.6 TIME-DEPENDENT PHENOMENA 275
2.20.7 REFERENCES 276

2.20.1 INTRODUCTION

The Mössbauer effect was discovered[1–3] in 1958 by Rudolf L. Mössbauer who received the Nobel Prize in physics for its discovery in 1961. Over the past 45 years the Mössbauer effect has developed into a well-established spectroscopic technique which has widely contributed[4–7] to coordination chemistry, inorganic and bioinorganic chemistry, and materials science.

Even though the Mössbauer effect has been observed[4,5] for almost 50 different elements and ca. 100 different nuclides, only a few of these elements are widely used as Mössbauer effect probes. The nuclides which are both experimentally viable and yield useful chemical information[8] are iron-57, tin-119,[9] antimony-121, and europium-151.[10] More difficult to use but of importance in coordination chemistry[8] are gold-197,[11] nickel-61, ruthenium-99, tellurium-125,[12] iodine-129,[13] dysprosium-161, tungsten-182,[11] and neptunium-237. Among these isotopes, iron-57 is by far the easiest, most informative, and most widely used[14] nuclide in both traditional coordination chemistry and in studies of biologically significant coordination complexes.

2.20.1.1 Fundamental Concepts of Recoil-free Absorption

A Mössbauer spectrum arises from the recoil-free emission and resonant absorption of a γ-ray by a nuclide. The intensity of the radiation emitted by a source containing the radioactive Mössbauer precursor nuclide, and transmitted through a solid absorber containing the Mössbauer nuclides in

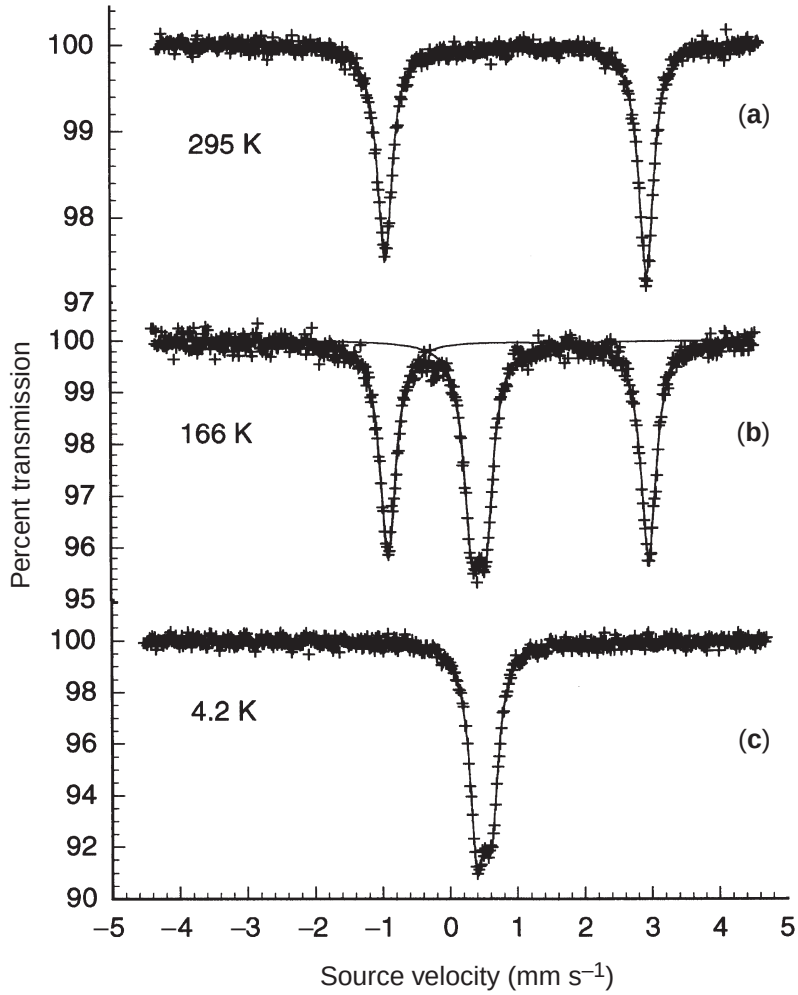

Figure 1 The high-spin (a), spin-crossover (b), and low-spin (c) Mössbauer spectra of {Fe[HC(3,5-$Me_2pz)_3]_2$}I_2, obtained at the indicated temperatures.

their ground state, is measured as a function of the γ-ray energy, an energy that is varied by Doppler shifting the source relative to the absorber. Some typical Mössbauer spectra are shown in Figure 1 as a plot of the percent transmission versus the source velocity relative to a stationary absorber. The hyperfine parameters discussed below are obtained from the energies of the absorption peaks, measured as relative velocities of the source and absorber, and the absorption area is a measure of the recoil-free fraction of the absorber, i.e., the fraction of the Mössbauer nuclei in the absorber undergoing recoil-free resonant absorption.

The recoil-free emission and resonant absorption processes necessary to observe the Mössbauer spectrum can only occur for nuclei bound into a solid. The fraction of such events depends[15] on the γ-ray energy and the vibrational properties of the crystal. Hence, in principle from temperature-dependent measurements of the absorption area, information about crystal dynamics, such as the Debye temperature, can be obtained.[16,17]

2.20.1.2 Advantages and Disadvantages of the Effect

Mössbauer spectroscopy is a nondestructive technique which probes a specific element which may occupy one or more crystallographic sites, may have one or more electronic configurations, and may or may not carry a magnetic moment. The absorbers may be in the form of single crystals, powders, foils, surfaces, or frozen solutions; solutions or liquids can not be studied. The influence of temperature, pressure, applied magnetic field, and electromagnetic irradiation is easily studied by Mössbauer spectroscopy.

Unfortunately, the requirements of recoil-free emission and resonant absorption and transmission through the absorber limit the useable energy range of the Mössbauer effect γ-ray to approximately 10–100 keV. Further, in order to obtain rather sharp absorption lines and a reasonable spectral resolution, the mean lifetime of the Mössbauer γ-ray precursor state should be between 1 ns and 100 ns. Further, the Mössbauer nuclide must have a sufficiently high isotopic abundance in the element to yield a usable signal-to-noise ratio over a reasonable acquisition time. Finally, the radioactive source containing the Mössbauer γ-ray precursor state must be easily prepared and have a mean lifetime of several weeks to be practical. These various requirements limit the number of nuclides available for typical Mössbauer spectral studies.

Iron-57 is the most important Mössbauer nuclide even though it has a natural abundance of only 2.2%. The half-life of its 14.41 keV excited state is 98.1 ns and the half-life of its precursor source, cobalt-57, is 270 days. As a result, the resolution of iron-57 Mössbauer spectroscopy, 6.5×10^{-13}—the ratio of the linewidth to the γ-ray energy—is excellent. Because the typical iron-57 hyperfine parameters are of the order of a few millimeters per second and range up to many times the natural linewidth of 0.194 mm s^{-1}, they are easily measured with excellent resolution.

The hyperfine parameters result from shifts in, or the removal of, the degeneracy of the nuclear energy levels[14,15] through the electric and magnetic interactions between the nucleus and its surrounding electronic environment. The expressions for the hyperfine parameters, the isomer shift, the quadrupole interaction, and the magnetic hyperfine field always contain two contributions, a nuclear contribution that is fixed for a given nuclide, and an electronic contribution that varies from compound to compound.

2.20.2 THE ISOMER SHIFT

The nuclear contribution to the isomer shift results from the change in size of the Mössbauer nuclide during its nuclear decay and the electronic contribution results from the differing electron density at the Mössbauer nucleus in the source and the absorber. The isomer shift is measured relative to a reference material, which for iron-57 is usually α-iron. The isomer shift for a given site in a compound is the center of gravity of all the absorption lines associated with the site. In practice, the isomer shift, δ, is given by Equation (1)

$$\delta = E_{\text{ref}} - E_{\text{abs}} \tag{1}$$

where E_{ref} and E_{abs} are the energies for the standard reference and the absorber, respectively. The isomer shift can also be written as

$$\delta = \frac{2\pi}{5} Ze^2 \left[|\Psi_{ns}(0)|^2_{\text{ref}} - |\Psi_{ns}(0)|^2_{\text{abs}} \right] \left(R^2_{\text{ex}} - R^2_{\text{gd}} \right) \tag{2}$$

where e is the charge of the electron, Ze is the charge of the nucleus, R_{ex} and R_{gd} are the nuclear radii in the excited and ground states, respectively, and $|\Psi_{ns}(0)|^2$ is the ns-electron probability density at the nucleus of the reference material and the absorber.

Because the ns-electrons are the only electrons that have a nonzero probability density at the nucleus, they are the only electrons that contribute directly to the isomer shift. However, the ns-electrons can be screened by intervening electrons, i.e., the 3d-electrons of iron, a screening which is responsible for the different isomer shifts observed for iron(II) and iron(III). As may be observed at 295 K in Figure 1a for the high-spin iron(II) complex, $\{Fe[HC(3,5\text{-}Me_2pz)_3]_2\}I_2$, where $HC(3,5\text{-}Me_2pz)_3$ is a tridentate ligand and pz is a pyrazolyl ring, the isomer shifts of high-spin iron(II) complexes[14] with pesudooctahedral nitrogen coordination are ca. 1.0–1.2 mm s^{-1}. In contrast, the isomer shifts of the analogous low-spin iron(II) complexes[14] (see the 4.2 K spectrum in Figure 1c) are ca. 0.4–0.5 mm s^{-1}. This dramatic change illustrates the sensitivity of the iron(II) isomer shift to its electronic configuration, i.e., high-spin $t_{2g}{}^4e_g{}^2$ or low-spin $t_{2g}{}^6$.

In a similar fashion, the isomer shifts of iron(III) complexes, which are usually different from those of iron(II), are also sensitive to spin state, with $t_{2g}{}^3e_g{}^2$ high-spin iron(III) typically having isomer shifts of 0.4–0.5 mm s^{-1} whereas the $t_{2g}{}^5$ low-spin iron(III) complexes typically have smaller isomer shifts of ca. 0.2 mm s^{-1}. Further, iron(IV) complexes[18] are also known to have relatively small isomer shifts in the range of -0.1 mm s^{-1} to 0.2 mm s^{-1}. Danon and co-workers[19] have observed an almost linear correlation of the isomer shifts with the oxidation states between iron(II) and iron(VI).

2.20.3 THE QUADRUPOLE INTERACTION

The interaction between a nonzero nuclear quadrupole moment and a surrounding nonspherical distribution of electric charges, as measured by the electric field gradient at the nucleus, gives rise to a quadrupole interaction. This hyperfine interaction, which also depends upon a nuclear and an electronic factor, is described by the Hamiltonian

$$H = \frac{V_{zz}Qe}{4\mathrm{I}(2\mathrm{I}-1)}\left[3I_z^2 - \mathrm{I}(\mathrm{I}+1) + \frac{\eta}{2}\left(I_+^2 + I_-^2\right)\right] \tag{3}$$

where Q is the nuclear quadrupole moment of the nuclear excited state, e is the charge of the electron, I is the nuclear spin, and I_z, I_+, and I_- are the z-component and the step-up and step-down nuclear spin operators. If V_{xx}, V_{yy}, and V_{zz} are the principal components of the electric field gradient tensor, such that $V_{xx} + V_{yy} + V_{zz} = 0$, then the asymmetry parameter, η, is given by

$$\eta = \frac{V_{xx} - V_{yy}}{V_{zz}} \tag{4}$$

with $|V_{zz}| \geq |V_{yy}| \geq |V_{xx}|$, and it follows that $0 \leq \eta \leq 1$. For iron-57, the quadrupole interaction results in a symmetric quadrupole doublet Mössbauer spectrum for a random powder absorber, with a quadrupole splitting, ΔE_Q, given by

$$\Delta E_Q = \frac{1}{2}eQV_{zz}\sqrt{1+\frac{\eta^2}{3}} \tag{5}$$

A slightly area asymmetric iron(II) doublet, characterized by a large quadrupole splitting, is shown in Figure 1a; the small asymmetry observed in the component areas of this doublet is the result of texture. The electric field gradient at the nucleus has two contributions,[20] a lattice and a valence contribution. For high-spin iron(III) ions which have a half-filled shell $3d^5$ electronic configuration, the valence contribution is zero and the only contribution to the quadrupole splitting is from the lattice. As a consequence, the quadrupole splittings of high-spin iron(III) coordination complexes[14] are usually small and of the order of 0.5–0.8 mm s^{-1}. In contrast, for high-spin iron(II) ions, the valence contribution, which results from the inequivalent electronic populations of the three t_{2g} orbitals in pseudooctahedral complexes or of the two e-orbitals in pseudotetrahedral complexes, dominates over the lattice contribution. As a result (see Figure 1a), high-spin iron(II) complexes,[14] with the $t_{2g}^4e_g^2$ electronic configuration in a pseudooctahedral environment, exhibit[21] quadrupole splittings of as high as 3.5 mm s^{-1}. In contrast, low-spin iron(II) ions, with the filled t_{2g}^6 set of orbitals, typically show (see Figure 1c) small quadrupole splittings of 0.2–0.3 mm s^{-1}, a splitting that arises only from a lattice contribution to the electric field gradient.

Hence, high-spin and low-spin iron(II) and iron(III) coordination complexes are easily distinguished through their isomer shifts and quadrupole splittings. Further, the coexistence of the high-spin and low-spin states at a spin crossover or a spin transition is easily observed at the appropriate temperature as is illustrated in Figure 1b, which indicates that {Fe[HC(3,5-$Me_2pz)_3]_2$}I_2 is ca. 50% high-spin and 50% low-spin at 166 K.[21]

2.20.4 ELECTRONIC SPIN-STATE STUDIES

There has been a multitude of Mössbauer spectral studies of electronic spin-state transitions in iron coordination compounds and the readers should consult one of the many reviews and books available[4,5,14,22–24] as only a few selected examples will be discussed herein.

In addition to the study[21] mentioned above of {Fe[HC(3,5-$Me_2pz)_3]_2$}I_2, a complex which undergoes a complete iron(II) spin-state crossover between 295 and 4.2 K, Reger and co-workers[25–29] have studied {Fe[HC(3,5-$Me_2pz)_3]_2$}$(BF_4)_2$ and found that it undergoes a *partial* iron(II) spin-state crossover at ca. 206 K from fully high spin between 295 K and 208 K to 50 percent high spin and 50% low spin between 205 K and 4.2 K. This partial spin-state crossover is apparently unique for a complex that contains only one crystallographic iron(II) site above the spin-state crossover temperature. The partial spin state crossover is accompanied by a crystallographic

phase transition in which one-half of the iron(II) sites change their pseudooctahedral coordination environment; similar phase transitions have been observed[28] in $\{M[HC(3,5\text{-}Me_2pz)_3]_2\}(BF_4)_2$, where M is cobalt(II), nickel(II), and copper(II), but, unlike the iron(II) complex, there is no change in the cobalt(II) high-spin state associated with the phase transition. Reger and co-workers have also shown through magnetic and Mössbauer spectral studies[27] that the related complex, $\{Fe[HC(pz)_3]_2\}(BF_4)_2$, in which the iron(II) is low-spin from 4.2 K to 295 K, undergoes a gradual spin-state transition between ca. 310 K and 450 K to the high-spin iron(II) state; the complex is completely high spin at 472 K.

Reedijk and co-workers have studied[30] the iron(II) spin-state crossover in $[Fe(teec)_6]X_2$, where X is BF_4, ClO_4, or PF_6, and teec is the monodentate 1-(2-chloroethyl)tetrazole ligand. Depending upon the anion and the rate of precipitation, these complexes exhibit differing, partial or complete, spin-state crossover behavior with gradual or sharp, one- or two-step, transitions both with and without hysteresis.

In contrast to iron(II) spin-state crossover complexes which usually show a cooperative behavior, iron(III) complexes exhibit a gradual, noncooperative, spin-state transition. There has been extensive Mössbauer spectral studies of these transitions, including ambient[31,32] and high-pressure studies[33] of the iron(III) trisdithiocarbamate complexes, the first iron complexes which were reported[34,35] in 1931 to undergo a spin-state transition.

Mössbauer spectroscopy has also been used in the search for intermediate iron(III) spin states. Trautwein and colleagues have shown[36] that $[Fe(L\text{-}N_4Me_2)(S_2C_6H_4)](ClO_4)\cdot 0.5H_2O$, where N_4Me_2 is *N*,*N*′-dimethyl-2,11-diaza[3.3](2,6)pyridinophane and $S_2C_6H_4$ is 1,2-benzenedithiolate, exhibits an unusual thermally induced iron(III) low-spin t_{2g}^5 to intermediate-spin $t_{2g}^4e_g^1$ transition as is confirmed by Mössbauer spectroscopy and a variety of other techniques. A similar formation of the essentially pure iron(III) intermediate spin state has also been reported[37,38] by Ikeue *et al.* for some saddle-shaped, six-coordinate iron(III) porphyrin complexes. The basis for this iron(III) intermediate spin state has been discussed in detail by Simonato *et al.*[39]

In the study of mixed valence iron complexes, Kojima and co-workers have used Mössbauer spectroscopy,[40] magnetic susceptibility,[41] and heat capacity[42] studies to show that the extended array honeycomb-like complex, $[(n\text{-}C_3H_7)_4][Fe^{II}Fe^{III}(dto)_3]$, where dto is the dithiooxalate dianion, $(C_2O_2S_2)^{-2}$, undergoes a reversible charge-transfer phase transition at ca. 120 K. Above 120 K the iron(III) ions are hexacoordinated to six dithiooxalate sulfurs, are low spin t_{2g}^5, and exhibit both a small quadrupole splitting and a small isomer shift, whereas the iron(II) ions are hexacoordinated to six dithiooxalate oxygens, are high spin $t_{2g}^4e_g^2$, and exhibit a large quadrupole splitting and a large isomer shift. Below 120 K the iron(II) ions are hexacoordinated to six dithiooxalate sulfurs, are low spin t_{2g}^6, and exhibit both a small quadrupole splitting and a small isomer shift, whereas the iron(III) ions are hexacoordinated to six dithiooxalate oxygens, are high spin $t_{2g}^3e_g^2$, and exhibit a relatively small quadrupole splitting and a small isomer shift. These Mössbauer spectral changes, as well as changes in the magnetic susceptibility and heat capacity, are consistent with the transfer at 120 K of an electron from the high-spin iron(II) sites to the low-spin iron(III) sites, a transfer which is also accompanied by changes in the spin state; this transfer corresponds to a new type of first-order phase transition.[41]

As might be expected, Mössbauer spectroscopy has been essential[43,44] in understanding the electronic properties of porphyrin and porphyrin-like iron complexes.[43–63] These complexes can be prepared in a variety of iron oxidation states and electronic spin states. Often for a given oxidation state, an intermediate spin state or an admixture of two spin states is observed[45–47,50–54] and, as a consequence, it is necessary to measure the Mössbauer spectra in an applied magnetic field. The resulting spectra are often very complex and the methods used to understand these spectra are discussed in Chapter 2.21.

Because a very large number of papers have dealt with the Mössbauer spectral study of porphyrin and porphyrin-like iron complexes, only a few recent papers will be discussed herein. Trautwein and co-workers have studied many iron porphyrin or porphyrin-like complexes including "picket-fence" porphyrins that exhibit either a single high-spin iron(II) state,[54,58] a single iron(III) state,[58] or iron(III) with a quantum mechanically mixed, $S = 5/2$, $3/2$, spin state.[55] Likewise, Kostka *et al.*[60] have used EPR and Mössbauer spectroscopy to study porphyrin-like iron(IV) complexes that are high spin with $S = 2$ and porphyrin-like iron(III) complexes that are intermediate spin with $S = 3/2$. Mössbauer spectroscopy has also been important in understanding the role of π-bonding in various iron porphyrin complexes[60,63] including some iron(III) π-cation radical complexes[57,61] and mixed ligand complexes.[56] Mössbauer spectral quadrupole splittings have been found[62] to be correlated with iron-57 NMR chemical shifts in low-spin diamagnetic iron(II) porphyrin complexes, a correlation that may be understood in terms of a valence cloud asymmetry.

Often, the observed iron-57 Mössbauer spectral hyperfine parameters, when combined with a knowledge of the magnetic properties of the complexes, can easily lead to an unambiguous assignment of the iron oxidation state, coordination number, and yield the extent of the distortion of its coordination environment. The same is also true for many of the other Mössbauer nuclides mentioned above.

2.20.5 MAGNETIC HYPERFINE FIELD

The magnetic interaction between the nuclear magnetic dipole moment of iron and the magnetic hyperfine field generated at the nucleus by the surrounding electrons and magnetic dipoles is described by the Hamiltonian

$$H = -\boldsymbol{\mu} \cdot \mathbf{H} = -g_N \mu_N \mathbf{I} \cdot \mathbf{H} \tag{6}$$

whose eigenvalues, E_m, are

$$E_m = -g_N \mu_N m_I H \tag{7}$$

where g_N is the nuclear Landé g-factor, μ_N is the nuclear Bohr magneton, **H** is the magnetic field at the nucleus, and **I** is the nuclear spin operator. For iron-57, this interaction results in a Mössbauer spectral sextet, and in the absence of any quadrupole interaction, this sextet is symmetric and, for a random powder absorber, the relative areas of its six lines are in the ratio 3:2:1:1:2:3. The overall sextet splitting is proportional to the hyperfine field experienced by the nucleus below the ordering temperature of the material, which can be ferromagnetic, antiferromagnetic, or ferrimagnetic. The measured hyperfine field in α-iron is 33 T or 10.6 mm s^{-1}, i.e., almost 50 times the experimental linewidth. Although in some complexes[64] the iron(III) hyperfine field may be as large as 62 T, high-spin iron(III) compounds typically exhibit hyperfine fields in the range of 45–55 T, whereas high-spin iron(II) compounds exhibit substantially lower fields in the range of 40–44 T. The 4.2 K spectrum of a mixed valence oxalate compound, $(PPh_4)[Fe^{II}Fe^{III}(ox)_3]$, which contains discrete valence iron(II) and iron(III) is shown[65] in Figure 2.

The magnetic hyperfine field is composed of three contributions: the Fermi contact, the dipolar, and the orbital contributions. The Fermi contact term, which in most iron-containing materials is dominant, results from the interaction between the nuclear magnetic moment and the unpaired electron spin density at the nucleus. The dipolar and orbital terms represent the dipolar interaction between the nuclear magnetic moment and the electronic spin and orbital moments of their

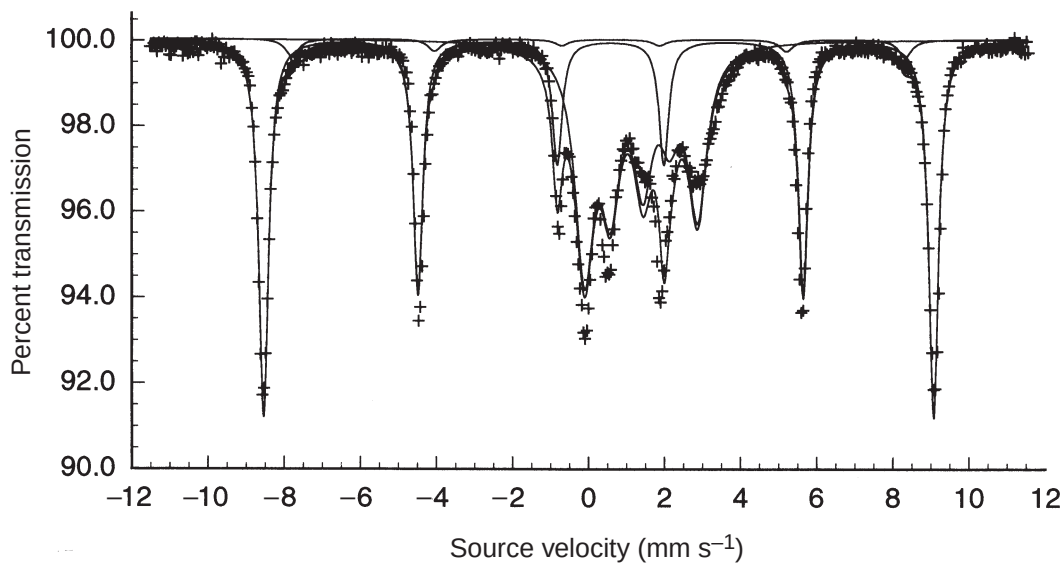

Figure 2 The magnetic Mössbauer spectrum of $(PPh_4)[Fe^{II}Fe^{III}(ox)_3]$, showing the outer high-spin iron(III) sextet and the inner high-spin iron(II) sextet.

parent atom. In iron-containing compounds, these two terms are usually small and opposed to the Fermi contact term. The difference in the contributions to the hyperfine field for iron(II) and iron(III) are immediately apparent in Figure 2. The outer sextet is assigned[65] to high-spin iron(III) in $(PPh_4)[Fe^{II}Fe^{III}(ox)_3]$, with the $t_{2g}^3e_g^2$ electronic configuration in a pseudooctahedral environment; the five unpaired electrons make essentially no orbital contribution to the moment. As a result this site exhibits a large hyperfine field of 54 T. In contrast, the inner sextet is assigned[65] to high-spin iron(II) with the $t_{2g}^4e_g^2$ electronic configuration in a pseudooctahedral environment. In this case the four unpaired electrons make a large orbital contribution to the moment, a contribution which subtracts from the Fermi contact term. As a result this site exhibits a small hyperfine field of ca. 6.5 T.

2.20.6 TIME-DEPENDENT PHENOMENA

Coordination complexes emitting or absorbing Mössbauer γ-rays often experience time-dependent interactions with their environment and, as a consequence of these time-dependent interactions, the complex will evolve[66] in time through the states determined by the applicable Hamiltonian. This time evolution, in which the complex goes from one state to another accessible state following a random path, is often referred to as relaxation.

There are three different relevant times to consider in the discussion of relaxation, i.e., the lifetime of the nuclear excited state, τ, the characteristic time, τ_L, needed for the nucleus to experience the electric or magnetic field, and the relaxation time, τ_R, i.e., the time interval during which the electric or magnetic field does not change its value or orientation. If τ_R is much smaller than τ_L, then the nucleus does not sense the changes in field and only responds to an average field. In contrast, if τ_R is much larger than τ_L, then the nucleus will sense the change in field and will experience more than one value. The appearance of the resulting spectrum is determined by the relationship between the three characteristic times. Usually, in iron-57 Mössbauer spectroscopy, τ is much larger than τ_L and a hyperfine split spectrum is observed, either a quadrupole doublet or a magnetic sextet. In addition, if τ_R is much larger than τ_L, then several overlapping hyperfine split spectra are observed for the various different values of the electric or magnetic field corresponding to the states between which the relaxation occurs. In contrast, if τ_R is much smaller than τ_L, an average hyperfine split spectrum corresponding to the average electric or magnetic field is observed.

By varying an external parameter, such as the temperature, the pressure, or an applied magnetic field, the relaxation time may be varied and its value obtained from the Mössbauer spectra by modeling[67,68] the line shape profile. An Arrhenius plot of the temperature or pressure dependence of the relaxation time yields the activation energy for the relaxation process.

In coordination complexes, the typical relaxation processes involve electronic spin-state relaxation, electronic valence state relaxation, structural relaxation, and paramagnetic relaxation. Only a few references to each example will be mentioned herein. The unsubstituted pyrazolyl borate and methane complexes[27,29] mentioned above nicely illustrate the case of electronic spin-state relaxation. Specifically, $Fe[HB(pz)_3]_2$ shows spin-state relaxation from the low-spin iron(II) state to the high-spin iron(II) state on heating from 295 K to 410 K. The activation energy for this spin-state relaxation is very sensitive to the size of the crystallites and is initially 7,300 cm^{-1}, a value which decreases to 1,860 cm^{-1} upon subsequent heating and cooling. The $\{Fe[HC(pz)_3]_2\}(BF_4)_2$ complex undergoes[27] an analogous spin-state transition between ca. 310 K and 450 K with an activation energy of 2,820 cm^{-1}, a value which is intermediate between the values observed for $Fe[HB(pz)_3]_2$.

A typical example of valence state relaxation from a valence trapped to a valence detrapped state has been observed[69] in the Mössbauer spectrum of $(Et_4N)[Fe_2(salmp)_2]$, where salmp is bis(salicylideneamino)-2-methylphenolate(3-). At 100 K, the Mössbauer spectrum consists of two doublets characteristic of trapped iron(II) and iron(III) valence states; upon warming an additional doublet appears, whose hyperfine parameters are intermediate between those of the iron(II) and iron(III) valence states and correspond to a valence averaged state. In contrast, a Mössbauer spectral study of $[L_2Fe_2(\mu\text{-}OH)_3](ClO_4)_2\cdot 2CH_3OH\cdot 2H_2O$, with L = *N*,*N*′,*N*″-trimethyl-1,4,7-triazacyclononane, reveals[70] a delocalized iron valence state, with an average valence of +2.5, even at 4.2 K, a delocalized valence state which gives rise to a double exchange mechanism.

The work of Fitzsimmons and co-workers[71–75] illustrates the value of Mössbauer spectroscopy in the study of dynamic molecular behavior. Specifically, they found that $[(C_6H_7)Fe(CO)_3]BF_4$ shows solid-state dynamic behavior at room temperature and above and static behavior at 78 K. Finally, low-temperature Mössbauer spectral studies have revealed[31,32] the onset of slow paramagnetic

relaxation in Fe[*N*,*N*′-dimethyldithiocarbamate]$_3$; it was possible from the temperature dependence of the observed relaxation rate to distinguish between the contributions of spin–lattice and spin–spin relaxation in this and several related complexes.

2.20.7 REFERENCES

1. Mössbauer, R. L. *Z. Phys.* **1958**, *151*, 124–143.
2. Mössbauer, R. L. *Naturwissenschaften* **1958**, *45*, 538–539.
3. Mössbauer, R. L. *Z. Naturforsch.* **1959**, *14a*, 211–216.
4. Long, G. J., Ed.; *Mössbauer Spectroscopy Applied to Inorganic Chemistry*, Plenum Press: New York, 1984 and 1986; Vols. 1 and 2.
5. Long, G. J.; Grandjean, F., Eds.; *Mössbauer Spectroscopy Applied to Inorganic Chemistry*, Plenum Press: New York, 1990, Vol. 3.
6. Long, G. J.; Grandjean, F., Eds.; *Mössbauer Spectroscopy Applied to Magnetism and Materials Science*, Plenum Press: New York, 1993 and 1996, Vols. 1 and 2.
7. Greenwood, N.; Gibb, T. *Mössbauer Spectroscopy*, Chapman and Hall: London, 1971.
8. Wilkinson, G.; Gillard, R. D.; McCleverty, J. A., Eds.; CCC (1987), Pergamon: Oxford, 1987, Vols. 1 to 6.
9. Parish, R. V. In *Mössbauer Spectroscopy Applied to Inorganic Chemistry*, Long, G. J., Ed.; Plenum Press: New York, 1984, Vol. 1, pp 527–575.
10. Grandjean, F.; Long, G. J. In *Mössbauer Spectroscopy Applied to Inorganic Chemistry*, Long, G. J., Grandjean, F., Eds.; Plenum Press: New York, 1989, Vol. 3, pp 513–597.
11. Williams, A. F. In *Mössbauer Spectroscopy Applied to Inorganic Chemistry*, Long, G. J., Ed.; Plenum Press: New York, 1987, Vol. 2, pp 429–479.
12. Berry, F. J. In *Mössbauer Spectroscopy Applied to Inorganic Chemistry*, Long, G. J., Ed.; Plenum Press: New York, 1987, Vol. 2, pp 343–390.
13. Parish, R. V. In *Mössbauer Spectroscopy Applied to Inorganic Chemistry*, Long, G. J., Ed.; Plenum Press: New York, 1987, Vol. 2, pp 391–428.
14. Hawker, P. N.; Twig, M. V. In CCC (1987), Wilkinson, G., Gillard, R. D., McCleverty, J. A., Eds.; Pergamon: Oxford, 1987, Vol. 4, pp 1180–1288. The readers should note that part D of Fig. 2 in this reference is incorrect and they should refer to the energy level diagram published in ref. 15.
15. Long, G. J.; Grandjean, F. In *Applications of Analytical Techniques to the Characterization of Materials*; Perry, D. L., Ed.; Plenum Press: New York, 1991, pp 119–151.
16. Herber, R. H. In *Chemical Mössbauer Spectroscopy*, Herber, R. H., Ed.; Plenum Press: New York, 1984; pp 199–216.
17. Kolk, B. In *Dynamic Properties of Solids*; Horton, G. K., Maradudin A. A., Eds.; North-Holland: Amsterdam, 1984; pp 5–506.
18. Russo, U.; Long, G. J. In *Mössbauer Spectroscopy Applied to Inorganic Chemistry*, Long, G. J., Grandjean, F., Eds.; Plenum Press: New York, 1989, Vol. 3, pp 289–329.
19. Guenzburger, D.; Esquivel, D. M. S.; Danon, J. *Phys. Rev. B* **1978**, *18*, 4561–4569.
20. Long, G. J. In *Mössbauer Spectroscopy*, Dickson, D. P. E., Berry F. J., Eds.; Cambridge University Press: Cambridge, 1986; pp 70–142.
21. Reger, D. L.; Little, C. A.; Smith, M. D.; Rheingold, A. L.; Lam, M.; Concolino, T.; Long, G. J.; Hermann, R. P.; Grandjean, F. *Eur. J. Inorg. Chem.* **2002**, 1190–1197.
22. Gütlich, P.; Goodwin, H. A., Eds.; *Spin Crossover Phenomena in Transition Metal Compounds*, Springer–Verlag: Berlin, **2004**.
23. Gütlich, P.; Garcia, Y.; Goodwin, H. A. *Chem. Soc. Rev.* **2000**, *29*, 419–427.
24. Gütlich, P.; Spiering, H. In *Inorganic Electronic Structure and Spectroscopy*, Solomon, E. I., Lever, A. B. P., Eds.; Wiley: New York, 1999, Vol. 2, pp 575–622.
25. Reger, D. L.; Little, C. A.; Rheingold, A. L.; Lam, M.; Concolino, T.; Mohan, A.; Long, G. J. *Inorg. Chem.* **2000**, *39*, 4674–4675.
26. Briois, V.; Sainctavit, P.; Long, G. J.; Grandjean, F. *Inorg. Chem.* **2001**, *40*, 912–918.
27. Reger, D. L.; Little, C. A.; Rheingold, A. L.; Lam, M.; Concolino, T.; Grandjean, F.; Briois, V.; Mohan, A.; Long, G. J. *Inorg. Chem.* **2001**, *40*, 1508–1520.
28. Reger, D. L.; Little, C. A.; Smith, M. D. *Inorg. Chem.* **2002**, *41*, 4453–4460.
29. Grandjean, F.; Long, G. J.; Hutchinson, B. B.; Ohlhausen, L.; Neill, P.; Holcomb, J. D. *Inorg. Chem.* **1989**, *28*, 4406–4414.
30. Stassen, A. F.; Dova, E.; Ensling, J.; Schenk, H.; Gütlich, P.; Haasnoot, J. G.; Reedijk, J. *Inorg. Chim. Acta* **2002**, *335*, 61–68.
31. Fiddy, J. M.; Hall, I.; Grandjean, F.; Russo, U.; Long, G. J. *Inorg. Chem.* **1987**, *26*, 4138–4139.
32. Fiddy, J. M.; Hall, I.; Grandjean, F.; Long, G. J.; Russo, U. *J. Phys.: Condens. Matter* **1990**, *2*, 10091–10107.
33. Fiddy, J. M.; Hall, I.; Grandjean, F.; Russo, U.; Long, G. J. *J. Phys.: Condens. Matter* **1990**, *2*, 10109–10122.
34. Cambi, L.; Cagnasso, A. *Atti Accad. Lincei* **1931**, *13*, 809–813.
35. Cambi, L.; Szego, L. *Ber.* **1933**, *66B*, 656–661.
36. Koch, W. O.; Schünemann, V.; Gerdan, M.; Trautwein, A. X.; Krüger, H.-J. *Chem. Eur. J.* **2002**, *4*, 686–691.
37. Ikeue, T.; Yamaguchi, T.; Ohgo, Y.; Nakamura, M.; Saitoh, T.; Takahashi, M.; Takeda, M. *Chem. Commun.* **2000**, 1989–1990.
38. Ikeue, T.; Ohgo, Y.; Yamaguchi, T.; Takahashi, M.; Takeda, M.; Nakamura, M. *Angew. Chem. Int. Ed.* **2001**, *40*, 2617–2620.
39. Simanoto, J.-P.; Pécaut, J.; Le Pape, L.; Oddou, J.-L.; Jeandy, C.; Shang, M.; Scheidt, W. R.; Wojaczynski, J.; Wolowiec, S.; Latos-Grazynski, L.; Marchon, J.-C. *Inorg. Chem.* **2000**, *39*, 3978–3987.
40. Kojima, N.; Aoki, W.; Seto, M.; Kobayashi, Y.; Maeda, Yu. *Synthetic Metals* **2001**, *121*, 1796–1797.

41. Kojima, N.; Aoki, W.; Itoi, M.; Ono, Y.; Seto, M.; Kobayashi, Y.; Maeda, Yu. *Solid State Commun.* **2001**, *120*, 165–170.
42. Nakamoto, T.; Miyazaki, Y.; Itoi, M.; Ono, Y.; Kojima, N.; Sorai, M. *Angew. Chem. Int. Ed.* **2001**, *40*, 4716–4719.
43. Munck, E. In *The Porphyrins*; Dolphin, D., Ed., Academic Press: New York, 1978, Vol. 4, pp 379–423.
44. Sams, J.; Tsin, T. In *The Porphyrins*; Dolphin, D., Ed.; Academic Press: New York, 1978, Vol. 4, pp 425–478.
45. Dolphin, D.; Sams, J.; Tsin, T. *Inorg. Chem.* **1977**, *16*, 711–713.
46. Summerville, D. A.; Cohen, I. A.; Hatano, K.; Scheidt, W. R. *Inorg. Chem.* **1978**, *17*, 2906–2910.
47. Reed, C. A.; Mashiko, T.; Bentley, S. P.; Kastner, M. E.; Scheidt, W. R.; Spartalian, K.; Lang, G. *J. Am. Chem. Soc.* **1979**, *101*, 2948–2958.
48. Masuda, H.; Taga, T.; Osaki, K.; Sugimoto, H.; Yoshida, Z.; Ogoshi, H. *Inorg. Chem.* **1980**, *19*, 950–955.
49. Mansuy, D.; Morgenstern-Badarau, I.; Lange, M.; Gans, P. *Inorg. Chem.* **1982**, *21*, 1427–1430.
50. Masuda, H.; Taga, T.; Osaki, K.; Sugimoto, H.; Yoshida, Z.; Ogoshi, H. *Bull. Chem. Soc. Jpn.* **1982**, *55*, 3891–3895.
51. Scheidt, W. R.; Geiger, D. K.; Hayes, R. J.; Lang, G. *J. Am. Chem. Soc.* **1983**, *105*, 2625–2632.
52. Toney, G.; ter Haar, L.; Savrin, J.; Gold, A.; Hatfield, W. E.; Sangaiah, R. *Inorg. Chem.* **1984**, *23*, 2561–2563.
53. Toney, G.; Gold, A.; Savrin, J.; ter Haar, L. W.; Sangaiah, R.; Hatfield, W. E. *Inorg. Chem.* **1984**, *23*, 4350–4352.
54. Mandon, D.; Ott-Woelfel, F.; Fischer, J.; Weiss, R.; Bill, E.; Trautwein, A. X. *Inorg. Chem.* **1990**, *29*, 2442–2447.
55. Gismelseed, A.; Bominaar, E. L.; Bill, E.; Trautwein, A. X.; Winkler, H.; Nasri, H.; Doppelt, P.; Mandon, D.; Fischer, J.; Weiss, R. *Inorg. Chem.* **1990**, *29*, 2741–2749.
56. Nasri, H.; Wang, Y.; Huynh, H. B.; Walker, F. A.; Scheidt, W. R. *Inorg. Chem.* **1991**, *30*, 1483–1489.
57. Scheidt, W. R.; Song, H.; Haller, K. J.; Safo, M. K.; Orosz, R. D.; Reed, C. A.; Debrunner, P. G.; Schulz, C. E. *Inorg. Chem.* **1992**, *31*, 939–941.
58. Bominaar, E. L.; Ding, X. Q.; Gismelseed, A.; Bill, E.; Winkler, H.; Trautwein, A. X.; Nasri, H.; Fischer, J.; Weiss, R. *Inorg. Chem.* **1992**, *31*, 1845–1854.
59. Fitzgerald, J. P.; Haggerty, B. S.; Rheingold, A. L.; May, L.; Brewer, G. A. *Inorg. Chem.* **1992**, *31*, 2006–2013.
60. Kostka, K. L.; Fox, B. G.; Hendrich, M. P.; Collins, T. J.; Rickard, C. E. F.; Wright, L. J.; Munck, E. *J. Am. Chem. Soc.* **1993**, *115*, 6746–6757.
61. Jayaraj, K.; Terner, J.; Gold, A.; Roberts, D. A.; Austin, R. N.; Mandon, D.; Weiss, R.; Bill, E.; Müther, M.; Trautwein, A. X. *Inorg. Chem.* **1996**, *35*, 1632–1640.
62. Polam, J. R.; Wright, J. L.; Christensen, K. A.; Walker, F. A.; Flint, H.; Winkler, H.; Grodzicki, M.; Trautwein, A. X. *J. Am. Chem. Soc.* **1996**, *118*, 5272–5276.
63. Nasri, H.; Ellison, M. K.; Chen, S.; Huynh, B. H.; Scheidt, W. R. *J. Am. Chem. Soc.* **1997**, *119*, 6274–6283.
64. Reiff, W. M.; Frommen, C. M.; Yee, G. T.; Sellers, S. P. *Inorg. Chem.* **2000**, *39*, 2076–2079.
65. Carling, S. G.; Hautot, D.; Watts, I. D.; Day, P.; Visser, D.; Ensling, J.; Gütlich, P.; Long, G. J.; Grandjean, F. *Phys. Rev. B* **2002**, *66*, 104407 (12 pages).
66. Hoy, G. R. In *Mössbauer Spectroscopy Applied to Inorganic Chemistry*, Long, G. J., Ed.; Plenum Press: New York, 1984, Vol. 1, pp 195–226.
67. Blume, M.; Tjon, J. A. *Phys. Rev.* **1968**, *165*, 446–455.
68. Tjon, J. A.; Blume, M. *Phys. Rev.* **1968**, *165*, 456–465.
69. Surerus, K. K.; Munck, E.; Snyder, B. S.; Holm, R. H. *J. Am. Chem. Soc.* **1989**, *111*, 5501–5502.
70. Ding, X.-Q.; Bominaar, E. L.; Bill, E.; Winkler, H.; Trautwein, A. X.; Drüeke, S.; Chaudhuri, P.; Wieghardt, K. *J. Chem. Phys.* **1990**, *92*, 178–186.
71. Fitzsimmons, B. W.; Hume, A. R. *J. Chem. Soc., Dalton Trans.* **1980**, 180–185.
72. Maeda, Y.; Ogawa, N.; Takashima, Y. *J. Chem. Soc., Dalton Trans.* **1987**, 627–632.
73. Fitzsimmons, B. W.; Sayer, I. *J. Chem. Soc., Dalton Trans.* **1991**, 2907–2909.
74. Fitzsimmons, B. W.; Marshall, W. G. *J. Chem. Soc., Dalton Trans.* **1992**, 73–76.
75. Brougham, D. F.; Barrie, P. J.; Hawkes, G. E.; Abrahams, I.; Motevalli, M.; Brown, D. A.; Long, G. J. *Inorg. Chem.* **1996**, *35*, 5595–5602.

Comprehensive Coordination Chemistry II
ISBN (set): 0-08-0437486

Volume 2, (ISBN 0-08-0443249); pp 269–277

2.21 Mössbauer Spectroscopy: Bioinorganic

E. MÜNCK and A. STUBNA
Carnegie Mellon University, Pittsburgh, PA, USA

2.21.1 INTRODUCTION 279
2.21.2 SPECTRA OF AN EXCHANGE-COUPLED [2Fe–2S] CLUSTER 281
2.21.3 VALENCE DELOCALIZATION AND DOUBLE EXCHANGE 282
2.21.4 HIGHER OXIDATION STATES OF DIIRON CLUSTERS 283
2.21.5 RAPID FREEZE–QUENCH STUDIES 284
2.21.6 MÖSSBAUER STUDIES OF CRYOREDUCED SAMPLES 284
2.21.7 SAMPLE CONSIDERATIONS 285
2.21.8 REFERENCES 285

2.21.1 INTRODUCTION

^{57}Fe Mössbauer spectroscopy is a powerful tool for studying the electronic structure of monomeric complexes, iron-containing clusters, and cluster assemblies. The technique measures transitions between the sublevels of the nuclear ground state ($I_g = 1/2$) and the levels of the 14.4 keV nuclear excited state ($I_e = 3/2$), see Figure 3.4 of Gütlich *et al.*[1] Because hyperfine splittings depend on electronic quantities such as charge distribution, symmetry, spin, and orbital angular momentum, the ^{57}Fe nucleus is a sensitive probe of the oxidation and spin state of an iron site and a good probe of the coordination environment. ^{57}Fe Mössbauer spectroscopy has been applied to many problems in coordination chemistry and magnetochemistry;[2,3] the fundamentals have been covered in basic texts.[1,4] Since the early 1970s, Mössbauer spectroscopy has been developed into an incisive tool for the study of metalloproteins.[5–10] In particular, complementary information obtained from Mössbauer and EPR spectroscopy has been exploited for the characterization of complex cluster systems.[7–9,11] The methodology developed for studies of metalloproteins is directly applicable to iron-containing crystals, polycrystalline samples, and (frozen) molecular solutions. Since the early 1990s, the synthesis and characterization of catalysts based on metal clusters found in biology has moved to the forefront of inorganic chemistry. The present article focuses on the information that can be obtained from a Mössbauer study.

The Mössbauer spectra of compounds with integer electronic spin such as Fe^{II} and Fe^{IV} complexes or $Fe^{III}Fe^{III}$ and $Fe^{II}Fe^{II}$ clusters generally exhibit simple patterns when the samples are studied in the absence of an applied magnetic field. The spectra consist of doublets from which one can extract the quadrupole splitting, ΔE_Q, and the isomer shift, δ (Figure 1a). The quadrupole splitting, or more exactly the electric field gradient (EFG) tensor (see below) contains a valence part and a ligand contribution. The valence contribution, together with the isomer shift, which measures the *s*-electron density at the nucleus and indirectly, through shielding, the *d*-electron population, provides generally sufficient information for assigning oxidation and spin states of the iron.[3,4] For a paramagnetic complex, integer or half-integral spin, additional

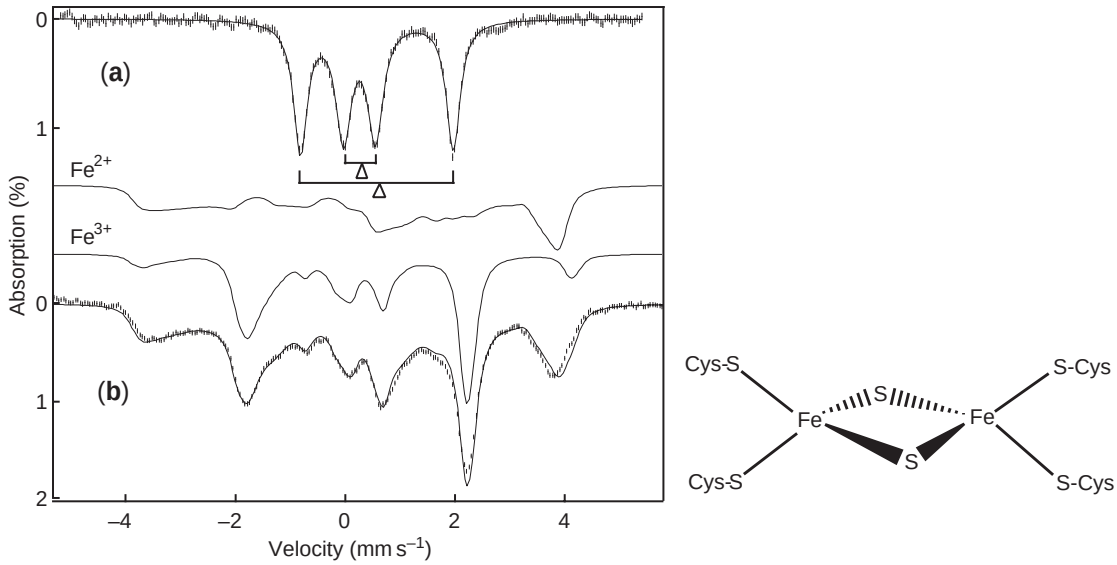

Figure 1 Structure of [2Fe–2S] cluster and Mössbauer spectra of the $[2Fe–2S]^{1+}$ cluster of the reductase of methane monooxygenase from *Methylosinus trichosporium OB3b*.[15] (a) The 200 K spectrum consists of two quadrupole doublets representing a ferric (inner doublet) and a ferrous site. The triangles mark the isomer shift of each site, obtained by taking the centroid of the spectrum. (b) 4.2 K spectrum, recorded in a field of 6.0 T applied parallel to the observed Mössbauer radiation. The solid lines above the experimental data show a decomposition of the high-field spectrum into contributions from the ferric and ferrous site. Details are described elsewhere.[15]

data concerning electronic structure can be obtained by studying the samples in applied magnetic fields. Many parameters can be extracted from an analysis of the Mössbauer spectra with a spin Hamiltonian such as

$$\mathrm{H} = \mathrm{H_e} + \mathrm{H_{hf}} \tag{1}$$

$$\mathrm{H_e} = D[\mathbf{S}_z^2 - \tfrac{1}{3}\mathrm{S}(\mathrm{S}+1)] + E(\mathbf{S}_x^2 - \mathbf{S}_y^2) + \beta\mathbf{S}\cdot\mathbf{g}\cdot\mathbf{B} \tag{2}$$

$$\mathrm{H_{hf}} = \mathbf{S}\cdot\mathbf{a}\cdot\mathbf{I} - g_n\beta_n\mathbf{B}\cdot\mathbf{I} + \tfrac{1}{2}eQV_{zz}[3\mathbf{I}_z^2 - \mathrm{I}(\mathrm{I}+1) + \eta(\mathbf{I}_x^2 - \mathbf{I}_y^2)]. \tag{3}$$

In Equation (2), D and E are the axial and rhombic zero-field splitting (ZFS) parameters, respectively, and $\mathbf{g}$ is the electronic g tensor. The magnetic hyperfine interactions of the electronic system with the ^{57}Fe nucleus are described by $\mathbf{S}\cdot\mathbf{a}\cdot\mathbf{I}$, and $-g_n\beta_n\mathbf{B}\cdot\mathbf{I}$ is the nuclear Zeeman term. The quadrupole interaction involves the traceless EFG tensor. The EFG tensor has principal components V_{xx}, V_{yy}, and V_{zz}. The asymmetry parameter $\eta = (V_{xx} - V_{yy})/V_{zz}$ can be confined to $0 \leq \eta \leq 1$ if the convention $|V_{zz}| \geq |V_{yy}| \geq |V_{xx}|$ is adopted. A quadrupole doublet yields the magnitude of $\Delta E_\mathrm{Q} = \frac{1}{2}eQV_{zz}\sqrt{1 + \frac{1}{3}\eta^2}$; determination of η and the sign of ΔE_Q requires the presence of magnetic hyperfine interactions (for diamagnetic compounds an applied field >2.0 T is required). Sites with axial symmetry have $\eta = 0$, but $\eta = 0$ does not imply this symmetry. (A d_{xy}-orbital, for instance, has tetragonal symmetry, yet this orbital can be an eigenstate in rhombic symmetry.) In Equations (2) and (3), the ZFS and EFG tensors are assumed to have a common principal axis system x, y, z. However, in symmetries lower than rhombic, all tensors in Equations (2) and (3) may have different principal axis systems.

Future research will generate an increasing number of complexes with less common oxidation states (Fe^{VI}, Fe^{V}, Fe^{IV}, and Fe^{I}) and novel coordination environments. Even "simple" Fe^{II} compounds still yield interesting spectroscopy. For instance, Holland and co-workers[12] have synthesized a series of three-coordinate, high-spin Fe^{II} complexes $[LFeX]^0$ (L = diketiminate; X = Cl^-, CH_3^-, $NHTol^-$, $NHtBu^-$). The complex with X = CH_3 yields low-temperature Mössbauer

spectra with unusually large magnetic hyperfine splittings, corresponding to internal magnetic field $\mathbf{B}_{\text{int}} = +82.0\,\text{T}$, the largest hyperfine field observed for an iron complex ($\mathbf{B}_{\text{int}}$ is defined in Equation (7); typical $\mathbf{B}_{\text{int}}$ values range from 10 to 50 T.). The positive sign of $\mathbf{B}_{\text{int}}$ indicates a large, unquenched orbital angular momentum, which was confirmed by the observation of an integer spin EPR signal corresponding to $g_z = 2.85$ (in $\text{H} = \beta\mathbf{S}\cdot\mathbf{g}\cdot\mathbf{B}$), the largest value observed for high-spin Fe^{II}. This large, unquenched orbital angular momentum results from an accidental near degeneracy of two orbitals with d_{z^2} and d_{yz} symmetry.[12]

2.21.2 SPECTRA OF AN EXCHANGE-COUPLED [2Fe–2S] CLUSTER

The power of Mössbauer spectroscopy is readily appreciated by considering a spin-coupled system, namely that of [2Fe–2S] clusters found in many ferredoxins that function in electron transfer (Figure 1).[13] In the biological environment the cluster alternates between the diferric state, designated $[2\text{Fe–2S}]^{2+}$, and the mixed valence $Fe^{II}Fe^{III}$ state, $[2\text{Fe–2S}]^{1+}$. In the 1+ state the electronic spins of the ferric, $S_a = 5/2$, and ferrous, $S_b = 2$, sites are antiferromagnetically coupled to yield a ground state with total spin $S = 1/2$.[11,14] The following discussion focuses on those aspects of Mössbauer spectroscopy that illustrate points of interest for the coordination chemist. In slightly modified form, the following arguments apply also to clusters with higher nuclearity.

The Mössbauer spectra of the $[2\text{Fe–2S}]^{1+}$ ferredoxins can be analyzed with the spin Hamiltonian

$$\text{H} = J\mathbf{S}_a\cdot\mathbf{S}_b + \text{H}_e(\text{a}) + \text{H}_{\text{hf}}(\text{a}) + \text{H}_e(\text{b}) + \text{H}_{\text{hf}}(\text{b}) \tag{4}$$

where J is the exchange coupling constant and a, b refer to the ferric and ferrous sites, respectively. The J values reported for ferredoxins are $>150\,\text{cm}^{-1}$, and the ZFS parameters $|\text{D}|$ for FeS_4 sites are typically $\approx 1\text{–}2\,\text{cm}^{-1}$ for Fe^{III} and $\approx 5\,\text{cm}^{-1}$ for Fe^{II}.

Under conditions when the electronic spin relaxes fast, the Mössbauer spectrum of a $[2\text{Fe–2S}]^{1+}$ ferredoxin exhibits two quadrupole doublets of equal intensity, indicating that the cluster contains two distinct Fe sites.[11,15] The 200 K Mössbauer spectrum in Figure 1a has one doublet with $\Delta E_{\text{Q}}(\text{a}) = 0.59\,\text{mm s}^{-1}$ and isomer shift, $\delta(\text{a}) = 0.26\,\text{mm s}^{-1}$, while the other exhibits $\Delta E_{\text{Q}}(\text{b}) = 3.00\,\text{mm s}^{-1}$ and $\delta(\text{b}) = 0.65\,\text{mm s}^{-1}$. The respective δ values are typical of high-spin ferric and high-spin ferrous sites with tetrahedral sulfur coordination (range $\delta = 0.22\text{–}0.30\,\text{mm s}^{-1}$ for Fe^{III} and $\delta = 0.65\text{–}0.72\,\text{mm s}^{-1}$ for Fe^{II}; octahedral high-spin sites with N/O coordination typically exhibit $\delta = 0.4\text{–}0.6\,\text{mm s}^{-1}$ for Fe^{III} and $\delta = 1.1\text{–}1.3\,\text{mm s}^{-1}$ for Fe^{II}; these values are quoted at 4.2 K relative to Fe metal at 298 K.).[1] The spectrum of Figure 1 shows that the cluster contains *localized* ferric and ferrous sites. With one exception[16] all ferredoxins studied to date exhibit localized valences.

For $[2\text{Fe–2S}]^{1+}$ clusters the exchange coupling ($J > 150\,\text{cm}^{-1}$) is very large compared to all other interactions. This suggests that one should analyze low-temperature EPR, Mössbauer, ENDOR, MCD, and magnetic susceptibility data for the (isolated) $S = 1/2$ ground state of the coupled system. The appropriate $S = 1/2$ spin Hamiltonian is given in Equation (5):

$$\text{H} = \beta\mathbf{S}\cdot\mathbf{g}\cdot\mathbf{B} + \{\mathbf{S}\cdot\mathbf{A}_a\cdot\mathbf{I}_a - g_n\beta_n\mathbf{B}\cdot\mathbf{I}_a + \text{H}_{\text{Q}}(a)\} + \{\mathbf{S}\cdot\mathbf{A}_b\cdot\mathbf{I}_b - g_n\beta_n\mathbf{B}\cdot\mathbf{I}_b + \text{H}_{\text{Q}}(b)\} \tag{5}$$

The tensors $\mathbf{g}$ and $\mathbf{A}$ of the coupled system are related, by use of the Wigner–Eckart theorem, to the local tensors by[11,14]

$$\mathbf{g} = \tfrac{7}{3}\mathbf{g}_a - \tfrac{4}{3}\mathbf{g}_b,\ \mathbf{A}_a = \tfrac{7}{3}\mathbf{a}_a \text{ and } \mathbf{A}_b = -\tfrac{4}{3}\mathbf{a}_b. \tag{6}$$

The spin projection factors 7/3 and $-4/3$ relate the tensors of the coupled system to the local tensors and reflect the orientation of the local spins relative to the system spin, $\mathbf{S} = \mathbf{S}_{\text{a}} + \mathbf{S}_{\text{b}}$. Since $g_{jb} \geq 2.0$ (j = x, y, z) the $(-4/3)$ factor of $\mathbf{g}_{\text{b}}$ leads to g values below $g = 2.00$.[14] For applied magnetic fields $B > 0.05\,\text{T}$ the electronic Zeeman interaction in Equation (5) is at least 20 times larger than the hyperfine interactions. Consequently, the expectation value of the electronic spin, $\langle\mathbf{S}\rangle$, is determined by the electronic Zeeman term, allowing us to replace the spin operator $\mathbf{S}$

with $<\mathbf{S}>$ in the magnetic hyperfine terms and to combine the expression $<\mathbf{S}>\cdot\mathbf{A}_i\cdot\mathbf{I}_i - g_n\beta_n\mathbf{B}\cdot\mathbf{I}_i$ for each iron site into $-\{\mathbf{B}_{\text{int}}(i) + \mathbf{B}\}g_n\beta_n\mathbf{I}_i$. The quantity

$$\mathbf{B}_{\text{int}}(i) = -<\mathbf{S}>\mathbf{A}_i/g_n\beta_n \tag{7}$$

is the internal magnetic field that acts on the magnetic moment of the ^{57}Fe nucleus, splitting the nuclear levels. Note that $\mathbf{B}_{\text{int}}$ is proportional to $<\mathbf{S}>$ and therefore depends on the electronic g tensor. More generally, $<\mathbf{S}>$ depends additionally on the ZFS (see Equation (2)) provided $S > 1/2$. By measuring $\mathbf{B}_{\text{int}}$ one can obtain information on purely electronic parameters such as the g-tensor, ZFSs, and, occasionally, exchange coupling constants. Although one could analyze the Mössbauer spectra by means of Equations (2)–(4), researchers generally use the coupled representation, Equation (5), as the point of departure when encountering clusters containing an unknown number of Fe sites with unknown (local) spin and oxidation states. In general, Equation (5) provides the common framework of reference for EPR, Mössbauer, ENDOR, low-temperature MCD, and magnetic susceptibility studies.

The 200 K spectrum of Figure 1a was recorded under conditions for which the electronic spin fluctuates fast compared to the nuclear precession frequencies. Consequently, $\mathbf{B}_{\text{int}}$, according to Equation (7), fluctuates also rapidly and magnetic hyperfine interactions are averaged out. However, at 4.2 K the electronic states have longer lifetimes (typically $>10^{-5}$ s) and the spectra exhibit paramagnetic hyperfine structure. The 6.0 T spectrum of Figure 1B has been decomposed into contributions of the ferric and ferrous sites. Analysis of such a spectrum is quite straightforward by use of a computer program such as WMOSS, available from Web Research, Inc. (Edina, MN). The A tensor of the ferric site is fairly isotropic and has negative components, while that of the ferrous site is quite anisotropic and has positive components. The signs are established by the observation that the magnetic splitting of the ferric site decreases with increasing applied field while that of the ferrous site increases. (Studies in strong applied fields are crucial for determining the spin coupling in polynuclear complexes, because such studies establish the signs of the A tensors and, with some knowledge about the properties of the local sites, the spin projection factors.) Since high-spin sites generally exhibit negative A-tensor components, the positive A values of the ferrous site indicate the sign reversal expressed by the relation $\mathbf{A}_b = -4/3\mathbf{a}_b$ of Equation (6). Moreover, the local tensors $\mathbf{a}_a$ and $\mathbf{a}_b$ are very close to those observed for ferric and ferrous rubredoxin, a protein containing a well-characterized tetrahedral $Fe(Cys)_4$ site. The Mössbauer data obtained for the [2Fe–2S] ferredoxins, together with chemical analyses and data from ENDOR, EPR, and susceptibility studies, revealed the existence of diiron clusters in these proteins. These data led, in the early 1970s, to a structural proposal that was confirmed by subsequent X-ray crystallographic studies.

In Equations (5) and (7) the system spin, S, enters the expressions for $\mathbf{B}_{\text{int}}$ at both iron sites, i.e., one spin, namely the cluster spin S, controls the hyperfine fields of the two sites. Because *two* Mössbauer spectra are observed for *one* spin system, it follows that the system must be a diiron cluster. This assertion is substantiated by determination of the EPR spin concentration (which yielded 1.06 ± 0.1 spins/2 Fe for the present case).[15] The strong correlation between an observed EPR signal and the associated Mössbauer spectrum can be used to considerable advantage.[7–9] Systematic use of this correlation led to the discovery of novel clusters and cluster assemblies,[13] e.g., the P and M clusters of nitrogenase, [3Fe–4S] clusters, the coupled heme–[4Fe–4S] chromophores in sulfite and nitrite reductase, and the delocalized $Fe^{IV}Fe^{III}$ dimer of Que and collaborators (see below); additional examples are given below and in Beinert *et al.*[13]

The exchange coupling in $[2Fe–2S]^{1+}$ clusters is large compared to the ZFSs of the constituent ferric and ferrous sites, resulting in an energetically isolated $S = 1/2$ ground state. However, if J is comparable with D_a or D_b, the spin multiplets are mixed by the ZFS terms, and the g and A values of the ground doublet become dependent on D_a and D_b (D/J mixing). Sage and co-workers[17] have given expressions for such mixing in binuclear $Fe^{II}Fe^{III}$ complexes, the presence of which is readily recognized by inspection of the ferric site A tensor. Thus, while the A tensors of mononuclear Fe^{III} sites with octahedral N/O coordination are generally isotropic to within a few percent, those of some Fe^{III} sites in $Fe^{III}Fe^{II}$ clusters, due to D/J mixing, display anisotropies reaching 50%.[17]

2.21.3 VALENCE DELOCALIZATION AND DOUBLE EXCHANGE

The $[2Fe–2S]^{2+}$ cluster described above has localized ferrous and ferric sites. Mössbauer spectroscopy has been used to characterize valence-*delocalized* systems that exhibit, in addition to the

familiar Heisenberg exchange $H = \mathbf{JS}_a \cdot \mathbf{S}_b$, an additional mechanism of coupling, referred to as spin-dependent delocalization or double exchange[18–20] Hagadorn *et al.*[21] have described a complex that can switch from a localized state into a delocalized one by a conformational change. The complex, $(Mes_2ArCO_2)_3Fe^{II}Fe^{III}(OCH\ Me_2)_2 \cdot Et_2O$ (Figure 2) features a pair of five-coordinate Fe sites bridged by two isopropoxide ligands and a carboxylate group. The complex can be crystallized in two forms. In form A the methyl–methyl axis of the propoxide groups is parallel to the Fe–Fe vector (Fe–Fe distance 2.75 Å), whereas form B adopts a conformation with the methyl–methyl axis perpendicular to the Fe–Fe vector with a smaller Fe–Fe distance (2.62 Å). Figure 2 shows 4.2 K Mössbauer spectra of both forms. The spectrum of form A consists of a superposition of two magnetic 6-line patterns. One belongs to a localized Fe^{III} ($\delta = 0.59\,mm\,s^{-1}$) and the other to a localized Fe^{II} ($\delta = 0.94\,mm\,s^{-1}$) site. In contrast, the two Fe sites of form B yield identical spectra with a $\delta = 0.76\,mm\,s^{-1}$, indicating a *delocalized* $Fe^{2.5+}Fe^{2.5+}$ cluster. Valence delocalization has the effect of ordering the spins of the two Fe sites parallel, yielding an $S = 9/2$ ground state in the present case.[21] Actually, the Fe sites of form A are not fully localized as indicated by the observation that the δ values of both sites are displaced already ca. 0.1–0.2 $mm\,s^{-1}$ towards the δ value of the fully delocalized state, indicating incipient delocalization. The spectra shown in Figure 2 show that Mössbauer spectroscopy is ideally suited to distinguish between valence-delocalized and valence-localized sites. Presently, it is not clear whether the $S = 9/2$ ground state of form A is the result of dominating ferromagnetic coupling, double exchange, or both. Wieghardt and co-workers[22] as well as Haase and co-workers[23] have reported additional examples of delocalized $Fe^{II}Fe^{III}$ dimers, while Achim *et al.*[16] have described a valence-delocalized state for a mutant $[2Fe–2S]^{1+}$ ferredoxin. Finally, double-exchange is a determining feature of the magnetic properties of two other cluster forms found in biological systems, namely $[3Fe–4S]^0$ and $[4Fe–4S]^{3+,2+,1+}$ clusters (see Figure 6 of Beinert *et al.*[13]).

2.21.4 HIGHER OXIDATION STATES OF DIIRON CLUSTERS

Biomimetic studies are currently focused on generating diiron complexes that can serve as structural and/or electronic models for oxidation states higher than Fe^{III} that are proposed to partake in the catalytic cycles of diiron proteins[25,26] such as methane monooxygenase and ribonucleotide reductase. Mössbauer spectroscopy has played a leading role in the characterization

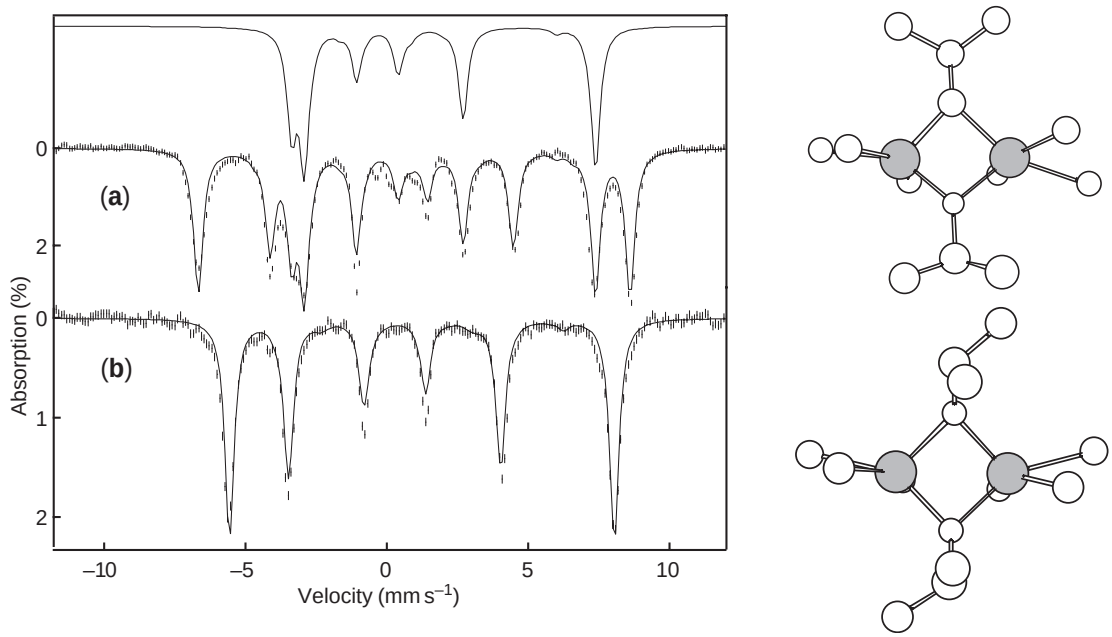

Figure 2 Core structure and Mössbauer spectra of $(Mes_2ArCO_2)_3Fe^{II}\ Fe^{III}(OCHMe_2)_2 \cdot Et_2O$. (a) Structure and 4.2 K spectrum of valence-localized form. The solid line drawn through the data is a fit to a ferric and a ferrous site (1:1 ratio); the theoretical curve for the ferrous site is shown above the data. (b) Structure and spectrum of the delocalized form. The two sites are identical and only one 6-line pattern is observed. The spectra of both forms were fitted to an $S = 9/2$ spin Hamiltonian.[21]

of these complexes. Two complexes, prepared by Que and co-workers[27,28] are dimers involving the TPA ligand (TPA = tris(2-pyridylmethyl) amine). $[Fe_2(O)_2(6\text{-}Me_3\text{-}TPA)_2]^{3+}$ has cluster spin $S = 1/2$ and exhibits localized *high-spin* Fe^{III} ($S_a = 5/2$, $\delta_a = 0.48\,mm\,s^{-1}$) and Fe^{IV} ($S_b = 2$, $\delta_b = 0.08\,mm\,s^{-1}$) sites.[27] This assignment is readily established from analysis of the Mössbauer spectra that proceeds as described for the [2Fe–2S] ferredoxin. The δ values are consistent with the octahedral N/O ligand structure and a higher oxidation state for one of the Fe sites. The spin states of the two sites were established using the following argument: The δ values establish the presence of localized ferric and ferryl sites; the a tensor of the ferric site is typical of high-spin Fe^{III} ($S = 5/2$), so in order to obtain a cluster spin of $S = 1/2$, the spin S_b of the Fe^{IV} site must be greater than 1; hence the Fe^{IV} site is high-spin. In contrast to $[Fe_2(O)_2(6\text{-}Me_3\text{-}TPA)_2]^{3+}$, $[Fe_2(\mu\text{-}O_2)(5\text{-}Et_3\text{-}TPA)_2]^{3+}$ has *low-spin* sites and, moreover, the cluster is a delocalized $Fe^{III}Fe^{IV}$ system ($\delta = 0.11\,mm\,s^{-1}$) as indicated by the observation that the two sites of this $S = 3/2$ complex yield identical Mössbauer spectra. While there seems to be agreement that the $S = 3/2$ ground state of this delocalized system is the result of strong double exchange,[28] a detailed coupling model has not yet been reported. The crystal structure shows that the *delocalized* complex has an $Fe_2(\mu\text{-}O)_2$ diamond core.[29] In the light of this result, it came as a surprise that resonance Raman spectra of the valence-*localized* $[Fe_2(O)_2(6\text{-}Me_3\text{-}TPA)_2]^{3+}$ complex indicated an Fe^{III}—O—Fe^{IV}=O structure.[27] An essential difference between the two complexes is the bulky substituent in the 5- or 6-position of the pyridyl ligands. Thus, the 6-methyl substituent introduces a steric hindrance that prevents formation of short Fe—N bonds, resulting in a high-spin site with only one μ-oxo bridge.

Costas *et al.*[30] have reported spectroscopic evidence for an $Fe^{IV}Fe^{IV}$ complex that can be considered a structural model for the putative $Fe^{IV}Fe^{IV}(\mu\text{-}O)_2$ core of methane monooxygenase intermediate **Q**.[31] The synthetic complex was prepared at $-80\,^{\circ}C$ in CH_2Cl_2 by decay of a mononuclear low-spin Fe^{III} peroxo precursor. The Mössbauer spectra showed that all iron in the sample is intermediate spin ($S = 1$) Fe^{IV}, but the data were compatible with either a mononuclear site or a weakly coupled ($|J| < 5\,cm^{-1}$) *symmetric* dimer. Combination of the Mössbauer technique with resonance Raman and EXAFS spectroscopies provided evidence for a bis–μ–oxo bridged diiron(IV) complex. The complex of Costas *et al.*[30] however, is not an electronic model for intermediate **Q**, as the latter contains high-spin Fe^{IV} sites.

2.21.5 RAPID FREEZE–QUENCH STUDIES

Recently, researchers have placed increased attention on characterizing short-lived catalytic intermediates. For proteins, the preparation method of choice is the rapid freeze–quench (RFQ) technique that allows one to prepare intermediates with lifetimes (at 4 °C) ranging from a few milliseconds to a few seconds by quenching the reactions, for instance, in cold (130 K) isopentane. Using RFQ it has been shown by Mössbauer spectroscopy[32] that methane monooxygenase intermediate **Q** contains an exchange-coupled $Fe^{IV}Fe^{IV}$ cluster; the two indistinguishable sites have $\delta = 0.08\,mm\,s^{-1}$ and small ΔE_Q values, indicating high-spin Fe^{IV} (high-spin sites are also indicated by the anticipated $FeN(O)_{4-5}$ coordination). RFQ has also been used to prepare the $Fe^{IV}Fe^{III}$ state of ribonucleotide reductase intermediate **X**; the EPR ($S = 1/2$, $g = 2.0$) and Mössbauer spectra of **X** were initially interpreted with a model comprising a diferric cluster and an $S = 1/2$ ligand-based radical mutually coupled to an $S = 1/2$ system. However, Mössbauer data of a localized $Fe^{III}Fe^{IV}$ complex prepared by Dong *et al.*[33] $[Fe_2(O)_2(6\text{-}Me\text{-}TPA)_2]^{3+}$, and subsequent ENDOR studies of **X** by Sturgeon *et al.*[34] established the $Fe^{IV}Fe^{III}$ nature of the cluster.

2.21.6 MÖSSBAUER STUDIES OF CRYOREDUCED SAMPLES

Interesting states have been attained by radiolytic reduction of complexes at 77 K, using either synchrotron X-rays or strong ^{60}Co or ^{137}Cs sources (typically such experiments require a dose of 2–4 Mrad). Using hydrated electrons at cryogenic temperatures offers the possibility to generate states that are difficult to access at room temperature (e.g., the reduced complex may not be stable). Moreover, this technique allows one to answer specific questions. For instance, in 1997 the $[4Fe\text{–}4S]^0$ cluster form of the Fe protein of nitrogenase was obtained by reduction with Ti^{III}-citrate, where the all-ferrous nature of the cluster was established by Mössbauer spectroscopy.[35] The X-ray structure of the Fe protein, obtained for the $[4Fe\text{–}4S]^{2+,1+}$ state, had shown that the cluster is suspended at the subunit interface of a protein homodimer, suggesting an idealized C_2

symmetry. The Mössbauer spectra of the Ti-citrate reduced cluster, however, revealed two types of ferrous sites in a 3:1 site ratio, raising the question of whether some rearrangement of the cluster ligands had occurred after reduction but prior to freezing the sample. This possibility was eliminated by radiolytic reduction of the $[4Fe–4S]^{1+}$ state at 77 K, which produced an all-ferrous state identical to that observed by reduction with Ti-citrate.[35] A subsequent X-ray study of the all-ferrous cluster revealed Fe–Fe distances ranging from 2.54 Å to 2.79 Å, but a unique site could not be identified in the crystal structure.[36] A distortion of the $[4Fe–4S]^{0}$ cluster at temperatures below that employed for measuring the crystal structure (110 K) can also be excluded, as the Mössbauer 3:1 site symmetry is observed from 1.5 K to 200 K. Such an electronically driven distortion at temperatures below 50 K has been demonstrated by Coucouvanis and co-workers,[37] who reported a Mössbauer study showing that the prismane $[Fe_6S_6Cl_6]^{2-}$ anion undergoes a distortion to lower symmetry both in the crystalline form and frozen solution. This transition to lower symmetry was confirmed by comparison of the 144 K and 20 K crystal structures.[37]

Presently, it would be interesting to prepare a model complex for the mixed-valence state (H_{ox}) of the dinuclear cluster of the H-center of Fe-hydrogenases. This cluster contains an Fe_2 (μ-$SR_2(CN)_2(CO)_3L_n$ core ($L = H_2O$ and a thiolate-linked $[4Fe–4S]^{2+}$ cluster). It is not clear whether H_{ox} is low-spin $Fe^{III}Fe^{II}$ or low-spin $Fe^{I}Fe^{II}$, or whether one redox equivalent is stored on a cluster ligand.[38] Structural $Fe^{II}Fe^{II}$ and $Fe^{I}Fe^{I}$ models for the H-cluster have been reported.[39] It would be interesting to reduce a $Fe^{II}Fe^{II}$ model complex radiolytically at 77 K into the mixed-valence state for Mössbauer and EPR studies. While this technique offers possibilities for accessing certain oxidation states, it should be noted that the radiolytically reduced complex often remains (at $T < 100$ K) in a constrained conformation characteristic of the oxidized (starting) state. Davydov and co-workers[40] have shown, however, for the $Fe^{II}Fe^{III}$ state of models for protein-bound diiron clusters, that annealing between 100 K and 150 K may relax the complex into the desired conformation. Krebs *et al.*[41] have reported Mössbauer and EPR studies of cryoreduced ribonucleotide reductase. Irradiation at 77 K produced an $S = 1/2$ $Fe^{II}Fe^{III}$ cluster which upon annealing at 180 K transformed into a cluster with an $S = 9/2$ ground state having localized valences as determined by Mössbauer spectroscopy. Finally, an interesting low-temperature Mössbauer study has been reported by Wieghardt and co-workers[42] who have produced a mononuclear $S = 3/2$ (nitrido)Fe^{V} complex by photoreduction via homolytic Fe-azide cleavage at 77 K.

2.21.7 SAMPLE CONSIDERATIONS

Researchers interested in preparing samples for a Mössbauer study are referred to http://mossbauer2. chem.cmu.edu/filesontoweb/CCCII.htm.

NOTE ADDED IN PROOF

Additional information for Section 2.21.4: Rhode and coworkers have recently published the first high-resolution X-ray structure of an Fe^{IV}=O complex, $[Fe^{IV}(O)(TMC)(NCCH_3)]^{2+}$ with TMC = 1,4,8,11-tetramethyl-1,4,8,11-tetraazacyclotetradecane.[43]

2.21.8 REFERENCES

1. Gütlich, P.; Link, R.; Trautwein, A. *Mössbauer Spectroscopy and Transition Metal Chemistry*; Springer-Verlag: Berlin, 1979.
2. Hawker, P. N.; Twigg, M. V. Iron(II) and Lower States. In *Comprehensive Coordination Chemistry, Vol. 4: The Synthesis, Reactions, Properties & Applications of Coordination Compounds*; Wilkinson, S. G., Ed.; Pergamon Press: New York, 1987; Chapter 44.1, pp 1181–1183.
3. Long, G. J.; Grandjean, F. , Eds. *Mössbauer Spectroscopy Applied to Inorganic Chemistry*; Plenum Press: New York, 1984, 1986, 1988; Vol. 1–3.
4. Greenwood, N.; Gibb, T. *Mössbauer Spectroscopy*; Chapman & Hall: London; 1971.
5. Lang, G. *Quart. Rev. Biophys.* **1970**, *3*, 1–60.
6. Debrunner, P. G. *Biol. Magn. Reson.* **1993**, *13*, 59–101.
7. Münck, E.; Surerus, K. K.; Hendrich, M. P. Combining Mössbauer Spectroscopy with Integer Spin Electron Paramagnetic Resonance. In *Methods in Enzymology, Vol. 227: Physical and Spectroscopic Methods for Probing Metal Ion Environments in Metalloproteins*; Riordan, J. F.; Vallee, B. L. , Eds.; Academic Press: New York, 1993; Chapter 17, pp 463–479.

8. Münck, E. Mössbauer Spectroscopy of Proteins: Electron Carriers. In *Methods in Enzymology, Vol. 54: Biological Oxidations*; Fleischer, S.; Packer, L. , Eds., Academic Press: New York, 1978; Chapter 20, pp 346–379.
9. Münck, E. Mössbauer Spectra of Hemeproteins. In *The Porphyrins*; D. Dolphin, Ed.; Academic Press: New York, 1978; Vol. 4, Chapter 8, pp 379–423.
10. Trautwein, A. X.; Bill, E.; Bominaar, E. L.; Winkler, H. *Struct. Bonding* **1991**, *78*, 1–95.
11. Sands, R. H.; Dunham, W. R. *Quart. Rev. Biophys.* **1974**, *7*, 443–504.
12. Andres, H.; Bominaar, E.; Smith, J. M.; Eckert, N. A.; Holland, P.; Münck, E. *J. Am. Chem. Soc.* **2002**, *124*, 3012–3025.
13. Beinert, H.; Holm, R. H.; Münck, E. *Science* **1997**, *277*, 653–659.
14. Münck, E. Aspects of ^{57}Fe Mössbauer Spectroscopy. In *Physical Methods in Bioinorganic Chemistry: Spectroscopy and Magnetism*; Que, L., Jr., Ed.; University Science Books: Sausalito, CA, 2000; pp 287–319.
15. Fox, B. G.; Hendrich, M. P.; Surerus, K. K.; Andersson, K. K.; Froland, W. A.; Lipscomb, J. D.; Münck, E. *J. Am. Chem. Soc.* **1993**, *115*, 3688–3701.
16. Achim, C.; Golinelli, M.-P.; Bominaar, E. L.; Meyer, J.; Münck, E. *J. Am. Chem. Soc.* **1996**, *118*, 8168–8169.
17. Sage, J. T.; Xia, Y.-M.; Debrunner, P. G.; Keough, D. T.; Jersey, J. D.; Zerner, B. *J. Am. Chem. Soc.* **1989**, *111*, 7239–7247.
18. Kahn, O. *Molecular Magnetism*; VCH Publishers: New York, 1993.
19. Papaefthymiou, V.; Girerd, J.-J.; Moura, I.; Moura, J. J. G.; Münck, E. *J. Am. Chem. Soc.* **1987**, *109*, 4703–4710.
20. Blondin, G.; Borshch, S.; Girerd, J. J. *Comments Inorg. Chem.* **1992**, *12*, 315–340.
21. Hagadorn, J. R.; Que, L., Jr.; Tolman, W. B.; Prisecaru, I.; Münck, E. *J. Am. Chem. Soc.* **1999**, *121*, 9760–9761.
22. Gamelin, D. R.; Bominaar, E. L.; Kirk, M. L.; Wieghardt, K.; Solomon, E. I. *J. Am. Chem. Soc.* **1996**, *118*, 8085–8097.
23. Dutta, S. K.; Ensling, J.; Werner, R.; Flörke, U.; Haase, W.; Gütlich, P.; Nag, K. *Angew. Chem. Int. Ed. Engl.* **1997**, *36*, 152–155.
24. Que, L.; Dong, Y. *Acc. Chem. Res.* **1996**, *29*, 190–196.
25. Waller, B. J.; Lipscomb, J. D. *Chem. Rev.* **1996**, *96*, 2625–2658.
26. Merkx, M.; Kopp, D. A.; Sazinsky, M. H.; Blazyk, J. L.; Muller, J.; Lippard, S. J. *Angew. Chem. Int. Ed. Engl.* **2001**, *40*, 2782–2807.
27. Zheng, H.; Yoo, S. J.; Müvck, E.; Que, L., Jr. *J. Am. Chem. Soc.* **2000**, *122*, 3789–3790.
28. Dong, Y.; Zang, Y.; Shu, L.; Wilkinson, E. C.; Que, L., Jr.; Kaufmann, K.; Münck, E. *J. Am. Chem. Soc.* **1997**, *119*, 12683–12684.
29. Hsu, H.-F.; Dong, Y.; Shu, L.; Young, V. G., Jr.; Que, L., Jr. *J. Am. Chem. Soc.* **1999**, *121*, 5230–5237.
30. Costas, M.; Rohde, J.-U.; Stubna, A.; Ho, R. Y. N.; Quaroni, L.; Münck, E.; Que, L., Jr. *J. Am. Chem. Soc.* **2001**, *123*, 12931–12932.
31. Shu, L.; Nesheim, J. C.; Kauffmann, K.; Münck, E.; Lipscomb, J. D.; Que, L., Jr. *Science* **1997**, *275*, 515–518.
32. Lee, S.-K.; Fox, B. G.; Froland, W. A.; Lipscomb, L. D.; Münck, E. *J. Am. Chem. Soc.* **1993**, *115*, 6450–6451.
33. Dong, Y.; Fujii, H.; Hendrich, M. P.; Leising, R. A.; Pan, G.; Randall, C. R.; Wilkinson, E. C.; Zang, Y.; Que, L., Jr.; Fox, B. G.; Kauffmann, K.; Münck, E. *J. Am. Chem. Soc.* **1995**, *117*, 2778–2792.
34. Sturgeon, B. E.; Burdi, D.; Chen, S.; Huynh, B.-H.; Edmondson, D. E.; Stubbe, J.; Hoffman, B. M. *J. Am. Chem. Soc.* **1996**, *118*, 7551–7557.
35. Yoo, S. J.; Angove, H. C.; Burgess, B. K.; Hendrich, M. P.; Münck, E. *J. Am. Chem. Soc.* **1999**, *121*, 2534–2545.
36. Strop, P.; Takahara, P. M.; Chiu, H.-J.; Angove, H. C.; Burgess, B. K.; Rees, D. C. *Biochemistry* **2001**, *40*, 651–656.
37. Krockel, M.; Trautwein, A. X.; Winkler, H.; Coucouvanis, D.; Kostikas, A.; Papaefthymiou, V. *Inorg. Chim. Acta.* **1998**, *283*, 111–117.
38. Popescu, C. V.; Münck, E. *J. Am. Chem. Soc.* **1999**, *121*, 7877–7884.
39. Gloaguen, F.; Lawrence, J. D.; Schmidt, M.; Wilson, S. R.; Rauchfuss, T. B. *J. Am. Chem. Soc.* **2001**, *123*, 12518–12527.
40. Davydov, R. M.; Menage, S.; Fontecave, M.; Graslund, A.; Ehrenberg, A. *J. Biol. Inorg. Chem.* **1997**, *2*, 242–255.
41. Krebs, C.; Davydov, R.; Baldwin, J.; Hoffman, B.; Bollinger, J. M., Jr.; Huynh, B. H. *J. Am. Chem. Soc.* **2000**, *122*, 5327–5336.
42. Grapperhaus, C. A.; Mienert, B.; Bill, E.; Weyhermüller, T.; Wieghardt, K. *Inorg. Chem.* **2000**, *39*, 5306–5317.
43. Rohde, J.-U.; In, J.-H.; Lim, M. H.; Brennessel, W. W.; Bukowski, M. R.; Stubna, A.; Münck, E.; Nam, W.; Que, L., Jr. *Science* **2003**, *299*, 1037–1039.

Comprehensive Coordination Chemistry II
ISBN (set): 0-08-0437486

Volume 2, (ISBN 0-08-0443249); pp 279–286

2.22
Optical (Electronic) Spectroscopy

C. REBER and R. BEAULAC
Université de Montréal, Montréal, Canada

2.22.1 GENERAL ASPECTS 287
2.22.1.1 Charge-transfer Transitions 289
2.22.2 SINGLE-CRYSTAL SPECTROSCOPY 292
2.22.2.1 Single-crystal Absorption Spectroscopy 292
2.22.2.2 Luminescence and Site-selective Spectroscopy of Single Crystals 294
2.22.3 OTHER MODERN OPTICAL SPECTROSCOPIC TECHNIQUES 297
2.22.4 REFERENCES 301

2.22.1 GENERAL ASPECTS

Optical spectroscopy provides a set of techniques for the detailed investigation of energies, bonding properties, and reactivities of the ground and excited electronic states[1–3] and it allows the direct observation of important optical materials characteristics, illustrated, for example, by the light-induced switching of spin-crossover complexes[4,5] or by doped solids for near-infrared to visible up-conversion.[6,7] Both of these phenomena make use of the rich electronic structure of transition metal compounds. Optical spectroscopic measurements are also of key importance for the development of new laser and phosphor materials,[8–10] and a number of non-linear optical processes[6,7] make use of the electronic structure of coordination compounds. An extremely wide variety of systems, ranging from traditional Werner complexes[11,12] and organometallics[13–16] in condensed phases and in the gas phase[17] to metal centers in enzymes[18–23] and nanoscale clusters[24] can be investigated with optical spectroscopic techniques, underlining the power of these methods.

The most important optical spectroscopic techniques in the area of coordination chemistry are absorption, luminescence, and excitation spectroscopy; their applications have been reviewed in detail.[1,11,25,26] Other methods include Raman spectroscopy, an optical spectroscopic technique that is mainly used to probe vibrational transitions involving the ground and excited electronic states, as described in Chapter 2.8, but it can also be applied to electronic transitions.[27] Resonance Raman spectroscopy has been developed into a powerful and widely used technique, discussed in Chapter 2.10. Time-resolved optical spectroscopic techniques have evolved since the 1980s from the nanosecond to the femtosecond range. The goal of this overview is to present a restricted number of examples that illustrate some of the fundamental concepts and new applications of optical spectroscopy, with references to other sections, where important techniques, phenomena, or compounds are discussed in detail. The basic aspects of the absorption spectroscopy of coordination compounds have been summarized in the first edition of this reference work.[29] A thorough introduction on ligand field theory and a systematic collection of characteristic absorption spectra for compounds with the d^1 to d^9 electron configurations are also given elsewhere in this volume and in a number of detailed reviews.[1,11,25,28]

A new generation of instruments for optical spectroscopy has become available since the 1980s. Both pulsed and continuous tunable laser excitation sources have been widely applied to time-resolved and selective spectroscopy.[30] Microscope spectrometers,[31] recognized to be important for a variety of techniques, are now commercially available, and fiber-optical probes are used for *in situ* measurements. CCD cameras and sensitive near-infrared detectors allow weak signals to be detected.[12] Computer-aided data acquisition permits precise statistics during the spectroscopic measurement and further enhances the signal/noise ratio, in particular for near-infrared spectroscopy.[32] Interferometers allow the measurement of very high quality optical absorption spectra throughout the near-infrared, visible, and ultraviolet wavelength regions, but the vast majority of absorption spectra are still measured with scanning instruments. The spectroscopy of systems under external perturbation has become more accessible with modern high-performance instrumentation. Such perturbations include light, for example in pump-probe Raman spectroscopy,[33] magnetic and electric fields, discussed in Chapters 2.23 and 2.25, or high pressure.[34–36] Spectroelectrochemistry also belongs to this category of methods, as discussed in Chapter 1.45.

The quantitative analysis of optical spectra with advanced theoretical models, has become important and has led to a more detailed understanding of a wide variety of new compounds, materials, and even complex systems such as metal centers in enzymes.[23] Many types of electronic structure calculations are used to characterize transitions, and quantitative potential energy surfaces have been successfully derived from absorption and luminescence spectra as well as from resonance Raman excitation profiles for a number of compounds.[2] A general and efficient approach for the quantitative analysis of spectra is discussed in Chapter 2.43.

Figure 1 illustrates schematically a few categories of transitions that have been studied with optical spectroscopy, with an emphasis on new developments. Figure 1a shows the traditional model view of a band in an optical spectrum,[25] corresponding to a transition between the ground state and a single excited state measured with absorption or luminescence spectroscopy. An aspect that has received particular attention is split electronic ground states, illustrated by the two lowest potential energy curves in Figure 1a. These splittings can be due to lifted degeneracies caused by symmetry lowering, spin–orbit coupling, or effects of magnetic exchange interactions between paramagnetic centers. They can be probed by all of the optical spectroscopic methods schematically illustrated in Figure 1a.[37–41] Luminescence spectroscopy often allows the direct observation of patterns corresponding to the ground-state levels. Electronic Raman spectroscopy, a method traditionally regarded as a curiosity in coordination chemistry, has been used recently to gain very detailed information.[27,41–43] Absorption spectroscopy can identify ground-state splittings through the temperature dependence of band intensities, reflecting the thermal population of different ground-state levels.[39,44,45] The combination of several optical spectroscopic techniques is often the most appropriate approach to determine such energy differences.

Figure 1b illustrates a category of optical spectroscopic phenomena outside the traditional limitation to a single initial and final state for an electronic transition. Interacting states, such as the two excited states shown in the figure, have been characterized in detail from optical spectra. They can correspond to excited states, such as different types of metal-centered ligand field or charge-transfer states,[12,46–48] or to the ground state and a low-energy excited state,[49] a situation that has been studied extensively for the optical characterization of spin-crossover compounds, described in Chapter 2.32, or for intervalence bands in mixed valence complexes,[50,51] as presented in Chapter 2.61. The representation of interacting states in Figure 1b is strictly qualitative, their coupling needs to be defined in detail for a quantitative analysis, as shown in Figure 5 of Chapter 2.43. The combination of several spectroscopic techniques and theoretical models is essential for the field of optical electron transfer, as described in detail in Chapter 7.11.

Figure 1c shows some fundamental aspects of selective spectroscopy.[29] The observed optical spectra of solutions or solids are always affected by inhomogeneous broadening, as illustrated by the superposition of several potential energy curves, corresponding to slightly different chromophores in a condensed-phase environment. Inhomogeneous broadening can mask small energy differences between nearby electronic states, as illustrated in Figure 10. Tuning a laser excitation source to an energy corresponding to a specific subset of chromophores can often significantly improve the resolution of optical spectra. This selective excitation is shown in Figure 1c as an arrow between the ground and excited states of one specific subset, denoted by the potential energy curves shown as solid lines. From this selectively excited set of chromophores, a better-resolved, line-narrowed luminescence spectrum can be observed.[29] Many studies report such line-narrowed luminescence transitions to higher-energy ground-state levels,[52–54] a technique used to simplify the experiment as no gated detection is needed to avoid excitation light. The approach has been extended to hole-burning[55,56] and to the detailed characterization of energy transfer processes.[57,58]

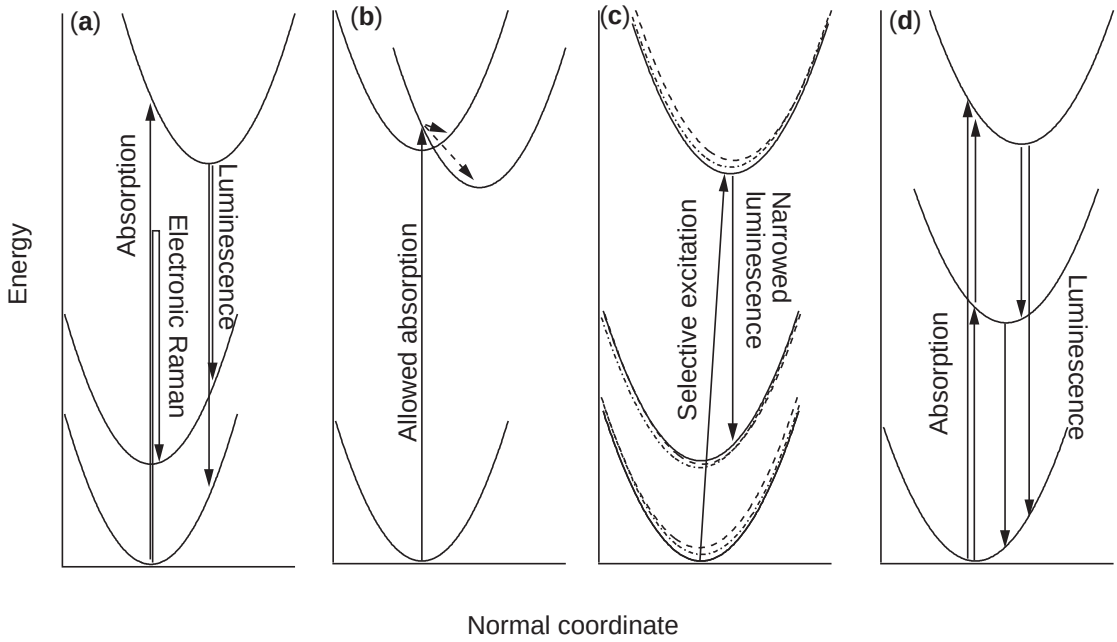

Figure 1 Schematic view of electronic transitions probed by optical spectroscopy. From left to right: (a) conventional absorption, luminescence, and electronic Raman transitions, (b) an absorption transition involving coupled final states, (c) selective spectroscopy probing only a subset of chromophores in a sample, (d) multiple absorption and luminescence transitions and a simple two-step up-conversion process.

Figure 1d shows an area of optical spectroscopy that has gained importance in recent years and is relevant for optical materials research. Luminescence from highly excited states can be observed even when exciting with photon energies that are not sufficient to reach the high-energy emitting state in a single step, leading to effects such as the up-conversion of near-infrared to visible light. In Figure 1d, a sequence of two low-energy absorptions, shown as short upward arrows, excite the luminescent entity to the high-energy emitting state, from which luminescence to the ground state can be observed. Such processes have been known for rare earth ions and their compounds, but have only recently been systematically studied for compounds of the *d*-block elements.[6,7] The properties of intermediate states have been characterized in detail with these experiments.[59]

Optical spectroscopic techniques have been applied to a wide variety of coordination compounds in the solid state, in solution and in the gas phase, underlining the general applicability and the detailed information that can be gained from these techniques. They provide very important photochemical information, as described in Section 7.3 (Volume 1) of the first edition of this work.[3,60–63] An illustrative recent example is the photodissociation reactions of gas-phase coordination compounds that reveal the highly resolved optical spectroscopic signatures of unexpected photofragments.[17,64–66]

2.22.1.1 Charge-transfer Transitions

Optical spectroscopy provides detailed experimental information on many categories of charge-transfer transitions, bands that can be observed for a wide variety of compounds. A typical example of well-resolved charge-transfer absorption bands is shown in Figure 2. The two bands in all spectra are ligand-to-metal charge-transfer (LMCT) transitions for *trans*-$OsO_2L_2^{2-}$ complexes, where L denotes either oxalate or malonate ions.[67–69] These complexes are representatives of a large family of metal–oxo compounds that have received much photochemical and spectroscopic attention.[70,71] The molar absorptivities of the bands shown are on the order of $10^3\,M^{-1}cm^{-1}$, higher by at least two orders of magnitude than those of metal-centered *d–d* transitions. Both the solution spectra in Figure 2a and the solid-state spectra in Figure 2b have resolved vibronic structure. The separation between resolved peaks corresponds to the symmetric O═Os═O stretching frequency in the excited state, indicating that the molecule only undergoes structural

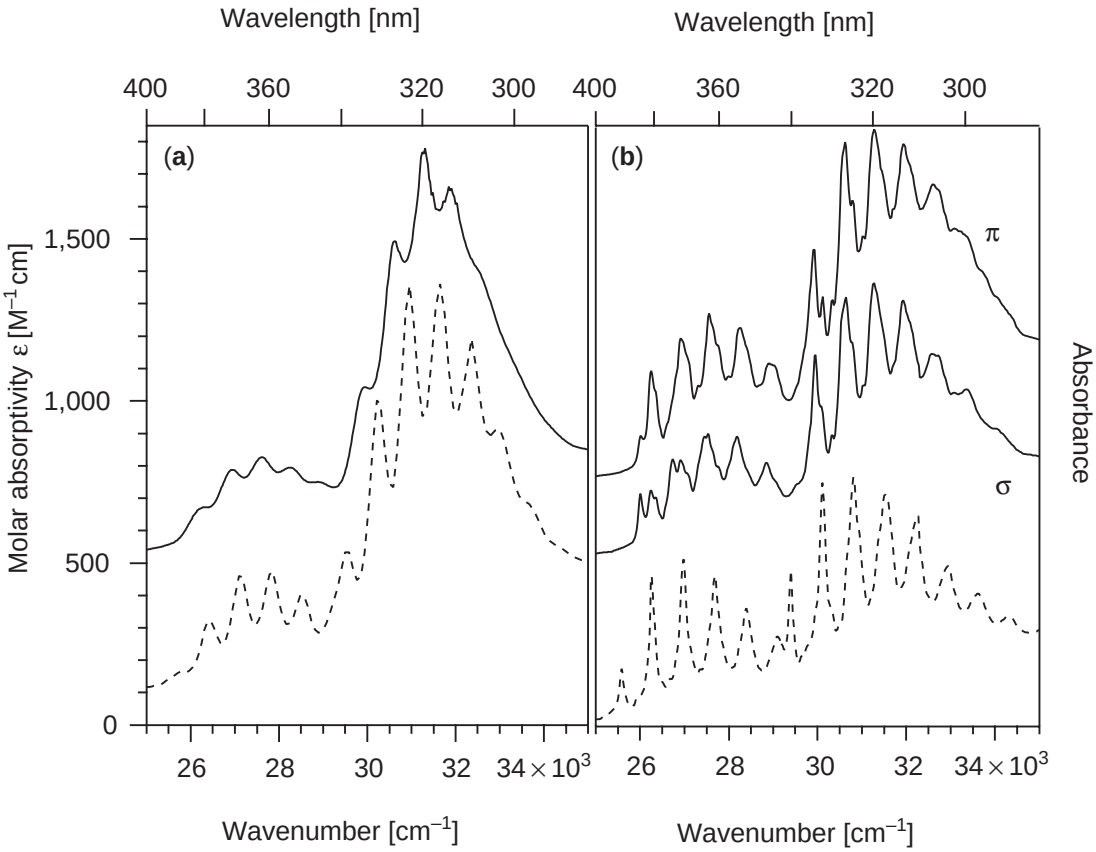

Figure 2 Charge-transfer (LMCT) absorption bands for *trans*-$OsO_2(malonate)_2^{2-}$ (top traces, solid lines) and *trans*-$OsO_2(oxalate)_2^{2-}$ (bottom traces, dotted lines). (a) Solution spectra at room temperature, (b) single-crystal spectra at 10 K. Traces shown as solid lines are shifted along the ordinate axis for clarity.

changes along the normal coordinate of this single mode as a consequence of the LMCT transition. A detailed normal coordinate analysis has shown that this mode consists of more than 98% of the two Os=O oscillators.[68] The average vibrational energies obtained from the absorption spectra are between 670 cm^{-1} and 705 cm^{-1}, lower by approximately 25% than the ground state vibrational frequency of 910 cm^{-1}, indicating that the metal—oxo bonds are significantly weakened in the LMCT excited state. The different patterns observed for the two closely related complexes in Figure 2 reveal transitions that are allowed for *trans*-$OsO_2(malonate)_2^{2-}$ in the C_i point group, but forbidden for *trans*-$OsO_2(oxalate)_2^{2-}$ with D_{2h} symmetry. The most intense set of peaks forming the low-energy band system in the spectrum of *trans*-$OsO_2(malonate)_2^{2-}$ is the one that is allowed in the higher D_{2h} symmetry and it is observed in π polarization, as expected from group theory.[69]

Most charge-transfer transitions show less vibronic resolution than the examples in Figure 2. Resonance Raman spectroscopy has often been used in these cases to analyze the structural changes between the initial and final states of the transition,[2,72,73] an approach especially relevant to metal centers in enzymes and to bioinorganic model compounds.[23,40,74] The full ensemble of optical spectroscopic techniques has been applied to the study of the lowest-energy metal-to-ligand charge-transfer (MLCT) bands in Ru(bipyridine)$_3^{2+}$ and related complexes. Other well-studied cases of MLCT transitions with resolved vibronic structure include a number of $W(CO)_5L$ complexes.[13,16,62,63]

Figure 3 shows the luminescence and absorption spectra of Ir(maleonitrile) $(CO)_2$(t-butylammonium), an iridium(I) compound with interesting charge-transfer bands.[75] The luminescence and excitation spectra are well resolved, and the Stokes shift is relatively small, indicating similar molecular structures in the ground and excited states. The luminescence decays uniformly with time, as shown in the inset to the figure. All these characteristics are typical of transitions often classified as intra-ligand charge-transfer (ILCT) bands. ILCT luminescence bands remain intense

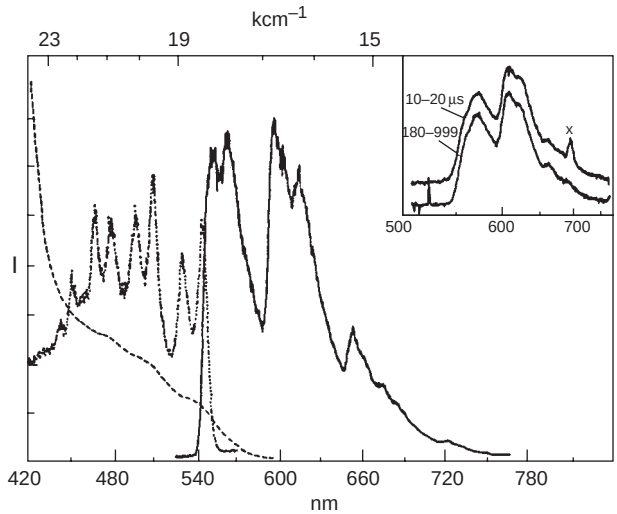

Figure 3 ILCT transitions of the (*t*-butylammonium)$Ir^{I}(CO)_2$(maleonitrile) complex. Luminescence and excitation spectra at 77 K show resolved structure. The dotted line gives the solution absorption spectrum

up to high temperatures and these compounds are promising candidates for applications as light-emitting diodes. Figure 4 presents a particularly well-resolved ILCT transition for the Pt(8-quinolinato-O,N)$_2$ complex in a Shpol'skii matrix of suitable n-alkanes.[76] The luminescence spectrum at 1.2 K shows many short progressions involving ligand-centered modes, a characteristic signature of an ILCT band. This rich structure has been fully analyzed.[76] The effects of a magnetic field on the region of the electronic origins are given in Figure 4b. This modern example illustrates the detailed information that can be gained from charge-transfer bands.

A category of compounds that has received much spectroscopic and photochemical interest due to the particularly rich charge-transfer spectra is square-planar platinum(II) complexes with nitrogen donor ligands.[77–80] The spectra in Figure 5 illustrate MLCT and ILCT transitions for complexes with diimine and pyrazolyl ligands, transitions that can be characterized from both absorption and luminescence spectroscopy. The nature of their emitting state can be modified, for example, by protonation, as illustrated in Figure 5, where two luminescence spectra with clear-cut differences are presented.[79] The broad, unresolved band in Figure 5a is typical for an MLCT

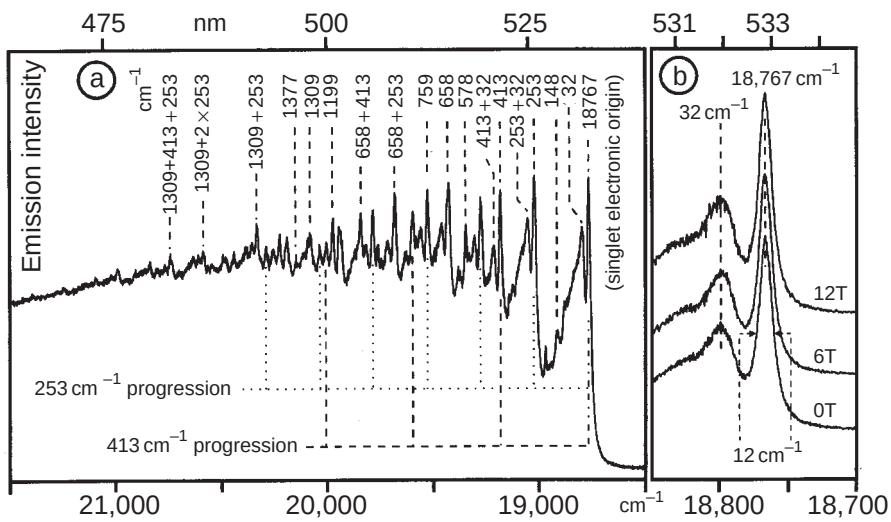

Figure 4 Site-selective spectroscopy of Pt(8-quinolinato-O,N)$_2$). (a) Luminescence spectrum with assignment of the vibronic structure, (b) effect of a magnetic field on the region of the electronic origins (reproduced by permission of the American Chemical Society from *Inorg. Chem.* **1997**, *36*, 3040–3048).

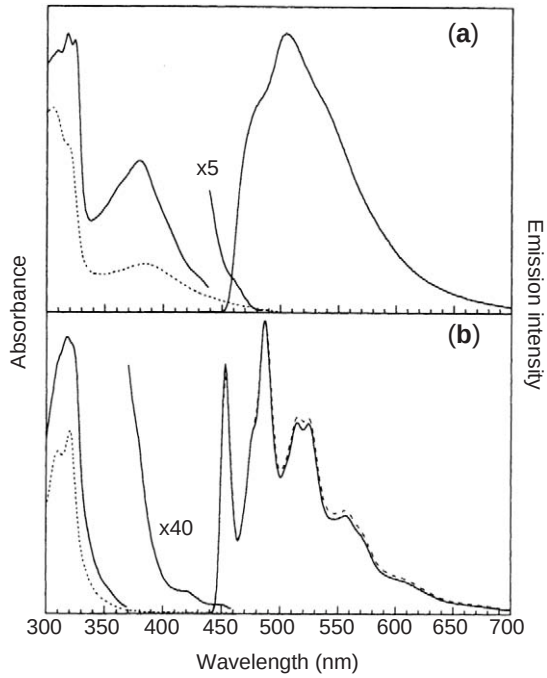

Figure 5 (a) Luminescence and excitation spectra of the MLCT transition of the Pt^{II}(bipyridine)(3,5-dimethylpyrazolate)$_2$ complex in ethanol–methanol (3:1) frozen glass at 77 K. (b) Luminescence and excitation spectra of the ligand-centered transition of the protonated form of the complex in (a) in ethanol–methanol (3:1) frozen glass at 77 K (reproduced by permission of the American Chemical Society from *Inorg. Chem.* **2000**, *39*, 2585–2592).

transition, where low-frequency metal–ligand modes contribute significantly to the vibronic structure, and the resulting spectra are often broad and not resolved. The narrower luminescence spectrum with resolved structure in Figure 5b is indicative of a ligand-centered transition and is very similar to the spectrum observed for the zinc(II) analogs of the platinum(II) compounds. Its vibronic structure is resolved because only high-frequency modes contribute significantly. Solution spectroscopy on these and related complexes is therefore sufficient to reveal the energetic order of electronic excited states. Single-crystal spectroscopy has led to the exact determination of zero-field splittings that can also be used to characterize excited electronic states.[81] The terpyridine ligand system has been studied in a series of detailed spectroscopic and photochemical investigations aimed at chemically tuning the emitting state of platinum(II) complexes.[78,80] A number of other categories of charge-transfer transitions, such as ligand-to-ligand (LLCT) bands,[82–84] have also been explored by detailed optical spectroscopy.

2.22.2 SINGLE-CRYSTAL SPECTROSCOPY

2.22.2.1 Single-crystal Absorption Spectroscopy

Polarized absorption spectra of single crystals have long been used to characterize the electronic structure of coordination compounds.[1,11,85] New examples of completely polarized bands include the unusual linear NiO_2^{2-} complex,[86,87] and the detailed chemical insight that can be obtained from polarized spectra has been illustrated for many low-symmetry complexes.[31,88–90] In addition to the polarization, single-crystal absorption spectra often show resolved vibronic structure that reveals detailed information on excited electronic states. Two examples are presented in Figures 6 and 7. The lowest-energy electronic transitions of $PdBr_4^{2-}$ are shown in Figure 6.[91] These weak bands were not observed in earlier spectroscopic studies, but they are important for the establishment of the energy order of the five molecular orbitals with predominant 4*d* character. All transitions are to triplet final states arising from the excitation of an electron from the occupied $d_{xz,yz}$, d_{xy}, and d_{z^2} metal-centered orbitals to the $d_{x^2-y^2}$ LUMO. Ligand-field calculations have

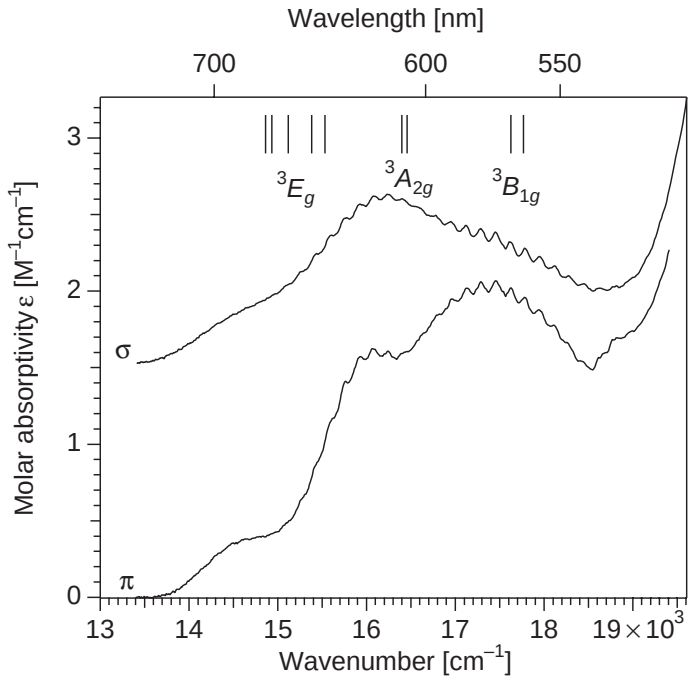

Figure 6 Polarized single-crystal absorption spectra of K_2PdBr_4 at 8 K. Vertical lines above the spectra indicate the lowest-energy calculated ligand-field states. The spectrum in σ polarization is shifted along the ordinate for clarity.

shown that these ^3E_g, $^3A_{2g}$, and $^3B_{1g}$ excited states have energies between 14,800 cm^{-1} and 17,800 cm^{-1},[92] as indicated by the vertical lines in Figure 6. They are lower in energy than all singlet excited states and are in satisfactory agreement with the experimental spectra. The triplet excited states have stronger Pd—Br antibonding character than the ground state and therefore long progressions in the symmetric stretching mode are observed in the spectra. The average progression interval is $165 \pm 2\,cm^{-1}$,[91] significantly lower than the ground state symmetric stretching frequency of 180 cm^{-1}, as expected from the bonding arguments presented above. The resolution of the absorption spectra is not sufficient to identify progressions involving other vibrational modes.

The polarized absorption spectra of *trans*-$NiCl_2(H_2O)_4$ in Figure 7 indicate strong mixing between excited states, as schematically illustrated in Figure 1b. In the O_h point group, the states involved in this mixing are the E_g levels arising from the $^3T_{1g}$ and ^1E_g excited states, interacting via spin–orbit coupling.[48] The most prominent feature of the spectra is the series of four vibronic maxima on the high-energy side of the band, denoted by the vertical lines above the σ-polarized spectrum in Figure 7. Their average spacing is $430 \pm 5\,cm^{-1}$, significantly higher than the frequencies of all ground-state metal–ligand vibrational modes. This interval is a direct manifestation of the interaction between states, illustrating that spin–orbit coupling does not only affect overall intensities, but that it can also have distinct vibronic signatures. The calculated spectrum included in Figure 7 shows that simple ligand-field concepts and spin–orbit coupling can be used to define a quantitative model that is in excellent agreement with the experimental data, as described in detail in Chapter 2.43. The polarization of these spectra also carries important information. In π polarization, the pattern appears to be doubled with a separation of 75 cm^{-1} between the two progressions. This doubling is a consequence of the splitting of the $^1E_g(O_h)$ excited state into $^1A_{1g}$ and $^1B_{1g}$ in the approximate D_{4h} point group symmetry of the complex, and the observed intensities in both polarizations can be explained from group theoretical arguments involving intensity borrowing from the triplet spin-orbit levels with identical symmetry and the symmetries of the available enabling modes.[48] The polarized spectra show directly the effect of the tetragonal symmetry of the complex on transition energies and intensities, and this information is of key importance to rule out alternative explanations for the band shape, which is observed as a double maximum in the room-temperature solution spectrum of many nickel(II) complexes, illustrated by the example in Figure 6 of Chapter 2.43. Table 1 in Chapter 2.43 summarizes such effects of mixing between electronic states for a number of different compounds.

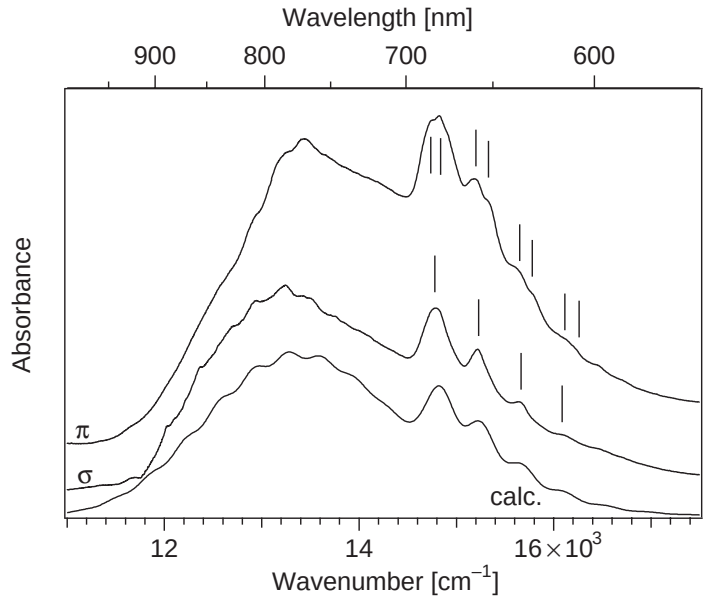

Figure 7 Polarized single-crystal absorption spectra of *trans*-$NiCl_2(H_2O)_4$ recorded at 5 K. Vertical lines above the experimental spectra indicate the single and double progressions observed in σ and π polarization, respectively. The bottom trace is a calculated spectrum obtained with the time-dependent theoretical approach described in Chapter 2.43.

Dramatic examples of interacting electronic states include intervalence bands in mixed-valence compounds[51,93] and many charge-transfer bands where coupled states influence the distribution of electron density, as well as the spin-crossover spectra.

Absorption spectroscopy can also be used to characterize splittings of the electronic ground state, caused, for example, by magnetic exchange coupling. For complexes containing two metal centers, the richest exchange splitting pattern is obtained for metal ions with the high-spin d^5 electron configuration, where pair spins from 0 to 5 are possible. For this configuration, all single-ion *d*–*d* transitions are spin forbidden and weak. Figure 8 shows the temperature dependence of an absorption band system for a specific spin–flip transition, $^6A_1 \rightarrow {}^4A_1$, in $((C_2H_5)_4N)_3Fe_2F_9$, a molecular crystal containing $Fe_2F_9^{3-}$ complexes with the two iron(III) centers bridged by three fluoride ligands.[94] This absorption transition is very sharp at 1.6 K, the lowest temperature in Figure 8. It shows a distinct temperature dependence, with new bands appearing and significant intensity changes in a narrow temperature range up to 14.4 K. Both the band positions and intensities in the polarized temperature-dependent absorption spectra contain quantitative information on the exchange interaction in the ground and excited states. It was determined from Figure 8 and from other temperature-dependent band systems in this compound that the ground state exchange interaction is ferromagnetic with the spin states spread over a range of approximately 20 cm^{-1}.[94] Even such small splittings in both the ground and excited states can be very precisely determined from temperature-dependent absorption intensities, as illustrated by the example in Figure 8. Other effects of magnetic exchange on absorption spectra include bands corresponding to double excitations, often observed in the near-ultraviolet spectral region.[95] Detailed spectra of such transitions have been recorded and models to analyze them quantitatively have been developed,[95] but the understanding of these cooperative transitions remains far from straightforward. The optical spectroscopy of other categories of exchange-coupled systems, including lanthanide ions or organic radical ligands, has received less attention.[96–98]

2.22.2.2 Luminescence and Site-selective Spectroscopy of Single Crystals

Luminescence spectroscopy of single crystals is a technique that often leads to spectra with well-resolved vibronic structure.[25,99–101] In the vast majority of coordination compounds, luminescence is observed only from the lowest-energy excited state and often the polarizations are less distinct than in absorption spectra. An illustrative example is the spectrum of the square

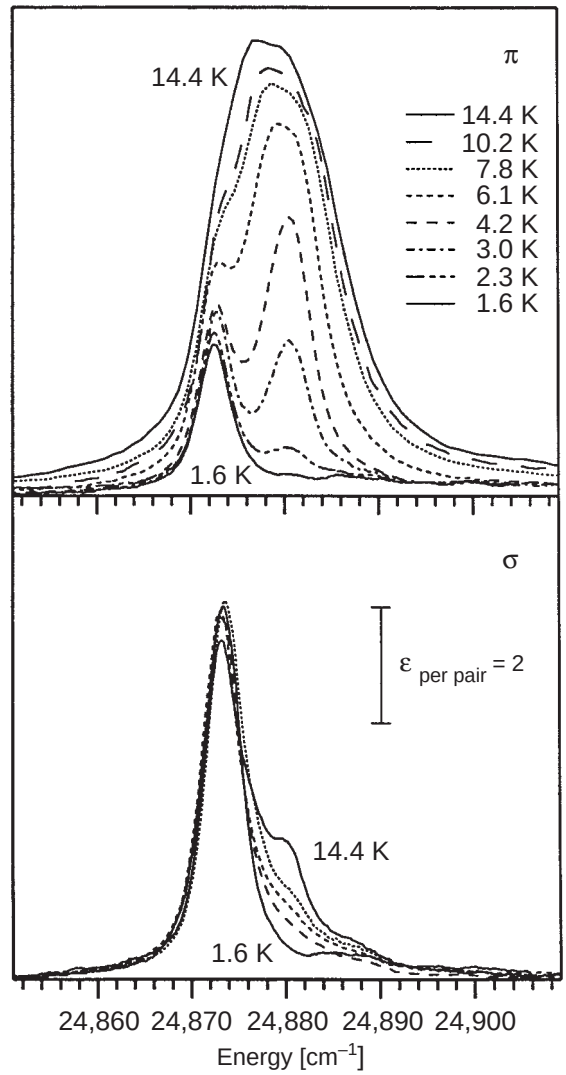

Figure 8 Absorption intensities leading to an optical determination of exchange splittings in the ground and excited states of $Fe_2F_9^{3-}$ (reproduced by permission of the American Chemical Society from *Inorg. Chem.* **2001**, *40*, 4319–4326).

planar $Pd(SCN)_4^{2-}$ complex with the d^8 electron configuration, shown in Figure 9.[102] This is a luminescence spectrum that is only observed at very low temperatures, as illustrated by the significant drop in intensity between 10 K and 30 K. The energy intervals between peaks forming the vibronic structure correspond to ground-state vibrational frequencies. In this example, with approximate D_{4h} point group symmetry, the totally symmetric Pd–S stretching mode with a frequency of 280 cm^{-1} and the in-plane S–Pd–S bending mode at approximately 140 cm^{-1} appear as easily observable vibronic progressions, with the intervals indicated in Figure 9. Luminescence spectra of other square planar complexes of palladium(II) and platinum(II) show vibronic structure involving the asymmetric stretching mode, as summarized in Table 1 of Chapter 2.13. The vibronic progressions allow the emitting state distortions along both totally symmetric and non-totally symmetric normal coordinates to be quantitatively determined from the calculated spectra shown in the figure, and they provide experimental insight on the Jahn–Teller effect in the emitting state and on σ and π metal–ligand bonding. Comprehensive overviews of the optical spectroscopy of other Jahn–Teller systems have been published.[100,103,104]

Site-selective spectroscopy has been very successfully applied to single crystals.[29,37] Figure 10 shows a particularly illustrative example revealing the ground-state magnetic exchange splittings in a bimetallic chromium(III) compound, $[(Bispicam)Cr^{III}(OH)_2(SO_4)Cr^{III}(Bispicam)]S_2O_6 \cdot 3H_2O$, where Bispicam denotes *N,N′*-bis(2-pyridylmethyl)-amine.[53] The two chromium(III) centers in this

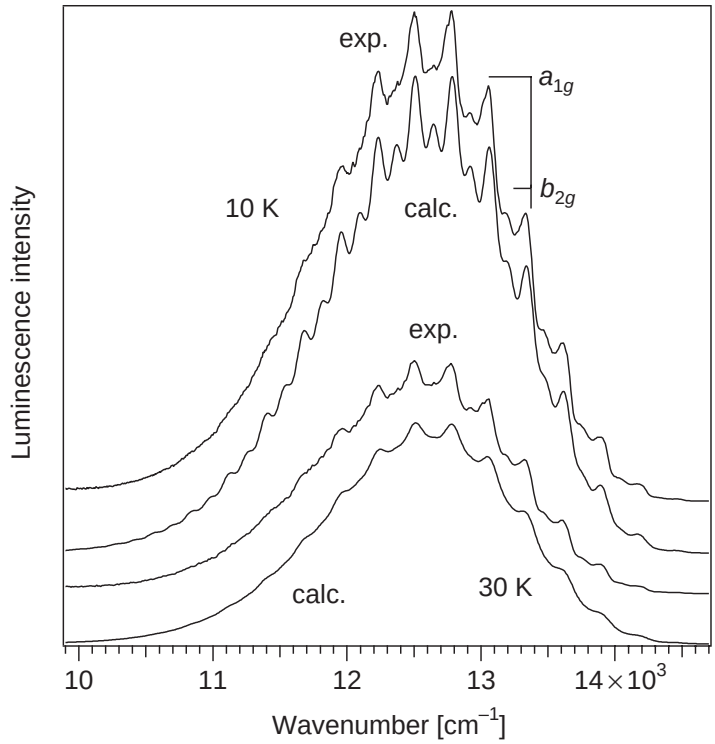

Figure 9 Single-crystal luminescence spectra of $Pd(SCN)_4^{2-}$ with resolved vibronic structure at 10 K and 30 K. Intervals corresponding to the a_{1g} totally symmetric Pd–S stretching mode and the b_{2g} S–Pd–S in-plane bending mode (D_{4h} labels) are given as horizontal lines. The calculated spectra were obtained with the approach described in Chapter 2.43.

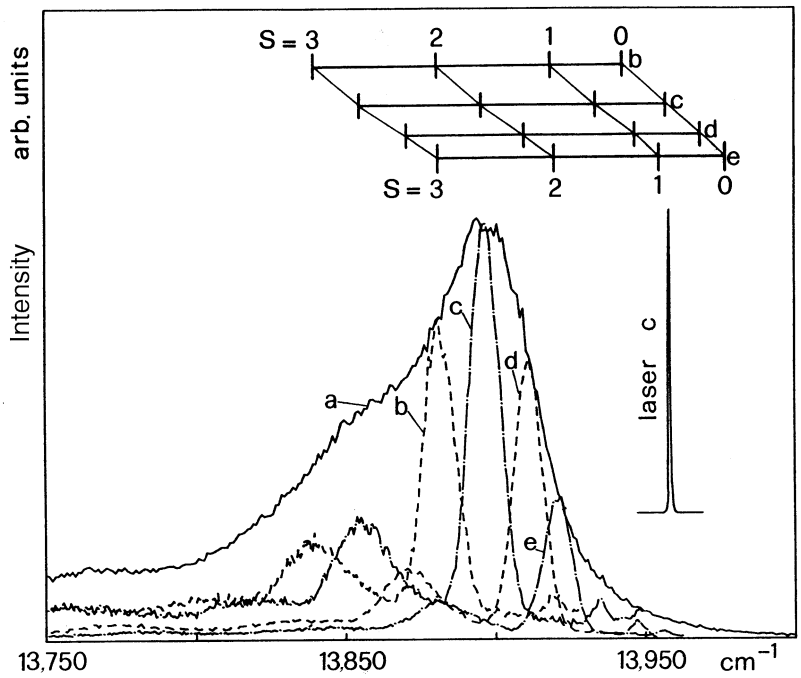

Figure 10 Selectively excited luminescence spectra for a bimetallic chromium(III) complex, [(Bispicam)-$Cr^{III}(OH)_2(SO_4)Cr^{III}$(Bispicam)]$S_2O_6 \cdot 3H_2O$, where Bispicam denotes *N*,*N*′-bis(2-pyridylmethyl)-amine. The traditional, unselectively excited luminescence spectrum is shown as trace (a). Traces (b) to (e) denote selectively excited luminescence spectra from specific subsets of molecules (reproduced by permission of Elsevier Science from *Chem. Phys. Lett.* **1987**, *133*, 429–432).

compound are bridged by a sulfate and two hydroxo ligands. The luminescence spectrum excited near one of the spin-allowed ligand-field absorption maxima shows no resolution and is denoted as trace *a* in Figure 10. For this spectrum, the inhomogeneous broadening is larger than the energy differences between levels of the ground state split by magnetic exchange effects. The selectively excited luminescence spectra for laser energies *b* to *e* very clearly reveal these ground state levels as distinct maxima. The observed energy differences increase as the luminescence transition energies decrease, confirming that the coupling between the paramagnetic centers is antiferromagnetic. The luminescence line-narrowing experiments allow not only a determination of average exchange parameters, but also a comparison of the exchange interaction in different subsets of molecules in the crystal. For the compound in Figure 10, the energy difference between the two lowest ground-state levels is obtained from the energy of the excitation laser and from the highest-energy resolved peak in the line-narrowed luminescence spectra. A systematic decrease from 23.9 cm^{-1} to 21.7 cm^{-1} is observed with increasing excitation energy from traces *b* to *e*, identifying the distinctly different subsets of complexes in the crystal. This example illustrates that even highly sensitive magnetic measurements on such crystals can lead to fallible results. Optical spectroscopy allows a direct determination of the ground-state energy differences, and provides a complementary approach to the magnetic measurements described in Chapter 2.31.

2.22.3 OTHER MODERN OPTICAL SPECTROSCOPIC TECHNIQUES

Ground–state splittings can not only be probed by the methods described in the two preceding sections, but also by electronic Raman spectroscopy, as shown schematically in Figure 1a. A modern example for the application of this technique is the electronic Raman spectroscopy of several vanadium(III) alums in Figure 11.[27] The experimental results were obtained on large single crystals of the highest quality. In perfectly octahedral coordination, the electronic ground state for d^2 ions such as vanadium(III) is $^3T_{1g}$, with spin–orbit levels separated by less than 300 cm^{-1}.[38] In the low-temperature electronic Raman spectra in Figure 11, broad bands are observed between 1,600 cm^{-1} and 2,200 cm^{-1} for the transition to the higher-energy ground state components. These energy differences are larger by almost an order of magnitude than the spin–orbit splittings, and they quantitatively reveal the low-symmetry effects of the crystal lattice on the ground state electronic structure of the chromophore. Figure 12 compares ground-state splittings observed in both luminescence and electronic Raman spectra for $V(urea)_6I_3$, another vanadium(III) complex with a distorted octahedral coordination sphere consisting of oxygen atoms.[43] Its electronic Raman band coincides in energy with the luminescence band observed for the transition from the emitting state to the higher-energy ground-state components, clearly indicating a ground-state splitting ΔE of approximately 1,500 cm^{-1}, significantly smaller than measured for the vanadium(III) alums in Figure 11. The luminescence spectrum shows bands at energies lower than 8,400 cm^{-1}, not present in the Raman spectrum and most likely corresponding to vibronic origins. Comparisons as shown in Figure 12 have become straightforward with modern instruments. Ground-state splittings larger by more than a factor of five than those described for the first-row transition metal compounds above are observed for second- and third-row complexes.[105]

External perturbations, such as pressure[35,36] or electric and magnetic fields, discussed in Chapters 2.23 and 2.25, often lead to dramatic optical spectroscopic effects. An example is the luminescence of samarium(II) ions doped into SrFCl shown in Figure 13, where pressure induces a large change in the spectrum.[35] Between ambient pressure and 67 kbar, the expected intraconfigurational $^5D_0 \rightarrow {}^7F_1$ luminescence transitions are observed as narrow lines. They show a pressure-dependent red shift of $-5\,cm^{-1}$/kbar, a value higher than the shift of the R_1 line of ruby, the longstanding pressure calibration standard. At higher pressures, shown in Figure 13 up to a limit of 310 kbar, a broad, unstructured transition dominates the spectrum, clearly corresponding to another category of electronic transition. Its final state has been assigned as arising from the lowest level of the $4f^5 5d^1$ electron configuration. The energies of the 5*d* orbitals are expected to change strongly with pressure, allowing the crossover to occur. Luminescence lifetimes as a function of pressure for the same solid show a decrease, as expected for increasing mixing of 5*d* character into the emitting state electron configuration.[106] Such spectroscopic experiments illustrate the potential for tuning luminescence properties over a wide range and give quantitative information on bonding and vibronic effects. Of particular recent interest have been systems where the emitting state changes with pressure, as illustrated in Figure 13. Many

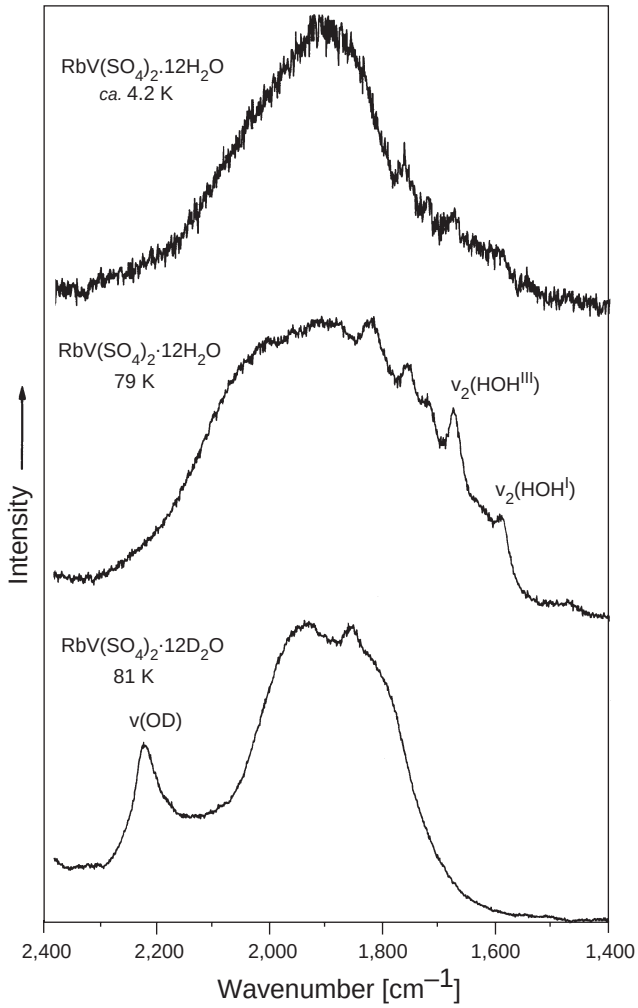

Figure 11 Polarized electronic Raman spectra of three different vanadium alums (reproduced by permission of the American Chemical Society from *Inorg. Chem.* **1996**, *35*, 5730–5736).

such studies have been reported for chromium(III) compounds.[35] More recently, other first-row metal compounds, such as octahedral VCl_6^{3-}, have been investigated.[107] The interactions between electronic ground and excited states have been probed for compounds of the heavier transition elements.[108] The magnetic exchange interaction in chromium(III) compounds similar to the example in Figure 10 has been studied as a function of external pressure, and shifts of electronic origins that are larger by an order of magnitude than those of the ruby R_1 line have been observed.[109,110] A recent development is the study of vibronic band shapes and resolved vibronic structure as a function of external pressure, applied, for example, to luminescence spectra of Jahn–Teller active titanium(III) ions doped into Al_2O_3[111] and to chromium(III) ions doped into chloride lattices,[112] where the effect of pressure on the Jahn–Teller effect in the $^4T_{2g}$ emitting state was determined. Room-temperature luminescence intensities from square planar complexes of palladium(II) and platinum(II) have been shown to increase significantly with pressure.[113] Pressure-induced changes of the high-frequency vibronic structure in *trans*-dioxo complexes of rhenium(V) have also been reported.[108]

Materials with multiple emitting states have become an important area where a variety of novel non-linear processes can be probed by optical spectroscopy.[6,7] A clear-cut example is illustrated in Figures 14 and15.[114] Luminescence from multiple excited states is observed from molybdenum (III) ions doped into several chloride and bromide elpasolite lattices. These ions have the same d^3 electron configuration as chromium(III), but due to their stronger crystal field, all quartet excited states are at very high energies, above the lowest sets of doublet states, as illustrated in the energy level scheme in Figure 14. Figures 14 and 15 show that luminescence is observed from both the

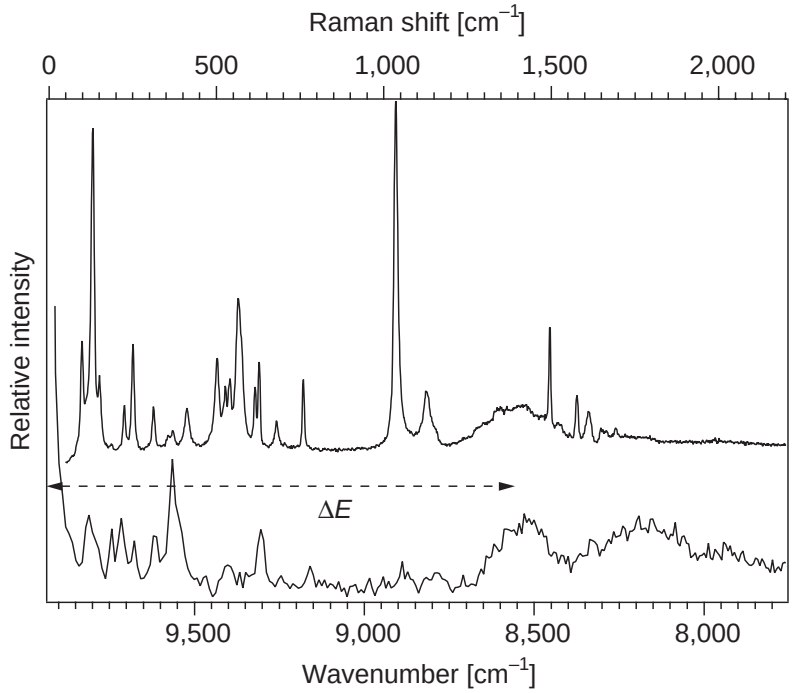

Figure 12 Electronic Raman spectrum (top trace and abscissa scale) and near-infrared luminescence spectrum (bottom trace and abscissa scale) of $V(urea)_6I_3$. The energy difference ΔE denoted by the horizontal double arrow indicates the ground state splitting.

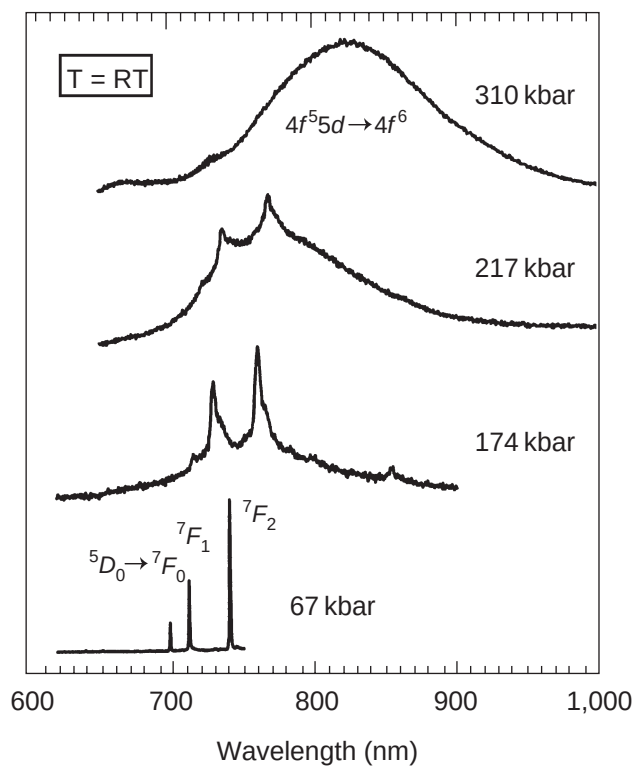

Figure 13 Pressure effect on the room-temperature luminescence spectrum of samarium(II) doped into SrFCl (reproduced by permission of Springer-Verlag from *Top. Curr. Chem.* **2001**, *213*, 1–94).

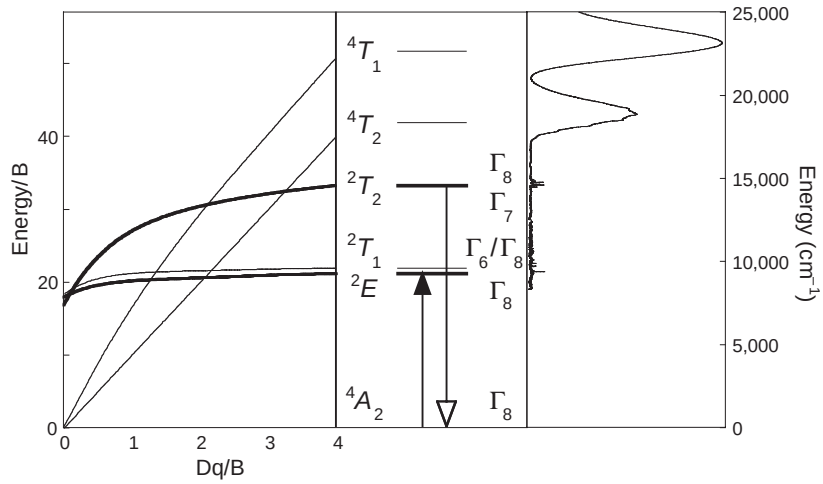

Figure 14 Schematic view of the relevant states and transitions for up-conversion processes and luminescence from higher excited states in halide elpasolites doped with molybdenum(III) (reproduced by permission of the American Chemical Society from *J. Phys. Chem. B* **2000**, *104*, 10222–10234).

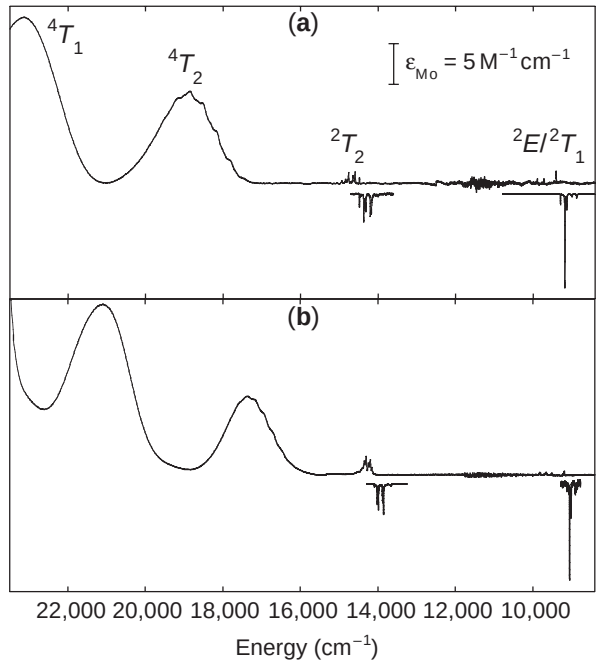

Figure 15 Absorption and luminescence spectra of molybdenum(III) ions doped into Cs_2NaYCl_6 (a) and Cs_2NaYBr_6 (b), an illustrative system for up-conversion. All spectra were measured at 10 K (reproduced by permission of the American Chemical Society from *J. Phys. Chem. B* **2000**, *104*, 10222–10234).

lowest energy ^2E and $^2T_1$ doublet states and also from the higher energy $^2T_2$ state, from which no luminescence is observed in chromium(III) compounds. Up-conversion has been achieved in these lattices by using red light to sequentially excite the molybdenum(III) centers to the ^2E, $^2T_1$ states and then to the higher doublet excited states, as schematically illustrated in Figure 1d. Several mechanisms for such phenomena have been discovered and their efficiency has been compared for a number of different transition metal and rare earth compounds,[6,7] but the area is far from fully explored. Even small structural changes, such as those caused by external pressure, can lead to different up-conversion mechanisms.[115] Many other intriguing optical spectroscopic effects have recently been discovered for materials with multiple emitting states, such as the optical bistability

for ytterbium(III) compounds,[116] and optical spectroscopy will continue to be a powerful tool for the development and characterization of new materials with interesting optical properties.

2.22.4 REFERENCES

1. Lever, A. B. P. *Inorganic Electronic Spectroscopy*; 2nd ed.; Elsevier Science Publishers B.V.: Amsterdam, 1984.
2. Zink, J. I.; Shin , K.-S. K. *Adv. Photochem.* **1991**, *16*, 119–214.
3. Zink, J. I. *Coord. Chem. Rev.* **2001**, *211*, 69–96.
4. Gütlich, P.; Hauser, A.; Spiering, H. *Angew. Chemie Int. Ed. Engl.* **1994**, *33*, 2024.
5. Gütlich, P.; Spiering, H.; Hauser, A. In *Inorganic Electronic Structure and Spectroscopy*; Solomon, E. I., Lever, A. B. P., Eds.; John Wiley & Sons, Inc: New York, 1999; Vol. II, pp 575–622.
6. Gamelin, D. R.; Güdel, H. U. *Acc. Chem. Res.* **2000**, *33*, 235–242.
7. Gamelin, D. R.; Güdel, H. U. *Top. Curr. Chem.* **2001**, *214*, 1–56.
8. Blasse, G. *Prog. Solid St. Chem.* **1988**, *18*, 79–171.
9. Caird, J. A.; Payne, S. A.; Staver, P. R.; Ramponi, A. J.; Chase, L. L.; Krupke, W. F. *IEEE J. Quant. Electr.* **1988**, *24*, 1077–1099.
10. Jacobsen, S. M.; Tissue, B. M.; Yen, W. M. *J. Phys. Chem.* **1992**, *96*, 1547–1553.
11. Ferguson, J. *Progr. Inorg. Chem.* **1970**, *12*, 159–293.
12. Bussière, G.; Beaulac, R.; Cardinal-David, B.; Reber, C. *Coord. Chem. Rev.* **2001**, *219–221*, 509–543.
13. Geoffroy, G. L.; Wrighton, M. S. *Organometallic Photochemistry*; Academic Press: New York, 1979.
14. Lees, A. J. *Chem. Rev.* **1987**, *87*, 711–743.
15. Davis, M. J.; Reber, C. *Inorg. Chem.* **1995**, *34*, 4585–4590.
16. Weiss, J.; Fischer, R. A.; Pelletier, Y.; Reber, C. *Inorg. Chem.* **1998**, *37*, 3316–3320.
17. Muraoka, P.; Byun, D.; Zink, J. I. *Coord. Chem. Rev.* **2000**, *208*, 193–211.
18. Brunold, T. C.; Gamelin, D. R.; Solomon, E. I. *J. Am. Chem. Soc.* **2000**, *122*, 8511–8523.
19. Brunold, T. C.; Gamelin, D. R.; Stemmler, T. L.; Mandal, S. K.; Armstrong, W. H.; Penner-Hahn, J. E.; Solomon, E. I. *J. Am. Chem. Soc.* **1998**, *120*, 8724–8738.
20. Randall, D. W.; Gamelin, D. R.; LaCroix, L. B.; Solomon, E. I. *J. Biol. Inorg. Chem.* **2000**, *5*, 16–29.
21. Solomon, E. I. *Inorg. Chem.* **2001**, *40*, 3656–3669.
22. Mandimutsira, B. S.; Yamarik, J. L.; Brunold, T. C.; Gu, W. W.; Cramer, S. P.; Riordan, C. G. *J. Am. Chem. Soc.* **2001**, *123*, 9194–9195.
23. Craft, J. L.; Mandimutsira, B. S.; Fujita, K.; Riordan, C. G.; Brunold, T. C. *Inorg. Chem.* **2003**, *42*, 859–867.
24. Radovanovic, P. V.; Gamelin, D. R. *J. Am. Chem. Soc.* **2001**, *123*, 12207–12214.
25. Brunold, T.; Güdel, H. U. In *Inorganic Electronic Structure and Spectroscopy*; Solomon, E. I., Lever, A. B. P., Eds.; John Wiley & Sons, Inc.: New York, 1999; Vol. I, pp 259–306.
26. McMillin, D. R. In *Physical Methods in Bioinorganic Chemistry*; Que, L., Jr, Ed.; University Science Books: Sausalito, 2000, pp 1–58.
27. Tregenna-Piggott, P. L. W.; Best, S. P. *Inorg. Chem.* **1996**, *35*, 5730–5736.
28. Lever, A. B. P.; Solomon, E. I. In *Inorganic Electronic Structure and Spectroscopy*; Solomon, E. I., Lever, A. B. P., Eds.; John Wiley & Sons, Inc.: New York, **1999**; Vol. I, pp 1–91.
29. Figgis, B. N. UV-Visible Spectra of Complexes. In *Comprehensive Coordination Chemistry*; Wilkinson, G., Ed.; Pergamon: Oxford, UK, 1987; Vol. 1, Chapter 6.5.3, pp 243–256.
30. Krausz, E.; Riesen, H. In *Inorganic Electronic Structure and Spectroscopy*; Solomon, E. I., Lever, A. B. P., Eds.; John Wiley & Sons, Inc: New York, **1999**; Vol. I, pp 307–352.
31. Chang, T.-H.; Zink, J. I. *J. Am. Chem. Soc.* **1984**, *106*, 287–292.
32. Oetliker, U.; Reber, C. *J. Near Infrared Spectr.* **1995**, *3*, 63–71.
33. Perng, J.-H.; Zink, J. I. *Inorg. Chem.* **1988**, *27*, 1403–1406.
34. Drickamer, H. G.; Bray, K. L. *Acc. Chem. Res.* **1990**, *23*, 55–61.
35. Bray, K. L. *Top. Curr. Chem.* **2001**, *213*, 1–94.
36. Grey, J. K.; Butler, I. S. *Coord. Chem. Rev.* **2001**, *219–221*, 713–759.
37. McCarthy, P. J.; Güdel, H. U. *Coord. Chem. Rev.* **1988**, *88*, 69–131.
38. Reber, C.; Güdel, H. U. *J. Lum.* **1988**, *42*, 1–13.
39. Jacobsen, S. M.; Güdel, H. U.; Daul, C. A. *J. Am. Chem. Soc.* **1988**, *110*, 7610.
40. Solomon, E. I.; Tuczek, F.; Root, D. E.; Brown, C. A. *Chem. Rev.* **1994**, *94*, 827–856.
41. Tregenna-Piggott, P. W. L.; Best, S. P.; Güdel, H. U.; Weihe, H.; Wilson, C. C. *J. Sol. Stat. Chem.* **1999**, *145*, 460–470.
42. Spichiger, D.; Carver, G.; Dobe, C.; Bendix, J.; Tregenna-Piggott, P. L. W.; Meier, R.; Zahn, G. *Chem. Phys. Lett.* **2001**, *337*, 391–397.
43. Beaulac, R.; Tremblay, J. C.; Bussière, G.; Reber, C. *Can. J. Analyt. Sci. Spectr.* **2001**, *46*, 152–161.
44. Cador, O.; Mathonière, C.; Kahn, O. *Inorg. Chem.* **2000**, *39*, 3799–3804.
45. Schenker, R.; Heer, S.; Güdel, H. U.; Weihe, H. *Inorg. Chem.* **2001**, *40*, 1482–1488.
46. Reber, C.; Zink, J. I. *J. Chem. Phys.* **1992**, *96*, 2681–2690.
47. Reber, C.; Zink, J. I. *Comm. on Inorg. Chem.* **1992**, *13*, 177–220.
48. Bussière, G.; Reber, C. *J. Am. Chem. Soc.* **1998**, *120*, 6306–6315.
49. Savoie, C.; Reber, C. *J. Am. Chem. Soc.* **2000**, *122*, 844–852.
50. Demadis, K. D.; Hartshorn, C. M.; Meyer, T. J. *Chem. Rev.* **2001**, *101*, 2655–2686.
51. Talaga, D. S.; Zink, J. I. *J. Phys. Chem. A* **2001**, *105*, 10511–10519.
52. Riesen, H.; Güdel, H. U. *Mol. Phys.* **1987**, *60*, 1221–1244.
53. Riesen, H.; Güdel, H. U. *Chem. Phys. Lett.* **1987**, *133*, 429–432.
54. Riesen, H.; Krausz, E. R.; Dubicki, L. *J. Lum.* **1989**, *44*, 97–103.
55. Riesen, H. *J. Phys. Chem. A* **2000**, *104*, 5469–5474.

56. Hughes, J. L.; Riesen, H. *J. Phys. Chem. A* 2003, *107*, 35–42.
57. von Arx, M. E.; Hauser, A.; Riesen, H.; Pellaux, R.; Decurtins, S. *Phys. Rev. B* **1996**, *54*, 15800–15807.
58. von Arx, M. E.; Burattini, E.; Hauser, A.; van Pieterson, L.; Pellaux, R.; Decurtins, S. *J. Phys. Chem. A* **2000**, *104*, 883–893.
59. Wermuth, M.; Güdel, H. U. *Chem. Phys. Lett.* **2000**, *323*, 514–521.
60. Kutal, C.; Adamson, A. W. Photochemical Processes. In *Comprehensive Coordination Chemistry*; Wilkinson, G., Ed.; Pergamon: Oxford, UK, 1987; Vol. 1, Chapter 7.3, pp 385–414.
61. Kirk, A. D. *Chem. Rev.* **1999**, *99*, 1607–1640.
62. Dahlgren, R. M.; Zink, J. I. *J. Am. Chem. Soc.* **1979**, *101*, 1448–1454.
63. Tutt, L.; Zink, J. I. *J. Am. Chem. Soc.* **1986**, *108*, 5830–5836.
64. Talaga, D. S.; Hanna, S. D.; Zink, J. I. *Inorg. Chem.* **1998**, *37*, 2880–2887.
65. Cheon, J.; Kang, H. K.; Zink, J. I. *Coord. Chem. Rev.* **2000**, *200*, 1009–1032.
66. Bitner, T. W.; Zink, J. I. *Inorg. Chem.* **2002**, *41*, 967–972.
67. Preetz, W.; Schulz, H. *Z. Naturforsch.* **1983**, *38b*, 183–189.
68. Struess, A.; Preetz, W. *Z. Naturforsch.* **1998**, *53b*, 823–828.
69. Stanislas, S.; Reber, C.; Beauchamp, A. L. *Inorg. Chem.* **2000**, *39*, 2152–2155.
70. Yam, V. W.-W.; Che, C.-M. *Coord. Chem. Rev.* **1990**, *97*, 93–104.
71. Miskowski, V. M.; Gray, H. B.; Hopkins, M. D. In *Advances in Trans. Met. Coord. Chem.*; Che, C.-M., Yam, V. W.-W., Eds.; JAI Press: Greenwich, CT, 1996; Vol. 1, pp 159–186.
72. Shin, K.-S. K.; Zink, J. I. *Inorg. Chem.* **1989**, *28*, 4358–4366.
73. Shin, K.-S. K.; Zink, J. I. *J. Am. Chem. Soc.* **1990**, *112*, 7148–7157.
74. Loppnow, G. R.; Fraga, E. *J. Am. Chem. Soc.* **1997**, *119*, 896–905.
75. Johnson, C. E.; Eisenberg, R.; Evans, T. R.; Burberry, M. S. *J. Am. Chem. Soc.* **1983**, *105*, 1795–1802.
76. Donges, D.; Nagle, J. K.; Yersin , H. *Inorg. Chem.* **1997**, *36*, 3040–3048.
77. Hissler, M.; Connick, W. B.; Geiger, D. K.; McGarrah, J. E.; Lipa, D.; Lachicotte, R. J.; Eisenberg, R. *Inorg. Chem.* **2000**, *39*, 447–457.
78. Michalec, J. F.; Bejune, S. A.; McMillin, D. R. *Inorg. Chem.* **2000**, *39*, 2708–2709.
79. Connick, W. B.; Miskowski, V. M.; Houlding, V. H.; Gray, H. B. *Inorg. Chem.* **2000**, *39*, 2585–2592.
80. McMillin, D. R.; Moore, J. J. *Coord. Chem. Rev.* **2002**, *229*, 113–121.
81. Yersin, H.; Donges, D. *Top. Curr. Chem.* **2001**, *214*, 81–186.
82. Vogler, A.; Kunkely, H. *Top. Curr. Chem.* **2001**, *213*, 143–182.
83. Wootton, J. L.; Zink, J. I. *J. Phys. Chem.* **1995**, *99*, 7251–7257.
84. Acosta, A.; Zink, J. I.; Cheon, J. *Inorg. Chem.* **2000**, *39*, 427–432.
85. Day, P. *Angew. Chem. Int. Ed. Engl.* **1980**, *19*, 290–301.
86. Hitchman, M. A.; Stratemeier, H.; Hoppe, R. *Inorg. Chem.* **1988**, *27*, 2506–2510.
87. Wexler, D.; Zink, J. I.; Reber, C. *J. Phys. Chem.* **1992**, *96*, 8757–8765.
88. Chang, T.-H.; Zink, J. I. *Inorg. Chem.* **1985**, *24*, 4499–4503.
89. Chang, T.-H.; Zink, J. I. *Inorg. Chem.* **1986**, *25*, 2736–2741.
90. Da Re, R. E.; Hopkins, M. D. *Inorg. Chem.* **2002**, *41*, 6973–6985.
91. Pelletier, Y.; Reber, C. *Inorg. Chem.* **1997**, *36*, 721–728.
92. Harvey, P. D.; Reber, C. *Can. J. Chem.* **1999**, *77*, 16–23.
93. Brunschwig, B. S.; Creutz, C.; Sutin, N. J. *Chem. Soc. Rev.* **2002**, *31*, 168–184.
94. Schenker, R.; Weihe, H.; Güdel, H. U. *Inorg. Chem.* **2001**, *40*, 4319–4326.
95. Schenker, R.; Weihe, H.; Güdel, H. U. *Inorg. Chem.* **1999**, *38*, 5593–5601.
96. Benelli, C.; Dei, A.; Gatteschi, D.; Güdel, H. U.; Pardi, L. *Inorg. Chem.* **1989**, *28*, 3089–3091.
97. Lescop, C.; Luneau, D.; Rey, P.; Bussière, G.; Reber, C. *Inorg. Chem.* **2002**, *41*, 5566–5574.
98. Tsukahara, Y.; Iino, A.; Yoshida, T.; Suzuki, T.; Kaizaki, S. *J. Chem. Soc.—Dalton Trans.* **2002**, 181–187.
99. Brunold, T. C.; Hauser, A.; Güdel, H. U. *J. Lumin.* **1994**, *59*, 321–332.
100. Brunold, T. C.; Hazenkamp, M. F.; Güdel, H. U. *J. Am. Chem. Soc.* **1995**, *117*, 5598–5599.
101. Larson, L. J.; Zink, J. I. *Inorg. Chem.* **1989**, *28*, 3519–3523.
102. Pelletier, Y.; Reber, C. *Inorg. Chem.* **2000**, *39*, 4535–4541.
103. Brunold, T. C.; Güdel, H. U.; Riley, M. J. *J. Chem. Phys.* **1996**, *105*, 7931–7941.
104. Riley, M. J. *Top. Curr. Chem.* **2001**, *214*, 57–80.
105. Wermuth, M.; Reber, C.; Güdel, H. U. *Inorg. Chem.* **2001**, *40*, 3693–3703.
106. Shen, Y. R.; Bray, K. L. *Phys. Rev. B* **1998**, *58*, 11944–11958.
107. Wenger, O. S.; Güdel, H. U. *Chem. Phys. Lett.* **2002**, *354*, 75–81.
108. Grey, J. K.; Triest, M.; Butler, I. S.; Reber, C. *J. Phys. Chem. A* **2001**, *105*, 6269–6272.
109. Riesen, H.; Güdel, H. U. *Inorg. Chem.* **1987**, *26*, 2347–2348.
110. Riesen, H.; Güdel, H. U. *J. Chem. Phys.* **1987**, *87*, 3166–3172.
111. García-Revilla, S.; Rodríguez, F.; Valiente, R.; Pollnau, M. *J. Phys.: Condens. Matter* **2002**, *14*, 447–459.
112. Wenger, O. S.; Valiente, R.; Güdel, H. U. *J. Chem. Phys.* **2001**, *115*, 3819–3826.
113. Grey, J. K.; Butler, I. S.; Reber, C. *J. Amer. Chem. Soc.* **2002**, *124*, 9384–9385.
114. Gamelin, D. R.; Güdel, H. U. *J. Phys. Chem. B* **2000**, *104*, 10222–10234.
115. Wenger, O. S.; Salley, G. M.; Güdel, H. U. *J. Phys. Chem. B* **2002**, *106*, 10082–10088.
116. Gamelin, D. R.; Lüthi, S. R.; Güdel, H. U. *J. Phys. Chem. B* **2000**, *104*, 11045–11057.

Comprehensive Coordination Chemistry II
ISBN (set): 0-08-0437486

Volume 2, (ISBN 0-08-0443249); pp 287–302

2.23
Stark Spectroscopy

K. A. WALTERS
Northern Kentucky University, Highland Heights, KY, USA

2.23.1 INTRODUCTION 303
2.23.2 STARK ABSORPTION SPECTROSCOPY 304
2.23.2.1 Theory 304
2.23.2.2 Experimental Considerations 305
2.23.2.3 Literature Examples 306
2.23.2.3.1 $Ru(bpy)_32+$ 306
2.23.2.3.2 $Ru(NH_3)_5L^{2+}$ 307
2.23.2.3.3 $(NH_3)_5$Ru-bridge-$Ru(NH_3)_5^{5+}$ 308
2.23.2.3.4 Biological systems 308
2.23.2.3.5 Second-order nonlinear optical chromophores 308
2.23.3 STARK EMISSION SPECTROSCOPY 308
2.23.3.1 Theory and Experimental Considerations 309
2.23.3.2 Literature Examples 309
2.23.3.2.1 $(bpy)Re(CO)_3Cl$ 309
2.23.3.2.2 Interfacial charge transfer 309
2.23.4 TRANSIENT DC PHOTOCONDUCTIVITY 310
2.23.4.1 Theory 310
2.23.4.2 Experimental Considerations 311
2.23.4.3 Literature Examples 311
2.23.4.3.1 $(bpy)Re(CO)_3Cl$ 311
2.23.4.3.2 Other transient DC photoconductivity measurements 311
2.23.5 SUMMARY 311
2.23.6 REFERENCES 312

2.23.1 INTRODUCTION

Many photophysical processes occurring within coordination and supramolecular complexes entail charge transfer (CT).[1] A key parameter is the distance over which the charge (i.e., electron or hole) is transferred, which can be used to extract, for example, electronic coupling parameters (H_{ab} values) from oscillator strengths, along with important information about solvent reorganization energies. In other cases, the CT distance magnitude is unimportant compared to whether CT occurs at all (i.e., does a specific optical transition comprise a CT transition?). Furthermore, more chemically significant questions arise: When charge is transferred, how is it ultimately distributed? Is molecular symmetry preserved when charges are transferred?

At first glance, determining CT distances appears to be trivial since electron-donor/-acceptor separation distances can be determined with molecular modeling or x-ray crystallography. These "geometric" distances, however, often significantly differ from the actual one-electron transfer distances. (Note, however, that more detailed calculations can suggest relative CT distances in a molecular series through comparison of excited-state electronic population redistribution. For more information, see Lever and Gorelsky, 2000[2]) How can "true" CT distances be obtained? In a simple two-state model, simple relationships exist between CT distances, initial state/final state

(e.g., ground state/excited state) vector dipole moment differences ($\Delta\mu_v$), the unit electronic charge (e), and the amount of charge actually transferred (q), as shown in Equation (1).

$$R_{12} \times e = R_{ab} \times q = \vec{\mu}_e - \vec{\mu}_g \tag{1}$$

In Equation (1), R_{12} and R_{ab} are the adiabatic and nonadiabatic CT distances, and $\vec{\mu}_e$ and $\vec{\mu}_g$ are the excited- and ground-state dipole moments. The adiabatic distance, the effective transfer distance for a full electronic charge, is typically the desired parameter. Due to initial state/final state mixing (present in all CT reactions), q is less than e and the nonadiabatic distance increases accordingly. This distance represents the hypothetical transfer distance of one electron with no state mixing or electronic coupling. Therefore, the difference between the two CT distances illustrates the extent that partial charge delocalization shortens the effective CT distance. A quantitative comparison is described by Equation (2), where c^2 is the quantity of delocalized charge.[3]

$$R_{12} = R_{ab}\left(1 - 2c^2\right) \tag{2}$$

Given Equation (1), experiments that measure $\Delta\mu$ should be capable of determining CT distances. Potential options include Stark absorption spectroscopy,[3,4] Stark emission spectroscopy,[5] transient DC photoconductivity (TDCP),[6] and transient microwave conductivity.[7] The first three techniques are described here, emphasizing comparative advantages and disadvantages. In choosing literature examples, coordination chemistry studies have been selected where possible, although a large number of reports on organic and biological molecules exist.

2.23.2 STARK ABSORPTION SPECTROSCOPY

The fundamental basis for Stark spectroscopy stems from Johannes Stark's discovery that electrical fields split lines in atomic spectra, which eventually led to his winning the 1919 Nobel Prize in physics. However, physicists did not begin to study Stark effects on the spectra of chemical systems until the 1970s.[8] The field of study was subsequently expanded to coordination compounds. Among the earliest reports are those by Boxer and co-workers beginning in 1989.[9,10]

2.23.2.1 Theory

The theory for Stark absorption spectroscopy is based on the initial work of Liptay and co-workers[11,12] and refinement by others.[13,14] In the basic experiment, an isotropic sample exhibiting a single absorption band in a rigid matrix (e.g., a clear solvent glass at low temperature or a polymer film) is assumed. During the measurement, an AC field is applied to the sample ($\mathbf{F}_{ext}$), leading to an effective field at the molecular level ($\mathbf{F}_{int}$) as defined in Equation (3).[3] In this equation, f typically ranges between 1.0 and 1.3 and depends upon analyte size and shape, as well as solvent polarity.[13,15]

$$\mathbf{F_{int}} = f \times \mathbf{F_{ext}} \tag{3}$$

The electric field perturbs the absorption band via direct manipulation of either the transition moment or the ground- and/or excited-state energies of the electronic transition (see Figure 1). These perturbations are modeled by deconvoluting the change in the absorption spectrum ($\Delta A(\upsilon)$) into a linear combination of the zeroth, first, and second derivatives of the unperturbed spectrum ($A(\upsilon)$), as described in Equation (4).

$$\Delta A(\upsilon) = \left\{ A_\chi A(\upsilon) + \frac{B_\chi \upsilon}{15hc} \frac{\mathrm{d}[A(\upsilon)/\upsilon]}{\mathrm{d}\upsilon} + \frac{C_\chi \upsilon}{30h^2c^2} \frac{\mathrm{d}^2[A(\upsilon)/\upsilon]}{\mathrm{d}\upsilon^2} \right\} \mathbf{F_{int}}^2 \tag{4}$$

The fitting coefficients A_χ, B_χ, and C_χ provide information on changes in the electronic transition moment, polarizability, and dipole moment, respectively, and are defined in Equations (5–7).

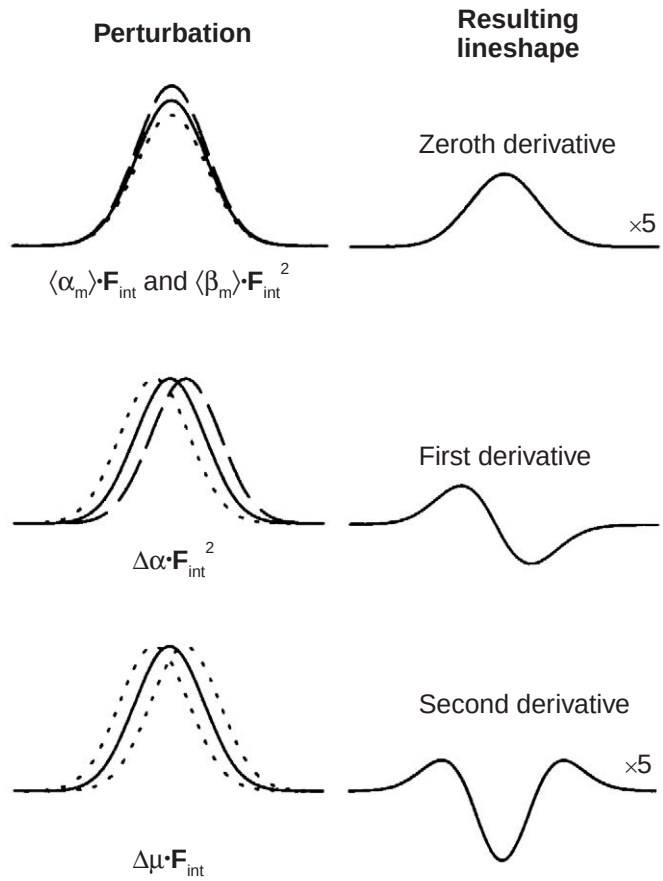

Figure 1 Origins of perturbation in Stark spectroscopy. The left panel shows changes in the unperturbed absorption spectrum (solid line) when an AC field is applied (dotted and dashed lines), leading to the delta absorption spectral line shape shown in the right column. (Adapted from Bublitz and Boxer, 1997[4]).

$$A_\chi = \frac{\langle \boldsymbol{\alpha}_\mathbf{m} \rangle}{3} + \tfrac{1}{30}\left(3\cos^2\chi - 1\right)\left(3\langle \boldsymbol{\beta}_\mathbf{m} \rangle - 2\langle \boldsymbol{\alpha}_\mathbf{m} \rangle\right) \tag{5}$$

$$B_\chi = \tfrac{5}{2}\,\mathrm{Tr}\Delta\alpha + \left(3\cos^2\chi - 1\right)\left(\tfrac{3}{2}\,\hat{\mathbf{g}}\cdot\Delta\alpha\cdot\hat{\mathbf{g}} - \tfrac{1}{2}\,\mathrm{Tr}\Delta\alpha\right) \tag{6}$$

$$C_\chi = |\Delta\mu_v|^2\left[5 + \left(3\cos^2\xi - 1\right)\left(3\cos^2\chi - 1\right)\right] \tag{7}$$

In these equations, $\langle \boldsymbol{\alpha}_\mathbf{m} \rangle$ and $\langle \boldsymbol{\beta}_\mathbf{m} \rangle$ are the scalar portions of the transition moment polarizability and hyperpolarizability tensors, $\mathrm{Tr}\Delta\alpha$ is the trace of the polarizability change, $\hat{\mathbf{g}}\cdot\Delta\alpha\cdot\hat{\mathbf{g}}$ is the polarizability change along the transition moment vector, $|\Delta\mu_v|$ is the vector change in dipole moment (its sign is not determined), and ξ is the angle between the transition dipole moment and the change in dipole moment vectors.[3] These coefficients are dependent on the incident angle of polarized light in relation to the electric field (χ), so recording Stark spectra at multiple χ values facilitates solution of the coefficient equations.

2.23.2.2 Experimental Considerations

As noted above, the sample is in a rigid matrix. The measurement is typically performed at cryogenic temperatures, where the absorption transitions are better resolved. The cryogen can also act as an insulator, thus increasing electric field stability. The sample is typically placed

between two glass or quartz plates coated with a transparent conductor (e.g., indium tin oxide), and a polarizer is placed in the optical path to obtain data for a single χ value.

To obtain the $\Delta A(\upsilon)$ spectrum, a lock-in amplifier is employed that is synchronized with the AC field generator. The signal is detected at twice the field modulation (typically 200–400 Hz) and is derived in Equation (8).

$$\Delta A = -\log\left(\frac{2\sqrt{2}\,V_{AC}}{V_{DC}} + 1\right) \tag{8}$$

In Equation (8), V_{AC} and V_{DC} are the detected AC (change in absorption) and DC (unperturbed absorption) spectra, respectively. Care must be taken to record a high-quality unperturbed spectrum, since its derivatives are the basis of the deconvolution.

2.23.2.3 Literature Examples

2.23.2.3.1 $Ru(bpy)_3^{2+}$

One issue that has troubled inorganic photochemists is the nature of the photoexcited electron following metal-to-ligand charge transfer (MLCT) excitation in Ru(2,2′-bipyridine)$_3^{2+}$-type systems. Two possibilities exist: i) localization on one bipyridine, or ii) delocalization across all three ligands. As illustrated in Scheme 1, both possibilities involve CT, but only in the localized process does CT entail a nonzero $\Delta\mu_v$. (Process 1 entails a change in octupolar moment, an effect that does not yield a Stark response.) Stark absorption measurements by Oh and Boxer on this system[10] produced a finite second derivative Stark signal, consistent with MLCT localization (see Figure 2, Panels B and C). Fitting yielded a $|\Delta\mu_v|$ of 8 ± 1 D. Since μ_g is zero, $|\Delta\mu_v|$ for Ru(bpy)$_3^{2+}$ must be positive. Also, because the measurement is based on light absorption, the timescale is instantaneous and the Franck-Condon region of the excited state is probed.

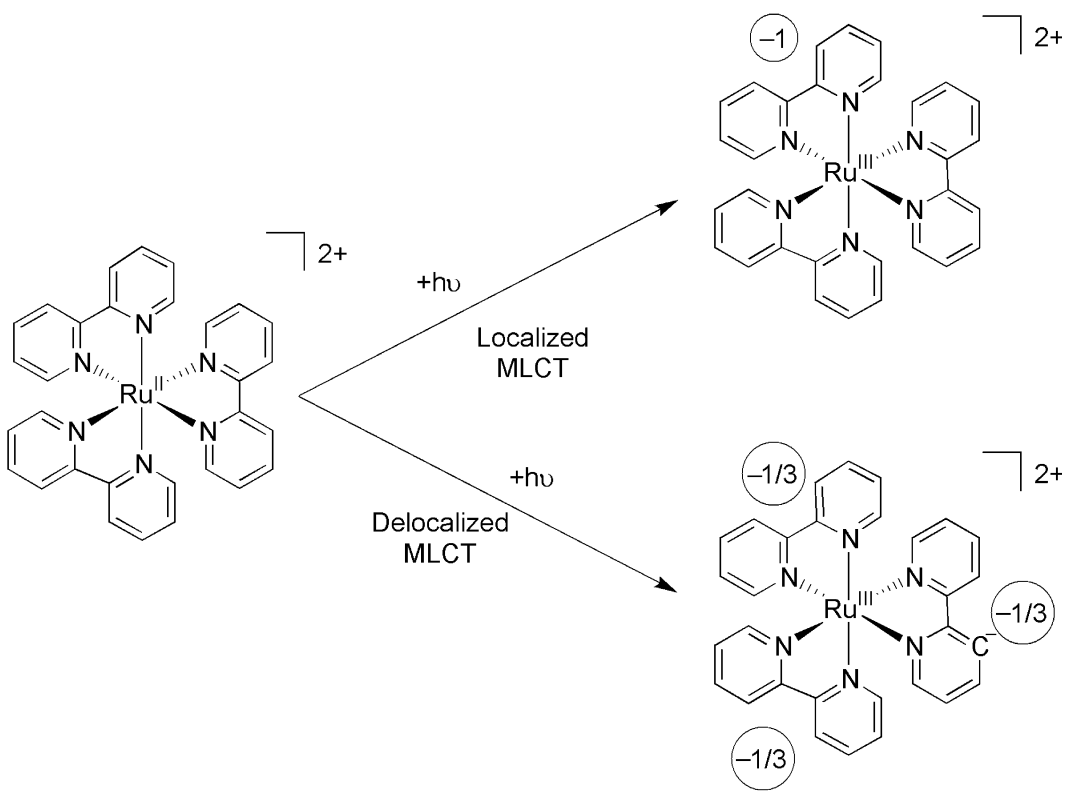

Scheme 1

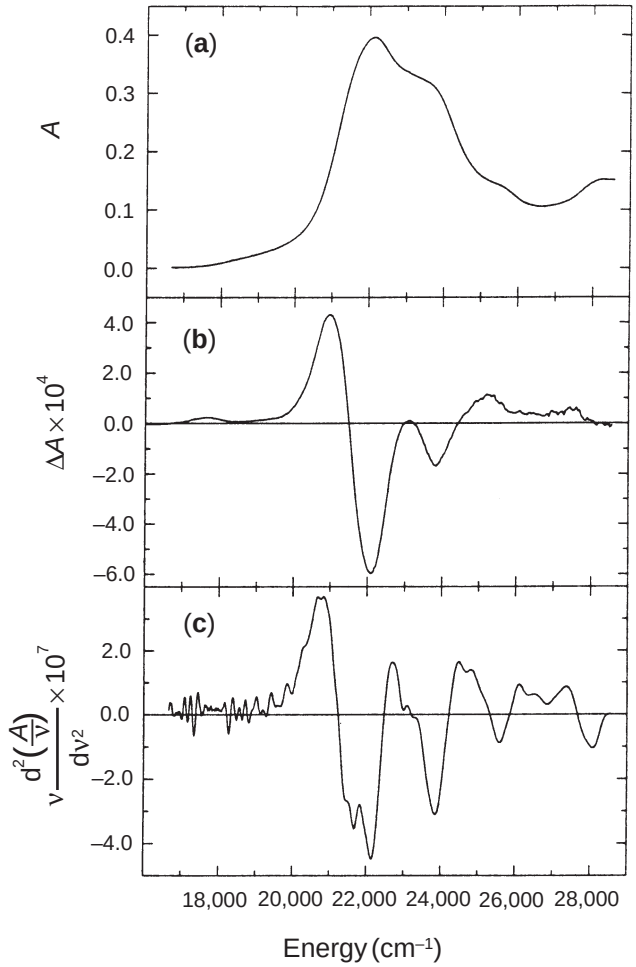

Figure 2 Stark absorption spectrum of $Ru(bpy)_3^{2+}$ in a PVA thin film at 77 K. (a) Unperturbed absorption spectrum. (b) Stark absorption spectrum ($\chi = 54.7°$). (c) Second derivative of unperturbed spectrum. (Reprinted with permission from *J. Am. Chem. Soc.* **1989**, *111*, 1130–1131.[10] © 1989 American Chemical Society).

2.23.2.3.2 $Ru(NH_3)_5L^{2+}$

An early report by Boxer and co-workers on MLCT within $Ru(NH_3)_5(pyrazine)^{2+}$ yielded the interesting result that R_{12} is only one-third the geometric distance between donor (Ru) and acceptor (pyrazine),[9] a finding that was replicated by computational studies.[16] Further work by Shin *et al.* on a family of $Ru(NH_3)_5L^{2+}$ systems yielded small adiabatic CT distances.[17] They concluded that substantial $d\pi$ (Ru)/π^* ligand backbonding, and the ensuing partial charge delocalization, is responsible in part for the different "geometric" and observed CT distances. Further experimental data analysis showed R_{12} was typically only 70% as large as R_{ab} for these systems, again suggesting partial delocalization based on Equation (2). In contrast, the ligand-to-metal charge transfer (LMCT) transition observed in oxidized complexes gave almost identical R_{12} and R_{ab} values, suggesting little ligand-to-metal charge delocalization.

A second explanation of the disparity between measured and geometric CT distances lies in valence electron polarization. As suggested by Brunschwig *et al.*[13] when the metal center is oxidized as a result of a MLCT transition, the ligand valence electrons are drawn towards the metal due to its increased charge. This "pull" opposes the movement of the optically excited electron, decreasing the observed dipole moment change. In a one-electron model (the basis for Equations (1) and (2) and associated theory), these multielectron self-polarization effects are manifest as a one-electron CT distance decrease. It is important to recognize that when evaluating parameters associated with the CT process, such as electronic coupling factors, a one-electron

description is usually implicit in the evaluation. Consequently, R_{12} is the most relevant distance to consider.[18]

2.23.2.3.3 $(NH_3)_5$Ru-bridge-Ru$(NH_3)_5^{5+}$

Stark measurements of "intervalence" transitions (IT) associated with mixed-valence species can yield information about its ground state electronic structure. IT within valence-localized (Robin and Day Class II)[19] complexes is accompanied by a nonzero dipole moment change. For the example shown in Equation (9), $|\Delta\mu_v|$ is large (ca. 21 D), confirming that a Class II description is appropriate.[9]

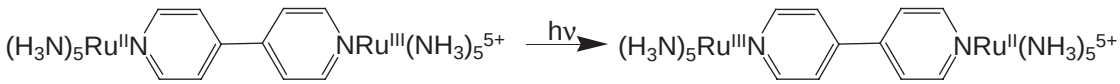

(9)

The corresponding R_{12} value is only about 40% as large as the geometric donor/acceptor distance, with most of the discrepancy reflecting polarization rather than delocalization effects.[9,16] Hupp and co-workers noted that the use of R_{12} in place of $R_{\text{geometric}}$ in solvent reorganization energy calculations resulted in good agreement with experimental measurements.[20]

Stark absorption measurements by Oh *et al.*[9] with the analogous pyrazine-bridged complex (the "Creutz-Taube" ion)[21] showed that almost no dipole moment change accompanies IT excitation, a result consistent with previous descriptions of the ion as a fully delocalized (Class III)[19] complex, see Equation (10). Other studies show that IT excitation is accompanied by charge redistribution from the bridging ligand to both metals simultaneously.[20] Consequently, in place of a dipole moment change IT excitation causes a *quadrupole* moment change, which is not detected with this method.

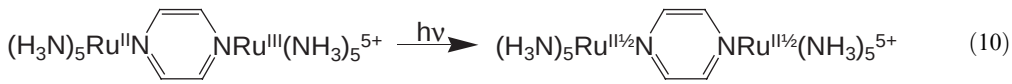

(10)

2.23.2.3.4 Biological systems

The only known reported Stark absorption study on coordination complexes in biological systems is one by Chowdhury *et al.*[22] on azurin copper-containing proteins. However, extensive Stark absorption research on other biological systems has been reported, including work on the photosynthetic reaction center[23] and various proteins.[24,25] The derived methodology and theory from these studies can be applied to future work on other inorganic coordination compounds.

2.23.2.3.5 Second-order nonlinear optical chromophores

Stark absorption spectroscopy has also been employed in studies of candidate chromophores for nonlinear photonic materials. Second-order nonlinear optical signals scale with the square of the first hyperpolarizability (β) of a molecule, which consequently scales with $|\Delta\mu_v|$. Although the lowest electronic transition is typically most important, β contributions from higher-energy transitions can also be significant. In at least two cases (neither of them involving inorganic materials), Stark absorption has been used to determine $|\Delta\mu_v|$ for several transitions within a single chromophore. One study focused on "push–pull" cyanine dyes,[26] while the second explored light-induced CT effects in a porphyrinic "push–pull" chromophore.[27]

2.23.3 STARK EMISSION SPECTROSCOPY

While Stark absorption spectroscopy is often a very good method for CT distance evaluation, electronic absorption bands sometimes overlap, making deconvolution difficult. Emission spectra,

however, almost always contain only a single electronic transition. Therefore, Stark emission spectroscopy has also been employed in CT measurements, albeit in a more limited manner.

2.23.3.1 Theory and Experimental Considerations

The theory for Stark emission spectroscopy closely follows the Stark absorption treatment, but minor modification of Equations (4) and (8) is required, as reflected in Equations (11) and (12).[28] Note that the unperturbed emission spectrum is also normalized before calculating any derivatives. The experimental requirements for Stark emission are identical to those for the Stark absorption measurement.

$$\Delta F(\upsilon) = \left\{ A_\chi F(\upsilon) + \frac{B_\chi \upsilon^3}{15hc} \frac{\mathrm{d}\left[F(\upsilon)/\upsilon^3\right]}{\mathrm{d}\upsilon} + \frac{C_\chi \upsilon^3}{30h^2c^2} \frac{\mathrm{d}^2\left[F(\upsilon)/\upsilon^3\right]}{\mathrm{d}\upsilon^2} \right\} \mathbf{F}_{\mathbf{int}}{}^2 \tag{11}$$

$$\Delta F = \frac{2\sqrt{2}\, V_{\mathrm{AC}}}{V_{\mathrm{DC}}} \tag{12}$$

2.23.3.2 Literature Examples

The majority of Stark emission work involves organic chromophores, with perhaps the earliest report attributed to Bischof and co-workers on 9,9′-bianthryl.[29] Groundbreaking Stark emission work was conducted by Boxer and co-workers on the photosynthetic reaction center.[5,30] One of the significant contributions of their research was the extension of the original Stark theory to include the possibility of additional excited states that could compete with CT emission (e.g., a "dark" electron transfer reaction). In these cases, the applied AC field alters the branching ratio for the competing excited-state decay processes and leads to an unexpected Stark emission spectrum. Rigorous analysis of this kind of data can provide a more complete magnitude and relative spatial arrangement profile of the dipole moments associated with the ground, excited, and deactivating intermediate states of the probed molecule.[5] This theory extension is important to consider when designing experiments on supramolecular systems with multiple excited-state deactivation pathways.

2.23.3.2.1 (bpy)Re(CO)$_3$Cl

The first known published application of Stark emission spectroscopy to coordination compounds was reported by Walters and co-workers and involved a series of (X_2-bpy)Re(CO)$_3$Cl complexes.[31] Substituents on the bipyridine ligand were altered to examine how electron-donating, -withdrawing, or -delocalizing moieties affected the CT distance. The unsubstituted bipyridine complex exhibited a $|\Delta\mu_v|$ of 9 D (ca. 2 eÅ) for MLCT emission. The substitution of electron-donating groups decreased the CT distance, while electron-withdrawing and -delocalizing groups exhibited the reverse effect.

2.23.3.2.2 Interfacial charge transfer

Walters *et al*. have also applied Stark emission spectroscopy to the problem of interfacial CT, focusing specifically on CT from adsorbed dye molecules to colloidal semiconductor particles.[32] The dyes are used in semiconductor regenerative solar cells as photosensitizers. While the majority undergo a molecule-localized photoexcitation followed by electron injection, a second possibility illustrated by organic dyes such as catechol on TiO_2 particles[33] exert a concerted, direct CT from the dye ground state to the semiconductor conduction band or adjacent surface states. If an observed emission were associated with the reverse direct charge recombination instead of simple relaxation of the surface-immobilized dye molecule,[34] Stark emission spectroscopy would return a nonnegligible $|\Delta\mu_v|$ value. In the study by Walters *et al*. eosin yellow on TiO_2 exhibited a $|\Delta\mu_v|$ identical to that obtained on a photoinactive surface, implying that direct CT does not occur with

this dye.[32] Brunschwig and co-workers, however, have obtained compelling evidence with Stark absorption spectroscopy on ferrocyanide/TiO_2 systems for direct CT.[35]

2.23.4 TRANSIENT DC PHOTOCONDUCTIVITY

A complementary technique to Stark spectroscopy, TDCP also measures dipole moment changes but additionally provides sign information. Notably, TDCP measures the *scalar* dipole moment difference ($\Delta\mu_s$), whereas Stark spectroscopy measures the *vector* difference. (The vector and scalar dipole moment changes will only be equivalent when μ_g and μ_e are collinear. In other cases, only the *vector* dipole moment difference can be equated with the actual CT distance, see Walters *et al*. 2002[31].) The pioneering work in this field was conducted by Smirnov and Braun in the early 1990s.[6,36] In this technique, a photo-induced transient displacement current is monitored that evolves as a result of analyte rotation within a high voltage (ca. 1.5 kV) DC field (see Scheme 2). The rotation of the excited-state dipole moment to align with the electric field causes a change in the effective capacitance of the TDCP cell, leading to the transient current.

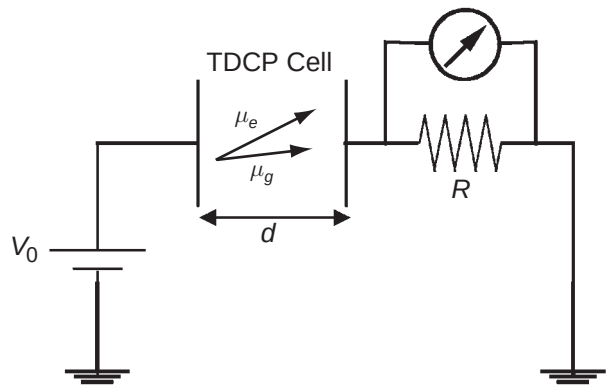

Scheme 2

2.23.4.1 Theory

The theory describing quantitative TDCP starts with the standard expression for electric field-induced polarization of a single analyte in fluid solution, P_{solute}.[37]

$$P_{\text{solute}} = n_i \frac{\mu_i^2 E_c}{3k_b T} \tag{13}$$

In Equation (13), n_i is the solute dipole concentration, μ_i is the solute dipole moment, E_c is the internal electric field, k_b is Boltzmann's constant, and T is temperature. If the temporal evolution of P_{solute} concomitant with photoexcitation is examined, Equation (14) is derived.

$$\Delta P_{\text{solute}}(t) = n_e(t)\left(\mu_e^2 - \mu_g^2\right)\frac{E_c}{3k_b T} \tag{14}$$

In Equation (14), $n_e(t)$ is the time-dependent, excited state dipole population. Note that the dipole moment difference is represented as a *difference of squares*, thus requiring independent determination of μ_g to calculate CT distances. The evolving transient current ($\upsilon(t)$) can be determined using $\Delta P_{\text{solute}}(t)$ via Equation (15).

$$\upsilon(t) + \tau_{RC}\frac{\mathrm{d}\upsilon(t)}{\mathrm{d}t} = \frac{\varphi R V_0}{d}\frac{\mu_e^2 - \mu_g^2}{3k_b T}\frac{\mathrm{d}n_e}{\mathrm{d}t} \tag{15}$$

In Equation (15), τ_{RC} is the time constant for the RC circuit created by the TDCP instrument, φ is a correction parameter that varies between 1.3 and 1.9 and accounts for analyte shape and solvent polarity,[38] and remaining parameters are defined in Scheme 2.

2.23.4.2 Experimental Considerations

Unlike Stark spectroscopic studies, TDCP experiments are conducted at room temperature on liquid solutions. However, a pulsed light source (i.e., laser) is required for excitation, and the solvent must be relatively nonpolar to avoid unwanted electrochemistry. For the same reason, analyte molecules must be neutral, although the DC voltage can be pulsed to reduce these side effects.[6]

TDCP cell design involves electrodes above and below the laser propagation direction, forming a narrow (ca. 2 mm) channel for the sample solution.[6,31] This design allows for the sample to flow through the cell continually, further reducing the possibility of sample degradation. Alternatively, indium tin oxide-coated glass can serve as both the cell windows and electrodes in a similar fashion to a Stark spectroscopy "sandwich" cell. Extensive RF shielding of the cell is necessary in order to diminish laser source noise.

2.23.4.3 Literature Examples

The majority of published TDCP work has been performed by Smirnov and Braun.[6] While the majority of their research has been on organic molecules, the extensive theoretical treatments and case study findings are relevant to experiments involving inorganic systems, including extension of TDCP theory to account for the slow rotational correlation time of large molecules.[38]

2.23.4.3.1 (bpy)Re(CO)$_3$Cl

The Stark emission study of various (X_2-bpy)Re(CO)$_3$Cl complexes reported by Walters and co-workers also included TDCP measurements.[31] The most remarkable finding was that all compounds exhibited a *negative* $\Delta\mu_s$, as evidenced by negative Gaussian transient band shapes (see example in Figure 3).[39] The resulting conclusion that μ_g is larger than μ_e, despite the MLCT nature of the excited state, was supported by semi-empirical calculations on manganese analogues of the rhenium series and provides a unique explanation for the negative solvatochromism observed in the absorption spectra of these complexes.[40,41] The complementary use of Stark emission and TDCP allowed for both the measurement of the absolute CT distance and, using vector algebra, determination of the spatial relationship of μ_g and μ_e across the series of complexes.

2.23.4.3.2 Other transient DC photoconductivity measurements

TDCP can also be used to confirm and/or assign the excited state of inorganic complexes. Vanhelmont *et al.* reported TDCP measurements of a platinum diimine thiolate complex and observed a negative $\Delta\mu_s$, which helped to establish the CT nature of the observed emission.[42] Another study confirmed the assigned CT emission of a rhenium complex containing a large, luminescent oxadiazole/phenylamine ligand, in contrast to the ligand-localized emission of the manganese analogue.[43]

2.23.5 SUMMARY

Three different techniques have been presented that all measure different "flavors" of photoinitiated CT distances. Indeed, a comparison of the techniques in Table 1 indicates many differences between them. Notably, the difference between *vector* and *scalar* dipole moment differences must be considered with respect to the geometry of the analyte, since scalar measurements do not necessarily yield the actual CT distances. Also, the analyte spectrum components must be clearly resolved. For example, Stark absorption on (bpy)Re(CO)$_3$Cl would be very difficult due to overlapping ligand π,π^* and MLCT bands. Alternatively, its emission spectrum exhibits only the MLCT band, allowing Stark emission to easily measure the CT distance. The need for Stark spectroscopy samples

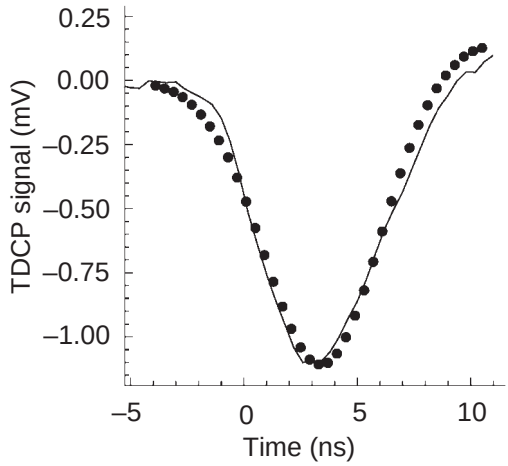

Figure 3 TDCP data of (bpy)Re(CO)$_3$Cl in 1:1 $CHCl_3$:Toluene. Points are experimental data, and the solid line is the simulated spectrum calculated from Equation (15) (Reprinted with permission from *Inorg. Chem.* **2000**, *39*, 1817–1819.[39] © 2000 American Chemical Society).

Table 1 Comparison of CT measurement methods.

Comparison	*Stark absorption*	*Stark emission*	*TDCP*
Measured dipole moment	Vector	Vector	Scalar
Sample environment	Rigid matrix (polymer or low temperature solvent glass)	Rigid matrix (polymer or low temperature solvent glass)	Room temperature nonpolar solution
Can analyte molecules be charged?	Yes	Yes	No
Probed excited state	Franck-Condon level of initially excited state	Vibrationally relaxed emitting state	Lowest-lying excited state (can be a dark state)
Can $\Delta\mu$ values for multiple electronic excited states be measured?	Yes, if individual spectral features are resolved	Yes, if individual spectral features are resolved	No
Is the sign of $\Delta\mu$ measured?	No	No	Yes
Is μ_g needed to determine $\Delta\mu$?	No	No	Yes
Other parameters measured	Change in molecular polarizability, angle between $\Delta\mu$ and transition dipole	Change in molecular polarizability, angle between $\Delta\mu$ and transition dipole	Rotational correlation times

to be in a rigid matrix is a potential obstacle for many measurements, as is the need for nonpolar solvents and analyte neutrality in TDCP measurements. In many cases, careful experiment design and the use of multiple techniques can be expected to provide useful descriptions of CT and redistribution within molecular coordination compounds.

2.23.6 REFERENCES

1. Meyer, T. J.; Taube, H. In *Comprehensive Coordination Chemistry*; Pergamon: Oxford, 1987; Vol. 1, pp 331–384.
2. Lever, A. B. P.; Gorelsky, S. I. *Coord. Chem. Rev.* **2000**, *208*, 153–167.
3. Vance, F. W.; Williams, R. D.; Hupp, J. T. *Int. Rev. Phys. Chem.* **1998**, *17*, 307–329.
4. Bublitz, G. U.; Boxer, S. G. *Ann. Rev. Phys. Chem.* **1997**, *48*, 213–242.
5. Lockhart, D. J.; Hammes, S. L.; Franzen, S.; Boxer, S. G. *J. Phys. Chem.* **1991**, *95*, 2217–2226.
6. Smirnov, S. N.; Braun, C. L. *Rev. Sci. Instrum.* **1998**, *69*, 2875–2887.

7. De Haas, M. P.; Warman, J. M. *Chem. Phys.* **1982**, *73*, 35–53.
8. Solomon, E. I.; Ballhausen, C. J.; Hoeg, J. H. *Chem. Phys. Lett.* **1975**, *34*, 222–224.
9. Oh, D. H.; Sano, M.; Boxer, S. G. *J. Am. Chem. Soc.* **1991**, *113*, 6880–6890.
10. Oh, D. H.; Boxer, S. G. *J. Am. Chem. Soc.* **1989**, *111*, 1130–1131.
11. Liptay, W. *Angew. Chem., Int. Ed. Engl.* **1969**, *8*, 177–188.
12. Liptay, W.; Walz, G.; Baumann, W.; Schlosser, H. J.; Deckers, H.; Detzer, N. *Z. Naturforsch. A* **1971**, *26*, 2020–2038.
13. Brunschwig, B. S.; Creutz, C.; Sutin, N. *Coord. Chem. Rev.* **1998**, *177*, 61–79.
14. Lockhart, D. J.; Boxer, S. G. *Biochemistry* **1987**, *26*, 664–668.
15. Bublitz, G. U.; Boxer, S. G. *J. Am. Chem. Soc.* **1998**, *120*, 3988–3992.
16. Reimers, J. R.; Hush, N. S. *J. Phys. Chem.* **1991**, *95*, 9773–9781.
17. Shin, Y. K.; Brunschwig, B. S.; Creutz, C.; Sutin, N. *J. Phys. Chem.* **1996**, *100*, 8157–8169.
18. Karki, L.; Lu, H. P.; Hupp, J. T. *J. Phys. Chem.* **1996**, *100*, 15637–15639.
19. Robin, M. B.; Day, P. *Adv. Inorg. Chem. Radiochem.* **1967**, *10*, 247–422.
20. Hupp, J. T.; Dong, Y.; Blackbourn, R. L.; Lu, H. *J. Phys. Chem.* **1993**, *97*, 3278–3282.
21. Creutz, C.; Taube, H. *J. Am. Chem. Soc.* **1973**, *95*, 1086–1094.
22. Chowdhury, A.; Peteanu, L. A.; Webb, M. A.; Loppnow, G. R. *J. Phys. Chem. B* **2001**, *105*, 527–534.
23. Lockhart, D. J.; Boxer, S. G. *Proc. Natl. Acad. Sci. USA* **1988**, *85*, 107–111.
24. Locknar, S. A.; Peteanu, L. A. *J. Phys. Chem. B* **1998**, *102*, 4240–4246.
25. Chowdury, A. C.; Locknar, S. A.; Premvardhan, L. L.; Peteanu, L. A. *J. Phys. Chem. A* **1999**, *103*, 9614–9625.
26. Bublitz, G. U.; Ortiz, R.; Marder, S. R.; Boxer, S. G. *J. Am. Chem. Soc.* **1997**, *119*, 3365–3376.
27. Karki, L.; Vance, F. W.; Hupp, J. T.; LeCours, S. M.; Therien, M. J. *J. Am. Chem. Soc.* **1998**, *120*, 2606–2611.
28. Lockhart, D. J.; Boxer, S. G. *Chem. Phys. Lett.* **1988**, *144*, 243–250.
29. Baumann, W.; Spohr, E.; Bischof, H.; Liptay, W. *J. Lumin.* **1987**, *37*, 227–233.
30. Lockhart, D. J.; Goldstein, R. F.; Boxer, S. G. *J. Chem. Phys.* **1988**, *89*, 1408–1415.
31. Walters, K. A.; Kim, Y. J.; Hupp, J. T. *Inorg. Chem.* **2002**, *41*, 2909–2915.
32. Walters, K. A.; Gaal, D. A.; Hupp, J. T. *J. Phys. Chem. B* **2002**, *106*, 5139–5142.
33. Persson, P.; Bergstroem, R.; Lunell, S. *J. Phys. Chem. B* **2000**, *104*, 10348–10351.
34. Ramakrishna, G.; Ghosh, H. N. *J. Phys. Chem. B* **2001**, *105*, 7000–7008.
35. Parise, A. R.; Brunschwig, B. S.; Sutin, N. Proceedings of the 24th DOE Solar Photochemistry Research Conference, Tahoe City, CA, June 3–7, 2001.
36. Smirnov, S. N.; Braun, C. L. *J. Phys. Chem.* **1992**, *96*, 9587–9591.
37. Debeye, P. *Polar Molecules* **1929**, Dover: New York.
38. Smirnov, S. N.; Braun, C. L.; Greenfield, S. R.; Svec, W. A.; Wasielewski, M. R. *J. Phys. Chem.* **1996**, *100*, 12329–12336.
39. Vanhelmont, F. W. M.; Hupp, J. T. *Inorg. Chem.* **2000**, *39*, 1817–1819.
40. Worl, L. A.; Duesing, R.; Chen, P.; Della Ciana, L.; Meyer, T. J. *J. Chem. Soc., Dalton Trans.* **1991**, 849–858.
41. Wrighton, M.; Morse, D. L. *J. Am. Chem. Soc.* **1974**, *96*, 998–1003.
42. Vanhelmont, F. W. M.; Johnson, R. C.; Hupp, J. T. *Inorg. Chem.* **2000**, *39*, 1814–1816.
43. Kim, Y.; Vanhelmont, F. W. M.; Stern, C. L.; Hupp, J. T. *Inorg. Chim. Acta* **2001**, *318*, 53–60.

Comprehensive Coordination Chemistry II
ISBN (set): 0-08-0437486

Volume 2, (ISBN 0-08-0443249); pp 303–313

2.24
Electronic Emission Spectroscopy

R. H. SCHMEHL
Tulane University, New Orleans, LA, USA
and
J. A. SIMON
Frostberg State University, Frostberg, MD, USA

2.24.1 GENERAL OVERVIEW AND BASIC CONCEPTS 315
2.24.2 LUMINESCENT EXCITED STATES OF COORDINATION COMPOUNDS 318
2.24.3 LUMINESCENCE SPECTROSCOPIC METHODS 319
2.24.3.1 First Row Complexes 320
2.24.3.2 Second and Third Row Complexes 321
2.24.3.3 Lanthanide Complexes 323
2.24.4 REFERENCES 323

2.24.1 GENERAL OVERVIEW AND BASIC CONCEPTS

Luminescence from discrete transition metal complexes was first observed for classical Werner complexes of Cr^{III} many years ago and early studies of metal complex luminescence provided the basis for characterizing the spin multiplicity and relaxation processes of excited states of complexes in solution and the solid state. This early work has been thoroughly documented in a number of books, monographs, and reviews on inorganic photochemistry.[1–6]

Emission from electronic excited states of transition metal complexes is generally observed from the ultraviolet to the near-infrared. Characterization of emission of molecular species involves measurement of three principal parameters: excited state energies, emission quantum yields, and lifetimes. Figure 1 shows a simple state diagram typical of a metal complex having a singlet ground state (i.e., low-spin d^6). Electronic excitation leads to population of a state having the same spin multiplicity as the ground state ($S_0 \rightarrow S_1$); excitation into higher energy excited states of the same spin multiplicity (i.e., $S_0 \rightarrow S_2$) also occurs. Relaxation of the Franck–Condon excited states to the thermally equilibrated excited state (state 0′ of S_1) generally occurs on the sub-ps time scale. In rare cases excitation into states higher in energy than S_1 results in direct relaxation to the ground state via emission of light (*vide infra*). Relaxation from the thermally equilibrated excited state can be via emission (k_r), nonradiative decay (k_{nr}), or intersystem crossing to the triplet (T_1) state. In addition, the excited state may react to yield net chemical products; for example, the excited molecule may participate in energy or electron transfer reactions with other chemical species. The T_1 state can also decay by radiative, nonradiative, and photoreaction paths. Figure 1b shows representative excitation and emission spectra that correspond to absorption into and emission from the S_1 state of the energy level diagram. The excited state energy is defined as the energy difference between the zeroeth vibrational level of the ground and excited states (E_0). The difference in the maxima for the absorption and emission transitions between the zeroeth vibrational levels is a consequence of the fact that the equilibrium nuclear displacements of the

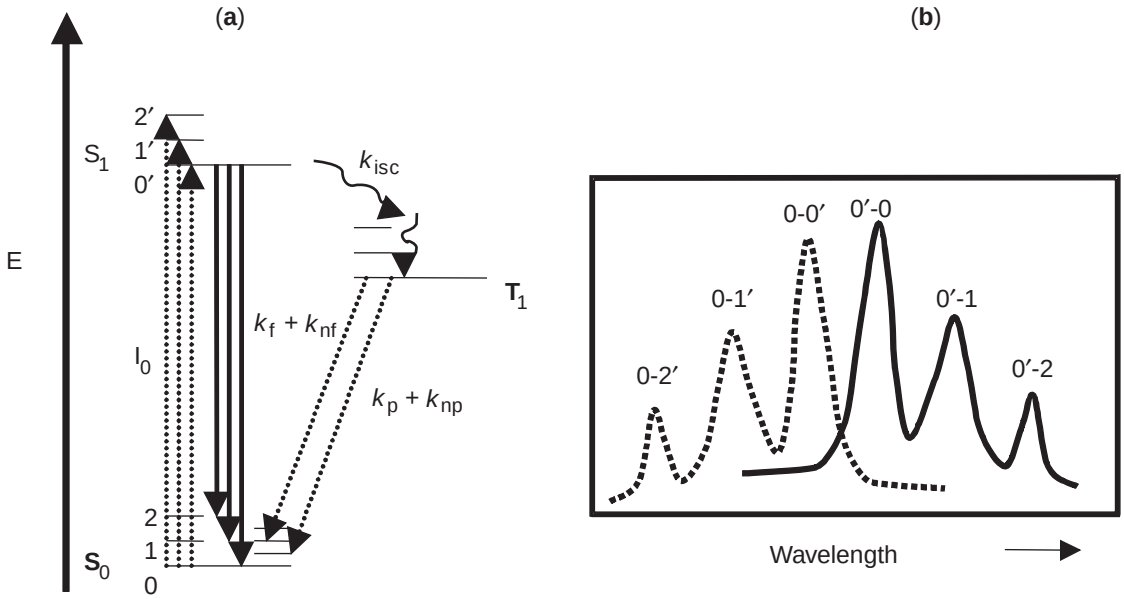

Figure 1 (a) Yablonski diagram showing electronic and vibrational levels as well as transitions between states. (b) S_0-S_1 absorption and emission from the S_1 electronic state structure.

ground and excited states differ (the excited state potential surface is distorted relative to the ground state).

Emission spectra provide information on the relative excited state distortion (the Huang–Rhys factor, S), the medium- and low-frequency vibrational modes associated with excited state relaxation ($h\omega$) and the zero–zero energy (E_0). An approach for fitting emission spectra has been discussed in detail in the work of Meyer and co-workers, and one expression for calculating the normalized luminescence intensity, I_ν, as a function of frequency ν is shown in Equation (1).[7,8] The expression shown employs a single, medium-frequency, acceptor vibrational mode, $h\omega_m$, the corresponding electron-vibrational coupling constant, S_m, and a term for the full width half maximum of the individual vibronic components, ν_h, which provides a measure of the average solvent (or medium) reorganizational energy associated with relaxation of the excited state. Figure 2 shows a typical emission spectrum of a Ru^{II} diimine complex obtained in a glass matrix at 77 K; the average medium frequency vibrational spacing is clearly evident and the degree of excited state distortion is experimentally related to the relative intensities of the two observed vibronic components.

$$I_\nu = \sum_m \left[\left(\frac{E_o - m h\omega_m}{E_o} \right)^3 \right] \frac{S_m^m}{m} \exp\left[-4 \ln 2 \left(\frac{\nu - E_o + m h\omega_m}{\nu_h} \right)^2 \right] \quad (1)$$

The observation of luminescence requires that the radiative decay rate constant be within a few orders of magnitude of the generally larger nonradiative decay constant. Excellent discussions of the factors influencing excited state relaxation of transition metal complexes have been published recently by Meyer[9,10], Endicott[11], Gudel[12] and others[13,14] Radiative decay rate constants are a function of the magnitude of the transition dipole moment and the emission frequency, increasing with increasing oscillator strength of the transition ($k_r \propto |M|^2$) and increasing emission frequency ($k_r \propto \nu^3$). Nonradiative relaxation rate constants are a function of a variety of factors including the emission energy ($k_{nr} \propto \exp(-E_{em})$; the Energy Gap Law), the degree of distortion of the excited state, the number and frequency of vibrational modes on the chromophore, and the degree of coupling with vibrational modes of the surrounding medium. A few examples from the literature are given below.

In the absence of reactions between two excited states or environmental effects resulting in significant inhomogeneities in the distribution of chromophores, emissive decay from a single excited state (i.e., either S_1 or T_1 of Figure 1) will follow first order kinetics and the observed rate

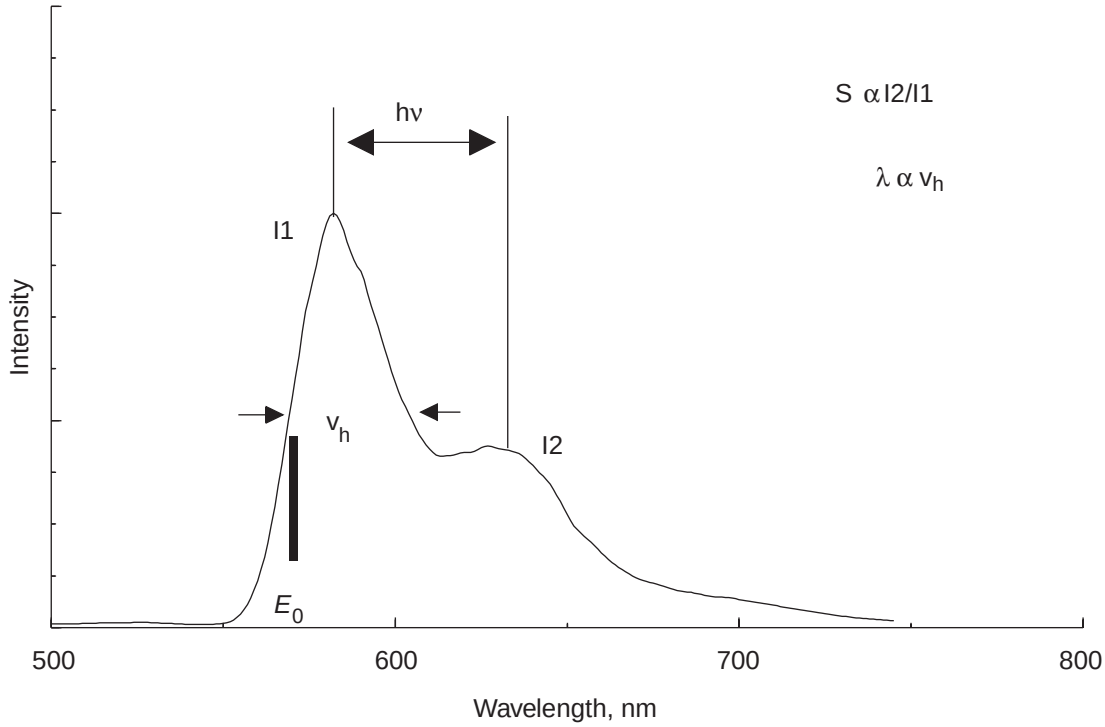

Figure 2 Emission spectrum fit with Equation (1). The value of E_0, the average of medium frequency vibrational modes contributing to nonradiative relaxation, hν, the degree of excited state distortion, proportional to the Huang–Rhys factor S, and the degree of inhomogeneous broadening of vibronic components, ν_h, can be obtained.

constant will equal the sum of the radiative and nonradiative decay rate constants. The excited state lifetime in such cases is simply the inverse of the observed decay rate constant (Equation (2)):

$$[\text{Ex. St}]_t = [\text{Ex. St.}]_0 \exp(-k_{obs}t) \text{ where } (k_{obs})^{-1} = \tau = (k_r + k_n)^{-1} \tag{2}$$

Emission quantum yields (Φ_{em} = fraction of excited states that emit) and lifetimes are related and experimental determination of both often allows unambiguous determination of radiative and nonradiative rate constants. In the case of exclusive emission from the initially formed excited state (S_1 in Figure 1), the emission quantum yield and lifetime are related by Equation (3)

$$\Phi_{em} = k_f/(k_f + k_{nf} + k_{isc}) = k_f\tau_f \tag{3}$$

In this case the radiative decay rate constant is obtained from the ratio of the emission yield and lifetime. However, even in this simple case the observed nonradiative decay is the sum of the rate constants for nonradiative relaxation of the singlet state and intersystem crossing. If emission is observed exclusively from a state with a spin multiplicity differing from the ground state (i.e., T_1 in Figure 1), the observed emission quantum yield will reflect the efficiency for populating the emissive excited state (Equation (4)).

$$\Phi_{em} = \left(\frac{k_{isc}}{k_r + k_{nf} + k_{isc}}\right)\left(\frac{k_p}{k_p + k_{np}}\right) = \eta_{isc}k_p\tau_p \tag{4}$$

The ratio of the emission quantum yield and lifetime of the triplet state emission (phosphorescence) yields the product of the intersystem crossing efficiency and radiative decay rate constant. Determination of intersystem crossing efficiencies is generally not straightforward and often techniques other than emission spectroscopy, such as time-resolved photoacoustic calorimetry,[15] are used.

Often more complicated excited state decay behavior is observed. For example, if the S_1-T_1 energy gap is small (Figure 1), back intersystem crossing may occur and the fluorescence ($S_1 \rightarrow S_0$) will consist of a prompt decay and a much longer-lived decay that is associated with the repopulation of the S_1 state from the T_1 state. An excellent discussion of such cases is given in books by Ferraudi[6] and Demas.[16]

2.24.2 LUMINESCENT EXCITED STATES OF COORDINATION COMPOUNDS

Since Comprehensive coordination chemistry (*CCC*, 1987) was published in 1987, the array of luminescent transition metal complexes has expanded considerably. A general overview of photochemical processes is presented in *CCC* (1987) Chapter 7.3 (Kutal and Adamson). Vogler and Kunkely published an excellent overview of luminescent excited states of coordination compounds in 2001, summarizing the tremendous diversity in luminescence exhibited by transition metal complexes.[17] General concepts relating to equilibration and relaxation of excited states of coordination compounds are elegantly presented in a recent article by Endicott.[18] Luminescent excited states of coordination complexes can be broadly categorized into four groups: excited states localized on a single metal, states involving charge transfer between a metal and a ligand, states involving more than one metal, and states localized on one ligand or involving charge transfer between two ligands.

Metal localized transitions: This class represents the ligand field *d–d* transitions and *f–f* transitions. The *d–d* transition is symmetry forbidden and the excited state formed very often leads to labilization of the complex. Emission is observed in some instances (mostly various ions in lattices, such as Ti^{III} in sapphire) from transition metal complexes and is widely known for octahedral Cr^{III} complexes (see *CCC* (1987) Chapters 6.5 and 35.4).[19]

Luminescence from *f–f* transitions of lanthanide complexes is by far the most commonly observed metal localized luminescence (see *CCC* (1987) Chapter 15.7; 39.2; 62.1). Both absorption and emission transitions are generally very narrow since *f*-orbitals are shielded from ligand interaction by other orbitals and *f–f* excitation results in very little distortion of the excited state relative to the ground state. Since *f–f* transitions are parity forbidden, *f–f* excited states are often intramolecularly sensitized by excitation of allowed transitions of coordinated ligands.[20]

Emission of various coordination compounds has also been assigned as arising from states formed via transitions between *nd* and $(n+1)s$-orbitals (i.e., for d^{10}complexes), *nd* and $(n+1)p$-orbitals, *ns* and $(n+1)p$-orbitals, and *nf* and $(n+1)d$-orbitals.[17] A limited number of examples exist for all of these cases.

Metal-to-ligand charge transfer (MLCT) transitions: An enormous amount of research has been conducted on coordination complexes having luminescent excited states in which charge transfer from the metal center to a ligand is involved. MLCT emission is most commonly observed in low-valence d^6, d^8, or d^{10} monometallic complexes having ligands with low-energy π^* levels. Several excellent reviews have been published on the photophysics of metal complexes having MLCT states.[21–23,9]

Ligand-to-metal charge transfer (LMCT) transitions: LMCT emission is much less commonly observed than MLCT luminescence. Complexes having metals in high oxidation states and strong electron donating ligands (halides, amides, carbanions, etc.) are likely to have relatively low-energy LMCT transitions, but often LMCT excitation results in ligand dissociation. Examples of luminescence from LMCT states include Sc^{III} and Ta^{V} cyclopentadienyl and imido[24] complexes.

Luminescent states unique to polymetallic complexes: Luminescence has been observed for $d^{10}-d^{10}$, d^8-d^8, d^7-d^7, and d^4-d^4 bimetallic complexes. An interesting phenomenon that has been observed in complexes that have no net metal–metal bond in the ground state (i.e., $d^{10}-d^{10}$) is that the metal–metal bond order *increases* upon excitation. For example, various $Pt^{II}-Pt^{II}$ dimers have a Pt—Pt bond order of zero in the ground state ($(\sigma_{dz}^*)^2\ (\sigma_{pz})^0$) but 1/2 in the excited state ($(\sigma_{dz}^*)^1\ (\sigma_{pz})^1$).[25] Emissive metal–metal bonded trimetallic clusters are also known.[26]

In addition, a number of ligand bridged polymetallic clusters, particularly copper clusters, are known to be luminescent. Assignment of optical transitions and emitting excited states in these complexes is often not straightforward. Among the clusters that have been studied, luminescence has been assigned as arising from all of the excited states mentioned above.

States Localized on a Ligand or Involving Charge Transfer Between Ligands: The emission of excited states localized on free ligands (intraligand, IL, states) is generally affected by coordination to metals. Very often, the emitting excited state of the free ligand is not the lowest energy

excited state in the coordination complex and the luminescence disappears because excitation energy drains into lower energy states (i.e., metal localized or charge transfer). If electronic interaction of the coordinated metal and ligand is weak or coordination of the metal yields no lower energy excited states (i.e., complexes of alkali ions, Al^{III}, Zn^{II}, etc.) IL fluorescence may be observed from ligands having emissive singlet excited states. Coordination of second and third row transition metals often enhances intersystem crossing in fluorescent ligands (due to the relatively large spin–orbit coupling coefficients of the metals), leading to observation of IL phosphorescence.[17]

It is also possible that coordination of a metal alters the electron affinity of a portion of the ligand, resulting in observation of absorption and emission from a charge transfer state localized on the ligand (intraligand charge transfer, ILCT).[27–29]

An interesting class of excited states of coordination complexes are those involving charge transfer between two different coordinated ligands, the so-called ligand-to-ligand charge transfer (LLCT) states. In this case the metal serves to link electron-donating and electron-accepting ligands. For example, Zn^{II}complexes having phenylthiol donor and phenanthroline acceptor ligands exhibit LLCT luminescence.[30–32] A number of examples of LLCT emission are known.[23]

2.24.3 LUMINESCENCE SPECTROSCOPIC METHODS

Techniques for the measurement of emission spectra and determination of luminescence quantum yields are well established and are presented in several books and review articles.[33,34,12] In addition, Demas's 1983 book on measurement of luminescence lifetimes still serves as an excellent resource for general approaches.[16]

Luminescence lifetimes measured using pulsed laser excitation involve either direct detection of emission decays with time or a technique known as time-correlated single photon counting (TCSPC). The latter technique involves repeated measurement of the delay time between the excitation pulse and the arrival of an emitted photon packet above a given discrimination level; the intensity–time decay profile accumulates over many millions of excitation pulses. The TCSPC experiment has the advantage that much better signal to noise can be obtained relative to the direct capture of the luminescence decay.

Often, assignment of electronic transitions in absorption and luminescence spectroscopy of coordination compounds is made difficult by the existence of nearly isoenergetic states of different orbital parentage. Useful information can be obtained via the use of polarization, high-resolution or magnetic-field-related techniques. The use of narrow-band laser excitation for laser selective photophysical studies of complexes in single crystals or other rigid environments was reviewed recently by Krausz *et al*. Selective excitation techniques have been used to characterize emitting excited states and examine intramolecular excitonic migration.[35] An excellent example of the use of both high-resolution emission spectroscopy and time-resolved emission is provided in a recent review by Yersin.[36]

The use of polarized excitation for anisotropy measurements in coordination complexes is widespread and is useful in correlating the relative orientation of excitation and emission dipoles.[37,38] For samples excited with vertically polarized light the anisotropy ratio is determined by measuring the intensity of emission of light polarized both parallel and perpendicular to the polarized excitation.[39] In this case the anisotropy, r, is given by Equation (5). For a chromophore in a rigid matrix, where loss of polarization does not occur via molecular rotation, the value of r is related to the relative orientation of the absorption and emission dipoles, θ. Thus, the measurement

$$r = \frac{I_{//} - I_{\perp}}{I_{//} + 2I_{\perp}} = \frac{2}{5}\left(\frac{3 < \cos^2\theta > -1}{2}\right) \tag{5}$$

of emission anisotropy is of fundamental value in relating excited states involved in absorption and emission.

Detailed information on emissive triplet excited states (having singlet ground states) can be obtained from optically detected magnetic resonance. Through the observation of emission intensity changes with varying microwave excitation frequency, the zero field splitting of the triplet states of ligand localized π–π^* and LLCT states has been determined. A review of the technique and its application to determination of zero field splitting in Rh^{III} and Pd^{II} coordination complexes has been published.[40]

A number of other techniques have been applied to the analysis of metal complex luminescence. Pressure effects on luminescence of coordination complexes in single crystals (either pure or doped) can also provide information of value in evaluating excited-state distortion or metal–metal interactions of ordered solid matrices.[41,42] The magnitude of transition dipole moments and polarizability can be determined using Stark spectroscopy, and Bublitz and Boxer wrote a recent review of the technique.[43] Two-photon excitation of transition metal complex chromophores has also been observed to yield luminescence. Recent work in this area has been reviewed by Lakowitz and co-workers.[34]

2.24.3.1 First Row Complexes

Luminescence is observed from coordination complexes of first row transition metals less often than from complexes of second or third row metals. This is a result of the presence of low-energy ligand field (LF) states into which the excitation is funneled that can rapidly deactivate through either non-radiative pathways to the ground state or photo-reaction pathways to products.[5,4] Recent reports relating to the luminescence of titanium,[44] chromium[45], and zinc complexes[46] provide examples of new emissive first row coordination compounds.

A large number of recent examples exist for luminescence from d^{10} metal systems such as copper(I), which can have no ligand field states. The interest in the photophysics of copper(I) complexes is sparked by the many possible coordination geometries and structures that are accessible since the coordinated metal imposes no electronic constraints to bonding and concomitant resulting variety of excited states that are observed.[47,48]

The tetrahedrally coordinated substituted copper bis-phenanthroline complexes have an emissive MLCT state as the lowest lying excited state. The $[Cu(phenanthroline)_2]^+$parent compound displays no emission in fluid solution. The transient photo-oxidation of the copper center to a d^9electron count causes the complex to distort in the excited state providing a non-radiative deactivation pathway to the ground state. Substitution of the phenanthroline ligand with methyl groups at the 2 and 9 positions results in a complex that emits in non-coordinating solvents such as chloroform and methylene chloride ($\lambda_{max}(CH_2Cl_2298) = 690\,nm$, $\tau = 0.090\,\mu s$, $\phi = 4 \times 10^{-4}$) but the emission is quenched in coordinating solvents such as methanol, water, and acetonitrile.[49] An excited state complex (exciplex) quenching mechanism was proposed in which the distortion of the complex in the excited state was large enough that the donating solvent could coordinate to the metal, stabilizing the excited state and increasing the non-radiative deactivation rates.

Bulky and pi delocalizing substituents on the phenanthroline ligands blue shift the emission.[50] The bulky 2,9 di-tert-butyl substituted phenanthroline ligand has been utilized as an efficient route to heteroleptic copper complexes as the bis complex is too sterically hindered to form. $[Cu(2,9\text{-di-tert-butyl-phenanthroline})(2,9\text{-di-methyl-phenanthroline})]^+$ has photophysical properties that are comparable to those of $[Ru(bpy)_3]^{2+}$($\lambda_{max}(CH_2Cl_2298) = 646\,nm$, $\tau = 0.73\,\mu s$, $\phi = 1\%$).[51] Studies of the temperature dependence of the emission of copper bis -phenanthroline complexes indicate that there are two MLCT states, of which the higher energy state is the primary photo emissive state.[52]

The cuprous ion will assemble under appropriate conditions into a variety of clusters and polymers that can have novel luminescent properties. The $Cu_4I_4(NC_5H_5)_4$ cluster, with a structure of two interpenetrating copper and iodide tetrahedra, has two non-equilibrated emissive excited states in fluid solution.[53] The low-energy excited state has been assigned as an iodide-to-ligand charge transfer state ($\lambda_{max}(RT) = 690\,nm$, $\tau = 10.6\,\mu s$, $\phi = 3.4 \times 10^{-4}$) and the high-energy emission has been assigned as a cluster-centered metal d-to-s excited state with a significant LMCT component ($\lambda_{max}(RT) = 480\,nm$, $\tau = 0.45\,\mu s$, $\phi = 0.09$). The two states are believed to distort in very different ways leading to a significant barrier between them that prevents efficient coupling and causes the dual emission as the states are populated by deactivation processes from higher energy states.[54]

A series of copper acetylide trimeric clusters, including $[Cu_3(\mu\text{-}PCH_3(C_6H_5)_2)_3(\mu_3\text{-}\eta_1CCC_6H_4OMe\text{-}p)(\mu_3\text{-}\eta_1CCC_6H_4OEt\text{-}p)]PF_6$, have been shown to luminesce with vibronically structured bands in the solid state and fluid solution ($\lambda_{max}(RT) = 479\,nm$, $\tau = 5.6\,\mu s$). The observed vibronic spacing is consistent with the acetylide stretching frequency and no emission was observed with electron-deficient acetylide ligands with nitro substituents leading to the assignment of the emitting state as an LMCT state.[55]

A square planar copper tetramer with a Cu_4N_4 core, $[CuN(Si(CH_3)_3)_2]_4$,displays a luminescence in fluid solution ($\lambda_{max}(CH_2Cl_2298) = 512\,nm$, $\tau = 30\,\mu s$) with similar properties in the solid at room temperature and 77 K.[56] The emission was assigned to a metal-centered excited state as the crystal structure reports a short copper–copper distance of 2.7 Å, less than the sum of the van der Waals radii of 2.8 Å, indicating significant copper–copper interactions. The large Stokes' shift observed for emission is consistent with the metal-centered assignment as population of the metal-centered state should lead to large distortions in the excited state.

The luminescence of a copper polymer, $[[\{(Ph_3P)_2Cu_2(\mu\text{-}Cl)_2(\mu\text{-pyrazine})\}_\infty]$, ($\lambda_{max}$(solid 20) = 615 nm, λ_{max}(solid 298) = 690 nm), was assigned as arising from an MLCT state based upon resonance Raman data in which pyrazine bands showed resonance enhancement.[57] The polymer structure had copper–copper distances of 3.059 Å, suggesting against a metal cluster-centered state.

2.24.3.2 Second and Third Row Complexes

Luminescence has been observed from a large number of later transition element complexes and a rich array of excited states have been observed. Related sections from *CCC* (1987) include Chapter 16.5 on Pt, Rh, and Ir complexes, 36.3 on Mo halide clusters, 43 on Re complexes, 45.4 on Ru polypyridyls, 46.4 on Os polypyridyls, 48.6 on Rh complexes, and sections of Chapter 52 on Pt complexes. Several recent reviews have been published on polynuclear d^{10} complexes,[58] the photophysics of gold complexes,[59] and platinum diimine complexes.[60,61] Many other more narrowly focused review articles have been published on transition metal complex luminescence; a significant number are published in the journal *Coordination Chemistry Reviews* and some of these reviews are cited in this chapter.

Metal-centered Excited States: A concise overview of luminescence from LF excited states is provided in a recent review.[17] Ligand field luminescence from coordination complexes is not common and is generally only observed in complexes having valences and ligands that result in relatively high-energy LMCT and MLCT transitions. For second and third row complexes the emission is very often from a spin-forbidden excited state (i.e.,^{3}LF state for complexes having singlet low-spin d^6ground states).

Metal-centered excited states involving transitions from an *nd* level to $(n+1)s$ or $(n+1)p$ orbitals have also been proposed to occur in coordination compounds.[62,63]

Other metal-centered transitions involve *d* to *p* excitation in metal–metal bonded systems. A fascinating example of such systems is the bimetallic complex $[Pt^{II}_2(\mu\text{-}P_2O_5H_2)_4]^{4-}$ which has two d^8 Pt^{II} centers with no formal metal–metal bond. The lowest–energy electronic transition is from a Pt—Pt antibonding (σ_{dz2}*) orbital to a bonding $(\sigma_{pz})^0$ level, yielding a strongly luminescent excited state with a Pt—Pt bond order of 0.5.[25] The complex is known to undergo a rich array of photoredox reactions, many of which involve two electrons. In addition, $Pd_2(dppm)_3$, a bimetallic d^{10}–d^{10} complex, also exhibits luminescence from a *d* to *p* excited state.[64] Time-resolved resonance Raman spectra support the assignment of the emissive excited state as being associated with a $d\sigma^* \rightarrow p\sigma$ transition in both complexes.

LMCT Excited States: While the observation of LMCT emission is relatively rare, a growing number of complexes exhibiting LMCT emission have been reported in recent years, principally for high valence early transition metal (d^0) complexes. In the early 1990s, Caspar and co-workers observed LMCT luminescence from a cyclopentadienyl Ta^V complex.[65] Subsequently, LMCT emission was reported from $Cp_2M^{IV}Cl_2$ and $[Zr(Cp^*)_2(ER)_2]$ (E = S, Se, R = alkyl, or aryl) complexes (M = Ti, Zr, Hf).[66,67] Imido complexes of Nb^V and $Ta^V$are also known to be luminescent and the excited states have been assigned as $M^V = N\ (\pi) \rightarrow M\ (d_{xy})$ charge transfer excited state.[24,68] Luminescence assigned as arising from a LMCT excited state has also been observed from Ce^{IV}complexes of the 2,2,6,6-tetramethyl-3,5-heptane-dionate anion.[69]

MLCT Excited States: An enormous number of d^6 complexes of second and third row transition elements have been shown to exhibit MLCT luminescence. MLCT emission from complexes of Mo^0, W^0, Re^I, Ru^{II}, Os^{II}, Rh^{III}, and Ir^{III} has been known for many years. Recently, MLCT emission has been documented to occur from Pt^{II} (d^8) and Au^I d^{10} complexes as well.

Among complexes having d^6 electron configurations, the ground states are singlets. MLCT excitation is followed by rapid intersystem crossing to yield the emissive excited state which has

a high degree of triplet character. Third row transition metals have much larger spin–orbit coupling matrix elements and, in some instances, direct singlet–triplet absorption is observed to have significant oscillator strength.

Stufkens has reviewed the photochemistry and photophysics of zerovalent d^6 complexes of diimine ligands; luminescence is observed from $[(CO)_4M(LL)]$ ($M = Mo^0$, W^0 and LL = diimine).[70] Other examples of zerovalent d^6 complexes exhibiting MLCT emission include the bimetallic complexes (μ-bpym)$[Mo(CO)_4]_2$, which exhibits weak emission with an onset at 700 nm in CH_2Cl_2.[71] and $[W(CO)_5]_2L$ (L = 2,1,3-benzothiadiazole, 2,1, 3-benzoselenadiazole) that shows weak near-IR (>750 nm) MLCT emission.[72]

A large amount of work has been published on Re^I complexes of the general type $[(L)Re(CO)_3(\alpha\text{-diimine})]^{0/+}$. These complexes exhibit $Re^I \rightarrow$ (diimine) MLCT emission at room temperature in solution and the emission energy can be tuned by variation of the diimine, ancillary ligand, L, and solvent. Several reviews have appeared that discuss the luminescence behavior of these complexes.[73,74] Recently, detailed temperature-dependent luminescence measurements have been made on several methylated phenanthroline (*m*-phen) complexes of the type $[ClRe(CO)_3(m\text{-phen})]$; the emission from the complexes was comprised of components from the ^{3}MLCT and *m*-phen localized π–π^* states.[75] Emission from this class of chromophores has been applied recently to immunoassays based on luminescence polarization of Re^I diimine complexes[76] and the development of unique luminescent arylethynylene polymers.[77]

By far the most widely studied complexes exhibiting MLCT emission are those of Ru^{II} and Os^{II}. The photochemistry and photophysics of Ru^{II} complexes has been of great interest since early reports of its potential use in photochemical water splitting. Since then, Ru^{II} complexes, particularly those of 2,2′-bipyridine and 1,10-phenanthroline, have been used as luminescent chemosensors and as sensitizers in dye-sensitized photoelectrochemical cells. Balzani and co-workers have written several excellent reviews of the luminescence behavior of diimine and triimine Ru^{II} complexes and multimetallic complexes having Ru^{II} ($d\pi$) $\rightarrow$ imine (π^*) transitions.[78,21,79,22] These reviews are broad in scope and have extensive lists detailing the photophysical properties of Ru^{II} complexes. Detailed photophysical studies of the luminescence of $[Ru^{II}(bpy)_3]^{2+}$, including Zeeman, Stark, and laser line narrowing measurements have also been reviewed.[80,81,35] The focus of this work has been in evaluating the zero field splitting parameters for the triplet excited state and addressing the issue of delocalization of the MLCT state.

Charge transfer luminescence has also been observed from diimine complexes of Rh^{III}, Ir^{III} and Pt^{II}. A review of Pt^{II} diimine complexes exhibiting MLCT emission was recently published.[60]

Exciplexes and Second Sphere Interactions: The concept of exciplex formation in inorganic systems has received considerable attention in recent years. Exciplexes can be observed when ground state complex formation is forbidden but the excited state complex has a shallow energy minimum that can radiatively decay to the ground state (Equation (6) and (7)). McMillin and co-workers postulated exciplex contributions to nonradiative relaxation of Cu^I phenanthroline

$$ML_n + Q \rightarrow \{ML_n, Q\} \quad \Delta G > 0 \tag{6}$$

$$ML_n^* + Q \rightarrow \{ML_n, Q\}^* \quad \Delta G < 0 \tag{7}$$

$$\{ML_n,Q\}^* \rightarrow ML_n + Q + h\nu$$

complexes in the mid 1980s.[82] Since that time, exciplex formation has been invoked in explaining the photophysical behavior of a number of luminescent second and third row coordination complexes. In the late 1980s Demas and co-workers reported exciplexes of Ru^{II} diimine complexes with Ag^+.[83] Horvath published two recent reviews of transition metal complex exciplexes, focusing on association of ruthenium diimine complexes with Ag^+ and dicyanocuprate with halides.[84,85] New reports have appeared in recent years, including solid state exciplexes between Tl^+ and $[Ag(CN)_2]^+$[86] and excited state complexes of Lewis bases and Pt^{II} terpyridyl complexes.[87,88]

In addition, formation of ground state complexes between chromophores and non-chromophoric species in solution, so called "second sphere" complexation, has also been shown to influence the

luminescence behavior of coordination complexes. Scandola and co-workers have shown that Ru^{II} diimine complexes having cyano ligands exhibit significant luminescence changes upon addition of various Lewis acids, which can be attributed to second sphere interactions.[89,90]

2.24.3.3 Lanthanide Complexes

The luminescence behavior of lanthanide complexes represents a rich and multi-faceted area. Lanthanides have large spin–orbit coupling constants and, as a result, ground and excited states are most precisely described by their spin–orbit coupled (J) states. In general, ligand perturbations of the valence shell (f) orbitals is small and luminescence associated with f–f transitions is sharp. In addition, coupling between states is weak and it is common to observe emission from states of varying energy and spin multiplicity. State diagrams for trivalent lanthanide ions in $LaCl_3$ are given in a monograph by Lund.[91]

Lanthanides commonly form complexes with oxygen donor ligands and, in the case of phenolic ligands, relatively low-energy LMCT transitions may exist that serve as energy traps that effectively quench f–f emission. Such is the case for Eu^{III} complexes of calix[n]arenes ($n = 5$ and 8), where mixing of the f–f and LMCT transitions results in very little emission from the lanthanide localized states.[92] However, it is also possible to sensitize f–f emission of lanthanides via excitation of higher-energy ligand localized excited states. In a recent comparison of solid state and solution luminescence of lanthanides, Choppin and Peterman illustrate the effectiveness of ligand-sensitized lanthanide luminescence.[20]

A number of lanthanide complexes have been shown to exhibit circularly polarized luminescence (CPL—the differential spontaneous emission of left- and right-circularly polarized light). In the absence of any externally applied fields, CPL is exhibited only by systems that have net chirality in their structures or are subject to chiral perturbations by their environment. CPL exhibited by the $4f$–$4f$ transitions of chiral lanthanide systems provides a sensitive probe of coordination and structure in solution. Applications are limited to systems which possess some element of chirality, but in many cases this merely requires that >1 ligand of interest has a chiral atom or carries a chiral label (such as a chiral substituent group).[93]

The photophysics of lanthanide complexes has drawn considerable attention in recent years, in part because of the potential applications of lanthanides (sensors, electroluminescent displays, etc.) and several recent reviews highlighting applications of luminescent lanthanide complexes have appeared. A discussion of infrared f–f luminescence of Yb^{III}, Nd^{III}, and Er^{III} in complexes having macrocyclic ligands such as porphyrins, cyclen derivatives, and calixarenes was published by Korovin and Rusakova.[94] In addition, DaSilva and co-workers describe the development of highly luminescent lanthanide complexes and their application as light-conversion molecular devices.[95]

2.24.4 REFERENCES

1. Sykora, J.; Sima, J. *Coord. Chem. Rev.* **1990**, *107*, v–xi, 1–225.
2. Balzani, V. C. V. *Photochemistry of Coordination Compounds*; Academic: New York, 1970.
3. Yersin, H.; Vogler, A.; Eds. *Photochemistry and Photophysics of Coordination Compounds*; Springer: Berlin, 1987.
4. Adamson, A. W.; Fleischauer, P. D.; Eds. *Concepts of Inorganic Photochemistry*; Wiley: New York, 1975.
5. Roundhill, D. M. *Photochemistry and Photophysics of Metal Complexes*; Plenum: New York, 1994.
6. Ferraudi, G. J. *Elements of Inorganic Photochemistry*; Wiley Interscience: New York, 1988.
7. Murtaza, Z.; Graff, D. K.; Zipp, A. P.; Worl, L. A.; Jones, W. E., Jr.; Bates, W. D.; Meyer, T. J. *J. Phys. Chem.* **1994**, *98*, 10504–10513.
8. Kober, E. M.; Caspar, J. V.; Lumpkin, R. S.; Meyer, T. J. *J. Phys. Chem.* **1986**, *90*, 3722–3734.
9. Chen, P. Y.; Meyer, T. J. *Chem. Rev.* **1998**, *98*, 1439–1477.
10. Graff, D.; Claude, J. P.; Meyer, T. J. *Adv. Chem. Ser.* **1997**, *253*, 183–198.
11. Endicott, J. F.; Perkovic, M. W.; Heeg, M. J.; Ryu, C. K.; Thompson, D. *Adv. Chem. Ser.* **1997**, *253*, 199–220.
12. Brunold, T. C.; Gudel, H. U. *Inorg. Electron. Struct. Spectrosc.* **1999**, *1*, 259–306.
13. Azumi, T.; Miki, H. *Top. Curr. Chem.* **1997**, *191*, 1–40.
14. Yersin, H.; Donges, D. *Top. Curr. Chem.* **2001**, *214*, 81–186.
15. Song, X.; Endicott, J. F. *Inorg. Chem.* **1991**, *30*, 2214–2221.
16. Demas, J. N. *Excited State Lifetime Measurements*; Academic Press: New York, 1983.
17. Vogler, A.; Kunkely, H. *Top. Curr. Chem.* **2001**, *213*, 143–182.
18. Endicott, J. F. *Inorg. Electron. Struct. Spectrosc.* **1999**, *2*, 291–341.
19. Porter, G. B. *Kinetics of Photophysical Processes*; Adamson, A. W. F., P. D., Ed.; Wiley: New York, 1975, pp 37–81.
20. Choppin, G. R.; Peterman, D. R. *Coord. Chem. Rev.* **1998**, *174*, 283–299.

21. Juris, A.; Balzani, V.; Barigelletti, F.; Campagna, S.; Belser, P.; Von Zelewsky, A. *Coord. Chem. Rev.* **1988**, *84*, 85–277.
22. Balzani, V.; Juris, A.; Venturi, M.; Campagna, S.; Serroni, S. *Chem. Rev.* **1996**, *96*, 759–833.
23. Lever, A. B. P.; Dodsworth, E. S. *Inorg. Electron. Struct. Spectrosc.* **1999**, *2*, 227–287.
24. Heinselman, K. S.; Hopkins, M. D. *J. Am. Chem. Soc.* **1995**, *117*, 12340–12341.
25. Roundhill, D. M.; Gray, H. B.; Che, C. M. *Acc. Chem. Res.* **1989**, *22*, 55–61.
26. Xiao, H.; Weng, Y.-X.; Wong, W.-T.; Mak, T. C. W.; Che, C.-M. *J. Chem. Soc., Dalton Trans.* **1997**, 221–226.
27. Pilato, R. S.; Van Houten, K. A. *Mol. Supramol. Photochem.* **1999**, *4*, 185–214.
28. Kaiwar, S. P.; Vodacek, A.; Blough, N. V.; Pilato, R. S. *J. Am. Chem. Soc.* **1997**, *119*, 3311–3316.
29. Yersin, H.; Donges, D.; Nagle, J. K.; Sitters, R.; Glasbeek, M. *Inorg. Chem.* **2000**, *39*, 770–777.
30. Crosby, G. A.; Highland, R. G.; Truesdell, K. A. *Coord. Chem. Rev.* **1985**, *64*, 41–52.
31. Jordan, K. J.; Wacholtz, W. F.; Crosby, G. A. *Inorg. Chem.* **1991**, *30*, 4588–4593.
32. Ikeda, S.; Yamamoto, S.; Azumi, T.; Crosby, G. A. *J. Phys. Chem.* **1992**, *96*, 6593–6597.
33. Krausz, E.; Riesen, H. *J. Mol. Struct.* **1997**, *406*, 61–74.
34. Lakowicz, J. R.; Gryczynski, I.; Szmacinski, H.; Malak, H.; Castellano, F. N.; Murtaza, Z.; Guo, X.-Q.; Li, L.; Lin, H.; Dattelbaum, J. D. *NATO ASI Ser., Ser. 3* **1998**, *52*, 3–19.
35. Krausz, E.; Riesen, H. *Coord. Chem. Rev.* **1997**, *159*, 9–40.
36. Yersin, H.; Strasser, J. *Coord. Chem. Rev.* **2000**, *208*, 331–364.
37. Riehl, J. P. *Acta Phys. Pol., A* **1996**, *90*, 55–62.
38. Michl, J. T. E.W. *Spectroscopy with Polarized Light*; VCH: New York, 1986.
39. Lakowicz. *Principles of Fluorescence Spectroscopy*, 2nd ed.; Kluwer Academic: New York, 1999.
40. Glasbeek, M. *Topics in Current Chemistry* **2001**, *213*, 95–142.
41. Bray, K. L. *Topics in Current Chemistry* **2001**, *213*, 1–94.
42. Van Eldik, R.; Ford, P. C. *Adv. Photochem.* **1998**, *24*, 61–146.
43. Bublitz, G. U.; Boxer, S. G. *Annu. Rev. Phys. Chem.* **1997**, *48*, 213–242.
44. Kenney, J. W. , III; Boone, D. R.; Striplin, D. R.; Chen, Y. H.; Hamar, K. B. *Organometallics* **1993**, *12*, 3671–3676.
45. Bussiere, G.; Beaulac, R.; Cardinal-David, B.; Reber, C. *Coord. Chem. Rev.* **2001**, *219–221*, 509–543.
46. Wang, S. *Coord. Chem. Rev.* **2001**, *215*, 79–98.
47. Armaroli, N. *Chem. Soc. Rev.* **2001**, *30*, 113–124.
48. Kutal, C. *Coord. Chem. Rev.* **1990**, *99*, 52–213.
49. Palmer, C. E. A.; McMillin, D. R. *Inorg. Chem.* **1987**, *26*, 3837–3840.
50. Miller, M. T.; Gantzel, P. K.; Karpishin, T. B. *Inorg. Chem.* **1999**, *38*, 3414–3422.
51. Miller, M. T.; Gantzel, P. K.; Karpishin, T. B. *J. Am. Chem. Soc.* **1999**, *121*, 4292–4293.
52. Felder, D.; Nierengarten, J.-F.; Barigelletti, F.; Ventura, B.; Armaroli, N. *J. Am.Chem. Soc.* **2001**, *123*, 6291–6299.
53. Ford, P. C.; Cariati, E.; Bourassa, J. *Chem. Rev.* **1999**, *99*, 3625–3647.
54. Vitale, M.; Ryu, C. K.; Palke, W. E.; Ford, P. C. *Inorg. Chem.* **1994**, *33*, 561–566.
55. Yam, V. W.-W.; Fung, W. K.-M.; Wong, M.-T. *Organometallics* **1997**, *16*, 1772–1778.
56. James, A. M., Laxman, R. K., Fronczek, F. R., Maverick, A. W. *Inorg. Chem.* **1998**, *37*, 3785–3791.
57. Henary, M.; Wootton, J. L.; Khan, S. I.; Zink, J. I. *Inorg. Chem.* **1997**, *36*, 796–801.
58. Yam, V. W.-W.; Lo, K. K.-W. *Chem. Soc. Rev.* **1999**, *28*, 323–334.
59. Vogler, A.; Kunkely, H. *Coord. Chem. Rev.* **2001**, *219–221*, 489–507.
60. Hissler, M.; McGarrah, J. E.; Connick, W. B.; Geiger, D. K.; Cummings, S. D.; Eisenberg, R. *Coord. Chem. Rev.* **2000**, *208*, 115–137.
61. Crosby, G. A.; Kendrick, K. R. *Coord. Chem. Rev.* **1998**, *171*, 407–417.
62. Kunkely, H.; Vogler, A. *Z. Naturforsch., B: Chem. Sci.* **1996**, *51*, 1067–1071.
63. Assefa, Z. M. B. G.; Staples, R. J.; Fackler, J. *Inorg. Chem.* **1995**, *34*, 4965–4968.
64. Harvey, P. D.; Gray, H. B. *J. Am. Chem. Soc.* **1988**, *110*, 2145–2147.
65. Paulson, S.; Sullivan, B. P.; Caspar, J. V. *J. Am. Chem. Soc.* **1992**, *114*, 6905–6906.
66. Loukova, G. V.; Smirnov, V. A. *Russian Chemical Bulletin Translation of Izvestiya Akademii Nauk, Seriya Khimicheskaya.* **2001**, *50*, 329–330.
67. Wing-Wah Yam, V.; Qi, G.-Z.; Cheung, K.-K. *J. Chem. Soc., Dalton Trans.* **1998**, 1819–1824.
68. Kunkely, H.; Vogler, A. *Inorg. Chem. Commun.* **2001**, *4*, 252–253.
69. Kunkely, H.; Vogler, A. *J. Photochem. Photobiol., A: Chemistry* **2001**, *146*, 63–66.
70. Stufkens, D. J. *Coord. Chem. Rev.* **1990**, *104*, 39–112.
71. Kaim, W.; Kohlmann, S.; Lees, A. J.; Snoeck, T. L.; Stufkens, D. J.; Zulu, M. M. *Inorg. Chim. Acta* **1993**, *210*, 65–159.
72. Kaim, W.; Kohlmann, S.; Lees, A. J.; Zulu, M. *Z. Anorg. Allg. Chem.* **1989**, *575*, 97–114.
73. Vogler, A.; Kunkely, H. *Coord. Chem. Rev.* **2000**, *200–202*, 991–1008.
74. Stufkens, D. J.; Vlcek, A., Jr. *Coord. Chem. Rev.* **1998**, *177*, 127–179.
75. Striplin, D. R.; Crosby, G. A. *Coord. Chem. Rev.* **2001**, *211*, 163–175.
76. Guo, X.-Q.; Castellano, F. N.; Li, L.; Lakowicz, J. R. *Anal. Chem.* **1998**, *70*, 632–637.
77. Walters, K. A.; Ley, K. D.; Cavalaheiro, C. S.; Miller, S. E.; Gosztola, D.; Wasielewski, M. R.; Bussandri, A. P.; van Willigen, H.; Schanze, K. S. *J. Amer. Chem. Soc.* **2001**, *123*, 8329–8342.
78. Balzani, V.; Juris, A. *Coord. Chem. Rev.* **2001**, *211*, 97–115.
79. Sauvage, J. P.; Collin, J. P.; Chambron, J. C.; Guillerez, S.; Coudret, C.; Balzani, V.; Barigelletti, F.; De Cola, L.; Flamigni, L. *Chem. Rev.* **1994**, *94*, 993–919.
80. Yersin, H.; Humbs, W.; Strasser, J. *Coord. Chem. Rev.* **1997**, *159*, 325–358.
81. Krausz, E.; Ferguson, J. *Prog. Inorg. Chem.* **1989**, *37*, 293–390.
82. McMillin, D. R.; Kirchhoff, J. R.; Goodwin, K. V. *Coord. Chem. Rev.* **1985**, *64*, 83–92.
83. Ayala, N. P.; Demas, J. N.; DeGraff, B. A. *J. Phys. Chem.* **1989**, *93*, 4104–4109.
84. Horvath, A.; Stevenson, K. L. *Coord. Chem. Rev.* **1996**, *153*, 57–82.
85. Horvath, A. *Coord. Chem. Rev.* **1997**, *159*, 41–54.
86. Omary, M. A.; Patterson, H. H. *Inorg. Chem.* **1998**, *37*, 1060–1066.
87. Crites Tears, D. K.; McMillin, D. R. *Coord. Chem. Rev.* **2001**, *211*, 195–205.
88. Pettijohn, C. N.; Jochnowitz, E. B.; Chuong, B.; Nagle, J. K.; Vogler, A. *Coord. Chem. Rev.* **1998**, *171*, 85–92.

89. Scandola, F.; Indelli, M. T. *Pure Appl. Chem.* **1988**, *60*, 973–980.
90. Balzani, V.; Sabbatini, N.; Scandola, F. *Chem. Rev.* **1986**, *86*, 319–337.
91. Lund, M. D. *Luminescence Spectroscopy* **1978**, Academic Press: New York.
92. Bunzli, J.-C. G.; Besancon, F.; Ihringer, F. *ACS Symp. Ser.* **2000**, *757*, 179–194.
93. Richardson, F. S. *J. Less-Common Met.* **1989**, *149*, 161–177.
94. Korovin, Y.; Rusakova, N. *Rev. Inorg. Chem.* **2001**, *21*, 299–329.
95. De Sa, G. F.; Malta, O. L.; De Mello Donega, C.; Simas, A. M.; Longo, R. L.; Santa-Cruz, P. A.; Da Silva, E. F., Jr., *Coord. Chem. Rev.* **2000**, *196*, 165–195.

Comprehensive Coordination Chemistry II
ISBN (set): 0-08-0437486

Volume 2, (ISBN 0-08-0443249); pp 315–325

2.25
Magnetic Circular Dichroism

W. R. MASON

Northern Illinois University, DeKalb, IL, USA

2.25.1 INTRODUCTION 327
2.25.2 MEASUREMENT OF MCD SPECTRA 328
2.25.3 THEORETICAL UNDERPINNINGS OF MCD 330
2.25.4 USE OF MCD SPECTROSCOPY 332
2.25.5 MCD LITERATURE AND SOME EXAMPLES 332
2.25.5.1 MCD Literature 332
2.25.5.2 Atomic Mercury Vapor 332
2.25.5.3 $BiBr_6^{3-}$ Ion 333
2.25.5.4 $M(Et\text{-}Xan)_2$ ($M = Ni^{II}$, Pd^{II}, and Pt^{II}; $Et\text{-}Xan = C_2H_5OCS_2^-$) 334
2.25.5.5 $Pt(P(Bu^t)_3)_2$ 334
2.25.5.6 $Pt(AuPPh_3)_8^{2+}$ and $Au(AuPPh_3)_8^{3+}$ Cluster Complexes 334
2.25.6 SUMMARY 335
2.25.7 REFERENCES 336

2.25.1 INTRODUCTION

Magnetic circular dichroism (MCD) spectroscopy is based upon the measurement of the differential absorption of circularly polarized light by a sample placed in a strong magnetic field oriented parallel to the direction of light propagation.[1–7] The magnetic field perturbs the electronic states involved in the absorption transitions, and will lift the degeneracy of degenerate states. The perturbation of electronic states allows an important experimental probe of the nature of the state(s) involved in the electronic transition. This is the primary value of MCD. It can assist in the interpretation of electronic transitions and can provide useful ground and/or excited state magnetic properties, which in some cases are difficult or impossible to obtain by any other means. When combined with conventional absorption spectroscopy, MCD adds another experimental dimension: MCD effects are sign dependent (positive or negative) and depend upon molecular magnetic moments in electronic states and the direction of the field. This anisotropic information is particularly useful for those samples that cannot be oriented conveniently in a polarized light beam (e.g., where single crystals can not be obtained). MCD spectra can be obtained from gases, solutions, or isotropic solids.

The origin of MCD is the Zeeman effect as it applies to atoms and molecules. Historically, the phenomenon is related to the Faraday Effect discovered by Michael Faraday in the 1840s. Faraday found that a property of matter placed in a magnetic field is that it will rotate the plane of polarized light. This magnetic optical rotation is related to MCD in the same way as optical rotation for chiral molecules is related to circular dichroism (CD).[7] A convenient way to explain MCD is presented in Figure 1 which shows the Zeeman splitting of an excited atomic *P* state (three-fold degenerate) by a magnetic field. Transitions from an *S* (nondegenerate) ground state are allowed for circular polarized light—left circularly polarized (lcp) light being allowed for the +1 Zeeman sublevel and right circularly polarized (rcp) light being allowed for the −1 sublevel.

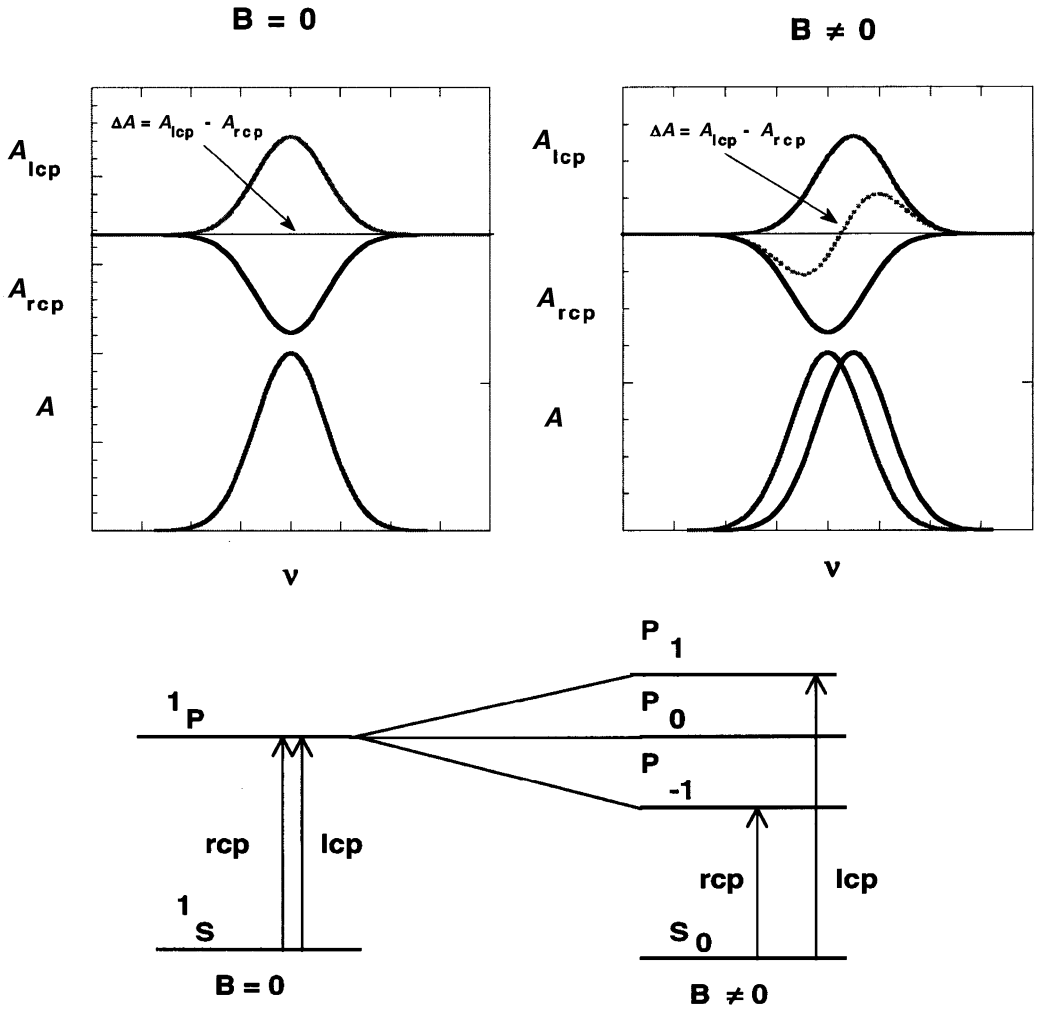

Figure 1 The effect of a magnetic field on an excited P state and the allowed absorptions by rcp and lcp light, respectively: the figures on the left are in the absence of a magnetic field while those on the right are in the presence of a longitudinal field along the direction of light propagation. In the top figures lcp and rcp absorptions are plotted in opposite directions and the $\Delta A = A_{\text{lcp}} - A_{\text{rcp}}$ is shown in between these absorptions.

The measurement (see Section 2.25.2) involves the difference in absorption between lcp and rcp light. Transitions to the 0 sublevel are strongly forbidden for both lcp and rcp light.

2.25.2 MEASUREMENT OF MCD SPECTRA

The measurement of MCD spectra requires a sensitive CD spectrometer and the sample in a strong magnetic field oriented along the light path. Figure 2 shows a sketch of a spectrometer which not only will measure the MCD (or CD in the absence of the field), but also the absorbance of the sample.[8] Simultaneous determination of absorbance A and the MCD (or CD) $\Delta A = A_{\text{lcp}} - A_{\text{rcp}}$ along the same light path is desirable in order to avoid errors which could develop by using two separate instruments. In Figure 2, monochromatic light is linearly polarized by a Rochon polarizer, and then the undeviated (ordinary) beam is converted to circularly polarized light by means of a quarter wave photoelastic modulator (PEM), and finally passed through the sample in a magnetic field. The absorbance of the sample is obtained by taking the log ratio of the input light intensity as measured by the deviated (extraordinary) beam from the Rochon polarizer and the intensity of the light passed through the sample. The MCD signal is obtained by detecting the modulated signal from the circularly polarized light passed through the

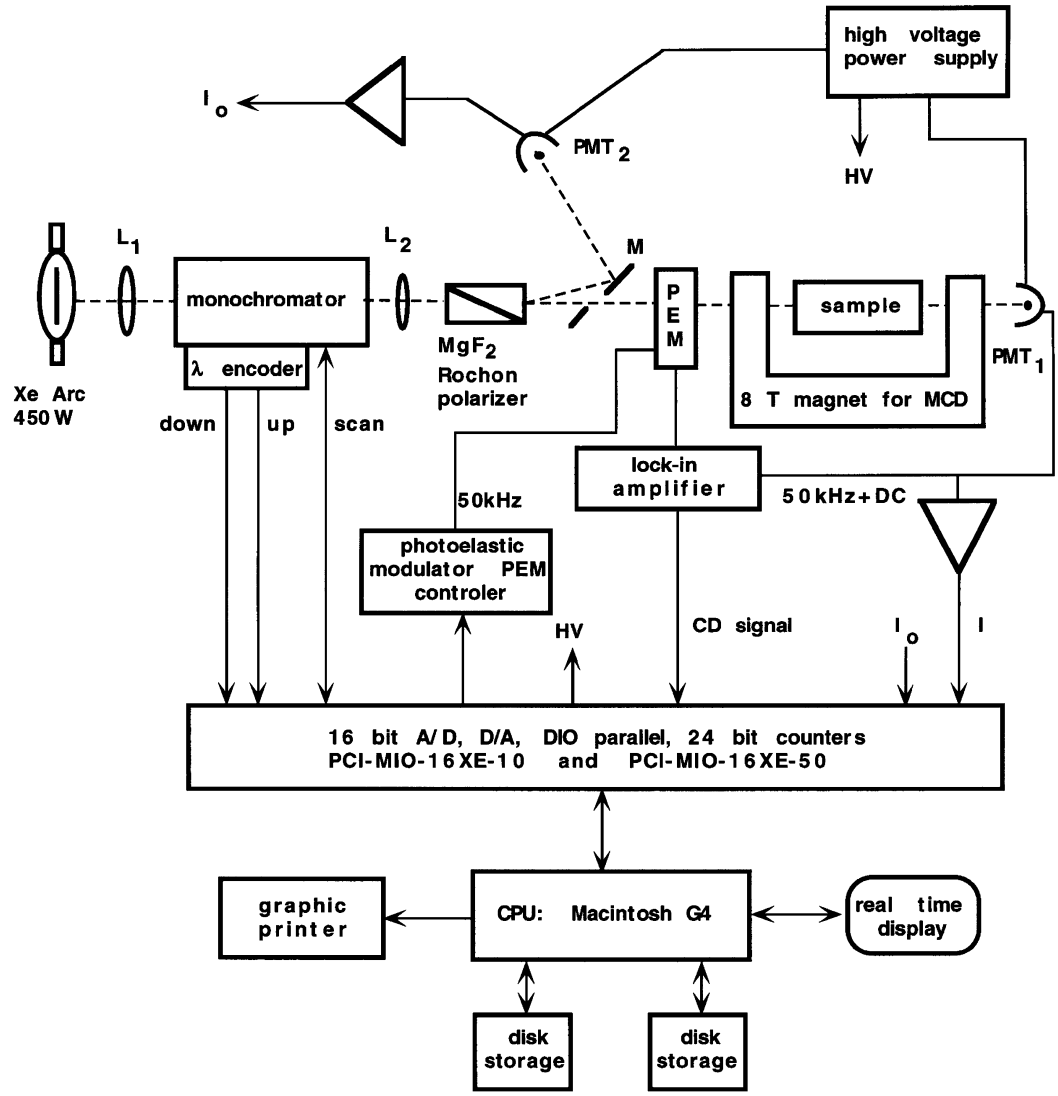

Figure 2 Block diagram of an MCD spectrometer similar to the one constructed in the author's laboratory (see reference 8 for a detailed description).

sample (see Mason[8] for the details of signal measurement, sensitivity, and calibration). Molar absorptivities are given by $\varepsilon = A/cl$, where c is the sample molar concentration and l is the path length in cm through the sample; and differential absorptivities are given by $\Delta\varepsilon = \Delta A/cl$. For MCD work $\Delta\varepsilon$ is often normalized by the field strength H in tesla: $\Delta\varepsilon_M = \Delta A/clH$. If a sample is optically active (such as for a protein or other biomolecule or for a chiral complex), then the CD spectrum determined with the field off is subtracted from the MCD + CD spectrum with the field on (the CD and MCD signals are additive). It is always sound practice to determine a solvent (or other supporting matrix) blank and subtract it from the sample spectrum in order to remove features due to the solvent alone.

Magnet systems for MCD measurements can be as simple as strong permanent magnets (fields up to ca. 1 T), or they can involve electromagnets (fields up to 1.5–2.0 T). The best magnets are superconducting systems (fields up to 10 T), which can be engineered with variable temperature sample holders where the sample temperature can be controlled from below 2.2 K to over 300 K. For low temperature work, care must be used to ensure that the sample matrix does not produce spurious signals due to strain birefringence from contraction upon cooling. Solid samples present problems if they are not isotropic. Birefringence (anisotropic index of refraction) in the sample can give signals that are sometimes considerably larger than the MCD signals, and thus obliterate the desired measurement.

2.25.3 THEORETICAL UNDERPINNINGS OF MCD

The theory of MCD was developed largely by Stephens and is formulated in terms of three parameters, which are known as A, B, and C terms.[7] The observed MCD spectra are given by Equation (1), where E is the energy; γ contains a collection of constants; μ_B is the

$$\frac{\Delta A}{E} = \gamma \mu_B H \left[A_1 \left(\frac{-\partial f(E)}{\partial E} \right) + \left(B_0 + \frac{C_0}{kT} \right) f(E) \right] \tag{1}$$

Bohr magneton; $f(E)$ is a spectroscopic line shape function (often approximated as a Gaussian); A_1, B_0, and C_0 are the A, B, and C term parameters (the subscripts indicate their relation to the spectral moment of order n, see below); k is Boltzmann's constant; and T is kelvin temperature. The dipole strength for the absorption band is given by Equation (2), where the parameter D_0 is proportional to the intensity. Equation (1) shows that A terms

$$\frac{A}{E} = \gamma D_0 f(E) \tag{2}$$

have a derivative line shape with a zero value at the absorption maximum, while B and C terms have an absorption line shape with a minimum or maximum at the absorption maximum. However, all three terms may be either positive or negative by virtue of the sign of the term parameters. Figure 3 shows the shapes of the MCD terms and their relation to the absorption band.

The interpretation of the MCD terms by means of electronic and magnetic properties of the electronic states of a molecule was formulated in terms of the Rigid Shift Model which assumes in a Born-Oppenheimer approximation that the band shape in the presence of the field is unchanged compared to the shape in the absence of the field, just shifted in energy as a result of the Zeeman interaction. The definitions of the A_1, B_0, and C_0 MCD parameters and D_0 are given in Equations (3–6), where the operators $\mu_z = -\mu_B(L_z + 2S_z)$ and $m_x = e\mathbf{x}$ or $m_y = e\mathbf{y}$, are the magnetic and electric moments, respectively,

$$A_1 = \frac{-2i}{\mu_B d_A} \sum (\langle J|\mu_z|J\rangle - \langle A|\mu_z|A\rangle)\langle A|m_x|J\rangle\langle J|m_y|A\rangle \tag{3}$$

$$\begin{aligned} B_0 = \mathrm{Im}\Bigg\{ \frac{-2}{\mu_B d_A} \sum \Bigg[\sum_{K \neq J} \frac{\langle J|\mu_z|K\rangle}{\Delta E_{KJ}} \left(\langle A|m_x|J\rangle\langle K|m_y|A\rangle - \langle A|m_y|J\rangle\langle K|m_x|A\rangle \right) \\ + \sum_{K \neq A} \frac{\langle K|\mu_z|A\rangle}{\Delta E_{KA}} \left(\langle A|m_x|J\rangle\langle J|m_y|K\rangle - \langle A|m_y|J\rangle\langle J|m_x|K\rangle \right) \Bigg] \Bigg\} \end{aligned} \tag{4}$$

$$C_0 = \frac{2i}{\mu_B d_A} \sum \langle A|\mu_z|A\rangle\langle A|m_x|J\rangle\langle J|m_y|A\rangle \tag{5}$$

$$D_0 = \frac{1}{2d_A} \sum (|\langle A|m_x|J\rangle|^2 + |\langle A|m_y|J\rangle|^2) \tag{6}$$

the state A is the ground state and states J and K are excited states, and d_A is the degeneracy of A. The A term depends upon magnetic moments of the ground and excited states, while the temperature-dependent C term is proportional to the ground state magnetic moment. The presence of C terms requires unpaired electrons and therefore ground state degeneracy. The origin of B terms is from a Zeeman interaction between a state J and all other states K, and the state A with all other states K, but the interactions are weighted by the inverse energy difference ΔE_{KJ} or ΔE_{KA} between the states K and J or K and A, respectively. They will be most important for close lying states. The MCD effects from the two states J and K, if the contribution from all others is small, will always be such that they will be of opposite sign, as shown in Figure 3. Furthermore,

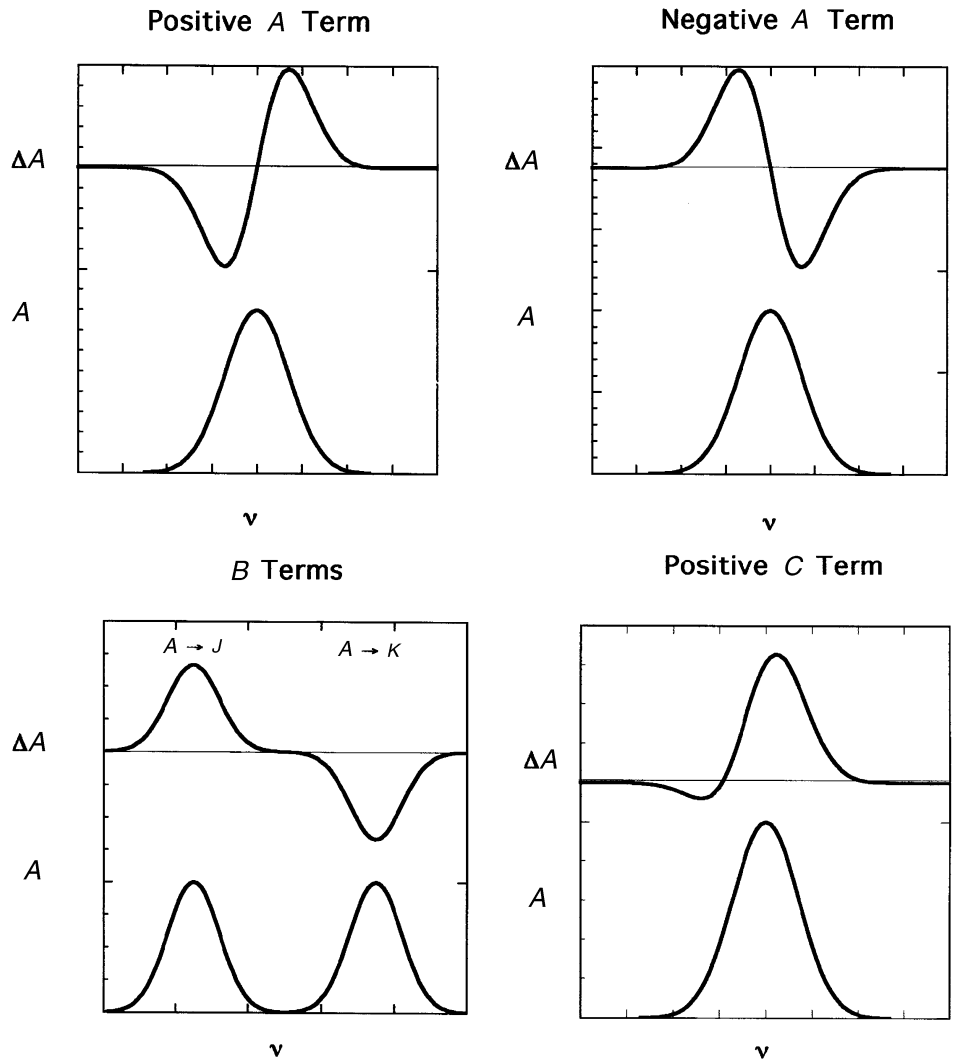

Figure 3 Graphical representation of a positive and a negative A term, two B terms resulting from magnetic interaction between two states J and K, and a positive C term.

if the two states J and K lie very close (within their bandwidths) they may give the appearance of an A term, and this case is referred to as a "pseudo A term." In the limit that J and K are in fact degenerate, then a true A term will be observed. The observed MCD features are the sum of contributions from the A, B, and C terms as shown in Equation (1), with relative intensities of approximately $1/\Gamma$, $1/\Delta E$, and $1/kT$, respectively, where Γ is the full-width-at-half-height of the transition. Thus at room temperature where $kT \cong 200\,\mathrm{cm}^{-1}$, and with $\Delta E = 10^4\,\mathrm{cm}^{-1}$ and $\Gamma = 10^3\,\mathrm{cm}^{-1}$, the relative intensities are approximately 10:1:50 for A, B, and C terms, respectively. For a narrow band ($\Gamma = 100\,\mathrm{cm}^{-1}$) at low temperature (10 K, $kT = 7\,\mathrm{cm}^{-1}$), the ratios become 100:1:1,000. Low temperature measurements are thus highly desirable, especially for systems that exhibit C terms.

In favorable cases, the A_1, B_0, and C_0 parameters can be obtained from experimental spectra by the method of spectral moments. Spectral moments are defined by integrations given in Equation (7), where $\alpha(E)$ is either the absorption $A(E)$ or the MCD

$$\langle \alpha \rangle_n = \int \alpha(E)(E - E^0)^n \mathrm{d}E \tag{7}$$

$\Delta A(E)$ band, and E^0 is the energy about which the moments of the band are taken (typically the absorption band maximum). The MCD parameters are then given by $\langle \Delta A \rangle_0 = 152.5$

$Hcl(B_0 + C_0/kT)$ and $\langle \Delta A \rangle_1 = 152.5\ HclA_1$. Often ratios of the MCD parameters, A_1/D_0, B_0/D_0, and C_0/D_0, are normalized to the absorption band strength (D_0) when comparing bands of different intensity; D_0 is given by zeroth moment of the absorption band $\langle A \rangle_0 = 326.6\ clD_0$.

2.25.4 USE OF MCD SPECTROSCOPY

An electronic structural model for a molecular system provides the basis for possible transition assignments which lead logically to a prediction of the A or C term signs, and depending on the approximations employed, estimates of the term magnitudes. The sign and approximate magnitude must agree with experiment for an interpretation to be considered satisfactory. For example, the observation of C terms is consistent only with electronic degeneracy in the ground state. The C_0/D_0 parameter ratio is then proportional to the ground state magnetic moment (g value), which in principle can be obtained independently (EPR or magnetic susceptibility). The observation of an A term confirms excited state degeneracy if the ground state is nondegenerate, and the A_1/D_0 parameter ratio is proportional to the excited state magnetic moment (excited state g value). Therefore, comparisons between the predicted moments for electronic states and those obtained from MCD spectroscopy can lead to important clues concerning wave function composition, and in cases where heavy atoms are present, the role of spin and orbital contributions to the magnetic moments. MCD B terms are somewhat more difficult to interpret because their sign and magnitude are dependent upon the relative energies of the most strongly interacting states in the presence of the field. Electronic structural models should be able to predict the distribution of states and, therefore, (in principle) the B term spectral pattern, which can be compared to experiment. Thus MCD spectra are a powerful compliment to electronic absorption spectra for the purpose of probing electronic structure.

2.25.5 MCD LITERATURE AND SOME EXAMPLES

2.25.5.1 MCD Literature

There are two older reviews that summarize the development of MCD spectroscopy and give examples of the early applications before the mid-1970 s.[1,2] Several less comprehensive reviews have appeared more recently and should be consulted for newer applications and examples.[3–6] By far the most important monograph which deals with the theoretical and symmetry aspects of MCD spectroscopy is the work by Piepho and Schatz.[7] This monograph contains an extensive treatment of high symmetry coefficients and the application of the Wigner-Eckart theorem to MCD theory. The text also contains a number of detailed examples. Recent applications of MCD spectroscopy have ranged from investigations of metalloenzymes and metalloproteins in bioinorganic chemistry to interpreting complicated 4*f* metal localized transitions in a variety of lanthanide compounds. For example, Oganesyan and Thomson,[9,10] Neese and Solomon,[11] and Pavel and Solomon[5] have developed models which demonstrate the use of temperature dependent C terms and field saturation studies to probe the spin states in various biomolecular systems. Mack and Stillman[12–17] have investigated a number of metal phthalocyanine and metal porphyrin systems and analyzed the absorption and MCD spectra simultaneously by means of a curve fitting algorithm. There have been various studies of lanthanide compounds,[18–23] but among the more interesting ones has been the interpretation of spectra for lutetium bisphthalocyanine, $Lu(Pc)_2$, a sandwich complex which exhibits intervalence transitions.[24,25] MCD spectroscopy has even been employed recently to study the plasmon resonance in colloidal gold nanoparticles.[26]

Several examples described below from the author's work[27–34] are illustrative, but by no means comprehensive. However, they were chosen to convey the flavor of using MCD spectroscopy in order to study electronic transitions and structure in several areas of coordination chemistry ranging from simple complexes to cluster complexes of heavy metals.

2.25.5.2 Atomic Mercury Vapor

Although atomic Hg vapor[27] is not a coordination compound, the MCD of Hg vapor illustrates the relationship between the atomic Zeeman effect and MCD spectral measurement. Figure 4

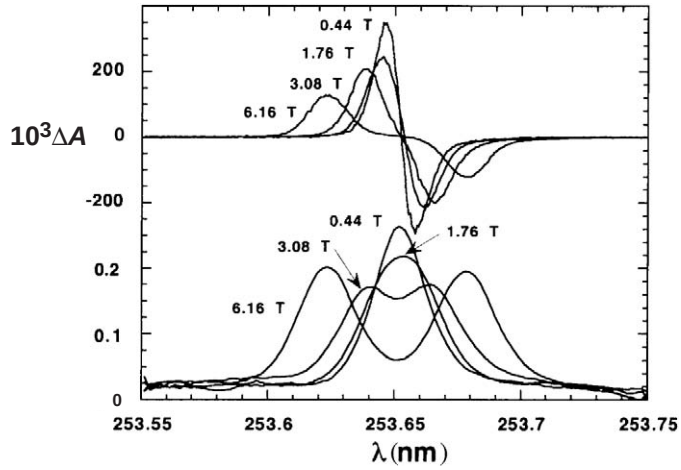

Figure 4 Electronic absorption (lower curves) and MCD (upper curves) spectra for Hg vapor at different magnetic field strength.[28]

shows the MCD and absorption spectra for Hg vapor in the region of the $^1S_0(6s^2) \rightarrow {}^3P_1(6s6p)$ atomic transition (253.65 nm) at different field strength. The strong spin-orbit coupling of the Hg atom provides significant singlet-triplet intermixing with the $^1S_0 \rightarrow {}^1P_0$ transition, which is located to higher energy (184.957 nm) thereby giving the band at 253.65 nm substantial intensity. At 0.44 T the MCD spectrum exhibits a very strong positive A term, while the absorption band broadens slightly. The band in the vapor state is very narrow being an atomic transition, so that at higher magnetic fields the absorption band is split into two resolved Zeeman components. At 6.2 T the excited atomic states are no longer degenerate. The absorption reveals two separate Zeeman transitions and the A term in the MCD now becomes two separate B terms of opposite sign. This example illustrates clearly the relationship between a degenerate state A term at low field and the pair of nondegenerate state B terms when the degeneracy is lifted by the stronger field.

2.25.5.3 $BiBr_6^{3-}$ Ion

Figure 5 presents the absorption and MCD spectra for the octahedral $BiBr_6^{3-}$ ion in acetonitrile solution.[28] The MCD spectrum shows two A terms for intense presumably dipole allowed bands. The lower energy positive A term is centered at 2.60 μm^{-1} (1 $\mu m^{-1} = 10^4\,cm^{-1}$), while the higher

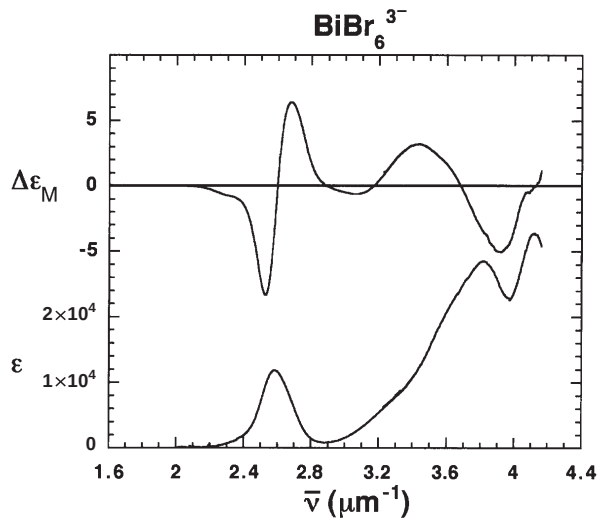

Figure 5 Electronic absorption (lower curve) and MCD (upper curve) spectra for $[Bu^n{}_4N][BiBr_4]$ in acetonitrile containing a 50-fold excess of $Bu^n{}_4NBr$ which produces the $BiBr_6^{3-}$ ion in solution.[28]

energy broad negative A term is at 3.7 μm^{-1}. The former band is assigned as the Bi^{3+} metal-centered $^1S_0(6s^2) \rightarrow {}^3P_1(6s6p)$ transition analogous to that for Hg vapor, while the latter is assigned to a ligand-to-metal charge transfer (LMCT) transition from occupied Br^- $4p$ orbitals to the LUMO $6p$ Bi^{3+} orbitals. The absorption and the MCD terms for these solution spectra are clearly much broader than for the Hg vapor case and are in keeping with the general characteristics of solution bandwidths (typically $10^3\ cm^{-1}$). The negative A term for the $BiBr_6^{3-}$ ion allows a choice between two LMCT transitions to allowed $T_{1u}(^1T_{1u})$ excited states, one each from the $t_{2g}{}^5t_{1u}$ and $t_{1g}{}^5t_{1u}$ excited configurations, respectively. The assignment is to the LMCT transition $^1A_{1g} \rightarrow T_{1u}(^1T_{1u},\ t_{2g}\ Br^- \rightarrow t_{1u}\ Bi^{3+})$, which predicts a negative A term. The alternative assignment to the LMCT transition $^1A_{1g} \rightarrow T_{1u}(^1T_{1u},\ t_{1g}\ Br^- \rightarrow t_{1u}\ Bi^{3+})$ can be ruled out because it predicts a positive A term, which is inconsistent with the observed spectrum.

2.25.5.4 M(Et-Xan)$_2$ (M = Ni^{II}, Pd^{II}, and Pt^{II}; Et-Xan = $C_2H_5OCS_2^-$)

The ethyl xanthato ligand forms bis chelate square complexes with Ni^{II}, Pd^{II}, and Pt^{II}. [29] These complexes are characterized by intense UV–vis spectra which contain a number of bands. The absorption and MCD spectra in acetonitrile solution are shown in Figure 6. Because the symmetry is low (approximately D_{2h}) the MCD features are all B terms. As can be seen from the figure the MCD spectra presents more individual features than the absorption spectra and, therefore, contains potentially more information. The assignment of these spectra was made in terms of LMCT transitions involving the S donor lone pairs to the empty dσ^* ($d_{x^2-y^2}$) orbital. At high energy, transitions that are believed to have metal-centered $5d \rightarrow 6p$ character were identified for the Pt^{II} and Ni^{II} complex, with a possibility for the Pd^{II} complex as well. The MCD for allowed metal localized transitions are often more intense than LMCT or ligand-localized transitions.

2.25.5.5 Pt(P(Bu^t)$_3$)$_2$

The $Pt(P(Bu^t)_3)_2$ complex[30,31] is a linear two-coordinate Pt^0 complex with a $5d^{10}$ metal electron configuration. This complex exhibits a rich spectrum in the 2.4–5.0 μm^{-1} region. Figure 7 shows the absorption and MCD in 2-methylpentane solution at 295 and 80 K (glass). There are three clear positive A terms which are ascribed to metal-to-ligand charge transfer (MLCT) transitions to Π_u states, which possess some $5d \rightarrow 6p$ metal-centered character. The MLCT character is supported by a large blue shift in the spectra for the isoelectronic and isostructural $Au(P(Bu^t)_3)_2^+$ complex ion. A careful consideration of the strong spin-orbit coupling for Pt^0 and Au^I shows that the excited MLCT/$d \rightarrow p$ states are spread over 1.0–1.5 μm^{-1}. The detailed assignment of the spectra lead to the conclusion that the predominantly $5d$ MOs of the complex are very close in energy with ordering $2\sigma_g{}^+(d_{z^2}) \sim \delta_g(d_{x^2-y^2},d_{xy}) > \pi_g(d_{xz},\ d_{yz})$. One of these, $\delta_g(d_{x^2-y^2},\ d_{xy})$, is non-bonding by symmetry, so that the $5d$ orbitals must have minimal involvement in metal–ligand bonding, even though they are very active spectroscopically.

2.25.5.6 Pt(AuPPh$_3$)$_8^{2+}$ and Au(AuPPh$_3$)$_8^{3+}$ Cluster Complexes

The measurement of MCD spectra as a companion to absorption spectra can often reveal more spectral features because of the bisignate nature of the MCD. This is illustrated nicely by the spectra obtained for the $Pt(AuPPh_3)_8^{2+}$ and $Au(AuPPh_3)_8^{3+}$ cluster complexes embedded in thin poly(methyl methacrylate) plastic films shown in Figure 8.[32–34] These complexes have metal-centered crown (D_{4d}) and centered icosahedral fragment (D_{2h}) structures, respectively. The absorption spectra show a number of features, but the MCD spectra reveal an even greater complexity. The transitions are assigned to intraframework metal–metal transitions among MOs constructed from the peripheral Au $6s$ valence orbitals. The low-energy portion of the MCD for the $Pt(AuPPh_3)_8^{2+}$ complex is more intense and differs significantly from that of the $Au(Au(PPh_3)_8^{3+}$ complex and is attributed to additional transitions from the occupied $5d$ orbitals on the center Pt to the gold-based framework LUMOs.

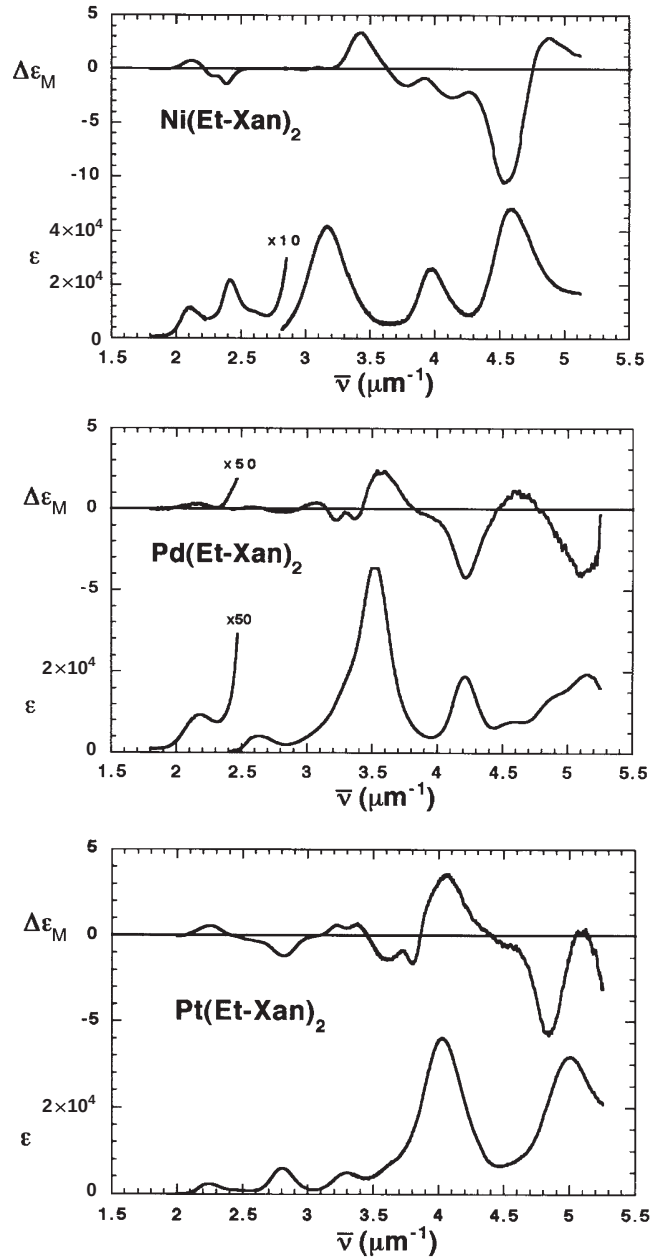

Figure 6 Electronic absorption (lower curves) and MCD (upper curves) spectra for $M(Et\text{-}Xan)_2$ in acetonitrile solution. $M = Ni^{II}$, top; $M = Pd^{II}$, center; $M = Pt^{II}$, bottom.[29]

2.25.6 SUMMARY

In general high-quality, sensitive MCD spectroscopy will be useful whenever a measurable absorption spectrum is obtained. However, unlike absorption spectroscopy where intensity is proportional to the transition dipole strength, the intensity of the MCD signals is proportional to *both* the transition dipole and the magnetic moment(s) of the state(s) involved in the transition. The magnetic moment operator (see Equations (3–5)) belongs to the rotational symmetry irrep R_z and depends upon the total orbital (L_z) and spin (S_z) angular momentum components of the electronic states. Therefore, signals will be relatively weak for dipole forbidden transitions and those that involve relatively low magnetic moments such as singlet to singlet (zero spin moment, $S_z = 0$) $\sigma \rightarrow \sigma^*$ transitions from states composed primarily of atomic *ns* orbitals (zero orbital moment, $L_z = 0$). Fortunately these types of transitions are not common. Alternatively, very strong MCD signals are found for the weak spin-forbidden $f \rightarrow f$ transitions observed for lanthanide ions, where spin and orbital magnetic

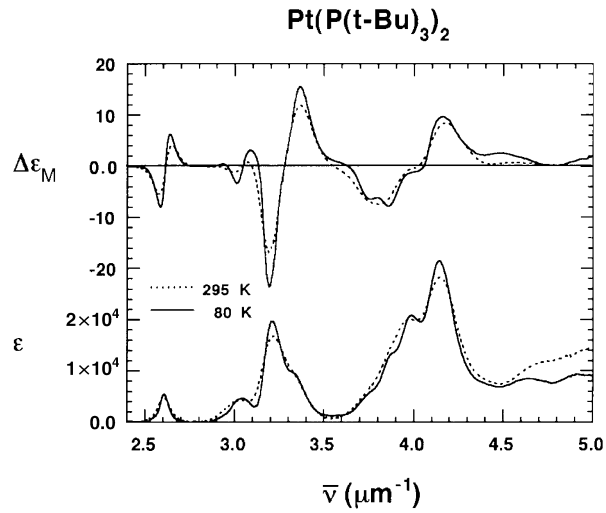

Figure 7 Electronic absorption (lower curves) and MCD (upper curves) spectra for $Pt(P(Bu^t)_3)_2$ in 2-methylpentane solution at 295 and 80 K.[30,31]

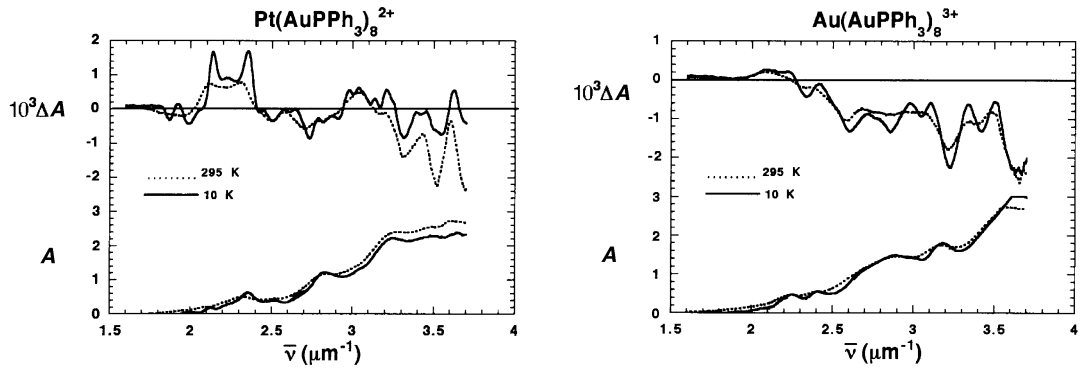

Figure 8 Electronic absorption (lower curves) and MCD (upper curves) spectra for $Pt(AuPPh_3)_8(NO_3)_2$ (left) and $Au(AuPPh_3)_8(NO_3)_3$ (right) in poly(methyl methacrylate) thin films at 295 and 10 K.[32–34]

moments can be quite high. Also in cases involving paramagnetic ground states, low temperature measurements can sometimes provide very strong MCD signals (*C* terms). Further, the bisignate nature of the MCD spectra offers a very useful probe of underlying weak transitions in a region of very intense absorption. Like absorption spectroscopy, MCD spectra can be rather complicated when close lying bands overlap. If the MCD signal changes sign, then clues can be obtained concerning the overlapping bands and close lying transitions, but if there are no sign changes, then the resolution problem is similar to that faced with absorption spectroscopy. Only by cooling the sample can one hope to experimentally resolve overlapping broadbands. In practice, MCD signals tend to be better resolved even at room temperature than do absorption signals (e.g., see Figures 7 and 8).

2.25.7 REFERENCES

1. Schatz, P. N.; McCaffery, A. J. *Quart. Rev.* **1969**, *23*, 552–584.
2. Stephens, P. J. *Adv. Chem. Phys.* **1976**, *35*, 197–264.
3. Ball, D. W. *Spectroscopy* **1991**, *1*, 18–24.
4. Hollebone, B. R. *Spectrochim. Acta Rev.* **1993**, *15*, 493–526.
5. Pavel, E. G.; Solomon, E. I. *Am. Chem. Soc. Symp. Ser.* **1998**, *692*, 119–135.
6. Andersson, L. A. *Encyclopedia of Spectroscopy and Spectrometry*; Lindon, J. C., Eds.; Academic Press: San Diego, 2000, pp 1217–1224.
7. Piepho, S. B.; Schatz, P. N. *Group Theory in Spectroscopy with Applications to Magnetic Circular Dichroism*; Wiley Interscience: New York, 1983.

8. Mason, W. R. *Anal. Chem.* **1982**, *54*, 646–648.
9. Oganesyan, V. S.; Thomson, A. J. *J. Chem. Phys* **2000**, *113*, 5003–5017.
10. Oganesyan, V. S.; George, S. J.; Cheesman, M. R.; Thomson, A. J. *J. Chem. Phys.* **1999**, *110*, 762–777.
11. Neese, F.; Solomon, E. I. *Inorg. Chem.* **1999**, *38*, 1847–1865.
12. Mack, J.; Stillman, M. J. *Inorg. Chem.* **2001**, *40*, 812–814, and references therein.
13. Mack, J.; Stillman, M. J. *Inorg. Chem.* **1997**, *36*, 413–425.
14. Ough, E. A.; Stillman, M. J. *Inorg. Chem.* **1995**, *34*, 4317–4325.
15. Mack, J.; Stillman, M. J. *J. Chem. Phys.* **1995**, *99*, 7935–7945.
16. Mack, J.; Stillman, M. J. *J. Am. Chem. Soc.* **1994**, *116*, 1292–1304.
17. Ough, E. A.; Stillman, M. J. *Inorg. Chem.* **1994**, *33*, 573–583.
18. Fluyt, L.; Heyde, K.; Gorller-Walrand, C. *Mater. Sci. Forum* **1999**, *315–317*, (Rare Earths '98), 424–430.
19. Heyde, K.; Binnemans, K.; Gorller-Walrand, C. *J. Chem. Soc., Faraday Trans.* **1998**, *94*, 843–849.
20. Gorller-Walrand, C.; Binnemans, K. *Bull. Soc. Chim. Belg.* **1997**, *106*, 685–689.
21. Binnemans, K.; Gorller-Walrand, C. *J. Alloys Compd.* **1997**, *250*, 326–331.
22. Fluyt, L.; Hens, E.; DeLeebeeck, H.; Gorller-Walrand, C. *J. Alloys Compd.* **1997**, *250*, 316–320.
23. Gorller-Walrand, C.; Verhoeven, P.; D'Olieslager, J.; Fluyt, L.; Binnemans, K. *J. Chem. Phys.* **1994**, *100*, 815–823.
24. Dunford, C. L.; Williamson, B. E.; Krausz, E. *J. Phys. Chem. A* **2000**, *104*, 3537–3543.
25. VanCott, T. C.; Gasyna, Z.; Schatz, P. N. *J. Phys. Chem.* **1995**, *99*, 4820–4830.
26. Zaitoun, M. A.; Mason, W. R.; Lin, C. T. *J. Phys. Chem. B* **2001**, *105*, 6780–6784.
27. Mason, W. R. *Inorg. Chem.* **1988**, *27*, 437–440.
28. Mason, W. R. *Inorg. Chem.* **1999**, *38*, 2742–2745.
29. Isci, H.; Dag, O.; Mason, W. R. *Inorg. Chem.* **1993**, *32*, 3909–3914.
30. Mason, W. R. *Inorg. Chem.* **2001**, *40*, 6316–6319.
31. Jaw, H.-R.; Mason, W. R. *Inorg. Chem.* **1989**, *28*, 4370–4373.
32. Mason, W. R. *Inorg. Chem.* **2000**, *39*, 370–374.
33. Adrowski, M. J.; Mason, W. R. *Inorg. Chem.* **1997**, *36*, 1443–1453.
34. Jaw, H.-R.; Mason, W. R. *Inorg. Chem.* **1991**, *30*, 275–278.

Comprehensive Coordination Chemistry II
ISBN (set): 0-08-0437486

Volume 2, (ISBN 0-08-0443249); pp 327–337

2.26 Magnetic Circular Dichroism of Paramagnetic Species

E. I. SOLOMON, M. L. NEIDIG, and G. SCHENK
Stanford University, Stanford, CA, USA

2.26.1 INTRODUCTION 339
2.26.2 BASIC PRINCIPLES AND APPLICATIONS OF MCD AND VTVH MCD 339
2.26.2.1 MCD 339
2.26.2.1.1 A-, B-, and C-terms 340
2.26.2.1.2 C-terms and paramagnetic systems 340
2.26.2.2 VTVH MCD 342
2.26.2.2.1 Kramers ions 344
2.26.2.2.2 Non-Kramers ions 346
2.26.3 REFERENCES 349

2.26.1 INTRODUCTION

Magnetic circular dichroism (MCD) spectroscopy and variable-temperature variable-field (VTVH) MCD are powerful methods for studying the excited and ground states of paramagnetic systems. Notably, these methods provide detailed insight into the geometric and electronic structures of catalytically active centers in inorganic and biological systems. In this review, we present the theoretical background for MCD and VTVH MCD and discuss their application.

2.26.2 BASIC PRINCIPLES AND APPLICATIONS OF MCD AND VTVH MCD

2.26.2.1 MCD

MCD spectroscopy combines the CD experiment with a longitudinal magnetic field, where the application of the magnetic field induces optical activity in any material so that all substances exhibit MCD activity. MCD probes the Zeeman splittings in the ground and excited states and the field-induced mixing between states.

MCD intensity for a transition from a ground state $|A\rangle$ to an excited state $|J\rangle$ is given by Equation (1):

$$\frac{\Delta A}{E} = \left(\frac{2N_0\pi^3\alpha^2 Cllge}{250\,hcn}\right)\beta H\left[\boldsymbol{A}_1\left(\frac{-\delta f(E)}{\delta E}\right) + \left(\boldsymbol{B}_0 + \frac{\boldsymbol{C}_0}{kT}\right)f(E)\right] \quad (1)$$

for broadband transitions when the MCD intensity is linear with field. Here, ΔA is the field-dependent difference between left- and right-circularly polarized light (lcp and rcp, respectively) absorption, $E = h\nu$, α is the electric permeability, $\boldsymbol{C}$ is the concentration, l is the path length, n is

the index of refraction, β is the Bohr magneton, H is the applied magnetic field, $f(E)$ is the absorption bandshape and $\delta f(E)/\delta(E)$ is its first derivative.[1–5] $\boldsymbol{A}_1$, $\boldsymbol{B}_0$, and $\boldsymbol{C}_0$ are the MCD ***A***-, ***B***-, and ***C***-terms, respectively. Note from Equation (1) that MCD intensity increases linearly with increasing magnetic field, while only C-term intensity is inversely proportional to temperature in the linear limit where $kT \gg g\beta H$.

2.26.2.1.1 A-, B-, and C-terms

$\boldsymbol{A}_1$ and $\boldsymbol{C}_0$ (see Chapter 2.14 for further details) are related to molecular electronic structure by Equations (2) and (3), where $|J\rangle$ is the excited state of the corresponding MCD transition, $|d_A|$ is the electronic degeneracy of the ground state $|A\rangle$ and the summation is over all components of $|A\rangle$ and $|J\rangle$. The first part of the ***A***-term expression is the difference between the excited and ground-state Zeeman terms, while the first part of the ***C***-term expression gives the Zeeman effect in the ground state. The second parts in both equations give the difference between the lcp (m_+) and rcp (m_-) electric dipole moments:

$$\boldsymbol{A}_1 = \frac{1}{|d_A|}\sum(\langle J|L_z + 2S_z|J\rangle - \langle A|L_z + 2S_z|A\rangle) \times (|\langle A|m_-|J\rangle|^2 - |\langle A|m_+|J\rangle|^2) \tag{2}$$

$$\boldsymbol{C}_0 = \frac{-1}{|d_A|}\sum\langle A|L_z + 2S_z|A\rangle(|\langle A|m_-|J\rangle|^2 - |\langle A|m_+|J\rangle|^2) \tag{3}$$

From the electric dipole term in Equations (2) and (3), the MCD selection rule is $\Delta M_L = \pm 1$, requiring that either the ground or excited state contains orbital angular momentum. Therefore, ***A***- and ***C***-term MCD transitions observed between spin degenerate orbital singlets occur by spin–orbit mixing with other states.

From Equation (2), either a degenerate ground or excited state is required for a system to exhibit ***A***-term intensity, whereas from Equation (3) ***C***-terms require a degenerate ground state. Figure 1 illustrates the ***A***- and ***C***-term mechanisms for a molecule having an angular momentum of $J = 1/2$ in the ground and excited states. In the absence of a magnetic field, the rcp and lcp transitions from the doubly degenerate ground state to the doubly degenerate excited state cancel, resulting in no observed MCD intensity. At high temperatures ($kT \gg g\beta H$) in the presence of a magnetic field (Figure 1a), the degeneracies of the ground and excited states are removed so that the rcp and lcp transitions combine to give an MCD transition with a derivative shape (temperature-independent ***A***-term). At lower temperatures ($kT \sim g\beta H$, Figure 1b), the lowest energy sublevel of the ground state is more populated than the higher energy sublevel, resulting in an intense ***C***-term MCD transition with an absorption bandshape:

$$\boldsymbol{B}_0 = \frac{2}{|d_A|}\mathrm{Re}\sum\left[\begin{array}{l}\displaystyle\sum_{K(K\neq J)}\frac{\langle J|L_z+2S_z|K\rangle}{\Delta E_{KJ}}(\langle A|m_-|J\rangle\langle K|m_+|A\rangle - \langle A|m_+|J\rangle\langle K|m_-|A\rangle) \\ \displaystyle + \sum_{K(K\neq A)}\frac{\langle K|L_z+2S_z|A\rangle}{\Delta E_{KA}}\left(\langle A|m_-|J\rangle\langle J|m_+|K\rangle - \langle A|m_+|J\rangle\langle J|m_-|K\rangle\right)\end{array}\right] \tag{4}$$

The relation between the $\boldsymbol{B}_0$-term and molecular properties is given by Equation (4), and is described in more detail in Chapter 2.14. ***B***-term intensity arises from field-induced mixing between the ground state $|A\rangle$ or excited state $|J\rangle$ and an intermediate state, $|K\rangle$, which is required to be close in energy. The first summation on the right of Equation (4) gives the Zeeman mixing of the intermediate state $|K\rangle$ into the excited state $|J\rangle$, and the second summation gives the Zeeman mixing of $|K\rangle$ into the ground state $|A\rangle$. From Equation (1) ***B***-term signals are temperature independent and have an absorption shape.

2.26.2.1.2 C-terms and paramagnetic systems

Though all three mechanisms (***A***-, ***B***-, and ***C***-term) may contribute to the MCD intensity for a paramagnetic species, the ***C***-term dominates at low temperature (see Equation (1)). As ground

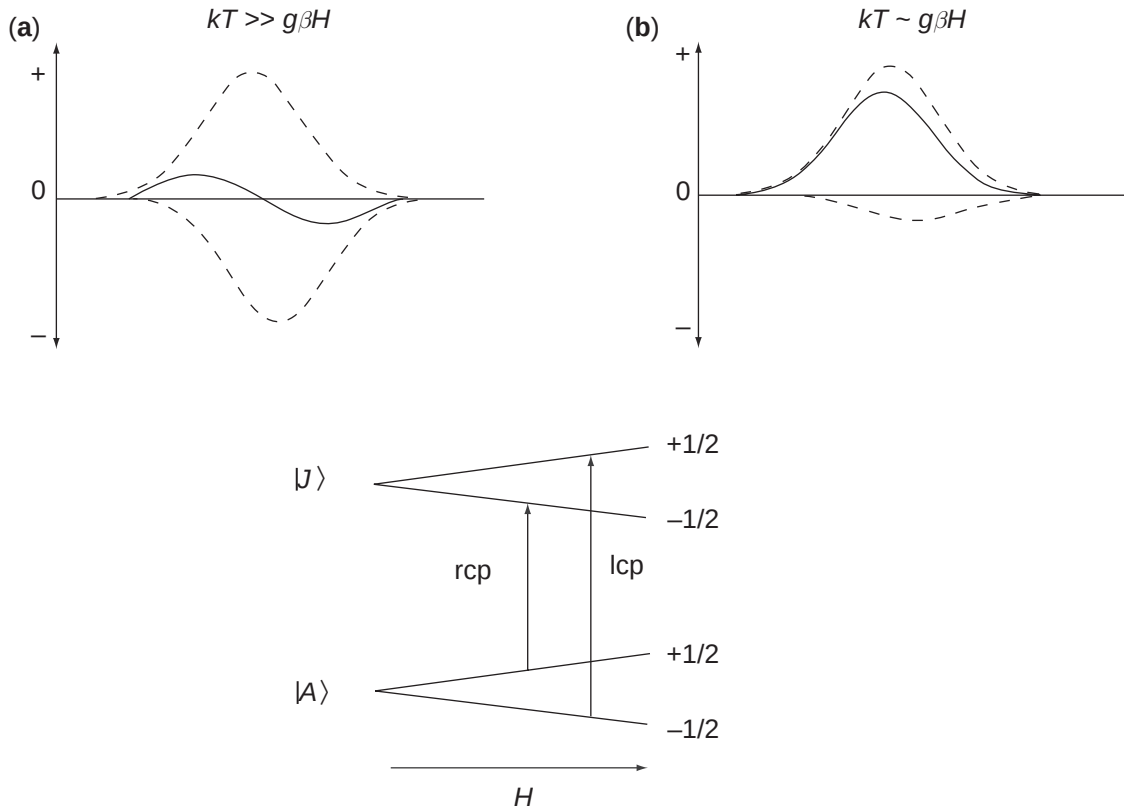

Figure 1 MCD mechanism for a molecule with $J = 1/2$ in the ground and excited states. (a) derivative shaped ***A***-term and its components when $kT \gg g\beta H$ and (b) absorption shaped ***C***-term and its component when $kT \sim g\beta H$. The selection rules for transitions of rcp and lcp light between the degenerate ground and excited states split by a magnetic field is shown at the bottom.

states are generally orbitally nondegenerate, the ground state degeneracy required for ***C***-term intensity usually involves the spin. From the selection rules for the MCD transition ($\Delta M_L = \pm 1$, $\Delta M_S = 0$), a nonzero ***C***-term is only obtainable from spin degeneracy through spin–orbit coupling (SOC). For high-symmetry paramagnetic metal species, orbitally doubly degenerate excited states exist having orbital angular momentum which will spin–orbit couple to the electron spin and produce a splitting of the excited state. A temperature-dependent pseudo-***A***-term will be produced from equal and opposite ***C***-terms, with the energy splitting of the ***C***-terms giving the in-state SOC. Pseudo-***A***-terms quantify the excited state SOC, allow assignment of orbitally degenerate excited states and have a sign, which can provide further insight into the one-electron orbitals involved in the transition.[6]

Most paramagnetic metal sites in biological systems have low symmetry and no orbital degeneracy. Thus, the ground-to-excited-state transition is electric-dipole allowed, but with a unidirectional transition moment in the molecule. From the expression for $\boldsymbol{C}_0$ for a frozen solution averaged over all molecular orientations relative to the external magnetic field in Equation (5), the selection rule for MCD intensity requires two perpendicular nonzero transition moments.[7] This condition is met for low-symmetry species with orbitally nondegenerate states through SOC, whereby two excited states with transition moments in different directions are mixed, resulting in nonzero ***C***-term intensity.[8] The coupling between two excited states will produce equal and opposite ***C***-terms, yielding a pseudo-***A***-term derived from nondegenerate states. More generally, SOC among a complete set of excited states should result in equal and opposite ***C***-term intensity distributed over the states, which will sum to zero. Any net ***C***-term intensity summed over excited states will result from further SOC into the ground state:

$$\boldsymbol{C}_0 \propto g_z M_x M_y + g_y M_x M_z + g_x M_y M_z \tag{5}$$

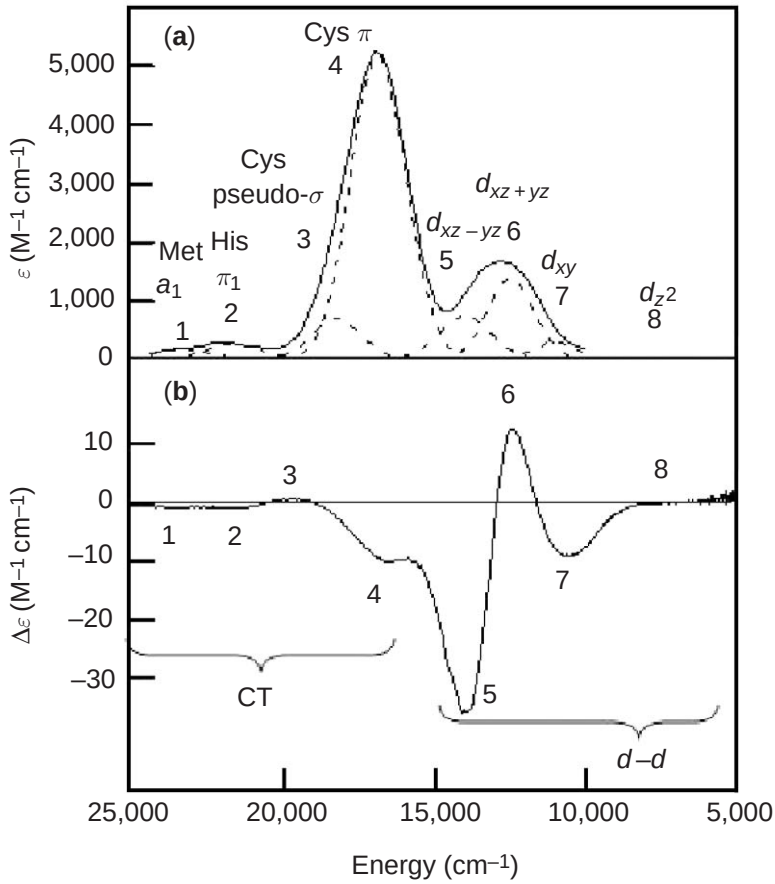

Figure 2 Low-temperature (a) absorption and (b) MCD of the blue copper protein plastocyanin. The use of $\boldsymbol{C}_0/\boldsymbol{D}_0$ led to the assignment of bands 1–4 to CT transitions and bands 5–8 to $d \rightarrow d$ transitions.

Thus, SOC determines the $\boldsymbol{C}$-term intensity, which is dependent on the magnitude of the SOC constant. Since the SOC constant will be greater for metal-centered than ligand-centered transitions, $d \rightarrow d$ excited states are expected to be more spin–orbit mixed than ligand-based charge transfer (CT) states and show larger low-temperature MCD intensity relative to absorption intensity. The MCD-to-absorption intensity ratio is often expressed as $\boldsymbol{C}_0/\boldsymbol{D}_0$, which is given experimentally by Equation (6):

$$\frac{\boldsymbol{C}_0}{\boldsymbol{D}_0} = \frac{kT}{\beta H}\left(\frac{\Delta\varepsilon}{\varepsilon}\right) \tag{6}$$

The application of low-temperature MCD and $\boldsymbol{C}_0/\boldsymbol{D}_0$ analyses to paramagnetic metal sites in biological systems has been a powerful method for identifying and studying $d \rightarrow d$ transitions. In addition, the sign and magnitude of the $\boldsymbol{C}_0/\boldsymbol{D}_0$ value allows the rigorous assignment of bands based upon electronic structure calculations, which include SOC and, thus, probe specific bonding interactions. Figure 2 shows the low-temperature MCD spectrum of the blue copper protein plastocyanin, where this method has been successfully applied to assign bands 5–8 to $d \rightarrow d$ transitions as these transitions are weak in absorption but intense in low-temperature MCD (bands 1–4 are assigned to CT transitions).[9] The assignments of these bands are given by the signs of the $\boldsymbol{C}$-terms and, thus, rigourously determined by the MCD experiment. These $d \rightarrow d$ transitions could then be used to correlate to crystallographically determined geometric structures and generate an electronic structure description of the plastocyanin active site.

2.26.2.2 VTVH MCD

Historically, MCD has mainly been used to probe the excited states of paramagnetic systems. More recently, this methodology has gained significance since it also provides insight into ground state

properties,[10] for example in ferrous systems, which are often inaccessible to EPR spectroscopy.[11] In the previous section the terms contributing to an MCD transition have been discussed. In particular, the ***C***-term contribution is greatly enhanced at low temperatures and high fields (see Equation (1)). In Figure 3 the dependence of the MCD intensity on the magnetic field at a fixed temperature is illustrated for a system with $S = 1/2$. At sufficiently low field the intensity increases linearly; at higher fields the intensity starts to level off and then saturates. The origin of this saturation behavior is developed from the insert in Figure 3a. In the absence of a magnetic field the $M_S = |1/2\rangle$ and $|-1/2\rangle$ sublevels of both states are degenerate and the right and left circularly polarized transitions cancel. Application of a field removes this degeneracy; the sublevels are split by the Zeeman term ($g\beta H$). As the field is increased and the temperature lowered, the $|-1/2\rangle$ sublevel of the ground state is dominantly Boltzmann populated, until, at low temperatures and high fields only this level is significantly populated. In this example only the lcp transition is observed and, thus, the MCD

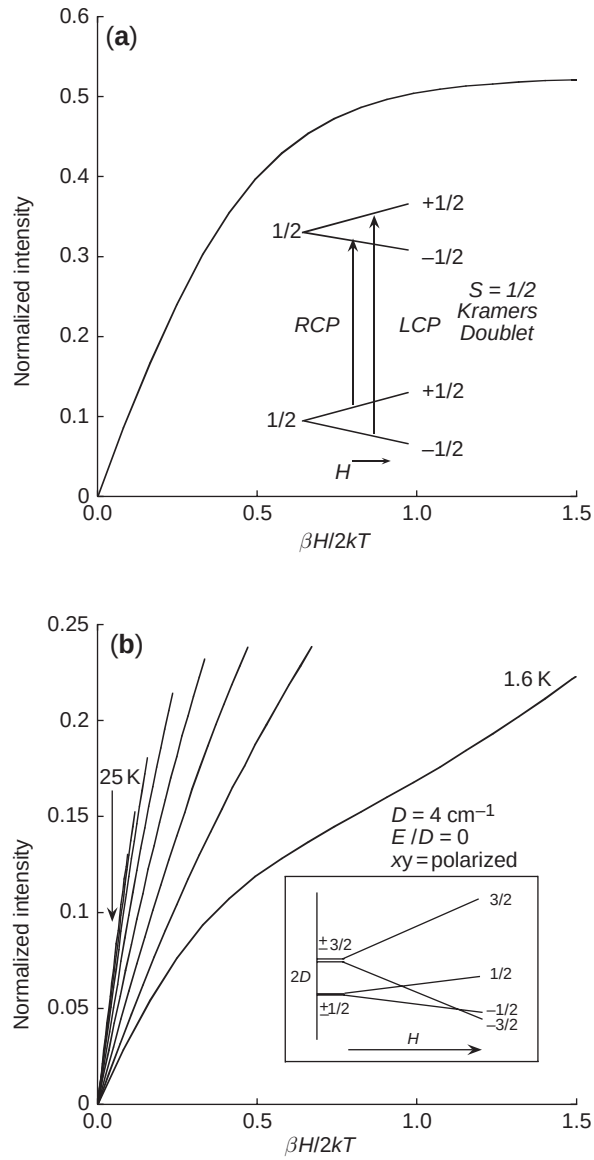

Figure 3 Field dependence of the MCD signal. (a) Saturation magnetization MCD for an $S = 1/2$ Kramers doublet. The inset shows a schematic representation of the transitions for lcp and rcp light from the ground to the excited state. (b) Simulation of the VTVH MCD behavior of an xy polarized transition for an axial $S = 3/2$ system with positive ZFS ($D = 4\,\mathrm{cm}^{-1}$, $E/D = 0$). The inset shows the energy splitting of the M_S sublevels as a function of the magnetic field, aligned along the z-axis.

signal saturates. The dependence of the intensity on the field is described by the Brillouin-type function for an isotropic $S = 1/2$ system:

$$\Delta\varepsilon = \text{const} \tanh\left(\frac{g\beta\mathrm{H}}{2kT}\right) \tag{7}$$

For a system with octahedral or tetrahedral symmetry, saturation data collected at different temperatures superimpose for all spin systems. For low-symmetry sites (e.g., protein-active sites) only isotherms for $S = 1/2$ systems superimpose in general. The spread or nesting behavior observed in VTVH MCD for systems with $S \neq 1/2$ is ascribed to the zero-field splitting (ZFS) of the M_S sublevels of the ground state, and is discussed in the next sections, first for Kramers-type systems (half-integer spin) and then for non-Kramers ions (integer spin), as exemplified by Fe^{II}.

2.26.2.2.1 Kramers ions

The VTVH MCD behavior for systems with $S > 1/2$ is complicated by the fact that the ground state is not a single doublet as in an $S = 1/2$ system. For illustrative purposes the case of an $S = 3/2$ system is discussed. Kramers theorem[12] postulates that for a system with half-integer spin all energy levels must be at least twofold degenerate. Application of a magnetic field removes the remaining degeneracies, as shown in Figure 3b for an $S = 3/2$ with positive ZFS (*vide infra*), removing the fourfold spin degeneracy of the quartet ground state, resulting in two doubly degenerate levels with $M_S = \pm 1/2$ and $M_S = \pm 3/2$ (Figure 3b inset). The energy levels are described by an effective spin Hamiltonian including the Zeeman effect and the ZFS. Assuming the D-tensor and the *g*-matrix to be coaxial, the energy levels are calculated using Equation (8):[13]

$$\mathcal{H}_{\text{spin}} = D[S_z^2 - 5/4] + E[S_x^2 - S_y^2] + \beta(g_x H_x S_x + g_y H_y S_y + g_z H_z S_z) \tag{8}$$

Here, D and E are the axial and rhombic ZFS parameters, respectively. Application of Equation (8) to the spin functions $|S, M_S\rangle$ with $S = 3/2$ results in a fourth order equation, which describes the behavior of the four energy levels in Figure 3b as a function of the magnitude of the external field and its orientation relative to the molecular frame. For an exact solution for the spin Hamiltonian the 4×4 matrix must be diagonalized at every field. For Kramer ions the parameters D and E can generally be determined by EPR spectroscopy.

VTVH MCD data for systems with $S > 1/2$ are in general more difficult to analyze than $S = 1/2$ systems, but additional information may be gained about the paramagnetic site.[11,14] Importantly, from the MCD magnetization curves the polarizations for each transition can be obtained, even for randomly oriented frozen samples.[14–16] Since MCD spectroscopy is orientation selective, only molecules that are suitably aligned in the magnetic field contribute to MCD intensity. For large ZFS, the $S = 3/2$ system can be approximated as a collection of non-interacting doublets. However, if the magnitude of D is similar to the Zeeman term ($g\beta H$), crossing between the spin levels has to be taken into account. A general expression (Equation (9)) for the analysis of VTVH MCD saturation magnetization curves[14] was derived, where the summation is carried out over all levels i of the ground state:

$$\frac{\Delta\varepsilon}{E} = \frac{\text{const}}{4\pi S}\int_0^{\pi}\int_0^{2\pi}\sum_i N_i(l_x\langle S_x\rangle_i M_{yz}^{\text{eff}} + l_y\langle S_y\rangle_i M_{xz}^{\text{eff}} + l_z\langle S_z\rangle_i M_{xy}^{\text{eff}})\sin\theta\,\mathrm{d}\theta\,\mathrm{d}\phi \tag{9}$$

which reduces to

$$\frac{\Delta\varepsilon}{\mathrm{E}} = -\frac{\text{const}}{4\pi}\int_0^{\pi}\int_0^{2\pi}\tanh\left(\frac{\gamma\beta\mathrm{H}}{2k\mathrm{T}}\right)\frac{\sin\theta}{\gamma}(l_x^2 g_x M_{yz}^{\text{eff}} + l_y^2 g_y M_{xz}^{\text{eff}} + l_z^2 g_z M_{xy}^{\text{eff}})\,\mathrm{d}\theta\,\mathrm{d}\phi \tag{10}$$

where $\gamma = \sqrt{G_x^2 + G_y^2 + G_z^2}$ and $G_p = l_p g_p$ with $p = x,y,z$ for a system with $S = 1/2$. E is the photon energy, N_i is the Boltzmann population of the i-th sublevel, $\langle S_p\rangle$ are the spin expectation

values in the p direction ($p = x, y, z$), l_p are the direction cosines describing the orientation of the applied field with respect to the molecular coordinate system, g_p are g-values of the molecule and M_{ij}^{eff} are the products of the relative polarizations of two electronic transitions. The angles between the incident light and the molecular z-axis and the xy plane are described by θ and Φ, respectively. These equations are valid for any system with an orbitally non-degenerate ground state with $S \geq 1/2$; note that for an isotropic system Equation (10) simplifies to a Brillouin-type function shown in Equation (7). In Figure 3b a simulation of the VTVH MCD behavior of an $S = 3/2$ system is shown, with $D = +4\,\text{cm}^{-1}$, $E/D = 0$ and the transition is assumed to be xy polarized. The saturation curves can readily be understood by an inspection of Equation (9). Since the transition is xy polarized only the third term contributes to MCD intensity, which selects the molecules whose z-axes are aligned along the magnetic field (g_z). At lowest temperature and low fields the $M_S = -1/2$ is lowest in energy (Figure 3b). Increasing the field gradually increases the Boltzmann population of this level, until at $\beta H/2kT = \sim 0.4$ the intensity starts to level off. However, no saturation of the signal is observed. This is due to the crossing between the $M_S = -1/2$ and $M_S = -3/2$ levels (Figure 3b). Since the spin expectation value for the latter is larger ($\langle S_z \rangle = 3/2$ compared to 1/2 for the former) the intensity increases. At higher temperatures the inflection point is less apparent since the $M_S = \pm 3/2$ doublet is thermally populated.

In principal, Equation (9) can be applied to obtain ground state parameters (g-values and ZFS parameters D and E) and the products of the relative polarizations. However, for VTVH MCD fitting the most reliable method is to determine the g-values and ZFS parameters from temperature-dependent EPR spectroscopy (Equation (8)) and calculate the effective polarization products with Equation (9) since this procedure reduces the number of variables in the fitting routine. From the M_{ij}^{eff} obtained, the polarizations in the p direction ($p = x, y, z$) can be determined using the following expression:

$$\%x = 100 \times \frac{(M_{xy}^{\text{eff}} M_{xz}^{\text{eff}})^2}{(M_{xy}^{\text{eff}} M_{xz}^{\text{eff}})^2 + (M_{xy}^{\text{eff}} M_{yz}^{\text{eff}})^2 + (M_{xz}^{\text{eff}} M_{yz}^{\text{eff}})^2} \tag{11}$$

where cyclic permutations of the p indices provide the other polarizations. Transitions polarized along different directions show a distinct nesting behavior that enables the determination of the polarization of a band in a spectrum and can be used to assign transitions. Test calculations show that the VTVH MCD behavior is (i) a weak function of E/D, (ii) a strong function of the sign of the ZFS parameter D, (iii) moderately sensitive towards the absolute magnitude of D, and (iv) strongly dependent on both the sign and magnitude of the polarization products M_{ij}^{eff}.

An example of an $S = 3/2$ system is the NO derivative of the mononuclear non-heme iron enzyme protocatechauate 3,4-dioxygenase (PCD), a member of the intradiol dioxygenases.[17] PCD catalyzes the cleavage of protocatechuate (PCA) to β-carboxy-*cis,cis*-muconate, with the incorporation of both atoms from molecular oxygen. Although an oxygen intermediate has been observed by stopped-flow spectroscopy[18] it cannot be trapped in sufficient amounts for spectroscopic analysis. In a recent study, NO was used as an O_2 analog to study the electronic structure of potential reaction intermediates.[19] NO reacts with the ferrous form of PCD to form an antiferromagnetically coupled Fe^{III}–NO^- complex. For the substrate-bound form the ZFS parameters D and E/D were estimated to be $4\,\text{cm}^{-1}$ and 0.175, respectively, using EPR spectroscopy.[20] The MCD spectrum and VTVH MCD saturation curves for five bands are shown in Figure 4; the effective polarization products M_{ij}^{eff} and the relative polarizations as determined with Equation (11) are summarized in Table 1. Often, NO reacts with Fe^{II} to form a short, strong bond with an Fe—N distance of around 1.75 Å (e.g., ref. 21). However, in the case of substrate-bound PCD the intermediate rhombicity observed from EPR indicates the absence of a dominating strong direction within the complex. This is in agreement with XAS pre-edge and EXAFS measurements, which preclude the presence of a single strong direction. VTVH MCD indicates that both bands 1 and 4 in Figure 4, assigned as a substrate to Fe^{III} CT transitions[19], define the dominant (z) direction. The remaining bands 2, 3, and 5 are x-polarized (Table 1), but attributed to the NO^- ligand from previous studies on Fe–NO model complexes.[21] Band 2 contains two weak, formally forbidden $Fe^{III} d \rightarrow d$ transitions, band 3 the two in-plane NO^- $2\pi^*$ to d_{xz} and $d_{x^2-y^2}$ CT transitions, and band 5 the intense out-of-plane NO^- $2\pi^*$ to d_{yz} CT transition. Hence, VTVH MCD provides direct insight into the electronic and geometric structure of the substrate- and NO-bound active site of PCD, revealing that, in contrast to most known high-spin Fe^{III}–NO^- complexes, the substrate and not the NO ligand defines the strongest bond due to the strong donor interaction from this catecholate ligand.

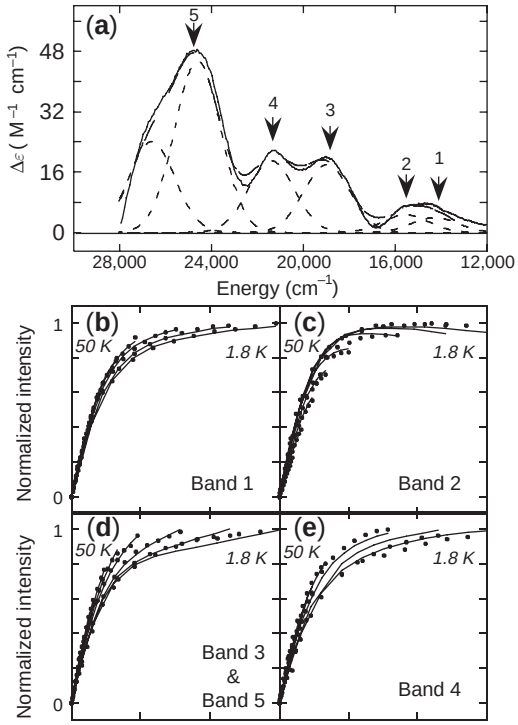

Figure 4 (a) Gaussian resolution (---) of the MCD spectrum of PCA- and NO-bound PCD at 5 K and 7 T. VTVH MCD data at various temperatures (ranging from 1.6 K to 50 K) and magnetic fields (between 0 T and 7 T) were collected at positions indicated by arrows: Band 1 (b) at 14,100 cm^{-1}, Band 2 (c) at 15,500 cm^{-1}, Band 3 (d) at 19,100 cm^{-1}, Band 4 (e) at 21,300 cm^{-1}, and Band 5 (d) at 24,780 cm^{-1}. Note that identical saturation behavior was observed for Bands 3 and 5, indicating that they have the same polarization.

Table 1 Effective transition moments from the VTVH MCD data for substrate- and NO-bound PCD.[19]

Transition	M_{xy}	M_{xz}	M_{yz}	*Polarization*
Band 1	0.22	1.1	0.5	z
Band 2	−1.0	1.7	0.28	x
Band 3 + 5	2.1	1.2	−0.50	x
Band 4	0.11	0.76	1.0	z

This observation is of functional significance since it supports a mechanism where the reduction potential of the iron is sufficiently lowered to favor substrate activation by Fe^{III}.[19]

2.26.2.2.2 Non-Kramers ions

The analysis of VTVH MCD data from non-Kramers-type systems has been reviewed previously [8,11,22,23] and is illustrated in brief for a ferrous system ($S = 2$) with negative ZFS (Figure 5, right panel). The VTVH MCD behavior of $S = 2$ systems with positive ZFS qualitatively resembles negative ZFS systems with a large δ and is thus not further discussed here.[11] Note, however, that the sign of ZFS relates to the geometry of the active site; negative and positive signs correspond to a weak and strong tetragonal distortion, respectively. For an $S = 2$ system with negative ZFS the $M_S = \pm 2$ doublet is lowest in energy (Figure 5). In contrast to Kramers-type systems a rhombic distortion splits this doublet (by an amount characterized by δ (Figure 5)) even in the absence of an external magnetic field. This splitting of the $M_S = \pm 2$ sublevel is the origin of the nesting which is generally observed for the saturation magnetization MCD data for non-Kramers ions as illustrated in Figure 6a. When these data are replotted to separate temperature from field dependence (Figure 6b), it is observed that at low-temperature saturation the MCD intensity

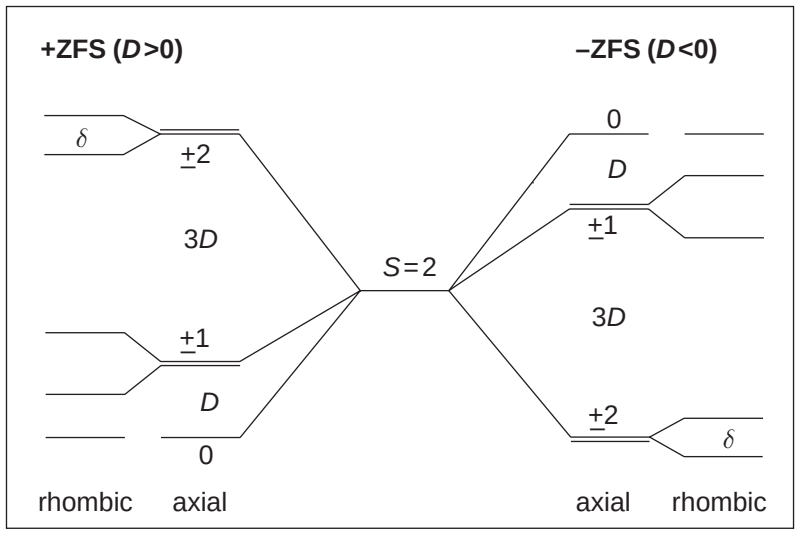

Figure 5 Energy splittings of the $S = 2$ sublevels for + ZFS (left) and –ZFS (right). In contrast to Kramers-type systems, rhombic distortion removes the degeneracy of the $M_S \geq \pm 1$ levels even in the absence of an external magnetic field.

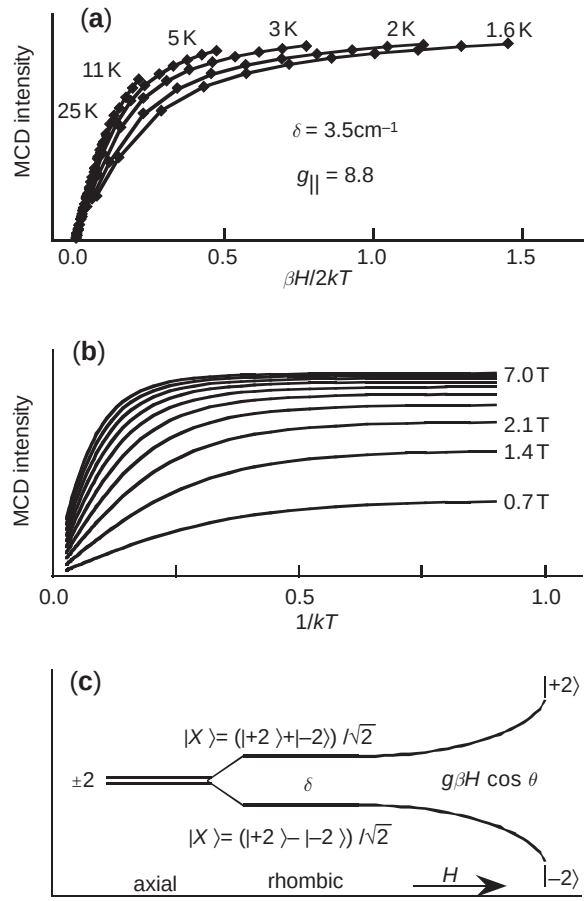

Figure 6 VTVH MCD data for a non-Kramers $S = 2$ system with negative ZFS (a). Replot of the data in Figure 6a to separate the temperature and field dependence. Note the increase in MCD intensity at low temperature saturates with increasing magnetic field (b). Rhombic and magnetic field splitting and mixing of an $M_S = \pm 2$ non-Kramers doublet (c).

increases in a nonlinear fashion, converging at high fields. This indicates that the wave function of the lowest component of the ground state is changing as a function of the magnetic field. This behavior is anticipated for a non-Kramers system, where rhombic distortion leads to a splitting of the $MS = \pm 2$ doublet (Figure 5). In the absence of a magnetic field the distortion leads to a mixing of the wave functions to produce $|X\rangle = (|+2\rangle + |-2\rangle)/\sqrt{2}$ and $|Y\rangle = (|+2\rangle - |-2\rangle)/\sqrt{2}$; equal amounts of $|+2\rangle$ and $|-2\rangle$ are mixed resulting in zero MCD intensity. As the field is increased the $MS = \pm 2$ doublet is further split by the amount $g\beta H\cos\theta$ (Figure 6c) and unequal amounts of $|+2\rangle$ and $|-2\rangle$ are mixed in a nonlinear fashion into the wave functions $|X\rangle$ and $|Y\rangle$ until they approach pure $|+2\rangle$ and $|-2\rangle$ at high magnetic field. It is this field dependence of the ground state wave function which leads to the observed saturation magnetization behavior in Figure 6a. In principal, the expression in Equation (9) can be applied to analyze VTVH MCD data, since this equation does not impose any restrictions on the spin of the system.[14] An expression that includes the non-Kramers behavior decribed above for a system with negative ZFS, and where the wave function is field-dependent, is given in Equation (12) (including orientation averaging)[11]

$$\Delta\varepsilon = \text{const}\left\{\int_0^{\pi/2} \frac{\cos^2\theta\,\sin\theta}{\Gamma} g_{\|}\beta H \tanh\left(\frac{\Gamma}{2kT}\right)\mathrm{d}\theta - \sqrt{2}\left(\frac{M_z}{M_{xy}}\right)\int_0^{\pi/2} \frac{\sin^3\theta}{\Gamma} g_{\perp}\beta H \tanh\left(\frac{\Gamma}{2kT}\right)\mathrm{d}\theta\right\} + B_0 H \quad (12)$$

where $= \sqrt{\delta^2 + (g_{\|}\beta H\cos\theta)^2 + (g_{\perp}\beta H\sin\theta)^2}$

which simplifies to Equation (7) for a simple isotropic system with $S = 1/2$, and includes a linear B-term to account for additional interactions amongst levels. VTVH MCD data can be computationally fit to Equation (12) to extract the ZFS splitting of the non-Kramers doublet ground state (δ), the ground state g-values ($g_{\|}$ and $g_{\perp}$), as well as the polarization ratio M_z/M_{xy}. Thus, VTVH MCD measurements on a non-Kramers system allow the determination of EPR parameters for a ground state that is often not accessible by EPR. For Fe^{II}-active sites these ground state parameters can be directly related to the ligand field parameters Δ and V (Scheme 1), which describe the splitting of the $^5T_{2g}$ ground state.[11] This provides a description of the t_{2g} d-orbital energies and a probe of specific metal–ligand π-interactions. In conclusion, the combination of these t_{2g} d-orbital splittings plus the e_g splittings observed by MCD (see ref. 11 for details) gives a complete energy-level diagram of the five d-orbitals of a metal ion site, and hence provides an experimental probe of its geometric and electronic structure.

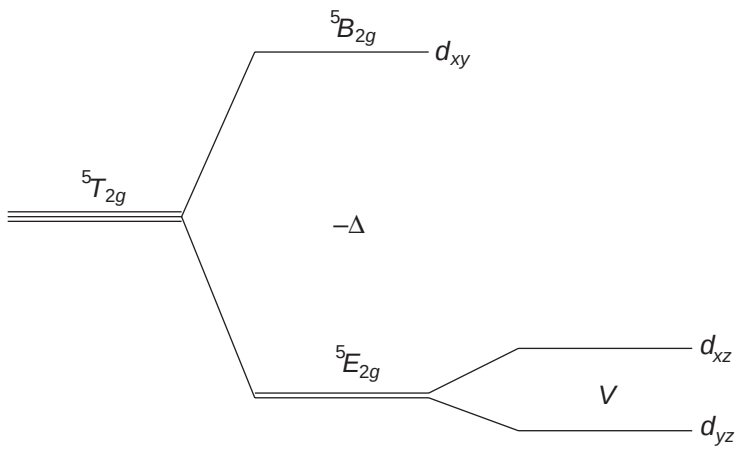

Scheme 1

ACKNOWLEDGEMENTS

This work was supported by the National Institutes of Health (GM-40392 to E.I.S.).

2.26.3 REFERENCES

1. Buckingham, A. D.; Stephens, P. J. *Annu. Rev. Phys. Chem.* **1966**, *17*, 399–419.
2. Stephens, P. J. *J. Chem. Phys.* **1970**, *52*, 3489–3516.
3. Stephens, P. J. *Annu. Rev. Phys. Chem.* **1974**, *25*, 201–232.
4. Stephens, P. J. *Adv. Chem. Phys.* **1976**, *35*, 197–264.
5. Piepho, S. B.; Schatz, P. N. *Group Theory in Spectroscopy: With Application to Magnetic Circular Dichroism*; John Wiley: New York, 1983.
6. Gebhard, M. S.; Deaton, J. C.; Koch, S. A.; Millar, M.; Solomon, E. I. *J. Am. Chem. Soc.* **1990**, *112*, 2217–2231.
7. Thomson, A. J.; Cheesman, M. R.; George, S. J. *Methods Enzymol.* **1993**, *226*, 199–232.
8. Solomon, E. I.; Hanson, M. A. *Bioinorganic Spectroscopy*. In Inorganic Electronic Structure and Spectroscopy; Solomon, E. I., Lever, A. B. P., Eds.; Wiley: New York, 1999; Vol. 2, pp 1–129.
9. Gewirth, A. A.; Solomon, E. I. *J. Am. Chem. Soc.* **1988**, *110*, 3811–3819.
10. Schatz, P. N.; Mowery, R. L.; Krausz, E. R. *Mol. Phys.* **1978**, *35*, 1537–1557.
11. Solomon, E. I.; Pavel, E. G.; Loeb, K. E.; Campochiaro, C. *Coor. Chem. Rev.* **1995**, *144*, 369–460.
12. Kramers, H. A. Proceedings of the Section of Sciences, Koninflife Akad. Van Wetenschappen; Amsterdam, 1930; pp 962–965.
13. Abragam, A.; Bleaney, B. *Electron Paramagnetic Resonance of Transition Ions*; Dover Publications: New York, 1986.
14. Neese, F.; Solomon, E. I. *Inorg. Chem.* **1999**, *38*, 1847–1865.
15. Oganesyan, V. S.; George, S. J.; Cheesman, M. R.; Thomson, A. J. *J. Chem. Phys.* **1999**, *110*, 762–777.
16. Oganesyan, V. S.; Thomson, A. J. *J. Chem. Phys.* **2000**, *113*, 5003–5017.
17. Fujisawa, H.; Hayaishi, O. *J. Biol. Chem.* **1968**, *243*, 267–281.
18. Bull, C.; Ballou, D. P.; Otsuka, S. *J. Biol. Chem.* **1981**, *256*, 12681–12686.
19. Wasinger, E. C.; Davis, M. I.; Pau, M.; Orville, A. M.; Zaleski, J. M.; Hedman, B.; Lipscomb, J. D.; Hodgson, K. O.; Solomon, E. I. *Inorg. Chem.* (in press).
20. Orville, A. M.; Lipscomb, J. D. *J. Biol. Chem.* **1993**, *268*, 8596–8607.
21. Brown, C. A.; Pavlosky, M. A.; Westre, T. E.; Zhang, Y.; Hedman, B.; Hodgson, K. O.; Solomon, E. I. *J. Am. Chem. Soc.* **1995**, *117*, 715–732.
22. Solomon, E. I. *Inorg. Chem.* **2001**, *40*, 3656–3669.
23. Solomon, E. S.; Brunold, T. C.; Davis, M. I.; Kemsley, J. N.; Lee, S-.K.; Lehnert, N.; Neese, F.; Skulan, A. J.; Yang, Y-.S.; Zhou, J. *Chem. Rev.* **2000**, *100*, 235–349.

Comprehensive Coordination Chemistry II
ISBN (set): 0-08-0437486

Volume 2, (ISBN 0-08-0443249); pp 339–349

2.27 Solvatochromism

E. S. DODSWORTH
York University, Toronto, Ontario, Canada
M. HASEGAWA
Gakuin University, Tokyo, Japan
and
M. BRIDGE and W. LINERT
Vienna University of Technology, Austria

2.27.1 INTRODUCTION 351
2.27.1.1 Causes of Solvatochromism 352
2.27.2 PARAMETERS AND MODELS FOR STUDYING SOLVATOCHROMISM 353
2.27.2.1 Introduction to Methods 353
2.27.2.2 Dielectric Continuum Theory 354
2.27.2.3 Empirical Parameters 355
2.27.2.4 Theoretical Simulations 356
2.27.3 EXAMPLES OF SOLVATOCHROMISM OF METAL COMPLEXES 356
2.27.3.1 Solvatochromism Resulting from Coordination by the Solvent 356
2.27.3.1.1 Solvatochromism of coordination compounds with nickel(II) or copper(II) 356
2.27.3.1.2 Solvatochromism of coordination compounds with oxo-vanadium(IV) 357
2.27.3.2 Solvatochromism Resulting from Intermolecular Interactions with the Solvent 357
2.27.3.2.1 Tris(bipyridine)ruthenium(II) 357
2.27.3.2.2 Carbonyl complexes 358
2.27.3.2.3 Platinum-group complexes 358
2.27.4 SOLVATOCHROMISM INVOLVING SPECIFIC INTERACTIONS—HYDROGEN BONDING 359
2.27.4.1 Cyano Complexes of the Iron Group 359
2.27.4.2 Ruthenium Ammine Complexes 361
2.27.4.2.1 Cyanamides of ruthenium 361
2.27.4.3 Bis(bipyridine)(3,4-diamino-3′,4′-diimino-3′,4′-dihydrodiphenyl)ruthenium(II) 362
2.27.5 CONCLUSION 362
2.27.6 REFERENCES 362

2.27.1 INTRODUCTION

One of the great beauties of inorganic chemistry is the wide variety of colors of metal complexes.[1] The electronic transitions, especially *d–d* bands of transition-metal complexes, have long been used to derive chemical information about these complexes (see Chapters 2.17 and 2.30). Solvatochromism refers to changes in electronic absorption spectra, and thus changes in color, with solvent. The phenomenon was first reported over a century ago[2] and was given the name solvatochromism by Hantzsch in 1922.[3] Inorganic complexes were not studied until later,[4] beginning with the work of Bos *et al*.[5] and then Bjerrum *et al*. in the 1950s.[6] Reichardt[2] defines solvatochromism as being due to the differential stabilization of ground and excited states by

intermolecular forces, and states that it "does not take into account spectral shifts due to fundamental alteration of the chromophore system by the solvent as a result of protonation, oxidation, complex formation ..." However, we do discuss here some complexes whose behavior lies outside this strict definition: in particular, species that change color due to coordination of a solvent molecule.[7]

Markedly solvatochromic complexes are usually highly polar or have strong specific interactions with the solvent.[1,8] Considerable work has focused on such solvent-dependent color changes, which provide a useful probe—one of very few such probes—into the nature of the Franck–Condon excited state.[8]

This chapter provides a brief summary of the underlying causes of solvatochromism, an overview of some of the parameters and equations that can be used to understand the phenomenon, and some discussion of specific examples. More detail can be found in some excellent recent reviews covering different aspects of the subject.[8–12]

2.27.1.1 Causes of Solvatochromism

The energy of a species is dependent upon how it interacts with its environment.[8] For a metal complex in fluid solution the environment may consist of other ions, and one or more types of solvent molecule. The solvent and ions may be more or less randomly arranged at any given time, or may on average be ordered to some degree by the electric field due to the solute molecule. Ordering may also occur due to interactions with specific parts of the complex, e.g., with highly polar groups, or by hydrogen bonding to ligands such as ammines or cyanides. Solvent–solute interactions compete with the solvent–solvent interactions which are disrupted by the presence of the solute.[10] Drago has proposed the dynamic cavity model, in which the solvent molecules rearrange to form cavities which contain the solute molecules and maximize the nonspecific solvent–solute interactions.[13]

The various types of interaction that occur between solvent and solute were described many years ago by Bayliss and McRae,[14] and recently calculated by Matyushov *et al.*[15] Depending upon the polarity of the solvent and solute, there are three main possible contributors to the solvent-induced shift (compared to the gas phase) in excitation energy, in the absence of specific interactions. Dispersion forces occur in all species, but are more significant for larger, more polarizable molecules. Dipole–induced dipole forces will occur in cases where the solute is polar, regardless of whether or not the solvent is polar. Dipole–dipole forces come into play where the solvent and solute are both polar. Polar solvents may also induce dipoles in nonpolar solutes, but this contribution is generally neglected.

On the timescale of electronic excitation, ca. 10^{-14} s, there is no reorientation of solvent (Franck–Condon (F-C) principle). Thus the solvent environment of the F-C excited state is that of the ground state, with the solvent equilibrated around the ground-state electronic distribution. However, the polarization of solvent electrons is fast and follows the excitation. The excited state is normally more polarizable than the ground state, and therefore the dispersion forces are increased in the excited state. In the absence of other interactions this results in a red shift of the transition, which is referred to by Bayliss and McRae as the polarization or general red shift.[14] The red shift depends upon the polarizability of the solvent and the oscillator strength of the transition, as well as on some of the higher energy transitions. For a nonpolar solute this will be the main cause of solvatochromism. However, few coordination complexes will fit this case, as many are charged and/or polar and therefore interact strongly with the solvent. The additional forces are often larger and their effects are superimposed upon the general red shift.

For a polar solute in a nonpolar solvent, dipole–induced dipole forces will have an effect, causing stabilization of the ground state where these forces are large. If the solute dipole moment decreases during the transition, the magnitude of the dipole–induced dipole forces will be smaller in the excited state than in the ground state. This results in a blue shift which increases with refractive index of the solvent, and which may override the general red shift. If the solute dipole moment increases in the excited state, the difference in dipole–induced dipole contributions will cause a red shift with increasing refractive index, which adds to the general red shift from the gas-phase energy.

For a polar solute in polar solvents, dipole–dipole interactions will stabilize the ground state of the solute according to the polarity of the solvent. In this case the solvent molecules will be oriented around the ground-state dipole and, if the dipole moment is increased by the transition, the excited state will be stabilized more by more polar solvents (those with higher dielectric constants). The resulting red shift will again add to the general red shift compared to the gas phase.

If, as is more common, the dipole moment decreases in the excited state (or changes direction) the resulting blue shift, which increases with increasing solvent polarity, will most probably cause an overall blue shift in the absorption, compared to the gas phase. In some complexes there will be a change in orientation of the dipole moment upon excitation, which can also give rise to negative solvatochromism.[16,17]

Solvent–solute interactions may be stronger and more specific than simple dipolar forces; there may be ordering of solvent molecules around specific parts of the molecule due to local dipoles, or there may be stronger interactions such as hydrogen bonding—which occurs, for example, in ammine and cyanide complexes and is discussed below.

A shift to the red of a transition with increasing solvent polarity is termed "positive solvatochromism" and a blue shift is termed "negative solvatochromism."[1,10] For transition-metal complexes most solvatochromic transitions are charge transfer in nature, being metal to ligand (MLCT), ligand to metal (LMCT), or ligand to ligand (LLCT). Such transitions often involve movement of an electron in a direction antiparallel to the ground-state dipole moment, and negative solvatochromism is commonly observed.[1]

The solvatochromic shift can be thought of in terms of two contributions: the differential solvation energy of the ground and equilibrium (non-F-C) excited states, Δ_{sol}; and the solvent or outer-sphere reorganization energy, χ_o, which can be regarded as being the destabilization of the excited state, i.e., the energy difference between the solvationally equilibrated and nonequilibrated excited states:[11,18–21]

$$E_{op} = E_{00}(g) + \Delta_{sol} + \chi_i + \chi_o \tag{1}$$

Here E_{op} is the transition energy, E_{00} (g) is the 0–0′ vibrational energy in the gas phase, and χ_i is the vibrational or inner-sphere reorganization energy, which is assumed here to be solvent independent. These various contributions to the energy and solvatochromic shifts are discussed in detail by Dodsworth and Lever;[20] in many cases they may be modeled using dielectric continuum theory (below). Both Streiff and McHale,[22] from resonance Raman studies of $[Ru(bpy)(NH_3)_4]^{2+}$ (where bpy = 2,2′-bipyridine), and Meyer and co-workers, from studies of cyano complexes,[23] have come to the conclusion that the variation in Δ_{sol} is larger than the variation in χ_o and causes most of the solvent dependence. However, hydrogen bonding is important in both these cases, and in general the relative contributions of Δ_{sol} and χ_o will depend on the magnitude of the ground- and excited-state dipole moments.[19,20]

Thus solvatochromism depends upon the way the electronic transitions in the visible region of the spectrum affect the solute dipole, and is most pronounced in molecules which have a large dipole moment, and/or which have strong specific interactions with the solvent environment.

In some cases the "ordering" of the solvent around the solute goes one step further and coordination at a vacant site may occur, leading to a pronounced solvent effect, as the change in stereochemistry may alter the spin state of the metal and/or drastically change the (relative) energies of the *d*-orbitals.[7] This leads to strong apparent solvatochromism in certain coordinatively unsaturated complexes, a number of examples of which are discussed below. Here the transitions are usually *d*–*d* in nature.

Emission spectra (see Chapter 2.19) are not covered in detail here, although the principles are the same as they are for absorption. Emission spectra of coordination compounds are often less solvatochromic than the corresponding absorption spectra.[23,24] Emission occurs from a relaxed, non-F-C, excited state. Thus, in the case of emission spectra in fluid solution the solvent will be oriented around the emitting state which, if polar, will be stabilized by polar solvents. This will lead to a red shift with increasing solvent polarity, as the ground state will not be similarly stabilized unless the dipole moment increases and does not change direction.[8]

The solvatochromism of intervalence (metal-to-metal) charge-transfer bands in dinuclear, mixed-valence complexes is a subject in itself, and will not be discussed here (but see Chapter 2.55).

2.27.2 PARAMETERS AND MODELS FOR STUDYING SOLVATOCHROMISM

2.27.2.1 Introduction to Methods

The ability of a solvent to solvate a particular species is often referred to in terms of the rather ill-defined idea of "solvent polarity."[2,9,10] This is not simply related to the overall dipole moment of the solvent, but may depend on the presence of polar groups and local dipoles, and the ability

to solvate will also depend on the polarizability of the solvent. Reichardt suggests that "solvent polarity" should be regarded as a measure of overall solvation capability, including all possible specific and nonspecific interactions.[10]

Since the solvating ability of a solvent is not easily described using well-defined parameters[10] such as dielectric constant, dipole moment, or refractive index, the solvatochromism of transition-metal complexes has most frequently been correlated with various empirical parameters. These may be derived from the behavior of one species or from an average of many different ones.[10,25] An advantage of such parameters is that, in many cases, one can be found that provides a good fit to the data and allows easy comparison of solvatochromic behavior in systems where the causes are similar, with or without specific interactions. Their empirical nature means that they are composite measures of specific and nonspecific interactions between the solvent and solute from which the parameter was derived. Thus a given parameter may be biased towards contributions from dipole–dipole forces or dipole–induced dipole forces, which have a large polarizability component; and hydrogen-bonding tendencies (as either a donor or acceptor) may or may not be reflected by the parameter. However, it is not the aim of this chapter to analyze the parameters themselves.

Potentially, the modeling of solvatochromic behavior using theoretical methods such as reaction field theory, in which the solvent is treated as a dielectric continuum and the solute as a point dipole in a spherical cavity, may provide more fundamental information than can be obtained using empirical parameters.[8,11] In principle this may allow calculation of ground- and excited-state dipole moments, gas-phase transition energies, and the relative magnitudes of some of the contributions to the solvatochromic shift. Deviations from the theory can also be useful in indicating the presence of specific interactions, and if either the solvent or solute has the potential to form hydrogen bonds with itself (alcohols, for example) or with another species, the dielectric continuum model is invalid[8,11] and empirical parameters are usually used.

2.27.2.2 Dielectric Continuum Theory

The various contributions to the solvatochromic shift (Equation (1), i.e., $\Delta_{sol} + \chi_o$) can be described using the reaction field method, such as is used in generating McRae's equation.[26] The solvent is treated as a dielectric continuum, and the solute as a point dipole in a spherical cavity embedded in the continuum. This assumes no short-range ordering of the solvent around the solute due to local bond dipoles or to hydrogen bonding. This approach has been used by a number of authors and various equations have been developed which differ slightly in the assumptions made, such as those of Kirkwood,[27] Ooshika,[28] Lippert,[29] and McRae.[26] The general theoretical background and some of these approaches are discussed by Marcus.[18] There have been many more recent discussions and attempts to improve upon these treatments.[21,30–37]

McRae's equation, which uses the Onsager[38] dielectric functions, has been used to interpret the solvatochromism of a number of coordination compounds. Meyer[19,23] and one of us[20] have also used Kirkwood's approach,[27] which is simpler since it neglects dispersion forces. Lippert's method is used for species in which absorption and emission data are available for the same excited state—when the difference between absorption and emission energies is known a number of terms in the equations will cancel, and it is then relatively simple to obtain the ground- and excited-state dipole moments.[8,29] This method is not usually applicable for coordination complexes as, if emission is observed, the emitting state is usually different from the main absorption band, e.g., in many cases absorption is to a singlet state and emission is from the corresponding triplet.

Applying McRae's equation,[26] and neglecting the Stark-effect (quadratic) term the shift, $\Delta\nu$, in the transition energy from the gas phase to that in a given solvent is expressed as:

$$\Delta\nu = A\frac{D_{op}-1}{2D_{op}+1} + B\frac{D_{op}-1}{2D_{op}+1} + C\left[\frac{D_s-1}{D_s+2} - \frac{D_{op}-1}{D_{op}+2}\right] \quad (2)$$

where A, B, and C are constants characteristic of the solute, D_{op} is the optical dielectric constant (equal to the square of the refractive index) of the solvent and D_s is the static dielectric constant of the solvent. The three terms including A, B, and C in the equation represent the three main types of contribution to the solvent-induced shift: dispersion forces, dipole–induced dipole forces, and dipole–dipole forces, respectively. A involves a sum over all the electronic transitions of the molecule, including those of the excited state. A simpler equation for this contribution is given by Bayliss,[39] but it is generally estimated to be rather small.[15,19,40] B and C depend upon the

ground- and excited-state dipole moments of the solute, μ_g and μ_e, and upon the cavity (assumed to be spherical) radius, a:

$$B = \frac{\mu_g^2 - \mu_e^2}{a^3} \tag{3}$$

$$C = \frac{2\mu_g(\mu_g - \mu_e)}{a^3} \tag{4}$$

There are a number of assumptions implicit in this equation, such as that the refractive index of the solvent in the visible-region wavelengths is the same as at zero frequency. This is reasonable for solvents other than water, but for water there is quite a large difference between the values at zero and visible-region frequencies.[26] The ground-state isotropic polarizability of the solute is assumed to be $a^3/2$.

McRae's approach and other similar approaches have been criticized by Brady and Carr,[34] and more recently by Klamt,[41] on the grounds that the orientational and electronic parts of the polarizability are not independent. Details are not given here but the reader is referred to their work, and to that of Tomasi *et al.*,[42] Brady and Carr, however, point out that in spite of the erroneous assumptions, statistically superior correlations are generally obtained with McRae's equation, compared to the corrected formulae.[34]

This model also breaks down theoretically in large solute molecules that have polar parts but are nonpolar overall, although good correlations may still be obtained in such cases. A further weakness, in practice, is that the A and B terms involving D_{op} are often small and ill defined, because of the errors inherent in poor statistical fits. Some of the scatter normally observed may result from solvent molecules whose dielectric constants are an average of the properties of a functional group and, for example, an aliphatic chain. Where there is some degree of preferential interaction between the solute and one part of the solvent molecule, the solute will "see" the part of the solvent that has dielectric properties differently from the average of the solvent as a whole.

2.27.2.3 Empirical Parameters

Many different empirical solvent parameters have been developed and these have been reviewed by Reichardt.[10] Here we discuss only those which are commonly used to correlate with solvatochromism of coordination complexes. Kosower's "Z values,"[43] derived from the absorption maximum of 1-ethyl-4-methoxycarbonylpyridinium iodide, were one of the earliest comprehensive solvent-polarity scales. These provide an empirical measure of the solvation behavior of a solvent, mainly reflecting dipole–dipole solute–solvent interactions, and they do not correlate well for nonpolar solvents. Reichardt and Dimroth's $E_T(30)$ values, developed a decade later, are sensitive to polar and hydrogen-bonding interactions, and also to some extent to other interactions such as dispersion forces.[2,44] These are based upon the spectrum of a pyridinium N-phenolbetaine, and have been applied to the solvatochromism of a number of coordination complexes. The $E_T(30)$ parameter is the original parameter, in kcal mol^{-1}, and there is also a normalized version of the scale, $E_T(N)$.[10]

Kamlet, Abboud, and Taft have developed in detail a set of parameters based on π^*, which is derived by averaging the behavior of a set of closely related solvatochromic probe molecules: substituted nitrobenzenes.[45–48] The π^* scale is normalized, with cyclohexane as the zero and DMSO having a value of 1.00. It reflects contributions from polarizability and polarity, but for solvents where polarizability is particularly important a second parameter δ is needed. The coefficient of δ, d, is 0.5 for polyhalogenated solvents and 1.0 for aromatics).[48] These authors define a "select solvent set" of nonchlorinated, nonprotonic, aliphatic solvents with a single, dominant bond dipole. This set is sometimes useful for correlations with other parameters, or with equations such as McRae's.[26] Two additional parameters, α and β, were developed for systems in which hydrogen-bond formation is a factor; the α scale reflects hydrogen-bond donating ability (acidity) and the β scale is for hydrogen-bond acceptor ability (basicity).[47,48] Equations of the form:

$$XYZ = XYZ_0 + s(\pi^* + d\delta) + a\alpha + b\beta \tag{5}$$

are used with the π^* scale. The relationships of these parameters to other empirical parameters and to various dielectric functions have been discussed by Abboud *et al.*[49] An updated version

of the π^* scale has been published, based on a single probe molecule, which is considered to be a superior approach compared to that of averaging data from several species.[25]

Gutmann's donor and acceptor number (DN and AN)[50,51] are designed to correlate with solvent effects where the interactions with the solute are dominated by those of the donor–acceptor type, including hydrogen bonding. These parameters have proved to be very useful for understanding the solvatochromism of a number of coordination complexes in which these types of interactions are important. Donor number is defined as the negative ΔH value for the interaction of the electron-pair donor/nucleophilic solvent (Lewis base) with 10^{-3} M $SbCl_5$ in 1,2-dichloroethane solution; it correlates with the β parameter of Kamlet *et al.* The acceptor number is based on the chemical shift of the ^{31}P NMR of triethylphosphineoxide in the acceptor solvent of interest. However, donor and acceptor properties cannot be completely explained by independent parameters, due to their mutual interactions. Donor and acceptor numbers of some solvents have been estimated from electronic absorption spectra of indicators such as $[Fe^{II}(phen)_2(CN)_2]$ and other metal complexes.[50,52,53] Although AN and $E_T(30)$ are considered to be linearly related, a detailed analysis[54] yields different groups of solvents characterized by their functional groups.

There are three parameters in the literature based on the solvatochromism of carbonyl complexes. Both Lees' E^*_{MLCT} parameter[55] and Walther's[56] earlier E_K are based on the solvatochromism of $[M(CO)_4(diimine)]$ complexes. Lees' parameter, which has been used in many subsequent studies, is based on the solvatochromism of bipyridinetetracarbonyltungsten(0).[55] The third scale is $E_{CT}(\pi)$, developed by Kaim's group.[57] This group have investigated the solvatochromism of a number of complexes, plotting much of their data against E^*_{MLCT}. However, in the case of $[M(CO)_5(\eta^2\text{-TCNE})]$ complexes (where M = Cr, W, and TCNE, tetracyanoethylene, is bound as an olefin) the solvatochromism differed qualitatively from that of other transition-metal carbonyls, and did not correlate with parameters such as E_T, Z, π^*, DN, or E^*_{MLCT}. The failure of these scales was attributed by Kaim to a specific type of π interaction between the complex and the solvent, in which a solvent molecule lies on the opposite side of the TCNE to the metal carbonyl fragment, and in the case of aromatic solvents lies coplanar with the TCNE. The solvent competes with the metal fragment for the π-accepting ability of the TCNE. The $E_{CT}(\pi)$ parameter scale is derived from the average of the results for the Cr and W complexes.

2.27.2.4 Theoretical Simulations

Relatively recently there have been attempts to model solvent effects on electronic spectra by incorporating them into theoretical calculations using methods such as INDO (discussed in Chapter 2.33 and in various reviews[12,58,59]). Most work has involved organic species, but a number of groups have calculated the spectra of ruthenium ammines surrounded by solvent molecules or in solution (see below).[60–67] Calculations without inclusion of solvent give charge-transfer band energies significantly higher than those observed. Dielectric continuum theory also breaks down for these species, because of their capacity for hydrogen-bond formation with acceptor solvents. The various methods of performing spectroscopic calculations involving solvent are reviewed by Hush and Reimers[12] specifically for transition-metal complexes, and also more generally by Zerner and co-workers.[68]

2.27.3 EXAMPLES OF SOLVATOCHROMISM OF METAL COMPLEXES

Some examples of the solvatochromic coordination compounds that have been most extensively studied are discussed here. Before discussion of true solvatochromic behavior, we comment on some examples where the solvent binds to a coordination site on the metal center, generating apparent solvatochromic behavior.

2.27.3.1 Solvatochromism Resulting from Coordination by the Solvent

2.27.3.1.1 Solvatochromism of coordination compounds with nickel(II) or copper(II)

Mixed-ligand coordination compounds with transition-metal ions such as nickel(II) and copper(II) show solvent-dependent color changes.[69–76] Recent reviews[7,52,77,78] discuss their features

in some depth and so only a summary is presented here. [M(diket)(diam)]: diket = β-diketone, diam = *N*-alkylated diamine, for instance, form square-planar complexes with Ni^{II} and also with Cu^{II}, in weakly donating solvents. With increasing solvent donor ability, two solvent molecules coordinate octahedrally. In the case of nickel(II) there is a change in spin state from square planar $S = 0$ nickel(II) through formation of the six-coordinate $S = 1$ species, thereby causing an abrupt change in the electronic absorption spectrum; solvents of intermediate donor ability can yield equilibrium mixtures of both stereochemistries (see Figure 3, ref. 78). Intermediate five-coordinate symmetries may also be involved. The formation of four-, five-, and six-coordinate copper(II) d^9 complexes upon solvent coordination does not involve a spin-state change, and generates a continuous change in spectrum rather than an abrupt one. In the case of copper, the coordination of anionic ligands can also cause significant changes in spectrum, analogous to the solvent effects. Generally, the square-planar structure is changed to square pyramidal with an anionic donor, or to octahedral with a donor solvent having a high donor strength, as seen from Figure 1 in ref. 79.

Highly sterically hindered diamines, such as *N*,*N*,*N*′,*N*′-tetramethylethylenediamine (tmen) and 1,2-dipiperidinoethane, form stable, mixed-ligand complexes such as $M(diket)(tmen)]^{n+}$ which often exhibit dramatic solvatochromic effects. For this reason they have been intensively studied.[52,77,78,80,81] This is reminiscent of the very early work by Lifschitz and co-workers,[5] who employed the hindered stilbenediamine ligand.

Copper(II) complexes with mixed ligands are also useful when quantitatively estimating the donating or accepting abilities of solvents. In the case of d^9 $[Cu(acac)(tmen)]^{2+}$ (acac = acetylacetonate), in the presence of a noncoordinating anion such as perchlorate, the shift in electronic spectrum with solvent reflects the formation of six-coordinate species with increasing donicity of the solvent.[78] Indeed this molecule is a useful reagent for assessing the donicity of solvents or solvent mixtures. Conversely, if a nondonor solvent such as dichloroethane is employed, one may ascertain the relative binding of various anions of differing donicity which influence the electronic spectrum in a manner similar to solvents of differing donicity.[77,79] Interestingly, if one studies solvent effects in the presence of the strongly binding chloride ion, the dominant factor then is the ability of the solvent to displace chloride, i.e., the ability of the solvent to solvate chloride, and the formation of six-coordinate di-solvent complexes then reflects the acceptor ability of the solvent rather than its donicity.[78]

2.27.3.1.2 Solvatochromism of coordination compounds with oxo-vanadium(IV)

Oxovanadium diketonate species have long been associated with solvatochromism involving the electronic absorption spectrum and also the (V = O) infrared stretching vibration.[82–92] The initial five-coordinate $OV(acac)_2$ species becomes solvated to form a six-coordinate species with concomitant shift in absorption transition energies and color change from blue to green. Formation constants can be calculated from the integral ratio of the most intense IR band originating from the (V = O) (A_1) stretching vibration of the free $[VO(acac)_2]$ and the coordinated $[VO(acac)_2]$ with solvent species. In pyridine (py) solution, a far IR band near 469 cm^{-1} in $[VO(acac)_2]$ splits into two frequencies, an observation interpreted in terms of an equilibrium mixture between *cis* and *trans* geometric isomers of $[VO(acac)_2(py)]$.

2.27.3.2 Solvatochromism Resulting from Intermolecular Interactions with the Solvent

2.27.3.2.1 Tris(bipyridine)ruthenium(II)

The title complex has no ground-state dipole moment, and shows the small degree of solvatochromism typical of a nonpolar complex.[19] However, the electronic spectrum of this complex has been debated for many years, the question being whether the visible region $Ru(d\pi) \rightarrow bpy(\pi^*)$ MLCT transitions give rise to localized or delocalized excited states.[93] The solvatochromism of this band correlates with the $(1 - D_{op})/(2D_{op} + 1)$ function of McRae's equation, shifting by about 300 cm^{-1} between nitrobenzene and water as solvents. Meyer's group[19] concluded that the shift was too large to be consistent with differences in dispersion forces and that the D_3 symmetry of the ground state must be broken in the F-C excited state, i.e., that the excited electron is localized on one of the three bipyridine ligands. The shift is then attributed to both changes in dispersion forces and in dipole–induced dipole forces.[19] Milder, however, has shown that the solvatochromism is less than that of one of the internal $bpy(\pi \rightarrow \pi^*)$ transitions, in the complex and in the

bpy ligand.[94] Since these are not expected to give polar excited states, it seems reasonable to conclude that the solvatochromism is due to the "general red shift," i.e., to differences in dispersion forces between the ground and excited states. The greater solvatochromism of the bpy($\pi \rightarrow \pi^*$) transition is consistent with the larger oscillator strength of this transition, using Bayliss' expression[39] for calculation of the dispersion force contribution.[40]

2.27.3.2.2 Carbonyl complexes

There have been many investigations[95] of the solvatochromism of $[M(CO)_4(diimine)]$ complexes (where M = Cr, Mo, or W, but most commonly Mo) since the earliest report by Saito *et al.*[96] These complexes are particularly well suited to the study of solvatochromism because they are neutral and yet highly polar (μ up to about 10 D),[97] and therefore are soluble in an exceptionally wide range of solvents—from hydrocarbons, such as hexane, to DMSO. They usually display strong negative solvatochromism,[95] and the visible-region, metal-to-diimine charge-transfer band may shift more than 3,000 cm^{-1} to the blue upon going from a nonpolar to a polar solvent. This main band is believed to be a *z*-polarized $b_2 \rightarrow b_2^*$ (in C_{2v} symmetry) transition; a second MLCT transition which is also solvatochromic is often seen at higher energies.

Saito[96] used McRae's equation to correlate with the solvatochromism, but later studies have used various empirical parameters. Burgess used E_T for a number of compounds which give separate linear correlations for hydroxylic and nonhydroxylic solvents.[98,99] Burgess[99,100] and Baxter and Connor[101] have also demonstrated the change in solvent sensitivity brought about by changing the substituents on the diimine ligand, and Kaim and co-workers have discussed in detail the factors affecting solvatochromism of carbonyl complexes with bidiazine ligands[102] and with other N-donor ligands.[103]

In an early report, tom Dieck and Renk observed that substitution of two of the carbonyls (in the axial positions, *trans* to each other) by phosphine ligands could reverse the direction of the solvatochromism.[104] This was interpreted as a change in the direction of charge transfer, from MLCT to LMCT, though alternative interpretations have been proposed.[1] A simpler explanation is that the increased metal–diimine mixing which occurs upon phosphine substitution, due to the increased electron richness of the metal, changes the nature of the transition to one with more metal–ligand bonding to antibonding character.[95] With a smaller change in dipole moment between the ground and excited states there may be little change in dipole–dipole forces, and the red shift resulting from the change in dispersion forces may be seen. This is consistent with the small changes in peak position seen for the complex in which the reversed solvatochromism is reported.

Investigations by Lees' group into the solvent effects on the lowest-energy excited states of dinuclear $[(OC)_5W—L—W(CO)_5]$ complexes (L = pz, 4,4′-bpy and 1,2-bis(4-pyridyl)ethane) showed that, like similar mononuclear complexes, the MLCT absorption bands exhibited strong negative solvatochromism.[105,106] Kaim and co-workers have also studied related dinuclear species.[103,107] Since these species have no net ground-state dipole moment, the solvatochromism was attributed by both groups to differences in the polarizability between the ground and excited states, causing differences in induced-dipolar and dispersion interactions. However, Dodsworth and Lever have proposed that these explanations are incompatible with the results of fitting data for various dinuclear systems to McRae's equation.[40,108] These correlations (e.g., see Figure 1 in ref. 108) show that dipole–dipole interactions are important despite the lack of a formal ground-state dipole moment. They suggest that the solvatochromism derives from the individual dipoles of each half of the molecule interacting with the solvent.[40,108] This conclusion is supported by work, including extended Hückel calculations, on related complexes by Granifo *et al.*[109]

2.27.3.2.3 Platinum-group complexes

The solvatochromism of square-planar complexes of the Ni group containing a diimine and a dithiolate ligand was first reported in 1973 by Miller and Dance, for Ni complexes.[110] These complexes have an intense band in the visible region, lying around 12–20,000 cm^{-1} depending upon the specific ligands present, and showing strong negative solvatochromism. There has been some uncertainty about the assignment of this band, which does not occur in the spectra of the corresponding bis(diimine) or bis(dithiolate) species. Most of these complexes formally contain a dithiolate dianion and are therefore neutral and soluble in a variety of solvents.

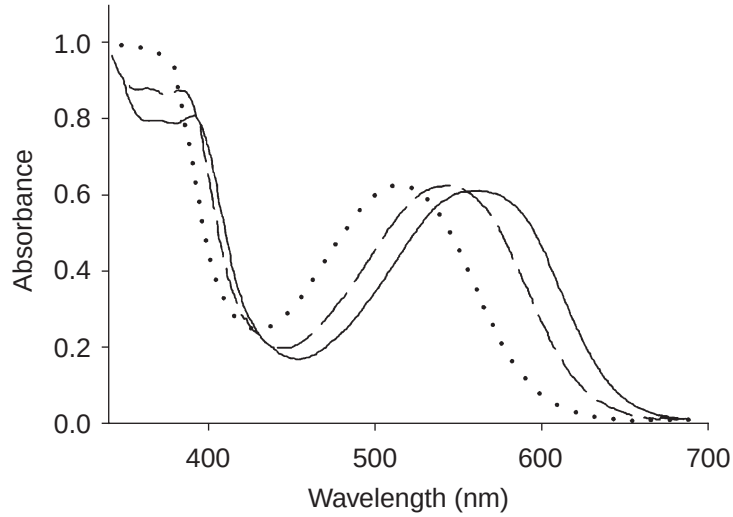

Figure 1 Absorption spectra of [Pt(Me_2bpy)(met)] in solvents of different polarity (adapted from ref. 113). Solvents: –chloroform; ---dichloromethane; ·····acetonitrile.

A plot of the solvatochromism of [Ni(tfd)(phen)] (tfd = $S_2C_2(CF_3)_2$; phen = 1,10-phenanthroline) against the product of solvent dipole moment and solvent concentration gave an obvious, though not completely linear, correlation for a variety of polar solvents, including alcohols and acetic acid. Miller and Dance concluded that the ground state is markedly dipolar and that one of the lower excited states is less so, i.e., that the solvatochromism reduces, reverses, or rotates the dipole. The effects of electron-withdrawing substituents on the two ligands on the redox potentials and spectra were also studied. The strong band was assigned to a strongly allowed $b_2 \rightarrow b_2^*$ LLCT transition, from an orbital mainly on the dithiolene, with some metal p_z character, to one mainly on the diimine, but with an estimated 20% metal *d* character and a significant dithiolene contribution. A more recent study of solvatochromism of related Ni complexes has been published by Chen *et al.*[111]

Eisenberg and co-workers have focused mainly on the related Pt complexes, which are similarly solvatochromic.[24,112–116] For example, the band in [Pt(Me_2bpy)(met)], where Me_2bpy is 4,4′-dimethyl-2,2′-bipyridine and met is *cis*-1,2-dicarbomethoxyethylene-1,2-dithiolate, shifts about 2,000 cm^{-1} to the blue on going from chloroform to acetonitrile: see Figure 1.[113] The solvatochromism of many of these complexes correlates well with Lees' E^*_{MLCT} parameter,[55] demonstrating that this parameter is a measure of solvent polarity rather than a reflection of specific interactions between polar solvents and the carbonyl groups in the [$W(CO)_4$bpy] from which it was derived. These authors assign the solvatochromic transition as being from a mixed Pt(*d*)/S(*p*) orbital to one which is mainly π^*(diimine), and characterize it as a mixed MLCT/LLCT transition.[114,117] Many of these complexes also emit in fluid solution, but the emission is generally less solvatochromic[24] or nonsolvatochromic[113] and may arise from a different state.[118,119] Transient DC photocurrent (TDCP) measurements, which give information about the change in dipole moment between the ground and excited states, have led Hupp to suggest that dimers are formed in the excited state.[119]

2.27.4 SOLVATOCHROMISM INVOLVING SPECIFIC INTERACTIONS—HYDROGEN BONDING

2.27.4.1 Cyano Complexes of the Iron Group

Solvatochromism of cyano complexes, particularly of the Fe group, has been investigated for many years.[4,6,11,99] Most of the complexes studied contain diimines as co-ligands, with the [M^{II}(diimine)$_2$$(CN)_2$] complexes having the advantage that they are neutral and soluble in a wide range of solvents. Indeed, the complex [$Fe^{II}$$(phen)_2(CN)_2$] has been proposed as a universal solvent polarity indicator by Burgess,[120] and has been used extensively to measure acceptor properties of solvents and cations.[4,7,50,121] In addition to its solubility, its usefulness stems from the combination of ligands that provide a strong visible region MLCT band—from the d^6 iron(II)

centre to the diimine ligand—coupled with the presence of cyanide ligands which interact strongly with the solvent or with other acceptors (e.g., BF_3, H^+, simple metal ions).[122,123] Acceptor solvents stabilize the ground state by withdrawing electron density, either through a simple donor–acceptor interaction with the cyanide lone pair of electrons, or through hydrogen bonding at the same site. This allows an increase in back-bonding to the cyanide ligands which stabilizes the metal orbitals, so that the MLCT energy increases with increasing acceptor ability. In some of these complexes there are two solvatochromic MLCT bands in the visible/near UV region, terminating on different π^* levels of the ligand.[124]

Burgess' group performed a number of early studies of $[Fe^{II}(bpy)_2(CN)_2]$ and related complexes.[99,125,126] The frequencies of maximum absorption of the visible region MLCT bands were plotted against Reichardt's E_T value, giving two correlation lines in each case, for potentially hydrogen-bonding and nonhydrogen-bonding solvents. Correlation with solvent AN gives a single straight line, the band shifting to higher energy with increasing AN (Figure 2).[7,124,127,128] The iron(III) complex $[Fe^{III}(phen)_2(CN)_2]^+$ also exhibits pronounced solvatochromism, but in this case for an LMCT band,[4,126] with an AN dependence of opposite slope to that for the MLCT band of the iron(II) complex.[129]

Burgess,[126] and later Toma,[124] noted the greater solvent sensitivity of the tetra- and pentacyano complexes compared to the dicyano species. $[Fe(CN)_5(2,6\text{-dimethylpyrazine})]^{3-}$ is particularly solvatochromic, with the main band shifting from 22,700 cm^{-1} in water to 16,250 cm^{-1} in DMA.[124] Similar behavior is observed for the related ruthenium complexes,[23,130–132] and a thorough study of solvent effects on the absorption and emission spectra and the $Ru^{III/II}$ potentials of a series of complexes containing 1–5 cyanide ligands has been carried out by Meyer and co-workers.[23] The solvatochromism of both absorption and emission was found to correlate well with AN rather than with dielectric continuum functions. The solvent sensitivity increases with the number of cyanides present, with the effects being additive, and it is greater for absorption than for emission. Where the absorption and emission involve the same excited state, and where dielectric continuum theory is applicable, the inner and outer reorganization energies are expected to be approximately equal for the two processes.[23] However, if there are strong specific interactions such as hydrogen bonding, the solvent–solute interactions may influence the nature of the ground state, and the χ_o terms for the absorption and emission processes are different; in fact, for the cyano complexes, $\chi_{o,gs}$ may be as much as twice the magnitude of $\chi_{o,es}$. The implications of vibronic structure, and the multiple states which exist in absorption spectra and are usually neglected when solvatochromism is studied, are also discussed in this paper.[23]

The polypyridyl ligand $\pi \rightarrow \pi^*$ bands of these complexes were also observed to be solvatochromic, though to a lesser extent than the MLCT bands. This is due to orbital mixing giving the $\pi \rightarrow \pi^*$ transitions some MLCT character, and to configuration interaction mixing transitions of the same symmetry.[23]

Sizova *et al.* have calculated the spectrum of $[Ru(CN)_5(pz)]^{3-}$ (pz = pyrazine) taking into account the solvent effect.[63]

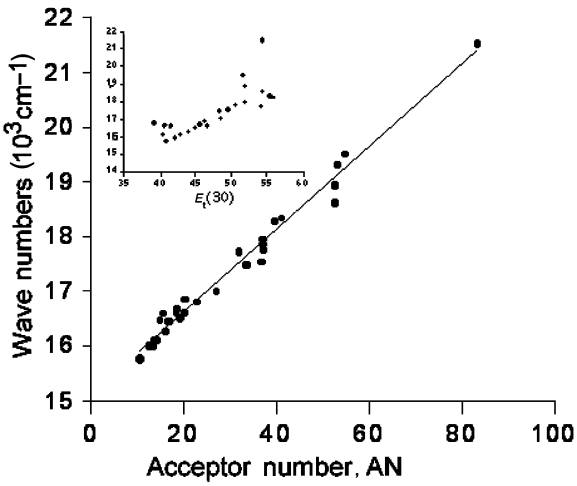

Figure 2 Linear relationship between the lower energy MLCT absorption maximum of $[Fe(phen)_2(CN)_2]$ and the acceptor number, AN. A plot of the same values against $E_T(30)$ is given in the insert (adapted from ref. 7).

2.27.4.2 Ruthenium Ammine Complexes

The LMCT and MLCT transitions in a variety of Ru^{II} and Ru^{III} polypyridyl-ammines are exceedingly solvent dependent,[11,133] with $[Ru(NH_3)_4(bqdi)]^{2+}$ (bqdi = benzoquinonediimine) being an interesting exception.[134] Meyer and co-workers have studied a series of Ru^{II} and Ru^{III} penta- and tetra-ammine complexes with pyridine-based co-ligands.[133] Neither the dielectric continuum model nor solvent dipole moment correlate with the charge-transfer energies of these complexes but, rather, parameters such as Gutmann's donor number or the Taft–Kamlet β parameter, which reflect the hydrogen-bond-accepting ability of the solvent, must be used. These give reasonable linear correlations for the complexes, with the slopes showing some tendency to increase with the number of coordinated ammines. The origin of these solvent effects was investigated in detail and found to lie largely in the solvent effect upon the $Ru^{III/II}$ redox potential. The donor solvents interact with the ammine protons, causing increased electron density on the ruthenium with increasing donor ability of the solvent. This effect is greater for Ru^{III} than for Ru^{II} complexes because of the greater acidity of the N—H groups. The donor–acceptor interactions are strong enough to cause preferential outer-sphere solvation in binary solvent mixtures, with the stronger donor being in closer proximity to the ion.[133]

Calculations have been performed on a number of these species; their MLCT energies are significantly overestimated by semi-empirical calculations, such as INDO/S, in which the solvent is not included.[11,60–67,135] Shin *et al.* used INDO in one of the earlier studies of $[Ru(NH_3)_5L]^{n+}$, where L = py, pz, pzH^+.[61] Inclusion of $15H_2O$ molecules was found to lower the calculated charge-transfer energies significantly, but not as low as the experimental values. Sizova *et al.* used a mixed INDO/CNDO method.[63] Zerner *et al.* have calculated the spectra of $[Ru(NH_3)_5py]^{2+}$, $[Ru(NH_3)_5py]^{3+}$, and some related species in several solvents,[60,66] using INDO/S and the self-consistent reaction field (SCRF) method. The INDO method tends to produce rather short hydrogen bonds,[60] so a hybrid quantum mechanics–molecular mechanics method was used to obtain structures for the later study.[66] Spectra were calculated quantum mechanically for the complex and first solvent shell, with a further solvent layer being modeled by point charges. The solvent structure was obtained by Monte Carlo simulations. A spherical SCRF was then used to include the longer-range interactions.

The calculated gas-phase MLCT energy of 35,900 cm^{-1} decreases when water is included in the calculation; two bands are predicted, at 24,500 cm^{-1} and 25,500 cm^{-1}, which agree well with the observed energy of 24,500 cm^{-1}. The calculations show that the solvent contributes about $1e^-$ to the Ru complex regardless of the quantum-mechanical method used, and this greatly improves the accuracy of the predicted MLCT band. The calculated spectrum changes little after the addition of 12 water molecules.[66]

Hush and Reimers have also performed calculations on ruthenium penta-ammine complexes using their model, ZHR-SS, which can be used for calculating the solvent-induced shift of absorption or emission bands.[12,62] This is a four-step method in which the gas-phase electronic structure and spectroscopy of the solute are determined, the structure of the solution is modeled, and the effect of the solvent structure on the electronic transitions is calculated. The gas-phase calculation of the solute is obtained at the highest level of theory possible. Using this method, calculated MLCT energies for $[Ru^{II}(NH_3)_5L]^{n+}$ (L = NH_3, py, pz, pzH^+) in aqueous solution are 3–6,000 cm^{-1} higher than observed, but significantly lower than the calculated energies in the absence of solvent.

More recently Ferretti and co-workers have used the polarizable continuum model (PCM) in conjunction with *ab initio* calculations to study the absorption spectra of $[Ru^{II}(NH_3)_5pz]^{2+}$ and $[Ru^{II}(NH_3)_5$4,4′-bpy$]^{2+}$ in several solvents.[64,65]

2.27.4.2.1 Cyanamides of ruthenium

The Crutchley group have done extensive studies of ruthenium cyanamide complexes, particularly with ammine co-ligands, including detailed investigations of substituent and solvent effects on oscillator strengths as well as transition energies.[136–140] These complexes have a well-defined LMCT band in the visible region which is assigned to a single transition, $b_1 \rightarrow b_1^*$.[136] For the complex $[Ru(NH_3)_5$(2,3-dichlorophenyl)cyanamide$]^{2+}$ the solvatochromism of the visible region CT band correlates well with DN[50,51] for a range of polar solvents of widely varying DN.[137]

For a series of phenylcyanamides with different substituents the oscillator strengths of the phenylcyanamide $\rightarrow Ru^{III}$ LMCT transitions correlate with the donor number of the solvent. The difference in oscillator strengths was found to be quite considerable, e.g., an increase in f of over 50% as DN decreases from 30 to about 2. Two of the complexes show linear correlations, while the others show evidence of curvature at low donor number, which is attributed to ion-pairing

effects. Donor solvents are believed to interact with the ammine protons, allowing electron density to move from the N—H bond to the Ru—ammine bond, thus increasing the electron density on the ruthenium. This in turn weakens the π-overlap with the negatively charged cyanamide ligand and decreases the oscillator strength.[139]

2.27.4.3 Bis(bipyridine)(3,4-diamino-3′,4′-diimino-3′,4′-dihydrodiphenyl)ruthenium(II)

The complex bis(bipyridine)(3,4-diamino-3′,4′-diimino-3′,4′-dihydrobiphenyl)ruthenium(II), $[Ru(bpy)_2(dadib)]^{2+}$, which comprises a donor diaminobenzene (opda) unit linked to an acceptor Ru^{II}(bqdi) unit, shows unusual solvatochromic behavior. In certain solvents, such as DMSO, two intense transitions are observed in the visible region, whereas in other solvents (e.g., water) there appears to be only one transition.[141,142] The solvent-induced shifts correlate fairly well with a dual-parameter fit involving the hydrogen-bond acceptor and donor parameters, α and β, of Taft, Kamlet, *et al.*[141] AM1 calculations on a model system using BF_2^+ as a simple acceptor unit in place of $[Ru(bpy)_2]^{2+}$,[141] and extended Hückel calculations on the complex[142] were used to demonstrate that the changes in the spectrum were caused by changes in the dihedral angle of the biphenyl unit, driven by changes in solvent–solute hydrogen bonding to the unbound amino groups at the remote end of the molecule. In donor solvents the amino-group lone pairs tend to conjugate with the opda ring, the ligand tends towards planarity, and a pathway exists for donation of electron density from the donor to the ruthenium. The effective symmetry of the complex is lowered and more than one $Ru(d\pi) \rightarrow \pi^*$ transition has significant intensity. In the presence of acceptors (e.g., water, H^+), the amino groups interact with these in preference to donating into the opda ring, the dihedral angle increases, and the complex resembles $[Ru(bpy)_2(bqdi)]^{2+}$, which has effective C_{2v} symmetry and only one intense, visible-region transition.[143]

2.27.5 CONCLUSION

Solvatochromism provides one of few probes into the nature of the F-C excited state. As such it can, for example, be used to estimate ground- and excited-state dipole moments[19,20,96] There are a number of studies using the electroabsorption or Stark-effect spectroscopy (electrochromism, see Chapter 2.18) and TDCP, which have provided complementary information about changes in dipole moments between ground and excited states for some complexes.[119,144–147] There is also scope for future work integrating studies of solvent effects on absorption spectra with other techniques such as NMR and IR, as well as with information from temperature and pressure effects upon absorption spectra: thermo- and piezo-chromism. Integrated studies with time-resolved resonance Raman spectroscopy, which also probes excited states, may be very worthwhile.[148] (References cited in this concluding section are intended as examples, rather than as an exhaustive list.)

Much remains to be understood about the structure of solvents in solution and the degree of local order caused by interaction with the solute. In particular, theoretical calculation of electronic spectra of coordination compounds in the presence of solvent has been limited to a narrow range of complexes, and mainly to water as a solvent.

Other related kinds of medium-dependent behavior have been observed, such as second-sphere coordination effects (e.g., with crown ethers,[149,150] cyclodextrins[151]), and solvatochromic species have been used as probes of their environment in polymers,[152,153] micelles,[154,155] zeolites,[156] inorganic glasses,[157] and surfaces,[158] etc. They may be used in this way either by virtue of their response to the electric field experienced in a particular environment, or because of specific interactions between the probe and the environment, e.g., hydrogen bonding. Solvatochromism is also a useful predictor of nonlinear optical behavior (see Chapter 9.14), because the same properties which give rise to strong solvatochromism are also necessary for large, second-order, nonlinear optical coefficients (β).[159–162]

2.27.6 REFERENCES

1. Lever, A. B. P. *Inorganic Electronic Spectroscopy*, 2nd ed.; Elsevier: Amsterdam, 1984; pp 208–212.
2. Reichardt, C. *Angew. Chem. Int. Ed. Engl.* **1965**, *4*, 29–40.
3. Hantzsch, A. *Ber. Dtsch. Chem. Ges.* **1922**, *55B*, 953–979.
4. Soukup, R. W.; Schmid, R. *J. Chem. Ed.* **1985**, *62*, 459–462.

5. Bos, J. G.; Lifschitz, I.; Dijkema, K. M. *Z. Anorg. Chem.* **1939**, *242*, 97–116 .
6. Bjerrum, J.; Adamson, A. W.; Bostrup, O. *Acta Chim. Scand.* **1956**, *10*, 329–331.
7. Linert, W.; Fukuda, Y. *Trends Inorg. Chem.* **1999**, *6*, 19–49.
8. Suppan, P. *J. Photochem. Photobiol.* **1990**, *50*, 293–330.
9. Reichardt, C. *Chem. Soc. Rev.* **1992**, 147–153.
10. Reichardt, C. *Chem. Rev.* **1994**, *94*, 2319–2358.
11. Chen, P.; Meyer, T. J. *Chem. Rev.* **1998**, *98*, 1439–1477.
12. Hush, N. S.; Reimers, J. R. *Chem. Rev.* **2000**, *100*, 775–786.
13. Drago, R. S. *J. Chem. Soc., Perkin Trans.* **1992**, *2*, 1827–1838.
14. Bayliss, N. S.; McRae, E. G. *J. Phys. Chem.* **1954**, *58*, 1002–1006.
15. Matyushov, D. V.; Schmid, R.; Ladanyi, B. M. *J. Phys. Chem. B* **1997**, *101*, 1035–1050.
16. Sullivan, B. P. *J. Phys. Chem.* **1989**, *93*, 24–26.
17. Vanhelmont, F. W. M.; Hupp, J. T. *Inorg. Chem.* **2000**, *39*, 1817–1819.
18. Marcus, R. A. *J. Chem. Phys.* **1965**, *43*, 1261–1274.
19. Kober, E. M.; Sullivan, B. P.; Meyer, T. J. *Inorg. Chem.* **1984**, *23*, 2098–2104.
20. Dodsworth, E. S.; Lever, A. B. P. *Chem. Phys. Lett.* **1984**, *112*, 567–570 (*Erratum: Chem. Phys. Lett* **1985**, *116*, 245).
21. Brunschwig, B. S.; Ehrenson, S.; Sutin, N. *J. Phys. Chem.* **1987**, *91*, 4714–4723.
22. Streiff, J.; McHale, J. L. *J. Chem. Phys.* **2000**, *112*, 841–850.
23. Timpson, C. J.; Bignozzi, C. A.; Sullivan, B. P.; Kober, E. M.; Meyer, T. J. *J. Phys. Chem.* **1996**, *100*, 2915–2925.
24. Huertas, S.; Hissler, M.; McGarrah, J. E.; Lachicotte, R. J.; Eisenberg, R. *Inorg. Chem.* **2001**, *40*, 1183–1188.
25. Laurence, C.; Nicolet, P.; Dalati, M. T.; Abboud, J.-L.; Notario, R. *J. Phys. Chem.* **1994**, *98*, 5807–5816.
26. McRae, E. G. *J. Phys. Chem* **1957**, *61*, 562–572.
27. Kirkwood, J. G. *J. Chem. Phys.* **1934**, *2*, 351–361.
28. Ooshika, Y. *J. Phys. Soc. Jpn* **1954**, *9*, 594–602.
29. Lippert, E. *Z. Elektrochem.* **1957**, *61*, 962–975.
30. Mataga, N.; Kaifu, Y.; Koizumi, M. *Bull. Chem Soc. Jpn* **1956**, *29*, 465–470.
31. Bakhshiev, N. G.; Knyazhanskii, M. I.; Minkin, V. I.; Osipov, O. A.; Saidov, G. V. *Russ. Chem. Rev.* **1969**, *38*, 740–754.
32. Block, H.; Walker, S. M. *Chem. Phys. Lett.* **1973**, *19*, 363–364.
33. Rettig, W. *J. Mol. Struct.* **1982**, *84*, 303–327.
34. Brady, J. E.; Carr, P. W. *J. Phys. Chem.* **1985**, *89*, 5759–5766.
35. Kolling, O. W. *J. Phys. Chem.* **1991**, *95*, 3950–3954.
36. Abe, T. *Bull. Chem Soc. Jpn* **1981**, *54*, 327–334.
37. Abe, T. *Bull. Chem Soc. Jpn* **1994**, *67*, 52–55.
38. Onsager, L. *J. Am. Chem. Soc.* **1936**, *58*, 1486–1493.
39. Bayliss, N. S. *J. Chem. Phys.* **1950**, *18*, 292–296.
40. Dodsworth, E. S.; Lever, A. B. P. *Coord. Chem. Rev.* **1990**, *97*, 271–284.
41. Klamt, A. *J. Phys. Chem.* **1996**, *100*, 3349–3353.
42. Aguilar, M. A.; Olivares del Valle, F. J.; Tomasi, J. *J. Chem. Phys.* **1993**, *98*, 7375–7384.
43. Kosower, E. M. *J. Am. Chem. Soc.* **1958**, *80*, 3253–3260.
44. Reichardt, C.; Dimroth, K. *Fortsch. Chem. Forsch.* **1968**, *11*, 1–73.
45. Abboud, J.-L.; Kamlet, M. J.; Taft, R. W. *J. Am. Chem. Soc.* **1977**, *99*, 8325–8327.
46. Kamlet, M. J.; Abboud, J.-L.; Taft, R. W. *J. Am. Chem. Soc.* **1977**, *99*, 6027–6038.
47. Kamlet, M. J.; Abboud, J.-L. M.; Taft, R. W. *Prog. Phys. Org. Chem.* **1981**, *13*, 485–630.
48. Kamlet, M. J.; Abboud, J.-L. M.; Abraham, M. H.; Taft, R. W. *J. Org. Chem.* **1983**, *48*, 2877–2887.
49. Abboud, J.-L. M.; Guiheneuf, G.; Essfar, M.; Taft, R. W.; Kamlet, M. J. *J. Phys. Chem.* **1984**, *88*, 4414–4420.
50. Gutmann, V. *The Donor–Acceptor Approach to Molecular Interactions* **1978**, Plenum: New York.
51. Gutmann, V. *Electrochim. Acta* **1976**, *21*, 661–670.
52. Linert, W.; Gutmann, V. *Coord. Chem. Rev.* **1992**, *117*, 159–183.
53. Linert, W.; Taha, A. *J. Coord. Chem.* **1993**, *29*, 265–276.
54. Fukuda, Y.; Mafune, K.; Nakagawa, H.; Linert, W. *J. Coord. Chem.* **1994**, *33*, 123–136.
55. Manuta, D. M.; Lees, A. J. *Inorg. Chem.* **1983**, *22*, 3825–3828.
56. Walther, D. *J. Prakt. Chem.* **1974**, *316*, 604–614.
57. Kaim, W.; Olbrich-Deussner, B.; Roth, T. *Organomets.* **1991**, *10*, 410–415.
58. Tomasi, J.; Persico, M. *Chem. Rev.* **1994**, *94*, 2027–2094.
59. Cramer, C. J.; Truhlar, D. G. *Chem. Rev.* **1999**, *99*, 2161–2200.
60. Stavrev, K. K.; Zerner, M. C.; Meyer, T. J. *J. Am. Chem. Soc.* **1995**, *117*, 8684–8685.
61. Shin, Y.-G. K.; Brunschwig, B. S.; Creutz, C.; Newton, M. D.; Sutin, N. *J. Phys. Chem.* **1996**, *100*, 1104–1110.
62. Zeng, J.; Hush, N. S.; Reimers, J. R. *J. Am. Chem. Soc.* **1996**, *118*, 2059–2068.
63. Sizova, O. V.; Baranovski, V. I.; Ivanova, N. V.; Panin, A. I. *Int. J. Quant, Chem.* **1997**, *63*, 853–860.
64. Ferretti, I.; Cacelli, A. *J. Chem. Phys.* **1998**, *109*, 8583–8590.
65. Cacelli, A.; Ferretti, I. *J. Phys. Chem. A* **1999**, *105*, 4438–4445.
66. Pearl, G. M.; Zerner, M. C. *J. Am. Chem. Soc.* **1999**, *121*, 399–404.
67. Streiff, J. H.; Edwards, W. D.; McHale, J. L. *Chem. Phys. Lett.* **1999**, *312*, 369–375.
68. Stavrev, K. K.; Tamm, T.; Zerner, M. C. *Int. J. Quant, Chem.* **1996**, *60*, 1585–1594.
69. Sone, K.; Fukuda, Y. *Rev. Inorg. Chem.* **1990**, *11*, 123–153.
70. Linert, W. *J. Chem. Inf. Comput. Sci.* **1992**, *32*, 221.
71. Taha, A.; Linert, W.; Fukuda, Y. *J. Coord. Chem.* **1993**, *30*, 53–62.
72. Tsiamis, C; Hatzidimitriou, A. G.; Tzavellas, L. C. *Inorg. Chem.* **1998**, *37*, 2903–2909.
73. Tsiamis, C.; Jannakoudakis, P. D.; Sachsinger, N.; Hennig, H. *Electrochem. Acta* **1993**, *38*, 2623–2630.
74. Tsiamis, C.; Youri-Tsochatzi, C.; Hatzidimitriou, A.; Gourdon, A. *Inorg. Chem. Acta* **1995**, *237*, 93–102.
75. Miyamae, H.; Kudo, H.; Hihara, G.; Sone, K. *Bull. Chem. Soc. Jpn* **1998**, *71*, 2621–2627.
76. Tsiamis, C.; Themeli, M. *Inorg. Chem. Acta* **1993**, *206*, 105–115 .

77. Berger, S. *Z. Phys. Chem.* **2002**, *216*, 1363–1364.
78. Linert, W.; Fukuda, Y.; Camard, A. *Coord. Chem. Rev.* **2001**, *218*, 113–152.
79. Linert, W.; Jameson, R. F.; Taha, A. *J. Chem. Soc., Dalton Trans.* **1993**, 3181–3186.
80. Bourdin, D.; Lavabre, D.; Beteille, J. P.; Levy, G.; Micheau, J. C. *Bull. Chem. Soc. Jpn* **1990**, *63*, 2985–2990.
81. Fukuda, Y.; Cho, M.; Sone, K. *Bull. Chem. Soc. Jpn* **1989**, *62*, 51–55.
82. Selbin, J.; Morpurgo, L. *J. Inorg. Nucl. Chem.* **1965**, *27*, 673–678.
83. Ebraheem, K. A. K.; Hamdi, S. T.; Asker, K. A.; Al-Sadoon, A. W. *Monats. Chem.* **1989**, *120*, 509–514.
84. Ebraheem, K. A. K.; Fahad, T. A. *Can. J. Spectr.* **1989**, *34*, 15–18.
85. Tsiamis, C.; Voulgaropoulos, B.; Charistos, D.; Voutsas, G. P.; Kavounis, C. A. *Polyhedron* **2000**, *19*, 2003–2010.
86. Ebraheem, K. A. K.; Hamdi, S. T.; Al-Duhan, I. A. *J. Saudi Chem. Soc.* **2002**, *6*, 245–256.
87. Sone, K.; Fukuda, Y. In *Ions and Molecules in Solution*; N. Tanaka, *et al.* Eds.; Elsevier: Amsterdam, 1983.
88. Linert, W.; Gutmann, V.; Sotriffer, A. *Vib. Spectrosc.* **1990**, *1*, 199–204.
89. Sone, K.; Fukuda, Y. In *Inorganic Chemistry Concepts*; Springer: Berlin, 1987; Vol. 10.
90. Linert, W.; Herlinger, E.; Margl, P.; Boca, R. *J. Coord. Chem.* **1993**, *28*, 1–16.
91. Selbin, J. *Chem. Rev.* **1965**, *65*, 153–175.
92. Gutmann, V.; Mayer, U. *Monatsh. Chem.* **1968**, *99*, 1383–1389.
93. Juris, A.; Balzani, V.; Barigelletti, F.; Campagna, S.; Belser, P.; von Zelewsky, A. *Coord. Chem. Rev.* **1988**, *84*, 85–277.
94. Milder, S. J. *Inorg. Chem.* **1989**, *28*, 868–872.
95. Stufkens, D. J. *Coord. Chem. Rev.* **1990**, *104*, 39–112 and references therein.
96. Saito, H.; Fujita, J.; Saito, K. *Bull. Chem. Soc. Jpn* **1968**, *41*, 863–874.
97. Balk, R. W.; Stufkens, D. J.; Oskam, A. *Inorg. Chem. Acta* **1978**, *28*, 133–143.
98. Burgess, J. *J. Organomet. Chem.* **1969**, *19*, 218–220.
99. Burgess, J.; Chambers, J. G.; Haines, R. I. *Trans. Met. Chem.* **1981**, *6*, 145–151.
100. bin Ali, R.; Burgess, J.; Kotowski, M.; van Eldik, R. *Trans. Met. Chem.* **1987**, *12*, 230–235.
101. Baxter, P. N. W.; Connor, J. A. *J. Organomet. Chem.* **1969**, *486*, 115–121.
102. Ernst, S.; Kaim, W. *J. Am. Chem. Soc.* **1986**, *108*, 3578–3586.
103. Kaim, W.; Kohlmann, S.; Ernst, S.; Olbrich-Deussner, B.; Bessenbacher, C.; Schultz, A. *J. Organomet. Chem.* **1987**, *321*, 215–226.
104. tom Dieck, H.; Renk, I. W. *Angew. Chem. Int. Ed. Engl.* **1970**, *9*, 793–795.
105. Manuta, D. M.; Lees, A. J. *Inorg. Chem.* **1986**, *25*, 3212–3218.
106. Zulu, M. M.; Lees, A. J. *Inorg. Chem.* **1988**, *27*, 3325–3331.
107. Kaim, W.; Kohlmann, S. *Inorg. Chem.* **1986**, *25*, 3306–3310.
108. Dodsworth, E. S.; Lever, A. B. P. *Inorg. Chem.* **1990**, *29*, 499–503.
109. Granifo, J.; Vargas, M. E.; Dodsworth, E. S.; Farrar, D. H.; Fielder, S. S.; Lever, A. B. P. *J. Chem. Soc., Dalton Trans.* **1996**, 4369–4378.
110. Miller, T. R.; Dance, I. G. *J. Am. Chem. Soc.* **1973**, *95*, 6970–6979.
111. Chen, C.-T.; Liao, S.-Y.; Lin, K.-J.; Chen, C.-H.; Lin, T.-Y. J. *Inorg. Chem.* **1999**, *38*, 2734–2741.
112. Zuleta, J. A.; Chesta, C. A.; Eisenberg, R. *J. Am. Chem. Soc.* **1989**, *111*, 8916–8917.
113. Bevilacqua, J. M.; Eisenberg, R. *Inorg. Chem.* **1994**, *33*, 2913–2923.
114. Cummings, S. D.; Eisenberg, R. *Inorg. Chem.* **1995**, *34*, 2007–2014.
115. Cummings, S. D.; Eisenberg, R. *J. Am. Chem. Soc.* **1996**, *118*, 1949–1960.
116. Paw, W.; Lachicotte, R. J.; Eisenberg, R. *Inorg. Chem.* **1998**, *37*, 4139–4141.
117. Zuleta, J. A.; Bevilacqua, J. M.; Proserpio, D. M.; Harvey, P. D.; Eisenberg, R. *Inorg. Chem.* **1992**, *31*, 2396–2404.
118. Crosby, G. A.; Kendrick, K. R. *Coord. Chem. Rev.* **1998**, *171*, 407–417.
119. Vanhelmont, F. W. M.; Johnson, R. C.; Hupp, J. T. *Inorg. Chem.* **2000**, *39*, 1814–1816.
120. Al-Alousy, A.; Burgess, J. *Inorg. Chem. Acta* **1990**, *169*, 167–170.
121. Linert, W.; Jameson, R. F.; Bauer, G.; Taha, A. *J. Coord. Chem.* **1997**, *42*, 211–229.
122. Schilt, A. A. *J. Am. Chem. Soc.* **1963**, *85*, 904–908.
123. Shriver, D. F.; Posner, J. *J. Am. Chem. Soc.* **1966**, *88*, 1672–1677.
124. Toma, H. E.; Takasugi, M. S. *J. Soln. Chem.* **1983**, *12*, 547–561.
125. Burgess, J. *Spec. Acta* **1970**, *26A*, 1369–1374.
126. Burgess, J. *Spec. Acta* **1970**, *26A*, 1957–1962.
127. Reichardt, C. *Solvents and Solvent Effects in Organic Chemistry*, 2nd ed. **1988**, Verlag Chemie: Weinheim, Germany.
128. Gutmann, V.; Resch, G. *Monats. Chem.* **1988**, *119*, 1251–1261.
129. Schmid, R.; Sapunov, V. N. In *Non–formal Kinetics*; Ebel, H. F. (Ed.); Verlag Chemie: Weinheim, Germany, 1982; *Monographs in Modern Chemistry*, Vol. 14.
130. Bignozzi, C. A.; Chiorboli, C.; Indelli, M. T.; Rampi Scandola, M. A.; Varani, G.; Scandola, F. *J. Am. Chem. Soc.* **1986**, *108*, 7872–7873.
131. Kato, M.; Yamauchi, S.; Hirota, N. *J. Phys. Chem.* **1989**, *93*, 3422–3425.
132. Maruyama, M.; Matsuzawa, H.; Kaizu, Y. *Inorg. Chem.* **1995**, *34*, 3232–3240.
133. Curtis, J. C.; Sullivan, B. P.; Meyer, T. J. *Inorg. Chem.* **1983**, *22*, 224–236.
134. Metcalfe, R. A.; Lever, A. B. P. *Inorg. Chem.* **1997**, *36*, 4762–4771.
135. Broo, A.; Larsson, S. *Chem. Phys* **1992**, *161*, 363–378.
136. Crutchley, R. J.; Naklicki, M. L. *Inorg. Chem.* **1989**, *28*, 1955–1958.
137. Saleh, A. A.; Crutchley, R. J. *Inorg. Chem.* **1990**, *29*, 2132–2135.
138. Crutchley, R. J.; McCaw, K.; Lee, F. L.; Gabe, E. J. *Inorg. Chem.* **1990**, *29*, 2576–2581.
139. Crutchley, R. J.; Saleh, A. A.; McCaw, K.; Aquino, M. A. S. *Mol. Cryst. Liq. Cryst.* **1991**, *194*, 93–101.
140. Naklicki, M. L.; Crutchley, R. J. *J. Am. Chem. Soc.* **1994**, *116*, 6045–6046.
141. Metcalfe, R. A.; Dodsworth, E. S.; Lever, A. B. P.; Pietro, W. J.; Stufkens, D. J. *Inorg. Chem.* **1993**, *32*, 3581–3582.
142. Metcalfe, R. A.; Dodsworth, E. S.; Fielder, S. S.; Stufkens, D. J.; Lever, A. B. P.; Pietro, W. J. *Inorg. Chem.* **1996**, *35*, 7741–7750.
143. Masui, H.; Lever, A. B. P.; Dodsworth, E. S. *Inorg. Chem.* **1993**, *32*, 258–267.
144. Reimers, J. R.; Hush, N. S. *J. Phys. Chem.* **1991**, *95*, 9773–9781.

145. Oh, D. H.; Sano, M.; Boxer, S. G. *J. Am. Chem. Soc.* **1991**, *113*, 6880–6890.
146. Bublitz, G. U.; Boxer, S. G. *Ann. Rev. Phys. Chem.* **1997**, *48*, 213–242.
147. Vance, F. W.; Williams, R. D.; Hupp, J. T. *Int. Rev. Phys. Chem.* **1998**, *17*, 307–329.
148. Turro, C.; Bossman, S. H.; Leroi, G. E.; Barton, J. K.; Turro, N. J. *Inorg. Chem.* **1994**, *33*, 1344–1347.
149. Ballardini, R.; Gandolfi, M. I.; Prodi, L.; Ciano, M.; Balzani, V.; Kohnke, F. H.; Shahriari-Zavareh, H.; Spencer, N.; Stoddart, J. F. *J. Am. Chem. Soc.* **1989**, *111*, 7072–7078.
150. Ando, I.; Ishimura, D.; Ujimoto, K.; Kurihara, H. *Inorg. Chem.* **1996**, *35*, 3504–3508.
151. Johnson, M. D.; Reinsborough, V. C.; Ward, S. *Inorg. Chem.* **1992**, *31*, 1085–1087.
152. Kotch, T. G.; Lees, A. J.; Fuerniss, S. J.; Papathomas, K. I.; Snyder, R. *Inorg. Chem.* **1991**, *30*, 4871–4872.
153. de Buyl, F.; Kirsch-De Mesmaeker, A.; Tossi, A.; Kelly, J. M. *J. Photochem. Photobiol. A: Chem.* **1991**, *60*, 27–45.
154. Thorp, H. H.; Kumar, C. V.; Turro, N. J.; Gray, H. B. *J. Am. Chem. Soc.* **1989**, *111*, 4364–4368.
155. Blandamer, M. J.; Burgess, J.; Shraydeh, B. *J. Chem. Soc., Faraday Trans.* **1993**, *89*, 531–533.
156. Dutta, P. K.; Turbeville, W. *J. Phys. Chem.* **1991**, *95*, 4087–4092.
157. McKiernan, J.; Pouxviel, J.-C.; Dunn, B.; Zink, J. I. *J. Phys. Chem.* **1989**, *93*, 2129–2133.
158. Zimmermann, Y.; Spange, S. *New J. Chem.* **2002**, *26*, 1179–1184.
159. Coe, B. J.; Chamberlain, M. C.; Essex-Lopresti, J. P.; Gaines, S.; Jeffery, J. C.; Houbrechts, S.; Persoons, A. *Inorg. Chem.* **1997**, *36*, 3284–3292.
160. Paley, M. S.; Harris, J. M.; Looser, H.; Baumert, J. C.; Bjorklund, G. C.; Jundt, D.; Twieg, R. J. *J. Org. Chem.* **1989**, *54*, 3774–3778.
161. Bosshard, C.; Knöpfle, G.; Prêtre, P.; Günter, P. *J. Appl. Phys.* **1992**, *71*, 1594–1605.
162. Simon, J.; Bassoul, P.; Norvez, S. *New J. Chem.* **1989**, *13*, 13–31.

Comprehensive Coordination Chemistry II
ISBN (set): 0-08-0437486

Volume 2, (ISBN 0-08-0443249); pp 351–365

2.28
Mass Spectrometry

D. ZAGOREVSKII
Rensselaer Polytechnic Institute, Troy, NY, USA

2.28.1 GENERAL 367
2.28.1.1 Introduction 367
2.28.1.2 Methods of Ionization and Mass Analysis 368
2.28.1.3 Analytical Information from Mass Spectral Data 370
2.28.2 MASS SPECTROMETRY IN COORDINATION CHEMISTRY 372
2.28.2.1 Analytical Applications of Mass Spectrometry 372
2.28.2.2 Interpretation of Mass Spectra of Metal Compounds 373
2.28.2.3 Thermochemistry of Organometallic Molecules and Ions 374
2.28.2.4 Chemistry of Metal–Ligand Bonds 375
2.28.2.5 Transformations of Molecules on Charged Metal Centers 376
2.28.2.6 Gas-phase Metal Negative Ion Chemistry 376
2.28.2.7 Elusive Neutral Organometallics Generated from Ions 377
2.28.2.8 Contributions of Coordination Chemistry to Mass Spectrometry 377
2.28.3 REFERENCES 378

2.28.1 GENERAL

2.28.1.1 Introduction

Mass spectrometry[1–10] is one of the most powerful modern physical-chemical methods for identifying compounds, and for studying their structure and reactivity. Recent developments in ionization and ion separation have made it possible to apply this technique to a wide range of individual compounds and mixtures. Mass spectrometry has a wide range of applications because of its sensitivity and selectivity. Mass spectrometers are used to solve a variety of analytical problems, ranging from molecular weight and elemental composition determination,[11,12] to the characterization of structures of complex bio-organic molecules and the analysis of polymers.[13] Isotope analyses can be performed on inorganic and organic substances. Mass spectrometry is the method of choice for many environmental,[14] industrial,[15] clinical,[16] and forensic[17] analyses. The determination of atom connectivities in simple and complex molecules, the elucidation of amino-acid sequences, and other structural applications have became a routine application of this technique. Importantly, mass spectrometry is a key technique in the expanding field of proteomics.[18–22]

Two general types of the application of mass spectrometry should be emphasized. One is the detection and characterization of compounds introduced into the mass spectrometer. In this case the mass spectrometer can be considered as a powerful detector. It is able to characterize individual compounds, or work online with (chromatographic) separation techniques.[23–27] Many applications of mass spectrometry, including analytical aspects, are based on the fact that this method involves physical or chemical transformations of the compounds being studied. These transformations may include evaporation, desolvation, electron transfer to or from the analyte, and chemical transformations before or after ionization. Chemical transformation can involve the formation of new bonds, or bond cleavage in ions of the compound under study.

The ability of mass spectrometry to induce chemical transformations makes this method a unique technique for obtaining information about the intrinsic properties of isolated ions and molecules, solvates, clusters, non-covalent complexes, etc. Mass spectrometry is a convenient method for measuring basic thermochemical values of neutral molecules, ions, and radicals. Various molecular properties, such as ionization energy, proton affinity, electron affinity, energy of solvation/desolvation, and bond dissociation energy can be directly measured in the gas phase by mass spectrometric methods (see also Chapter 2.12).

Every mass spectrometry experiment involves the following principal steps: the sample (analyte) is transferred to the ion source of the mass spectrometer; ions of the analyzed compound are generated and transformed to the gas phase; ions are separated and analyzed according to their mass-to-charge ratio; the ions are detected; and the corresponding signals are recorded, stored, and converted into a mass spectrum. Analyzers and detectors must operate at low pressures of 10^{-3}–10^{-9} Torr, which requires powerful vacuum-pumping systems. This is essential for a successful mass analysis, as collisions between the ions and background molecules must be prevented. A generalized layout of a mass spectrometer is shown in Figure 1.

2.28.1.2 Methods of Ionization and Mass Analysis

The delivery of a compound or a mixture of compounds to the ion source can be achieved in different ways, including batch (heatable-reservoir, direct probe); membrane and chromatographic inlets (gas chromatography (GC), thin-layer chromatography (TLC); high-performance liquid chromatography (HPLC); supercritical fluid chromatography; and capillary electrophoresis (CE)). Ions are formed and/or transferred at the ion source. In some cases, the sample delivery system and the ion source form the same instrumental unit. Different types of ion sources have been designed to enable the ionization of various types of compounds, and to accommodate

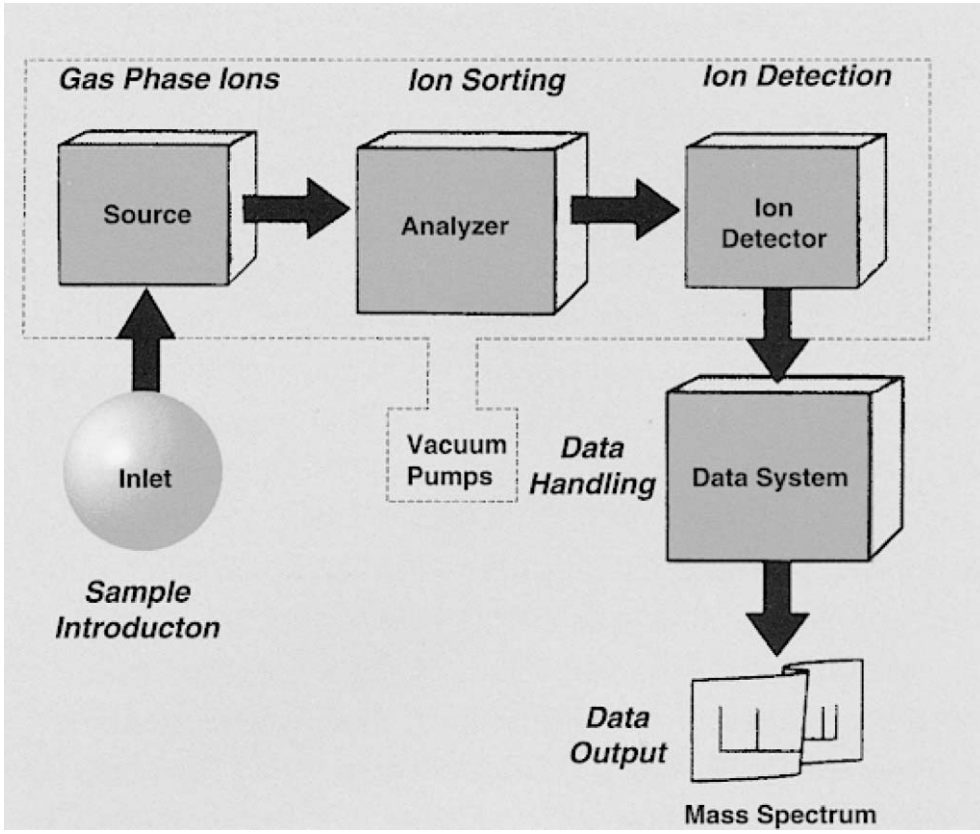

Figure 1 The components of a mass spectrometer (reproduced by permission of the American Society for Mass Spectrometry from *What is Mass Spectrometry?* **1998**).

various types of interfaces for the delivery of ions into the gas phase. As a result, mass spectrometry allows the analysis of various types of molecule in various physical and chemical states, including gases, volatile and non-volatile liquids and solids, non-polar and ionic molecules, compounds having various thermal stabilities, different molecular weights, etc.

All modern mass spectrometers are operated and controlled by computers. Their primary purpose is to transform the results to the form of a mass spectrum—a graph of ion intensity as a function of mass-to-charge ratio. The computers on modern mass spectrometers also perform a variety of other functions, such as regimes of ionization, transmission of ions through the mass spectrometer, separation and detection of ions, and collection and interpretation of the data. They often control the delivery of analytes into the mass spectrometer.

Ionization is a critical step in any mass spectrometric experiment. For substances existing in the ionized form, the ions must be delivered to the gas phase. For uncharged analytes, two general approaches can be used for producing ions in the gas phase. In the first approach, neutral molecules are delivered to the gas phase and then ionized. The second approach is based on making the ions in the condensed phase and delivering them to the gas phase.

Ionization methods[28] that are based on the first approach are electron ionization (EI),[4,28,29] resonance electron capture (REC),[30,31] chemical ionization (CI),[32] negative ion chemical ionization (NICI),[33,34] field ionization (FI),[35] atmospheric pressure chemical ionization (APCI),[36] photoionization (PI),[37] and thermospray ionization (TSP).[38] In the EI method, gaseous molecules are ionized by interaction with high-energy (30–100 eV) electrons. The internal energy of molecular radical-ions ($M^{\cdot+}$) often exceeds their dissociation limit(s). As a result, EI mass spectra usually display intense peaks of fragment ions. Photoionization involves the interaction of gaseous molecules with photons. Molecular ions are usually observed. The degree of their fragmentation depends on the energy of the ionizing photons. In the REC method, molecules react with low-energy (usually 0–10 eV) electrons. If the electron affinity of the analyte is negative, than negatively charged molecular ions ($M^{\cdot-}$) are generally observed. Chemical ionization methods are based on the interaction between neutral molecules of the analyte and reactant ions in the gas phase. These interactions involve various types of processes that can be designed for specific purposes. For example, negatively charged reactant ions may transfer an electron to a molecule if the latter has a higher electron affinity. The opposite process, the transfer of an electron from the molecule to a positively charged reactant ion, takes place if the ionization energy of the molecule is lower than that of the neutral counterpart of the reactant. The most common type of chemical ionization reaction is a transfer of a charged species from the reactant ion to a molecule. Other reactions, taking place in CI conditions, result in the formation of charged adducts, deprotonation, abstraction of a hydrogen atom or other atoms from the neutral molecule. These reactions may occur in a diluted gas phase (CI, NICI) or at atmospheric pressure (APCI, TSP). In APCI, primary ions are formed by corona discharge. These ions ionize solvent molecules, which further react with molecules of analytes. The TSP method is based on the co-evaporation of analyte and some ionic compound (e.g., ammonium acetate) from solution to the gas phase, where reactions between neutral molecules and the ions take place and the ionization occurs. In FI, a molecule in the vapor state is ionized in the strong electric field.

The other approach to making ions is ionization in the condensed phase and delivering ions to the gas phase. One of the most popular methods of this type is electrospray ionization (ESI; see also Section 2.28.2).[39,40] In this technique, ions are formed in solution and then electrosprayed to the gas phase, where desolvation takes place prior to mass analysis. A variety of desorption ionization (DI) methods is used for the analysis of nonvolatile samples. Ions can be formed and desorbed from solution or from the solid phase by applying strong electric fields (field desorption, FD);[35,41] bombarding the sample by fast-moving atoms (fast-atom bombardment, FAB)[42,43] or ions (secondary ion mass spectrometry, SIMS);[42,43] by heavy-atom (^{252}Cf) fission products (plasma desorption, PD);[44,45] or by a laser beam (laser desorption, LD, or matrix-assisted laser desorption ionization, MALDI).[46–48] In these methods, ionization may take place either in the condensed phase, followed by evaporation of the ions; in the gas phase, as a result of interactions with matrix ions; or in a supercompressed gas.

Separation of ions according to their mass-to-charge ratio is another basic step in each mass spectral experiment. This can be done using magnetic (B) or electrostatic (E) analyzers (sector instruments);[5,6,26,28] quadrupole mass filter (Q)[49] or quadrupole ion trap analyzer (ITD);[50] ion cyclotron resonance (ICR)[51–53] cells; or by time-of-flight (TOF)[54] analyzers. Combinations of various mass analyzers are used to achieve high resolution, mass accuracy, or other parameters. Each type of mass analyzer has its advantages and limitations (Table 1). For example, commercial quadrupole filters or ion traps have a limited mass range (up to 2,000–4,000 Da) and a rather

Table 1 Characteristics of the most popular mass analyzers.

Mass analyzer	*Quantity Measured*	*Mass/Mass-to-charge ranges*	*Resolution at 1,000 Da/charge*	*Mass measurement accuracy*	*Dynamic range*	*Operating pressure* (Torr)	*Cost*
Sector magnet	Momentum/Charge	100,000/10^4	10^5	<5 ppm	10^7	10^{-6}	$$$$
Time-of- flight	Flight time	Unlimited/10^6	10^3–10^4	0.1–0.01%	10^4	10^{-6}	$$
Quadrupole ion trap	Frequency	4,000/10^4–10^5	10^3–10^4	0.1%	10^4	10^{-3}	$
Quadrupole	Filters for m/z	4,000/10^4–10^5	10^3	0.1%	10^5	10^{-5}	$
Cyclotron resonance	Frequency	~10,000/10^5	10^6	<10 ppm	10^4	10^{-9}	$$$$

poor mass resolution. However, these mass analyzers have some valuable advantages, such as the ability to work at relatively high pressure, which makes it easy to couple them with ionization techniques operating at atmospheric pressure. Quadrupole analyzers are usually the first choice in experiments, involving GC and HPLC separation of mixtures. Quadrupole filters are more convenient than quadrupole ion traps when compounds of unknown masses are being analyzed. At the same time, ion traps can achieve very high sensitivity and low detection limits in the analysis of known target compounds. Compared with quadrupoles, ion traps have a limited application in quantitative analyses.

Magnetic analyzers are often used in various combinations with electrostatic sectors. Sector instruments are characterized by good ion transmission. Depending on the order of these analyzers, very high resolution and wide mass ranges can be achieved. Sector instruments suffer from a relatively low scan rate, which makes their application in GC-MS and LC-MS studies somewhat limited. At the same time, some types of tandem mass spectrometry experiments with mass-selected ions[55–57] can be performed only on this type of equipment.

High resolution is a superior property of FTICR instruments. This type of mass analyzer also has exclusive advantages when it comes to studies of ion-molecule reactions.

TOF analyzers are characterized by simplicity, high sensitivity, high ion transmission, high spectrum acquisition rate, and the ability to determine very high molecular masses. Although the dynamic range and resolution of conventional TOF analyzers are relatively low, the resolution can be significantly improved by using reflectron mode, resulting in a mass accuracy in the range of 0.1–0.01%.

Some ionization techniques (EI, FAB, and SIMS) are compatible with all mass analyzers. PD, LD, and MALDI are most suited to TOF analyses. Atmospheric pressure ionization methods (TSP, ESI, APCI) are best coupled with quadrupole and ion trap instruments. Sector and FTICR instruments can also operate with chromatographic interfaces; however, a significant reduction of pressure in the system is required. Consequently, in FTICR, the ion source and the ICR cells must be separated by a distance of about 1 m. Powerful ion optics is required for the transmission of ions for these long distances. This inconvenience, however, is offset by the advantages of FTICR, such as extremely high resolution and the ability to store the ions of interest for long periods.

2.28.1.3 Analytical Information from Mass Spectral Data

Various types of analytical information about the analyzed molecule can be obtained using mass spectrometry. The determination of the molecular weight is one of the most common goals. The observation of molecular species (molecular ions, molecular adducts, or ions formed by a loss of specific neutrals from the analyzed and ionized molecule) are often sufficient proof for the presence of the desired molecule. Accurate mass measurements of molecular species provide information about the elemental composition of ions and their precursor molecules; consequently, mass spectrometry has largely replaced traditional elemental analysis. Mass spectrometry is a powerful technique for both qualitative and quantitative analyses. GC, HPLC, TLC, and CE are separation techniques compatible with mass spectrometry. When combined with such chromatographic methods, mass spectrometry becomes a unique method for the identification of submicromolar quantities of analytes.

Mass spectrometry is a convenient method for identifying structures of compounds, either in their pure form or in mixtures. It should be noted that in mass spectrometry "structure" refers to atom and group connectivity, rather than to bond distances and bond angles. Also, the elucidation of structures of ions is performed by inducing their chemical transformations and detecting the reaction products. In other words, a mass spectrometer should be considered as a mini-chemical laboratory, in which ions can be produced and their structure and reactivity can be studied.

Some ionization methods (EI, CI) can directly provide information about an ion's structure by producing unimolecular dissociations (simple bond cleavage and rearrangements) of energy-rich molecular ions. The atom/group connectivity in the parent ion can usually be reconstructed from the analysis of the dissociation pathways. Other ionization methods may or may not result in fragmentation of molecular ions or other molecular species. If such fragmentation does take place, it often results in product ions that cannot be used for unequivocal identification. In ESI and APCI, fragmentation of ions can be forced by additional acceleration of the ions through the region between the ion source and the mass analyzer. Collisions (in-source dissociation) of these ions with residual air or solvent molecules may induce some structure-specific fragmentation. The assignment of fragments to precursor ions in all these cases may be questionable if the sample is not pure and when the background is high. Experiments with mass-selected ions are the most suitable approach to the investigation of structures and group connectivity in gas phase ions.

Tandem mass spectrometry methods[10,55–57] (also abbreviated as MS/MS or MS^n) are used to characterize individual compounds in mixtures or to determine an individual compound's structure. They are based on the separation of the ions of interest from all other ions, both in space and in time. Separation in space is achieved by coupling two or more mass analyzers, such as BE, EBE, QQ, BEE, etc. Separation in time is achieved using a single mass analyzer (ion trap or ICR), which performs two steps of mass analysis. Once mass separation is completed, various types of experiment can be performed in order to identify the structures of the ions. In a traditional MS/MS experiment, dissociation products of mass-selected ions are detected. However, different types of experiment, such as the detection of precursor ions for a specific fragment and the identification of ions that have lost a neutral fragment of specific mass, are often available.

Ions having internal energies slightly exceeding their dissociation limit may (metastably) decompose (fragmentation rate constants 10^5–$10^6\,s^{-1}$) during the flight from the ion source to the detector. Metastable ion studies[55] can be performed on sector and TOF (post-source dissociation) instruments. Metastable ions may provide useful information about ion structures, but usually represent reactions with the lowest activation energies.

Additional energy is necessary to initiate dissociation pathways with higher activation energies. Collision-induced dissociation (CID), also known as collisional activated dissociation (CAD), can be achieved by collision of the mass-selected ions with a neutral target gas (He, Ar, or others).[58] Two collision-induced activation regimes can be used. Low-energy collisions (<200 eV) are observed on triple-quadrupole, ion trap, and ICR instruments. Excitation results mainly in higher vibrational states. The CID mass spectra obtained on these instruments are sensitive to the nature of the target gas. The efficiency of low-energy collisions for high-mass ions is rather poor.

High-energy collisions (up to 10 keV of translational energy) are accessible on sector and time-of-flight instruments. The excitation energy is rapidly converted into various vibrational modes of the excited ions, inducing their extensive fragmentation. This type of collision experiment is very efficient when high-energy fragmentation pathways must be observed, or if high-mass ions are to be analyzed.

Other methods of activation of stable ions are used in structural analysis. The ions can be collided with a surface (surface-induced dissociation, SID), reacted with electrons, or subjected to photodissociation.[59]

Ion–molecule reactions[60,61] are a true chemical way of identifying ion structures in the gas phase. These reactions are often more structure specific than metastable or collision-induced dissociations. Ion–molecule reactions can be applied to the identification of structural, geometrical, and stereo isomers.[62] Conclusions about structures can be made from the qualitative analyses of reaction products, or by measuring the kinetics and thermodynamics of the processes. Ion traps and ICR spectrometers are the best for studying ion–molecule reactions, because they permit reactions to be monitored over a long period of time. At the same time, various instruments and techniques, such as flowing afterglow and selected-ion flow tube,[63] Knudcen cell mass spectroscopy,[64] and others, can be successfully applied to the investigation of ion–molecule interactions.

In conclusion, the choice of ionization method and mass analyzer usually depends on the nature of the analyte and the particular purpose of the experiment, but they should be compatible with

each other. The characterization of an unknown compound usually requires the use of a combination of several mass spectrometry techniques. Structural information about the compound can be obtained by a variety of methods based on a study of the reactivity of ions in the gas phase.

2.28.2 MASS SPECTROMETRY IN COORDINATION CHEMISTRY

2.28.2.1 Analytical Applications of Mass Spectrometry

Mass spectrometry has made significant contributions to coordination and organometallic chemistry.[65–87] One of the most important applications of mass spectrometry is the determination of the molecular weight and elemental composition of metal compounds, and identification of their structure. Mass spectrometry was first applied to the analysis of relatively volatile metal complexes using electron impact and chemical ionization techniques. Further development of ionization techniques has made it possible to analyze and to study the structure of a wide range of organometallics, including nonvolatile, ionic, multiply charged, polymetallic, and high-molecular-weight derivatives. Some of the above ionization techniques allow identification of metal-containing intermediates directly from the condensed phase[88–91] (see also Chapter 2.30) providing beneficial information about reaction mechanisms.

A typical procedure for mass spectral characterization of an unknown metal complex by mass spectral methods includes several stages. The determination of the molecular weight of the analyte is a first step. The molecular weight can be obtained from the observation of "molecular species." The latter may be positively or negatively, singly or multiply charged molecular ions, ions of protonated (MH^+) or deprotonated ($[M–H]^-$) molecules, or adducts of M with various positively or negatively charged ions. The type of molecular species produced depends on the ionization mode and can be predicted in most cases. The use of more than one ionization technique greatly benefits the correct identification of the molecular ion. The nonobservation of the (expected) molecular ions is often overlooked and considered as a failed identification of the (metal) compound. In many of these cases, however, the analysis of the whole set of mass spectral data may provide the necessary information for positive identification of the molecule without the observation of $M^{\cdot+}$ or $M^{\cdot-}$ ions.

Volatile and thermally stable complexes can be analyzed by EI, CI, APCI, and TSP methods. ESI is a likely first choice for analysis of nonvolatile and thermally unstable molecules. Most ionic compounds can be directly analyzed in the ESI. Several approaches can be employed for the ionization of neutral metal-containing complexes.[88–91] They include either oxidation or reduction of the metal atom, which may be achieved in an electrochemical cell or using metal electrospray capillary as an electrode. Chemical derivatization of complexes, including ligand removal or substitution reactions, quaternization of nitrogen or phosphorus atoms in ligands, and metallation of complexes using metal ions, are common ways to make metal-containing molecules amenable for ESI analysis.

Desorption methods are also useful for the ionization of both ionic and neutral molecules. FD, LD, FAB, and SIMS have been used for the characterization of nonvolatile metal complexes.[92,93] MALDI is probably the most convenient method for analysis of high-molecular-weight analytes, such as complex biomolecules, metal-containing polymers, etc.

After the molecular weight has been deduced, the elemental composition of the molecular ion can be determined. The isotope distribution of peaks of the molecular ion may provide a thorough preliminary evaluation of the quantity and type of metal atoms. This analysis is based on the fact that most metal atoms have specific isotope distributions. The next step towards the determination of the elemental composition is to measure accurate mass(es) of the molecular ion(s). These measurements require a mass analyzer with appropriate mass resolution. Sector instruments, TOF mass spectrometers, and ICR spectrometers are the most suitable for accurate mass measurement.

Detailed information about the structure of the metal complex can be obtained by using various mass spectral resources. Processes of electron attachment and removal, e.g., ionization and redox reactions, may give an insight about the oxidation state of the metal, its coordination saturation, and the number of ligands in the coordination sphere. However, the most convenient and direct way of elucidating structures of ions in mass spectrometry can be achieved by studying their reactivity. Two general types of reactions are used for this purpose. One of them is unimolecular dissociation of mass-selected ions of interest. Ions that are formed with a small excess of internal energy above their dissociation limit may fragment on the flight from the ion

source to detector. These transitions provide information about the weakest bonds in the ion. For stable ions, a variety of methods can be applied to increase the internal energy of the ions and to induce their dissociation. The other type of process that is used for studying atom connectivities in gas-phase, metal-containing ions includes reactions of these ions with neutral molecules.

The most common question that is addressed in the elucidation of the structure of organometallic compounds is what the ligands are that surround the central metal atom(s). A common approach to this problem is to break the metal–ligand bond(s). This dissociation may occur upon ionization of molecular ions having an excess of internal energy. A sequential loss of metal–ligand bonds can also be achieved by activation of the ion. The observed mass loss leads to the knowledge of the elemental composition of the ligand. Similar information can be obtained from ligand substitution ion–molecule reactions. Coordinatively saturated molecular ions are usually inert to neutral reactants.

The recognition of atom connectivity in ligands is not always a straightforward task and a combination of experimental data should be considered. Reactions involving radical and neutral molecule losses, as well as migration of groups to the metal atom, are the most informative for the recognition of the structure and location of substituents in the ligand. The most abundant processes are those involving atoms and groups located in close proximity to the metal atom, for example, groups in α- and β-positions of the substituent in ligands. It is useful to compare the mass spectral behavior of the unknown compound with the reactivity of similar derivatives having a well-established structure.

Some isomeric organometallic complexes may be recognized using mass spectral methods.[94] The difference in the mass spectra of isomers usually comes from the interaction of the metal atom with electronegative groups or unsaturated bonds in the substituent. These interactions increase the bond strength between the metal atom and the ligand, resulting in a preferential loss of other ligands. If an electronegative group is involved in such an interaction, then its migration to the metal atom may occur. The extent of the latter reaction depends on how close the migrating group is to the metal atom.

Another effect that may result in differentiation of isomers is a metal-catalyzed loss of neutral molecules from a ligand(s). The isomer having an electronegative group in closer proximity to the metal atom usually easily loses this group as a part of a neutral molecule.

2.28.2.2 Interpretation of Mass Spectra of Metal Compounds

The interpretation of mass spectra of positively charged metal-containing ions is based on two general concepts.

The concept of valence change[95] has been applied to rationalize and predict the fragmentation of a variety of metal σ-complexes. It operates on the following assumptions:

(i) The metal atom contains an even number of electrons in the parent neutral molecule;
(ii) Stabilization of molecular ions occurs when the metal atom can increase its oxidation state (OS). Fragmentation of these complexes involves a loss of even-electron species (molecules);
(iii) If the metal atom has only one stable OS, then molecular ions are of low intensity and their fragmentation will likely involve loss of a radical, followed by losses of neutral molecules;
(iv) If the metal atom can be easily reduced, then the dissociation of molecular ions will involve a predominant loss of two radicals.

The valence-change effect is illustrated by the behavior of aluminum (one stable OS: III) and iron (two stable OSs: III and II) trisacetyacetonates, $Mt(acac)_3$ (Scheme 1). Both complexes produced modest molecular ions in the EI mass spectra, with the dominant loss of one β-diketonate ligand producing $Mt(acac)_2^+$ ions in which metal atoms retained their stable OS III. The Fe derivative also underwent a significant loss of the second ligand, giving rise to ions having the metal atom in the OS II. The abundance of this process in the EI mass spectrum of $Al(acac)_3$ was very low, due to the low stability of Al^{II}. The dissociation of complexes having two metals with two stable oxidation states follows the same rules.

The most successful interpretation of mass spectra of transition metal π-complexes is based on the concept of charge localization on the metal atom.[80,94] Ionization energies of the majority of organometallic molecules are lower than those of the ligands, but differ only slightly from the ionization energies of the free metal atoms. Accordingly, the ionization of transition metal

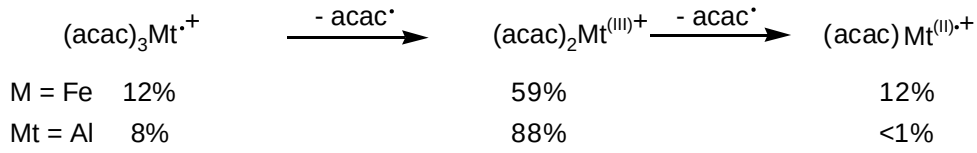

Scheme 1

complexes most likely involves the removal of an electron from the metal atom. As a result, on the decomposition of molecular ions of transition metal hydrocarbon ions the positive charge usually remains on the metal-containing fragment. The other consequence of the charge localization on the metal atom is that the dissociations of organometallic ions become controlled by the central metal atom. Unlike ionized metal-free organic molecules, their metal complexes lose even-electron neutrals rather than radicals. Also mechanisms of similar reactions in the coordinated and metal-free organic molecules are often different. A direct participation ("catalysis") of the metal atom in transformations of the ligand regulates these mechanisms (Scheme 2).

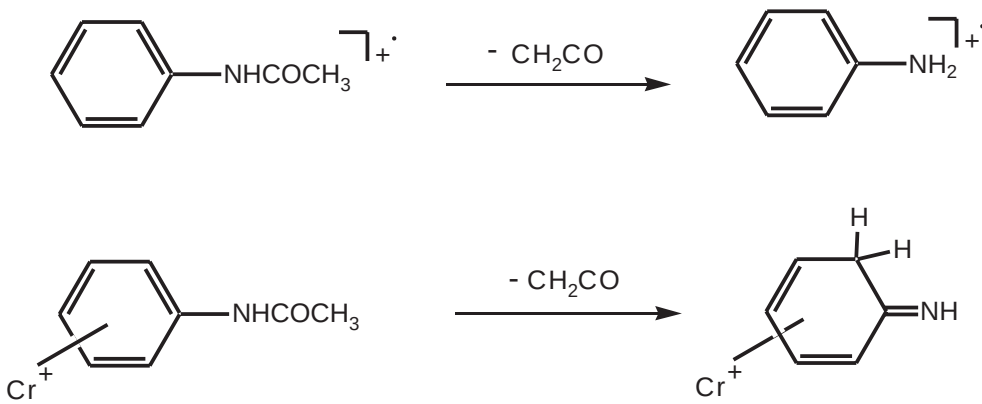

Scheme 2

The formation of neutral, metal-containing species upon fragmentation of organometallic ions does not contradict the initial charge localization on the metal atom. The positively charged metal atom is easily attacked by electronegative groups in a ligand, forming stable, metal-containing molecules.

$$C_5H_5FeC_5H_4COCl^+ \rightarrow C_5H_5Fe^{II}Cl + C_5H_4CO^+ \quad (1)$$

This effect is common for the interaction of metal ions with functionalized organic reactants:

$$Mg^+ + ClCH_2CH_2Cl \rightarrow Mg^{II}Cl_2 + C_2H_4^+ \quad (2)$$

2.28.2.3 Thermochemistry of Organometallic Molecules and Ions

Mass spectrometry can be used to determine the fundamental thermochemical parameters of organometallic molecules (see also Chapter 2.12), such as ionization energies (IEs), electron and proton affinities. IEs can be obtained by determining the ionization thresholds of electron-induced ionization (vertical IE), or photoionization (adiabatic IE). The electron exchange between a positively charged ion and a neutral molecule (electron-transfer bracketing) allows the estimation of adiabatic IEs. In this approach, various reference compounds are introduced and the observation of (direct or reverse) electron-transfer reactions indicates which molecule has a lower IE. If it is possible to establish accurately a pressure for the neutral reactant, then the electron-transfer equilibrium can be measured, giving IE values with high accuracy.

Similar experiments, involving electron transfer between an anion and a neutral molecule, yield relative or absolute EAs. The method has been used to determine relative free energies for electron attachment for a variety of metallocenes and β-diketonate molecules. Electron photodetachment spectroscopy of negatively charged ions[96] is another source for obtaining electron affinities of molecules. These data provide an important component of thermochemical cycles involving oxidation/reduction of metal complexes, and serve as a basis for obtaining other thermochemical values.

The understanding of substituent effects in metal complexes is one of the goals of electron-transfer equilibrium studies. For example, alkyl substitution in metallocenes predictably decreased their IEs. At the same time, it has been shown that the gas-phase EAs can be increased by a larger alkyl substituent in the hydrocarbon ligand.

Anion-transfer reactions to/from metal complexes are sources for the anion affinities of organometallic molecules.[63,64] To illustrate: the hydroxide affinity of $(CO)_5Fe$ has been determined by measurement of the equilibrium constant for hydroxide transfer exchange between $(CO)_5Fe$ and SO_2. This value was used to estimate the heat of formation of $(CO)_4FeCOOH^-$. Ion–molecule reactions of these ions and their collision-induced dissociation gave rise to a variety of negatively charged species having a coordinatively unsaturated metal atom. A study of their reactivity is a good source for obtaining the thermochemical characteristics of elusive metal complexes that cannot be produced otherwise.

Proton-transfer equilibrium measurements and proton-transfer bracketing methods are sources for proton affinity values of organometallic complexes. The determination of the site of protonation, i.e., metal atom vs. a ligand, is a fundamental dilemma of any study on the protonation of metal complexes. It was demonstrated, for example, that $Fe(CO)_5$ was protonated exclusively at the metal atom, whereas the results for the proton transfer to ferrocene can be explained by the formation of a metal-protonated form and a ring-protonated form, involving the agostic interaction of the proton with the metal atom.

Cation-exchange reactions are a common source for obtaining cation (CH_3^+, Na^+, NH_4^+, etc.) affinities of neutral molecules.

2.28.2.4 Chemistry of Metal–Ligand Bonds

Knowledge of metal–ligand bond energies is fundamental information for organometallic chemistry. It is essential for the understanding of catalytic reaction mechanisms, which often involve the cleavage or formation of these bonds. Mass spectrometry offers a series of experimental methods for determining absolute and relative bond strengths between a positively or negatively charged metal center and ligands[69–71,76] (see also Chapter 2.12). Direct determination of metal–ligand bond dissociation energies (BDE) can be performed by measuring appearance energies (AEs) of the molecular and fragment ions. The best results are obtained from AEs of ions produced by metastable dissociation of mass selected precursors. Kinetic energy release distribution[97] during metastable dissociation of ions is another source for the quantitative characterization of metal–ligand bonds. The experimental results obtained by this method require theoretical calculations in order to extract the information on the enthalpy change for the observed processes.

Appearance energy measurements and photodissociation of ions were used for measuring BDEs in anions.[63] Energy-resolved, collision–induced dissociation is another source for obtaining information about bond stabilities. The general trend in metal–ligand bonds is that they decrease by going from anions to neutrals and to positively charged ions. In L_nMtX^- complexes, the ligands X having the highest electron affinity are usually those forming the strongest Mt—X bonds.

A large number of both relative and absolute bond energies in metal-containing ions have been measured by the kinetic method.[98] The method operates with an abundance of products formed by competitive ligand loss. The metal–ligand bond enthalpies can be determined from the metastable and collision-induced dissociation of LMt^+L' ions, where L and L′ are different molecules. The general trend in metal–ligand BDEs is that the larger alkyl derivatives are bound to the metal atom more strongly than their smaller homologs. A particular advantage of the kinetic method is that it can probe ions containing thermally unstable ligands—chemistry which is difficult to study in the condensed phase.

Ion–molecule ligand-exchange reactions are a convenient method for obtaining relative and absolute metal–ligand BDE. By using this approach, the affinities of molecules for a variety of

"bare" and ligated metal ions have been determined. Two-ligand systems, $D^0(Mt^+ - 2L)$, as well as negatively and doubly charged positive ions, have been characterized.

Monitoring the thresholds of endothermic reactions by the guided ion-beam technique is one of the methods used to obtain the most accurate bond energies (see also Chapter 2.12). Similar measurements can be performed employing the FTICR technique. General types of endothermic reactions studied to obtain BDEs are as follows (Mt^+ is a "bare" or ligated metal ion).

$$Mt^+ + RX \rightarrow MtX^+ + R \quad (3)$$

$$Mt^+ + RX \rightarrow MtX + R^+ \quad (4)$$

$$MtY^+ + RX \rightarrow MtX^+ + RY \quad (5)$$

If the thermochemistry of reactants (Mt^+, MtY^+, RX) and one of the reaction products (R, R^+ RY) is well established, then using the experimentally measured threshold energy of reaction, one can calculate M^+—X and M—X bond strengths.

The results on metal–ligand BDEs obtained by different methods are usually in good agreement with each other. However, a critical analysis of the experimental techniques, understanding their limitations and sources of errors as well as the knowledge of trends in changing BDEs, is highly recommended before accepting a specific thermochemical value.

2.28.2.5 Transformations of Molecules on Charged Metal Centers

Mass spectrometry is widely used for studying reaction mechanisms involving metal-containing reaction intermediates. A great majority of these studies involve the investigation of transformations of organic molecules on ligated or "bare" metal ions.[66–71,79,80,84] The gas-phase reactivity of charged metal clusters[87] was the subject of multiple investigations in a search for mechanisms of reactions on metal surfaces. Reactions (1)–(5) provide a few examples from a large number of processes involving bond cleavage within ligands. Particular interest in this field of research is focused on intrinsic mechanisms of metal-ion-induced C—H, C—C, and C–heteroatom bond activation reactions, being models for the elementary stages of important homogeneous and heterogeneous catalytic processes, metal ion biochemistry, synthesis of electronic and ceramic materials, etc. Unlike positively charged metal atoms, their negatively charged counterparts showed inertness toward saturated hydrocarbons and olefins.[83] Other small molecules, including H_2, CO, NO, N_2, CO_2, O_2, NH_3, and CH_3OH, were subjected to reactions with positively and negatively charged metal-containing ions.

A series of experiments on the reactivity of metal ions with nitriles, RCN, led to the discovery of the remote functionalization mechanism.[72,73] The initial interaction of the metal ion involves coordination at the nitrile group. The insertion of the metal atom into a C—H or C—C bond occurs only after the alkyl chain becomes long enough (at least three or four methylene groups) to interact with a remote bond. The dissociation of the metal-hydride or metal-alkyl intermediate results in a loss of H_2 alkene or alkane molecules, depending on the structure of the hydrocarbon group R.

Important reactive metal-containing intermediates (e.g., metal-benzyne complexes, $MtCO_2^+$) and processes (e.g., decarbonylation, oxidation, reductive addition) of practical interest have been characterized using various mass spectral methods, and provide insight as to the mechanisms of organometallic reactions.

2.28.2.6 Gas-phase Metal Negative Ion Chemistry

Negatively charged metal-containing complexes play an important role in inorganic and organometallic chemistry in solution. Various industrial processes involve anionic reagents, metal substrates, or else proceed via nucleophilic reactions. Mass spectrometry provides tools for the identification of anionic reaction products and intermediates, and for the study of their reactivity in the gas phase.[83] This method has been useful for the investigation of unimolecular dissociation

and ion–molecule reactions of metal-containing anions, in order to obtain information about their and their neutral counterparts' reactivity and thermochemistry.

A variety of thermochemical data were obtained for negatively charged metal complexes. For example, appearance energy measurements; photodissociation, energy-resolved, collision-induced dissociation, electron-, proton- and anion-transfer reactions to and from negatively charged ions, were all used for obtaining a variety of thermochemical parameters for ions, molecules, and radicals.

Although the general approach to the study of gas-phase reactions of negatively charged ions by mass spectrometry is very similar to that for the chemistry of their positively charged counterparts, some specifics can be mentioned. First, some ionization techniques (NICI, REC) are designed for the production of negatively charged ions in the gas phase.[82] Most of the work on negative ion chemistry[83] has been carried out with the use of ICR (or FTICR), flowing afterglow techniques (FA)[63] and Knudcen cell mass spectrometry.[64]

The Knudcen cell method is used to characterize negative-ion equilibria taking place in the saturated vapor over binary mixtures containing metal compounds. This technique is especially valuable for measurements of the heats of formation of fluorides, MtF_n^- fluoride ion affinities, $D[MtF_n - F^-]$, and high (>5 eV) electron affinities.

The main advantage of the FA method is that ions are carried through the flow tube to the mass spectrometer in the "stream" of a buffer gas at relatively high pressure (0.1–1.0 Torr). During this time they become thermally equilibrated and achieve thermal energy distribution. Ion–molecule reactions of the ions can be studied by the addition of small flows of neutral reagents along the length of the flow tube. Reliable kinetic measurements for ligand-attachment and ligand-substitution reactions have been performed for MtL_n^- ions.

The overall contribution of negative metal ion chemistry to the gas-phase ion chemistry of metal complexes is relatively small, but it should not be overlooked.

2.28.2.7 Elusive Neutral Organometallics Generated from Ions

Neutralization-reionization mass spectrometry (NR MS) (see also Chapter 2.34) is a unique mass spectral technique that allows the generation of neutral species from their charged counterparts. The major application of NR MS is to produce unstable reaction intermediates that cannot be isolated or characterized by other means, to yield new, previously unknown molecules and radicals. The method has been used successfully to generate a variety of organometallic species.[85,86] A wide range of elusive metal-containing molecules (AuF, PrF, C_5H_5FeF, $C_5H_5Rhacac$, etc.) and radicals (NiCCH, $C_5H_5FeC_5H_4CO$, $(C_5H_5)_2Zr$ and others) have been generated and characterized for the first time using the NR MS method. The observation of these species in the gas phase suggests their possible formation in other than gas-phase experimental conditions, at least as short-lived reaction intermediates. This information is used by chemists to confirm and evaluate the mechanisms of organometallic reactions, including elementary steps of catalytic transformations on metal centers.

2.28.2.8 Contributions of Coordination Chemistry to Mass Spectrometry

Complexes of metals have contributed to various fields of mass spectrometry. They may serve as standards for mass calibration. Molecules with well-established ionization energies, bond dissociation energies, proton affinities, etc., are used for the determination of the thermochemical characteristics of other molecules and ions. Metal complexes have played an important role in establishing concepts of interpretation of mass spectral data, and in understanding ionization and ionic fragmentation mechanisms. The presence of a metal atom often changes dramatically the dissociation pathways of organic molecules. For this reason, coordination with metal ions can be used for the generation of organic and inorganic molecules and radicals with unusual atom connectivities.

Metal-containing ions are useful reactants for the identification of organic compounds by mass spectrometry. The formation of metal adducts is especially advantageous when traditional methods of ionization (EI, CI) do not result in stable molecular ions or protonated species. Chemical ionization with metals and metal-containing ions provides high selectivity and sensitivity to specific types of analytes (unsaturated and functionalized hydrocarbons, peptides, crown ethers,

polymers, etc.) and can be successfully used in GC-MS experiments. Regio- and stereospecific dissociation of metal adducts may allow the distinguishing of isomers.

The formation of complexes between analytes and metal (-containing) ions is commonly observed and used in other methods of ionization. ESI mass spectra of organic compounds very often display adducts with Na^+ and K^+ ions. Solvents, glassware, and impure chemicals are common sources of these ions. Intentional "doping" of solutions by alkali-metal ions in ESI is widely used to improve the ionization of (non-polar) analytes, and to determine the number of mobile hydrogen atoms in molecules.

Adducts with metal ions are important for the successful MALDI analyses of nonpolar compounds. Similarly to the ESI method, their formation very often takes place as a result of the presence of traces of metal salts. Addition of small amounts of Na^+ and K^+ ions is used for helping the ionization of analytes whose proton affinities are low. Transition-metal ions have been successfully applied when no other ionizing reagents work. For example, Ag^+ ions are extremely effective in the MALDI analysis of polymers[13] having no heteroatoms.

In conclusion, mass spectrometry provides a variety of opportunities for the qualitative and quantitative analyses of metal compounds. It is a convenient method for studying the reactivity of nonsolvated, metal-containing ions, and for the generation and characterization of reaction intermediates. Thermochemical properties of ions and neutrals can be obtained from these studies.

2.28.3 REFERENCES

1. *What is Mass Spectrometry?* The American Society for Mass Spectrometry, 1998, 3rd ed.; (http://www.asms.org/whatisms/index.html).
2. Lindon, J. C.; Tranter, G. E.; Holmes, J. L., Eds., *Encyclopedia of Spectroscopy and Spectrometry*, Academic Press: San Diego, CA, 2000.
3. Gross, M. L., Ed., *Mass Spectrometry in Biological Sciences: The Tutorial*, Kluwer Academic: Dordrecht, Netherlands, 1991.
4. McLafferty, F. W.; Turecek, F. *Interpretation of Mass Spectra*, 3rd ed.; University Science Books: Mill Valley, CA, 1993.
5. Chapman, J. S. *Practical Organic Mass Spectrometry*, 2nd ed.; Wiley: Chichester, UK, 1993.
6. Watson, J. T. *Introduction to Mass Spectrometry*, 3rd ed.; Lippincott-Raven: Philadelphia, PA, 1997.
7. Lambert, J. B.; Shurvell, H. E.Lightner, D. A.; Cooks, R. G. *Organic Structural Spectroscopy*, Prentice Hall: Upper Saddle River, NJ 1998; Part IV, pp 346–478.
8. Johnstone, R. A. W.; Rose, M. E. *Mass Spectrometry for Chemists and Biochemists*, 2nd ed.; Cambridge University Press: Cambridge, UK, 1996.
9. de Hoffmann, E.; Charette, J.; Stroobant, V. *Mass Spectrometry: Principles and Applications*, Wiley: Chichester, UK, 1996.
10. Russell, D. H. *Experimental Mass Spectrometry*, Plenum Press: New York, 1994.
11. Beauchemin, D. *Trends Anal. Chem.* **1991**, *10*, 71–76.
12. Adams, F.; Gijbels, R.; Van Grieken, R. *Inorganic Mass Spectrometry*, Wiley: New York, 1988.
13. Montaudo, G.; Lattimer, R. R. *Mass Spectrometry of Polymers*, CRC Press: Boca Raton, FL, 2002.
14. Barceló, D., Ed., *Applications of LC-MS in Environmental Chemistry*, Elsevier, Amsterdam, 1996.
15. White, F. A.; Wood, G. M. *Mass Spectrometry: Applications in Science and Engineering*, Wiley: New York, 1986.
16. Lawson, A. M. *Clinical Biochemistry: Principles, Methods and Applications. Vol. 1: Mass Spectrometry*, De Gruyten: Berlin, 1989.
17. Yinon, Y., Ed., *Forensic Applications of Mass Spectrometry*, CRC Press: Boca Raton, FL, 1995.
18. Chapman, J. R., Ed., *Protein and Peptide Analysis by Mass Spectrometry*, Humana Press: Totowa, NJ, 1996.
19. Kinter, M.; Sherman, N. E. *Protein Sequencing and Identification using Tandem Mass Spectrometry*, Wiley: New York, 2000.
20. Snyder, P. A. *Interpreting Protein Mass Spectra: A Comprehensive Resource*, Oxford University Press: Washington, DC, 2000.
21. Housby, J. N. *Mass Spectrometry and Genomic Analysis*, Kluwer Academic: Dordrecht, Netherlands, 2001.
22. Dass, C. *Principles and Practice of Biological Mass Spectrometry*, Wiley: New York, 2001.
23. Odham, G.; Larsson, L.; Mardh, P.-A., Eds., *Gas Chromatography/Mass Spectrometry Applications in Microbiology*, Plenum Press: New York, 1984.
24. Niessen, W. M. A., Ed., *Current practice of Gas Chromatography-Mass Spectrometry*, Marcel Dekker: New York, 2001.
25. Arpino, P. J. *Mass Spectrom. Rev.* **1992**, *11*, 3–40.
26. Niessen, W. M. A., Ed., *Liquid Chromatography-Mass Spectrometry*, 2nd ed.; Marcel Dekker: New York, 1999.
27. Niessen, W. M. A.; Voyksner, R. D., Eds., *Current Practice of Liquid Chromatography-Mass Spectrometry*, Elsevier: Amsterdam, 1998.
28. Ashcroft, A. E. *Ionization Methods in Organic Mass Spectrometry*, The Royal Society of Chemistry: Cambridge, UK, 1997.
29. Reed, R. I. *Ion Production by Electron Impact*, Academic Press: New York, 1962.
30. Illenberger, E.; Smirnov, B. M. *Physics – Uspekhi* **1998**, *41*, 651–685.

31. Laramee, J. A.; Cody, R. B.; Deinzer, M. L. In *Encyclopedia of Analytical Chemistry*, Mayers, R.A., Ed.; Wiley: Chichester, UK, 2000, pp 11651–11679.
32. Harrison, A. G. *Chemical Ionization Mass Spectrometry*, 2nd ed.; CRC Press: Boca Raton, FL, 1992.
33. Melton, C. E. *Principles of Mass Spectrometry and Negative Ions*, Marcel Dekker: New York, 1970.
34. Budzikiewicz, H. *Mass Spectrom. Rev.* **1986**, *5*, 345–380.
35. Beckey, H.-D. *Principles of Field Ionization and Field Desorption Mass Spectrometry*, Pergamon Press: Oxford, UK, 1977.
36. Carrol, D. I.; Dzidic, I.; Horning, E. C.; Stillwell, R. N. *Appl. Spectr. Rev.* **1981**, *17*, 337–406.
37. Berkowitz, J. *Photoadsorption, Photoionization, and Photoelectron Spectroscopy*, Academic Press: New York, 1979.
38. Arpino, P. *Mass Spectrom. Rev.* **1990**, *9*, 631–669.
39. Cole, R. B., Ed., *Electrospray Ionization Mass Spectrometry: Fundamentals, Instrumentation, and Applications*, Wiley: New York, 1997.
40. Pramanik, B. N.; Ganguly, A. K.; Gross, M. L., Eds., *Applied Electrospray Mass Spectrometry*, Marcel Dekker: New York, 2002.
41. Prokai, L. *Field Desorption Mass Spectrometry*, Marcel Dekker: New York, 1990.
42. De Pauw, E.; Agnello, A.; Derwa, F. *Mass Spectrom. Rev.* **1991**, *10*, 283–301.
43. Lyon, P. A., Ed., *Desorption Mass Spectrometry: Are SIMS and FAB the Same*, American Chemical Society: Washington, DC, 1985.
44. Holland, G.; Tanner, S. D., Eds., *Plasma Source Mass Spectrometry: New Developments and Applications*, Royal Society of Chemistry: Cambridge, UK, 1999.
45. Loon van, J. C.; Barefoot, R. R.; Barefoot, R. R. *Plasma Source Mass Spectrometry*, CRC Press: Boca Raton, FL, 2001.
46. Lubman, D. M. *Lasers and Mass Spectrometry*, Oxford University Press: Oxford, UK, 1990.
47. Karas, M.; Hillenkamp, F. *Int. J. Mass Spectrom. Ion Processes* **1989**, *92*, 231–242.
48. Hillenkamp, F. In *Biological Mass Spectrometry: Present and Future*, Matsuo, T.; Caprioli, R. M.; Gross, M. L.; Seyama, Y., Eds.; Wiley: New York, 1994, pp 101–126.
49. Dawson, P. H. *Mass Spectrom. Rev.* **1986**, *5*, 1–37.
50. March, R. E.; Hughes, R. J. *Quadrupole Storage Mass Spectrometry*, Wiley: New York, 1989.
51. Buchanan, M. V. *Fourier Transform Mass Spectrometry: Evolution, Innovation, and Applications*, American Chemical Society: Washington, DC, 1986.
52. Lehman, T. A.; Bursey, M. M. *Ion Cyclotron Resonance Spectroscopy*, Wiley: New York, 1976.
53. Marshall, A. G.; Hendrickson, C. L.; Jackson, G. S. *Mass Spectrom. Rev.* **1998**, *17*, 1–35.
54. Cotter, R. J. *Time-of-flight Mass Spectrometry*, American Chemical Society: Washington, DC, 1994; ACS Symposium Series, Vol. 549.
55. Cooks, R. G.; Beynon, J. H.; Caprioli, R. M.; Lester, G. R. *Metastable Ions*, Elsevier: Amsterdam, 1973.
56. Busch, K. L.; Glish, G. L.; McLuckey, S. A. *Mass Spectrometry/Mass Spectrometry*, VCH: New York, 1988.
57. Jennings, K. R., Ed. *Fundamentals of Gas Phase Ion Chemistry*, Kluwer Academic: Dordrecht, Netherlands, 1991.
58. Hayes, R. N.; Gross, M. L. *Methods in Enzymology, Vol. 193: Mass Spectrometry*, Academic Press: New York, 1990.
59. Morris, M.; Riederer, D. E., Jr.; Cooks, R. G. In *Biological Mass Spectrometry: Present and Future*, Matsuo, T.; Caprioli, R. M.; Gross, M. L.; Seyama, Y., Eds.; Wiley: New York, 1994, pp 239–247.
60. Farrar, J. M.; Saunders, W. H. *Techniques for the Study of Ion/Molecule Reactions*, Wiley: New York, 1988.
61. Brodbelt, J. S. *Mass Spectrom. Rev.* **1997**, *16*, 91–110.
62. Splitter, J. S.; Turecek, F., Eds., *Applications of Mass Spectrometry to Organic Stereochemistry*, VCH: New York, 1994.
63. Squires, R. R. *Int. J. Mass Spectrom. Ion Processes,* **1992**, *118/119*, 503–518.
64. Sidorov, L. N. In *Encyclopedia of Spectroscopy and Spectrometry*, Lindon, J. C.; Tranter, G. E.; Holmes, J. L., Eds.; Academic Press: San Diego, CA, 2000, pp 915–923.
65. Bruce, M. I. In *Advances in Organometallic Chemistry*, Stone, F. G. A.; West, R., Academic Press: New York, 1968; Vol. 6, pp 273–333.
66. Cais, M.; Lupin, M. S. In *Advances in Organometallic Chemistry*, Stone, F. G. A.; West, R.; Eds.; Academic Press: New York, 1970; Vol. 8, pp 211–333.
67. Charalambous, J., Ed., *Mass Spectrometry of Metal Compounds*, Butterworth: London, 1975.
68. Zagorevskii, D. V. In *Encyclopedia of Spectroscopy and Spectrometry*; Lindon, J. C.; Tranter, G. E.; Holmes, J. L., Eds.; Academic Press: San Diego, CA, 2000, pp 1726–1733.
69. Freiser, B. S. *Acc. Chem. Res.* **1994**, *27*, 353–360.
70. Freiser, B. S. *J. Mass Spectrom.* **1996**, *31*, 703–715.
71. Freiser, B. S., Ed., *Organometallic Ion Chemistry*, Kluwer Academic: Dordrecht, Netherlands, 1996.
72. Eller, K.; Schwarz, H. *Chem. Rev.* **1991**, *91*, 1121–1177.
73. Eller, K. *Coord. Chem. Rev.* **1993**, *126*, 93–147.
74. Kiser, R. W. In *Characterization of Organometallic Compounds*, Tsutsui, M., Eds.; Wiley Interscience: New York, 1969, pp 137–211.
75. Litzov, M. R.; Spalding, P. H. *Mass Spectrometry of Inorganic and Organometallic Compounds*; Elsevier: Amsterdam, 1973.
76. Marks, T. J., Ed., *Bonding Energetics in Organometallic Chemistry*; American Chemical Society: Washington, DC, 1990.
77. Martinho Simoes, J. A.; Beauchamp, J. L. *Chem. Rev.* **1990**, *90*, 629–688.
78. *Mass Spectrometry* (Specialist Periodic Report) (1971–1989), The Chemical Society: London; Vols.1–10.
79. Miller, J. M.; Wilson, G. L. In *Advances in Inorganic Chemistry and Radiochemistry*; Emeleus, H. J., Ed.; Academic Press: New York, 1976; Vol. 18, pp 229–285.
80. Muller, J. *Angew. Chem. Intern. Ed.* **1972**, *11*, 653–665.
81. Russell, D. H., Ed., *Gas Phase Inorganic Chemistry*, Plenum Press: New York, 1989.
82. Gregor, I. K.; Guilhaus, M. *Mass Spectrom. Rev.* **1984**, *3*, 39–84.

83. Squires, R. R. *Chem. Rev.* **1987**, *87*, 623–646.
84. Zagorevskii, D. V.; Nekrasov, Y. S. *Mass Spectrom. Rev.* **1995**, *14*, 21–48.
85. Zagorevskii, D. V.; Holmes, J. L. *Mass Spectrom. Rev.* **1999**, *18*, 87–118.
86. Zagorevskii, D. V. *Coord. Chem. Rev.* **2002**, *225*, 5–34.
87. Fisher, K. In *Progress in Inorganic Chemistry,* Karlin, K. D., Ed.; Wiley, New York, 2001; Vol. 50, pp 343–432.
88. Colton, R.; D'Agostino, A.; Traldi, P. *Mass Spectrom. Rev.* **1995**, *14*, 79–106.
89. Gatlin, C. L., Turecek, F. In *Electrospray Ionization Mass Spectrometry*, Cole, R. B., Ed.; Wiley: New York, 1997, pp 527–570.
90. Traeger, J. C. *Int. J. Mass Spectrom.* **2000**, *200*, 387–401.
91. Traeger, J. C.; Colton, R. In *Advances in Mass Spectrometry*, Karjalainen, E. J.; Hesso, A. E.; Jalonen, J. E.; Karjalainen, U. P., Eds.; Elsevier: Amsterdam, 1998, pp 637–659.
92. Schulten, H. R. *Int. J. Mass Spectrom. Ion Phys.* **1979**, *32*, 97–283.
93. Gower, J. L. *Biomed. Mass Spectrom.* **1985**, *12*, 191–196.
94. Nekrasov, Y. S.; Zagorevskii, D. V. In *Applications of Mass Spectrometry to Organic Stereochemistry*; Splitter, J. S.; Turecek, F., Eds.; VCH: New York, 1994, pp 657–671.
95. Lacey, M. J.; Shannon, J. S. *Org. Mass Spectrom.* **1972**, *6*, 931–937.
96. Wetzel, D. M.; Brauman, J. I. *Chem. Rev.* **1987**, *87*, 607–622.
97. Van Koppen, P. A. M.; Bowers, M. T.; Beauchamp, J. L.; Dearden, D. V. In *Bonding Energetics in Organometallic Chemistry*; Marks, T. J., Ed.; American Chemical Society: Washington, DC, 1990, pp 34–54.
98. Cooks, R. G.; Patrick, J. S.; Kotiano, T.; McLuckey, S. A. *Mass Spectrom. Rev.* **1994**, *13*, 287–339.

Comprehensive Coordination Chemistry II
ISBN (set): 0-08-0437486

Volume 2, (ISBN 0-08-0443249); pp 367–380

2.29 Neutralization–Reionization Mass Spectrometry

D. ZAGOREVSKII
Rensselaer Polytechnic Institute, Troy, NY, USA

2.29.1 REFERENCES 386

Neutralization–reionization mass spectrometry (NR MS) is one of many tandem mass spectrometry methods.[1–12] Unlike other mass spectrometry techniques, NR MS is aimed at producing *neutrals* from ions. The premise of the experiments is that gas phase ions having unusual structures and atom connectivities can be easily accessed from ionization of stable molecules and fragmentation of their ions. If these ions are successfully neutralized, then stable neutrals, having the same atom connectivity, can be generated as stable species in the gas phase. Generation of otherwise unstable or unknown neutrals in a NR MS experiment is one of the ways of proving that particular reaction intermediate, molecule, or radical do exist at some specific experimental conditions.

Another application of NR MS is to study ion structures and mechanisms of reactions of ions in the gas phase. This method has some advantages over other tandem mass spectrometry methods of elucidation of ion structures. One of them is the ability to detect neutral products of ion fragmentation.

Scheme 1 shows the instrumental and functional arrangement of NR MS experiments that include the following most common steps:

(i) The generation of positively or negatively charged ions whose neutral counterparts are intended to be produced.
(ii) Structural characterization of the ions to determine that they possess the desired atom and group connectivity.
(iii) Mass separation of the ions of interest from all other ions using a mass analyzer and their transmission to a field-free region (FFR) where their neutralization will be performed.
(iv) Acceleration of the ions to translational energies of 3–10 keV, to ensure efficient processes of neutralization and reionization.
(v) Neutralization of the fast-moving mass-selected ions is achieved by collisions with a target gas.
(vi) Deflection of all remaining charged species from the beam of fast-moving neutrals by placing a charged deflector electrode after the neutralization region.
(vii) Reionization of the neutrals by collisions with target molecules.
(viii) Detection of the ions produced by reionization of neutrals.
(ix) Further mass spectrometry experiments on mass-selected reionized species to obtain information about their structure.

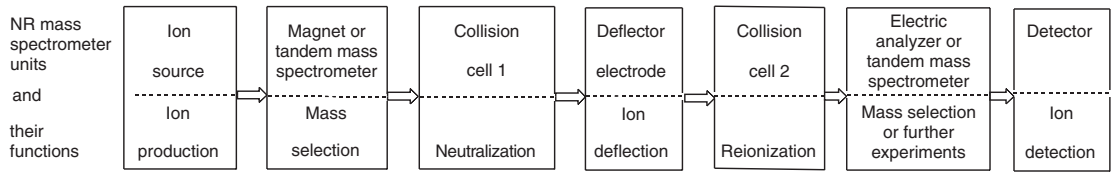

Scheme 1

A variety of instruments have been used for conducting NR studies. In pioneer studies of neutralization of metal-containing ions,[13] a single-sector mass spectrometer was used for mass separation of the ion of interest.[13,14] After collision of the ions with metal vapors, the remaining ions were removed from the beam by electrostatic deflection. The information on the extent of fragmentation and stability of neutrals was obtained from the analysis of the neutral beam-scattering profiles acquired with a translatable detector. Sector mass spectrometers with different sets of magnet and electric analyzers are the most commonly used instruments in NR MS studies. Quadrupole analyzers have been used in neutralization–reionization for mass selection of precursor ions and for mass analysis of products of NR. In order to perform neutralization and reionization on these instruments, the ions leaving the first quadrupole should be accelerated and the ions formed after the NR event should be decelerated before their mass analysis.[15]

Similar to any mass spectrometric experiment, ions that are intended to be converted to neutrals in NR MS should be first generated by appropriate ionization methods. In principle, all ionization methods described in Chapter 2.28 may be used for the generation of ions for NR MS studies. However, only a limited number of ionization techniques have found practical use for this purpose. They are electron impact, chemical ionization, fast atom bombardment, and secondary ion mass spectrometry. One of the reasons for not using other methods is that NR MS experiments are mostly carried out on sector instruments. The mass spectrometers of this type are usually equipped with relatively "old" methods of ionization. The second reason for using these methods is that they provide high ion fluxes of ions of interest. This condition is crucial for many NR MS experiments because of the overall low total efficiency (<0.1%) of the neutralization–reionization process.

Ions for NR MS can be produced by ion–molecule reactions. Reactions of "reactant" ions with molecules of analyte are used in CI, FAB, and SIMS ionization methods. Ions of interest can also be generated by introducing specific neutral molecules to the ion source. This method is widely used for making ions having a new metal–ligand bond. Using multi-sector tandem mass spectrometers allows the use of dissociations of mass-selected ions as a single source for ions of interest.[16] These reactions are intended for the production of a single isomer.

Ionic precursors of the sought neutrals should be structurally characterized. Ions in the gas phase may exist in various isomeric forms, so it is important to make sure that (i) the right isomer is formed, and (ii) that the ions of interest are isomerically pure. Neutralization is considered as a vertical Franck–Condon process and it is expected that the neutrals will retain the "structure" of the ion that has been neutralized.

NR MS itself is a powerful method for the assignment of structures to ions and for the study of ion and neutral dissociation mechanisms. There are two distinct advantages of this method as compared with, for example, CID mass spectra. First, the amount of internal energy that is transferred to the ion and the neutral during the NR process usually exceeds the amount of energy transferred in collisional activation. Reactions having high activation energies can be readily accessed in the NR event. Some of these reactions can be very important for characterization of the atom connectivity in the ion. The second advantage of NR MS over other methods of elucidation of ion structures is that neutral products of ion dissociations, as well as all other neutrals formed in the course of the NR MS experiment, are detected as ions. This gives a broader vision of mechanisms of dissociation of ions compared with the analysis of the charged products of reaction only.

The ions of interest should be mass-separated from all other ionic species. High resolution sometimes is required to separate ions of different elemental composition, but the same nominal mass. For example, the NR MS study of $FeC_2H_4^+$ ions required their separation from $FeCO^+$ ions.[17] It should be noted that increasing the resolution is associated with losses in intensity of ion currents, making it difficult to obtain a reliable NR mass spectrum. Isotope labeling is widely used for separation of ions having different elemental composition but the same mass-to-charge ratio.

Acceleration of the ions to translational energies of 4–10 kV before or after the mass separation will ensure effective neutralization. Neutralization takes place in the first collision cell and involves an electron transfer to or from the projectile ion. The neutrals formed in this process leave the collision cell together with the remaining ions. The latter are then removed from the beam of fast moving neutrals by applying a positive or negative potential (500–1,000 V) to the deflector electrode. As a result, only the neutrals are allowed to reach the second collision cell where they collide with another target gas. As a consequence of these collisions, the ionization of some neutrals takes place allowing their further detection as charged species.

One of the most common goals for conducting NR MS experiments is to generate a neutral molecule or a radical. The experimental evidence for the stability of a neutral formed in the course of a neutralization–reionization experiment is the observation of a so-called "recovery" signal or "survivor ions" in NR mass spectra. The recovery signal appears at the same mass (or energy) as the original ions passing through the corresponding FFR without been neutralized–reionized. The observation of the recovery signal indicates that the neutrals' lifetime exceeded the time between neutralization and reionization events. Depending on the mass of the ion and the experimental setting, this time varies from less than 1 μs to a few μs.

The observation or nonobservation of a recovery signal depends on several factors. First, collisional neutralization of ions may produce neutrals in their dissociative state(s). Electron transfer between the ion and the target is considered as a vertical Franck–Condon process. If the geometry of the ion is close to that of the neutral, the latter has a good chance of being formed as a stable species. When the geometry of the ion and the neutral are significantly different then the neutral is likely to be unstable.

The nonobservation of the recovery signal does not necessarily testify that the particular neutral cannot be produced. A low dissociation barrier for neutrals is a common rationale for their instability. Another possible reason for nonobservation of survivor ions is unfavorable experimental conditions. One of the most critical factors determining the stability or instability of neutrals is the nature of the target gas used for neutralization.[1,3,18] The closer the ionization energy (IE) of the target to the IE of the sought neutral the better chances for this neutral to survive in the experimental time frame. Also, charge transfer is the most efficient when the IE of the target is close to the IE of the projectile ion. Ionization energies of metal complexes are usually low and their best neutralization can be achieved by using targets having low IEs (dimethyldisulfide, NO, amines).

Negatively charged ions can also be subjected to collisional neutralization. In these cases oxygen is the most commonly used target gas.

Reionization is another important and critical stage of NR MS experiments. Two types of processes can contribute to the collisional ionization of neutrals: an electron transfer between the fast moving neutral and a target molecule, and ejection of the electron from the projectile neutral. The first process is generally a softer one, producing ions with lower internal energies. For this reason, molecules with high electron affinities (O_2, NO_2) are preferred targets in the reionization stage.

The interpretation of NR mass spectra is not always a simple task. Survivor ions, if present, can be easily recognized by their position on the mass or energy scale. They also appear as very sharp peaks unlike all other ions in NR mass spectra. Ions other than survivor ions may originate from different sources.

To illustrate, the NR mass spectrum of $C_5H_5FeBr^+$ ions[19] is shown in Figure 1. The highest mass peak corresponds to survivor ions. Their observation indicated that stable in the experimental time of frame neutral C_5H_5FeBr complex has been formed. $C_5H_5Fe^+$ and $FeBr^+$ ions might originate from the dissociation of the reionized $C_5H_5FeBr^+$ or from collisional ionization of the corresponding neutrals arising from unstable neutral C_5H_5FeBr (Scheme 2). The observation of $C_5H_5^+$ and Br^+ ions reflects the formation of neutral C_5H_5 and Br radicals from the dissociation of collisionally excited $C_5H_5FeBr^+$ ions. Other processes can also be considered as sources for $C_5H_5^+$ and Br^+ ions.

NR mass spectra usually contain a larger variety of peaks than CID mass spectra of the same ions, providing complementary information about ions and neutrals involved in the dissociation and neutralization–reionization processes. Special procedures of detecting neutral fragments of ionic dissociation and products of decomposition of intermediate neutrals have been developed. Neutral and ion decomposition difference (NIDD) mass spectrometry was developed[20] to identify dissociation products of unstable neutrals formed by neutralization of the corresponding ions. In this technique, the NR mass spectra are compared with the charge-stripping spectra (CS) recorded in similar conditions. The CS involves a one-step two-electron transfer from the

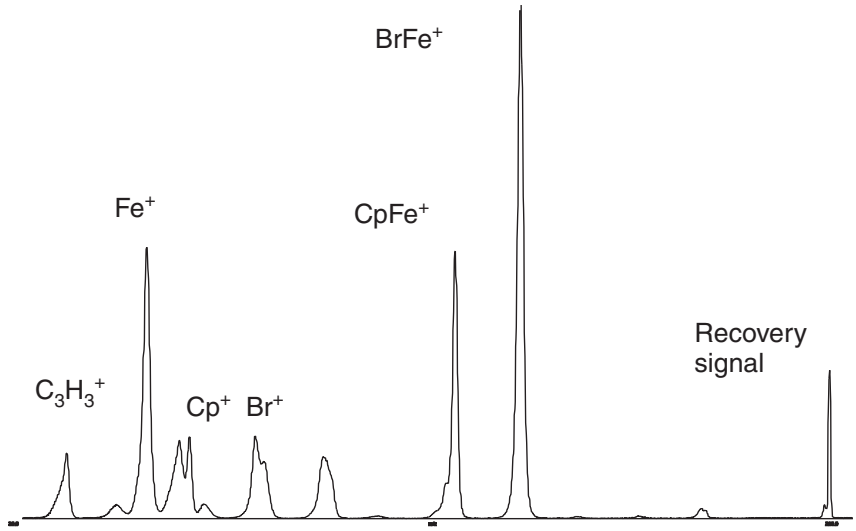

Figure 1 Neutralization–reionization mass spectrum of $CpFe^{79}Br^+$ and CID mass spectrum of survivor ions (reproduced by permission of Elsevier from *J. Am. Soc. Mass Spectrom.*, **1995**, *6*, 1143–1153; © 1995, American Society for Mass Spectrometry).

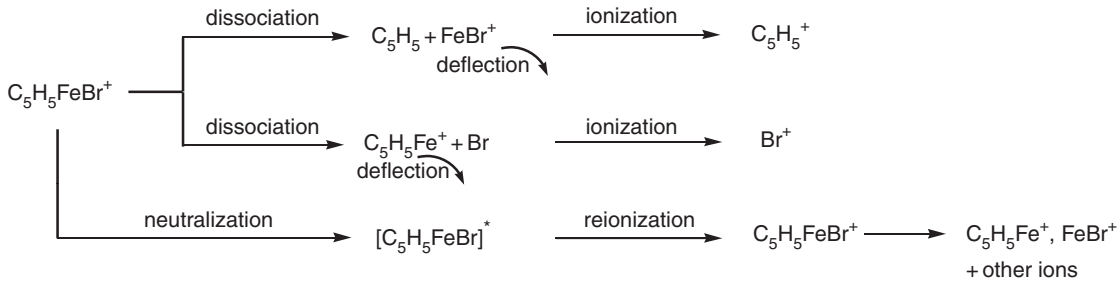

Scheme 2

projectile, a negatively charged ion. The resulting mass spectrum is a fingerprint of the ions formed after the charge reversal because the corresponding neutrals are not formed in the process. In the NR process, the removal of electrons from the ion is separated in time. A part of the NR mass spectrum originates from the collisional ionization of neutrals formed in the period of time between neutralization and reionization. By subtracting the CS mass spectrum from the NR mass spectrum of the same ions recorded with the "same" experimental conditions, the products of the dissociation of neutrals (arising in the NR conditions) may be retrieved.

Neutral products of dissociation of ions can be analyzed using collision-induced dissociative ionization (CIDI)[6] and neutral fragment reionization (N_fR)[21] methods. In the first method, unlike NR MS, no collision gas is introduced in the first collision cell. All precursor and product ions are deflected before reaching the second cell. Neutral products of metastable dissociation are collisionally analyzed in the second cell and detected. In N_fR experiments, similar to NR MS, a collision gas is introduced to the first collision cell to increase the degree of fragmentation. The requirement to this gas is that it should not cause neutralization of the ions. Helium is used for this purpose.

A key question in NR MS experiments is whether or not the intermediate neutrals retain the atom connectivity of the precursor ions. Structures of neutrals generated in NR MS experiments can be elucidated by comparison of CID mass spectra of the ion *prior* to their neutralization with CID mass spectra of the ions surviving neutralization–reionization. If the CID mass spectra are close to each other then it is a good indication that the structures of the ions before and after the NR event are the same.

The observation of significant differences between the CID mass spectra of the ions before neutralization and after reionization usually indicates that the intermediate neutrals did not retain

the atom connectivity of the precursor ions. The isomerization of neutrals may be very fast, e.g., it may be completed in a few microseconds before the reionization event will take place.[22]

The NR MS method has made significant contributions to organometallic and coordination chemistry.[23–25] The main purpose of the majority of NR MS experiments in this field is to test whether or not a particular neutral metal derivative is stable in the gas phase. Such observation is a good indication for the possible involvement of these species in the reactions taking place in the gas phase (such as interstellar processes) and their likely formation and stability in the condensed phase. The importance of the latter is indisputable because metal complexes are involved as reactants or catalysts in numerous chemical processes. These studies have been performed on a variety of metal complexes, such as very simple two-atomic species, metal solvates, and polyatomic transition metal derivatives.

Table 1 shows some neutral metal complexes generated in NR MS experiments. The stability (or instability) of neutrals may be predicted in many cases. Ions containing σ ligands are expected to survive neutralization–reionization. Similar predictions can be made for π-cyclopentadienyl complexes. A favorable Franck–Condon factor (small changes in metal–ligand bond distances) and relatively high bond dissociation energies are the major factors contributing to the stability of MtR_n, $C_5H_5MtR_n$, and similar molecules.

As a rule, complexes with even-electron ligands, such as solvates, alkene, benzene complexes, do not produce survivor ions. This may be reversed, however, by changing the experimental conditions (target gas, experimental time frame, etc.). Sometimes, adding a ligand increases the stability of complexes. For example, neutral LFeCO showed an unexpectedly higher stability compared with FeL.[26]

Some of the complexes listed in Table 1 were previously known while others had never been isolated or characterized. Successful NR MS experiments have been performed on systems with coordinatively and electron unsaturated metal complexes as well as electron-enriched systems. Among the latter is zirconocene,[27] which has been sought by chemists for a long time. Some bis-arene[28] and "unusual" bis-cyclopentadienyl complexes[29,30] were generated by NR MS for the first time.

Future studies in neutralization–reionization mass spectrometry of organometallics will be extremely helpful in the generation and characterization of various types of neutral complexes, including suspected reaction intermediates and so far unknown molecules. NR MS experiments are performed in the gas phase, where there are no interactions between the sought neutral and

Table 1 Some metal derivatives generated by neutralization–reionization mass spectrometry.

σ-Complexes with no metal–carbon bond

FeR, R = H, F, Cl, Cl_2, Cl_3, Br, I, NH_2, O, OH, O_2, O_3, S, OCH_3, OOCH
PrF, PrF_2, AuF, CuN, CuO, CuNO, CuO_2, MnH, MnOH, SnH, SnCl,
SnBr, SnI, FLi_2, HOK_2, HSK_2, $HOLi_2$, $HONa_2$, $HSNa_2$

σ-Complexes with metal–carbon bond

$FeCH_n$ (n = 0–3), MtCCH (Mt = Fe, Co, Ni), FeCN, FeC_6H_5, $MnCH_3$, MnC_6H_5, $AlCH_2$, $AlCH_3$, $SnCH_3$, SnC_6H_5

Metal "solvates"

Cu(HCN), $Cu(NH_3)_n$ (n = 1,2), NiL and NiL_2 (L = CO, H_2O, NH_3)
FeL and Fe(CO)L (L = CO, C_2H_4, C_4H_6, NH_3)

Coordinatively unsaturated π-cyclopentadienyl complexes

C_5H_5Mt (Mt = Fe, Co, Ni, Ti, Rh), MnC_5H_4R (R = H, CH_3, CHO, $COCH_3$, CN),
C_5H_5FeR (R = O, OH, NH_2, F, Cl, Br, I, OCH_3)

17–20-electron complexes

$(C_5H_5)_2M$ (M = Fe, V, Cr, Ti, Zr, Rh), $C_5H_5FeC_5H_4X$ (X = O, CO, CH_2),
$C_5H_5RhC_5H_4R$ (R = COOH, $COOCH_3$, CH_2OH), C_5H_5Rh(acac)

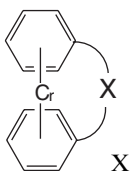

X = SS, $(CH_2)_n$, CH_2O, CH_2OCH_2, CH_2NH

other molecules. For this reason, NR MS cannot directly confirm the mechanism of a specific reaction in the condensed phase, but it provides the *experimental* evidence for the intrinsic stability of such species and therefore for their *possible existence* in other experimental conditions.

2.29.1 REFERENCES

1. Wesdemiotis, C.; McLafferty, F. W. *Chem. Rev.* **1987**, *87*, 485–500.
2. Terlouw, J. K.; Schwarz, H. *Angew. Chem., Int. Ed. Engl.* **1987**, *26*, 805–815.
3. Holmes, J. L. *Mass Spectrom. Rev.* **1989**, *8*, 513–539.
4. Schwarz, H. *Pure Appl. Chem.* **1989**, *61*, 685–692.
5. Holmes, J. L. *Adv. Mass Spectrom.* **1989**, *11*, 53–79.
6. Terlouw, J. K. *Adv. Mass Spectrom.* **1989**, *11*, 984–1010.
7. McLafferty, F. W. *Science* **1990**, *247*, 925–929.
8. Sülzle, D.; Drewello, T.; Schwarz, H. In *Sulfur-centered Reactive Intermediates in Chemistry and Biology*, Chatgilialoglu, C.; Asmus, K.-D., Eds. Plenum Press: New York, 1990; pp 185–192.
9. McLafferty, F. W. *Int. J. Mass Spectrom. Ion Process.* **1992**, *118/119*, 221–235.
10. Turecek, F. *Org. Mass Spectrom.* **1992**, *27*, 1087–1097.
11. Polce, M. J.; Wesdemiotis, C. In *Mass Spectrometry in the Biological Sciences*, Gross, M. L., Ed. Kluwer Academic: Dordrecht, 1992; pp 303–310.
12. Wesdemiotis, C. In *Encyclopedia of Spectroscopy and Spectrometry*, Lindon, J. C.; Tranter, G. E.; Holmes, J. L., Eds. Academic Press: San Diego, CA, 2000; pp 1469–1479.
13. Hudgins, D. M.; Porter, R. F. *Rapid. Commun. Mass Spectrom.* **1988**, *2*, 197–199.
14. Gellene, G. I.; Porter, R. F. *Acc. Chem. Res.* **1983**, *16*, 200–207.
15. Turecek, F.; Gu, M.; Shaffer, S. A. *J. Am. Soc. Mass Spectrom.* **1992**, *3*, 493–501.
16. Zagorevskii, D. V.; Aubry, C.; Holmes, J. L. *Eur. Mass Spectrom.* **2000**, *6*, 89–96.
17. Schröder, D.; Fiedler, A.; Schwarz, H. *Int. J. Mass Spectrom. Ion Process.* **1994**, *134*, 239–248.
18. Hop, C. E. C. A.; Holmes, J. L. *Org. Mass Spectrom.* **1991**, *26*, 476–480.
19. Zagorevskii, D. V.; Holmes, J. L.; Zverev, D. V.; Orlova, T. Yu.; Nekrasov, Yu. S. *J. Am. Soc. Mass Spectrom.* **1995**, *6*, 1143–1153.
20. Shalley, C. A.; Hornung, G.; Schröder, D.; Schwarz, H. *Chem. Soc. Rev.* **1998**, *27*, 91–104.
21. Cordero, M. M.; Wesdemiotis, C. In *Biological Mass Spectrometry: Present and Future*, Matsuo, T.; Caprioli, R. M.; Gross, M. L.; Seyama, Y., Eds. Wiley: New York, 1994; pp 119–126.
22. Schroeder, D.; Kretzschmar, I.; Schwarz, H.; Rue, C.; Armentrout, P. *Inorg. Chem.* **1999**, *38*, 3474–3480.
23. Zagorevskii, D. V.; Holmes, J. L. *Mass Spectrom. Rev.* **1994**, *13*, 133–154.
24. Zagorevskii, D. V.; Holmes, J. L. *Mass Spectrom. Rev.* **1999**, *18*, 87–118.
25. Zagorevskii, D. V. *Coord. Chem. Rev.* **2002**, *225*, 5–34.
26. Schröder, D.; Barsch, S.; Schwarz, H. *Chem. Phys. Lett.* **1999**, *309*, 407–413.
27. Zagorevskii, D. V.; Holmes, J. L. *Organometallics* **1995**, *14*, 5041–5043.
28. Zagorevskii, D. V.; Kuck, D.; Holmes, J. L. In *Proceedings of the 48th Conference on Mass Spectrometry and Allied Topics*, Long Beach, CA, June 11–15, 2000; pp 937–938.
29. Zagorevskii, D. V.; Holmes, J. L. *Organometallics* **1997**, *16*, 1969–1973.
30. Zagorevskii, D. V.; Chen, H.; Holmes, J. L.; Nekrasov, Yu. S.; Chizhevski, I. T.; Rastova, N. I.; Kolobova, N. E. *Org. Mass Spectrom.* **1993**, *28*, 463–469.

Comprehensive Coordination Chemistry II
ISBN (set): 0-08-0437486

Volume 2, (ISBN 0-08-0443249); pp 381–386

2.30 Electrospray Mass Spectrometry

W. HENDERSON
University of Waikato, Hamilton, New Zealand
and
J. S. McINDOE
University of Cambridge, UK

2.30.1 THE IONIZATION PROCESS 387
2.30.2 STRUCTURAL INFORMATION 389
2.30.3 APPLICATIONS 389
2.30.4 COMPLICATIONS 390
2.30.5 REFERENCES 390

Electrospray mass spectrometry (ESMS) was developed primarily by Fenn and co-workers in the mid 1980s, an achievement for which Fenn won the 2002 Nobel Prize for Chemistry.[1] Initially exploited for the analysis of thermally fragile and high-molecular-weight materials including proteins and polymers, recently there has been an exponential increase in applications involving coordination complexes. It is a very gentle ionization process (involving transfer of solution ions to the gas phase), and therefore typically yields molecular ions with little or no fragmentation. The simplicity (and thus ease of interpretation) of spectra obtained by this technique is of great benefit. However, ions generated by the electrospray ionization process can be easily fragmented using established techniques such as collision-induced dissociation (CID).

Reviews covering the basic principles behind electrospray ionization mass spectrometry,[2–6] and applications in inorganic, coordination,[7–11] and organometallic[12,13] chemistry have appeared.

2.30.1 THE IONIZATION PROCESS

In the electrospray process, a dilute solution is sprayed from a metal capillary held at a high voltage (ca. 3,000 V) into a chamber which is at atmospheric pressure. A fine spray of charged solution droplets is produced, from which the solvent is evaporated by a stream of warm gas (usually nitrogen) to give gas-phase ions. The nature of the desolvation process has been the subject of much debate, with the two main theories proposed involving either ion evaporation from the surface of the charged droplet, or a more catastrophic process involving a Coulombic explosion. The gas-phase ions are separated using a variety of techniques. Modern instruments may be found with quadrupole, quadrupole ion trap, Fourier transform ion cyclotron resonance (FTICR), magnetic sector, or time-of-flight (TOF) mass analyzers, with tandem (MS/MS) mass spectrometers becoming increasingly popular. The key features of electrospray ionization are that the sample is introduced as a dilute solution (so direct analysis of reaction mixtures can be easily carried out), the gentle nature of this ionization process, and the ability to couple with liquid chromatographic (LC) separation techniques, giving LC–MS. Sample volatility is not a requirement, unlike ionization techniques such as electron impact. Like all forms of mass spectrometry,

Table 1 Major types of positive ions observed for various types of coordination compounds.*

Complex	*Major positive ion species***
$[L_n^aM]$	$[L_n^aM+H]^+$, $[L_n^aM+H+\text{solvent}]^+$, $[2L_n^aM+H]^+$ (and analogous ions from the presence of Na^+, K^+, NH_4^+)
$[L_n^bM]$	$[L_n^bM]^{\cdot+}$
$[L_n^cM]$	$[L_n^cM+Ag]^+$, $[L_n^cM+\text{solvent}+Ag]^+$ (with added Ag^+)
$[L_nMX_m]$	$[M-X]^+$, $[M+\text{solvent}-X]^+$
$[L_nM]^+$	$[L_nM]^+$, $[(L_nM)_2+\text{anion}]^+$
$[L_nM]^{2+}$	$[L_nM]^{2+}$, $[L_nM+\text{anion}]^+$, $[L_nM-H]^+$, $[L_nM+\text{solvent}-H]^+$
$[L_nM]^{3+}$	$[L_nM]^{3+}$, $[L_nM+\text{anion}]^{2+}$, $[L_nM+(\text{anion})_2]^+$, $[L_nM-H]^{2+}$, $[L_nM+\text{solvent}-H]^{2+}$, $[L_nM+(\text{solvent})_2-2H]^+$

[a] With basic sites. [b] Electron-donating. [c] With unsaturated groups; X: halide. * At higher fragmentation energies, weakly associated solvent molecules are lost first followed by stripping of neutral monodentate ligands. Formally charged ligands are difficult to remove by CID, as are chelating ligands and those with high hapticity. ** Negative ions of significant intensity are generally seen only for neutral complexes bearing acidic protons, or for anionic complexes. Spectra are typically uncomplicated, consisting of $[L_nM-H]^-$ ions or $[L_nM]^{x-}$, respectively.

ESMS requires very little sample for analysis, picomolar concentrations being easily accessible under ideal conditions. For many types of coordination complex, the electrospray technique can be considered to give a representative picture of the species present in solution. Indeed, in cases where other solution techniques (such as NMR spectroscopy, ESR spectroscopy) have been used to identify solution species present, there is generally good agreement between the various methods.[14]

The isotopic richness of elements present in most coordination complexes means that the use of a simulation program (if not included with the mass spectrometry software, available separately[15] or online (e.g., the "Chemputer" at http://www.shef.ac.uk/chemistry/chemputer/isotopes.html)) is important in ion assignment. Accurate mass determination ($\pm 0.0001\, m/z$) is less commonly employed due to the high likelihood of ambiguity in the ion composition at high mass.

For coordination complexes, observed ions can be generated by a range of processes, one or more of which may operate for a given complex. The principal types of ions commonly observed are summarized in Table 1.

(i) Charged complexes may give the parent ions (if the charge density of the ion is relatively low) or less-highly charged fragment ions derived from the parent, if the charge density is high. Electrospray ionization is equally amenable to the analysis of cations or anions, by reversal of the appropriate potentials in the instrument.

(ii) Neutral complexes M can ionize by aggregation with a solution cation (X^+) to give detectable $[M+X]^+$ positive ions, providing that a suitable "basic" site (e.g., ether, amine, ketone, alcohol) is present in the complex. In the case of protic solvents or mixtures thereof (e.g., alcohols, alcohol–water or acetonitrile–water mixtures, in which most complexes, even "sparingly soluble" ones, are sufficiently soluble) the cation is typically a proton, or an adventitious (or deliberately added) alkali metal[16] or ammonium cation present in the solvent. An example, that of $Cr(acac)_3$, (Figure 1) illustrates the observation of dominant $[M+H]^+$ and $[2M+NH_4]^+$ ions, together with several low-intensity ancillary ions. Alternatively, non-protic solvents (e.g., tetrahydrofuran) in combination with a suitable cation source such as potassium iodide[17] can be used for compounds susceptible to protonolysis.

(iii) Coordination complexes which contain a relatively labile anionic ligand can ionize by loss of this ligand to give a detectable cation, which can be solvated, depending on the fragmentation conditions chosen. A wide range of transition metal halide complexes have been found to ionize via this pathway.[18]

(iv) In some special cases, the charged probe tip can act as an electrochemical cell, giving oxidized ions in the electrospray spectrum.[19] Thus, electron-rich substrates such as alkyl-substituted metalloporphyrins can be oxidized to give $[M]^{\cdot+}$ ions rather than, e.g., protonated $[M+H]^+$ ions.[20,21] Alternatively, electrochemical ionization can be carried out prior to analysis.[22]

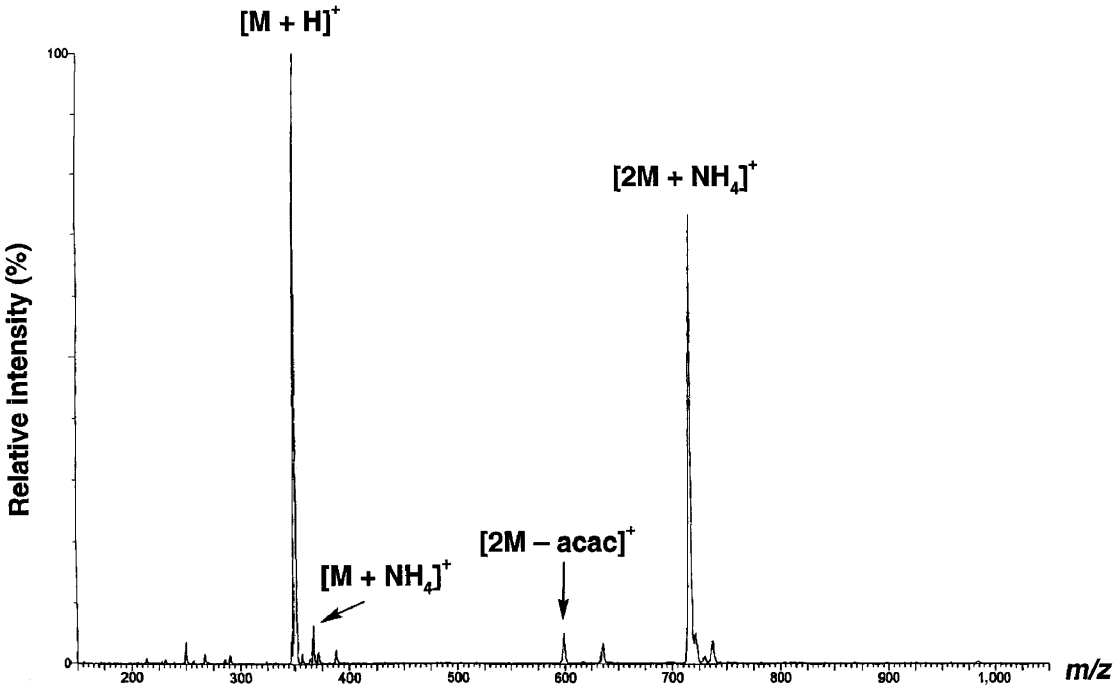

Figure 1 Positive ion electrospray mass spectrum of $Cr(acac)_3$ in MeCN–H_2O solvent, using a cone voltage of 25 V. acac = $CH_3COCHCOCH_3$.

(v) For the characterization of ligands by ESMS, coordination complexes may be generated *in situ* by addition of a suitable metal ion; the use of Ag^+ ions has been used to derivatize a range of phosphine and arsine ligands, allowing mass spectrometric characterization.[23] Complexes with arene ligands can also interact with Ag^+ ions.

2.30.2 STRUCTURAL INFORMATION

Electrospray ionization is a very convenient and successful means of generating gas-phase ions from a variety of substrates. These ions can then be subjected to fragmentation processes in order to yield structural information. CID can be easily achieved in most commercial electrospray mass spectrometers by acceleration of the ions by means of an applied cone voltage (a potential difference applied across two cones which accelerates the ions, causing collisions with gas and residual solvent molecules) or its equivalent. The advantage of this approach is that the degree of fragmentation can be carefully tuned. A singly charged parent ion will often undergo loss of neutral ligand molecules in the initial stages, whereas a multiply charged ion will typically fragment by loss of a charged species or gain of a counterion, to reduce the charge on the parent ion.

Energy-dependent electrospray ionization mass spectrometry (EDESI-MS) uses a map of cone voltage versus m/z upon which ion intensity is plotted, which provides a complete picture of the fragmentation pattern particularly suitable for the structural analysis of mixtures.[24,25]

2.30.3 APPLICATIONS

Many types of coordination compounds have been characterized by ESMS; a selection of examples is given in Table 2.

ESMS is particularly useful for the analysis of solutions containing rapidly exchanging,[26] or paramagnetic species, which are less readily accessed by other solution techniques such as NMR spectroscopy. Studies of kinetically labile equilibria have been carried out, and it was concluded that it would only be difficult to quantify species distributions which change during the 5 μs timescale for ion desorption from an evaporating droplet.[27] Metal–ligand binding constants and relative stabilities of metal–ligand combinations can be determined, such as between alkali metal cations and crown ethers,

Table 2 Coordination complexes which have been studied by ESMS.

Class of complex	*References*
Oxo, nitrido, and imido complexes	42–44
Metal phosphine complexes	18,45,46
Metal halide complexes	18,47
Polyoxometallate anions	48–51
Alkoxide complexes	28–31,52
Thiolate complexes	53,54
Dithiocarbamate complexes	55
Polypyridyl complexes including supramolecular derivatives	56–58
Macrocyclic complexes	59,60
Metallodendrimers	61,62
Diketonate complexes	63
Metal derivatives of peptides and proteins	64,65

cryptands, or other macrocycles.[28–31] Reactive intermediates[32] and complexes formed during catalytic processes can also be detected.[33,34] Electrochemical cells can also be coupled to ES instruments, such that charged species generated electrochemically can then be analyzed directly.[35] ESMS is ideal for the rapid screening of microscale reactions (thus minimizing wastage), and directing subsequent synthetic chemistry on the macroscopic scale. An example is the coordination chemistry of the metalloligands $[Pt_2(\mu\text{-}E)_2(PPh_3)_4]$ (E = S, Se), which form chalcogenide-bridged aggregate cations with a diverse range of metal–halide substrates.[36,37]

2.30.4 COMPLICATIONS

Low-mass, highly charged ions have a limited stability in the gas phase, and anions will either lose electrons or negatively charged fragments, while small, charged cations will often react with the solvent with the formation of, e.g., oxo or hydroxo species.[38–40] Copper(II) complexes often undergo reduction to copper(I).[41] Spectra may be complicated by competing ionization processes, such as addition of H^+, Na^+, K^+, or NH_4^+ ions to a single, pure substrate; spiking the analyte solution with an excess of the authentic cation(s) typically resolves this complication.

2.30.5 REFERENCES

1. Whitehouse, C. M.; Dreyer, R. N.; Yamashita, M.; Fenn, J. B. *Anal. Chem.* **1985**, *57*, 675–679.
2. Cole, R. B., Ed., *Electrospray Ionization Mass Spectrometry; Fundamentals, Instrumentation and Applications*, 1997, Wiley-Interscience, New York.
3. Hofstadler, S. A.; Bakhtiar, R.; Smith, R. D. *J. Chem. Educ.* **1996**, *73*, A82–A88.
4. Voyksner, R. D. *Environ Sci. Technol.* **1994**, *28*, 118A–127A.
5. Kebarle, P.; Tang, L. *Anal. Chem.* **1993**, *65*, 972A–986A.
6. Fenn, J. B.; Mann, M.; Meng, C. K.; Wong, S. F.; Whitehouse, C. M. *Mass Spectrom. Rev.* **1990**, *9*, 37–70.
7. Fisher, K. J. *Prog. Inorg. Chem.* **2001**, *50*, 343–432.
8. Stewart, I. I. *Spectrochim. Acta.* **1999**, *B54*, 1649–1695.
9. Traeger, J. C.; Colton, R. In *Advances in Mass Spectrometry: Proceedings of the 14th International Mass Spectrometry Conference, Tampere, Finland, 25–29 August 1997*, Eds. Karjalainen, E. J.; Hesso, A. E.; Jalonen, J. E.; Karjalainen, U. P. **1998**, *14*, 637–659.
10. Stewart, I. I.; Horlick, G. *Trends Anal. Chem.* **1996**, *15*, 80–90.
11. Hop, C. E. C. A.; Bakhtiar, R. *J. Chem. Educ.* **1996**, *73*, A162–169.
12. Traeger, J. C. *Int. J. Mass Spectrom.* **2000**, *200*, 387–401.
13. Henderson, W.; Nicholson, B. K.; McCaffrey, L. J. *Polyhedron* **1998**, *17*, 4291–4313.
14. Colton, R.; D'Agostino, A.; Traeger, J. C. *Mass Spectrom. Rev.* **1995**, *14*, 79–106.
15. Arnold, L. J. *J. Chem. Educ.* **1992**, *69*, 811.
16. Coll, R. K.; Chand, S.; McIndoe, J. S. *Polyhedron* **1998**, *17*, 507–511.
17. Saf, R.; Mirtl, C.; Hummel, K. *Tetrahedron Lett.* **1994**, *35*, 6653–6656.
18. Henderson, W.; Evans, C. *Inorg. Chim. Acta* **1999**, *294*, 183–192.
19. de la Mora, J. F.; Van Berkel, G. J.; Enke, C. G.; Cole, R. B.; Martinez-Sanchez, M.; Fenn, J. B. *J. Mass Spectrom.* **2000**, *35*, 939–952.
20. Vandell, V. E.; Limbach, P. A. *J. Mass Spectrom.* **1998**, *33*, 212–220.

21. Van Berkel, G. J.; McLuckey, S. A.; Glish, G. L. *Anal. Chem.* **1992**, *64*, 1586–1593.
22. Johnson, K. A.; Shira, B. A.; Anderson, J. L.; Amster, I. J. *Anal. Chem.* **2001**, *73*, 803–808.
23. Bonnington, L. S.; Coll, R. K.; Gray, E. J.; Flett, J. I.; Henderson, W. *Inorg. Chim. Acta* **1999**, *290*, 213–221.
24. Butcher, C. P. G.; Dyson, P. J.; Johnson, B. F. G.; McIndoe, J. S.; Langridge-Smith, P. R. R.; Whyte, C. *Rapid Commun. Mass Spectrom.* **2002**, *16*, 1595–1598.
25. Dyson, P. J.; Hearley, A. K.; Johnson, B. F. G.; Khimyak, T.; McIndoe, J. S.; Langridge-Smith, P. R. R. *Organometallics* **2001**, *20*, 3970–3974.
26. Wang, H.; Agnes, G. R. *Anal. Chem.* **1999**, *71*, 3785–3792.
27. Wang, H.; Agnes, G. R. *Anal. Chem.* **1999**, *71*, 4166–4172.
28. Kempen, E. C.; Brodbelt, J. S. *Anal. Chem.* **2001**, *73*, 384–390.
29. Young, D.-S.; Hung, H.-Y.; Liu, L. K. *Rapid Commun. Mass Spectrom.* **1997**, *11*, 769–773.
30. Oshima, T.; Matsuda, F.; Fukushima, K.; Tamura, H.; Matsubayashi, G.; Arakawa, R. *J. Chem. Soc. Perkin Trans. 2* **1998**, 145–148.
31. Kempen, E. C.; Brodbelt, J. S.; Bartsch, R. A.; Jang, Y.; Kim, J. S. *Anal. Chem.* **1999**, *71*, 5493–5500.
32. Bonchio, M.; Licini, G.; Modena, G.; Moro, S.; Bortolini, O.; Traldi, P.; Nugent, W. A. *Chem. Commun.* **1997**, 869–890.
33. Hoffmuller, W.; Maurus, M.; Severin, K.; Beck, W. *Eur. J. Inorg. Chem.* **1998**, *6*, 729–731.
34. Wilson, S. R.; Wu, Y. H. *Organometallics* **1993**, *12*, 1478–1480.
35. Zhou, F.; van Berkel, G. J. *Anal. Chem.* **1995**, *67*, 3643–3649.
36. Yeo, J. S. L.; Vittal, J. J.; Henderson, W.; Hor, T. S. A. *J. Chem. Soc., Dalton Trans.* **2001**, 315–321.
37. Fong, S.-W. A.; Yap, W. T.; Vittal, J. J.; Hor, T. S. A.; Henderson, W.; Oliver, A. G.; Rickard, C. E. F. *J. Chem. Soc., Dalton Trans.* **2001**, 1986–2002.
38. Peschke, M.; Blades, A. T.; Kebarle, P. *Int. J. Mass Spectrom.* **1999**, *185/186/187*, 685–699.
39. Stewart, I. I.; Horlick, G. *Anal. Chem.* **1994**, *66*, 3983–3993.
40. Cheng, Z. L.; Siu, K. W. M.; Guevremont, R.; Berman, S. S. *Org. Mass Spectrom.* **1992**, *27*, 1370–1376.
41. Lavanant, H.; Virelizier, H.; Hoppilliard, Y. *J. Am. Soc. Mass Spectrom.* **1998**, *9*, 1217–1221.
42. Lau, T.-C.; Wu, Z.; Wang, J.; Siu, K. W. M.; Guevremont, R. *Inorg. Chem.* **1996**, *35*, 2169–2170.
43. Lau, T.-C.; Wang, J.; Siu, K. W. M.; Guevremont, *J. Chem. Soc. Chem. Commun.* **1994**, 1487–1488.
44. Andersen, U. N.; McKenzie, C. J.; Bojesen, G. *Inorg. Chem.* **1995**, *34*, 1435–1439.
45. Colton, R.; Dakternieks, D. *Inorg. Chim. Acta* **1993**, *208*, 173–177.
46. Colton, R.; Harrison, K. L.; Mah, Y. A.; Traeger, J. C. *Inorg. Chim. Acta* **1995**, *231*, 65–71.
47. Lipshutz, B. H.; Stevens, K. L.; James, B.; Pavlovich, J. G.; Snyder, J. P. *J. Am. Chem. Soc.* **1996**, *118*, 6796–6797.
48. Deery, M. J.; Howarth, O. W.; Jennings, K. R. *J. Chem. Soc., Dalton Trans.* **1997**, 4783–4788.
49. Deery, M. J.; Fernandez, T.; Howarth, O. W.; Jennings, K. R. *J. Chem. Soc., Dalton Trans.* **1998**, 2177–2183.
50. Takara, S.; Ogo, S.; Watanabe, Y.; Nishikawa, K.; Kinoshita, I.; Isobe, K. *Angew. Chem., Int. Ed. Engl.* **1999**, *38*, 3051–3053.
51. Walanda, D. K.; Burns, R. C.; Lawrance, G. A.; von Nagy-Felsobuki, E. I. *J. Chem. Soc., Dalton Trans.* **1999**, 311–321.
52. Løver, T.; Henderson, W.; Bowmaker, G. A.; Seakins, J. M.; Cooney, R. P. *J. Mater. Chem.* **1997**, *7*, 1553–1558.
53. Howard-Lock, H. E.; LeBlanc, D. J.; Lock, C. J. L.; Smith, R. W.; Wang, Z. *Chem. Commun* **1996**, 1391–1392.
54. Nomiya, K.; Kondoh, Y.; Nagano, H.; Oda, M. *J. Chem. Soc., Chem. Commun.* **1995**, 1679–1680.
55. Bond, A. M.; Colton, R.; Gatehouse, B. M.; Mah, Y. A. *Inorg. Chim. Acta* **1997**, *260*, 61–71.
56. Marquis-Rigault, A.; Dupont-Gervais, A.; Van Dorsselaer, A.; Lehn, J.-M. *Chem. Eur. J.* **1996**, *2*, 1395–1398.
57. Funeriu, D. P.; Lehn, J.-M.; Baum, G.; Fenske, D. *Chem. Eur. J.* **1997**, *3*, 99–104.
58. Arakawa, R.; Matsuo, T.; Nozaki, K.; Ohno, T.; Haga, M. *Inorg. Chem.* **1995**, *34*, 2464–2467.
59. Stang, P. J.; Cao, D. H.; Chen, K.; Gray, G. M.; Muddiman, D. C.; Smith, R. D. *J. Am. Chem. Soc.* **1997**, *119*, 5163–5168.
60. Ralph, S. F.; Sheil, M. M.; Hick, L. A.; Geue, R. J.; Sargeson, A. M. *J. Chem. Soc Dalton Trans.* **1996**, 4417–4424.
61. Huck, W. T. S.; van Veggel, F. C. J. M.; Reinhoudt, D. N. *Angew. Chem., Int. Ed. Engl.* **1996**, *35*, 1213–1215.
62. Moucheron, C.; Kirsch-De Mesmaeker, A.; Dupont-Gervais, A.; Leize, E.; Van Dorsselaer, A. *J. Am. Chem. Soc.* **1996**, *118*, 12834–12835.
63. Hall, B. J.; Brodbelt, J. S. *J. Am. Soc. Mass Spectrom.* **1999**, *10*, 402–413.
64. Fabris, D.; Hathout, Y.; Fenselau, C. *Inorg. Chem.* **1999**, *38*, 1322–1325.
65. Luo, X.; Huang, W.; Mei, Y.; Zhou, S.; Zhu, L. *Inorg. Chem.* **1999**, *38*, 1474–1480.

Comprehensive Coordination Chemistry II
ISBN (set): 0-08-0437486

Volume 2, (ISBN 0-08-0443249); pp 387–391

2.31
Magnetism: General Introduction

D. GATTESCHI and R. SESSOLI
Università degli Studi di Firenze, Sesto Fiorentino, Italy
and
A. CORNIA
Università degli Studi di Modena e Reggio Emilia, Modena, Italy

2.31.1 INTRODUCTION 393
2.31.2 PARAMAGNETIC SYSTEMS 394
2.31.3 ORIGIN OF THE MAGNETIC INTERACTION: EXCHANGE AND SUPEREXCHANGE 399
2.31.4 HIGH-FIELD MAGNETIZATION AND TORQUE MEASUREMENTS 403
2.31.4.1 High-field Magnetization: The MST Method 404
2.31.4.2 Torque Magnetometry 408
2.31.4.2.1 Basic definitions 408
2.31.4.2.2 The TST method 411
2.31.5 DYNAMIC MAGNETIC PROPERTIES 412
2.31.6 REFERENCES 416

2.31.1 INTRODUCTION

One of the distinctive properties of transition-metal compounds is the presence of unpaired electrons in the partially filled *d*-shell which give rise to magnetic properties. The metal ions are therefore paramagnetic, which means that they are attracted by an applied magnetic field. The paramagnetism has its origins in both the spin and orbital moments of the unpaired electrons. In general, the passage from isolated ions to coordination compounds is associated with the quenching of the orbital moment, and the paramagnetic properties can be described to a first approximation by considering the orbital contribution as a perturbation on the spin term. It is the presence of the unquenched orbital contribution that makes the measurement of the paramagnetic properties an important tool for the structural characterization of transition-metal coordination compounds. In fact magnetic measurements have long been used in order to obtain structural information. Magnetochemistry[1,2] was extensively developed in the 1950s in conjunction with the first impact of quantum mechanics in transition-metal chemistry as a fundamental tool for the characterization of coordination compounds. In the eighties there was a gradual shift from simple paramagnetic properties to all kinds of cooperative magnetic phenomena, with the investigation of complex zero-, one-, two-, and three-dimensional molecule-based magnetic materials.[3–5] This shift of interest was accompanied by a progressive increase in the complexity of the magnetic techniques used to investigate transition-metal compounds. In the early stages the measurement of the effective magnetic moment at room temperature was enough, now it is almost routine to measure down to the liquid helium region and below, in both d.c. and a.c. mode. Sophisticated techniques are also used for the investigation of single crystals.

This chapter is organized as follows. In Section 2.31.2, we will briefly review the magnetic techniques that are traditionally used to investigate simple paramagnets, while in Section 2.31.3 we will describe the origin of the interactions responsible for the various forms of cooperative magnetism. Finally, Sections 2.31.4 and 2.31.5 will be devoted to advanced experimental techniques which are now currently used (or will soon become wide spread) for the investigation of the static and dynamic magnetic properties of molecule-based magnetic materials.

2.31.2 PARAMAGNETIC SYSTEMS

The first information which is possible to obtain from the measurement of the paramagnetic susceptibility of the compounds is the number of unpaired electrons per metal ion, n. In fact in the spin-only limit, and assuming that no interaction between the magnetic centers occurs, the molar magnetic susceptibity χ_m is given by the Curie law:

$$\chi_m = \frac{N_A \mu_B^2 g^2}{3k_B T} S(S+1) = \frac{C}{T} \tag{1}$$

where T is the absolute temperature, N_A is Avogadro's number, μ_B is the Bohr magneton, k_B is Boltzmann constant, $S = n/2$ is the spin value of the given ion, g (value of 2.0023) is Lande's factor for the free electron and:

$$C = \frac{N_A \mu_B^2 g^2}{3k_B} S(S+1) \tag{2}$$

Orbital contributions in general determine departures of the g value from the free electron value, and introduce magnetic anisotropy.[6] Equation (1) shows that the quantity $\chi_m T$ is independent of temperature. Sometimes instead of χ_m a dimensionless quantity, the so-called effective magnetic moment $\mu_{eff} = 2.828\sqrt{(\chi_m T)}$ is used, but in the recent literature the $\chi_m T$ value is usually reported. The spin-only $\chi_m T$ and μ_{eff} values for various numbers of unpaired electrons are given in Table 1. It is much more common for the magnetic susceptibility to use cgs rather than SI units and we will use the former throughout this chapter.

Another important quantity is the magnetization (M), which is expected to depend on temperature and on the applied magnetic field through the Brillouin function. (Note: in this chapter M will be used to indicate both the magnetization and the magnetic spin quantum number, though in different contexts.) The saturation magnetization, which corresponds to the selective population of the lowest-lying state $M = -S$ in a magnetic field, is given by:

$$M_{sat} = N_A \mu_B g S \tag{3}$$

Therefore the direct measurement of the saturation magnetization is another way of determining the number of unpaired electrons of a given compound. To reach the saturation magnetization it is necessary to have a large B/T ratio, where B is the applied magnetic field. Experiments are performed at low T (typically in the liquid helium region or below) and at high fields. Standard magnetometers range from $B = 5\,T$ to $12\,T$, but higher fields are achieved in special centers. Values of 20–30 T can be achieved in static fields, while pulsed field experiments have been reported up to 800 T. Also the sensitivity of commercial magnetometers has strongly increased

Table 1 Spin-only $\chi_m T$ (emu K mol^{-1}) and μ_{eff} values.

n	S	$\chi_m T$	μ_{eff}
1	1/2	0.376	1.73
2	1	1.003	2.83
3	3/2	1.880	3.88
4	2	3.008	4.90
5	5/2	4.387	5.92

and most apparatus is no longer based on force methods (Gouy or Faraday balances) but rather on direct measurement of the magnetic flux variation in a detection coil, which is coupled to a superconducting quantum interference device (SQUID).[2] A SQUID is a superconducting ring with a nonsuperconducting junction where the magnetic field generated by the sample can penetrate in quantized quantities, the so-called fluxons. This results in a high sensitivity of the instrumentation which can measure down to 10^{-8} emu. An alternative measurement method is that employed by the so-called vibrating sample magnetometers (VSM). The sample vibrates inside the coil at a frequency of the order of 50 Hz and the induction is measured with a lock-in amplifier.[2] The latter type of equipment is particularly suited for high field applications.

Going back to Equation (1) we underline that it can be considered as the magnetic counterpart of the ideal-gas law, being based on the assumption of isotropic noninteracting centers. The measurement of the temperature dependence of the magnetic susceptibility therefore provides information on the existence of inter-ion interactions or magnetic anisotropy. The simplest way of taking into account the above factors is through the Curie–Weiss law:

$$\chi_{\mathrm{m}} = \frac{C}{T - \theta} \tag{4}$$

The constants C and θ are usually determined by plotting $1/\chi_{\mathrm{m}}$ vs. T. If the nonzero value of θ depends on inter-ionic interactions a negative θ corresponds to antiferro- and a positive one to ferromagnetic couplings. The sign of θ is not always indicative of the type of magnetic order that occurs at low temperature. A nice example of this can be found in a very simple compound, manganese(III) formate, which can be obtained by treating $KMnO_4$ with formic acid at low temperature. The structure consists of a three-dimensional network of manganese(III) ions connected by formate ions (see Figure 1).[7] In the cavities, carbon dioxide, water, and formic acid molecules are entrapped. The magnetic properties of this compound are shown in Figure 2. The $1/\chi$ vs. T plot shows a linear behavior and the slope agrees well with that expected for $S = 2$, $C = 2.91\ \mathrm{emu\ K\ mol^{-1}}$, thus confirming the oxidation state of the metal ions. The positive θ, $\theta = 18.7\ \mathrm{K}$, is indicative of ferromagnetic interactions, but below a critical temperature (27 K) the susceptibility suddenly decreases as expected for an antiferromagnet. As a possible explanation, antiferromagnetic interactions between layers of ferromagnetically coupled spins have been suggested.[7]

It must be stressed, however, that a nonzero θ is not by itself an indication of inter-ionic interactions. In fact, in low-symmetry environments, which are quite common in transition-metal compounds, the $2S + 1$ states belonging to the S ground multiplet are split even in zero applied

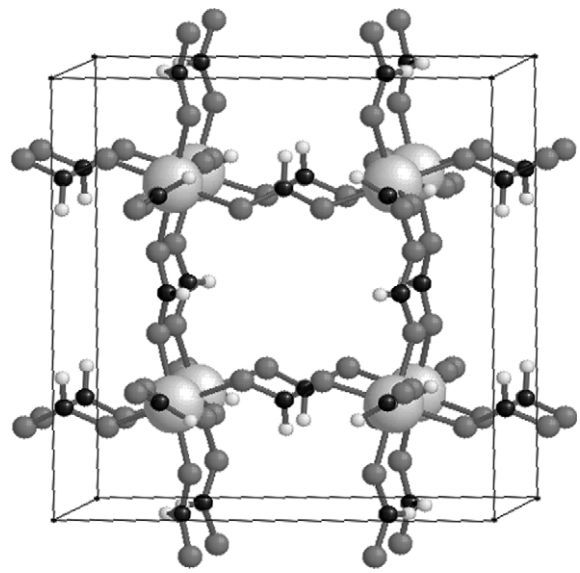

Figure 1 View of the three-dimensional cubic network of $Mn(HCOO)_3$. The metal atoms are light gray, oxygen ones are dark gray, carbon and hydrogen atoms are black and white respectively (after Cornia *et al.*).[7]

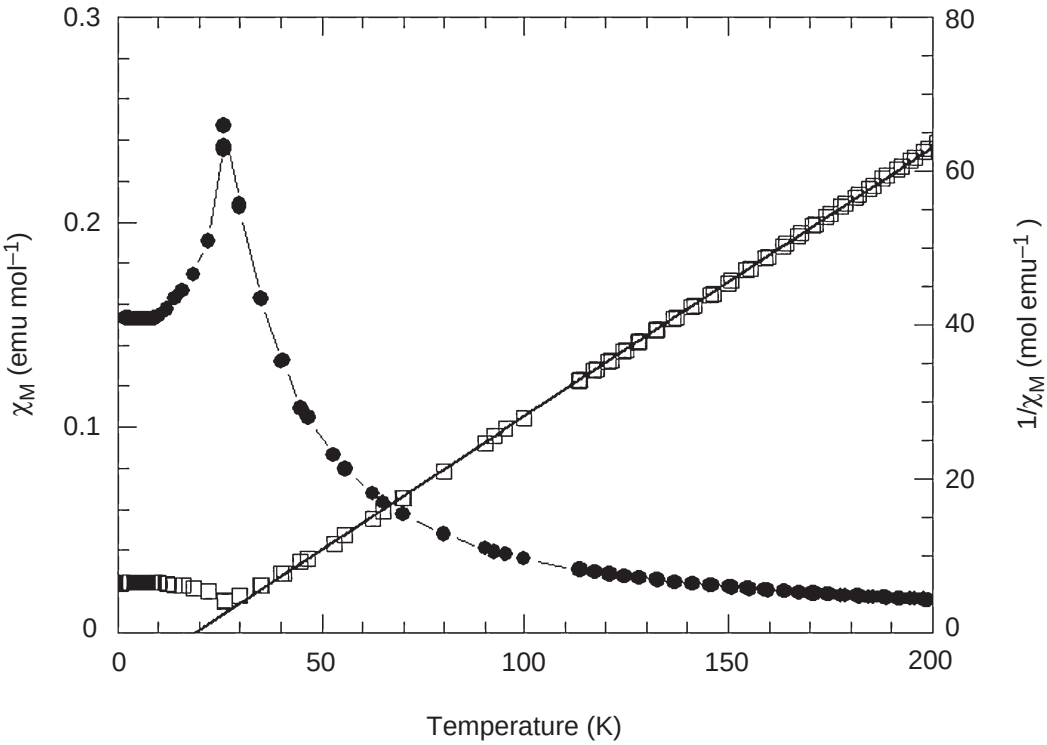

Figure 2 Temperature dependence of the magnetic susceptibility (•) and of $1/\chi$(□) in $Mn(HCOO)_3$. The solid line corresponds to the best fit of the high temperature data ($T > 50$ K) with a Curie–Weiss law (after Cornia *et al.*).[7]

magnetic field (zero field splitting, zfs).[8] This gives rise to magnetic anisotropy and the Curie–Weiss law is followed.

The presence of zfs is particularly apparent at low temperatures. It is best determined through magnetic anisotropy measurements, but reasonable values can be obtained also on polycrystalline samples (powders). This method has been strongly advocated by Hendrickson,[9,10] who also developed suitable computer programs to fit the field dependence of the magnetization. In Figure 3 we show the results obtained on a tetranuclear cluster with formula $Mn_4O_3Cl_4(O_2CC_6H_3Cl_2)_3(Py)_3$ comprising one manganese(IV) ($S = 3/2$) and three manganese(III) ($S = 2$) centers.[10] The data are plotted as a function of B/T, and the experiments were performed by measuring the temperature dependence of the magnetization at a given field. In principle it would be possible also to measure the field dependence of the magnetization at a given temperature. The two procedures are absolutely equivalent as long as the ground multiplet is well separated from the excited ones.

The first important result which emerges from the data of Figure 3 is that at high field the magnetization tends to the limit $M_{sat} = 9N_A\mu_B$ expected for an $S = 9/2$ ground state with $g = 2$. This is only one of the numerous spin states which can be obtained by coupling three $S = 2$ and one $S = 3/2$ spins. This result suggests that the ground spin state can be described by putting the spins of the manganese(III) ions parallel to each other, to give a resulting spin $S = 6$, and antiparallel to the spin of manganese(IV).

The second important piece of information is that there must be a magnetic anisotropy (zfs) operative in the cluster. In fact, for zero zfs all the curves in Figure 3 would superimpose and coincide with the Brillouin function. The zfs of the $S = 9/2$ multiplet is described by the following spin Hamiltonian:

$$\mathbf{H} = D[\mathbf{S}_z^2 - \tfrac{1}{3}S(S+1)] + E'(\mathbf{S}_x^2 - \mathbf{S}_y^2) \tag{5}$$

where the D and E' parameters can be obtained by fitting the experimental data. D (axial zfs parameter) is zero in cubic symmetry, while E' (rhombic zfs parameter) is zero in axial symmetry.

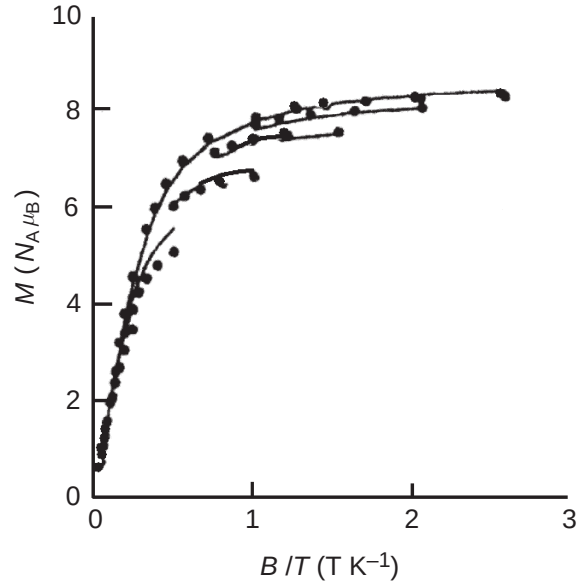

Figure 3 Field dependence of the magnetization of $Mn_4O_3Cl_4(O_2CC_6H_3Cl_2)_3(Py)_3$ at five different temperatures. The data are reported vs. the B/T ratio. The solid line corresponds to the magnetization calculated assuming a ground $S = 9/2$ state with magnetic anisotropy (after Wemple *et al.*).[10]

A positive D gives a ground state corresponding to the smallest M value in the z direction (i.e., $M = 0$ for integer and $M = \pm 1/2$ for half-integer S). This corresponds to the smallest magnetic component along z and the axial anisotropy is thus of the easy-plane type, i.e., at low temperature the spin will be preferentially oriented *perpendicular* to z. For negative D the $M = \pm S$ states, which correspond to the maximum magnetic component along z, lie lowest in energy and the resulting axial anisotropy is of the easy-axis type, i.e., at low temperature the spin will be preferentially oriented *parallel* to z.

Although D and E' can vary independently, in practice it is convenient to restrict the variation in the range:

$$0 \leq |E'/D| \leq 1/3 \tag{6}$$

Varying the E'/D ratio beyond these limits is equivalent, from the symmetry point of view, to a change of the quantization axis.[11,12] This is apparent from the plot of Figure 4, for instance. At $E'/D = 0$, the three levels of $S = 1$ are grouped in two blocks at energies $E(\pm 1) = (1/3)D$ and $E(0) = -(2/3)D$ (the states are labeled using the M components). At $E'/D = 1/3$ the states are heavily admixed, and the three levels have energies $-(2/3)D$, 0, and $(2/3)D$, respectively. This corresponds to the maximum splitting between pairs of neighboring levels. A further increase of the E'/D ratio determines an increase in the separation between the middle and the highest level, while the energy gap between the middle and the lowest level decreases, until at $E'/D = 1$ the energies become $-(2/3)D$ (twofold degenerate state) and $(4/3)D$. In other words, the pattern of levels is similar to that already met at $E' = 0$, only reversed. This is equivalent to choosing the unique axis parallel to x rather than parallel to z.

Equation (5) embodies the simplest spin Hamiltonian which can be used to describe the zfs of the S multiplets. It is totally satisfactory for $S < 2$. For $S \geq 2$, fourth-order terms (depending on $\mathbf{S}_\alpha{}^4$), and for $S \geq 3$, sixth-order terms (depending on $\mathbf{S}_\alpha{}^6$) must in principle also be added.[8]

The magnetization of the S multiplet is calculated as $-\mathrm{d}E/\mathrm{d}B$ by diagonalizing the matrix representative of $\mathbf{H}$ *plus* the Zeeman operator. It must be stressed, however, that the determination of the sign of the zfs parameter D, which gives information on the type of magnetic anisotropy, is extremely difficult on the basis of polycrystalline powder measurements only, unless the low temperature limit, where $k_B T$ is small compared to D *is reached.*

The values of the spin Hamiltonian parameters already provide some useful information, but in order to be fully exploited they require comparison with the values calculated using some fundamental theory. Molecular orbital approaches, especially after the successful introduction

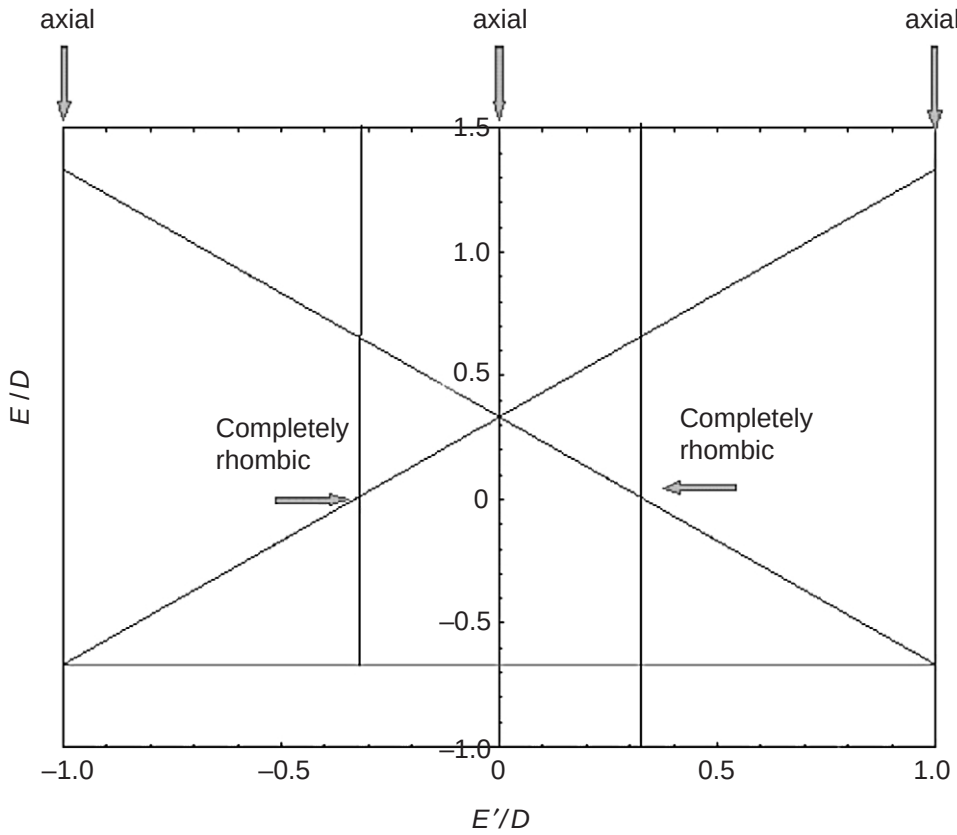

Figure 4 Calculated energy levels for a spin triplet, $S = 1$, as a function of the E'/D ratio.

of density functional theory (DFT) methods,[13–15] are becoming widespread, but for comparison within series of compounds the ligand field models,[6,16] which allowed the first explanation of the magnetic properties of transition-metal compounds, are still a very useful tool. The original compounds that were studied were coordination compounds of high symmetry, because in this case the number of ligand field parameters is reduced to a minimum. However, the 1990s have seen interest growing for low-symmetry transition-metal compounds, therefore treatments are needed which take into account all the parameters required for low-symmetry environments. In 1998, Bencini *et al.*[17] developed a computer program which can be used in an environment with no symmetry at all to calculate not only the second-order, but also fourth-order contributions to the zfs of the S multiplets. The method has been successfully used to analyze the zfs parameters obtained through high-frequency EPR experiments on simple transition-metal compounds.[18] Similar results and programs have also been reported by other groups.[19]

The temperature dependence of the magnetization has been used[20] to determine the nature of the S multiplet and the zfs in a cluster, believed to contain four manganese ions, present in the water oxidizing complex, WOC, of Photosystem II.[21,22] The manganese cluster is an active part of the catalyst which oxidizes water to oxygen, in a four-step process corresponding to the loss of one electron at a time. Among the intermediate forms one was reported to show an EPR spectrum characterized by $g = 4.1$.[23,24] Since the manganese ions present in the cluster are either manganese(III) or manganese(IV), such a large deviation from the free electron value 2.0023 can only be associated with a large zfs. EPR theory suggests that the observed signal arises either from the perpendicular signal of an axial $S = 3/2$ or from a system with $S = 5/2$ in a completely rhombic environment ($|E'/D| \sim 1/3$). Accurate measurements using a SQUID magnetometer suggest that the latter is the correct explanation.[20] Again the experimental work could not distinguish between the two sets of values, $D = +1.7\,\mathrm{cm}^{-1}$, or $D = -1.05\,\mathrm{cm}^{-1}$ and $E'/D = 0.25$. A model compound was also reported to have similar spin Hamiltonian parameters.[25]

2.31.3 ORIGIN OF THE MAGNETIC INTERACTION: EXCHANGE AND SUPEREXCHANGE

The origin of the magnetic interaction between simple paramagnetic centers is well described in many excellent books and reviews to which the interested reader is directed.[4,26–28] Here we simply recall that the interaction can be often considered as the formation of a weak covalent bond between two suitably chosen building blocks. We may imagine that on each building block the unpaired electrons are in molecular orbitals which are usually denoted as "magnetic orbitals."[29,30] If the two magnetic orbitals have a nonzero overlap, the spins will pair (antiferromagnetic coupling) and a weak covalent bond will form between the two magnetic centers. By contrast, if the overlap is zero the spins will tend to stay parallel to each other (ferromagnetic coupling), provided that areas of relatively large overlap density are present. These qualitative rules were proposed in the 1960s by Goodenough and Kanamori.[31–33] A simple clear example was worked out by Kahn *et al.*[34] who synthesized a dinuclear compound of formula $CuVO(fsa)_2en{\cdot}CH_3OH$ (Figure 5). The unpaired electron on the copper(II) center is in the $d(x^2-y^2)$ orbital, while on the oxovanadium(IV) center the unpaired electron lies in the $d(xy)$ orbital. It is apparent that the two orbitals are orthogonal to each other, independent of the angle Cu—O—V at the bridging oxygen ligand. However the magnetic orbital is not exactly localized on the metal ions, but will have a nonzero density on the oxygen ligand as well. In fact, the interaction between the magnetic orbitals is named *exchange interaction* if they overlap directly or *superexchange* if they overlap at a formally diamagnetic bridging ligand. It is this area of common overlap that determines the observed ferromagnetic coupling. If the two magnetic centers did not interact with each other a simple paramagnetic behavior would be expected, which corresponds to the sums of the Curie laws, Equation (1), for the two ions. A simple way of determining whether a compound follows the Curie law is to plot $\chi_m T$ vs. T in a wide temperature range as shown in Figure 6. It is apparent that the experimental curve lies above the theoretical one for two noninteracting spins $S = 1/2$,

$$\chi_m T = \frac{N_A \mu_B^2 (g_{Cu}^2 + g_V^2)}{4k_B} \tag{7}$$

The deviations from the Curie law are associated with the fact that the interaction between the copper(II) and oxovanadium(IV) centers gives rise to a singlet state and a triplet state, separated by an energy Δ. At low temperature the triplet will be selectively populated and the value of $\chi_m T$ will tend to the value expected for $S = 1$, $\sim 1.00\,\text{emu K mol}^{-1}$. From the fit of the temperature dependence of $\chi_m T$, which reflects the variation of the thermal population of the singlet and

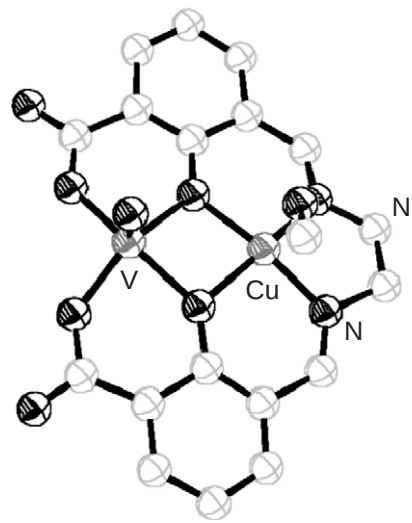

Figure 5 ORTEP view of the structure of $CuVO(fsa)_2en{\cdot}CH_3OH$ (after Kahn *et al.*).[34] The carbon and oxygen atoms are shown in pale and dark gray, respectively. The other atoms are labeled.

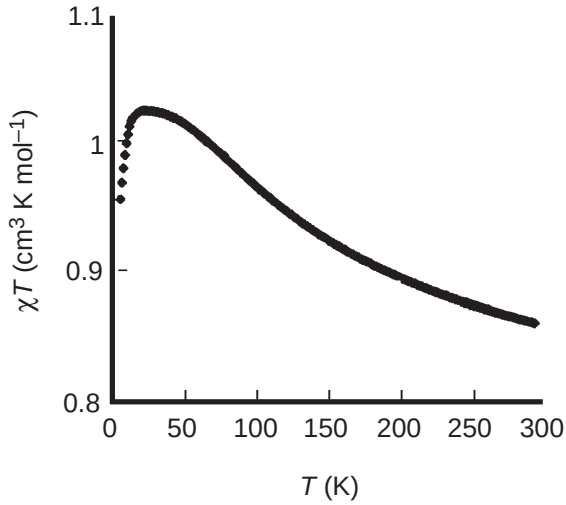

Figure 6 Temperature dependence of the $\chi_m T$ product of $CuVO(fsa)_2en{\cdot}CH_3OH$ (reproduced by permission of the American Chemical Society from *J. Am. Chem. Soc* **1978**, *100*, 3931–3933).

triplet states, it is possible to obtain the energy separation Δ. Therefore magnetic measurement can directly provide information on the interaction between the two metal centers.

Exchange and superexchange interactions are described, in the simplest way, by the spin Hamiltonian:[35]

$$\mathbf{H} = J\mathbf{S}_1{\cdot}\mathbf{S}_2 \tag{8}$$

Different notations where J is substituted by $-J$, $-2J$, $+2J$ are often encountered in the literature. They are all equivalent to each other from a theoretical point of view, but of course comparison between the spin Hamiltonian parameters can be made only if the same convention is used. According to this spin Hamiltonian, a ferromagnetic coupling corresponds to a negative J while an antiferromagnetic coupling is associated with a positive J.

The eigenstates of Equation (8) can be grouped into multiplets having different values of the total spin S and the susceptibility can be easily calculated by taking into account the energy $E(S)$ and the Boltzmann population of the different multiplets:

$$\chi_m = \frac{N_A g^2 \mu_B^2}{3k_B T} \frac{\sum_S S(S+1)(2S+1)e^{-E(S)/k_B T}}{\sum_S (2S+1)e^{-E(S)/k_B T}} \tag{9}$$

where the summations extend over all permitted S values, i.e., $|S_1 - S_2| \leq S \leq S_1 + S_2$.

The above treatment is valid for pairs but can be easily extended to larger numbers of interacting ions by including in the spin Hamiltonian (Equation (8)) all possible pairwise interactions and extending in a similar way the sums in Equation (9). The number of S states is $(2S_i + 1)$ for a pair of spins S_i but increases rapidly as more spins are added. More details on the procedure for the calculation of the thermodynamic properties of high-nuclearity spin clusters will be available in Volume 7.

Perhaps the most complete study of exchange interactions in a class of molecule-based magnetic materials containing pairs of different transition-metal ions has been performed on the series of Prussian-blue analogs.[36] The compounds have general formula $C_nA_p[B(CN)_6]_q{\cdot}xH_2O$, where C is a monovalent cation, usually nonmagnetic, while A and B are magnetic cations, octahedrally coordinated to the N- and C-donor atoms, respectively, of the bridging cyanide ligands. Some typical structures are shown in Figure 7. In octahedral symmetry the d-orbitals are of either e_g- or t_{2g}-symmetry, as depicted in Figure 8. The t_{2g}-orbitals on a B center have nonzero overlap with the t_{2g}-orbitals on the A center, but zero overlap with the e_g orbitals. Therefore the t_{2g}–t_{2g} interaction is expected to be antiferromagnetic, while the t_{2g}–e_g interaction must be ferromagnetic.

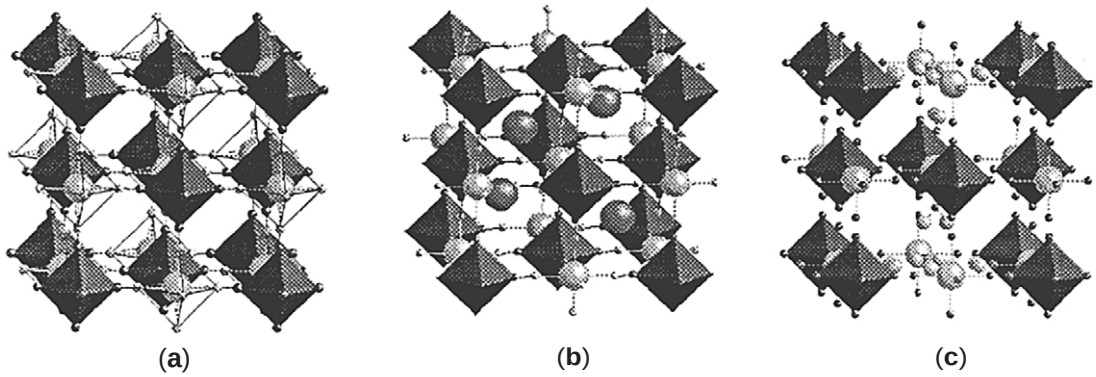

Figure 7 Typical structures of cubic Prussian-blue analogs: (a) A(III)[B(III)$(CN)_6$], A_1B_1; (b) Cs(I)A(II)[B(III)$(CN)_6$], $Cs_1A_1B_1$; (c) $\{A(II)\}_3[B(III)(CN)_6]_2 \cdot xH_2O$, A_3B_2. [$B(CN)_6$] are the dark solid octahedra surrounded by CN (very small spheres), A are the light small spheres, C are the gray medium size spheres in (b); in (c) H_2O are shown by the small light-gray spheres.

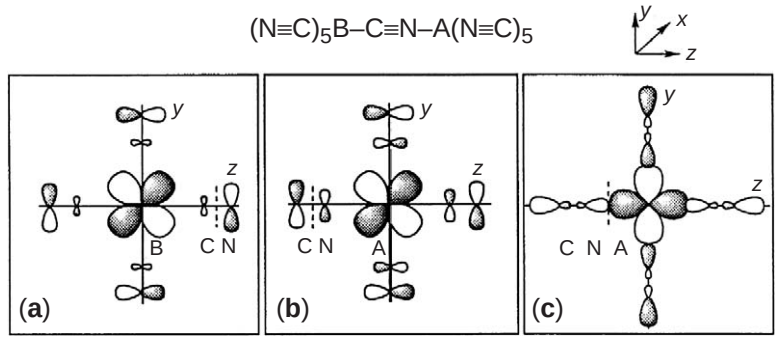

Figure 8 Local magnetic orbitals in an isolated $(NC)_5$–B–CN–$A(NC)_5$ binuclear unit: (a) t_{2g} magnetic orbitals at the B site; (b) t_{2g} magnetic orbitals at the A site; (c) e_g magnetic orbitals at the A site.

The observed exchange interaction J can then be expressed as a sum of pairwise interactions between magnetic orbitals on the two sites:

$$J = \frac{1}{4S_1S_2}\sum_{i,j} J_{ij} \tag{10}$$

where i and j run over all magnetic orbitals on the centers 1 and 2, respectively. For instance, chromium(III) has a d^3 electron configuration, with three unpaired electrons in the t_{2g}-orbitals, while copper(II) and nickel(II) have d^9 and d^8 configurations with one and two unpaired electrons in the e_g orbitals, respectively. In the Cr^{III}–Cu^{II} derivative the interacting magnetic orbitals are $d(x^2-y^2)$ on copper(II) and $d(xz)$, $d(yz)$, $d(xy)$ on chromium(III), so that overall ferromagnetic coupling is expected. Indeed the coupling was found to be ferromagnetic, as shown in Figure 9. Similar considerations hold for the Cr^{III}–Ni^{II} derivative. On the other hand, vanadium(II) has a d^3 configuration with three unpaired electrons in the t_{2g}-orbitals and the Cr^{III}–V^{II} interaction is antiferromagnetic. The coupling constants observed throughout the series are given in Table 2 along with the number of ferromagnetic and antiferromagnetic pathways.

The above treatment considers that the unpaired electrons are localized on the metal centers. While this is certainly a good approximation in the majority of cases, another mechanism based on spin polarization may sometimes be operative.[37] Spin polarization is of fundamental importance for organic radicals,[38] where in general the unpaired spin density is delocalized on a number of atoms.[27,28,39] It has been invoked to explain magnetic coupling in $[Fe(Cp^*)_2]^+(TCNE)^-$,[40,41] the first organometallic compound with magnetic orbitals of s and p character to show a

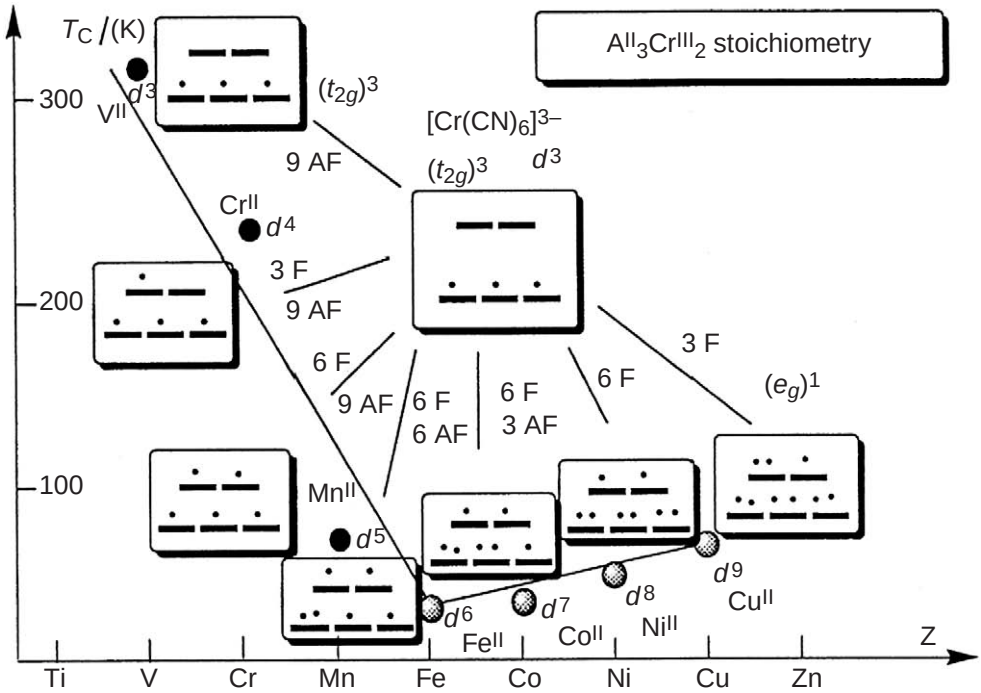

Figure 9 Experimental variation of T_C with Z, the atomic number of the A(II) cation in the series $\{A(II)\}_3[Cr(III)(CN)_6]_2$, electronic structures and expected exchange pathways (black dots ferrimagnets; gray dots ferromagnets) (after Verdaguer *et al.*).[36]

Table 2 Electronic structure, exchange pathways, and interactions in A^{II}-NC-B^{III} magnetic pairs.[a]

Cr^{III} (t_{2g}^3)	V^{II} (t_{2g}^3)	Cr^{II} $(t_{2g}^3)(e_g)$	Mn^{II} $(t_{2g}^3)(e_g^2)$	Fe^{II} $(t_{2g}^4)(e_g^2)$	Co^{II} $(t_{2g}^5)(e_g^2)$	Ni^{II} $(t_{2g}^6)(e_g^2)$	Cu^{II} $(t_{2g}^6)(e_g^3)$
AF pathways	9	9	9	6	3	0	0
F pathways	0	3	6	6	6	6	3
Interaction[a]	AF	AF	AF	af	af	F	F

[a] Upper case notation indicates a strong coupling, either ferromagnetic (F) or antiferromagnetic (AF) in nature, while lower-case notation indicates a weak coupling.

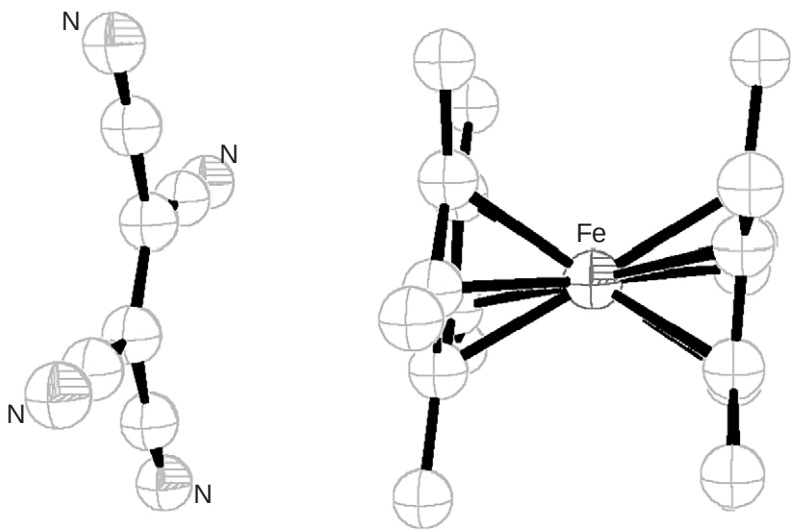

Figure 10 Schematic view of the $[Fe(Cp^*)_2]^{\cdot+}$ and the $TCNE^{\cdot-}$ ions. The noncarbon atoms have been labeled.

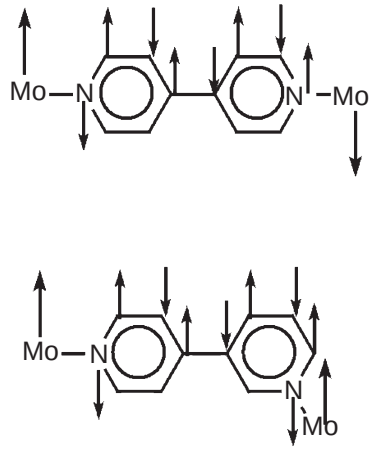

Figure 11 Sketch of the mechanism of spin polarization responsible for the antiferro- (up) and ferromagnetic (down) coupling between molybdenum(V) ions bridged by 4,4′- and 4,5′-bipyridine, respectively (after Bayly *et al.*).[46]

transition to ferromagnetic order at ~4 K. A sketch of the interacting cation and anion is shown in Figure 10. At the lowest level of approximation the unpaired electron of the cation is localized on the iron ion. However, for a more correct description one must take into account spin correlation effects, by considering excited states which mix into the ground state. Formally this corresponds to transferring to the Cp* ligand a fraction of unpaired electron, with a spin opposed to that on the metal center. The negative spin density on the Cp* ring interacts antiferromagnetically with the spin density on the $TCNE^-$ moiety, thus giving rise to an effective ferromagnetic coupling between the iron(III) and $TCNE^-$ centers.[42] It must be stressed that other justifications for the observed ferromagnetic coupling are also possible.

Spin polarization has also been invoked in order to justify the observed alternance of ferro- and antiferromagnetic coupling in dinuclear molybdenum(V) complexes bridged by pyridine type ligands.[43–46] The sketch of Figure 11 is self explanatory: when the bridge is 4,4′-bipyridine the coupling is antiferromagnetic, while for 4,5′-bipyridine the coupling is ferromagnetic. It must be stressed that the procedure outlined in Figure 11 for the spin polarization mechanism is oversimplified, and one should take into account other factors, such as the angle between the aromatic rings. However, the model is simple and has certainly some predictive power for experimentalists.

2.31.4 HIGH-FIELD MAGNETIZATION AND TORQUE MEASUREMENTS

The complexity of the systems investigated in molecular magnetism is continually increasing and the number of independent parameters is so large that measuring the temperature dependence of the magnetic susceptibility is no longer sufficient to characterize the materials. In fact several sets of parameters can often equally well simulate the experimental $\chi_m T$ vs. T curves and additional information are therefore necessary. For instance, the manifold nature of magnetic levels in molecular systems can be probed in considerable detail by exploiting Zeeman interactions with a strong magnetic field at very low temperature. Under these conditions, the evolution of the ground spin state properties as a function of applied field provides a wealth of information about quantities of interest in the spin Hamiltonian, such as intramolecular exchange-coupling interactions and magnetic anisotropies. For this purpose, the field dependence of the magnetization (M), differential susceptibility (dM/dB), or magnetic torque (τ) is usually measured as a function of applied field B on powder or single-crystal samples. High-field magnetization or differential susceptibility measurements have been generally applied to polycrystalline samples and only occasionally to single crystals, due to their intrinsic low sensitivity. By contrast, single crystals are now very conveniently investigated by torque magnetometry (TM). This technique was used at the beginning of magnetochemistry, but the available apparatus required large single crystals, which were difficult to prepare. Now the sensitivity of modern torquemeters allows one to handle very small samples (down to the microgram size).[47] In the following sections, we will describe two

leading techniques for the high-field characterization of molecule-based magnetic materials, namely the magnetization step (MST) and the torque step (TST) methods. They rely on a thermodynamic technique for determining the energies and splitting of individual spin levels and can be regarded as "thermodynamic spectroscopies."[48,49]

2.31.4.1 High-field Magnetization: The MST Method

Though mainly applied to powder samples, the MST method well serves to illustrate the principles underlying the high-field characterization of molecular magnetic systems. The MST technique was initially developed for investigating exchange-coupled metal pairs, triplets, quartets, etc. in dilute magnetic semiconductors and related materials.[50–58] These paramagnetic clusters embedded in a nonmagnetic matrix bear direct structural and magnetic resemblance to molecular systems. The MST method can be applied to antiferromagnetically coupled clusters, in which Zeeman interaction of the spins with an external magnetic field is competitive with intramolecular exchange-coupling interactions. Hence, sufficiently strong magnetic fields induce the progressive decoupling of the spins, resulting in crossovers in the nature of the ground spin state. The simplest molecular compounds to which this approach has been applied are antiferromagnetic dimers, such as $[Fe_2(salen)_2Cl_2]$[59] and $[Fe_2(C_2O_4)(acac)_4]$.[60] Here, isotropic intradimer exchange interactions are dominant and the spin levels $E(S,M)$ are well described by the formula

$$E(S,M) = \frac{J}{2}S(S+1) + g\mu_B MB \tag{11}$$

which follows directly from the spin Hamiltonian

$$\mathbf{H} = J\mathbf{S}_1\cdot\mathbf{S}_2 + g\mu_B\mathbf{S}\cdot\mathbf{B} \tag{12}$$

for two exchange-coupled spins $\mathbf{S}_1$ and $\mathbf{S}_2$ in a magnetic field $\mathbf{B}$ ($B=|\mathbf{B}|$). In Equation (11), S is the total-spin quantum number of the dinuclear species while $M=-S, -S+1,\ldots, S-1, S$ labels the total spin component along $\mathbf{B}$. For two high-spin ferric ions $S_1=S_2=5/2$ and S thus ranges from 0 to 5. In the presence of antiferromagnetic interactions ($J>0$) the ground state has $S=0$ in zero applied field, as shown in Figure 12a. By contrast, in a strong magnetic field the $S=5$ state must lie lowest, the high magnetic field limit being reached when the external field overcomes the AF interaction. By sweeping the magnetic field, it is thus possible to observe the crossovers from $S=0$ to 1, from 1 to 2, etc. as depicted in Figure 12b. These occur at evenly spaced magnetic field values B_n given by:

$$B_n = n\frac{J}{g\mu_B} \quad \text{with} \quad n=1,2\ldots5 \tag{13}$$

At each crossover the value of $|M|$ in the ground state changes by one unit, so that the magnetization exhibits a sudden step-like increase at low temperature ($k_BT \ll J$). Alternatively, when dM/dB is measured (as in pulsed-field experiments) each MST shows up as a peak in the dM/dB vs. B plot (Figure 12c). Because the position of the steps is directly related to the magnitude of the exchange constant through Equation (13), the MST method represents a useful alternative to the traditional approach based on the temperature variation of magnetic susceptibility for the determination of J values, provided that the experiment is performed at sufficiently low temperature (typically below 1 K). In fields up to 55 T, $[Fe_2(salen)_2Cl_2]$ exhibits two peaks in the dM/dB vs. B curve,[59] whereas $[Fe_2(C_2O_4)(acac)_4]$ shows all five predicted peaks because of its comparatively smaller coupling constant (Figure 13).[60] The values $J=16.8(4)\,cm^{-1}$ and $7.2(2)\,cm^{-1}$ have been obtained for the two compounds, respectively, by reasonably assuming $g=2.00$ for the high-spin ferric ion.

The MST has allowed precise measurements of exchange-coupling interactions in higher-nuclearity spin clusters as well. In the manganese(II) cluster $[Mn_3(CH_3CO_2)_6(bpy)_2]$,[61] featuring a linear spin topology, the crossover between the $S=5/2$ and $S=7/2$ states at about 16 T was used to determine the nearest-neighbor coupling constant, $J=4.4\,cm^{-1}$. This value is in very good agreement with that deduced from χ_m vs. T data. In larger exchange-coupled systems, the MST method becomes an even more powerful tool because the magnetic fields required to

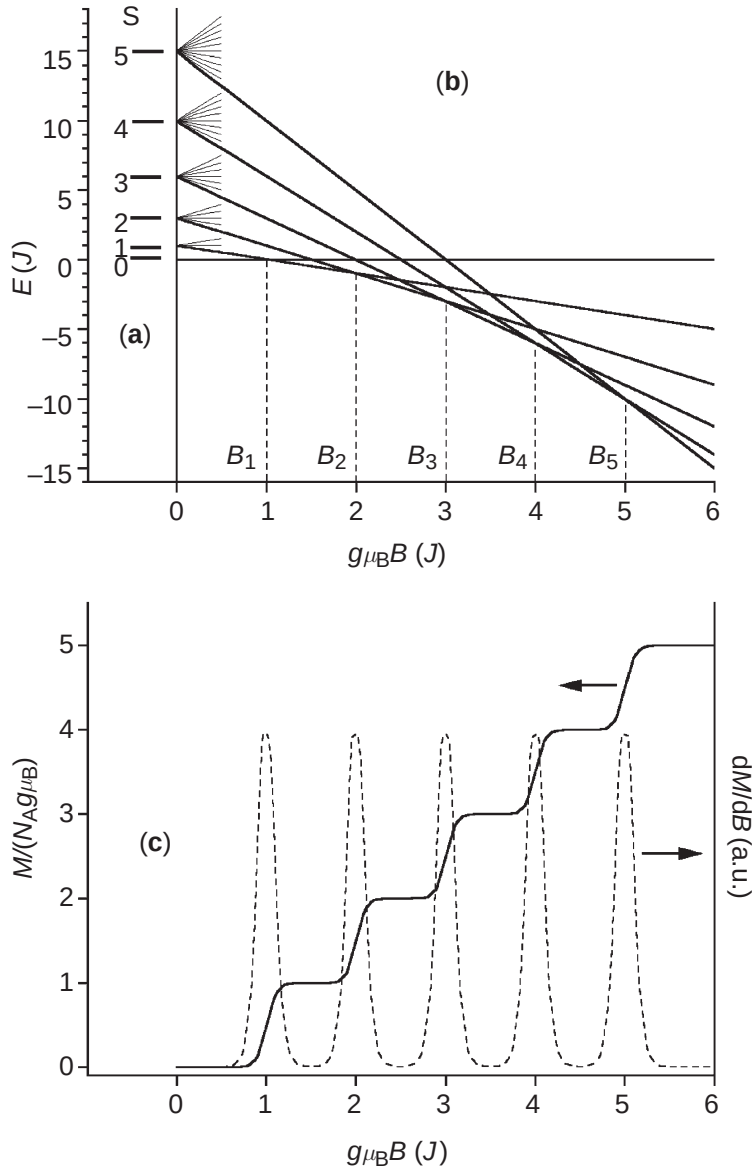

Figure 12 (a) Calculated spin levels for a dimer of antiferromagnetically coupled $S_i = 5/2$ spins in zero magnetic field. (b) Evolution of the spin levels in a magnetic field B. The crossover fields B_n are marked by dashed vertical lines. (c) Molar magnetization (M) and differential susceptibility (dM/dB) of the dimer at low temperature.

induce successive crossovers are often smaller than for dimers with comparable J values. For instance, in ring-like clusters comprising $2N$ antiferromagnetically coupled spins $\mathbf{S}_i$, the energies of the first excited exchange multiplets (Δ_S) and the crossover fields are approximated by the expressions:[62–67]

$$\Delta_S = \frac{J}{N} S(S+1) \tag{14a}$$

$$B_n = n\frac{2J}{Ng\mu_B} \quad \text{with } n = 1, 2 \ldots 2NS_i \tag{14b}$$

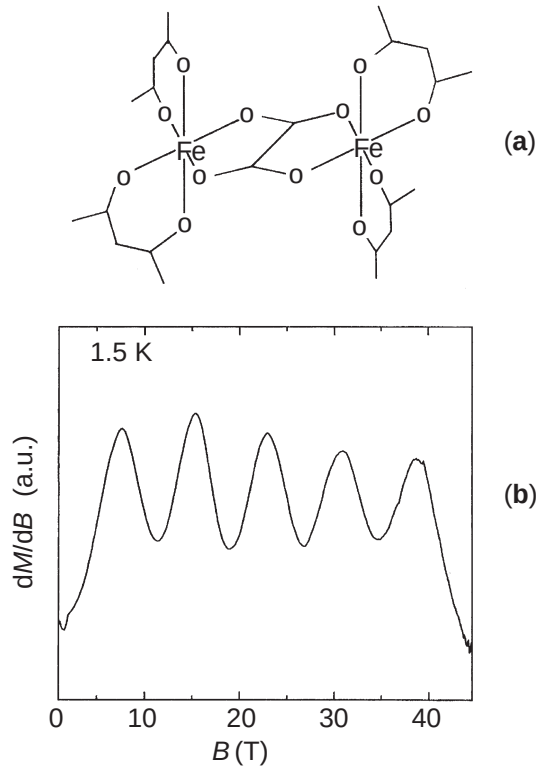

Figure 13 (a) Molecular structure of $[Fe_2(C_2O_4)(acac)_4]$. (b) Differential susceptibility measured in pulsed fields at 1.5 K (after Shapira *et al.*).[60]

For a given J value, Δ_S and B_n are thus expected to decrease with increasing N, following the evolution of the ring toward a chain-like gapless system. Pulsed-field experiments up to 52 T on the compounds $[Na\subset Fe_6(OCH_3)_{12}(dbm)_6]Cl$ ($N=3$, $J=20\,cm^{-1}$)[62,68] and $[Fe_{12}(OCH_3)_{24}(dbm)_{12}]$ ($N=6$, $J=22\,cm^{-1}$)[64,69] revealed *three* and *four* steps in the magnetization, respectively, at $T<1$ K. In the field range from 0 T to 42 T, *nine* MSTs have been observed in the decairon(III) cluster $[Fe_{10}(OCH_3)_{20}(CH_2ClCO_2)_{10}]$ ($N=5$, $J\sim10\,cm^{-1}$) due to the combined effects of a small coupling constant and a large number of spins in the ring (Figure 14).[63] From the position of the MSTs approximate J values can be obtained by using Equation (14b), more accurate estimates requiring exact diagonalization of Heisenberg Hamiltonian.

For a given spin topology the largest exchange constants which can be measured by the MST method are dictated by the maximum available magnetic field. On the other hand, very weak exchange interactions require very low temperatures to resolve the MSTs, so that the use of dilution refrigerators is often mandatory. Utilizing magnetic explosion generators[70,71] magnetic fields of megagauss strength can now be achieved which allow the complete decoupling of the spins, yielding a field-induced quasiferromagnetic state. An outstanding experiment on the dodecanuclear manganese cluster $[Mn_{12}O_{12}(CH_3CO_2)_{16}(H_2O)_4]\cdot4H_2O\cdot2CH_3COOH$, Mn12Ac, in fields up to 600 T has revealed a cascade of discrete quantum jumps of the magnetization at low temperature, reflecting the stepwise modulation from the ground state $S=10$ to $S=22$. The latter corresponds to the state of higher spin multiplicity for four manganese(IV), $S_i=3/2$, and eight manganese(III), $S_i=2$, ions of the cluster.[72]

The amount of information that can be extracted from high-field magnetization measurements on single-crystals is considerably larger than that obtained with powder measurements. For a given orientation of the magnetic field, the position of the MSTs is not only determined by the exchange constants, but also by anisotropic terms such as single-ion zfs and dipolar and anisotropic-exchange interactions.[53,55,56] The resulting angular dependence of crossover fields is completely lost in polycrystalline samples due to powder averaging. The results of angle-resolved measurements on single-crystals of $Pb_{1-x}Eu_xS$ have been interpreted in terms of exchange

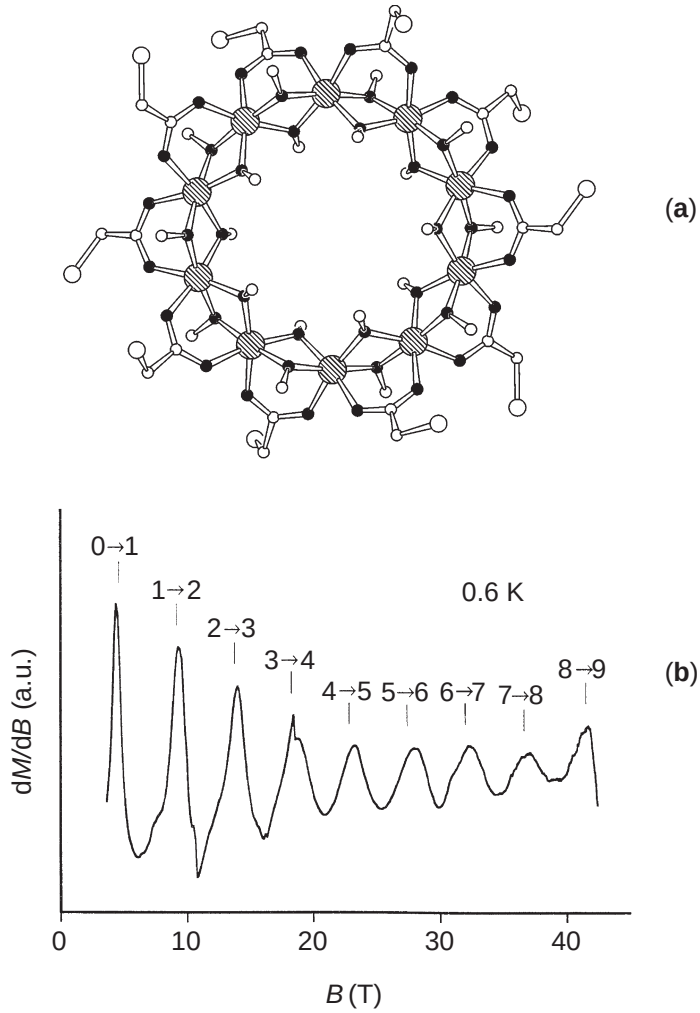

Figure 14 (a) Molecular structure of $[Fe_{10}(OCH_3)_{20}(CH_2ClCO_2)_{10}]$. Atom code: large hatched circles = Fe; small black circles = O; small empty circles = C; medium-size empty circles = Cl. (b) Differential susceptibility measured in pulsed fields at 0.6 K (after Taft *et al.*).[63]

anisotropy between couples of europium(II) ions.[53] Weak magnetic interactions can also be revealed by the width and shape of the MSTs.[50] Under isothermal conditions, the expected full-width at half-maximum (ΔB) of the peaks in dM/dB vs. B curves is given by

$$\Delta B = 3.5255 \frac{k_B T}{g \mu_B} \tag{15}$$

Departures from Equation (15) observed on single-crystal samples of $Cd_{1-x}Mn_xSe$ have been ascribed to Dzyaloshinski-Moriya (DM) interactions[56] within noncentrosymmetric couples of manganese(II) ions. The DM interactions (Equation (16)) are indeed able to mix the spin wave functions near B_n, thus leading to a rounding of the steps.

$$\mathbf{H}_{DM} = \mathbf{d}_{12} \cdot \mathbf{S}_1 \times \mathbf{S}_2 \tag{16}$$

However, possible extrinsic sources of line broadening, such as strain effects and crystal mosaicity,[73] must be carefully ruled out before any interpretation of single-crystal measurements is attempted. Finally, it must be noted that the very fast sweeping rates typical of pulsed-field experiments may lead to thermal nonequilibrium conditions at the crossovers. In this case, the observed lineshape is also strongly influenced by magnetocaloric effects.[59]

2.31.4.2 Torque Magnetometry

2.31.4.2.1 Basic definitions

TM represents a versatile macroscopic method for the characterization of anisotropic magnetic materials. Excellent reviews describe the earliest developments of TM, which was initially used to investigate paramagnetic anisotropy in simple transition-metal complexes.[74,75] Prominent modern applications of TM include the characterization of High-T_c superconductors,[76–78] organic conductors,[79–83] magnetic nanowires,[84,85] nanoparticles,[84] thin films and multilayers,[86–91] as well as chain molecular magnets[92] and molecular magnetic clusters.[47,49,93–101]

Magnetic torque ($\boldsymbol{\tau}$) is the mechanical couple acting on a magnetically anisotropic substance in a homogeneous magnetic field **B**. It originates from the noncollinearity of **B** and the sample magnetization **M**:

$$\boldsymbol{\tau} = \mathbf{M} \times \mathbf{B} \tag{17}$$

Without loss of generality, we can assume that **M** and **B** lie on the xz-plane of an orthogonal coordinate frame so that the $\boldsymbol{\tau}$ vector will be necessarily parallel to the y-axis, with $\tau_x = \tau_z = 0$ and $\tau_y = |\boldsymbol{\tau}|$ (Figure 15). Labeling the polar angles of **M** and **B** with φ and θ, respectively, Equation (17) can be rewritten in scalar form as follows

$$\tau_y = MB \sin(\theta - \varphi) \tag{18}$$

where $M = |\mathbf{M}|$ and $B = |\mathbf{B}|$. If the direction of **M** with respect to the crystal axes is known, as in permanently magnetized substances, φ is simply fixed by the sample orientation and Equation (18) can be directly exploited to measure the magnetization. Notice that the torque signal is maximum for $(\theta - \varphi) = \pi/2, 3\pi/2$, etc. while it vanishes at $(\theta - \varphi) = 0, \pi$, etc., i.e., when **M** is either parallel or antiparallel to **B**. However, TM is most useful to investigate magnetic anisotropy in paramagnetic materials, which feature a field induced magnetization.[47] For an anisotropic paramagnet with spin S and principal magnetic directions along x, y, and z (Figure 15), two limiting regimes can be envisaged which lead to different torque behaviors. In the weak-field limit, τ_y is simply proportional to B^2 and to the difference between the principal susceptibilities in the xz-plane,[47,74,75] as given by the formula

$$\tau_y = B^2(\chi_{zz} - \chi_{xx})\sin\theta\cos\theta \tag{19}$$

By contrast, in the strong-field limit τ_y saturates and becomes field independent due to Zeeman quenching of magnetic anisotropy. For axial anisotropy along z and no g-anisotropy, the molecular torque follows the simple law

$$\tau_y = -2DS(S - 1/2)\sin\theta\cos\theta \tag{20}$$

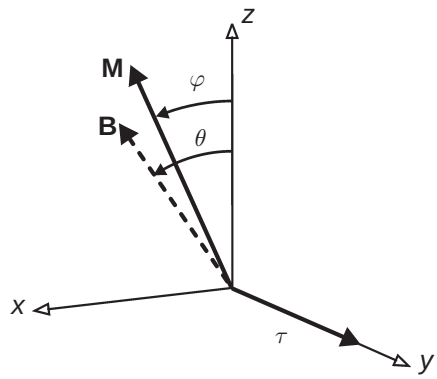

Figure 15 Reference frame used in the discussion of TM, with the definition of the θ and φ angles. **M** and **B** lie on the xz-plane.

where D denotes the axial zfs parameter.[47,98] Notice the angular modulation of the torque provided by the $\sin\theta\ \cos\theta$ term in both Equations (19) and (20). Zero torque is expected whenever the magnetic field is applied along a principal direction, i.e., for $\theta = 0,\ \pi/2,\ \pi,\ 3\pi/2$, etc., while $|\tau_y|$ is maximum for $\theta = \pi/4,\ 3\pi/4$, etc. Equation (19) combined with an average (powder) susceptibility measurement has been largely exploited for the determination of the principal magnetic susceptibilities from low-field torque data.[74,75] On the other hand, Equation (20) constitutes the basis of the TST method, which will be described in the following section.

The complete field-dependence of τ_y allows one to investigate anisotropy terms in much greater detail. For instance, it has been used to extract both second- and fourth-order anisotropy parameters of the ground $S = 10$ state in Mn12Ac (Figure 16a). When the magnetic field is applied close to the hard magnetic plane of the molecule, a bell-shaped torque curve is recovered (Figure 16b). The torque signal exhibits a quadratic field dependence in low fields, passes through a maximum at ~6.2 T and follows an asymptotic behavior in high fields. The best-fit spin

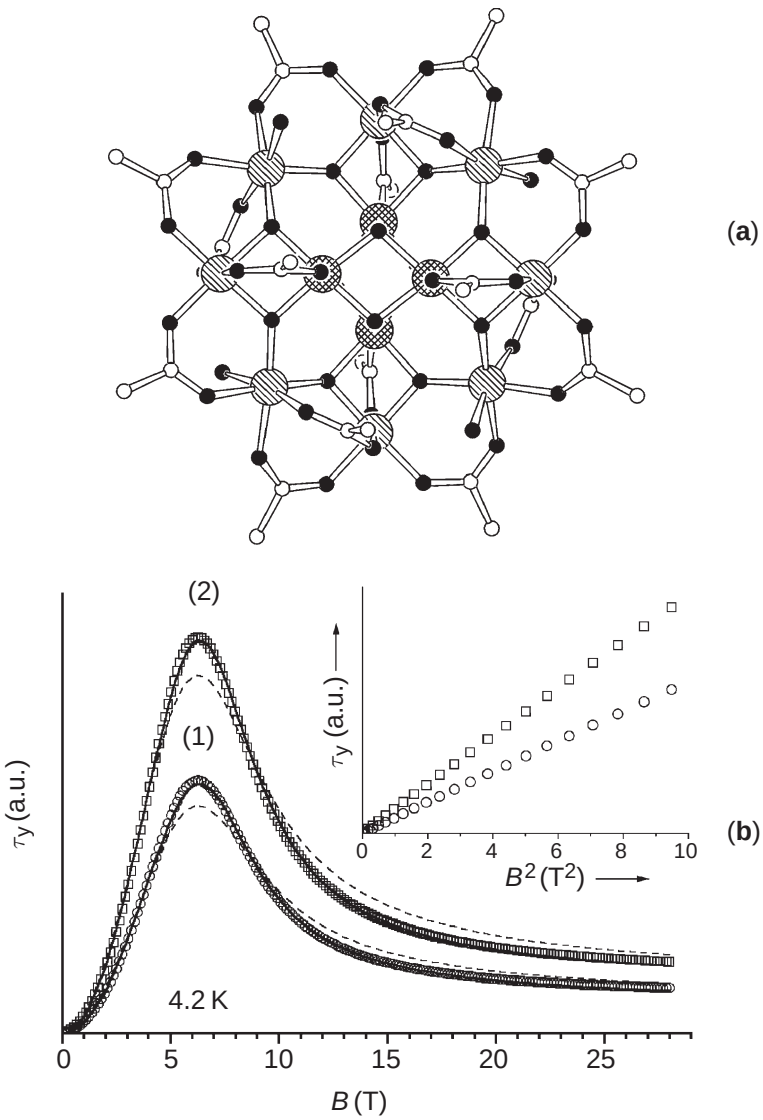

Figure 16 (a) Molecular structure of $[Mn_{12}O_{12}(CH_3CO_2)_{16}(H_2O)_4]$ viewed along the easy magnetic axis (S_4). Same atom code as in Figure 14a, with large hatched circles = Mn. (b) Torque curves recorded at 4.2 K by applying the magnetic field at $\theta = 89.2°$ (line 1) and 88.9° (line 2) from the S_4-axis and best-fit calculated data with (solid lines) and without (dashed lines) fourth-order anisotropy terms. The inset shows the B^2 dependence of τ_y in low fields.

Hamiltonian parameters leading to the solid lines in Figure 16b are in excellent agreement with those determined by spectroscopic techniques, such as inelastic neutron scattering and high-frequency EPR.[94] Notice the much worse fit obtained by neglecting fourth-order anisotropy terms (dashed lines).

We conclude this section by noticing that the design of new torquemeters with increased performance has considerably expanded the potential of modern TM. Micromechanical torquemeters based on miniaturized cantilever[84,88,102–105] or rotor[106] devices are now available whose sensitivity is considerably higher than that of commercial SQUIDs. In addition, they are extremely easy to handle and particularly suitable to operate in high magnetic fields or in the restricted confines of ^{3}He/^{4}He cryostats and dilution refrigerators. Schematic views of cantilever- and rotor-based torquemeters are shown in Figure 17. In both cases, the sample is firmly anchored to the mobile part of the torquemeter, which becomes sensitive to the torque component responsible for cantilever flexion or wheel rotation (τ_y). In the late 1990s, microfabricated cantilevers were realized which allow the detection of *two* torque components at the same time.[103,104] Detection of the torque signal can rely on capacitive, piezoresistive, piezoelectric, or optical methods, in either static or dynamic mode. Cantilever torquemeters with capacitive detection are in particularly widespread use due to their simple design and tunable sensitivity.[102,105] Their functional principle is extremely simple: the cantilever (Si or Cu/Be) is part of a parallel-plate condenser whose

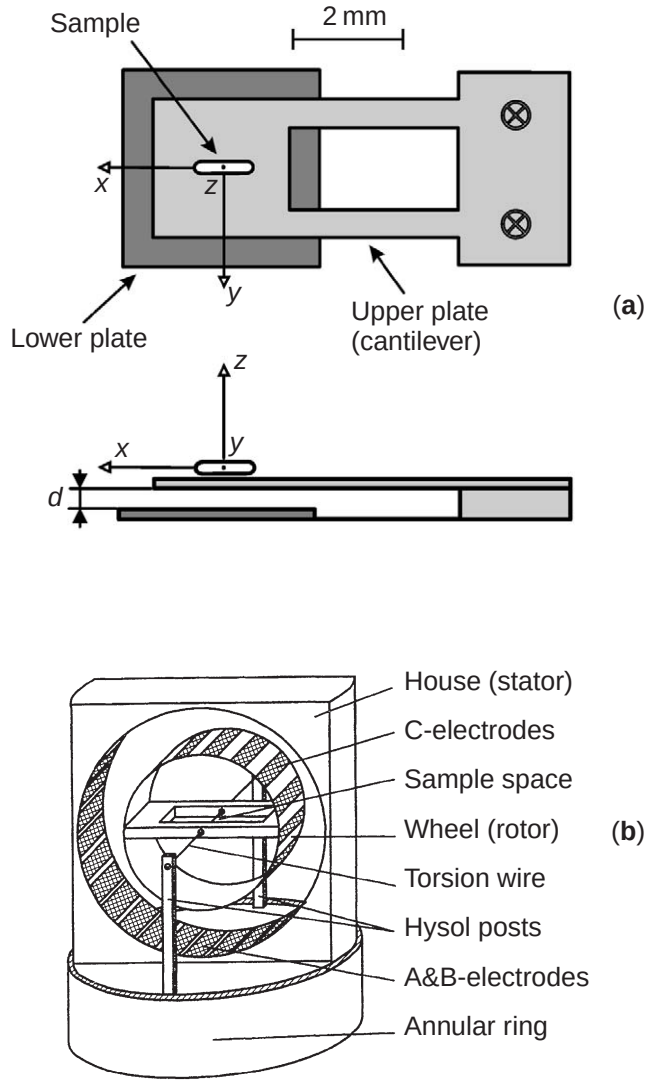

Figure 17 Schematic drawing of cantilever (a) and wheel (b) torquemeters. The size of the gap between the electrodes is exaggerated to show more clearly the electrode configuration (after Wiegers *et al.*).[106]

capacitance is a function of the plate-to-plate separation d (Figure 17a). The sensitivity of the device can be modulated by a proper design of the cantilever (thickness, leg width) or by adjusting the plate-to-plate separation. In a magnetic field, the torque acting on the sample leads to a small deflection of the cantilever which is detected as a change of capacity. For small displacements and a fully elastic response of the spring, the detected capacitance variation is simply proportional to the torque.

2.31.4.2.2 The TST method

In antiferromagnetic clusters, the torque method has been extensively used to detect ground spin state crossover (see Section 2.31.4.1). When the two multiplets involved have different anisotropies, as is usually the case, the ground spin change results in an abrupt, step-like variation of the torque signal at low temperature. After each step, the torque signal reaches a plateau whose height is proportional to the D parameter of the ground state (Equation (20)). Consequently, torque vs. B curves show a staircase structure similar to that obtained in magnetization measurements. In this field, the TST method has proven to be superior to the MST technique because it can be applied to single-crystal samples with a mass of a few micrograms only. In the octachromium(III) ring $[Cr_8F_8(Bu^tCO_2)_{16}]$ (Figure 18) torque data at $T = 0.4\,K$ and $B = 0$–$10\,T$

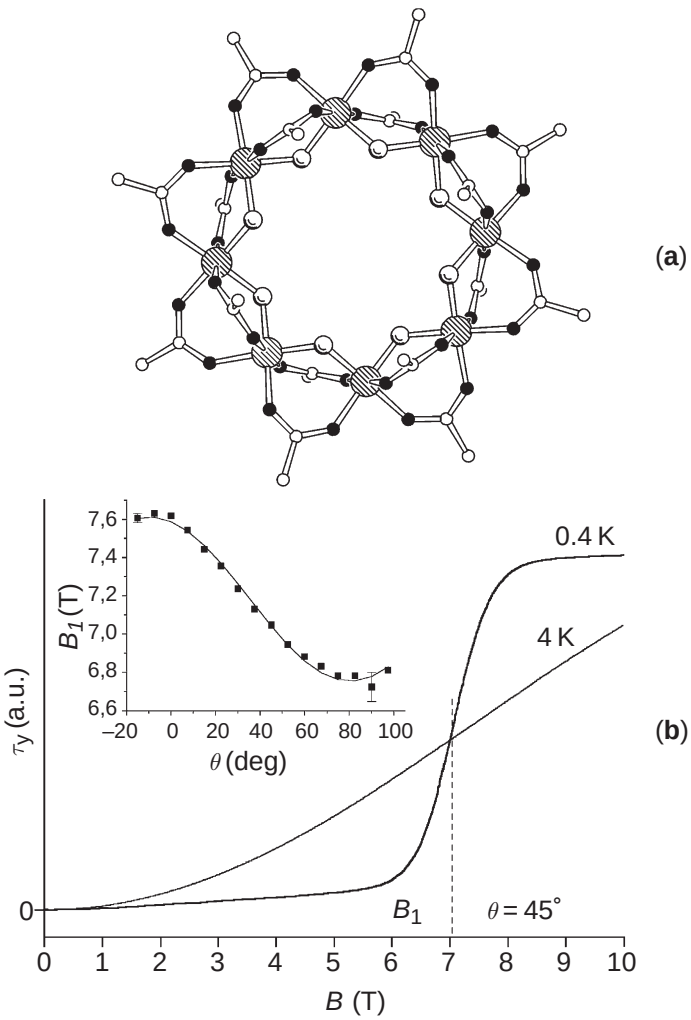

Figure 18 (a) Molecular structure of $[Cr_8F_8(Bu^tCO_2)_{16}]$. Atom code: large hatched circles = Cr; small black circles = O; small empty circles = C; medium-size empty circles = F. (b) Torque signal measured at $\theta \sim 45°$ from the ring axis at two temperatures (4 K and 0.4 K) The inset shows the θ dependence of B_1 and the best-fit curve calculated with the parameters Δ_1 and D_1 given in the text (solid line).

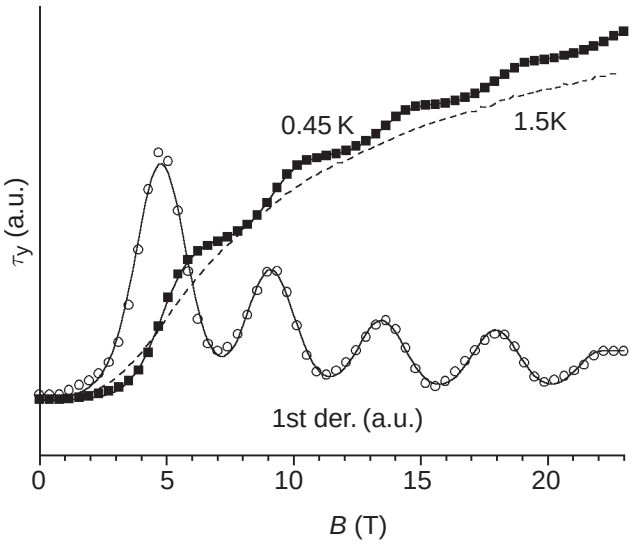

Figure 19 Torque curves recorded at 1.5 K and 0.45 K on $[Fe_{10}(OCH_3)_{20}(CH_2ClCO_2)_{10}]$ at $\theta \sim 50°$ from the ring axis (see Figure 14a for the molecular structure). The first derivative of the torque is also shown. Solid lines provide the best fit to experimental data (after Cornia *et al.*).[99]

have provided the angular variation of the crossover field for the $S = 1 \leftarrow 0$ transition. In particular, B_1 is larger (7.6 T) when the field is parallel to the tetragonal molecular axis as compared with the perpendicular orientation (6.8 T), which is indicative of a hard-axis type anisotropy. The smooth angular variation of the step position has been elegantly used to extract the singlet-triplet energy gap $\Delta_1 = 6.509(8)$ cm^{-1} and the triplet's zero-field splitting $D_1 = 1.59(3)$ cm^{-1}. The latter value compares extremely well with that obtained by high-frequency EPR (1.63 cm^{-1}),[97] further showing that high-field TM is competitive with spectroscopic techniques for the evaluation of spin Hamiltonian parameters. In addition, its applicability is far more general, since EPR resonances from excited states may be unobservable due to fast electronic relaxation, excessive dipolar broadening, or large zero-field splitting.[47,49] The detection of ground-state modulation by TM can be extended to successive crossovers in order to probe the energy and anisotropy of higher excited states. The angular dependence of B_2 has been used to investigate the $S = 2$ spin state in hexa- and octanuclear iron(III) rings.[49,98] Alternatively, the D_S parameters of higher excited states can be evaluated from D_1 and from the relative height of the torque plateaus using Equation (20). This approach has been used to determine the zero-field splitting parameters from D_2 to D_5 in $[Fe_{10}(OCH_3)_{20}(CH_2ClCO_2)_{10}]$ with measurements up to 23 T (Figure 19).[99]

In some cases, the sign of magnetic anisotropy can be abruptly reversed at the crossover fields. The magnetic anisotropy of the 3×3 grid $[Mn_9(2POAP)_6]^{6+}$ (Figure 20) changes from a easy-axis to hard-axis type at 7.5 T as the ground state switches from $S = 5/2$ to 7/2.[100] This result probably reflects the different projection of single-ion anisotropies on the $S = 5/2$ and 7/2 states. The cluster can in fact be regarded as a central manganese(II), $S_C = 5/2$, ion *plus* an outer ring (R) of eight manganese(II) ions antiferromagnetically coupled to give $S_R = 0$, 1, 2, etc. The two spin subsets are weakly magnetically coupled affording the total spin states of the grid. Since the ground $S = 5/2$ state originates from $S_R = 0$ and $S_C = 5/2$, its anisotropy is ruled by the central ion only. By contrast, the first-excited $S = 7/2$ state derives from $S_R = 1$ and thus embeds anisotropic contributions from the outer metal ions as well.

2.31.5 DYNAMIC MAGNETIC PROPERTIES

Until now we have only addressed the static properties of the magnetization, neglecting the dynamic properties[107] which were the focus of great interest among physicists in the 1950s.[108] However a renewed interest in the dynamics of the magnetization has followed the discovery that in Mn12Ac the magnetization relaxes very slowly at low temperature.[109] For example, if the system is magnetized by applying a strong magnetic field and then the field is removed, the

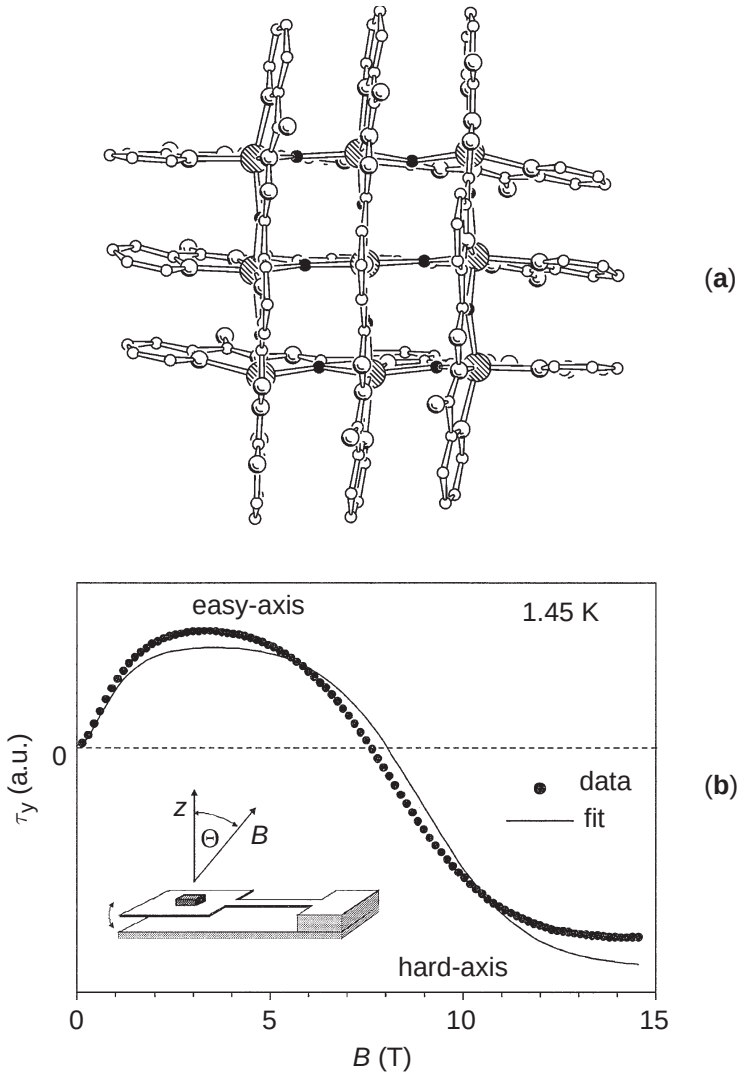

Figure 20 (a) Molecular structure of $[Mn_9(2POAP)_6]^{6+}$. Same atom code as in Figure 14a, with large hatched circles = Mn, medium-size empty circles = N. (b) Field dependence of the torque at 1.45 K and $\theta \sim 24°$ from the idealized S_4 molecular axis (z) (after Waldmann *et al.*).[100]

magnetization relaxes to zero with a characteristic time of approximately two months at around 2 K. At these temperatures a large hysteresis appears, in the magnetization cycle, whose origin is a property of the isolated cluster and not a cooperative phenomenon. These molecules have been named single molecule magnets, SMM, for the analogies they present with bulk magnets.[110]

Information on the dynamics of the magnetization can be now obtained in many chemistry laboratories because most commercial SQUID magnetometers can measure also in the a.c. (alternating current) mode. Very schematically, a weak magnetic field (usually <1 Oe) oscillating at the frequency ν is applied parallel to the principal field and the response is measured. As the amplitude of the oscillating field is small, the ratio $\Delta M/\Delta H$ approaches the limit dM/dH and the "true" susceptibility is measured. The signal is proportional to χ and not to M and therefore the a.c. mode is particularly well suited for low or zero static field measurements without loss of sensitivity. Zero or near-zero field measurements are often necessary to characterize the critical behavior when a phase transition to bulk magnetism occurs. More important is the fact that the response in an oscillating field is a complex quantity:

$$\chi(\omega) = \chi'(\omega) - i\chi''(\omega) \tag{21}$$

where $\omega = 2\pi\nu$. The complex susceptibility is related to the relaxation time τ of the magnetization according to the Casimir and Duprè equations:[111]

$$\chi'(\omega) = \chi_S + \frac{\chi_T - \chi_S}{1 + \omega^2\tau^2} \qquad \chi''(\omega) = \frac{(\chi_T - \chi)\omega\tau}{1 + \omega^2\tau^2} \tag{22}$$

where χ_S is the adiabatic susceptibility, which is measured in the limit $\omega \gg \tau^{-1}$, and χ_T is the isothermal one. The latter corresponds to the limit for which $\omega \ll \tau^{-1}$ and the magnetization relaxes fast enough to follow the oscillating field.

The most rigorous procedure to investigate the dynamic properties of a magnetic compound is to measure the complex susceptibility at a given temperature and at different frequencies and to evaluate the frequency corresponding to the maximum in χ'' for which $\tau^{-1} = \omega$ (see Figure 21). The complex susceptibility can be plotted as χ'' vs. χ' in the so called Cole–Cole plot.[112,113] If the relaxation mechanism is described by one relaxation time the data follow a semicircle with the center on the x-axis. On the contrary, a distribution of relaxation times gives a semicircle whose center falls below the x-axis. More often the susceptibility is measured at a limited number of frequencies by varying the temperature almost continuously. In fact, if the relaxation time, τ, changes with the temperature, the condition $\tau^{-1} = \omega$, corresponding to the maximum value of χ'', is met at different temperatures depending on the a.c. frequency. In Figure 22 is reported the temperature and frequency dependence of both χ' and χ'' for the molecular cluster of formula $[Fe_8O_2(OH)_{12}(tacn)_6]Br_8 \cdot 9H_2O$,[114] one example of the known SMMs.[115] A nonzero χ'' is frequently observed in ordered magnetic materials, but not in the paramagnetic phase. The presence of a nonzero χ'' is now considered a fingerprint of SMM behavior,[116–124] because it denotes the presence of slow relaxation of the magnetization. However it is important to stress that a normal paramagnet can have nonzero χ'' if a moderate static magnetic field is applied.[125] This field in fact removes the degeneracy of spin-up and spin-down states and the much faster spin–spin relaxation mechanism is no more efficient. The spin–lattice relaxation rates below the liquid helium temperature can slow down to the kHz range and can be monitored with commercial a.c. susceptometers. In high-spin clusters with a large magnetic anisotropy such as the SMMs, the relaxation occurs through a multistep Orbach process which involves the different components of the $2S+1$ manifold of the ground spin state, whose degeneracy is removed by the magnetic anisotropy (zfs).[126] Therefore also in zero static field the spin–spin mechanism is inefficient. The spin–lattice relaxation time increases at low temperature following the Arrhenius law, $\tau = \tau_0 \exp(\Delta/kT)$, where Δ is $|D|S^2$, and χ'' becomes different from zero when $\tau \approx \omega^{-1}$. Molecular clusters behaving

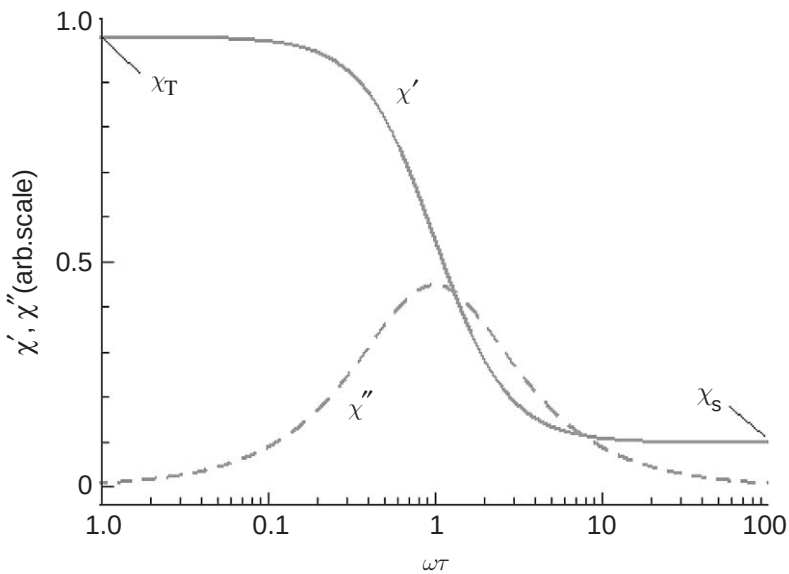

Figure 21 Frequency dependence of the in-phase (χ') and out-of-phase (χ'') magnetic susceptibility. χ_T and χ_S are the isothermal and adiabatic susceptibility, respectively.

like SMM are not the only case of slow relaxation of the magnetization in the paramagnetic phase. Very recently one-dimensional materials comprising anisotropic metal ions like cobalt (II)[127,128] and manganese(III)[129] have also shown similar behavior.

When monitoring the dynamics of the magnetization at very low temperature the relaxation becomes so slow (day, months, years, etc.) that the a.c. susceptibility is no longer measured as the adiabatic limit is attained. In this case a commercial magnetometer can still be used for

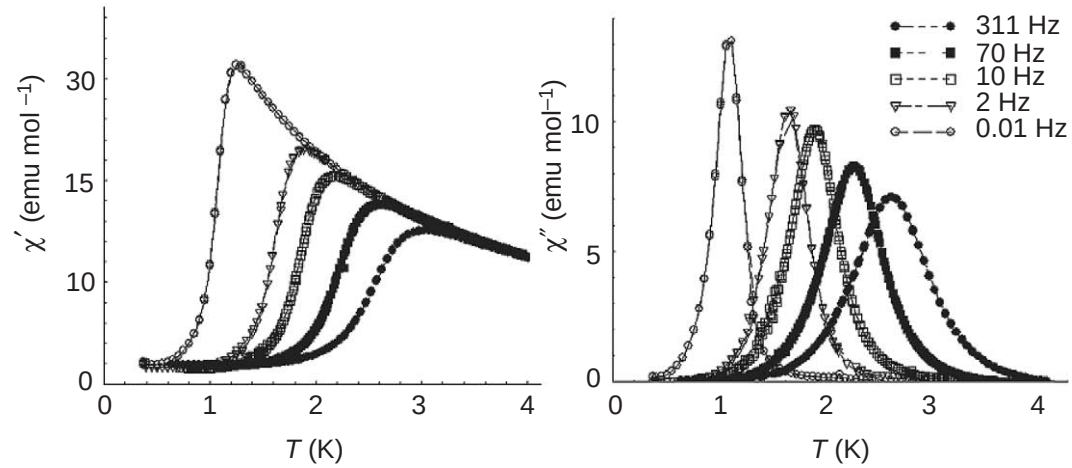

Figure 22 Temperature and frequency dependence of the in-phase (χ') and out-of-phase (χ'') magnetic susceptibility of the molecular cluster $[Fe_8O_2(OH)_{12}(tacn)_6]Br_8 \cdot 9H_2O$.

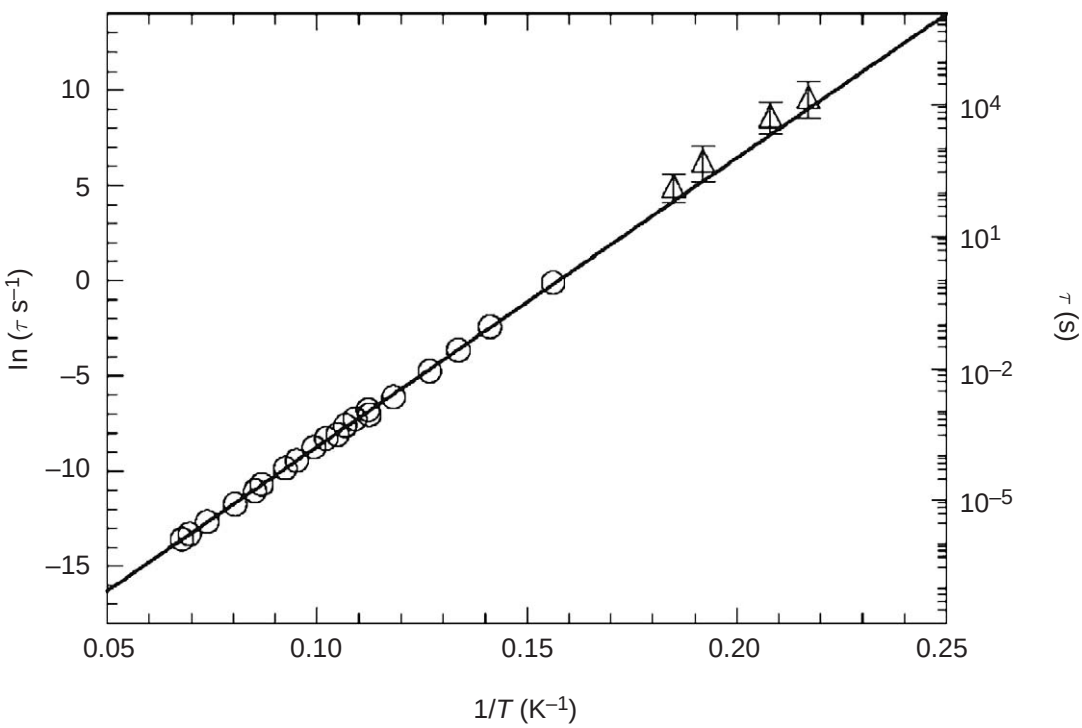

Figure 23 Temperature dependence of the relaxation time of the magnetization of the chain compound $[Co(hfac)_2NITPhOMe]_n$. The empty circles represents the data extracted from a.c. susceptibility while the triangles represents those extracted from the time decay of the remanent magnetization. The line corresponds to the best fit with the Arrhenius law with $\Delta = 152(\pm 1)$ K and $\tau_0 = 4(\pm 1) \times 10^{-11}$ s.

the characterization of the materials by measuring the time dependence of the magnetization. The most commonly used procedure consists in cooling the sample in a magnetic field, then removing the field and monitoring the decay of the magnetization as a function of the elapsed time.[130] If only one process is responsible for the relaxation and the sample is homogeneous the relaxation is described by a single exponential decay, and the characteristic time can easily be extracted from the experimental curves. By combining a.c. susceptibility and magnetization decay measurements the relaxation time of the magnetization of a Co^{II}-nitronyl-nitroxide chain compound of formula $[Co(hfac)_2NITPhOMe]_n$, has been measured and found to follow the Arrhenius law for ~10 decades of characteristic time, as shown in Figure 23.[127,128] By constrast, in SMMs the investigation of the decay of the magnetization at low temperature has revealed, in some cases, deviations from the Arrhenius behavior,[131,132] which have been associated with under-barrier tunneling relaxation processes.[133]

The strong interdisciplinary character of the research in molecular magnetism has introduced many chemists working in this field to more sophisticated techniques,[27] usually considered the realm of physicists. These techniques range from neutron scattering[134–136] to the use of synchrotron light, as in X-ray magnetic circular dichroism,[137–139] from muon spin resonance[140–145] to microcalorimetry,[146,147] as well as unconventional magnetometry. In this last case a very interesting low temperature magnetometer is constituted by an array of micrometer-sized SQUID devices,[148] where the sample is directly placed on the SQUID junctions. Such an experimental set-up, as the cantilever torquemeter described in Section 2.31.4.2, allows the characterization of oriented single crystal of micrometer dimensions.[149] The investigation of the magnetic anisotropy, a fundamental feature in the magnetism of coordination compounds, can therefore be easily extended to those substances for which the growth of large crystals is very difficult.

2.31.6 REFERENCES

1. Carlin, R. L. *Magnetochemistry*; Springer-Verlag: Berlin, **1986**.
2. O'Connor, C. J. *Magnetochemistry-Theory and Experimentation*; Wiley: New York, **1972**.
3. de Jongh, L. J.; Miedema, A. R. *Adv. Phys.* **1974**, *23*, 1–260.
4. Kahn, O. *Molecular Magnetism*; VCH: Weinheim, Germany, **1993**.
5. Gatteschi, D.; Kahn, O.; Miller, J. S.; Palacio, F., Eds. *Magnetic Molecular Materials*; NATO ASI; Kluwer: Dordrecht, The Netherlands, 1991.
6. Griffith, J. S. *The Theory of Transition Metal Ions*; Cambridge University Press: Cambridge, UK, **1961**.
7. Cornia, A.; Caneschi, A.; Dapporto, P.; Fabretti, A. C.; Gatteschi, D.; Malavasi, W.; Sangregorio, C.; Sessoli, R. *Angew. Chem., Int. Ed. Engl.* **1999**, *38*, 1780–1782.
8. Abragam, A.; Bleaney, B. *Electron Paramagnetic Resonance of Transition Ions*; Dover: New York, **1986**.
9. Hendrickson, D. N.; Christou, G.; Schmitt, E. A.; Libby, E.; Bashkin, J. S.; Wang, S.; Tsai, H.-L.; Vincent, J. B.; Boyd, P. D. W.; Huffman, J. C.; Folting, K.; Li, Q.; Streib, W. E. *J. Am. Chem. Soc.* **1992**, *114*, 2455–2457.
10. Wemple, M. W.; Tsai, H.-L.; Folting, K.; Hendrickson, D. N.; Christou, G. *Inorg. Chem.* **1993**, *32*, 2025–2031.
11. Bencini, A.; Gatteschi, D. *Transition Metal Chemistry* **1982**, *8*, 1–178.
12. Bencini, A.; Gatteschi, D. Electron Paramagnetic Resonance Spectroscopy. In *Inorganic Electronic Structure and Spectroscopy*; Lever, A. B. P.; Solomon E. I., Eds.; Wiley Interscience: New York, 1999; Vol. 1, pp 93–159.
13. Hohenberg, P.; Kohn, W. *Phys. Rev.* **1964**, B864–B871.
14. Kohn, W.; Sham, L. *Phys. Rev.* **1965**, *140*, A1133–A1138.
15. Barone, U.; Bencini, A.; Fantucci, P., Eds. In *Recent Advances in Density Functional Methods (Part III)*; World Scientific: Singapore, 2002.
16. Lever, A. B. P.; Solomon, E. I. Ligand Field Theory and the Properties of Transition Metal Complexes. In *Inorganic Electronic Structure and Spectroscopy*; Lever, A. B. P.; Solomon, E. I., Eds.; Wiley Interscience: New York, 1999; Vol. 1, pp 1–91.
17. Bencini, A.; Ciofini, I.; Uytterhoeven, M. G. *Inorg. Chim. Acta* **1998**, *274*, 90–101.
18. Gatteschi, D.; Sorace, L.; Sessoli, R.; Barra, A. L. *Applied Magnetic Resonance* **2001**, *21*, 299–310.
19. Tregenna-Piggott, P. L. W.; Weihe, H.; Bendix, J.; Barra, A. L.; Güdel, H. U. *Inorg. Chem.* **1999**, *38*, 5928–5929.
20. Horner, O.; Rivière, E.; Blondin, G.; Un, S.; Rutherford, A. W.; Girerd, J.-J.; Boussac, A. *J. Am. Chem. Soc.* **1998**, *120*, 7924–7928.
21. Yachandra, V. K.; Sauer, K.; Klein, M. P. *Chem. Rev.* **1996**, *96*, 2927–2950.
22. Zouni, A.; Witt, H. T.; Kern, J.; Fromme, P.; Krauss, N.; Saenger, W.; Orth, P. *Nature* **2001**, *409*, 739–743.
23. Boussac, A.; Girerd, J.-J.; Rutherford, A. W. *Biochemistry* **1996**, *35*, 6984–6989.
24. Boussac, A.; Un, S.; Horner, O.; Rutherford, A. W. *Biochemistry* **1998**, *37*, 4001–4007.
25. Dubé, C. E.; Sessoli, R.; Hendrich, M. P.; Gatteschi, D.; Armstrong, W. H. *J. Am. Chem. Soc.* **1999**, *121*, 3537–3538.
26. Gatteschi, D. *Adv. Mater.* **1994**, *6*, 635–645.
27. Miller, J. S.; Drillon, M., Eds. *Magnetism: Molecules to Materials. Models and Experiments*; Wiley-VCH: Weinheim, Germany, 2001; Vol. 1.
28. Miller, J. S.; Drillon, M., Eds. *Magnetism: Molecules to Materials. Molecule Based Materials*; Wiley-VCH: Weinheim, Germany, 2001; Vol. 2.
29. Anderson, P. W. *Phys. Rev.* **1959**, *115*, 2–13.

30. Anderson, P. W. Exchange in insulators: superexchange, direct exchange, and double exchange. In *Magnetism*; Rado, G. T.; Suhl, H., Eds.; Academic Press: New York, 1963; Vol. 1, p 25.
31. Goodenough, J. B. *J. Phys. Chem. Solids* **1958**, *6*, 287.
32. Goodenough, J. B. *Magnetism and the Chemical Bond*; Interscience: New York, **1963**.
33. Kanamori, J. *J. Phys. Chem. Solids* **1959**, *10*, 87.
34. Kahn, O.; Tola, P.; Galy, J.; Coudanne, H. *J. Am. Chem. Soc.* **1978**, *100*, 3931–3933.
35. Van Vleck, J. H. *The Theory of Electric and Magnetic Susceptibility*; Oxford University Press: Oxford, UK, **1932**.
36. Verdaguer, M.; Bleuzen, A.; Marvaud, V.; Vaissermann, J.; Seuileman, M.; Desplanches, C.; Scuiller, A.; Train, C.; Garde, R.; Gelly, G.; Lomenech, C.; Rosenman, I. V. P.; Cartier, C.; Villain, F. *Coord. Chem. Rev.* **1999**, *190–192*, 1023–1047.
37. McConnel, H. M. *J. Chem. Phys.* **1963**, *39*, 1910.
38. Izuoka, A.; Murata, S.; Sagawara, T.; Iwamura, H. *J. Am. Chem. Soc.* **1987**, *109*, 2631–2639.
39. Miller, J. S.; Drillon, M., Eds. *Magnetism: Molecules to Materials. Nanosized Magnetic Materials*; Wiley-VCH: Weinheim, Germany, 2002; Vol. 3.
40. Miller, J. S.; Calabrese, J. C.; Rommelmann, H.; Chittipeddi, S.; Zhang, J. H.; Reiff, W. M.; Epstein, A. J. *J. Am. Chem. Soc.* **1987**, *109*, 769–781.
41. Miller, J. S.; Epstein, A. J. *Chem. Commun.* **1998**, 1319–1325.
42. Kollmar, C.; Couty, M.; Kahn, O. *J. Am. Chem. Soc.* **1991**, *113*, 7994–8005.
43. McCleverty, J. A.; Ward, M. D. *Acc. Chem. Res.* **1998**, *31*, 842–851.
44. Thompson, A. M. W. C.; Gatteschi, D.; McCleverty, J. A.; Navas, J. A.; Rentschler, E.; Ward, M. D. *Inorg. Chem.* **1996**, *35*, 2701–2703.
45. Ung, V. A.; Thompson, A. M. W. C.; Bardwell, D. A.; Gatteschi, D.; Jeffery, J. C.; McCleverty, J. A.; Totti, F.; Ward, M. D. *Inorg. Chem.* **1997**, *36*, 3447–3454.
46. Bayly, S. R.; Humphrey, E. R.; De Chair, H.; Paredes, C. G.; Bell, Z. R.; Jeffery, J. C.; McCleverty, J. A.; Ward, M. D.; Totti, F.; Gatteschi, D.; Courric, S.; Steele, B. R.; Screttas, C. G. *J. Chem. Soc., Dalton. Trans.* **2001**, 1401–1414.
47. Cornia, A.; Gatteschi, D.; Sessoli, R. *Coord. Chem. Rev.* **2001**, 219–221, 573–604.
48. Waldmann, O.; Koch, R.; Schromm, S.; Müller, P.; Zhao, L.; Thompson, L. K. *Chem. Phys. Lett.* **2000**, *332*, 73–78.
49. Waldmann, O.; Koch, R.; Schromm, S.; Schülein, J.; Müller, P.; Bernt, I.; Saalfrank, R. W.; Hampel, F.; Balthes, E. *Inorg. Chem.* **2001**, *40*, 2986–2995.
50. Gratens, X.; Bindilatti, V.; Ter Haar, E.; Oliveira, N. F.; Shapira, Y.; Montenegro, F. C. *Phys. Rev. B* **2001**, *64*, art. no. 214424.
51. Gratens, X.; Ter Haar, E.; Bindilatti, V.; Oliveira, N. F.; Shapira, Y.; Liu, M. T.; Golacki, Z.; Charar, S.; Errebbahi, A. *J. Phys., Condens. Matter* **2000**, *12*, 3711–3718.
52. Bindilatti, V.; Ter Haar, E.; Oliveira, N. F.; Shapira, Y.; Liu, M. T. *Phys. Rev. Lett.* **1998**, *80*, 5425–5428.
53. Bindilatti, V.; Ter Haar, E.; Oliveira, N. F.; Liu, M. T.; Shapira, Y.; Gratens, X.; Charar, S.; Isber, S.; Masri, P.; Averous, M.; Golacki, Z.; McNiff, E. J. *Phys. Rev. B* **1998**, *57*, 7854–7862.
54. Liu, M. T.; Shapira, Y.; Ter Haar, E.; Bindilatti, V.; Mcniff, E. J. *Phys. Rev. B* **1996**, *54*, 6457–6464.
55. Bindilatti, V.; Oliveira, N. F.; Shapira, Y.; McCabe, G. H.; Liu, M. T.; Isber, S.; Charar, S.; Averous, M.; McNiff, E. J.; Golacki, Z. *Phys. Rev. B* **1996**, *53*, 5472–5480.
56. Bindilatti, V.; Vu, T. Q.; Shapira, Y.; Agosta, C. C.; McNiff, E. J.; Kershaw, R.; Dwight, K.; Wold, A. *Phys. Rev. B* **1992**, *45*, 5328–5338.
57. Shapira, Y. *J. Appl. Phys.* **1990**, *67*, 5090–5095.
58. Foner, S.; Shapira, Y.; Heiman, D.; Becla, P.; Kershaw, R.; Dwight, K.; Wold, A. *Phys. Rev. B* **1989**, *39*, 11793–11799.
59. Shapira, Y.; Liu, M. T.; Foner, S.; Dubé, C. E.; Bonitatebus, P. J. *Phys. Rev. B* **1999**, *59*, 1046–1054.
60. Shapira, Y.; Liu, M. T.; Foner, S.; Howard, R. J.; Armstrong, W. H. *Phys. Rev. B* **2001**, *63*, art. no. 094422.
61. Ménage, S.; Vitols, S. E.; Bergerat, P.; Codjovi, E.; Kahn, O.; Girerd, J. J.; Guillot, M.; Solans, X.; Calvet, T. *Inorg. Chem.* **1991**, *30*, 2666–2671.
62. Caneschi, A.; Cornia, A.; Fabretti, A. C.; Foner, S.; Gatteschi, D.; Grandi, R.; Schenetti, L. *Chem. Eur. J.* **1996**, *2*, 1379–1387.
63. Taft, K. L.; Delfs, C. D.; Papaefthymiou, G. C.; Foner, S.; Gatteschi, D.; Lippard, S. J. *J. Am. Chem. Soc.* **1994**, *116*, 823–832.
64. Abbati, G. L.; Caneschi, A.; Cornia, A.; Fabretti, A. C.; Gatteschi, D. *Inorg. Chim. Acta* **2000**, *297*, 291–300.
65. Chiolero, A.; Loss, D. *Phys. Rev. Lett.* **1998**, *80*, 169–172.
66. Meier, F.; Loss, D. *Phys. Rev. Lett.* **2001**, *86*, 5373–5376.
67. Normand, B.; Wang, X.; Zotos, X.; Loss, D. *Phys. Rev. B* **2001**, *63*, art. no. 184409.
68. Caneschi, A.; Cornia, A.; Lippard, S. J. *Angew. Chem., Int. Ed. Engl.* **1995**, *34*, 467–469.
69. Nakano, H.; Miyashita, S. *J. Phys. Soc. Jpn.* **2001**, *70*, 2151–2157.
70. Zvezdin, A. K.; Plis, V. I.; Popov, A. I. *Physics of the Solid State* **2000**, *42*, 1100–1105.
71. Zvezdin, A. K.; Plis, V. I.; Popov, A. I.; Barbara, B. *Physics of the Solid State* **2001**, *43*, 185–189.
72. Platonov, V. V.; Barbara, B.; Caneschi, A.; Clark, D. A.; Fowler, C. M.; Gatteschi, D.; Lubashevsky, I. A.; Mukhin, A. A.; Plis, V. I.; Popov, A. I.; Rickel, D. G.; Sessoli, R.; Tatsenko, O. M.; Zvezdin, A. K. submitted for publication.
73. Rubo, Y. G.; Thorpe, M. F.; Mousseau, N. *Phys. Rev. B* **1997**, *56*, 13094–13102.
74. De W. Horrocks, W.; De W. Hall, D. *Coord. Chem. Rev.* **1971**, *6*, 147–186.
75. Mitra, S. *Prog. Inorg. Chem.* **1977**, *22*, 309–408.
76. Hofer, J.; Schneider, T.; Singer, J. M.; Willemin, M.; Keller, H.; Sasagawa, T.; Kishio, K.; Conder, K.; Karpinski, J. *Phys. Rev. B* **2000**, *62*, 631–639.
77. Zhukov, A. A.; De Groot, P. A. J.; Kokkaliaris, S.; Di Nicolo, E.; Jansen, A. G. M.; Mossang, E.; Martinez, G.; Wyder, P.; Wolf, T.; Kupfer, H.; Asaoka, H.; Gagnon, R.; Taillefer, L. *Phys. Rev. Lett.* **2001**, *87*, art. no. 017006.
78. Willemin, M.; Schilling, A.; Keller, H.; Rossel, C.; Hofer, J.; Welp, U.; Kwok, W. K.; Olsson, R. J.; Crabtree, G. W. *Phys. Rev. Lett.* **1998**, *81*, 4236–4239.

79. Harrison, N.; Balicas, L.; Brooks, J. S.; Tokumoto, M. *Phys. Rev. B* **2000**, *62*, 14212–14223.
80. Harrison, N.; Biskup, N.; Brooks, J. S.; Balicas, L.; Tokumoto, M. *Phys. Rev. B* **2001**, *63* art. no. 195102.
81. Uji, S.; Shinagawa, H.; Terashima, T.; Yakabe, T.; Terai, Y.; Tokumoto, M.; Kobayashi, A.; Tanaka, H.; Kobayashi, H. *Nature* **2001**, *410*, 908–910.
82. Mola, M. M.; Hill, S.; Qualls, J. S.; Brooks, J. S. *Physica B* **2001**, 294–295, 422–426.
83. Weiss, H.; Kartsovnik, M. V.; Biberacher, W.; Balthes, E.; Jansen, A. G. M.; Kushch, N. D. *Phys. Rev. B* **1999**, *60*, R16259–R16262.
84. Stipe, B. C.; Mamin, H. J.; Stowe, T. D.; Kenny, T. W.; Rugar, D. *Phys. Rev. Lett.* **2001**, *86*, 2874–2877.
85. Henry, Y.; Ounadjela, K.; Piraux, L.; Dubois, S.; George, J. M.; Duvail, J. L. *European Phys. J. B* **2001**, *20*, 35–54.
86. Hohne, R.; Kleint, C. A.; Pan, A. V.; Krause, M. K.; Ziese, M.; Esquinazi, P. *J. Magn. Magn. Mater.* **2000**, *211*, 271–277.
87. Lohndorf, M.; Moreland, J.; Kabos, P.; Rizzo, N. *J. Appl. Phys.* **2000**, *87*, 5995–5997.
88. Harris, J. G. E.; Awschalom, D. D.; Matsukura, F.; Ohno, H.; Maranowski, K. D.; Gossard, A. C. *Appl. Phys. Lett.* **1999**, *75*, 1140–1142.
89. Platt, C. L.; Berkowitz, A. E.; David, S.; Fullerton, E. E.; Jiang, J. S.; Bader, S. D. *Appl. Phys. Lett.* **2001**, *79*, 3992–3994.
90. Hopfl, T.; Sander, D.; Hoche, H.; Kirschner, J. *Rev. Sci. Instrum.* **2001**, *72*, 1495–1501.
91. Poulopoulos, P.; Flevaris, N. K.; Krishnan, R.; Porte, M. *J. Appl. Phys.* **1994**, *75*, 4109–4113.
92. Meira-Belo, L. C.; Leitão, U. A.; Pereira, C. L. M.; Doriguetto, A.; Fernandes, N. G.; Stumpf, H. O. *J. Magn. Magn. Mater.* **2001**, *226–230*, 2018–2020.
93. Cornia, A.; Affronte, M.; Gatteschi, D.; Jansen, A. G. M.; Caneschi, A.; Sessoli, R. *J. Magm. Magn. Meter.* **2001**, *226–230*, 2012–2014.
94. Cornia, A.; Affronte, M.; Jansen, A. G. M.; Gatteschi, D.; Caneschi, A.; Sessoli, R. *Chem. Phys. Lett.* **2000**, *322*, 477–482.
95. Perenboom, J. A. A. J.; Brooks, J. S.; Hill, S.; Hathaway, T.; Dalal, N. S. *Physica B* **1998**, *246–247*, 294–298.
96. Perenboom, J. A. A. J.; Brooks, J. S.; Hill, S.; Hathaway, T.; Dalal, N. S. *Phys. Rev. B* **1998**, *58*, 330–338.
97. Van Slageren, J.; Sessoli, R.; Gatteschi, D.; Smith, A. A.; Helliwell, M.; Winpenny, R. E. P.; Cornia, A.; Barra, A. L.; Jansen, A. G. M.; Rentschler, E.; Timco, G. A. *Chem. Eur. J.* **2002**, *8*, 277–285.
98. Cornia, A.; Affronte, M.; Jansen, A. G. M.; Abbati, G. L.; Gatteschi, D. *Angew. Chem., Int. Ed. Engl.* **1999**, *38*, 2264–2266.
99. Cornia, A.; Jansen, A. G. M.; Affronte, M. *Phys. Rev. B* **1999**, *60*, 12177–12183.
100. Waldmann, O.; Zhao, L.; Thompson, L. K. *Phys. Rev. Lett.* **2002**, *88*, art. no. 066401.
101. Waldmann, O.; Schülein, J.; Koch, R.; Müller, P.; Bernt, I.; Saalfrank, R. W.; Andres, H. P.; Güdel, H. U.; Allenspach, P. *Inorg. Chem.* **1999**, *38*, 5879–5886.
102. Naughton, M. J.; Ulmet, J. P.; Narjis, A.; Askenazy, S.; Chaparala, M. V.; Hope, A. P. *Rev. Sci. Instrum.* **1997**, *68*, 4061–4065.
103. Brugger, J.; Despont, M.; Rossel, C.; Rothuizen, H.; Vettiger, P.; Willemin, M. *Sens. Actuators* **1999**, *73*, 235–242.
104. Willemin, M.; Rossel, C.; Brugger, J.; Despont, M. H.; Rothuizen, H.; Vettiger, P.; Hofer, J.; Keller, H. *J. Appl. Phys.* **1998**, *83*, 1163–1170.
105. Rossel, C.; Willemin, M.; Gasser, A.; Bothuizen, H.; Meijer, G. I.; Keller, H. *Rev. Sci. Instrum.* **1998**, *69*, 3199–3203.
106. Wiegers, S. A. J.; Van Steenbergen, A. S.; Jeuken, M. E.; Bravin, M.; Wolf, P. E.; Remenyi, G.; Perenboom, J. A. A. J.; Maan, J. C. *Rev. Sci. Instrum.* **1998**, *69*, 2369–2374.
107. Morrish, A. H. *The Physical Principles of Magnetism*; Wiley: New York, **1966**.
108. Gorter, C. J. *Paramagnetic Relaxation*; Elsevier: Amsterdam, **1947**.
109. Sessoli, R.; Gatteschi, D.; Caneschi, A.; Novak, M. A. *Nature (London)* **1993**, *365*, 141–143.
110. Christou, G.; Gatteschi, D.; Hendrickson, D. N.; Sessoli, R. *MRS Bull.* **2000**, *25*, 66–71.
111. Casimir, H. B. J.; Duprè, F. K. *Physica* **1938**, *5*, 507–511.
112. Cole, K. S.; Cole, R. H. *J. Chem. Phys.* **1941**, *9*, 341–351.
113. Dekker, C.; Arts, A. F. M.; DeWijn, H. W.; van Duyneveldt, A. J.; Mydosh, J. A. *Phys. Rev. B* **1989**, *40*, 11243–11251.
114. Wieghardt, K.; Pohl, K.; Jibril, I.; Huttner, G. *Angew. Chem., Int. Ed. Engl.* **1984**, *23*, 77–78.
115. Barra, A. L.; Debrunner, P.; Gatteschi, D.; Schulz, Ch. E.; Sessoli, R. *Europhys. Lett.* **1996**, *35*, 133–138.
116. Eppley, H. J.; Aubin, S. M. J.; Wemple, M. W.; Adams, D. M.; Tsai, H.-L.; Grillo, V. A.; Castro, S. L.; Sun, Z. M.; Folting, K.; Huffman, J. C.; Hendrickson, D. N.; Christou, G. *Molecular Cryst. Liq. Cryst.* **1997**, *305*, 167–179.
117. Brechin, E. K.; Yoo, J.; Nakano, M.; Huffman, J. C.; Hendrickson, D. N.; Christou, G. *Chem. Commun.* **1999**, 783–784.
118. Caneschi, A.; Gatteschi, D.; Sessoli, R.; Barra, A.-L.; Brunel, L. C.; Guillot, M. *J. Am. Chem. Soc.* **1991**, *113*, 5873–5874.
119. Barra, A. L.; Caneschi, A.; Gatteschi, D.; Goldberg, D. P.; Sessoli, R. *J. Solid State Chem.* **1999**, *145*, 484–487.
120. Yamaguchi, A.; Ishimoto, H.; Awaga, K.; Yoo, J. S.; Nakano, M.; Hendrickson, D. N.; Brechin, E. K.; Christou, G. *Physica B* **2000**, *284–288*, 1225–1226.
121. Yoo, J.; Brechin, E. K.; Yamaguchi, A.; Nakano, M.; Huffman, J. C.; Maniero, A. L.; Brunel, L. C.; Awaga, K.; Ishimoto, H.; Christou, G.; Hendrickson, D. N. *Inorg. Chem.* **2000**, *39*, 3615–3623.
122. Aubin, S. M. J.; Sun, Z.; Eppley, H. J.; Rumberger, E. M.; Guzei, I. A.; Folting, K.; Gantzel, P. K.; Rheingold, A. L.; Christou, G.; Hendrickson, D. N. *Inorg. Chem.* **2001**, *40*, 2127–2146.
123. Benelli, C.; Cano, J.; Journaux, Y.; Sessoli, R.; Solan, G. A.; Winpenny, R. E. P. *Inorg. Chem.* **2001**, *40*, 188–189.
124. Cadiou, C.; Murrie, M.; Paulsen, C.; Villar, V.; Wernsdorfer, W.; Winpenny, R. E. P. *Chem. Commun.* **2001**, 2666–2667.
125. Carlin, R. L.; van Duyneveldt, A. J. *Magnetic Properties of Transition Metal Compounds*; Springer: New York, **1977**.
126. Villain, J.; Hartman-Boutron, F.; Sessoli, R.; Rettori, A. *Europhys. Lett.* **1994**, *27*, 159–164.
127. Caneschi, A.; Gatteschi, D.; Lalioti, N.; Sangregorio, C.; Sessoli, R.; Venturi, G.; Vindigni, A.; Rettori, A.; Pini, M. G.; Novak, M. A. *Angew. Chem. Int., Ed. Engl.* **2001**, *40*, 1760–1763.

128. Caneschi, A.; Gatteschi, D.; Lalioti, N.; Sangregorio, C.; Sessoli, R.; Venturi, G.; Vindigni, A.; Rettori, A.; Pini, M. G.; Novak, M. A. *Europhys. Lett.* **2002**, *58*, 771–777.
129. Clérac, R.; Miyaska, H.; Yamashita, M.; Coulon, C. J. *Am. Chem. Soc.* **2002**, 12837–12844.
130. Sessoli, R. *Mol. Cryst. Liq. Cryst.* **1995**, *274*, 145–157.
131. Sangregorio, C.; Ohm, T.; Paulsen, C.; Sessoli, R.; Gatteschi, D. *Phys. Rev. Lett.* **1997**, *78*, 4645–4648.
132. Aubin, S. M. J.; Dilley, N. R.; Pardi, L.; Krzystek, J.; Wemple, M. W.; Brunel, L. C.; Maple, M. B.; Christou, G.; Hendrickson, D. N. *J. Am. Chem. Soc.* **1998**, *120*, 4991–5004.
133. Fort, A.; Rettori, A.; Villain, J.; Gatteschi, D.; Sessoli, R. *Phys. Rev. Lett.* **1998**, *80*, 612–615.
134. Caciuffo, R.; Amoretti, G.; Murani, A.; Sessoli, R.; Caneschi, A.; Gatteschi, D. *Phys. Rev. Lett.* **1998**, *81*, 4744–4747.
135. Amoretti, G.; Carretta, S.; Caciuffo, R.; Casalta, H.; Cornia, A.; Affronte, M.; Gatteschi, D. *Phys. Rev. B* **2001**, *64*, art. no. 104403.
136. Andres, H.; Clemente-Juan, J. M.; Basler, R.; Aebersold, M.; Güdel, H. U.; Borras-Almenar, J. J.; Gaita, A.; Coronado, E.; Büttner, H.; Janssen, S. *Inorg. Chem.* **2001**, *40*, 1943–1950.
137. Arrio, M. A.; Scuiller, A.; Sainctavit, P.; Moulin, C. C. D.; Mallah, T.; Verdaguer, M. *J. Am. Chem. Soc.* **1999**, *121*, 6414–6420.
138. Dujardin, E.; Ferlay, S.; Phan, X.; Desplanches, C.; Moulin, C. C. D.; Sainctavit, P.; Baudelet, F.; Dartyge, E.; Veillet, P.; Verdaguer, M. *J. Am. Chem. Soc.* **1998**, *120*, 11347–11352.
139. Ghigna, P.; Campana, A.; Lascialfari, A.; Caneschi, A.; Gatteschi, D.; Tagliaferri, A.; Borgatti, F. *Phys. Rev. B* **2001**, *64*, art. no. 132413.
140. Blundell, S. J. *Contemporary Physics* **1999**, *40*, 175–192.
141. Lascialfari, A.; Gatteschi, D.; Borsa, F.; Shastri, A.; Jang, Z. H.; Carretta, P. *Phys. Rev. B* **1998**, *57*, 514–520.
142. Schenck, A. *Muon Spin Rotation Spectroscopy: Principles and Applications in Solid State Physics*; Hilger: Bristol, UK, **1986**.
143. Nuttall, C. J.; Carling, S. G.; Day, P. *Solid State Commun.* **1999**, *110*, 39–43.
144. Verdaguer, M.; Blundell, S. J. *Philos. Trans. R. Soc. London, Ser. A* **1999**, *357*, 2936–2937.
145. Salman, Z.; Keren, A.; Mendels, P.; Scuiller, A.; Verdaguer, M. *Physica B* **2000**, *289–290*, 106–109.
146. Fominaya, F.; Fournier, T.; Gandit, P.; Chaussy, J. *Rev. Sci. Instrum.* **1997**, *68*, 4191–4195.
147. Fominaya, F.; Villain, J.; Gandit, P.; Chaussy, J.; Caneschi, A. *Phys. Rev. Lett.* **1997**, *79*, 1126–1129.
148. Wernsdorfer, W.; Hasselbach, K.; Benoit, A.; Barbara, B.; Mailly, D.; Tuaillon, J.; Perez, J. P.; Dupuis, V.; Dupin, J. P.; Giraud, G.; Perex, A. *J. Appl. Phys.* **1995**, *78*, 7192–7195.
149. Wernsdorfer, W.; Sessoli, R. *Science* **1999**, *284*, 133–135.

Comprehensive Coordination Chemistry II
ISBN (set): 0-08-0437486

Volume 2, (ISBN 0-08-0443249); pp 393–419

2.32
Electronic Spin Crossover

P. GÜTLICH
Johannes-Gutenberg-Universität, Mainz, Germany
and
H. A. GOODWIN
University of New South Wales, Sydney, Australia

2.32.1 OCCURRENCE OF SPIN TRANSITIONS 421
2.32.2 CONSEQUENCES OF SPIN TRANSITIONS 422
2.32.3 THE GENERATION OF COOPERATIVITY 423
2.32.4 REFERENCES 425

2.32.1 OCCURRENCE OF SPIN TRANSITIONS

Octahedral complexes of d^{4-7} ions may be high-spin (HS) or low-spin (LS), the particular configuration depending, for a given metal ion, on the relationship between the strength of the ligand field and the spin pairing energy. Progressive change in the field strength may result in the two spin states being almost equi-energetic and the configuration may then change with the application of some external perturbation, such as variation in temperature, pressure, radiation, or a magnetic field. This is referred to as the spin crossover situation and the change in spin state as a spin transition. In order for a spin transition to occur the difference in the Gibb's free energies for the two spin states involved must be of the order of thermal energy, k_BT.

The earliest examples of spin transitions were those in the iron(III) dithiocarbamates described by Cambi and co-workers in the 1930s, and later studied in detail.[1] Their occurrence and significance in biological systems were recognized early, and their role in the function of many heme protein active sites is crucial.[2] The 1960s saw increased activity in the field, principally relating to cobalt(II), iron(II), and iron(III) systems. Later, limited data became available for manganese(II)[3] and (III),[4] and for chromium(II).[5] Spin transitions in the d^6 ion Co^{III} occur, but are much less common than for iron(II), in part because of the much higher fields induced by this smaller ion. Nevertheless, there has been extensive study, principally by Rao and co-workers, of the transitions in perovskite-type cobaltate(III) systems where the coordination center is CoO_6.[6] For the only other Co^{III} system-type described, the CoO_6 core is also involved.[7] For the second transition series, transitions for niobium[8] and molybdenum species[9] have been proposed but there are no examples for the third series.

Since it is for six-coordinate iron(II) that spin crossover—$t_{2g}{}^6e_g{}^0$ ($^1A_{1g}$, LS) $\longleftrightarrow$ $t_{2g}{}^4e_g{}^2$ ($^5T_{2g}$, HS)—seems to occur most widely and has been most thoroughly characterized, iron(II) systems are primarily considered here. The field has been reviewed many times, two recent articles providing a lead into the extensive literature.[10,11] The majority of systems known contain an $[FeN_6]$ coordination center but the donor-atom sets N_4O_2,[12] N_4S_2,[13] S_6,[14] and P_4Cl_2[15] are also known. The $[FeN_6]$ systems are generally cationic but uncharged species are known, most notably

[Fe(1,10-phenanthroline)$_2$(NCS)$_2$],[16] bis[hydro-tris(pyrazolyl-borato)]iron(II)[17] and related systems.

The initial reports of synthetic iron(II) spin crossover involved [Fe(diimine)$_2$(NCS)$_2$] complexes where the diimine was either 1,10-phenanthroline or 2,2′-bipyridine.[16] The spin crossover situation persists in such complexes for a wide range of diimine species and for certain unidentate pyridine derivatives,[18] bridging diimine systems and bis(unidentate) systems. In addition, mixed aromatic–aliphatic N_4 quadridentate donors have been incorporated into this general class.[19] The anionic groups can be varied and spin crossover is also observed in [Fe(diimine)$_2$X$_2$] systems when $X^- = NCSe^-$,[16] $[NCBH_3]^-$,[20] $TCNQ^-$,[21] $[N(CN)_2]^-$,[22] and $2X^- = [WS_4]^{2-}$.[23]

Many $[FeN_6]^{2+}$ systems are derivatives of the well-known LS [Fe(2,2′-bipyridine)$_3$]$^{2+}$ or [Fe(2,2″:2′,6′-terpyridine)$_2$]$^{2+}$ ions, the crossover situation being attained by the introduction of sterically hindering groups adjacent to the donor atoms or by replacement of the pyridine rings by five-membered heterocycles.[11] This is illustrated by the spin crossover systems tris(6-methyl-2,2′-bipyridine)iron(II)[24] and bis(2,4-bis(pyridin-2-yl)thiazole)iron(II) ions.[25] In addition, the $[FeN_6]$ system can exhibit spin crossover behavior when six unidentate donors are involved, the classic examples being the [Fe(N-alkyl-tetrazole)$_6$]X$_2$ species, which are almost regular octahedral,[26] or when a sexadentate system is coordinated, e.g., the mixed aliphatic/heterocyclic tetrakis(2-pyridylmethyl)ethylenediamine).[27] The only completely saturated donor system would seem to be the encapsulating sexadentate species described by Martin *et al.*[28]

2.32.2 CONSEQUENCES OF SPIN TRANSITIONS

Accompanying the LS $\longleftrightarrow$ HS conversions are profound changes in all those properties which depend on the electronic arrangement, such as spectral, magnetic, and structural properties. The changes in these properties provide means of detecting and monitoring a spin transition, most commonly by measurement of the temperature-dependence of magnetic susceptibility, optical, vibrational and Mössbauer spectra, crystal structure and heat capacity.[10] For iron(II) the HS $\rightarrow$ LS change results in complete de-population of the essentially antibonding e_g orbitals and hence a significant (up to 0.2 Å) contraction in the iron–donor atom distance. This presents a barrier to the conversion, particularly in a solid system where it can instigate a major change in the overall lattice. Thus it is found that a thermally induced spin transition in the solid state can take a number of courses, depending on, among other factors, the nature of the lattice and the extent of cooperativity associated with the spin and/or structural change. The principal pathways observed are represented by the spin transition curves (HS fraction (γ_{HS}) vs. T) in Figure 1.

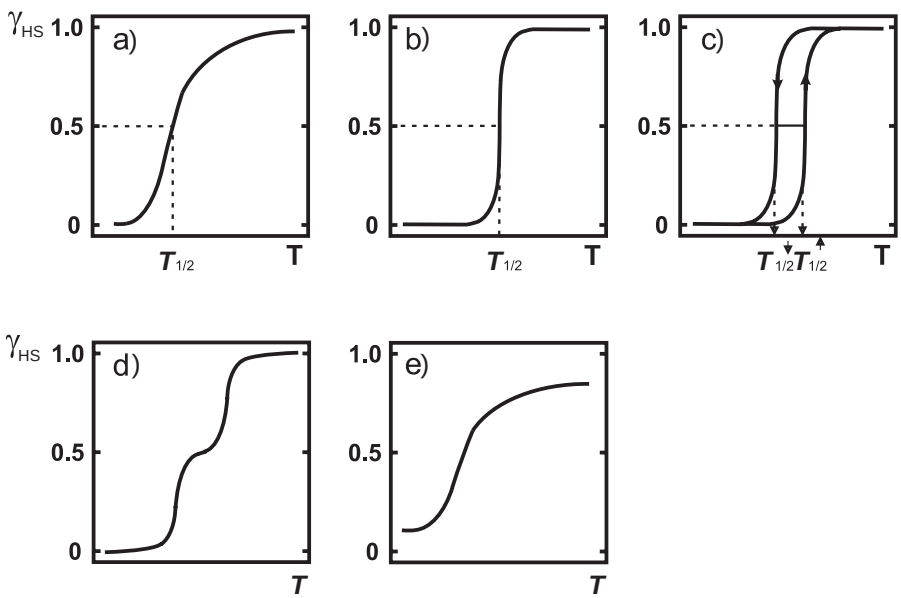

Figure 1 Classification of spin transition curves.

Transitions have been classified as gradual (a), abrupt (b), with hysteresis (c), two-step (d), and incomplete (e). There is a degree of cooperativity involved in the propagation of the structural and electronic changes throughout the solid. This arises from both short- and long-range interactions, and principally accounts for the differences in the spin transition curves $\gamma_{HS}(T)$. A thermal spin transition may also be accompanied by a phase transition. For transitions in the solution phase cooperativity is generally minimal and the transition curve follows the gradual course of Figure 1a. In this instance analysis of the transition in terms of a simple thermal equilibrium involving a Boltzmann distribution over all vibronic levels of the two spin states is usually straightforward and leads to meaningful thermodynamic parameters. The driving force for the transition is the considerable entropy gain of ca. 12–20 cal mol^{-1} K^{-1} for the LS → HS conversion, made up of a magnetic component, $\Delta S_{mag} = R[\ln(2S+1)_{HS} - \ln(2S+1)_{LS}]$, ca. 3 cal mol^{-1} K^{-1}, and a larger intramolecular vibrational entropy contribution arising from the much higher degeneracies in the HS state. The enthalpy change for the LS → HS conversion is typically 2–4 kcal mol^{-1} and is associated primarily with the rearrangement of the coordination sphere.

Heat capacity studies confirmed a strong cooperative interaction through coupling of the electron state and the phonon system for solid $[Fe(phen)_2NCS)_2]$ and $[Fe(phen)_2NCSe)_2]$.[29] The evolution of transitions of increasingly more continuous character by metal-dilution techniques also confirms the cooperative nature of the transition in the concentrated solid.[30,31] Detailed study of these effects has led to various models for the interaction mechanism responsible for the cooperativity. One of the most appropriate takes as its basis the change in size and shape of the complex ion accompanying a transition.[32,33] It is proposed that such a significant change at every "point defect" where a spin transition occurs sets up pressure (an "image pressure") which is communicated to the surroundings via phonon interactions. In the course of the spin transition the lattice expands at many point defects and accelerates the transition in other centers. Thus the nature of the cooperative interactions in a solid is elastic, and the model uses typical quantities from elasticity theory to account for the experimental results.

Cooperativity leading to hysteresis, along with the implications of the response of spin transition systems to radiation (see Chapter 2.33) has been the impetus for much of the recent interest in the field. The occurrence of hysteresis imparts bistability on the system and hence the properties of the compounds depend on the history of the sample. Since the properties, for example color, of spin transition systems change dramatically with temperature, this bistability can be very readily detected and offers potential for exploitation in memory, switching, and display devices.[34]

Because of the contraction in the Fe-donor atom distance, the HS → LS conversion is favored by an increase in pressure. From both solution studies and crystal structure determinations the decrease in molecular volume has been estimated as typically 20 $Å^3$. Thus, an increase in pressure generally results in an increase in the transition temperature, but changes in the width of the hysteresis loop, the steepness of the transition curve, and changes in the residual fractions of HS and LS species at the extremes of the temperature range for the transition are also observed.[35] Relatively simple species such as FeO[36] and FeS[37] in addition to some iron(II)-containing minerals have been shown to undergo pressure-induced HS ⟷ LS transitions and these are relevant to the behavior of iron-containing minerals under the pressures experienced in the Earth's crust and mantle.

2.32.3 THE GENERATION OF COOPERATIVITY

The principal strategies applied to enhance cooperativity of a spin transition are (i) incorporation of a hydrogen-bonded network, (ii) incorporation of π-stacking moieties and (iii) coordination of bridging ligands. A further possible route to cooperativity is the coupling of disorder–order and spin transitions. This has not been explored widely. A disorder–order transition involving the ethanol solvate orientation occurs along with a spin transition in $[Fe(pic)_3]Cl_2 \cdot EtOH$[38] and it was proposed that this ordering of the solvate molecule may trigger the spin transition. A similar synergism between an order–disorder transition and a spin transition has been proposed for $[Fe(dppen)_2Cl_2] \cdot 2(CH_3)_2CO$ (dppen = *cis*-1,2-bis(diphenylphosphino)ethene).[39] This approach remains an interesting one for possible exploitation in increasing cooperativity.

Incorporation of hydrogen bonding centers within the ligand leading to a network of interactions with the associated anions and/or solvent molecules has been achieved in a number of systems. The classic example is the 2-picolylamine (pic) system, $[Fe(pic)_3]X_2.(solvent)_n$, in which the nature of the spin transition curve depends on both X and the solvent; e.g., the chloride

monohydrate shows a strongly cooperative transition, while the dihydrate is low-spin.[40] $[FeN_6]X_2 \cdot nH_2O$ salts containing the tridentate 2,6-bis(pyrazol-3-yl)pyridine (3bpp) similarly have properties which depend markedly on the extent of hydration. The >NH groups of the pyrazolyl moieties in this ligand are involved in hydrogen bonding and for the triflate salt monohydrate, for example, a highly cooperative transition is observed with an extremely broad hysteresis (140 K).[41]

π-Stacking is believed to be the source of the cooperativity in some systems where there is no other obvious means of propagation of the spin change through the crystal. The $[Fe(phen)_2(NCS)_2]$ model has been modified by the incorporation of aromatic substituents into the bidentate moiety, which enhance π-stacking interactions and produce highly cooperative transitions. This is illustrated by the derivative of dipyrido[3,2-a:2′,3′-c]phenazine (dpp). In the structure of $[Fe(dpp)_2(NCS)_2]$ the dpp ligands of adjacent molecules stack with an interplanar separation of 3.5 Å and a dihedral angle of 0.6°. It is this interaction which is believed to be responsible for the high cooperativity of the transition.[42] The ligand 3,5-bis (pyridin-2-yl)-4-amino-1,2,4-triazole (abpt) is involved in two remarkable systems of the $[Fe(diimine)_2X_2]$ type. Unlike most systems of this general class the derivatives of abpt have a *trans* arrangement of the X groups. This allows for stacking of the imine systems within chains of metal centers in $[Fe(abpt)_2(NCS)_2]$ and $[Fe(abpt)_2(NCSe)_2]$.[43] In addition to this form of stacking, in $[Fe(abpt)_2(TCNQ)_2]$ the $TCNQ^-$ anions also stack leading to a range of π-type interactions.[21] In neither system, however, is the cooperativity strong. In systems of the kind $[M(diimine)_3]^{n+}$ and $[M(terimine)_2]^{n+}$ general structural motifs are frequently observed which allow interactions between the aromatic moieties of neighboring complex ions.[44,45] It is feasible that these interactions may be operative in influencing the cooperativity in certain spin crossover systems, e.g., in the $[Fe(2,6\text{-bis(benzimidazol-2-yl)pyridine})_2]^{2+}$ salts, even when other possible mechanisms such as hydrogen bonding may additionally be present.[46] This is also indicated by the similarly cooperative transitions observed for $[Fe(3bpp)_2][BF_4]_2$ and $[Fe(1bpp)_2][BF_4]_2$ (1bpp = 2,6-bis-(pyrazol-1-yl) pyridine) despite the much reduced scope for hydrogen bonding in the latter system.[47,48] Hydrogen bonding seems to be associated with the cooperativity of the transitions in a family of cobalt(II) systems, e.g., in $[Co(H_2fsa_2en)(py)_2]$ (H_2fsa_2en is the dianion of the Schiff base from condensation of 1,2-diamino-ethane and 3-carboxy-salicylaldehyde), but again stacking of the quadridentate ligands is evident.[49]

The aim of increasing cooperativity of a spin transition by linking the metal coordination centers by actual chemical bonds to give multinuclear or polymeric systems has been actively pursued. Binuclear species of the type $[Fe(diimine)_2X_2]$ have been obtained by replacing one of the diimine molecules with bridging bipyrimidine. Cooperativity is certainly present in some of these and the transition may be selective in that it occurs in one of the bridged metal centers at a higher temperature than in the other, the systems being considered as possible "binary triggers."[50]

A novel tetranuclear system which involves a square grid-like array of FeN_6 centers is formed from the polypyridine system 4,6-bis(2′,2″-bipyrid-6′-yl)-2-phenyl-pyrimidine.[51] Evidence for cooperativity within the tetrameric unit was obtained but inter-molecular cooperativity is weak and no thermal hysteresis was observed.

The trinuclear system $Fe_3(ettrzH)_6(H_2O)_6](CF_3SO_3)_6$ (ettrz = 4-ethyl-1,2,4-triazole) is of considerable interest. The structure consists of linear Fe_3 units, the central iron having N_6 coordination and the two equivalent terminal Fe atoms having N_3O_3 coordination. The triazole moieties bridge through the N1 and N2 atoms.[52] Only the $[FeN_6]$ center undergoes a spin transition. The basic structural features of this are retained in an extensive series of chain-like polymeric derivatives of triazole (trzH), the triazolate anion (trz) and 4-substituted triazoles.

The cooperative spin transition in $[Fe(trzH)_2(trz)][BF_4]$ was first reported in 1977[53] but the special relevance of this and related systems to the significance of cooperativity associated with spin transition systems came to be recognized much later, principally through the work of the groups of Lavrenova[54] and Kahn.[34] The special features of the transitions are their cooperative nature and, due to the associated hysteresis, the conferring of bistability on the systems. Furthermore, the systems are very visibly thermochromic, the high-spin forms being white and the low-spin pink–violet. The absence of charge-transfer absorption in the visible region for these systems allows the clear detection of the widely separated ligand field bands for the high-spin and low-spin species and these determine the color in the separate spin states. Moreover, the spin transitions in many of the systems studied occur close to room temperature. These aspects are all of importance in any application of spin transition systems in switching or display devices or sensors.[34] To date there has been no X-ray structure reported for these Fe^{II} triazole derivatives but the essential structural features have been established by EXAFS.[55]

The ability of 4,4′-bis-1,2,4-triazole (btr) to link two metal centers has led to a three-dimensional network in $[Fe(btr)_3][ClO_4]_2$ in which limited cooperativity is found.[56] When two tetrazole moieties are linked by a 1,2-propyl bridge a chain structure is obtained with Fe^{II} containing $[FeN_6]^{2+}$ centers. The observed transition displays virtually no cooperativity and it is believed that this is associated with the flexible nature of the bridge, which apparently acts as a kind of "shock absorber" to the structural changes occurring within the immediate environment of the metal centers and vitiates their synchronized transmission through the crystal.[57] The use of relatively more rigid bridges between two 4-pyridyl groups in systems of the kind $[FeN_4(NCS)_2]$ has been no more successful in increasing cooperativity. In both [Fe(1,2-bis-(4-pyridyl)ethene)$_2$(NCS)$_2$][58] and [Fe(1,4-bis(4-pyridyl)-butadiyne)$_2$(NCS)$_2$][59] continuous transitions occur, despite both systems involving remarkable interlocked networks. In contrast, $[Fe(btr)_2(NCS)_2]$, which has a layer-type structure, undergoes a very abrupt transition with hysteresis.[60]

Perhaps the most promising of the new polymeric systems is the class represented by the general formula $[Fe(py)_2M(CN)_4]$ where M refers to a bivalent ion from periodic Group 10. These are structurally related to the Hofmann clathrate compounds and consist of two-dimensional sheets made up of alternating square–planar $M(CN)_4$ units and octahedral $Fe(NC)_4(py)_2$ units linked through bridging cyano groups. The cooperative transition for M = Ni was first reported in 1996[61] and more recently where M = Pd, Pt and where the network has been extended to three-dimensions by the replacement of pyridine by the bridging pyrazine, with higher transition temperatures and retention of the cooperativity.[62]

Undoubtedly, progress in the field has been substantial but a fuller understanding of the factors controlling cooperativity and their operation remains one of the challenges of the spin crossover field. This will be essential if the unique possibilities for practical applications of spin crossover systems are to be realized.

2.32.4 REFERENCES

1. Martin, R. L.; White, A. H. *Trans. Met. Chem.* **1968**, *4*, 113–198.
2. Hoa, G. H. B.; McLean, M. A.; Sligar, S. G. *Biochem. Biophys. Acta* **2002**, *36572*, 1–12.
3. Köhler, F. H.; Schlesinger, B. *Inorg. Chem.* **1992**, *31*, 2853–2859.
4. Garcia, Y.; Kahn, O.; Ader, J.-P.; Buzdin, A.; Meurdesoif, Y.; Guillot, M. *Phys. Lett.* **2000**, *A 271*, 145–154.
5. Sorai, M.; YumotoY.; Halepoto, D. M.; Larkworthy, L. F. *J. Phys. Chem. Solids* **1993**, *54*, 421–430.
6. Rao, C. N. R. *Int. Revs. Phys. Chem.* **1985**, *4*, 19–38.
7. Kläui, W.; Eberspach, W.; Gütlich, P. *Inorg. Chem.* **1987**, *26*, 3977–3982.
8. Imoto, H.; Simon, A. *Inorg. Chem.* **1982**, *21*, 308–319.
9. Chisholm, M. H.; Kober, E. M.; Ironmonger, D. J.; Thornton, P. *Polyhedron* **1985**, *4*, 1869–1874.
10. Gütlich, P.; Hauser, A.; Spiering, H. *Angew. Chem., Int. Ed. Engl.* **1994**, *33*, 2024–2054.
11. Gütlich, P.; Garcia, Y.; Goodwin, H. A. *Chem. Soc. Rev.* **2000**, *29*, 419–427.
12. Boinnard, D.; Bousseksou, A.; Dworkin, A.; Savariault, J. M.; Varret, F.; Tuchagues, J. P. *Inorg. Chem.* **1994**, *33*, 271–281.
13. Grillo, V. A.; Gahan, L. R.; Hanson, G. R.; Stranger, R.; Hambley, T. W.; Murray, K. S.; Moubaraki, B.; Cashion, J. D. *J. Chem. Soc. Dalton Trans.* **1998**, 2341–2348.
14. Womes, M.; Jumas, J.-C.; Olivier-Fourcade, J.; Aubertin, F.; Gonser, U. *Chem. Phys. Lett.* **1993**, *201*, 555–558.
15. Levason, W.; McAuliffe, C. A.; Khan, M. M.; Nelson, S. M. *J. Chem. Soc. Dalton* **1975**, 1778–1783.
16. König, E. *Coord. Chem. Rev.* **1968**, *3*, 471–495.
17. Hannay, C.; Hubin-Franskin, M.-J.; Grandjean, F.; Briois, V.; Itié, J.-P.; Polian, A.; Trofimenko, S.; Long, G. J. *Inorg. Chem.* **1997**, *36*, 5580–5588.
18. Roux, C.; Zarembowitch, J.; Gallois, B.; Granier, T.; Claude, R. *Inorg. Chem.* **1994**, *33*, 2273–2279.
19. Toftlund, H. *Coord. Chem. Rev.* **1989**, *94*, 67–108.
20. Edwards, M. P.; Hoff, C. D.; Curnutte, B.; Eck, J. S.; Purcell, K. F. *Inorg. Chem.* **1984**, *23*, 2613–2619.
21. Kunkeler, P. J.; van Koningsbruggen, P. J.; Cornelissen, J. P.; van der Horst, A. N.; van der Kraan, A. M.; Spek, A. L.; Haasnoot, J. G.; Reedijk, J. *J. Am. Chem. Soc.* **1996**, *118*, 2190–2197.
22. Moliner, N; Gaspar, A. B.; Muñoz, M. C.; Niel, V.; Cano, J.; Real, J. A. *Inorg. Chem.* **2001**, *40*, 3986–3991.
23. Czernuszewicz, R. S.; Nakamoto, K.; Strommen, D. P. *Inorg. Chem.* **1980**, *19*, 793–797.
24. Onggo, D.; Hook, J. H.; Rae, A. D.; Goodwin, H. A. *Inorg. Chim. Acta* **1990**, *173*, 19–30.
25. Childs, B. J.; Craig, D. C.; Scudder, M. L.; Goodwin, H. A. *Inorg. Chim. Acta* **1998**, *274*, 32–41.
26. Wiehl, L. *Acta Cryst.* **1993**, *B49*, 289–304.
27. Chang, H.-R.; McCusker, J. K.; Toftlund, H.; Wilson, S. R.; Trautwein, A. X.; Winkler, H.; Hendrickson, D. N. *J. Am. Chem. Soc.* **1990**, *112*, 6814–6827.
28. Martin, L. L.; Martin, R. L.; Murray, K. S.; Sargeson, A. M. *Inorg. Chem.* **1990**, *29*, 1387–1394.
29. Sorai, M.; Seki, S. *J. Phys. Chem. Solids* **1974**, *35*, 555–570.
30. Sorai, M.; Ensling, J.; Gütlich, P. *Chem. Phys.* **1976**, *18*, 199–209.
31. Jung, J.; Schmitt, G.; Wiehl, L.; Knorr, K.; Spiering, H.; Gütlich, P. *Z. Phys. B* **1996**, *100*, 523–534.
32. Spiering, H.; Willenbacher, N. *J. Phys.:Condens. Matter* **1989**, *1*, 10089–10105.

33. Willenbacher, N.; Spiering, H. J. Phys.C: SolidStatePhys. **1989**, *21*, 1423–1439.
34. Kahn, O.; Martinez, C. J. *Science* **1998**, *279*, 44–48.
35. Ksenofontov, V.; Spiering, H.; Schreiner, A.; Levchenko, G.; Goodwin, H. A.; Gütlich, P. *J. Phys. Chem. Solids* **1999**, *60*, 393–399.
36. Hemley, R. J.; Mao, H. K.; Gramsch, S. A. *Mineral. Mag.* **2000**, *64*, 157–184.
37. Rueff, J.-P.; Kao, C. C.; Struzhkin, V. V.; Badro, J.; Shu, J.; Hemley, R. J.; Mao, H. K. *Phys. Rev. Lett.* **1999**, *82*, 3284–3287.
38. Mikami, M.; Konno, M.; Saito, Y. *Acta Cryst.* **1980**, *B36,* 275–287.
39. König, E.; Ritter, G.; Kulshreshtha, S. K.; Waigel, Sacconi, L. *Inorg. Chem.* **1984**, *23*, 1241–1246.
40. Sorai, M.; Ensling, J.; Hasselbach, K. M.; Gütlich, P. *Chem. Phys.* **1977**, *20*, 197–208.
41. Buchen, T.; Gütlich, P.; Sugiyarto, K. H.; Goodwin, H. A. *Chem. Eur. J.* **1996**, *2*, 1134–1138.
42. Zhong, Z. J.; Tao, J.-Q.; Yu, Z.; Dun, C.-Y.; Liu, Y.-J.; You, X.-Z. *J. Chem. Soc. Dalton Trans.* **1998**, 327–328.
43. Moliner, N.; Munoz, M. C.; Létard, S.; Létard, J.-F.; Solans, X.; Burriel, R.; Castro, M.; Kahn, O.; Real, J. A. *Inorg. Chim. Acta* **1999**, *291*, 279–288.
44. Dance, I. G.; Scudder, M. L. *J. Chem. Soc. Dalton Trans.* **1998**, 1341–1350.
45. Scudder, M. L.; Goodwin, H. A.; Dance, I. G. *New J. Chem.* **1999**, *23*, 695–705.
46. Boca, R.; Boca, M.; Dlhan, L.; Falk, K.; Fuess, H.; Haase, W.; Jarosciak, R.; Papankova, B.; Renz, F.; Vrbova, M.; Werner, R. *Inorg. Chem.* **2001**, *40*, 3025–3033.
47. Buchen, T.; Gütlich, P.; Goodwin, H. A. *Inorg. Chem.* **1994**, *33*, 4573–4576.
48. Holland, J. M.; McAllister, J. A.; Kilner, C. A.; Thornton-Pett, M.; Bridgeman, A. J.; Halcrow, M. A. *J. Chem. Soc. Dalton Trans.* **2002**, 548–554.
49. Zarembowitch, J. *New J. Chem.* **1992**, *16*, 255–267.
50. Ksenofontov, V.; Spiering, H.; Reiman, S.; Garcia, Y.; Gaspar, A. B.; Moliner, N.; Real, J. A.; Gütlich, P. *Chem. Phys. Lett.* **2001**, *348*, 381–386.
51. Breuning, E.; Ruben, M.; Lehn, J.-M.; Renz, F.; Garcia, Y.; Ksenofontov, V.; Gütlich, P.; Wegelius, E.; Rissanen, K. *Angew. Chem., Int. Ed. Engl.* **2000**, *39*, 2504–2507.
52. Vos, G.; de Graaff, R. A. G.; Haasnoot, J. G.; van der Kraan, A. M.; de Vaal, P.; Reedijk, J. *Inorg. Chem.* **1984**, *23*, 2905–2910.
53. Haasnoot, J. G.; Vos, G.; Groeneveld, W. L. *Z. Naturforsch.* **1977**, *32b*, 1421–1430.
54. Erenburg, S. B.; Bausk, N. V.; Lavrenova, L. G.; Mazalov, L. N. *Nucl. Instrum. Methods Phys. Res. A* **2000**, *448*, 351–357.
55. Michalowicz, A.; Moscovici, J.; Charton, J.; Sandid, F.; Benamrane, F.; Garcia, Y. *J. Synchrotron Rad.* **2001**, *8*, 703–1430.
56. Garcia, Y.; Kahn, O.; Rabardel, L.; Chansou, B.; Salmon, L.; Tuchagues, J. P. *Inorg. Chem.* **1999**, *38*, 4663–4670.
57. van Koningsbruggen, P. J.; Garcia, Y.; Kahn, O.; Fournès, L.; Kooijman, H.; Spek, A. L.; Haasnoot, J. G.; Moscovici, J.; Provost, K.; Michalowicz, A.; Renz, F.; Gütlich, P. *Inorg. Chem.* **2000**, *39*, 1891–1990.
58. Real, J. A.; Andrés, E.; Muñoz, M.; Julve, M.; Granier, T.; Bousseksou, A.; Varret, F. *Science* **1995**, *268*, 265–267.
59. Moliner, N.; Muñoz, C.; Létard, S.; Solans, X.; Menéndez, N.; Goujon, A.; Varret, F.; Real, J. A. *Inorg. Chem.* **2000**, *39*, 5390–5393.
60. Vreugdenhil, W.; Van Dieman, J. H.; De Graaff, R. A. G.; Haasnoot, J. G.; Reedijk, J.; van der Kraan, A. M.; Kahn, O.; Zarembowitch, J. *Polyhedron* **1990**, *9*, 2971–2979.
61. Kitazawa, T.; Gomi, Y.; Takahashi, M.; Takeda, M.; Enomoto, M.; Miyazaki, A.; Enoki, T. *J. Mater. Chem.* **1996**, *6*, 119–121.
62. Niel, V.; Martinez-Agudo, J. M.; Muñoz, M. C.; Gaspar, A. B.; Real, J. A. *Inorg. Chem.* **2001**, *40*, 3838–3839.

Comprehensive Coordination Chemistry II
ISBN (set): 0-08-0437486

Volume 2, (ISBN 0-08-0443249); pp 421–426

2.33
Excited Spin State Trapping (LIESST, NIESST)

A. HAUSER
Université de Genève, Switzerland
and
P. GÜTLICH
Johannes-Gutenberg-Universität, Mainz, Germany

2.33.1 LIGHT-INDUCED EXCITED SPIN STATE TRAPPING (LIESST) 427
2.33.2 NUCLEAR DECAY INDUCED EXCITED SPIN STATE TRAPPING (NIESST) 430
2.33.3 RELAXATION 430
2.33.4 CONCLUSIONS 433
2.33.5 REFERENCES 433

2.33.1 LIGHT-INDUCED EXCITED SPIN STATE TRAPPING (LIESST)

In general, coordination compounds of transition metal ions with a d^5 to d^7 electron configuration do not show any luminescence for ligand-field strengths in the vicinity of the crossover point between the high-spin (HS) and the low-spin (LS) states in the respective Tanabe–Sugano diagram. Low-lying ligand-field states form a perfect ladder for efficient nonradiative decay of higher excited states back to the ground state. This is particularly true for the spin-crossover compounds (see Chapter 2.32). Nevertheless, these compounds do possess interesting photophysical properties, to be discussed for iron(II) d^6 in the following.

Figure 1 shows the potential well of the $^1A_1$ (LS) state of iron(II), and at slightly higher energy the one for the $^5T_2$ (HS) state, which becomes thermally populated at elevated temperatures. In addition, the higher excited ligand-field states with $S = 0$, 1, and 2 and possible MLCT states are indicated.[1–7] In the case of ligands for which the weak ligand-field transitions are not obscured by strong MLCT bands, the former can be easily assigned. Figure 2 shows absorption spectra of $[Fe(ptz)_6](BF_4)_2$ (ptz = 1-propyltetrazole),[8–10] a prototype for the class of compounds with tetrazole and related ligands.[11–13] At 295 K, the one band in the near infrared corresponds to the spin-allowed $^5T_2 \rightarrow {}^5E$ transition of the HS species. The thermal spin transition of this compound occurs at ~135 K,[4–7] and as a consequence, the two absorption bands in the visible of the 20 K spectrum correspond to the spin-allowed transitions $^1A_1 \rightarrow {}^1T_1$ and $^1A_1 \rightarrow {}^1T_2$ of the LS species. Additionally, the weak spin-forbidden transitions $^1A_1 \rightarrow {}^3T_1$ and $^1A_1 \rightarrow {}^3T_2$ can be located in the near infrared. Another prototype for a spin-crossover system with pyridyl ligands is provided by $[Fe(mepy)_3tren]^{2+}$, (mepy)$_3$tren = tris{4-[(6-methyl)-2-pyrridyl]-3-aza-3-butenyl}amine.[14,15] Figure 3 gives its absorption spectra at 295 K and at 20 K doped into an inert host lattice.[16–18] The intensity of the strong MLCT band at 550 nm is much higher for complexes in the LS state due to the

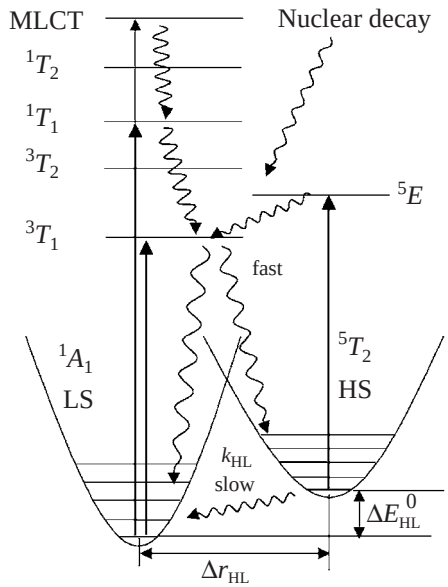

Figure 1 The electronic structure of iron(II) spin-crossover complexes. The mechanisms of LIESST, reverse-LIESST, and NIESST are indicated by curly arrows.

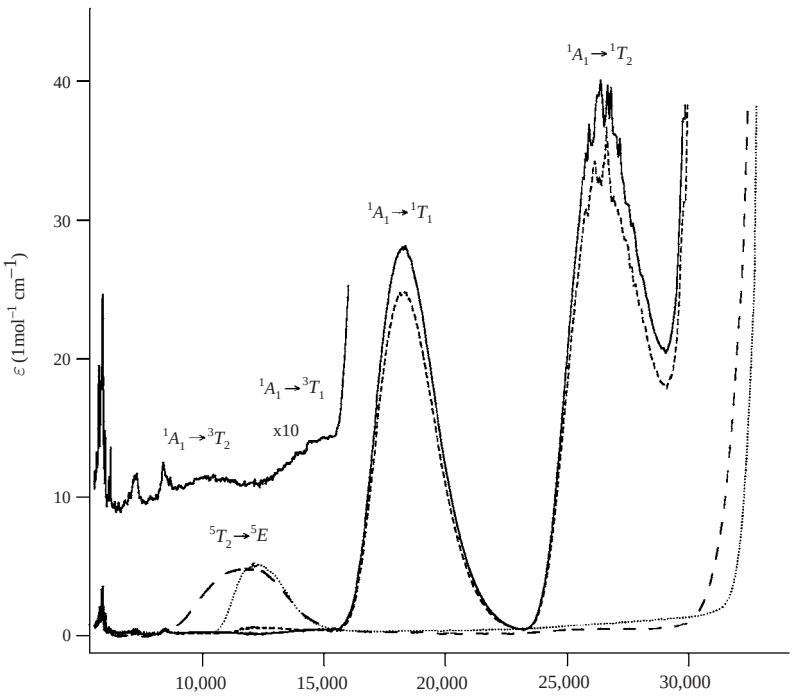

Figure 2 Single-crystal absorption spectra (cm^{-1}) of $[Fe(ptz)_6](BF_4)_2$: (– – –) at 295 K, (—) at 10 K, (· · · · · ·) at 10 K following irradiation at 514.5 nm (the spectrum following irradiation at 980 nm is identical), and (- - -) at 10 K and irradiation at 820 nm. The spectra following irradiation at the different wavelengths provide clear-cut evidence for the processes depicted in Figure 1.

shorter metal–ligand bond length and the resulting larger overlap between metal-centered and ligand-centered orbitals.

Irradiation of spin-crossover compounds in the visible results in an efficient conversion of the complexes from the LS to the HS state. This was first realized by McGarvey *et al.*[19,20] who determined the dynamics of the HS → LS relaxation of spin-crossover complexes in solution using

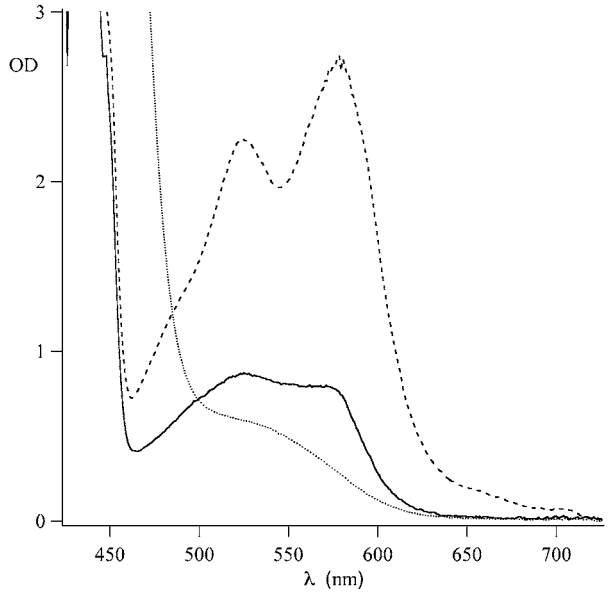

Figure 3 Single-crystal absorption spectra of $[Zn_{1-x}Fe_x(mepy)_3tren](PF_6)_2$, $x = 0.05\%$ at 295 K (· · · · · ·), at 10 K (- - -), and at 10 K following irradiation at 514.5 nm (—).

laser flash photolysis. At low temperatures, the HS → LS relaxation slows down considerably, and below 50 K some systems can be trapped quantitatively in the HS state. Experimental evidence for such "Light-induced Excited Spin State Trapping (LIESST)" is provided by the absorption spectra at 20 K of $[Fe(ptz)_6](BF_4)_2$ following irradiation into the $^1A_1 \rightarrow {}^1T_1$ ligand-field band,[4–10] and of $[Zn_{1-x}Fe_x(mepy)_3tren]$ following irradiation into the MLCT band,[16–18] which are included in Figures 2 and 3, respectively. Since the discovery of LIESST in 1983, a large number of systems showing this effect have been found for a variety of spin-crossover systems such as in neat solids,[21–24] in mixed crystals,[25,26] in amorphous matrices[27] and in Langmuir–Blodgett films.[28]

The mechanism for LIESST is sketched in Figure 1: a double intersystem crossing step takes the excited complex to the HS state, where, as result of the energy barrier between the HS and the LS state due to the large difference in metal–ligand bond length and the small value of the zero-point energy difference, ΔE^0_{HL}, it stays trapped at sufficiently low temperatures. The quantum efficiency of the double intersystem crossing step is close to unity.[8–10] Sub-picosecond experiments show that the process is very fast indeed and highly nonadiabatic.[29,30] Thus, even though the triplet state does play an important role in the vibronic coupling between the singlet and the quintet manifolds, it cannot be considered a true intermediate state in the relaxation process.

The lifetime of the light-induced HS state even below 10 K is finite, but for some compounds it does reach values of 10^6 s or more.[4–10,16–18,21–28] At somewhat higher temperatures, a thermally activated relaxation back to the LS ground state invariably sets in (see below). The scheme of Figure 1 suggests that the complexes may also be pumped back to the ground state optically by irradiating into the $^5T_2 \rightarrow {}^5E$ band. This process is much less efficient than the forward process. Indeed, it can only be observed for compounds which do not have intense MLCT bands with tails all the way into the near infrared. Even then, the reverse process is usually not quantitative. Because of the spectral overlap of the spin-forbidden transitions of the LS species with the $^5T_2 \rightarrow {}^5E$ band, a steady state-type situation results, with a LS population which depends upon the precise irradiation wavelength within the $^5T_2 \rightarrow {}^5E$ band. This is demonstrated by the absorption spectrum of $[Fe(ptz)_6](BF_4)_2$ following irradiation at 930 nm as shown in Figure 2. On the other hand, irradiation into the spin-forbidden $^1A_1 \rightarrow {}^3T_1$ band on the low-energy side of the HS band again results in quantitative LIESST.[4–10]

In a limited number of systems which stay in the HS state down to low temperatures but sufficiently close to the crossover point, it is possible to populate the LS state as metastable state by irradiation in the near infrared.[31–33] Cooperative effects can result in a true light-induced bistability for such systems, which can persist to quite high temperatures.[31–33] In exchange-coupled binuclear iron spin-crossover systems, which are in the LS state at low temperatures, it is also possible to induce the HS state by irradiation. Although the individual iron centers are

now in the HS state, the overall state of the binuclear complex is diamagnetic below 10 K due to antiferromagnetic coupling between the two metal centers.[34,35]

With respect to lifetimes of the light-induced HS states of the order of minutes to days, LIESST is restricted to iron(II) spin-crossover compounds with a small zero-point energy difference, ΔE^0_{HL}, between the HS and the LS state. From the point of view of the double intersystem crossing step, LIESST is more general than that. It can also be observed for LS systems[36] provided sufficiently fast excitation and detection methods are being used for monitoring the (in this case) much faster decay of the light-induced HS state (see below).

2.33.2 NUCLEAR DECAY INDUCED EXCITED SPIN STATE TRAPPING (NIESST)

^{57}Fe Mössbauer spectroscopy provides an elegant technique to generate excited electronic states in coordination compounds and to simultaneously identify them via the characteristic hyperfine interactions, and even measure their lifetimes within the time window given by the lifetime of the excited nuclear state of ~140 ns.[37–39] To this end, the compound of interest doped with ^{57}Co is used as Mössbauer source towards a single-line absorber. The decay of ^{57}Co to ^{57}Fe by electron capture (EC) is accompanied by energy release, which leads to electronic excitations of the nucleogenic ^{57}Fe ion. Thus, several years prior to the discovery of LIESST, anomalous resonance signals were observed in such *Mössbauer emission spectra* of ^{57}Co-labeled coordination compounds for which the corresponding Fe^{II} complexes are LS complexes. These signals can be assigned to metastable HS states of the nucleogenic $^{57}Fe^{II}$.[40] The proposed mechanism for this "Nuclear Decay-induced Excited Spin State Trapping (NIESST)" is much the same as for LIESST (see Figure 1), but with an intramolecular light source provided by the ^{57}Co(EC)^{57}Fe nuclear decay.

NIESST was first observed on $[M(phen)_3](ClO_4)_2$ (phen = 1,10-phenantroline).[40] The neat iron compound is a LS compound at all temperatures, and so are $[^{57}Fe(phen)_3]^{2+}$-doped systems with ~0.1% ^{57}Fe. Thus, the Mössbauer absorption spectra for $M = {}^{57}Fe_x/Co_{1-x}$, $x = 0.001$, of Figure 4a simply consist of a typical Fe^{II}–LS quadrupole doublet. The Mössbauer emission spectra for $M = {}^{57}Co_x/Co_{1-x}$, $x = 0.001$, of Figure 4b are similar down to 250 K (A), except for a small fraction of Fe^{III}–LS (B), which arises from the loss of a valence electron after the nuclear decay. At lower temperatures, however, two typical Fe^{II}–HS doublets (C,D) appear at the expense of the Fe^{II}–LS doublet. Time-differential Mössbauer emission spectroscopy[41,42] shows that the relaxation from the highly excited states to the HS state occurs rapidly, and it allows the determination of the lifetime of the metastable HS state. For the above system, the lifetime at 80 K is ~500 ns, and it decreases rapidly at higher temperatures. Time-differential Mössbauer emission spectra on $[^{57}Co/Mn(bpy)_3](PF_6)_2$ and laser pump probe experiments on the corresponding $[Fe/Mn(bpy)_3](PF_6)_2$ system between 10 K and 130 K gave values for the lifetimes of the metastable HS states in very good agreement with each other.[43] Thus, the NIESST phenomenon actually proves that the light-induced transient states in LS complexes are indeed HS states.

For complexes with a somewhat lower ligand-field strength such as in ^{57}Co-labeled $[Fe(phen)_2(NCS)_2]$, in which the thermal LS ↔ HS transition occurs at a temperature of $T_{1/2} \approx 175$ K, the Mössbauer emission spectrum consists of the typical Fe^{II}–HS doublet at all temperatures down to 4.2 K.[44] A similar behavior was observed in the Mössbauer emission spectra of a whole series of ^{57}Co-doped Fe^{II} spin-crossover compounds and their Co^{II} analogs.[45–48] In all the spin-crossover systems, metastable Fe^{II}–HS states originating from the ^{57}Co nuclear decay are "trapped" at temperatures below the thermal transition temperature with an efficiency of nearly 100% with respect to the decay events.

2.33.3 RELAXATION

The HS → LS relaxation is basically a unimolecular process, and in diluted mixed crystals corresponding relaxation curves are single exponential. In Figure 5, HS → LS relaxation rate constants for several spin-crossover complexes doped into inert host lattices as well as for some LS complexes are plotted as k_{HL} on a log scale vs. $1/T$. Figure 5 includes data obtained by optical spectroscopy,[16–18] by Mössbauer line shape analysis,[49,50] and by Mössbauer emission.[44] Above ~50 K, these curves show the classical behavior of a thermally activated process, as is expected based on the energy barrier between the two states, and in agreement with results from

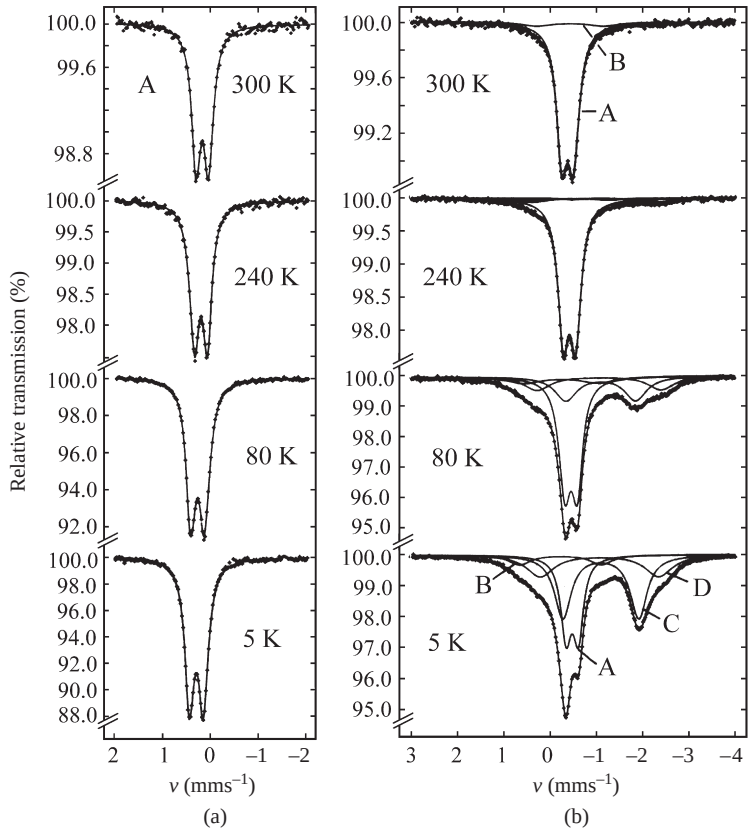

Figure 4 (a) ^{57}Fe Mössbauer absorption spectra of $[^{57}Fe/Co(phen)_3](ClO_4)_2$ as a function of temperature versus ^{57}Co/Rh (295 K) as source. (b) Time-integral Mössbauer emission spectra of a $[^{57}Co/Co(phen)_3](ClO_4)_2$ source as a function of temperature versus $K_4[Fe(CN)_6]$ (295 K) as absorber. A: Fe^{II}–LS, B: Fe^{III}–LS, C: Fe^{II}–HS1, D: Fe^{II}–HS2. In (a) the source was moved relative to the absorber; in (b) the absorber was moved relative to the source. For direct comparison, the sign of the velocities must be changed either in (a) or in (b).[40]

pulsed laser experiments on spin-crossover compounds in solution at elevated temperatures.[19,20,51–53] At low temperatures, however, there are deviations from the simple Arrhenius behavior towards a much less temperature-dependent tunneling process. Such a process was first theoretically proposed by Buhks *et al.*[54] in 1980, and Xie and Hendrickson provided the first experimental evidence in 1987.[55,56] According to Buhks *et al.*, the experimental activation energy should decrease with increasing zero-point energy difference, ΔE^0_{HL}, between the two states. At the same time, the low-temperature tunneling rate constant should increase exponentially. For spin-crossover compounds, the thermal transition temperature is a direct measure of this energy difference. Figure 6 shows the low-temperature tunneling rate constant for a series of complexes as a function of the corresponding thermal transition temperature.[57–59] The predicted exponential increase from less than $10^{-6}\,s^{-1}$ for $[Fe(ptz)_6]^{2+}$ with a transition temperature of 95 K when doped into the inert zinc host, to $10^4\,s^{-1}$ for $[Fe(mepy)(py)_2tren]^{2+}$ with a transition temperature of 370 K when embedded in a polymer matrix, is obvious.[16–18]

The zero point energy difference between the two states cannot only be varied chemically, it can also be influenced physically by applying an external pressure. Because of the large difference in volume, ΔV_{HL}, between the two states, external pressure destabilizes the HS state with respect to the LS state by a work term, $p\Delta V_{HL}$. This had been realized by several research groups, who determined activation volumes for the HS → LS relaxation of spin-crossover complexes in solution at and around ambient temperatures.[57–59] With activation volumes of the order of $-10\,Å^3$ per molecule, the resulting acceleration is of the order of 30% per kbar external pressure at ambient temperature. In the tunneling regime the effect of external pressure is much more striking. The low-temperature tunneling rate constant for $[Fe(mepy)_3tren]^{2+}$ doped into the inert zinc host increases from $10^{-1}\,s^{-1}$ (lifetime of 10 s) at 1 bar to $10^8\,s^{-1}$ (lifetime of 10 ns) at 27 kbar, with an initial increase by a factor of 10 per kbar.[60–62] This is in accordance with the

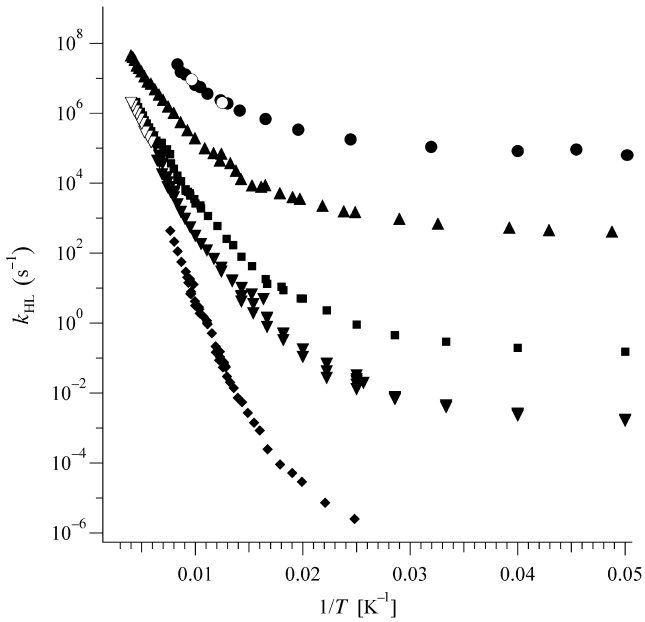

Figure 5 k_{HL} on a log scale plotted against $1/T$ for a series of iron(II) spin-crossover and low-spin complexes diluted in inert host lattices: $[Zn:Fe(ptz)_6](BF_4)_2$ (■), $[Mn:Fe(pic)_3]Cl_2EtOH$ (▼) from laser pulse excitation, (▽) $[Fe(pic)_3]Cl_2EtOH$ from Mössbauer lineshape analysis, $[Zn:Fe(mepy)_3tren](PF_6)_2$ (■), $[Zn:Fe(bpy)_3tren](PF_6)_2$ (▲), $[Mn:Fe(bpy)_3tren](PF_6)_2$ (●) from laser pulse excitation, (○) from time-differential Mössbauer emission.

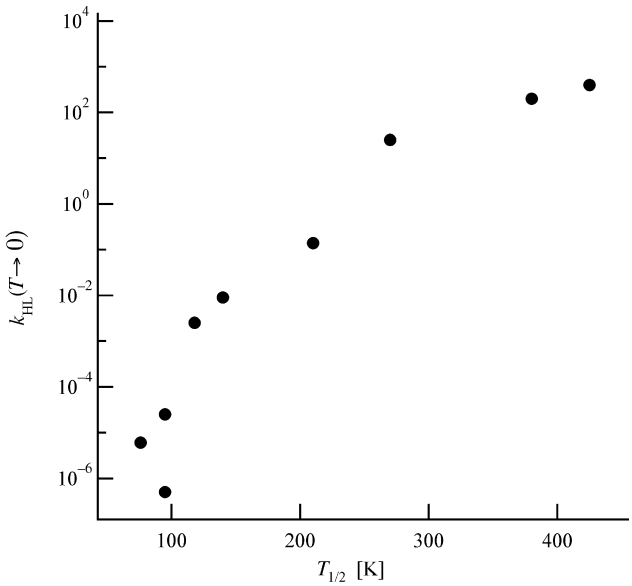

Figure 6 The low-temperature tunneling rate constant as function of chemical variation of the zero-point energy difference between the HS and the LS state as expressed by the transition temperatures of series of spin-crossover complexes.

theory of Buhks *et al.*[54] and an effective volume difference between the states of 25 $Å^3$ per molecule.

For other spin-crossover systems, in particular of iron(III), a light-induced perturbation of the spin equilibrium in solution[63] and the solid state[64,65] is also possible, but because of the substantially smaller metal–ligand bond length difference between the HS and the LS state, the lifetime of the metastable HS state at low temperatures is on the order of milliseconds at best,[64,65] with the exception of strongly cooperative systems.[66]

In neat spin-crossover compounds, cooperative effects of elastic origin[67,68] influence the relaxation behavior. Corresponding HS → LS relaxation curves following irradiation are no longer single exponential, but have a distinct sigmoidal shape.[69–71] This self-accelerating behavior can be rationalized in the mean-field approach to cooperative effects, which states that there is an internal or lattice pressure proportional to the LS fraction.[4–7,67,68] During the relaxation the internal pressure increases, leading to an exponential increase in the relaxation rate constant similar to the effect of external pressure.[70,71] Frequently observed deviations from mean-field behavior are thought to be due to nearest-neighbor interactions and the build-up of correlation[72,73] and inhomogeneous broadening.[74,75]

2.33.4 CONCLUSIONS

LIESST and NIESST are fascinating phenomena, the discovery of which has helped to develop an in-depth understanding of the photophysical behavior of iron(II) coordination compounds in general and spin-crossover compounds in particular. The principles that have evolved from this understanding are valid in a very general way, and can be applied to the photophysics of coordination compounds of other transition metal ions. Iron(II) spin-crossover systems possess, at least in principle, the necessary properties for applications in optical data storage and processing devices,[76–79] and, as is obvious from the extensive list of references since the early 1990s, have therefore received a lot of attention from researchers worldwide. In a wider context, research on the photophysical properties of spin-crossover compounds is part of the international effort for the search of light-induced metastable and bistable systems[80] such as the tautomeric Co^{III} catecholate complexes with their metastable LMCT state,[81,82] the Nitro-prussides with the inversion of the coordinating NO in the metastable state,[83,84] and the Prussian Blue analogs with their metastable metal–metal charge transfer states.[85–87]

2.33.5 REFERENCES

1. Sugano, S.; Tanabe, Y.; Kamimura, H. *Multiplets of Transition Metal Ions, Pure and Applied Physics*, Vol. 33; Academic Press: New York, 1970.
2. Shriver, D. T.; Atkins, P. W.; Langford, C. H. *Inorganic Chemistry*, 3rd ed.; Oxford University Press, Oxford, 1980.
3. Lever, A. B. P. *Inorganic Electronic Spectroscopy, Studies in Physical and Theoretical Chemistry 33*; Elsevier: Amsterdam, 1984.
4. Gütlich, P. *Structure and Bonding* **1981**, *44*, 83.
5. König, E. Progr. *Inorg. Chem.* **1987**, *35*, 527.
6. Gütlich, P.; Hauser, A.; Spiering, H. *Angew. Chem. Int. Ed. Engl.* **1994**, *33*, 2024.
7. Gütlich, P.; Hauser, A.; Spiering, H. In *Inorganic Electronic Structure and Spectroscopy*.; Solomon, E. I.; Lever, A. B. P., Eds. Wiley: New York, 1999, Vol. 2, p 575, and references therein.
8. Decurtins, S.; Gütlich, P.; Hasselbach, K. M.; Spiering, H.; Hauser, A. *Inorg. Chem.* **1985**, *24*, 2174.
9. Decurtins, S.; Gütlich, P.; Köhler, C. P.; Spiering, H.; Hauser, A. *Chem. Phys. Lett.* **1984**, *105*, 1.
10. Hauser, A. J. *Chem. Phys.* **1991**, *94*, 2741.
11. Van Koningsbruggen, P. J.; Garcia, Y.; Kahn, O.; Fournes, L.; Kooijman, H.; Spek, L.; Haasnoot, J. G.; Moscovici, J.; Provost, K.; Michalowicz, A.; Renz, F.; Gütlich, P. *Inorg. Chem.* **2000**, *39*, 1891.
12. Stassen, A. F.; De Vos, M.; Van Koningsbruggen, P. J.; Renz, F.; Ensling, J.; Kooijman, H.; Spek, A. L.; Haasnoot, J. G.; Gütlich, P.; Reedijk, J. *Eur. J. Inorg. Chem.* **2000**, *10*, 2231.
13. Roubeau, O.; Alcazar Gomez, J. M.; Balskus, E.; Kolnaar, J. J. A.; Haasnoot, J. G.; Reedijk, J. *New J. Chem.* **2001**, *25*, 144.
14. Hoselton, M. A.; Wilson, L. J.; Drago, R. S. *J. Am. Chem. Soc.* **1975**, *97*, 1722.
15. Dose, E. V.; Hoselton, M. A.; Sutin, N.; Tweedle, M. F.; Wilson, L. J. *J. Am. Chem. Soc.* **1978**, *100*, 1141.
16. Hauser, A.; Vef, A.; Adler, P. *J. Chem. Phys.* **1991**, *95*, 8710.
17. Hauser, A. *Comments Inorg. Chem.* **1995**, *17*, 17.
18. Hauser, A. *Coord. Chem. Rev.* **1991**, *111*, 275.
19. McGarvey, J. J.; Lawthers, I. J. *Chem. Soc. Chem. Commun.* **1982**, 906.
20. Toftlund, H. *Coord. Chem. Rev.* **1989**, *97*, 67.
21. Moliner, N.; Gaspar, A. B.; Munoz, M. C.; Niel, V.; Cano, J.; Real, J. A. *Inorg. Chem.* **2001**, *40*, 3986.
22. Capes, L.; Létard, J.-F.; Kahn, O. *Chem. Eur. J.* **2000**, *6*, 2246.
23. Hayami, S.; Gu, Z.; Einaga, Y.; Kobayasi, Y.; Ishikawa, Y.; Yamada, Y.; Fujishima, A.; Sato, O. *Inorg. Chem.* **2001**, *40*, 3240.
24. Herber, R. H. *Inorg. Chem.* **1987**, *26*, 173.
25. Hauser, A.; Gütlich, P.; Spiering, H. *Inorg. Chem.* **1986**, *25*, 4245.
26. Buchen, T.; Schollmeyer, D.; Gütlich, P. *Inorg. Chem.* **1996**, *35*, 155.
27. Baldenius, K.-U.; Camplen, A. K.; Hönk, H.-D.; Rest, A. J. *J. Mol. Struct.* **1987**, *157*, 295.
28. Létard, J.-F.; Nguyen, O.; Soyer, H.; Mingotaud, C.; Delhaes, P.; Kahn, O. *Inorg. Chem.* **1999**, *38*, 3020.
29. McCusker, J. K.; Walda, K. N.; Dunn, R. C.; Simon, J. D.; Magde, D.; Hendrickson, D. N. *J. Am. Chem. Soc.* **1992**, *114*, 6919.

30. McCusker, J. K.; Walda, K. N.; Dunn, R. C.; Simon, J. D.; Magde, D.; Hendrickson, D. N. *J. Am. Chem. Soc.* **1993**, *115*, 298.
31. Hinek, R.; Gütlich, P.; Hauser, A. *Inorg. Chem.* **1994**, *33*, 567.
32. Hinek, R.; Spiering, H.; Gütlich, P.; Hauser, A. *Chem. Eur. J.* **1996**, *2*, 1435.
33. Hinek, R.; Spiering, H.; Schollmeyer, D.; Gütlich, P.; Hauser, A. *Chem. Eur. J.* **1996**, *2*, 1427.
34. Letard, J.-F.; Real, J. A.; Moliner, N.; Gaspar, A. B.; Capes, L.; Cador, O.; Kahn, O. *J. Am. Chem. Soc.* **1999**, *121*, 10630.
35. Chastanet, G.; Létard, J.-F.; Gaspar, A. B.; Real, J. A. *Chem. Comm.* **2001**, *819*.
36. Hauser, A. *Chem. Phys. Lett.* **1990**, *173*, 507.
37. Gütlich, P. In *Mössbauer Spectroscopy Applied to Inorganic Chemistry*, Long, J. G., Ed., Plenum: New York, 1984, Vol. 1, p 287.
38. Gütlich, P.; Link, R.; Trautwein, A. X. *Mössbauer Spectroscopy and Transition Metal Chemistry*; Springer: Berlin, 1978.
39. Sano, H.; Gütlich, P. In *Hot Atom Chemistry*, Matsuura, T., Ed., Kodanski: Tokyo, 1984, pp 265–302.
40. Ensling, J.; Fitzsimmons, B. W.; Gütlich, P. *Angew. Chem.* **1970**, *9*, 637.
41. Grimm, R.; Gütlich, P.; Kankeleit, E.; Link, R. J. *Chem. Phys.* **1977**, *67*, 5491.
42. Albrecht, R.; Alflen, M.; Gütlich, P.; Kajcsos, Zs.; Schulze, R.; Spiering, H.; Tuczek, F. *Nucl. Instrum. Methods A* **1987**, *257*, 209.
43. Deisenroth, S.; Hauser, A.; Spiering, H.; Gütlich, P. *Hyperf. Interact.* **1994**, *93*, 1573.
44. Ensling, J.; Gütlich, P.; Hasselbach, K. M.; Fitzsimmons, B. W. *Chem. Phys. Lett.* **1976**, *42*, 232.
45. Fleisch, J.; Gütlich, P. *Chem. Phys. Lett.* **1976**, *42*, 237.
46. Fleisch, J.; Gütlich, P. *Chem. Phys. Lett.* **1977**, *45*, 29.
47. Fleisch, J.; Gütlich, P.; Köppen, H. *Radiochem. Radioanalyt. Lett.* **1980**, *42*, 279.
48. Hauser, A.; Adler, P.; Deisenroth, S.; Gütlich, P.; Hennen, C.; Spiering, H.; Vef, A. *Hyperfine Interactions* **1994**, *90*, 77.
49. Adler, P.; Spiering, H.; Gütlich, P. *Inorg. Chem.* **1987**, *26*, 3840.
50. Adler, P.; Hauser, A.; Vef, A.; Spiering, H.; Gütlich, P. *Hyp. Int.* **1989**, *47*, 343.
51. Beattie, J. K. *Adv. Inorg. Chem.* **1988**, *32*, 1.
52. König, E. *Struct. Bonding* **1991**, *76*, 51.
53. Bacci, M. *Coord. Chem. Rev.* **1988**, *86*, 245.
54. Buhks, E.; Navon, G.; Bixon, M.; Jortner, J. *J. Am. Chem. Soc.* **1980**, *102*, 2918.
55. Xie, C.-L.; Hendrickson, D. N. *J. Am. Chem. Soc.* **1987**, *109*, 6981.
56. Conti, A.; Xie, C. L.; Hendrickson, D. N. *J. Am. Chem. Soc.* **1989**, *111*, 1171.
57. McGarvey, J. J.; Lawthers, I.; Heremans, K.; Toftlund, H. *Inorg. Chem.* **1990**, *29*, 252.
58. McGarvey, J. J.; Lawthers, I.; Heremans, K.; Toftlund, H. *J. Chem. Soc. Chem. Com.* **1984**, 1575.
59. DiBenedetto, J.; Arkle, V.; Goodwin, H. A.; Ford, P. C. *Inorg. Chem.* **1985**, *24*, 456.
60. Schenker, S.; Hauser, A.; Wang, W.; Chan, I. Y. *J. Chem. Phys.* **1998**, *109*, 9870.
61. Jeftic, J.; Hauser, A. *Chem. Phys. Lett.* **1996**, *248*, 458.
62. Jeftic, J.; Hauser, A. *J. Phys. Chem. B* **1997**, *101*, 10262.
63. Lawthers, I.; McGarvey, J. J. *J. Am. Chem. Soc.* **1984**, *106*, 4280.
64. Schenker, S.; Hauser, A. *J. Am. Chem. Soc.* **1994**, *116*, 5497.
65. Schenker, S.; Hauser, A.; Dyson, R. M. *Inorg. Chem.* **1996**, *35*, 4676.
66. Hayami, S.; Gu, Z.; Shiro, M.; Einaga, Y.; Fujishima, A.; Sato, O. *J. Am. Chem. Soc.* **2000**, *122*, 7126.
67. Spiering, H.; Meissner, E.; Köppen, H.; Müller, E. W.; Gütlich, P. *Chem. Phys.* **1982**, *68*, 65.
68. Köhler, C. P.; Jakobi, R.; Meissner, E.; Wiehl, L.; Spiering, H.; Gütlich, P. *J. Phys. Chem. Solids* **1990**, *51*, 239.
69. Hauser, A.; Jeftic, J.; Romstedt, H.; Hinek, R.; Spiering, H. *Coord. Chem. Rev.* **1999**, *190–192*, 471.
70. Buchen, T.; Guetlich, P.; Goodwin, H. Y. *Inorg. Chem.* **1994**, *33*, 4573.
71. Jeftic, J.; Hinek, R.; Capelli, S.; Hauser, A. *Inorg. Chem.* **1997**, *36*, 3080.
72. Spiering, H.; Kohlhaas, Th.; Romstedt, H.; Hauser, A.; Bruns-Yilmas, C.; Kusz, J.; Gütlich, P. *Coord. Chem. Rev.* **1999**, *190–192*, 629.
73. Romstedt, H.; Hauser, A.; Spiering, H. *J. Phys. Chem. Solids* **1998**, *59*, 265.
74. Hauser, A.; Adler, J.; Gütlich, P. *Chem. Phys. Lett.* **1988**, *152*, 468.
75. Buchen, T.; Gütlich, P. *Chem. Phys. Lett.* **1994**, *220*, 3.
76. Kahn, O.; Kröber, J.; Jay, C. *Adv. Mater.* **1992**, *4*, 718.
77. Kröber, J.; Codjovi, E.; Kahn, O.; Grolière, F.; Jay, C. *J. Am. Chem. Soc.* **1993**, *115*, 9810.
78. Garcia, Y.; van Koningsbruggen, P. J.; Codjovi, E.; Lapouyade, R.; Kahn, O.; Rabardel, L. *J. Mater. Chem.* **1997**, *7*, 857.
79. Kahn, O.; Martinez, C. J. *Science* **1998**, *279*, 44.
80. Gütlich, P.; Garcia, Y.; Woike, Th. *Coord. Chem. Rev.* **2001**, *219–221*, 839.
81. Adams, D. M.; Dei, A.; Rheingold, A. L.; Hendrickson, D. N.; *J. Am. Chem. Soc.* **1993**, *115*, 8221.
82. Adams, D. M.; Hendrickson, D. N. *J. Am. Chem. Soc.* **1996**, *118*, 11515.
83. Delley, B.; Schefer, J.; Woike, Th. *J. Chem. Phys.* **1997**, *107*, 10067.
84. Carducci, M. D.; Pressprich, M. R.; Coppens, P.; *J. Am. Chem. Soc.* **1997**, *119*, 2669.
85. Sato, O.; Iyoda, T.; Fujishima, A.; Hashimoto, K. *Science* **1996**, *272*, 704–705.
86. Escax, V.; Bleuzen, A.; Cartier dit Moulin, C.; Villain, F.; Goujon, A.; Varret, F.; Verdaguer, M. *J. Am. Chem. Soc.* **2001**, *123*, 12536.
87. Goujon, A.; Roubeau, O.; Varret, F.; Dolbecq, A.; Bleuzen, A.; Verdaguer, *M. Eur. Phys. J. B* **2000**, *14*, 115.

Comprehensive Coordination Chemistry II
ISBN (set): 0-08-0437486

Volume 2, (ISBN 0-08-0443249); pp 427–434

2.34
Notes on Time Frames

A. B. P. LEVER
York University, Toronto, Ontario, Canada

2.34.1 INTRODUCTION 435
2.34.2 TIME FRAMES OF SELECTED PHYSICAL MEASUREMENTS 436
2.34.2.1 Vibrational Spectroscopy 436
2.34.2.2 Electronic Spectroscopy, Magnetic Circular Dichroism, etc. 436
2.34.2.3 Mössbauer Spectroscopy 436
2.34.2.4 Electrochemistry 436
2.34.2.5 Diffraction Processes 436
2.34.2.6 Photoelectron Spectroscopy 437
2.34.2.7 Mass Spectroscopies 437
2.34.2.8 NMR Spectroscopies 437
2.34.2.9 Electron Paramagnetic Resonance 437
2.34.3 REFERENCES 437

2.34.1 INTRODUCTION

One may consider trivially that if one wishes to record the infrared spectrum of a species one has just prepared in the laboratory, it must remain stable for a sufficient length of time to allow one to take the sample physically from the preparation laboratory to the infrared laboratory. Obviously if the sample only exists for 10 seconds at $-40\,^{\circ}C$, special conditions must be arranged to obtain physical data before the sample decomposes.

However, this article deals with the intrinsic lifetime associated with a particular physical technique. Thus, suppose there exists *cis* and *trans* isomers of a species and that these interchange in equilibrium in solution at a rate of 10^9 times per second–is it possible to record the physical properties of each species separately or will one observe the properties of an average of the two species. Here we address the intrinsic lifetime of a physical process. Thus, for example, the intrinsic lifetime of the infrared experiment is the time for a vibration, or about 10^{-14} s. Thus, an infrared spectrum is capable of freezing out this equilibrium and we observe a spectrum which is a summation of the individual spectra of the *cis* and *trans* isomers; it is as though we have frozen the equilibrium or taken a very high-speed snapshot. Electronic spectroscopy is even faster, ca. 10^{-15} s and will freeze out vibrations of a molecule. On the other hand, the NMR experiment is much slower (*vide infra*) and we would observe an NMR spectrum comprised of an average of the exchanging species. Cooling the sample in the NMR spectrometer may cause the equilibrium to slow down such that the interchange becomes slower than the NMR timescale and then separate resonances would appear for each isomeric species.

More specifically we note two other topical areas where the lifetime of a particular technique is crucial in understanding the significance of the results.

In mixed valence species,[1] especially symmetric species such as the dinuclear ruthenium Creutz-Taube (CT) ion, questions arise as to whether the valence states are localized, in the CT ion $Ru^{II} \cdots Ru^{III}$, or delocalized, formally, $Ru^{2.5} \cdots Ru^{2.5}$. The former can become the latter if an electron exchanges rapidly between the two ruthenium centers. Thus, a snapshot taken faster than

the electron exchange will show a localized valency and a snapshot slower than the exchange will reveal a delocalized species (see Chapter 2.60).

Another area of intense interest is the question of whether the excited state of the tris(bipyridine)ruthenium(II) cation is localized or delocalized. It has long been known from excited state resonance Raman spectroscopy[2] that the relaxed excited MLCT state is localized in one bipyridine ring, i.e., can be written as $[Ru^{III}(bpy)_2(bpy^-)]^{2+}*$, but the question arises as to whether the actual excitation leads directly to a localized or delocalized state. Clearly the time frame of the probing experiment is critical; in this case femtosecond spectroscopy leads to the conclusion that a delocalized state is initially formed but that localization follows extremely rapidly thereafter.[3–5] Without going into detail here, it is also true that the coupling of a molecule to its environment (crystal, solvent, etc.) also plays a crucial role in determining the dynamics of any process.[6]

2.34.2 TIME FRAMES OF SELECTED PHYSICAL MEASUREMENTS

2.34.2.1 Vibrational Spectroscopy

This technique has a time frame of a single vibration or approximately 1×10^{-14} s. Obviously depending on frequency ν, simply $t = 1/\nu$, with longer periods for the lower frequencies, e.g., νC=C ca. 20 fs, νC—H ca. 10 fs.

2.34.2.2 Electronic Spectroscopy, Magnetic Circular Dichroism, etc.

The time of excitation to the Franck-Condon state is approximately 1 fs (10^{-15} s). Thus, these techniques will "freeze out" any equilibrium that involves the actual movement of nuclei, such as a *cis–trans* interconversion. Electron exchange can, however, be faster than a vibration. These very fast electron transfer processes can be probed by exposing a sample to laser radiation with a pulse shorter than 10^{-14} s, i.e., the realms of femtosecond (10^{-15} s) and attosecond (10^{-18} s) spectroscopy.[7,8]

2.34.2.3 Mössbauer Spectroscopy

The time depends on the nuclide under study, corresponding with the lifetime of the nuclear excited state. For example, it is 19 ns for ^{57}Fe, 18.3 ns for ^{119}Sn, and 3.5 ns for ^{121}Sb.[9]

2.34.2.4 Electrochemistry

Electrochemical timescales are of importance when one desires to measure the kinetics of an electrochemical process. Changing the rate of mass transport by convection, the shape or size of the electrode, and scan rate can vary the timescale. There is a quadratic dependence of the timescale upon the radius of the electrode, favoring microelectrodes, therefore, for rapid kinetic measurements. A timescale as short as 10 μs can be accessed using a microjet electrode. The reader is referred to an excellent analysis by Bond and co-workers.[10]

2.34.2.5 Diffraction Processes

The fundamental physical process is scattering of a photon (or electron or neutron) as it passes an atom, and the time involved is therefore extremely short. For X-rays it is of the order of 10^{-19} s, for electrons, up to an order of magnitude slower (10^{-18} s), and for typical neutrons about 10^{-15} s. However these numbers are not really meaningful since the actual experiment usually takes hours or days and so a time-average is observed over this long timescale. Nevertheless using pulsed synchrotron techniques (see Chapter 2.13) time resolved X-ray crystallography is achievable down to much shorter timescales even to the picosecond regime.[11–13]

2.34.2.6 Photoelectron Spectroscopy

If the timescale of a spectroscopic method is defined as the natural lifetime of a state, and the natural lifetime is defined as the reciprocal of the Einstein coefficient for spontaneous emission decay (e.g., neglecting decays from radiationless transition, energy transfer in collision, and photochemical reactions), the time scale is then energy dependent because the spontaneous radiation decay is proportional to the cubic power of transition energy. Thus, for a photoelectron process with direct photoionization, the lifetime of an excited electronic state of a molecular ion can range from about 10 ns (10^{-8} s) (in the vis–UV region) to about 10 fs (10^{-14} s) (in the X-ray region, say ~1,000 eV). However, for threshold photoionization, which produces molecular ions in their ground electronic state, the lifetime can then be very long. For ZEKE that is based on delayed electric field ionization, the lifetime is of the order of a microsecond (10^{-5}–10^{-6} s).

2.34.2.7 Mass Spectroscopies

The actual ionization process takes place in about 10^{-15} s. This is followed by possible fragmentation after 10^{-13} s and deactivation to the ground state in about 10^{-8} s. The ion may arrive at the detector in about 10^{-6} s but depending on the design of the spectrometer, these ions may be stored indefinitely after their formation.[14,15] The threshold CID processes have a time scale of 100–500 μs ($1–5 \times 10^{-4}$ s).

2.34.2.8 NMR Spectroscopies

The timescale is the reciprocal of the frequency, which in NMR depends on the magnetic field strength and the particular element to be analyzing. For protons, conventional spectrometers range from 100 MHz to 600 MHz and the intrinsic time will be the reciprocal of this. Thus, in the latter case the snapshot time is 1.7 ns (the time for the spin to flip). However, of greater importance for time dependence in NMR is the signal averaging time which depends on the difference in frequency between the signals being averaged. For example, if two equilibrating species give a signal 0.1 ppm apart on a 400 MHz spectrometer, this difference will be 40 Hz and the time resolution is the inverse, i.e., 2.5 s. Thus, two such species would give separate signals only if they equilibrate *slower* than 2.5 times per second. Similarly for a 2 ppm separation on a 400 MHz machine, the difference is 800 Hz with a time of 1.25 ms. Signal averaging is not seen in most other forms of spectroscopy due to the much larger differential frequencies and hence shorter times involved, much too short for chemical processes.

2.34.2.9 Electron Paramagnetic Resonance

The timescale depends on the type of EPR measurement that is performed, the g and A-anisotropy for the molecule, and the magnetic field and frequency of the experiment. The timescale can range from about 10^{-6} s to 10^{-12} s. The larger the inequivalence that is averaged, the faster the rate that is required to average it, and the shorter the timescale (see Section 2.34.2.8) The relationship between operating frequency, ν, and time is given by $(2\pi\nu)^{-1}$ s,[16,17] if the energy difference that defines the EPR timescale is the spectrometer frequency. In other cases the energy difference to be averaged is related to nuclear hyperfine interaction, which is not dependent on spectrometer frequency. In still other cases, the energy difference to be averaged is determined by a combination of *g* anisotropy and hyperfine interaction, and the resulting energy difference may be several orders of magnitude smaller than the spectrometer frequency, but still frequency dependent.

2.34.3 REFERENCES

1. Demadis, K. D.; Hartshorn, C. M.; Meyer, T. J. *Chem. Rev.* **2001**, *101*, 2655–2685.
2. Bradley, P. G.; Kress, N.; Hornberger, B. A.; Dallinger, R. F.; Woodruff, W. H., Jr. *J. Am. Chem. Soc.* **1981**, *103*, 744.
3. Yeh, A. T. S. C. V.; McCusker, J. K. *Science* **2000**, *289*, 935–938.
4. Bhasikuttan, A. C.; Suzuki, M.; Nakashima, S.; Okada, T. *J. Am. Chem. Soc.* **2002**, *124*, 8398–8405.
5. Shaw, G. B.; Brown, C. L.; Papanikolas, J. M. *J. Phys. Chem. A* **2002**, *106*, 1483–1495.

6. Webb, M. A.; Knorr, F. J.; McHale, J. L. *J. Raman Spectrosc.* **2001**, *32*, 481–485.
7. Hentschel, M; Kienberger, R.; Spielmann, C.; Reider, G. A.; Milosevic, N.; Brabec, T.; Corkum, P.; Heinzmann, U.; Drescher, M.; Krausz, F. *Nature* **2001**, *414*, 509–513.
8. Windhorn, L.; Witte, T.; Yeston, J. S.; Proch, D.; Motzkus, M.; Kompa, K. L.; Fuß, W. *Chem. Phys. Lett.* **2002**, *357*, 85–90.
9. Long, G. J.; Grandjean, F. E. *The Time Domain in Surface and Structural Dynamics* 1988, Kluwer Academic Publishers: Dordrecht, The Netherlands.
10. Eklund, J. C.; Bond, A. M.; Alden, J. A.; Compton, R. G. *Adv. Phys. Org. Chem.* **1999**, *32*, 1–120.
11. Perman, B.; Šrajer, V.; Ren, Z.; Teng, T. -Y.; Pradervand, C.; Ursby, T.; Bourgeois, D.; Schotte, F.; Wulff, M.; Kort, R.; Hellingwerf, K.; Moffat, K. *Science* **1998**, *279*, 1806–1950.
12. Genick, U. K.; Borgstahl, G. E. O.; Ng, K.; Ren, Z.; Pradervand, C.; Burke, P. M.; Teng, T.-Y.; McRee, D. E.; Getzoff, E. D. *Science* **1997**, *275*, 1471–1475.
13. Šrajer, V.; Teng, T. Y. U. T.; Pradervand, C.; Ren, Z.; Adachi, S.; Schildkamp, W.; Bourgeois, D.; Wulff, M.; Moffat, K. *Science* **1996**, *274*, 1726–1729.
14. Lambert, J. B.; Shurvell, H. E.; Lightner, D. A.; Cooks, R. G. *Organic Structural Spectroscopy* 1998. *Part IV*, 346–478. Prentice Hall: Upper Saddle River, NJ.
15. de Hoffman, E.; Stroobant, V. *Mass Spectrometry, Principles and Applications* 2002, Wiley: Chichester, U.K.
16. Weil, J. A.; Bolton, J. R.; Wertz, J. E. *Electron Paramagnetic Resonance Spectroscopy: Elementary Theory and Practical Applications* 1994, Wiley: New York.
17. Dei, A.; Gatteschi, D.; Sangregorio, C.; Sorace, L.; Vaz, M. G. F. *Chem. Phys. Lett.* **2003**, *368*, 162–167.

Comprehensive Coordination Chemistry II
ISBN (set): 0-08-0437486

Volume 2, (ISBN 0-08-0443249); pp 435–438

2.35
Ligand Field Theory

R. J. DEETH
University of Warwick, Coventry, UK

2.35.1 THE NATURE OF LFT 439
2.35.2 LIGAND FIELD PARAMETERS 439
2.35.3 "*d*–*d*" ELECTRONIC TRANSITION INTENSITIES 441
2.35.4 APPLICATIONS AND REFINEMENTS 441
2.35.5 LFT IN THE FUTURE 441
2.35.6 REFERENCES 442

Ligand field theory (LFT) was already a relatively mature subject when *Comprehensive Coordination Chemistry* (*CCC*, 1987) was published and virtually all of Figgis' original Chapter 6 remains valid in terms of the mathematical techniques and the interpretation of the spectral and magnetic properties of high-symmetry, cubic systems. In 2000, Figgis, in collaboration with Hitchman,[1] published the long-awaited updated edition of his classic text on LFT which covers the intervening developments in theory and applications especially with regard to the angular overlap model (AOM), the topic of the next section. However, the issue of the physical significance and transferability of ligand field parameters remains a contentious issue which was debated, sometimes hotly, during the late 1980s to early 1990s. Figgis was fairly skeptical and states in *CCC* (1987) that the "physical significance to be attached to the meaning of ligand field parameters is . . .very limited."

In contrast, the "Gerloch school" attempted to make a direct connection between the ligand field parameter values and the nature of the metal–ligand bonding.[2–11] The physical basis for interpreting the significance of ligand field parameters was developed by Woolley[12] whose starting point was the density functional theorem. His analysis leads to different expressions for the AOM e_σ and e_π parameters, previously introduced by Schäffer and Jørgenson[13] in the context of the Wolfsberg–Helmholtz approximation, and to different interpretations of phenomena such as *d*–*s* mixing,[4] phase-coupled ligators,[8] bent bonding,[9,10] and parameter transferability.[6,14] These issues are discussed further in Chapter 2.36.

2.35.1 THE NATURE OF LFT

LFT is an example of effective operator theory and can be employed to construct multiplet states arising from d^n (or f^n) configurations. Hence, it is strictly only applicable to systems where the ground state and the lower energy excited states are dominated by *d*-(or *f*-) orbital contributions. LFT is thus most relevant for relatively ionic Werner-type transition metal (TM) complexes.

Within this approximation, the mathematics for evaluating the multiplets and their relative energies is straightforward and all the necessary equations were well-established by the start of the 1960s. In a sense, therefore, LFT is an "exact" model and Figgis' Chapter 6 in *CCC* (1987) remains a definitive account of the mechanics of how to carry out actual LFT calculations of the "*d*–*d*" (or "*f*–*f*") spectroscopic and magnetic properties of TM complexes. The major advancements since *CCC* (1987) are in developing methods and computer codes (see Chapter 2.52) for extracting ligand field parameter values and what these mean in terms of metal–ligand bonding.

2.35.2 LIGAND FIELD PARAMETERS

LFT is a parametric approach in which the symmetry of the complex is treated explicitly but the bonding is handled implicitly through the ligand field parameters. These parameters describe the three contributions to the overall Hamiltonian, H: the ligand field, H_{LF}, interelectronic repulsion, H_{ER} and spin orbit coupling, H_{LS}. The relative importance of each of these terms depends on the element's position in the periodic table.

First and second transition series: $H_{LF} > H_{ER} \approx H_{LS}$
Third transition series: $H_{LF} \approx H_{ER} \approx H_{LS}$
Lanthanoids: $H_{ER} > H_{LS} > H_{LF}$
Actinoids: $H_{ER} \geq H_{LS} \geq H_{LF}$

Within the normal central field approximation, H_{ER} and H_{LS} are spherically symmetric. Interelectronic repulsion in a complex is thus treated using the same electrostatic theory as for atomic spectroscopy. It is parameterized either within the original Condon–Shortley F_0, F_2, F_4, scheme or the later Racah A, B, C scheme. Since LFT only gives energy differences, values for F_0 (and A) cannot be determined. There is a simple mapping between the Condon–Shortley and Racah schemes and they will give identical energies if used in full-basis calculations. However, Racah noted that in free atoms or ions, the energy difference between the terms of maximum spin multiplicity required only one parameter, B. Hence, the Racah scheme is more popular for analyzing "*d–d*" spectra since B is sufficient for calculating the spin-allowed transitions of a high-spin complex.

Spin–orbit coupling is also based on atomic theory and requires only the one-electron spin–orbit coupling constant, ζ. In addition, the calculation of magnetic moments includes Steven's orbital reduction parameter, k. Figgis gives a comprehensive account in *CCC* (1987) of calculating magnetic properties and includes additional terms such as the Trees correction.

The ligand field potential, V_{LF}, defines the energies of the *d*-(or *f*-) orbitals and is the only part of a conventional LFT calculation which includes the symmetry of the complex. Hence, H_{LF} is the only part of the Hamiltonian which can make general *direct* contact with M—L bonding. H_{ER} and H_{LS} may still be relevant but only in terms of the overall, averaged nature of the metal–ligand interaction.

There are two important points to emphasize with regard to V_{LF}. First, contributions to V_{LF} are not computed from first principles. Instead, the potential is constructed parametrically and the parameter values are determined by fitting calculated properties to experiment. Secondly, there are two distinct ways in which V_{LF} can be constructed–globally or via ligand superposition.

The global approach is exemplified by the original crystal field theory (CFT). V_{LF} is described as a linear combination of spherical harmonics which progressively lowers the symmetry from spherical to cubic and on to still lower symmetries. For high symmetries such as octahedral and tetrahedral (i.e., cubic), the global scheme is simple and elegant. The *d*-orbital splitting depends on a single parameter, Δ. Since many complexes are (approximately) octahedral or tetrahedral, the global approach has been widely applied. However, as is well known, the e_g–t_{2g} splitting in octahedral symmetry is a competition between σ-and π-bonding effects which the single global parameter cannot separate. Furthermore, as the symmetry is lowered, the number of global parameters increases and since they include both symmetry (i.e., angular) and bonding (i.e., radial) contributions, the connection between parameter values and the nature of individual M—L interactions is difficult and sometimes impossible to extract. In other instances, the global scheme does not describe the bonding correctly.

For example, in tetragonal symmetry, the global scheme has three parameters, Dq, Ds, and Dt. For tetragonal macrocyclic tetraaza Ni^{II} complexes with an NiN_4X_2 core, there are also three AOM parameters, $e_\sigma(N)$, $e_\sigma(X)$, and $e_\pi(X)$ (*vide infra*) and hence the two parameters sets can be directly mapped onto each other. Values for Dq, Ds and Dt were derived by analyzing the *d–d* spectra and assignments were made based on the "reasonableness" of the ligand field parameter values and their variations. However, when the values are converted to their corresponding AOM values, Cl^- is predicted to be a π-acceptor. Equally acceptable assignments of the *d–d* transition energies can be obtained with more reasonable AOM parameter values.[15]

As alluded to above, the superposition method, typified by the AOM, overcomes many of the problems of the global scheme and is discussed in detail in Chapter 2.52. V_{LF} is constructed as a superposition of contributions from individual M—L bonds which explicitly separates the angular and radial parts. The former is implicit in the geometry so that the AOM energy parameters focus

exclusively on the radial part. Furthermore, the individual M–L perturbations can be factored into local σ and π components as monitored by the AOM e_σ and e_π energy parameters. In octahedral symmetry, the σ–π competition arises naturally since the *d*-orbital splitting is given by $3e_\sigma$–$4e_\pi$. Furthermore, by assuming two or more ligands are chemically equivalent, the number of AOM parameters can be kept manageable even for complexes with no symmetry which would, in principle, require a maximum of 14 independent global variables. Hence, by *CCC* (1987), the general consensus was that the best way to parameterize V_{LF} was via a superposition method like the AOM. Chapter 2.52 provides more details and describes applications of the AOM.

2.35.3 "*d–d*" ELECTRONIC TRANSITION INTENSITIES

Perhaps the most significant theoretical advance in LFT arose out of the Gerloch group during the late 1980s culminating in a comprehensive review published in 1997.[16] It concerned one of the most basic properties of the electronic spectrum which hitherto had not been readily calculable; namely the transition intensities.

In the spirit of the ligand superposition model, Gerloch and co-workers developed a parametric approach for calculating "*d–d*" transition intensities. In essence, the relative intensities of the "*d–d*" electric dipole transitions are expressed in terms of local t_λ intensity parameters which parallel the e_λ energy parameters. The intensity parameters are further qualified in terms of their *P* and *F* contributions. That is, since the basic parity selection rule is $\Delta l = \pm 1$, only *p* or *f* contributions (i.e., $l = 1$ or 3) are relevant for "*d–d*" transitions. The method has been applied both to non-centrosymmetric (static) and centrosymmetric (dynamic) species, the latter requiring the additional development of normal coordinate analysis methods for handling the vibronic intensity mechanism.

The review describes the application of the CLF intensity model to 43 chromophores. The ability to reproduce the observed intensity distributions, including those from experiments using linearly and circularly polarized light, is impressive. For example, the band areas for both the unpolarized absorption and CD spectra of Co(α-isospartein)Cl_2 are virtually perfect while in centrosymmetric complexes such as $[PtCl_4]^{2-}$, $[PtBr_4]^{2-}$, and $[PdCl_4]^{2-}$ the vibronic analysis can also establish the relative importance of the possible contributing ungerade vibrational modes to the overall intensity. In these cases, the e_u mode accounts for more than half of the total.

Despite all the effort, however, the CLF spectral intensities model has not been widely adopted even though the latest version of the CAMMAG program (Chapter 2.54) provides the means to carry out the calculations. In the absence of a "champion" and in the light of the continuing rapid development of alternative, more widely applicable methods based on molecular orbital schemes, it seems likely that the promising CLF approach will languish.

2.35.4 APPLICATIONS AND REFINEMENTS

Even a cursory examination of the literature reveals that ligand field concepts are still widely employed to interpret and rationalize diverse experimental data on varied transition metal systems and the present volume contains myriad examples. Chapter 2.36 focuses specifically on the applications of the superposition models. However, the basic methods for carrying out LFT calculations have not altered significantly. Chapter 2.52 has overviews of available software packages.

There have been some refinements of certain ligand field concepts. For example, the familiar "double hump" behavior of the ligand field stabilization energy has been reanalyzed by Johnson and Nelson who demonstrate the need to include contributions from *d–d* interelectron repulsion along with the conventional *d*-orbital splitting components.[17–20] Also, there have been some attempts to reconcile the predictions of LFT with the results emerging from DFT. This theme is taken up again in Chapter 2.35.

2.35.5 LFT IN THE FUTURE

There is little doubt that as a pedagogic tool for introducing coordination chemistry, symmetry, and spectroscopy, LFT will remain a valuable part of the undergraduate syllabus. As such, many of the basic concepts derived from LFT will remain in service. However, the methodology of LFT

has been fully developed in that we cannot do better LFT calculations. Thus, given the fundamental limitations on the quantities which LFT can compute, it seems only a matter of time before more sophisticated methods, most likely based on DFT, will replace actual LFT calculations. One possible exception here is the development of empirical modeling schemes like the ligand field molecular mechanics (LFMM) method[21] and the AOM extension of the General Utility Lattice Program (GULP) for simulating solid state systems.[22] These models combine an AOM calculation of the ligand field stabilization energy with a conventional molecular mechanics/dynamics treatment to deliver a fast, empirical molecular modeling method capable of treating very large systems like metalloenzymes and oxide materials but in a way which captures the important electronic effects arising from incomplete *d*-shells (see Chapter 2.35). Perhaps the best example of the latter is the Jahn-Teller distortions of six-coordinate d^9 Cu^{II} [23,24] complexes and d^4 Mn^{III} in $LaMnO_3$ and Mn_2O_3.[22] By targeting the modeling of large systems beyond the reach of quantum electronic structure methods like DFT, the LFMM method and extended GULP may continue to stimulate interest in LFT for some years to come.

2.35.6 REFERENCES

1. Figgis, B. N.; Hitchman, M. A. *Ligand Field Theory and Its Applications* **2000**, Wiley: New York.
2. Gerloch, M.; Woolley, R. G. *J. Chem. Soc., Dalton Trans.* **1981**, 1714–1717.
3. Gerloch, M.; Woolley, R. G. *Prog. Inorg. Chem.* **1983**, *31*, 371–446.
4. Deeth, R. J.; Gerloch, M. *Inorg. Chem.* **1984**, *23*, 3846–3853.
5. Deeth, R. J.; Gerloch, M. *Inorg. Chem.* **1984**, *23*, 3853–3861.
6. Deeth, R. J.; Gerloch, M. *Inorg. Chem.* **1985**, *24*, 1754–1758.
7. Deeth, R. J.; Gerloch, M. *Inorg. Chem.* **1985**, *24*, 4490–4493.
8. Deeth, R. J.; Duer, M. J.; Gerloch, M. *Inorg. Chem.* **1987**, *26*, 2573–2578.
9. Deeth, R. J.; Duer, M. J.; Gerloch, M. *Inorg. Chem.* **1987**, *26*, 2578–2582.
10. Deeth, R. J.; Gerloch, M. *Inorg. Chem.* **1987**, *26*, 2582–2585.
11. Bridgeman, A. J.; Gerloch, M. *Prog. Inorg. Chem.* **1997**, *45*, 179–281.
12. Woolley, R. G. *Mol. Phys.* **1981**, *42*, 703–720.
13. Schaeffer, C. E.; Jorgensen, C. K. *Mol. Phys.* **1965**, *9*, 401.
14. Woolley, R. G. *Chem. Phys. Lett.* **1985**, *118*, 207–212.
15. Deeth, R. J.; Kemp, C. M. *J. Chem. Soc., Dalton Trans.* **1992**, 2013–2017.
16. Bridgeman, A. J.; Gerloch, M. *Coord. Chem. Rev.* **1997**, *165*, 315–446.
17. Johnson, D. A.; Nelson, P. G. *J. Chem. Soc., Dalton Trans.* **1995**, 3483–3488.
18. Johnson, D. A.; Nelson, P. G. *Inorg. Chem.* **1999**, *38*, 4949–4955.
19. Johnson, D. A.; Nelson, P. G. *Inorg. Chem.* **1995**, *34*, 3253–3259.
20. Johnson, D. A.; Nelson, P. G. *Inorg. Chem.* **1995**, *34*, 5666–5671.
21. Deeth, R. J. *Coord. Chem. Rev.* **2001**, *212*, 11–34.
22. Woodley, S. M.; Battle, P. D.; Catlow, C. R. A.; Gale, J. D. *J. Phys. Chem. B* **2001**, *105*, 6824–6830.
23. Burton, V. J.; Deeth, R. J.; Kemp, C. M.; Gilbert, P. J. *J. Am. Chem. Soc.* **1995**, *117*, 8407–8415.
24. Burton, V. J.; Deeth, R. J. *J. Chem. Soc., Chem. Commun.* **1995**, 573–574.

Comprehensive Coordination Chemistry II
ISBN (set): 0-08-0437486
Volume 2, (ISBN 0-08-0443249); pp 439–442

2.36
Angular Overlap Model

T. SCHÖNHERR
Heinrich-Heine-Universität, Düsseldorf, Germany
M. ATANASOV
Bulgarian Academy of Sciences, Sofia, Bulgaria
and
H. ADAMSKY
Heinrich-Heine-Universität, Düsseldorf, Germany

2.36.1 INTRODUCTION 443
2.36.2 THE THEORY OF THE AOM 444
2.36.2.1 The Original Version of the AOM 444
2.36.2.2 AOM Parametrization and the CLF Model 444
2.36.3 APPLICATIONS OF THE AOM 445
2.36.3.1 Orthoaxial Complexes 445
2.36.3.2 Non-orthoaxial Complexes 447
2.36.3.3 Stereochemistry and Reactivity 448
2.36.3.4 Photochemistry 448
2.36.4 EXTENSIONS OF THE AOM 449
2.36.4.1 *s–d* Mixing 449
2.36.4.2 Orbital Phase Coupling (Orgel Effect) 450
2.36.4.3 Misdirected Ligand Lone Pairs 452
2.36.4.4 Higher Coordination Spheres 452
2.36.4.5 Vibronic Coupling 452
2.36.4.6 Polynuclear TM Systems 453
2.36.5 ADVANTAGES AND DRAWBACKS OF THE AOM 453
2.36.5.1 Advantages 453
2.36.5.2 Drawbacks 453
2.36.6 REFERENCES 454

2.36.1 INTRODUCTION

Since its invention in 1963–1965[1–6] the angular overlap model (AOM) has become a powerful tool for the interpretation of spectra and magnetism of d^n transition metal (TM) complexes. While the physical background and the formalism of the AOM has been outlined elsewhere in some detail,[7,8] we confine ourselves here to a brief account of the theory (Section 2.36.2), including a recent development—the cellular ligand field (CLF) model. Emphasis will be given to the applications of the AOM in Section 2.36.3, including examples pertaining to thermochemical and photochemical reactions. More advanced applications of the AOM, in the framework of the numerous extensions introduced since the mid-1980s, will be the topic of Section 2.36.4. Finally, in Section 2.36.5, the advantages and drawbacks of the AOM will be summarized. (A comparison of the AOM with other LF approaches in view of the potential of DFT is presented in Chapter 2.50.)

2.36.2 THE THEORY OF THE AOM

2.36.2.1 The Original Version of the AOM

The AOM parametrizes the ligand field using *local* contributions to the ligand field potential (CFT and the conventional LFT define global (i.e., symmetry-adapted) parameters—see Chapter 2.35) that arise from interactions of the metal *d*-orbitals with valence orbitals of the individual ligating atoms (ligators). Starting from metal-*d* and ligand orbitals that are optimally aligned for σ (d_{z^2}–p_z) and π (d_{zx}–p_x, d_{yz}–p_y) *overlap*, the perturbed metal orbital energies are described by corresponding parameters e_σ, $e_{\pi s}$, and $e_{\pi c}$, ($e_{\pi s} = e_{\pi c}$ ($= e_\pi$) in cases of isotropic π-bonding, e.g., for halide ligands), respectively (Figure 1). Interactions of δ-type are treated similarly, however they are small and usually subsumed under the σ,π parameters (cf. Equation (23) in ref. 8). Contributions from all ligators, which represent the *chromophore*, are added to yield a simple diagonal (5×5) ligand field matrix V_{LF} (*additive potential*). The power of the AOM, however, comes from its ability to describe low-symmetry effects adequately. Thus, for any arbitrary orientation of metal and ligand orbitals, *angular* geometric factors $F_{M\lambda}$ are introduced, yielding also off-diagonal matrix elements in V_{LF}. The master equation of the AOM, Equation (1), defines the general matrix element V_{ij}^{AOM} between *d*-orbitals *i* and *j*,[9,10] the effect of each ligand (1) is accounted for by the model parameters $e_{\lambda l}$ ($\lambda = \sigma, \pi, \delta$), and by the geometric positions of the ligating atoms.

$$V_{ij}^{AOM} = \Sigma_l \Sigma_\lambda F_{\lambda i}(\Theta_l, \Phi_l, \Psi_l) \cdot F_{\lambda j}(\Theta_l, \Phi_l, \Psi_l) \cdot e_{\lambda l} \tag{1}$$

The $F_{M\lambda}$ are described by using the Eulerian angles Θ_l, Φ_l, and Ψ_l as outlined in Chapter 2.52. Spin-orbit coupling, which may be important even for lighter TM complexes by affecting magnetic susceptibilities as well as EPR and optical spectra, is accounted for by the operator $\mathbf{V_{SO}}$ (parameter ζ), while the Zeeman operator $\mathbf{V_{mag}}$ describes the interaction of the spin and orbital momenta of the *d*-electrons with an external field. In the case of d^n, $n \geq 2$, the matrices V_{AOM}, V_{SO}, and V_{mag} are constructed by using the many-electron wave function and supplemented with contributions from the operators for the interelectronic repulsion $\mathbf{V_{ee}}$ (described by Racah parameters) and the orbit–orbit interaction $\mathbf{V_{Trees}}$ (Trees parameter α). For details see Chapters 2.35 and 2.52.

2.36.2.2 AOM Parametrization and the CLF Model

In its initial formulation the AOM was developed as a MO approach. Each metal *d*-orbital overlaps the corresponding ligand *p*-orbitals of the same symmetry (σ or π) to yield one bonding and one antibonding function, the latter usually mainly metal-localized. Then, nondegenerate perturbation theory in combination with the Wolfsberg–Helmholz approximation yields for the antibonding energy change $\Delta\varepsilon_{ab}$[11]

$$\Delta\varepsilon_{ab}(\lambda) = e_{\lambda l} \approx S_{ML}(\lambda)^2 H_L^2/(H_M - H_L), \quad \lambda = \sigma, \pi \tag{2}$$

where S_{ML} is the overlap integral and H_M and H_L represent the metal and ligand valence state ionization potentials. Equation (2) regards a complex molecule as being the sum of its constituent atoms, a notion which is very useful in chemistry. It serves as a theoretical basis that supposes the parameters $e_{\lambda l}$ to be highly transferable from one complex to another, implying that the chemical

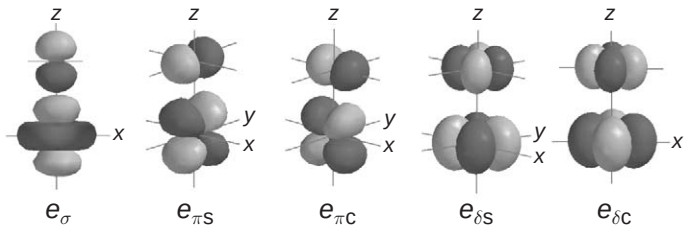

Figure 1 AOM parametrization for the M–L system within the standard orientation.

environment leads only to negligible variations in $S_{ML}(\lambda)$, H_L, and H_M from molecule to molecule. In turn, dependencies such as $e_{\lambda l} \sim S_{ML}(\lambda)^2$ have been invoked to successfully approximate bond length variations in ligand field treatments, thus lowering the degree of parametrization.[12–14] Transferability of AOM parameters between different complexes of the same TM in a particular oxidation state has been suggested.[8,11–13] However, such conclusions have been criticized by others, with particular regard to the influence of the trans-effect on AOM parameters.[15,16]

An interesting attempt toward further understanding of the AOM parameters and the AOM itself is the CLF model developed by Gerloch *et al.*[17–19] It is based on the assumption that metal–ligand covalent bonding is mainly due to metal 4*s*, 4*p*, and ligand-*p* and -*s* functions. Thus, the CLF presupposes that 3*d*-orbitals (electrons) can be regarded as spectators (probes) of the electron density due to the remaining electrons on the bonding and nonbonding orbitals χ. By spherically averaging the potential **V** due to this density, one arrives at mean "*d*"-orbitals and mean "*d*"-orbital energies. In a second step, the deviation of **V** from spherical symmetry $<\mathbf{V}> - \mathbf{V}' = \mathbf{V} - <\mathbf{V}>$ is used to define $e_{\lambda l}$ as

$$e_{\lambda l} \approx <d_\lambda|\mathbf{H}|d_\lambda> + \Sigma_\lambda <d_\lambda|\mathbf{H}'|\chi_\lambda><\chi_\lambda|\mathbf{H}'|d_\lambda>/(\varepsilon_d - \varepsilon_\chi) \tag{3}$$

where $\mathbf{H} = \mathbf{V} + \mathbf{T}$ and $\mathbf{H}' = \mathbf{V}' + \mathbf{T}$, **T** is the kinetic energy operator and ε_d and ε_χ are the energies of the orbitals *d* and χ. The first term in Equation (3) is referred to as the static term; it is formally similar to the electrostatic matrix element in crystal field (CF) theory. The second term, comprising the sum over χ, is called the dynamic contribution to $e_{\lambda l}$, which is the covalent term and can be approximated by Equation (2). Arguments have been presented[15,20] to show that the static term is considerably smaller than the dynamic one, especially when $\lambda = \pi$ rather than $\lambda = \sigma$. It should be noted that an equation of the form (3) was set up much earlier by Schmidtke[21] in an attempt to decompose AOM e_σ and e_π energies into CF and overlap contributions. Extensive reviews covering the achievements of the CLF as a rationale for the AOM have been published.[17,22] Calculations based on first principles following the recipes of the CLF are still lacking. Because DFT calculations tend to indicate that metal *d*-orbitals are strongly involved in bonding, in most cases considerably more strongly than metal 4*s* and 4*p* orbitals, the initial interpretation as given by Equation (2) seems more feasible, not least because of the usefulness of this equation for practical purposes. The same view was taken in ref. 7.

2.36.3 APPLICATIONS OF THE AOM

2.36.3.1 Orthoaxial Complexes

In octahedral complexes the *d*-orbitals are split by symmetry into subsets e_g (d_{z^2}, $d_{x^2-y^2}$) and t_{2g} (d_{xy}, d_{yz}, d_{zx}) that are of pure σ- and π-type, respectively. They also remain so in lower symmetry, presuming the Cartesian axes to be directed toward the ligand nuclei (orthoaxial chromophores). For such complexes the AOM matrix is diagonal in most cases providing the *d*-orbital perturbation energy directly. As illustrated in Figure 2, the *d*-level scheme is readily derived by using the definitions for the AOM parameters.[7–9] Thus, a ligand on the *x*-axis contributes $3e_\sigma/4$ to $d_{x^2-y^2}$, $e_\sigma/4$ to d_{z^2}, and e_π (or $e_{\pi s}$, $e_{\pi c}$) to d_{xy}, d_{zx}. A ligand on the *z*-axis perturbs d_{z^2} by e_σ, and both d_{zx}, d_{yz} by e_π. Contributions for each orbital are added to yield the total energy ε_{di}. Of some importance is the special situation for NH_3 and amine ligands. They are assumed to show no relevant π interaction (i.e., $e_\pi(N) = 0$), the corresponding hybrid functions being involved in stronger σ-bonds. Thus, according to the relation

$$10Dq = 3e_\sigma - 4e_\pi \tag{4}$$

e_σ(Cr–N) is simply given by $10Dq/3$ in such cases. In d^3 complexes, the LF parameter $10Dq$ (or Δ), which defines the spectrochemical series (see Chapter 2.35), is an observable quantity, namely the energy of the first spin-allowed transition $^4A_{2g} \rightarrow {}^4T_{2g}$. For $[Cr(NH_3)_6]^{3+}$, having $e_\pi = 0$, $e_\sigma = 7{,}200\,cm^{-1}$ can be obtained directly as one third of the energy of the first broad spectral band. In tetragonal trans-$[MA_4B_2]$ (D_{4h}) or $[MA_5B]$ (C_{4v}) complexes, symmetry predicts three independent variables Δ_A, Δ_t, and Δ_e for the *d*-level splitting, while, on the other hand, four AOM parameters generally appear (e_σ and e_π for each ligand). However, in the particular case of

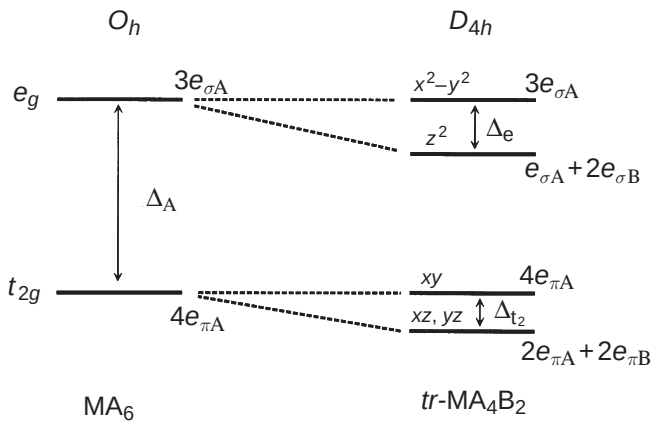

Figure 2 *d*-Orbital energies for a octahedral [MA_6] and tetragonal *trans*-[MA_4B_2] complexes given in terms of four AOM interaction parameters. The three independent parameters for the orbital splittings are included.

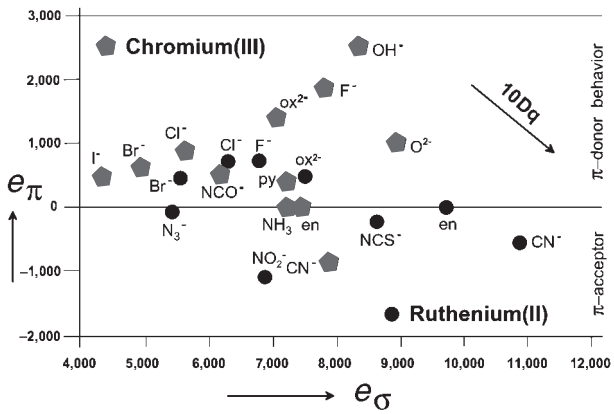

Figure 3 Two-dimensional *Spectrochemical Series* for chromium(III) and ruthenium(II) complexes.

am(m)ine complexes, all such parameters can still be deduced from experiment. Two famous examples analyzed the tetragonally split transitions $^4A_{2g} \rightarrow {}^4T_{2g}$, $^4T_{1g}{}^a$, $^4T_{1g}{}^b$ in the absorption spectra of chromium(III) complexes.[23–25] The determination of bonding parameters due to σ and π interaction leads to the so-called two-dimensional spectrochemical series for each metal ion.[26] AOM parameters for Cr(III) are depicted in Figure 3 together with the trend for the spectrochemical series[7,19] according to Equation (4). Herein we find large parameter values for F^- and OH^-, characterizing these ligands as strong σ- and π-donors, even though the overall ligand fields are rather weak due to their large antibonding M–L interactions of π-type. This result has important implications for photochemistry (see Section 2.36.3.4).

A similar sequence of e_σ and e_π parameter values for Ru^{2+} has been derived from metal-to-ligand charge transfer bands in *cis*-[$Ru(bpy)_2L_2$] compounds.[27] It was assumed that the energy of the lowest bipyridine π*-orbital does not vary across the series, which is certainly a crude approximation. However, the trends in values of e_σ and e_π are quite similar to Cr^{III}; in addition, as expected, π-donation is less important for the d^6 Ru^{II} than π-back donation.

A study of the optical spectra of symmetrically and asymmetrically substituted ethylenediamine complexes of Ni^{II} with known structures by Lever *et al.*[28] is a good example of how AOM parameters can be derived from the spectra of low symmetric (rhombic) species and, additionally, allows one to check the concept of parameter transferability. e_σ Parameters for the Ni—N bond vs. the Ni—N bond distance are depicted in Figure 4. Here, data for the Ni—NH_3 bond reported for *trans*-[$Ni(NH_3)_4(NCS)_2$] and $[Ni(NH_3)_6]^{2+}$ are also included.[28] With increasing steric

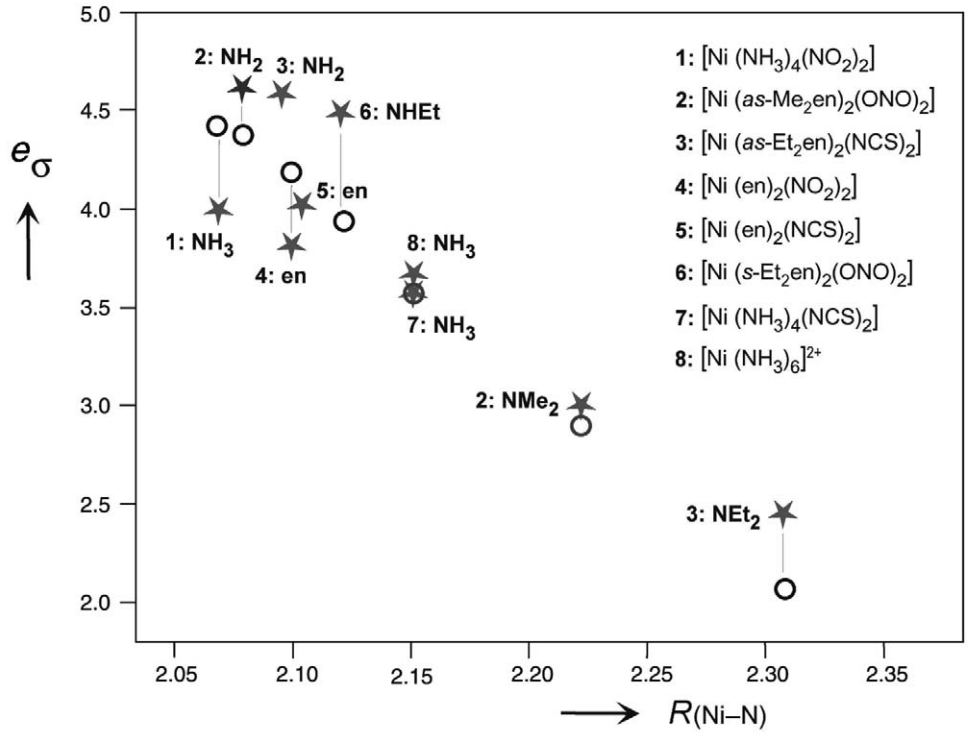

Figure 4 Metal–ligand distances and e_σ parameter values (in $10^{-3}\,cm^{-1}$) for Ni(II) amine complexes as fitted from *d–d* spectra (stars, adopted from McClure[26]) and calculated by using overlap integrals (circles).

hindrance connected with the dialkylamino group in the order NH_2, NHEt, NMe_2, NEt_2 ligands, the Ni—N bond length gets longer and this is nicely reflected in decreasing values of the parameter e_σ. In Figure 4 we also plot values of e_σ deduced by a scaling according to square of the Ni—N overlap integral (calculated using a sp^3 hybrid function for N) where we take $e_\sigma = 3583\,cm^{-1}$ and $R = 2.15$ Å (for *trans*-[Ni$(NH_3)_4(NCS)_2$]) as reference. The data show that for the Ni—N bond the values of e_σ deduced from the spectra are consistent with Equation (2), the behavior at larger distances being possibly influenced by additional longer-range crystal field (ionic) contributions. The e_σ parameters for the rhombic complexes also agree with those found for the higher symmetry species: i.e., the notion of AOM parameter transferability seems to be justified here.

2.36.3.2 Non-orthoaxial Complexes

The problem of parameter redundancy that might appear in high-symmetry complexes is weakened when the coordination geometry deviates from orthoaxiality.[8,29] Then, additional off-diagonal matrix elements appear that depend on electronic (AOM) and on geometrical parameters which are due to the angular geometry of the chromophore. Thus, insofar as the molecular structure is known, AOM parameters can be derived from the analysis of *d–d* transitions. On the other hand, the angular geometry of the chromophore can be deduced if sufficient spectroscopic data are available (*spectrum–structure correlations*). An example for the latter case is given by the spectroscopy on the $[Cr(ox)_3]^{3-}$ impurity centers in Cr^{III}-doped $NaMg[Al(ox)_3]\cdot 8H_2O$.[30] The electronic spectrum in high-resolution including ground $^4A_{2g}$ and excited ^2E_g zero-field splitting could be rationalized only if a trigonal twist angle of 14° and, in addition, a trigonal compression of the CrO_6 polyhedron ($\delta\theta = 4°$) were taken into account. Along the same lines, an interpretation of the spectra of $Mn^{5+}(d^2)$ doped into spodiosite and apatite oxidic host structures showed that the geometry of the tetrahedral sites is significantly modified by Mn^{5+} when incorporated into positions of P^{5+} with a smaller ionic radius.[31] In a series of papers, Gerloch *et al.* have shown that an accurate fit of AOM parameters is also possible by taking into account EPR and magnetic susceptibility data.[32–35] As has been argued earlier,[28] electronic transition energies deduced from

spectral data allow one to deduce at most four parameters from four orbital energy differences in ligand fields of low symmetry. It is noted, however, that the 5×5 ligand field matrix depends on a total of 14 different diagonal and off-diagonal matrix elements. All of these in low symmetry affect the orbital and many-electronic wave functions. These matrix elements will also influence the expectation values of the Zeeman and the orbital moment operators when applied on these wavefunctions, and thus the *g*- and magnetic susceptibility tensors. The latter observables can be used in turn to deduce a larger number of AOM parameters. The formalism behind this strategy has been elaborated by Gerloch *et al.*[32–35] A study on the optical spectra, the *g*- and magnetic susceptibility tensor in tetrakis(diphenylmethylarsine oxide) nitrato cobalt(II) and nickel(II) serves as a typical and well-documented example where as many as eight AOM parameters could be derived from the spectra along with equations which, however, show parameter correlations (two for Co and three for Ni).[36] Further useful information can be obtained from EPR spectra, an example for that is given in ref. 37.

2.36.3.3 Stereochemistry and Reactivity

Structural predictions on the basis of LFSEs as calculated by using the AOM have been pioneered by Burdett and others.[38–40] An instructive implication for thermochemical substitution reactions in square planar complexes was given by Lee.[41] He calculated the activation energy which accompanies the substitution of X by Y in the square pyramidal *trans*-[ML_2TX] complex. Y enters the coordination sphere at the axial position to form a square pyramid, which subsequently reorients toward a trigonal bipyramid with X, Y, and T forming the trigonal plane. A simple expression for the activation energy E_a in terms of σ-bond contributions and considering π-back donation

$$E_a \equiv \Delta_{LFSE} = e_{\sigma T} + e_{\sigma X} - e_{\sigma L} - (1/2)e_{\sigma Y} + 4(e_{\pi^* T} - e_{\pi T}) \quad (5)$$

has led to the following conclusions: trans-ligand T activities are in the reverse order of their corresponding 10Dq values, i.e., $I^- > Br^- > Cl^- > F^- > OH^- > NH_3$. Like 10Dq, $e_{\sigma T}$ values decrease with increasing trans-activity. The trans-ligand T has the effect of reducing the values of $e_{\sigma X}$, and more effective T-ligands are those which also generate smaller $e_{\sigma T}$ values. Both effects tend to decrease the activation energy E_a. The entering group Y contributes only $-(1/2)e_{\sigma Y}$ and tends also to decrease E_a as well. This is borne out by the fact that the nucleophilicity of amines with respect to four-coordinate planar d^8 metals increases with increasing amine basicity.[42] Finally, ligands T for which π-back donation is operative tend to further reduce the activation energy. In such cases $e_{\pi^* T}$ and $e_{\pi T}$ are both negative, but $|e_{\pi^* T}| > |e_{\pi T}|$ leads to a negative $4(e_{\pi^* T} - e_{\pi T})$ contribution to E_a (Equation (5)). The latter result is also supported by more sophisticated calculations,[43] which show that if π-bonding is possible in the transition state, it dictates the reaction path.

2.36.3.4 Photochemistry

The photochemical substitution in octahedrally coordinated complexes is usually governed by Adamson's rules:[44] (i) the leaving ligand is located on the axis characterized by the weakest ligand field; (ii) on the labilized axis, the leaving ligand is the one possessing the stronger ligand field. A detailed AOM treatment that gives a rationale of both rules and goes further to cover exceptions to these rules has been given by Vanquickenborne and Ceulemans.[45,46] Their model approximates the *bonding* energy of a given ligand in the ground state (I) and in the photoactive excited state (I^*) by summing up the orbital energies of occupied bonding and antibonding orbitals. Assuming that bonding orbitals (mostly ligand centered) are stabilized to the same extent as the antibonding ones (mostly $3d$) are destabilized, it follows that I and I^* are just given by the number and distribution of holes between the metal $3d$-orbitals in a given electronic state. Instructive examples are *trans*-[$Cr(L_{eq})_4(L_{ax})_2$] complexes. With a $t_{2g}^3 e_g^4$ hole-configuration in the $^4A_{2g}$ ground state of Cr(III), the *bonding* energies of L_{eq} and L_{ax} are calculated to be $I(L_{ax}) = 2e_\sigma^{ax} + 2e_\pi^{ax}$, and $I(L_{eq}) = 2e_\sigma^{eq} + 2e_\pi^{eq}$, respectively. As expected, thermochemical reactions will lead to substitution of the more weakly bound ligand. This can be easily judged based on reported AOM parameter values for Cr^{III} (see Figure 3). On the other hand, upon excitation the photoactive state has to be

considered, which usually is the lowest excited state. In tetragonal symmetry this depends on the splitting of the $^4T_{2g}$ excited state. The state sequence can be derived from the ligand field parameters involved:

$$E(^4B_{2g}) - E(^4E_g) = 2(e_\pi^{ax} - e_\pi^{eq}) - (3/2)(e_\sigma^{ax} - e_\sigma^{eq}) = (1/2)(10Dq^{eq} - 10Dq^{ax}) \quad (6)$$

If one assumes $10Dq^{ax} < 10Dq^{eq}$, ^4E_g becomes the photoactive state, otherwise $^4B_{2g}$. An inspection of the wave functions of ^4E_g and $^4B_{2g}$ shows that a $^4A_{2g} \rightarrow {}^4E_g$ excitation corresponds to a $d_{zx,yz}{}^1 \rightarrow (3/4)\ (d_{z^2}{}^1) + (1/4)\ (d_{x^2-y^2}{}^1)$ excitation, while $^4A_{2g} \rightarrow {}^4B_{2g}$ is due to a $d_{xy}{}^1 \rightarrow d_{x^2-y^2}{}^1$ excitation. Configurational mixing with higher ^4E_g states increases (decreases) the relative amount of d_{z^2} ($d_{x^2-y^2}$) in ^4E_g. Energy expressions for $I^*(L_{ax})$ and $I^*(L_{eq})$ in dependence on the e_σ and e_π parameters are listed in Table 1 for the excitations from d_{xy} or $d_{zx,yz}$ into d_{z^2} and $d_{x^2-y^2}$. With $^4B_{2g}$ as the photoactive state ($d_{xy}{}^1 \rightarrow d_{x^2-y^2}{}^1$) the weakening of the Cr—L_{eq} bond is proportional to $10Dq^{eq}$, while the Cr—L_{ax} bond is not altered.

$$I(M - L_{eq}) - I^*(M - L_{eq}) = (1/4)(3e_\sigma^{eq} - 4e_\pi^{eq}) = (5/2)Dq^{eq} \quad (7)$$

With ^4E_g as the photoactive state, the labilization of L_{eq} and L_{ax} is given by

$$I(M - L_{eq}) - I^*(M - L_{eq}) = (1/8)(3e_\sigma^{eq} - 4e_\pi^{eq}) = (5/4)Dq^{eq} \quad (8a)$$

$$I(M - L_{ax}) - I^*(M - L_{ax}) = (1/4)(3e_\sigma^{ax} - 4e_\pi^{ax}) = (5/2)Dq^{ax} \quad (8b)$$

It follows that for a given value of 10Dq the Cr—L_{ax} bond absorbs twice as much of the excitation energy as the Cr—L_{eq} bond does. This difference increases upon configurational mixing. If the quantity (I–I^*) is the crucial parameter for the photo-substitution, Equations (8a) and (8b) lead to Adamson's rules: if $10Dq^{ax} > 10Dq^{eq}$, only the equatorial ligands are labilized according to Equation (7). In the opposite case, i.e., $10Dq^{ax} < 10Dq^{eq}$, these equations show that axial ligands are labilized at least twice as much as the equatorial ligands. This is the first of Adamson's rules. However, in either case, the labilization is proportional to the 10Dq value of the ligand—this is equivalent to his second rule. Although deviations from this behavior might occur in certain cases, correct predictions for the leaving ligand have been made for a series of trivalent chromium and cobalt complexes.[45]

The leaving ligand treatment within the AOM has been extended[46] to the following steps of the photoisomerization process—the isomerization of the resulting five-coordinate species, followed by the nucleophilic attack of the entering ligand. The electronic structure control of the latter two steps was based on state correlation diagrams, but nicely translated into orbital pictures of the Woodward–Hoffman rules of conservation of orbital symmetry.

2.36.4 EXTENSIONS OF THE AOM

2.36.4.1 *s–d* Mixing

When the symmetry is sufficiently low, some of the 3*d*-orbitals may become totally symmetric and start to mix with 4*s*. This leads to a depression of the energies of those *d*-orbitals involved in such

Table 1 AOM expressions for the bonding energies of the L_{ax} and L_{eq} ligands in *trans*-[$Cr(L_{eq})_4(L_{ax})_2$] complexes of Cr^{III} in the ground state (I) and in the $e_g \rightarrow t_{2g}$ singly excited configuration (I^*). Ligand labilization energy expressions (I–I*) are listed in parentheses.

Ligand ground state			$\rightarrow d_{z^2}$	$\rightarrow d_{x^2-y^2}$
L_{ax}	$2e_\sigma^{ax} + 2e_\pi^{ax}$	$d_{xy} \longrightarrow$	$e_\sigma^{ax} + 2e_\pi^{ax}(e_\sigma^{ax})$	$2e_\sigma^{ax} + 2e_\pi^{ax}(0)$
		$d_{zx,yz} \longrightarrow$	$e_\sigma^{ax} + 3e_\pi^{ax}(e_\sigma^{ax} - e_\pi^{ax})$	$2e_\sigma^{ax} + 3e_\pi^{ax}(-e_\pi^{ax})$
L_{eq}	$2e_\sigma^{eq} + 2e_\pi^{eq}$	$d_{xy} \longrightarrow$	$7/4e_\sigma^{eq} + 3e_\pi^{eq}(1/4e_\sigma^{eq} - e_\pi^{eq})$	$5/4e_\sigma^{eq} + 3e_\pi^{eq}(3/4e_\sigma^{eq} - e_\pi^{eq})$
		$d_{zx,yz} \longrightarrow$	$7/4e_\sigma^{eq} + (5/2)e_\pi^{eq}(1/4e_\sigma^{eq} - (1/2)e_\pi^{eq})$	$5/4e_\sigma^{eq} + (5/2)e_\pi^{eq}(3/4e_\sigma^{eq} - (1/2)e_\pi^{eq})$

a mixing. A way of accounting for this effect is the extension of the *nd* basis to include the $(n+1)s$-orbital. Then the AOM matrix element of Equation (1) must be supplemented with[47,48]

$$\mathcal{V}_{ij}^{sd} = -\left(\Sigma_{(l)} F_{\sigma i}(\Theta_l, \Phi_l)[e_{sd\sigma}(l)]^{1/2}\right)\cdot\left(\Sigma_{(l)} F_{\sigma j}(\Theta_l, \Phi_l)[e_{sd\sigma}(l)]^{1/2}\right) \quad (9)$$

where $e_{sd\sigma}(l)$ represents the parameter for *s–d* mixing. It can be approximated by perturbation theory as

$$e_{sd\sigma}(l) \cong <(n+1)s|\mathbf{V}_l|nd_{z^2}>^2 / |\varepsilon_{nd z^2} - \varepsilon_{(n+1)s}| \quad (10)$$

The effect of *s–d* mixing is very pronounced in square planar MA_4 and in linear MA_2 systems and has been extensively studied for Cu^{II} and Pt^{II} complexes.[49,50] For example, in the case of quadratic $[CuCl_4]^{2-}$, having a single hole in the *d* subshell, AOM expressions for the transition energies are readily obtained (see Table 2). Calculated values of e_σ, e_π, and e_{sd} (5,350 cm^{-1}, 1,200 cm^{-1}, and 1,400 cm^{-1}) are very close to those deduced from the spectrum of pseudo-tetrahedral $[CuCl_4]^{2-}$ and imply a nice parameter transferability between the two geometries.[51,52] The large effect of *s–d* mixing is reflected here by the relatively high energy of the $^2A_{1g}$ excited state.

Electronic spectra of linear $CuCl_2$[53] and $NiCl_2$,[53,54] supported by later first principles calculations,[55,56] show that the energy of the d_{z^2} orbital ($= e_\sigma - 4e_{sd}$) is very low, even lower than that of the d_{zx},d_{yz} orbitals ($2e_\pi$). This is again a manifestation of considerable *s–d* mixing. The resulting d_{xy},$_{x^2-y^2} \leq d_{z^2} < d_{zx}$,$d_{yz}$ orbital sequence is consistent with a $^2\Pi$ and with a $^3\Sigma$ ground state for CuX_2 (X = F, Cl) and $NiCl_2$, respectively. Further examples of *s–d* mixing have been reported with the unique paramagnetic NiO_4 chromophore in Li_2NiO_2[57] and the NiO_2N_2 chromophore in $Ni[t\text{-}Bu_2P(O{=}NR)]_2$.[58] In the latter case, alternative interpretations of the observed high-spin ground state, which is very unusual for planar Ni(II) complexes, have been extensively discussed.[59–61] Optical spectra of the linear chromophores NiO_2^{2-} in $K_2[NiO_2]$[62] and NiO_2^{3-} in $K_3[NiO_2]$ and $KNa_2[NiO_2]$[63] are other key examples illustrating the role of *s–d* mixing. In the latter compounds a $d_{z^2} > d_{zx}$,$d_{dyz} > d_{x^2-y^2}$ order of *d*-orbital energies and $^3\Pi_g$ [$Ni^{II}(d^8)$] and $^2\Sigma_g$ [$Ni^{I}(d^9)$] ground states have been proposed based on optical and EPR spectra for $Ni^{I}(d^9)$.[62,63] For a review on this topic see ref. 64.

2.36.4.2 Orbital Phase Coupling (Orgel Effect)

Frontier orbitals in chelate ligands are frequently part of an extended π-electron network. In such cases perturbations from bonding and antibonding *delocalized* ligand π-MOs, rather than separate and independent ligand π-functions, govern the respective LF potential. This effect was predicted by Orgel early on[65] and was first incorporated into the AOM by Ceulemans *et al.*[66] Following Atanasov *et al.*[67] we consider a bidentate ligand L–L with in-phase (ψ) and out-of-phase (χ) combinations of the π(L) orbitals (see Figure 5). In order to get appropriate metal-*d* functions of the same symmetry (b_1 or a_2 in C_{2v}), linear combinations according to Table 3 have to be taken, which result in different parameters $e_{\pi s}$ and $e_{\pi s}'$ for the respective three-center interactions (*non-additive model*).

Within the new basis ($d\psi$, $d\chi$) the AOM matrix $\mathcal{V}_{\pi s}'$ is diagonal, but the formalism requires a representation in the initial basis. This can be easily obtained by a simple transformation, i.e., $\mathcal{V}_{\pi s} = \mathcal{T}^{-1}\ \mathcal{V}_{\pi s}'\ T$ (cf. Equation (7) in ref. 67). If we set $e_{\pi s} = e_{\pi s}'$, the degeneracy of the *d*-orbitals restores the conventional (*additive*) model assuming holohedrized D_{4h} symmetry.

Table 2 LF states and transition energies of square-planar $[CuCl_4]^{2-}$.

State energy	*Transition energy*	*Exp.* (cm^{-1})[51]
$E(^2B_{1g}) = -3e_\sigma$	0	
$E(^2A_{1g}) = -e_\sigma + 4e_{sd}$	$2e_\sigma + 4e_{sd}$	16,300
$E(^2E_g) = -2e_\pi$	$3e_\sigma - 2e_\pi$	13,650
$E(^2B_{2g}) = -4e_\pi$	$3e_\sigma - 4e_\pi$	11,250

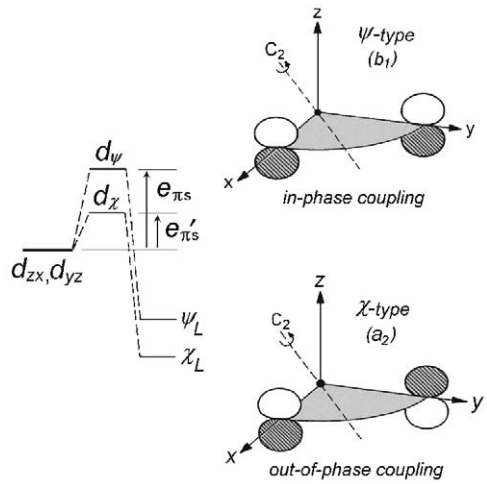

Figure 5 Parametrization for M(L–L) chelates with an extended π-electron system (notation according to local C_{2v} symmetry) (adapted from Schönherr,[8] Figure 7).

Table 3 Symmetry adapted wave functions and interaction parameters in a M(L–L) system for phase-coupled frontier orbitals of π-type.

Symmetry	*Metal*	*Ligand*	*M–L interaction*
b_1	$d\psi = (1/2)\ (d_{zx} + d_{yz})$	ψ	$e_{\pi s}$
a_2	$d\chi = (1/2)\ (d_{zx} - d_{yz})$	χ	$e_{\pi s}'$

For orthoaxial tris-chelate complexes the trigonal AOM matrix in the basis d_{xy}, d_{yz}, d_{zx} is readily derived by cyclic permutation of x, y, and z leading to

$$\mathcal{V}_{\pi}^{trig} = \begin{bmatrix} (e_{\pi s} + e_{\pi s}') & \frac{1}{2}(e_{\pi s} - e_{\pi s}') & \frac{1}{2}(e_{\pi s} - e_{\pi s}') \\ \frac{1}{2}(e_{\pi s} - e_{\pi s}') & (e_{\pi s} + e_{\pi s}') & -\frac{1}{2}(e_{\pi s} - e_{\pi s}') \\ \frac{1}{2}(e_{\pi s} - e_{\pi s}') & -\frac{1}{2}(e_{\pi s} - e_{\pi s}') & (e_{\pi s} + e_{\pi s}') \end{bmatrix} \tag{11}$$

An inspection of Equation (11) shows that the phase-coupling effect leads to a splitting of the t_{2g} orbital subset with Δ_{t2} $(= \varepsilon_{eg} - \varepsilon_{a1g}) = (3/2)(e_{\pi s} - e_{\pi s}')$. Using the concept of phase-coupling, the polarized electronic spectrum of $[Cr(acac)_3]$ (acac: acetylacetonate) could be rationalized, which shows a distinct splitting of 800 cm^{-1} of the $^4A_{2g} \rightarrow {}^4T_{2g}$ transition with an energy order $^4A_1 < {}^4E$.[67,68] It should be noted that the geometry of the CrO_6 chromophore is very close to an octahedron in this complex, and the small deviations toward a trigonal elongation would lead to much smaller splitting with opposite level ordering. However, since the acac ligand has a HOMO and a LUMO of ψ- and χ-type, respectively, Δ_{t2} is positive, resulting in the correct level scheme. Taking the value of Δ_{t2} as deduced from the spin-allowed transitions, the magnitude and the sign of the excited state ^2E_g splitting of 220–290 cm^{-1}, as reported from the spectra of the Cr^{3+}-doped Ga and Al host lattices, could also be reproduced.[68] Recent *ab initio* calculations lend full support to this first manifestation of the Orgel effect.[69] The system $[Cr(bpy)_3]^{3+}$ presents an example in which the ordering of HOMO (χ) and LUMO (ψ) frontier orbitals are just opposite to acac.[70] Further examples, e.g., $[Co(C_{10}H_{20}N_8)]^{2+}$, [Co(salen)], and [Co(amben)], which display the effect of different types of phase-coupling on the order of energies of π-orbitals, and therefore anisotropy of the g-tensor, can be found in Ceulemans *et al.*[71] A detailed overview on the treatment of conjugated bidentate ligands within the parametrization of the AOM has been given by Schäffer and Yamatera.[72]

2.36.4.3 Misdirected Ligand Lone Pairs

Metal–ligand bonding is usually such that it allows a decomposition of the M–L interaction into components of σ-and π-type. This implies a pseudo-symmetry of the electron density around a given M—L bond that is not lower than C_{2v} (cf. Figure 1). A lowering of this symmetry to C_s or C_1 may be due to rigidity of a chelate ligand or to nonbonding lone pairs on a ligator atom. The misalignment of ligand orbitals in such cases (*misdirected valency*) precludes a full separation of σ and π metal–ligand bonding. Following an idea of Liehr,[73] the concept of misdirected valency was introduced into the AOM by Gerloch *et al.*[74–77] who used this model to explain the band splitting in planar Co^{II} and trigonal–bipyramidal Ni(II) complexes. In Figure 6 we illustrate this using a ligand orbital that is misplaced by the angle δ with respect to the M–L axis (σ) in the chelate plane, and further by the angle ω out of this plane. With such low M–L symmetry (C_1), the angle δ causes an off-diagonal AOM matrix element $e_{\sigma\pi c}$ between d_{z^2} and d_{zx}, while the angle ω introduces $e_{\sigma\pi s}$ between d_{z^2} and d_{yz}. Thus the initial local AOM matrix, separating contributions of σ- and π-type, does not remain diagonal. A case study for a symmetric tris-chelate complex is given elsewhere.[68] An illustrative example is provided by Ni—NCS bonding, which has been thoroughly discussed by Gerloch *et al.*[75,76] Surprisingly, the NCS ligand has been suggested to be a π-donor in *trans*-$[Ni(NH_3)_4(NCS)_2]$ ($e_\pi > 0$),[78] but a π-acceptor in *trans*-$[Ni(en)_2(NCS)_2]$ ($e_\pi < 0$).[28] However, accounting for the large deviations from the linear Ni–N–CS arrangement in the [en] complex, the effect of bent bonding due to the lone pair on N should result in a non-zero value for the $e_{\sigma\pi}$(NCS) parameter if sp_z-hybrids of the free linear N–CS ligand, rather than a sp^2-rehybridization, are assumed. It was shown in Duer *et al.*[77] that accounting for the misaligned bonds in the [en] complex by using one additional $e_{\sigma\pi}$(NCS) parameter, a positive value for e_π is derived from the spectral fit. Thus the π-donor effect of NCS^- in the [en] complex is restored. Another impressive manifestation of misaligned valence orbitals was reported by Dubicki *et al.* who investigated H_2O bonding by analyzing the zero field splitting of $[Cr(H_2O)_6]^{3+}$ in the $CsCr(SeO_4)_2 \cdot 12H_2O$ crystal.[37,79] Misdirected M—L bonds can also be expected, for example, in TM-doped lattices.[8,80] Due to highly charged cations in the second coordination sphere of oxidic structures, this effect was manifested in spectra and bonding parameters of coordination polyhedra of Ni^{II} and Cu^{II}.[80] This is the main topic of Chapter 1.36.

2.36.4.4 Higher Coordination Spheres

Ligands (or atoms) extending beyond the first coordination sphere of TM act as electrostatic perturbers, covalent forces being negligibly small at such large distances. In an AOM description, crystal field contributions to the parameters e_σ and e_π are assumed to decrease according to an $a\,(1/R^3) + b\,(1/R^5)$ law.[14] Interesting examples are the fine structures observed in the intraconfigurational transitions of $K_3[Cr(CN)_6]$,[14] of Cr^{III} in the spectrum of ruby,[81] and of the Mn^{VI} ion doped in Cs_2SO_4.[82] All these systems exhibit an electrostatic influence from the asymmetric cationic surroundings of the chromophores due to the outer ions K^+, Al^{3+}, or Cs^+, respectively. Recently, the contribution of the second coordination sphere in Cr^V-doped YVO_4 and YPO_4 solids has been manifested both spectroscopically and by DFT.[83]

2.36.4.5 Vibronic Coupling

Vibronic coupling in TM complexes, such as the Jahn–Teller effect in electronically degenerate states in octahedral or tetrahedral symmetries, leads to geometrical distortions resulting in lower

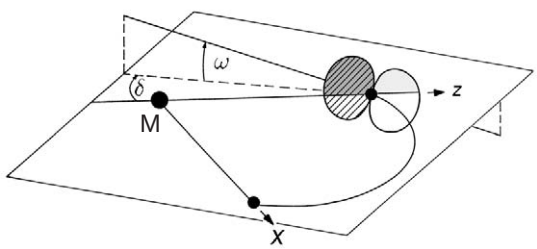

Figure 6 Misdirected valency: Displacement of ligand frontier orbital from M—L bonding axis (adapted from Schönherr,[8] Figure 8).

symmetric polyhedra. Bacci has proposed an interesting application of the AOM to evaluate vibronic coupling constants.[84,85] Later on, the first and second order vibronic coupling constants were used to formulate the *epikernel principle* of Jahn–Teller coupling.[86] The use of vibronic coupling constants within the AOM formalism in order to explain geometrical structures and electronic spectra in Jahn–Teller distorted tetrahedra of Ni(II) and Cu(II) is reviewed elsewhere.[87]

2.36.4.6 Polynuclear TM Systems

An extension of the AOM to polynuclear TM complexes without direct M—M bonds has been given.[88,89] Atanasov and Schmidtke have described a generalization to systems involving TM—TM bonds.[90] An application to the parametrization of exchange coupling constants within the Anderson model of superexchange led to a quantification of the Goodenough–Kanamori rules.[91] AOM parameters deduced from the spectra involve not only covalent (overlap) but also ionic (crystal field) terms. Complexes of TM in their oxidation states +2 and +3 with ligands such as F^- and O^{2-} can be considered to a high degree as ionic, in contrast to ligands such as CN^-. Thus the large values of the AOM parameters for the former ligands may reflect crystal field contributions to the ligand field in addition to the covalent (overlap) energy. While multiplet energies in TM complexes are affected both by ionicity and metal–ligand overlap, magnetic exchange coupling between magnetic TM ions mediated via bridging ligands mirrors solely TM–L covalency. The use of phenomena such as exchange coupling and hyperfine transferred magnetic fields to deduce the covalent terms of the ligand field metal–ligand interactions utilizing an AOM parametrization of extended structures has been illustrated for $KAlCuF_6$.[92] A recent critical review of this topic can be found in Schäffer.[93]

2.36.5 ADVANTAGES AND DRAWBACKS OF THE AOM

2.36.5.1 Advantages

(A1) *Meaningful parametrization:* A chemically meaningful interpretation of bonding parameters deduced from spectroscopy permits one to explore chemical trends. As an example, the two-dimensional spectrochemical series serves as a means to classify ligands according to their σ and π bonding behavior.
(A2) *Low symmetry:* The local structure of the covalent part of the LF potential allows for an additive scheme of contributions from various ligands. Therefore, the AOM is designed to treat isolated complexes of low symmetry as well as dissolved complexes, doped materials, etc. This contrasts with the global character of the CF parametrization.
(A3) *Accuracy:* In particular cases multiplet *splitting* can be rationalized in high precision, e.g., energy separations of some ten wave numbers or much less (zero field splittings in EPR) have been correctly reproduced. Thereby, even slight angular distortions of the chromophore from higher symmetric arrangements can be derived (*spectrum–structure correlations*). This is far beyond the ability of any other quantum chemical method up to date.
(A4) *Flexibility:* Peculiarities in the electronic structures of the TM or the ligands require specific extensions of the relatively simple framework of the conventional AOM which can be easily derived within the underlying MO approach. Moreover, the potential to treat multiplet splitting of mononuclear TM complexes as well as exchange coupling in bridged TM complexes (which cannot be treated in CF theory) opens new perspectives for applications of the AOM.

2.36.5.2 Drawbacks

(D1) *Limited basis:* The power of the AOM is to calculate energy splitting of d^n-states, while, on the other hand, absolute energies cannot be derived. Because the set of explicitly used wave functions is limited to the five *d*-orbitals, there is no reliable access to charge transfer states, which generally affect the energy of d^n-states.[94] The latter also influence greatly the spectral intensities of *d–d* transitions, which, therefore, cannot be reasonably predicted within the framework of the LFT, although some effort has been undertaken for special[95] and more general cases.[96]

(D2) *Over-parametrization:* The more ligator atoms are involved in mixed-ligand complexes the larger is the number of AOM parameters to be determined with the inherent uncertainty in their determination from experiment. This may lead to an over-parametrized scheme, in particular when experimental data are scarce.

2.36.6 REFERENCES

1. Jørgensen, C. K.; Pappalardo, R.; Schmidtke, H.-H. *J. Chem. Phys.* **1963**, *39*, 1422–1430.
2. Jørgensen, C. K.; Schmidtke, H.-H. *Z. Phys. Chem.* **1963**, *38*, 118–120.
3. Perkins, W. G.; Crosby, G. A. *J. Chem. Phys.* **1965**, *42*, 407–414.
4. Schmidtke, H.-H. *Z. Naturforsch.* **1964**, *19a*, 1502–1510.
5. Schäffer, C. E.; Jørgensen, C. K. *Mol. Phys.* **1965**, *9*, 401–412.
6. Schäffer, C. E.; Jørgensen, C. K. *Math.-fys. Medd. Selsk* **1965**, *34(13)*, 1–20.
7. Figgis, B. N. Theory and Background, Ligand Field Theory. The Angular Overlap model. In *Comprehensive Coordination Chemistry*; Wilkinson, G. Ed.; Volume 1, Pergamon Press, Oxford, 1987; pp 225–231.
8. Schönherr, T. *Top. Curr. Chem.* **1997**, *191*, 87–152.
9. Schäffer, C. E. *Struct. Bond.* **1968**, *5*, 68–95.
10. Schäffer, C. E. *Pure Appl. Chem.* **1970**, *24*, 361–392.
11. Bertini, I.; Gatteschi, D.; Scozzofava, A. *Inorg. Chem.* **1975**, *14*, 812–815.
12. Hitchman, M. A.; Waite, T. D. *Inorg. Chem.* **1976**, *15*, 2150–2154.
13. Waite, T. D.; Hitchman, M. A. *Inorg. Chem.* **1976**, *15*, 2155–2158.
14. Hoggard, P. E.; Lee, K.-W. *Inorg. Chem.* **1988**, *27*, 2335–2339.
15. Gerloch, M.; Harding, J. H.; Woolley, R. G. *Struct. Bond.* **1981**, *46*, 1–46.
16. Smith, D. W. *Inorg. Chem.* **1978**, *17*, 3153–3156.
17. Gerloch, M.; Woolley, R. G. *Prog. Inorg. Chem.* **1984**, *31*, 371–446.
18. Gerloch, M. In *Understanding Molecular Properties*; Avery, J. S.; Dahl, J. P.; Hansen, A. E., Eds.; Reidel, Dordrecht, 1987, pp 111–142.
19. Gerloch, M.; Constable, E. C. *Transition Metal Chemistry*; VCH, New York, 1994, p 128.
20. Woolley, R. G. *Mol. Phys.* **1981**, *42*, 703–720.
21. Schmidtke, H.-H. *Theor. Chim. Acta* **1971**, *20*, 92–104.
22. Bridgeman, A. J.; Gerloch, M. *Prog. Inorg. Chem.* **1997**, *45*, 179–281.
23. Barton, T. J.; Slade, R. C. *J. Chem. Soc. Dalton Trans.* **1975**, 650–657.
24. Glerup, J.; Mønsted, O.; Schäffer, C. E. *Inorg. Chem.* **1976**, *15*, 1399–1407.
25. Glerup, J.; Mønsted, O.; Schäffer, C. E. *Inorg. Chem.* **1980**, *19*, 2855–2857.
26. McClure, D. S. In *Advances in the Chemistry of Coordination Compounds*, Kirschner, S., Ed.; MacMillan, New York, 1961; p 498.
27. Hoggard, P. E.; Clanet, P. P. *Polyhedron* **1987**, *6*, 1621–1623.
28. Lever, A. B. P.; Walker, I. M.; McCarthy, P. J.; Mertes, K. B.; Jircitano, A.; Sheldon, R. *Inorg. Chem.* **1983**, *22*, 2252–2258.
29. Hoggard, P. E. *Coord. Chem. Rev.* **1986**, *70*, 85–120.
30. Schönherr, T.; Spanier, J.; Schmidtke, H.-H. *J. Phys. Chem.* **1989**, *93*, 5969–5972.
31. Atanasov, M.; Reinen, D.; Adamsky, H. *Chem. Phys.* **1996**, *202*, 155–165.
32. Gerloch, M.; McMeeking, R. F. *J. Chem. Soc. Dalton Trans.* **1975**, 2443–2451.
33. Gerloch, M.; Hanton, L. R. *Inorg. Chem.* **1980**, *19*, 1692–1698.
34. Gerloch, M; Manning, M. *Inorg. Chem.* **1981**, *20*, 1051–1056.
35. Gerloch, M. *Magnetism and Ligand-field Analysis*; Cambridge University Press, Cambridge, UK; 1983.
36. Fenton, N. D.; Gerloch, M. *Inorg. Chem.* **1987**, *26*, 3273–3277.
37. Dubicki, L.; Bramley, R. *Chem. Phys. Lett.* **1997**, *272*, 55–60.
38. Burdett, J. K. *Inorg. Chem.* **1976**, *15*, 212–219.
39. Burdett, J. K. *Molecular Shapes: Theoretical Models in Inorganic Stereochemistry*, Wiley, New York, 1980.
40. Purcell, K. F.; Kotz, J. C. *Inorganic Chemistry*; Saunders: Philadelphia, 1977, Chapter 9.
41. Lee, L. *J. Chem. Educ.* **1994**, *71*, 644–645.
42. Cattalini, L.; Orio, A.; Doni, A. *Inorg. Chem.* **1966**, *5*, 1517–1519.
43. Armstrong, D. R.; Fortune, P.; Perkins, P. G. *Inorg. Chim. Acta* **1974**, *9*, 9.
44. Adamson, A. W. *J. Phys. Chem.* **1967**, *71*, 798–808.
45. Vanquickenborne, L. G.; Ceulemans, A. *J. Am. Chem. Soc.* **1977**, *99*, 2208–2214.
46. Vanquickenborne, L. G.; Ceulemans, A. *Coord. Chem. Rev.* **1983**, *48*, 157–202 and cited references.
47. Smith, D. W. *Inorg. Chim. Acta* **1977**, *22*, 107–110.
48. Vanquickenborne, L. G.; Beyens, D.; Ceulemans, A. *Inorg. Chim. Acta* **1982**, *61*, 199–206.
49. Deeth, R. J. *J. Chem. Soc. Dalton Trans.* **1993**, 1061–1064.
50. Vanquickenborne, L. G.; Ceulemans, A. *Inorg. Chem.* **1981**, *20*, 796–800.
51. Ferguson, J. *J. Chem. Phys.* **1964**, *40*, 3406–3410.
52. Harlow, R. L.; Wells, W. J. III; Watt, G. W.; Simonsen, S. H. *Inorg. Chem.* **1974**, *13*, 2106–2111.
53. DeKock, C. W.; Gruen, D. M. *J. Chem. Phys.* **1966**, *44*, 4387–4398.
54. DeKock, C. W.; Gruen, D. M. *J. Chem. Phys.* **1967**, *46*, 1096–1105.
55. Bridgeman, A. J. *J. Chem. Soc. Dalton Trans.* **1996**, 2601–2607.
56. Wang, S. G.; Schwarz, W. H. E. *J. Chem. Phys.* **1998**, *109*, 7252–7262.
57. Reinen, D; Atanasov, M; Nikolov, G.; Steffens, F. *Inorg. Chem.* **1988**, *27*, 1678–1686.
58. Frömmel, T.; Peters, W.; Wunderlich, H.; Kuchen, W. *Angew. Chem. Int. Ed. Engl.* **1993**, *32*, 907–908.
59. Mink, H. J.; Schmidtke, H.-H. *Chem. Phys. Lett.* **1994**, *231*, 235–240.

60. Mink, H.-J.; Schmidtke, H.-H. *Chem. Phys. Lett.* **1995**, *247*, 310–312.
61. Bridgeman, A. J.; Gerloch, M. *Chem. Phys. Lett.* **1995**, *247*, 304–309.
62. Hitchman, M. A.; Stratemeier, H.; Hoppe, R. *Inorg. Chem.* **1988**, *27*, 2506–2510.
63. Möller, A.; Hitchman, M.; Krausz, E.; Hoppe, R. *Inorg. Chem.* **1995**, *34*, 2684–2691.
64. Schäffer, C. E. *Inorg. Chim. Acta* **1995**, *240*, 581–592.
65. Orgel, L. E. *J. Chem. Soc.* **1961**, 3683–3686.
66. Ceulemans, A.; Dendooven, M.; Vanquickenborne, L. G. *Inorg. Chem.* **1985**, *24*, 1153–1158; ibid. 1159–1165.
67. Atanasov, M.; Schönherr, T.; Schmidtke, H.-H. *Theor. Chim. Acta* **1987**, *71*, 59–73.
68. Atanasov, M.; Schönherr, T. *Inorg. Chem.* **1990**, *29*, 4545–4550.
69. Ribbing, C.; Pierloot, K.; Ceulemans, A. *Inorg. Chem.* **1998**, *37*, 5227–5232.
70. Schönherr, T.; Atanasov, M.; Hauser, A. *Inorg. Chem.* **1996**, 35, 2077–2084.
71. Ceulemans, A.; Debuyst, R.; Dejehet, F.; King, G. S. D.; Vanhecke, M.; Vanquickenborne, L. G. *J. Phys. Chem.* **1990**, *94*, 105–113.
72. Schäffer, C. E.; Yamatera, H. *Inorg. Chem.* **1991**, *30*, 2840–2853.
73. Liehr, A. D. *J. Phys. Chem.* **1964**, *68*, 665–772.
74. Deeth, R. J.; Duer, M. J.; Gerloch, M. *Inorg. Chem.* **1987**, *26*, 2573–2578.
75. Deeth, R. J.; Duer, M. J.; Gerloch, M. *Inorg. Chem.* **1987**, *26*, 2578–2582.
76. Deeth, R. J.; Gerloch, M. *Inorg. Chem.* **1987**, *26*, 2582–2585.
77. Duer, M. J.; Fenton, N. D.; Gerloch, M. *Int. Rev. Phys. Chem.* **1990**, *9*, 227–280.
78. Bertini, I.; Gatteschi, D.; Scozzofava, A. *Inorg. Chem.* **1976**, *15*, 203–207.
79. Riesen, H.; Dubicki, L. *Inorg. Chem.* **2000**, *39*, 2206–2211.
80. Reinen, D.; Atanasov, M.; Lee, S.-L. *Coord. Chem. Rev.* **1998**, *175*, 91.
81. Lee, K.-W.; Hoggard, P. E. *Inorg. Chem.* **1990**, 29 850–854.
82. Brunold, T. C.; Güdel, H. U.; Riley, M. J. *J. Chem. Phys.* **1996**, *105*, 7931–7941.
83. Hazenkamp, M. F.; Stückl, A. C.; Cavalli, E.; Güdel, H. U. *Inorg. Chem.* **2000**, *39*, 251–254.
84. Bacci, M. *Chem. Phys. Lett.* **1978**, *58*, 537–540.
85. Bacci, M. *Chem. Phys.* **1979**, *40*, 237–244.
86. Ceulemans, A.; Vanquickenborne, L. G. *Struct. Bond.* **1989**, *71*, 125–159.
87. Reinen, D.; Atanasov, M. *Magn. Res. Rev.* **1991**, *15*, 167–239.
88. Glerup, J. *Acta Chem. Scand.* **1972**, *26*, 3775–3787.
89. Bencini, A.; Gatteschi, D. *Inorg. Chim. Acta* **1978**, *31*, 11–18.
90. Atanasov, M.; Schmidtke, H.-H. *Chem. Phys.* **1988**, *124*, 205–222.
91. Atanasov, M.; Angelov, S. *Chem. Phys.* **1991**, *150*, 383–393.
92. Atanasov, M; Hitchman, M. A.; Hoppe, R.; Murray, K. S.; Moubaraki, B.; Reinen, D.; Stratemeier, H. *Inorg. Chem.* **1993**, *32*, 3397–3401.
93. Schäffer, C. E. *Inorg. Chim. Acta* **2000**, *300-302*, 1035–1076.
94. Atanasov, M. *Chem. Phys.* **1995**, *195*, 49–58.
95. Acevedo, R.; Flint, C. D. *Theor. Chim. Acta* **1986**, *69*, 225–233.
96. Bridgeman, A. J.; Gerloch, M. *Coord. Chem. Rev.* **1997**, *165*, 315–446.

Comprehensive Coordination Chemistry II
ISBN (set): 0-08-0437486

Volume 2, (ISBN 0-08-0443249); pp 443–455

2.37
Molecular Mechanics

R. J. DEETH
University of Warwick, Coventry, UK

2.37.1 MOLECULAR MECHANICS 457
2.37.2 THE MM STRAIN ENERGY 457
2.37.3 FORCE FIELD PARAMETERS 458
2.37.4 MOLECULAR MECHANICS FOR COORDINATION COMPLEXES 459
2.37.5 STRUCTURE 460
2.37.5.1 Macrocycle Hole Size 461
2.37.5.2 Metal Hydrides and Alkyls 462
2.37.5.3 Transition States 462
2.37.6 SPECTROSCOPY 462
2.37.7 ELECTRON TRANSFER 462
2.37.8 BIOINORGANIC 464
2.37.9 FUTURE TRENDS 464
2.37.10 REFERENCES 465

2.37.1 MOLECULAR MECHANICS

At the start of the 1980s, the theoretical methods for computing molecular structures of coordination compounds were severely limited. *Ab initio* methods based on the Hartree-Fock approximation and its extensions were too expensive and/or inaccurate,[1] molecular density functional theory (DFT) was still in its infancy[2] and extended Hückel theory (EHT), although very successful at generating the molecular orbital structure, ignored the interactions necessary for computing sensible bond lengths. In contrast, a new method had become popular for "organic" molecules, which was both extremely computationally efficient and also capable of reliable accuracy. The method ignored quantum effects and was instead based on the much simpler classical equations for bond stretching, angle bending, etc. This molecular mechanics (MM) method was fast enough to enable all the internal degrees of freedom to be optimized simultaneously.[3] After some earlier forays into Co^{III} chemistry, by the mid-1980s, inorganic chemists took up the challenge and set about implementing MM for transition metal (TM) species.

2.37.2 THE MM STRAIN ENERGY

The essence of MM is the strain energy U_{total} that, in its simplest form, consists of four energy terms:

$$U_{\text{total}} = \sum E_r + \sum E_\theta + \sum E_\phi + \sum E_{\text{nb}} \quad (1)$$

where $\sum E_r$ is the total bond deformation energy, $\sum E_\theta$ is the total angle deformation energy, $\sum E_\phi$ is the total torsion deformation energy, $\sum E_{\text{nb}}$ is the total nonbonded (van der Waals and electrostatic) interaction energy, and the summations run over all in relevant internal coordinates.

The individual energy terms are described using simple expressions. For example, the bond stretch term E_r for the bond between atoms i and j of length r_{ij} can be treated via a simple Hooke's law expression:

$$E_r = \tfrac{1}{2}k_r(r_{ij} - r_0)^2 \tag{2}$$

where k_r is a force constant and r_0 is the "ideal" distance between the relevant atomic centers. Similarly, the angle bending potential energy can be described by a harmonic function:

$$E_\theta = \tfrac{1}{2}k_\theta(\theta_{ijk} - \theta_0)^2 \tag{3}$$

where k_θ is the force constant for the angle θ_{ijk} made by atoms i, j, and k and θ_0 is its "ideal" value. The periodicity of torsion angles requires a more complex equation:

$$E_\phi = \tfrac{1}{2}k_\phi[1 + \cos\{m(\phi_{ijkl} + \phi_{\text{offset}})\}] \tag{4}$$

where k_ϕ is the height of the rotation barrier about the torsion angle ϕ_{ijkl}, m is the periodicity, and ϕ_{offset} is the offset of the minimum energy from a staggered conformation. Nonbonded van der Waals interactions can be computed from, for example, a Lennard-Jones 6–12 potential:

$$E_{\text{nb}}(\text{vdW}) = \frac{A}{d_{ij}^{12}} - \frac{B}{d_{ij}^{6}} \tag{5}$$

where d_{ij} is the distance between atoms i and j, and A and B are derived from atom-based parameters. Nonbonded electrostatic interactions, $E_{\text{nb}}(\text{elec})$, can be calculated via Coulomb's law:

$$E_{\text{nb}}(\text{elec}) = \frac{q_i q_j}{\varepsilon\, d_{ij}} \tag{6}$$

where q_i and q_j are the partial charges on atoms i and j and ε is the dielectric constant.

In addition to these basic energy terms, a number of additional/alternative terms can be considered: for example, a Morse function for bond length distortions, nonbonding terms for L–M–L angle bending,[4] out-of-plane deformation terms to enforce planarity in aromatic or sp^2-hybridized systems, explicit terms for hydrogen bonding, cross terms linking bond lengths to angle bends, electronic terms to represent the ligand field stabilization energy,[5] and so on. The collection of energy terms and their associated parameters is often referred to as the force field (FF).

2.37.3 FORCE FIELD PARAMETERS

The advantage of a FF approach is the high computational efficiency, which allows large systems and/or many smaller systems (e.g., conformational searches, virtual high-throughput screening) to be treated in a reasonable time. The main disadvantage of the FF is that the results are only as good as the parameters. In particular, FF parameters developed for one class of compound may not be transferable to another. Likewise, parameters developed with respect to a particular strain energy expression will not in general be applicable to any other.

These issues are discussed by Comba and Hambley[6] who also provide a detailed account of how to derive FF parameters as do Norrby and Brandt.[7] Computer programs which have been applied to modeling various coordination compounds include versions of MM2 and MM3,[8] SHAPES,[9] and modified versions of MacroModel,[10] CHARMM,[11] AMBER,[12] MOMEC,[6] and DOMMINO.[13] Most FFs in coordination chemistry employ MM2[14–16] or AMBER,[12] or something based on these, to treat the "organic" parts of the molecule which may be modified to account for the effects of binding to a metal cation.[17] All the above schemes rely on an extensive table of FF parameters spanning all the various combinations of bond, angles torsions, etc.

The alternative approach is the "generic" FF in which some or all the parameters are derived from atom-based properties. The DREIDING FF[18] and the universal force field (UFF)[19,20] are examples of this approach. They avoid the necessity of developing new parameters every time a new type of bond is encountered but can suffer from reduced accuracy relative to a "specialist" FF. The VALBOND FF takes elements from both approaches and uses a conventional parametrization for all terms except the angle bend, where general but fitted atom-pair-based parameters are used.[21,22]

In general, development of FF parameters is based on reproducing a test set of experimental properties—structures, vibrational data, conformational energies, etc. Increasingly, experimental data is being supplemented (or even replaced) by computed data, a trend which is likely to become increasingly popular.[23–26]

2.37.4 MOLECULAR MECHANICS FOR COORDINATION COMPLEXES

For practical implementations of MM for coordination complexes, the most significant difference compared to carbon-based chemistry is how to treat high coordination numbers. For carbon, the simple harmonic expression Equation (3) is sufficient since, for a given hybridization, the valence angles are identical—viz. 180°, 120°, and 109.5° for *sp*, sp^2, and sp^3, respectively. In contrast, square planar, five-coordinate, and six-coordinate structures require at least two "ideal" angles. Two main solutions to this problem have emerged. The first is to use a more sophisticated expression for L–M–L angles and the second is to remove explicit L–M–L angle terms altogether.

The first solution has been implemented in the DREIDING program[18] which employs a harmonic cosine function and in the SHAPES FF[9] which uses a Fourier term. The VALBOND program[27] implements a multiple minima expression based on Pauling's strength functions which describe the ideal angles between hybrid orbitals.

The second solution is used in the MOMEC program[6] and the ligand field molecular mechanics (LFMM) method[13] as implemented in DOMMINO.[5] In both cases, instead of using an L–M–L angle bend term, explicit ligand–ligand 1,3-nonbonded interactions are permitted which, in the spirit of VSEPR theory or points on a sphere (POS), facilitate the treatment of any coordination number.

The other distinguishing features of coordination complexes are the electronic effects arising from the *d* configuration. For example, low-spin d^8 complexes are invariably square planar rather than tetrahedral while six-coordinate d^9 systems are severely tetragonally distorted rather than regularly octahedral. Square planar geometries can (and have[9]) been accommodated within the more sophisticated angular potential functions. Jahn–Teller effects are more difficult since they affect the M—L bond lengths. If the M—L distances are significantly different, conventional MM requires independent sets of parameters even though the ligand might be identical in each case. MOMEC has a facility for modeling the Jahn–Teller distortions in six-coordinate Cu^{2+} amine complexes by adding an explicit energy term based on the first-order model developed by Deeth and Hitchman[28] which represents the change in electronic energy accompanying a tetragonal elongation—the Q_θ mode (Equations (7)–(9)). The energy depends on the ligand field stabilization energy (LFSE), Δ, and the ideal bond length for the hypothetical, regular octahedral precursor system, r_0. The structure is forced along the distortion mode using Lagrangian constraints until the minimum energy is obtained.[29]

$$Q_\theta = (1/12)^{1/2}(\delta x_1 + \delta x_2 + \delta y_3 + \delta y_4 - 2\delta z_5 - 2\delta z_6) \tag{7}$$

$$E_{JT}^{xy} = [(-0.0119, 8)(\delta x)(\Delta)]/r_0 \tag{8}$$

$$E_{JT}^{z} = [(-0.0239, 6)(\delta x)(\Delta)]/r_0 \tag{9}$$

With the possible exception of $[Cu(imidazole)_6]^{2+}$, the structural data in Table 1 are in good agreement with experiment (see also Figure 1).

DOMMINO achieves the same result but in a completely general way by including an explicit calculation of the LFSE within the strain energy expression.[30] Hence, the Jahn–Teller distortions are automatically accounted. In addition, other effects attributed to LFSE changes are

Table 1 Experimental and calculated structures of some Cu^{II} complexes.[29]

Compound	*Equatorial X-ray/ calculated*	*Axial X-ray/ calculated*
$[Cu(tach)_2]^{2+}$	2.07/2.07	2.35/2.34
$[Cu(bipy)_3]^{2+}$	2.03/2.04	2.34/2.34
$[Cu(phen)_3]^{2+}$	2.04/2.04	2.33/2.35
$[Cu(terpy)_2]^{2+}$	2.04/2.04	2.29/2.34
$[Cu(en)_3]^{2+}$	2.08/2.06	2.34/2.37
$[Cu(9\text{-ane-}N_3)_2]^{2+}$	2.06/2.06	2.32/2.35
$[Cu(pzpy)_2]^{2+}$	2.01/2.03	2.39/2.36
$[Cu(tptz)(pcc)]^{2+}$	2.03/2.06	2.38/2.37
$[Cu(imidazole)_6]^{2+}$	2.03/2.01	2.59/2.39

tach = 1,3,5-Triaminocyclohexane; bipy = 2,2′-bipyridine; phen = 1,10-phenanthroline; terpy = 2,2′:6′,2″-terpyridine; en = ethylenediamine. See Figure 1 for structural diagrams of pzpy, tptz, and pcc ligands.

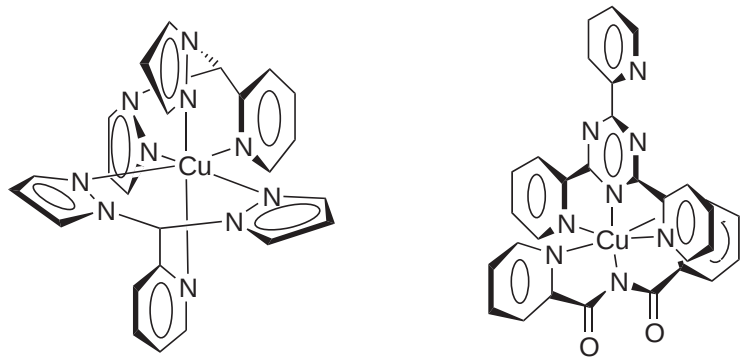

$[Cu(pzpy)_2]^{2+}$ $[Cu(tpz)(pcc)]^{2+}$

Figure 1 Schematic representations of the mixed-ligand systems given in Table 1.

automatically treated. For example, in d^8 Ni^{II} amine complexes, the Ni–N distance in six-coordinate high-spin species is around 2.1 Å and ~1.9 Å for four-coordinate low-spin compounds. The shorter bond length results from the higher LFSE. Hence, in the LFMM method, a single set of Ni–N parameters treats both cases to within about ±0.01 Å in contrast to "conventional" MM which uses separate parameters for each spin state.

Finally, π-bonded ligands present interesting challenges for MM. Three approaches have appeared so far: (i) rigid ligand, (ii) dummy atom, and (iii) explicit σ bonds.

The first method simply treats the ligand as a fixed, rigid body and its position is determined by mutual interligand repulsion. This approach is easy to implement but not very accurate.

The dummy atom and explicit σ bonds methods give better results but are more difficult to parametrize. In the former, a dummy atom, D, is placed at the centroid of the ligand carbon framework and kept in place by M—D bond stretch and M–D–C angle bend terms.[31] In the latter, each M—C interaction is explicitly parametrized. The main applications cover cyclopentadiene systems and Pd-allyl systems.[32]

2.37.5 STRUCTURE

Accurate molecular structure is a critical requirement of any MM scheme. Under favorable conditions, well parametrized schemes can generally reproduce metal–ligand distances to around ±0.01 Å, L–M–L angles to about ±3° and torsions to about ±8°. These limits are of the order of experimental precision for, for example, single crystal X-ray diffraction experiments or within the variations attributed to crystal packing and/or hydrogen bonding effects.

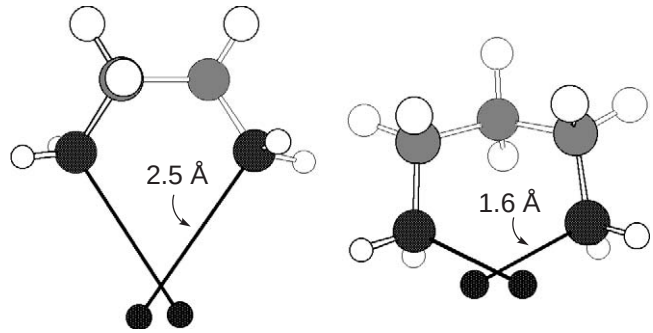

Figure 2 Illustration of effect of chelate ring size on ideal metal–ligand distance.

The most accurate FFs are obtained for those metal centers associated with regular coordination geometries. For example, low-spin d^6 Co^{III} and low-spin d^8 Ni^{II} or Pt^{II} have regular octahedral and square planar geometries respectively which are relatively easy to capture within by MM using specially designed FF parameters. More generic approaches such as UFF and Gajewski *et al.*'s MM2 extension[15] are less accurate (~0.05 Å on bond lengths) but more widely applicable. Similar errors are obtained for the rather more demanding Cu^{II} centers using the LFMM method. However, LFMM has the advantage of employing single sets of FF parameters for multiple coordination numbers and spin states.[30]

Although the absolute MM strain energy is arbitrary, referring to some hypothetical "strain free" system, variations between isomeric species are meaningful and MM has been used to compute isomer distributions and stabilities.[6] Another significant application is the use of MM to model stability constants and thus attempt to design ligands which bind selectively to specific metal centers. If the coordinated ligand has any conformational flexibility, it is important to account for contributions from all energetically accessible structures.[33–35] At the least this involves building all possible isomers and optimizing them individually but an automated procedure is obviously preferable. However, full conformational searches of inorganic complexes are complicated due to the various coordination geometries that TM ions can adopt and the difficulties in conducting conformational searches with systems that have connected ring systems, such as the ones formed when a metal ion binds a multidentate ligand. Two promising methods which address these issues are the "random kick" (Cartesian stochastic Monte Carlo search) method and the Monte Carlo dihedral and positional method.[36] The methods were tested on three Co^{III} complexes, $[Co(dien)_2]^{3+}$, $[Co(dien)(dpt)]^{3+}$, and $[Co(hexamethylcyclam)Cl_2]^{+}$.

By comparing the change in strain energy when a ligand is coordinated to a metal, the stability can be studied as a function of chelate ring size. An increase in chelate ring size from five to six increases the selectivity towards smaller metal ions. This effect is attributed to the directionality of the donor atom lone pairs. For a constant donor atom–donor atom distance in the unstrained ligand, the vectors describing the ideal lone pair directions intersect at 2.5 Å from the donor atoms for the five-membered ethane-1,2-diamine chelate but at 1.6 Å for the six-membered propane-1,3-diamine (Figure 2).

2.37.5.1 Macrocycle Hole Size

Molecular mechanics has been employed widely to the design of metal-ion-selective ligands. The calculations usually concern determining the hole size of a macrocyclic ligand system.

A common approach is to map the strain energy as a function of the M—L distance. However, the results can depend on how the M—L distance is scanned. For example, a very large M—L bond stretch force constant in conjunction with a range of r_0 values overestimates the strain energies. Another issue concerns how to scan systematically the cavity size if the ligand contains different donor atoms with different geometric and/or energetic requirements. A neat solution to the latter problem has been proposed by Comba *et al.*[34] who describe a mathematical method based on Lagrangian multipliers which allows the optimum geometry of the host molecule to be determined in the absence of a specific metal ion.

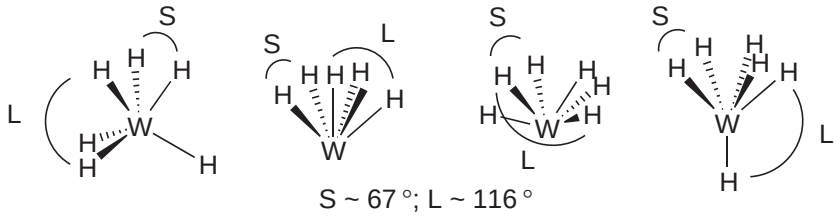

Figure 3 Possible isomers of WH_6 which conform to the ideal angles for sd^5 hybridization.

2.37.5.2 Metal Hydrides and Alkyls

As described in Section 2.37.3, one of the main difficulties for TM systems is how to treat the angle term at the metal center. This becomes even more critical for predicting the structures of metal hydrides and alkyls. For example, $W(Me)_6$ is not octahedral but rather a distorted trigonal prism. In a series of elegant papers, Landis and co-workers[21,22,37–39] explored the factors determining this unusual structure (and those for a range or other hydride and alkyl species) and concluded that the geometries could be rationalized in terms of sd^n hybridization patterns. Just as there are "ideal" angles between sp, sp^2, and sp^3 hybrid orbitals, so too are there ideal angles between sd^n hybrids. The difference is that for sd^4 and sd^5 there are *two* ideal values, 67° and 117°. Using the strength functions introduced by Pauling, Landis developed and implemented in the VALBOND program new angular potential functions to describe this behavior and successfully computed the nonoctahedral structure of WL_6 species (L = H, Me). As shown in Figure 3, there are four possible isomers of WH_6 which conform to these angular constraints.

2.37.5.3 Transition States

Since MM is normally parametrized using ground state data, its applicability to transition states (TSs) is limited. FFs like the Merck molecular force field (MMFF) make extensive use of quantum chemical (QC) results in order to model torsional barriers.[26] Similarly, Norrby uses QC calculations to model TSs.[7] A reaction path for a model reaction is computed using *ab initio* theory and the TS located. The Hessian matrix is computed for the TS but the single negative eigenvalue is reassigned a large positive value. The modified Hessian is then employed to refine a set of MM parameters for the reaction in question. Thus, the quantum chemical TS optimization is converted into an energy minimization problem in MM. Although the response of the MM minimum responds to additional steric strains in the opposite sense to the true TS, the MM is sufficiently close to provide a reasonable description of various asymmetric reaction processes such as osmium-catalyzed dihydroxylation.

2.37.6 SPECTROSCOPY

An obvious application of MM is to compute vibrational energies. However, for this to be successful, the FF parameters must be developed appropriately and this is not always done. By fitting calculated values to well-assigned experimental data, the skeletal modes of a range of metallocenes have been computed. The derived FF parameters were used to optimize the structures for $[M(Cp)_2]$ ($M = Fe^{II}$, Ru^{II}, Os^{II}, V^{II}, Co^{II}, Co^{III}, Fe^{III}, or Ni^{II}), including strapped ferrocenes. Good accuracy was obtained both for structural parameters (bonds to ±0.01 Å, angles to ~3–4°) and barriers to rotation of the Cp rings.[32]

Comba has pioneered the use of MM to determine the structure with a subsequent angular overlap model (AOM) calculation of the "*d–d*" transition energies and, where applicable, EPR *g*-values and hyperfine coupling constants.[40,41] This combination provides a powerful method for designing novel compounds with particular spectroscopic properties and for the determination of solution structures.

2.37.7 ELECTRON TRANSFER

Both the thermodynamics (redox potentials) and kinetics (rates) of electron transfer reactions have steric contributions amenable to MM. The $Co^{3+/2+}$ couple is the most studied[42] with recent work also on the $Cu^{2+/1+}$ couple.[43]

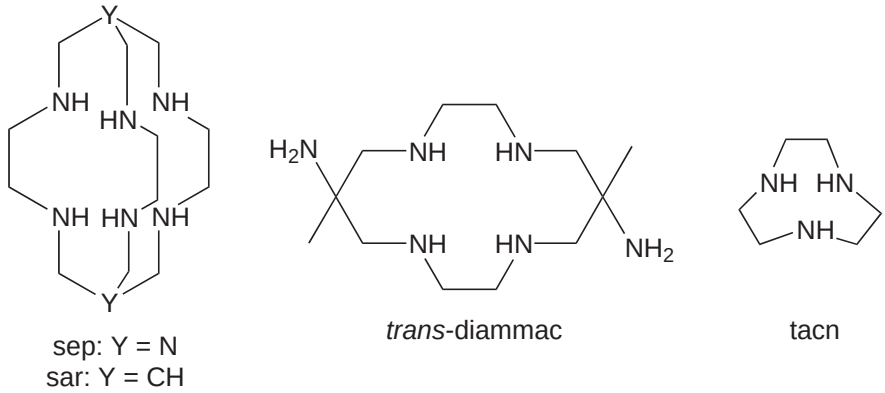

Figure 4 Amine ligands used to form Co^{III} complexes.

Reduction potentials for hexaamine cobalt(III) complexes span more than 0.9 V. A constraining ligand like *trans*-diammac (Figure 4) leads to relatively short Co—N bonds which stabilize the Co^{III} state and give low reductions potential (−0.63 V). Conversely, 2,3-dimethyl-2,3-diaminobutane (tmen) gives relatively long Co—N bonds destabilizing the Co^{III} state leading to a high potential (+0.28 V). MM calculations of the strain energy difference for the lowest energy conformations of Co^{II} and Co^{III} amine complexes yield a good correlation with experimental reduction potentials.

According to the Marcus theory, the inner sphere reorganization energy makes a significant contribution to the rate of outer-sphere electron transfer (ET). By assuming the other contributions (e.g., solvent reorganization) remain constant, reasonably good estimates of the self-exchange rates for hexaaminecobalt(III/II) complexes can be derived from the MM strain energies (Table 2).

The data listed in Table 2 were computed assuming that the TS for electron transfer corresponds to the crossing point of the absolute strain energy curves from the reduced and oxidized reactants. While this definition can correctly yield a TS in which electron transfer is isoenergetic it does not generally give the lowest energy point satisfying this criterion. Xie *et al.*[43] describe an alternative procedure wherein the vertical reorganization energy, λ_{in}, is given by

$$\lambda_{in} = E_v(Cu^I) + E_v(Cu^{II}) - E_{rel}(Cu^I) - E_{rel}(Cu^{II}) \tag{10}$$

where E_v is the vertical (unoptimized) strain energy computed for the given oxidation state but using the geometry of the other state and E_{rel} is the strain energy for the optimized structure of the given oxidation state. From these calculations plus an estimate of the solvation reorganization, perfect agreement between experimental and theoretical self-exchange ET rate constants was obtained for $[Cu(bib)_2]^{2+/+}$ (bib = 2,2′-bis(2-imidazolyl)biphenyl, Figure 5).

Table 2 Observed and calculated redox couples.[42]

Compound	$E_{1/2}$ (*obs*) (V)	$E_{1/2}$ (*calc*) (V)
$[Co(en)_3]^{3+/2+}$	−0.18	−0.10
$[Co(tmen)_3]^{3+/2+}$	+0.28	+0.28
$[Co(trans\text{-}diammac)]^{3+/2+}$	−0.63	−0.63
$[Co(sar)]^{3+/2+}$	−0.45	−0.32
$[Co(sep)]^{3+/2+}$	−0.30	−0.20
$[Co(tacn)_2]^{3+/2+}$	−0.41	−0.55
$[Co(NH_3)_6]^{3+/2+}$	+0.06	−0.14

en = Ethylenediamine; tmen = tetramethylethylenediamine. See Figure 4 for structural diagrams of other ligands.

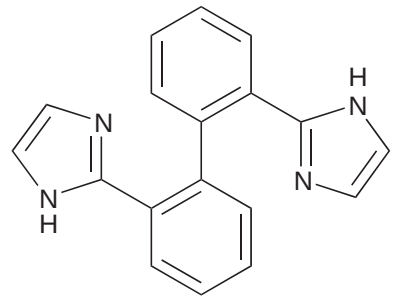

Figure 5 Structure of bib ligand.

2.37.8 BIOINORGANIC

There has been an explosion of interest in bioinorganic chemistry during the previous two decades. Although MM techniques, including molecular dynamics (MD), for modeling purely "organic" proteins and nucleic acids are well developed,[44] applications involving transition elements lag behind. This appears to be through a lack of suitable software since the two main programs, AMBER and CHARMM, have limited TM capabilities and tend to be restricted either to highly rigid systems, like Fe-porphyrins, or to electronically simple metals like Zn^{II} which can be treated as hard charged spheres. This situation is changing. Commercial software packages now facilitate the development of new parameters for TM systems. For example, Reichert and Welch[45] have developed new parameters for Ga^{III}, In^{III}, Tc^{V}, and Gd^{III} using the SYBYL program in order to understand their biological behavior, and designing new ligands for the coordination of metals utilized as imaging agents in diagnostic medicine. Many more applications of MM/MD to bioinorganic systems can be anticipated.

Another factor hampering application of MM to biological molecules is that the metal center is often found in an unusual coordination environment and there are insufficient related model complexes upon which to build a reasonable MM parametrization. For example, the type I blue copper center contains a highly distorted CuN_2S_2 center which is neither planar nor tetrahedral. This places extra demands on the MM approach. However, the development of sophisticated DFT methods are enabling these unusual structures to be modeled from first principles.[46] It should then be possible to develop MM parameters based on the DFT data.[47]

Given the biological significance of the heme unit, the geometry of metalloporphyrins and other tetrapyrroles have been extensively studied by MM including the MD simulation of hydrogen peroxide binding to the heme iron in cytochrome *c* peroxidase. and the structure and internal dynamics of (carbonmonoxy)myoglobin.[48] For the isolated metalloporphyrin systems, MM2 has been used to study the conformation as a function of (i) metal ion size, (ii) axial ligation, (iii) phenyl group orientation in tetraphenyl porphyrinato complexes, and (iv) the flexibility of the porphyrin macrocycle.

MM studies on metal-nucleotide and metal–DNA interactions are dominated by platinum-based anticancer drugs.[49] There have been numerous studies on the interaction of cisplatin, *cis*-$[PtCl_2(NH_3)_2]$ with DNA focusing on the intrastrand adduct between adjacent guanine bases.

2.37.9 FUTURE TRENDS

The high computational efficiency of MM will always make it an attractive method for large systems, like proteins and nucleic acids, for molecular dynamics simulations and for virtual high-throughput screening. However, the MM method must be capable of handling low symmetry environments with unusual ligand combinations and be able to treat the structural consequences of the incomplete *d* shell either explicitly as in the LFMM model[50] implicitly by considering the nonspherical contributions to the geometries around TM centers.[51]

The rapid increase in computer power coupled with the development of ever-more sophisticated DFT methods will, perhaps paradoxically, provide computational routes to the development of improved MM parameters which will eventually filter down into widely available computer packages. There is a continuing bright future for the application of molecular mechanics/dynamics to ever more complex problems in coordination and bioinorganic chemistry.

2.37.10 REFERENCES

1. Veillard, A. *Chem. Rev.* **1991**, *91*, 743–766.
2. Slater, J. C. *The Self-consistent Field for Molecules and Solids*; McGraw-Hill: USA, 1974; Vol. 4.
3. Burkert, U.; Allinger, N. L. *Molecular Mechanics*; American Chemical Society: Washington, DC, 1982.
4. Bernhardt, P. V.; Comba, P. *Inorg. Chem.* **1992**, *31*, 2638–2644.
5. Burton, V. J.; Deeth, R. J.; Kemp, C. M.; Gilbert, P. J. *J. Am. Chem. Soc.* **1995**, *117*, 8407–8415.
6. Comba, P.; Hambley, T. W. *Molecular Modeling of Inorganic Compounds*; VCH: Weinheim, 1995.
7. Norrby, P. O.; Brandt, P. *Coord. Chem. Rev.* **2001**, *212*, 79–109.
8. Brandt, P.; Norrby, T.; Akermark, E.; Norrby, P. O. *Inorg. Chem.* **1998**, *37*, 4120–4127.
9. Allured, V. S.; Kelly, C. M.; Landis, C. R. *J. Am. Chem. Soc.* **1991**, *113*, 1–12.
10. *Macro Model*; Schrödinger Inc., Portland, OR, USA.
11. Brooks, B. R.; Bruccoleri, R. E.; Olafson, B. D.; States, D. J.; Swaminathan, S.; Karplus, M. *J. Comput. Chem.* **1983**, *4*, 187–217.
12. Pearlman, D. A.; Case, D. A.; Caldwell, J. W.; Ross, W. S.; Cheatham, T. E.; Debolt, S.; Ferguson, D.; Seibel, G.; Kollman, P. *Comput. Phys. Commun.* **1995**, *91*, 1–41.
13. Deeth, R. J.; Foulis, D. L. *Phys. Chem. Chem. Phys.* **2002**, *4*, 4292–4297.
14. Casewit, C. J.; Colwell, K. S.; Rappe, A. K. *J. Am. Chem. Soc.* **1992**, *114*, 10046–10053.
15. Gajewski, J. J.; Gilbert, K. E.; Kreek, T. W. *J. Comp. Chem.* **1998**, *19*, 1167–1178.
16. Beagley, B.; Edge, N. C.; Jaiboon, N.; James, J. J.; McAuliffe, C. A.; Thorp, M. S.; Watkinson, M.; Whiting, A.; Wright, D. C. *Tetrahedron* **1996**, *52*, 10193–10204.
17. Bol, J. E.; Buning, C.; Comba, P.; Reedijk, J.; Strohle, M. *J. Comp. Chem.* **1998**, *19*, 512–523.
18. Mayo, S. L.; Olafson, B. D.; Goddard, W. A. *J. Phys. Chem.* **1990**, *94*, 8897–8909.
19. Rappe, A. K.; Casewit, C. J.; Colwell, K. S.; Goddard, W. A.; Skiff, W. M. *J. Am. Chem. Soc.* **1992**, *114*, 10024–10035.
20. Rappe, A. K.; Colwell, K. S.; Casewit, C. J. *Inorg. Chem.* **1993**, *32*, 3438–3450.
21. Landis, C. R.; Cleveland, T.; Firman, T. K. *J. Am. Chem. Soc.* **1998**, *120*, 2641–2649.
22. Firman, T. K.; Landis, C. R. *J. Am. Chem. Soc.* **2001**, *123*, 11728–11742.
23. Halgren, T. A. *J. Comput. Chem.* **1996**, *17*, 490–519.
24. Halgren, T. A. *J. Comput. Chem.* **1996**, *17*, 520–552.
25. Halgren, T. A. *J. Comput. Chem.* **1996**, *17*, 553–586.
26. Halgren, T. A.; Nachbar, R. B. *J. Comput. Chem.* **1996**, *17*, 587–615.
27. Root, D. M.; Landis, C. R.; Cleveland, T. *J. Am. Chem. Soc.* **1993**, *115*, 4201–4209.
28. Deeth, R. J.; Hitchman, M. A. *Inorg. Chem.* **1986**, *25*, 1225–1233.
29. Comba, P.; Zimmer, M. *Inorg. Chem.* **1994**, *33*, 5368–5369.
30. Burton, V. J.; Deeth, R. J. *J. Chem. Soc., Chem. Commun.* **1995**, 573–574.
31. Doman, T. N.; Landis, C. R.; Bosnich, B. *J. Am. Chem. Soc.* **1992**, *114*, 7264–7272.
32. Fey, N. *J. Chem. Technol. Biotechnol.* **1999**, *74*, 852–862.
33. Comba, P. *Coord. Chem. Rev.* **1999**, *186*, 81–98.
34. Comba, P.; Okon, N.; Remenyi, R. *J. Comp. Chem.* **1999**, *20*, 781–785.
35. Comba, P. *Coord. Chem. Rev.* **1999**, *182*, 343–371.
36. Bartol, J.; Comba, P.; Melter, M.; Zimmer, M. *J. Comput. Chem.* **1999**, *20*, 1549–1558.
37. Firman, T. K.; Landis, C. R. *J. Am. Chem. Soc.* **1998**, *120*, 12650–12656.
38. Landis, C. R.; Cleveland, T.; Firman, T. K. *J. Am. Chem. Soc.* **1995**, *117*, 1859–1860.
39. Landis, C. R.; Firman, T. K.; Root, D. M.; Cleveland, T. *J. Am. Chem. Soc.* **1998**, *120*, 1842–1854.
40. Bernhardt, P. V.; Comba, P. *Inorg. Chem.* **1993**, *32*, 2798–2803.
41. Comba, P.; Hambley, T. W.; Hitchman, M. A.; Stratemeier, H. *Inorg. Chem.* **1995**, *34*, 3903–3911.
42. Comba, P.; Sickmuller, A. F. *Inorg. Chem.* **1997**, *36*, 4500–4507.
43. Xie, B. P.; Wilson, L. J.; Stanbury, D. M. *Inorg. Chem.* **2001**, *40*, 3606–3614.
44. Wang, W.; Donini, O.; Reyes, C. M.; Kollman, P. A. *Ann. Rev. Biophys. Biomolec. Struct.* **2001**, *30*, 211–243.
45. Reichert, D. E.; Welch, M. J. *Coord. Chem. Rev.* **2001**, *212*, 111–131.
46. Ryde, U.; Olsson, M. H. M.; Pierloot, K.; Roos, B. O. *J. Mol. Biol.* **1996**, *261*, 586–596.
47. Comba, P.; Remenyi, R. *J. Comput. Chem.* **2002**, *23*, 697–705.
48. Marques, H. M.; Brown, K. L. *Coord. Chem. Rev.* **2002**, *225*, 123–158.
49. Scheeff, E. D.; Briggs, J. M.; Howell, S. B. *Mol. Pharmacol.* **1999**, *56*, 633–643.
50. Deeth, R. J. *Coord. Chem. Rev.* **2001**, *212*, 11–34.
51. Woodley, S. M.; Battle, P. D.; Catlow, C. R. A.; Gale, J. D. *J. Phys. Chem. B* **2001**, *105*, 6824–6830.

Comprehensive Coordination Chemistry II
ISBN (set): 0-08-0437486

Volume 2, (ISBN 0-08-0443249); pp 457–465

2.38 Semiempirical SCF MO Methods, Electronic Spectra, and Configurational Interaction

S. I. GORELSKY
Stanford University, CA, USA

2.38.1 INTRODUCTION 468
2.38.2 BASIC EQUATIONS 469
2.38.2.1 Zero Differential Overlap Approximations 470
2.38.2.2 Basis Sets 471
2.38.2.3 Fock Matrix Elements in Semiempirical ZDO Methods 471
2.38.2.3.1 CNDO 471
2.38.2.3.2 INDO 471
2.38.2.3.3 NDDO 472
2.38.2.4 One-electron Terms 472
2.38.2.5 Two-center Two-electron Integrals 473
2.38.2.5.1 γ_{AB} approximation 473
2.38.2.5.2 Other approaches 473
2.38.2.6 Orthogonalization Corrections 474
2.38.3 CURRENTLY USED SEMIEMPIRICAL METHODS FOR TM SPECIES 475
2.38.3.1 INDO/1 475
2.38.3.2 INDO/S 476
2.38.3.3 CINDO-E/S 476
2.38.3.4 MINDO/SR 476
2.38.3.5 SINDO1 477
2.38.3.6 MSINDO 477
2.38.3.7 MNDO/d 477
2.38.3.8 AM1/d 477
2.38.3.9 PM3(tm) 477
2.38.3.10 PM3d 478
2.38.3.11 PM5 478
2.38.3.12 NDDO/MC 478
2.38.3.13 SAM1 478
2.38.4 CALCULATION OF ENERGIES AND INTENSITIES OF ELECTRONIC TRANSITIONS 479
2.38.4.1 Single-transition Approximation 479
2.38.4.2 Configuration Interaction with Single Excitations 480
2.38.4.3 Direct Methods 481
2.38.4.3.1 Random-phase approximation 481
2.38.4.4 Time-dependent Density Functional Theory 482
2.38.4.5 Delta Methods 482
2.38.4.5.1 ΔSCF 482
2.38.4.5.2 Correlated methods 482
2.38.4.6 Transition State Method of Slater 483
2.38.5 SIMULATIONS OF ELECTRONIC SPECTRA 483
2.38.6 CONCLUSIONS 484
2.38.7 REFERENCES 484

2.38.1 INTRODUCTION

At present, *ab initio* methods, density functional methods, molecular mechanics, and semiempirical self-consistent field (SCF) molecular orbital (MO) methods serve as the major computational tools of quantum chemistry.[1–8] There is a trade-off between accuracy and computational effort in these methods. The most accurate results are obtained from high-level *ab initio* calculations multi-configuration self-consistent field (MCSCF), multi-reference configuration interaction (MRCI), full configuration interaction (FCI), complete active space (CAS), or coupled-cluster (CC) calculations with extended basis sets.[1–3] Such calculations require the highest computational effort and are extremely expensive for large molecules containing transition metal (TM) elements. On the other hand, semiempirical SCF MO calculations are fast, but of a limited reliability. Actual applications have to balance the required accuracy against the available computational resources. The combined use of several computational tools may well be the best approach to solve a given chemical problem by performing initial explorations at the semiempirical level followed by density functional and (if possible) high-level *ab initio* calculations.

In this chapter, because of the space constraint, only all-valence electron semiempirical SCF MO methods are briefly discussed. Please refer to other reviews[6–13] and the original publications (see references in Table 1) for more information.

In the 1960s, several semiempirical SCF methods were proposed by Pople and co-workers: the *complete neglect of differential overlap* (CNDO) method,[14–18] the *intermediate neglect of differential overlap* (INDO) method,[16,19–20] and the *neglect of differential diatomic overlap* (NDDO) approximation[14–16] (Table 1). In 1968, Bene and Jaffé parametrized the CNDO method to study electronic spectra (CNDO/S).[31–34] Ridley and Zerner developed the INDO method to predict electronic spectra (INDO/S).[60–61] In 1977, an alternative semiempirical approach with configuration interaction (CI), *local neglect of differential overlap for spectroscopy* (LNDO/S), was proposed.[106–111]

In the late 1960s and early 1970s, Dewar and co-workers developed the *modified* INDO (MINDO) methods.[39–48] In 1976, the *modified neglect of diatomic overlap* (MNDO) method[112–133] was introduced. Further refinements were made to MNDO and improved parametrizations, AM1 (*Austin model 1*),[137–152] PM3 (*parametric method 3*),[154–157] and PM5 (*parametric method 5*),[244] were developed. In 1992, Dewar and co-workers released a new model, *semi-ab initio model 1* (SAM1).[207–211] In 1998, Li *et al*. introduced a new charge model and parametrization for the INDO/S method.[242] The new model, called *charge model 2 for INDO/S* (CM2/INDO/S2), has better accuracy for $n \rightarrow \pi^*$ transition energies. In 1999, Voityuk *et al*. introduced a new semiempirical scheme, *neglect of diatomic differential overlap, Garching–Gainesville parametrization* (NDDO-G), for calculating geometries and spectroscopic properties.[243]

Recognizing the importance of orthogonalization effects (see Section 2.38.2.6), which are neglected in many semiempirical SCF MO methods, INDO-based methods with orthogonalization corrections, SINDO,[87–88] SINDO1,[89–95] and MSINDO,[101–103] have been developed. The *orthogonalization models 1* and *2* (OM1 and OM2)[235–238] go beyond the established MNDO-type methods by employing orthogonalization corrections and offer significant improvements in accuracy.

Originally all these methods employed *sp* basis sets without *d*-orbitals. Therefore, they could not be applied to most TM compounds. Parameter development for TM elements has proven to be more difficult than for the main-group elements. This is mostly because of the complicated electronic structure of TM compounds.[2,3,72] In 1966, Santry and Segal extended the CNDO/2 method to *d*-orbitals.[18] After that, CNDO was extended to TM elements.[35–38,55–59,245–254] Zerner and co-workers extended the INDO formalism for TM elements.[62–82] In 1980, Böhm and Gleiter developed their CNDO and INDO formalism for the elements H to Br, including first-row TM elements.[255–260] In 1981, Blyholder and co-workers extended the MINDO/3 model to TM elements (MINDO/SR).[158–174] In 1986, Zerner and co-workers applied the INDO method to study the electronic structure of lanthanide complexes.[78] In 1990, the LNDO/S method was extended to *d*-orbitals.[110–111] SINDO1[96–100] and MSINDO[104–105] were extended for the treatment of TM elements in 1991 and 2000 respectively. In the 1990s, the NDDO formalism was extended to *d*-orbitals and TM elements (MNDO/d,[228–234] NDDO/MC,[198–206] PM3(tm),[217–227] PM3d,[240–241] and AM1/d[239]).

There have been two approaches for parametrization of semiempirical methods. One approach aims at reproducing *ab initio* MO calculations with the same minimal basis set. This approach is taken in the method of *partial retention of diatomic differential overlap* (PRDDO).[84–86] The second approach aims at reproducing experimental data and/or high-level *ab initio* or density functional theory (DFT) calculations. Severe limitations of low-level *ab initio* calculations are well known now, especially for TM species.[1–3] As a result, parametrizations of modern semiempirical SCF MO methods follow the second approach.

Table 1 Development of all-valence electron semiempirical SCF MO methods.[a]

Year[b]	*CNDO, INDO, and LNDO types*	*NDDO and PRDDO types*
2002		**PM5**[290]
2001		PM5[244]
2000	**MSINDO**[104–105]	
1999		**AM1/d**,[239] NDDO-G[243]
1998	MSINDO,[101–103] CM2/INDO/S2[242]	
1996		OM2[237–238]
1995		**MNDO/d**,[233–234] **PM3d**[240–241]
1994		**SAM1**,[212–216] **PM3(tm)**,[217–236] ENDDO[205]
1992	**CINDO-E/S**[180–197]	SAM1[207–211]
1991	**SINDO1**[97–100]	**NDDO/MC**,[198–216] MNDO/d,[228–232] OM1,[235–236] PM3[154–157]
1988		
1987	**GRINDOL**[177–179]	
1986	**CNDO-S**[2173–176]	
1984		AM1[137–153]
1981	**MINDO/SR**[158–172]	**PRDDO**[85–86]
1980	SINDO1[89–96]	MNDOC[134–136]
1977[c]	**ZINDO**,[d 62–82] LNDO/S[106–111]	
1976	RINDO[83]	MNDO[112–133]
1974	MINDO/3[46–50]	
1973	(Z)INDO/S[60–61] SINDO,[87–88]	PRDDO[84]
1970	RCNDO,[51–55] **CNDO/2**[55–59]	
1969	MINDO/2,[43] **CNDO-R**[35–38]	
1968	MINDO/1[39–42]	
1967	CNDO/S,[31–34] INDO/1[16–19–20]	
1965	CNDO/1,[14–16] CNDO/2[16–18,21–30]	

[a] Methods applicable for compounds, containing TM elements with a *spd* basis, are bold type. [b] Paper submission dates are taken into consideration. [c] According to *A Users Guide to ZINDO*. [d] (Z)INDO/1 and (Z)INDO/S.

2.38.2 BASIC EQUATIONS

Semiempirical SCF MO approaches are formulated within the same conceptual framework as *ab initio* methods.[1–2] The elements of the Fock matrix, $F^{\alpha}_{\mu\nu}$, are defined as

$$F^{\alpha}_{\mu\nu} = H^{\text{core}}_{\mu\nu} + G^{\alpha}_{\mu\nu} \tag{1}$$

where $H^{\text{core}}_{\mu\nu}$ is the one-electron core Hamiltonian matrix element containing the kinetic energy and nuclear attraction of an electron, i.e.,

$$H^{\text{core}}_{\mu\nu} = \left(\mu \left| -\frac{\nabla^2}{2} - \sum_{\text{A}} \frac{Z_A}{R_A} \right| \nu\right) \tag{2}$$

and

$$G^{\alpha}_{\mu\nu} = \sum_{\lambda,\sigma} [P_{\lambda\sigma}(\mu\nu|\lambda\sigma) - P^{\alpha}_{\lambda\sigma}(\mu\lambda|\nu\sigma)] \tag{3}$$

$\boldsymbol{P}^{\alpha}$ is the density matrix for α spin electrons,[1,2] with elements defined by

$$P^{\alpha}_{\lambda\sigma} = \sum_i \eta_i^{\alpha} c^{\alpha}_{\lambda i}(c^{\alpha}_{\sigma i}) \tag{4}$$

where $\eta_i{}^{\alpha}$ are the occupation numbers of α spin real MO, $\phi_i{}^{\alpha}$. Similar expressions (Equations (1), (3), and (4)) are applicable for β spin electrons. The total density matrix $\boldsymbol{P}$ is given by

$$\boldsymbol{P} = \boldsymbol{P}^{\alpha} + \boldsymbol{P}^{\beta} \tag{5}$$

For the spin-restricted closed-shell SCF method,[1]

$$\boldsymbol{P}^{\alpha} = \boldsymbol{P}^{\beta}, \qquad \boldsymbol{F} = \boldsymbol{F}^{\alpha} = \boldsymbol{F}^{\beta} \tag{6}$$

The following energy terms and interactions are included in semiempirical methods:

(i) One-center one-electron energies $U_{\mu\mu}$ (part of $H^{\text{core}}_{\mu\mu}$),
(ii) Two-center one-electron integrals representing electrostatic core–electron attractions (part of $H^{\text{core}}_{\mu\mu}$),
(iii) Two-center one-electron resonance integrals $H^{\text{core}}_{\mu\nu}$,
(iv) Two-center two-electron integrals $(\mu\nu|\lambda\sigma)$ representing electrostatic electron–electron repulsions,
(v) Two-center core-core repulsions.

The solution of the Roothaan–Hall equation[1] provides MO energies (ε_i) and coefficients ($c_{\mu i}$). The Mulliken notation[1,2] is used in this chapter for the two-electron repulsion integrals (TERIs): $(\mu\nu|\lambda\sigma)$ is defined by

$$(\mu\nu|\lambda\sigma) = \int \chi^*_{\mu}(\vec{r}_1)\chi_{\nu}(\vec{r}_1) r_{12}^{-1} \chi^*_{\lambda}(\vec{r}_2)\chi_{\sigma}(\vec{r}_2)\mathrm{d}\tau_1\mathrm{d}\tau_2 \tag{7}$$

where $r_{12} = |\vec{r}_1 - \vec{r}_2|$ is the interelectronic distance; $\mathrm{d}\tau_1$ and $\mathrm{d}\tau_2$ are the volume elements for integration over the coordinates of electrons 1 and 2 respectively. The functions χ are the atomic orbitals (AOs) and Greek subscripts denote the particular AOs involved. Because of the large number of integrals $(\mu\nu|\lambda\sigma)$, the evaluation and manipulation of these two-electron integrals is a major difficulty in Hartree–Fock (HF) calculations.[1]

Semiempirical MO methods follow a different path. Instead of trying to calculate the necessary integrals accurately, they are replaced by approximations. These approximations not only help to save computing time, they also can include some corrections that are missing in the classical HF theory.[1–2] For example, electron correlation effects (neglected in the HF theory) in the semiempirical methods can be included in an average sense by a suitable representation of the TERIs and by the overall parametrization.

2.38.2.1 Zero Differential Overlap Approximations

If AOs of different atoms did not overlap with one another, overlap integrals would vanish, and so would the integrals $(\mu\nu|\lambda\sigma)$ if χ_{μ} and χ_{ν} were AOs of different atoms or if χ_{λ} and χ_{σ} were AOs of different atoms. The number of the TERIs that had to be calculated would then be far less. This is the basis of the NDDO approximation,[14] the most rigorous of several so-called zero differential overlap (ZDO) approximations. In the NDDO approximation, the integrals $(\mu\nu|\lambda\sigma)$ are neglected unless χ_{μ} and χ_{ν} are AOs of the same atom, and χ_{λ} and χ_{σ} are AOs of the same atom:

$$\chi^A_{\mu}(r_1)\chi^B_{\nu}(r_1)\mathrm{d}\tau_1 \rightarrow \delta_{AB}\chi^A_{\mu}(r_1)\chi^A_{\nu}(r_1)\mathrm{d}\tau_1 \tag{8}$$

$$\chi^A_{\lambda}(r_2)\chi^B_{\sigma}(r_2)\mathrm{d}\tau_2 \rightarrow \delta_{AB}\chi^B_{\lambda}(r_2)\chi^B_{\sigma}(r_2)\mathrm{d}\tau_2 \tag{9}$$

where the superscripts A and B refer to atoms and δ_{AB} is the Kronecker delta. Thus the nonzero TERIs in NDDO methods are either one-center ($A = B$) or two-center ($A \neq B$) integrals. All the

three- and four-center TERIs are neglected. The NDDO approximation has been justified by explicit calculations which demonstrated that the three- and four-center TERIs are indeed very small.

CNDO and INDO are more drastic approximations than NDDO. The CNDO approximation assumes the following transformation:[14–18,72]

$$\chi_\mu^A(r_1)\chi_\nu^B(r_1)\mathrm{d}\tau_1 \rightarrow \delta_{\mu\nu}\chi_\mu^A(r_1)\chi_\mu^A(r_1)\mathrm{d}\tau_1 \tag{10}$$

So, in CNDO, all the TERIs are neglected except one- and two-center Coulomb integrals, $(\mu\mu|\lambda\lambda)$. Moreover, in order for this approximation to have rotational invariance (a calculation must give the same result if a molecule is rotated in the molecular coordinate system) it is necessary to make the further approximation that the two-electron integrals $(\mu\mu|\lambda\lambda)$ are independent of the specific orbitals χ_μ or χ_λ: $(\mu\nu|\lambda\sigma) = \delta_{\mu\nu}\,\delta_{\lambda\sigma}\,\gamma_{AB}$.

The INDO model, in addition to the Coulomb integrals, also contains the one-center exchange integrals, $(\mu\nu|\nu\mu)$, and the one-center hybrid TERIs, $(\mu\nu|\lambda\sigma)$.[62–93] These extra terms, which are the next largest two-electron integrals after the Coulomb integrals, increase the accuracy of the INDO model (compared to CNDO) and preserve rotational invariance.[14,93,261]

2.38.2.2 Basis Sets

Semiempirical MO methods neglect the explicit consideration of atomic inner shells and usually use only a minimal basis set for the valence electrons (all-valence semiempirical methods). Sometimes this basis is enhanced by addition of polarization, Rydberd, and ghost orbitals.[18,49–53,83,177–179,215,228–232]

An orthogonalized basis is assumed in the ZDO-based semiempirical models. Thus, the overlap matrix $\boldsymbol{S}$ is the identity matrix:

$$S_{\mu\nu} = \delta_{\mu\nu} \tag{11}$$

2.38.2.3 Fock Matrix Elements in Semiempirical ZDO Methods

Application of the ZDO approximations (CNDO, INDO, and NDDO) to Equation (1) allows derivation of equations for the Fock matrix in different semiempirical methods.

2.38.2.3.1 CNDO

Diagonal term for the μ-th AO on atom A:

$$F_{\mu\mu}^\alpha = H_{\mu\mu}^{\mathrm{core}} - P_{\mu\mu}^\alpha\gamma_{AA} + \sum_{B\neq A}\sum_{\lambda}^{B} P_{\lambda\lambda}\gamma_{AB} \tag{12}$$

Off-diagonal term for the μ-th AO on atom A and the ν-th AO on atom B:

$$F_{\mu\nu}^\alpha = H_{\mu\nu}^{\mathrm{core}} - P_{\mu\nu}^\alpha\gamma_{AB} \tag{13}$$

2.38.2.3.2 INDO

Diagonal term for μ-th AO on atom A:

$$F_{\mu\mu}^\alpha = H_{\mu\mu}^{\mathrm{core}} + \sum_{\lambda,\sigma}^{A}[P_{\lambda\sigma}(\mu\mu|\lambda\sigma) - P_{\lambda\sigma}^\alpha(\mu\lambda|\mu\sigma)] + \sum_{B\neq A}\sum_{\lambda}^{B} P_{\lambda\lambda}\gamma_{AB} \tag{14}$$

Off-diagonal term for μ-th AO and ν-th AO on the same atom A:

$$F^{\alpha}_{\mu\nu} = H^{\text{core}}_{\mu\nu} + \sum_{\lambda,\sigma}^{A} [P_{\lambda\sigma}(\mu\nu|\lambda\sigma) - P^{\alpha}_{\lambda\sigma}(\mu\lambda|\nu\sigma)] \tag{15}$$

Off-diagonal term for μ-th AO on atom A and ν-th AO on atom B:

$$F^{\alpha}_{\mu\nu} = H^{\text{core}}_{\mu\nu} - P^{\alpha}_{\mu\nu}\gamma_{AB} \tag{16}$$

2.38.2.3.3 NDDO

Diagonal term for the μ-th AO on atom A:

$$F^{\alpha}_{\mu\mu} = H^{\text{core}}_{\mu\mu} + \sum_{\lambda,\sigma}^{A} [P_{\lambda\sigma}(\mu\mu|\lambda\sigma) - P^{\alpha}_{\lambda\sigma}(\mu\lambda|\mu\sigma)] + \sum_{B\neq A}\sum_{\lambda,\sigma}^{B} P_{\lambda\sigma}(\mu\mu|\lambda\sigma) \tag{17}$$

Off-diagonal term for the μ-th AO and the ν-th AO on the same atom A:

$$F^{\alpha}_{\mu\nu} = H^{\text{core}}_{\mu\nu} + \sum_{\lambda,\sigma}^{A} [P_{\lambda\sigma}(\mu\nu|\lambda\sigma) - P^{\alpha}_{\lambda\sigma}(\mu\lambda|\nu\sigma)] + \sum_{B\neq A}\sum_{\lambda,\sigma}^{B} P_{\lambda\sigma}(\mu\nu|\lambda\sigma) \tag{18}$$

Off-diagonal term for the μ-th AO on atom A and the ν-th AO on atom B:

$$F^{\alpha}_{\mu\nu} = H^{\text{core}}_{\mu\nu} - \sum_{\lambda}^{A}\sum_{\sigma}^{B} P^{\alpha}_{\lambda\sigma}(\mu\lambda|\nu\sigma) \tag{19}$$

2.38.2.4 One-electron Terms

Core matrix elements $H^{\text{core}}_{\mu\nu}(\mu,\nu \in A)$ are given by

$$H^{\text{core}}_{\mu\nu} = \delta_{\mu\nu}U_{\mu\mu} + \sum_{B\neq A}\left(\mu\left|\frac{-Z_B}{R_B}\right|\nu\right) \tag{20}$$

where $U_{\mu\mu}$ are the one-center core integrals, which are used as adjustable parameters or defined from atomic spectral data. The core-electron attraction integrals, $(\mu|-Z_B/R_B|\nu)$, are frequently evaluated using effective core potentials[205] or using the corresponding two-center TERI:[44,81,106]

$$\left(\mu\left|\frac{-Z_B}{R_B}\right|\nu\right) = -Z_B(\mu\nu|s^B s^B) \tag{21}$$

where Z_B is the core charge on atom B and s^B is a s-orbital of atom B.

Off-diagonal matrix elements $H^{\text{core}}_{\mu\nu}$ between AOs on different atoms ($\mu \in A$, $\nu \in B$), which are also referred to as "resonance integrals" $\beta_{\mu\nu}$ in the literature, are usually estimated by the Wolfsberg–Helmholz formula,[262]

$$H^{\text{core}}_{\mu\nu} = \frac{\beta^A_\mu + \beta^B_\nu}{2} S_{\mu\nu} \tag{22}$$

or by similar expressions. The bonding parameters, β_μ and β_ν, are chosen empirically to yield the best agreement with experimental data. The proportionality between $H^{\text{core}}_{\mu\nu}$ and $S_{\mu\nu}$ appears to be a reasonable approximation, having been adopted by a majority of existing semiempirical methods.

Under the ZDO approximation the orthogonalization procedure gives rise to significant changes in the core Hamiltonian matrix. There is also an observation that the interactions between neighboring atoms are too large for the usual parametric schemes within the

ZDO-based methods. Taking this into account, Kolb and Thiel suggested another empirical formula for the resonance integral:[236]

$$H_{\mu\nu}^{\text{core}} = \frac{\beta_\mu^A + \beta_\nu^B}{2}\sqrt{R_{AB}}e^{-(\alpha_\mu+\alpha_\nu)R_{AB}^2} \tag{23}$$

where α_μ and β_μ are adjustable parameters that are specific to a given AO type. The factor $e^{-(\alpha_\mu+\alpha_\nu)R^2}$ in Equation (23) makes the function decay faster than the overlap and the factor $\sqrt{R}$ produces extrema at internuclear distances below 1 Å that are also found for $H_{\mu\nu}^{\text{core}}$ in a similar region.[236,238] Neto and Zerner applied this formula to INDO/1 and reported considerable accuracy improvement (relative to the original INDO/1 parametrization) in the calculated geometries.[82]

2.38.2.5 Two-center Two-electron Integrals

2.38.2.5.1 γ_{AB} approximation

Calculation of the two-center TERIs differs in CNDO, INDO, and NDDO schemes. The γ_{AB} approximation is used in the CNDO, and INDO, models. Under this approximation the average electrostatic repulsion between an electron on atom A (in any orbital) and an electron on atom B (in any orbital) is represented by γ_{AB}, which is a function of internuclear distance between atoms A and B and the one-center Coulomb integrals, $\gamma_{AA} = (s_A s_A | s_A s_A)$ and $\gamma_{BB} = (s_B s_B | s_B s_B)$:

$$\gamma_{AB} = \text{f}(R_{AB}, \gamma_{AA}, \gamma_{BB}) \tag{24}$$

This function should behave appropriately in the long- ($\gamma_{AB} = {R_{AB}}^{-1}$ at $R_{AB} \to \infty$) and short-range ($\gamma_{AB} = \gamma_{AA}$ at $R_{AB} = 0$) limits. Several functions have been suggested in the literature. One of them is the Dewar–Sabelli formula:[263]

$$\gamma_{AB} = \frac{1}{\sqrt{R_{AB}^2 + \frac{1}{4}(1/\gamma_{AA} + 1/\gamma_{BB})^2}} \tag{25}$$

The Klopman–Ohno formula,[264–266]

$$\gamma_{AB} = \frac{1}{\sqrt{R_{AB}^2 + \delta_{AB}^2}} \tag{26}$$

where

$$\delta_{AB} = \frac{2}{\gamma_{AA} + \gamma_{BB}} \tag{27}$$

and the Mataga–Nishimoto formula,[267,268]

$$\gamma_{AB} = \frac{f_\gamma}{R_{AB} + f_\gamma \delta_{AB}} \tag{28}$$

where $f_\gamma = 1$ or 1.2,[11,60] are also frequently used. All quantities in Equations (25)–(28) are in atomic units.[1]

All these functions depend on the properties (γ_{AA} and γ_{BB}) of the two atoms involved, but do not differentiate between the AOs involved. As a result, the electrostatic interactions between *s*-, *p*-, and *d*-type AOs (with the same radial extent) are the same.

2.38.2.5.2 Other approaches

There are other approaches for calculations of the TERIs. The uniformly charged sphere model [269–271] is used in LNDO/S, the multipole model[228] is used in MNDO/d, AM1/d, and PM3(tm); the bipolar expansion of the Klopman–Ohno potential[272] is used in PM3d.

In the NDDO/MC method, the TERIs are calculated using the model Coulomb hole function in the electronic repulsion potential:[198–204]

$$(\mu\nu|\lambda\sigma) = \int \chi_\mu^*(r_1)\chi_\nu(r_1)\frac{\theta(r_{12}-\delta)}{r_{12}}\chi_\lambda^*(r_2)\chi_\sigma(r_2)\mathrm{d}\tau_1\mathrm{d}\tau_2 \tag{29}$$

where $\theta(r_{12}-\delta)=0$ when $r_{12}\leq\delta$ and 1 when $r_{12}>\delta$.

In SINDO1 and MSINDO, the TERIs are evaluated analytically over *s*-functions with different exponents for *s*-, *p*-, and *d*-type AOs.[273] SAM1 uses an *ab initio*-style approach, which involves the analytical evaluation of the TERIs and subsequent scaling.[207,215]

Both the one- and two-center TERIs used in semiempirical SCF methods are smaller than the corresponding integrals obtained from *ab initio* calculations. This has been attributed to the implicit inclusion of correlation effects in semiempirical values.

2.38.2.6 Orthogonalization Corrections

Ab initio SCF methods solve the Roothaan–Hall pseudoeigenvalue problem

$$\boldsymbol{Fc}=\boldsymbol{Sc}\varepsilon \tag{30}$$

where $\boldsymbol{F}$, $\boldsymbol{S}$, and $\boldsymbol{c}$ are the Fock, overlap, and eigenvector matrices respectively, and ε is the diagonal matrix of MO energies. Orthogonalization of the basis $\{\chi\}$ leads to a standard eigenvalue problem,

$${}^{\lambda}\boldsymbol{F}{}^{\lambda}\boldsymbol{c}={}^{\lambda}\boldsymbol{c}\varepsilon \tag{31}$$

where the superscript λ denotes quantities expressed in an orthogonalized basis $\{{}^{\lambda}\chi\}$. This transformation can be achieved through a symmetric orthogonalization:[274,275]

$${}^{\lambda}\chi=\chi\boldsymbol{S}^{1/2} \tag{32}$$

$${}^{\lambda}\boldsymbol{c}=\boldsymbol{S}^{1/2}\boldsymbol{c} \tag{33}$$

$${}^{\lambda}\boldsymbol{F}=\boldsymbol{S}^{-1/2}\boldsymbol{F}\boldsymbol{S}^{-1/2} \tag{34}$$

$${}^{\lambda}\boldsymbol{S}=\mathbf{1}(\text{identity matrix}) \tag{35}$$

Semiempirical ZDO methods solve an equation,

$${}^{\mathrm{ZDO}}\boldsymbol{F}\ {}^{\mathrm{ZDO}}\boldsymbol{C}={}^{\mathrm{ZDO}}\boldsymbol{C}\,\varepsilon \tag{36}$$

However, the transformation $\boldsymbol{F}\rightarrow{}^{\lambda}\boldsymbol{F}$ is not explicitly performed. This observation suggests that the semiempirical Fock matrix ${}^{\mathrm{ZDO}}\boldsymbol{F}$ implicitly refers to an orthogonalized basis:

$${}^{\mathrm{ZDO}}\boldsymbol{F}\approx{}^{\lambda}\boldsymbol{F} \tag{37}$$

The neglect of all the three- and four-center TERIs in the ZDO approximation is in agreement with this assumption because these integrals are indeed very small in an orthogonalized basis. The problem is, however, that the standard ZDO-based semiempirical methods do not employ an orthogonalized basis. This leads to some deficiencies. For example, the gaps between bonding and antibonding MOs are underestimated and the calculated barriers to internal rotations are too low.[13,238]

The Fock matrix contains one-electron ($\boldsymbol{H}^{\mathrm{core}}$) and two-electron ($\boldsymbol{G}$) terms (Equation (1)), which can be separated:

$${}^{\lambda}\boldsymbol{F}={}^{\lambda}\boldsymbol{H}^{\mathrm{core}}+{}^{\lambda}\boldsymbol{G} \tag{38}$$

$${}^{\lambda}H^{\mathrm{core}}=\boldsymbol{S}^{-1/2}\boldsymbol{H}^{\mathrm{core}}\boldsymbol{S}^{-1/2} \tag{39}$$

$${}^{\lambda}\boldsymbol{G}=\boldsymbol{S}^{-1/2}\boldsymbol{G}\,\boldsymbol{S}^{-1/2} \tag{40}$$

To account for the orthogonalization effects arising from these transformations, different approaches may be taken. The orthogonalization of the core Hamiltonian matrix according to Equation (39) is possible. However, the direct use of Equation (40) is not practical since it requires the calculation of all the TERIs and would greatly decrease the computational efficiency of the semiempirical methods. So, several approaches were introduced in the literature to apply orthogonalization corrections to the ZDO-based semiempirical methods.[13,205,235–238,276] Since the orthogonalization procedure produces a much larger change in the core Hamiltonian matrix than in the two-electron matrix $\boldsymbol{G}$, in the semiempirical methods such as CNDO-S^2, SINDO1, MSINDO, and NDDO/MC, orthogonalization corrections are applied only to the core Hamiltonian matrix, $\boldsymbol{H}^{\text{core}}$, and the two-electron matrix is left unchanged:

$$^{\lambda}\boldsymbol{G} = {}^{\text{ZDO}}\boldsymbol{G} \tag{41}$$

2.38.3 CURRENTLY USED SEMIEMPIRICAL METHODS FOR TM SPECIES

Currently the INDO- and NDDO-based methods are most frequently used for examining TM species. The CNDO-based methods, which were popular in the 1970s and 1980s to study molecular systems containing TM elements, are rarely used nowadays. More accurate INDO and NDDO methods have replaced CNDO methods at small cost in computing time.

The availability of TM and lanthanide elements in semiempirical SCF MO methods is shown in Table 2. See Chapter 2.58 for information about different quantum mechanical program packages. Note that atomic parameters and element availability may differ in different program packages.

2.38.3.1 INDO/1

This semiempirical method (often referred to as ZINDO/1), although not specifically parameterized to favor any experimental quantity, can be used for calculation of binding energies, geometries, ionization energies, and dipole moments of TM and lanthanide species.[76–82] In INDO/1, the one-center TERIs are calculated theoretically over Slater-type AOs and scaled (if necessary).

Table 2 Parameter availability for TM elements and the lanthanides in modern semiempirical SCF MO methods.

	TM elements			
Method	*First row*	*Second row*	*Third row*	*Lanthanides*
AM1	Zn[a]		Hg[a]	Eu,[b] Gd[b]
AM1/d[c]	Sc–Cr, Fe–Cu	Zr, Mo, Pd, Ag	Pt	
CINDO-E/S	Ti–Ni	Zr, Mo, Ru–Pd		
CNDO-S^2	Fe,Ni	Pd		
GRINDOL	Ti–Ni	Y–Cd		
MINDO/3	Zn[a]			
MINDO/SR	Sc–V, Fe–Ni			
MNDO	Zn[a]		Hg[a]	
MNDO/d[d]	Sc–Cr, Fe–Cu, Zn[a]	Zr, Mo, Pd, Ag, Cd[a]	Hf, Pt, Hg[a]	
MSINDO	Sc–Zn			
NDDO/MC	Cr–Ni	Ag		
PM3	Zn[a]	Cd[a]	Hg[a]	
PM3d	Cr			
PM3(tm)	Ti–Cu	Zr, Mo–Pd	Hf–Pt	Gd
PM5	Sc–Cr, Fe–Cu, Zn[a]	Zr, Mo, Pd, Ag, Cd[a]	Pt, Hg[a]	
SAM1	Fe, Cu, Zn			
SINDO1	Sc–Zn			
(Z)INDO1 and (Z)INDO/S	Sc–Zn	Y–Cd	Au	Ce–Lu

[a] A *sp* basis is employed for these elements. [b] Using the "sparkle" model.[150,151] [c] Only parameters for Mo are published and recommended for general use; parameters for other TM elements are preliminary.[290] [d] Only parameters for Zn, Cd, and Hg are recommended for general use; parameters for other TM elements are preliminary.[286,290]

In general, INDO/1-predicted geometries agree with experimental data reasonably well with the average absolute error in bond lengths around 5%.[80,81,277] The calculated stretching frequencies are overestimated by approximately 40%.[81] INDO/1 can also reliably predict spin states in a variety of different coordination environments.[225] INDO/1 is available in *HyperChem* and the *ZINDO* semiempirical package.

2.38.3.2 INDO/S

This is a popular semiempirical method (often referred to as ZINDO/S or ZINDO) for calculation of electronic spectra of both organic molecules and TM species.[60–75,277,278,320] The INDO/S parametrization was carried out at the CIS level (see Section 2.38.4.2). The Slater–Condon integrals, which are used to evaluate the TERIs, were taken from atomic spectroscopy data. The calculated transition energies are chosen to match energies of absorption maxima, ω_{max}, as opposed to absorption band origins.

Instead of standard overlap integrals $S_{\mu\nu}$, the "weighted" overlap $\bar{S}_{\mu\nu}$ is adopted in INDO/S:[11,60–62,64]

$$\bar{S}_{\mu\nu} = \sum_{m=0}^{l} f_{l,m} g_{\mu\nu} S_{\mu(\mathrm{m})\nu(\mathrm{m})} \tag{42}$$

where $g_{\mu\nu}$ are the Eulerian rotation factors required to convert from the local diatomic coordinate system to the molecular system, $S_{\mu(\mathrm{m})\nu(\mathrm{m})}$ are the σ or π or δ components of the overlap integrals in the local diatomic system, and $f_{l,m}$ are empirical weighting factors for σ ($m=0$), π ($m=1$), and δ ($m=2$) types of interactions ($l=0$, 1, 2 for *s*-, *p*-, and *d*-type orbitals respectively). They are chosen to reproduce the MO energy spread of model *ab initio* calculations.[60–62] Usually, $f_{1,0}=1.267$, $f_{1,1}=0.585$–0.68, and all other $f_{l,m}=1$.

Generally, INDO/S reproduces the energies of electronic transitions below 45,000 cm^{-1} within 2,000 cm^{-1}.[11,60–66,69–75,277,278] Charge transfer (CT) bands in non-solvatochromic systems and *d*–*d* transitions are particularly well reproduced. The oscillator strengths calculated using the dipole length approximation at the CIS level are usually overestimated by a factor of 2–3.[11,60,69,277,278] The INDO/S calculations with the random-phase approximation (RPA) (see Section 2.38.4.3.1) produce more accurate transition intensities.[69,72] Solvent effects on absorption spectra can be estimated by using the self-consistent reaction field (SCRF) method[279,280] or other approaches.[71,74,280–284] INDO/S is available in *Gaussian 98*, *HyperChem*, and the *ZINDO* and *CNDO/INDO* semiempirical packages.

2.38.3.3 CINDO-E/S

This is another method (also referred to as CINDO/S) for calculation of electronic spectra of TM complexes.[180–197] The method uses a mixed INDO/CNDO approximation (INDO/S for TM elements and CNDO/S for the main-group elements). Generally, CINDO-E/S results are similar to Zerner's INDO/S.

CINDO-E/S parameters are available for first- and second-row TM elements.[183,184] User-friendly software for performing CINDO-E/S calculations has never been distributed.

2.38.3.4 MINDO/SR

MINDO/SR[158–172] is an extension of MINDO/3[44–50] that permits the treatment of TM compounds. One of the features of the method is that the matrix elements $H_{\mu\nu}^{\mathrm{core}}$ involving an orbital of a TM atom are assumed to be proportional to $S_{\mu\nu}/R_{AB}$, where $S_{\mu\nu}$ is the overlap integral between the AOs μ and ν centered on the atoms A and B respectively, and R_{AB} is their internuclear distance.[158]

MINDO/SR parameters are available for a majority of first-row TM elements. The MINDO/SR code has not been distributed.

2.38.3.5 SINDO1

SINDO1[89–100] is a semiempirical method based on the INDO model and derives its name from an approximate transformation to symmetrically orthogonalized orbitals. Since the new version of this method, MSINDO (see Section 2.38.3.6), is more accurate,[105] the newly developed version should be used instead of SINDO1.

2.38.3.6 MSINDO

MSINDO[101–105] is a new semiempirical method and is based on SINDO1. Two sets of orbital exponents are employed in MSINDO: one for calculating one-center integrals and another for calculating two-center integrals. Orthogonalization corrections are restricted to the core Hamiltonian matrix elements. The set of atomic parameters is increased (comparing with SINDO1), however bond parameters[97] are no longer used.[101] MSINDO parameters are available for first-row TM elements.[105] The parameter development for second-row TM elements is to begin in 2002.[285]

MSINDO provides significant improvements over SINDO1 for predicting ground-state properties (heats of formation, geometries, ionization energies, and dipole moments) of molecules. Mean errors for heats of formation and bond lengths for a reference molecule set, which includes all 10 first-row transition elements, are 7.4 kcal mol^{-1} and 0.03 Å respectively. For SINDO/1, the corresponding mean errors are 10.7 kcal mol^{-1} and 0.07 Å. The MSINDO code and documentation is available from the authors.

2.38.3.7 MNDO/d

MNDO/d[228–234,157,158] is an extension of the MNDO method.[112–131] The implementation of the method is analogous to MNDO, with minor variations. For the first- and second-period elements, MNDO/d uses the same parameters as MNDO. MNDO/d parameters have been published for Zn, Cd, and Hg.[233] Currently, these are the only TM parameters that are recommended for general use.[286] There are preliminary parameter sets for other TM elements (e.g., Ti, Fe, Ni, Cu, Zr, Ag, Hf) which are listed in the MNDO97 code.[234] The parameter development for Cr, Mo, W, Ru, and Rh is in progress in Thiel's research group.[286,287] The MNDO/d parameters for 16 TM elements have been independently developed by J. J. P. Stewart.[290] MNDO/d is available in *AMPAC, HyperChem 7, MOPAC, Spartan, Titan,* and *UniChem*.

2.38.3.8 AM1/d

AM1/d[239] is an extension of the AM1 method[137–153] to a *spd* basis. The AM1 formalism and parametrization are unchanged for all main-group elements. The method uses the multipole model[228] to calculate the TERIs and was parametrized to reproduce the heats of formation and equilibrium geometries. AM1/d parameters are available for 16 TM elements.[244,290] Currently, only the Mo parameters have been published and are recommended for general use.[239] Parameter development for other TM elements is in progress.[288,290] Mean absolute errors for heats of formation and bond lengths for a reference set, which includes Mo species, are 6.5 kcal mol^{-1} (50 comparisons) and 0.044 Å (83 comparisons) respectively.[239] AM1/d is available in *MOPAC 2000* or higher.

2.38.3.9 PM3(tm)

PM3(tm)[217–227] is an extension of the PM3 method.[152–157] The PM3 parametrization are unchanged for all main-group elements, Zn, Cd, and Hg. PM3(tm) uses the multipole model[228] to calculate the TERIs and was parametrized to reproduce equilibrium and transition-state geometries of TM and organometallic species. Thus, this method focuses on structural predictions.

In general, PM3(tm)-predicted geometries agree with experimental data well with the average error in bond lengths around 3%. PM3(tm) parameters are available for most TM elements.[219]

It appears that the predictive ability is excellent for the group 4–9 TMs but diminishes for the other TMs.[223] The method can also reliably predict spin states in a variety of different coordination environments.[225] PM3(tm) calculations can be performed using *HyperChem 7, Spartan*, and *Titan*. PM3(tm) is not available by default in *MOPAC* but can be added via an external parameter file.

2.38.3.10 PM3d

PM3d[240,241] is another extension of the PM3 method for TM species. Instead of the multipole model,[228] the Klopman–Ohno potential expansion into the real spherical harmonics[272] is used to calculate the TERIs. The method was parametrized to reproduce the heats of formation, ionization potentials, dipole moments, and equilibrium geometries. The parameters are available for C, N, O, H, and Cr.[240,241] No further parameter development is planned.[289] Mean absolute errors for heats of formation and bond lengths for a reference molecule set, which includes 23 Cr compounds, are 14.8 kcal mol^{-1} and 0.05 Å respectively.[241] PM3d is available from the authors (http://quark.unn.runnet.ru/TCG_SOFTWARE.htm).

2.38.3.11 PM5

PM5 is a new re-parametrization of the MNDO method.[244] Currently, PM5 parameters are available for main-group elements and 16 TM elements, however the parameters have not been published yet.[290] Average errors for heats of formation, ionization potentials, and bond lengths in the new parametrization are reduced quite considerably compared to those from MNDO/d, AM1/d, and PM3 calculations.[244,290] PM5 is available in *MOPAC 2002*.

2.38.3.12 NDDO/MC

This NDDO-based method is available for prediction of binding energies and molecular geometries.[198–206] Its features include orthogonalization corrections to the core Hamiltonian matrix, the use of a modified formula for the resonance integral, and the model Coulomb hole function (Equation (29)) in the electronic repulsion potential in calculations of the TERIs.

Mean absolute errors for binding energies and bond lengths for a reference molecule set, which includes 36 Co and Ni compounds, are 5.0 kcal mol^{-1} and 0.064 Å respectively.[198] NDDO/MC has been also applied to calculate transition energies using the CIS approach (see Section 2.38.4.2).[206] User-friendly software for performing NDDO/MC calculations has never been distributed.

2.38.3.13 SAM1

SAM1 is an expansion of the NDDO model with focus on thermochemical and structural predictions.[207–216] It can also be useful in the calculation of vibrational frequencies, as long as certain deficiencies are recognized.[210] In SAM1, the TERIs are calculated using a minimal basis set of Gaussian functions to compute these integrals directly, limiting the actual number of integrals calculated by the NDDO approximation. The values of the computed integrals are then scaled.

SAM1 differs from AM1 in derivation of the one-center TERIs. At the first stage of the parametrization, Slater orbital exponent values are derived using atomic data. These orbital exponents are then used to calculate all the one-center two-electron integrals in the *spd* basis and these values are then fixed. The second stage is a "molecular" parametrization where the usual parameters from the NDDO models are augmented with the needed parameters for SAM1.

The method was parametrized more carefully and with more extensive searches of the parameter hypersurface. SAM1 parameters are only available for 3 TM elements (Fe, Cu, and Zn). No further parameter development is planned.[291] SAM1 is available in *AMPAC*.

2.38.4 CALCULATION OF ENERGIES AND INTENSITIES OF ELECTRONIC TRANSITIONS

The accurate prediction of electronic transition energies and intensities remains a challenging area of quantum chemistry. Many of the early successes of MO theory involved qualitative interpretations of electronic spectra. The development of the Hückel model[292,293] made semiquantitative calculations for conjugated organic molecules possible for the first time. The crystal field model (see Chapter 2.35) was successfully applied to calculate *d–d* transitions in TM complexes.

Much of our qualitative understanding of electronic transitions and the language we use to describe them derives from the independent particle approximation (IPA). Typically, one interprets features in absorption spectra of TM complexes as *d–d*, MLCT, LMCT, or LLCT transitions, etc., in an attempt to describe these processes in terms of the simple MO picture. However, such a description is approximate and the actual electron excitation process is more complex. Within the Born–Oppenheimer approximation,[1] the interaction between specific UV or visible light and matter leads to transitions between quantum states that belong to separate potential energy surfaces. In general, the absorption of a photon takes a state characterized by distinct electronic, vibrational, and rotational quantum numbers to another state with a different set of quantum numbers. The energy required for transitions between different electronic states is typically much larger than energy differences between vibrational and rotational states so typically observed low-resolution spectra are often characterized by absorption peaks that grossly represent the electronic part of the transition, with the underlying vibrational and rotational features unresolved. This is especially true for TM species in solution where the fine structure of absorption bands is rarely resolved.

Here we discuss the most common ways to calculate electronic spectra. Note that these methods can be used not only with semiempirical methods, but with other quantum mechanical methods as well.

2.38.4.1 Single-transition Approximation

Let's assume that the MO model is a valid first-order approximation and that the radiation field causes a single electron to be promoted from the occupied MO ϕ_i to the MO ϕ_a, which is not occupied in the ground electronic state. Furthermore, the MOs in the ground and excited states are the same (the *frozen orbital* approximation)[1] and there is no interaction between excited states so that an excited state can be represented by one excitation, $\phi_i \rightarrow \phi_a$. This is the so-called single-transition approximation (STA).[294]

In the case that the ground state is a closed-shell singlet, excitation of an electron from ϕ_i with MO eigenvalue ε_i to ϕ_a with MO eigenvalue ε_a gives rise to a singlet and a triplet configuration (the case where both ϕ_i and ϕ_a are degenerate orbitals is not considered here). In STA, the energy corresponding to a singlet–singlet transition is given by:[294]

$$\omega_{\text{singlet } i \rightarrow a} = \varepsilon_a - \varepsilon_i - J_{ia} + 2\,K_{ia} \tag{43}$$

where $J_{ia} = (ii|aa)$ and $K_{ia} = (ia|ai)$ are the molecular two-center Coulomb and exchange integrals respectively.[1] The energy of the corresponding singlet–triplet transition is:

$$\omega_{\text{triplet } i \rightarrow a} = \varepsilon_a - \varepsilon_i - J_{ia} \tag{44}$$

Similar expressions exist for electronic states of other multiplicities.[70] Note that, unlike the Hückel method,[292,293] the STA model does not predict that the transition energy is equal to a difference of MO eigenvalues, $\varepsilon_a - \varepsilon_i$. Rather, it allows for a certain amount of interaction between electrons and correctly predicts unequal energies for electronic transitions that differ in the multiplicity.

Oscillator strengths, f_I, of electronic transitions in the dipole length and velocity formulations are:[2]

$$f_I^r = \tfrac{2}{3}\omega_I \langle \Psi_0 | \boldsymbol{r} | \Psi_I \rangle^2 \tag{45}$$

$$f_I^{\nabla} = \frac{2}{3\omega_I} \langle \Psi_0 | \nabla | \Psi_I \rangle^2 \tag{46}$$

where $\boldsymbol{r}$ and ∇ are the dipole length and velocity operators respectively. In STA, transition moments are:

$$\langle\Psi_0|\boldsymbol{r}|\Psi_I\rangle^{\mathrm{STA}} = \sqrt{2}\langle i|\boldsymbol{r}|a\rangle \tag{47}$$

$$\langle\Psi_0|\nabla|\Psi_I\rangle^{\mathrm{STA}} = \sqrt{2}\langle i|\nabla|a\rangle \tag{48}$$

for the I-th electronic transition corresponding to the $\phi_i \rightarrow \phi_a$ excitation.

Although the STA model may be qualitatively appealing, it does not provide quantitatively satisfactory predictions. The principal reason for this is the fact that electronic transitions can rarely be described as just single excitations. There is a better theoretical approach than STA, which does not discard the intuitively attractive one-electron picture. This method is known as configuration interaction with single excitations (CIS or SECI) or the Tamm–Dancoff approximation (TDA).[2,3,72,295]

2.38.4.2 Configuration Interaction with Single Excitations

All possible Slater determinants can be described by reference to the HF determinant, Φ_0. So, the exact wave function for any electronic state of the system can be written as

$$\Psi_I = C_{0,I}\Phi_0 + \sum_{i,a} C_{ia,I}\Phi_i^a + \sum_{\substack{i<j\\a<b}} C_{iajb,I}\Phi_{ij}^{ab} + \sum_{\substack{i<j<k\\a<b<c}} C_{iajbkc,I}\Phi_{ijk}^{abc} + \cdots \tag{49}$$

where Φ_i^a are singly excited determinants, Φ_{ij}^{ab} are doubly excited determinants, Φ_{ijk}^{abc} are triply excited determinants, etc., and indexes i, j, k and a, b, c refer to occupied and unoccupied MOs of the HF ground state respectively.[1] Multiply excited states are of less interest in electronic spectroscopy than singly excited states since the electronic transitions from the ground state to multiply excited states are forbidden. However, such states can interact and mix with singly excited states, thereby affecting their properties.

An infinite set of N-electron determinants, $\{\Phi_i^a, \Phi_{ij}^{ab}, \Phi_{ijk}^{abc}, \ldots\}$, is a complete set for the expansion of any N-electron wave function, and the energies of the ground and excited states of the system are the eigenvalues of the Hamiltonian matrix. This procedure is called configuration interaction (CI).[1–3] Practical applications of this method to large molecular systems are often restricted to the CI expansion with single excitations (CIS) or to the CI expansion with single and double excitations (CISD).[2]

In the CIS method, each excited state is approximated by a linear combination of frozen-orbital single-electron excitations, Φ_i^a. First, the set of single-electron excitations is used to construct the CIS matrix, $\boldsymbol{A}$. For spin singlet-singlet transitions,

$$A_{iajb} = \langle{}^1\Phi_i^a|H|{}^1\Phi_j^b\rangle - \langle{}^1\Phi_0|H|{}^1\Phi_0\rangle\delta_{ij}\delta_{ab} = (\varepsilon_a - \varepsilon_i)\delta_{ij}\delta_{ab} + 2(ai|jb) - (ab|ji) \tag{50}$$

Then, the eigenvalue problem is solved:

$$\boldsymbol{A}\boldsymbol{C}_I = \omega_I \boldsymbol{C}_I \tag{51}$$

The eigenvalues, ω_I, are the transition energies. Since only single excitations are used in the CIS approximation, this approach fails in the description of excited states with significant contributions from doubly and triply excited determinants, Φ_{ij}^{ab}, Φ_{ijk}^{abc}.

Transition moments in the dipole length and velocity formulations are given by:

$$\langle\Psi_0|\boldsymbol{r}|\Psi_I\rangle^{\mathrm{CIS}} = \sqrt{2}\sum_{i,a} C_{ia,I}\langle i|\boldsymbol{r}|a\rangle \tag{52}$$

$$\langle\Psi_0|\nabla|\Psi_I\rangle^{\mathrm{CIS}} = \sqrt{2}\sum_{i,a} C_{ia,I}\langle i|\nabla|a\rangle \tag{53}$$

The CIS approximation is used in a majority of semiempirical SCF methods to calculate energies and oscillator strengths of electronic transitions (CNDO/S, INDO/S, CINDO-E/S, NDDO/MC, NDDO-G).

2.38.4.3 Direct Methods

When applied to spectroscopy, the response methods, also called Green's function methods or Liouville methods, yield the energies and the intensities of electronic transitions *directly*.[1,2] Starting with the generalized Schrödinger equation,

$$\boldsymbol{H}|\Psi_I\rangle = E_I|\Psi_I\rangle \tag{54}$$

let's define an excitation operator $\boldsymbol{\Theta}_I$ that when operating on the ground state $|\Psi_0\rangle$, generates an excited state $|\Psi_I\rangle$:

$$\boldsymbol{\Theta}_I|\Psi_0\rangle = |\Psi_I\rangle \tag{55}$$

If the Liouvillian operator $\boldsymbol{L}_I$ is defined from the commutator $[\boldsymbol{H}, \boldsymbol{\Theta}_I]$:

$$\boldsymbol{L}_I = [\boldsymbol{H}\boldsymbol{\Theta}_I] = \boldsymbol{H}\boldsymbol{\Theta}_I - \boldsymbol{\Theta}_I\boldsymbol{H} \tag{56}$$

$$\boldsymbol{L}_I|\Psi_0\rangle = \boldsymbol{H}\boldsymbol{\Theta}_I|\Psi_0\rangle - \boldsymbol{\Theta}_I\boldsymbol{H}|\Psi_0\rangle = \boldsymbol{H}|\Psi_I\rangle - \boldsymbol{\Theta}_I E_0|\Psi_0\rangle = E_I|\Psi_I\rangle - E_0\boldsymbol{\Theta}_I|\Psi_0\rangle = E_I|\Psi_I\rangle - E_0|\Psi_I\rangle = \omega_I|\Psi_I\rangle \tag{57}$$

the transition energies ω_I appear naturally as a consequence of these calculations. Note that Ψ_0 occurs on the left side of Equation (57), but Ψ_I on the right. This points out one of the difficulties of this method: it is not easy to extract information on the individual excited states. On the good side, this methodology generally provides not only accurate transition energies, but also reliable transition intensities.[2]

2.38.4.3.1 Random-phase approximation

The simplest of the direct methods is the RPA.[2,69,72,296–302] This approximation uses the SCF wave function for Ψ_0 and the excitation operator $\boldsymbol{\Theta}_I$,

$$\boldsymbol{\Theta}_I(i \rightarrow a) = [(\boldsymbol{a}^+_{a\alpha}\boldsymbol{a}_{i\alpha} + \boldsymbol{a}^+_{a\beta}\boldsymbol{a}_{i\beta}) + (\boldsymbol{a}_{a\alpha}\boldsymbol{a}^+_{i\alpha} + \boldsymbol{a}_{a\beta}\boldsymbol{a}^+_{i\beta})]/\sqrt{2} \tag{58}$$

where $\boldsymbol{a}^+_a$ is the *creation* operator, which creates an electron in spin orbital ψ_a, and $\boldsymbol{a}_a$ is the *annihilation* operator, which removes an electron from ψ_a.[1]

$$\boldsymbol{a}^+_a|\psi_k \ldots \psi_l\rangle = |\psi_a\psi_k \ldots \psi_l\rangle \tag{59}$$

$$\boldsymbol{a}_a|\psi_a\psi_k \ldots \psi_l\rangle = |\psi_k \ldots \psi_l\rangle \tag{60}$$

RPA with real orbitals can be expressed as a non-Hermitian eigenvalue problem,

$$\begin{pmatrix} A & B \\ B & A \end{pmatrix}\begin{pmatrix} Z \\ Y \end{pmatrix} = E\begin{pmatrix} 1 & 0 \\ 0 & -1 \end{pmatrix}\begin{pmatrix} Z \\ Y \end{pmatrix} \tag{61}$$

where $\boldsymbol{A}$ is the CIS matrix, $\boldsymbol{E}$ is the diagonal matrix of transition energies, and the (Z, Y) vector denotes the RPA eigenvector solution of Equation (61). The matrix elements for $\boldsymbol{B}$ are

$$B_{iajb} = 2(ia|jb) - (aj|bi) \tag{62}$$

for singlet–singlet transitions. The $\boldsymbol{B}$ matrix represents interaction between the ground state and doubly excited states. The HF ground state is used to evaluate the $\boldsymbol{A}$ and $\boldsymbol{B}$ matrices. However, the PRA ground state will consist of the HF ground state plus doubly excited states, i.e., the effects of configuration interaction are, to some extent, taken into account. This, as expected, is an improvement over CIS.

In RPA, transition moments in the dipole length and in the velocity formulations are:

$$\langle\Psi_0|\boldsymbol{r}|\Psi_I\rangle^{\mathrm{RPA}} = \sqrt{2}\sum_{i,a}(Z_{ia,I} + Y_{ia,I})\langle i|\boldsymbol{r}|a\rangle \tag{63}$$

$$\langle\Psi_0|\nabla|\Psi_I\rangle^{\mathrm{RPA}} = \sqrt{2}\sum_{i,a}(Z_{ia,I} - Y_{ia,I})\langle i|\nabla|a\rangle \tag{64}$$

An attractive aspect of CIS and RPA is that they both use a common set of MOs for the ground and excited states, which helps in developing qualitative interpretations of the excitation process and in calculation of transition moments. It is straightforward to evaluate $\langle i|\boldsymbol{r}|a\rangle$ and $\langle i|\nabla|a\rangle$ provided ϕ_i and ϕ_a both belong to the same orthonormal MO set. When different MO sets are used for different electronic states (to get the best possible solution), the resultant nonorthogonality of ϕ_i from one MO set and ϕ_a from another MO set causes complications.

RPA can be used with semiempirical methods to calculate electronic spectra.[2,69,72] More sophisticated direct methods employ better reference functions (CC, MCSCF, etc.) and/or include more terms in the excitation operator $\boldsymbol{\Theta}_I$.[2]

2.38.4.4 Time-dependent Density Functional Theory

Another important method to calculate transition energies and intensities is time-dependent density functional theory (TDDFT) (see Chapter 2.40).

2.38.4.5 Delta Methods

2.38.4.5.1 ΔSCF

When it is possible to describe an excited state by a single configuration wave function, the attractive approach to estimate transition energies is via separate evaluation of SCF energies for both the ground and excited states.[2,3,72] Subtraction of the resulting energies gives transition energies in a ΔSCF treatment:

$$\omega_I = E_I - E_0 \tag{65}$$

However, in addition to the need to run multiple SCF calculations to obtain the electronic energies, E_I, of many excited states, the ΔSCF approach has a number of undesirable features that severely limit its applicability. First, one encounters the problem of variational collapse.[2] If a molecule possesses no symmetry elements, it is impossible to obtain SCF solutions for any state other than the lowest energy state of a given multiplicity. Second, many excited states cannot be adequately approximated by any single determinant and one must resort to low-spin restricted open-shell approaches which can be difficult to converge.

2.38.4.5.2 Correlated methods

Conceptually one of the simplest ways to study excited states at the correlated level of theory is by means of ΔE methods, in which the energy of the system, E, is obtained with some post-HF method.[2,3,72] While the problem of variational collapse severely complicates efforts to calculate transition energies by ΔSCF, it is not so difficult to obtain ΔCI transition energies, provided the same reference function is used for both states. In this case, the orbitals are usually optimized for the ground state. Correlated energies are then obtained by diagonalization of the Hamiltonian matrix in the basis of the reference determinant and some suitable set of excited configurations. In this way, wave functions for the ground and excited states as well as transition energies are easily obtained. Despite the conceptual simplicity of this approach, it is not often used in practice. All the CI wave functions are based on a common reference state, Φ_0, and the MOs making up Φ_0 are optimized for the ground state. Since computational considerations frequently limit ΔCI approaches to ΔCISD, insufficient orbital relaxation is included, and therefore excited states are not described as well as the ground state. As a result of this imbalance, ΔCISD typically overestimates transition energies. In fact, CIS and RPA are preferable to ΔCISD because these two approaches offer a balanced description of the ground and excited states.[2,3]

One can avoid the "orbital problem" associated with ΔCI calculations by using MCSCF. The MOs are optimized for each state of interest and the ground and excited states are treated in an even-handed way. Dynamic correlation can then be included by performing MRCI calculations. This approach can be used to obtain very accurate transition energies. However, it is inconvenient

for the study of multiple excited states because separate orbital optimizations and CI calculations are required for each electronic state. Moreover, the use of different MOs for different electronic states complicates the calculations of transition intensities.

A way to include many of the advantageous features of both the ΔCI and ΔMCSCF-CI approaches is to use "state-averaged" orbitals. In these calculations, a common set of orbitals designed to describe a set of electronic states is used in a subsequent CI calculation. Such a procedure is relatively efficient and is expected to work well, provided the optimal MOs for all the electronic states of interest are not very different. If there is a significant difference between the electronic states, such a state-averaged scheme cannot work too well because all electronic states will be described poorly. In addition, the size of the configuration space required in these calculations is larger than that needed for state-specific MCSCF calculations, resulting in great computational demands.

2.38.4.6 Transition State Method of Slater

This approach to obtain approximate transition energies was proposed by Slater.[303,304] It is based on the idea that the total electronic energy of a molecular system in DFT is a function of MO occupation numbers. Instead of basing the calculation on the ground state, the calculation is done for what is called "the transition state": a state in which the occupation numbers for relevant MOs are half-way between those of the initial (ground) and final (excited) state. For example, the difference of the orbital energies, $\varepsilon_a - \varepsilon_i$, calculated for the configuration $(\ldots)(\phi_i\ \alpha)^1(\phi_i\ \beta)^{0.5}(\phi_a\ \beta)^{0.5}$, which is halfway between the initial electronic state $(\ldots)(\phi_i\ \alpha)^1(\phi_i\ \beta)^1$ and the final state $(\ldots)(\phi_i\ \alpha)^1(\phi_a\ \beta)^1$, is used to estimate the energy of the electronic transition $\phi_i \rightarrow \phi_a$. With the development of other methods (in particular, TDDFT), this approximation is rarely used nowadays.

2.38.5 SIMULATIONS OF ELECTRONIC SPECTRA

Since the electronic spectra of TM complexes usually contain many overlapping absorption bands, comparing experimental and calculated electronic spectra is not a straightforward task. The experiment provides an electronic spectrum in the form of a frequency- (or wavelength-) dependent molar absorbance function, $\varepsilon(\omega)$—an absorption curve. Theoretical calculations usually deliver only transition energies and intensities. So, to compare experimental and calculated data one has to either *deconvolute* the experimental absorption spectrum or calculate the absorption curve from available quantum mechanical information. Deconvolution may appear to be an easy task but, strictly speaking, it has an infinite number of solutions (due to overlapping absorption bands). Thus, deconvolution results can be ambiguous and, in fact, misleading.

The methods available for predicting band shapes are often restricted to small molecular systems as they involve statistical mechanics,[73,305–310] or use an accurate treatment of the potential and attempt to solve the nuclear problem on this potential.[311–315] Zerner and co-workers[316] suggested an empirical method for reproducing the molecular absorption spectra for large systems in condensed phases. The band shape is modeled using an empirical parameter to estimate the half-bandwidth for each transition. In addition to generating a shape for allowed transitions, a procedure is developed for estimating the oscillator strength for forbidden transitions.

Alternatively, absorption profiles of TM complexes can be obtained from a simple model.[278,317] Instead of evaluating the half-bandwidths $\Delta_{1/2,I}$ for each electronic transition, $\Delta_{1/2,I}$ can be taken as empirical parameters (1,000–7,000 cm^{-1}), which depend on the CT characters of the electronic transitions: higher CT character implies large $\Delta_{1/2}$ values and low CT character implies small $\Delta_{1/2}$ values. Then, an absorption profile is calculated as a sum of Gaussian-shaped bands using the following equation:

$$\varepsilon(\omega) = 2.174 \times 10^8 \sum_I \frac{f_I}{\Delta_{1/2,I}} \exp\left(-2.773 \frac{(\omega - \omega_I)^2}{\Delta_{1/2,I}^2}\right) \tag{66}$$

where molar absorbance, ε, is given in units of $mol^{-1}\,L\,cm^{-1}$. The sum in Equation (66) includes all allowed electronic transitions with energies, ω_I (expressed in cm^{-1}), half-bandwidths, $\Delta_{1/2,I}$

(expressed in cm^{-1}), and oscillator strengths f_I. So the total integrated intensity under an absorption profile obtained from Equation (66) is equal to a sum of the oscillator strengths:[293]

$$4.32 \times 10^{-9} \int \varepsilon(\omega) \mathrm{d}\omega = \sum_I f_I \tag{67}$$

The Gaussian band shape can be chosen because low-resolution spectroscopic bands (such as CT absorption bands of TM complexes in solution) follow this shape closely.[278,316,318]

2.38.6 CONCLUSIONS

In this chapter, semiempirical SCF MO methods for TM species are presented. The advantages of semiempirical SCF MO methods include a substantial reduction in the required computation time and, consequently, an increase in ability to execute calculations on much larger molecules. If an appropriate semiempirical method and semiempirical parameters are carefully chosen, results can be surprisingly accurate.

The disadvantages are the loss of the variational principle (one can obtain a total energy that is below the true total energy), the limited applicability (methods can only be applied to molecules containing elements that have been parametrized), and the danger of spurious results. There are no perfect semiempirical methods. They all can produce incorrect results, especially for molecular systems which are different from the structures used for parametrizations (the problem of parameter transferability).

Since the early 1970s, semiempirical MO methods have been able to provide significant insight into chemical problems which were too large for study using more sophisticated methods. In recent years, fast personal computers and user-friendly software for computational quantum chemistry have created an opportunity to run semiempirical SCF MO calculations in *every chemical laboratory*. Nowadays, researchers start to look more and more at high-level *ab initio* techniques and DFT to solve chemical problems. So, one may think that the increasing speed of computers spells death to semiempirical SCF MO methods. This would be true if chemistry ended at gas-phase reactions of small- and medium-size molecules. However, chemistry continues to grow, chemical structures under study become bigger and bigger. Studies of large molecular systems such as bioinorganic systems are currently out of reach of high-level *ab initio* methods. On the other hand, modern semiempirical SCF MO methods are becoming more reliable and accurate and can handle molecules with hundreds of atoms. So, there is very little danger that semiempirical methods will go out of use in the near future.[319]

ACKNOWLEDGEMENTS

The author would like to thank Drs. George Blyholder, Thomas Bredow, David Gallagher, Warren J. Hehre, Andrew J. Holder, Stanislav K. Ignatov, Olga V. Sizova, James J. P. Stewart, Walter Thiel, Alexander A. Voityuk, and Georgii M. Zhidomirov for the information they provided. Special thanks to Drs. A. B. P. Lever and René Fournier for their input and suggestions.

2.38.7 REFERENCES

1. Szabo, A.; Ostlund, N. S. *Modern Quantum Chemistry* **1996**, Dover Publications: Mineola, NY.
2. Martin, C. H.; Zerner, M. C. Electronic Structure Calculations on Transition Metal Complexes: *Ab Initio* and Approximate Models. In *Electronic Structure and Spectroscopy of Inorganic Compounds*; Solomon, E. I., Lever, A. B. P., Eds.; Wiley: New York, 1999; Vol. 1, Chapter 10, pp 555–659.
3. Bartlett, R. J.; Stanton, J. F. Applications of Post-Hartree-Fock Methods: A Tutorial. In *Reviews in Computational Chemistry*; Lipkowitz, K. B., Boyd, D. B., Eds.; VCH Publishers: New York, 1994; Vol. 5; pp 65–169.
4. Thiel, W. *J. Mol. Struct. (Theochem)* **1997**, *398–399*, 1–6.
5. Reynolds, C. H. *J. Mol. Struct. (Theochem)* **1997**, *401*, 267–277.
6. Segal, G. A., Ed. *Semiempirical Methods of Electronic Structure Calculation* **1977**, Plenum Press: New York.
7. Sadlej, J. *Semi-Empirical Methods of Quantum Chemistry* **1979**, Wiley: New York.
8. Clark, T. *A Handbook of Computational Chemistry: A Practical Guide to Chemical Structure and Energy Calculations* **1985**, Wiley: New York.

9. Thiel, W. *Tetrahedron* **1988**, *44*, 7393–7408.
10. Stewart, J. J. P. Semiempirical Molecular Orbital Methods. In *Reviews in Computational Chemistry*; Lipkowitz, K. B., Boyd, D. B., Eds.; VCH Publishers: New York, 1990; Vol. 1, Chapter 2, pp 45–81.
11. Zerner, M. C. Semiempirical Molecular Orbital Methods. In *Reviews in Computational Chemistry*; Lipkowitz, K. B., Boyd, D. B., Eds.; VCH Publishers: New York, 1991; Vol. 2, Chapter 8, pp 313–365.
12. Thiel, W. Perspectives on Semiempirical Molecular Orbital Theory. In *Advances in Chemical Physics*; Prigogine, I., Rice, S. A., Eds.; Wiley: New York, 1996; Vol. 93, pp 703–757.
13. Thiel, W. Semiempirical Methods. In *Modern Methods and Algorithms of Quantum Chemistry* Proceedings; 2nd Ed., Grotendorst, J., Ed.; John von Neumann Institute for Computing: Jülich, 2000; Vol. 3, pp 261–283.
14. Pople, J. A.; Santry, D. P.; Segal, G. A. *J. Chem. Phys.* **1965**, *43*, S129–S135.
15. Pople, J. A.; Segal, G. A. *J. Chem. Phys.* **1965**, *43*, S136–S151.
16. Pople, J. A.; Beveridge, D. L. *Approximate Molecular Orbital Theory* **1970**, McGraw-Hill: New York.
17. Pople, J. A.; Segal, G. A. *J. Chem. Phys.* **1966**, *44*, 3289–3296.
18. Santry, D. P.; Segal, G. A. *J. Chem. Phys.* **1967**, *47*, 158–174.
19. Pople, J. A.; Beveridge, D. L.; Dobosh, P. A. J. *Chem. Phys.* **1967**, *47*, 2026–2033.
20. Dixon, R. N. *Mol. Phys.* **1967**, *12*, 83–90.
21. Sichel, J. M.; Whitehead, M. A. *Theor. Chim. Acta* **1967**, *7*, 32–40.
22. Sichel, J. M.; Whitehead, M. A. *Theor. Chim. Acta* **1968**, *11*, 220–238.
23. Sichel, J. M.; Whitehead, M. A. *Theor. Chim. Acta* **1968**, *11*, 239–253.
24. Sichel, J. M.; Whitehead, M. A. *Theor. Chim. Acta* **1968**, *11*, 254–262.
25. Sichel, J. M.; Whitehead, M. A. *Theor. Chim. Acta* **1968**, *11*, 263–270.
26. Boyd, R. J.; Whitehead, M. A. *J. Chem. Soc. A* **1969**, 2598–2600.
27. Boyd, R. J.; Whitehead, M. A. *J. Chem. Soc. Dalton Trans.* **1972**, 73–77.
28. Boyd, R. J.; Whitehead, M. A. *J. Chem. Soc. Dalton Trans.* **1972**, 78–81.
29. Boyd, R. J.; Whitehead, M. A. *J. Chem. Soc. Dalton Trans.* **1972**, 81–87.
30. Fischer, H.; Kollmar, H. *Theor. Chim. Acta* **1969**, *13*, 213–219.
31. Del Bene, J.; Jaffé, H. H. *J. Chem. Phys.* **1968**, *48*, 1807–1813.
32. Del Bene, J.; Jaffé, H. H. *J. Chem. Phys.* **1968**, *48*, 4050–4055.
33. Del Bene, J.; Jaffé, H. H. *J. Chem. Phys.* **1968**, *49*, 1221–1229.
34. Del Bene, J.; Jaffé, H. H. *J. Chem. Phys.* **1969**, *50*, 1126–1129.
35. Brown, R. D.; Roby, K. R. *Theor. Chim. Acta* **1970**, *16*, 175–193.
36. Brown, R. D.; Roby, K. R. *Theor. Chim. Acta* **1970**, *16*, 194–216.
37. Brown, R. D.; James, B. H.; O'Dwyer, M. F. *Theor. Chim. Acta* **1970**, *17*, 264–278.
38. Brown, R. D.; James, B. H.; McQuade, T. J. V.; O'Dwyer, M. F. *Theor. Chim. Acta* **1970**, *17*, 279–292.
39. Baird, N. C.; Dewar, M. J. S. *Theor. Chim. Acta* **1967**, *9*, 1–16.
40. Baird, N. C.; Dewar, M. J. S. *J. Chem. Phys.* **1969**, *50*, 1262–1274.
41. Baird, N. C.; Dewar, M. J. S.; Sustmann, R. *J. Chem. Phys.* **1969**, *50*, 1275–1280.
42. Baird, N. C.; Dewar, M. J. S.; Sustmann, R. *J. Am. Chem. Soc.* **1969**, *91*, 352–355.
43. Dewar, M. J. S.; Lo, D. H.; Haselbach, E. *J. Am. Chem. Soc.* **1970**, *92*, 590–598.
44. Dewar, M. J. S.; Lo, D. H.; Ramsden, C. A. *J. Am. Chem. Soc.* **1975**, *97*, 1285–1293.
45. Dewar, M. J. S.; Lo, D. H.; Ramsden, C. A. *J. Am. Chem. Soc.* **1975**, *97*, 1294–1301.
46. Dewar, M. J. S.; Lo, D. H.; Ramsden, C. A. *J. Am. Chem. Soc.* **1975**, *97*, 1302–1306.
47. Dewar, M. J. S.; Lo, D. H.; Ramsden, C. A. *J. Am. Chem. Soc.* **1975**, *97*, 1307–1311.
48. Dewar, M. J. S.; Lo, D. H.; Ramsden, C. A. *J. Am. Chem. Soc.* **1975**, *97*, 1311–1318.
49. Zhanpeisov, N. U.; Zhidomirov, G. M. *J. Struct. Chem.* **1992**, *33*, 128–130.
50. Zhanpeisov, N. U.; Zhidomirov, G. M.; Baerns, M. *J. Struct. Chem.* **1994**, *35*, 9–12.
51. Salahub, D. R.; Sandorfy, C. *Theor. Chim. Acta* **1971**, *20*, 227–242.
52. Salahub, D. R.; Sandorfy, C. *Chem. Phys. Lett.* **1971**, *8*, 71–74.
53. Salahub, D. R. *Theor. Chim. Acta* **1971**, *22*, 325–329.
54. Salahub, D. R. *Theor. Chim. Acta* **1971**, *22*, 330–336.
55. Allen, G. C.; Clack, D. W. *J. Chem. Soc. A* **1970**, 2668–2672.
56. Clack, D. W.; Farrimond, M. S. *J. Chem. Soc. A* **1971**, 299–304.
57. Allen, G. C.; Clack, D. W.; Farrimond, M. S. *J. Chem. Soc. A* **1971**, 2728–2733.
58. Clack, D. W.; Farrimond, M. S. *J. Chem. Soc. Dalton Trans.* **1972**, 29–33.
59. Clack, D. W.; Hush, N. S.; Yandle, J. R. *J. Chem. Phys.* **1972**, *57*, 3503–3510.
60. Ridley, J.; Zerner, M. C. *Theor. Chim. Acta* **1973**, *32*, 111–134.
61. Ridley, J. E.; Zerner, M. C. *Theor. Chim. Acta* **1976**, *42*, 223–236.
62. Bacon, A. D.; Zerner, M. C. *Theor. Chim. Acta* **1979**, *53*, 21–54.
63. Zerner, M. C.; Loew, G. H.; Kirchner, R. F.; Mueller-Westerhoff, U. T. *J. Am. Chem. Soc.* **1980**, *102*, 589–599.
64. Anderson, W. P.; Edwards, W. D.; Zerner, M. C. *Inorg. Chem.* **1986**, *25*, 2728–2732.
65. Krogh-Jespersen, K.; Westbrook, J. D.; Potenza, J. A.; Schugar, H. J. *J. Am. Chem. Soc.* **1987**, *109*, 7025–7031.
66. Kotzian, M.; Rosch, N.; Pitzer, R. M.; Zerner, M. C. *Chem. Phys. Lett.* **1989**, *160*, 168–174.
67. Baker, J. D.; Zerner, M. C. *Chem. Phys. Lett.* **1990**, *175*, 192–196.
68. Baker, J. D.; Zerner, M. C. *J. Phys. Chem.* **1991**, *95*, 2307–2311.
69. Baker, J. D.; Zerner, M. C. *J. Phys. Chem.* **1991**, *95*, 8614–8619.
70. Cory, M. G.; Zerner, M. C. *Chem. Rev.* **1991**, *91*, 813–822.
71. Stavrev, K. K.; Zerner, M. C.; Meyer, T. J. *J. Am. Chem. Soc.* **1995**, *117*, 8684–8685.
72. Zerner, M. C. Intermediate Neglect of Differential Overlap Calculations on the Electronic Spectra of Transition Metal Complexes. In *Metal–Ligand Interactions*, Russo, N., Salahub, D. R., Eds.; Kluwer Academic Publishers: Amsterdam, 1996; pp 493–531.
73. Coutinho, K.; Canuto, S.; Zerner, M. C. *Int. J. Quantum Chem.* **1997**, *65*, 885–891.
74. Pearl, G. M.; Zerner, M. C. *J. Am. Chem. Soc.* **1999**, *121*, 399–404.
75. Cory, M. G.; Zerner, M. C. *J. Phys. Chem. A* **1999**, *103*, 7287–7293.

76. Head, J. D.; Zerner, M. C. *Chem. Phys. Lett.* **1985**, *122*, 264–270.
77. Head, J. D.; Zerner, M. C. *Chem. Phys. Lett.* **1986**, *131*, 359–366.
78. Culberson, J. C.; Knappe, P.; Rösch, N.; Zerner, M. C. *Theor. Chim. Acta* **1987**, *71*, 21–39.
79. Cundari, T. R.; Zerner, M. C.; Drago, R. S. *Inorg. Chem.* **1988**, *27*, 4239–4241.
80. Anderson, W. P.; Cundari, T. R.; Drago, R. S.; Zerner, M. C. *Inorg. Chem.* **1990**, *29*, 1–3.
81. Anderson, W. P.; Cundari, T. R.; Zerner, M. C. *Int. J. Quantum Chem.* **1991**, *39*, 31–45.
82. Da Motto Neto, J. D.; Zerner, M. C. *Int. J. Quantum Chem.* **2001**, *81*, 187–201.
83. Haque, W. *J. Chem. Phys.* **1977**, *67*, 3629–3635.
84. Halgren, T. A.; Lipscomb, W. N. *J. Chem. Phys.* **1973**, *58*, 1569–1591.
85. Marynick, D. S.; Lipscomb, W. N. *Proc. Natl. Acad. Sci. USA* **1982**, *79*, 1341–1345.
86. Marynick, D. S. PRDDO. In *Encyclopedia of Computational Chemistry*, Schleyer, P. v. R. Ed.; Wiley: Chichester UK, 1998; Vol. 3, pp 2153–2160.
87. Coffey, P.; Jug, K. *J. Am. Chem. Soc.* **1973**, *95*, 7575–7580.
88. Jug, K. *Theor. Chim. Acta* **1973**, *30*, 231–242.
89. Nanda, D. N.; Jug, K. *Theor. Chim. Acta* **1980**, *57*, 95–106.
90. Jug, K.; Nanda, D. N. *Theor. Chim. Acta* **1980**, *57*, 107–130.
91. Jug, K.; Nanda, D. N. *Theor. Chim. Acta* **1980**, *57*, 131–144.
92. Mishra, P. C.; Jug, K. *Theor. Chim. Acta* **1982**, *61*, 559–579.
93. Schulz, J.; Iffert, R.; Jug, K. *Int. J. Quantum Chem.* **1985**, *27*, 461–464.
94. Iffert, R.; Jug, K. *Theor. Chim. Acta* **1987**, *72*, 373–378.
95. Jug, K.; Iffert, R.; Schulz, J. *Int. J. Quantum Chem.* **1987**, *32*, 265–277.
96. Jug, K.; Krack, M. *Int. J. Quantum Chem.* **1992**, *44*, 517–531.
97. Li, J.; Correa de Mello, P.; Jug, K. *J. Comput. Chem.* **1992**, *13*, 85–92.
98. Li, J.; Jug, K. *J. Comput. Chem.* **1992**, *13*, 93–101.
99. Soudackov, A. V.; Jug, K. *Int. J. Quantum Chem.* **1997**, *62*, 403–418.
100. Jug, K.; Bredow, T. SINDO1: Parameterization and Applications. In *Encyclopedia of Computational Chemistry*; Schleyer, P. v. R. Ed.; Wiley: Chichester UK, 1998; Vol. 4, pp 2599–2609.
101. Ahlswede, B.; Jug, K. *J. Comput. Chem.* **1999**, *20*, 563–571.
102. Ahlswede, B.; Jug, K. *J. Comput. Chem.* **1999**, *20*, 572–578.
103. Jug, K.; Geudtner, G.; Homann, T. *J. Comput. Chem.* **2000**, *21*, 974–987.
104. Jud, K.; Kunert, L.; Köster, A. M. *Theor. Chem. Acc.* **2000**, *104*, 417–425.
105. Bredow, T.; Geudtner, G.; Jug, K. *J. Comput. Chem.* **2001**, *22*, 861–887.
106. Lauer, G.; Schulte, K.-W.; Schweig, A. *J. Am. Chem. Soc.* **1978**, *100*, 4925–4935.
107. Hase, H.-L.; Lauer, G.; Schulte, K.-W.; Schweig, A. *Theor. Chim. Acta* **1978**, *48*, 47–57.
108. Schulz, R.; Schweig, A; Zittlau, W. *J. Mol. Struct.(Theochem)* **1985**, *121*, 115–120.
109. Heidenreich, A.; Norbert, M.; Schweig, A. *Z. Naturforsch.* **1986**, *41A*, 1415–1424.
110. Heidenreich.A.; Doctoral Dissertation Universität Marburg, 1990.
111. Hanekamp, G.; Heidenreich, A.; Krause, D.; Meyer, H.; Müller, T.; Schweig, A. *J. Mol. Struct.* **1994**, *327*, 193–200.
112. Dewar, M. J. S.; Thiel, W. *J. Am. Chem. Soc.* **1977**, *99*, 4899–4907.
113. Dewar, M. J. S.; Thiel, W. *J. Am. Chem. Soc.* **1977**, *99*, 4907–4917.
114. Dewar, M. J. S.; Thiel, W. *Theor. Chim. Acta* **1977**, *46*, 89–104.
115. Dewar, M. J. S.; McKee, M. L. *J. Am. Chem. Soc.* **1977**, *99*, 5231–5241.
116. Dewar, M. J. S.; Rzepa, H. S. *J. Am. Chem. Soc.* **1978**, *100*, 777–784.
117. Dewar, M. J. S.; McKee, M. L.; Rzepa, H. S. *J. Am. Chem. Soc.* **1978**, *100*, 3607–3607.
118. Davis, L. P.; Guidry, R. M.; Williams, J. R.; Dewar, M. J. S.; Rzepa, H. S. *J. Comput. Chem.* **1981**, *2*, 433–445.
119. Dewar, M. J. S.; McKee, M. L. *J. Comput. Chem.* **1983**, *4*, 84–103.
120. Dewar, M. J. S.; Rzepa, H. S. *J. Comput. Chem.* **1983**, *4*, 158–169.
121. Dewar, M. J. S.; Healy, E. F. *J. Comput. Chem.* **1983**, *4*, 542–551.
122. Dewar, M. J. S.; Healy, E. F.; Stewart, J. J. P. *J. Comput. Chem.* **1984**, *5*, 358–362.
123. Dewar, M. J. S.; Grady, G. L.; Stewart, J. J. P. *J. Am. Chem. Soc.* **1984**, *106*, 6771–6773.
124. Dewar, M. J. S.; Grady, G. L.; Merz, K. M., Jr.; Stewart, J. J. P. *Organometallics* **1985**, *4*, 1964–1966.
125. Dewar, M. J. S.; Holloway, M. K.; Grady, G. L.; Stewart, J. J. P. *Organometallics* **1985**, *4*, 1973–1980.
126. Dewar, M. J. S.; Merz, K. M., Jr. *Organometallics* **1985**, *4*, 1967–1972.
127. Voityuk, A. A.; Bliznyuk, A. A.; Burshtein, K. Ya. *J. Struct. Chem.* **1987**, *28*, 9–12.
128. Dewar, M. J. S.; Reynolds, C. H. *J. Comput. Chem.* **1986**, *7*, 140–143.
129. Dewar, M. J. S.; Friedheim, J.; Grady, G.; Healy, E. F.; Stewart, J. J. P. *Organometallics* **1986**, *5*, 375–379.
130. Dewar, M. J. S.; Merz, K. M., Jr. *Organometallics* **1986**, *5*, 1494–1496.
131. Dewar, M. J. S.; Grady, G. L.; Healy, E. F. *Organometallics* **1987**, *6*, 186–189.
132. Voityuk, A. A. *J. Struct. Chem.* **1988**, *29*, 120–146.
133. Kolb, M.; Thiel, W. *J. Comp. Chem.* **1993**, *14*, 37–44.
134. Thiel, W. *J. Am. Chem. Soc.* **1981**, *103*, 1413–1420.
135. Thiel, W. *J. Am. Chem. Soc.* **1981**, *103*, 1420–1425.
136. Schweig, A.; Thiel, W. *J. Am. Chem. Soc.* **1981**, *103*, 1425–1431.
137. Dewar, M. J. S.; Zoebisch, E. G.; Healy, E. F.; Stewart, J. J. P. *J. Am. Chem. Soc.* **1985**, *107*, 3902–3909.
138. Dewar, M. J. S.; Storch, D. M. *J. Am. Chem. Soc.* **1985**, *107*, 3898–3902.
139. Dewar, M. J. S.; Jie, C. *Organometallics* **1987**, *6*, 1486–1490.
140. Dewar, M. J. S.; Zoebisch, E. G. *J. Mol. Struct. (Theochem)* **1988**, *180*, 1–21.
141. Dewar, M. J. S.; Jie, C.; Zoebisch, E. G. *Organometallics* **1988**, *7*, 513–521.
142. Dewar, M. J. S.; Merz, K. M. Jr. *Organometallics* **1988**, *7*, 522–524.
143. Dewar, M. J. S.; Jie, C. *J. Mol. Struct. (Theochem)* **1989**, *187*, 1–13.
144. Dewar, M. J. S.; Jie, C. *Organometallics* **1989**, *8*, 1544–1547.
145. Dewar, M. J. S.; Jie, C. *Organometallics* **1989**, *8*, 1547–1549.
146. Dewar, M. J. S.; Yuan, Y.-C. *Inorg. Chem.* **1990**, *29*, 3881–3890.

147. Dewar, M. J. S.; Holder, A. A. *Organometallics* **1990**, *9*, 508–511.
148. Dewar, M. J. S.; Healy, E. F.; Holder, A. J.; Yuan, Y.-C. *J. Comp. Chem.* **1990**, *11*, 541–542.
149. Dewar, M. J. S.; Healy, E. F.; Kuhn, D. R.; Holder, A. J. *Organometallics* **1991**, *10*, 431–435.
150. de Andrade, A. V. M.; da Costa, N. B. Jr.; Simas, A. M.; de Sá, G. F. *Chem. Phys. Lett.* **1994**, *227*, 349–353.
151. Cundari, T. R.; Saunders, L. C. *J. Chem. Inf. Comput. Sci.* **1998**, *38*, 523–528.
152. Hutter, M. C.; Reimers, J. R.; Hush, N. S. *J. Phys. Chem. B* **1998**, *102*, 8080–8090.
153. Bräuer, M.; Kunert, M.; Dinjus, E.; Kluβmann, M.; Döring, M.; Görls, H.; Anders, E. *J. Mol. Struct. (Theochem)* **2000**, *505*, 289–301.
154. Stewart, J. J. P. *J. Comp. Chem.* **1989**, *10*, 209–220.
155. Stewart, J. J. P. *J. Comp. Chem.* **1989**, *10*, 221–264.
156. Stewart, J. J. P. *J. Comp. Chem.* **1990**, *11*, 543–544.
157. Stewart, J. J. P. *J. Comp. Chem.* **1991**, *12*, 320–341.
158. Blyholder, G.; Head, J.; Ruette, F. *Theor. Chim. Acta* **1982**, *60*, 429–444.
159. Blyholder, G.; Head, J.; Ruette, F. *Inorg. Chem.* **1982**, *21*, 1539–1545.
160. Blyholder, G.; Head, J.; Ruette, F. *Surf. Sci.* **1983**, *131*, 403–418.
161. Ruette, F.; Blyholder, G.; Head, J. *J. Chem. Phys.* **1984**, *80*, 2042–2048.
162. Ruette, F.; Blyholder, G.; Head, J. *Surf. Sci.* **1984**, *137*, 491–505.
163. Ruette, F.; Hernandez, A.; Ludena, E. *Surf. Sci.* **1985**, *151*, 103–127.
164. Ruette, F.; Ludena, E.; Hernandez, A.; Castro, G. *Surf. Sci.* **1986**, *167*, 393–400.
165. Ruette, F.; Ludena, E.; Hernandez, A. *Int. J. Quantum Chem.* **1986**, *29*, 1351–1364.
166. Ruette, F.; Blyholder, G. *Theor. Chim. Acta* **1988**, *74*, 137–150.
167. Blyholder, G.; Lawless, M. *J. Am. Chem. Soc.* **1989**, *111*, 1275–1281.
168. Rodriguez, L. J.; Ruette, F.; Castro, G. R.; Ludena, E. V.; Hernandez, A. J. *Theor. Chim. Acta* **1990**, *77*, 39–56.
169. Rodriguez-Arias, E. N.; Rincon, L.; Ruette, F. *Organometallics* **1992**, *11*, 3677–3683.
170. Rodriguez, L. J.; Ruette, F. *J. Mol. Struct. (Theochem)* **1993**, *287*, 179–184.
171. Poveda, F. M.; Sierraalta, A.; Villaveces, J. L.; Ruette, F. *J. Mol. Catal. A: Chem.* **1996**, *106*, 109–118.
172. Primera, J. R.; Sánchez, M.; Romero, M.; Sierraalta, A.; Ruette, F. *J. Mol. Struct. (Theochem)* **1999**, *469*, 177–190.
173. Filatov, M. J.; Gritsenko, O. V.; Zhidomirov, G. M. *Theor. Chim. Acta* **1987**, *72*, 211–222.
174. Filatov, M. Yu.; Gritsenko, O. V.; Zhidomirov, G. M. *J. Struct. Chem.* **1988**, *29*, 349–356.
175. Filatov, M. J.; Gritsenko, O. V.; Zhidomirov, G. M. *J. Mol. Catal.* **1989**, *54*, 462–477.
176. Filatov, M. J.; Talsi, E. P.; Gritsenko, O. V.; Zhidomirov, G. M.; Zamaraev, K. I. *J. Chem. Soc. Dalton Trans.* **1990**, 3265–3269.
177. Leszczynski, J.; Lipinski, J. *Z. Naturforsch.* **1987**, *42a*, 160–166.
178. Lipinski, J. *Int. J. Quantum Chem.* **1988**, *34*, 423–435.
179. Roszak, S.; Lipinski, J. *Int. J. Quantum Chem.* **1992**, *44*, 831–837.
180. Baranovskii, V. I.; Sizova, O. V.; Panin, A. I.; Ivanova, N. V. *J. Struct. Chem.* **1990**, *31*, 1–7.
181. Sizova, O. V.; Baranovskii, V. I. *J. Struct. Chem.* **1993**, *34*, 191–197.
182. Sizova, O. V.; Ivanova, N. V.; Baranovskii, V. I.; Nikolskii, A. B. *J. Struct. Chem.* **1994**, *35*, 433–442.
183. Sizova, O. V.; Baranovskii, V. I. *J. Struct. Chem.* **1994**, *35*, 425–432.
184. Sizova, O. V.; Baranovskii, V. I. *J. Comp. Chem.* **1995**, *16*, 586–594.
185. Sizova, O. V.; Panin, A. I.; Baranovskii, V. I.; Ivanova, N. V. *J. Struct. Chem.* **1996**, *37*, 171–180.
186. Sizova, O. V.; Panin, A. I.; Ivanova, N. V. *J. Struct. Chem.* **1996**, *37*, 181–191.
187. Sizova, O. V.; Ivanova, N. V.; Baranovskii, V. I.; Panin, A. I. *Russ. J. Coord. Chem.* **1996**, *22*, 556–562.
188. Sizova, O. V.; Ivanova, N. V.; Baranovskii, V. I.; Panin, A. I. *Russ. J. Coord. Chem.* **1996**, *22*, 642–650.
189. Sizova, O. V.; Baranovskii, V. I.; Ivanova, N. V.; Panin, A. I. *Russ. J. Coord. Chem.* **1997**, *23*, 197–204.
190. Sizova, O. V.; Baranovskii, V. I.; Ivanova, N. V.; Panin, A. I. *Int. J. Quantum Chem.* **1997**, *63*, 853–860.
191. Sizova, O. V.; Baranovskii, V. I.; Ivanova, N. V.; Panin, A. I. *Int. J. Quantum Chem.* **1997**, *65*, 183–193.
192. Baranovski, V. I.; Sizova, O. V. *Chem. Phys. Lett.* **1999**, *315*, 130–134.
193. Sizova, O. V.; Ivanova, N. V.; Nikol'skii, A. B.; Panin, A. I.; Baranovskii, V. I.; Ershov, A. Yu. *Russ. J. Gen. Chem.* **1999**, *69*, 576.
194. Leshchev, D. V.; Baranovskii, V. I.; Sizova, O. V.; Panin, A. I. *J. Struct. Chem.* **2000**, *40*, 493–502.
195. Ivanova, N. V.; Sizov, V. V.; Nikolskii, A. B.; Panin, A. I. *J. Struct. Chem.* **2000**, *40*, 620–623.
196. Sizova, O. V.; Ivanova, N. V.; Baranovskii, V. I.; Panin, A. I.; Nikol'skii, A. B. *Russ. J. Gen. Chem.* **2000**, *70*, 823–828.
197. Rogachevsky, I. V.; Baranovski, V. I. *Spectrochim. Acta A* **2000**, *56*, 2699–2705.
198. Filatov, M. J.; Zilberberg, I. L.; Zhidomirov, G. M. *Int. J. Quantum Chem.* **1992**, *44*, 565–585.
199. Filatov, M. J.; Pelmenschikov, A. G.; Zhidomirov, G. M. *J. Mol. Catal.* **1993**, *80*, 243–251.
200. Zilberberg, I. L.; Zhidomirov, G. M.; Skuratovskii, I. Ya. *J. Mol. Struct. (Theochem)* **1993**, *285*, 129–136.
201. Filatov, M. J.; Elizarova, G. L.; Gerasimov, G. V.; Zhidomirov, G. M.; Parmon, V. N. *J. Mol. Catal.* **1994**, *91*, 71–82.
202. Zilberberg, I. L.; Milov, M. A.; Zhidomirov, G. M. *J. Struct. Chem.* **1999**, *40*, 350–357.
203. Milov, M. A.; Zilberberg, I. L.; Ruzankin, S. F.; Zhidomirov, G. M. *J. Struct. Chem.* **2000**, *41*, 200–205.
204. Milov, M. A.; Zilberberg, I. L.; Ruzankin, S. F.; Zhidomirov, G. M. *J. Mol. Catal.* **2000**, *158*, 309–312.
205. Zhidomirov, G. M.; Zhanpeisov, N. U.; Zilberberg, I. L.; Yudanov, I. V. *Int. J. Quantum Chem.* **1996**, *58*, 175–184.
206. Zilberberg, I. L.; Zhidomirov, G. M. *J. Struct. Chem.* **1999**, *40*, 187–191.
207. Dewar, M. J. S.; Jie, C.; Yu, J. *Tetrahedron* **1993**, *49*, 5003–5038.
208. Holder, A. J.; Dennington II, R. D.; Jie, C. *Tetrahedron* **1994**, *50*, 627–638.
209. Holder, A. J.; Evleth, E. M. In *Modeling the Hydrogen Bond*, Smith, D. A. Ed.; American Chemical Society: Washington, DC, 1994; pp 113–124.
210. Holder, A. J.; Dennington II, R. D. *J. Mol. Struct. (Theochem)* **1997**, *401*, 207–218.
211. Holder, A. J. SAM1 semiempirical parameters for transition metals. Book of Abstracts, 210th ACS National Meeting, Chicago, IL, August 20–24 (1995), COMP-113, American Chemical Society: Washington, DC.
212. Holder, A. J. SAM1 semiempirical parameters for transition metals. Book of Abstracts, 212th ACS National Meeting, Orlando, FL, August 25–29 (1996), COMP-198, American Chemical Society: Washington, DC.

213. Holder, A. J.; Ward. R.; White. D. A.; Jie. C. SAM1 semiempirical calculations for iron and selected other first row transition metals. Book of Abstracts, 216th ACS National Meeting, Boston, August 23–27 (1998), COMP-174, American Chemical Society: Washington, DC.
214. White, D. A.; Holder A. J.; Jie, C. SAM1 semiempirical calculations for selected first row transition metals. Book of Abstracts, 216th ACS National Meeting, Boston, August 23–27 (1998), COMP-182, American Chemical Society: Washington, DC.
215. Holder, A. J. SAM1 In *Encyclopedia of Computational Chemistry*, Schleyer, P. v. R. Ed.; Wiley: Chichester, UK, 1998; Vol. 4, pp 2542–2544.
216. Liotard, D. A.; Holder, *A. J. Chem. Inf. Comput. Sci.* **1999**, *39*, 587–593.
217. Hehre, W. J.; Yu, J. Semi-empirical models for transition metals. Book of Abstracts, 210th ACS National Meeting, Chicago, IL, August 20–24 (1995), COMP-077; American Chemical Society: Washington, DC.
218. Hehre, W. J.; Yu, J. Book of Abstracts, 211th ACS National Meeting, New Orleans, LA, March 24–28 (1996), PMSE-216; American Chemical Society: Washington, DC.
219. *Spartan 02 Windows Tutorial and User's Guide*. Wavefunction, Inc.: Irvine, CA, 2001.
220. Børve, K. J.; Jensen, V. R.; Karlsen, T.; Støvneng, J. A.; Swang, O. *J. Mol. Model.* **1997**, *3*, 193–202.
221. Decker, S. A.; Donini, O.; Klobukowski, M. *J. Phys. Chem. A* **1997**, *101*, 8734–8740.
222. Cundari, T. R.; Saunders, L.; Sisterhen, L. L. *J. Phys. Chem. A* **1998**, *102*, 997–1004.
223. Cundari, T. R.; Deng, J. *J. Chem. Inf. Comput. Sci.* **1999**, *39*, 376–381.
224. Cundari, T. R.; Deng, J. *Int. J. Quantum Chem.* **2000**, *77*, 421–432.
225. Ball, D. M.; Buda, C.; Gillespie, A. M.; White, D. P.; Cundari, T. R. *Inorg. Chem.* **2002**, *41*, 152–156.
226. Bosque, R.; Maseras, F. *J. Comp. Chem.* **2000**, *21*, 562–571.
227. Zakharian, T. Y.; Coon, S. R. *Comput. Chem.* **2001**, *25*, 135–144.
228. Thiel, W.; Voityuk, A. A. *Theor. Chim. Acta* **1992**, *81*, 391–404.
229. Thiel, W.; Voityuk, A. A. *Int. J. Quantum Chem.* **1992**, *44*, 807–829.
230. Thiel, W.; Voityuk, A. A. *J. Mol. Struct. (Theochem)* **1994**, *313*, 141–154.
231. Malagoli, M.; Thiel, W. *Chem. Phys.* **1996**, *206*, 73–85.
232. Thiel, W.; Voityuk, A. A. *Theor. Chim. Acta* **1996**, *93*, 315.
233. Thiel, W.; Voityuk, A. A. *J. Phys. Chem* **1996**, *100*, 616–626.
234. *UniChem 5.0 Guide to MNDO97*. Oxford Molecular Ltd., Oxford, UK, 2000.
235. Kolb.M. Ph.D. Thesis, Universität Wuppertal, 1991.
236. Kolb, M.; Thiel, W. *J. Comput. Chem.* **1993**, *14*, 775–789.
237. Weber. W. Ph.D. Thesis Universität Zürich, 1996.
238. Weber, W.; Thiel, W. *Theor. Chem. Acc.* **2000**, *103*, 495–506.
239. Voityuk, A. A.; Rösch, N. *J. Phys. Chem. A* **2000**, *104*, 4089–4094.
240. Ignatov, S. K.; Razuvaev, A. G.; Kokorev, V. N.; Aleksandrov, Yu. A. *J. Struct. Chem.* **1995**, *36*, 538–543.
241. Ignatov, S. K.; Razuvaev, A. G.; Kokorev, V. N.; Aleksandrov, Yu. A. *J. Phys. Chem.* **1996**, *100*, 6354–6358.
242. Li, J.; Williams, B.; Cramer, C. J.; Truhlar, D. G. *J. Chem. Phys.* **1999**, *110*, 724–733.
243. Voityuk, A. A.; Zerner, M. C.; Rösch, N. *J. Phys. Chem. A* **1999**, *103*, 4553–4559.
244. Stewart, J. J. P. *MOPAC 2002 Manual Fujitsu Ltd.*, 2001; http://www.cachesoftware.com/mopac/Mopac2002manual/.
245. Baranovskii, V. I.; Sizova, O. V. *Dokl. Akad. Nauk SSSR* **1971**, *200*, 871–873.
246. Tondello, E. *Inorg. Chim. Acta* **1974**, *11*, L5–L6.
247. Serafini, A.; Savariault, J.-M.; Cassoux, P.; Labarre, J.-F. *Theor. Chim. Acta* **1975**, *36*, 241–247.
248. Serafini, A.; Pélissier, M.; Savariault, J.-M.; Cassoux, P.; Labarre, J.-F. *Theor. Chim. Acta* **1975**, *39*, 229–239.
249. Savariault, J.-M.; Serafini, A.; Pélissier, M.; Cassoux, P. *Theor. Chim. Acta* **1976**, *42*, 155–161.
250. Baranovskii, V. I.; Sizova, O. V.; Ivanova, N. V. *J. Struct. Chem.* **1976**, *17*, 478–506.
251. Baba-Ahmed, A.; Gayoso, J. *Theoret. Chim. Acta* **1983**, *62*, 507–521.
252. Yakovlev, V. N.; L'vovskii, V. E.; Panona, N. S. *J. Struct. Chem.* **1986**, *27*, 656–657.
253. Boca, R. *Int. J. Quantum Chem.* **1987**, *31*, 941–950.
254. Boca, R. *Int. J. Quantum Chem.* **1988**, *33*, 159–167.
255. Böhm, M. C.; Gleiter, R. *Theor. Chim. Acta* **1981**, *59*, 127–151.
256. Böhm, M. C.; Gleiter, R. *Theor. Chim. Acta* **1981**, *59*, 153–179.
257. Böhm, M. C. *Theor. Chim. Acta* **1981**, *60*, 233–268.
258. Böhm, M. C. *Theor. Chim. Acta* **1982**, *61*, 539–558.
259. Böhm, M. C. *Theor. Chim. Acta* **1983**, *62*, 351–372.
260. Böhm, M. C. *Theor. Chim. Acta* **1983**, *62*, 373–396.
261. Figey, H. P.; Geerlings, P.; van Alsenoy, C. *Int. J. Quantum Chem.* **1977**, *11*, 705–713.
262. Wolfsberg, M.; Helmholz, L. *J. Chem. Phys.* **1952**, *20*, 837–843.
263. Dewar, M. J. S.; Sabelli, N. L. *J. Chem. Phys.* **1962**, *66*, 2310–2316.
264. Klopman, G. *J. Am. Chem. Soc.* **1964**, *86*, 4550–4557.
265. Ohno, K. *Theor. Chem. Acta* **1964**, *2*, 219–227.
266. Ohno, K. Molecular Orbital Calculations of II Electron Systems. In *Advances in Quantum Chemistry*, Löwdin, P.-O., Ed.; Academic Press: New York, 1967; Vol. 3, pp 239–322.
267. Mataga, N.; Nishimoto, K. *Z. Physik. Chem. (Frankfurt)* **1957**, *12*, 335–338.
268. Mataga, N.; Nishimoto, K. *Z. Physik. Chem. (Frankfurt)* **1957**, *13*, 140–157.
269. Parr, R. G. *J. Chem. Phys.* **1952**, *20*, 1499–1499.
270. Pariser, R.; Parr, R. G. *J. Chem. Phys.* **1953**, *21*, 466–471.
271. Pariser, R.; Parr, R. G. *J. Chem. Phys.* **1953**, *21*, 767–776.
272. Ignatov, S. K.; Razuvaev, A. G.; Kokorev, V. N. *J. Struct. Chem.* **1994**, *35*, 443–446.
273. Harris, F. E. *J. Chem. Phys.* **1969**, *51*, 4770–4778.
274. Löwdin, P. O. *J. Chem. Phys.* **1950**, *18*, 365–375.
275. Löwdin, P.-O. On the Nonorthogonality Problem. In *Advances in Quantum Chemistry*; Löwdin, P.-O., Ed.; Academic Press: New York, 1970; Vol. 5, 185–199.
276. Kollmar, C.; Böhm, M. C. *Theor. Chim. Acta* **1995**, *92*, 13–47.

277. Gorelsky, S. I.; Dodsworth, E. S.; Lever, A. B. P.; Vlcek, A. A. *Coord. Chem. Rev.* **1998**, *174*, 469–494.
278. Gorelsky, S. I.; Lever, A. B. P. *J. Organomet. Chem.* **2001**, *635*, 187–196; **2002**, *659*, 202.
279. Karelson, M. M.; Zerner, M. C. *J. Phys. Chem.* **1992**, *96*, 6949–6957.
280. Stavrev, K. K.; Tamm, T.; Zerner, M. C. *Int. J. Quantum Chem. Quantum Chem. Symposium* **1996**, *30*, 1585–1594.
281. Zeng, J.; Craw, J. S.; Hush, N. S.; Reimers, J. R. *J. Phys. Chem.* **1994**, *98*, 11075–11088.
282. Zeng, J.; Hush, N. S.; Reimers, J. R. *J. Am. Chem. Soc.* **1996**, *118*, 2059–2068.
283. Hush, N. S.; Reimers, J. R. *Chem. Rev.* **2000**, *100*, 775–786.
284. Klamt, A. *J. Phys. Chem.* **1996**, *100*, 3349–3353.
285. Bredow, T. Private communication, May 2002.
286. Thiel, W. Private communication, May 2002.
287. Liu, Z. Ph.D. Thesis, Emory University, 2000.
288. Voityuk, A. A. Private communication, May 2002.
289. Ignatov, S. K. Private communication, April 2002.
290. Stewart, J. J. P.; Gallagher,D. Private communications, May–October 2002.
291. Holder, A. J. Private communication, April 2002.
292. Hückel, E. *Z. Physik* **1931**, *70*, 204–286.
293. Sandorfy, C. *Electronic Spectra and Quantum Chemistry*; Prentice Hall: Englewood Cliffs, NJ, 1964.
294. Roothaan, C. C. J. *Rev. Mod. Phys.* **1951**, *23*, 69–89.
295. Elliott, J.; Flowers, B. H. *Proc. Roy. Soc. (London)* **1975**, A242,57–80.
296. Thouless, D. J. *Quantum Mechanics of Many Body Systems*; 1st ed.; Academic Press: New York, 1961.
297. Altick, P. L.; Glassgold, A. E. *Phys. Rev.* **1964**, *133*, A632–A646.
298. Dunning, T. H.; McKoy, V. *J. Chem. Phys.* **1967**, *47*, 1735–1747.
299. Oddershede, J. Polarization Propagator Calculations. In *Advances in Quantum Chemistry*; Löwdin, P.-O., Ed.; Academic Press: New York, 1978; Vol. 11, pp 275–352.
300. Jørgensen, P.; Simons, J. *Second Quantization-based Methods in Quantum Chemistry* **1981**, Academic Press: New York.
301. Hansen, A. E.; Voigt, B.; Rettrup, S. *Int. J. Quantum Chem.* **1983**, *23*, 595–611.
302. Zakrzewski, V. G.; Dolgounitcheva, O.; Ortiz, J. V. *Int. J. Quantum Chem., Quantum Chem. Symp.* **1996**, *30*, 1241–1247.
303. Slater, J. C. Statistical Exchange-correlation in the Self-consistent Field. In *Advances in Quantum Chemistry*; Löwdin, P.-O., Ed.; Academic Press: New York, 1972; Vol. 6, pp 1–92.
304. Slater, J. C. *Quantum Theory of Molecules and Solids*; McGraw-Hill: New York, 1974; Vol. 4.
305. Warshel, A. *J. Phys. Chem.* **1979**, *83*, 1640–1652.
306. Blair, J. T.; Krogh-Jespersen, K.; Levy, R. M. *J. Am. Chem. Soc.* **1989**, *111*, 6948–6956.
307. DeBolt, S. E.; Kollman, P. A. *J. Am. Chem. Soc.* **1990**, *112*, 7515–7524.
308. Levy, R. M.; Kitchen, D. B.; Blair, J. T.; Krogh-Jespersen, K. *J. Phys. Chem.* **1990**, *94*, 4470–4476.
309. Luzhkov, V.; Warshel, A. *J. Am. Chem. Soc.* **1991**, *113*, 4491–4499.
310. Gao, J. *J. Am. Chem. Soc.* **1994**, *116*, 9324–9328.
311. Campagnola, P. J.; Lavrich, D. J.; DeLuca, M. J.; Johnson, M. A. *J. Chem. Phys.* **1991**, *94*, 5240–5242.
312. Karwowski, J. *Int. J. Quantum Chem.* **1994**, *51*, 425–437.
313. Bielińska-Wąż, D.; Karwowski, J. *Phys. Rev. A* **1995**, *52*, 1067–1071.
314. Baczyński, A.; Radomska, D. *J. Fluoresc.* **1995**, *5*, 91–98.
315. Bielinska-Wąż, D.; Karwowski, J. Determining the Shapes of Molecular Electronic Bands from their Intensity Distribution Moments. In *Advances in Quantum Chemistry*; Löwdin, P.-O., Ed.; Vol. 28; Academic Press: San Diego, CA, 1997; pp 159–169.
316. Pearl, G. M.; Zerner, M. C.; Broo, A.; McKelvey, J. *J. Comput. Chem.* **1998**, *19*, 781–796.
317. Gorelsky, S. I.; SWizard program, http://www.obbligato.com/software/swizard/.
318. Endicott, J. F. Charge-transfer Excited States of Transition Metal Complexes. In *Electron Transfer in Chemistry*; Balzani, V., Ed.; Wiley-VCH: Weinheim, 2001; Vol. 1, Chapter 7, pp 238–270.
319. Boyd, D. B. *J. Mol. Struct. (Theochem)* **1997**, *401*, 219–225.
320. Shapley, W. A.; Reimers, J. R.; Hush, N. S. *Int. J. Quantum Chem.* **2002**, *90*, 424–438.

Comprehensive Coordination Chemistry II
ISBN (set): 0-08-0437486

Volume 2, (ISBN 0-08-0443249); pp 467–489

2.39
Density Functional Theory

L. NOODLEMAN, T. LOVELL, W.-G. HAN, T. LIU, R. A. TORRES, and F. HIMO
The Scripps Research Institute, La Jolla, CA, USA

2.39.1 INTRODUCTION 491
2.39.2 FUNDAMENTAL ISSUES 492
2.39.3 EXCHANGE-CORRELATION POTENTIALS 494
2.39.4 THE IMPORTANCE OF SPIN 495
2.39.5 SPIN POLARIZED SYSTEMS 496
2.39.6 SPIN-COUPLED SYSTEMS: METAL-RADICAL SYSTEMS AND SPIN-COUPLED DINUCLEAR COMPLEXES 497
2.39.7 GEOMETRIES OF TRANSITION METAL DIMER COMPLEXES 500
2.39.8 INTERACTION ENERGY WITH PROTEIN AND SOLVENT ENVIRONMENTS 500
2.39.9 IRON-OXO DIMER PROTEINS 501
2.39.10 IRON–SULFUR COMPLEXES 504
2.39.11 METAL–LIGAND RADICAL SYSTEMS 508
2.39.12 CONCLUSIONS 508
2.39.13 REFERENCES 509

2.39.1 INTRODUCTION

Density functional theory (DFT) constitutes a family of methodologies for quantum mechanical electronic structure calculations with broad applications to organic and main group molecules as well as more complicated systems.[1–3] These methods are of particular value for transition metal complexes where electron correlation effects can be large,[4,5] and for systems of similar complexity like metals, solid-state compounds, and surfaces.[6] The problems that can be studied effectively include electronic structure, charge and spin distributions, molecular geometries, and reaction pathway energetics.[5,7] There are now a variety of applications both to ground state and to excited state energies, properties, and pathways.[8–11] For an alternative methodology to the ΔSCF methods for excited states discussed in this review, see the contribution on time-dependent DFT (TDDFT) in this volume (Chapter 2.40). DFT methods for medium- and large-sized systems combine high computational efficiency with very good physical accuracy.

The plan of this short review is: (i) a summary of some fundamental issues to provide perspective on practical calculations; (ii) a brief summary of some practical aspects of DFT calculations with additional specific methodologies, in particular, different exchange-correlation potentials, the importance of spin polarized calculations in many cases, the uses of the broken symmetry (BS) and spin projection method, fitting of the electrostatic potential (ESP) to create an active site point charge model, use of electrostatic/dielectric methods to represent the extended environment, and coupling to the quantum cluster; (iii) a short summary of some representative applications, including spin-polarized transition metal complexes, spin-coupled metal–ligand radical complexes, spin-coupled dinuclear metal complexes, and redox and coupled electron–proton transfer energetics.

2.39.2 FUNDAMENTAL ISSUES

From a fundamental viewpoint, the goal of DFT is to obtain the "best", ultimately "universal" forms for the "exact" exchange and correlation energy, E_{xc}, and the corresponding exchange-correlation potential ν_{xc}. These in combination with the Coulomb potential of the electron density V_{Coul} and the nuclear electron attraction potential V_{Ne} can then be used to construct the Kohn–Sham (KS) potential, ν_s:

$$\nu_s = V_{Ne} + V_{Coul} + \nu_{xc} \tag{1}$$

This local density dependent one-electron potential operates on the KS orbitals, and gives accurate one-electron orbitals, electron densities, and energies. We have used the notation of Baerends and Gritsenko (with a few minor changes) and our current discussion follows the logic of their argument.[1,12] For a good perspective on reduced density matrices, which forms a foundation for these arguments, see McWeeny.[13]

It is useful to distinguish "exact KS" theory from practical approximate KS-DFT methods. In the "exact KS" theory, it is assumed that the exact correct electron density is obtained (or known from preceding work). There is then no remaining "correlation contribution" to the nuclear-electron attraction energy V. However, because the one-electron KS orbitals are solutions to a local one-electron potential ν_s, the kinetic energy (T_s) of the KS wave function $\Psi_s[\rho]$ is the sum of the orbital kinetic energies. The KS potential acts like a local external potential, and the KS total kinetic energy T_s is not the "true" total kinetic energy of the interacting system T, with the difference being the correlation contribution to the kinetic energy $T_c = T - T_s$ within KS-DFT theory. This will enter into some important equations below.

Defining the "true" electronic total energy of the system as $E_{elect} = T + V_{Ne} + W$ and the total system energy as $E_{tot} = E_{elect} + V_{NN}$, where V_{NN} is the nuclear–nuclear electrostatic repulsion energy, with the total kinetic energy of the system as T, the total nuclear–electron attraction as V_{Ne}, and the total electron–electron repulsion energy as W, the last can be decomposed into

$$W = W_{Coul} + W_{xc} \tag{2}$$

where $W_{Coul} = (1/2)\int \rho(1)\rho(2)/r_{12}\, d1\, d2$ is the classical Coulomb repulsion of the electron density with $\rho(1)$ the electron density at position r_1 with spin index $S_1 = \alpha$ or β and W_{xc} is the exchange-correlation term in the total $e^- - e^-$ repulsion. This result occurs because the correlated joint probability density $\Gamma(1,2)$ is not just equal to the product of the one electron probability densities. Instead

$$\Gamma(1,2) = \rho(1)\rho(2) + \Gamma_{xc}(1,2) \tag{3}$$

$\Gamma(1,2)$ can be separated into four terms for $\alpha\alpha$, $\beta\beta$, $\alpha\beta$, and $\beta\alpha$. In a related way, the conditional probability density for finding an electron at position 2 when another electron is known to be a position 1 is given by

$$\rho_{cond}(2|1) = g(1,2)\rho(2) = \Gamma(1,2)/\rho(1) = \rho(2) + \Gamma_{xc}(1,2)/\rho(1) = \rho(2) + \rho_{xc}{}^{hole}(2|1) \tag{4}$$

This defines the important exchange-correlation hole density $\rho_{xc}{}^{hole}(2|1)$ as the difference between the conditional probability density and the ordinary electron density. The following total charge integral rules hold for parallel $\alpha\alpha$ and $\alpha\beta$ antiparallel electron spins:

$$\int \rho_{xc}{}^{hole}{}_{\alpha\alpha}\, dr_2 = -1 \tag{5}$$

$$\int \rho_{xc}{}^{hole}{}_{\alpha\beta}\, dr_2 = 0 \tag{6}$$

Equation (5) represents the Fermi hole, which is a consequence of the Pauli exclusion principle, and represents the combined exchange and correlation of parallel spin electrons. (It applies also for the $\beta\beta$ integral.) Note that exchange alone will also satisfy this integral. Equation (6)

represents the behavior of the Coulomb type hole for opposite spin electrons; while electron correlation allows these electrons to avoid one another, this is less effective than for parallel spin electrons, and is not a consequence of the Pauli antisymmetry principle. Correspondingly, the Pauli principle requires that no two parallel spin electrons can be at the same position simultaneously, or equivalently,

$$\rho_{\mathrm{xc}}{}^{\mathrm{hole}}{}_{\alpha\alpha}(1|1) = -\rho_{\alpha}(1) \tag{7}$$

(with an analogous equation for β), while there is no such guarantee for opposite spin electrons. These and other limits are used to determine reasonable forms for the exchange-correlation hole functions, and to find ν_{xc}.

The exchange-correlation term in the total $e^- - e^-$ can be defined in terms of these densities by

$$W_{\mathrm{xc}} = (1/2)\int \rho(1)\rho_{\mathrm{xc}}{}^{\mathrm{hole}}(2|1)/r_{12}\,\mathrm{d}1\,\mathrm{d}2 = (1/2)\int \rho(1)\nu_{\mathrm{xc}}{}^{\mathrm{hole}}(1)\,\mathrm{d}1 \tag{8}$$

so that

$$\nu_{\mathrm{xc}}{}^{\mathrm{hole}}(1) = \int \rho_{\mathrm{xc}}{}^{\mathrm{hole}}(2|1)/r_{12}\,\mathrm{d}2 \tag{9}$$

The exact total energy equation is

$$E_{\mathrm{tot}} = T + V_{\mathrm{Ne}} + V_{\mathrm{NN}} + W_{\mathrm{Coul}} + W_{\mathrm{xc}} \tag{10}$$

However, using T_{s} instead, this can be rewritten as

$$E_{\mathrm{tot}} = T_{\mathrm{s}} + V_{\mathrm{Ne}} + V_{\mathrm{NN}} + W_{\mathrm{Coul}} + E_{\mathrm{xc}} \tag{11}$$

which defines $E_{\mathrm{xc}} = (T - T_{\mathrm{s}}) + W_{\mathrm{xc}}$. It is also useful to define the total potential energy

$$V_{\mathrm{tot}} = V_{\mathrm{Ne}} + V_{\mathrm{NN}} + W_{\mathrm{Coul}} + W_{\mathrm{xc}},\ \text{so}\ E_{\mathrm{tot}} = T + V_{\mathrm{tot}}.$$

The major goal is to find a good functional form for the exchange-correlation energy density per particle $\varepsilon_{\mathrm{xc}}$ where

$$E_{\mathrm{xc}} = \int \rho(1)\varepsilon_{\mathrm{xc}}(1)\,\mathrm{d}1 \tag{12}$$

From these equations above and the variational principle, $\delta E/\delta\rho = 0$, the proof that $\nu_{\mathrm{xc}} = \delta E_{\mathrm{xc}}[\rho]/\delta\rho(r)$ is fairly straightforward. Defining $T_{\mathrm{c}} = T - T_{\mathrm{s}}$, a kinetic correlation energy density $\nu_{\mathrm{c,kin}}$ is readily defined

$$T_{\mathrm{c}} = \int \rho(1)\nu_{\mathrm{c,kin}}\,\mathrm{d}1 \tag{13}$$

Then the central equations follow

$$\varepsilon_{\mathrm{xc}} = (1/2)\nu_{\mathrm{xc}}{}^{\mathrm{hole}} + \nu_{\mathrm{c,kin}} \tag{14}$$

$$\nu_{\mathrm{xc}} = \nu_{\mathrm{xc}}{}^{\mathrm{hole}} + \nu_{\mathrm{c,kin}} + \nu_{\mathrm{resp}} \tag{15}$$

The problem of evaluating the contribution of the kinetic correlation energy density $\nu_{\mathrm{c,kin}}$ to ν_{xc} is even more difficult than for $\nu_{\mathrm{xc}}{}^{\mathrm{hole}}$, and it would be better to treat this term more directly. (Note that in the potential ν_{xc}, the derivative $\delta T_{\mathrm{c}}/\delta\rho(r)$ gives two complicated terms $\nu_{\mathrm{c,kin}} + \nu_{\mathrm{resp}}$. Also, the functional derivative of $\nu_{\mathrm{xc}}{}^{\mathrm{hole}}$ contributes to ν_{resp}. As a number of authors have pointed out, there is a contrast between the family of correlation methods which starting from the Hartree–Fock (HF) wave function build in more and more correlation into the many-electron wave

function, and DFT methods where the correlation (and exchange) are built into ε_{xc} and the exchange-correlation potential ν_{xc}.

We propose instead a type of middle ground.[14] From an examination of spin polarized and BS approaches, and some general results based on the virial theorem, we employ a strategy where general exchange and correlation effects are built into the potential ν_{xc} (called "dynamic" correlation), while important wave function specific correlation effects are built into the BS method (called "nondynamic" or "near-degeneracy" correlation).

It is evident that $\nu_{xc}{}^{\alpha}$, the exchange-correlation potential operating on α electrons need not be the same as $\nu_{xc}{}^{\beta}$ operating on β electrons for two possible reasons: either (i) there can be different total numbers of α versus β electrons (N_α, N_β), or (ii) there can be differences in the local α versus β density (ρ_α, ρ_β) whether or not the total numbers are different. Since the exchange-correlation holes are different for parallel vs. antiparallel spin electrons and more efficient for electrons of the same spin index, if there is sufficient freedom in the spin orbital density, these electron densities (ρ_α, ρ_β) and corresponding potentials may separate into distinctive α and β parts. Let us consider a case where this is energetically favored in accordance with the variational principle and compare with the spin restricted case.

The virial theorem is a useful analysis tool here.[15,16] It is based on a scaling argument involving electron and nuclear coordinates of very general validity, applying in an exact theory to molecules and to the separated atoms or fragments, as well as in HF theory, in many CI-based methods, and in the simplest DFT (Slater exchange).[17] For more complicated DFTs, the same general principles outlined below should hold, but the "exactness" of the theorem depends on assigning which part of E_{xc} is the kinetic energy ($T - T_s$) compared to the potential energy (W_{xc}). The virial theorem for the equilibrium geometry only, but for either ground or excited states is

$$T = -E_{tot} = -V_{tot}/2 \tag{16}$$

recalling $E_{tot} = T + V_{tot}$. Now comparing the spin-restricted (RS) vs. BS energies, we find that $E_{BS} < E_{RS}$ (both are negative) since by the variational principle the BS state would not arise without energy stabilization compared to RS. Further, for the KS type kinetic energy T_s, $T_s(\mathrm{BS}) > T_s(\mathrm{RS})$ (both positive), so for the corresponding kinetic correlation energies,

$$T_c(\mathrm{BS}) = (T - T_s(\mathrm{BS})) < T_c(\mathrm{RS}) = (T - T_s(\mathrm{RS})) \tag{17}$$

One expects then that the correlation kinetic energy term in E_{xc} and generating also $\nu_{c,kin}$ will be smaller and more tractable within BS than in spin-restricted form. Qualitatively, the increased T_s(BS) compared to T_s(RS) corresponds to localization of α and β spin densities in different regions of space.

2.39.3 EXCHANGE-CORRELATION POTENTIALS

The earliest exchange-correlation potentials attempted only to create a local exchange potential that would correspond to a local exchange hole (of the same spin as the reference electron and centered on the reference electron position) integrating to $-1e^-$ (the hole density is "positively charged"). This is called the Slater exchange potential, and was used in the older X-α theory.[17] It is proportional to $\rho_\alpha{}^{1/3}$ for up-spin α electrons and to $\rho_\beta{}^{1/3}$ for down-spin β electrons. The corresponding total exchange energies are $-C_x\int\rho_\alpha{}^{4/3}\,\mathrm{d}r$ and $-C_x\int\rho_\beta{}^{4/3}\,\mathrm{d}r$. Later, Becke (1986, 1988)[18] found a greatly improved gradient dependent expression for the exchange-energy. Meanwhile, work on the exchange-correlation energy of a free-electron gas due to Ceperly and Alder with subsequent parametrization by Vosko, Wilk, and Nusair (VWN) led to an accurate solution of this problem for a uniform electron gas with densities ρ_α and ρ_β. This is usually called the "local density approximation" (LDA) or "local spin density" (LSD) approximation. For inhomogeneous systems (molecules), LSD leads to strong overbinding, and in general the exchange plus correlation contribution to the molecular binding energy is too large. (The exchange energy E_x in the LSD total energy is just the Slater exchange energy.) The Becke gradient-dependent exchange term provides a major improvement in binding energies. Further, gradient corrections to the correlation energy yield further improvements. The first from Stoll *et al.*[19] simply eliminates the parallel spin contribution to the correlation energy, while in Perdew's work (1986),[20,21] both parallel spin and anti-parallel spin correlation terms are modified by gradient dependent energy

expressions. The generalized-gradient (GGA) corrected exchange-correlation potentials in greatest use now are mainly the Becke88-Perdew86 (BP86) potential referred to above, the Perdew–Wang91 for both exchange and correlation (PW91), Becke88–Perdew–Wang91(BPW91),[22] and the BLYP (Becke for exchange, with Lee–Yang–Parr for correlation).[1] Current experience indicates that the PW91 exchange potential is similar to Becke88 exchange, so that BPW91 and PW91 give similar energetics. The older Becke88-Stoll potential behaves quite similarly to BP86. PW91 for both exchange and correlation terms in transition metal complexes shows good quality answers for spin coupling parameters as detailed later, and reasonable protonation and redox energetics, indicating that this, in common with BPW91, is probably preferable to BP86 for most problems. This is also the experience of others for energetics of first and second row molecules,[23] and for some transition metal complexes.[24] Despite some quantitative deficiencies, the BP86 potential has provided valuable results for energetic trends for complexes through the first row transition metal series, and for related active sites in enzymes (see examples below).[25–27]

Hybrid potentials involve some combination of "exact" HF exchange mixed into the DFT-GGA potential, the most common being the B3LYP functional. The exchange-correlation energy is:

$$E_{xc}^{B3LYP} = (1 - A)E_x^{Slater} + AE_x^{HF} + BE_x^{Becke} + CE_c^{LYP} + (1 - C)E_c^{VWN} \tag{18}$$

The fundamental justification for mixing the HF exchange energy term (E_x^{HF}) lies in the "adiabatic connection formula"[3] which predicts that there will be some HF exchange energy contribution to a high-quality expression for E_{xc}. One can show that integrating over electron–electron coupling strength from the noninteracting limit ($\lambda = 0$) to full strength ($\lambda = 1$, the true physical $e^- - e^-$ repulsion strength) allows one to circumvent (in principle) the more difficult parts of the exchange-correlation potential evaluation.[3] In practice, the coupling strength integration formula is not evaluated from first principles. Instead, the functional form of $E_{xc}{}^{B3LYP}$ is fit to experimental heats of formation to extract the parameters A, B, C. The HF mixing parameter turns out to be $A = 0.2$. A more complete story can be found in Becke (1993).[28] This fitting improves the predictions of atomization energies for the G2 test set of 55 small molecules involving first and second row elements from about 12 kcal mol^{-1} error in BP86 to 2 kcal mol^{-1} in B3LYP. Siegbahn has also shown that for some reactions including OH bond splitting from the high-oxidation state complex $MnO_3(OH)^-$, for transition metal–CO bond dissociation energies in $M(CO)_n$ (error range 0–4 kcal mol^{-1} vs. 2–9 kcal mol^{-1}) and for CO versus O_2 binding to an Fe^{II}-porphyrin model, B3LYP gives better energies than GGA-based functionals (BP86 and BLYP).[5] A larger set of examples for energetics encompassing both main group and transition metal containing molecules is summarized in Koch and Holthausen.[3] DFT-GGA methods are computationally faster than hybrid DFT-HF methods when efficient programs using density fitting (Jaguar, ADF, ORCA)[2,29,30] are used, typically by a factor of two or greater, which is significant for very large systems. Basis sets need to be of high quality for transition metal complexes (at least double zeta plus polarization on the metal, or better, and similarly for the ligands) to obtain good accuracy, and this increases computation time. Methods selection then needs to be combined with model complex selection to solve problems practically.

2.39.4 THE IMPORTANCE OF SPIN

From Hund's Rules, it is well known that the ground state of most free atoms and ions is the high-spin (HS) state, depending only on the filling of the *s*, *p*, or *d* subshells. This same behavior persists for many transition metal complexes because the field of the surrounding ligands is either of weak or moderate strength. Further, much of bioinorganic chemistry is the chemistry of high-spin transition metal sites, although these may be spin coupled to low, or more rarely higher, net spin for the complex. The two general divisions of spin-coupled complexes in transition metal and bioinorganic chemistry are (i) dinuclear (or polynuclear complexes); and (ii) metal complexes coupled to free radicals. These are often redox active catalytic centers which carry out some of the most difficult molecular reactions in biology. Where low or intermediate spin transition metal complexes are involved in catalytic cycles, spin crossover may well be part of the catalytic cycle. Because of the form of the exchange-correlation hole (see above), electrons of the same spin can avoid one another more efficiently than electrons of opposite spin. This leads to different electron distributions for the spin-up (α), and spin-down (β) electrons.

2.39.5 SPIN POLARIZED SYSTEMS

We begin by summarizing the energetics of some representative transition metal systems. The energetics of bond formation in transition metal complexes are governed in part by the valence state of the relevant transition metal ion. The $3d^{(n-1)}4s^1 \rightarrow 3d^n$ promotion energies of the first row transition metal series (M^+ cations) are relevant to the energetics of these ions in high-spin complexes since during bond formation 4*s* electrons are removed and replaced by *sd*-orbital hybridization with a smaller 4*s* contribution. We have calculated these promotion energies for the first row transition metal series ($Sc^+ - Cu^+$) using the BP86 GGA exchange-correlation potential and large basis sets.[31] The typical saw-toothed pattern of the experimental excitation energies is extremely well reproduced. After the experimental data is corrected for relativistic effects, the average error is 0.2 eV (5 kcal mol^{-1}) with a maximum error of 0.5 eV (11 kcal mol^{-1}); these excitation energies span a 5 eV range from -3.5 eV to $+1.5$ eV. Results of similar quality have been calculated by others using both GGA (BP86) and hybrid B3LYP.[32] Similarly, the ionization potentials (IPs) for gas phase $M^{2+,3+}$ (IP^{III}) and $M^{1+,2+}$ (IP^{II}) ionization have been calculated with errors of 0.5–1.0 eV, but now the energies are of the magnitude of 15–20 eV for IP^{II} and 25–40 eV for IP^{III}. These energies are far larger than comparable IPs of cationic transition metal complexes because of two factors: (i) metal–ligand bonding produces large electron relaxation effects, with substantial charge transfer from the ligands to the metal on oxidation. These effects are quite large on $M^{II} \rightarrow M^{III}$ oxidation; (ii) Either solvent, counterion, or protein environments drastically reduce IP_{red} for cationic complexes. For future reference, the conversion between IP_{red}(env) including the environment and the standard redox potential (E^0) versus a standard H electrode is:

$$E^0 = IP_{red}(env) + \Delta SHE \tag{19}$$

in electron volts (energy) or volts (potential), and where there is some uncertainty in the conversion constant $\Delta SHE = -4.43 \pm 0.05$ eV for a standard hydrogen electrode.

Turning now to transition metal complexes, we have calculated redox potentials for all the aqueous $M^{3+} \rightarrow M^{2+}$ ions of the first row transition metal series. The quantum cluster contained the finite $M(H_2O)_{18}{}^{2+,3+}$ complex surrounded by continuum solvent for Fe and Mn.[7,33] For the other metal ions in the series, we extrapolated the solvation energies by comparison of the $M(H_2O)_{18}{}^{2+,3+}$ with smaller $M(H_2O)_6{}^{2+,3+}$ clusters calculated by the same type of quantum chemistry. The average redox potential error was 0.20 eV (maximum 0.35 eV) out of a 2 eV range of known redox potentials. Further, very reasonable predictions of redox potentials were made beyond the currently observed range for Sc, Ti, Ni, Cu, and Zn. We also examined the coupled electron–proton transfer that occurs when Fe^{3+} and Mn^{3+} cations are reduced in aqueous solution at pH = 7, since at normal pH, one coordinated ligand is $(OH)^-$ which is then converted to H_2O.[26,33] The overall calculated coupled redox potential is 0.41 eV vs. 0.48 eV (exp.) for $Fe^{3+,2+}$, while for $Mn^{3+,2+}$ aquo system, the calculated redox potential 0.79 V shows a larger deviation from experiment 1.15 V, but still shows the proper qualitative trend compared to $Fe^{3+,2+}$. By contrast, the simple redox potential, relevant to the observed redox processes in highly acidic media give 1.59 V calculated (1.56 V, exp.) for $Mn^{3+,2+}$ aquo, and 0.77 V calculated (1.06 V, exp.) for $Fe^{3+,2+}$ aquo ions, so the Fe complex shows the larger error.[33] This is a consequence of partial cancellation of the pK_a (0.4 V or 9 kcal mol^{-1}) and simple redox errors in Fe aquo, while these errors add in the Mn aquo redox reaction. There are some conclusions of broad validity that may be drawn. For transition metal complexes in solution, both intrinsic errors in the DFT method, and the difficulty of representing a complicated environment must be dealt with together, and these problems are even more important when the transition metal complex is charged.

We have recently investigated large quantum clusters for the active sites of Mn and Fe superoxide dismutases (SODs) embedded in an electrostatic/dielectric description of the protein/solvent environment. Large quantum clusters are needed because this enzyme active site, like many others, contains an extended charged H-bond network. The coupled electron transfer/proton transfer to the metal bound (OH^-) is analogous to that in the metal-aquo complexes.[4,26] The $Fe^{3+,2+}$SOD coupled redox/protonation energy is quite good, while the $Mn^{3+,2+}$ SOD-coupled redox energy deviates substantially from experiment, by 0.65 eV. Part of this probably has the same origin as for the Mn aquo complex, but additional groups not included in the current quantum clusters, particularly tryptophan could affect the coupled redox/protonation properties. The Trp ring has the potential for a π-cation interaction with

the active site cluster.[34] Despite these quantitative deficiencies, coupled redox potentials for a series of homologous and mutant Mn SODs give a extremely good representation of experimental redox trends.[26]

Using the same method, we evaluated the hydration enthalpies of $Fe^{3+,2+}$ and $Mn^{2+,3+}$ aqueous ions. For Fe^{3+}, a close comparison can be made with the subsequent and careful study of Martin *et al*. for Fe^{3+} hydration using a $Fe(H_2O)_6{}^{3+}$ quantum cluster, B3LYP potential, and a Poisson equation continuum method for solvation, similar to the one we used but with different numerical methods.[35] The gas phase energy of formation in our work was $-652\,\mathrm{kcal\,mol^{-1}}$ while that for Martin *et al*. was $-670\,\mathrm{kcal\,mol^{-1}}$ (excluding zero point energy effects in both cases). The calculated solvation free energies were $-444\,\mathrm{kcal\,mol^{-1}}$ (Li *et al*.) vs. $-441\,\mathrm{kcal\,mol^{-1}}$ (Martin *et al*.).[33] The calculations disagree by only $15\,\mathrm{kcal\,mol^{-1}}$ (1.5 %) or $2.5\,\mathrm{kcal\,mol^{-1}}$ per average Fe^{3+}—(OH_2) bond. We have also examined the calculated binding energies for all $M^{II}(H_2O)_6$ and $M^{III}(H_2O)_6$ complexes of the first transition metal series using the BP86 xc (exchange-correlation) potential. The double bowl shape of the experimental hydration enthalpies is reproduced, and after accounting for solvation, the total hydration enthalpies are very reasonable, with errors per M^{II}–(H_2O) and M^{III}–(H_2O) in the range of 2.5–5.0 $\mathrm{kcal\,mol^{-1}}$. Further, these B88P86 calculations correctly predict that all of the hydrated metal ions will stay high-spin rather than low-spin in solution, except for Co^{III}. Only for Co^{III} is the low-spin state the experimental ground state, a result consistent with our calculations, which indicate a near degeneracy between HS and LS, but with LS slightly lower.

Finally, we want to emphasize the importance of spin-polarization for these and other high-spin systems on the energy level scheme for the molecular orbitals. Spin polarization in HS systems often leads to strong stabilization of majority spin metal levels, with ligand-based orbitals and then minority spin metal orbitals lying higher in energy, producing the inverted energy level scheme depicted in Figure 1, as confirmed also by photoelectron and optical spectroscopy.[31,36]

2.39.6 SPIN-COUPLED SYSTEMS: METAL-RADICAL SYSTEMS AND SPIN-COUPLED DINUCLEAR COMPLEXES

As in previous work, an antiferromagnetic (AF) spin-coupled state within DFT is represented by a "BS" state, where the spin-up (α) electron density occupies a different region of space from the spin-down (β) electron density.[14,37] These two densities are different, but there is usually overlap between them. This idea is broad enough to cover a number of different situations, encompassing metal–radical interactions and spin-coupled dinuclear and polynuclear transition metal complexes. (Ligand radicals are most often $S = 1/2$ as in semiquinones, tyrosine, or tryptophan radicals, but molecular oxygen is $S = 1$.) The integrated net spin density may sum to zero (when the ground state is a singlet, total spin $S_t = 0$), or nonzero (when the ground state has higher spin, for example $S_t = 1/2$, 3/2, 5/2, etc. or $S_t = 1$, 2, 3). In some cases, the spin-aligned high-spin (HS) state may be the ground state, and the broken symmetry state lies higher. Further, while typically the transition metal is in a high-spin state for each metal site, intermediate (IS) or low-spin (LS) metal sites are not precluded. One just needs to start with an appropriate guess at the spin density distribution; this is often best done by starting with a parallel spin aligned state, and then interchanging α with β electron densities on different metal and/or ligand sites as needed. This can usually be quite effectively done with the electron fit densities used in various programs (particularly in the Amsterdam Density Functional codes, ADF). If the broken symmetry state is not energetically favored (within a given exchange-correlation potential and at any given geometry), then the variational principle requires that the spin density disappears and the self-consistent-field (SCF) solution will converge instead to the ordinary nonbroken symmetry case.

To be concrete, we examine a dinuclear transition metal complex with the same metal ion and spin on each site. Then a BS state is constructed by the spin flip procedure and solution of the SCF problem. We will analyze the spin-coupling energy assuming a Heisenberg spin Hamiltonian of the form $H_{spin} = JS_1 \cdot S_2$, to determine the Heisenberg coupling constant J. The pure spin states form a Heisenberg ladder obeying the Lande interval rule, $E(S) - E(S-1) = JS$ for successive states, and with total spins ranging from $S_{min} = |S_1 - S_2|$, $S_{max} = |S_1 + S_2|$ in integer steps. For dominant AF coupling, the spin-coupling interactions give "spin-bonding" for BS, and "spin-

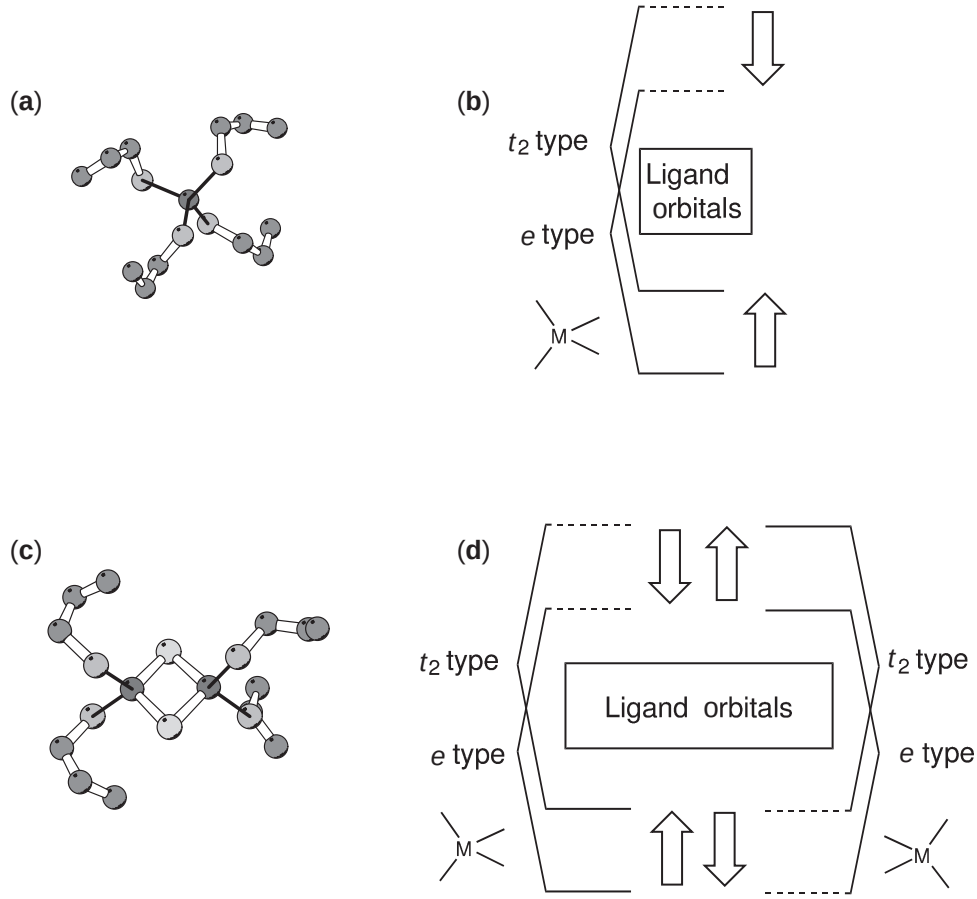

Figure 1 The inverted level scheme is shown for iron–sulfur monomer and dimer complexes. (a) $Fe(SR)_4$ complex. (b) Splitting into lower energy majority spin Fe 3*d* orbitals (spin-up), ligand orbitals (center), and higher energy mainly Fe 3*d*-based minority spin (ligand) field orbitals, with *e* below the t_2 type. (c) $Fe_2S_2(SR)_4$ complex. (d) Broken symmetry level structure containing similar spin-dependent and ligand field splitting to (b), but now with left–right spin localization for lower majority spin and higher minority spin Fe 3*d* levels. Note that the ligand field ordering with *e* below t_2 applies only to the minority spin orbitals, and the level ordering can be different for deeper majority spin orbitals.

antibonding" for the spin aligned HS state. In this dimer, the energy difference between HS and the singlet ground state is:

$$E(\mathrm{HS}) - E(S=0) = JS_{\max}(S_{\max} + 1)/2 \tag{20}$$

where $S^{\max}$ is the maximum total system spin. By contrast, the energy difference between HS and BS is

$$E(\mathrm{HS}) - E(\mathrm{BS}) = JS_{\max}^2/2 \tag{21}$$

The BS state is the "semiclassical analog" of the singlet ground state. The BS state is not a pure spin state; instead, it is a specific weighted average of pure spin states, and lies above the pure spin ground state when $E(S=0)$ is below $E(\mathrm{HS})$. To see this more clearly, we consider the expansion of $\Psi(\mathrm{BS})$ and the corresponding energy $E(\mathrm{BS})$ over pure spin states

$$\Psi(\mathrm{BS}) = \sum_S C(S)\Psi(S) \tag{22}$$

$$E(\mathrm{BS}) = \langle\Psi(\mathrm{BS})|H|\Psi(\mathrm{BS})\rangle = \sum_S C(S)^2 \langle\Psi(S)|H|\Psi(S)\rangle = \sum_S C(S)^2 E(S) \tag{23}$$

since the electronic Hamiltonian does not connect states of different total spin. In the weak metal–metal interaction regime, valid for most spin-coupled dimers, $C(S) = C_1(S)$, where $C_1(S)$ is a standard Clebsch-Gordon coefficient $C_1(S) = C(S_1S_2,S;M_1M_2)$, where S_1, S_2 are the principal spins of the two metal sites, and M_1, M_2 are their z components, specifying the spin alignment in the broken symmetry state. For nonequivalent spin sites, we need a more general equation for E(HS) – E(BS). Let S_A and S_B be spin quantum numbers for A and B subunits. Then using the spin algebra of raising/lowering operators acting on HS and BS,[38] we find

$$< S_A.S_B >_{HS,BS} = \pm S_A S_B \tag{24}$$

with the + and − signs for HS and BS respectively, and where the right-hand side involves only quantum numbers. Then

$$E(S_{max}) - E(BS) = 2JS_A S_B \tag{25}$$

This equation can be readily generalized to polynuclear complexes with multiple Heisenberg J parameters.

If the overlap of the magnetic orbitals (the orbitals that are different for α versus β spin) is larger, more general methods based on projected-unrestricted-Hartree–Fock (PUHF) methods can be used for transition metal–ligand radical, dinuclear complexes, or organic diradicals.[39,40] For organic diradicals, the question of whether symmetry breaks at the proper point along the reaction path for Cope rearrangements (sigmatropic shifts) has been investigated.[41,42] Depending on the systems studied, the authors concluded either that unrestricted UBPW91 performs better than UB3LYP, or that the two methods perform similarly and bracket the expected enthalpies of transition states and diradical intermediates.

An interesting case is the singlet–triplet problem, where a general solution is obtained valid from the weak coupling regime where $E(BS) = [E(S=1) + E(S=0)]/2$ to the strong coupling regime where the spin density vanishes $E(BS) = E(S=0)$.[43] The general singlet–triplet equation is:

$$E(BS) = [(1 + S_{ab}^2)E(S=0) + (1 - S_{ab}^2)E(S=1)]/2 \tag{26}$$

where S_{ab} is the spatial overlap of the two nonorthogonal magnetic orbitals (ϕ_a,ϕ_b for α and β spin), $S_{ab} \to 0$ gives weak coupling, $S_{ab} \to 1$ gives strong coupling. This flexibility is particularly valuable when following the potential energy surface (PES) as a bond is broken to produce a diradical. We have recently examined "twisted stilbene,"[43] and others have examined many other organic diradical systems.[39]

The BS plus spin projection method discussed here is closely connected to the simple open-shell singlet method for optical excitations based on the Slater sum rule and ΔSCF (self-consistent-field total energy difference method). The "mixed spin excited state" is like the BS state, also of mixed spin. The Slater sum rule method[44] is also quite effective for multiplet problems for excited states of transition metal complexes as shown in the work of Dahl and Baerends.[8,45]

Proceeding to mixed-valence dimers (as in diiron complexes with high-spin Fe^{2+}, Fe^{3+} sites), the higher total spin states can gain stabilization energy from a spin-dependent delocalization (SDD) mechanism (also called resonance delocalization or "double exchange")[10,46] with a spin Hamiltonian of the form $H_{spin} = JS_1 \cdot S_2 \pm B(S_{tot} + 1/2)$, while for lower total spin states (and for BS), vibronic coupling and solvent effects can quench the resonance term and leave only the Heisenberg spin coupling $JS_1 \cdot S_2$. Calculation of the BS and HS states is again feasible to extract J and B parameters. Further, the extension of these methods to polynuclear complexes (most prominantly $Fe_mS_n(SR)_p$) is straightforward.

Both $J(x)$ and $B(x)$ can be geometry dependent, as we have demonstrated, with the most important effects when J is fairly strong, and the E(HS) geometric minimum differs significantly from that of E(BS).[6,7] For $B(x)$, the clearest effects are observed in HS delocalized mixed-valence dimers including Fe_2S_2 and $Fe_2(OH)_3$ where $S_{tot} = 9/2$, and optical spectroscopy allows an assessment of $2B(x)(S_{tot} + 1/2)$. For $J(x)$, a more accurate evaluation would include the path dependence, both in calculations and in modeling of experimental magnetic susceptibility. From a theoretical perspective, if a path is traced from E(HS) to E(BS) in Cartesian steps (and somewhat beyond these limits), the bounds on $J_{path}(x)$ are $|J_{adiabatic}| < |J_{path}| < |J_{vert,BS}|$. The solvent and protein environment can also modulate the $J_{path}(x)$ over the path. It seems, however, that presently this is less important than the quality of the exchange-correlation potential in determining J.

2.39.7 GEOMETRIES OF TRANSITION METAL DIMER COMPLEXES

In Figure 2, we present the calculated optimized geometries of 11 ligand bridged transition metal complexes containing manganese–oxo, iron–oxo and –hydroxo, copper–oxo and –peroxo, and iron–sulfur type bridging sites and simple, but representative terminal ligands (simple amines and methyl-sulfide).[7,47] The simple VWN-Stoll exchange-correlation potential gives excellent geometries compared with related synthetic complexes. We note particularly that the dramatic changes in Cu—Cu distance for $Cu^{III}_2(\mu\text{-}O)_2$ versus $Cu^{II}_2(O_2^{2-})$ (peroxo) coordination (Complexes (**8**) and (**9**)) are well-portrayed, while for the iron systems, the contrasts between $Fe^{III}_2O(OAc)_2$, $Fe^{II}_2(OH)(OAc)_2$, and $Fe^{III}_2(OH)(OAc)_2$ (Complexes (**5**)–(**7**)) (OAc = acetate) are clearly in very good agreement with experiment. For the latter, protonation of complex $5 \rightarrow 7$ causes a larger change than $1e^-$ reduction, complex $7 \rightarrow 6$, in M–M distance. These predicted geometries are fairly representative of the quality of predictions for changes in protonation or redox for transition metal dimers, and applies to GGA type as well as to the simpler VWN-Stoll potential.

2.39.8 INTERACTION ENERGY WITH PROTEIN AND SOLVENT ENVIRONMENTS

Many transition metal complexes are polar and often charged so that there are strong interactions with the surrounding solvent and counterion environment.[7] For metalloproteins, the transition metal active site cluster may again be charged and often embedded in an extensive polar or charged protein network, with substantial interactions with aqueous solvent as well.[48] To evaluate these interactions, the active site quantum cluster may be represented as a charge distribution which interacts with its environment by both screened charge–charge and

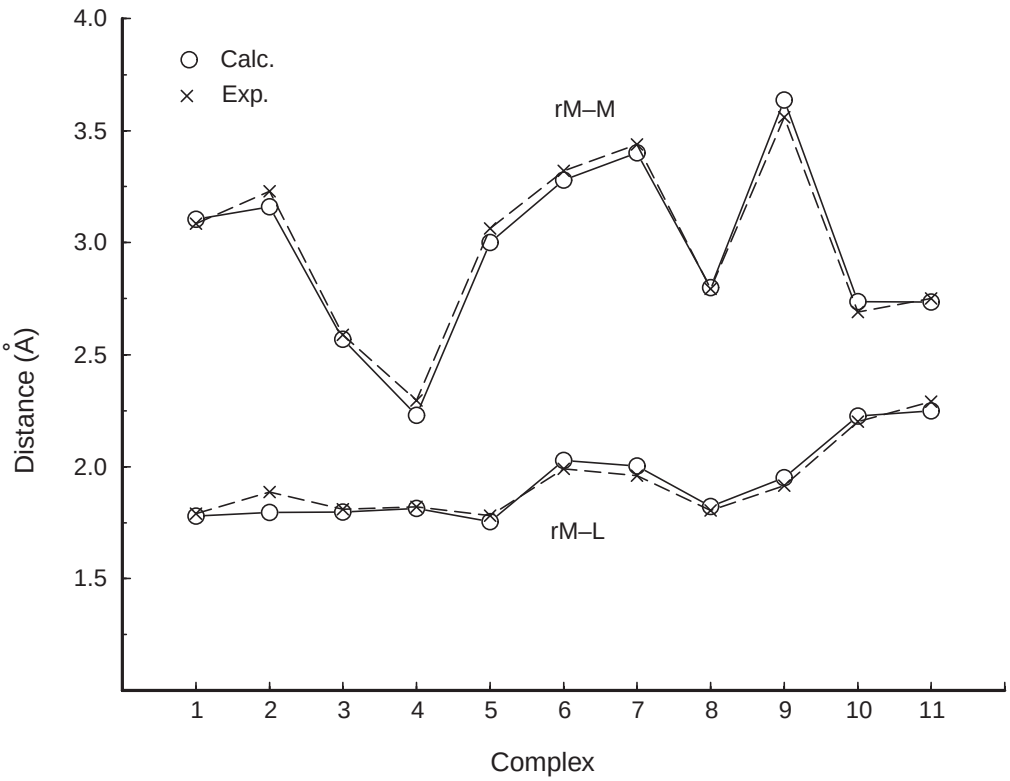

Figure 2 DFT calculated optimized geometries for 11 ligand-bridged transition metal complexes (VWN-Stoll potential) compared with related experimental synthetic systems. Metal–metal (rM–M) and metal-bridging ligand (rM–L) distances are given. The core complexes are; (**1**) $[Mn^{III}_2O(OAc)_2]^{2+}$; (**2**) $[Mn^{III}Mn^{IV}O(OAc)_2]^{3+}$; (**3**) $[Mn^{III}Mn^{IV}O_2(OAc)]^{3+}$; (**4**) $[Mn^{IV}_2(\mu\text{-}O)_3]^{2+}$; (**5**) $[Fe^{III}_2O(OAc)_2]^{2+}$; (**6**) $[Fe^{II}_2(OH)(OAc)_2]^{+}$; (**7**) $[Fe^{III}_2(OH)(OAc)_2]^{3+}$; (**8**) $[Cu^{III}_2(\mu\text{-}O)_2]^{2+}$; (**9**) $[Cu^{II}_2(O_2)]^{2+}$; with simple $(NH_3)_3$ as terminal ligands to each metal ion in the calculations, and tridentate nitrogen ligands in the synthetic analogs. For iron–sulfur complexes: (**10**) $[Fe^{III}_2S_2(SR)_4]^{2-}$; (**11**) $[Fe^{II}Fe^{III}S_2(SR)_4]^{3-}$; where $(SR)^- = (S\text{-methyl})^-$ in the calculations, and organic thiolates (complex (**10**)), or cysteine (complex (**11**)). See Li and Noodleman (1998).[7]

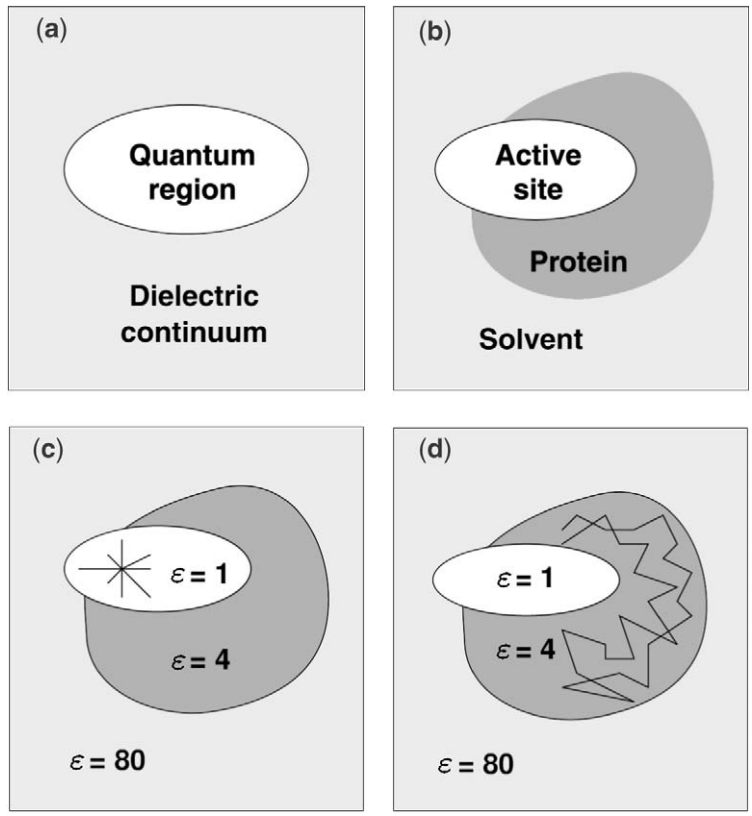

Figure 3 Schematic partitioning of space and assignment of different dielectric regions. (a) Quantum region vs. continuum solvent; (b) three region model: active site (quantum region); protein, and solvent; (c) dielectric model for (b) showing generating charges for reaction field potential from the quantum cluster (d) same dielectric model showing protein generating charges for the protein field potential.

charge–polarization energies, with the latter arising from dipolar polarization of the solvent and protein dielectric media. Figure 3 shows a schematic representation of these interactions. The effective cluster charge distribution is determined from an ESP outside a van der Waals envelope around the quantum cluster. The protein is considered as a dielectric medium with embedded charges with the protein partial charges usually extracted from some force field model or other models that give good solvation energies.[49] The interaction energies arise from a reaction field energy E_{react} for the dielectric response to the cluster ESP charges, while the protein field energy E_{protein} gives the screened charge–charge interactions of the protein charges with the cluster charges. Appropriate potentials are constructed by solutions of the Poisson–Boltzmann equation. The simplest version of this method, called the "single step" (or "rigid charge") method evaluates these energies after a gas phase quantum calculation and quantum ESP charge fitting.[50] A more complicated method allows the protein and reaction field potentials to be added to the DFT Hamiltonian and iterated to self-consistency, giving a self-consistent-reaction-field (SCRF).[48,50]

Some examples of the use of these methods for iron–sulfur complexes will be discussed later. The methods have utility for redox potentials,[48] pK_a calculations,[27] reaction path energetics,[50,51] and understanding how surrounding protein side chains (or main chains) can stabilize an active site cluster electronically or geometrically.[52]

2.39.9 IRON-OXO DIMER PROTEINS

We will compare some aspects of the reaction pathway and properties of the O_2 carrier protein hemerythrin (Hr) with the early parts of the reaction cycles of the structurally related enzymes methane monooxygenase hydroxylase (MMOH) and ribonucleotide reductase (RNR). A general structural comparison of these three proteins is given in Figure 4 for the diferric and diferrous

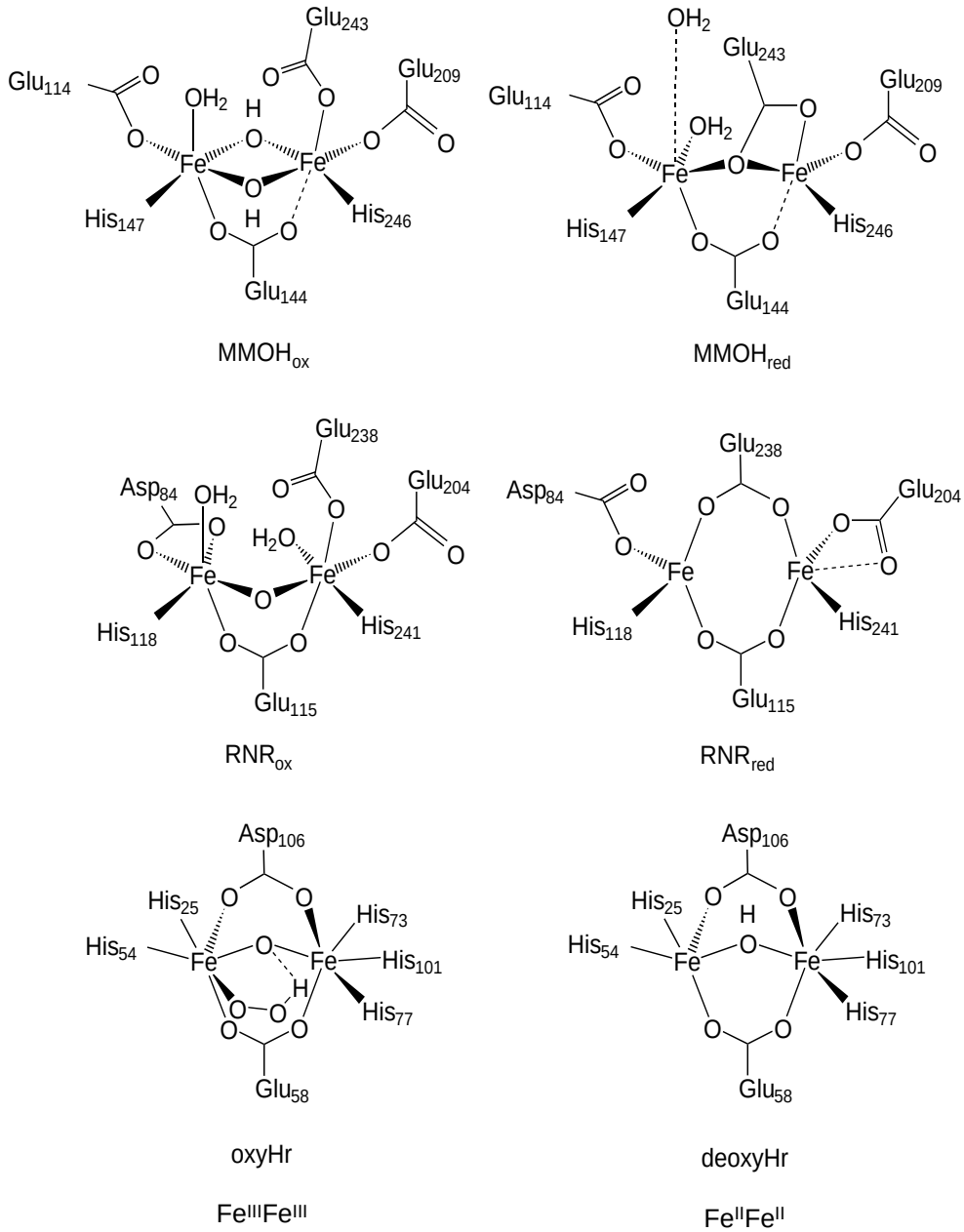

FeIIIFeIII

FeIIFeII

Figure 4 Active site structures and corresponding oxidation states for iron-oxo dimer proteins: methane monooxygenase (MMOH); ribonucleotide reductase (RNR); and hemerythrin (Hr).

forms.[53–55] Hemerythrin functions as a reversible carrier for molecular oxygen, while MMOH and RNR undergo redox-dependent cluster activations which then prepare the active sites for subsequent reactions with molecular oxygen and then with substrates by producing high-valent iron-oxo (or oxo, hydroxo) intermediates. MMOH hydroxylates methane to methanol, and can perform hydroxylation and other quite diverse transformations on a variety of hydrocarbons. The iron-oxo dimer site of RNR generates a stable tyrosine radical, which then serves as a catalytic radical transfer site for reduction of ribonucleotides to deoxyribonucleotides.

In contrast to MMOH and RNR, Hr has the diferrous form as the "resting unreacted" state, and there is a single five-coordinate site for end-on binding of O_2. After O_2 binding, a Fe end-on bound hydroperoxide $(OOH)^-$ intermediate is formed, with the iron centers becoming diferric. In Hr, the O_2 binding step occurs comparatively earlier, and the oxidation states of the first two intermediates are reversed compared to RNR and MMO. The resting states of both are diferric

($MMOH_{ox}$, RNR_{ox}) and the interaction with reductases allows the formation of the diferrous forms after net two-electron transfer and coupled protonation. These reactions open up the active sites of MMOH and RNR for initial bidentate coordination to 2Fe and reaction with molecular oxygen driving the reaction further into the catalytic cycle. As can be seen by comparing the diferrous and diferric structures of RNR and MMO, along with computational analysis of likely reaction steps along these paths, the activation of the 2Fe sites involves both electronic charge transfer and protonation of the bridging $(OH)^-$ in MMO, and μ-O in RNR with the pathway facilitated by protonation of a nearby monodentate glutamate residue. This is the same Glu that undergoes a carboxylate shift to μ1,1 OCO bidentate in MMOH and μ1,3 OCO bidentate in RNR.

Based on Brunold and Solomon's combined DFT and spectroscopic work,[54,55] the reaction pathway of Hr can be followed in some detail (see Figure 5). The deoxyHr form has a resting diferrous oxidation state that can donate electron density to the O_2 as it binds. The single bridging OH^- of deoxyHr transfers its proton to stabilize the developing end-on peroxide from O_2; the bound hydroperoxide can still form a hydrogen bond to the remaining bridging oxo of the $Fe^{III}OFe^{III}$ unit. The high covalency of the bridging diferric-oxo unit allows for a stable intermediate. In the diferric oxyHr, the stronger AF coupling compared to diferrous deoxyHr provides part of the driving force for O_2 binding, an effect estimated as about 6.6 kcal mol^{-1} comparing the high-spin with the $S=0$ state of oxyHr. This is based on the experimental J coupling, which is in reasonable qualitative agreement with the calculated J coupling for a simplified model. Considering the O_2 dissociation process, the presence of a very weakly coupled manifold of deoxyHr spin states with $S_{tot}=0$–4 and the product triplet $O_2(^3\Sigma_g^-)$ (formed from the bonded O_2 ($^1\Delta_g$ state) allows for a more pronounced barrier with a crossover between the $S_{tot}=0$ state of oxyHr and the family of deoxyHr spin states.

The protonation states of these systems play important roles in the chemical transformations along the reaction pathways, but these are difficult to examine directly via X-ray crystallography in the absence of very high-resolution structures. Even here, only some states of a reaction cycle may be available. It is therefore valuable to examine theoretical calculations both of active site geometries and of Heisenberg J couplings, which reflect the coordinating ligands, the protonation state of bridging (OH_n) groups, and the Fe site oxidation states. Evalution of pK_as by combined DFT and electrostatics methods further clarifies the picture of protonation states for MMOH. These computational results can be compared with spectroscopic observations and X-ray structures of synthetic model systems as well as protein structures.

Table 1 shows how Heisenberg J parameters calculated for different Fe oxidation states and bridges compare with experiment. The diferric-oxo AF couplings are much stronger than

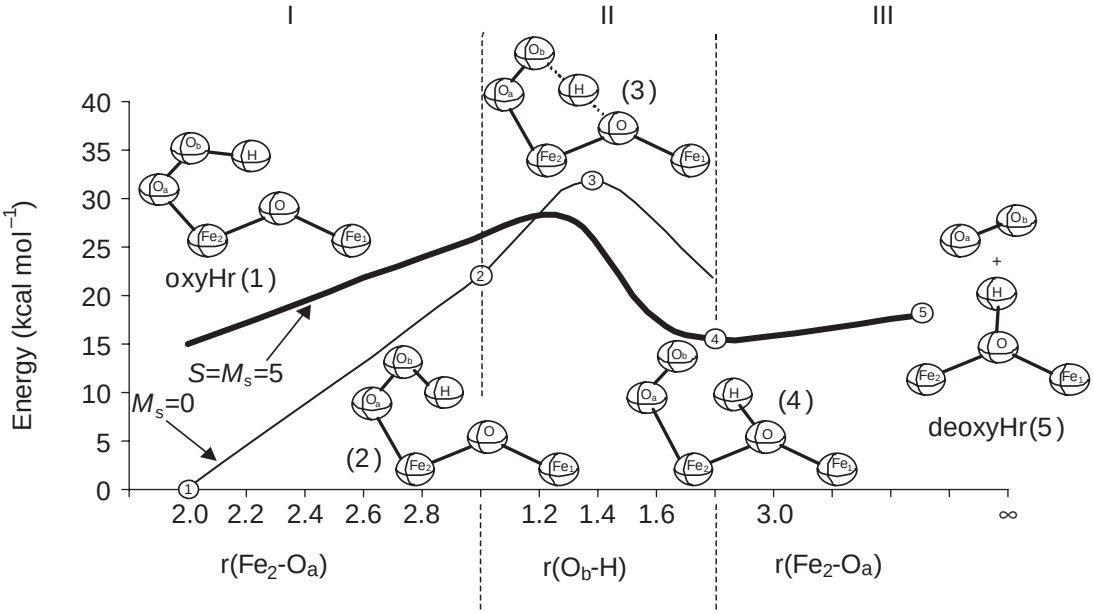

Figure 5 Reaction pathway of oxygen binding to hemerythrin. Adapted and simplified from Brunold and Solomon (1999).[54,55]

Table 1 Heisenberg J coupling parameters for iron-oxo dimer complexes ($H = -2JS_1 \cdot S_2$).

System	*Fe state*	*Bridge*	J(calc.)	J(exp.)	*Potential*[a]
oxyHr	Fe^{III}_2	O	−214	−77	BP86
MMOH(ox)	Fe^{III}_2	$(OH)_2$	−35	−4 to −10	PW91
RNR(ox)	Fe^{III}_2	O	−130	−90 to −108	PW91
deoxyHr	Fe^{II}_2	OH	7	−14	BP86
RNR(red)	Fe^{II}_2	*	13	−0.5	PW91
MMOH(red)	Fe^{II}_2	*	32	+0.35	PW91

* Carboxylate bridges only. [a] BP86 from Brunold and Solomon.[54,55] PW91 from Lovell *et al.*[53,56]

diferric-hydroxo type, while the diferrous couplings are generally weaker still. The protonation state of the bridging oxygen ligands is also strongly reflected in the iron-bridging oxygen bond lengths as we have demonstrated in Lovell *et al.*[52,53,56] Based on evaluation of protonation energetics and tautomeric states, as well as orbital and structural analysis, we proposed the carboxylate shift mechanism in Figure 6 for the proton coupled two-electron redox process which gives the diferrous MMOH(red) state. The proton is carried by Glu243 as it undergoes the carboxylate shift. The energetics of the subsequent steps of the reaction cycle have been considered by a number of groups. It is important to assess both structures and spectroscopic properties of predicted intermediates by comparison of calculated structures and properties with experiment.[57] These comparisons will further test the intermediates and related transition states that have been proposed based on calculated DFT energies.[5,58–60]

2.39.10 IRON–SULFUR COMPLEXES

Iron–sulfur proteins are very widespread electron transfer (eT) agents in nearly all organisms, functioning in the electron transport chain in mitochondria, in photosynthetic electron transport, and in bacterial electron transport.[37,61] Also, eT may be coupled to proton transfer (pT) with significance for energy transduction for some complexes in these systems. In addition, redox reactions can be part of catalytic transformations, involving single or multiple electrons. For these reasons, it is important to understand the fundamental basis for the general range of redox potentials comparing different cluster types and oxidation states, as well as the narrower variations in potentials among fairly homologous proteins or mutants. A connection can also be drawn between redox properties of FeS proteins, and analogous properties of related synthetic FeS clusters, which helps to isolate the distinctive effects of the protein environment compared to "simpler" solvent media. Electronic structure and spin coupling are closely linked to redox problems as well.

Several groups have conducted extensive analyses of electronic structures, properties, and geometries of iron–sulfur complexes as well as redox and protonation energetics.[38,48,51,62–64] In Figure 7, we present schematically, the typical spin-coupling and localization/delocalization structures seen for oxidized and reduced 1Fe−, 2Fe−, and 4Fe−sulfur-containing complexes. The specific cluster compositions are: $[Fe(SR)_4]^{1-,2-}$, $[Fe_2S_2(SR)_4]^{2-,3-}$, and $[Fe_4S_4(SR)_4]^{2-,3-}$. The high-potential $[Fe_4S_4(SR)_4]^{1-,2-}$ is also fairly common, and there is recent interest also in the highly reduced $[Fe_4S_4(SR)_4]^{3-,4-}$ couple. (By convention, the clusters are often referred to by the oxidation state of the core unit, omitting the $(SR)^-$ groups from the charge count.) The $(SR)^-$ group can represent deprotonated *S-Cys*$^-$ or various organic thiolates in synthetic analogs. The 2Fe cluster is typically trapped valence for the additional electron of the reduced form, but there is a Cys → Ser mutant form having a physical mixture of delocalized $S_{tot} = 9/2$ with $S_{tot} = 1/2$ states. The 4Fe clusters by contrast typically have one or more delocalized mixed-valence pairs, depending on the cluster oxidation state. The state depicted pictorially is $[Fe_4S_4(SR)_4]^{2-}$, which has four nearly equivalent $Fe^{2.5+}$ sites, divided into two delocalized mixed valence $Fe^{2.5+}$–$Fe^{2.5+}$ pairs, each internally with parallel spin vectors, and with opposite AF spin alignment for the top versus bottom pairs. It is clear from the nature of the "resonance delocalization" energy that electron delocalization is energetically facilitated by having parallel spin Fe sites. Having two pairs of such sites allows for four antiferromagnetic Fe–Fe pairs and two ferromagnetic pairs. Thus the number of AF coupling interactions is maximized with no cost to pairwise electron delocalization. With one electron more (or less), there is only one delocalized mixed-valence pair

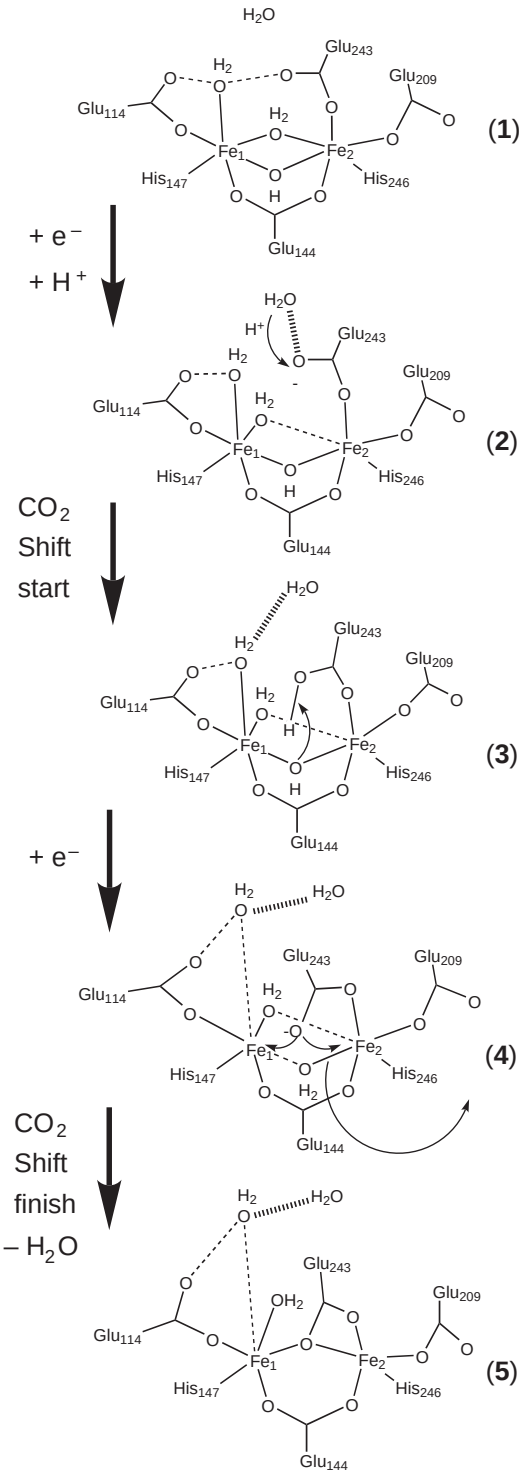

Figure 6 The carboxylate shift mechanism proposed for the two-electron–one-proton transition from $MMOH_{ox}$ to $MMOH_{red}$ (adapted from Lovell *et al.*, 2001).[56]

at the cost of some energy (loss of a B term energy). By contrast, in reduced 2Fe2S clusters, the delocalization allowed by having parallel spin vectors is directly opposed the Heisenberg interaction, strongly favoring AF spin alignment. The usual state is then trapped valence $S_t = 1/2$ with only minor partial delocalization, the Cys → Ser mutant with $S_{tot} = 9/2$ being the exception (in a physical mixture with $S_t = 1/2$), possibly due to a diminished J parameter (smaller AF coupling term). In 4Fe reduced clusters, there is a single delocalized $2Fe^{2.5+}$ pair and an alternate $2Fe^{2+}$

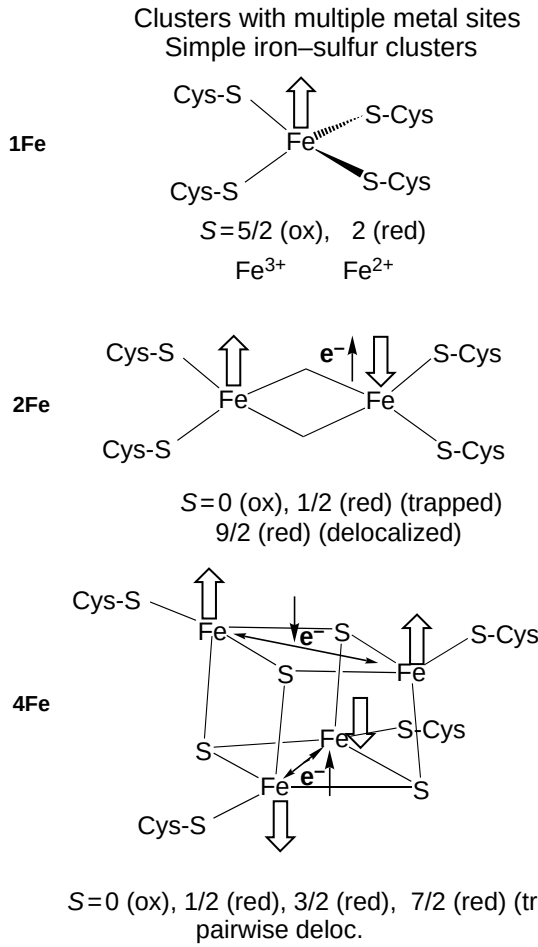

Figure 7 1Fe–, 2Fe–, and 4Fe–sulfur clusters in oxidized and reduced states showing electron trapping or delocalization. Large arrows show main spin vectors, while the small arrows (labeled e^-) depict minority spin Fe 3*d* electrons (reprinted from Noodleman *et al.*[37] with permission from Elsevier from *Curr. Opin. Chem. Biol.*, **2002**, *6*, 259–273).

pair. If these interact mainly through a Heisenberg AF coupling interaction, the $S_{tot} = 1/2$ state results. If there is substantial resonance delocalization between the $2Fe^{2.5+}$ pair and the $2Fe^{2+}$ pair, an $S_{tot} = 3/2$ state often results, from competition of the interlayer resonance B term with the Heisenberg interaction which favors $S_{tot} = S_{min} = 1/2$. By contrast, the purely trapped valence $S_{tot} = 7/2$ spin state, formally composed from $3Fe^{2+}$ and $1Fe^{3+}$ site is rare (seen for example in Se-substituted clostridial 4Fe ferredoxins), and probably depends on some cluster distortion (Se is somewhat larger than the S that is substituted at the core cluster sites). However, the $S_{cubane} = 7/2$ motif is much more common in superclusters containing 8Fe or 7Fe1Mo as seen in the Fe_8S_7 and $MoFe_7S_9$ core clusters of the P cluster (oxidized) and the MoFe cofactor centers in nitrogenase, respectively.[37] Here, cluster distortions and links between the component cubanes are significant.

We now examine trends in redox potentials between 1Fe–, 2Fe–, and 4Fe–sulfur complexes, and comment on the important energy contributions. Our first paper on redox trends in model Fe–S clusters in solution across different cluster types and redox couples is Mouesca *et al.* (1994),[38] with a follow-up analysis by Mouesca and Lamotte (1998).[65] More recently, we have extended these calculations to iron–sulfur complexes in complete protein/solvent environments using both single-step Poisson–Boltzmann-based methods for the protein and solvent environment for 4Fe4S (Torres *et al.* 2003),[66] to proton-coupled electron transfer in the Rieske 2Fe2S protein (containing a $(CysS)_2FeS_2Fe(NHis)_2$ type active site, Ullmann *et al.*, 2002),[51] and to more complicated SCRF methods in some cases for 2Fe2S ferredoxin type centers with terminal SCys coordination (Li *et al.*, 1998),[48] (Liu *et al.*, 2003, in preparation).

There has also been a considerable effort to predict redox potential shifts among fairly homologous proteins with the same cluster type and redox couple.[67] These can be examined by

full combined electronic structure plus Poisson–Boltzmann methods (as above),[68] or more simply by the electrostatics based methods alone,[69] once good cluster charges are obtained for both oxidation states. Usually these charges are obtained from electronic structure calculations, and subsequent charge fitting to the ESP. The latter methods have been shown to have value for comparing redox shifts due to different H-bonding networks and extent of solvent access, but they cannot be used to compare different cluster types or redox couples. They can, however, be extended to include protein and solvent structure and dynamics.[70,71]

Returning to the general theme, we can ask how different electronic contributions to the redox potential compare with environmental protein and solvent effects, and which of these (if any) is decisive for various trends. The electronic term is clearly complicated, and it is helpful to separate off the spin-coupling part of this by examining the Heisenberg (J term) and resonance delocalization (B term) parts. To get a proper reference state where the J term is "turned off", we consider the "spin nonbonding" state to be the spin barycenter, the spin multiplicity $(2S_{\text{tot}}+1)$ weighted average of the Heisenberg spin states. The B term(s) are easily "turned off" for resonance delocalized pairs of a spin-coupled system.[38,65,72] Referring Heisenberg spin-coupling energy of the ground state to the "spin nonbonding" state, and the corresponding resonance B term energy to the state where this interaction is "turned off", we obtain redox energy terms ΔJT and ΔBT (JT means "J term", BT means "B term"). The redox potential of a cluster in a solvent environment takes the form

$$E_0 = E(\text{vac})^0_{\text{uncoupled}} + \Delta E_{\text{PB}} + \Delta JT + \Delta BT \tag{27}$$

where $E(\text{vac})^0_{\text{uncoupled}} = IP(\text{red})_{\text{uncoupled}} + \Delta(\text{SHE})$ is the spin-uncoupled redox energy in vacuum, ΔE_{PB} is the solvation contribution from the Poisson–Boltzmann equation for the cluster in the dielectric environment, and ΔJT, ΔBT are the spin coupling terms above. The most interesting and surprising results can be qualitatively summarized: ordering experimental redox potentials from the most negative to the most positive we see: $2\text{Fe}(2\text{-},3\text{-}) \leq 4\text{Fe}(2\text{-},3\text{-}) < 4\text{Fe}(1\text{-},2\text{-})$ (indicating the number of Fe sites and true cluster charge). This is the expected ordering if redox potentials were governed by electron–electron ($e^- - e^-$) repulsion which increases with the cluster charge (roughly as $(Q^2_{\text{red}} - Q^2_{\text{ox}})$ and with decreasing cluster size (as $1/R_{\text{eff}}$, with R_{eff} an effective radius. However, the equivalent e–e repulsion-like term theoretically is $E(\text{vac})^0_{\text{uncoupled}}$ which has the same ordering of clusters, but gives extremely negative redox potentials with enormous differences between the successive clusters. By contrast, the solvation redox term ΔE_{PB} is also extremely large (from +8.4 eV to +7.6 eV to +4.6 eV) and nearly compensating for these same clusters. Adding these two terms alone gives a much smaller theoretical span in redox potentials than seen from experiment, and with some redox couples in the wrong order. The agreement in the ordering of redox potentials (and sensible if not precise agreement in their values) is restored only after addition of the spin coupling terms $\Delta JT + \Delta BT$. For the 4Fe(2-,3-) versus the 4Fe(1-,2-) couple, the largest effect is due to ΔBT, which makes the 4Fe(2-,3-) couple about −0.5 eV more negative, and 4Fe(1-,2-) about + 0.5 eV more positive because 4Fe(2-) has two delocalized mixed valence pairs while 4Fe(3-) and 4Fe(1-) each have one. The ΔJT term is also quite significant for these same clusters. Overall, all the relevant terms in the equation above are large, and what is most important depends on the problem being examined. In our early work, the overall redox potential errors compared to experiment in synthetic systems were in the range of 0–0.5 eV for 1Fe (1-,2-), 4Fe clusters 4Fe(1-,2-), 4Fe(2-,3-) and similarly about 0.4–0.5 eV for 2Fe(2-,3-). These calculations did not include geometry optimization, and only synthetic rather than protein systems were studied. In very recent work on 4Fe clusters (Torres *et al.*, 2003) with geometry optimization (BP86 potential) and considering clusters both in solvent and in protein environments, the overall redox error was reduced to typically 0.1–0.3 eV (2–5% of $\Delta E_{\text{react}} + \Delta E_{\text{protein}}$). The correct typically positive shift from synthetic clusters to clusters in protein environments was obtained, and redox shifts between homologous proteins for the same redox couple were fairly well reproduced provided the experimental difference was not too small >0.1 eV.

Similarly, for 2Fe(2-,3-) clusters in protein environments, the redox shift between Anabaena ferredoxin (a single domain protein) and phthalate dioxygenase reductase (PDR, a three-domain protein which is reasonably homologous in the first domain) was reasonably reproduced; PDR has a more positive potential by about 0.2 eV and the theoretical shift prediction is close to this, whether by a single cycle Poisson–Boltzmann calculation or with more elaborate SCRF methodology. This redox shift can be traced mainly to one additional strong N—H—S hydrogen bond

that occurs in PDR, while the analogous potential H bond cannot happen in Anabaena ferredoxin because of the position of the peptide backbone. The redox energy contributed by the nearby 8 or 9 N—H—S hydrogen bonds (involving both inorganic S and CysS) is substantial 0.8 to 1.1 eV (called $\Delta E_{\text{protein}}$), but this is far less than the enormous reaction field contribution, 7.5 to 7.6 eV (ΔE_{react}), associated with solvent and protein dielectric polarization (dominated largely by orientational polarization of the solvent and protein). Nonetheless, the difference between the PDR and ferredoxin proteins is largely due to this difference in peptide group to sulfur H-bonding since the protein shapes in the homologous domain and solvent access are evidently quite similar. We have recently reexamined this redox problem with improved SCRF methods and including also much larger quantum clusters. Now much better X-ray structures are available for Anabaena ferredoxin than previously. While the redox shift predictions are of similar accuracy to those obtained previously, and the active site geometries are better, the absolute redox potentials still deviate considerably 0.5–0.6 eV from experiment. This is perhaps not too surprising since this error is about 7% of $\Delta E_{\text{react}} + \Delta E_{\text{protein}}$.

The Rieske 2Fe2S center is part of the cytochrome bc_1 complex in the electron transfer chains of mitochondria and bacteria, and there are similar b_6f complexes in chloroplasts and algae. The bc_1 complex couples electron transfer from ubiquinol to proton translocation via the proton motive Q cycle originally proposed by Mitchell. Our DFT calculations (PW91 potential) in the protein environment,[51] in agreement with experimental measurements,[73] show that the redox potential is pH dependent, and involves protonation of the two histidines bound to one Fe site (the same Fe being reduced). The predicted pK_a of these histidines, 6.9 and 8.8 for oxidized (but involving both His), and 11.3, 12.8 for the reduced system are in very good agreement with experimental values, 7.5 and 9.2 (oxidized), and >10 (reduced). The DFT predicted redox potential is about 0.32 eV more negative than the experimental redox potential at low pH, which is reasonable and consistent with results in related systems.

We should also mention a very surprising redox potential result for the complicated active site of the FeMo cofactor of nitrogenase having a $MoFe_7S_9$ type core.[74–76] Here our DFT (BP86) calculations for the $M_{OX} \rightarrow M_N$ resting state redox potential give a value much more positive than experiment by 0.8 eV, which is very anomalous compared to all other iron–sulfur clusters studied. A possible explanation for this anomaly has recently emerged: the Rees group has found a previously undetected atom (possibly nitrogen) at the center of the MoFe cluster which is observed only with very high resolution X-ray crystallography.

2.39.11 METAL–LIGAND RADICAL SYSTEMS

There is a large and growing literature on metalloenzymes with ligand radical intermediates. A number of broken symmetry DFT studies have been made of Compound I systems: high-valent $Fe^{IV}=O$ (ferryl) ($S=1$) heme intermediates coupled to either a porphyrin radical ($S=1/2$), or alternatively axial ligand radicals, including tryptophan, cysteine, or tyrosine as possibilities. Histidine is also an axial ligand, but not usually a radical. Spin coupling is an important indicator of the nature of the electronic state and for comparison with experimental magnetic properties.[77–80] The enzymes studied include several distinctive peroxidases, cytochrome P450s, and catalase. Whether the axial ligand forms a ligand radical in place of the porphyrin can depend on a number of factors, particularly on H-bonding which can stabilize the spin paired form. These factors are important in the energetics of the catalytic cycle.

Many other metalloenzymes with associated or coupled ligand radicals are known. Himo *et al.*[4,81] have studied the catalytic cycle of galactose oxidase where a Cu^{II} center is spin coupled to a bound tyrosine radical in the substrate binding state. After proton transfer to the Tyr-O in the first step of the catalytic cycle, the radical center moves to the Cu^{II} bound tyrosine which is cross-linked to cysteine-S. In subsequent steps of the reaction, the ligand radical is propagated to the substrate, and the Cu is reduced to Cu^{I} by e^- transfer. Then, a reaction with O_2 regenerates the Cu^{II}-tyrosine radical starting state.

2.39.12 CONCLUSIONS

Our goal has been to outline the general framework of DFT and to illustrate these principles with applications to geometries, electronic structures, energetics, and reaction pathways for transition

metal complexes. We have emphasized in particular dinuclear and polynuclear complexes, and coupled metal–ligand systems. The protein and solvent environment in metalloenzymes can often exercise an important stabilizing influence. For example, iron–sulfur complexes would very likely not be stable at all in the absence of the protein/solvent environment (or solvent/counterions for related synthetic analogues). Further, the protein/solvent can direct reactivity along particular pathways, often influenced by H-bonding and proton transfer. The accuracy of current DFT generalized gradient methods and hybrid DFT-HF methods is often quite good for identifying and systematizing important energetic features of redox active enzymes and for distinguishing feasible from unlikely reaction pathways. The typical quantitative accuracy of these methods, very roughly 2–9 kcal mol^{-1} for GGA-DFT (BP86, BLYP, PW91, BPW91) with the last three somewhat more accurate in recent studies, and 2–5 kcal mol^{-1} for hybrid DFT-HF methods (B3LYP) can be improved even further. There is an ongoing effort to improve both GGA and hybrid methods from a careful analysis of exchange, correlation, and kinetic energy terms, and from careful selection of families of molecules as test cases. More attention could be paid to this same strategy in the context of spin-coupled transition metal complexes.

ACKNOWLEDGMENTS

We want to thank our collaborators D. A. Case and D. Bashford and former group members J. Li, J. L. Chen, G.M Ullmann, and J.-M. Mouesca for their contributions to the work reviewed here. This work was supported by NIH Grants GM43278 and GM39914.

2.39.13 REFERENCES

1. Kohn, W.; Becke, A. D.; Parr, R. G. *J. Phys. Chem.* **1996**, *100*, 12974–12980.
2. Velde, G. T.; Bickelhaupt, F. M.; Baerends, E. J.; Guerra, C.; Fonseca; van Gisbergen, S. J. A.; Snijders, J. G.; Ziegler, T. *J. Comp. Chem.* **2001**, *22*, 931–967.
3. Koch, W.; Holthausen, M. C. *A Chemist's Guide to Density Functional Theory*; Wiley-VCH, Weinheim, Germany, 2001.
4. Lovell, T.; Himo, F.; Han, W.-G.; Noodleman, L. *Coor. Chem. Rev.* **2003**, in press.
5. Siegbahn, P. E. M.; Blomberg, M. R. A. *Annu. Rev. Phys. Chem.* **1999**, *50*, 221–249.
6. Springborg, M., Ed., *Density Functional Methods in Chemistry and Materials Science*; Wiley: New York, 1997.
7. Li, J.; Noodleman, L. Electronic Structure Calculations; Density Functional Methods for Spin Polarization, Charge Transfer and Solvent Effects in Transition Metal Complexes. In Solomon, E. I.; Hodgson, K. O., Ed., *ACS Symposium Series 692: Spectroscopic Methods in Bioinorganic Chemistry*, American Chemical Society: Washington, DC 1998, pp 179–197.
8. Daul, C.; Baerends, E. J.; Vernooijs, P. *Inorg. Chem.* **1994**, *33*, 3538–3543.
9. Adams, D. M.; Noodleman, L.; Hendrickson, D. N. *Inorg. Chem.* **1997**, *36*, 3966–3984.
10. Noodleman, L.; Baerends, E. J. *J. Am. Chem. Soc.* **1984**, *106*, 2316–2327.
11. Van Gisbergen, S. J. A.; Groeneveld, J. A.; Rosa, A.; Snijders, J. G.; Baerends, E. J. *J. Phys. Chem. A* **1999**, *103*, 6835–6844.
12. Baerends, E. J.; Gritsenko, O. V. *J. Phys. Chem. A* **1997**, *101*, 5383–5403.
13. McWeeny, R. *Methods of Molecular Quantum Mechanics*, 2nd ed.; Academic Press: San Diego, 1992; pp 45–50, 371–387.
14. Noodleman, L.; Case, D. A. *Adv. Inorg. Chem.* **1992**, *38*, 423–470.
15. Lowdin, P. O. *J. Mol. Spectr.* **1959**, *3*, 46–66.
16. Darvesh, K. V.; Boyd, R. J. *J. Chem. Phys.* **1987**, *87*, 5329–5332.
17. Slater, J. C. *The Self-consistent Field for Molecules and Solids: Quantum Theory of Molecules and Solids*; McGraw-Hill: New York, 1974.
18. Becke, A. D.; In Salahub, D. R.; Zerner, M. C., Ed., *The Challenge of d and f Electrons*, American Chemical Society: Washington, DC, 1989, 165–179.
19. Stoll, H.; Pavlidou, C. M. E.; Preuss, H. *Theoret. Chim. Acta* **1978**, *149*, 143–149.
20. Perdew, J. P. *Phys Rev. B* **1986**, *33*, 8822–8824.
21. Perdew, J. P. *Phys. Rev. B* **1986**, *34*, 7406.
22. Perdew, J. P.; Wang, Y. *Phys. Rev. B* **1992**, *45*, 13244.
23. Cohen, A. J.; Handy, N. C. *Chem. Phys. Lett.* **2000**, *316*, 160–166.
24. Eriksson, L. A.; Petterson, L. G. M.; Siegbahn, P. E. M.; Wahlgren, U. *J. Chem. Phys.* **1995**, *102*, 872–878.
25. Ziegler, T. *Can. J. Chem.* **1995**, *73*, 743–761.
26. Han, W.-G.; Lovell, T.; Noodleman, L. *Inorg. Chem.* **2002**, *41*, 205–218.
27. Konecny, R.; Li, J.; Fisher, C. L.; Dillet, V.; Bashford, D.; Noodleman, L. *Inorg. Chem.* **1999**, *38*, 940–950.
28. Becke, A. D. *J. Chem. Phys.* **1993**, *98*, 5648–5652.
29. Neese, F. *ORCA— an ab initio, Density Functional and Semiempirical Program, Version 2.1* Max Planck Institut für Strahlenchemie, Mülheim, Germany, 2001.
30. Friesner, R. A.; Beachy, M. D. *Curr. Opin. Struct. Biol.* **1998**, *8*, 257–262.

31. Li, J.; Noodleman, L.; Case, D. A.; In Solomon, E. I.; Lever, A. B. P., Eds.; *Inorganic Electronic Structure and Spectroscopy, Vol. 1 Methods*; Wiley; 1999, 661–724.
32. Koch, W.; Hertwig, R. H. In von Schleyer, P. R. Ed.; *Encyclopedia of Computational Chemistry*; Wiley: New York, 1998, pp 689–700.
33. Li, J.; Fisher, C. L.; Chen, J. L.; Bashford, D.; Noodleman, L. *Inorg. Chem.* **1996**, *35*, 4694–4702.
34. Zaric, S. D.; Popovic, D. M.; Knapp, E. W. *Chem. Eur. J.* **2000**, *6*, 3935–3942.
35. Martin, R. L.; Hay, P. J.; Pratt, L. R. *J. Phys. Chem. A* **1998**, *102*, 3565–3573.
36. Butcher, K. D.; Gebhard, M. S.; Solomon, E. I. *Inorg. Chem.* **1990**, *29*, 2067.
37. Noodleman, L.; Lovell, T.; Liu, T.; Himo, F.; Torres, R. A. *Curr. Opin. Chem. Biol.* **2002**, *6*, 259–273.
38. Mouesca, J.-M.; Chen, J. L.; Noodleman, L.; Bashford, D.; Case, D. A. *J. Am. Chem. Soc.* **1994**, *116*, 11898–11914.
39. Goldstein, E.; Beno, B.; Houk, K. N. *J. Am. Chem. Soc.* **1996**, *118*, 6036–6043.
40. Rodriguez, J. H.; McCusker, J. K. *J. Chem. Phys.* **2002**, *116*, 6253–6270.
41. Staroverov, V. N.; Davidson, E. R. *J. Am. Chem. Soc.* **2000**, *122*, 7377–7386.
42. Leach, A. G.; Catak, S.; Houk, K. N. *Chem. Eur. J.* **2002**, *8*, 1290–1299.
43. Han, W.-G.; Lovell, T.; Liu, T.; Noodleman, L. *Chem. Phys. Chem.* **2002**, *3*, 167–178.
44. Ziegler, T.; Rauk, A.; Baerends, E. J. *Theor. Chim. Acta* **1977**, *43*, 261–271.
45. Doclo, K.; De Corte, D.; Daul, C.; Gudel, H. U. *Inorg. Chem.* **1998**, *37*, 3842–3847.
46. Anderson, P. W.; Hasegawa, H. *Phys. Rev.* **1955**, *100*, 675–681.
47. Fan, L.; Ziegler, T. *J. Chem. Phys.* **1991**, *95*, 7401–7408.
48. Li, J.; Nelson, M. R.; Peng, C. Y.; Bashford, D.; Noodleman, L. *J. Phys. Chem. A* **1998**, *102*, 6311–6324.
49. Sitkoff, D.; Sharp, K. A.; Honig, B. *J. Phys. Chem.* **1994**, *98*, 1978–1988.
50. Asthagiri, D.; Dillet, V.; Liu, T.; Noodleman, L.; Etten, R. L.; van Bashford, D. *J. Am. Chem. Soc.* **2002**, *124*, 10225–10235.
51. Ullmann, G. M.; Noodleman, L.; Case, D. A. *J. Biol. Inorg. Chem.* **2002**, *7*, 632–639.
52. Lovell, T.; Li, J.; Noodleman, L. *J. Biol. Inorg. Chem.* **2002**, *7*, 799–809.
53. Lovell, T.; Li, J.; Noodleman, L. *Inorg. Chem.* **2001**, *40*, 5251–5266.
54. Brunold, T. C.; Solomon, E. I. *J. Am. Chem. Soc.* **1999**, *121*, 8277–8287.
55. Brunold, T. C.; Solomon, E. I. *J. Am. Chem. Soc.* **1999**, *121*, 8288–8295.
56. Lovell, T.; Li, J.; Noodleman, L. *Inorg. Chem.* **2001**, *40*, 5267–5278.
57. Lovell, T.; Han, W.-G.; Liu, T.; Noodleman, L. *J. Am. Chem. Soc.* **2002**, *124*, 5890–5894.
58. Dunietz, B. D.; Beachy, M. D.; Cao, Y.; Whittington, D. A.; Lippard, S. J.; Friesner, R. A. *J. Am. Chem. Soc.* **2000**, *122*, 2828–2839.
59. Gherman, B. F.; Dunietz, B. D.; Whittington, D. A.; Lippard, S. J.; Friesner, R. A. *J. Am. Chem. Soc.* **2001**, *123*, 3836–3837.
60. Siegbahn, P. E. M. *J. Biol. Inorg. Chem.* **2001**, *6*, 27–45.
61. Beinert, H. *J. Biol. Inorg. Chem.* **2000**, *5*, 2–15.
62. Beinert, H.; Holm, R. H.; Munck, E. *Science* **1997**, *277*, 653–659.
63. Gamelin, D. R.; Bominaar, E. L.; Kirk, M. L.; Wieghardt, K.; Solomon, E. I. *J. Am. Chem. Soc.* **1996**, *118*, 8085–8097.
64. Sigfridsson, E.; Olsson, M. H. M.; Ryde, U. *Inorg. Chem.* **2001**, *40*, 2509–2519.
65. Mouesca, J.-M.; Lamotte, B. *Coord. Chem. Rev.* **1998**, *178–180*, 1573–1614.
66. Torres, R. A.; Lovell, T.; Noodleman, L.; Case, D. A. *J. Am. Chem. Soc.* **2003**, *125*, 1923–1936.
67. Jensen, G. M.; Warshel, A.; Stephens, P. J. *Biochemistry* **1994**, *33*, 10911–10924.
68. Ludwig, M. L.; Ballou, D. P.; Noodleman, L.; Phthalate Dioxygenase Reductase. In Wieghardt, K.; Huber, R.; Poulos, T.; Messerschmidt, A., Eds.; *Handbook of Metalloproteins*; Wiley: Chichester, 2001, pp 652–667.
69. Correll, C. C.; Ludwig, M. L.; Bruns, C. M.; Karplus, P. A. *Protein Sci.* **1993**, *2*, 2112–2133.
70. Yang, Y.; Beck, B. W.; Shenoy, V. S.; Ichiye, T. *J. Am. Chem. Soc.* **1993**, *115*, 7439–7444.
71. Koerner, J. B.; Ichiye, T. *J. Phys. Chem. B* **1997**, *101*, 3633–3643.
72. Noodleman, L.; Peng, C. Y.; Case, D. A.; Mouesca, J.-M. *Coord. Chem. Rev.* **1995**, *144*, 199–244.
73. Zu, Y.; Fee, J. A.; Hirst, J. *J. Am. Chem. Soc.* **2001**, *123*, 9906–9907.
74. Lovell, T.; Li, J.; Liu, T.; Case, D. A.; Noodleman, L. *J. Am. Chem. Soc.* **2001**, *123*, 12392–12410.
75. Lovell, T.; Li, J.; Case, D. A.; Noodleman, L. *J. Am. Chem. Soc.* **2002**, *124*, 4546–4547.
76. Lovell, T.; Li, J.; Case, D. A.; Noodleman, L. *J. Biol. Inorg. Chem.* **2002**, *7*, 735–749.
77. Harris, D. L. *Curr. Opin. Chem. Biol.* **2001**, *5*, 724–735.
78. Kuramochi, H.; Noodleman, L.; Case, D. A. *J. Am. Chem. Soc.* **1997**, *119*, 11442–11451.
79. Green, M. T. *J. Am. Chem. Soc.* **2001**, *123*, 9218–9219.
80. Ogliaro, F.; Cohen, S.; Filatov, M.; Harris, N.; Shaik, S. *Angew. Chem. Int. Ed. Engl.* **2000**, *39*, 3851–3855.
81. Himo, F.; Eriksson, L. A.; Maseras, F.; Siegbahn, P. E. M. *J. Am. Chem. Soc.* **2000**, *122*, 8031.

Comprehensive Coordination Chemistry II
ISBN (set): 0-08-0437486

Volume 2, (ISBN 0-08-0443249); pp 491–510

2.40 Time-dependent Density Functional Resonance Theory

S. J. A. VAN GISBERGEN
Scientific Computing and Modelling N.V., Amsterdam, The Netherlands
and
E. J. BAERENDS
Vrije Universiteit, Amsterdam, The Netherlands

2.40.1 INTRODUCTION 511
2.40.2 BASIC EQUATIONS 512
2.40.3 ACCURACY 514
2.40.4 SOME RELEVANT APPLICATIONS OF TDDFT 514
2.40.5 REFERENCES 515

2.40.1 INTRODUCTION

Time-dependent density functional theory (TDDFT) is the extension of density functional theory (DFT) (see Chapter 2.39) to time-dependent problems. It has become popular in chemistry since formulations have appeared that allow excitation energies and other important properties to be easily implemented in standard DFT software packages, including Gaussian, ADF, Turbomole, CADPAC, Q-Chem, and several others.

Runge and Gross[1] were among those to provide a solid theoretical framework for TDDFT. They showed that DFT can be extended to problems where a time-dependent external perturbation is present, such as the oscillating electric field of a laser. The theory was originally applied in physics to simple systems, such as atoms or idealized metal surfaces. Initially the focus was on frequency-dependent polarizabilities and hyperpolarizabilities. TDDFT also allows the treatment of problems that fall outside the scope of standard perturbation theory,[2] such as high harmonic generation, but this field is still in its infancy and will not be further discussed here.

Two factors have caused the current strong interest of chemists in TDDFT. One is the formulation which allowed excitation energies to be calculated in a way similar to what was known from time-dependent Hartree–Fock (HF) methods. The other was a formulation in terms of localized basis set expansions, which made it possible to calculate the desired properties in existing molecular DFT codes. The groups of Gross[2,3] and Casida and co-workers[4–7] both played important roles in the popularization of TDDFT applications in chemistry. Many other groups soon followed.[8–24]

The following properties, previously not (easily) accessible within DFT, have become available: excitation energies and oscillator strengths,[4,12] frequency-dependent polarizabilities[4,8] and

hyperpolarizabilities,[25] circular dichroism spectra,[26,27] optical rotatory strengths, optical rotatory dispersion,[28] Raman intensities (determined at experimental laser frequency),[29] van der Waals dispersion coefficients,[30] excited-state geometries, dipole moments, and IR frequencies.[31] The current popularity of TDDFT is related to the popularity of DFT itself. It can be efficiently implemented to treat systems with several hundred atoms, it allows accurate treatment of transition metal compounds, and it provides an intuitive chemical picture, as it shows which orbitals are important for the molecular property under study. For further theoretical background information on TDDFT, the authors suggest refs. 2, 4, and 32–35.

2.40.2 BASIC EQUATIONS

The basic quantity in TDDFT is the time-dependent electron density. Many important spectroscopic properties can be derived from it. As in ordinary (ground-state) DFT, the density is obtained from an auxiliary system of independent electrons which move in an effective potential, the time-dependent Kohn–Sham (KS) potential. With the exact KS potential, $v_s[\rho](\mathbf{r}, t)$, the density of the noninteracting electron system will be equal to the true electron density. In practice, the KS potential contains the exchange-correlation (xc) potential, $v_{xc}(\mathbf{r}, t)$, for which approximations are needed.

To put these words in the form of equations: the exact time-dependent density $\rho(\mathbf{r}, t)$ can be obtained from the time-dependent KS equations:

$$i\frac{\partial}{\partial t}\phi_j(\mathbf{r}, t) = \left[-\frac{\nabla^2}{2} + v_s[\rho](\mathbf{r}, t)\right]\phi_j(\mathbf{r}, t) \tag{1}$$

as the sum of the squares of the noninteracting KS orbitals:

$$\rho(\mathbf{r}, t) = \sum_{j=1}^{N} |\phi_j(\mathbf{r}, t)|^2 \tag{2}$$

The potential $v_s[\rho](\mathbf{r}, t)$ is called the time-dependent KS potential and written as:

$$v_s[\rho](\mathbf{r}, t) = v(\mathbf{r}, t) + \int d\mathbf{r}' \frac{\rho(\mathbf{r}', t)}{|\mathbf{r} - \mathbf{r}'|} + v_{xc}(\mathbf{r}, t) \tag{3}$$

Here, $v(\mathbf{r}, t)$ is the external field, which may include a time-dependent component, such as an oscillating electric field associated to a laser beam, and $v_{xc}(\mathbf{r}, t)$ is the time-dependent xc potential, the unknown part of $v_s(\mathbf{r}, t)$, which has to be approximated for practical applications.

Although the full time-dependent electron density contains much useful information, it is hard and expensive to compute, and not needed for many basic properties. Most applications in chemistry therefore use only linear (or nonlinear) response theory to obtain the first-order (or higher-order) change in the electron density due to a time-dependent electric perturbation. Most properties of interest (such as excitation energies and oscillator strengths) can be obtained from the linear response equations.

In general theory, the first-order time-dependent density can be calculated from the *exact* linear response function χ acting on an external perturbing time-dependent potential $v_1(\mathbf{r}', t')$:

$$\rho_1(\mathbf{r}, t) = \int d\mathbf{r}' \int dt' \chi(\mathbf{r}, t; \mathbf{r}', t') v_1(\mathbf{r}', t') \tag{4}$$

Similarly, for the KS system of noninteracting electrons, one finds the first-order change in the density from[2]

$$\rho_1(\mathbf{r}, t) = \int d\mathbf{r}' \int dt' \chi_s(\mathbf{r}, t; \mathbf{r}', t') v_{s,1}(\mathbf{r}', t') \tag{5}$$

where χ_s is the *noninteracting* linear density–density response function, and $v_{s,1}(\mathbf{r}, t)$ is the KS potential in first order of the external field, which differs from $v_1(\mathbf{r}, t)$ in two terms which depend on ρ_1:

$$v_{s,1}(\mathbf{r}, t) = v_1(\mathbf{r}, t) + \int d\mathbf{r}' \frac{\rho_1(\mathbf{r}', t)}{|\mathbf{r} - \mathbf{r}'|} + \int d\mathbf{r}' \int dt' f_{xc}[\rho_0](\mathbf{r}, t; \mathbf{r}', t')\rho_1(\mathbf{r}', t') \tag{6}$$

Here the xc kernel f_{xc} has been introduced. It is the functional derivative of the time-dependent xc potential $v_{xc}(\mathbf{r}, t)$ with respect to the time-dependent density $\rho(\mathbf{r}, t)$:

$$f_{xc}(\mathbf{r}, t; \mathbf{r}', t') = \frac{\delta v_{xc}(\mathbf{r}, t)}{\delta \rho(\mathbf{r}', t')} \tag{7}$$

These equations are usually Fourier transformed from the time domain to the frequency domain. In the frequency representation, the KS response function is written in terms of the unperturbed KS orbitals $\varphi_j(\mathbf{r})$, their occupation numbers ε_j, and their orbital energies φ_j as:

$$\chi_s(\mathbf{r}, \mathbf{r}'; \omega) = \sum_{j,k} (\eta_k - \eta_j) \frac{\phi_j(\mathbf{r})\phi_k^*(\mathbf{r})\phi_j^*(\mathbf{r}')\phi_k(\mathbf{r}')}{\omega - (\varepsilon_j - \varepsilon_k) + i\delta} \tag{8}$$

where δ is a positive infinitesimal.

The first-order change in the electron density determines the change in the dipole moment under the influence of an external perturbation. In the most common case of an electric perturbation, the corresponding property is the frequency-dependent polarizability, which is directly related to (vertical) excitation energies ω_i, oscillator strengths f_i, and transition dipole moments μ_i.[36]

$$\alpha_{av}(-\omega; \omega) = \sum_i \frac{f_i}{\omega_i^2 - \omega^2} = \frac{2}{3} \sum_i \frac{\omega_i \mu_i^2}{\omega_i^2 - \omega^2} \tag{9}$$

where α_{av} is the average polarizability, equal to the average of the α_{xx}, α_{yy}, and α_{zz} components and i labels the excitations. From this equation it is clear that the poles of the polarizability tensor are directly related to the exact excitation energies. Although only the dipole-allowed and spin-allowed transitions have a nonzero contribution in this summation, the TDDFT approach also allows the determination of triplet excitation energies, as well as excitation energies with zero oscillator strength.

It has been shown explicitly by Casida[4] that the poles of the polarizability (i.e., the excitation energies) occur at the eigenvalues ω_i of the following eigenvalue equation

$$\Omega \mathbf{F}_i = \omega_i^2 \mathbf{F}_i \tag{10}$$

where the components of the four-index matrix Ω are given by

$$\Omega_{ia\sigma,jb\tau} = \delta_{\sigma\tau}\delta_{ij}\delta_{ab}(\varepsilon_a - \varepsilon_i)^2 + 2\sqrt{(\varepsilon_a - \varepsilon_i)} K_{ia\sigma,jb\tau} \sqrt{(\varepsilon_b - \varepsilon_j)} \tag{11}$$

where σ and τ label the spin directions. The desired excitation energies are equal to ω_i, and the oscillator strengths are obtained from the eigenvectors $\mathbf{F}_i$.[4] For a spin-restricted calculation, the Ω-matrix can be split in two separate singlet and triplet matrices Ω^S and Ω^T, by performing a unitary transformation.[12,37] The KS orbital energy differences $\varepsilon_a - \varepsilon_i$, which occur on the diagonal of this matrix, are usually a very important part of Ω. If the coupling matrix K, which contains the Coulomb and xc terms, would be zero, the excitation energies would be identical to the orbital energy differences between occupied and virtual KS orbitals, and the oscillator strengths would depend directly on the corresponding KS orbitals. This shows the physical significance of both the occupied and virtual KS orbitals and their orbital energies. In this respect, TDDFT differs from time-dependent HF, where no such significance can be attributed to the virtual orbital energies.

The Coulomb term in the coupling matrix K is usually much more important than the xc term, related to f_{xc}. The K-matrix affects both the diagonal and off-diagonal components of Ω. The

off-diagonal components induce a mixing of the various primitive orbital replacements $i \rightarrow a$ and $j \rightarrow b$ (where i, j are occupied KS orbitals and a, b are virtual). In other words, the eigenvectors F_i which determine the oscillator strengths, will have multiple nonzero components. This makes it possible to determine spectra in which such mixing effects are crucial. In optical spectra of porphyrins, for example, the low-energy, low-intensity Q band and the intense B band at higher energy (cf. free base porphin example below), both derive from the same primitive occupied to virtual KS orbital transitions, but mixed with different signs. A different method to obtain excited-state properties in DFT, the so-called ΔSCF method,[38–43] on the other hand, is not well suited to treat such subtle cases.

2.40.3 ACCURACY

The quality of the results are, in addition to more technical issues, determined by the quality of the approximations for the xc potential v_{xc} and the xc kernel f_{xc}, which is the functional derivative of v_{xc}. The xc potential determines the KS orbital energies. The orbital energy differences between occupied and virtual orbitals give a reasonable zero-order estimate for the excitation energy. It is therefore not surprising that a reliable xc potential is important. The xc kernel is usually of less importance, and even the simple adiabatic local density approximation (ALDA) which is often used, appears to be satisfactory in most cases. There have been many suggestions for improved xc potentials.[44–48] These aim to improve the shape of the xc potential, including the incorrect asymptotic behavior of the usual LDA and GGA potentials. The asymptotic behavior strongly affects the position of the high-lying virtuals. It is important for polarizabilities, hyperpolarizabilities, and Rydberg excitations, but not so much for valence excitations. Valence excitations are usually well described at the LDA or GGA level. Deviations from experiment are typically 0.1–0.5 eV, and also for coordination compounds. Certain types of charge-transfer excitations may be less accurate.

There are certain situations in which the accuracy of time-dependent DFT applications may be unsatisfactory, due to the fact that the currently used xc approximations are not satisfactory in these cases. Multiple excitations are not yet well described, for example. It is generally believed that treatment of such excitations requires an xc kernel f_{xc} which is frequency-dependent and significantly more complicated than the currently popular adiabatic approximation which is almost universally employed. In practice it turns out that excitations, which in theories based on HF have a significant multiple-excitation character, may still be surprisingly well described at the TDDFT level. If, however, an excitation is almost purely a multiple excitation, the current TDDFT descriptions are likely to miss it completely.

Another area where one needs to be careful is photochemistry. If the excited-state potential energy curves between two open-shell fragments are studied with TDDFT, artifacts may occur at bond lengths beyond the equilibrium geometry. The simplest example is H_2,[49,50] where the TDDFT first singlet excitation energy tends to zero, whereas the experimental curve tends towards about 10 eV. Again, the xc kernel f_{xc} is to blame and a general solution is not yet in sight, although a partial remedy to the problem has been suggested.[49]

Finally, optical properties of conjugated polymers are currently poorly described.[51–55] This is due to the fact that the local functionals currently in use (LDA and GGAs) fail to capture subtle charge displacements at the ends of a long molecular chain. Recently, a solution to this important problem, using the sophisticated "ultra nonlocal" Vignale–Kohn xc functional, has come much closer.[56]

2.40.4 SOME RELEVANT APPLICATIONS OF TDDFT

A few recent relevant applications of TDDFT to absorption spectra are listed in this section. The list is far from complete and primarily intended to give some starting points in the literature which show how TDDFT can be applied in practice to chemically interesting systems. Many other applications can be found in the references of these listed papers.

Applications have appeared, among several others, on the following transition metal compounds: MnO_4^-, $Ni(CO)_4$, $Mn_2(CO)_{10}$,[57] $M(CO)_6$ (M = Cr, Mo, W),[58] ruthenium diimine[59] and other ruthenium complexes,[60] $CpMn(CO)_3$,[61] MF_6 (M = Cr, Mo, W),[62] and several other metal complexes.[63]

Table 1 Comparison of TDDFT dipole-allowed singlet excitation energies and oscillator strengths of free base porphin from ref. 65 to experimental and theoretical literature values.

		Experiment		*TDDFT*[a]		*CASPT2*[b]	
State	*Assignment*	*Excitation energy*	*Oscillator strength*[c]	*Excitation energy*	*Oscillator strength*[c]	*Excitation energy*	*Oscillator strength*[c]
1^1B_{3u}	Q_x	1.98–2.02 (Q_x)[d]	0.01	2.16	0.01	1.63	0.004
1^1B_{2u}	Q_y	2.33–2.42 (Q_y)[d]	0.06	2.29	0.0005	2.11	0.002
2^1B_{2u}	B_y	3.13–3.33 (B)[e]	1.15[f]	3.01	0.04	3.08	0.911
2^1B_{3u}	B_x	3.13–3.33 (B)[e]		2.98	0.1338	3.12	0.704
3^1B_{2u}	N_y	3.65(N)	<0.1[f]	3.41	0.8962	3.42	0.458
3^1B_{3u}	N_x	3.65(N)		3.47	0.7293	3.53	0.833
4^1B_{2u}	L_y	4.25(L)	~0.1[f]	3.77	0.1688	3.96	0.341
4^1B_{3u}	L_x	4.25(L)		3.76	0.1272	4.04	0.202

[a] Using the BP/ALDA approximations. [b] Ref. 77. [c] Oscillator strengths taken from ref. 79. [d] From refs. 79–81. [e] Band maxima in vapor or solution. Refs. 79, 81, and 82. [f] Summed oscillator strengths for the x and y bands.

Because of space limitations, we will only briefly discuss the most basic application in the area of porphyrin optical spectra. Much work has already been done in this area, both with TDDFT and related methods.[64] The TDDFT applications include free base porphin[64–66] and its ss-octahalogenated derivatives,[67] the porphyrinato-porphyrazinato-zirconium(IV) complex,[68] NiP, NiPz, NiTBP, and NiPc,[69] zinc phthalocyanine,[70] chlorophyll *a*,[71] zinc complexes of porphyrin, tetraazaporphyrin, tetrabenzoporphyrin, phthalocyanine,[72] phenylene-linked free-base and zinc porphyrin dimers,[73] metal bis(porphyrin) complexes[74] a series of porphyrin-type molecules,[64] and many more. We refer to ref. 75 for an extensive discussion of TDDFT calculations on the spectra of porphyrins and porphyrazines, as well as their interpretation. For further theoretical work on porphyrines, we mention ref. 76 and other papers in that special issue.

In Table 1, the experimental spectrum of FBP consists of the Q_x and Q_y bands, the B band (Soret band), and the N and L bands at higher energy. The assignment of this spectrum has been heavily debated, but there now seems to be agreement[64,65,77] on the main assignments as presented in Table 1. These assignments differ from earlier work based on other high-level theoretical methods. This assignment indicates that the B, N, and L bands are in fact overlapping pairs of x and y bands. This makes sense because the FBP D_{2h} symmetry is only a slight distortion, caused by the presence of the two central hydrogens, of the D_{4h} symmetry of metal porphyrins. Of course, any reasonable assignment for this molecule requires a method that yields excitation energies that are accurate up to a few tenths of an eV at most.

It is fair to note that the oscillator strengths of both the TDDFT and CASPT2 results still leave much room for improvement. The deficiency for the TDDFT case for this molecule is not shared by other choices for the xc functionals, and also does not show up in similar studies on metal-porphyrin spectra, where excellent agreement with experiment is usually obtained.[69] A calculation on a system of this size can nowadays be performed in a few minutes. So-called linear scaling techniques[78] make TDDFT calculations on molecules with hundreds of atoms feasible.

In summary, TDDFT enables reliable theoretical predictions of optical spectra, and many other properties, of large coordination compounds. In view of algorithmic and hardware improvements, and ongoing research to improve the xc functionals, the future prospects for TDDFT and its application to coordination chemistry seem bright.

2.40.5 REFERENCES

1. Runge, E.; Gross, E. K. U. *Phys. Rev. Lett.* **1984**, *52*, 997.
2. Gross, E. K. U.; Dobson, J. F.; Petersilka, M. In *Density Functional Theory*, Springer Series, *Topics in Current Chemistry*; Nalewajski, R. F., Ed.; Springer: Heidelberg, Germany, 1996.
3. Petersilka, M.; Gossmann, U. J.; Gross, E. K. U. *Phys. Rev. Lett.* **1996**, *76*, 1212–1215.
4. Casida, M. E. In *Recent Advances in Density-Functional Methods*; Chong, D. P., Ed.; World Scientific: Singapore, 1995, p 155.

5. Casida, M. E. In *Recent Developments and Applications of Modern Density Functional Theory*; Seminario, J. M., Ed.; Elsevier: Amsterdam, 1996.
6. Casida, M. E.; Jamorski, C.; Bohr, F.; Guan, J.; Salahub, D. R. *Theoretical and Computational Modeling of NLO and Electronic Materials;* Karna, S. P; Yeates, A. T., Eds.; ACS: Washington, DC, 1996; 145–163.
7. Jamorski, Ch.; Casida, M. E.; Salahub, D. R. *J. Chem. Phys.* **1996**, *104*, 5134–5147.
8. van Gisbergen, S. J. A.; Snijders, J. G.; Baerends, E. J. *J. Chem. Phys.* **1995**, *103*, 9347–9354.
9. van Gisbergen, S. J. A.; Osinga, V. P.; Gritsenko, O. V.; van Leeuwen, R.; Snijders, J. G.; Baerends, E. J. *J. Chem. Phys.* **1996**, *105*, 3142–3151.
10. van Gisbergen, S. J. A.; Snijders, J. G.; Baerends, E. J. *Phys. Rev. Lett.* **1997**, *78*, 3097–3100.
11. van Gisbergen, S. J. A.; Snijders, J. G.; Baerends, E. J. *Comput. Phys. Commun.* **1999**, *118*, 119–138.
12. Bauernschmitt, R.; Ahlrichs, R. *Chem. Phys. Lett.* **1996**, *256*, 454–464.
13. Bauernschmitt, R.; Häser, M.; Treutler, O.; Ahlrichs, R. *Chem. Phys. Lett.* **1997**, *264*, 573–578.
14. Colwell, S. M.; Handy, N. C.; Lee, A. M. *Phys. Rev.* **1996**, *A53*, 1316–1322.
15. Handy, N. C.; Tozer, D. J. *J. Comput. Chem.* **1999**, *20*, 106–113.
16. Caillie, C. Van; Amos, R. D. *Chem. Phys. Lett.* **1998**, *291*, 71–77.
17. Yabana, K.; Bertsch, G. F. *Phys. Rev.* **1996**, *B54*, 4484–4487.
18. Yabana, K.; Bertsch, G. F. *Int. J. Quantum Chem.* **1999**, *75*, 55.
19. Stener, M.; Decleva, P.; Lisini, A. *J. Phys.* **1995**, *B28*, 4973–5000.
20. Görling, A.; Heinze, H. H.; Ruzankin, S. Ph.; Staufer, M.; Rösch, N. *J. Chem. Phys.* **1999**, *110*, 2785–2799.
21. Vasiliev, I.; Öğüt, S.; Chelikowsky, J. R. *Phys. Rev. Lett.* **1999**, *82*, 1919–1922.
22. Stratmann, R. E.; Scuseria, G. E.; Frisch, M. J. *J. Chem. Phys.* **1998**, *109*, 8218–8224.
23. Hirata, So; Head-Gordon, M. *Chem. Phys. Lett.* **1999**, *302*, 375–382.
24. Hirata, So; Lee, T. J.; Head-Gordon, M. *J. Chem. Phys.* **1999**, *111*, 8904.
25. van Gisbergen, S. J. A.; Snijders, J. G.; Baerends, E. J. *J. Chem. Phys.* **1998**, *109*, 10644–10656.
26. Furche, F.; Ahlrichs, R.; Wachsmann, C.; Weber, E.; Sobanski, A.; Vögtle, F.; Grimme, S. *J. Am. Chem. Soc.* **2000**, *122*, 1717.
27. Autschbach, J.; Ziegler, T.; van Gisbergen, S. J. A.; Baerends, E. J. *J. Chem. Phys.* **2002**, *116*, 891.
28. Grimme, S. *Chem. Phys. Lett.* **2001**, *339*, 380–388.
29. van Gisbergen, S. J. A.; Snijders, J. G.; Baerends, E. J. *Chem. Phys. Lett. 1996* **259**, 599–604.
30. Osinga, V. P.; van Gisbergen, S. J. A.; Snijders, J. G.; Baerends, E. J. *J. Chem. Phys.* **1997**, *106*, 5091–5101.
31. Caillie, C. Van; Amos, R. D. *Chem. Phys. Lett.* **2000**, *317*, 159–164.
32. Gross, E. K. U.; Ullrich, C. A.; Gossmann, U. J. Density Functional Theory of Time-Dependent Systems. In NATO ASI Series, Vol. 337; Gross, E. K. U., Dreizler, R. M., Eds.; Plenum: New York, 1995.
33. Singh, R.; Deb, B. M. *Phys. Lett.* **1999**, *311*, 48–94.
34. Maitra, N. T.; Burke, K.; Appel, H.; Gross, E. K. U.; van Leeuwen, R. A Celebration of the Contributions of Robert Parr. In *Reviews in Modern Quantum Chemistry*; Sen, K. D., Eds.; World Scientific, Singapore, 2002, pp 1155–1185.
35. van Leeuwen, R. *Int. J. Mod. Phys.* **2001**, *B15*, 1969–2023.
36. Craig, P.; Thirunamachandran, T. *Molecular Quantum Electrodynamics*; Academic Press: New York, 1984.
37. Petersilka, M.; Gross, E. K. U. *Int. J. Quantum Chem. Symp.* **1996**, *30*, 181–189.
38. Ziegler, T.; Rauk, A.; Baerends, E. J. *Theor. Chim. Acta* **1977**, *43*, 261–271.
39. von Barth, U. *Phys. Rev.* **1979**, *A20*, 1693–1703.
40. Daul, C. *Int. J. Quantum Chem.* **1994**, *52*, 867.
41. Dickson, R. M.; Ziegler, T. *Int. J. Quantum Chem.* **1996**, *58*, 681–687.
42. Adams, D. M.; Noodleman, L.; Hendrickson, D. N. *Inorg. Chem.* **1997**, *36*, 3966–3984.
43. Han, W. G.; Lovell, T.; Liu, T. Q.; Noodleman, L. *Comput. Phys. Commun.* **2002**, *3*, 167.
44. van Leeuwen, R.; Baerends, E. J. *Phys. Rev.* **1994**, *A49*, 2421–2431.
45. Tozer, D. J.; Handy, N. C. *J. Chem. Phys.* **1998**, *109*, 10180–10189.
46. Schipper, P. R. T.; Gritsenko, O. V.; van Gisbergen, S. J. A.; Baerends, E. J. *J. Chem. Phys.* **2000**, *112*, 1344–1352.
47. Grüning, M.; Gritsenko, O. V.; van Gisbergen, S. J. A.; Baerends, E. J. *J. Chem. Phys.* **2001**, *114*, 652–660.
48. Handy, N. C.; Tozer, D. J. *J. Comput. Chem.* **1999**, *20*, 106–113.
49. Casida, M. E.; Gutierrez, F.; Guan, J. G.; Gadea, F. X.; Salahub, D.; Daudey, J. P. *J. Chem. Phys.* **2000**, *113*, 7062–7071.
50. Gritsenko, O. V.; van Gisbergen, S. J. A.; Görling, A.; Baerends, E. J. *J. Chem. Phys.* **2000**, *113*, 8478–8489.
51. Champagne, B.; Perpète, E. A.; van Gisbergen, S. J. A.; Baerends, E. J.; Snijders, J. G.; Soubra-Ghaoui, C.; Robins, K.; Kirtman, B. *J. Chem. Phys.* **1998**, *109*, 10489–10498.
52. van Gisbergen, S. J. A.; Schipper, P. R. T.; Gritsenko, O. V.; Baerends, E. J.; Snijders, J. G.; Champagne, B.; Kirtman, B. *Phys. Rev. Lett.* **1999**, *83*, 694–697.
53. Champagne, B.; Perpète, E. A.; Jacquemin, D.; van Gisbergen, S. J. A.; Baerends, E. J.; Soubra-Ghaoui, C.; Robins, K.; Kirtman, B. *J. Phys. Chem.* **2000**, *A104*, 4755–4763.
54. Gritsenko, O. V.; van Gisbergen, S. J. A.; Schipper, P. R. T.; Baerends, E. J. *Phys. Rev.* **2000**, *A62*, 012507.
55. Fabian, J. *Theor. Chim. Acta* **2001**, *106*, 199–217.
56. van Faassen, M.; de Boeij, P. L.; van Leeuwen, R.; Berger, J. A.; Snijders, J. G. *Phys. Rev. Lett.* **2002**, *88*, 186401.
57. van Gisbergen, S. J. A.; Groeneveld, J. A.; Rosa, A.; Snijders, J. G.; Baerends, E. J. *J. Phys. Chem.* **1999**, *A103*, 6835–6844.
58. Rosa, A.; Baerends, E. J.; van Gisbergen, S. J. A.; van Lenthe, E.; Groeneveld, J. A.; Snijders, J. G. *J. Am. Chem. Soc.* **1999**, *121*, 10356–10365.
59. Gorelsky, S. I.; Lever, A. B. P. *J. Org. Chem.* **2001**, *635*, 187–196.
60. Turki, M.; Daniel, Ch.; Zalis, S., Jr.; Vlcek, A.; van Slageren, J.; Stufkens, D. J. *J. Am. Chem. Soc.* **2001**, *123*, 11431–11440.
61. Full, J.; González, L.; Daniel, Ch. *J. Phys. Chem.* **2001**, *A105*, 184–189.
62. Adamo, C.; Barone, V. *Theor. Chim. Acta* **2000**, *105*, 169–172.
63. Boulet, P.; Buchs, M.; Chermette, H.; Daul, C.; Gilardoni, F.; Rogemond, F.; Schlapfer, C. W.; Weber, J. *J. Phys. Chem.* **2001**, *A105*, 885–894.

64. Parusel, A. B. J.; Grimme, S. *J. Porphyrins Phthalocyanines* **2001**, *5*, 225–232.
65. van Gisbergen, S. J. A.; Rosa, A.; Ricciardi, G.; Baerends, E. J. *J. Chem. Phys.* **1999**, *111*, 2499–2506.
66. Sundholm, D. *Phys. Chem. Chem. Phys.* **2000**, *2*, 2275–2281.
67. Nguyen, T. A.; Day, P. N.; Pachter, R. *J. Phys. Chem.* **2000**, *A104*, 4748–4754.
68. Ricciardi, G.; Rosa, A.; van Gisbergen, S. J. A.; Baerends, E. J. *J. Phys. Chem.* **2000**, *A104*, 635–643.
69. Rosa, A.; Ricciardi, G.; Baerends, E. J.; van Gisbergen, S. J. A. *J. Phys. Chem.* **2001**, *A105*, 3311–3327.
70. Ricciardi, G.; Rosa, A.; Baerends, E. J. *J. Phys. Chem.* **2001**, *A105*, 5242–5254.
71. Sundholm, D. *Chem. Phys. Lett.* **1999**, *302*, 480–484.
72. Nguyen, T. A.; Pachter, R. *J. Chem. Phys.* **2001**, *114*, 10757–10767.
73. Yamaguchi, Y.; Yokomichi, Y.; Yokoyama, S.; Mashiko, S. *Int. J. Quantum Chem.* **2001**, *84*, 338–347.
74. Ricciardi, G.; Rosa, A.; Baerends, E. J.; van Gisbergen, S. J. A. *J. Am. Chem. Soc.* **2002**, *124*, 12319–12394.
75. Baerends, E. J.; Ricciardi, G.; Rosa, A.; van Gisbergen, S. J. A. *Coord. Chem. Rev.* **2002**, *230*, 5–27.
76. Ghosh, A. *J. Porphyrins Phthalocyanines* **2001**, *5*, 187–189.
77. Serrano-Andrés, L.; Merchán, M.; Rubio, M.; Roos, B. O. *Chem. Phys. Lett.* **1998**, *295*, 195–203.
78. van Gisbergen, S. J. A.; Guerra, C. Fonseca; Baerends, E. J. *J. Comput. Chem.* **2000**, *21*, 1511–1523.
79. Edwards, L.; Dolphin, D. H.; Gouterman, M.; Adler, A. D. *J. Mol. Spectrosc.* **1971**, *38*, 16–32.
80. Kim, B. F.; Bohandy, J. *J. Mol. Spectrosc.* **1978**, *73*, 332.
81. Nagashima, U.; Takada, T.; Ohno, K. *J. Chem. Phys.* **1986**, *85*, 4524.
82. Rimington, C.; Mason, S. F.; Kennard, O. *Spectrochim. Acta* **1958**, *12*, 65.

Comprehensive Coordination Chemistry II
ISBN (set): 0-08-0437486

Volume 2, (ISBN 0-08-0443249); pp 511–517

2.41
Molecular Orbital Theory (SCF Methods and Active Space SCF)

B. O. ROOS and U. RYDE
University of Lund, Sweden

2.41.1 THE MOLECULAR ORBITAL 519
2.41.2 THE MANY-ELECTRON WAVE FUNCTION AND THE NATURAL ORBITALS 520
2.41.2.1 The First-order Density Matrix and the Natural Spin-orbitals 521
2.41.2.2 Spin Integration and the Natural Orbitals 521
2.41.3 THE HARTREE–FOCK METHOD 523
2.41.4 ACTIVE ORBITALS AND MULTICONFIGURATIONAL WAVE FUNCTIONS 525
2.41.4.1 Bond Dissociation 526
2.41.4.2 The Complete Active Space SCF Model–CASSCF 528
2.41.5 THE COORDINATION OF NICKEL WITH ETHENE 529
2.41.6 THE FERROCENE MOLECULE 530
2.41.6.1 Computational Details 530
2.41.6.2 The Electronic Structure of Ferrocene 532
2.41.7 THE $[Re_2Cl_8]^{2-}$ ION 533
2.41.8 BLUE COPPER PROTEIN MODELS 534
2.41.8.1 CuSH 535
2.41.8.2 $Cu^{2+}(NH_3)_3X$ 536
2.41.8.3 Electronic Spectra 536
2.41.9 CONCLUSIONS 538
2.41.10 REFERENCES 539

2.41.1 THE MOLECULAR ORBITAL

The molecular orbital (MO) is the basic concept in contemporary quantum chemistry.[1–3] It is used to describe the electronic structure of molecular systems in almost all models, ranging from simple Hückel theory to the most advanced multiconfigurational treatments. Only in valence bond (VB) theory is it not used. Here, polarized atomic orbitals are instead the basic feature. One might ask why MOs have become the key concept in molecular electronic structure theory. There are several reasons, but the most important is most likely the computational advantages of MO theory compared to the alternative VB approach. The first quantum mechanical calculation on a molecule was the Heitler–London study of H_2[4] and this was the start of VB theory. It was found, however, that this approach led to complex structures of the wave function when applied to many-electron systems and the mainstream of quantum chemistry was to take another route, based on the success of the central-field model for atoms introduced by by Hartree in 1928 and developed into what we today know as the Hartree–Fock (HF) method, by Fock, Slater, and co-workers (see Ref. 5 for a review of the HF method for atoms). It was found in these calculations of atomic orbitals that a surprisingly accurate description of the electronic structure could be achieved by assuming that the electrons move independently of each other in the mean field created by the electron cloud. Some correlation was introduced between electrons with

parallel spin, through the fulfillment of the Pauli exclusion principle, which required that the total wave function was written as an antisymmetrized product of atomic spin-orbitals, instead of a simple product.

At the same time, molecular orbitals were used in simplified treatments of the pi-electrons in conjugated organic molecules.[6] Similar empirical or semiempirical electron-structure models were developed and successfully applied in other areas of chemistry. They have been described in other chapters of this book. The field was therefore open for development of a nonempirical HF theory for molecules. A key paper was published by Roothaan in 1951.[7] Albeit not the first to do so, he gave a clear and detailed description of an HF procedure for molecules that could almost be used as a manual for the development of a computer code. The computers were not quite ready, though, and it was to take another 10 years before the first general-purpose codes were produced.

Today we know that the HF method gives a very precise description of the electronic structure for most closed-shell molecules in their ground electronic state. The molecular structure and physical properties can be computed with only small errors. The electron density is well described. The HF wave function is also used as a reference in treatments of electron correlation, such as perturbation theory (MP2), configuration interaction (CI), coupled-cluster (CC) theory, etc. Many semi-empirical procedures, such as CNDO, INDO, the Pariser–Parr–Pople method for π-electron systems, etc. are based on the HF method. Density functional theory (DFT) can be considered as HF theory that includes a semiempirical estimate of the correlation error. The HF theory is the basic building block in modern quantum chemistry, and the basic entity in HF theory is the molecular orbital.

Below we shall describe this model in more detail and study its possibilities and limitations (because it has serious limitations), but first a few words about electron densities and molecular orbitals in general.

2.41.2 THE MANY-ELECTRON WAVE FUNCTION AND THE NATURAL ORBITALS

Building wave functions in molecular quantum chemistry starts from generating a "basis set," which normally consists of atom-centered functions obtained from calculations on individual atoms. Let us assume that there are m of these atomic orbitals (AOs) and call them (χ_p, $p = 1, m$). We can construct the MOs, φ_i as a linear expansion in these basis functions (the LCAO method; LCAO = linear combination of atomic orbitals). A spin function has to be attached to each molecular orbital and we define the molecular spin orbitals, (SO) as:

$$\psi_i = \phi_i \theta_i = \sum_p a_{ip} \chi_p \theta_i \tag{1}$$

The spin function θ_i can take two values (α or β), so with m linearly independent basis functions we can construct $2m$ SOs.

Now, suppose that our system has n electrons. We can then build $N = \binom{2m}{n}$ Slater determinants, Φ_K, by occupying n of the $2m$ SOs in all possible ways. The total wave function, Ψ, can be expanded in this n-electron basis:

$$\Psi = \sum_K C_K \Phi_K \tag{2}$$

The variation principle can be used to determine the expansion coefficients, C_K. This leads to the well known secular equation:

$$\sum_L (H_{KL} - \delta_{KL} E) C_L = 0 \tag{3}$$

In the limit of a complete basis set, this equation becomes equivalent to the Schrödinger equation. For a finite basis set, Equation (2) represents the best wave function (in the sense of the variation principle) that can be obtained. It is called the "Full CI" (FCI) wave function. It serves as a calibration point for all approximate wave-function methods. It is obvious that many of the coefficients in Equation (3) are very small. We can consider most approximate MO models in quantum chemistry as approximations in one way or the other, where one attempts to include the most important of the configurations in Equation (2). We notice that the FCI wave function and

energy are invariant to unitary transformations of the MOs. We could actually use the original AO basis set, properly orthonormalized. We may then ask the question of whether there is any special representation of the MOs that will concentrate as much information as possible in as few configurations as possible. An answer to this question was given by P.-O. Löwdin in a famous article from 1955,[8] in which he gives strong indications that the fastest convergence of the CI expansion is obtained when the orbitals used are the natural spin-orbitals.

2.41.2.1 The First-order Density Matrix and the Natural Spin-orbitals

The probability density of electrons $\rho^{(s)}(x)$ in a quantum-mechanical system is given by the diagonal element of the "first-order reduced-density matrix," $\rho^{(s)}(x;x')$ (the superscript s indicates that these quantities depend on the electron-spin:

$$\rho^{(s)}(x;x') = n \int \psi(x';x_2,x_3 \ldots,x_n)^* \psi(x;x_2,x_3 \ldots,x_n) \mathrm{d}x_2 \mathrm{d}x_3 \ldots \mathrm{d}x_n \tag{4}$$

$x_i = (\mathbf{r}_i, \zeta_i)$, where $\mathbf{r}_i$ is the space and ζ_i the spin variable for electron i. If we know this matrix, we can compute all one-electron properties of our system. To compute also the two-electron properties, including the total energy, we need to know also the second-order reduced-density matrix. We can represent the density matrix in our basis of SOs as:

$$\rho^{(s)}(x;x') = \sum_{i,j} D_{i,j}^{(s)} \psi_i(x')^* \psi_j(x) \tag{5}$$

The matrix $\mathbf{D}^{(s)}$ is Hermitian and can be brought to diagonal form by a unitary rotation of the orbitals. The new orbitals are called the "Natural Spin-orbitals" (NSOs), $\lambda_i^{(s)}$. In terms of them, the density matrix is given as:

$$\rho^{(s)}(x;x') = \sum_i \eta_i^{(s)} \lambda_i^{(s)}(x')^* \lambda_i^{(s)}(x) \tag{6}$$

The quantities $\eta_i^{(s)}$ are called the "occupation numbers" of the NSOs and fulfill the condition: $0 \leq \eta_i^{(s)} \leq 1$.[8]

2.41.2.2 Spin Integration and the Natural Orbitals

The electron spin can be separated out in $\rho^{(s)}(x;x')$. If we do that and integrate over the spin variables, we obtain the charge-density matrix, $\rho(\mathbf{r};\mathbf{r}')$, which we shall also call the 1-matrix. It can be expanded in the MOs:

$$\rho(\mathbf{r};\mathbf{r}') = \sum_{i,j} D_{i,j} \phi_i(\mathbf{r}')^* \phi_j(\mathbf{r}) \tag{7}$$

Again, we can diagonalize the matrix $\mathbf{D}$ and obtain a representation of the 1-matrix in diagonal form:

$$\rho(\mathbf{r};\mathbf{r}') = \sum_i \eta_i \lambda_i(\mathbf{r}')^* \lambda_i(\mathbf{r}) \tag{8}$$

The orbitals λ_i are called "Natural Orbitals" (NO). Their occupation numbers, $\eta_i \leq$ fulfill the condition: $0 \leq \eta_i \leq 2$.

The natural orbitals have properties that are very stable, independently of how the wave function has been obtained. We find for all molecular systems that the NOs can be divided into three different classes: One group of orbitals have occupation numbers close to 2. These orbitals may be considered as almost doubly occupied. We call them "strongly occupied." There is another large group of orbitals that have occupation numbers close to zero (typically smaller than 0.02). These are the "weakly occupied" NOs. For stable, closed-shell molecules close to their equilibrium geometry, we shall find only these two types of NOs. However, in more complex situations (molecules far from equilibrium geometry, excited states, radicals, ions, etc.) we find a

third class of NOs, with occupation numbers that are neither small nor close to two. In open-shell systems (radicals, transition-metal compounds, etc.) we find one or more orbitals with occupation numbers close to one. If we follow a chemical reaction over a barrier, we may find cases where an occupation number changes from two to zero, while another moves in the opposite direction. An example is given in Figure 1, which shows how the occupation numbers of the NOs vary when two ethene fragments approach each other and form cyclobutane (the approach is along the symmetry-forbidden reaction path, which keeps D_{2h} symmetry).

The figure shows the four orbitals with occupation numbers that deviate most from two or zero. At large distances they are the π-bonding and antibonding orbitals of the two ethene fragments. They have occupation numbers of about 1.9 and 0.1, respectively. Close to the transition state for the reaction, one of the bonding orbitals becomes antibonding and weakly occupied, while another orbital becomes bonding and strongly occupied. A picture of the four orbitals in this region is shown in Figure 2. The two first orbitals have occupation numbers close to one, the third about 1.9, and the fourth 0.1.

At the end of the reaction we have two new bonding orbitals from the ring. They are single bonds, which typically have occupation numbers close to two. The importance of this analysis is that it is valid for the exact wave function. Whether it remains true for approximate methods depends on the method. Below we shall discuss an approach that takes these features of the electronic structure explicitly into account. But first, we shall look more closely at the situation where all occupied orbitals have occupation numbers close to two. This situation is common for most molecules in their ground electronic state, close to their equilibrium geometry. It is a natural first approximation to assume that the occupation numbers are exactly two or zero, which can be

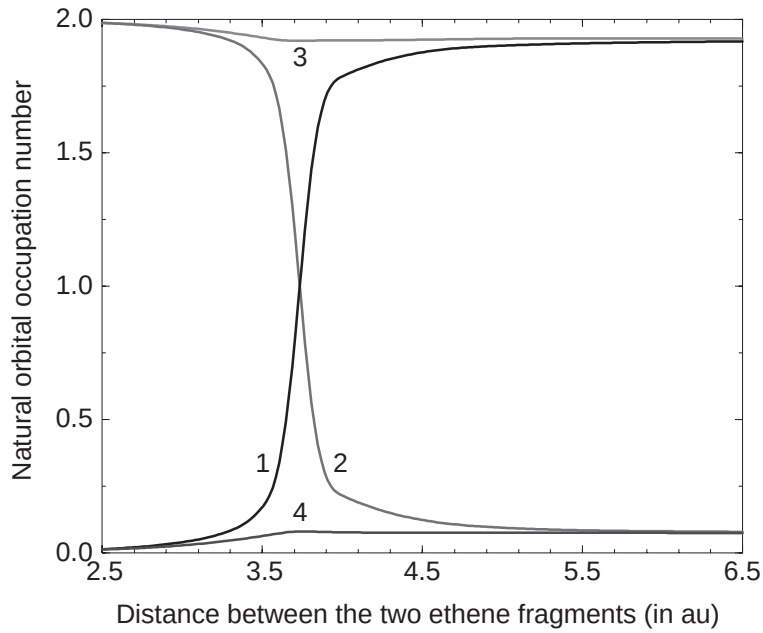

Figure 1 Natural orbital occupation numbers for the active orbitals (1–4) in C_4H_8 as a function of the distance between the two C_2H_4 fragments. The NOs are shown in Figure 2.

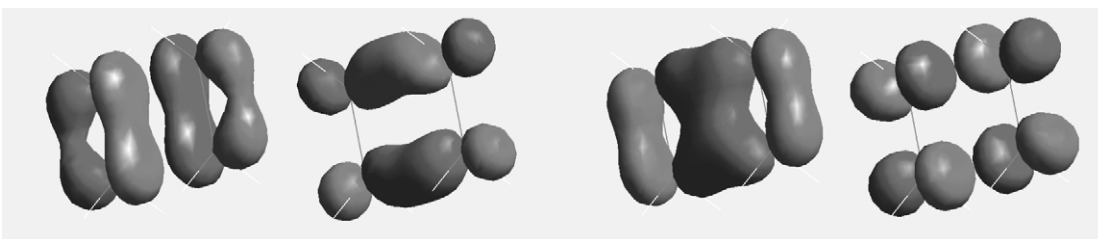

Figure 2 The four natural orbitals in C_4H_8, which change character during the reaction. The distance between the two ethene fragments is 2 Å.

shown to be equivalent to assuming that the total wave function is a single configuration (Slater determinant). This is the closed-shell HF model.[7]

2.41.3 THE HARTREE–FOCK METHOD

The simplest approximation we can make of the full CI expansion of the wave function is to assume that one configuration is enough to describe the wave function. This is equivalent (in the spin-orbital formulation) to select n SOs from the full set. The corresponding wave function is the antisymmetrized product of these SOs:

$$\psi_{UHF} = \hat{A}\{\psi_1(x_1)\psi_2(x_2)\cdots\psi_n(x_n)\} \tag{9}$$

where $\hat{A}$ is the antisymmetrizer ($\hat{A} = \Sigma_p(-1)^p\hat{P}$; the summation running over all permutations with parity p, $\hat{P}$, of the electron coordinates). In this model, we thus divide the SO space into an occupied and an unoccupied (virtual) part. Obviously, the quality of this wave function will strongly depend on how we choose the occupied orbitals (in contrast to full CI, which is invariant to this choice). The HF orbitals are those which make the energy corresponding to Equation (9) stationary. We shall not attempt to derive the corresponding equations here; the reader is referred to existing literature on the subject (see for example ref. 9). The final result is an equation for the orbitals that can be written in the form:

$$\hat{F}\psi_i = \varepsilon_i\psi_i \tag{10}$$

where $\hat{F}$ is a one-electron operator, which for a molecule has the following form:

$$\hat{F} = \hat{T} - \sum_A \frac{Z_A}{|\mathbf{r} - \mathbf{R}_A|} + \hat{J} - \hat{K} \tag{11}$$

Here, $\hat{T}$ is the kinetic-energy operator and the second term gives the Coulomb attraction between the electron and the nuclei A. The third and fourth terms describe the interaction between one electron and all other electrons. The first of them is the Coulomb operator:

$$\hat{J}\psi_i(x_1) = \int \frac{\rho(x_2;x_2)}{r_{12}}\psi_i(x_1)\mathrm{d}x_2 \tag{12}$$

This term is thus completely classical and describes the Coulomb repulsion between an electron in spin-orbital ψ_i and the total electron density, ρ. We note that ρ is given in terms of the orbitals. The HF equation is thus not linear but has to be solved self-consistently—that is, until the input density used to construct $\hat{J}$ equals the output density. The efficiency of current SCF programs lies in their ability to achieve fast convergence in this iterative process, and many ingenious convergence procedures have been derived for this purpose.

The second term is the exchange operator. It results from the antisymmetry of the wave function and may be written as:

$$\hat{K}\psi_i(x_1) = \int \frac{\rho(x_2;x_1)}{r_{12}}\psi_i(x_2)\mathrm{d}x_2 \tag{13}$$

It is easy to see by inserting the definition from Equation (5) of ρ that while all electrons contribute to $\hat{J}$, only those with the same spin as ψ_i will be included in $\hat{K}$. It may be shown that this contribution to the total energy is negative. The exchange terms thus lower the energy of the system, because electrons with parallel spins avoid one another, resulting in a reduction of the repulsion. The antisymmetry of the wave functions results in zero probability for finding two electrons with the same spin in the same point in space. This is the so-called Fermi hole. The HF model does not prevent electrons with opposite spins from occupying the same point in space, which has important consequences for the energy error of the HF model: the so-called "correlation energy." It arises mainly from the interaction of pairs of electrons with opposite spins and can, to a good approximation, be written as a sum of pair energies. The success of second-order

perturbation theory (MP2) for computing the correlation energy is based on this property of the HF wave function.

We also notice that the exchange operator is nonlocal, because the results depend on the value of ψ_i in all points in space. One of the challenges in DFT theory is to model the nonlocal exchange with a local operator.

The eigenvalue of the HF orbital ψ_i, ε_i, can be identified as an energy of the electron in that orbital. The background is Koopmanns' theorem, which states that removing one electron from an occupied orbital, without modifying the remaining ones, results in an energy increase $-\varepsilon_i$, thus relating the eigenvalues of the occupied orbitals to the ionization energies of the molecule. In the same way, it may be shown that the energies of the virtual orbitals give a measure of the electron affinity. It is important to emphasize that these relations are only approximate, because they do not include relaxation of the density and electron-correlation effects. They are nevertheless important conceptually, because they give a model of the electronic structure where the electrons move in well-defined molecular orbitals with an equally well-defined orbital energy. This is the shell model for molecules, except for one little detail.

The formalism given above assigns one spin-orbital to each electron. In principle they all have different space parts. However, if you perform such a calculation for the water molecule, you will find that orbitals for α and β spin are pairwise identical. The result is five occupied MOs, each with two electrons of opposite spin. The concept of the closed shell is thus a result in HF theory. Not all molecules behave in this way, but many do so when they are close to their equilibrium geometry. The pairing is self-consistent for an even number of electrons, that is, if the electrons are paired in identical orbitals, the HF equation for α and β spin orbitals will be identical and will thus give a paired solution. The only question is whether the solution is stable (is a minimum). It may be shown that this property of the solution is related to the energy difference between the closed-shell state and the lowest triplet state. When this energy is too low, the paired solution becomes unstable, and another solution, with different orbitals for different spins, appears with a lower energy. Such a wave function is no longer an eigenfunction of the total spin and may also break the molecular point-group symmetry.

A closed-shell structure for a ground-state molecular wave function is possible only for an even number of electrons. An open shell will always lead to spin polarization, that is, different orbitals for different spins for all electrons. The model with this property is called "Unrestricted Hartree–Fock," UHF. It is possible to impose the restriction of pairing also for open-shell systems, but this is then an additional condition that will lead to a higher energy than the corresponding UHF solution. Such an approach is called "Restricted Hartree–Fock," RHF. It may be constructed in such a way that the wave function is an eigenfunction of the total spin, which is not a property of the UHF approach.[10] However, as we shall discuss below, open-shell systems need in general a higher-order treatment, where more than one determinant is used to expand the wave function.

The HF approach is surprisingly accurate for normal closed-shell molecules involving only light (first- and second-row) atoms. Bond distances are usually represented with an accuracy of 0.02 Å or better and the accuracy in bond angles is a few degrees. Physical properties like dipole moments etc. are predicted with errors of the order of 10%. For an extensive error analysis of different quantum chemical methods, see for example ref. 11. It should be noticed, however, that for systems including heavier atoms, the errors may be larger also when the system is a closed shell. A typical example is ferrocene, where the metal–ring distance is overestimated with 0.23 Å at the HF level.[12] The error can be related to strong electron-correlation effects in the 3*d* shell of iron. Thus, one cannot use the HF approach with confidence for studies of coordination compounds. Electron correlation has to be invoked already when the wave function is determined.

HF theory cannot be used to compute properties that are related to processes where electron pairs are formed or broken. The correlation error depends strongly on the number of such pairs. Examples of such processes are dissociation of a chemical bond, ionization, excitation, passing a transition state in a chemical reaction, etc. The possible applications of HF theory are thus severely limited. Methods to compute the correlation energy starting from an HF reference wave function are described in several articles in this book. The most commonly used methods today for ground-state systems are probably second-order perturbation theory and DFT.

However, in several cases it is not possible to use HF theory at all. It is based on the assumption that the natural orbitals have occupation numbers close to either two or zero (in the closed-shell case). We saw in the example of C_4H_8 that this is not always the case. Some orbitals may drastically change their occupation during a chemical process. In strongly correlated

systems, like some transition metals, the HF method might give large errors even if the occupation numbers are not very different from zero, one, or two. In such cases it is necessary to extend the theory and allow for occupation numbers different from two or zero.

2.41.4 ACTIVE ORBITALS AND MULTICONFIGURATIONAL WAVE FUNCTIONS

Let us take a closer look at the $C_2H_4 + C_2H_4 \rightarrow C_4H_8$ reaction. Why do the orbitals change their occupation numbers? Let us introduce the following notations:

- φ_1 ethene bonding but antibonding between the two (orbital 1 in Figure 2)
- φ_2 ethene antibonding but bonding between the two (orbital 2)
- φ_3 bonding between all four carbons (orbital 3)
- φ_4 antibonding between all four carbons (orbital 4).

At large distances between the two moieties, the orbitals φ_1 and φ_3 will be doubly occupied. This gives a wave function that we symbolically can write as (forgetting all other electrons):

$$\psi_1 = (\varphi_1)^2(\varphi_3)^2 \tag{14}$$

When cyclobutane has been formed the two orbitals that form the new bonds, φ_2 and φ_3, will instead be occupied and we get the wave function:

$$\psi_2 = (\varphi_2)^2(\varphi_3)^2 \tag{15}$$

So, orbital φ_3 is always occupied and its occupation number changes only little during the reaction. Orbital φ_4 is always weakly occupied. Orbitals φ_1 and φ_2, however, change their occupation, φ_1 from zero to two and φ_2 in the opposite way.

What will happen to the energies along the reaction path for these two HF configurations? The energy surface for ψ_1 will clearly become repulsive when the two ethene molecules approach each other, because ϕ_1 is antibonding. ψ_2 will, however, become repulsive when we dissociate the new bonds, since this configuration cannot give ethene double bonds. The electronic configuration will have to change from ψ_1 to ψ_2 at some point along the reaction path. This will happen at the point where the two potentials cross, that is, where they have the same energy. If they are used as basis functions in a two-by-two CI calculation, one obtains:

$$\psi = \frac{1}{\sqrt{2}}(\psi_1 - \psi_2) \tag{16}$$

The natural orbitals of this wave function will be the same, but now φ_1 and φ_2 will have the occupation number one. This is the crossing point shown in Figure 1. So, we have three wave functions: Equation (14), valid at infinite distance; Equation (15), valid at the C_4H_8 equilibrium geometry; and Equation (16), valid in the transition-state region. How do we write a wave function that is valid for the full reaction path? The obvious choice is to abandon the single-configuration (HF) approach and write:

$$\psi = C_1\psi_1 + C_2\psi_2 \tag{17}$$

and determine not only the orbital but also the configuration-mixing coefficients by the variation principle. The example illustrates a chemical process where we need to go beyond the single-determinant approach in order to understand the electronic structure. But note that the basic quantity is still the natural orbitals. It is obvious that this example illustrates a whole class of chemical processes: chemical reactions that involve a change of electronic configuration.

Let us take another example which is of interest in coordination chemistry. It concerns the nickel atom and its lower excited states. The ground state is ^3D ($3d^9 4s$), but 0.03 eV higher is ^3F ($3d^8 4s^2$). These values are averaged over the J components. 1.70 eV higher we find the closed-shell ^1S ($3d^{10}$) state. If we compute these relative energies at the RHF level, we find $\Delta E(^3D \rightarrow {}^3F) = -1.63$ eV and $\Delta E(^3D \rightarrow {}^1S) = 4.33$ eV. It turns out to be very difficult to compute these energies accurately (see for example Ref. 13 for a discussion of results at different levels of

theory). The reason is strong radial correlation effects in the (almost) filled $3d$ shell. Actually, it was noted early on that for the copper atom a large fraction of the correlation energy could be recovered if an electron configuration $4s3d^9 3d'$ was used, instead of $4s3d^{10}$.[14] This "double-shell" effect has been found to be important for a quantitative understanding of the electronic spectra of transition metals with more than a half-filled d-shell, not only for free atoms but also for complexes.[15] The occupation numbers of the orbitals in the second d-shell are not very large (of the order of 0.01–0.02), but their contribution to the energy is large. The example shows that there is not always a trivial relation between the occupation numbers and the importance of a natural orbital for the description of the electronic structure and the energetics of a molecular system.

How can we extend HF theory to incorporate the effects of the most important natural orbitals, even in cases where the occupation numbers are not close to two or zero? Actually, Löwdin gave an answer to this question in his 1955 article, where he derived something he called the "extended HF equations."[8] The idea was to use the full CI wave function, Equation (2), but with a reduced number of orbitals, and determine the expansion coefficients and the molecular orbitals variationally. His derivation was formal only and had no impact on the general development at the time. It was not until 20 years later that a similar idea was suggested and developed into a practical computational procedure. The approach is today known as the "complete active space SCF" method, CASSCF.[16]

The CASSCF method is based on some knowledge of the electronic structure and its transformation during a molecular process (chemical reaction, electronic excitation, etc.). This knowledge can, if necessary, be achieved by making experiments on the computer. Let us use C_4H_8 as an example. We noticed that four of the MOs in this molecule will change their occupation numbers considerably along the reaction path. Four electrons are involved in the process. We shall call these orbitals "active." The other electrons remain in doubly occupied orbitals. Such orbitals will be called "inactive." The inactive and active orbitals together constitute a subset of the MO space. Remaining orbitals are empty. We can define configurations in this subspace by occupying the four active orbitals with the four electrons in all possible ways. It is left to the reader to show that the number of such configurations with the spin quantum number zero (singlet states) is 20. The number of Slater determinants is $\binom{8}{4} = 70$, which includes, in addition to the singlet states, 3×15 triplet and 5×1 quintet states. Of the twenty singlet configurations, only eight have the correct symmetry. The wave function is thus in this case a linear combination of these eight configuration functions (CFs). Above, we discussed the electronic structure in terms of only two CFs, so it is clear that we do not need to invoke all eight functions. However, the selection of individual configurations to use in the construction of the total wave function is a complicated procedure that easily becomes biased. The CAS approach avoids this by specifying only the inactive and active orbitals.

The choice of the active orbitals is in itself nontrivial. Again, we can use C_4H_8 as an example: we chose the four orbitals that changed character along the reaction path. Two of them are C—C σ-bonding in the final molecule, and the other two are antibonding in the same bonds. Thus we have a description where two of the bonds are described by two orbitals each, while the two other C—C bonds (those of the original ethene moieties) are inactive. If we optimize the geometry of the C_4H_8 molecule with such an active space, we shall find it to be rectangular and not quadratic. The D_{4h} symmetry of the molecule demands that the four C—C bonds are treated in an equivalent way. Thus we need an active space consisting of eight orbitals and eight electrons. The resulting wave function will comprise 1,764 CFs, which will be reduced to a few hundred because of the high symmetry.

2.41.4.1 Bond Dissociation

Another example that illustrates the breakdown of the HF approximation concerns the dissociation of a chemical bond. Assume that two atoms A and B are connected with a single bond involving two electrons, one from each atom. To a good approximation we can describe the bond with the electronic configuration $\psi_1 = (\sigma)^2$, where:

$$\sigma = N(\sigma_A + \sigma_B) \tag{18}$$

and σ_A and σ_B are two atomic orbitals, one on each atom. This wave function is, however not valid at large interatomic distances, because it contains ionic terms, where both electrons reside on the same atom. Here, the wave function is better described in terms of the localized orbitals:

$$\psi_\infty = (\sigma_A(1)\sigma_B(2) + \sigma_A(2)\sigma_B(1))\Theta \tag{19}$$

where Θ is a spin function for a singlet state with two electrons. This wave function can also be written as:

$$\psi_{\infty} = \frac{1}{\sqrt{2}}(\psi_1 - \psi_2) \tag{20}$$

where ψ_1 is the bonding configuration given above and $\psi_2 = (\sigma^*)^2$, where σ^* is the antibonding orbital:

$$\sigma^* = N^*(\sigma_A - \sigma_B) \tag{21}$$

Thus, the wave function is described by two electronic closed-shell configurations at infinite distance between the atoms. The situation is actually identical to what was obtained in the transition-state region for the cyclobutane reaction. The reason is also the same: the two configurations $(\sigma)^2$ and $(\sigma^*)^2$ become degenerate at dissociation and will mix with equal weights. It is clear that a wave function that describes the full potential curve for the dissociation of a single bond should have the form:

$$\psi = C_1\psi_1 + C_2\psi_1 \tag{22}$$

The two natural orbitals σ and σ^* will have the occupation numbers $\eta = 2C_1^2$ and $\eta = 2^*C_2^2$, respectively. At infinite distance they will both be one, but near equilibrium almost all of the occupation will reside in the bonding orbital. For weak bonds, an intermediate situation obtains and we can actually define a bond order, *BO*, from the natural orbital occupation numbers:

$$BO = \frac{\eta - \eta^*}{\eta + \eta^*} \tag{23}$$

which becomes one when η^* is zero and zero when both are one.

An illustration of a more complicated, multibonding situation is given by the chromium dimer. Here, six weak bonds are formed between the 3*d* and 4*s*-orbitals of the two Cr atoms. CASSCF calculations with 12 electrons in the 12 valence orbitals provide the NO occupation numbers given in Table 1 at the equilibrium geometry.

The computed total bond order, using the formula given above, is 4.4. Effectively, two Cr atoms form a quadruple bond even if all twelve electrons are involved. One notices that the occupation number of the antibonding δ-orbital is large, indicating a weak bond. In Figure 3 we show how the NO occupation numbers vary with the interatomic distance.

The vertical line indicates the equilibrium distance. We can see how the 4*s* bond is formed at larger distances than the 3*d* bonds, and also that the 3*dσ* and 3*dπ* bonds are stronger than the 3*dδ* bond.[17]

The general conclusion we can draw from the above exercises is that, in order to describe the formation of a chemical bond, we need to invoke both the bonding and antibonding orbitals. It is only for strong bonds close to equilibrium that the bonding orbital dominates the wave function.

Another conclusion we can draw is that if we are in a situation where two or more electronic configurations (of the same symmetry) have the same or almost the same energy, they will mix strongly and a quantum-mechanical model that takes only one of them into account will not be valid.

Table 1 NO occupation numbers at the equilibrium geometry of bonds between 3*d* and 4*s*-orbitals of two Cr atoms.

Orbital pair	*Bonding*	*Antibonding*	*Bond order*
4*s*	1.890	0.112	0.89
3*dσ*	1.768	0.227	0.77
3*dπ*	3.606	0.394	1.61
3*dΔ*	3.134	0.868	1.13

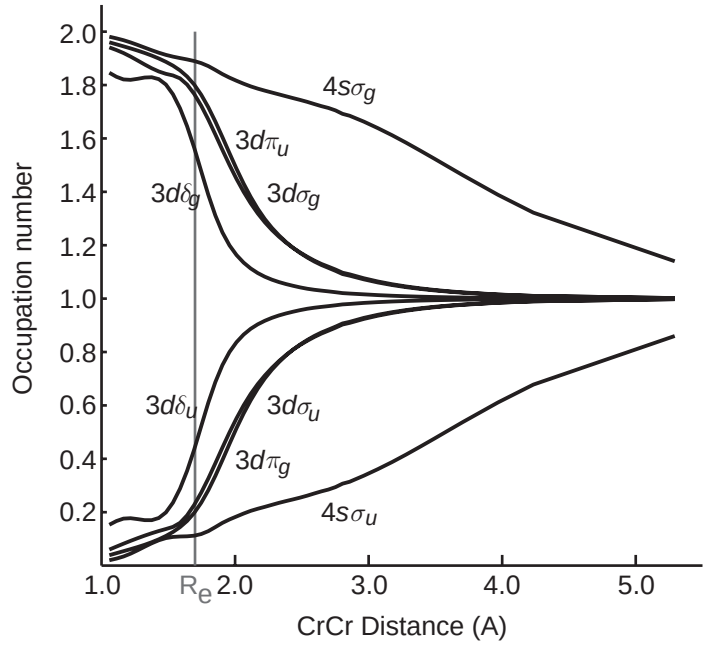

Figure 3 Natural orbital occupation numbers for the bonding and antibonding orbitals in Cr_2 as a function of the distance between the two atoms.

2.41.4.2 The Complete Active Space SCF Model–CASSCF

The CASSCF model has been developed to make it possible to study situations with near-degeneracy between different electronic configurations and considerable configurational mixing. In Figure 4 we illustrate the partitioning of the orbital space into inactive, active, and virtual.

The wave function is a full CI in the active orbital space. By using spin-projected configurations, we can select those terms in the full CI wave function that have a given value of the total spin. When the system has symmetry, we can also add the condition that the selected terms shall belong to a given, irreducible representation of the molecular point group. The wave function will then be well defined with respect to these properties. It will considerably reduce the length of the CI expansion. In the example of C_4H_8, we could decrease the size from a total of seventy CFs to eight by selecting only the terms for which $S=0$ (singlets) and which belong to the totally

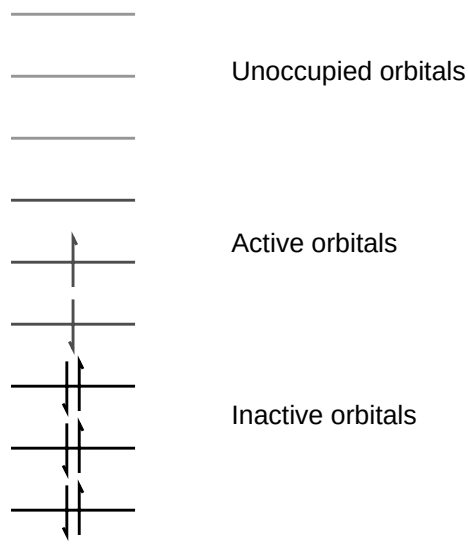

Figure 4 The partitioning of the orbital space into inactive, active, and virtual in the CASSCF method.

symmetric representation of the D_{2h} point group. Apart from these restrictions, our wave function is completely general. It may contain an arbitrary number of open shells, and it may belong to any of the irreducible representations of the point group. With the CASSCF approach it becomes equally simple to study the potential of the $^{13}\Sigma_g^+$ Cr_2 as it is to study the $^1\Sigma_g^+$ ground state (both dissociate to ground-state Cr atoms).

We shall not discuss here in any detail how one proceeds to optimize a CASSCF wave function. The reader is referred to the existing literature.[11,16,18] Instead we shall continue with some study cases, to illustrate how the multiconfigurational approach is used in practical applications. But, before that, a few words about the remaining error.

The CASSCF model allows us to include into the wave functions contributions from the most important NOs that describe the most important correlation effects among the electrons. This type of correlation is often called "static" or "nondynamic." It is usually long range and describes effects on the electronic structure leading to separation of the electrons in a pair. Typical examples are dissociation of a chemical bond, or the C_4H_8 reaction described above. This partitioning of the electron correlation is not strict, as is illustrated by the Ni atom, where the separation of the electrons through the introduction of a second 3*d* shell is not long range. The remaining error is called "dynamic correlation" and is caused by the instantaneous correlation of electrons in the region where the interelectronic distance is close to zero—the cusp region. It can be treated by the CASSCF method only for very small molecules with few electrons, because a large number of NOs are needed for an accurate description. A thorough discussion of the convergence of the dynamic correlation energy in CI like methods may be found in ref. 11.

Only a few accurate methods exist today for the treatment of the dynamic correlation energy in cases where the nondynamic effects are large. For systems where HF theory is adequate, a number of different approaches exist, the most accurate being CC theory. The most commonly used approach for large molecules is probably Møller–Plesset second-order perturbation theory, MP2. We again refer to ref. 11 for a detailed discussion of these methods. They are all based on an HF reference function. DFT may also be considered to belong to this type of method, even if it is not so clear how well the method will work in the case of near-degeneracy. Some applications indicate that it might work reasonably well, but others give less accurate results.

It has not yet been possible to extend the CC approaches in a systematic way to the multiconfigurational regime. For small molecules it is possible in this case to use large multireference CI methods, where the most important configurations in a CASSCF wave function are used as reference functions, and the CI expansion comprises all single and double excitations from the occupied orbitals to virtual or other (partially) occupied orbitals. The size of such a CI expansion grows, however, too quickly to be of interest for larger molecules.

An alternative approach was developed about ten years ago. It may be regarded as an extension of the MP2 method to the case where the reference function (the zeroth-order approximation) is not a HF but a CASSCF wave function.[19–21] It has been named CASPT2. We shall not describe the method in detail here, but it will be used in the illustrations discussed below. The accuracy is limited by the possibility of choosing an adequate active space for the CASSCF wave function, and by the fact that the remaining correlation effects are treated only to second order in perturbation theory. Nevertheless, it has been used successfully in a large number of studies of a variety of properties of ground and excited states in organic and inorganic molecules and coordination compounds involving transition metals, lanthanides, and actinides. Also metal-containing active sites in proteins have been studied. We shall below give a few examples.

2.41.5 THE COORDINATION OF NICKEL WITH ETHENE

As a first example we use the complex formed between a nickel atom and the ethene molecule. This compound is a prototype for coordination of a transition metal to a double bond in an organic molecule. It is traditionally understood in terms if the Dewar–Chatt–Duncanson (DCD) model,[22,23] where the bonding is described as donation of electrons from the ethene π-orbital to Ni and a corresponding back-donation from Ni(3*d*) to the π^*-orbital. However, it is not obvious that the binding may be described by such a simple model, because there is no empty Ni orbital into which electrons may be donated. The dissociation of the molecule gives Ni in the $3d^9 4s$, ^{1}D, state with one occupied 4*s*-orbital, which would prevent an effective back-donation. A number of studies of this compound have been performed using the CASSCF/CASPT2 method.[24–26] From these studies a somewhat more complex picture of the bonding has emerged, which is not in

conflict with the DCD model, but explains how the problem with the 4*s*-orbital is solved by the bonding mechanism. This explanation is multiconfigurational in nature, and resembles in a way our preceding discussions about how a configuration changes to another one in the course of a chemical reaction. Let us take a closer look at these results. The molecule has C_{2v} symmetry, with nickel bonded at the center of the C—C bond perpendicular to the ethene plane.

The Ni atom in its ground state has one singly occupied 3*d* and one 4*s*-orbital coupled to a triplet. The situation resembles two radicals, but here we have both electrons on the same atom. With two radicals we can form the bonding and antibonding combination of the localized radical orbitals and write the wave function as a linear combination of two configurations, as was discussed above in the section on bond dissociation (Equation (16)). We can do the same here and form the orbitals $3d+4s$ and $3d-4s$. The wave function then has the symbolic form:

$$\psi = C_1(3d + 4s)^2 + C_2(3d - 4s)^2 \tag{24}$$

This is an equally valid representation of the ^{1}D state. The $3d+4s$-orbital is the hybrid that points towards the C—C bond of the ethene molecule, while the other hybrid points away from ethene.

The coefficient C_1 will start to decrease when the nickel atom approaches the ethene double bond, while C_2 will increase to a value close to one. Thus, the electron pair which causes the repulsion is moved out of the way, and binding can take place between the $3d+4s$-orbital on Ni and the π-orbital on ethene. The two orbitals are shown in Figure 5 as $9a_1$ and $10a_1$ (bottom left). It is evident from the shape of $9a_1$ that a rather covalent bond is formed. The occupation number of this orbital is close to two, because there is no low-lying orbital that can be used for correlation.

The second bond is formed between the $3d_{xz}$-orbital (*xz* is the NiCC plane) and the empty ethene π^*-orbital. This bond is also quite covalent (orbital $5b_2$ in the figure), but weaker. The occupation number is 1.91, with 0.09 electrons in the corresponding antibonding $6b_2$-orbital. The other orbitals in Figure 5 are the doubly occupied 3*d*-orbitals of Ni and the corresponding correlating orbitals, the 3*d*′-orbitals of the Ni double shell. It can be seen from the pictures that the latter orbitals occur in pairs with the 3*d*-orbitals and have a clear 4*d* character.

The covalency of the Ni–ethene bond is a result of the multiconfigurational treatment. The charge of the Ni atom at the HF level is +0.9, which reduces to +0.5 when the extra NOs are added. For a more detailed discussion of the bonding, including also a discussion of the bond energy, we refer to the original article.[26] What we have seen here is another example of the need for a multiconfigurational treatment for the complete understanding of the binding mechanism.

2.41.6 THE FERROCENE MOLECULE

As a second example of the coordination of a transition metal to carbon, we shall look at the binding in another prototype molecule, ferrocene. This molecule was a challenge to *ab initio* quantum chemistry for a long time, because of the difficulty in computing the iron–ring distance. Calculations at the HF level overestimate this distance by as much as 0.20 Å. Adding correlation at the MP2 level leads instead to a distance that is 0.17 Å too short.[26] Only highly correlated calculations, which include all valence electrons, the semi-core of Fe, and the dispersion interaction between the two cyclopentadienyl rings, were able to reproduce the experimental bond distance.[26,27] Here we shall not discuss these problems in detail, but only illustrate how the bonding mechanism is described in a multiconfigurational approach. It should be mentioned, however, that when the most important NOs are included in the wave function (as described below) the bond distance is reduced from 1.86 Å (SCF result) to 1.72 Å, now only 0.06 Å longer than the experimental value. Thus, a semiquantitative result may be obtained already at this level of theory. Higher accuracy can be obtained only by adding dynamical correlation effects. Before starting the discussion of the electronic structure, it might be of some interest for the reader to show in some detail how the calculations of the NOs were performed. We therefore give below computational details.

2.41.6.1 Computational Details

A new set of calculations was performed for the present discussion. This were done on a Linux-equipped laptop. The MOLCAS quantum-chemistry software was used.[28] The basis set was of the

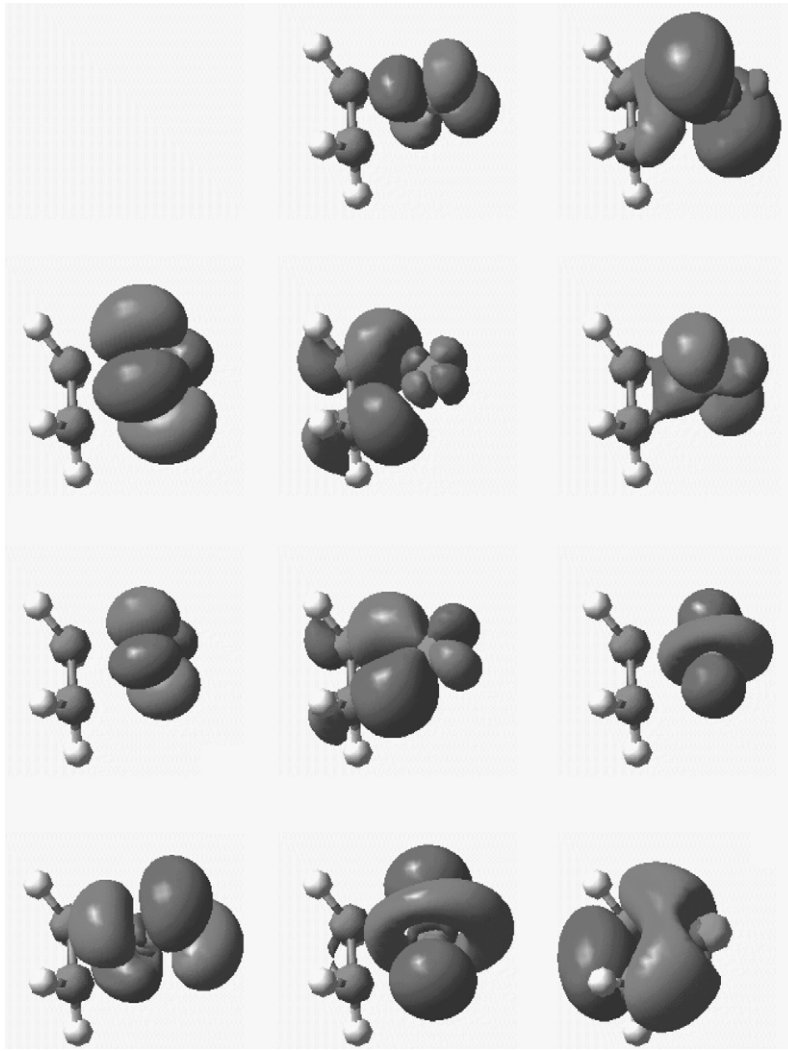

Figure 5 Natural orbitals in the NiC_2H_4 molecule. Counted from left to right and from bottom up, the orbitals are (occupation numbers within parentheses): $9a_1$ (2.00), $10a_1$ (1.98), $11a_1$ (1.97), $12a_1$ (0.03), $13a_1$ (0.02), $5b_2$ (1.91), $6b_2$ (0.09), $4b_1$ (1.98), $5b_1$ (0.02), $2a_2$ (1.98), $3a_2$ (0.02).

Atomic Natural Orbital type (ANO-L of the MOLCAS library[29,30]). The ANOs are well suited to multiconfigurational calculations, because they have been determined from correlated calculations on the atoms. Thus, the basis set contains functions that are optimized for atomic correlation. For iron, the basis set contained 7 *s*-type, 6 *p*-type, 3 *d*-type, and 1 *f*-type ANOs. 3*s*2*p*1*d* was used for carbon and 2*s*1*p* for hydrogen. This is a rather limited basis set. It cannot be used to compute energy-related quantities, but for the present purpose of demonstrating the NOs and their occupation, it is satisfactory. The geometry chosen was from an earlier study[26]: Fe–ring distance = 1.643 Å, r(C–C) = 1.423 Å, and r(C–H) = 1.086 Å. The symmetry of the molecule is D_{5h}. In practice C_{2v} was used, but the full symmetry was preserved in the calculation.

A CASSCF calculation was performed with input orbitals from a preceding SCF calculation. The active space was chosen according to the 10-electron rule: The five 3*d*-orbitals were first chosen. For each doubly occupied orbital, an empty correlating orbital of the same symmetry was added. This could be either a 3*d*′-orbital (the double shell) or an empty ligand orbital (π^* from the ring), or a combination of both determined by the CASSCF orbital-optimization procedure. For each empty 3*d*′-orbital an occupied ligand orbital of the same symmetry was added. This gave an active space with 10 electrons in 10 orbitals. This way of selecting active orbitals for a coordination compound is quite general. It was used above for NiC_2H_4. More examples and a more detailed discussion may be found in ref. 15.

2.41.6.2 The Electronic Structure of Ferrocene

Fe^{2+} has the electronic configuration $(3d\sigma)^2(3d\delta)^4$ in ferrocene, where we have assumed that the z-axis is the fivefold symmetry axis. Rewritten in the D_{5h} symmetry it is $(a_1')^2(e_2')^4$. The empty 3d-orbitals are 3$d\pi$ (e_1''). The 10 ligand π-orbitals have the symmetries: a_1', a_2'', e_1', e_1'', e_2', and e_2'' with the following occupation: $(a_1')^2(a_2'')^2(e_1')^2(e_1'')^2$. Following the recipe given above, we thus choose the following active space (introducing also the correct numbering of the orbitals). (8,9)a_1', (4,5)e_1'' and (4,5)e_2'.

What bonding mechanism will this active space result in? Let us first look at the doubly occupied 3d-orbitals. 8a_1' will only interact repulsively with the ring, because the ring π-orbital of the same symmetry is also occupied. We thus expect a rather isolated orbital and the correlating orbital 9a_1' will then describe the double-shell effect and also be localized to iron. The orbitals are shown in Figure 6. They have the expected shape.

The situation is different for the four electrons in the 4e_2'-orbital pair. The correlating orbital is now the empty ligand orbital pair 5e_2'. Back-transfer from Fe to the rings is thus possible and a bonding and antibonding pair or orbitals may be formed. As can be seen from the picture, the delocalization is rather limited in the doubly occupied orbital. The corresponding correlating orbital pair 5e_2' is partly 4d in character but shows also an interesting ring–ring bonding feature, which would be absent in a staggered conformation. The total population in this pair is 0.11 electrons.

The 4e_1''-orbital pair should be mainly located on the rings. It is, however, extensively delocalized onto the 3$d\pi$-orbitals and an almost covalent bond is formed. The Mulliken population analysis gives 0.74 electrons in each of the 3$d\pi$-orbitals. The corresponding correlating pair is a mixture of 4d and ring π-orbitals. It has a total occupation of 0.14 electrons.

In total, 0.27 electrons are moved from the strongly to the weakly occupied orbitals, thus illustrating the difference in the picture of the bonding that the CASSCF model gives compared to HF. It is interesting to see that quite a redistribution occurs among the 3d-electrons. The

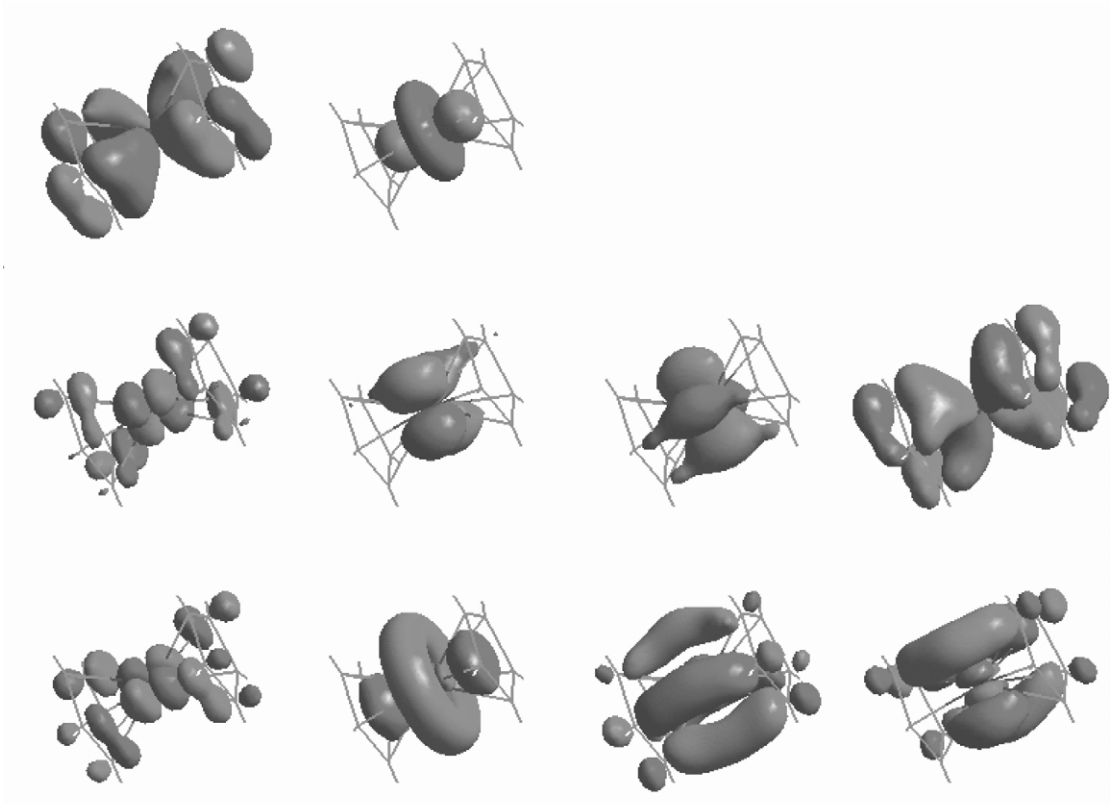

Figure 6 Natural orbitals in the ferrocene molecule. Counted from right to left and from top down, the orbitals are (occupation numbers within parentheses): 8a_1'(1.96), 4e_1''(1.95), 4e_1''(1.95), 4e_2'(1.94), 4e_2'(1.94), 5e_1''(0.07), 5e_2'(0.05), 5e_2'(0.05), 9a_1'(0.03), 5e_1''(0.07).

Mulliken population analysis gives a total of 6.78 electrons in these orbitals, to be compared to 6 in the free ion (note that the populations also include the correlating 4*d*-orbitals). Of these, 1.48 go into the 3*dπ*-orbitals, which are empty in the free ion, and 0.53 electrons are moved out of the 3*dδ*-orbitals. The total charge of the Fe atom is +0.82. The difference between this number and the total number of 3*d* electrons is due to the population of 4*p*.

The multiconfigurational picture of the electronic structure in ferrocene shows a molecule with (of course) strong ionic bonding, but in addition prominent covalent features, mainly arising from ligand-to-metal charge transfer from the filled ligand orbitals of e_1'' symmetry to the corresponding empty 3*dπ*-orbitals. The bond is reasonably strong, with an antibonding population of 0.07 in each orbital of the degenerate pair. One pair of weakly occupied orbitals also exhibits pronounced ring–ring bonding. There is a clear difference between this picture and the one obtained at the SCF level, which gives an ion more similar to free Fe^{2+}. The number of electrons in the different 3*d*-orbitals is at that level of theory: 1.89 (3*dσ*), 0.94 (3*dπ*), and 3.78 (3*dδ*). The most pronounced difference is found in the population of the bonding 3*dπ*-orbitals.

2.41.7 THE $[Re_2Cl_8]^{2-}$ ION

This ion was one of the prototypes of multiple bonding between two transition-metal ions. It was discovered and characterized in 1965 by Cotton and Harris.[31] The Re—Re bond distance was determined to be only 2.24 Å, and it was concluded that it is a quadruple bond. A similar short bond had earlier been found in the trinuclear complex $[Re_3Cl_{12}]^{3-}$[32]. These ions were to form the conceptual basis for the forthcoming development of the field multiple metal–metal bonding in transition-metal chemistry.

So, is there really a quadruple bond between the Re atoms in $[Re_2Cl_8]^{2-}$? In 1965 it was impossible to give a final theoretical answer to this question. The theoretical models that could be used were not advanced enough. The multiconfigurational approach we have access to today is, however, capable of giving a conclusive answer to the question. We know from the preceding discussion that a single bond is formed when the occupation number of the bonding orbital is close to two, while the corresponding antibonding orbital has a small occupation number. The ion has been studied in recent extensive CASSCF/CASPT2 calculations, which involve an optimization of the ground-state geometry, a characterization of the electronic structure and a detailed analysis of the electronic spectrum.[33] The calculation used a large relativistic ANO basis set and included spin-orbit coupling. We refer to the full article for all details. Here we shall only present the NOs and see what they tell us about the nature of the chemical bond.

Rhenium appears in the complex as Re^{3+}, with the electronic configuration $(5d)^4$. If we place the *z*-axis along the Re—Re bond and the Cl ions in the planes bisecting the *xz*- and *yz*-planes, we can write the configuration as $(5d_{z^2})(5d_{x^2-y^2})(5d_{xz})(5d_{yz})$ with all spins parallel. The $(5d_{xy})$-orbital is empty because of the interaction with the Cl 3*p*-orbitals. We can thus, in principle, form a quadruple bond between the two Re ions. Cotton noted already in 1965 that this bonding pattern explains the eclipsed structure of the ion, which allows one of the the 3*dδ*-orbitals to be involved in the Re—Re bonding.[34]

Let us now perform a CASSCF calculation with all the 5*d* orbitals active, and in addition the two Cl orbitals that interact with $(5d_{xy})$. This gives 12 orbitals and 12 electrons. We perform the calculation in D_{2h} symmetry, but can classify the orbitals using the full D_{4h} point group.

The resulting NOs are shown in Figure 7 with their occupation numbers (the active orbitals are for simplicity numbered from one up). We can clearly see the pairing of orbitals into bonding and antibonding. The sum of the occupation numbers for each such pair is very close to 2.0. Most strongly occupied are the two Re—Cl bonding orbitals, which involve the $5d_{xz}$-metal orbital. The two orbitals are mainly located on the Cl ions, but a population analysis gives a gross atomic population of 0.7 for each of the $5d_{xz}$-orbitals. The occupation numbers are close to two. The two corresponding antibonding orbitals (bottom left in the figure) are mainly $5d_{xz}$ in character and are only weakly populated.

The remaining eight orbitals in the figure describe the Re—Re bond. Most strongly bonding is, as expected, the *σ*-orbital, $1a_{1g}$, which has an occupation number of 2.41. Next in strength is the pair of *π*-orbitals, $1e_u$, with a total occupation number of 3.74. Finally, the *δ*-bonding orbital is occupied with 1.54 electrons. The corresponding antibonding orbitals have occupation numbers two minus that of the bonding orbital.

So, is this a quadruple bond? Formally it would seem so, because we have four bonding orbitals. But we remember from the preceding discussion that a bond is broken if the bonding

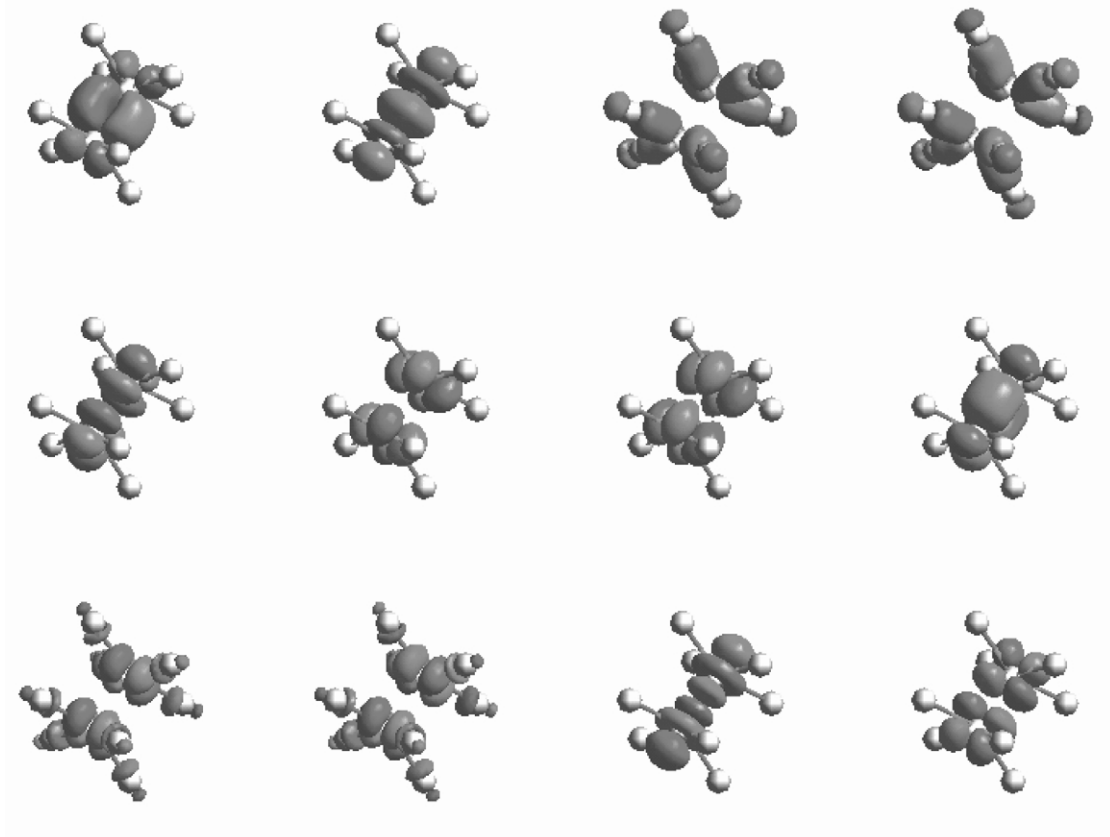

Figure 7 Natural orbitals in the $[Re_2Cl_8]^{2-}$ ion. Counted from right to left and from top down, the orbitals are (occupation numbers within parentheses): $1b_{1u}$(1.98), $1b_{1g}$(1.98), $1a_{1g}$(2.41), $1e_u$(2.41), $1e_u$(2.41), $1b_{2g}$(1.54), $1b_{2u}$(0.46), $1e_g$(0.13), $1e_g$(0.13), $1a_{2u}$(0.08), $2b_{1u}$(0.02), $2b_{1g}$(0.02).

and antibonding orbitals have the same occupation number one, and it is fully formed when the bonding orbital is occupied by two electrons. Here we clearly see intermediate situations. The bond formation varies in the order: $\sigma > \pi > \delta$. Thus it does not seem reasonable to talk about a quadruple bond. If we define the covalent bond order for the orbital pairs i, BO_i, according to Equation (23), we obtain: $BO_\sigma = 0.92$, $BO_\pi = 1.75$, and $BO_\delta = 0.54$. The summed bond order is 3.21, which is considerably less than four. It seems more appropriate to say that $[Re_2Cl_8]^{2-}$ has an effective triple bond. The weak δ-bond is reflected in the electronic spectrum of the ion, which shows a transition at 14,700 cm^{-1} due to the excitation $\delta \rightarrow \delta^*$.[35] It is clear that the weak multiple bonding, occurring between transition metals in bimetallic systems, can be understood only in a multiconfigurational framework that allows the natural orbitals to have occupation numbers different from two and zero. This is a general finding for such complexes. It was earlier demonstrated for the diatomic Cr_2. More details about the Re complex will be published separately.[33]

2.41.8 BLUE COPPER PROTEIN MODELS

The earlier sections of this chapter have been concerned mostly with the multiconfigurational description of the electronic structure of compounds involving a transition metal. In this final section, our goal is slightly different. We shall show an example where the approach has been used to study the bonding and spectroscopic properties in an important class of transition-metal compounds, the so called blue copper proteins. The emphasis will now be on the results obtained and the comparison of different quantum-chemical methods. Only a brief summary can be given here and the reader is referred to the original literature for more details.

Blue copper proteins transfer electrons between various biological systems, e.g., between the two photosystems in photosynthesis (plastocyanin). They are characterized by a number of unusual properties, viz., a bright blue color, an unusually high reduction potential, and distinctive

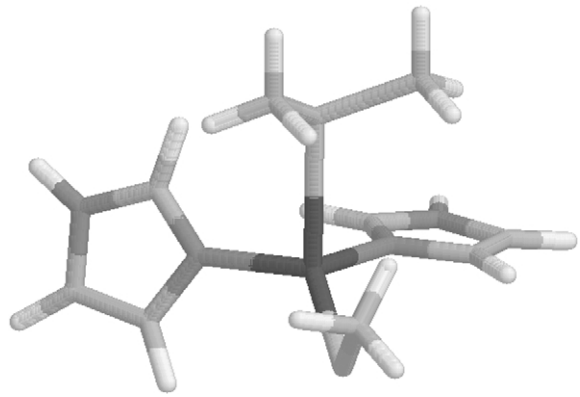

Figure 8 One of the models used in the study of the active site in the blue copper protein plastocyanin. Histidine ligands have been replaced with imidazole, cysteine with SCH_3^-, and methionine with $S(CH_3)_2$.

electronic spin resonance spectra. The active site of these proteins consists of a copper ion bound to the protein in a trigonal geometry involving one cysteine and two histidine residues. The coordination sphere is normally completed by one or two weak axial ligands, e.g., methionine, glutamine, or a backbone carbonyl group (see Figure 8). The reason for the unusual properties and the strange geometry has been much discussed, but it seems now generally accepted that it comes mostly from the choice of metal ligands (in particular the cysteine thiolate ligand), rather than from mechanical strain enforced by the protein.[36–38]

2.41.8.1 CuSH

Let us first look at the very simple $CuSH^{0/+}$ model as a representative of the important $Cu^{2+}-S^-$ interaction of the blue copper proteins. This system is so small that it can be studied with most theoretical methods and with extended basis sets. We have studied three states of this model (neutral CuSH and $CuSH^+$ in the $^2A'$ and $^2A''$ states).[39] All three states give similar results and a typical example is given in Table 2. From this comparison, it can be seen that the HF and CASSCF methods give poor geometries and energies. However, the MP2, CCSD(T), and CASPT2 methods give similar results, which indicates that the system is not especially multi-configurational in nature. This is confirmed by the weight of the major CF, which is 0.96. The three DFT functionals tested give quite differing results, especially for the Cu—S bond length. B3LYP seems in general to give the best results, although the Cu—S bond length is often somewhat too long with this method. A notable result for this model is the strong basis-set dependence of the CASPT2 method, whereas the DFT results change very little (less than 1 pm and 1° when the basis set is enlarged; the CASPT2 geometry changes by up to 8 pm and 4° when the basis set is enlarged from ANO–S to ANO—L.)[39] This is a typical feature of wave-function

Table 2 The structure of the $^2A''$ state of $CuSH^+$, optimized with various methods and an ANO–S basis set (Cu: 17*s*12*p*9*d*4*f*/6*s*4*p*3*d*2*f*; C: 13*s*10*p*4*d*/4*s*3*p*2*d*; H: 7*s*3*p*/2*s*1*p*). Distances in pm, angle in degrees, energy difference to the $^2A'$ state in kJ mol^{-1}.

Method	*Cu–S*	*S–H*	*Cu–S–H*	ΔE
HF	243.1	133.5	100.1	66
CASSCF	236.7	134.0	100.6	67
LDA	207.8	137.3	95.1	94
BP86	213.3	136.8	95.8	91
B3LYP	217.7	135.5	97.0	86
MP2	218.7	135.7	98.2	92
CCSD(T)	219.2	136.2	96.9	93
CASPT2	219.5	135.7	97.5	81
CASPT2/ANO–L[a]	214.8	134.6	97.9	86

[a] Cu: 21*s*15*p*10*d*6*f*4*g*/7*s*6*p*5*d*4*f*3*g*; C: 17*s*12*p*5*d*4*f*/6*s*5*p*4*d*3*f*; H: 8*s*4*p*3*d*/3*s*2*p*1*d*.

based methods, where the correlation energy is computed in a CI framework. The DFT methods, which are based on the density alone, depend much less on the basis set.

2.41.8.2 $Cu^{2+}(NH_3)_3X$

Next, we will look at complexes of the form $Cu^{2+}(NH_3)_3X$, where X is related to the thiolate ligand in the blue copper proteins, e.g., SH^-, OH^-, SeH^-, PH_2^-, and Cl^-. Such complexes have been employed to explain why the blue copper proteins exhibit a trigonal structure, whereas most Cu(II) complexes assume a tetragonal structure.[40] For all these complexes, local minima representing both a tetragonal and a trigonal structure could be optimized. However, the relative stability of the trigonal structure increases as we move down and to the left in the periodic table, as can be seen in Table 3. It is also stabilized by negatively charged X ligands. The relative energies were calculated by both the CASPT2 and B3LYP methods. The two methods give rather similar results, with maximum and average differences of 18 kJ mol^{-1} and 8 kJ mol^{-1}, and they therefore give the same predictions of the most stable structure for all complexes, except for the two complexes where the two geometries are almost degenerate, $Cu(NH_3)_3(SH)(SH)^+$ and $Cu(NH_3)_3(PH_2)^+$.

Relativistic corrections (Darwin contact and mass–velocity terms calculated at the CASSCF level) are also given in the table. For most complexes, this correction is small and insignificant. However, for three complexes ($Cu(NH_3)_3(SH)^+$, $Cu(NH_3)_3(SeH)^+$, and $Cu(NH_3)_3(SH_2)^+$, the corrections are large (14–16 kJ mol^{-1}) and positive (favoring the tetragonal state). The reason for this is that relativistic corrections in general favor the structure with the lowest Cu 3*d* population. For the three complexes exhibiting large relativistic effects, the Cu 3*d* population for the tetragonal structure is 9.3–9.4, whereas it is 9.9 for the trigonal structure. For all the other complexes the CASSCF Cu 3*d* are similar for the tetragonal and the trigonal structures, either close to 9.3 or close to 9.9 (representing either d^9 or d^{10} states. This is not in accordance with the B3LYP results, where the Cu 3*d* populations are always similar (within ~0.1) for the two geometries, but it varies continuously between 9.3 and 9.7 (in general, it is lower for complexes with stable tetragonal states and higher for those with more stable trigonal states). This gives also an explanation for the tetrahedral distortion of the complexes with stable trigonal structures (both trigonal and tetrahedral): In the latter complexes much charge is donated from the large, soft, and polarizable negatively charged X ligand, giving rise to an electronic structure close to Cu^+, which is closed-shell (d^{10}) and therefore prefers a tetrahedral structure.

2.41.8.3 Electronic Spectra

Finally, we will discuss the electronic spectra of blue copper proteins. The absorption spectrum of plastocyanin, the best studied blue copper protein, is dominated by a bright band at 16,700 cm^{-1} (600 nm), giving rise to its bright blue color. However, a more thorough investigation of the experimental spectrum identifies at least six more absorption bands below 22,000 cm^{-1}, as is shown in Table 4.[41] Several different methods have been used to interpret this spectrum, ranging from the semi-empirical CNDO/S method, over various DFT methods (Xα and time-dependent

Table 3 Energy difference (kJ mol^{-1}) between the trigonal and tetragonal structures of the various model complexes.

Model	*B3LYP*	*CASPT2*	*CASPT2 + Rel. Corr.*
$Cu(NH_3)_4^{2+}$	46.0	42.8	42.2
$Cu(NH_3)_3(OH_2)^{2+}$	33.9	33.9	33.5
$Cu(NH_3)_3Cl^+$	38.2	49.3	47.4
$Cu(NH_3)_3(OH)^+$	19.7	37.6	35.9
$Cu(NH_3)_3(SH)^+$	3.1	−1.7	14.4
$Cu(NH_3)_3(SeH)^+$	−5.8	−18.2	−4.7
$Cu(NH_3)_3(PH_2)^+$	2.6	−4.4	−5.1
$Cu(NH_3)_2(SH)(SH_2)^+$	−12.6	−21.1	−7.0

Table 4 The experimental spectrum of plastocyanin[41] compared to spectra calculated with the $X\alpha$, CASPT2, and time-dependent B3LYP methods.[41,44,47] All excitation energies are given in cm^{-1}. Significant oscillator strengths are indicated in parentheses. The assignment is based on the CASPT2 calculations[44] and the results of the other methods are ordered so that excitations with the same character are found on the same row (even if the authors of the Xα investigation give a different assignment of several bands in the experimental spectrum[41]). The assignment invokes a coordinate system where the Cu ion is at the origin, the z-axis is along the Cu–S_{Met} bond, and the Cu–S_{Cys} bond is situated in the xy-plane. Two excitations studied with the CASPT2 method could be studied only by severe approximations (see the text) and are therefore marked by square brackets.

Experimental	*CASPT2*	*B3LYP*	*Xα*	*Assignment*[a]
5,000	4,119	4,206	4,527	σ^*
10,800 (.0031)	10,974	9,441 (.0013)	8,691	d_{z^2}
12,800 (.0114)	13,117 (.0015)	12,827 (.0142)	11,942 (.046)	d_{yz}
13,950 (.0043)	13,493 (.0003)	13,673 (.0010)	15,064	d_{xz}
16,700 (.0496)	17,571 (.1032)	18,364 (.0733)	16,940 (.078)	π
18,700 (.0048)				
21,390 (.0035)	20,599 (.0014)	20,267 (.0002)	25,313	σ
23,440	[31,264]	20,806 (.0003)	15,895, 36,700	Met
32,500	[34,992]	21,327 (.0006)	14,770, 52,894	His

[a] Singly occupied orbital in the excited state.

B3LYP calculations) to CASPT2.[41–45] The results of the various calculations are also shown in Table 4, together with calculated oscillator strengths and an assignment of the various excitations.

All methods agree that in the ground state, the singly-occupied orbital is comprised of the Cu $3d_{xy}$-orbital and a S_{Cys} $3p$-orbital, forming an antibonding π interaction (some authors use a coordinate system that is rotated 45° relative to ours).[41,43] The bright blue line arises from the excitation to the corresponding π-bonding interaction, and its high intensity arises from the strong overlap between these two orbitals. This interaction also explains the trigonal structure of the plastocyanin site: By the π-bond, S_{Cys} overlaps with two of the four lobes of the Cu $3d_{xy}$-orbital. The two histidine ligands form normal σ bonds to copper, overlapping with the remaining two lobes of the singly occupied Cu $3d_{xy}$-orbital, whereas any additional ligand (methionine in plastocyanin) can overlap only with doubly occupied orbitals, and therefore forms weak axial interactions at long distances.

The normal Cu–S_{Cys} σ-antibonding interaction is found as the first excited state in plastocyanin, at an excitation energy of 5,000 cm^{-1}. In some other proteins, e.g., nitrite reductase, this state becomes the ground state, giving rise to a strongly tetrahedrally distorted (owing to the charge transfer from S_{Cys}) tetragonal structure with σ bonds to all four ligands.[45,46] This state overlaps strongly with the corresponding σ-bonding interaction, found at slightly higher energy than the π bond (21,900 cm^{-1} in nitrite reductase), giving this enzyme a green colour.[46] Other proteins exist that have intermediate structures and spectra, e.g., cucumber basic protein and pseudoazurin.[45]. Moreover, various mutant proteins have been constructed with other ligand sets (but still a cysteine ligand) that have more tetragonal structures and even brighter excitations to the Cu–S_{Cys} σ-orbital, giving them a yellow colour. In fact, the intensity ratio between the yellow and blue bands of all blue copper proteins can be rationalized by the transition of the structure from trigonal to tetragonal, e.g., as described by the angle between the planes defined by the N–Cu–N and S_{Cys}–Cu–S_{Met} atoms.[45]

Table 4 shows that the accuracy of the CASPT2 method is impressive for this complicated system (a chromophore in a protein); the six lowest excitations are calculated with an error of less than 1,000 cm^{-1}. Owing to the size of the system, several approximations had to be invoked to make the calculations possible. The chromophore was modeled by $Cu(imidazole)_2(SH)(SH_2)^+$, at the crystal geometry and with a point-charge model of the surrounding protein. However, this model is too small to give accurate results. Therefore, the excitation energies have been corrected (by up to 2,600 cm^{-1}) for truncation effects by using data from the $Cu(imidazole)_2(SCH_3)(S(CH_3)_2)^+$ model, optimized with the B3LYP method and C_s symmetry (Figure 8). Moreover, the calculations had to be performed with quite small basis sets, e.g., without polarizing functions on the N, C, and H atoms. The two excitations with the highest energy (charge-transfer excitations to the methionine and histidine residues, respectively) could be studied only with the symmetric $Cu(imidazole)_2(SCH_3)(S(CH_3)_2)^+$ model at the optimized geometry. Therefore, these excitation energies are much less accurate, especially for the former

excitation, which is very sensitive to the geometry of the model and also to the size of the basis sets. Finally, it should be noted that our assignment left one band unassigned, mainly on the basis that this band is not present in the spectrum of the related protein nitrate reductase.[45,46]

The plastocyanin spectrum calculated with the time-dependent B3LYP method (using the $Cu(imidazole)_2(SCH_3)(S(CH_3)_2)^+$ model optimized with B3LYP without symmetry; no point-charge model) is also included in Table 4.[47] It can be seen that the result is quite similar to both the CASPT2 and the experimental results for the six lowest excitations; the largest difference to the CASPT2 is 1,500 cm^{-1} for the second excitation, and the largest difference to experiments is 1,700 cm^{-1} for the bright blue line. However, for the true charge-transfer excitations to the methionine and histidine ligands, the difference is much larger. The B3LYP calculations show one excitation to methionine at 21,327 cm^{-1}, compared to the experimental line at 23,440 cm^{-1}, and the CASPT2 result at 31,264 cm^{-1}. However, as was discussed above, for this excitation the CASPT2 results are not reliable. Similarly, B3LYP gives four excitations to the two histidine residues: two around 21,500 cm^{-1} and two close to 35,500 cm^{-1}, all with a low calculated intensity. In the experimental spectrum, there is only one line at 32,500 cm^{-1}, and with CASPT2, only one excitation could be studied, giving an energy of 34,992 cm^{-1}. Thus, these results indicate that B3LYP gives rise to spurious charge-transfer excitations. Similar results have been obtained also for other (mostly organic) models (see for example the discussion of charge-transfer bands in polypeptides in ref. 48).

Finally, Table 4 also contains excitations for plastocyanin calculated with the density functional Xα method.[41] Once again, the result is similar to the other calculations and experiments for the six lowest excitations, whereas the discrepancy is much larger for the charge-transfer excitations. In general, Xα seems to give the least accurate results, except for the blue line (which may be because the method was parameterized to reproduce the electronic spin resonance g-values for the ground state). It should also be noted that the authors of this investigation made a different assignment of several bands in the spectrum, based also on other spectroscopic experiments and selection rules.[41]

In conclusion, we have seen that it is possible to study the spectrum of a chromophore in a protein with theoretical methods. CASPT2 seems to give the most accurate results, provided that a reasonable chemical model can be studied and proper active orbitals can be selected (five Cu 3d-orbitals, five correlating Cu 3d'-orbitals, and all orbitals involved in charge-transfer excitations). DFT, especially the time-dependent methods also gives reasonable results at a much lower cost and with a smaller basis-set dependence. It should be noted, however, that the assignment of the various excitations is much easier to perform at the CASPT2 level than with DFT (the orbitals are more pure).

2.41.9 CONCLUSIONS

In this chapter we have tried to illustrate through some examples how a multiconfigurational model describes the electronic structure in coordination compounds. The key concept has been the NOs, which are the generalization of the HF orbitals to a situation where more than one electronic configuration is needed to describe the electronic structure. The examples (with the exception of the blue proteins) have been confined to the ground state. It is evident, however, that the multi-configurational approach is even more essential in discussions of excited states and photochemistry.

Many theoretical studies of coordination compounds are today successfully performed using DFT. This is all to the good, as long as one is aware of the pitfalls within this approach. The problem of charge-transfer processes was mentioned above. The definition of spin and the inclusion of spin-orbit coupling in heavier systems is another problem, which is of major concern in studies of electronic spectroscopy and photochemical reactions. Strongly degenerate situations can hardly be treated with DFT. One example is the Cr_2 molecule, which was discussed above. We have also tried to use DFT for the $[Re_2Cl_8]^{2-}$ ion, but failed to converge the calculations.

The virtue of a wave-function-based multiconfigurational approach is the complete generality, meaning that any type of electronic structure may be studied with exactly defined spin and other symmetry properties. The major problem with the approach is the size of the active space, which limits the possibilities to compute the effects of dynamic electron correlation. Today the only possible approach for large molecules with many electrons is CASPT2, which is limited with respect to the active space and in some applications gives severe intruder-state problems. It is hoped that in the near future we shall have access alternative methods where these limitations are removed.

2.41.10 REFERENCES

1. Hund, E. *Z. Physik* **1927**, *40*, 742.
2. Lennard-Jones, J. E. *Trans. Faraday Soc.* **1929**, *25*, 668.
3. Mulliken, R. S. *Phys. Rev.* **1928**, *32*, 186.
4. Heitler, W. F. *Z. Physik* **1927**, *44*, 455.
5. Hartree, D. R. *The Calculation of Atomic Structures*; Wiley Interscience: New York, 1957.
6. Hückel, E. *Z. Physik* **1930**, *60*, 423.
7. Roothaan, C. C. J. *Revs. Mod. Phys.* **1951**, *23*, 69.
8. Lòwdin, P.-O. *Phys. Rev.* **1955**, *97*, 1474.
9. Almlöf, J.; Ahlrichs, R. Notes on Hartree–Fock theory and related topics. In *European Summer School in Quantum Chemistry*, *Book II*; Roos, B. O., Widmark, P.-O., Eds.; Lund University: Sweden, 2000.
10. Roothaan, C. C. J. *Revs. Mod. Phys.* **1960**, *32*, 179.
11. Helgaker, T.; Jörgensen, P.; Olsen, J. *Molecular Electronic Structure Theory*; Wiley: Chichester, UK, 2000.
12. Lüthi, H. P.; Ammeter, J. H.; Almlöf, J.; Faegri, K. *J. Chem. Phys.* **1982**, *77*, 2002.
13. Andersson, K.; Roos, B. O. *Chem. Phys. Lett.* **1992**, *191*, 507.
14. Froese-Fischer, C. *J. Phys. B* **1977**, *10*, 1241.
15. Roos, B. O.; Andersson, K.; Fülscher, M. P.; Malmqvist, P.-Å.; Serrano-Andrés, L.; Pierloot, K.; Merchán, M. In *Advances in Chemical Physics: New Methods in Computational Quantum Mechanics*; Prigogine, I., Rice, S. A., Eds.; Wiley: New York, 1996; Vol. XCIII, pp 219–331.
16. Roos, B. O. In *Advances in Chemical Physics: Ab initio Methods in Quantum Chemistry-II*; Lawley, K. P., Ed.; Wiley: Chichester, UK, 1987; Chap. 69, p 339.
17. Roos, B. O. These calculations were performed with the CASSCF module of the MOLCAS quantum chemistry software. The active space chosen was the 3*d* and 4*s* orbital of each Cr atom (12) with 12 active electrons..
18. Roos, B. O. In *European Summer School in Quantum Chemistry*, *Book II*; Roos, B. O., Widmark, P.-O., Ed., Lund University: Sweden, 2000.
19. Andersson, K.; Malmqvist, P.-Å.; Roos, B. O.; Sadlej, A. J.; Wolinski, K. *J. Phys. Chem.* **1990**, *94*, 5483–5488.
20. Andersson, K.; Malmqvist, P.-Å.; Roos, B. O. *J. Chem. Phys.* **1992**, *9*, 1218–1226.
21. Roos, B. O.; Andersson, K.; Fülscher, M. P.; Serrano-Andrés, L.; Pierloot, K.; Merchán, M.; Molina, V. *J. Mol. Struct. (Theochem.)* **1996**, *388*, 257–276.
22. Chatt, J.; Duncanson, L. A. *J. Chem Soc.* **1953**, 2939 .
23. Dewar, M. J. S. *Bull. Soc. Chim. Fr.* **1951**, 79 .
24. Widmark, P.-O.; Roos, B. O.; Siegbahn, P. E. M. *J. Phys. Chem.* **1985**, *89*, 2180.
25. Widmark, P.-O.; Sexton, G.-J.; Roos, B. O. *J. Mol. Struct. (Theochem.)* **1986**, *135*, 235.
26. Pierloot, K.; Persson, B. J.; Roos, B. O. *J. Phys. Chem.* **1995**, *99*, 3465–3472.
27. Park, C.; Almlöf, J. *J. Chem. Phys.* **1991**, *95*, 1829.
28. Andersson, K.; Baryz, M.; Bernhardsson, A.; Blomberg, M. R. A.; Carissan, Y.; Cooper, D. L.; Cossi, M.; Fleig, T.; Flescher, M. P.; Gagliardi, L.; de Graaf, C.; Hess, B. A.; Karlstrom, G.; Lindh, R.; Malmqvist, P.-Å.; Neogrdy, P.; Olsen, J.; Roos, B. O.; Schimmelpfennig, B.; Schtz, M.; Seijo, L.; Serrano-Andrés, L.; Siegbahn, P. E. M.; Ståring, J.; Thorsteinsson, T.; Veryazov, V.; Wierzbowska, M.; Widmark, P.-O. MOLCAS Version 5.2; Dept of Theoretical Chemistry, University of Lund: Lund, Sweden, 2001.
29. Pou-Amérigo, R.; Merchán, M.; Nebot-Gil, I.; Widmark, P.-O.; Roos, B. O. *Theor. Chim. Acta* **1995**, *92*, 149.
30. Widmark, P.-O.; Malmqvist, P.-Å.; Roos, B. O. *Theor. Chim. Acta* **1999**, *77*, 291–306.
31. Cotton, F. A.; Harris, C. B. *Inorg. Chem.* **1965**, *4*, 330.
32. Bertrand, J. A.; Cotton, F. A.; Dollase, W. A. *J. Am. Chem. Soc.* **1963**, *85*, 1349.
33. Gagliardi, L.; Roos, B. O. *Inorg. Chem.* **2003**, *42*, 1599.
34. Cotton, F. A. *Inorg. Chem.* **1965**, *4*, 334.
35. Trogler, W. C.; Gray, H. B. *Acc. Chem. Res.* **1978**, *11*, 232.
36. Randall, D. W.; Gamelin, D. R.; LaCroix, L. B.; Solomon, E. I. *J. Biol. Inorg. Chem.* **2000**, *5*, 16–29.
37. Gray, H. B.; Malmström, B. G.; Williams, R. P. J. *J. Biol. Inorg. Chem.* **2000**, *5*, 551–559.
38. Ryde, U.; Olsson, M. H. M.; Roos, B. O.; De Kerpel, J. O. A.; Pierloot, K. *J. Biol. Inorg. Chem.* **2000**, *5*, 565–574.
39. Ryde, U.; Olsson, M. H. M. *Int. J. Quantum Chem.* **2001**, *81*, 335–347.
40. Olsson, M. H. M.; Ryde, U.; Roos, B. O.; Pierloot, K. *J. Biol. Inorg. Chem.* **1998**, *3*, 109–125.
41. Gewirth, A. A.; Solomon, E. I. *J. Am. Chem. Soc.* **1988**, *110*, 3811–3819.
42. Larsson, S.; Broo, A.; Sjölin, L. *J. Phys. Chem.* **1995**, *99*, 4860–4865.
43. Penfield, K. W.; Gewirth, A. A.; Solomon, E. I. *J. Am. Chem. Soc.* **1985**, *107*, 4519–4529.
44. Pierloot, K.; De Kerpel, J. O. A.; Ryde, U.; Roos, B. O. *J. Am. Chem. Soc.* **1997**, *119*, 218–226.
45. Pierloot, K.; De Kerpel, J. O. A.; Ryde, U.; Olsson, M. H. M.; Roos, B. O. *J. Am. Chem. Soc.* **1998**, *120*, 13156–13166.
46. LaCroix, L. B.; Shadle, S. E.; Wang, Y.; Averill, B. A.; Hedman, B.; Hodgson, K. O.; Solomon, E. I. *J. Am. Chem. Soc.* **1996**, *118*, 7755–7768.
47. Borin, A. C.; Olsson, M. H. M.; Ryde, U.; Roos, B. O. To be published.
48. Tozer, D. J.; Amos, R. D.; Handy, N. C.; Roos, B. O.; Serrano-Andrés, L. *Mol. Phys.* **1999**, *97*, 859–868.

Comprehensive Coordination Chemistry II
ISBN (set): 0-08-0437486
Volume 2, (ISBN 0-08-0443249); pp 519–539

2.42 Valence Bond Configuration Interaction Model

F. TUCZEK
Christian-Albrechts-Universität, Kiel, Germany
and
E. I. SOLOMON
Stanford University, CA, USA

2.42.1	INTRODUCTION	541
2.42.2	THE VBCI MODEL: COPPER(II) DIMERS (d^9–d^9, d^1–d^1)	542
2.42.3	APPLICATION TO COPPER PEROXO DIMERS: DISTORTION OF THE Cu_2O_2 CORE	546
2.42.4	APPLICATION TO LINEAR AND BENT IRON(III)–IRON(III) OXO DIMERS (d^5–d^5)	549
2.42.5	EVALUATION OF U, Δ, AND h_{dp} FROM PHOTOELECTRON SPECTROSCOPY	554
2.42.6	SUMMARY AND CONCLUSION	556
2.42.7	REFERENCES	557

2.42.1 INTRODUCTION

Dimer formation from two mononuclear transition-metal units has important consequences for spectroscopy.[1] The most obvious example for this phenomenon is the appearance of high-intensity, low-energy "dimer bands" in the UV–vis absorption spectra of binuclear copper[2–4] and iron–oxo complexes.[5–7] Several possible assignments for these features which are absent in the spectra of corresponding monomeric complexes have been considered, including $d \rightarrow d$ simultaneous pair excitations (SPEs) and low-energy charge-transfer (CT) transitions. With respect to *d*–*d* spectra, intensity enhancement of ligand-field (LF) transitions of Mn^{II},[8–11] Cr^{III} [12] and other dimer combinations have also been well-known effects of dimer interactions. By analogy to the ground state, energy splittings in the spin-flip LF excited states of these systems have been analyzed in terms of a Heisenberg Hamiltonian. This formalism, however, does not account for exchange interactions in LF excited states of orbital configurations different from that of the ground state, which, e.g., applies to all LF states of Cu^{II} dimers. In this case the dimer splitting of each excited state depends on additional interactions which probe individual superexchange pathways between different combinations of *d* orbitals.[13]

CT spectra of transition-metal systems equally show evidence for binuclear interactions.[14] Interest in this topic has been stimulated by the fact that metalloproteins often exhibit intense bands at energies well below that of protein absorption, which are due to CT transitions from ligands like oxide, sulfide, phenolate, thiolate, or peroxide to *d*-orbitals of the metal center(s) of the active site. Apart from providing a characteristic spectroscopic fingerprint of the respective metalloprotein in a specific physicochemical state, these transitions also sensitively probe

metal-ligand bonding. Importantly, the ligand → metal CT spectra of these ligands in mononuclear sites are clearly distinct from a situation where they act as a bridge between two or more metal centers.[15–17] In the past years, the correlation between binding geometry and CT spectrum has been a major theme of bioinorganic electronic spectroscopy, an important aspect of these studies having been to define how for a particular binding mode the CT spectrum of the monomer (one metal center bound to the ligand) changes upon going to the dimer bridged by this ligand.

From group theory each monomer CT transition splits into two transitions in the dimer. The first observation of this type of dimer splitting was made in a spectral comparison between an end-on terminally azido coordinated Cu^{II} complex and the corresponding *cis* μ-1,3 azido bridged dimer.[18] If the dimer contains paramagnetic metal centers, each CT excited state in addition exhibits a magnetic splitting due to coupling of a single electron in a ligand orbital with these unpaired electrons in metal orbitals. In the case of Cu^{II} dimers, e.g., each excited monomer state thus splits into *four* excited states, two singlets and two triplets. It has been found that the CT singlet states apart from that splitting also exhibit a large shift to lower energy, which has been interpreted as being due to a large antiferromagnetic interaction in the CT excited state. This in fact has been found to be the origin of the "dimer bands," i.e., these are assigned as singlet–singlet CT bands shifting into the visible part of the spectrum upon dimer formation.[4]

The valence bond configuration interaction (VBCI) model provides a coherent explanation for all of these spectroscopic phenomena in terms of a valence-bond (VB) description which in a minimum basis comprises the highest occupied orbitals (HOMOs) of the metal and the bridging ligand. From the various configurations within this active space, ground (GS), charge–transfer (CT) and metal–metal-CT (MMCT) states can be formed which interact by a number of electron transfer integrals (i.e., covalent interactions). This configuration interaction (CI) scheme leads to the above-mentioned energy shifts and splittings of charge transfer transitions.[19] In addition, the VBCI model allows quantitative predictions regarding the magnetic coupling in the electronic ground state, which is expressed by the sign and magnitude of $-2J$. More specifically, it allows the evaluation of CT excited-state contributions to the magnetic coupling constant of the electronic ground state and thus correlates excited-state effects with ground-state properties. This allows us to directly experimentally probe the various superexchange pathways involved in the ground-state magnetic coupling $-2J$. In the present short review, the VBCI model is developed first on a prototypical example and then applied to peroxo-bridged Cu^{II} and Fe^{III}–oxo dimers. A final paragraph deals with the evaluation of model parameters from photoelectron spectroscopy and the relationship between the VBCI and cluster-CI models.

2.42.2 THE VBCI MODEL: COPPER(II) DIMERS (d^9–d^9, d^1–d^1)

For the sake of simplicity, the VBCI model is exemplified on a copper(II) dimer bridged by a ligand L (Figure 1). Each $S = 1/2$ Cu^{II} center contains nine electrons, the unpaired electron on each half of the dimer being in the highest, singly occupied orbital (SOMO), which is an antibonding combination of a metal d orbital (e.g., $d_{x^2-y^2}$) with orbitals of the surrounding ligands, including the p orbital of the bridging ligand that mediates the coupling between the two metals. It has proven useful to express the electronic states of this system in a localized valence bond (VB) basis, i.e., use $d_{x^2-y^2}$ type orbitals d_A and d_B centered on Cu_a and Cu_b; the connection to a delocalized (dimer MO) basis will be made below. In the VB description, the $S = 0$ and 1 singlet and triplet ground state wavefunctions of the Cu^{II} dimer are given as

$$ {}^1\Psi_+^{GS} = \frac{1}{\sqrt{2}} \left(\left| d_A^+ \bar{p} \, p^+ \bar{d}_B \right| - \left| \bar{d}_A \, \bar{p} \, p^+ d_B^+ \right| \right) \tag{1a} $$

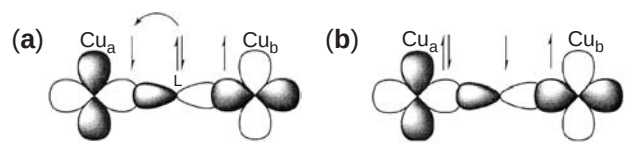

Figure 1 Copper dimer bridged by a ligand L. (a) ground state. (b) CT excited state. Relevant ligand and metal orbitals are included.

$$^3\Psi_-^{GS}(M_S = 0) = \frac{1}{\sqrt{2}}\left(\left|\overset{+}{d}_A\,\overset{-}{p}\,\overset{+}{p}\,\overset{-}{d}_B\right| + \left|\overset{-}{d}_A\,\overset{-}{p}\,\overset{+}{p}\,\overset{+}{d}_B\right|\right) \tag{1b}$$

These two states transform according to two different irreducible representations of the point group of the dimer as the spatial part of the triplet wavefunction is antisymmetric with respect to interchange of the two electrons (i.e., halves of the dimer), and that of the singlet is symmetric. The energies of these states are evaluated from the Hamiltonian

$$\hat{H} = \sum_{i=1}^{4} \hat{h}(i) + \sum_{i<j;i=1}^{4} e^2/r_{ij} \tag{2}$$

containing one- and two-electron contributions. Applying $\hat{H}$ to Equation (1a) and (1b) gives an energy difference between these two states represented by the exchange integral J_{AB}. In the VBCI model, however, energy splittings due to two-electron integrals are in general neglected (except for "on-site" interactions, i.e., both electrons i and j on one Cu center; see below) and thus singlet and triplet ground states are considered as degenerate in zeroth order (Figure 2, "zeroth order singlets and triplets").

Charge–transfer (CT) transitions are possible by excitation of an electron from the bridging ligand orbital into the SOMO's d_A and d_B leading to two locally excited (i.e., $Cu^I_{A,B}$) configurations Φ_A^{CT} and Φ_B^{CT}, the other center remaining in the Cu^{II} ground state (Figure 1b). These two Cu^ICu^{II} mixed-valence configurations are strictly degenerate at an energy Δ above the ground state, which corresponds to the energy difference between the metal $d_{A,B}$ and ligand p-orbitals. Removal of the electron from the doubly occupied bridging ligand p orbital leaves an unpaired electron in this orbital behind which couples with the other unpaired electron on a Cu^{II} center to form the locally excited singlet and triplet charge transfer states

$$^1\Phi_A^{CT} = \frac{1}{\sqrt{2}}\left(\left|\overset{+}{d}_A\,\overset{-}{d}_A\,\overset{+}{p}\,\overset{-}{d}_B\right| - \left|\overset{+}{d}_A\,\overset{-}{d}_A\,\overset{-}{p}\,\overset{+}{d}_B\right|\right) \tag{3a}$$

$$^1\Phi_B^{CT} = \frac{1}{\sqrt{2}}\left(\left|\overset{+}{d}_B\,\overset{-}{d}_B\,\overset{+}{p}\,\overset{-}{d}_A\right| - \left|\overset{+}{d}_B\,\overset{-}{d}_B\,\overset{-}{p}\,\overset{+}{d}_A\right|\right) \tag{3b}$$

$$^3\Phi_A^{CT}(M_S = 0) = \frac{1}{\sqrt{2}}\left(\left|\overset{+}{d}_A\,\overset{-}{d}_A\,\overset{+}{p}\,\overset{-}{d}_B\right| + \left|\overset{+}{d}_A\,\overset{-}{d}_A\,\overset{-}{p}\,\overset{+}{d}_B\right|\right) \tag{3c}$$

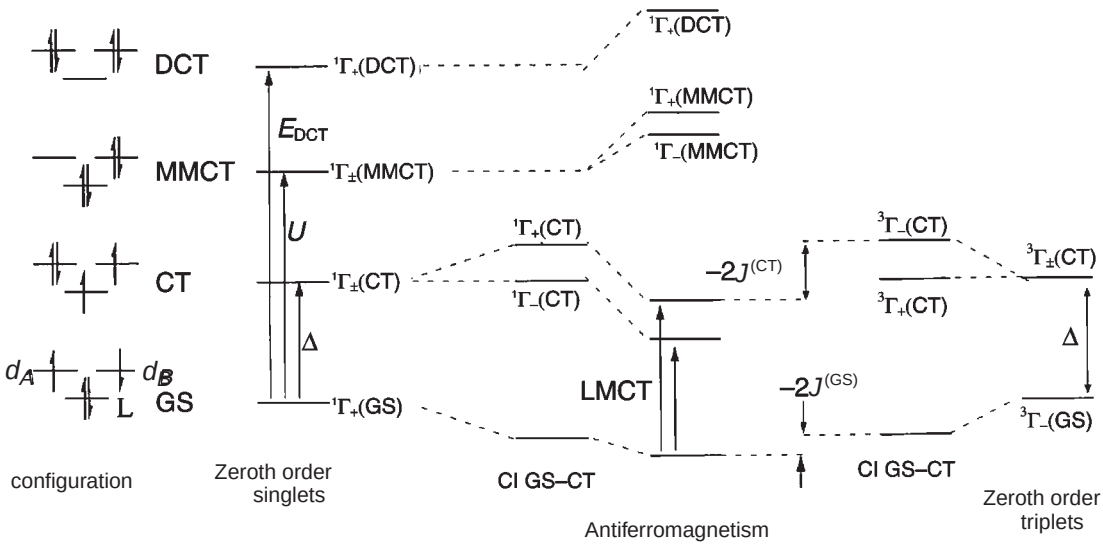

Figure 2 VBCI scheme of a bridged dimer. Left: GS, CT, MMCT, and DCT configurations. Second and last column: 0th order singlets and triplets. Center: Levels and energies after GS–CT configuration and CI with MMCT and DCT states.

$$^3\Phi_B^{CT}(M_S=0)=\frac{1}{\sqrt{2}}\left(\left|\overset{+}{d}_B\,\overset{-}{d}_B\,\overset{+}{p}\,\overset{-}{d}_A\right|+\left|\overset{+}{d}_B\,\overset{-}{d}_B\,\overset{-}{p}\,\overset{+}{d}_A\right|\right) \tag{3d}$$

+/− combinations of these local CT configurations finally generate the following spin- and symmetry-adapted CT states of the dimer

$$^1\Psi_+^{CT}=\frac{1}{\sqrt{2}}\left(^1\Phi_A^{CT}+{}^1\Phi_B^{CT}\right) \tag{4a}$$

$$^1\Psi_-^{CT}=\frac{1}{\sqrt{2}}\left(^1\Phi_B^{CT}-{}^1\Phi_B^{CT}\right) \tag{4b}$$

$$^3\Psi_+^{CT}=\frac{1}{\sqrt{2}}\left(^3\Phi_A^{CT}+{}^3\Phi_B^{CT}\right) \tag{4c}$$

$$^3\Psi_-^{CT}=\frac{1}{\sqrt{2}}\left(^3\Phi_A^{CT}-{}^3\Phi_B^{CT}\right) \tag{4d}$$

Thus, as a result of spin coupling (two $s=1/2=>S=1,\ 0$) and spatial degeneracy (+/− combinations of local excitations), each CT state of a monomeric subunit (one Cu^{II} center) corresponds to $2\times2=4$ states in the Cu^{II}–Cu^{II} dimer. Out of the four CT states given in Equation (4), two have the same spin and spatial symmetry of the singlet and triplet ground states (Equation (1)), respectively, which leads to configuration interaction (CI)

$$\left\langle ^1\Psi_+^{CT}\middle|\hat{H}\middle|^1\Psi_+^{GS}\right\rangle=\left\langle ^3\Psi_-^{CT}\middle|\hat{H}\middle|^3\Psi_-^{GS}\right\rangle=\sqrt{2}\left\langle d_A\middle|\hat{h}\middle|p\right\rangle=\sqrt{2}\,h_{d_Ap}=\sqrt{2}\,h_{d_Bp}=h_{dp} \tag{5}$$

h_{d_Ap} is a matrix element of the one-electron part $\hat{h}$ of the dimer Hamiltonian $\hat{H}$ which scales with the overlap between the metal d_A or d_B and the bridging ligand p orbital and thus is a measure of covalency present in the dimer. Typically, this transfer matrix element is on the order of several thousand wavenumbers.[20] For reasons of symmetry, $^1\Psi_-^{CT}$ does not interact with $^1\Psi_+^{GS}$ and $^3\Psi_+^{CT}$ does not interact with $^3\Psi_-^{GS}$; in addition, singlets do not interact with triplets. Thus, the triplet GS and CT energies result from the zero-order energies 0 (GS) and Δ (CT) and the 2×2 secular determinant

$$\begin{array}{c} \quad\ ^3\Psi_-^{GS} \quad\ ^3\Psi_-^{CT} \\ \begin{vmatrix} -E & h_{dp} \\ h_{dp} & \Delta-E \end{vmatrix} \end{array}=0 \tag{6}$$

As a consequence, the triplet CT states $^3\Psi_+^{CT}$ and $^3\Psi_-^{CT}$ split by an energy $h_{dp}{}^2/\Delta$ with $^3\Psi_-^{CT}$ being at higher energy than $^3\Psi_+^{CT}$, and $^3\Psi_-^{GS}$ is lowered by the same amount (Figure 2, second column from right). The same applies to the singlet CT excited and ground states, respectively, only with the energetic sequence of the CT states inverted and $^1\Psi_+^{GS}$ lowered by $h_{dp}{}^2/\Delta$. Thus, as a result of the GS–CT interaction, the two ground states $^1\Psi_+^{GS}$ and $^3\Psi_-^{GS}$ are still degenerate, but lowered in energy by the metal-bridging ligand interaction (Figure 2, columns "CI GS–CT"). This energy is twice as large as for an isolated Cu^{II} monomer binding to the ligand which in the dimer forms the bridge.[20]

The GS and CT states considered so far do not exhaust the possible configurations available from the three-orbital (two d, one p) four-electron scheme. Starting from a CT configuration, the unpaired electron localized at Cu_A or Cu_B may be transferred into the bridging ligand orbital p, leading to two Cu^{III}–L(↑↓)–Cu(I) states

$$^1\Psi_{\pm}^{\mathrm{MMCT}} = \frac{1}{\sqrt{2}}\left(\left|\overset{+}{d}_{\mathrm{A}}\,\overset{-}{d}_{\mathrm{A}}\,\overset{+}{p}\,\overset{-}{p}\right| \pm \left|\overset{+}{d}_{\mathrm{B}}\,\overset{-}{d}_{B}\,\overset{+}{p}\,\overset{-}{p}\right|\right) \tag{7}$$

The energy of these states is the so-called Mott–Hubbard U.[21,22] Starting from the Cu^{II}–L(↑↓)–Cu^{II} ground state, this transition effectively corresponds to a metal → metal charge transfer (MMCT). In the VBCI scheme the MMCT transition, however, is not allowed in this direct manner since the corresponding metal–metal transfer matrix element h_{AB} is generally small and therefore neglected. In contrast to the ground and CT configurations which generate singlet and triplet states, the MMCT states (Equation (7)) are now inherently of singlet character (due to the Pauli principle, there is no possibility of a parallel alignment of electrons, either on the metal or the ligand orbital); therefore, these states only interact with singlet CT states and selectively stabilize these states below the energy of their triplet counterparts (see below).

Finally, starting from a CT configuration, the second electron in the ligand orbital may also be excited into a metal orbital, leading to the double CT (DCT) configuration Cu^{I}–L(□□)–Cu^{I}. This now directly corresponds to a single electronic state which is a singlet and totally symmetric:

$$^1\Psi_{+}^{\mathrm{DCT}} = \left|\overset{+}{d}_{\mathrm{A}}\,\overset{-}{d}_{\mathrm{A}}\,\overset{+}{d}_{\mathrm{B}}\,\overset{-}{d}_{\mathrm{B}}\right| \tag{8}$$

The energy of this state is denoted by E_{DCT}. Based on the singlet GS, CT, MMCT, and DCT states and taking into account the respective configuration interaction matrix elements, the VBCI determinants for the $^1\Psi_+$ and $^1\Psi_-$ states are given by

$$\begin{array}{c} {\scriptstyle ^1\Psi_+^{\mathrm{GS}}\quad ^1\Psi_+^{\mathrm{CT}}\quad ^1\Psi_+^{\mathrm{MMCT}}\quad ^1\Psi_+^{\mathrm{DCT}}} \\ \begin{vmatrix} -E & h_{dp} & 0 & 0 \\ h_{dp} & \Delta - E & h_{dp} & \sqrt{2}h_{dp} \\ 0 & h_{dp} & U-E & 0 \\ 0 & \sqrt{2}h_{dp} & 0 & E_{\mathrm{DCT}}-E \end{vmatrix} = 0 \end{array} \qquad \begin{array}{c} {\scriptstyle ^1\Psi_-^{\mathrm{CT}}\quad ^1\Psi_-^{\mathrm{MMCT}}} \\ \begin{vmatrix} \Delta - E & h_{dp} \\ h_{dp} & U-E \end{vmatrix} = 0 \end{array} \tag{9}$$

The determinant for the $^3\Psi_-$ states is given by Equation (6); for $^3\Psi_+$ only one state exists. Solution of Equations (6) and (9) leads to the VBCI energy-level scheme represented by the two central rows of Figure 2. Several important points should be observed from this energy diagram:

The two singlet CT states are greatly lowered with respect to the two triplet CT states, which leads to a large stabilization of the singlet → singlet CT transitions of bridging ligands in dimers. As a measure of this antiferromagnetic interaction in the excited state (ESAF), it is meaningful to take (as in the ground state) the energy difference between the $^3\Psi_-$ and the $^1\Psi_+$ state, which is approximately given by

$$-2J^{\mathrm{CT}} \equiv E\left[^3\Psi_-^{\mathrm{CT}}\right] - E\left[^1\Psi_+^{\mathrm{CT}}\right] = \frac{h_{dp}^2}{U-\Delta} + \frac{h_{dp}^2}{(E_{\mathrm{DCT}}/2)-\Delta} \tag{10}$$

The first contribution is due to CI between the $^1\Psi_+$ CT state and the MMCT state (Equation (7)), the second one to CI with the DCT state (Equation (8)).

The singlet ground state component is depressed in energy below the triplet state GS component as it interacts with a singlet CT state that is admixed with a (singlet) MMCT state and thus is at lower energy than the corresponding triplet CT state. In fourth-order perturbation theory, J^{GS} is given by

$$-2J^{\mathrm{GS}} \equiv E\left[^3\Psi_+^{\mathrm{GS}}\right] - E\left[^1\Psi_+^{\mathrm{GS}}\right] = \frac{h_{dp}^4}{\Delta^2 U} + \frac{h_{dp}^4}{\Delta^2(E_{\mathrm{DCT}}/2)} \tag{11}$$

Note that the GS coupling again contains AF contributions from the MMCT and DCT states. This mechanism is referred to as *superexchange*. Equation (11), however, differs from Anderson superexchange in that not only the first term (MMCT) contributes to $-2J^{GS}$ through intermediacy of the CT state but also the DCT state.[23] Further, with λ being the amount of CT character mixed into the ground state,

$$\lambda = -\frac{h_{dp}}{\Delta} \tag{12}$$

and $U - \Delta \approx U$, the GS coupling (Equation (11)) is related to the CT excited-state coupling (10) by

$$-2J^{GS} = \lambda^2 \left(-2J^{CT}\right) \tag{13}$$

With h_{dp} being on the order of $10^3\,cm^{-1}$ and Δ on the order of $10^4\,cm^{-1}$, λ is on the order of 0.5–0.1, and therefore $-2J^{GS}$ is one to two orders of magnitude smaller than $-2J^{CT}$. The p orbital provides a *superexchange pathway* between d_A and d_B. Knowing $-2J^{CT}$ and λ (or h_{dp}) for a specific CT state, the contribution of the corresponding superexchange pathway to the coupling constant $-2J^{GS}$ of the electronic ground state can be determined. This is of particular interest if there are several unpaired electrons per mononuclear site and therefore several superexchange pathways (see Section 2.42.4).

Both singlet and triplet CT states are split, and this splitting can be determined experimentally by, e.g., optical absorption spectroscopy if both transitions from the respective GS spin component to each of the split components of the CT state are electric-dipole (ED) allowed. This is the case if the dimer does not have a center of symmetry. In that case the +/− would correspond to g/u (gerade/ungerade) combinations and only the $g \leftrightarrow u$ transition would have ED intensity.

The VBCI splitting of the triplet CT states, which is approximately given by ${h_{dp}}^2/\Delta$ (*vide supra*), corresponds to the HOMO/LUMO splitting of the dimer at the same level of approximation. This follows from consideration of the sym/antisym combinations of the copper SOMOs and their interaction with the ligand HOMO generating one non-bonding and one antibonding copper MO.[19] In addition, the triplet CT state energies predicted by MO and VB theory are identical. This allows one to obtain *ab initio* VBCI parameters h_{dp} and Δ from triplet MO ground state or CT transition-state calculations (see below). Due to additional MMCT and DCT interactions (Figure 2), the VBCI splitting of singlet CT states becomes smaller than the limiting value ${h_{dp}}^2/\Delta = \Delta E$(HOMO–LUMO) or can even be reversed with respect to the order predicted by the prototypical VBCI scheme of Figure 2 (see next Section).

2.42.3 APPLICATION TO COPPER PEROXO DIMERS: DISTORTION OF THE Cu_2O_2 CORE

The VBCI model has been employed for the interpretation of the optical absorption and CD spectra of of peroxo bridged Cu^{II} dimers like oxy-Hemocyanin and corresponding small-molecule analogs (Figure 3).[15–17,24–26] Hemocyanin (Hc), the oxygen-transport protein of mollusks and arthropods, contains a binuclear Cu(I) active site that reversibly binds dioxygen as peroxide in a side-on bridging (μ–η^2:η^2) geometry (Scheme 1(A)).[27] The highest occupied molecular orbitals of peroxide are a doubly degenerate π^* set which split in energy upon bonding to a metal center: a σ-bonding orbital within the plane of the metal–peroxo bond, π^*_σ, (cf. Scheme 1(A)) and a π-bonding orbital vertical to this plane, π^*_v. As σ- is much stronger than π-bonding, the π^*_σ orbital is much lower in energy than the π^*_v orbital, and the $\pi^*_\sigma \rightarrow d_{x^2-y^2}$ CT transition is expected to be at much higher energy than the $\pi^*_v \rightarrow d_{x^2-y^2}$ transition. From overlap considerations with respect to $d_{x^2-y^2}$, the intensity of the π^*_σ will also be considerably higher than that of the π^*_v transition. In agreement with this qualitative picture, the two intense bands in the optical absorption spectrum of oxy–Hc at $17{,}200\,cm^{-1}$ ($\varepsilon = 1{,}000\,M^{-1}\,cm^{-1}$) and $29{,}000\,cm^{-1}$ ($\varepsilon = 20{,}000\,M^{-1}cm^{-1}$) have been assigned to the ED allowed transitions to the π^*_v and π^*_σ CT states, respectively, and the positive feature in the CD spectrum near 480 nm ($21{,}000\,cm^{-1}$; $\Delta\varepsilon = 1\,M^{-1}\,cm^{-1}$) as the MD allowed transition to the g component of the π^*_v CT state (Figure 3).

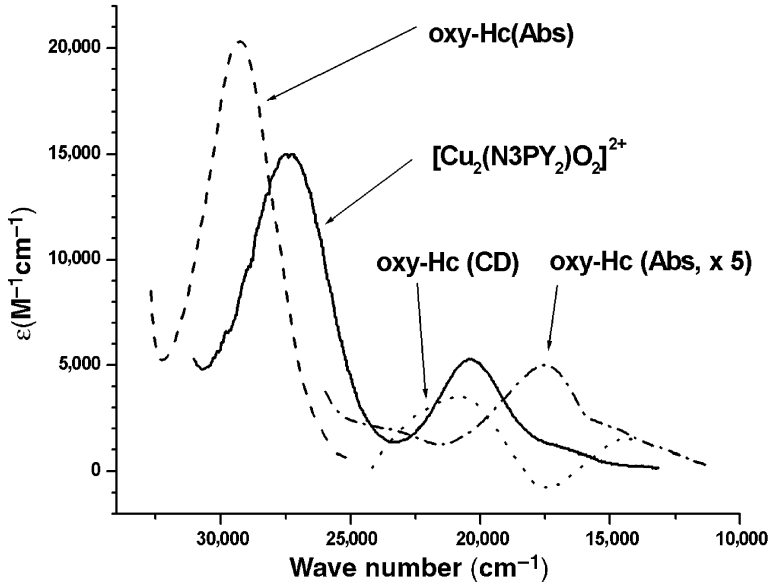

Figure 3 Optical absorption and CD spectrum of oxy-Hemocyanin and the model complex $[Cu_2(N3PY2)O_2]^{2+}$. While the spectrum of oxy-Hc is typical for μ-η^2:η^2 Cu peroxo systems with an almost planar Cu_2O_2 unit, the model complex has a bent side-on peroxo bridged (butterfly) structure (see text; adapted from ref. 31).

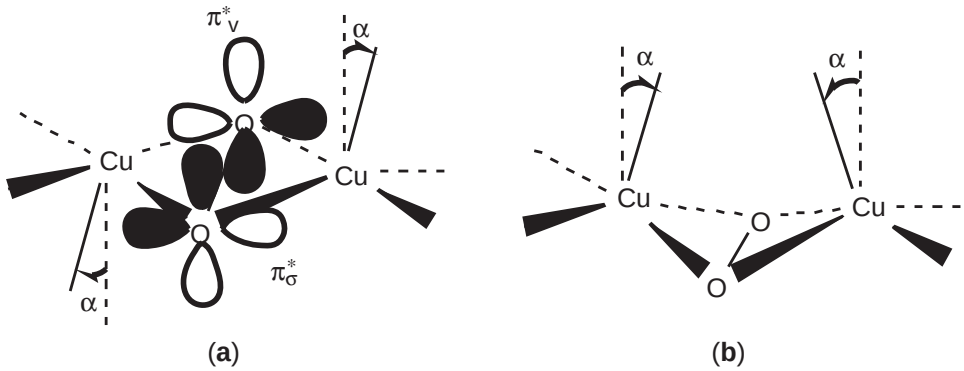

Scheme 1

In order to reproduce these transition energies with the VBCI model, parameters derived from DFT calculations and spectroscopy were used.[28] Initially, the active site of oxy-Hc was modeled using a simplified $[(NH_3)_4Cu_2(O_2)]^{2+}$ planar core (symmetry D_{2h}), and the relative energies of the MO triplet states were determined with SCF-Xα-SW transition-state calculations.[29] From these values the zeroth-order energies for the π^*_σ CT (Δ_σ) and the π^*_v CT states (Δ_v) as well as the magnitude of the in-plane transfer element $(h_{d\pi})_\sigma$ were calculated. The zeroth-order energy for the MMCT state was assumed to be equal to the Mott–Hubbard energy U, which for Cu^{II} dimers was found by PES to be 6.5 eV (cf. Section 2.42.5).[30] In planar D_{2h} symmetry, however, the out-of-plane π^*_v orbital has no overlap with the Cu $d_{x^2-y^2}$ orbitals, and hence the transfer matrix element $(h_{d\pi})_v$ between π^*_v and $d_{x^2-y^2}$ vanishes; consequently, no splitting of the π^*_v states is predicted in this symmetry. In order to reproduce the experimentally observed splitting of these states, the actual dimer geometry has to be considered. Inclusion of the transaxial ligands lowers the symmetry to C_{2h}, and due to the pyramidal coordination the quantization axis of each copper center is tilted with respect to the Cu_2O_2 plane (α in Scheme 1(A)). This leads to a nonzero value of the matrix element $(h_{d\pi})_v$. An estimate of its magnitude was obtained from the value of $(h_{d\pi})_\sigma$ and the relative, experimentally determined oscillator strengths of the π^*_σ and π^*_v absorption bands.

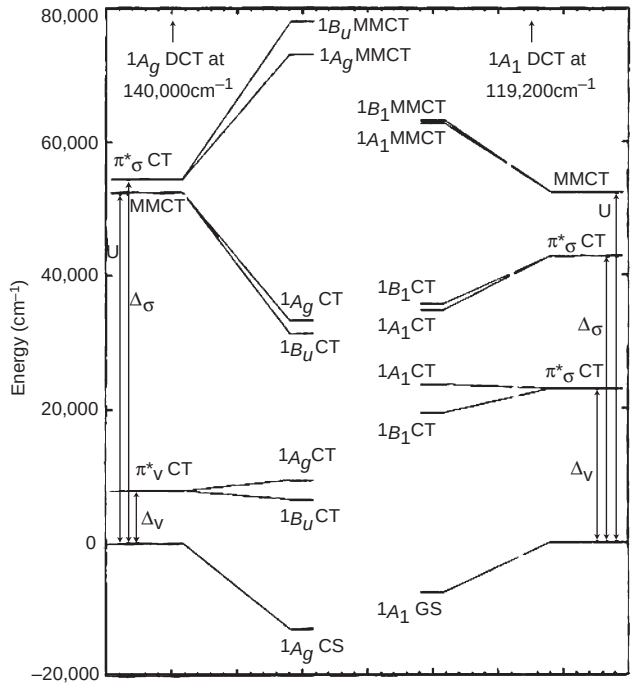

Figure 4 VBCI diagram for a side-on peroxide-bridged copper dimer in planar (left) and butterfly (right) geometries. Unperturbed singlet states are shown for both planar and butterfly geometries (far left and far right, respectively) and after CI is introduced between the GS, CT, and higher energy CT states (MMCT and DCT, DCT omitted from diagram for clarity) (center left, planar; center right, butterfly) (reproduced by permission of the American Chemical Society from *J. Am. Chem. Soc.* **1999**, *121*, 1299).

Using these parameters, the VBCI energy level scheme shown on the left side of Figure 4 was obtained. Importantly,

the A_g component of the $\pi^*_\sigma \rightarrow Cu^{II}$ CT transition (electric dipole forbidden) was calculated to be $\approx$2,000 cm^{-1} above the electric-dipole allowed B_u component (observed experimentally at 345 nm), and
the splitting of the two components of the $\pi^*_v \rightarrow Cu^{II}$ transition was calculated to be $\approx$3,000 cm^{-1} with the CD-active band (A_g component) being above the electric-dipole allowed band (B_u component), in agreement with the experimental observation.

More recently, the above treatment was also applied to Cu_2O_2 cores that exhibit a butterfly structure, i.e., bent around the O–O axis (Scheme 1(b)).[31] As compared to the planar Cu_2O_2 cores the absorption spectra of these systems exhibit one additional intense band in the 420–490 nm region (cf. Figure 3). Resonance Raman Spectroscopy shows that this feature is one component of the $\pi^*_\sigma \rightarrow Cu^{II}$ transition which becomes allowed in the lower symmetry (C_{2v}) of the bent geometry. To apply the VBCI model to the C_{2v} butterfly core, values for Δ_σ, $(h_{d\pi})_\sigma$, Δ_v and $(h_{d\pi})_v$ derived from DFT triplet CT transition-state calculations were employed. In analogy to the C_{2h} case (*vide supra*), a non-vanishing value of $(h_{d\pi})_v$ results from a nonplanar geometry (Scheme 1(B)). The Δ_σ and $(h_{d\pi})_\sigma$ parameters obtained are smaller than those calculated for the planar C_{2h} model, reflecting the loss of interaction between the peroxide π^*_σ and the Cu $d_{x^2-y^2}$ orbitals in the butterfly core. Due to the greater interaction between the peroxide π^*_v and the Cu $d_{x^2-y^2}$ orbitals, on the other hand, the magnitude of the zeroth-order energy Δ_v and the transfer matrix element $(h_{d\pi})_v$ are larger than those of the planar core. Diagonalization of the VBCI matrices using these parameters gives the energies for the π^*_σ and π^*_v CT states as shown in Figure 4, right, with the following results:

The A_1 component of the π^*_σ CT is now calculated to be approx. 900 cm^{-1} *below* the B_1 component, in contrast to the results obtained for oxy–Hc (C_{2h}), where the A_g component of the π^*_σ CT was calculated to be approximately 2,000 cm^{-1} *above* the B_u component. This order of π^*_σ CT state components is in agreement with the experiment.

The splitting between the two components of the π^*_v CT state is calculated to be $\approx$4,000 cm^{-1}, compared with the splitting of $\approx$2,900 cm^{-1} calculated for the planar C_{2h} core. This is in good agreement with the spectroscopic data which show the splitting of the π^*_v states to be approximately 5,000–6,000 cm^{-1}, compared with the $\approx$3,000 cm^{-1} splitting in oxy–Hc.

Thus, the VBCI model accounts for the spectroscopic properties of Cu^{II} peroxo systems with both planar and bent μ–η^2:η^2 Cu_2O_2 cores and correctly reproduces the spectroscopic–structural correlations observed experimentally. It shows that the π^*_σ interaction produces the superexchange pathway for AF coupling in the GS and provides an experimentally calibrated VBCI estimate of $-2J^{GS}$.

2.42.4 APPLICATION TO LINEAR AND BENT IRON(III)–IRON(III) OXO DIMERS (d^5–d^5)

If the metal centers contain several unpaired electrons, in principle each unpaired electron on one subunit can couple with each unpaired electron on the other unit if a bridging ligand orbital exists that overlaps with both metal orbitals involved. As described in Section 2.42.2 the corresponding superexchange pathway is mediated by CT, MMCT, and DCT states, and spectroscopic information from the CT spectrum can be used to determine the relative contribution of *this specific pathway* to the cumulative ground-state coupling constant $-2J^{GS}$.

This has been employed in the study of linear and bent μ-oxo bridged Fe^{III} dimers which are models for the met form of hemerythrin, an oxygen transport protein found in marine invertebrates.[7] Core atoms and coordinate frames for the bent, tribridged structure (**1**) and the monobridged, almost linear structure (**2**) are given in Scheme 2. The 300 and 10 K absorption spectra of (**1**) and (**2**) are shown in Figure 5A and 5B, respectively. These spectra can be divided into three different regions. Region I exclusively contains ligand-field (LF) bands whereas region II shows both LF- and low-energy CT bands. In region III only CT bands are present. The spectra in part exhibit spectacular temperature effects. In Figure 5A for (**1**), most bands decrease in intensity or disappear upon cooling except for the most intense peak at 21,000 cm^{-1} which almost doubles in intensity at 10 K. For structure (**2**) (Figure 5B), the intensity at 21,000 cm^{-1} decreases and that of the band at 25,000 cm^{-1} increases at low temperature. In region III, variable temperature dependencies are found for (**2**).

These findings can be understood in terms of dimer exchange interactions. Both (**1**) and (**2**) contain high-spin Fe^{III} centers which are antiferromagnetically coupled, i.e., the ground state (GS) splits into six total spin states due to antiferromagnetic coupling between two $s = 5/2$ monomers to give the total spin $S = 0, 1, 2, 3, 4, 5$ states with $S = 0$ being lowest in energy. A phenomenological description of the GS spin ladder shown in the bottom of Figure 6 is provided by the Heisenberg Hamiltonian $H = -2J^{GS}\ \boldsymbol{s}_A \cdot \boldsymbol{s}_B$ with $s_A = s_B = 5/2$; experimentally determined J^{GS} values are $-120\ cm^{-1}$ for (**1**) and $-95\ cm^{-1}$ for (**2**). Also shown in Figure 6 (middle) are the dimer states resulting from a LF transition of one center to a quartet LF state. In this case coupling of the $s = 5/2$ GS on one half of the dimer and an $s = 3/2$ excited LF state on the other half generates $S = 1, 2, 3, 4$ dimer states with a splitting described by a LF excited state J^{LF}. Due to $+/-$ combinations of local excitations at A and B, each individual S state again splits into two states represented by Γ_+ and Γ_-, giving a total of 8 dimer states for each quartet LF transition in

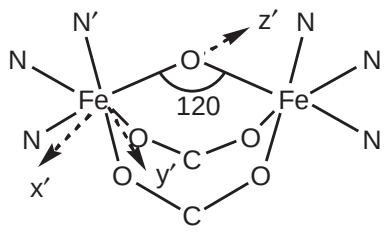

(**1**)

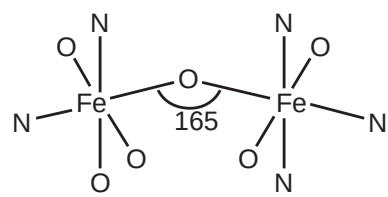

(**2**)

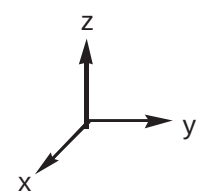

Scheme 2

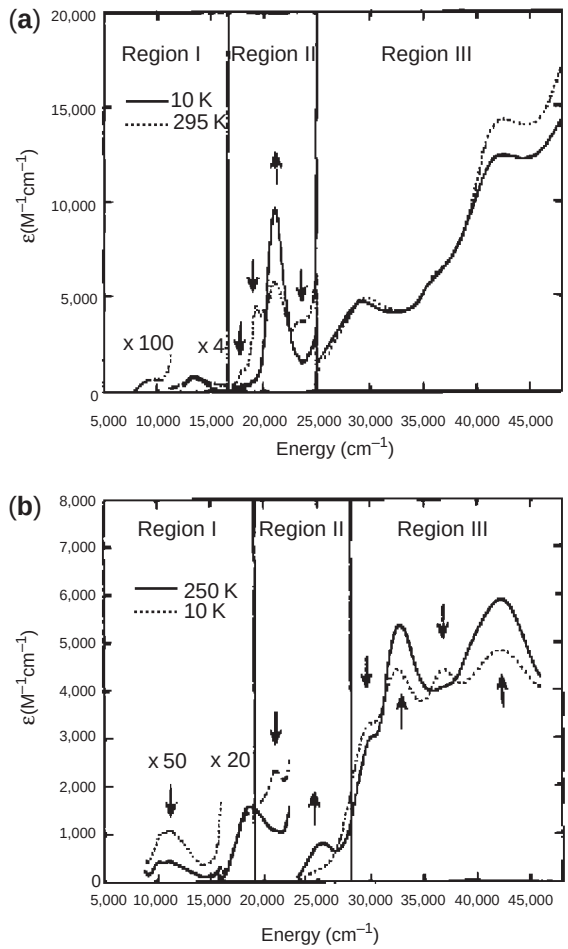

Figure 5 Absorption spectra for (**1**) (a) and (**2**) (b). Arrows indicate the change in intensity with decreasing temperature. (reproduced by permission of the American Chemical Society from *Inorg. Chem.* **1995**, *34*, 688).

the monomer. Finally, the top portion of Figure 6 gives the excited states resulting from a spin-allowed CT of the monomer. These dimer CT states are obtained by coupling a $^6\Gamma$ CT state generated by excitation of one electron from a ligand orbital into one of the singly occupied metal orbitals of Fe_A or Fe_B with the $^6A_1$ ground state on the other half of the dimer. In this case, +/− combinations lead to 12 CT states in the dimer. At low temperature, when only the $S=0$ component of the GS is populated, there can be spin-allowed ($\Delta S=0$) transitions for CT but not for LF states whereas both spin-allowed LF and CT transitions are possible from higher S states of the GS at elevated temperatures. This allows assignment of a spin multiplicity to each spin-allowed LF or CT transition in Figure 5 based on the temperature dependence of its intensity.

In order to further elucidate the origin of CT bands in 5, VBCI calculations have been performed on (**1**) and (**2**). For simplicity, a linear dimer with C_{2v} molecular symmetry (**2′**) taken as a model for (**2**) will be considered first. The analysis will then be extended to a singly bridged, bent Fe–O–Fe dimer (**1′**) which is taken as a model for (**1**). Figure 7 shows the metal-bridging ligand orbital interactions in the linear (**2′**; left) and the bent structure (**1′**; right). In the linear dimer (**2′**), oxo → Fe CT transitions are possible from $p_x \rightarrow d_{xz}$ ("out-of-plane (o.o.p.) π"; the Fe–O–Fe plane for (**2′**) is yz), $p_y \rightarrow d_{yz}$ ("in-plane (i.p.) π") and $p_z \rightarrow d_z^2$ ("σ"). Based on the scheme given in Figure 6, each of these three orbitally allowed CT transitions gives rise to $^{2S+1}A_1{}^{CT}$ and $^{2S+1}B_2{}^{CT}$ states ($S=0,\ldots,5$). However, not all of these states are important. The $^1A_1$ GS can have CT transitions to the states of $^1B_2$ (parallel polarization) and $^1A_1$ symmetry (perpendicular polarization with respect to Fe–Fe). VBCI matrices of all $^1A_1$ and $^1B_2$ states are necessary to describe this CT spectrum, and the $^1A_1$ matrix is needed to account for the $^1A_1$ GS

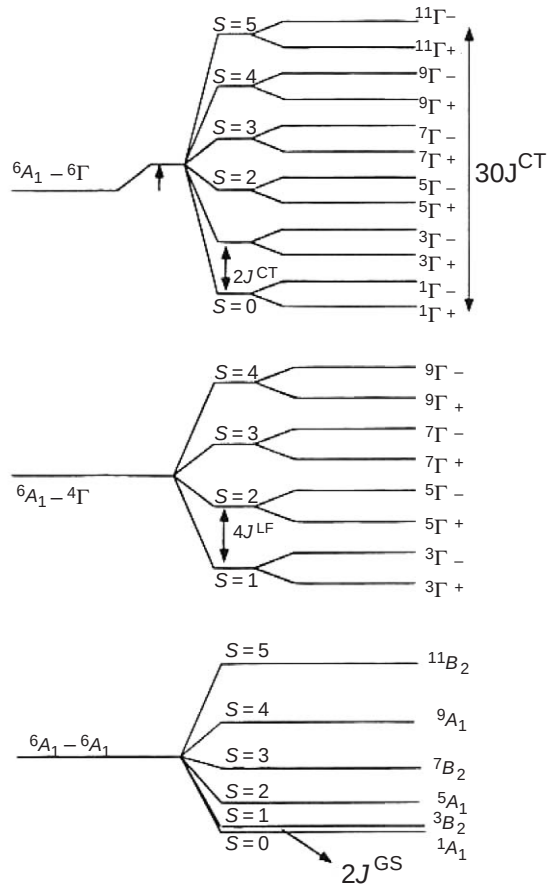

Figure 6 Energy level diagrams giving the GS, ligand field (LF) and charge transfer (CT) excited state manifolds of binuclear Fe^{III} h.s. dimers (taken from ref. 7).

stabilization (note that due to the linear symmetry the individual π and σ CT states do not mix with each other but all contribute to the ground state AF coupling). The high-spin matrices $^{11}A_1$ and $^{11}B_2$ are relevant since from DFT transition-state calculations of the high-spin states, $^{11}A_1$ and $^{11}B_2$, VBCI parameters can be extracted and the total splitting of the GS $^{11}B_2 - {}^1A_1 = -30\ J^{GS}$ allows the determination of J^{GS} (cf. Section 2.42.2). The results of this protocol are shown in Figure 8. Based on the two high-spin o.o.p. π transitions $p_x \rightarrow d_{xz}$ ($^{11}B_2 \rightarrow {}^{11}A_1$, $^{11}B_2$), the two high-spin i.p. π transitions $p_y \rightarrow d_{yz}$ ($^{11}B_2 \rightarrow {}^{11}A_1$, $^{11}B_2$) and the two high-spin σ transitions $p_z \rightarrow d_z{}^2$ ($^{11}B_2 \rightarrow {}^{11}A_1$, $^{11}B_2$) the six VBCI parameters $h_{d_{xz}p_x}$, $h_{d_{yz}p_y}$, $h_{d_{z^2}p_z}$, Δ_x, Δ_y, and Δ_z were obtained by fitting the appropriate VBCI matrices to the calculated transition energies (right half of Figure 8). Values for U and E_{DCT} were obtained from photoelectron spectroscopy (7 eV[7]) and by doubling the corresponding CT energies, respectively. These parameters were then used in the $^1A_1$ and $^1B_2$ VBCI matrices to obtain the singlet energy level scheme given on the left half of Figure 8.

The important results from this treatment of the linear dimer (**2′**) are:

The $^1A_1$ GS level is stabilized by $-10{,}530\ cm^{-1}$ and the $^{11}B_2$ level by $-8{,}460\ cm^{-1}$, giving a J^{GS} value of $-69\ cm^{-1}$ (GSAF; expt. value for (**2**): $-95\ cm^{-1}$).

The i.p. π CT levels $^1A_1$ and $^1B_2$ are greatly lowered in energy with respect to their $S = 5$ high-spin counterparts. Defining in analogy to the ground state $-30J^{CT} = E(^{11}B_2) - E(^1A_1)$ gives for these states a CT excited coupling constant (ESAF) of $J^{CT} = -600\ cm^{-1}$, about nine times larger than GSAF.

Due to the large transition energy for the σ transition, the corresponding $p_z \rightarrow d_{z^2}$ CT states lie at energies above the MMCT and DCT states of the π transitions.

The normalized, squared coefficients of the CT states in the $^1A_1$ GS wavefunction have been taken as a measure of the relative importance of the various superexchange pathways.

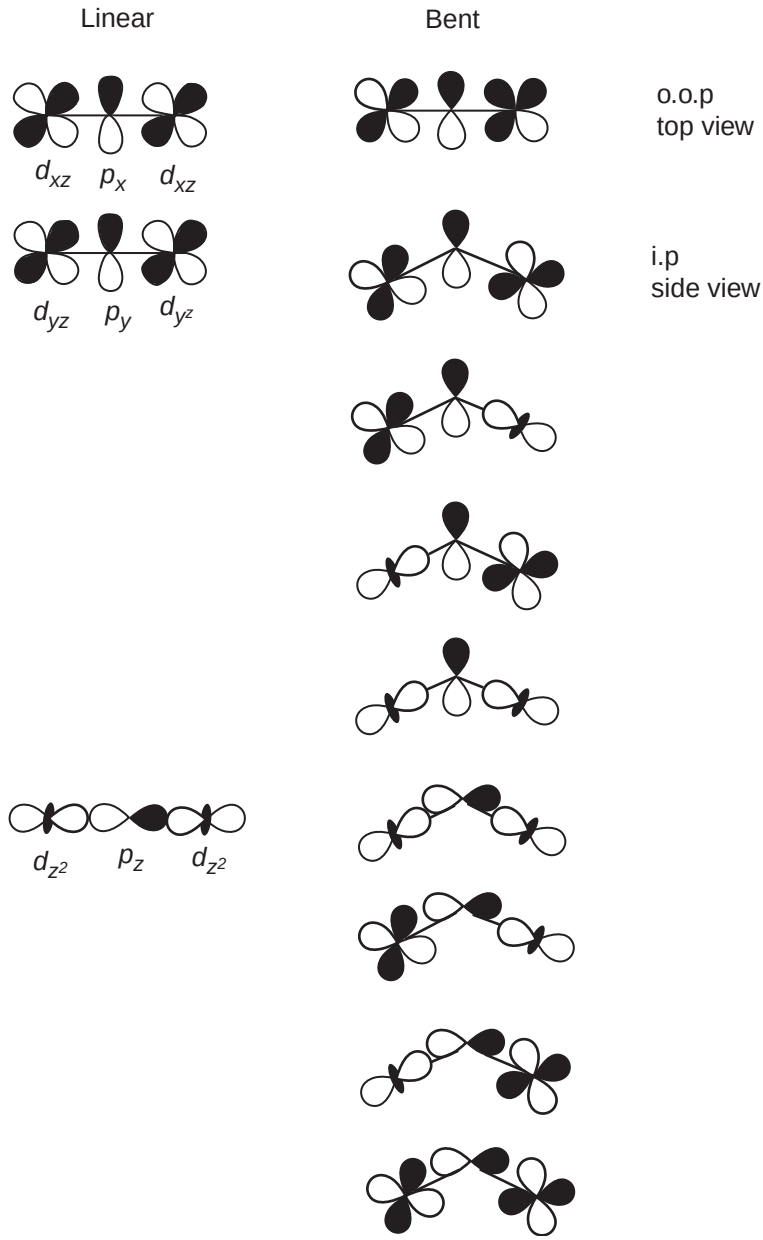

Figure 7 Diagrams for the major superexchange pathways in the Fe^{III}–O–Fe^{III} unit. The linear pathways are given on the left and the pathway in the bent dimer on the right (taken from ref. 7).

This gives 40% and 45% CT character in the ground state deriving from the o.o.p and i.p. π transitions, respectively, and 13.8% from the σ transition, indicating the dominant role of π superexchange pathways to the AF coupling in linear μ-oxo dimers.

This analysis has then been extended to the bent Fe–O–Fe dimer **1**′ (Figure 7, right). While the o.o.p. π interactions are identical to the linear dimer **2**′, the i.p. π (d_{yz}) and σ (d_{z^2}) orbital interactions become mixed. For the i.p. oxo p_y orbital, there are now two possible CT transitions: $p_y \rightarrow d_{yz}$ and $p_y \rightarrow d_{z^2}$. Thus a new CT transition, $p_y \rightarrow d_{z^2}$ needs to be added to the VBCI matrices described above. In addition, this opens new possibilities for MMCT ($d_{z^2} \leftrightarrow d_{yz}$) and DCT ($d_{z^2} \leftarrow p_y \rightarrow d_{z^2}$) states. Likewise, there is a new CT transition from $p_z \rightarrow d_{yz}$ which has to be taken into account. This interaction also generates new MMCT and DCT states. The new interactions mediate the "mixed π/σ" superexchange pathways.

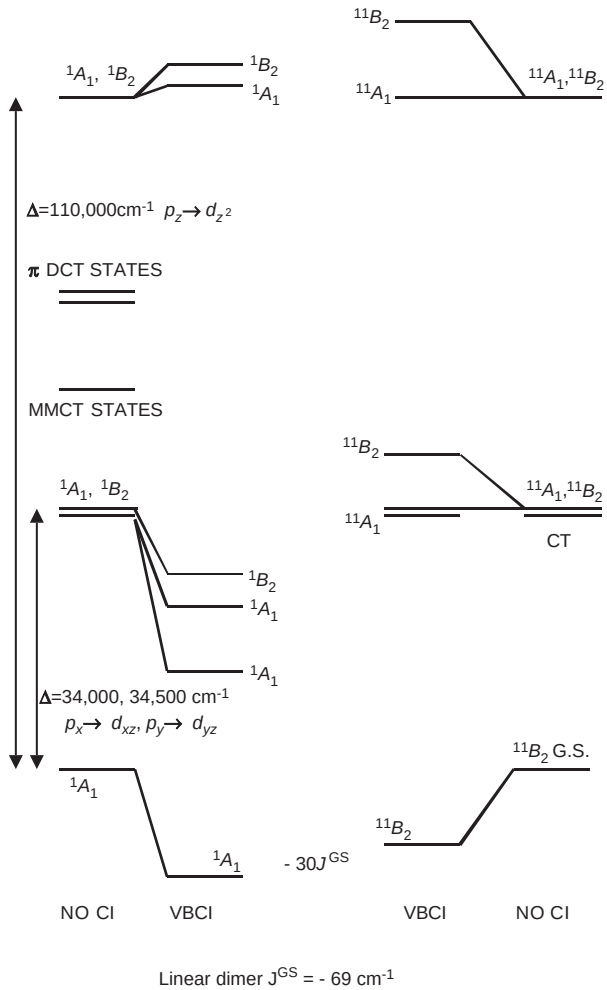

Figure 8 Energy level scheme giving the result of the VBCI analysis on the linear structure 2′. The $S=0$ states are given on the left and the $S=5$ states on the right (taken from ref. 7).

In order to also apply the VBCI model to this case, the high-spin problem again has been treated first. In particular, the ten $^{11}A_1$, $^{11}B_2$ CT excited states resulting from the five possible oxo → Fe transitions $p_x \rightarrow d_{xz}$ (o.o.p. π), $p_y \rightarrow d_{yz}$ (i.p. π), $p_y \rightarrow d_{z^2}$ (mixed π/σ), $p_z \rightarrow d_{yz}$ (mixed π/σ) and $p_z \rightarrow d_{z^2}$ (σ) were calculated by DFT, and by fitting the appropriate $^{11}A_1$ and $^{11}B_1$ VBCI matrices to the resulting energies, the corresponding five VBCI transfer integrals and five Δ-values have been determined. The corresponding energy level scheme is shown on the right-hand side of Figure 9. U and E_{DCT} have been parameterized as in the linear case.

Using these VBCI parameters in the treatment of the singlet, $^1A_1$ and $^1B_2$, states, the energy levels shown on the left-hand side of Figure 9 are obtained. The important points to observe from this diagram are:

The $^1A_1$ GS is lowered by $-10{,}465\,cm^{-1}$ in energy and the $^{11}B_2$ state by $-8{,}345\,cm^{-1}$, giving a GS J value of $-71\,cm^{-1}$ (GSAF; expt. value: $-120\,cm^{-1}$).

The singlet i.p. and o.o.p π transitions from oxo $p_{x,y}$ to $d_{xz,yz}$ are greatly lowered in energy with respect to their undecet counterparts (ESAF).

The $^1A_1$ and $^1B_2$ CT states deriving from the in-plane $p_y \rightarrow d_{yz}$ π transition are at lower energy than their o.o.p. $p_x \rightarrow d_{xz}$ counterparts. In agreement with this VBCI prediction, the lowest-energy CT transitions in the absorption spectrum of (**1**) at $18{,}400\,cm^{-1}$ (shoulder in mull spectrum; not

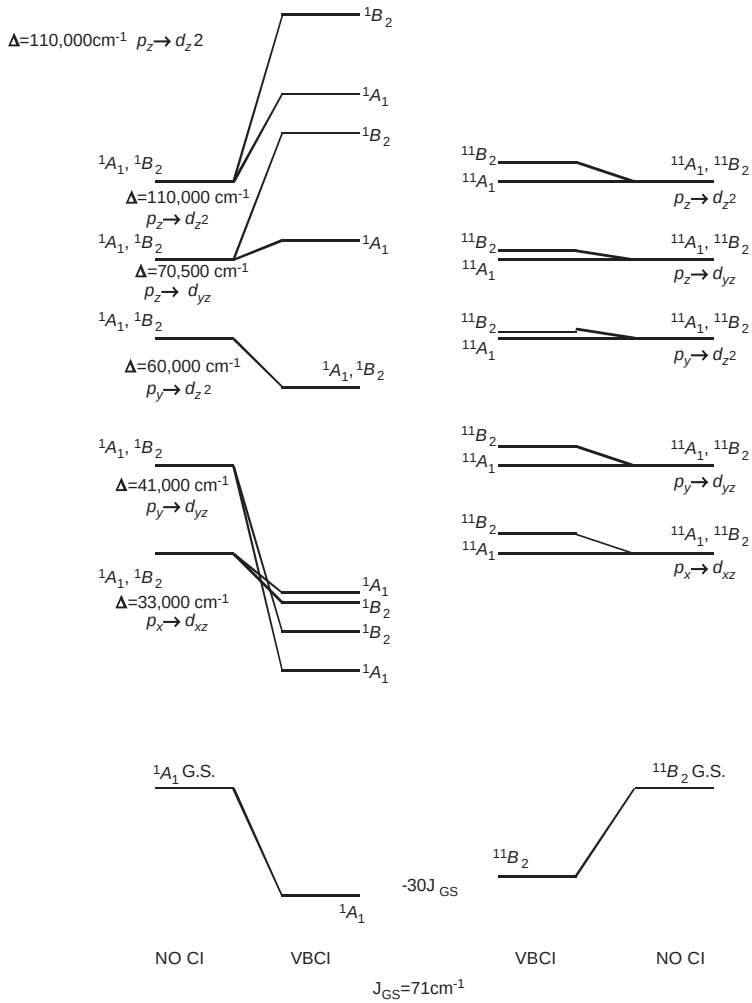

Figure 9 Energy level scheme giving the result of the VBCI analysis on the bent structure 1′. The $S=0$ states are given on the left and the $S=5$ states on the right (taken from ref.7).

visible in Figure 5A) and 20,500 cm^{-1} are assigned to $^1A_1 \rightarrow {}^1A_1$ and $^1A_1 \rightarrow B_2$ components of the $p_y \rightarrow d_{yz}$ CT transition, respectively. In contrast, the lowest component of the o.o.p. $p_x \rightarrow d_{xz}$ transition is only observed at 25,960 cm^{-1}, more than 5,000 cm^{-1} above its i.p. counterpart. This "inverted" ordering of the i.p. and o.o.p. π transitions is due to additional i.p. mixed π/σ interactions (*vide supra*) which significantly decrease the energy of the i.p. states.

Based on the normalized CT contributions in the GS wavefunctions, the relative importance of the i.p. and o.o.p. π superexchange pathways has decreased in the bent with respect to the linear dimer. This loss of π interaction is compensated by an increase of the importance of the σ pathway, which is due to the energetic lowering of the $p_z \rightarrow d_{z^2}$ CT state, and in particular by the new, mixed π/σ pathways $p_y \rightarrow d_{z^2}$ and $p_z \rightarrow d_{yz}$ which in the bent geometry account for 4 and 12% CT character in the GS wavefunction, respectively. The combined effects of increase of σ interaction and additional, mixed π/σ interactions lead to the observed increase of AF coupling upon lowering the Fe–O–Fe angle in μ-oxo Fe^{III} dimers.

An analogous treatment has been applied to Mn oxo dimers.[32]

2.42.5 EVALUATION OF U, Δ, AND h_{dp} FROM PHOTOELECTRON SPECTROSCOPY

As shown in the previous sections, diagonalization of the VBCI matrices involves the CT energies Δ, transfer integrals $h_{d\pi}$ (or h_{dp}) and Mott–Hubbard gaps U. While experimental information on

Δ and h_{dp} can be obtained from CT spectra, U in general is not accessible by this technique as the corresponding transitions are high energy and probably very diffuse. For these reasons, U values derived from photoelectron spectroscopy (PES) have been used in Sections 2.42.3 and 2.42.4. Whereas we have calculated Δ and h_{dp} from DFT on the high-spin states, these can also be derived from PES data using the so-called impurity or cluster CI models of PES.[23,33–35] These calculations involve diagonalization of the Anderson Hamiltonian with part or all of the translational symmetry of the lattice being neglected in favor of an explicit treatment of on-site electron–electron interactions. While in the impurity approach the bandwidth of the *d*-states is neglected but the finite bandwidth of the O $2p$ states is taken into account, the cluster CI (or local cluster) model totally neglects the bandwidth of both *d* and *p* states and only includes an oxygen–oxygen nearest-neighbor hybridization T_{pp} via differences in energy for the different symmetry levels. In addition, the oxygen levels are shifted upon metal–oxygen mixing. These calculations have proven very useful for the interpretation of photoelectron and inverse photoelectron spectroscopic data of ionic solids and in addition have allowed to understand their magnetic properties. In this section the relationship of these treatments to the VBCI model of isolated dimers and the evaluation of VBCI/cluster–CI parameters from the analysis of PES data will briefly be discussed.

An example is provided by a planar array of alternating Cu and O centers derived from, e.g., a Y–Ba–Cu oxide high-T_{c} superconductor (Figure 10).[23] The basic assumption of the cluster CI model is that a $(CuO_4)^{6-}$ square–planar cluster can be considered as a separable unit of this CuO plane (Figure 10, solid lines). If this condition is not met (i.e., if the bandwidth of *p* states is large with respect to the O $2p \rightarrow$ Cu $3d$ CT energy), the model breaks down. The electronic structure of the local cluster is described with the model Hamiltonian (Equation (14))

$$\hat{H} = \sum_m \varepsilon_d(m) d_m^+ d_m + \sum_m \varepsilon_p(m) p_m^+ p_m + \sum_m T_{pd}(m)(d_m^+ p_m + p_m^+ d_m) + \sum_{m,m',n,n'} U(m,m',n,n') d_m^+ d_{m'} d_n^+ d_{n'} \tag{14}$$

Here the operator d_m^+ creates a Cu $3d$ hole with an energy $\varepsilon_d(m)$ and the operator p_m^+ a ligand O $2p$ hole with an energy $\varepsilon_p(m)$. The oxygen–oxygen–hybridization is already included in the different $\varepsilon_p(m)$. The third term describes the mixing between the Cu $3d$ states and the ligand orbitals; $T_{dp}(m)$ is the transfer integral for the Cu $3d$–O $2p$ ligand hybridization (mixing). The last term describes the two-particle Cu $3d$ Coulomb- and exchange interactions U; the indices m, m', n, and n' denote orbital and spin quantum numbers. The energies $\varepsilon_d(m)$, $\varepsilon_p(m)$ and the integrals $T_{dp}(m)$ do not depend on spin. For each symmetry/spin label m, diagonalization of the 2×2 interaction matrix

$$\begin{array}{cc} |3d^9\rangle & |3d^{10}L\rangle \\ \begin{vmatrix} -E & T_{dp} \\ T_{dp} & \Delta - E \end{vmatrix} & \end{array} \tag{15}$$

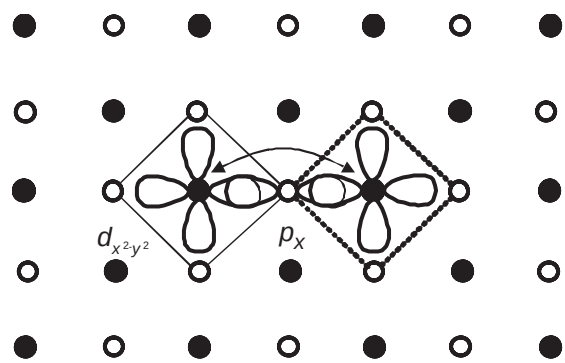

Figure 10 Section from a square Cu–O lattice with CuO_4 cluster (solid lines) and relevant orbital. Neighboring cluster dotted lines.

leads to a one-hole ground state (GS) and a one-hole excited state (CT). Here, $|3d^9\rangle$ refers to a state with one hole in the d-shell, and $|3d^{10}L\rangle$ to a state with a hole in the p shell. Δ is given by the energy difference between metal and ligand orbital, $\Delta = \varepsilon(d) - \varepsilon(p)$. Since the transfer integrals $T_{dp} = T_i$ are of different magnitude for different combinations of d and p orbitals, this leads to the splitting of the (one-hole) ligand-field states. As $T_{x^2-y^2,p} = T(b_1) = T_1$ is the largest transfer matrix element, the GS of lowest energy has the hole in the $b_{1g} = d_{x^2-y^2}$ orbital.

Photoemission leads to removal of an electron leading to a second hole in the CuO_4 cluster. Ionization of a b_{1g} electron, e.g., produces final states with a second hole in a b_{1g} level. This generates three possible configurations $|d^8>$, $|d^9L>$ and $|d^{10}L^2>$ at energies U, Δ_1 and $2\Delta_1$, respectively. The d^8 and $d^{10}L^2$ configurations each produce one singlet state while the d^9L state produces both a singlet state and a triplet state. The singlets all have the same spin and spatial symmetry and can undergo CI which involves the parameters U, Δ_1 and T_1.

Diagonalization of the respective matrix gives the energy level scheme for the final states. The same can be done with the states resulting from removal of an electron from a non-b_{1g} orbital; in this case the final state CI matrices are only slightly larger. The theoretical PE spectrum can then be evaluated by forming the electric dipole operator matrix elements between the ground state and the various final states. It has been pointed out that nonlocal effects are important for a detailed understanding of the local cluster energy level scheme, cf. ref. 35. A fit to the measured spectrum will afford values for the various CT energies Δ_i, the transfer matrix elements T_i and U.[30]

The parameters derived from this treatment of the local CuO_n cluster can then be employed in cluster–CI calculations to evaluate the coupling that arises between two Cu centers due to virtual charge fluctuations (superexchange). In the simplest case, the cluster–CI calculation is based on a three-center linear unit with a central ligand atom and two cations (Figure 10), i.e. the mixing of the copper centers of two neighboring CuO_4 clusters (solid and dotted lines in Figure 10) with the terminal oxygen atoms is neglected and only their interaction via one σ-bridging oxygen p orbital is considered. The determination of the two-hole wavefunctions, the interaction matrices and the energy level scheme is entirely analogous to the VBCI procedure for isolated Cu dimers outlined in Section 2.42.2. Importantly, the transfer integral t used in the cluster CI superexchange calculation is related to the transfer integral $T_1 = T(b_{1g})$ of the single CuO_4 cluster by $t = 1/2\ T_1$. In the case of a 3D cubic lattice (rock salt structure), the superexchange transfer integral t is related to the transfer integral $T_1 = T(e_g)$ of the CuO_6 cluster by $t = T_1/\sqrt{3}$. Using these values and U and Δ parameters corrected for crystal-field and electrostatic effects, the Néel temperatures of transition-metal oxides have been successfully reproduced.[23]

2.42.6 SUMMARY AND CONCLUSION

The preceding sections have shown that the VBCI model accounts for the electronic structure of bridged dimers. This has been demonstrated for the d^9-d^9 (d^1-d^1) and the d^5-d^5 case, respectively. The VBCI model in a valence-bond (VB) formalism considers the configurations and state of a transition-metal dimer bridged by a ligand and evaluates configuration interaction (CI) between these states by metal–ligand transfer matrix elements. This allows an understanding of the shifts and splittings of CT bands. In addition, the VBCI-assisted interpretation of CT spectra allows us to determine the relative contributions of specific superexchange pathways to the antiferromagnetic coupling of the ground state. In general, two-electron integrals are neglected in VBCI calculations except for on-site contributions. In this limit the VBCI model is equivalent to Cluster CI calculations of solid-state theory and thus also accounts for the high-energy part of the spectrum probed in photoelectron and related spectroscopies. Based on these VB approaches, it is therefore possible to arrive at a consistent understanding of the electronic structure of highly correlated transition-metal systems on an energy scale of several cm^{-1} to about $10^5\,cm^{-1}$, both in isolated polynuclear molecules and in 2- and 3D extended solids.

ACKNOWLEDGMENTS

EIS acknowledges funding by NIH DK31450 and the NSF Biophysics program.

2.42.7 REFERENCES

1. Lever, A. B. P. *Inorganic Electronic Spectroscopy* **1984**, Elsevier: New York.
2. Hansen, A. E.; Ballhausen, C. J. *Trans. Faraday Soc.* **1965**, *61*, 631–639.
3. Dubicki, L. *Aust. J. Chem.* **1972**, *25*, 1141–1149.
4. Desjardins, S. R.; Wilcox, D. E.; Musselman, R. L.; Solomon, E. I. *Inorg. Chem.* **1987**, *26*, 288–300.
5. Schugar, H. J.; Rossman, G. R.; Barraclough, C. G.; Gray, H. B. *J. Am. Chem. Soc.* **1972**, *94*, 2683–2690.
6. Schugar, H. J.; Rossman, G. R.; Thibeault, J.; Gray, H. B. *Chem. Phys. Lett.* **1970**, *6*, 26.
7. Brown, C. A.; Remar, G. J; Musselman, R. L.; Solomon, E. I. *Inorg. Chem.* **1995**, *34*, 688–717.
8. McClure, D. S. *J. Chem. Phys.* **1963**, *39*, 2850–2855.
9. Lohr, L. L.; McClure, D. S. *J. Chem. Phys.* **1968**, *49*, 3516–3521.
10. Ferguson, J.; Guggenheim, H. J.; Tanabe, Y. *J. Phys. Soc. Jpn.* **1966**, *21*, 692–704.
11. Meltzer, R. S.; Lowe, M.; McClure, D. S. *Phys. Rev.* **1969**, *180*, 561–578.
12. Schenker, R.; Weihe, H.; Güdel, H. U. *Inorg. Chem.* **1999**, *38*, 5593–5601, and references therein.
13. Ross, P. K.; Allendorf, M. D.; Solomon, E. I. *J. Am. Chem. Soc.* **1989**, *111*, 4009–4021.
14. Tuczek, F.; Solomon, E. I. *Coord. Chem. Rev.* **2001**, *219–221*, 1075–1112.
15. Solomon, E. I.; Baldwin, M. J.; Lowery, M. D. *Chem. Rev.* **1992**, *92*, 521–542.
16. Solomon, E. I.; Tuczek, F.; Root, D. E.; Brown, C. A. *Chem. Rev.* **1994**, *94*, 827–856.
17. Solomon, E. I.; Sundaram, U. M.; Machonkin, T. E. *Chem. Rev.* **1996**, *96*, 2563–2605.
18. Pate, J. E.; Ross, P. K.; Thamann, T. J.; Reed, C. A.; Karlin, K. D.; Sorrell, T. N.; Solomon, E. I. *J. Am. Chem. Soc.* **1989**, *111*, 5198–5208.
19. Tuczek, F.; Solomon, E. I. *Inorg. Chem.* **1993**, *32*, 2850–2862.
20. Tuczek, F. In *Spectroscopic Methods in Bioinorg. Chem.*; American Chemical Society: Washington, DC, 1998.
21. Mott, N. F. *Proc. Roy. Soc. London* **1949**, *A62*, 416.
22. Hubbard, J. *Proc. Roy. Soc. London* **1964**, *A277*, 237.
23. Zaanen, J.; Sawatzki, G. A. *Can. J. Phys.* **1987**, *65*, 1262.
24. Kitajima, N.; Fujisawa, K.; Moro-oka, Y.; Toriumi, K. *J. Am. Chem. Soc.* **1989**, *111*, 8975–8976.
25. Kitajima, N.; Fujisawa, K.; Fujimoto, C.; Moro-oka, Y; Hashimoto, S.; Kitagawa, T.; Toriumi, K.; Tatsumi, K.; Nakamura, A. *J. Am. Chem. Soc.* **1992**, *114*, 1277–1291.
26. Blackman, A. G.; Tolman, W. B. *Struct. Bonding (Berlin)* **2000**, *97*, 179–211.
27. Magnus, K. A.; Ton That, H.; Carpenter, J. E. *Chem.Rev.* **1994**, *94*, 727–735.
28. Tuczek, F.; Solomon, E. I. *J. Am. Chem. Soc.* **1994**, *116*, 6916–6924.
29. Ross, P. K.; Solomon, E. I. *J. Am. Chem. Soc.* **1991**, *113*, 3246–3259.
30. Didziulis, S. V.; Cohen, S. L.; Gewirth, A. A.; Solomon, E. I. *J. Am. Chem. Soc.* **1988**, *110*, 250–268.
31. Pidcock, E.; Obias, V.; Abe, M.; Liang, H.-C.; Karlin, K. D.; Solomon, E. I. *J. Am. Chem. Soc.* **1999**, *121*, 1299–1308.
32. Brunold, T. C.; Gamelin, D. R.; Solomon, E. I. *J. Am. Chem. Soc.* **2000**, *122*, 8511–8523.
33. Sawatzki, G. A. *Int. J. Mod. Phys. B* **1988**, *1*, 779–802.
34. Eskes, H.; Tjeng, L. H.; Sawatzki, G. A. *Phys. Rev. B* **1990**, *41*, 288–299.
35. Atanasov, M.; Reinen, D. *J. Electr. Spectr. Reatl. Phenom.* **1997**, *86*, 185–199.

Comprehensive Coordination Chemistry II
ISBN (set): 0-08-0437486

Volume 2, (ISBN 0-08-0443249); pp 541–557

2.43 Time-dependent Theory of Electronic Spectroscopy

C. REBER and J. LANDRY-HUM
Université de Montréal, Montréal, Canada

2.43.1 INTRODUCTION AND OVERVIEW OF THE APPROACH 559
2.43.2 LUMINESCENCE AND ABSORPTION SPECTRA FOR ELECTRONIC TRANSITIONS BETWEEN ONE–DIMENSIONAL HARMONIC POTENTIAL ENERGY SURFACES 560
2.43.3 LUMINESCENCE AND ABSORPTION SPECTRA FOR ELECTRONIC TRANSITIONS BETWEEN POTENTIAL ENERGY SURFACES FROM ELECTRONIC STRUCTURE CALCULATIONS AND BETWEEN MULTIDIMENSIONAL POTENTIAL ENERGY SURFACES 565
2.43.4 OTHER ELECTRONIC TRANSITIONS 571
2.43.5 REFERENCES 571

2.43.1 INTRODUCTION AND OVERVIEW OF THE APPROACH

Experimental information on the electronic structure of a wide variety of systems of interest to coordination chemistry, from classic Werner complexes to metalloproteins and nanoscale clusters, is obtained from a number of optical spectroscopic techniques, among them absorption, luminescence, and resonance Raman spectroscopy. The physical processes governing electronic transitions probed by these methods obviously determine the timescales and resolution of the experimental results. In order to gain insight on molecular quantities from spectra, theoretical models are needed. Electronic structure calculations, as presented in the preceding sections, have become more accurate over the past decades. They are most often carried out for molecules frozen at their ground-state structure, and vibronic processes leading to structural changes in excited states are generally neglected despite their important influence on spectra. It is therefore often hard to rigorously compare spectroscopic results to computational data.

The time-dependent theory of spectroscopy bridges this gap. This approach has received less attention than the traditional time-independent view of spectroscopy, but since 1980, it has been very successfully applied to the field of coordination chemistry.[1–3] The intrinsic time dependence of external perturbations, for example oscillating laser fields used in electronic spectroscopy, is also explicitly treated by modern computational methods such as time-dependent density functional theory, a promising approach to the efficient calculation of electronic spectra and excited-state structures not based on adjustable parameters, as described in Chapter 2.40. In contrast, the time-dependent theory of spectroscopy outlined in the following often relies on parameters obtained by adjusting a calculated spectrum to the experimental data. It provides a unified approach for several spectroscopic techniques and leads to intuitive physical pictures often qualitatively related to classical dynamics. The concepts at its core, time-dependent wave functions (wave packets) and autocorrelation functions, can be measured with femtosecond (fs) techniques,[4] which often illustrate concepts very similar to those presented in the following for the analysis of steady-state spectra. The time-dependent approach therefore unifies spectroscopic

transitions, scattering processes, and dynamics of molecules both in the ground and excited electronic states. Recent text books and chapters in advanced comprehensive volumes illustrate the basic theory and its link to the traditional time-independent formalism of quantum mechanics.[1,5–7]

This overview proceeds from basic to more advanced examples, emphasizing the link between purely theoretical models and experimental spectra. The implementation of the formalism, efficient algorithms and programming details have been published and lead to calculations that can easily be carried out on personal computers.[8–14]

2.43.2 LUMINESCENCE AND ABSORPTION SPECTRA FOR ELECTRONIC TRANSITIONS BETWEEN ONE–DIMENSIONAL HARMONIC POTENTIAL ENERGY SURFACES

The traditional view of an electronic absorption or luminescence transition is shown in Figure 1. The Franck–Condon picture for an allowed transition relates the intensity of each vibronic band in a spectrum to the square of the overlap of vibrational eigenfunctions for potential energy surfaces representing the initial and final electronic states. Analytical expressions for these overlap integrals exist for a few special cases, such as one-dimensional harmonic potentials with identical force constants for the initial and final states of the electronic transition.[15] Anharmonic potential energy surfaces, such as those obtained in numerical form from electronic structure calculations, are harder to treat in the traditional framework and closed formula solutions generally do not exist. The time-dependent approach is mathematically equivalent to the time-independent Franck–Condon picture, but can be easily generalized to numerical potentials given as arrays of energy values along one or several normal coordinates. Important parameters that are directly

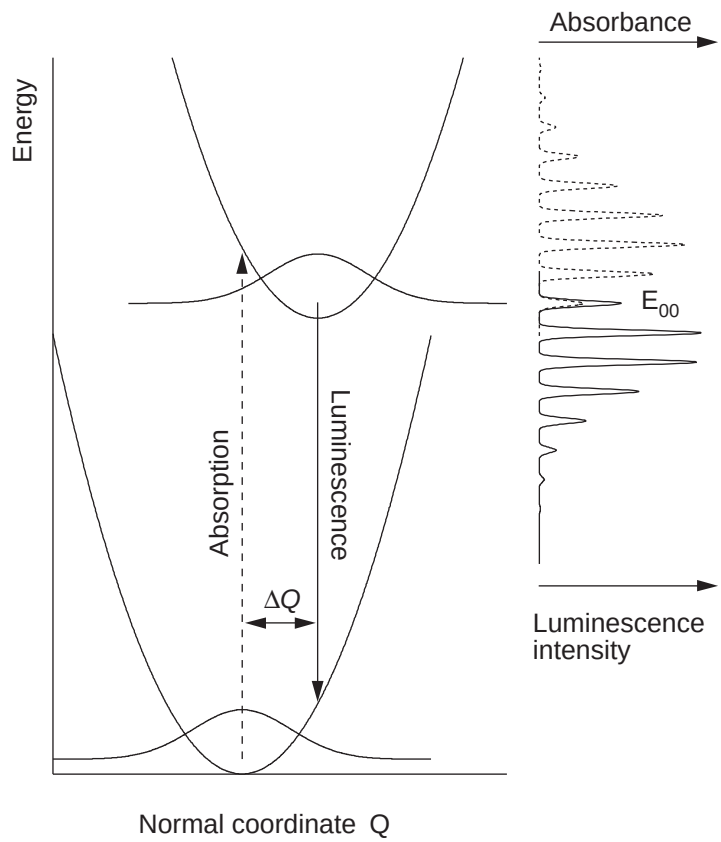

Figure 1 Electronic absorption and luminescence transitions between initial and final states represented by harmonic potential energy curves. The solid and dotted spectra denote calculated luminescence and absorption spectra, respectively. The electronic origin transition, E_{00}, and the offset between potential energy minima, ΔQ, are indicated.

determined from spectra such as those shown in Figure 1 are the vibrational frequencies of the two potential energy curves and their energy offset, which is defined by the electronic origin transition denoted as E_{00} in Figure 1. The most important parameter that can not be read directly from the spectra is the offset of the potential minima ΔQ along the normal coordinate ΔQ, illustrated in Figure 1. It is adjusted to lead to the best agreement between experimental and calculated spectra. In general, ΔQ_i values for i multiple coordinates ΔQ_i are easily determined from fit procedures and the effects of potential energy surfaces that are no longer harmonic can be analyzed, as illustrated by the examples in Figures 8 and 10.

Figure 2 illustrates the approach to the time-dependent calculation of electronic spectra. In this example, we show the final state of the luminescence transition in Figure 1 and calculate the luminescence spectrum. In the time-dependent picture of an allowed electronic transition, the initial wavefunction, corresponding to the lowest-energy eigenfunction of the excited state in Figure 1, is placed onto the final state surface, where it is no longer an eigenfunction and evolves with time. This evolution of the time-dependent wavepacket $\phi(t)$ is obtained from solutions of the time-dependent Schrödinger equation, with ϕ given as a starting point. Figure 2 illustrates the time-dependent wavefunction at three times, corresponding to 0, 10, and 50 fs. At time 0, the wavepacket ϕ is identical to the eigenfunction of the excited state. After 10 fs, the wavepacket has moved away from its initial position, and after 50 fs, a time corresponding to approximately half the vibrational period, it is near the turning point. This example shows a special situation: harmonic potentials with identical force constants for the initial and final states. The time-dependent wavefunction does therefore retain its Gaussian shape and it simply moves across the harmonic potential well. In general, the shape of the wavefunction changes significantly as it moves, as illustrated by published animations and wavepacket snapshots.[16–18]

The quantity that defines the shape of a spectrum is the autocorrelation function $<\phi|\phi(t)>$ of the wavepacket moving on the final state potential energy surface.[19] Its absolute value as a function of time is illustrated in the bottom panel of Figure 2. It corresponds to the overlap of the wavefunction ϕ at time 0 with the wavepacket $\phi(t)$ at longer times and it obviously depends on the shape of the potential energy surface in the region explored by the wavepacket, as illustrated,

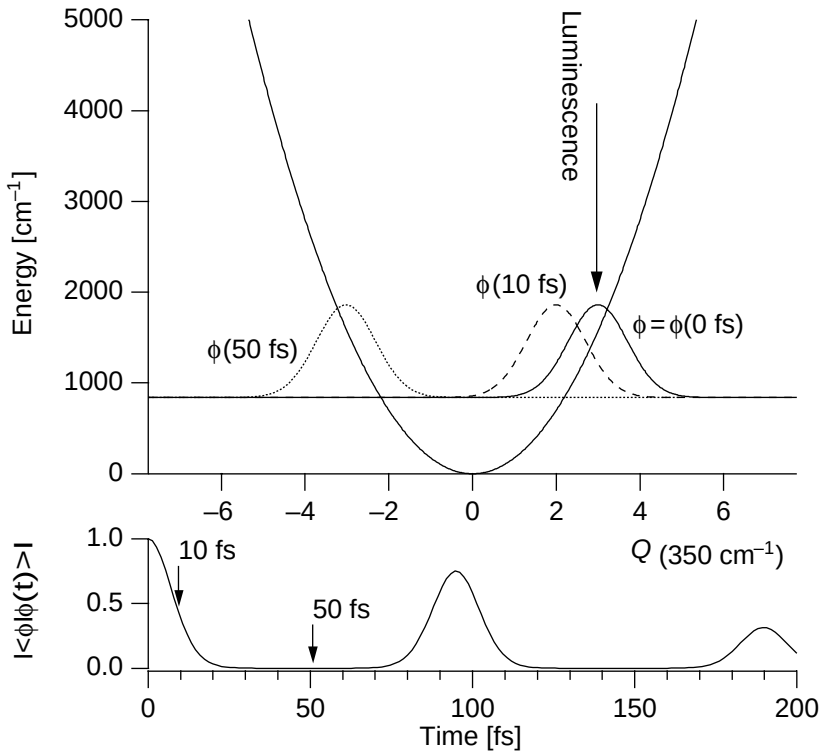

Figure 2 Time-dependent view of the luminescence transition in Figure 1. Only the potential energy curve of the final state is shown. Time-dependent wave functions are given for times of 0, 10, and 50 fs. The bottom panel shows the absolute value of the autocorrelation function, visualized as the overlap between the time-dependent wavefunction $\phi(t)$ and the wavefunction at time zero. The first recurrence at 95 fs occurs after a single vibrational period of the 350 cm^{-1} vibrational frequency used to define the harmonic potential energy curve.

for example, by the initial drop of the autocorrelation from its maximum value over the first few tens of fs. At longer times, the autocorrelation reaches a maximum after each vibrational period, as shown in Figure 2.

The absorption spectrum is given by the Fourier transform of the autocorrelation function as:[2]

$$I_{\mathrm{abs}}(\omega) = C\omega \int_{-\infty}^{\infty} \mathrm{e}^{\mathrm{i}\omega t} \langle \phi | \phi(\mathrm{t}) \rangle \mathrm{e}^{-\left(\Gamma^2 t^2 + (\mathrm{i}E_{00}/\hbar)\mathrm{t}\right)} \mathrm{d}t \tag{1}$$

The luminescence spectrum is given by an equation closely related to Equation (1):[2]

$$I_{\mathrm{lum}}(\omega) = C\omega^3 \int_{-\infty}^{\infty} \mathrm{e}^{\mathrm{i}\omega t} \langle \phi | \phi(\mathrm{t}) \rangle \mathrm{e}^{-\left(\Gamma^2 t^2 + (\mathrm{i}E_{00}/\hbar)\mathrm{t}\right)} \mathrm{d}t \tag{2}$$

In both equations, ω denotes the wave number abscissa of the calculated spectrum, E_{00} is the energy of the electronic origin transition, Γ is a phenomenological damping factor determining the width of each vibronic line in the calculated spectrum, and C is an adjustable scaling factor. The resolution in most condensed-phase experimental spectra is inferior by orders of magnitude than the limit imposed by the Heisenberg uncertainty relation on the width of a spectroscopic transition. Most often, the resolution is determined by inhomogeneous broadening. Its effect can be included in the model in Figure 2 via the damping factor Γ, typically treated as an adjustable parameter to reduce the autocorrelation at long times. The damping factor Γ determines the width of each vibronic band in Figure 1, and it should be chosen small enough not to influence the overall width of a spectrum. It also determines up to which time the autocorrelation function has to be calculated, as illustrated in Figure 3, where $<\phi|\phi(t)>$ values insignificantly different from zero are calculated at times longer than approximately 450 fs.

Figure 3 shows the absolute values of the autocorrelation functions for three different offsets ΔQ, defining three different initial positions for ϕ on the final state potential energy surface in Figure 2. The slope of the potential surface at the initial position determines the decrease of the autocorrelation function from its initial value of 1, and it depends on the offset ΔQ between the minima of the potentials along the normal coordinate in Figures 1 and 2. For an offset ΔQ of zero, the center of the wavepacket ϕ encounters a flat potential surface. No decrease of the absolute value of the autocorrelation is expected with time, as the overlap remains 1 at all times. The slow decrease seen for the solid line in Figure 3 is therefore caused by the damping factor Γ and the calculated spectrum is narrow. For an offset ΔQ of 1, the decrease at short times is faster, due to the nonzero slope of the potential surface at $\mathrm{Q} = \pm 1$, and the calculated spectrum shows a large overall bandwidth. This trend is even more pronounced for the larger offset $\Delta Q = 3$, the

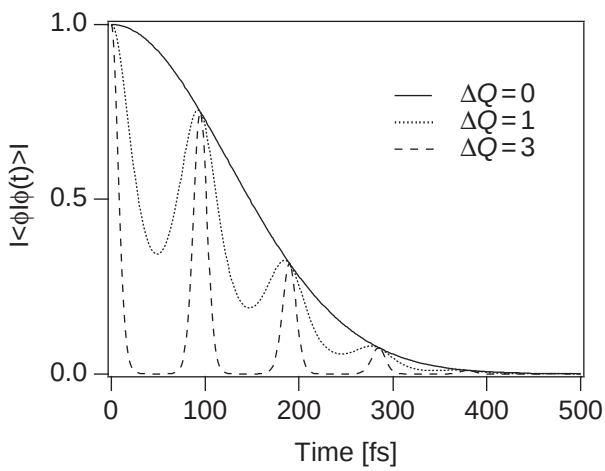

Figure 3 Absolute values of the autocorrelation functions used to calculate the spectra in Figure 4 for different values of ΔQ, given in the Figure. The initial drop of the autocorrelation is related to the slope of the potential energy surface directly below the excited state potential minimum. Recurrences occur at each vibrational period, independent of the value used for ΔQ.

situation for which time-dependent wave functions are shown in Figure 2. Another quantity influencing the initial decrease is the vibrational frequency of the final state potential.[16–18] It is often illustrative to inspect the initial decrease of the autocorrelation in order to analyze spectroscopic effects or to compare spectra of related molecules.

The spectra calculated from the autocorrelation functions in Figure 3 are given in Figure 4. The top panel shows absorption and luminescence spectra for an offset ΔQ of zero, a situation that corresponds to many spin–flip transitions in the spectra of transition metal complexes. Absorption and luminescence spectra are shown in Figure 4a and they consist of a single line with a maximum at E_{00}, the energy of the electronic origin. The spectra for a small offset $\Delta Q = 1$ are shown in Figure 4b. A short vibronic progression with four easily discernible members is observed with an interval corresponding to the ground or excited state vibrational frequencies in luminescence and absorption spectra, respectively. A larger offset $\Delta Q = 3$ leads to a longer vibronic progression consisting of at least twelve members and to the largest overall bandwidth of the three calculated spectra, shown in Figure 4c. A resolved progression in an experimental spectrum can therefore be directly analyzed with this model and leads to a quantitative estimate for ΔQ along the normal coordinate. Such values are important for the characterization of metal–ligand bonding and structural changes in excited states and for excited-state dynamics relevant to transition metal photochemistry.[1,20] Representative examples for ΔQ values determined from fits of calculated spectra to experimental data are given in Table 1. It is interesting to note that similar ΔQ values are observed for many different types of transitions, emphasizing the need for detailed analyses of the spectra of interest. The transformation of ΔQ values in dimensionless units to changes of bond lengths and angles has been published for many compounds[1,21,22] and the use of normal coordinate analysis calculations has also been illustrated in detail.[22–24] The spectroscopic signatures of even slight changes in the parameters describing the potential energy surfaces in Figure 1 are easily calculated and can be compared to variations of the experimental spectra. Recent examples of studies reporting such detailed effects and analyzing them with time-dependent theory include the pressure dependence of resolved vibronic structure in luminescence spectra.[22,25]

A special category of transition that has received significant attention, mainly because of the well resolved bands, is intraconfigurational *d–d* transitions. These involve initial and final states with identical electron configurations, and a ΔQ value of zero is expected, leading to luminescence and absorption spectra as shown in Figure 4a. In experimental spectra, short progressions, similar to those illustrated in Figure 4b, are sometimes observed. In these cases, the offset ΔQ is

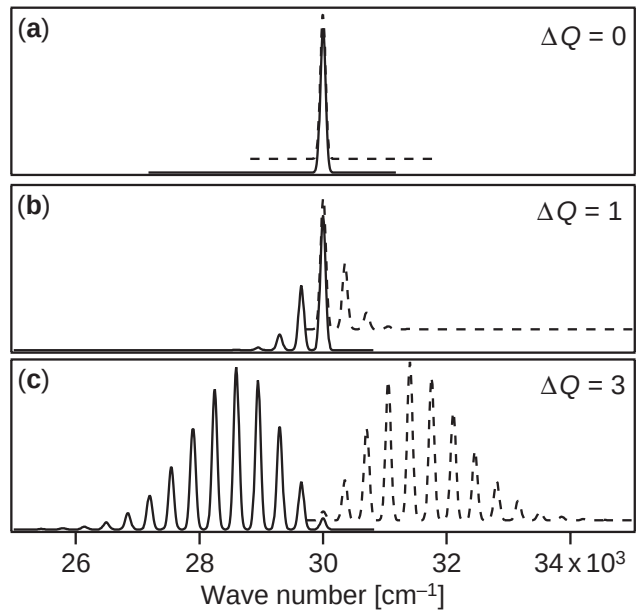

Figure 4 Luminescence and absorption spectra calculated for different offsets ΔQ between potential minima along the normal coordinate in Figure 1 are shown as solid and dotted lines, respectively. The interval between members of the vibronic progression corresponds to the vibrational energy of the final state, chosen as 350 cm^{-1} for the potential curves in Figures 1 and 2. Values of the offset ΔQ are given for each pair of spectra.

different from zero due to spin–orbit coupling to a nearby excited state with a large ΔQ value. This effect is illustrated in Figure 5 for the potential energy curves in the range of the lowest-energy intraconfigurational transition of the $Ni(H_2O)_6^{2+}$ complex, where two states of E_g symmetry interact.[26] The minimum of the harmonic (diabatic) final state of the intraconfigurational transition to the ^1E_g state is at $Q = 0$, directly above the minimum of the ground state potential energy surface. The anharmonic (adiabatic) potential has its minimum offset by an amount ΔQ due to coupling with the $^3T_{1g}$ state, and a short progression is observed in the experimental spectrum. Table 1 summarizes several compounds where nonzero ΔQ values arise from coupling between states, and it is interesting to note that values almost as large as those for charge–transfer

Table 1 Representative ΔQ values (Figures 1 and 5) in dimensionless units determined from absorption or luminescence spectra with time-dependent theory. Only the largest offsets ΔQ are given for transitions where more than four modes are involved.

Type of electronic transition	*Coordination geometry, compound (host lattice for doped solids)*	*Normal coordinate (where indicated in the reference), vibrational frequency* (cm^{-1})	ΔQ (dim.-less units)	*References*
d–d intraconfigurational (spin–flip) transition	**Octahedral**			
	$TiCl_6^{4-}$ ($MgCl_2$)	ν(Ti–Cl),260	0.01[a]	56
	VCl_6^{3-} (Cs_2NaYCl_6)	ν(V–Cl), 291	0.02[a]	56
	CrF_6^{3-} (K_2NaAlF_6)	ν(Cr–F), 568	0.00[a]	56
	CrF_6^{3-}	ν(Cr–F), 415	0.11	32
	MnF_6^{3-}	ν(Mn–F), 595	0.00[a]	56
	$NiCl_6^{4-}$ ($CsMgCl_3$)	ν(Ni–Cl), 255	0.80[a]	26
	trans-$NiCl_2(H_2O)_4$	ν(Ni–OH_2), 364	0.94[a]	26
	$Ni(H_2O)_6^{2+}$	ν(Ni–OH_2), 397	0.88[a]	26
	Tetrahedral			
	MnO_4^{3-} (Li_3PO_4)	ν(Mn–O), 800	0.00	57
	MnO_4^{3-} ($Ba_5(VO_4)_3Cl$)	ν(Mn–O), 754	0.00	57
	Linear			
	NiO_2^{2-}	ν(Ni–O), 590	1.43[a]	56
d–d interconfigurational transition	**Octahedral**			
	$TiCl_6^{4-}$ ($MgCl_2$)	ν(Ti–Cl), 200	3.05[a]	56
	VCl_6^{3-} (Cs_2NaYCl_6)	ν(V–Cl), 215	3.53[a]	56
	CrF_6^{3-} (K_2NaAlF_6)	ν(Cr–F), 510	2.12[a]	56
	CrF_6^{3-}	ν(Cr–F), 415	2.68	32
	MnF_6^{3-}	ν(Mn–F), 490	2.49[a]	56
	$CrCl_6^{3-}$ ($Cs_2NaScCl_6$)	ν_{a1g}(Cr–Cl), 298 ν_{eg}(Cr–Cl), 236	2.37[b] 2.41[b]	22
	$NiCl_6^{4-}$ ($CsMgCl_3$)	ν(Ni–Cl), 255	2.78[a]	26
	trans-$NiCl_2(H_2O)_4$	ν(Ni–OH_2), 364	4.11[a]	26
	$Ni(H_2O)_6^{2+}$	ν(Ni–OH_2), 397	4.11[a]	26
	Tetrahedral			
	MnO_4^{3-} (Li_3PO_4)	ν(Mn–O), 800	1.03[a]	57
	MnO_4^{3-} ($Ba_5(VO_4)_3Cl$)	ν(Mn–O), 754	1.60[a]	57
	Linear			
	NiO_2^{2-}	ν(Ni–O), 500	2.98[a]	56
	Square planar			
	$PtCl_4^{2-}$	ν_{b1g}(Pt–Cl), 304 ν_{a1g}(Pt–Cl), 329	2.25, 2.23 2.58, 2.70	21 58
	$PdBr_4^{2-}$	ν_{b1g}(Pd–Br), 167 ν_{a1g}(Pd–Br), 187	1.73 3.90	59
	$Pd(SCN)_4^{2-}$	ν_{a1g}(Pd–SCN), 280 δ_{b2g}(NCS—Pd–SCN), 179	3.74 1.61	60

Table 1 continued

Type of electronic transition	*Coordination geometry, compound (host lattice for doped solids)*	*Normal coordinate (where indicated in the reference), vibrational frequency* (cm^{-1})	ΔQ (dim.-less units)	*References*
	$Pt(SCN)_4^{2-}$	ν_{a1g}(Pt–SCN), 300	4.86	17
		δ_{b2g}(NCS—Pt–SCN), 151	1.67	
LMCT transition	**Octahedral**			
	trans-OsO_2(oxalate)$_2^{2-}$	ν_{sym}(Os = O), 701	2.10[a]	44
MLCT transition	*trans*-$W(N_2)_2$(1,2-bis (diphenylphosphino) ethane)$_2$	65	0.92	61
		125	1.34	
		ν(W–P), 176	1.09	
		δ(W–N_2), 450	0.97	
		ν(W–N), 524	1.02	
		ν(N–N), 2000	0.35	
MMCT transition	$[(CO)_5Cr^0$-CN-$Os^{III}(NH_3)_5](CF_3SO_3)_2$		2 states	62
		ν(Cr–CN), 396	2.20, 1.00	
		ν(Os–NC), 488	1.30, 2.50	
		ν(C–N), 2100	0.17, 0.27	
LLCT transition	*Square planar*			
	Ni(1,2-maleonitrile) (biacetylbisaniline)	ν(Ni–N), 273	1.33	63
		ν(Ni–S), 330	0.62	
		ν(C–S,C–CN), 520	1.05	
		ν(C–N), 1542	1.05	
	Pd(1,2-maleonitrile) (biacetylbisaniline)	ν(Pd–N), 258	1.32	63
		ν(Pd–S), 360	0.71	
		ν(C–S,C–CN), 520	0.89	
		ν(C–N), 1550	1.82	

[a] Converted from Å units given in the reference to dimensionless units with $\Delta Q = 0.1722Q[Å]\sqrt{\omega m}$ where ω denotes the vibrational frequency in wave number (cm^{-1}) units and m the mass of the ligand in g/mole. [b] Calculated from the Huang–Rhys parameter S given in the reference with $\Delta Q = 2\sqrt{S}$.

transitions have been determined. The time-dependent theoretical calculations allow a quantitative determination of these detailed effects through the comparison of experimental and calculated vibronic intensity distributions. The relative intensities of the transitions to the $^3T_{1g}$ and ^1E_g excited states in Figure 5 can be calculated with the time-dependent approach, but the limitation to the anharmonic (adiabatic) approximation used above to determine ΔQ is no longer valid as wave packet amplitude transfer between potential energy surfaces becomes an important effect.[2,3,26]

Forbidden transitions often gain their main intensity through enabling modes, leading to electric dipole intensity for vibronic origins. In the literature, these vibronic origins and their progressions are usually treated with the same models as true electronic origins and their vibronic patterns. In a strict approach, the coordinate dependence of the transition dipole along the normal coordinate of the enabling mode has to be multiplied to the eigenfunction of the initial state in order to obtain the wavepacket ϕ.[27] This has been shown recently to lead to characteristic spectroscopic signatures that can not be analyzed with the traditional assumption of an allowed transition.[28] The time-dependent approach is easily extended to include such forbidden transitions.

2.43.3 LUMINESCENCE AND ABSORPTION SPECTRA FOR ELECTRONIC TRANSITIONS BETWEEN POTENTIAL ENERGY SURFACES FROM ELECTRONIC STRUCTURE CALCULATIONS AND BETWEEN MULTIDIMENSIONAL POTENTIAL ENERGY SURFACES

In this section, we present two model cases where spectra are calculated from potential energy surfaces obtained from electronic structure calculations. The first example is the $Ni(H_2O)_6^{2+}$

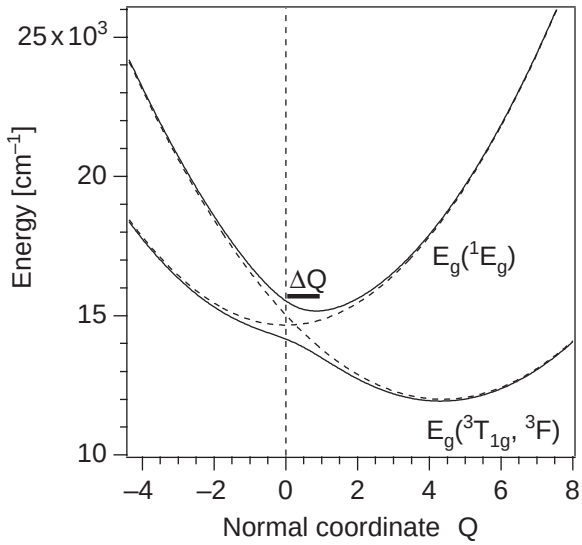

Figure 5 Potential energy curves for the final state of an intraconfigurational absorption transition in proximity to an excited state arising from a different electron configuration. The potential energy curves and labels of electronic states (O_h point group) apply to $Ni(H_2O)_6^{2+}$.[26] The ground state potential energy minimum is at $Q = 0$, given as a vertical dotted line. The offset between the minima of the harmonic (diabatic, dotted line) $E_g(^1E_g)$ state and the ground state is zero. Spin–orbit coupling leads to the anharmonic (adiabatic, solid line) curves and to a nonzero offset ΔQ, given by the horizontal bar. The $E_g(^3T_{1g})$ excited state has a large offset, as given in Table 1.

complex, one of the coordination compounds whose absorption spectrum is shown in many textbooks. *Ab initio* calculations using the CASSCF and CASPT2 methods were carried out for a series of points along the Ni–OH_2 totally symmetric stretching coordinate and a harmonic potential curve along this coordinate was defined for the ground state and for each triplet excited state from the calculated energies.[29] These potential energy curves were then used to calculate the absorption spectrum from Equation (1) without any adjustable parameters. The ΔQ value for the $^3T_{1g}(^3F)$ excited state obtained from this calculation is 3.11, lower by approximately 25% than the value of 4.11 obtained from fitting harmonic model potentials and leading to the best agreement between experiment and calculation shown in Figure 8 of Chapter 2.22, illustrating the difficulty of calculating precise ΔQ values from first principles even for simple coordination compounds. Nevertheless, Figure 6 shows that the overall agreement is remarkably good and that a quantitative link between electronic structure calculations and experimental absorption spectra can be established with the time-dependent approach described here. Calculated spectra of similar good quality can be expected for many other compounds of the first-row transition metals, but detailed effects can not be calculated exactly, as computational methods are most often based on the Born–Oppenheimer approximation and energetically close electronic states can lead to effects where this approximation is no longer valid. Examples for such discrepancies are the middle band in the spectrum of $Ni(H_2O)_6^{2+}$, where the interaction between the two excited E_g states illustrated in Figure 5 leads to the double maximum in the experimental spectrum shown in Figure 6 and to an unusual series of resolved peaks in the low-temperature single-crystal spectrum of the *trans*-$NiCl_2(H_2O)_4$ complex in Figure 7 of Chapter 2.22.[26] The distinct interference dips in the absorption spectra of octahedral chromium(III) complexes, sometimes called Fano antiresonances, are another illustrative example of an intricate spectroscopic effect that can be analyzed in a straightforward way with the time-dependent approach.[3,30–32]

Potential energy surfaces for second- and third-row metals are challenging for modern computational methods, as illustrated by the analysis of the luminescence spectrum of *trans*-$ReO_2(ethylenediamine)_2^+$, a well-studied compound for which the detailed experimental spectra indicate a large ΔQ value along the normal coordinate of the high-frequency symmetric O═Re═O stretching mode.[33,34] The solid line in Figure 7 shows a calculated potential energy curve along this coordinate obtained with an advanced DFT method.[35] It is compared to the harmonic potential curve defined by the ground state Raman frequency of 880 cm^{-1} and shown as a dotted line. The anharmonicity of the solid potential energy curve is obvious, and anharmonic potential surfaces need to be routinely used for the analysis of spectra for compounds of 4*d* and 5*d*

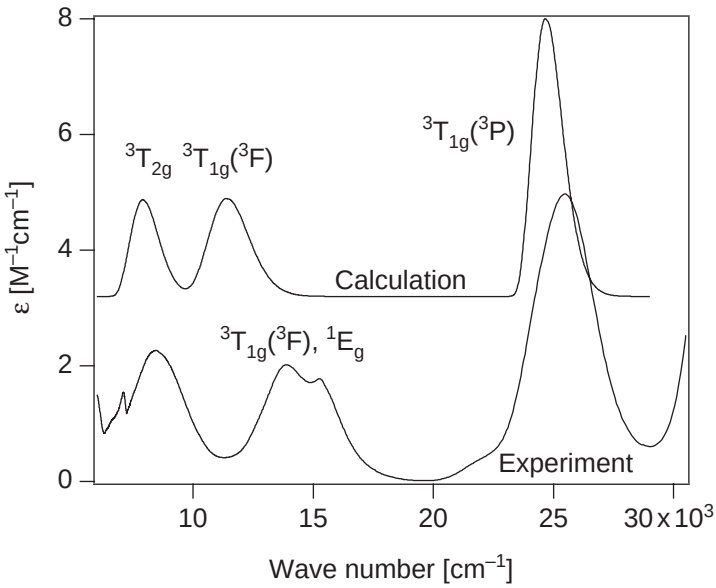

Figure 6 Experimental spectrum of $Ni(H_2O)_6^{2+}$ in aqueous solution, compared to the spectrum calculated from potential energy curves obtained from *ab initio* calculations. The calculated spectrum does not involve adjustable parameters.

metals. The spectra calculated from the potential energy surfaces in Figure 7 are compared to the experimental spectrum in Figure 8. For these calculations, the excited state vibrational frequency was set to 780 cm^{-1}, a value determined from the absorption spectrum, the electronic origin E_{00} was set to 14, 410 cm^{-1}, and a value of 1.90 was determined for ΔQ in order to best reproduce the intensity distribution and bandwidth of the experimental spectrum. The calculated spectrum obtained from the anharmonic potential in Figure 7 is closer to the experimental result than the calculation using the harmonic potential, but a significant discrepancy remains, most likely due to the neglected spin–orbit coupling in the DFT calculation. Other time-dependent studies in this area include high-quality calculations of potential energy surfaces and excited state dynamics involving multiple states, work that has led to detailed insight on the photochemical properties of several first and second row transition metal compounds,[36] including, for example, ruthenium(II) complexes with α-diimine ligands.[37,38]

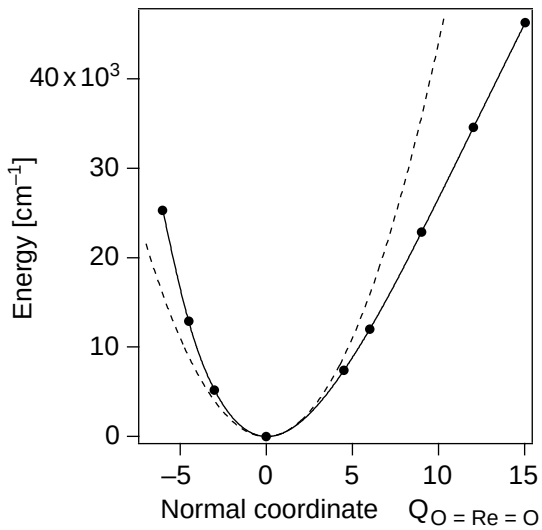

Figure 7 Potential energy curve along the symmetric O═Re═O coordinate of *trans*-ReO_2(ethylenediamine)$_2^+$ from DFT calculations, shown as dots and interpolated solid line. The dotted line shows a harmonic curve calculated from the observed vibrational frequency of 880 cm^{-1}.

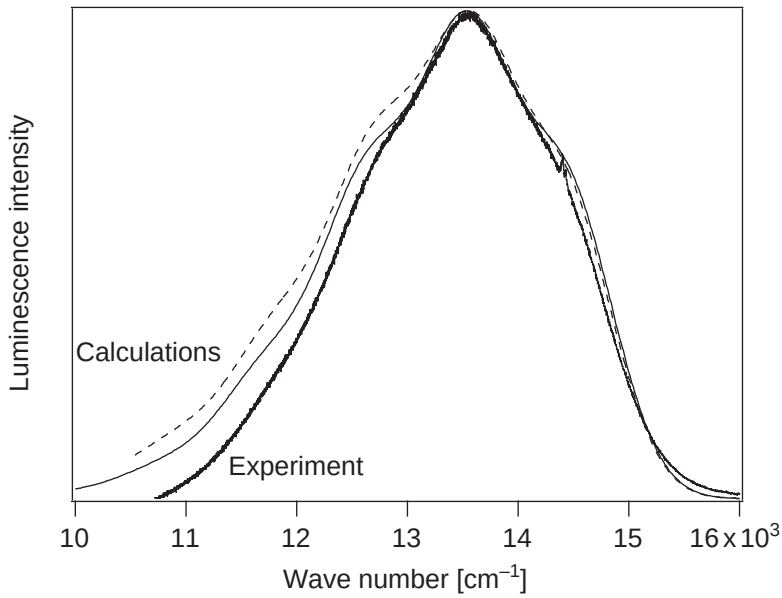

Figure 8 Experimental luminescence spectrum of crystalline *trans*-ReO_2(ethylenediamine)$_2$Cl at room temperature. The calculated spectra were obtained from the one-dimensional potential energy curve calculated by DFT and from the harmonic curve, both shown in Figure 7.

The time-dependent approach is efficient to calculate spectra for transitions between multidimensional potentials.[39] In the absence of coupling between coordinates, autocorrelation functions are calculated separately along each normal coordinate, and the total autocorrelation is obtained as the *product* of the individual autocorrelation functions obtained for coordinates with nonzero values of ΔQ.[1] It is obvious from the solid line in Figure 3 that coordinates along which the wavepacket explores a flat area of the potential curve, such as the example for $\Delta Q = 0$ in Figures 3 and 4, do not change the product and can therefore be neglected. Resolved vibronic structure involving many coordinates has been fully analyzed with this approach.[40] Illustrative examples are compiled in Table 1. Detailed insight has also been obtained from spectra that are not well enough resolved to show each vibronic line, a phenomenon denoted as the missing mode effect (MIME).[39,41,42] These analyses of experimental spectra have allowed the identification of normal coordinates with the largest ΔQ values, modes of relevance for photochemical observations.[20,39] Electronic structure calculations need therefore only be carried out along a few select coordinates, an important shortcut over the calculation of full multidimensional potential surfaces.

If the coordinates are coupled, the total autocorrelation is no longer a product of the autocorrelation along each individual coordinate, and multidimensional wave packets and potential energy surfaces must be used. The storage requirements of wave packets on multidimensional coordinate grids become prohibitive if more than two coordinates are involved, and efficient computational methods have been developed to solve this problem.[43,44] Some of the effects of coupled coordinates are seen from the two-dimensional potential energy surfaces shown in Figure 9. They allow easy visual detection of coupling from cross-sections parallel to the normal coordinates. If these cross-sections show a variation other than a simple shift along the energy axis, coupling is present. Such a variation is obvious from the comparison of cross-sections along the left-hand and right-hand vertical axes in Figure 9b. The top half of the left-hand axis defines a wider curve than the top half of the right-hand vertical axis, a difference that indicates coupled coordinates. Analytical equations for potential energy surfaces have coupling terms that are easily identified, such as the well-known Q_1Q_2 product of two coordinates, which leads to a Duschinsky rotation.[45,46]

An example where spectroscopic manifestations of coupling between coordinates are observed is the low-temperature, single-crystal luminescence spectrum of *trans*-ReO_2(vinylimidazole)$_4^+$ in Figure 10.[34] The overall shape of this spectrum is similar to that of *trans*-ReO_2(ethylenediamine)$_2^+$ in Figure 8, but vibronic peaks corresponding to two different modes are resolved. A spectrum calculated from the two-dimensional harmonic potential energy surface

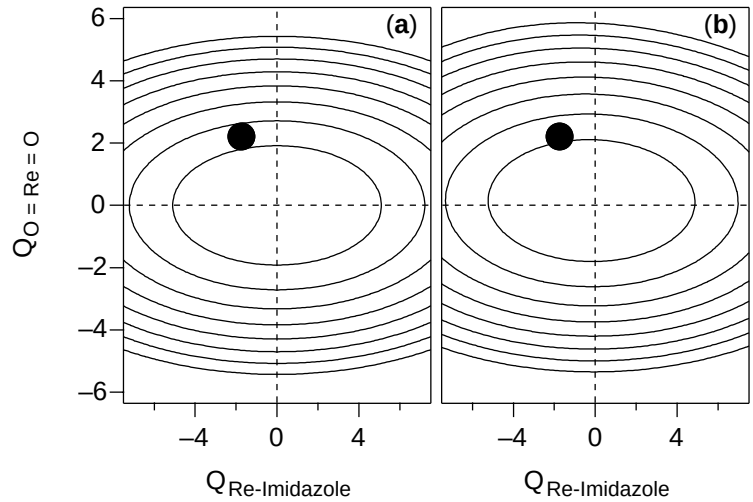

Figure 9 Two-dimensional potential energy surfaces for *trans*-ReO_2(vinylimidazole)$_4$Cl along the O═Re═O coordinate and a low-frequency Re–N(imidazole) mode. Elliptical contours are observed for the harmonic potential (top), the bottom potential includes coupling between normal modes and electronic states and is flattened in the area below the excited state minimum, indicated by the dot.

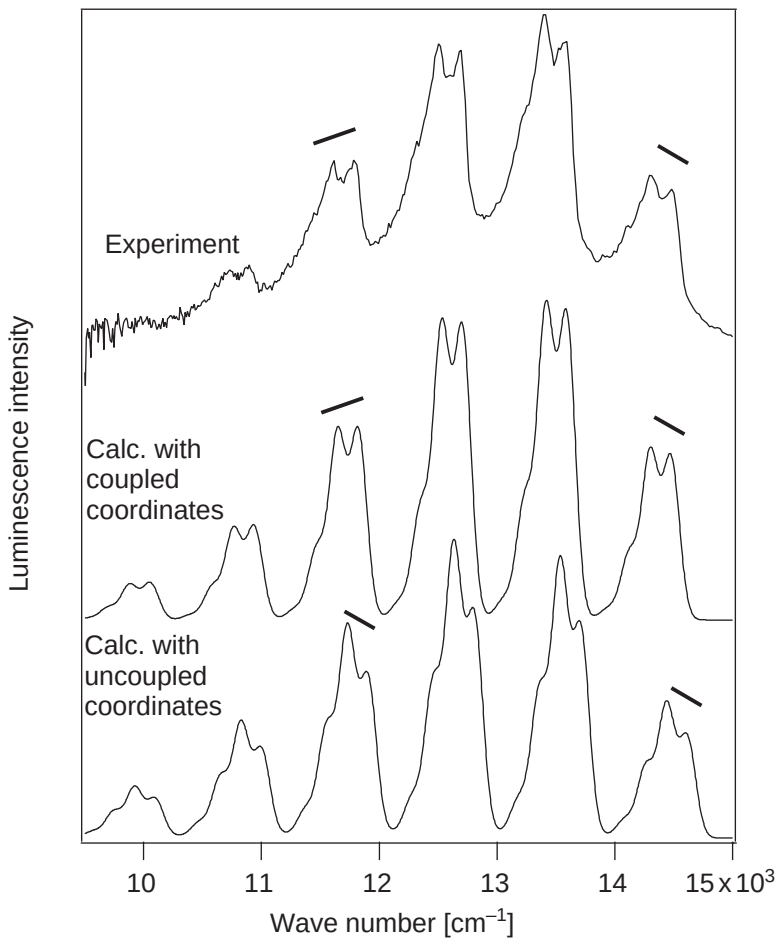

Figure 10 Comparison of the experimental low-temperature, single-crystal luminescence spectrum of *trans*-ReO_2(vinylimidazole)$_4$Cl with calculated spectra using a harmonic potential energy surface for the ground state and a potential energy surface derived including the coupling between the ground state and excited states of identical symmetry, giving rise to coupled coordinates. The potential energy surfaces used to calculate this spectrum are shown in Figure 9.

in Figure 9 leads to a good overall agreement with the experimental spectrum, but it fails to reproduce the vibronic intensity distributions given by the sloped lines. The calculated spectrum arising from the two-dimensional potential energy surface with coupled coordinates in Figure 9b shows that the vibronic intensity distributions emphasized by the sloping lines in Figure 10 are a manifestation of coupled coordinates. The origin of the coupling is the interaction between ground and excited states and only coordinates with nonzero offsets ΔQ can be involved. The comparison of absolute autocorrelation functions in Figure 11 provides a link between the potential energy surfaces in Figure 9 and the calculated spectra in Figure 10. The initial drop in Figure 11a is less rapid for the potential with coupled coordinates in Figure 9b, where the dot indicating the emitting state potential minimum and the position of ϕ is in a slightly flatter area than on the harmonic surface in Figure 9a. This difference in the decrease of the autocorrelation function at short times and the differences at longer times, illustrated in Figure 11b and by the difference trace in Figure 11c, are all contributing to the variation of vibronic intensities given by the sloping lines and allow a detailed characterization of the physical origin of coupling between coordinates.[34] This example illustrates the intuitive understanding of detailed spectroscopic effects that can be gained from the time-dependent approach. Intervalence bands in mixed-valence compounds are a particularly intricate category of transitions involving potential energy surfaces with coupled normal coordinates that have recently been analyzed with time-dependent theory.[47,48]

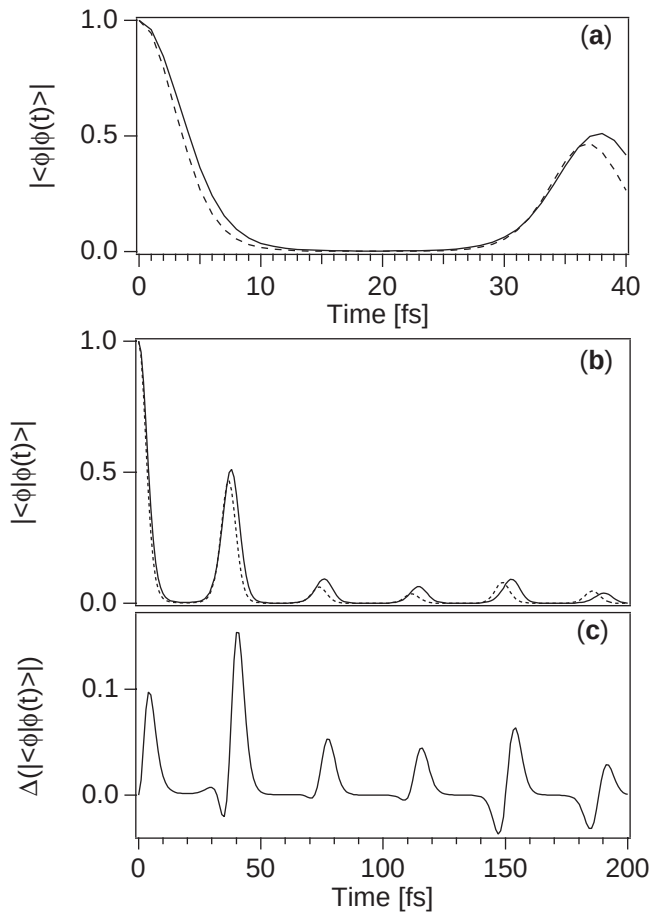

Figure 11 Autocorrelation functions used to calculate the spectra in Figure 10 from the potential energy surfaces in Figure 9. Dotted and solid lines correspond to autocorrelation functions obtained from the potential surfaces in Figures 9a (harmonic potential energy surface) and 9b (potential energy surface with coupled coordinates), respectively. a) short-time comparison over the time interval for the initial decrease of the autocorrelation function; b) comparison over a time interval corresponding to several vibrational periods; c) difference trace between the autocorrelation functions in b.

2.43.4 OTHER ELECTRONIC TRANSITIONS

A very important application of time-dependent theory is the calculation of resonance Raman excitation profiles, based on the same principles outlined for absorption and luminescence transitions in Figures 1 and 2. A number of recent detailed reviews describe the approach and specific applications to transition metal compounds.[1,19,49–54] Resonance Raman spectroscopy allows to obtain precise ΔQ values and other information selectively for all normal coordinates whose Raman bands are resonance enhanced, even if the electronic spectra are not resolved. This situation occurs often in the spectroscopy of metal centers in enzymes, where the time-dependent theory of resonance Raman spectroscopy has been successfully applied.[55]

2.43.5 REFERENCES

1. Zink, J. I.; Shin, K.-S. K. *Adv. Photochem.* **1991**, *16*, 119–214.
2. Reber, C.; Zink, J. I. *Comm. Inorg. Chem.* **1992**, *13*, 177–220.
3. Reber, C.; Zink, J. I. *J. Chem. Phys.* **1992**, *96*, 2681–2690.
4. Zewail, A. H. *J. Phys. Chem. A* **2000**, *104*, 5660–5694.
5. Heller, E. J. *J. Chem. Phys.* **1975**, *62*, 1544–1555.
6. Tannor, D. *Introduction to Quantum Mechanics A Time-Dependent Perspective* 2003, University Science Books: Sausalito, CA.
7. Schatz, G. C.; Ratner, M. A. *Quantum Mechanics in Chemistry* 1993, Prentice Hall: Englewood Cliffs, NJ.
8. Feit, M. D.; Fleck, Jr., J. A.; Steiger, A. *J. Comp. Phys.* **1982**, *47*, 412–433.
9. Kosloff, D.; Kosloff, R. *J. Comp. Phys.* **1983**, *52*, 35–53.
10. Kosloff, R. *J. Phys. Chem.* **1988**, *92*, 2087–2100.
11. Tanner, J. J. *J. Chem. Ed.* **1990**, *67*, 917–921.
12. Bandrauk, A. D.; Shen, H. *Chem. Phys. Lett.* **1991**, *176*, 428–432.
13. Hansen, J. C.; Kouri, D. J.; Hoffman, D. K. *J. Chem. Ed.* **1997**, *74*, 335–342.
14. Nowak, A. M.; Eno, L. *Chem. Educ.* **2000**, *5*, 175–180.
15. Brunold, T.; Güdel, H. U. *Inorganic Electronic Structure and Spectroscopy*; Solomon, E. I., Lever, A. B. P., Eds.; John Wiley: New York, 1999, pp 259–306.
16. Triest, M.; Bussière, G.; Bélisle, H.; Reber, C. *J. Chem. Ed.* **2000**, *77*, 670–670, full article: http://jchemed.chem.wisc.edu/JCEWWW/Articles/index.html.
17. Triest, M.; Masson, S.; Grey, J. K.; Reber, C. *PhysChemComm* **2000**, article *12*, 64–70, available at: http://www.rsc.org/is/journals/current/PhyschemComm/pcccon.htm.
18. Masson, S.; Triest, M.; Reber, C. *Chem. Educator* **2001**, *6*, 147–152, electronic article available at http://link.springer.de/link/service/journals/00897/bibs/0006003/0630147cr.htm.
19. Heller, E. J. *Acc. Chem. Res.* **1981**, *14*, 368–375.
20. Zink, J. I. *Coord. Chem. Rev.* **2001**, *211*, 69–96.
21. Preston, D. M.; Güntner, W.; Lechner, A.; Gliemann, G.; Zink, J. I. *J. Am. Chem. Soc.* **1988**, *110*, 5628–5633.
22. Wenger, O. S.; Valiente, R.; Güdel, H. U. *J. Chem. Phys.* **2001**, *115*, 3819–3826.
23. Brunold, T. C.; Hauser, A.; Güdel, H. U. *J. Lumin.* **1994**, *59*, 321–332.
24. Wootton, J. L.; Zink, J. I.; Diaz Fleming, G.; Campos Vallette, M. *Inorg. Chem.* **1997**, *36*, 789–795.
25. Grey, J. K.; Butler, I. S.; Reber, C. *J. Am. Chem. Soc.* **2002**, *124*, 11699–11708.
26. Bussière, G.; Reber, C. *J. Am. Chem. Soc.* **1998**, *120*, 6306–6315.
27. Tannor, D. J. *J. Phys. Chem.* **1988**, *92*, 3341–3350.
28. Bitner, T. W.; Zink, J. I. *J. Am. Chem. Soc.* **2000**, *122*, 10631–10639.
29. Landry-Hum, J.; Bussière, G.; Daniel, C.; Reber, C. *Inorg. Chem.* **2001**, *40*, 2595–2601.
30. Bussière, G.; Reber, C.; Neuhauser, D.; Walter, D. A.; Zink, J. I. *J. Phys. Chem. A* **2003**, *107*, 1258–1267.
31. Neuhauser, D.; Park, T.-J.; Zink, J. I. *Phys. Rev. Lett.* **2000**, *85*, 5304–5307.
32. Schenker, R.; Triest, M.; Reber, C.; Güdel, H. U. *Inorg. Chem.* **2001**, *40*, 5787–5794.
33. Winkler, J. R.; Gray, H. B. *Inorg. Chem.* **1985**, *24*, 346–355.
34. Savoie, C.; Reber, C. *J. Am. Chem. Soc.* **2000**, *122*, 844–852.
35. Landry-Hum, J.; Tessier, V.; Ernzerhof, M.; Reber, C. *Coord. Chem. Rev.* **2002**, *233–234*, 63–73.
36. Guillaumont, D.; Daniel, C. *J. Am. Chem. Soc.* **1999**, 11733–11743.
37. Turki, M.; Daniel, C. *Coord. Chem. Rev.* **2001**, *216*, 31–43.
38. Turki, M.; Daniel, C.; Zalis, S.; Vlcek, A.; van Slageren, J.; Stufkens, D. J. *J. Am. Chem. Soc.* **2001**, *123*, 11431–11440.
39. Tutt, L.; Zink, J. I. *J. Am. Chem. Soc.* **1986**, *108*, 5830–5836.
40. Hollingsworth, G. J.; Shin, K.-S. K.; Zink, J. I. *Inorg. Chem.* **1990**, *29*, 2501–2506.
41. Tutt, L.; Tannor, D.; Heller, E. J.; Zink, J. I. *Inorg. Chem.* **1982**, *21*, 3858–3859.
42. Tutt, L. W.; Zink, J. I.; Heller, E. J. *Inorg. Chem.* **1987**, *26*, 2158–2160.
43. Anderson, S. M.; Zink, J. I.; Neuhauser, D. *Chem. Phys. Lett.* **1998**, *291*, 387–392.
44. Cromp, B.; Triest, M.; Carrington, Jr., T.; Reber, C. *Spectrochim. Acta A* **1999**, *55*, 575–583.
45. Duschinsky, F. *Acta Physicochim. URSS* **1937**, *7*, 551–566.
46. Wexler, D.; Zink, J. I. *J. Phys. Chem.* **1993**, *97*, 4903–4909.
47. Talaga, D. S.; Zink, J. I. *J. Phys. Chem.* **1996**, *100*, 8712–8721.
48. Talaga, D. S.; Zink, J. I. *J. Phys. Chem. A* **2001**, *105*, 10511–10519.
49. Heller, E. J.; Sundberg, R. L.; Tannor, D. *J. Phys. Chem.* **1982**, *86*, 1822–1839.
50. Shin, K.-S. K.; Zink, J. I. *Inorg. Chem.* **1989**, *28*, 4358–4366.
51. Shin, K.-S. K.; Zink, J. I. *J. Am. Chem. Soc.* **1990**, *112*, 7148–7157.

52. Reber, C.; Zink, J. I. *J. Phys. Chem.* **1992**, *96*, 571–576.
53. Myers, A. B. *Chem. Phys.* **1994**, *180*, 215–230.
54. Myers, A. B. *Acc. Chem. Res.* **1997**, *30*, 519–523.
55. Loppnow, G. R.; Fraga, E. *J. Am. Chem. Soc.* **1997**, *119*, 896–905.
56. Wexler, D.; Zink, J. I.; Reber, C. *J. Phys. Chem.* **1992**, *96*, 8757–8765.
57. Wexler, D.; Zink, J. I. *Inorg. Chem.* **1995**, *34*, 1500–1506.
58. Reber, C.; Zink, J. I. *J. Phys. Chem.* **1991**, *95*, 9151.
59. Pelletier, Y.; Reber, C. *Inorg. Chem.* **1997**, *36*, 721–728.
60. Pelletier, Y.; Reber, C. *Inorg. Chem.* **2000**, *39*, 4535–4541.
61. Larson, L. J.; Zink, J. I. *Inorg. Chem.* **1989**, *28*, 3519–3523.
62. Wootton, J. L.; Zink, J. I. *J. Am. Chem. Soc.* **1997**, *119*, 1895–1900.
63. Wootton, J. L.; Zink, J. I. *J. Phys. Chem.* **1995**, *99*, 7251–7257.

Comprehensive Coordination Chemistry II
ISBN (set): 0-08-0437486

Volume 2, (ISBN 0-08-0443249); pp 559–572

2.44
Electronic Coupling Elements and Electron Transfer Theory

M. D. NEWTON
Brookhaven National Laboratory, Upton, NY, USA

2.44.1 INTRODUCTION 573
2.44.2 KINETIC FRAMEWORK 574
2.44.2.1 Energetics in the Weak Coupling Limit 574
2.44.2.2 Transition State Theory 575
2.44.2.3 Features of the Coupling Element (H_{if}) 576
2.44.2.3.1 Orbital vs. many-electron wave function coupling 576
2.44.2.3.2 Spin dependence 577
2.44.2.3.3 Spin-orbit coupling 577
2.44.3 FORMULATION OF ELECTRONIC STATES AND COUPLING ELEMENTS 577
2.44.3.1 Resonant D and A Sites 577
2.44.3.1.1 Superexchange pathway analysis 577
2.44.3.2 Nonresonant D and A Sites 578
2.44.3.2.1 The Generalized Mulliken Hush model 578
2.44.4 COMPUTATIONAL APPLICATIONS AND COMPARISONS WITH EXPERIMENT 579
2.44.4.1 Role of Metal/Ligand Mixing 579
2.44.4.1.1 Electronically saturated ligands 580
2.44.4.1.2 Metallocene-based electron transfer systems 580
2.44.4.2 Alternative Initial and Final States 581
2.44.4.2.1 Near-degeneracy 581
2.44.4.2.2 High-spin vs. low-spin states 582
2.44.4.3 The Role of Activation Parameters in Determination of H_{if}Values 584
2.44.5 SUMMARY 585
2.44.6 REFERENCES 585

2.44.1 INTRODUCTION

Coordination complexes continue to play a central role in the ongoing field of electron transfer (ET) chemistry, one characterized by rapidly expanding mechanistic understanding,[1] whose implications for the design of novel systems and processes of technological significance (e.g., molecular electronics and sensor devices) are being intensively pursued.[2,3] Numerous recent reviews dealing with electronic and energetic factors of relevance to thermal and optical ET processes have been published, offering an overview of experimental, theoretical, and computational means of probing basic ET mechanisms.[4–11] It is well recognized that these probes working in tandem provide very powerful tools for quantitative elucidation of the different factors controlling ET dynamics and for the formulation of compact predictive models. In the present review we focus on mechanistic issues of particular importance for ET systems based on transition metal complexes (TMC). Because of the complexity of the electronic structure of TMCs, reliable quantum chemical modeling remains a major challenge, but a number of promising computational approaches are now available for treating ET systems,[10–32] and rapid expansion of such capability is proceeding steadily, based on *ab initio* and density functional techniques.[33–36]

Basic models for energetics and kinetics are presented briefly in Section 2.44.2. The formulation of initial and final electronic states and associated electronic coupling elements is given in Section 2.44.3, followed by a number of illustrative computational applications in Section 2.44.4. These applications offer detailed examples of calculated electronic coupling elements, showing the consequences of ligand (L)–metal (M) mixing, structural variation, and alternative choices of initial and final states on the overall efficiency of the ET process, and the extent to which meaningful contact may be established between theory and experiment. Unifying features of thermal and optical ET are emphasized.

2.44.2 KINETIC FRAMEWORK

The basic ingredients of kinetic theory for ET, and the closely related theory for optical ET, have been covered in detail in recent literature.[4–6,37–46] Here we consider applications to ET involving TMCs. The first task in modeling ET is to characterize the initial (ψ_i) and final (ψ_f) electronic states in the process (plus any other intermediate states which may be significant). We assume that initial (ψ_i) and final (ψ_f) states are known, corresponding to a simple two-state approximation (TSA). Procedures for dealing with multiple electronic states (i.e., beyond the TSA, as for example in cases of near-degeneracy) are addressed below.

Unless noted otherwise we use the term "electron transfer" generally to denote both electron (ET) and hole (HT) transfer. The charge-localized initial and final states are denoted generically as DBA and D^+BA^- to reflect the fact that in typical situations it is convenient to represent the donor/acceptor (D/A) interaction as being mediated by an intervening "bridge" (B) or "spacer." For intramolecular ET, e.g., as in binuclear TMCs, the entire DBA assembly is a bonded molecular system. In cases of bimolecular ET between TMCs it may be useful to view the M ions as the local D and A sites, with the L in direct contact serving collectively as the B.[16]

In activated ET a thermal fluctuation brings the system from equilibrium to the transition state (TS), where D and A are "resonant." In the optical ET process, the photon energy allows energy conservation in the vertical process. We present explicit rate constant expressions for the thermal process (k_{ET}), which may occur either in ground or excited state manifolds, provided the initial state ψ_i (either ground or photoexcited) is thermally equilibrated with respect to the nuclear modes of the system.[42] For example, in the case of photoexcited TMCs, ψ_i may be a triplet state originating (via intersystem crossing) from an initially excited singlet. For thermal ET, ψ_i and ψ_f are nonstationary charge-localized states, denoted below as "diabatic."[4,5]

The nuclear modes for each electronic state may be represented classically or quantum mechanically and are generally assumed to be harmonic.[42,47] Solvent modes are generally treated as a low-frequency classical continuum, whereas higher frequency molecular modes of the "solute" (DBA) may be treated quantum mechanically. This review is confined to so-called "outer-sphere ET,"[37–39] in which the formal bonding within the inner spheres is maintained throughout the reaction.

2.44.2.1 Energetics in the Weak Coupling Limit

We adopt as the ET reaction coordinate, η, the vertical free energy difference for ψ_i and ψ_f at an arbitrary configuration of the nuclear coordinates.[4,5,42] The energy quantities needed to formulate k_{ET} in the standard framework of transition state theory (TST) are then given in terms of the free energy profiles shown in Figure 1, drawn for the limiting case of diabatic states,[4,5,40] where $G_i(\eta)$ and $G_f(\eta)$ intersect in a cusp (the consequences of finite coupling between these states are pursued below). The horizontal and vertical shifts of the free energy minima of ψ_i and ψ_f lead, respectively, to the kinetically crucial reorganization free energies (λ_i and λ_f) and reaction driving force ($-\Delta G^o$). For weakly coupled D and A sites (the nonadiabatic limit presented below), the ET process is Franck–Condon controlled and the actual charge transfer can occur only at the crossing point ($\eta^\dagger$) characterized by activation energy, $G^\dagger$.

For a harmonic system (shifted parabolas of fixed curvature), simple Marcus expressions[38] relate the various quantities displayed in Figure 1:

$$\eta_{i,f} = \lambda \pm \Delta G^o \tag{1}$$

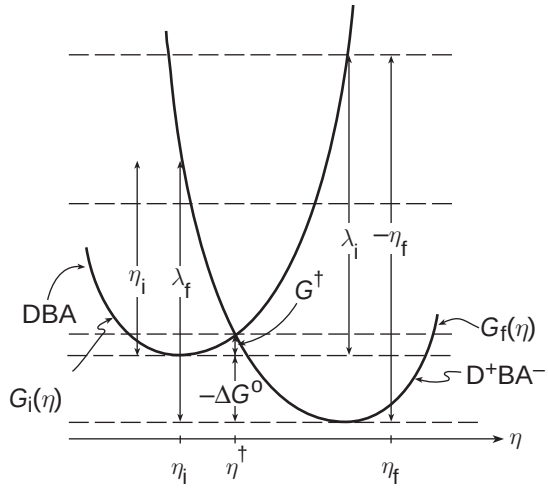

Figure 1 Free energy profiles along the reaction coordinate (η) for the initial and final diabatic states, indicating the reorganization energy (η), activation free energy ($G^\dagger$), and reaction driving force ($-\Delta G^o$).[4,5]

$$G^\dagger = \frac{(\eta_i)^2}{4\lambda} = \frac{(\lambda + \Delta G^o)^2}{4\lambda} \tag{2}$$

where $\lambda = \lambda_i = \lambda_f$ and λ has the form $k_\eta(\eta_i - \eta_f)^2/2$. The total reorganization energy λ may be decomposed into a sum of individual terms of the same form, $\lambda = \Sigma_j \lambda_j$, based on those normal coordinates (q_j) of the harmonic system which undergo a shift in equilibrium coordinate. For the solvent polarization contribution, λ_s, an equivalent expression in terms of dielectric continuum theory was derived by Marcus[48] (see also Vath *et al.*, 1999;[49] Elliott *et al.*, 1998;[50] Derr and Elliott, 1999[51]).

Aside from activation energetics, coupling between ψ_i and ψ_f is required for ET to occur. While the overall coupling may be a complex vibronic phenomenon,[42,47] a quantity of central importance is the electronic coupling matrix element,

$$H_{if} = \int \psi_i \, H_{el} \psi_f \, d\tau \tag{3}$$

(H_{el} is the electronic Hamiltonian). In general, H_{if} varies with nuclear coordinates and may be evaluated at the TS ($\eta^\dagger$). Coordinate dependence is neglected in the Condon approximation.[52]

2.44.2.2 Transition State Theory

The TST thermal rate constant for unimolecular ET may be represented as[37]

$$k_{ET} = \nu_n \, \kappa_{el} \, \kappa_n \tag{4}$$

where the effective fraction of the reactant species in the TS ($\eta^\dagger$) is given by the nuclear factor, κ_n, and the fraction of activated species which successfully pass through the crossing region and on to products per unit time is given by the product of an effective nuclear frequency, ν_n, and the electronic transmission factor, κ_{el}. In bimolecular ET processes the overall second-order rate constant must be constructed in terms of the unimolecular k_{ET} evaluated for the relevant range of inter-reactant coordinates (translational and orientational).

For classical nuclear motion and sufficiently strong electronic coupling (H_{if}), we obtain the adiabatic limit,[37]

$$\kappa_{el} = 1 \tag{4}$$

$$\kappa_n = \exp(-G^\dagger/k_B T) \tag{5}$$

where k_B is the Boltzmann constant. $G^\dagger$ may be expressed as,

$$G^\dagger = H^\dagger - TS^\dagger$$
$$S^\dagger = \frac{-dG^\dagger}{dT} \tag{6}$$

We will neglect the distinction between $H^\dagger$ and the activation *energy* (E_a). In Arrhenius form,

$$k_{ET} = A\exp(-H^\dagger/k_B T) \tag{7}$$

where $A = \nu_n \kappa_{el} \exp(S^\dagger/k_B)$ and $H^\dagger = -k_B d(\ln k_{ET})/d(1/T)$.

The nonadiabatic kinetic regime (denoted by the superscript "na"), pertains when electronic coupling is strongly "rate limiting," and expressions for $\kappa_{el} = \kappa_{el}^{na} \ll 1$ may be obtained on the basis of the Golden Rule.[4,5,37] For classical, harmonic nuclear motion in the general case, the Landau–Zener model yields,[37]

$$\kappa_{el} = 2\left[\frac{1-\exp(-\gamma/2)}{2-\exp(-\gamma/2)}\right] \tag{8}$$

where $\gamma = [(2\pi H_{if}^2/\hbar)/(4\pi k_B T\lambda)^{1/2}]/\nu_n$ (κ_{el} ranges from zero to unity).

In the nonadiatic limit, Equation (8) yields,

$$\kappa_{el}^{na} \cong \gamma \tag{9}$$

We thus have (see Equations (4) and (5)),

$$k_{ET}^{na} = \frac{2\pi H_{if}^2/\hbar}{(4\pi k_B T\lambda)^{1/2}} \exp\left(-G^\dagger/k_B T\right) \tag{10}$$

where the prefactor corresponds to $\nu_n \kappa_{el}^{na}$. An adiabatic process may be understood in terms of dynamics on a single energy surface, whereas nonadiabatic dynamics intrinsically involves more than one energy surface.[4,5,42,47] The "adiabatic states" (denoted ψ_i and ψ_f) manifest an avoided crossing in the TS region.[4,5,53] Adiabatic states at point $\eta^\dagger$ (where the diabatic curves cross) are separated by a gap,[4,5,37,39]

$$\Delta E_{12} = 2|H_{if}| \tag{11}$$

A double-well adiabatic energy profile will occur provided that the coupling magnitude ($|H_{if}|$) is below a threshold determined by λ and ΔG^o (e.g., $2|H_{if}| < \lambda$ when $\Delta G^o = 0$).[39] The double-well situation corresponds to some degree of charge localization (i.e., for the adiabatic states, as well as for the diabatic states, which by construction are charge-localized[52]), and is generally denoted as belonging to the Robin-Day Class II[54] (especially for mixed-valence binuclear TMCs) in contrast to the delocalized, single-well Robin-Day Class III.[54] The cases considered in Section 2.44.4 are all of the Class II type.

2.44.2.3 Features of the Coupling Element (H_{if})

H_{if} may often be decomposed into separate factors. Three examples are discussed here.

2.44.2.3.1 Orbital vs. many-electron wave function coupling

H_{if} is typically found to be closely approximated by an orbital matrix element, H_{DA},

$$H_{if} = S_{if} H_{DA} \sim H_{DA} \tag{12}$$

where the overlap integral S_{if} (an electronic "Franck–Condon factor" reflecting the electronic "core" of the system) is close to unity ($S_{if} \gtrsim 0.9$).[4,5,16,40]

2.44.2.3.2 Spin dependence

When ET occurs between TMCs with paramagnetic "cores," the spatial coupling element may be scaled by a factor, $f(S_c, S)$, depending on the spin quantum number of each core (taken here as S_c for both cores) and the overall spin quantum number (S) of the DBA system (including the spin of the transferring electron, assumed to be "high-spin" coupled to each core spin),[55,56]

$$f(S_c, S) \propto \left[(2S+1)^2/2(2S_c+1)(2S_c+2)\right]^{1/2} \tag{13}$$

Thus an appreciable increase in κ_{el} (and hence degree of adiabaticity) may occur as S increases from its low-spin (ls) to high-spin (hs) limits.

2.44.2.3.3 Spin-orbit coupling

In cases such as $Co(NH_3)^{2+/3+}$ exchange,[15] the spatial matrix element may be appreciably attenuated by a factor reflecting the degree of spin-orbit coupling between the ground and higher energy spin states.

Finally, we note that nuclear quantum effects may be included in terms of vibronic coupling elements, in which the electronic elements (H_{if}) are scaled by nuclear Franck–Condon factors ($S_{FC} \leq 1$), thus increasing the degree of nonadiabatic character.[42,47]

Nuclear coordinates may affect H_{if} magnitudes in a number of other ways (e.g., conformational gating[57,58]). We note that the variation of H_{if} with r_{DA} (effective D/A separation distance) may often be expressed to good approximation as

$$(H_{if})^2 \propto \exp(-\beta r_{DA}) \tag{14}$$

One may also attempt to fit the r_{DA} dependence of the overall rate constant using the exponential form of Equation (14). If $G^{\dagger}$ has its own appreciable r_{DA}-dependence (generally, for $r_{DA} \lesssim 10$ Å), such a fit may yield an effective decay coefficient β departing appreciably from that governing H_{if} (Equation (14); e.g., see Brunschwig *et al.*, 1984;[59] Yonemoto *et al.*, 1994;[60] Jortner *et al.*, 1998;[61] Davis *et al.*, 2002[62]).

2.44.3 FORMULATION OF ELECTRONIC STATES AND COUPLING ELEMENTS

We now require a specification of electronic states and associated properties in a form capable of detailed implementation using the techniques of computational quantum chemistry. It is often convenient to express the desired diabatic quantities in terms of the corresponding adiabatic quantities.

2.44.3.1 Resonant D and A Sites

At the TS for thermal ET we may assume that ψ_1 and ψ_2 are 50:50 mixtures of the resonant charge-localized reactant and product states in the TSA, and H_{if} is given by 1/2 the adiabatic splitting, ΔE_{12} (Equation (11)).[4,5,20,40,63]

2.44.3.1.1 Superexchange pathway analysis

The overall B-mediated D/A coupling implicit in H_{if} may often be usefully analyzed in terms of the superexchange (se) model.[40,64–69] The simplest example of the se model is the perturbative

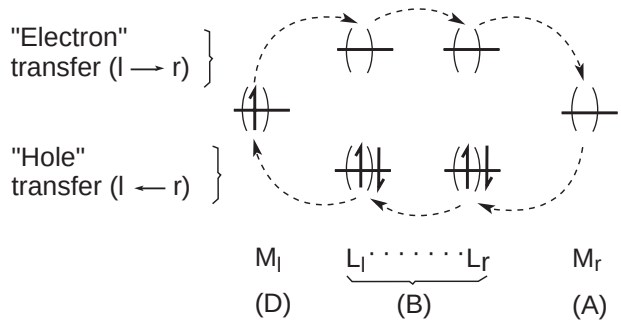

Figure 2 Schematic orbital representation of B-mediated superexchange of the "electron" (top, left to right) and "hole" (bottom, right to left) type, illustrated for the case of intermolecular ET between two ML complexes, where D≡M_l, B≡$L_l \cdots L_r$, and A≡M_r.[4,5] The virtual intermediate states for the hole and electron processes involve, respectively, charge-localization in the filled ("valence") and empty ("conduction") bands of the B.

expression derived by McConnell, which represents H_{if} as a single nearest-neighbor (NN, sometimes denoted as "tight binding") pathway involving n B sites, with one state per site,[64]

$$H_{if} = T_{D1}\left(\prod_{j=1}^{n-1} t_{jj+1}/\Delta_j\right)(T_{nA}/\Delta_n) \tag{15}$$

where T and t denote NN transfer (or "hopping") integrals, and Δ_j denotes the vertical gap separating the energies of the jth B state and the resonant D/A sites. For homologous Bs (T, t, and Δ independent of site), Equation (15) is seen to yield the pure exponential behavior introduced in Equation (14). Competing ET and HT for a model binuclear TMC are displayed schematically in Figure 2 for the case $n = 2$. As the gap separating D/A and B levels is reduced, thermal occupation of charge-localized B sites may become significant.[4,5,61,70] For discussion of the possible influence of solvent on the gaps (and hence also H_{if}) (see Newton, 2001;[4] 2003;[5] Calzado and Sanz, 1998;[22] Reimers and Hush, 1999;[27] Newton and Cave, 1997).[68]

2.44.3.2 Nonresonant D and A Sites

It is desirable to have a means of defining diabatic states (ψ_i and ψ_f) and H_{if} which is free of the constraint of D/A resonance, e.g., in the case of optical ET where one may obtain estimates of H_{if} to be compared with corresponding values inferred from thermal kinetics, and which may be of value in predicting thermal kinetics when thermal H_{if} estimates are not available.[4,5,50,71–75]

2.44.3.2.1 The Generalized Mulliken Hush model

To proceed further we adopt the Generalized Mulliken Hush (GMH) criterion for defining the diabatic states, i.e., those that exhibit the maximum degree of charge localization.[4,5,68,76] According to this criterion, for any given space of electronic states (defined in terms of a set of n adiabatic states), the diabatic states are those which diagonalize the projection of the electronic dipole moment vector operator ($\bar{\mu}$) in the direction of the charge transfer process, and hence maximize the differences among the state dipole moments (projected on the same reference direction). In the traditional Mulliken-Hush (MH) approach[77] it is assumed that a two-state adiabatic space (ψ_1 and ψ_2) is adequate for representing ψ_i and ψ_f (cf. Cave and Newton, 1997;[78] Bixon *et al.*, 1994[79]).

Adopting a two-state space and the above criterion, together with the assumption that ψ_i and ψ_f are orthonormal, and the reference charge transfer direction as that defined by the adiabatic dipole moment shift,

$$\bar{\mu}_{12} \equiv \bar{\mu}_{22} - \bar{\mu}_{11} \tag{16}$$

where $\bar{\mu}_{ij} = \int \psi_i \bar{\mu} \psi_j \, d\tau$ leads to the following GMH result,

$$|H_{if}| = \mu_{12} \Delta E_{12} / \Delta\mu_{if}| \tag{17}$$

where

$$\mu_{if} = \left[(\Delta\mu_{12})^2 + 4 (\mu_{12})^2 \right]^{1/2} \tag{18}$$

Here ΔE_{12} is the vertical adiabatic energy gap introduced in Equation (11) for the special case of resonant D and A sites). The natural definition of the effective D/A separation, r_{DA}, now becomes,[76]

$$r_{DA} \equiv \Delta\mu_{if}/e \tag{19}$$

where e is the magnitude of the electronic charge. In the case of symmetrically delocalized adiabatic states, Equation (17) yields Equation (11).

A great advantage of the GMH model (Equations (17) and (18)) is that it can be applied to an arbitrary nonresonant situation, yielding H_{if} and r_{DA} entirely in terms of spectroscopic (i.e., adiabatic state) information, whether from experiment or from quantum calculations.

2.44.4 COMPUTATIONAL APPLICATIONS AND COMPARISONS WITH EXPERIMENT

We present results of theoretical calculations based mainly on semiempirical (INDO) quantum chemical electronic structure calculations, and in one case (Section 2.44.4.3), on large-scale MD simulations.[17] The "spectroscopic" Hamiltonian (INDO/s) parametrized by Zerner and co-workers for systems including both organic and transition M-based moieties,[80] is very useful for treating electronic properties of TMCs, including evaluation of H_{if}.[4,5,40] Alternatively, the method is not parametrized for calculating features of potential energy surfaces, so that necessary bond lengths and force constants must be obtained from independent sources. Given our particular focus on H_{if}, it is notable that in several cases where comparison has been made, INDO/s results for H_{if} are found typically to be within ~25% of *ab initio* SCF results[81] (see also Newton, 2000[69]).

2.44.4.1 Role of Metal/Ligand Mixing

While ET between TMCs may often be viewed nominally as metal-to-metal charge transfer (MMCT), the actual contact between the TMCs (whether in a bimolecular process or in a binuclear complex) is often established primarily by the Ls.[16,22,40,65,82,83] Hence the effectiveness of the overall MM electronic coupling (manifested in H_{if}) depends crucially on the extent to which the transferring charge is partially delocalized onto the Ls, both in the initial (ψ_i) and final (ψ_f) states at the TS. This will be true whether the Ls are in direct contact (as in encounter complexes in bimolecular ET between TMCs with single coordination shells), or indirectly, as mediated by tethers. The specific examples considered in Sections 2.44.4.1.1 and 2.44.4.1.2 involve bimolecular ET processes.

The influence of ML mixing on H_{if} can be cast in terms of superexchange theory (Section 2.44.3.1.1), as illustrated in Figure 2, where the collective B is represented by a pair of Ls ($n = 2$) in contact. The relative importance of ET and HT transfer is then controlled by the ML hopping integrals (T, in Equation (15)) and, respectively, the energy gaps for metal-to-ligand charge transfer (MLCT) and ligand-to-metal charge transfer (LMCT) (the L–L coupling element t (see Equation (15)) is also needed to "complete the circuit").[16]

For a binuclear TMC system, one may employ a simpler se model based on a single B site ($n = 1$ in Equation (15)), yielding the following superposition of ET and HT pathways, developed specifically for ET involving low-spin Ru^{2+} and Ru^{3+} sites.[4,5,71,74]

$$H_{if} = \frac{T_{ML} T_{M'L}}{2\Delta E_{ML}} + \frac{T_{LM'} T_{LM}}{\Delta E_{LM}} \tag{20}$$

where ML (M′L) and LM (LM′) refer, respectively, to MLCT and LMCT processes, and ΔE_{ML} and ΔE_{LM} are effective MLCT and LMCT energy gaps.[40,71] Equation (20) has been used with reasonable success[71,74] to correlate optical data for MLCT and LMCT (right-hand side) with H_{if} estimates based on optical data for MMCT (left-hand side), also known as the intervalence transition (IT).

A measure of the extent of ML mixing is reflected in GMH effective D/A separation distances (r_{DA}) inferred from experimental optical data (Equations (18) and (19)), as illustrated in Table 1 (see also Brunschwig *et al.* 1998[6]). The r_{DA} values are appreciably less than the nominal values based on molecular structure, and the spectroscopic (adiabatic) value can be significantly smaller than the diabatic value.[4,5]

2.44.4.1.1 Electronically saturated ligands

Water and ammonia are familiar examples of electronically saturated Ls which lack low-lying orbitals and, hence, are expected to serve as electron donors, thus leading to dominance of the HT se pathway (via LMCT) in establishing the magnitude of H_{if}.[40] Electron exchange in some model aquo and ammine $Fe^{2+/3+}$, $Ru^{2+/3+}$, and $Co^{2+/3+}$ complexes with a common linear ML···LM geometry yielded proportionality between H_{if} and the square of the ML covalency parameter, thus underscoring the role of L-mediated overall M–M coupling.[82] Alternatively, H_{if} magnitudes for complexes of a given ML_6 type can depend strongly on the relative orientation of the TMCs in the bimolecular TS, displaying variations of nearly an order of magnitude.[40] For the relatively "intimate" face-to-face (F–F) approach geometry, intermolecular L···M (and perhaps even M···M) as well as L···L contacts may be significant. Complexity of contacts precludes any simple variation of H_{if} with r_{DA} (of the type expected for homologous DBA systems (Equation (14)) if comparisons are made among systems with different orientations.

2.44.4.1.2 Metallocene-based electron transfer systems

In exchange between ferrocene/ferrocenium (Fc/Fc^+) or the cobalt analog (Cc/Cc^+, where Cc denotes cobaltocene), the unsaturated cyclopentadienyl (Cp) L can serve as an electron donor (LMCT), but also an A (via a somewhat higher energy MLCT process).[16,80] Thus the relative importance of ET and HT pathways for H_{if} is not immediately obvious. Group theory and analysis of INDO/s results for H_{if} suggest that ET and HT are, respectively, the dominant se pathways for the ferrocene and cobaltocene exchange. Using quasi-cylindrical symmetry, we find that the transferring charge for Fc and Cc resides in orbitals, respectively, of $\delta\,(3d_{x^2-y^2}$ or $3d_{xy})$ and $\pi\,(3d_{xz}$ or $3d_{yz})$ symmetry (where z is the quasi-cylindrical axis), while the highest occupied and lowest unoccupied orbitals of Cp are, respectively, of π and δ symmetry. Hence the LMCT

Table 1 Effective separation of D/A sites (r_{DA} (Å)).

ET system	*From molecular geometry*[a]	*From two-state analysis of spectral data*[b]	
		Diabatic	*Adiabatic*
$(NH_3)_5\,(Ru^{2+}L)$[c]			
MLCT[d] L = pz	3.5	2.2	1.0
MLCT[d] L = pzH^+	3.5	2.1	<0.1
MLCT[d] L = bpy	5.6	3.4	2.9
MLCT[d] L = $bpyH^+$	5.6	4.3	3.6
$(NH_3)_5\,(Ru^{2+}L\ Ru^{3+})\ NH_3)_5$[c]			
IT[e] L = pz	6.8	1.4	<0.1
IT[e] L = bpy	11.3	5.2	5.1r

[a] Based on separation of M and L midpoint (for MLCT cases) or $r_{MM'}$ (for IT cases), where M and M′ denote Ru atom sites. (Table 2 of Newton, 2001;[4] 2003,[5] reproduced by permission of Wiley-VCH). [b] Based on spectral data analyzed in terms of the two-state GMH model (Equation (17)). In the analysis a value of $f = 1.3$ was used to relate the local to the applied external electric field in the Stark measurements $(\vec{E}_{loc} = f\,\vec{E}_{ext})$. [c] pz ≡ pyrazine.[6,93,94]

Table 2 Calculated and experimental estimates of H_{if} for $(CpFeCp)^{o/+}$ and $(CbCoCp)^{o/+}$[a].

Encounter geometry[b]	Intermolecular contact[c]		Fe(δ)[d]		Co(π)[d]	
	r_{MM}	r_{CC}	Calc	Exp[84]	Calc	Exp[84]
Coaxial (D_{5h})	6.75	3.39	135	35	920	175
T-shaped (C_s)	6.50	3.63	99		70	

[a] Newton *et al.* (1991).[16] [b] Lowest-energy structures.[16] [c] M–M and shortest bimolecular carbon–carbon contact distances (Å).
[d] Symmetry-type of D and A orbitals, based on pseudo-cylindrical symmetry.

pathway (with lower energy gap) does not couple to the transferring electron on Fc, leaving the higher energy ET pathway (via MLCT) as the symmetry-allowed route for H_{if}.[16] Table 2 shows that calculated H_{if} values based on the lowest energy encounter complexes (separated by ≥ 3 kcal mol^{-1} from other structures)[16] bracket experimental values.[84] The results for Cc imply the adiabatic ET regime ($\kappa_{el} \sim 1$), whereas Fc appears to be near the nonadiabatic/adiabatic boundary. Further good agreement between calculation and experiment has been obtained for intramolecular ET between Fc and Fc^+ sites linked by an acetylenic (A) or an ethylenic (E) group in DBA structures denoted, respectively, as $(FcAFc)^+$ and $(FcEFc)^+$.[85–87]

2.44.4.2 Alternative Initial and Final States

Implementation of the TSA becomes ambiguous in cases of near degeneracy (e.g., Newton *et al.*, 1991;[16] Broo and Larsson, 1992;[20] Cacelli and Ferretti, 1998;[28] Elliott *et al.*, 1998;[50] Zerner *et al.*, 1980;[80] Newton, 2003;[85] Shin *et al.*, 1996[88]) (common in open shell TMCs, where, for example, perturbation of idealized octahedral symmetry may lead to splitting of t_{2g} and e_g states) or other situations where the appropriate choice of ψ_i and ψ_f is not obvious.[15,17,89,90] The choice in general involves a tradeoff including thermal access (in the case of initial states), and the state-dependence of activation energy ($G^\dagger$) and coupling (H_{if}).[15,17]

2.44.4.2.1 Near-degeneracy

In cases of near-degeneracy in D or A manifolds, one component state may couple effectively to the B (hopping integral T in Equation (15)), while the other couples weakly due to the nodal structure. An example is provided in Table 3 for the case of Fc and Fc+ linked by unsaturated Bs of the type "APA" and "VPV," where A, E, and P denote, respectively, an acetyenic, an ethylenic, and a *p*-phenylenic moiety.[85] In the isolated ferrocene molecule the $3d_{x^2-y^2}$ and $3d_{xy}$ orbitals (and hole states) are degenerate, but due to different orientation of nodal planes in the tethered DBA systems, $3d_{x^2-y^2}$ (which overlaps with a Cp MO having a finite contribution at the carbon atom linked to the B) lies above the $3d_{xy}$ orbital (which has a node at the linked Cp carbon atom). Thus, the hole ground states ($3d_{x^2-y^2}$) are the ones which yield good overall D/A coupling. Nevertheless, the weakly coupled $3d_{xy}$ hole states are calculated to lie only 0.05–0.06 eV higher and thus are thermally accessible at room temperature.

Michl and co-workers have discussed the potential role of $(C_4R_4)Co(C_5H_5)$ complexes in conductive two-dimensional assemblies, in which the cyclobutadiene rings may be linked via suitable substituents R.[85] Denoting the complex as CbCoCp, where R = H for the present discussion, we note that it may be viewed as basically isoelectronic (as far as the relevant Co and L MOs are concerned) with ferrocene (CpFeCp).[5,85] In Table 4 we compare the calculated low-lying hole states of CbCoCp and CpFeCp.[85] The primary feature of interest is the relative order of the nondegenerate $3d_{x^2-y^2}$ and $3d_{xy}$ hole states in $(CbCoCp)^+$. While the overall symmetry of the CbCoCp structure can be at most C_s, the local C_{4v} symmetry of the CbCo moiety plays an important role, with the antibonding Cb pi MO (b_1) mixing with the Co $3d_{x^2-y^2}$ orbital and pushing it below the $3d_{xy}$ orbital (b_2), whose nodal planes contain the Cb carbon atoms and thus in the local C_{4v} symmetry do not mix with any of the Cb pi MOs. This result has implications for electronic coupling when CbCoCp units are linked, since as discussed above, the $3d_{xy}$ orbitals yield much less favorable coupling than the $3d_{x^2-y^2}$ orbitals.

Table 3 Quasi-degenerate hole states in $(FcAPA\ Fc)^+$ and $(Fc\ EPEFc)^+$.[a]

Fe 3d-hole type[b]		H_{if} (cm^{-1})	*Relative energy* (eV)[c]
$(FcAPAFc)^+$	$3d_{x^2-y^2}$	177	0.000
	$3d_{xy}$	2	0.058
$(FcEPEFc)^+$	$3d_{x^2-y^2}$	140	0.000
	$3d_{xy}$	0.4	0.051

[a] Reproduced by permission of the American Chemical Society from *ACS Symposium Series*, **2003**, 844, 196 (A, P, and E denote, respectively, acetylenic, phenylene, and vinyl moieties). [b] Dominant character of calculated hole state, where z is the Fc axis and the *x*-axis is aligned with the single bonds linking the Fc Cp rings to the B. [c] Based on INDO/s SCF/CI calculations.

Table 4 Comparison of low-lying hole states for ferrocene and $(C_4H_4)Co(C_5H_5)$.[a]

	Hole state[b]	*Relative energy* (eV)[c]
Ferrocene	$3d_{x^2-y^2}$, $3d_{xy}$	0
	$3d_{z^2}$	0.48
$(C_4H_4)Co(C_5H_5)$[b]	$3d_{xy}$	0
	$3d_{z^2}$	0.27
	$3d_{x^2-y^2}$	0.33

[a] Reproduced by permission of the American Chemical Society from *ACS Symposium Series*, **2003**, 844, 196
[b] The 3*d*-type hole states are based on a coordinate system where the *z*-axis is perpendicular to the ring planes and where the *x*-and *y*-axis are parallel to the diagonals of the C4 ring. [c] The ground and low-lying excited states were obtained from separate direct SCF calculations.

Other examples of near-degeneracy effects involve ET in low-spin $Fe^{2+/3+}$ and $Ru^{2+/3+}$ couples complexed to aza aromatic Ls. The case of tris bpy Fe^{2+} and Fe^{3+} sites linked by three polymethylene chains ($(CH_2)_m$) with approximate C_3 symmetry (schematically represented by structure **1**(m) is especially interesting.[50] While the ls t_{2g} states of the Fe^{3+} site are split into ground (^2A) and excited (^2E) states separated by only $\sim 100\,cm^{-1}$, the larger spin orbit coupling constant (estimated at $\sim 440\,cm^{-1}$) requires the use of spin-orbit adapted states in analyzing both the thermal and optical ET processes, in which a single thermally accessible initial state is significantly coupled to two separate final states, estimated to be split by $\sim 3k_BT$ at room temperature.[50] If the spin orbit coupling were absent, only the ground state ET process would have appreciable weight.[50]

2.44.4.2.2 High-spin vs. low-spin states

The mechanism of $Co^{2+/3+}$ $(NH_3)_6$ aqueous exchange requires careful consideration of the roles of hs and ls electronic states.[4,5,15,17,89,90] For Co^{2+} and Co^{3+}, these states correspond, respectively, to the $t_{2g}^5e_g^2$(hs)/$t_{2g}^6e_g$(ls) and $t_{2g}^5e_g$(hs)/t_{2g}^6(ls) electronic configurations. The (zeroth-order) ground states are hs(2+) and ls(3+). In the absence of spin-orbit mixing, the ground state process, while

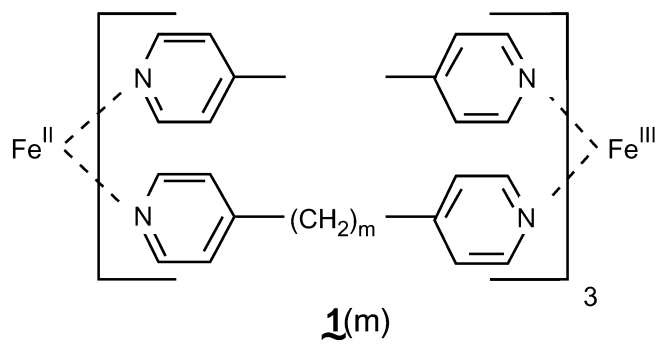

1(m)

formally spin-allowed, would be extremely slow, since it involves a "three-electron" process.[15] Spin-orbit mixing of the excited configurations with their ground state counterparts yields a "one-electron" process (transfer of an electron between e_g orbitals at the two sites), but at the cost of a very small κ_{el} value (estimated to be $\sim 10^{-3}$ for an apex-to-apex encounter complex, and $\sim 10^{-4}$ when orientational averaging is included[15]). Alternatively, a thermally excited purely ls mechanism has the advantage of a reduced reorganization energy and also adiabatic behavior ($\kappa_{el} \sim 1$), which would at least partially offset the energy penalty for thermal hs to ls excitation. In fact, detailed calculations based on both *ab initio* and INDO/s methods, indicate that the net tradeoff unequivocally favors the ground-state (spin-orbit-enhanced) route.[15] The small κ_{el} values cited above correspond to an effective H_{if} in which a large spatial matrix element linking e_g orbitals on the two sites ($\sim 600\,cm^{-1}$ for the apex-to-apex geometry) is scaled by a spin-orbit attenuation factor $\gamma^{so} = 0.014$.[4,5,15]

In comparison with the above picture for $Co^{2+/3+}$ exchange, a contrasting situation is depicted in Figure 3 for reduction of Co^{3+} by a reduced bpy^- L at the Ru^{2+} site in a tethered binuclear complex[14] (see Figure 4), dealt with in more detail in Section 2.44.4.3. Here, the preference for the ls mechanism is dominated by the more favorable κ_{el} for the ls final state (ψ_f). The attenuation factor γ^{so} is expected (on the basis of the approach given in Newton, 1991[15]) to be appreciably larger than the value of 0.014 cited above for $Co^{2+/3+}$ exchange, since the spin-orbit mixing controlling H_{if} in the former case is first-order, in contrast to the second-order mixing in the latter case.[4,5] The activation free energies ($G^{\dagger}$) for the hs and ls processes are estimated to be comparable, due to compensating effects involving inner-shell reorganization energy and driving force

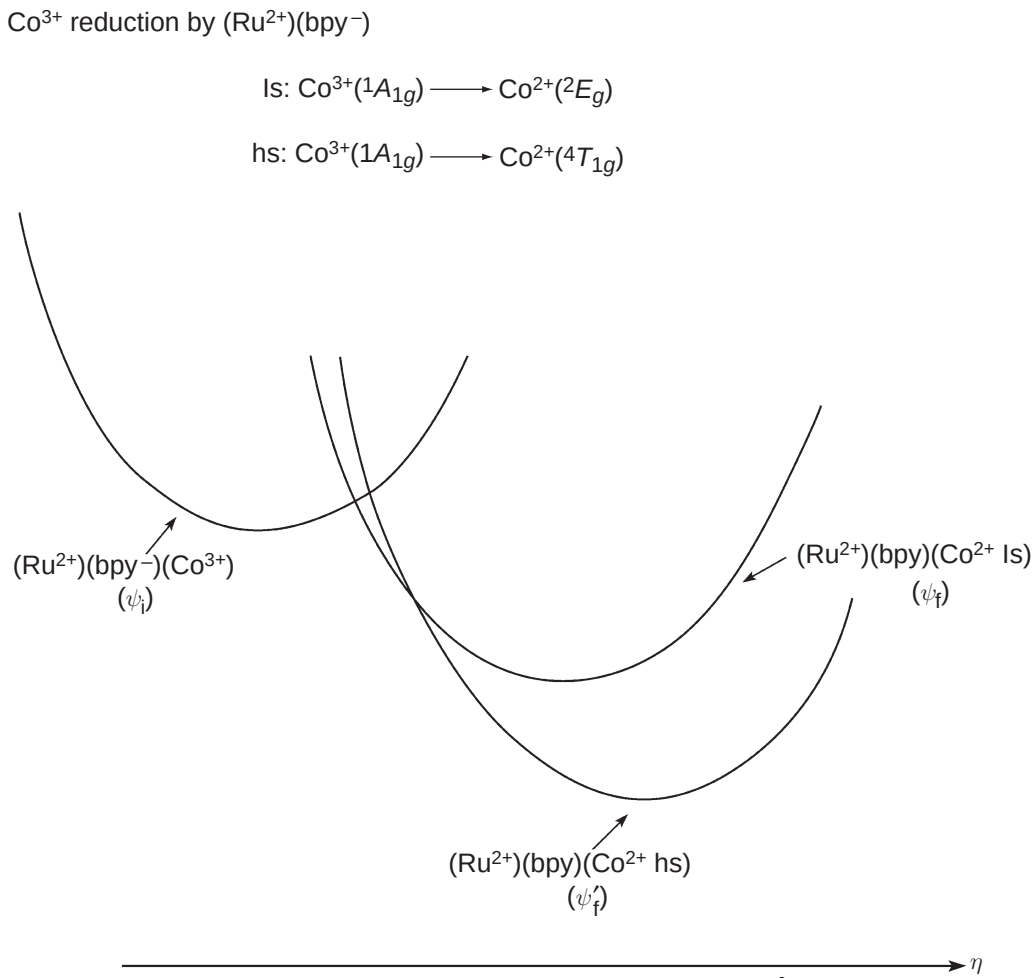

Figure 3 Schematic depiction of energy profiles for reduction of an $(-O^-Co^{3+}(NH_3)_5)$ A site by a tethered $(bpy)_2Ru^{2+}(bpy^-)$ D site[17] (see detailed structure in Figure 4) (figure 7 of Derr and Elliott, 1999,[51] reproduced by permission of Elsevier Science).

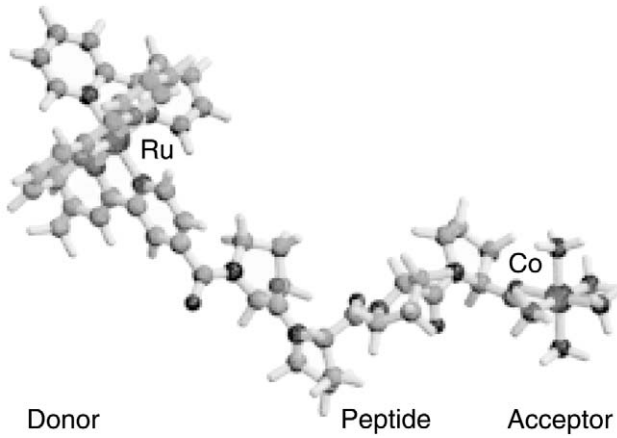

Figure 4 Diagram of the ET system discussed in Section 2.44.4.3. The peptide B contains four proline residues, the D is a derivative of $(bpy)_2Ru^{2+}(bpy^-)$ (with the transferring electron in the initial state largely localized on the bpy L linked to the B), and the A is $-O^-Co^{3+}(NH_3)_5$. (reproduced by permission of the American Chemical Society from *J. Phys. Chem. B* **1999**, 103, 7367).

$(-\Delta G^o)$, each of which is larger for the hs process.[4,5] Thus the hs ground final state (ψ_f') is expected to be formed not directly, but rather via intersystem crossing from the initially formed ls excited state (ψ_f). For related behavior see Yoshimura *et al.* (1997)[89] and Song *et al.* (1993).[90]

2.44.4.3 The Role of Activation Parameters in Determination of H_{if}Values

As a final computational example, we illustrate the importance of understanding activation parameters (both entropic and enthalpic) in comparing calculated H_{if} values with experiment. The DBA system is displayed in Figure 4, consisting of a derivatized $[(bpy)_2Ru^{2+}(bpy^-)]$ D group, a $(pro)_4$ B (where pro≡proline and the tetrapeptide is in a polyproline II helical conformation), and a $[-O^-Co^{3+}(NH_3)_5]$ A group. The nominal redox process corresponds schematically to Equation (21) (see Figure 3),

$$Ru^{2+}(bpy^-)(Co^{3+}) \longrightarrow Ru^{2+}(bpy)(Co^{2+}) \tag{21}$$

where the excess electron localized on the bpy linked (by a carbonyl group) to the $(pro)_4$ B reduces the Co^{3+} site. This system is of interest for detailed theoretical study because it is a member of a homologous series for which a large body of kinetic data exists.[92]

The details of the theoretical computations (based on MD simulation and quantum chemical calculations) are given in Ungar *et al.* (1999).[17] The rate constant (k_{ET}) was expressed in terms of the results of the computer simulations,[17] using a nonadiabatic TST model (Equation (10)). Since the experimental results were analyzed in terms of a phenomenological Arrhenius model,[92] agreement between experiment (left-hand side) and theory (right-hand side) would yield the following two equations. For the weakly temperature-dependent prefactor we have:

$$(k_B T/h)\exp\left(S^{\dagger\prime}/k_B\right) = \left(2\pi H_{if}^2/\hbar\right)(4\pi k_B T\lambda)^{1/2}\exp\left(S^{\dagger}/k_B\right) \tag{22}$$

and for the Boltzmann factor:

$$\exp\left[-\left(H^{\dagger}\right)^{exp}/k_B T\right] = \exp\left[-\left(H^{\dagger}\right)^{calc}/k_B T\right] \tag{23}$$

In Equation (22), $S^{\dagger}$ is the "true" activation entropy (see Equation (6)). By contrast, $S^{\dagger\prime}$ is a "pseudo"-entropy of activation, which includes the contribution from the nonadiabatic prefactor (see Equations (9) and (10)) in addition to the quantity $S^{\dagger}$ defined in Equation (6). Thus in order to infer the value of H_{if} from the experimental data ($S^{\dagger\prime}$), one must know the value of $S^{\dagger}$ (not directly available from the data of Ogawa, 1993[92]).

Table 5 Experimental vs. calculated activation parameters.[a,b]

Experiment[92]	*Calculation*[17]
$S^{\dagger\prime} = 5.5 \pm 0.8$ eu	$S^{\dagger} = 18.3 \pm 5$ eu
$H^{\dagger} = 9.4 \pm 0.2$ kcal mol^{-1}	$H^{\dagger} = 11.2 \pm 1.5$ kcal mol^{-1}
$\lvert H_{if}\rvert = 0.1-2.0$ cm^{-1}	$\lvert H_{if}\rvert = 0.5-5.0$ cm^{-1}

[a] Table 8 of Newton, 2001,[4] reproduced by permission of Wiley-VCH. Results for ET in system displayed in Figure 4. [b] See Equations (22) and (23).

The primary results are summarized in Table 5. The experimental $S^{\dagger\prime}$ value together with the calculated $S^{\dagger}$ value and Equation (22) yields an estimate of H_{if} ($0.1-2.0$ cm^{-1}) close to the calculated range ($0.5-5.0$ cm^{-1}). Given the estimated uncertainties,[17] the experimental and calculated activation energies ($H^{\dagger}$) are seen to be in reasonable accord as well. Note that failure to distinguish between the $S^{\dagger\prime}$ and $S^{\dagger}$ values in Table 5 amounts to an error of a factor of $\sim$20 in the inferred H_{if} magnitude, and also offers an example in which even if ΔS° were available from experiment, it would not be a useful guide to estimating $S^{\dagger}$.[4,5,17]

2.44.5 SUMMARY

This review has focused on the evaluation and analysis of the kinetic quantities primarily responsible for controlling transfer of an electron between TMC complexes, either in bimolecular processes, or in analogous intramolecular processes in which the TMCs are tethered by molecular bridging units. The primary focus is on electronic coupling elements (H_{if}), formulated in a unified framework encompassing thermal and optical ET (i.e., for cases of both resonant and nonresonant D and A sites). The thermal ET treatment spans the nonadiabatic and adiabatic limits within the context of the TST.

Examples of computational applications of the theory are presented for several TMC-based systems, exploiting detailed electronic structure calculations (based for the most part on the all-valence electron INDO/s method) and MD simulations. The TMCs sampled include cases of electronically saturated (aquo and ammine) and unsaturated (cyclopentadiene, cyclobutadiene, and 2,2′-bipyridine) Ls, and the role of ML mixing in determining overall H_{if} magnitudes is discussed in detail (including the perspective gained from superexchange theory) as well as the dependence on intersite geometry (separation distance and relative orientation). In situations where direct comparison is possible, calculated and experimental estimates of H_{if} values are in reasonable accord, and the detailed results of the calculations are shown to be of value in the analysis of the experimental data.

In selecting ψ_1 and ψ_2 for use within the conventional TSA, ambiguities may arise in the case of open shell TMCs, e.g., due to near-degeneracy within M *d*-orbital manifolds or alternative hs and ls states, as discussed for some illustrative examples.

Detailed treatment of ET between Ru and Co coordination complexes tethered by a tetraproline B has led to estimates of entropy as well as enthalpy of activation, a distinction shown to be crucial when it comes to extracting the H_{if} magnitude from the Arrhenius prefactor.[17]

ACKNOWLEDGMENTS

This research was carried out at Brookhaven National Laboratory under contract DE-AC02-98CH10886 with the US Department of Energy and supported by its Division of Chemical Sciences, Office of Basic Energy Sciences.

2.44.6 REFERENCES

1. Balzani, V., Ed., *Electron Transfer in Chemistry*; Wiley-VCH: Weinheim, 2001, Vol. I–V.
2. Jortner, J.; Ratner, M., Eds., *Molecular Electronics*; Blackwell Science: Oxford, 1997.
3. de Silva, A. P., Ed., *Molecular-level Electronics*; Wiley-VCH: Weinheim, 2001, Vol. V, Part 1.

4. Newton, M. D. Electron Transfer: Theoretical Models and Computational Implementation. In *Principles and Theories*; Piotrowiak, P., Ed.; Wiley-VCH: Weinheim, 2001, Vol. I , Part 1, pp 3–63.
5. Newton, M. D. *Coord. Chem. Rev.* **2003**, in press.
6. Brunschwig, B. S.; Creutz, C.; Sutin, N. *Coord. Chem. Rev.* **1998**, *177*, 61.
7. Crutchley, R. J. *Adv. Inorg. Chem.* **1994**, *41*, 273.
8. Gray, H. B.; Winkler, J. R., Eds., *Biological Systems*; Wiley-VCH: Weinheim, 2001, Vol. III, Part 1.
9. Konstanttinos, K. D.; Demadis, D.; Hartshorn, C. M.; Meyer, T. J. *Chem. Rev.* **2001**, *101*, 2655.
10. Endicott, J. F.; Uddin, Md. J. *Coord. Chem. Rev.* **2001**, *219*, 687.
11. Endicott, J. F. Charge-Transfer Excited States of Transition Metal Complexes. In *Principles and Theories*; Piotrowiak, P., Ed.; Wiley-VCH: Weinheim, 2001, Vol. I, Part 1, p 238.
12. Stuchebrukhov, A. A.; Marcus, R. A. *J. Phys. Chem.* **1995**, *99*, 7581.
13. Daizadeh, I.; Medvedev, E. S.; Stuchebrukhov, A. A. *Proc. Natl. Acad. Sci. USA* **1997**, *94*, 3703.
14. Thompson, M. A.; Zerner, M. C. *J. Am. Chem. Soc.* **1991**, *113*, 8210.
15. Newton, M. D. *J. Phys. Chem.* **1991**, *95*, 30.
16. Newton, M. D.; Ohta, K.; Zhong, E. *J. Phys. Chem.* **1991**, *95*, 2317.
17. Ungar, L. W.; Newton, M. D.; Voth, G. A. *J. Phys. Chem. B* **1999**, *103*, 7367.
18. Zeng, J.; Hush, N. S.; Reimers, J. R. *J. Phys. Chem.* **1995**, *99*, 10459.
19. Zeng, J.; Hush, N. S.; Reimers, J. R. *J. Am. Chem. Soc.* **1996**, *118*, 2059.
20. Broo, A.; Larsson, S. *Chem. Phys.* **1992**, *161*, 363.
21. Kurnikov, I. V.; Zusman, L. D.; Kurnikova, M. G.; Farid, R. S.; Beratan, D. N. *J. Am. Chem. Soc.* **1997**, *119*, 5690.
22. Calzado, C. J.; Sanz, J. F. *J. Am. Chem. Soc.* **1998**, *120*, 1051.
23. Zhang, L. Y.; Friesner, R. A.; Murphy, R. B. *J. Chem. Phys.* **1997**, *107*, 450.
24. Hasegawa, J.; Ohkawa, K.; Nakatsuji, H. *J. Phys. Chem. B* **1998**, *102*, 10420.
25. Ohtsuka, Y.; Ohkawa, K.; Nakatsuji, H. *J. Comp. Chem.* **2001**, *22*, 521.
26. Kim, J.; Stuchebrukhov, A. *J. Phys. Chem.* **2000**, *104*, 8606.
27. Reimers, J. R.; Hush, N. S. *J. Phys. Chem.* **1999**, *103*, 3066.
28. Cacelli, I.; Ferretti, A. *J. Chem. Phys.* **1998**, *109*, 8583.
29. Bencini, A.; Ciofini, I.; Daul, C. A.; Ferretti, A. *J. Am. Chem. Soc.* **1999**, *121*, 11418.
30. Cacelli, I.; Ferretti, A. *J. Phys. Chem.* **1999**, *103*, 4438.
31. Pearl, G. M.; Zerner, M. C. *J. Am. Chem. Soc.* **1999**, *121*, 399.
32. Blomberg, M. R. A.; Siegbahn, P. E. M.; Babcock, G. T. *J. Am. Chem. Soc.* **1998**, *120*, 8812.
33. Mainz, D. T.; Klicic, J. J.; Friesner, R. A.; Langlois, J.-M.; Perry, J. K. *J. Comp. Chem.* **1997**, *18*, 1863.
34. Friesner, R. A.; Dunietz, B. D. *Acc. Chem. Res.* **2001**, *34*, 351.
35. Okazaki, I.; Sato, F.; Kashiwagi, H. *J. Molec. Struc.-Theochem.* **1999**, *461–462*, 325.
36. Siegbahn, P. E. M.; Blomberg, M. R. A. *Chem. Rev.* **2000**, *100*, 421.
37. Sutin, N. *Prog. Inorg. Chem.* **1983**, *30*, 441.
38. Marcus, R. A.; Sutin, N. *Biochim. Biophys. Acta* **1985**, *811*, 265.
39. Brunschwig, B. S.; Sutin, N. *Coord. Chem. Rev.* **1999**, *187*, 233.
40. Newton, M. D. *Chem. Rev.* **1991**, *91*, 767.
41. Newton, M. D. *Adv. Chem. Phys.* **1999**, *106*, 303. Erratum: the factor of 1/4 in Equation (3.27a) should be replaced by the factor 4.
42. Jortner, J.; Bixon, M. *Adv. Chem. Phys.* **1999**, *106*, 35.
43. Stuchebrukhov, A. A. *Adv. Chem. Phys.* **2001**, *118*, 1.
44. Skourtis, S. S.; Beratan, D. N. Single- and Multi-electron Transfer Processes. In *Principles and Theories*; Piotrowiak, P., Ed.; Wiley-VCH: Weinheim, 2001, Vol. I, Part 1, pp 109–125.
45. Gould, I. R.; Noukakis, D.; Gomez-Jahn, L.; Young, R. H.; Goodman, J. L.; Farid, S. *Chem. Phys.* **1993**, *176*, 439.
46. Marcus, R. A. *J. Phys. Chem.* **1989**, *93*, 3078.
47. Jortner, J.; Bixon, M. *J. Chem. Phys.* **1988**, *88*, 167.
48. Marcus, R. A. *J. Chem. Phys.* **1956**, *24*, 966.
49. Vath, P.; Zimmt, M. B.; Matyushov, D. V.; Voth, G. A. *J. Phys. Chem. B* **1999**, *103*, 9130.
50. Elliott, C. M.; Derr, D. L.; Matyushov, D. V.; Newton, M. D. *J. Am. Chem. Soc.* **1998**, *120*, 11714.
51. Derr, D. L.; Elliott, C. M. *J. Phys. Chem. A* **1999**, *103*, 7888.
52. Onuchic, J. N.; Beratan, D. N.; Hopfield, J. J. *J. Phys. Chem.* **1986**, *90*, 3707.
53. Newton, M. D.; Sutin, N. *Ann. Rev. Phys. Chem.* **1984**, *35*, 437.
54. Robin, M. B.; Day, P. *Adv. Inorg. Chem. Radiochem.* **1967**, *10*, 247.
55. Cox, P. A. *Chem. Phys. Lett.* **1980**, *69*, 340.
56. Girerd, J.-J. *J. Chem. Phys.* **1983**, *79*, 1766.
57. Hoffman, B. M.; Ratner, M. A. *J. Am. Chem. Soc.* **1987**, *109*, 6237.
58. Brunschwig, B. S.; Sutin, N. *J. Am. Chem. Soc.* **1989**, *111*, 7454.
59. Brunschwig, B. S.; Ehrenson, S.; Sutin, N. *J. Am. Chem. Soc.* **1984**, *106*, 6858.
60. Yonemoto, E. H.; Saupe, G. B.; Schmehl, R. H.; Hubig, S. M.; Riley, R. L.; Iverson, B. L.; Mallouk, T. E. *J. Am. Chem. Soc.* **1994**, *116*, 4786.
61. Jortner, J.; Bixon, M.; Langenbacher, T.; Michel-Beyerle, M. E. *Proc. Natl. Acad. Sci. USA* **1998**, *95*, 12759.
62. Davis, W. B.; Hess, S.; Naydenova, I.; Haselsberger, R.; Ogrodnik, A.; Newton, M. D.; Michel-Beyerle, M.-E. *J. Am. Chem. Soc.* **2002**, *124*, 2422.
63. Braga, M.; Broo, A.; Larsson, S. *Chem. Phys.* **1991**, *156*, 1.
64. McConnell, H. M. *J. Chem. Phys.* **1981**, *74*, 6746.
65. Larsson, S. *J. Am. Chem. Soc.* **1981**, *103*, 4034.
66. Curtiss, L. A.; Naleway, C. A.; Miller, J. R. *Chem. Phys.* **1993**, *176*, 387.
67. Shepard, M. J.; Paddon-Row, M. N.; Jordan, K. D. *Chem. Phys.* **1993**, *176*, 289.
68. Newton, M. D.; Cave, R. J. *Molecular Electronics*; Jortner, J.; Ratner, M. A, Eds.; Blackwell Science: Oxford, 1997, pp 73–118.
69. Newton, M. D. *Int. J. Quant. Chem.* **2000**, *77*, 255.

70. Davis, W. B.; Wasielewski, M. R.; Ratner, M. A.; Mujica, V.; Nitzan, A. *J. Phys. Chem. A* **1997**, *101*, 6158.
71. Creutz, C.; Newton, M. D.; Sutin, N. *J. Photochem. Photobiol. A: Chem.* **1994**, *82*, 47.
72. Salaymeh, F.; Berhane, S.; Yusof, R.; de la Rosa, R.; Fung, E. Y.; Matamoros, R.; Lau, K. W.; Zheng, Q.; Kober, E. M.; Curtis, J. C. *Inorg. Chem.* **1993**, *32*, 3895.
73. Dong, Y.; Hupp, J. T. *Inorg. Chem.* **1992**, *31*, 3170.
74. Evans, C. E. B.; Naklicki, M. L.; Rezvani, A. R.; White, C. A.; Kondratiev, V. V.; Crutchley, R. J. *J. Am. Chem. Soc.* **1998**, *120*, 13096.
75. Nelsen, S. F.; Ismagilov, R. F.; Gentile, K. E.; Powell, D. R. *J. Am. Chem. Soc.* 121 (1999) 7108.
76. Cave, R. J.; Newton, M. D. *Chem. Phys. Lett.* **1996**, *249*, 15.
77. Hush, N. S. *Electrochim. Acta* **1968**, *13*, 1005.
78. Cave, R. J.; Newton, M. D. *J. Chem. Phys.* **1997**, *106*, 9213.
79. Bixon, M.; Jortner, J.; Verhoeven, J. W. *J. Am. Chem. Soc.* **1994**, *116*, 7349.
80. Zerner, M. C.; Loew, G. H.; Kirchner, R. F.; Mueller-Westerhoff, U. T. *J. Am. Chem. Soc.* **1980**, *102*, 589.
81. Newton, M. D. Cluster Models for Condensed-Phase Electron Transfer Processes. In: *Cluster Models for Surface and Bulk Phenomena*; Pacchioni, G.; Bagus, P. S.; Parmigiani, F, Eds.; Plenum Press: New York, 1992, pp 551–563.
82. Newton, M. D. *J. Phys. Chem.* **1988**, *92*, 3049.
83. Richardson, D. E.; Taube, H. *J. Am. Chem. Soc.* **1983**, *105*, 40.
84. McManis, G. E.; Nielson, R. M.; Gochev, A.; Weaver, M. J. *J. Am. Chem. Soc.* **1989**, *111*, 5533.
85. Newton, M. D. *ACS Symposium Series*, 2003, *844*, 196.
86. Plenio, H.; Hermann, J.; Sehring, A. *Chem. Eur. J.* **2000**, *6*, 1820.
87. Ribou, A.-C.; Launay, J.-P.; Sachtleben, M. L.; Li, H.; Spangler, C. W. *Inorg. Chem.* **1996**, *35*, 3735.
88. Shin, Y.-G. K.; Brunschwig, B. S.; Creutz, C.; Newton, M. D.; Sutin, N. *J. Phys. Chem.* **1996**, *100*, 1104.
89. Yoshimura, A.; Nozaki, K.; Ohno, T. *Coord. Chem. Rev.* **1997**, *159*, 375.
90. Song, X.; Lei, Y.; Van Wallendal, S.; Perkovic, M. W.; Jackman, D. C.; Endicott, J. F.; Rillema, D. P. *J. Phys. Chem.* **1993**, *97*, 3225.
91. Harrison, R. M.; Brotin, T.; Noll, B. C.; Michl, J. *Organometallics* **1997**, *16*, 3401.
92. Ogawa, M. Y.; Wishart, J. F.; Young, Z.; Miller, J. R.; Isied, S. S. *J. Phys. Chem.* **1993**, *97*, 11456.
93. Reimers, J. R.; Hush, N. S. *J. Phys. Chem.* **1991**, *95*, 9773.
94. Oh, D. H.; Sano, M.; Boxer, S. G. *J. Am. Chem. Soc.* **1991**, *113*, 6880.

Comprehensive Coordination Chemistry II
ISBN (set): 0-08-0437486

Volume 2, (ISBN 0-08-0443249); pp 573–587

2.45
Metal–Metal Exchange Coupling

R. J. CRUTCHLEY
Carleton University, Ottawa, ON, Canada

2.45.1 INTRODUCTION 589
2.45.2 THEORETICAL APPROACHES TO MAGNETIC EXCHANGE 590
2.45.3 METAL–LIGAND COUPLING ELEMENTS AND EXCHANGE 593
2.45.4 REFERENCES 594

2.45.1 INTRODUCTION

The field of molecular magnetic materials is of great current interest and activity because of the potential application of these materials to problems of magnetic shielding and lightweight magnetic devices.[1–3] To achieve these goals requires an understanding of the metal–metal exchange coupling that occurs between two magnetic centers. The simplest approach is to consider a system composed of two metals ions A and B, each with spin S_A and S_B, respectively. The exchange coupling between metal ions is generally formulated in terms of the spin Hamiltonian,

$$H = JS_A \cdot S_B \tag{1}$$

where the exchange coupling constant J is positive if the spins on the metal ions are parallel and negative if they are paired. In the case of $S_A = S_B = \frac{1}{2}$, antiferromagnetic exchange results in a singlet ground state and an excited triplet state separated in energy by $-J$. Ferromagnetic coupling of the $\frac{1}{2}$ spins results in the formation of a triplet ground state and a singlet excited state with separation energy J. The preference for a singlet or triplet ground state is determined by the relative magnitude of ferromagnetic (J_F) and antiferromagnetic (J_{AF}) terms,

$$J = J_F - J_{AF} \tag{2}$$

where J_{AF} represents the energy released as a result of the coupling of spins, and J_F is the overall spin pairing energy. The value of J can be determined experimentally by temperature-dependent magnetic susceptibility studies or estimated from theoretical models of J_F and J_{AF}. Qualitative predictions of the sign of J can be made based on Goodenough–Kanamori rules.[4,5] These rules were formulated based on the symmetry of the orbitals containing the unpaired electrons and the electron configuration of metal ions in terms of crystal field theory. With respect to the $S_A = S_B = \frac{1}{2}$ case described above, antiferromagnetism is predicted if there is direct contact of the orbitals on adjacent paramagnetic ions or, in the case of a bridging ligand, there is overlap of the delocalized orbitals which contain the unpaired electrons (a weak bonding interaction). The latter is referred to as the superexchange mechanism. Ferromagnetism occurs when the unpaired electrons occupy orthogonal orbitals and exchange coupling (J_F) results in parallel alignment of spins. There have been a number of theoretical models developed to calculate values of J_F and J_{AF}. These are briefly discussed in the following section.

2.45.2 THEORETICAL APPROACHES TO MAGNETIC EXCHANGE

The first model for isotopic exchange was developed by Anderson[6] who used an unrestricted Hartree–Fock(HF) formalism in his treatment of superexchange in insulators. In his derivation, Anderson considered singlet and triplet states

$$\psi_{\pm} = \frac{1}{\sqrt{2}}|\varphi_A(1)\varphi_B(2) \pm \varphi_A(2)\varphi_B(1)| \tag{3}$$

where + holds for the singlet and − for the triplet, and φ_A and φ_B are orthogonal magnetic orbitals. φ_A and φ_B are derived from a linear combination of the two highest singly occupied molecular orbitals (mostly *d*-orbital character for transition metal ions). The energy gap J between triplet and singlet states was then calculated by a perturbation treatment, using the effective Hamiltonian,

$$H = h(1) + h(2) + \frac{1}{r_{12}} \tag{4}$$

yielding

$$J = 2K_{AB} - \frac{2b^2}{U} \tag{5}$$

where the ferromagnetic term $2K_{AB}$ is the potential exchange, representing pairing energy, and b is the transfer integral, representing the energy released when electrons are able to delocalize into molecular orbitals. U is the difference in energy between states in which two unpaired electrons are on separate metal ions and paired electrons are on one metal ion.

Hay, Thibeault, and Hoffmann[7] showed that J_{AF} can be analyzed in terms of pairwise interactions of dimeric molecular orbitals with the square of the splitting in energy between the members of a pair being a measure of the stabilization of the low-spin state. Their final result

$$J = 2K_{AB} - \frac{\Delta\varepsilon^2}{U} \tag{6}$$

where $\Delta\varepsilon$ is the difference in energy between the linear combinations of the two highest singly occupied molecular orbitals, was shown to be equivalent to Anderson's treatment of exchange coupling. Extended Hückel theory was used to evaluate the effect of geometry, electronegativity, and substituents on the splitting energy $\Delta\varepsilon$.

Girerd, Journaux, and Kahn[8] re-examined exchange coupling and their solution for the energy between singlet and triplet states

$$J = 2K_{AB} - \frac{4(b + l)^2}{U} \tag{7}$$

is essentially the Anderson model; however, it included the two-electron ionic integral l for the MMCT event (see below).

It is possible to describe the antiferromagnetic term in Equation (5) in the same conceptual basis as that for Marcus electron-transfer theory[9–11] and the Hush model for intervalence transitions.[12–14] Bertrand considered the case of electron transfer between biological molecules coupled by an exchange interaction.[15] This is represented schematically by two metal sites separated by a bridging medium L (Scheme 1).

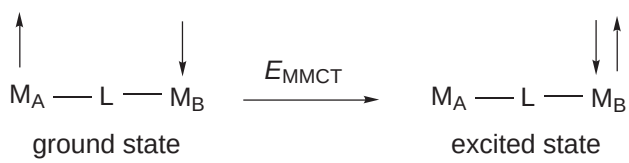

Scheme 1

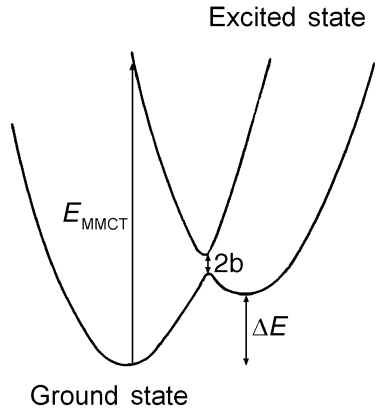

Figure 1 Potential energy diagram of metal-to-metal charge transfer.

In the ground state, the antiparallel alignment of unpaired electrons is the most stable because this arrangement permits a configuration interaction with the metal–metal charge transfer excited state. The potential energy diagram representing this interaction is shown in Figure 1. This is essentially identical to the MMCT case for an asymmetrical mixed-valence complex[16] except that the energy of the excited MMCT state includes a contribution from pairing energy. The singlet ground state is stabilized by antiferromagnetic exchange,[15]

$$J = 2K_{AB} - \frac{2b^2}{E_{MMCT}} \tag{8}$$

Here b represents the resonance exchange integral for electron transfer between the metal centers.

Tuczek and Solomon[17] examined both molecular orbital and valence bond configuration interaction (VBCI) models of magnetic exchange and showed that the VBCI model accounts for both the sign and magnitude of charge transfer state splitting observed in Cu azide systems. In this model, ground state antiferromagnetism is derived from configuration interaction with metal-to-metal and double charge transfer states and has the form

$$-J_{AF} = \frac{c{h_{ML}}^4}{\Delta E^2}\left(\frac{1}{U} + \frac{2}{E_{DCT}}\right) \tag{9}$$

where c is a constant, h_{ML}, the transfer integral (metal–ligand coupling element) corresponds to a one-electron charge transfer between the bridging ligand and the metal (i.e., a LMCT transition), ΔE is the energy difference between the ground state and the LMCT excited state associated with h_{ML}, and E_{DCT} is the difference in energy between the ground and double charge transfer states (Scheme 2).

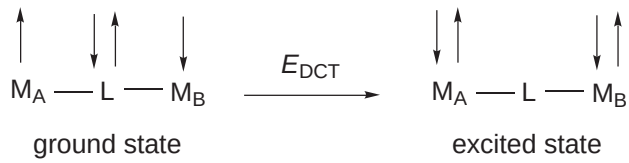

Scheme 2

The singlet double charge transfer state corresponds to the simultaneous transition of one bridging ligand electron to each metal ion. It is not accounted for by Anderson theory and is expected to have a significant contribution to ground state antiferromagetism if the bridging ligand is very polarizable.[18]

Weihe, Güdel, and Toftlund,[19] have extended the above valence bond treatment to three additional cases where a bridging ligand orbital simultaneously interacts with a half-filled orbital localized on metal A and an empty orbital on metal B, a full orbital localized on metal A and a half-filled orbital on metal B and finally a full orbital localized on A and an empty orbital

localized on metal B. All of the treatments demonstrated the need to include higher-order effects in order to properly account for magnetic properties.

Configuration interaction treatments must invoke orthogonal magnetic orbitals and, as a consequence, there is no direct antiferromagnetic contribution to the singlet state. Instead, the stabilization of the singlet state arises through an interaction between the ground state configuration and an excited state configuration. An alternative approach using nonorthogonal magnetic orbitals was suggested by Kahn.

In Kahn's approach,[8,20] magnetic exchange was likened to the formation of a weak bond or, in other words, the overlap of localized singly occupied orbitals. Incorporating nonorthogonal magnetic orbitals in the description of triplet and singlet states (Equation (3)) and applying the effective Hamiltonian (Equation (4)) to solve for the energy gap between these two states yielded

$$J = 2(K_{AB} - kS^2) + 4tS - \frac{4|t + l - (k + K_{AB})S|^2}{k_0 - k} \tag{10}$$

where S is the overlap integral of two magnetic orbitals, k, k_0, and t are two-center Coulomb repulsion, one-center Coulomb repulsion, and resonance exchange integrals, respectively. It is important to recognize that the integrals K_{AB}, k, t, and l do not have the same values according to whether the orthogonalized or nonorthogonalized magnetic orbitals are used as a basis set.[20]

If one assumes that configuration interaction is small, simplification of Equation (10) leads to

$$J = 2(K_{AB} - kS^2) - 2\Delta S \tag{11}$$

where Δ is the energy gap between the two molecular orbitals built from the bonding and antibonding combinations of the magnetic orbital for the triplet state.[21] The term Δ is formally equivalent to $\Delta\varepsilon$ which appears in Equation (6). If asymmetric systems are studied where magnetic orbitals have different energies, singlet–triplet splitting energy has the final form[22]

$$J = 2(K_{AB} - kS^2) - 2S(\Delta^2 - \delta^2) \tag{12}$$

where δ is the difference in energy between the magnetic orbitals.

Quantitative calculations of the magnetic exchange interaction require an accurate description of the electronic structure of the system in both ground and excited states. This is achieved by invoking HF molecular orbital theory and by using extensive configuration interaction (CI) to correlate the magnetic electrons. Calculations at the *ab initio* level are possible for large molecules, if the pseudopotential approach can properly model the effect of core electrons. De Loth *et al.*[23] were the first to perform such calculations on the singlet–triplet state energy gap of dinuclear copper(II) acetate. Their results showed that direct superexchange mechanism only cancels the direct exchange (the terms in Equation (5)). Double spin polarization, and higher order contributions, involving superexchange and polarization of ligand and 3*d*-orbitals, had to be invoked to provide enough stabilization of the singlet state to match with experiment. This work has been followed by a number of similar calculations of J for other dinuclear copper(II) complexes[24–26] and complete active-space multiconfigurational calculations of oxo-bridged systems.[27,28]

A list of second-order contributions and corrections in the *ab initio* calculation of J is available.[20] The spin polarization mechanism of exchange is different from the charge transfer mechanisms discussed so far and is perhaps best illustrated by the exchange between metals ions bridged by the azide ligand (Scheme 3).

The highest occupied molecular orbital of the azide ligand is nonbonding and its molecular orbital can schematically represented as shown in Scheme 3 (the center nitrogen has little contribution to the MO).[21] To minimize repulsion between electrons in this nonbonding orbital, the most probable electron distribution is one in which an electron with α spin is localized at one terminal nitrogen while the β spin electron is localized on the other terminal nitrogen. For the end-on bonding case, the bonding nitrogen electron density (say with α spin) will delocalize towards the *d*-orbitals, with the extent of delocalization depending on the overlap integral and the relative energy differences between azide and metal orbitals. This gives an instantaneous α density in the metal *d*-orbitals, causing each mostly metal unpaired electron to adopt β spin. Thus, a triplet ground state is favored by end-on coordination of the azide bridging ligand. Similar arguments[21] lead to the prediction of a singlet ground state for terminal coordination of the azide.

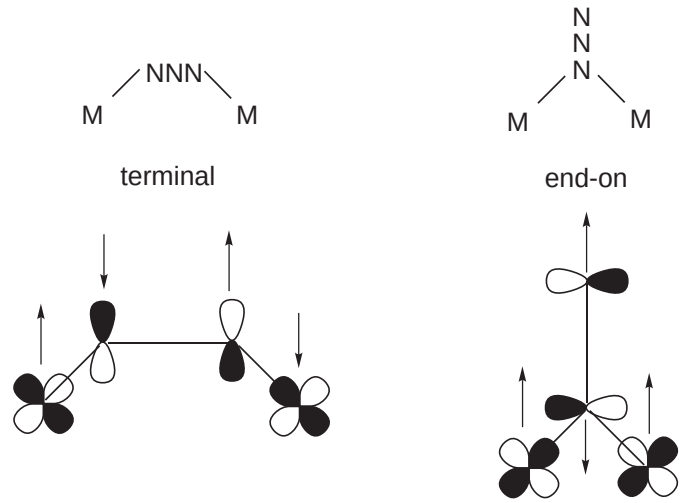

Scheme 3

Noodleman and Norman suggested that the low spin state could be described by a broken spin and space symmetry single-determinate wave function models and would therefore require less computational effort.[29,30] In this regard, Rappé *et al.* compared *ab initio* full CI and HF broken symmetry (HF-BS) calculations and found that HF-BS gave results in close agreement with large-CI calculations.[31–33] More recently, Bencini *et al.* examined broken symmetry (BS/DFT) and single-determinant density (SD/DFT) functional theory of magnetic exchange and found that BS/DFT provided acceptable semi-quantitative results and was therefore a useful tool for the rationalization of magneto-structural correlations.[34] Further theoretical studies of magnetic exchange interactions in copper(II) azido bridged complexes have shown remarkable agreement with experiment.[35]

2.45.3 METAL–LIGAND COUPLING ELEMENTS AND EXCHANGE

The VBCI method (Equation (9)) can lead to calculated values of J_{AF} provided reasonable estimates of the metal–ligand coupling element h_{ML} and charge transfer energies are available. Creutz, Newton, and Sutin (CNS) have shown[36,37] that the value of the metal–ligand coupling element can be determined from experimental charge transfer (CT) band properties by using the expression from Mulliken and Hush,[12–14]

$$h_{ML} = \frac{3.03 \times 10^2}{r}(\nu_{max} f)^{1/2} \tag{13}$$

where ν_{max} is the band maximum in cm^{-1}, f is the oscillator strength of a single metal–ligand chromophore, and r is the transition moment length which is usually taken to be the separation between donor and acceptor in Å. Equation (13) is frequently assumed to be applicable only to very weakly coupled systems, however, CNS have shown that this equation is exact in the two-state model provided overlap can be neglected and the CT transition is polarized along the donor–acceptor axis.

Crutchley *et al.* prepared a series of dinuclear Ru^{III} complexes in which the magnitude of antiferromagnetic exchange and the spectral properties of the ligand-to-metal CT transition were dramatically dependent upon the nature of the bridging ligand and the nature of the outer coordination sphere.[38] Metal–ligand coupling values were calculated by using Equation (13) and these values were placed into Equation (9) to derive calculated values of antiferromagnetic exchange $-J_{AF}$. Good agreement was found between $-J_{AF}$ and experimental values of antiferromagnetic exchange $-J_{est}$ that were derived from room-temperature magnetic moments of the complexes in solution by using

$$-J_{est} = kT \ln\left(\frac{3.0003g^2}{\mu_{eff}^2} - 3\right) \tag{14}$$

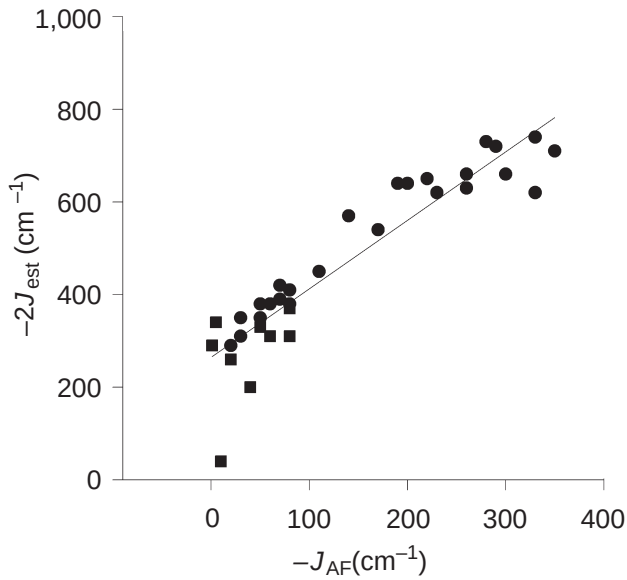

Figure 2 Plot of calculated versus estimated antiferromagnetic exchange constants for the complexes in aprotic solvents (solid circles) and the complexes in aqueous solutions (solid squares). The equation for the line is $J_{est} = 1.5,\ J_{AF} - 260,\ R^2 = 0.86$ (reproduced with permission from ref. 38; © 1998, American Chemical Society).

Thompson and Ramaswamy showed that this expression,[39] when fitted to literature values of $-J$ for a wide selection of antiferromagnetically coupled Cu^{II} dimers, gave a sensible mean g value (2.198 ± 0.008) for Cu^{II} and a mean room-temperature (295.6 ± 4.5 K). The use of this equation for Ru^{III} dimers assumes that orbital angular momentum is largely quenched and the coordination geometry is the same for all the complexes in solution.

Crutchley *et al.*'s plot of the estimated vs. calculated antiferromagnetic exchange constants for the complexes in aprotic (solid circles) and water (solid squares) is shown in Figure 2. The strong correlation between $-J_{est}$ and $-J_{AF}$ in aprotic solvents suggests that both Equations (9) and (13) are realistic models, however, the linear least-squares fit of the data points ($J_{est} = 1.5J_{AF} - 260$) is at odds with Equation (2), which predicts unity slope and positive intercept for constant J_F. This can be partially accounted for by assigning a value of 1.5 to c in Equation (9). The data derived from aqueous solutions shows considerably more scatter but an intercept centered in the origin, suggesting that J_F is very small for these complexes. The difference between aprotic and water data have led these authors to conclude that there are two superexchange mechanisms operative in these complexes.[38]

The study by Crutchley *et al.* demonstrates that a relatively unsophisticated level of theory in conjunction with spectroscopy may be all that is necessary to predict trends in antiferromagnetic exchange derived from frontier orbitals. However, for a quantitative understanding, it is also clear from Section 2.45.2 that *ab initio* CI calculations, involving all the single and double excitations of the valence electrons, are required to get reasonable agreement with experiment.

2.45.4 REFERENCES

1. Novoa, J. J.; Deumal, M. *Struct. Bond.* **2001**, *100*, 33–60.
2. Inoue, K. *Struct. Bond.* **2001**, *100*, 61–91.
3. Leuenberger, M. N.; Loss, D. *Nature* **2001**, *410*, 789–793.
4. Goodenough, J. B. *J. Phys. Chem. Solids* **1958**, *6*, 287–297.
5. Kanamori, J. J. *J. Phys. Chem. Solids* **1959**, *10*, 87–98.
6. Anderson, P. W. *Phys. Rev.* **1959**, *115*, 2–13.
7. Hay, P. J.; Thibeault, J. C.; Hoffmann, R. *J. Am. Chem. Soc.* **1975**, *97*, 4884–4899.
8. Girerd, J. J.; Journaux, Y.; Kahn, O. *Chem. Phys. Lett.* **1981**, *82*, 534–538.
9. Marcus, R. A. *J. Chem. Phys.* **1956**, *24*, 966–978.
10. Marcus, R. A. *J. Chem. Phys.* **1957**, *26*, 867–871.
11. Marcus, R. A. *J. Chem. Phys.* **1957**, *26*, 872–877.
12. Hush, N. S. *Prog. Inorg. Chem.* **1967**, *8*, 391–444.

13. Hush, N. S. *Trans. Faraday Soc*. **1961**, *57*, 557–580.
14. Hush, N. S. *Electrochim. Acta* **1968**, *13*, 1005–1023.
15. Bertrand, P. *Chem. Phys. Lett*. **1985**, *113*, 104–107.
16. Brunschwig, B. S.; Sutin, N. *Coord. Chem. Rev*. **1999**, *187*, 233–254.
17. Tuczcek, F.; Solomon, E. I. *Inorg. Chem*. **1993**, *32*, 2850–2862.
18. Brown, C. A.; Remar, G. J.; Musselman, R. L.; Solomon, E. I. *Inorg. Chem*. **1995**, *34*, 688–717.
19. Weihe, H.; Güdel, H. U.; Toftlund, H. *Inorg. Chem*. **2000**, *39*, 1351–1362.
20. Kahn, O. *Molecular Magnetism*; VCH Publishers: New York, 1993.
21. Kahn, O. In *Magneto–Structural Correlations in Exchange Coupled Systems*; Willet, R. D.; Gatteschi, D.; Kahn, O., Eds.; Reidel: Dordrecht, Holland, 1985, pp 37–56.
22. Morgenstern-Badarau, I.; Rerat, M.; Kahn, O.; Jaud, J.; Galy, J. *Inorg. Chem*. **1982**, *21*, 3050–3059.
23. de Loth, P.; Cassoux, P.; Daudey, J. P.; Malrieu, J. P. *J. Am. Chem. Soc*. **1981**, *103*, 4007–4016.
24. Miralles, J.; Daudey, J. P.; Cabollol, R. *Chem, Phys. Lett*. **1992**, *198*, 555–562.
25. Miralles, J.; Castell, O.; Caballol, R.; Malrieu, J. P. *Chem. Phys*. **1993**, *173*, 33–43.
26. Castell, O.; Miralles, J.; Caballol, R. J. P. *Chem. Phys. Lett*. **1994**, *179*, 337–384.
27. Wang, C.; Fink, K.; Staemmler, V. *Chem. Phys*. **1995**, *201*, 87–84.
28. Fink, K.; Fink, R.; Staemmler, V. *Inorg. Chem* **1994**, *33*, 6219–6229.
29. Noodleman, L.; Norman, J. G. Jr. *J. Chem. Phys*. **1979**, *70*, 4903–4006.
30. Noodleman, L. *J. Chem. Phys*. **1981**, *74*, 5737–5743.
31. Hart, J. R.; Rappé, A. K.; Gorun, S. M.; Upton, T. H. *J. Phys. Chem*. **1992**, *96*, 6255–6263.
32. Hart, J. R.; Rappé, A. K.; Gorun, S. M.; Upton, T. H. *J. Phys. Chem*. **1992**, *96*, 6264–6269.
33. Hart, J. R.; Rappé, A. K.; Gorun, S. M.; Upton, T. H. *Inorg. Chem*. **1992**, *31*, 5254–5743.
34. Bencini, A.; Totti, F.; Daul, C. A.; Dolco, K.; Fantucci, P.; Barone, V. *Inorg. Chem*. **1997**, *36*, 5022–5030.
35. Adamo, C.; Barone, V.; Bencini, A.; Totti, F.; Ciofini, I. *Inorg. Chem*. **1999**, *38*, 1996–2004.
36. Creutz, C.; Newton, M. D.; Sutin, N. *J. Photochem. Photobiol. A: Chem*. **1994**, *82*, 47–59.
37. Cave, R. J.; Newton, M. D. *Chem. Phys. Lett*. **1996**, *249*, 15–19.
38. Naklicki, M. L.; White, C. A.; Plante, L. L.; Evans, C. E. B.; Crutchley, R. J. *Inorg. Chem*. **1998**, *37*, 1880–1885.
39. Thompson, L. K.; Ramaswamy, B. S. *Inorg. Chem*. **1986**, *25*, 2664–2665.

Comprehensive Coordination Chemistry II
ISBN (set): 0-08-0437486

Volume 2, (ISBN 0-08-0443249); pp 589–595

2.46 Solvation

W. LINERT and M. BRIDGE
Institute of Applied Synthetic Chemistry, Vienna, Austria
H. OHTAKI
Ritsumeikan University, Kusatsu, Japan

2.46.1 INTRODUCTION 597
2.46.2 DEVELOPMENT OF SOLUTION CHEMISTRY UNTIL 1957 597
2.46.3 IONIC HYDRATION 598
2.46.4 STRUCTURE OF HYDRATED IONS 598
2.46.5 SECOND HYDRATION SHELL OF IONS 601
2.46.5.1 Li^+ 601
2.46.5.2 Na^+ 602
2.46.5.3 K^+ 602
2.46.5.4 Cs^+ 602
2.46.5.5 NH_4^+ 602
2.46.5.6 Ag^+ 602
2.46.5.7 Mg^{2+} 602
2.46.5.8 Ca^{2+} 602
2.46.5.9 Sr^{2+} 603
2.46.5.10 Mn^{2+} to Zn^{2+} 603
2.46.5.11 Cd^{2+}, Hg^{2+}, and Sn^{2+} 603
2.46.5.12 Al^{3+}, Cr^{3+}, and Fe^{3+} 603
2.46.6 DYNAMIC PROPERTIES OF WATER MOLECULES IN HYDRATION SHELLS OF IONS 603
2.46.7 IONIC HYDRATION UNDER EXTREME CONDITIONS 603
2.46.8 IONIC SOLVATION IN NONAQUEOUS SOLVENTS 605
2.46.9 PREFERENTIAL SOLVATION OF IONS IN MIXED SOLVENTS 606
2.46.10 THEORETICAL CONSIDERATION OF IONIC SOLVATION 609
2.46.11 CONCLUSION 609
2.46.12 REFERENCES 609

2.46.1 INTRODUCTION

A brief review of ionic hydration from the past to the present, from the static to the dynamic points of view, and a summary of the results of ionic solvation in neat and mixed nonaqueous solvents are given.

2.46.2 DEVELOPMENT OF SOLUTION CHEMISTRY UNTIL 1957

Over 100 years have passed since Arrhenius published his *Dissociation Theory of Electrolytes* in 1887.[1] Prior to this it was believed that electrolytes did not dissociate into ions in water until current was passed, and Arrhenius' work was not well received. It was some decades after this that Born's theory of ionic solvation,[2] and then, Debye and Hückel's theory of ionic activities in

solution were published,[3] with Bjerrum's ion-pair formation theory[4] following shortly after. While physical chemists welcomed these theories, there were still many contradictions between the results obtained from theory and those obtained practically. Many of these were resolved when Frank-Wen[5] and Samoilov[6] proposed their theories for "structure-making and structure breaking of ions" and "negative hydration," respectively, at the *Faraday Discussion* in 1957. Then, ionic solvation was discussed by taking into account the structure of solvents, especially the water structure for ionic hydration.

2.46.3 IONIC HYDRATION

Since electrolyte solutions contain at least two ionic components, i.e., cations and anions, and thermodynamic properties of both ions are not separately measured by experiments, some assumptions have to be introduced when separating measured properties into cationic and anionic ones. Thus, hydration numbers of individual ions are not determinable without assumption.

Table 1 summarizes the different methods employed for the determination of ionic solvation numbers and what they measure. While each method has distinct advantages over others, it is often useful to use more than one method, e.g., the Jahn–Teller distorted structure of the hexa-hydrated copper(II) ion in water was revealed by XRD,[7] but by neutron diffraction (ND) the elongated Cu—OH_2 bonds at the axial position were not clearly visible.[8]

2.46.4 STRUCTURE OF HYDRATED IONS

The hydration structure of most single atomic cations and anions in water has been determined by MD, ND, and EXAFS methods. However, orientation of water molecules in the solvation shells is not so well elucidated. Although ND can determine the distances between the central ion and hydrogen atoms and between the ion and the oxygen atom of a solvated water molecule, from which the tilt angle of the water molecule can be estimated, discrepancies between the experi-

Table 1 Methods employed for studies on ionic hydration.

Method	*Region*
Diffraction (X-ray, neutron)	Mainly the 1^{st} shell; when the isomorphous substitution method is applied, the 2^{nd} shell can be studied
X-ray absorption (EXAFS, XANES)	1^{st} shell
Electron diffraction	1^{st} shell of ions in quickly frozen solution (solid)
Computer simulations (molecular dynamics, Monte Carlo)	1^{st} and 2^{nd} shells
Spectroscopy	
Visible, UV, IR	1^{st} shell
Raman	1^{st} shell
NMR (chemical shift, line broadening)	1^{st} shell
Mössbauer	1^{st} shell
Thermodynamics	
Enthalpy and entropy of hydration	Not clear
Compressibility	Mainly the is' shell
Activity	Mainly the lit shell, but not clear
Vapor pressure, boiling and melting points	Mainly the is' shell, but not clear
Density	Not clear
Solubility, salting out	Mainly the is' shell, but not clear
Mobilities	
Transport number	Not clear
Mobility, diffusion coefficient	Not clear
Reaction kinetics	
Isotope dilution	1^{st} shell
NMR	1^{st} shell

mental results from ND and those from MD simulations have been found in some cases, due probably to a large scattering of experimental data in ND measurements.

Rates of exchange of hydrated water molecules in solution previously were examined by the relaxation methods developed by Eigen and colleagues.[9] The development of the NMR method for measurement of the dynamic properties of solvated ions has largely replaced these in recent years and has accelerated the accumulation of experimental results. The data generated has been summarized in many books,[10–19] and reviews.[20,21]

Table 2 summarizes selected results among various experimental results reported.[21] Generally, results from NMR agree with those obtained from diffraction methods. However, if we define the hydration number to be the number of water molecules in the nearest neighbor of an ion, the results obtained by the diffraction methods are more reliable than those by NMR, because NMR cannot measure the number of water molecules moving fast within less than ca. 10^{-9} s well. Alternatively, the hydration numbers found by XRD, ND, and EXAFS methods for alkali and alkali earth metal ions do not always agree with the results derived by Frank-Wen's and Samilov's considerations, because the hydrated water molecules determined by diffraction methods do not always imply water molecules strongly combined with the central ions.

Table 2 Selected values of hydration numbers and bond angles of ion–water interactions in the first hydration shell of cations and anions determined by NMR, X-ray, neutron diffraction, and EXAFS (for details see Ohtaki and Radnai, 1993[21] and references therein).

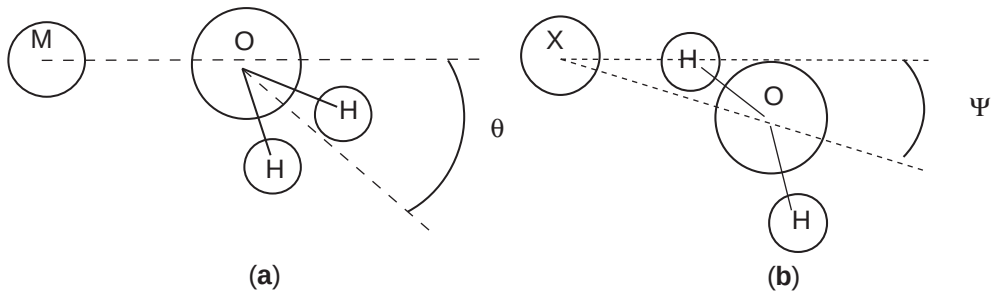

Orientation of water molecule: a: M = cation, b: × = anion bond length number *n*, NMR X-ray, neutron diffraction, EXAFS.

Ion	*Hydration number, n*	*Nucleus*	*T* (°C)	*Method*	*Hydration number, n*	*Bond length* (r_{M-O}, r_{M-O})(pm)	*Bond angle* (θ, ψ)(°)	*Method*[a]
H^+	2.5	^1H			3	244		X
					1	290		
					4	288	$\theta = 0$	N
					3.3	195	$\theta = 52$	N
Li^+	3.0	^1H	broad T	Tcs	5.5	195	$\theta = 40$	N
Na^+	3.5	^1H	broad T	Tcs	6	244–248		X
K^+	3.0	^1H	broad T	Tcs	6	280		X
Rb^+	3.5	^1H	broad T	Tcs				
Cs^+	3.0				8	295	$\theta = 54.75$	N
NH_4^+					4	280–288		X
						304		X
Ag^+					4	243		X
Be^{2+}	4	^1H	−20–100	pa	4	167		X
Mg^{2+}	6	^1H	−67–90	pa	6	212		X
Ca^{2+}	6.0	^1H	broad T		6	244		X
					5.5	240	$\theta = 51$	N
					8	246		E,X
Sr^{2+}	5.0	^1H	20–100	pa	8	264		X
Ba^{2+}	5.7	^1H	−20–100	pa	9.5	290		X
Cr^{2+}					4[b]	208		E
Mn^{2+}					6	220		X
Fe^{2+}	5.6, 5.8	^1H	−40–80	cs	6	213	$\theta = 32$	N
Co^{2+}	5.9	^1H	−38–63.7	pa	6	208		X

Table 2 continued

Ion	*Hydration number, n*	*Nucleus*	*T* (°C)	*Method*	*Hydration number, n*	*Bond length* (r_{M-O}, r_{M-O})(pm)	*Bond angle* (θ, ψ)(°)	*Method*[a]
Ni^{2+}	6	^{17}O	<127	cs	6	204		X
					5.8	205	$\theta = 30$	N
Cu^{2+}					4	194		X
					2	238		
Zn^{2+}	5.9–6.4	^{1}H	120	cs	6	204		X
Cd^{2+}	4.6	^{1}H	−20–100	pa	6	231		X
Hg^{2+}	4.9	^{1}H	−20–100	pa	6	241		X
Sn^{2+}					3.6	234		X
Pb^{2+}	5.7	^{1}H	−20–100	pa				
Al^{3+}	6.0	^{1}H	−35–52	pa	6	187		X
Sc^{3+}	5.1	^{1}H		pa	6	187		X
Cr^{3+}	6.0	$^{17}0$	20	pa	6	199.7		X
					6	197		X
					5	195	$\theta = 36$	N
Fe^{3+}					6	201	$\theta = 41$	N
Ga^{3+}	5.89	$^{17}0$	35	pa	6	196		X
Y^{3+}					8	236		X
Rh^{3+}					6	206		X
In^{3+}	5.8–6.0	^{1}H	−89–99	pa	6	215		X
Ti^{3+}					5	223.6		X
Bi^{3+}					8	241		X
La^{3+}	6.0 6.4	^{1}H	−105–120	cs	9.1	258		X
					6	252		X
					3	264		
Ce^{3+}	4.5–5.5	^{1}H	–110	cs				
Pr^{3+}					9.2	254		X
Nd^{3+}					8.9	251		X
Sm^{3+}					8.8	247		X
Eu^{3+}					8.3	245		X
Gd^{3+}	8 or 9	^{1}H			8.0	237		X
Tb^{3+}					8.0	240		X
Dy^{3+}					7.9	239		N
Er^{3+}					8.0	236		X
Tm^{3+}					8	233	$\theta = 12$	N
Yb^{3+}					8	233	$\theta = 12$	N
Lu^{3+}					8.0	234		X
Sn^{4+}	6.0	^{1}H		pa	8.0	234		X
Th^{4+}	9.1	^{1}H		pa	7.9–8.1	248.6		X
					10	245		X
U^{4+}					7.9	250		X
					10	242		X
F^{-}					6	269		X
Cl^{-}					5.3–6.2	222–226	$\psi =$ 0–6	N
Br^{-}					8	320		X
I^{-}					8.3	358		X
NO_3^{-}					7.2	340[c]		X
$C1O^{-}$					8	380[c]		X
SO_4^{2-}					8.2	379		X

[a] Broad *T*: values obtained from temperature *T* and concentration *c* dependencies of chemical shifts over a broad range of *T* and *c*; cs: determined from chemical shifts; pa: determined from peak area; X: X-ray diffraction; N: neutron diffraction; E: EXAFS; [b] Cr^{2+}—OH_2 bonds elongated along the axis were not observed; [c] X—OH_2 distance beyond the O atom directly combined with X.

According to the results by ND, water molecules around an ion are not directed towards the dipole of the water molecule but tilt by θ. An explanation of the tilt angle in terms of the sp^3 structure of a water molecule is no longer acceptable, as it does not appear as if water molecules have the sp^3 electronic configuration such as the ST2 type[22] but rather have two positive charges at the hydrogen atoms and one negative charge at a point very close to the central oxygen atom. No electronic orbitals expanded in the opposite area from the hydrogen atoms beyond the oxygen

atom are observed by molecular orbital calculations.[23] The three-point model for the water molecule has been widely accepted following the success by Matsuoka, Clementi, and Yoshimine[24] with various modifications for the electronic charge distribution and bond lengths.

The tilt of water molecules in the hydration shell is interpreted in terms of hydrogen bonding of the water molecule with water molecules on the second hydration shell. A nonzero tilt angle allows the formation of three hydrogen bonds, while zero angles can only allow two hydrogen bonds, and thus, the former can form a more stable hydration sphere than the latter.

2.46.5 SECOND HYDRATION SHELL OF IONS

Information on the second hydration shell of ions is much poorer than that of the first hydration shell (see Table 3). The quantitative analysis of radical distribution curves in the long r range is difficult and much less reliable. Reliable information in the structure of the second shell may be obtained by the isomorphous substitution method in XRD measurements and the isotopic substitution method in ND measurements. Of course, such methods cannot be applied to every electrolyte solution. In most works in which some attempts have been made to determine the structure of the second hydration shell of ions, suitable structural models have been introduced. In some other cases fitting procedures between experimental and theoretical $G(r)$ functions have been continued until a more or less satisfactory agreement is obtained between them. Details about the distance between a central ion and water molecules in the second hydration shell, $n_{MO(2)}$, the rmsd, $l_{MO(2)}$, the number of water molecules in the second hydration shell of the ion, $n_{MO(2)}$, and $l_{O(1)-O(2)}$ and $l_{O(1)-O(2)}$ values between water molecules in the first and second hydration shells are given in Ohtaki and Radnai (1993).[21]

2.46.5.1 Li^+

The $r_{MO(2)}$ value of 441 pm has been evaluated from a model of the octahedral structure of the hydrated Li^+ ion with additional 12 water molecules around the hydrated ion in which each water molecule in the first hydration shell is hydrogen bonded with two water molecules with the C_{3v} arrangement. Alternatively, the water molecules in the first hydration shell of Li^+ is found to have an orientation which is favorable to form three hydrogen bonds with water molecules in the

Table 3 Structural parameters of the second hydration shell of cations derived from radial distribution functions obtained by computer simulations salt.

Salt	*H_2O/salt molar ratio*	$r_{MO(2)}$(pm)	$n_{MO(2)}$	*Water model*	*Method*[a]
Li^+	200	400	14.2	CI	MC
LiCl	25	450		ST2	MD
LiI	25	430		ST2	MD
LiI	25	419	12	ST2	MD
LiI	25	441	12.4	ST2	MD, X
Na^+	200	450		CI	MC
NaCl	25–100	444–447		ST2	MD
$NaCl_a$	25	480	17.4	BJH	MD
K^+	200	530		CI	MC
KCl	25	460		ST2	MD
CsF	25	530		ST2	MD
CsF	25	530		ST2	MD
CsCl	25	490		ST2	MD
NH_4CI	25	506		ST2	MD
$BeCI_2$	50	373	12	BJH	MD
$MgCl_2$[b]	50	447	9	CF	MD
$Mg^{2+} + 37NH_3$	164	430		MCY	MD
$CaCI_2$	50	453		CF	MD, X
$SrCI_2$	50	500	16–18	BJH	MD
Zn^{2+}	200	420		MCY	MC

[a] At 235 °C and 3 kbar pressure. [b] Analyzed by the SNM method.

second hydration, the orientation helping to construct a more stable hydration structure than that forms only two hydrogen bonds. Therefore, the $n_{MO(2)}$ value of 12 may be better explained, in terms of three water molecules binding to each water molecule in a tetrahedrally hydrated Li^+ ion associated with a $n_{MO(1)}$ value of 6 (given in references in Table 1). The $r_{O(1)–O(2)}$ distance of 272 pm, which is shorter than the water–water intermolecular distance in the bulk, fit the intensity data. Results of MD and MC simulations show the number of water molecules in the second hydration shell of 12.0–14.2 with a $r_{MO(2)}$ value of 400–450 pm.

2.46.5.2 Na^+

The number of water molecules in the second hydration shell of Na^+ estimated by MD and MC simulations is 12.4 and the $r_{MO(2)}$ value is ranged from 441 pm to 480 pm. The evaluation of the structural parameters of the second hydration shell of Na^+ from the radial distribution curve may be difficult.

2.46.5.3 K^+

The structure of the second hydration shell of K^+ may be diffused, because the ion–water interactions of K^+ are not so strong. An MC simulation calculation reveals that the number of water molecules in the second hydration shell of K^+ is 17.7 and the $r_{MO(2)}$ distance is 460–530 pm.

2.46.5.4 Cs^+

No value has been proposed for $r_{MO(2)}$ of Cs^+. The $r_{MO(2)}$ value estimated by MD (see Table 3) studies may provide such information.

2.46.5.5 NH_4^+

It may be impossible to determine experimentally the second hydration structure of NH_4^+ by the XRD method, because the method can hardly distinguish between oxygen and nitrogen atoms in ammonium salt aqueous solutions. An attempt made by MD simulations for the estimation of the structure of the second hydration structure of NH_4 shows that the N—O(2) distance is 506 pm.

2.46.5.6 Ag^+

The structure of the second hydration shell of Ag^+ has been explored from the peak shape of the radial distribution curves of silver(I) perchlorate and nitrate solutions. Ag^+—O(2) distance of 430–440 pm and the number of water molecules in the second hydration shell of Ag^+ of about 5–9 have been estimated. The $r_{O(1)–O(2)}$ value is about 285 pm.

2.46.5.7 Mg^{2+}

The number of water molecules in the second hydration shell of Mg^{2+} is estimated to be about 12 and the $r_{MO(2)}$ value is 410–428 pm according to the results by XRD measurements, but the $r_{MO(2)}$ value estimated by MD simulations is 430–447 pm which is longer than the experimental value. The O(1)—O(2) distance estimated by the XRD studies is 275–281 pm, which is shorter than the water–water distance in the bulk water.

2.46.5.8 Ca^{2+}

The number of water molecules in the second coordination sphere of Ca^{2+} should be larger than that of Be^{2+} and Mg^{2+}, because Ca^{2+} has a larger ionic surface than the other two. In fact, the

$r_{MO(2)}$ value of Ca^{2+} (440–460 pm) is larger than those of Be^{2+} and Mg^{2+}. Nevertheless, the estimated value of $n_{MO(2)}$, for Ca^{2+} (1.0–5.9) is smaller than those for Be^{2+} and Mg^{2+}, and the result may be difficult to be reasonably explained.

2.46.5.9 Sr^{2+}

An XRD study shows the result that $r_{MO(2)}$ is 492–494 pm and $n_{MO(2)}$ is 9.3–14.9, the latter value is much larger than the corresponding value of Ca^{2+}. The $r_{MO(2)}$ distance estimated by an MD simulation is 500 pm.

2.46.5.10 Mn^{2+} to Zn^{2+}

The structural parameters of the second hydration shell of the divalent transition metal ions in the first row of the periodic table from Mn^{2+} to Zn^{2+}, summarized in Ohtaki and Radnai (1993),[21] does not show clear conclusions for the structural change of the ions with the atomic number.

2.46.5.11 Cd^{2+}, Hg^{2+}, and Sn^{2+}

It seems strange that the $r_{MO(2)}$ value of Hg^{2+} is smallest among the values of Cd^{2+}, Hg^{2+}, and Sn^{2+} and even smaller than the values of ions from Mn^{2+} to Zn^{2+}. More investigation may be necessary for the $r_{MO(2)}$ value of Hg^{2+}.

2.46.5.12 Al^{3+}, Cr^{3+}, and Fe^{3+}

The strongly hexahydrated trivalent ions may have a stronger second hydration shell than mono- and divalent ions. Many authors have adopted structural models with 12 water molecules in the second hydration shell of the trivalent ions. However, the tilt angle of water molecules in the first hydration shell of Cr^{3+} and Fe^{3+} ions is in favor of the construction of three hydrogen bonds with water molecules in the second hydration shell. Thus, for the evaluation of orientation of water molecules and the $n_{MO(2)}$ value; more detailed investigations may be needed. The $r_{MO(2)}$ values may be shortest in Al^{3+} and longest in Fe^{3+}.

2.46.6 DYNAMIC PROPERTIES OF WATER MOLECULES IN HYDRATION SHELLS OF IONS

Dynamic properties, such as the residence time and rotational behavior of water molecules in the hydration shells of ions, can be found from kinetic and dynamic studies of electrolyte solutions. NMR, quasi-elastic neutron scattering (QENS), and MD studies may provide such information. The residence times of water molecules in the first hydration shell of various ions are summarized in Table 4. The residence time values of the oxygen atom, τ_o, depend remarkably on the ions. Generally speaking, among ions in the same group the larger the ionic radius, the smaller the τ_o value. Irregularity in the order of the magnitude of the τ_o values observed in the first transition metal ions has been explained by applying ligand field theory to the stability of penta- or hepta-coordinated reaction intermediates.[25]

Exchange reactions of water molecules have been thoroughly investigated using the NMR method. The results are summarized in Table 5.

2.46.7 IONIC HYDRATION UNDER EXTREME CONDITIONS

Structural studies of water on the molecular level have been performed since the XRD studies by Mayer,[26] Stewart,[27,28] and Amaldi,[29] and the theoretical work by Bernal and Fowler[30] in the 1930s. Water structure at supercooled temperatures and in the glassy state has also been investigated from the various viewpoints of chemistry, physics, geology, biology, and engineering.[31,32]

Table 4 Residential time of water molecule in the bulk and of oxygen and hydrogen atoms of hydrated water molecules in the first hydration shell of ions (τ_{H_2O}, τ_O, and τ_H) (for details see Ohtaki and Radnai, 1993[21] and references therein).

Ion	τ_{H_2O} (s)	τ_O (s)	τ_O (s)	*Method*[a]
Li^+	4.8×10^{-12}			MD
		3.3×10^{-11}		MD
			$\sim 3 \times 10^{-11}$	MR
Na^+	3.8×10^{-12}	$9\ 9 \times 10^{-12}$		MD
K^+	4.8×10^{-12}	$4\ 0 \times 10^{-12}$		MD
		$<10 \times 10^{-10}$		QENS
Cs^+		$<10 \times 10^{-10}$		QENS
Be^{2+}		3×10^{-4}		NMR
Mg^{2+}		2×10^{-6}		NMR
			$\geq 5 \times 10^{-5}$	QENS
Ca^{2+}		$<10^{-10}$		NMR
			$\leq 10 \times 10^{-10}$	QENS
Mn^{2+}		3.2×10^{-8}		NMR
Fe^{2+}		3.13×10^{-7}		NMR
Co^{2+}		8.8×10^{-7}		NMR
Ni^{2+}		3.7×10^{-5}		NMR
			$\geq 5 \times 10^{-9}$	QENS
		1×10^{-4}		NMR
Cu^{2+}		5×10^{-9}		NMR
		$\leq 10^{-10}$		QENS
Zn^{2+}		$>10^{-4}$		QENS
Ti^{3+}		1.0×10^{-5}		NMR
V^{3+}		6×10^{-4}		NMR
		$1.8–2.2 \times 10^{-5}$		NMR
Cr^{3+}			2×10^{-6}	NMR
			$\geq 5 \times 10^{-9}$	QENS
Fe^{3+}		6×10^{-3}		NMR
			$\geq 5 \times 10^{-9}$	QENS
Co^{3+}		10^{-5}		NMR
Al^{3+}		0.78		NMR
			$\geq 5 \times 10^{-9}$	QENS
Ga^{3+}		5.5×10^{-5}		NMR
			$= 5 \times 10^{-9}$	QENS
Nd^{3+}			$>10^{-10}$	QENS
Tb^{3+}		$1.3–4.8 \times 10^{-8}$		NMR
Dy^{3+}		$3.1–7.1 \times 10^{-3}$		NMR
			$>10^{-10}$	QENS
Ho^{3+}		$1.6 \times 10^{-8} – 1.1 \times 10^{-7}$		NMR
		$7.4 \times 10^{-9} – 1.9 \times 10^{-7}$		NMR
Tm^{3+}		$1.5–3.0 \times 10^{-7}$		NMR
F^-	5.5×10^{-12}	20.3×10^{-12}		MD
			$\leq 10^{-10}$	QENS
Cl^-	4.1×10^{-12}	4.5×10^{-12}		MD
			$\leq 10^{-10}$	QENS

[a] QENS: quasi-elastic neutron scattering.

In recent years, the solution XRD technique with a special cell arrangement was effectively applied to structural studies at high temperatures and high pressures (HTHP) and the conclusions on the structure of water in the supercritical region seem to be that supercritical water consists of small clusters having hydrogen bonds and monodispersed gas-like particles. Recent studies on the structure of supercritical water are summarized in some articles.[33–35] The structures of hydrated ions in supercritical water have not been so widely investigated and a rather limited number of results have been reported.[36,37]

Table 5 Rate constants of water exchange reactions of hydrated cations and thermodynamic parameters of the reaction at 25 °C (for details see Ohtaki and Radnai, 1993[21] and references therein).

Ion	*Hydration number, n*	*Reaction, k* (s^{-1})	$\Delta H^{\#}$ (kJ mol^{-1})	$\Delta S^{\#}$ (kJ mol^{-1})	$\Delta V^{\#}$ ($cm^3\,mol^{-1}$)	*Mechanism*[a]
Be^{2+}	4	7.3×10^{2}	59.2	8.4	−13.6	A
V^{2+}	6	8.7×10^{1}	61.8	0.4	4.1	I_a
Mn^{2+}	6	2.1×10^{7}	32.9	5.7	−5.4	I_a
Fe^{2+}	6	4.39×10^{6}	41.4	21.2	3.8	I_a–I_d
Co^{2+}	6	3.18×10^{6}	46.9	37.2	6.1	I_a–I_d
Ni^{2+}	6	3.37×10^{4}	52.3	17.2	7.1	I_d
Cu^{2+}	4	1.0×10^{4}	192	−16.8		
	2	3.0×10^{8}	87.8			
Zn^{2+}	6	3.0×10^{7}				
Ru^{2+}	6	1.8×10^{-2}	87.8	16.1	−0.4	I
Pd^{2+}	4	5.6×10^{2}	49.5	−26	22	I_a or A
Pt^{2+}	4	3.9×10^{-4}	89.7	−9	−4.6	I_a or A
$A1^{3+}$	6	1.29	84.7	41.6	5.7	I_d
Ga^{3+}	6	4.0×10^{2}	67.1	30.1	5.0	I_d
Ti^{3+}	6	1.8×10^{5}	43.4	1.2	−12.1	I_a or A
V^{3+}	6	5.0×10^{2}	49.4	−27.8	−8.9	I_a
Vo^{2+}	5	7.41×10^{2}	55.6	−6.3		
Cr^{3+}	6	2.4×10^{-6}	108.6	11.6	−9.6	I_a
Fe^{3+}	6	6.8×10^{4}	40.3	80	−5.4	I_a
Ru^{3+}	6	$3\ 5 \times 10^{-6}$	89.8	−48.3	−8.3	I_a
Rh^{3+}	6	2.2×10^{-9}	131.2	29.3	−4.2	I_a
Gd^{3+}	8	11.9×10^{8}	12.0	−30.9		I_a
Tb^{3+}	8	5.58×10^{8}	12.1	−36.9	−5.7	I_a
Dy^{3+}	8	4.34×10^{8}	16.6	−24.0	−6.0	I_a
Ho^{3+}	8	2.14×10^{8}	16.4	−30.5	−6.6	I_a
Er^{3+}	8	1.33×10^{8}	18.4	−27.8	−6.9	I_a
Tm^{3+}	8	0.47×10^{8}	22.7	−16.6	−6.0	I_a
Yb^{3+}	8	0.47×10^{8}	23.3	−21.0		I_a

[a] A: association mechanism, I: interchange mechanism, I_a: associative interchange mechanism, I_d: dissociative interchange mechanism, I_a–I_d: not distinguishable between I_a and I_d mechanisms.

2.46.8 IONIC SOLVATION IN NONAQUEOUS SOLVENTS

Since most electrolytes are less soluble in nonaqueous solvents than in water, studies on the solvation phenomena of ions in nonaqueous solution are much less frequent than those in aqueous solution. Many alcohols and some nonaqueous solvents such as DMF, DMSO, and acetonitrile (AN) have relative medium dielectric constants with donor and acceptor properties comparable with those of water and many electrolytes can be dissolved in these solvents. Donor and acceptor interactions between ions and solvent molecules can be compared with those with water molecules.

The copper(II) ion has a distorted octahedral structure in DMF similar to that in aqueous solution.[7,38] EXAFS measurements show that the nickel(II) ion forms an octahedral solvate structure in various nitriles (acetonitrile, propionitrile, butylnitrile, isobutylnitrile, valeronitrile, and benzonitrile) similar to that in water.[39] The length of the Ni—O bond in the nitriles did not vary significantly from the Ni—O bond length found in water.[39–41]

The cobalt(II) ion in 1,3-propanediamine (a bidentate ligand with two nitrogen atoms and having a strong donor property) combines with three solvent molecules to form an octahedral hexa-coordinated solvate.[42] The Co—N length was longer than the Co—O length in water, the difference possibly arising from the bidentate character of the formation of a five-membered ring of the solvent rather than the different atomic sizes of the nitrogen and oxygen atoms in 1,3-propanediamine and water, respectively. In *n*-propylamine it forms an equilibrium mixture of octahedral hexa-coordinated and tetrahedral tetra-coordinated solvates while in 1,1,3,3-tetramethylurea (TMU) the cobalt(II) ion forms a tetra-coordinated solvate[43] probably due to steric hindrance between ligating solvent molecules.

The solvation structures of Ln^{3+} in DMF and DMA have been compared using EXAFS and no significant differences between the structure in DMF and that in DMA were observed.[44]

The silver(I) ion can form various coordination structures depending on the coordinating solvent and ligand molecules. The hard and soft properties of the ligand atoms also affect the coordination structure of silver(I) ion solvates. For example, silver(I) forms a tetra-coordinated solvate in oxygen-donating solvents such as water[45–47] and DMF[48] and in nitrogen-donating solvents such as ammonia,[49] AN,[48–50] and pyridine.[49,51] It was found that Ag^+ forms a tetrahedral structure in DMSO with four Ag—O bonds in the first coordination solvate shell by means of EXAFS.[52] Conversely one Ag—S bond together with three Ag—O bonds were observed in the same solvent by XRD.[53] A reexamination of the structure of the Ag^+ solvate in DMSO is currently being undertaken by one of the authors.

In DMSO, mercury(II) and cadmium(II) were found to form regularly octahedral hexasolvates with the DMSO coordinating via the oxygen atom.[54] The crystal and molecular structures of both solvate products were elucidated by Sandstrom,[55,56] confirming both to be octahedral. The Raman spectra of perchlorate solutions of Hg^{II}, Cd^{II}, and Zn^{II} in DMSO provide further proof that the metal ions are all coordinated via O.[54]

The solvated yttrium(III) ion has been shown by XAFS and large angle X-ray scattering to coordinate eight solvent molecules in both DMSO and DMF, but only six in *N*,*N*′-dimethylpropyleneurea due to steric effects. XRD results show the ionic radii of Y^{III} to increase about 0.12 Å from six to eight coordination.[57]

Gallium(III) ion takes the six-coordinate solvation structure in trimethyl phosphate (TMP) as in water from the measurement of EXAFS and the comparison between some metal ion solvation.[58] The results also show the bond length between the solvated metal ion (Mn^{II}, Fe^{II}, Co^{II}, Ni^{II}, Cu^{II}, or Ga^{III}) and oxygen atom of each solvent (EtOH, MeOH, DMSO, TMP) is much similar to that in water. However, the coordination number of the Zn^{II} ion even in the larger ionic radius than the Gd^{II}, decreases in DMA[59] and TMP, i.e., the coordination of DMA or TMP with such metal ions may influence their charge density than ionic radius.

Further structural data of solvated ions in typical nonaqueous solvents are summarized in Table 6.

2.46.9 PREFERENTIAL SOLVATION OF IONS IN MIXED SOLVENTS

Mixed solvents have been widely used in thermodynamic and kinetic studies on ionic interactions in solution with changing solvent properties of the reaction medium. Dielectric constants and viscosities of solvents are changed by altering the solvent composition of the mixtures. Theories proposed for the explanation of the variation of thermodynamic and kinetic data usually assume a homogeneous continuum medium with specific bulk properties, and the theories which are successfully applied to a neat medium usually fail when applied to mixed solvent systems. The disagreement of theoretical values with experimental ones has traditionally been put down to the inadequacy of the simple assumption of continuum of the solvents. The different solvent composition in the solvation shell from that in the bulk may be another more important factor for causing these discrepancies.

It could reasonably be expected that in a mixed solvent, the solvent with the larger affinity to an ion might be preferentially solvated with it. The solvent composition of the first solvation shell of the main species formed in various mixed AN-DMF mixtures, together with individual bond lengths are summarized in Table 6. While the accuracy of the results may not be so high the variation of the solvent composition of the solvation shell with the composition in the bulk is clearly recognizable.

An attempt to introduce a quantitative measure of preferential solvation of ions concluded that it occurs primarily due to the difference in the Gibbs energies of solvation of the two solvents under study.[60] Solvent–solvent interaction is another important factor controlling preferential solvation. This is illustrated by the solvation of Co^{II} in mixtures of TMU and water.[61] TMU is a much stronger donor solvent than water and, thus, would be expected to preferentially solvate with cations over water. However in H_2O–TMU mixtures with a larger portion of water, the Co^{II} ion preferentially solvated with water. The results can be explained in terms of strong TMU–H_2O intermolecular interactions in the bulk, which result in the disappearance of free TMU. In mixtures containing TMU as a major portion, Co^{II} is preferentially solvated with TMU, while spectrophotometric evidence shows that Co^{II} forms the tetra-solvated $[Co(TMU)_4]^{2+}$ in neat TMU.

Yokoyama *et al.*[62] have determined the solvent composition in the solvation shell of Co^{2+} in various amide–water mixtures by XRD. The Gibb's free energy of solvation and the Gutmann's donor number of the amides are not significantly different but they have differing abilities for hydrogen bonding with water molecules due to different numbers of free amino groups in their

Table 6 Selected values of ion–ligand atom distances (r_{M-X}) and number of solvent molecules (n) coordinated the ion in various solvents.

Ion	*DMSO* *r*(pm)	*DMF* *n*	*DMA* *r*(pm)	*AN* *n*	*DMTF* *r*(pm)	*DMPU* *n*	*Py* *r*(pm)	*PDA* *n*		
Ca^{2+}	232	6	229	6						
Sr^{2+}	254	6	255	6						
Ba^{2+}	276	6	275	6						
Cu^{+}	209	4	199	4	233[m]	4				
Ag^{+}	224[a] 257[b]	4	233	4	226	4	255[m]	4	241	4
Au^{+}	219	4	228[m]	4	216	4				
Mn^{2+}	220	6	210	5						
Fe^{2+}	210	6	214	6	202	4				
Co^{2+}	209.5	6	213	6	211.6	6	200	5	217	6
Ni^{2+}	206.3	6	206.7	6	200	5				
Cu^{2+}	198	6[c]	201	6[c]	199[d]	6[c]	192	4		
	–	284	–							
Zn^{2+}	212	6	208	6	236[m]	4	195	4		
Cd^{2+}	229	6	230	6	270[m]	6	229	6		
Hg^{2+}	239	6[e]	257.2[m]	4						
Hg^{2+}	222	4	221[k]	2	222	4	267			
Sn^{2+}		4[g]								
Ph^{2+}	289	6								
Pd^{2+}			223							
Pt^{2+}	207[h]	4[i]	200	4[i]	230	4[i]	221.5			
Sc^{3+}	209	6								
Fe^{3+}	202	6								

Table 6 continued

Ion	*DMSO* *r*(pm)	*DMF* *n*	*DMA* *r*(pm)	*AN* *n*	*DMTF* *r*(pm)	*DMPU* *n*	*Py* *r*(pm)	*PDA* *n*
Y^{3+}	236	8[i]	224	6				
Bi^{3+}	241	8[j]	279	6	232	6		
La^{3+}	250	8[j]	248.6	7.3	247.5	6.5	244	~7
Ce^{3+}	247.4	8.1	245.2	6.6				
Pr^{3+}	244.7	7.4	242.0	6.9				
Nd^{3+}	243.8	7.4	240.2	6.1				
Sm^{3+}	241.6	8.9	236.7	8.4				
Eu^{3+}	238.5	7.7	234.7	6.7				
Gd^{3+}	238.5	7.5	233.3	7.2				
Tb^{3+}	236.9	7.5	231.9	7.3				
Dy^{3+}	236.0	7.7	230.5	7.0				
Ho^{3+}	234.6	7.8	229.3	6.9				
Er^{3+}	233.6	7.2	227.3	7.6				
Tm^{3+}	232.5	7.5	226.7	6.8				
Yb^{3+}	230.9	7.5	223.8	6.3				
Lu^{3+}	229.8	7.9	222.1	6.0				
Ga^{3+}	196	6	224	4	192	5		
In^{3+}	214	6	261	6	214	6		

DMA: *N*,*N*-dimethylacetamide; AN: acetonitrile; DMTF: *N*,*N*-dimethylthioformamide; DMPU: 1,3-dimethylpropylene urea; Py: pyridine; TMU: tetramethylurea; PDA: 1,3-propanediamine; [a] three M—O bonds; [b] one M—S bond; [c] Jahn–Teller distorted octahedron; [d] four equatorial Cu—O bonds; [e] second-order Jahn–Teller distorted octahedron; [f] Hg—Hg bond length: 250 pm; [g] two bonds are longer than the other two; [h] two M—O bonds and two M—S bonds; [i] square-planar; [j] square antiprism; [k] Hg—Hg bond length: 254pm; [l] linear; [m] M—S bond; [n] square pyramid; [o] bidentate ligand.

molecules. Moreover, they have different substituents resulting in different volumes of bulkiness of the molecules, which may cause steric hindrance in the solvation sphere of the ion. When amino protons are substituted with alkyl groups, the amino group in the molecule attracts fewer water molecules in the bulk so that the concentration of free water molecules increases, the result being that Co^{2+} can be solvated with more water molecules than with the amide. The different volumes of solvent molecules with bulky substituents may be an additional reason for making different degrees of preferential solvation of the amides.

Umebayashi *et al.*[62–66] have applied Raman spectrophotometry to the determination of the total solvation number of various ions together with the composition of the solvent molecules in the first solvation shell. The total number of solvated molecules in the first coordination sphere, as well as the numbers of individual solvent molecules, of Mn^{II}, Ni^{II}, Cu^{II}, and Zn^{II} in DMF–DMA and DMF–TMU mixtures were determined.

Previous results showed that divalent metal ions, with the exception of Mn^{II}, are stabilized in DMF better than DMA,[67] which is the opposite of what could be expected given the solvation abilities of DMF and DMA.

2.46.10 THEORETICAL CONSIDERATION OF IONIC SOLVATION

In the last few decades, some investigators have attempted to extend molecular dynamics for use in solution state with the distinct expansively of computer chemistry. It means that the total micro-view, such as the conformation of the coordination in the ionic solvation state, and the macro-view, such as the design for new ionic liquid or new functional phenomena, of ionic solvation can be discussed with some experimental data.

The translational motion of the Li^{I} ion in water, for instance, speeds up the solvation by ca. 20% by using of the density functional theory (DFT) with some approximation.[68] The computational progress toward ionic solvation has been arriving to discuss the more complicate area such as heat capacity changes (by a Monte Carlo calculation),[69] surface effects on aqueous ionic solvation (by a Molecular Dynamics).[70]

2.46.11 CONCLUSION

Ionic solvation is one of the most fundamental subjects in solution chemistry. The extension of studies in aqueous solution to nonaqueous solution and mixed solvents and of solvent composition from single-component to multi-component leads to both interesting results and a widening view for chemistry in aqueous solution itself.

ACKNOWLEDGMENTS

Thanks for financial support are due to the "*Fonds zur Förderung der Wissenschaftlichen Forschung in Österreich*" (Project 15874-N03).

2.46.12 REFERENCES

1. Arrhenius, S. *Z. Phys. Chem.* **1887**, *1*, 631.
2. Born, M. *Z. Physik* **1920**, *1*, 45.
3. Debye, P.; Huckel, E. *Phys. Z.* **1923**, *24*, 185, 305.
4. Bjerrum, N. *Det. Kgl. Danske Videnskab. Math.-fys. Medd.* **1926**, *7*, 1.
5. Frank, H. S.; Wen, W.-Y. *Disc. Faraday Soc.* **1957**, *24*, 133.
6. Samoilov, O. *Disc. Faraday Soc.* **1957**, *24*, 141.
7. Ohtaki, H.; Maeda, M. *Bull. Chem. Soc. Jpn.* **1974**, *47*, 2197.
8. Enderby, J. E. In Proceedings of the 7th International Symposium on Solute–Solute–Solvent Interactions, Reading, U.K., July 15–19, 1985.
9. Eigen, M.; DeMaeyer, L. *Z. Elektrochem.* **1955**, *59*, 986.
10. Burgess, J. H. *Metal Ions in Solution*; Ellis Horwood: New York, 1978.
11. Conway, B. E. *Ionic Hydration in Chemistry and Biophysics*; Elsevier: Amsterdam, 1981.
12. Burgess, J. H. *Ions in Solution: Basic Principles of Chemical Interactions*; Ellis Horwood: Chichester, U.K., 1988.
13. Marcus, Y. *Ion Solvation*; Wiley: Chichester, U.K., 1988.
14. Bockris, J. O. M.; Reddy, A. K. N. Eds., *Modern Electrochemistry, Ionics*; 2nd ed., Plenum: New York, 1988; Vol. 1.

15. Ohtaki, H. *Yoeki Kagaku (Solution Chemistry)* (in Japanese), Shokabo: Tokyo, 1985.
16. Ohtaki, H. *Yoeki no Kagaku (Chemistry of Solutions)* (in Japanese), Dai-Nippon Tosho: Tokyo, 1990.
17. Ohtaki, H. *Ion no Suiwa (Hydration of Ions)*, (in Japanese), Kyoritsu Shuppan: Tokyo, 1990.
18. Ohtaki, H.; Tanaka, N.; Nakahara, S.; Miyahara, Y.; Yamatera, H.; Yamamoto, Y. Eds., *Ion to Yobai (Ions and Solvents)* (in Japanese), Kagaku Sosetsu No. 11, ed. Chemical Society of Japan, Gakkai Shuppan Center, 1976.
19. Ohtaki, H.; Nakahara, M.; Nomura, H. Eds., *Yoeki no Bunshiron-teki Byozo (Molecular Pictures of Solutions)* (in Japanese), Kikan Kagaku Sosetsu No. 25, Chemical Society of Japan, Gakkai Shuppan Center, 1995.
20. Marcus, Y. *Chem. Rev.* **1993**, *88*, 1475.
21. Ohtaki, H.; Radnai, T. *Chem. Rev.* **1993**, *93*, 1157.
22. Stillinger, F. H.; Rahman, A. *J. Chem. Phys.* **1974**, *60*, 1545.
23. Kern, C. W.; Karplus, M. The Water Molecule. In *Water – A Comprehensive Treatise*; Franks, F., Ed., Plenum: New York, 1972; Vol. 1.
24. Matsuoka, O.; Clementi, E.; Yoshimine, M. *J. Chem. Phys.* **1976**, *64*, 1351.
25. Basolo, F.; Pearson, R. G. *Mechanisms of Inorganic Reactions*; Wiley: New York, 1958.
26. Mayer, A. W. *Ann. Phys.* **1930**, *5*, 701.
27. Stewart, G. W. *Phys. Rev.* **1930**, *35*, 1462.
28. Stewart, G. W. *Phys. Rev.* **1931**, *37*, 9.
29. Amaldi, W. *Phys. Z.* **1931**, *32*, 914.
30. Bernal, J. D.; Fowler, R. H. *J. Chem. Phys.* **1933**, *1*, 515.
31. Franks, F. Ed. *Water—A Comprehensive Treatise*; Plenum: New York, 1982; Vol. 7, p 215.
32. Angel, C. A. *Ann. Phys. Chem.* **1983**, *34*, 593.
33. Ohtaki, H.; Radnai, T.; Yamaguchi, T. *Chem. Soc. Rev.* **1997**, *41*.
34. Nakahara, M.; Yamaguchi, T.; Ohtaki, H. *Recent Res. Devel. Phys. Chem.* **1997**, *1*, 17.
35. Radna, T.; Ohtaki, H. *Mol. Phys.* **1996**, *87*, 103.
36. Pfund, D. M.; Darab, J. G.; Fulton, J. L.; Ma, Y. *J. Phys. Chem.* **1994**, *98*, 13102.
37. Wallen, S. L.; Palmer, B. J.; Fulton, J. L. *J. Chem. Phys.* **1998**, *108*, 4039.
38. Ozutsumi, K.; Ishiguro, S.; Ohtaki, H. *Bull. Chem. Soc. Jpn.* **1988**, *61*, 945.
39. Inada, Y.; Funahashi, S. *Anal. Sci.* **1997**, *13*, 373.
40. Ohtaki, H.; Yamaguchi, T.; Maeda, M. *Bull. Chem. Soc. Jpn.* **1976**, *49*, 71.
41. Soper, A. K.; Neilson, G. W.; Enderby, J. E.; Howe, R. A. *J. Phys. Chem., Solid State Phys.* **1977**, *10*, 1793.
42. Aizawa, S.; Iida, S.; Matsuda, K.; Funahashi, S. *Inorg. Chem.* **1996**, *35*, 1338.
43. Ozutsumi, O.; Asaka, A.; Iinomi, N.; Ohtaki, H. *Rits SR Center Activity Report*, Ritsumeikan University, 1996, p 39.
44. Ishiguro, S.; Umebayashi, Y.; Kato, K.; Takahashi, R.; Ozutsumi, K. *J. Chem. Soc., Faraday Trans.* **1998**, *94*, 3607.
45. Yamaguchi, T.; Lindqvist, O.; Boyce, J. B.; Claesson, T. *Acta Chem. Scand.* **1984**, *A38*, 423.
46. Yamaguchi, T.; Johansson, G.; Holmberg, B.; Maeda, M.; Ohtaki, H. *Acta Chem. Scand.* **1984**, *A38*, 437.
47. Sandstrom, M.; Neilson, G. W.; Johansson, G.; Yamaguchi, T. *J. Phys. Chem., Solid State Phys.* **1985**, *18*, L1115.
48. Ozutsumi, K.; Kitakaze, A.; Iinomi, M.; Ohtaki, H. *J. Mol. Liq.* **1997**, *73/74*, 385.
49. Yamaguchi, T.; Wakita, H.; Nomura, M. *J. Chem. Soc., Chem. Commun.* **1988**, 433.
50. Nilsson, K.; Oskarsson, A. *Acta Chem. Scand.* **1984**, *A38*, 79.
51. Nilsson, K.; Oskarsson, A. *Acta Chem. Scand.* **1982**, *A36*, 605.
52. Tsutsui, Y.; Sugimoto, K.; Wasada, H.; Inada, Y.; Funahashi, S. *J. Phys. Chem. A* **1997**, *101*, 2900.
53. Ozutsumi, K.; Ohtaki, H. *Structure of Mixed Solvents and Preferential Solvation of Metal Ions* Proceedings of the 26th International Conference on Solution Chemistry, Fukuoka, Japan, July 26–31, 1999.
54. Sandstrom, M.; Persson, I.; Ahrland, S. *Acta Chem. Scand.* **1978**, *A32*, 607.
55. Sandstrom, M. *Acta Chem. Scand.* **1978**, *A32*, 519.
56. Sandstrom, M.; Persson, I. *Acta Chem. Scand.* **1978**, *A32*, 95.
57. Lindqvist-Reis, P.; Naslund, J.; Persson, I.; Sandstrom, M. *J. Chem. Soc. Dalton Trans.* **2000**, *16*, 2703.
58. Inada, Y.; Hayashi, H.; Sugimoto, K.; Funahashi, S. *J. Phys. Chem. A* **1999**, *103*, 1401.
59. Ozutsuni, K.; Koide, M.; Suzuki, H.; Ishiguro, S. *J. Phys. Chem.* **1993**, *97*, 500.
60. Ozutsumi, K.; Ikuno, N.; Suzuki, T.; Ohtaki, H. Proceeding of the 49th National Conference on Coordination Chemistry, Sapporo, Japan, Sept 24–26, 1999.
61. Ikuno, N.; Asaka, T.; Ueohmae, M.; Ozutsumi, K.; Ohtaki, H. *Preferential Solvation Structure of Cobalt (II) Ion in Water -1,1,3,3,- Tetramethylnrea Mixtures* Proceedings of the 21st National Symposium on Solution Chemistry, Sapporo, Japan, Oct 8–10, 1998.
62. Yokoyama, H.; Tada, Y. *Preferential Solvation of Cobalt (II) Ion in Water-Amide Mixtures* Proceeding of the 65th Annual Meeting of Electrochemical Society of Japan, Tokyo, April 1–3, 1998.
63. Yokoyama, H.; Tada, Y.; Ohtsu, H.; Tanabe, M.; Hirano, R. *Study of Selective Solvation of Cobalt (II) Iron in Mixed Solvents by X-ray Diffraction Measurements Using Imaging-plate Detector* Proceedings of the 21st National Symposium on Solution Chemistry, Sapporo, Japan, Oct 8–10, 1998.
64. Yokoyama, H.; Tada, Y.; Ohtsu, H.; Tanabe, M.; Hirano, R. *Preferential Solvation of Cobalt (II) Iron in Amide-water Mixtures* Proceedings of the 26th International Conference on Solution Chemistry, Fukuoka, Japan, July 26–31, 1999.
65. Umebayashi, Y.; Matsumoto, K.; Watanabe, M.; Katoh, K.; Ishiguro, S. *Anal. Sci.* **2002**, in press.
66. Umebayashi, Y.; Watanabe, M.; Ishiguro, S. Proceedings of the 26th International Conference on Solution Chemistry, Fukuoka, Japan, July 26–31, 1999.
67. Koide, M.; Ishiguro, S. *J. Solution Chem.* **1995**, *24*, 511.
68. Biswas, R.; Bagch, B. *J. Phys. Chem.* **1996**, *100*, 4261.
69. Madan, B.; Sharp, K. *J. Phys. Chem.* **1996**, *100*, 7713.
70. Jungwirth, P.; Tobias, D. J. *J. Phys. Chem. B* **2000**, *104*, 7702.

Comprehensive Coordination Chemistry II
ISBN (set): 0-08-0437486

Volume 2, (ISBN 0-08-0443249); pp 597–610

2.47
Topology: General Theory

R. B. KING
University of Georgia, Athens, GA, USA

2.47.1 INTRODUCTION 611
2.47.2 TOPOLOGY AND POLYHEDRA 611
2.47.3 POLYHEDRAL ISOMERIZATIONS 617
2.47.4 SUMMARY 620
2.47.5 REFERENCES 620

2.47.1 INTRODUCTION

Topology is the mathematics of neighborhood relationships in space independent of metric distance. Topology thus embraces geometrical concepts but is more general since it seeks structural insights independent of metric ideas and algebraic structure. The concept of connectivity remains in topology, which in a chemical structure tells us how the atoms are joined when all ideas of distances and angles are removed. This apparently simple notion of connectivity still embodies a considerable amount of structural information and in chemistry is typically depicted by the various types of structural formulas used by chemists.

The ideas of topology may be expressed abstractly in what is called point-set or general topology,[1,2] which may be regarded as a generalization of geometry. In this connection, geometry is concerned with objects in space and their transformations. Topology has a similar concern but allows transformations that are less restrictive. Thus, transformations that stretch and deform but do not tear (i.e., transformations that are *continuous*) are allowed in topology. Concepts such as distance disappear upon stretching and deformation but concepts such as adjacency and nearness are preserved.

A number of recent books discuss diverse applications of topology to chemical problems[3–6] including chemical reactivity[7] and chirality.[8] This article focuses on applications of topology to problems of interest to coordination chemists, particularly the study of coordination polyhedra and their rearrangements.

2.47.2 TOPOLOGY AND POLYHEDRA

An important concept in topology is that of a *topological space*, which can be defined formally by introducing the idea of an *open set*. In this connection let X be a nonempty set. A family T of subsets of X is then defined as a *topology* on X if T obeys the following axioms:

(i) The full space X and the empty set Ø belong to T.
(ii) The union of any number of subsets in T belongs to T.
(iii) The intersection of the elements of any finite collection of subsets in T belongs to T.

The members of T are called open sets and the pair (x,T) is called a *topological space*.

The most important topological space used to model chemical structures is that of a graph. In this connection a graph is defined as a nonempty set V (the "vertices") together with a (possibly empty) set E (the "edges"—disjoint from V) of two-element subsets of (distinct) elements of V.[9] A graph thus represents a finite topology (V,T) in which its edges E as well as V and the empty set Ø are the open sets in the topology T on the set V, corresponding to the vertices. In the most obvious use of graphs to model chemical structures, the vertices of the graph represent the atoms and the edges represent chemical bonds.

The concept of a graph leads very naturally to the concept of a polyhedron, which essentially is a way of embedding a graph into three-dimensional space, $\Re^3$. A graph G forming a polyhedron Π may be called the *1-skeleton*[10] of the polyhedron; the vertices and edges of G form the vertices and edges of Π. The embedding of G into $\Re^3$ to form Π leads to the two-dimensional *faces* of Π.

Polyhedra are very useful for describing diverse chemical structures. In coordination chemistry polyhedra can appear as *coordination polyhedra* in which the vertices represent ligands surrounding a central atom which is often, but not always, a metal; and *cluster polyhedra* in which the vertices represent multivalent atoms and the edges represent bonding distances. *Deltahedra*, in which all faces are triangles, are a special type of polyhedra that appear often in chemical structures.

The simplest and most important polyhedra are the so-called *simple* polyhedra, which can be continuously deformed into spheres (i.e., are topologically homeomorphic to a sphere). The simple polyhedra of chemical interest generally have the additional property of convexity. All vertices of a convex polyhedron lie entirely on one side of each of its faces so that a convex polyhedron can be laid on a flat tabletop with any face down. Convexity is not a topological property, for convex polyhedra in general can be continuously transformed into nonconvex polyhedra.

Convex polyhedra in $\Re^3$ exhibit the following relationships between possible numbers and types of vertices (v), edges (e), and faces (f): In this connection the following elementary relationships are particularly significant:[11]

(i) Euler's relationship:[10]

$$v - e + f = 2 \tag{1}$$

This arises from the properties of ordinary three-dimensional space.

(ii) Relationship between the edges and faces:

$$\sum_{i=3}^{v-1} if_i = 2e \tag{2}$$

In Equation (2) f_i is the number of faces with i edges (i.e., f_3 is the number of triangular faces, f_4 is the number of quadrilateral faces, etc.). This relationship arises from the fact that exactly two faces share each edge of the polyhedron. Since no face can have fewer edges than the three of a triangle, the following inequality must hold in all cases:

$$3f \leq 2e \tag{3}$$

(iii) Relationship between the edges and vertices:

$$\sum_{i=3}^{v-1} iv_i = 2e \tag{4}$$

In Equation (4) v_i is the number of vertices of degree i (i.e., having i edges meeting at the vertex). This relationship arises from the fact that each edge of the polyhedron connects exactly two vertices. Since no vertex of a polyhedron can have a degree less than three, the following inequality must hold in all cases:

$$3v \leq 2e \tag{5}$$

(iv) Totality of faces:

$$\sum_{i=3}^{v-1} f_i = f \tag{6}$$

(v) Totality of vertices:

$$\sum_{i=3}^{v-1} v_i = v \tag{7}$$

Equation (6) relates the f_is to f and Equation (7) relates the v_is to v.

In generating actual polyhedra, the operations of capping and dualization are often important. *Capping* a polyhedron Π_1 consists of adding a new vertex above the center of one of its faces Φ_1 followed by adding edges to connect the new vertex with each vertex of Φ_1. If Φ_1 has k edges, then the capping process can be more specifically described as k-capping.

The capping process gives a new polyhedron Π_2 having one more vertex than Π_1. If a triangular face is capped (i.e., 3-capping), the following relationships will be satisfied in which the subscripts 1 and 2 refer to Π_1 and Π_2 respectively:

$$v_2 = v_1 + 1;\ e_2 = e_1 + 3;\ f_2 = f_1 + 2 \tag{8}$$

Such a capping of a triangular face is found in the capping of a tetrahedron to form a trigonal bipyramid (Figure 1a). In general, if a face with f_k edges is capped (i.e., k-capping), the following relationships will be satisfied:

$$v_2 = v_1 + 1;\ e_2 = e_1 + f_k;\ f_2 = f_1 + f_k - 1 \tag{9}$$

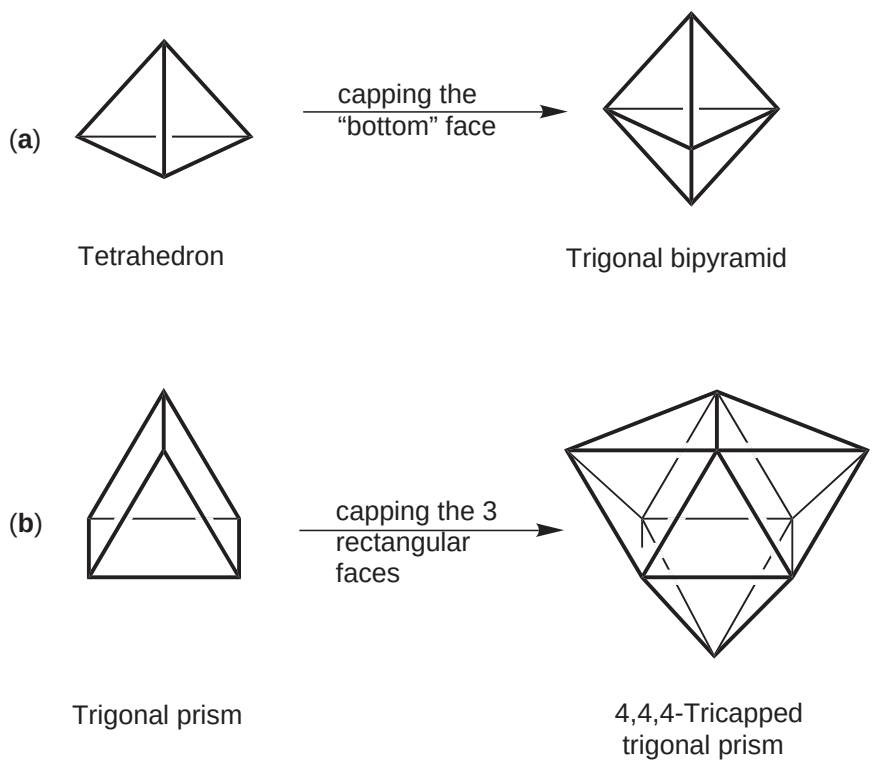

Figure 1 (a) Capping one face of a tetrahedron to give a trigonal bipyramid; (b) Capping the three rectangular faces of a trigonal prism to give the 4,4,4-tricapped trigonal prism found in nine-coordinate complexes such as ReH_9^{2-}.

Application of such a capping process to each of the three rectangular faces of a trigonal prism generates the 4,4,4-tricapped trigonal prism found in the rare examples of nine-coordinate complexes such as ReH_9^{2-} (Figure 1b).

Another process of interest in polyhedral topology is the *dualization* of polyhedra. A given polyhedron Π can be converted into its dual Π* by locating the centers of the faces of Π* at the vertices of Π and the vertices of Π* above the centers of the faces of Π. Two vertices in the dual Π* are connected by an edge when the corresponding faces in Π share an edge. Examples of the process of dualization are the conversion of a trigonal bipyramid into a trigonal prism (Figure 2a) and the conversion of an octahedron to a cube (Figure 2b). The tetrahedron is an example of a self-dual polyhedron; i.e., dualization of a tetrahedron gives another tetrahedron (Figure 2c).

The process of dualization has the following properties:

(i) The numbers of vertices and edges in a pair of dual polyhedra Π and Π* satisfy the relationships $v^* = f, e^* = e, f^* = v$ in which the starred variables refer to the dual polyhedron Π*. Thus, for the trigonal bipyramid (Π)/trigonal prism (Π*) dual pair depicted in Figure 2a $v^* = f = 6$, $e^* = e = 9$, $f^* = v = 5$.

(ii) Dual polyhedra have the same symmetry elements and thus belong to the same symmetry point group. Thus, in the example above, both the trigonal bipyramid and the trigonal prism have the D_{3h} symmetry point group. Also note in general that the dualization of a prism gives the corresponding bipyramid and vice versa.

(iii) Dualization of the dual of the polyhedron leads to the original polyhedron.

(iv) The degrees of the vertices of a polyhedron correspond to the number of edges in the corresponding face polygons in its dual.

The problem of the classification and enumeration of polyhedra is a complicated one. Thus, there appear to be no formulas, direct or recursive, for which the number of combinatorially distinct polyhedra having a given number of vertices, edges, faces, or any given combination of these elements can be calculated.[12,13] Duijvestijn and Federico have enumerated by computer the polyhedra having up to 22 edges according to the numbers of vertices, edges, and faces and their

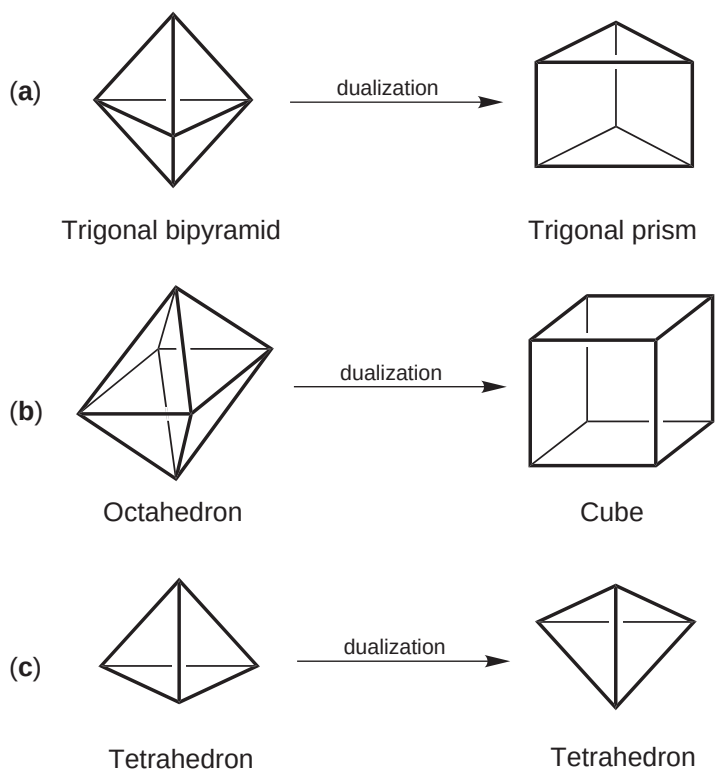

Figure 2 (a) Dualization of the trigonal bipyramid to give the trigonal prism; (b) dualization of a regular octahedron to give a cube; (c) dualization of a tetrahedron to give another tetrahedron indicating the self-dual nature of the tetrahedron.

symmetry groups, and present a summary of their methods, results, and literature references to previous work.[14] Their work shows that there are 1, 2, 7, 34, 257, 2,606, and 32,300 topologically distinct polyhedra having 4, 5, 6, 7, 8, 9, and 10 faces or vertices, respectively. Tabulations are available for all 301 (=1 + 2 + 7 + 34 + 257) topologically distinct polyhedra having eight or fewer faces[15] or eight or fewer vertices.[16] These two tabulations are essentially equivalent by the dualization relationship discussed above.

The following polyhedra are the most important as coordination polyhedra (Table 1):

Coordination number 4: The tetrahedron ($e = 6$, $f = 4$) is the only topologically distinct three-dimensional coordination polyhedron. Many four-coordinate complexes have square planar coordination, but the square is a two-dimensional polygon rather than a three-dimensional polyhedron.

Coordination number 5: The two possible five-coordinate polyhedra are the trigonal bipyramid ($e = 9$, $f = 6$) and square pyramid ($e = 8$, $f = 5$).

Coordination number 6: Among the seven topologically distinct polyhedra having six vertices, the octahedron ($e = 12$, $f = 8$) is the coordination polyhedron found in almost all six-coordinate complexes. However, the trigonal prism ($e = 9$, $f = 5$) occurs in a few early transition metal complexes. There are three pairs of topologically distinct six-vertex polyhedra with the same numbers of edges and faces. The octahedron/bicapped tetrahedron pair ($e = 12$, $f = 8$) is the most readily recognizable such pair (Figure 3).

Coordination number 7: Several polyhedra are found in seven-coordinate complexes of which the pentagonal bipyramid, capped octahedron, and capped trigonal prism are the most important (Figure 4a). Note that the pentagonal bipyramid and capped octahedron are both deltahedra with necessarily the same numbers of edges and faces ($e = 15$, $f = 10$).

Coordination number 8 (Figure 4b): The deltahedron found in eight-coordinate complexes is the bisdisphenoid ($e = 18$, $f = 12$), also called the dodecahedron. However, this terminology is confusing since one of the five Platonic regular polyhedra ($v = 20$, $e = 30$, $f = 12$) is also called the dodecahedron. The square antiprism ($e = 16$, $f = 10$) is also found in some eight-coordinate complexes. The cube ($e = 12$, $f = 6$) is rarely found in eight-coordinate complexes, at least partially because a set of eight hybrid orbitals at the vertices of a cube requires participation of at least one *f*-orbital.

Coordination number 9: This coordination number, which is obviously the highest that can be obtained from the nine orbitals of the sp^3d^5 manifold using simple two-center two-electron

Table 1 Properties of some polyhedra encountered in coordination chemistry.

Polyhedron	*Point group, G*	*Size of G*	*No. of vertices*	*No. of edges*	*No. of faces*
Tetrahedron[a]	T_d	24	4	6	4
Trigonal bipyramid[a]	D_{3h}	12	5	9	6
Square pyramid	C_{4v}	8	5	8	5
Octahedron[a]	O_h	48	6	12	8
Bicapped tetrahedron[a]	C_{2v}	4	6	12	8
Pentagonal pyramid	C_{5v}	10	6	10	6
Trigonal prism	D_{3h}	12	6	9	5
Pentagonal bipyramid[a]	D_{5h}	20	7	15	10
Capped octahedron[a]	C_{3v}	6	7	15	10
Capped trigonal prism	C_{2v}	4	7	13	8
Bisdisphenoid[a]	D_{2d}	8	8	18	12
Square antiprism	D_{4d}	8	8	16	10
Tricapped trigonal prism[a]	D_{3h}	12	9	21	14
Bicapped square antiprism[a]	D_{4d}	16	10	24	16
Edge-coalesced icosahedron[a]	C_{2v}	4	11	27	18
Icosahedron[a]	I_h	120	12	30	20

[a] These polyhedra are deltahedra (i.e., all faces are triangles).

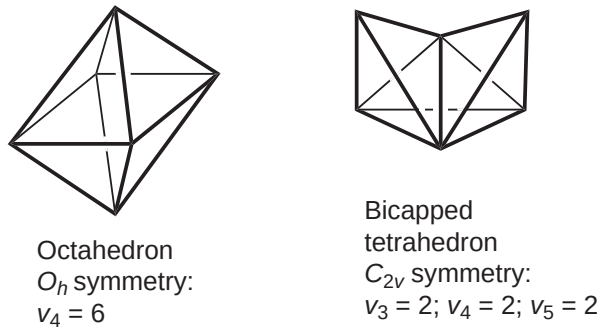

Figure 3 The octahedron and bicapped tetrahedron, which are examples of topological nonequivalent polyhedra with the same numbers of vertices, edges, and faces. Note that the octahedron has all vertices of degree 4 whereas the bicapped tetrahedron has two vertices of degree 3, two vertices of degree 4, and two vertices of degree 5.

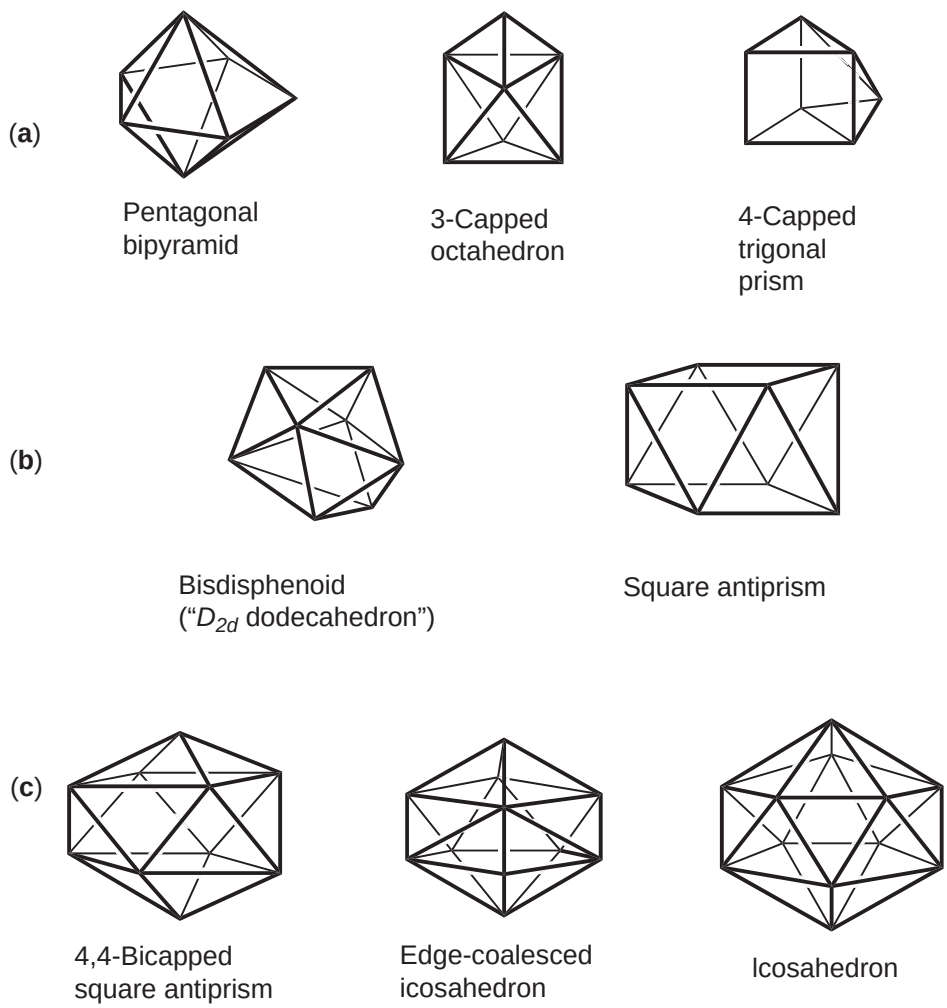

Figure 4 (a) The three most common polyhedra for coordination number 7; (b) The two most common polyhedra for coordination number 8; (c) The common deltahedra with 10, 11, and 12 vertices.

bonding, is rare. Normally, the tricapped trigonal prism ($e = 21$, $f = 14$) is found in such complexes (Figure 1b).

The deltahedra with more than nine vertices listed in Table 1 (Figure 4c) are not normally encountered as coordination polyhedra (except for a few lanthanide and actinide complexes

where *f*-orbitals can be involved). However, they are found in cluster structures including deltahedral boranes of the type $B_nH_n^{2-}$ ($n = 10$, 11, and 12) as well as corresponding carboranes, metallaboranes, and metallacarboranes.

2.47.3 POLYHEDRAL ISOMERIZATIONS

The role of polyhedra in the static description of chemical structures, including those of coordination compounds, makes the dynamic properties of polyhedra also of considerable interest. The central concept in the study of dynamic properties of polyhedra is that of a *polyhedral isomerization*, which may be defined as the deformation of a specific polyhedron Π_1 until the vertices define a new polyhedron Π_2. Of particular interest are sequences of two polyhedral isomerization steps $\Pi_1 \rightarrow \Pi_2 \rightarrow \Pi_3$ in which the polyhedron Π_3 is equivalent to the polyhedron Π_1 but with some permutation of the vertices. Such a polyhedral isomerization process is called a *degenerate* polyhedral isomerization with Π_2 as the *intermediate polyhedron*. A degenerate polyhedral isomerization in which the intermediate Π_2 is a planar polygon may be called a *planar polyhedral isomerization*.

Polyhedral isomerizations may be treated from either the microscopic or macroscopic points of view. The microscopic view uses the details of polyhedral topology to elucidate possible single polyhedral isomerization steps. The macroscopic view presents the relationships between different polyhedral isomers as graphs called *topological representations* in which the vertices depict different permutational isomers of a given polyhedron and the edges depict single degenerate polyhedral isomerization steps.[17] Typically, the midpoints of the edges correspond to an intermediate polyhedron.

First consider some microscopic aspects of polyhedral isomerizations. As early as 1966, Lipscomb[18] described framework rearrangements (isomerizations) in boranes and carboranes in terms of diamond–square–diamond (dsd) processes. Such a dsd process in a polyhedron occurs at two triangular faces sharing an edge and is depicted in Figure 5. In this figure a configuration such as **Ia** can be called a *dsd* situation, the edge AB a *switching edge*, and the quadrilateral face ABCD in structure **Ib** a *pivot face*.[19] If a, b, c, and d are the degrees of vertices A, B, C, and D, respectively, in the original diamond (**Ia**), then the requirement for a degenerate dsd process is the following:

$$c = a - 1 \quad \text{and} \quad d = b - 1 \quad \text{or} \quad c = b - 1 \quad \text{and} \quad d = a - 1 \tag{10}$$

A deltahedron with e edges has e distinct dsd situations; if at least one of these dsd situations is degenerate by satisfying Equation (10), then the deltahedron is *inherently fluxional*.[19] The inherent rigidity/fluxionality of deltahedra having various numbers of vertices is summarized in Table 2. From the point of view of coordination chemistry note that the trigonal bipyramid and bisdisphenoid, which are favored coordination polyhedra for coordination numbers five and eight, respectively, are inherently fluxional whereas the octahedron found in six-coordinate complexes is inherently rigid. This relates to the stereochemical nonrigidity of five- and eight-coordinate complexes observed experimentally in contrast to the relative rigidity of six-coordinate complexes.

Now consider some macroscopic aspects of polyhedral isomerizations as depicted by topological representations,[17] which are graphs in which the vertices correspond to isomers and the edges correspond to isomerization steps. For isomerizations of a polyhedron having n vertices, the number of vertices in the topological representation is the isomer count I defined by the following

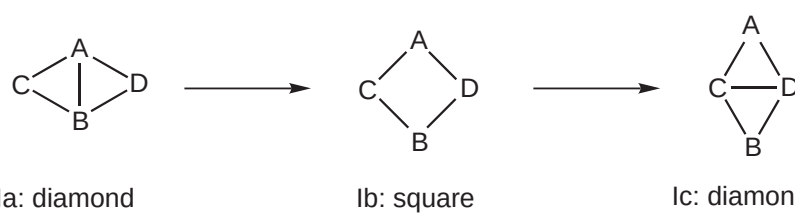

Figure 5 The dsd process occurring at two triangular faces sharing an edge (the "diamond").

Table 2 Inherent fluxionality/rigidity of deltahedra.

Vertices	*Deltahedron*	*Inherently rigid or fluxional*
4	Tetrahedron	Rigid
5	Trigonal bipyramid	Fluxional
6	Octahedron	Rigid
7	Pentagonal bipyramid/Capped octahedron	ML_7→Fluxional Boranes →Rigid
8	Bisdisphenoid	Fluxional
9	Tricapped trigonal prism	Fluxional
10	Bicapped square antiprism	Rigid
11	Edge-coalesced icosahedron	Fluxional
12	Icosahedron	Rigid

equation where $|R|$ is the number of proper rotations in the symmetry point group of the polyhedron in question:

$$I = \frac{n!}{|R|} \tag{11}$$

The degree of a vertex in the topological representation corresponds to the number of distinct permutational isomers that can be generated in a single isomerization from the isomer represented by the vertex in question; this number δ is called the *connectivity*. For topologically distinct polyhedra depicted in the same topological representation, the isomer counts I and I' and connectivities δ and δ' must satisfy the so-called closure condition,[17] i.e.:

$$I\delta = I'\delta' \tag{12}$$

A simple illustration of these ideas is provided in the topological representation of polyhedral rearrangements in four-coordinate compounds of the type ML_4. The favored coordination polyhedron for most such complexes is the tetrahedron, which can undergo degenerate planar isomerization into its enantiomer through a square planar intermediate (Figure 6).[17] The isomer count for the tetrahedron, I_{tet}, is $4!/|T| = 24/12 = 2$ and the isomer count for the square, I_{sq}, is $4!/|D_4| = 24/8 = 3$. A topological representation for this process is a so-called $K_{2,3}$ bipartite graph, which is derived from the trigonal bipyramid by deletion of the three equatorial–equatorial edges. The two axial vertices correspond to the two tetrahedral isomers and the three equatorial vertices correspond to the three square planar isomers. The connectivities of the tetrahedral (δ_{tet}) and square planar (δ_{sq}) isomers are 3 and 2, respectively, in accord with the degrees of the corresponding vertices of the $K_{2,3}$ graph (Figure 6). Since $I_{tet}\delta_{tet} = I_{sq}\delta_{sq} = 6$, the closure condition (Equation (12)) is satisfied for this topological representation.

The topological representations for polyhedral rearrangements in five- and six-coordinate compounds are considerably more complicated.[17] Thus, the 20-vertex Desargues–Levy graph (Figure 7a) is a topological representation of isomerizations of the 20 trigonal bipyramid permutation isomers through the 30 square pyramid isomer intermediates represented by the edge midpoints; these isomerizations correspond to Berry pseudorotations in five-coordinate complexes.[20,21] If the 20 trigonal bipyramidal permutation isomers are depicted as the corresponding 10 pairs of enantiomers, then the topological representation reduces to the Petersen's graph (Figure 7b), which is of interest since it has both threefold and fivefold symmetry. A topological representation of six-vertex polyhedral isomerizations is a double group regular dodecahedron with a K_5 complete graph (i.e., a pentagon and pentagram with all five vertices in common) in each of the 12 faces (Figure 8). The 30 edge midpoints of the dodecahedron (spades, ♠, in Figure 8) correspond to the 30 octahedron permutation isomers. Similarly, the $(12)(10) = 120$ edge midpoints of the 12 K_5 graphs on the dodecahedron (diamonds, ♦, in Figure 8) correspond to the 120 trigonal prism intermediates in trigonal twist processes[17,22,23] (e.g., Bailar twist[24] or Ray and Dutt twist[25] triple dsd processes).

Polyhedra having more than six vertices have isomer counts too large (Equation (11)) for topological representations of their rearrangements to be depicted graphically in a tractable manner by methods similar to those used for polyhedra with four to six vertices described above (Figures 6–8). However,

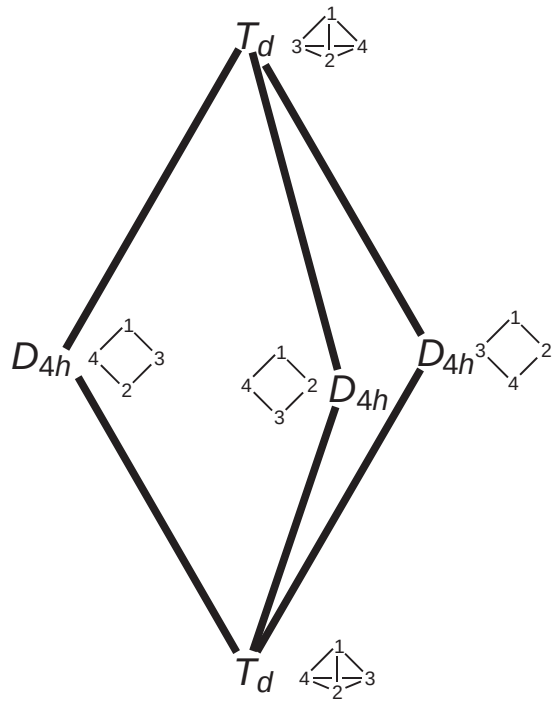

Figure 6 The $K_{2,3}$ bipartite graph as a topological representation of the degenerate planar isomerization of a tetrahedron (T_d) into its enantiomer through a square planar intermediate (D_{4h}). The isomers corresponding to the vertices of the $K_{2,3}$ bipartite graph are depicted next to the vertex labels.

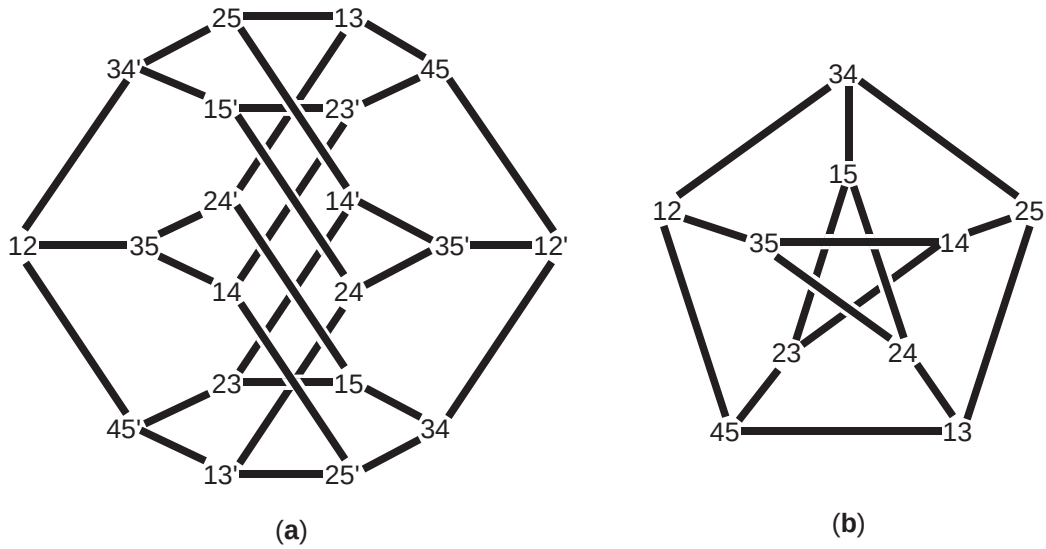

Figure 7 Topological representation of the isomerizations of trigonal bipyramids through dsd processes (Berry pseudorotations). The two digits represent labels for the axial positions with primes used to indicate enantiomers. (a) The Desargues–Levy graph as a topological representation for dsd isomerizations of the 20 trigonal bipyramid isomers; (b) The Petersen's graph as a topological representation for dsd isomerizations of the 10 enantiomer pairs of the trigonal bipyramid isomers.

in the case of eight-vertex polyhedra a tractable graphical topological representation can be obtained by "hyperoctahedral restriction" since the 384-operation symmetry group of the four-dimensional analog of the cube or tesseract contains the symmetries of all of the eight-vertex polyhedra of actual or potential chemical significance.[26]

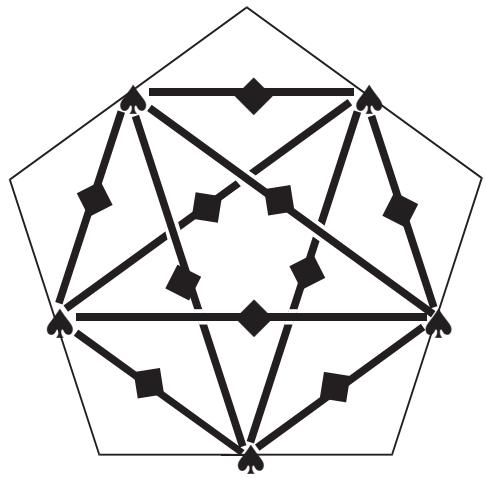

Figure 8 One of the twelve pentagonal faces of the I_h double group pentagonal dodecahedron used as a topological representation for the degenerate triple dsd isomerization of the octahedron (O_h) through a trigonal prismatic intermediate (D_{3h}). The five spades (♠) at the midpoints of the sides of the face represent five of the 30 octahedron permutational isomers whereas the 10 diamonds (♦) at the midpoints of the edges of the K_5 graph drawn on the face represent 10 of the 120 trigonal prism permutational isomers.

2.47.4 SUMMARY

Ideas from the mathematical discipline of topology lead to graphs, which can be used to model chemical structures in which vertices represent atoms and edges represent chemical bonds. Graphs also appear as the skeletons of polyhedra, which are frequently used to describe structures in coordination chemistry. Fundamental to the description of polyhedra is Euler's theorem relating the numbers of vertices, edges, and faces in a given polyhedron. Interconversions between many pairs of polyhedra having the same numbers of vertices can be described either microscopically through dsd processes or macroscopically through graphs known as topological representations. Such ideas originating from topology provide useful insight into a number of problems of interest to coordination chemists including the structures, bonding, and rearrangements of metal coordination and cluster compounds.

2.47.5 REFERENCES

1. Dugundji, J. *Topology*. Allyn and Bacon, Boston, 1966.
2. Munkres, J. R. *Topology*. Prentice-Hall, Englewood Cliffs, NJ, 1975.
3. Merrifield, R. E.; Simmons, H. E. *Topological Methods in Chemistry*. Wiley-Interscience, New York, 1989.
4. Balaban, A. T., Ed., *From Chemical Topology to Three-dimensional Geometry*. Plenum, New York, 1997.
5. Bonchev, D.; Rouvray, D. H., Ed., *Chemical Topology: Applications and Techniques*. Gordon and Breach, Amsterdam, 2000.
6. Diudea, M. V.; Gutman, I.; Lorentz, J. *Molecular Topology*. Nova Science Publishers, Huntington, New York, 2001.
7. Schipper, P. E. *Symmetry and Topology in Chemical Reactivity*. World Scientific, Singapore, 1994.
8. Flapan, E. *Where Topology Meets Chemistry: A Topological Look at Molecular Chirality*. Cambridge University Press, Cambridge, U.K., 2000.
9. Behzad, M.; Chartrand, G. *Introduction to the Theory of Graphs*. Allyn and Bacon, Boston, 1971.
10. Grünbaum, B. *Convex Polytopes*. Interscience Publishers, New York, 1967.
11. King, R. B. *J. Am. Chem. Soc.* **1969**, *91*, 7211–7216.
12. Harary, F.; Palmer, E. M. *Graphical Enumeration*. Academic Press, New York, 1973, p 224.
13. Tutte, W. T. *J. Combin. Theory Ser. B.* **1980**, *28*, 105–126.
14. Duijvestijn, A. J. W.; Federico, P. J. *Math. Comput.* **1981**, *37*, 523–532.
15. Federico, P. J. *Geom. Ded.* **1975**, *3*, 469–481.
16. Britton, D.; Dunitz, J. D. *Acta Cryst.* **1973**, *A29*, 362–371.
17. Muetterties, E. L. *J. Am. Chem. Soc.* **1969**, *91*, 1636–1643.
18. Lipscomb, W. N. *Science* **1966**, *153*, 373–378.
19. King, R. B. *Inorg. Chim. Acta* **1981**, *49*, 237–240.
20. Berry, R. S. *J. Chem. Phys.* **1960**, *32*, 933–938.
21. Holmes, R. R. *Acc. Chem. Res.* **1972**, *5*, 296–303.
22. Muetterties, E. L. *J. Am. Chem. Soc.* **1968**, 5097–5102.

23. Eaton, S. S.; Eaton, G. R. *J. Am. Chem. Soc.* **1973**, *95*, 1825–1829.
24. Bailar, J. C., Jr. *J. Inorg. Nucl. Chem.* **1958**, *8*, 165–175.
25. Ray, P.; Dutt, N. K. *J. Indian Chem. Soc.* **1943**, *20*, 81–92.
26. King, R. B. *Theor. Chim. Acta* **1981**, *59*, 25–45.

Comprehensive Coordination Chemistry II
ISBN (set): 0-08-0437486

Volume 2, (ISBN 0-08-0443249); pp 611–621

2.48
Topology: Assemblies

G. F. SWIEGERS
Commonwealth Scientific and Industrial Research Organisation (CSIRO), Melbourne, Vic., Australia

2.48.1 INTRODUCTION 623
2.48.2 STRUCTURAL CLASSIFICATION OF METALLOCYCLIC 3-D ASSEMBLIES 623
2.48.3 THE ASSEMBLY-DESCRIPTOR METHOD OF CLASSIFYING SELF-ASSEMBLY PROCESSES 624
2.48.4 EXAMPLES OF 3-D METALLOCYCLIC ASSEMBLIES 625
2.48.4.1 Face-occupied Polyhedra 625
2.48.4.2 Cube or Cuboctahedron? 626
2.48.4.3 Truncated Tetrahedron 628
2.48.4.4 Dodecahedron 628
2.48.5 TOPOLOGICAL TRANSFORMATIONS IN ASSEMBLIES 629
2.48.6 CONCLUSIONS 631
2.48.7 REFERENCES 631

2.48.1 INTRODUCTION

The spontaneous self-assembly of multinuclear 3-D molecular polyhedra is an important method of preparing spheroidal or pseudospheroidal molecules.[1] Frameworks of this type enclose cavities which allow them to act as artificial containers in which novel chemistry, biology, and molecular science can be carried out.[1] The principles of topology apply to such species in the same way that they apply to mononuclear complexes. However, interpretation of their topology can be complicated by ambiguity in assigning mathematically based topological structures to real chemical molecules.

This section examines several representative, self-assembled 3-D molecular polyhedra in terms of their topological properties. The intention of this work is to: (i) illustrate the application of topology to self-assembled molecular polyhedra; (ii) provide some pertinent examples to illustrate the concepts; and (iii) describe a method of recognizing possible topological transformations in this field.

This work is designed to be complementary to the preceding Chapter 2.47.

2.48.2 STRUCTURAL CLASSIFICATION OF METALLOCYCLIC 3-D ASSEMBLIES

Because of the wide diversity of architectures available, a coherent classification of metallocyclic molecular polyhedra according to topological principles was notably absent, until MacGillivray and Atwood formalized the description of such species as spheroidal or pseudospheroidal moieties.[2] In their analysis they demonstrated that assemblies of this type could be cataloged according to the principles of solid geometry in which the Platonic and Archimedean solids—along with prisms, anti-prisms, duals, and irregular polyhedra—served as models of spheroidal design. This comparative approach is topologically consistent, since most of these solids can be

Table 1 The number of vertices, edges, and faces in Platonic and Archimedean solids.

Solid	*Vertices*	*Edges*	*Faces (sides to the face)*
Platonic solids			
Tetrahedron	4	6	4(3)
Cube	8	12	12(4)
Octahedron	6	12	8(3)
Dodecahedron	20	30	20(5)
Icosahedron	12	30	20(3)
Archimedean solids			
Truncated tetrahedron	12	18	4(3), 4(6)
Cuboctahedron	12	24	8(3), 6(4)
Truncated cube	24	36	8(3), 6(8)
Truncated octahedron	24	36	6(4), 8(6)
Rhombicuboctahedron	24	48	8(3), 18(4)
Snub cube	24	60	32(3), 6(4)
Icosidodecahedron	30	60	20(3), 12(5)
Rhombitruncated cuboctahedron	48	72	12(4), 8(6), 6(8)
Truncated dodecahedron	60	90	20(3), 12(10)
Truncated icosahedron	60	90	12(5), 20(6)
Rhombicosidodecahedron	60	120	20(3), 30(4), 12(5)
Snub dodecahedron	60	150	80(3), 12(5)
Rhombitruncated icosidodecahedron	120	180	30(4), 20(6), 12(10)

continuously deformed into spheres. In practice however, this method relies on a sometimes subjective recognition of the relationship between idealized polyhedral structures and the chemical building blocks of which 3-D molecular polyhedra are composed. Table 1 lists the names and the number of vertices, edges, and faces for each of the Platonic and Archimedean solids. Space precludes the inclusion of diagrammatic depictions of their structures; these can be viewed elsewhere.[2]

2.48.3 THE ASSEMBLY-DESCRIPTOR METHOD OF CLASSIFYING SELF-ASSEMBLY PROCESSES

The assembly descriptor classification has recently been devised as a means of comparing self-assembly processes in the formation of molecular polygons.[3,4] However, it can be of assistance when classifying the structure of a particular molecular polyhedron. The system abbreviates the properties of each component of an assembly in terms of their geometry and topicity. Thus a building block is listed as angular, A (i.e., subtends an angle of $<180°$ between its binding sites), or linear, L (i.e., subtends an angle of ca. 180° between its binding sites). The building block topicity is specified using a superscript, followed by an "a" to indicate acceptor sites (i.e., a metal ion) or a "d" for donor sites (i.e., a ligand).

Thus, the *in situ* reaction of octahedral Fe^{II} with one equivalent of the tridentate phosphine *triphos* produces the tritopic, angled acceptor unit $Fe(triphos)^{2+}$ (Scheme 1), which is classified an A^{3a} building block since it is able to bind three strong donors on the underside of the Fe^{II} ion (*triphos* = 1,1,1-tris(diphenylphosphinomethane)ethane). The ditopic, linear dicyano ligand (1) is considered to be an L^{2d} component. When these materials are combined in solution in the correct stoichiometry, an $A^{3a}{}_4L^{2d}{}_6$ assembly having the formula $[((triphos)Fe)_4(1)_6]^{8+}$ is formed spontaneously.[5] A clue to the likely topology of this ensemble is given by its assembly descriptor: 6 equivalents of a linear ditopic component, which must make up the edges of the polyhedron, co-exist with 4 equivalents of an angled component, which presumably occupy the vertices. A scan of Table 1 indicates that the tetrahedron is the only symmetrical solid which contains four vertices and six edges. And indeed, the structure of $[((triphos)Fe)_4(1)_6]^{8+}$ in the solid state is a tetrahedron, albeit with a BF_4^- anion encapsulated in its central cavity.[5]

However, not all of the edges, vertices, or faces of a polyhedral assembly need be occupied. Moreover, other geometric solids also exhibit a 4:6 ratio of vertices to edges, e.g., the cube (8:12), and the truncated tetrahedron (12:18). The assembly descriptor of an ensemble consequently

cannot provide an unambiguous topological assignment. Because the assembly components must occupy vertices, edges, or faces of a structure, the topology of a particular polyhedron must nevertheless be consistent with the stoichiometry and topicity of its building blocks, i.e., with its assembly descriptor.

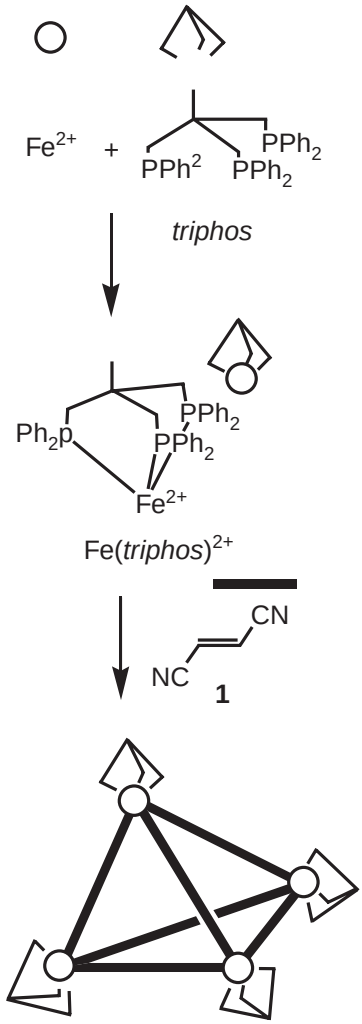

Scheme 1

2.48.4 EXAMPLES OF 3-D METALLOCYCLIC ASSEMBLIES

2.48.4.1 Face-occupied Polyhedra

Most multinuclear molecular polyhedra have metal ions at the vertices and ligands on the edges of the structure. However, increasing numbers of face-occupied polyhedral assemblies are being reported. One example is shown in Scheme 2, which depicts the reaction of $Ti(^{i}OPr)_4$ with the tritopic ligand (**2**) to generate the face-occupied, *T*-symmetric $A^{3a}{}_4A^{3d}{}_4$ assembly $[Ti_4(2)_4]^{8-}$ ($^{i}OPr = i$-propoxide).[6] While the edges of this structure are vacant, the face occupation clearly defines a tetrahedral topology in which the four vertices are occupied by the metal ions and the

four faces by the ligands. The structure displays the property of convexity which is common to all simple polyhedra; i.e., the tetrahedron looks the same regardless of the face on which it is stood.

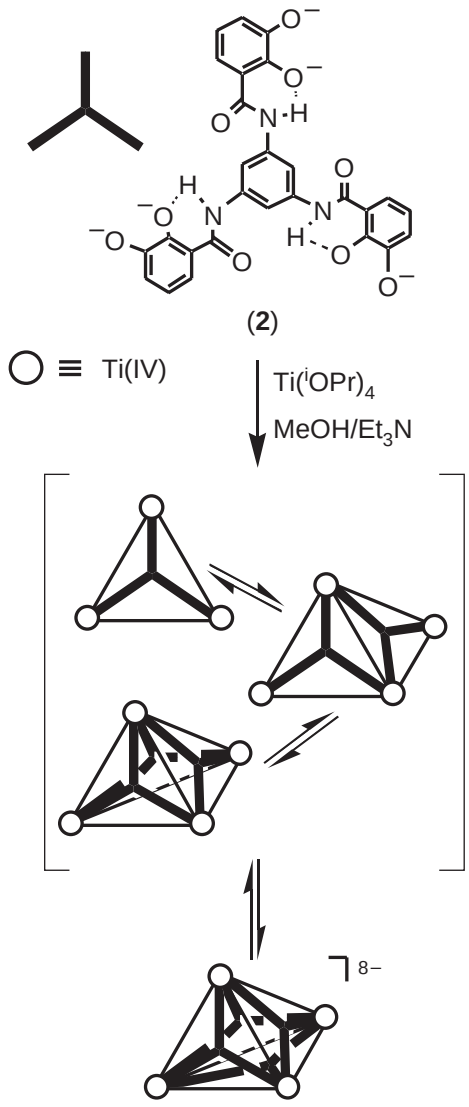

Scheme 2

2.48.4.2 Cube or Cuboctahedron?

The capacity of molecular polyhedra to be face- or edge-occupied can complicate their classification when the distinction between an edge, a corner, and a face is not absolute. An example of such a problem involves the neutral $A^{3a}{}_8A^{2d}{}_{12}$ complex $[Cu_{12}(3)_8]$ (Scheme 3), which is formed by treatment of the deprotonated ligand (**3**) with $Cu(NO_3)_2$.[7] Because the resulting complex contains 8 tritopic centers and 12 linking ditopic components, it fits the topological description of a truncated cube, whose vertices are occupied by the ligands and whose edges are occupied by the metal ions; the 12 faces of the cube are unoccupied. This structure is depicted as the upper product in Scheme 3. However, from a purely visual point of view, the corner faces in a truncated

cube are normally small relative to the other faces, while in $[Cu_{12}(\mathbf{3})_8]$ the ligands occupying the truncated faces are relatively large. The structure can therefore also be considered as a cuboctahedron, whose 12 vertices are occupied by the metal ions and whose 8 three-sided faces are occupied by the ligands; the edges and the four-sided faces of the cuboctahedron are vacant. This organization is depicted as the bottom product in Scheme 3.

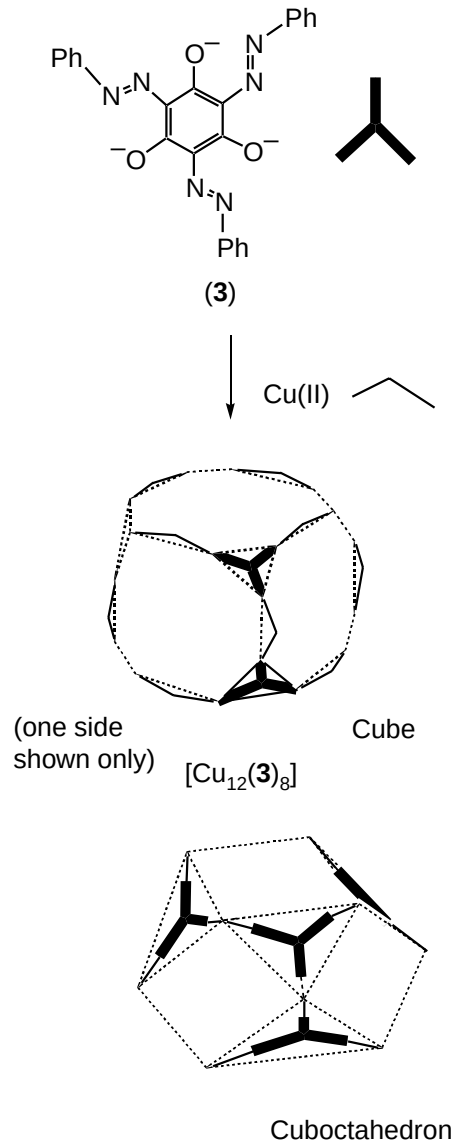

Scheme 3

Which is the more accurate description? Several approaches can be used to decide; none is conclusive. One involves visually comparing the assembly with an edge-occupied example of each of the proposed solids; that which is the most similar provides the best description. Another is to compare the extent of occupation of the structure; the mathematical solid having the most shape-defining units occupied within the polyhedron is considered the more accurate description. By both these measures, $[Cu_{12}(\mathbf{3})_8]$ is closest to a cuboctahedron. As a cube or truncated cube, 12 of its faces are unoccupied, while as a cuboctahedron only the 4 four-sided faces are unoccupied. Moreover, while an example of an edge-occupied cuboctahedron or truncated cube is not known, it is clear that the shape of $[Cu_{12}(\mathbf{3})_8]$ would be closer to the former structure than it is to a cube (like the $A^{3a}{}_8L^{2d}{}_{12}$ assembly $[\{([9]ane\text{-}S_3)Ru\}_8(\mathbf{4})_{12}]^{16+}$ (Scheme 4))[8] or a truncated cube. Purists would argue, however, that the principles of topology demand selection of the least complicated

and most symmetrical of the possible solids, without regard to niceties of appearance. In that case $[Cu_{12}(\mathbf{3})_8]$ would be a cube,[7] since this is a Platonic solid which is simpler than the cuboctahedron or truncated cube, which are Archimidean solids.

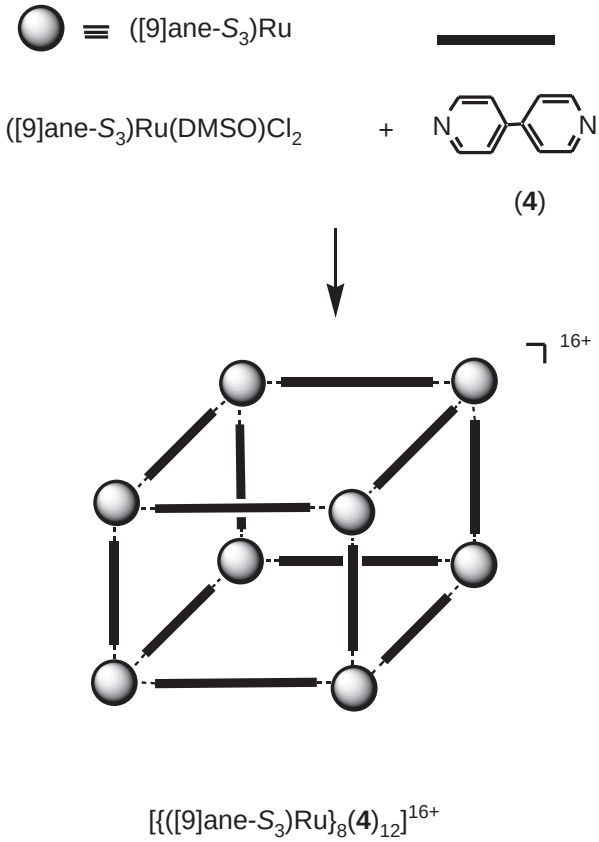

Scheme 4

2.48.4.3 Truncated Tetrahedron

A similar dilemma arises in the formation of partially filled, face-occupied octahedra. An example is given in Scheme 5, which depicts the reaction of the planar A^{3d} benzene tri(ethynyl pyridyl) ligand (**5**) with the triflate of the shape-defining, ditopic A^{2a} metal ion, Pd(*binap*) (*binap* = 2,2′-bis(diphenylphosphino)-1,1′-binaphthyl).[9] The resulting chiral $A^{2a}{}_6A^{3d}{}_4$ assembly $[((R\text{-}binap)Pd)_6(5)_4]^{12+}$ adopts a C_2-symmetric shape in which alternate, opposing faces of an octahedron are occupied on top and bottom (depicted as the upper product in Scheme 5). However, an alternative depiction is that of a truncated tetrahedron which is derived by capping the corners of a tetrahedron, as shown at the bottom of Scheme 5. Most authors consider assemblies like $[((R\text{-}binap)Pd)_6(5)_4]^{12+}$ to be truncated tetrahedral, because this is the more completely filled structure.[1] Symmetry does not distinguish the two topologies, since both the partially filled octahedron and the truncated tetrahedron exhibit *T*-symmetry, as does $[((R\text{-}binap)Pd)_6(5)_4]^{12+}$ itself.

2.48.4.4 Dodecahedron

The pinnacle of achievement in the assembly of 3-D polyhedra is probably the spontaneous formation of $A^{3a}{}_{20}L^{2d}{}_{30}$ dodecahedra by Stang and co-workers. The correct stoichiometric combination of tri(4′-pyridyl)methanol (**6**) (directing angles 108°) (Scheme 6) with a linear bidentate unit, such as bis[4,4′-*trans*-$Pt(PR_3)_2OTf$]benzene (**7**) (directing angle 180°; R = Et, Ph;

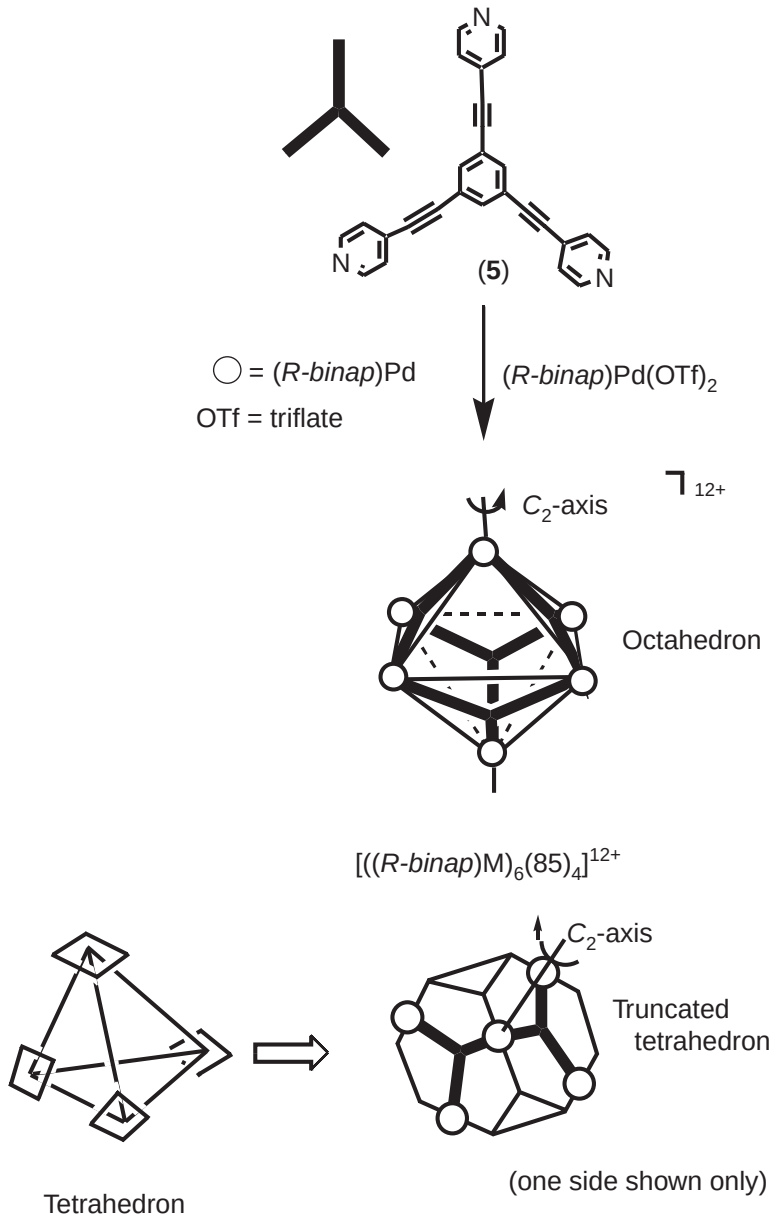

Scheme 5

OTf = triflate), produced the first reported $A^{3a}{}_{20}L^{2d}{}_{30}$ molecular dodecahedra $[(\mathbf{6})_{20}(\mathbf{7})_{30}]^{60+}$ in quantitative yield.[10] The success of this procedure rested on the rigidity of the building blocks, which were able to correctly transmit the directing angles over nanometer-scale distances. Flexible linkers permitted the formation of defects which could not self-correct in the thermodynamic equilibrium. The dodecahedra enclose spheroids of diameter 5–8 nm. The self-assembly of each dodecahedron involved the *in situ* formation of 60 coordination bonds between 50 individual molecules in solution.

2.48.5 TOPOLOGICAL TRANSFORMATIONS IN ASSEMBLIES

The assembly descriptor method of classifying molecular polyhedra allows a ready comparison of the stoichiometry and topicity of the building blocks in assemblies having widely different

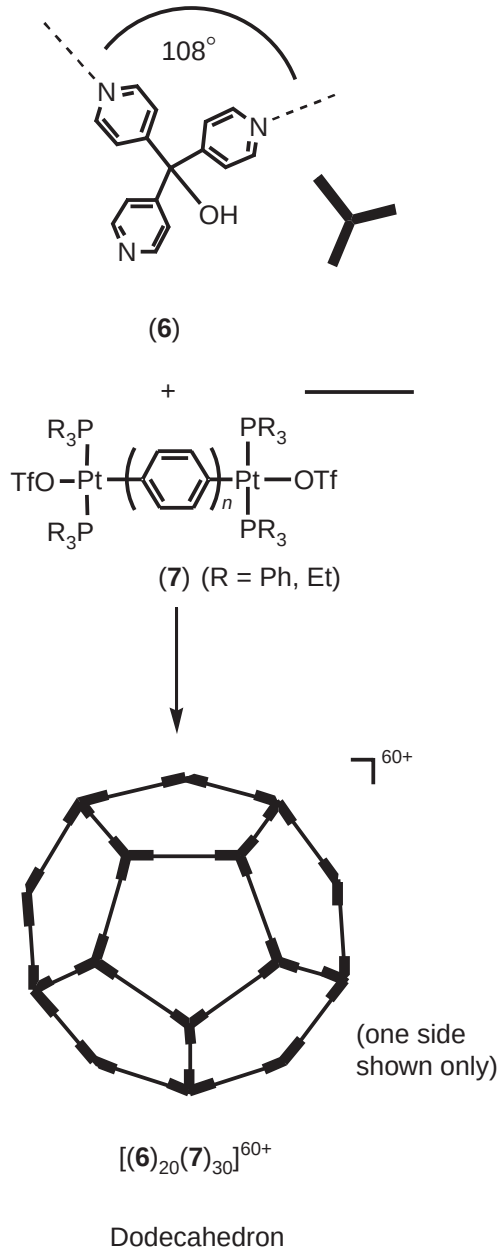

Scheme 6

shapes.[3,4] This is potentially useful when studying possible topological transformations. For example, an edge-occupied $A^{3a}{}_4L^{2d}{}_6$ tetrahedron has the same component ratio and topicity as the following Platonic solids: edge-occupied $A^{3a}{}_8L^{2d}{}_{12}$ cubes, and $A^{3a}{}_{20}L^{2d}{}_{30}$ dodecahedra. The only difference in these assemblies is the directing angles, which are 109.5° for a tetrahedron, 90° for a cube, and 108° for a dodecahedron. An ensemble of one of these shapes which has been formed in a kinetically labile, thermodynamic self-assembly process should therefore spontaneously transform itself to another of the geometries if the directing angle of its A^{3a} components are changed *in situ*. Alterations of this type have been achieved in unrelated systems by electrochemical switching between a Cu^{I} (109.5°) and a Cu^{II} (90°) couple.[11] Topological transformations can also be induced by the presence of third-party molecules.[12] Transformations of such species differ from those of mononuclear complexes, in that connectivity is not maintained. Self-assembly conditions allow structures to dissociate and reassociate in a new shape if a thermodynamic driver is present.

2.48.6 CONCLUSIONS

While the development of new 3-D self-assembled metallocyclic architectures has thrown up some topological challenges, it undoubtedly constitutes an increasingly important avenue of research. As the field grows, more ambiguities of greater complexity can be anticipated. However, these should not obscure the practical potential that 3-D metallocycles hold in areas as diverse as "smart" catalysts or molecular information storage systems.

2.48.7 REFERENCES

1. Leininger, S.; Olenyuk, B.; Stang, P. J. *Chem. Rev.* **2000**, *100*, 853–908.
2. MacGillivray, L. R.; Atwood, J. L. *Angew. Chem. Int. Ed. Engl.* **1999**, *38*, 1018–1033.
3. Swiegers, G. F.; Malefetse, T. J. *Chem. Eur. J.* **2001**, *7*, 3636–3643.
4. Swiegers, G. F.; Malefetse, T. J. *Coord. Chem. Rev.* **2002**, *225*, 91–121.
5. Mann, S.; Huttner, G.; Zsolnai, L.; Heinze, K. *Angew. Chem. Int. Ed. Engl.* **1996**, *35*, 2808–2809.
6. Caulder, D. L.; Bruckner, C.; Powers, R. E.; Konig, S.; Parac, T. N.; Leary, J. A.; Raymond, K. N. *J. Am. Chem. Soc.* **2001**, *123*, 8923–8938.
7. Abrahams, B. F.; Egan, S. J.; Robson, R. *J. Am. Chem. Soc.* **1999**, *121*, 3535–3536.
8. Roche, S.; Haslam, C.; Adams, H.; Heath, S. L.; Thomas, J. A. *Chem. Commun.* **1998**, 1681–1682.
9. Stang, P. J.; Olenyuk, B.; Muddiman, D. C.; Smith, R. D. *Organometallics* **1997**, *16*, 3094–3096.
10. Olenyuk, B.; Levin, M. D.; Whiteford, J. A.; Shield, J. E.; Stang, P. J. *J. Am. Chem. Soc.* **1999**, *121*, 10434–10435.
11. For example: Collin, J.-P.; Gaviña, P.; Sauvage, J.-P. *Chem. Commun.* **1996**, 2005–2006.
12. Caulder, D. L.; Raymond, K. N. *Dalton Trans.* **1999**, 1185–1200 and references therein.

Comprehensive Coordination Chemistry II
ISBN (set): 0-08-0437486

Volume 2, (ISBN 0-08-0443249); pp 623–631

2.49
Electrode Potential Calculations

D. E. RICHARDSON
University of Florida, Gainesville, FL, USA

2.49.1 INTRODUCTION 633
2.49.2 CONVENTIONS FOR SOLUTION AND GAS-PHASE REDOX ENERGETICS 634
2.49.2.1 Standard Electrode Potentials 634
2.49.2.2 Electron Conventions for Gas-phase Oxidation and Reduction 634
2.49.2.3 Single Electrode Potentials 634
2.49.2.4 Other Reference Couples 635
2.49.3 SOLVATION ENERGIES 635
2.49.3.1 Differential Solvation Energies 635
2.49.3.2 The Born Equation 637
2.49.3.3 Other Solvation Energy Models 637
2.49.3.4 Organic Examples of Complete Electrode Potential Calculations 637
2.49.4 SURVEY OF CALCULATIONS FOR TRANSITION METAL COMPLEXES 638
2.49.4.1 Coordination Complexes: Complete Calculations for Aquo Ions 638
2.49.4.2 Complete Calculations for Other Coordination Complexes 639
2.49.4.3 Metalloproteins: General Considerations 639
2.49.4.4 Metalloproteins: Calculations of Bonding Contributions to Electrode Potentials 639
2.49.4.5 Metalloproteins: Complete Calculations of Electrode Potentials 640
2.49.4.6 Future Applications 640
2.49.5 REFERENCES 640

2.49.1 INTRODUCTION

Electron transfer reactions and oxidation–reduction reactions in general are among the most commonly encountered transformations for coordination compounds in solution. Theoretical calculations of the relevant electrode potentials for redox couples are difficult since absolute energy differences between two different electronic configurations must be determined for transition metal complexes. In addition, the role of solvation must be factored in since the impact of the differential solvation energy is substantial.[1,2] Density functional theory (DFT) and appropriate semiempirical methods described earlier in this volume can provide reasonably accurate methods for calculating molecular ionization energies for gas-phase complexes. However, solvation energetics cannot yet be treated at higher levels of theory, such as DFT, and one must resort to rather severe approximations to model the solvent bath. In addition, electrode potentials are fundamentally differential *free energies*, so entropies and heat capacities must be included in complete calculations of the molecular energy changes. Nevertheless, progress has been substantial, and electrode potentials for coordination complexes, even including active sites in metalloproteins, can now be estimated from theory with reasonable accuracy.

2.49.2 CONVENTIONS FOR SOLUTION AND GAS-PHASE REDOX ENERGETICS

2.49.2.1 Standard Electrode Potentials

Comparison of experimental electrode potentials with those calculated by theory requires a common convention for the thermodynamics of oxidation and reduction reactions. The thermodynamics of condensed-phase oxidation–reduction processes are tabulated by using the convention of the *standard electrode potential*,[3] which is defined as the Gibbs free energy per electron for an electrochemical cell reaction involving reduction by dihydrogen to produce the aqueous proton with all reactants at standard conditions ($E^\circ = -\Delta G^\circ/nF$, where n is the number of electrons and F is the Faraday constant). For example, the half cell defining the ferric/ferrous electrode potential as $E^\circ = 0.770\,\text{V}$ (Equation (1)) is an abbreviation for the reaction in Equation (2), for which the standard free energy change $\Delta G^\circ = -17.8\,\text{kcal mol}^{-1}$ when all aqueous species are at unit activity and H_2 is at 1 atm. In standard electrode potential half cells, "e^-" is an abbreviation for $1/2H_2(g) - H^+(aq)$, with the normal hydrogen electrode (NHE, $H^+(aq) + e^- = 1/2H_2(g)$) thereby assigned a value of $E^\circ = 0\,\text{V}$ exactly.

$$Fe^{3+}(aq) + e^- = Fe^{2+}(aq) \quad (1)$$

$$Fe^{3+}(aq) + 1/2H_2(g) = Fe^{2+}(aq) + H^+(aq) \quad (2)$$

2.49.2.2 Electron Conventions for Gas-phase Oxidation and Reduction

The standard electrode potential convention is a different approach from that normally taken with thermodynamic quantities related to chemical change in electron number for gas-phase molecules and ions. Ionization potentials and electron affinities are referenced to the electrostatic zero potential energy of the infinitely separated electron in a field-free vacuum.[4] The electron itself is conventionally treated as an ideal gas (the *thermal electron convention*) or as a subatomic particle with no heat capacity or entropy (the *ion convention*). Ionization/electron attachment enthalpies under the two conventions differ by $1.48\,\text{kcal mol}^{-1}$ at 298 K,[4] while the corresponding free energies under the two conventions are only equal at 0 K and 297 K.[5]

The ion convention is favored by those who apply mass spectrometric equilibrium methods for the determination of electron attachment energies.[4] In such experiments, gas-phase equilibria of the general form $A^q + R \rightarrow A + R^q$ are investigated (q is typically $+1$ or -1 and R is a reference compound). These equilibria are completely analogous to solution redox equilibrium reactions studied in solution or via an electrochemical cell. To obtain values for the energy of the reaction $A^+ + e^- \rightarrow A$ (if $q = +1$), a value must be assigned to the reference couple $R^+ + e^- \rightarrow R$, and this is done from experiment (e.g., photoelectron spectroscopy) and/or theory without consideration of the electron thermochemistry above 0 K.

It is important to note that gas-phase energies for ionization and electron attachment used for thermochemical cycles involving solution electrode potentials must strictly be adiabatic free energies rather than vertical energies as obtained in photoelectron spectroscopy and related techniques. The energy of an adiabatic ionization reaction will reflect the final geometry (bond distances, angles) of the ionized acceptor, while a vertical ionization is the energy for the process with the original nuclear positions frozen.[4] Furthermore, free energies for the gas-phase process must be estimated with appropriate inclusion of heat capacity and entropy differences for the initial and final states.[5] It is also possible to estimate the difference between vertical and adiabatic energies for solution redox couples, as shown by Gorelsky *et al.* who used outer-sphere charge transfer transitions to derive estimated total reorganization energies for many coordination redox couples.[6]

2.49.2.3 Single Electrode Potentials

Gas-phase ionization energies or electron affinities for molecular species calculated by quantum mechanics do not include the thermodynamic properties of the free electron and can be compared directly to the tabulations of experimental data for these processes in the ion convention. To relate condensed- and gas-phase redox thermochemistry directly, however, a common convention must be adopted. Electrode potentials can be converted to the gas-phase convention for reaction in which there is a change in the number of electrons. The *single electrode potential* (E_s°) can be

defined as the potential for a half cell in which the e^- is a free electron. For the NHE, E_s° is estimated by summing the Gibbs energies at 25 °C of Equations (3)–(5) giving Equation (6) and $E_s^\circ = 4.44$ V.[7] The value of 4.44 V is estimated to be accurate to within ~50–100 mV. The difficulty in estimating a more accurate absolute free energy for the hydrogen electrode arises from the limitations of various experimental approaches used to obtain the approximate free energy change for Equation (4), which cannot be quantified by direct experiment (the values for Equations (3) and (5) are known accurately).[7–12] High-level *ab initio* theoretical calculations on Equation (4) using a fully polarizable continuum model for solvation of $H^+(H_2O)_n$ supermolecule clusters[13] support a value of $\Delta G^\circ = 262.4$ kcal mol^{-1} (this value results in $E_s^\circ = 4.34$ V for the NHE).

$$H^+(g) + e^-(g) = H(g) \qquad \Delta G^\circ = -314.1 \text{ kcal mol}^{-1} \tag{3}$$

$$H^+(aq) = H^+(g) \qquad \Delta G^\circ = 260.0 \text{ kcal mol}^{-1} \tag{4}$$

$$H(g) = 1/2H_2(g) \qquad \Delta G^\circ = -48.5 \text{ kcal mol}^{-1} \tag{5}$$

$$H^+(aq) + e^-(g) = 1/2H_2(g) \qquad \Delta G^\circ = -102.6 \text{ kcal mol}^{-1} \tag{6}$$

Since standard electrode potentials are referenced to the NHE, the values of E_s° for other half cells can be obtained readily. For example, the value for Equation (7) is 5.21 V.

$$Fe^{3+}(aq) + e^-(g) = Fe^{2+}(aq) \qquad E_s^\circ = 5.21 \text{ V} = -120 \text{ kcal mol}^{-1} \tag{7}$$

Most authors apply the value of 4.44 V (or a related estimate) to the theoretically calculated free energies for redox couples and report calculated potentials vs. NHE. This approach is of course equivalent to that above.

Single electrode potentials can be partitioned into enthalpic and entropic components ($E_s^\circ = -\Delta G_s^\circ/nF = (-\Delta H_s^\circ + T\Delta S_s^\circ)/nF$). Entropic contributions to the free energy change can be substantial when large electron configuration changes occur between the oxidized and reduced complexes.[14] When high-spin to low-spin interconversions occur the resulting shifts in low-frequency metal–ligand vibrations can lead to large entropy changes.[14,15]

2.49.2.4 Other Reference Couples

A second method to allow comparison of theory with experiment in electrode potential calculations is to establish a reference couple in the calculations and compare all other calculated energies to that couple, bypassing the issue of conversion to the standard potential directly. The differential energies can then be compared to the experimentally observed differences for the same species. This approach is not fundamentally different from the use of a standard couple, such as the NHE, rather than an assumed value for the reference electrode potential, in the experimental determination of electrode potentials. For example, the ferrocenium/ferrocene couple is commonly used as a reference in the electrochemistry of organometallic compounds, which are often studied in nonaqueous media.[16] Quantum calculations of the electrochemical potentials could be referenced to the calculated ferrocenium/ferrocene potential, and the experimental values would then be directly comparable to the calculations. Such an approach could be especially useful in cases where rather subtle effects are being considered, as in the study of substituent effects or systematic alterations in the ligand environment of a metal complex. Of course, what is lost is an overall appreciation for the origin of the absolute energetics of the redox process, including a division of the potentials into metal–ligand bonding energies and differential solvation energies.[1,2]

2.49.3 SOLVATION ENERGIES

2.49.3.1 Differential Solvation Energies

A thermochemical cycle is shown in Figure 1, which illustrates the separation of condensed-phase electrode potentials into inner-sphere bonding and outer-sphere solvation contributions. Of

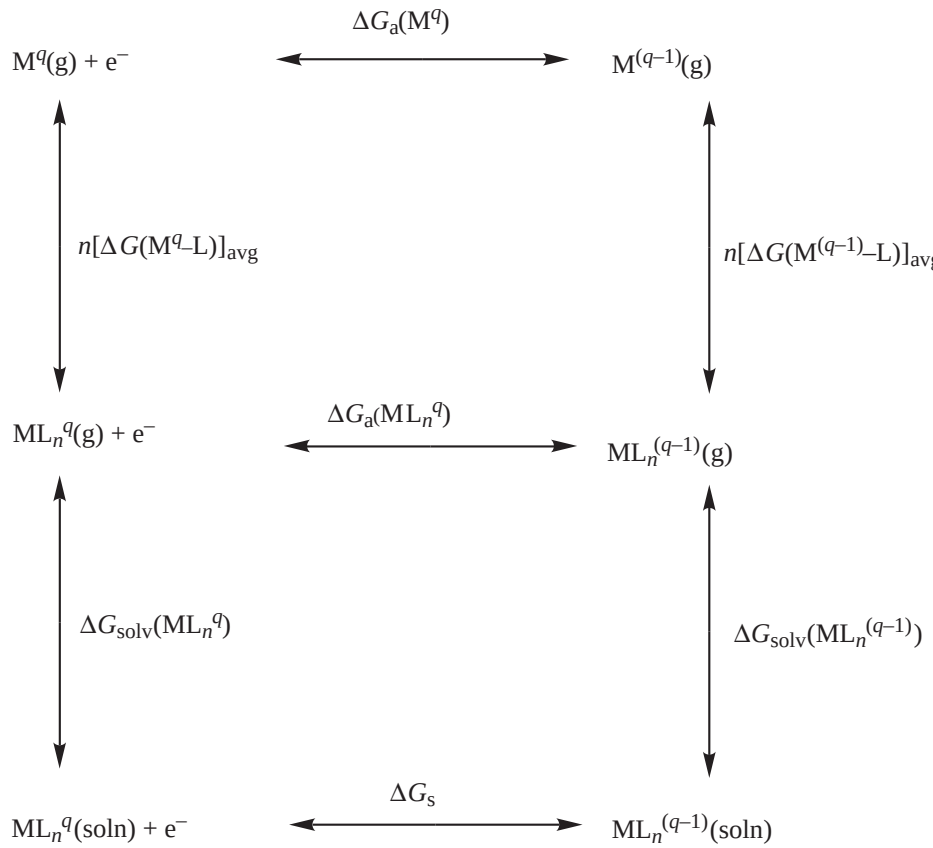

Figure 1 Thermochemical cycles illustrating the relationship of gas-phase electron attachment energies, average metal–ligand bond energies, and differential solvation energies to single electrode potentials in solution.

course, such a partitioning is completely arbitrary, but it does reflect both the experimentally and theoretically accessible quantities. From this cycle, the differential solvation free energy is defined by

$$\Delta\Delta G^\circ_{solv} = \Delta G^\circ_{solv}(ML_n^{q-1}) - \Delta G^\circ_{solv}(ML_n^{q}) = \Delta G_s^\circ - \Delta G_a^\circ \tag{8}$$

which shows that the $\Delta\Delta G^\circ_{solv}$ value is also given by the difference between the single electrode free energy in solution ΔG_s° and the gas-phase electron attachment energy ΔG_a° for the fully ligated but unsolvated complex. Note that electron attachment refers here to addition of an electron to a species having any charge q, not just to the case when $q = 0$.

Differential solvation energies can be quite large for highly charged species with small molecular radii compared to larger complexes with low charge. In addition, the sign of $\Delta\Delta G^\circ_{solv}$ obviously depends on the sign of the charges on the complexes. For example, the estimated $\Delta\Delta G^\circ_{solv}$ value for decamethylferrocene(+/0) is $24\,kcal\,mol^{-1}$,[17] while $\Delta\Delta G^\circ_{solv}$ for the $[Fe(CN)_6](3-/4-)$ couple is estimated to be $-250\,kcal\,mol^{-1}$.[2]

Experimental values for gas-phase ionization and electron attachment free energies are available for a relatively small number of coordinatively saturated transition metal coordination complexes[2,18–22] and organometallic compounds.[17,22–26] High-quality theoretical approaches, such as DFT, can be used to calculate these same gas-phase energies, and most of the attention has been on organometallic compounds rather than gas-phase coordination complex ions.[27,28] Calculation of solution electrochemical energies, which are readily obtained experimentally for many coordination complexes, is normally done by modifying the calculated gas-phase energies with estimates of differential solvation energies based on nonquantum models such as the dielectric continuum reaction field model.

2.49.3.2 The Born Equation

The Born equation[29] is a very simple but surprisingly useful dielectric continuum model for solvation energetics. From the Born equation

$$\Delta G_{el} = \frac{-(qe)^2}{8\pi\varepsilon_0 a}\left(1 - \frac{1}{D_s}\right) \tag{9}$$

electrostatic solvation free energies are derived for a conducting sphere of radius a and charge q in a dielectric continuum with static dielectric constant D_s. In Equation (9), ε_0 is the vacuum permittivity and e is the elementary charge. The definition for ΔG_{el} is the electrostatic free energy change when a charge on a conducting sphere in a vacuum is transferred to a sphere of equal radius in the dielectric medium. The relationship of $\Delta\Delta G^{\circ}_{solv}$ to the Born equation can be illustrated readily for the cases where $q = +1$ or 0. For example, if $q = 0$, then the $\Delta\Delta G^{\circ}_{solv}$ value is the free energy change for Equation (10).

$$ML_n^{-}(g) + ML_n^{0}(solv) \longrightarrow ML_n^{-}(solv) + ML_n^{0}(g) \tag{10}$$

It is apparent that the free energy change for Equation (10) is reasonably modeled by the Born equation for roughly spherical complexes since the chemical change involves transfer of a charge from the gas-phase complex to a neutral complex of approximately equal dimensions in solution. Thus comparisons of experimental $\Delta\Delta G^{\circ}_{solv}$ values with theoretical models often begin with the Born model, and the value of a can be adjusted to an effective thermochemical radius that yields agreement between $\Delta\Delta G^{\circ}_{solv}$ and ΔG°_{el} values.[30] Large differences between the effective radii and structural radii from known molecular dimensions are usually indications of specific interactions (such as hydrogen bonding or Lewis acid–base interactions) between the first solvation shell and the inner-sphere ligands.[30,31]

2.49.3.3 Other Solvation Energy Models

Most coordination complexes are not well modeled as spheres of uniform charge (e.g., metalloprotein active sites are an extreme example). Therefore, more sophisticated dielectric continuum reaction field models are generally employed to take into account the shape of the complex and even account for the dielectric properties of the ligands themselves. Furthermore, the charge distribution and/or polarity of the complex can be used to model discretely the reaction field energies at various points on the exterior surface of the solute.[32] There are many variations of such solvent models, some of which are available in standard quantum chemistry programs.

It is certainly possible to model solvation for redox energetics by extending the quantum calculation to include solvent molecules in the first solvation shell and beyond. Of course, such calculations rapidly become impractical as layers of solvent are added. Since solvation of ions is strongly correlated with the dipolar density of the solvent (i.e., the solvent molecular dipole divided by molecular volume),[33] intermediate models treating solvent molecules as dipolar structures are often a reasonable compromise.[34–39] Some solvation models used in literature redox potential calculations are discussed in the survey below. It is notable that experimental stepwise energies of outer-sphere solvation (i.e., the energies of the sequential binding of solvent molecules in the first solvation shell of complex ions) have become accessible for multicharged ions as a result of solvent cluster methods in mass spectrometry, in particular electrospray ionization.[40–48] These experimental values provide a useful benchmark for examining the quality of quantum mechanical calculations for solvent binding energies when the solvent is treated at the molecular level.

2.49.3.4 Organic Examples of Complete Electrode Potential Calculations

Several groups have performed high-quality theoretical calculations on organic redox couples such as quinones and anilines.[49–59] These calculations provide a calibration of the level of

accuracy that can be expected for various theoretical methods for combining ionization energy calculations with approximate solvation models. (Ionization energies for organic molecules can typically be obtained more accurately by theory and/or experiment than those for coordination compounds.) For example, Winger *et al.*[55] compared semiempirical and DFT approaches (combined with various dielectric continuum models for the solvation energies) to calculate the electrode potentials of aniline and a set of 21 mono- and disubstituted anilines, and they found both methods could yield good agreement with experiment (mean unsigned errors <100 mV or about 2 kcal mol^{-1} in the best cases). As another example, Wright and Reynolds[50] calculated the electrode potentials of a series of nitroimidazoles (by using a combination of DFT for the solute and a semiempirical modified Born method (AM1 SM2) for the solvent) with a mean accuracy of about 80 mV.

2.49.4 SURVEY OF CALCULATIONS FOR TRANSITION METAL COMPLEXES

2.49.4.1 Coordination Complexes: Complete Calculations for Aquo Ions

A fundamental study of transition metal aquo complexes was reported in 1996 by Li *et al.*[60] Specifically, they investigated the application of DFT calculations to the Mn(3+/2+) and Fe(3+/2+) aqueous redox couples and modeled the solvent reaction field by a dielectric continuum.[61] They used discrete cluster approximations for the DFT part of the calculations in which the six inner-sphere and, in some calculations, twelve outer-sphere waters were treated quantum mechanically. The geometry of the inner-sphere cluster (six-coordinated waters) was obtained with DFT and excellent agreement with known structural metrics was confirmed. The structure of the first solvation shell was treated less accurately, and a cluster model was chosen with two hydrogen-bound waters per inner-sphere water. They further employed a numerical finite difference method to calculate the solvent reaction field potential induced by the charge distribution of the clusters (comparisons were also obtained in which the first solvation shell was not explicitly modeled but simply included in the solvent continuum). A self-consistent approach was used in which the DFT energy was recalculated to obtain the molecular charge distributions in the reaction field followed by a reaction field recalculation with the new cluster charges until convergence was obtained. The solute interior was defined by the Connolly method[62,63] in which a probe sphere of radius 140 pm is computationally rolled on the van der Waals surface of the molecular cluster.

In the study of Li *et al.*[60] good agreement was found between experimental and theoretical hydration energies, with somewhat better agreement for the full 18-water cluster compared to the 6-water cluster. The authors carefully partition the components of the redox energy (free energy) calculation to include geometry relaxation and relativistic corrections:

$$E^{\circ}_{\text{redox}} = \text{IP(g)} - \Delta\Delta E_{\text{solv}} + T\Delta S(\text{aq}) + \Delta\text{NHE} + \Delta E_{\text{rel}} + \Delta E_{\text{geom}} \tag{11}$$

(all quantities in volts). The authors used 4.43 V as the absolute potential of NHE (thus $\Delta\text{NHE} = -4.43$ V in Equation (11)), and the entropy change $T\Delta S$(aq) was obtained from literature data (0.55 V). (Entropy increases upon reduction of a positively charged metal complex as a the result of the more loosely bound ligands in the reduced form and, predominantly, the reduced polarization and orientation of the solvent around an ion of lower charge.) The geometry relaxation term accounts for the difference between the vertical ionization potential (of ML_n^{2+}) and the adiabatic energy in which the bond lengths and angles are relaxed to their equilibrium values following ionization.

The calculated electrode potentials (vs. NHE) for the Mn(3+/2+) and Fe(3+/2+) couples using the full 18-water model are 1.59 V and 1.06 V, respectively, and these values compare favorably with the experimental values of 1.56 V and 0.77 V. It was shown clearly that calculated potentials are closer to experiment when a larger portion of the solvation shell is treated quantum mechanically. For the 6-water model, the deviation of theory from experiment was ca. 1 V, and when all waters were modeled only by a continuum, the deviations of theory from experiment exceed 2 V. This observation can be understood in terms of the dielectric saturation that occurs in the vicinity of an ion in solution and the resulting failure of the dielectric continuum model with a single dielectric constant to account for the energetic contributions by solvent molecules in the inner-sphere and the strongly hydrogen bound first solvation shell.[30]

2.49.4.2 Complete Calculations for Other Coordination Complexes

Reynolds and co-workers applied DFT methods to the calculation of redox potentials for Co(3+/2+) couples where the cobalt is ligated by various ligands such as ammonia, ethylenediamine (en), diethylenediamine (dien), and oxalate.[64–66] In their work, the $[Co(dien)_2](3+/2+)$ couple was used a reference, and solvation was treated by the Poisson–Boltzmann method, which had been shown to calculate solvation energies with high accuracy.[67] The boundary between the solute interior and the solvent was based on atomic radii and a 140 pm radius for water. In later work, Reynolds and co-workers[66] proposed a modification of the solvation model to account for solute polarization, which they considered a major source of error in the Poisson–Boltzmann method for complexes with more highly polarizable ligands (dien compared to water, for example). Reasonable agreement was found between theory and experiment for relative electrode potentials of the cationic Co complexes (errors of the order of 50–300 mV), but larger errors were generally encountered for the anionic $[Co(ox)_3]^{3-/4-}$ couple. The experimental trends in the ionic strength dependence were reproduced closely by the Poisson–Boltzmann solvation model. The work by Reynolds and co-workers shows how sensitive electrode potential calculations are to the quality of quantum modeling of the complex and the specifics of the solvent treatment.

The small number of papers applying high-level theory to the complete calculation of electrode potentials for classical coordination complexes (which often have well-documented and accurately known electrode potentials) makes it difficult to judge the ultimate accuracy that can be expected for new calculations. The field would benefit from broad comparative studies of modern quantum theoretical methods applied to a variety of ligand, metal oxidation state, and charge combinations.

Ziegler and co-workers reported DFT with self-consistent reaction field calculations on multielectron redox reactions for dinuclear iron complexes $[Fe_2(CO)_6(\mu_2\text{-}PR_2)_2]^{0/-1/-2}$ ($R = CH_3,\ CF_3$).[68] They did calculations on all three oxidation states for the complexes to construct energy profiles for the addition of two electrons to the $q = 0$ oxidation state. It was found that inclusion of solvent and/or ion pairing effects was necessary to predict the experimentally observed disproportionation reaction of the singly reduced complex. It was also found that CO ligands are important in the delocalization of added electron density due to reduction. Interestingly, the authors also conclude that ion pairing with the anionic complexes should be modeled to produce the most realistic calculations.

2.49.4.3 Metalloproteins: General Considerations

Holm *et al.*[69] have referred to metalloproteins as "elaborated inorganic complexes," and it is computationally and conceptually useful to consider the immediate environment of a transition metal in a protein active site as a coordination complex surrounded by an unusual solventlike environment provided by the folded polypeptide of the protein.[35] In many cases, redox active metal binding sites are sufficiently embedded in the protein matrix such that the actual solvent (water and/or lipid membranes) may have little impact on the redox thermochemistry of the site. Specific features of the active site beyond the first coordination shell (e.g., hydrogen bonds, charged peptide side chains) can have a significant impact on the redox properties of the site. Spectroscopic probes based on the properties of the metal "reporter" can then provide detailed information about the bonding and electronic structure of the redox active site.[69–73] Thus, rather spatially limited theoretical calculations on redox active metal sites can be used to complement and interpret experimental data.

The protein matrix can be modeled as a continuum, but generally a much lower dielectric constant (of the order of 2–20) must be chosen than for water (78) to fit experimental data.[35,39] Since reaction fields of lower dielectric constant disfavor more highly charged complexes, differences in redox potentials for metal site models in polar solvents vs. the active site itself can be significant. Simple estimates can be done by using the Born equation (Equation (9)). For example, the electrode potential of a $ML_n(-1/-2)$ redox couple with a 400 pm radius is predicted to shift positively by $\sim$1.3 V when transferred from water to a medium with dielectric constant 4.

Several groups have investigated how solvent models affect theoretical predictions for redox energetics for metalloproteins such as azurin,[74] heme proteins,[75–78] and iron–sulfur proteins.[34,79]

2.49.4.4 Metalloproteins: Calculations of Bonding Contributions to Electrode Potentials

Solomon and co-workers[69–73,80] have investigated the redox properties of blue copper proteins (plastocyanin and azurin) and other copper or iron proteins via a combination of experiment and

theory (Xα/density functional). These calculations and accompanying experiments focus on the important bonding contributions to redox properties of metalloproteins. For example, with respect to the blue copper site, they conclude that the relatively high potential is explained primarily by (i) the unusually low energy of the redox orbital ($d_{x^2-y^2}$) in the distorted tetrahedral stereochemistry of the site and (ii) the relatively high effective Cu nuclear charge that results from the nature of the donor ligands (particularly the long Cu—S bond to methionine). Thus, theory suggests that entactic state considerations are not the source of the high potential but rather the nature of ligation in the active site determines the potential. This point of view is supported by Ryde and co-workers, who have used purely theoretical approaches (DFT coupled to molecular mechanics) to examine the inner-sphere bonding and the role of protein strain in the blue copper proteins.[81–84]

Other similar theoretical examinations of the role of bonding in the thermodynamics and other properties of redox metalloproteins have appeared. They include binuclear copper-A sites[85] and cytochrome P450.[86]

2.49.4.5 Metalloproteins: Complete Calculations of Electrode Potentials

A relatively large number of theoretical studies on the complete calculation of redox potentials of transition metal active sites in metalloproteins have been published. Metalloproteins studied include manganese superoxide dismutase,[87–90] iron superoxide dismutase,[88] copper–zinc superoxide dismutase,[91] iron–sulfur proteins,[92–97] cytochrome f,[98] components of the photosynthetic reaction center,[13,99,100] and peroxidases.[101]

In their pioneering study of DFT/solvent continuum methods applied to metalloprotein iron–sulfur active site models, Mouesca and co-workers[92] found good correspondence between theoretical and experimental electrode potentials for one-, two-, and four-iron clusters. The largest errors were found to be about 0.5 V ($\sim$12 kcal mol^{-1}). The authors point out that this error is less than 10% of the large contributing terms to the overall potentials, such as the differential solvation energies.

A series of papers on manganese superoxide dismutase (MnSOD)[87–90] nicely illustrate the complexity of electrode potential calculations for metalloproteins. In a relatively simple approach, the crystallographic atom positions in the immediate vicinity of the active site (Mn and its peptide ligands along with bound water) were used to obtain energies for both the active and reduced forms via DFT. Solvation in an aqueous environment was treated by self-consistent dielectric continuum methods used in the calculations for aqueous couples described above.[60] In later calculations on the same site, the authors used DFT to geometry optimize the reduced and oxidized forms of the active site and accounted for the protein reaction field as a dielectric continuum with a dielectric constant of 4. In this latter work, the final calculated electrode potential (vs. NHE) was 0.06 V, which is comparable to the experimental values of 0.26 V and 0.31 V for MnSOD from two bacterial sources. Again, the errors are small relative to the large contributors to the overall redox energy.

Calculations for the electrode potential of iron SOD also gave good agreement of theory (0.16 V) with experiment (0.25 V).[88] The combined DFT/electrostatics approach used by these authors also was found to reproduce the trends in electrode potentials of MnSODs when calculated for various native proteins and a mutant MnSOD.

2.49.4.6 Future Applications

Calculations of electrode potentials for metal complexes in solution and metalloproteins have progressed remarkably with increasing computational power and the greater sophistication of combined quantum/classical models. It is clear that the portion of the problem accessible to quantum methods will continue to expand in the future, revealing even more subtle aspects of the relation of redox thermochemistry to structure, bonding, and solvation.

2.49.5 REFERENCES

1. Buckingham, D. A.; Sargeson, A. M. In *Chelating Agents and Metal Chelates*, Dwyer, F. P.; Mellor, P. D., Ed.; Academic Press: New York, 1964; pp 237–282.
2. Richardson, D. E. *Inorg. Chem.* **1990**, *29*, 3213–3217.

3. Bard, A. J.; Parsons, R.; Jordan, J., Eds., *Standard Electrode Potentials in Aqueous Solution* **1985**, Marcel Dekker: New York.
4. Lias, S. G.; Bartmess, J. E.; Liebman, J. F.; Holmes, J. L.; Levin, R. D.; Mallard, W. G. *Gas-phase Ion and Neutral Thermochemistry* **1988**, American Institute of Physics: New York.
5. Sharpe, P.; Richardson, D. E. *Thermochim. Acta* **1992**, *202*, 173–179.
6. Gorelsky, S. I.; Kotov, V. Y.; Lever, A. B. P. *Inorg. Chem.* **1998**, *37*, 4584–4588.
7. Trasatti, S. *Pure Appl. Chem.* **1986**, *58*, 955–966.
8. Trasatti, S. *Electrochim. Acta* **1990**, *35*, 269–271.
9. Reiss, H. *J. Electrochem. Soc.* **1988**, *135*, C247–C258.
10. Trasatti, S. *Int. J. Hydrogen Energy* **1987**, *12*, 589–589.
11. Hansen, W. N.; Hansen, G. J. *Phys. Rev. Lett.* **1987**, *59*, 1049–1052.
12. Pleskov, Y. V. *J. Phys. Chem.* **1987**, *91*, 1691–1692.
13. Zhang, L. Y.; Friesner, R. A. *J. Phys. Chem.* **1995**, *99*, 16479–16482.
14. Richardson, D. E.; Sharpe, P. *Inorg. Chem.* **1993**, *32*, 1809–1812.
15. Richardson, D. E.; Sharpe, P. *Inorg. Chem.* **1991**, *30*, 1412–1414.
16. Noviandri, I.; Brown, K. N.; Fleming, D. S.; Gulyas, P. T.; Lay, P. A.; Masters, A. F.; Phillips, L. *J. Phys. Chem. B* **1999**, *103*, 6713–6722.
17. Ryan, M. F.; Richardson, D. E.; Lichtenberger, D. L.; Gruhn, N. E. *Organometallics* **1994**, *13*, 1190–1199.
18. Sharpe, P.; Alameddin, N. G.; Richardson, D. E. *J. Am. Chem. Soc.* **1994**, *116*, 11098–11108.
19. Sharpe, P.; Eyler, J. R.; Richardson, D. E. *Inorg. Chem.* **1990**, *29*, 2779–2787.
20. Sharpe, P.; Richardson, D. E. *Coord. Chem. Rev.* **1989**, *93*, 59–85.
21. Sharpe, P.; Richardson, D. E. *J. Am. Chem. Soc.* **1991**, *113*, 8339–8346.
22. Richardson, D. E. In *Organometallic Ion Chemistry*, Freiser, B. S., Ed.; Kluwer: Dordrecht 1996; pp 259–282.
23. Richardson, D. E.; Christ, C. S.; Sharpe, P.; Eyler, J. R. *J. Am. Chem. Soc.* **1987**, *109*, 3894–3902.
24. Richardson, D. E.; Ryan, M. F.; Khan, M. N. I.; Maxwell, K. A. *J. Am. Chem. Soc.* **1992**, *114*, 10482–10485.
25. Ryan, M. F.; Siedle, A. R.; Burk, M. J.; Richardson, D. E. *Organometallics* **1992**, *11*, 4231–4237.
26. Ryan, M. F.; Eyler, J. R.; Richardson, D. E. *J. Am. Chem. Soc.* **1992**, *114*, 8611–8619.
27. Fey, N. *J. Chem. Technol. Biotechnol.* **1999**, *74*, 852–862.
28. Ishimura, K.; Hada, M.; Nakatsuji, H. *J. Chem. Phys.* **1902**, *117*, 6533–6537.
29. Born, M. *Z. Physik* **1920**, *1*, 45.
30. Millen, W. A.; Watts, D. W. *J. Am. Chem. Soc.* **1967**, *89*, 6051–6056.
31. Drago, R. S.; Richardson, D. E.; George, J. E. *Inorg. Chem.* **1997**, *36*, 25–32.
32. Bashford, D.; Case, D. A. *Ann. Rev. Phys. Chem.* **2000**, *51*, 129–152.
33. Mu, L.; Drago, R. S.; Richardson, D. E. *J. Chem. Soc., Perkin Trans. 2* **1998**, 159–167.
34. Stephens, P. J.; Jollie, D. R.; Warshel, A. *Chem. Rev.* **1996**, *96*, 2491–2513.
35. Warshel, A.; Papazyan, A. *Curr. Opin. Struct. Biol.* **1998**, *8*, 211–217.
36. Papazyan, A.; Warshel, A. *J. Chem. Phys.* **1997**, *107*, 7975–7978.
37. Papazyan, A.; Warshel, A. *J. Phys. Chem. B* **1997**, *101*, 11254–11264.
38. Papazyan, A.; Warshel, A. *J. Phys. Chem. B* **1998**, *102*, 5348–5357.
39. Warshel, A.; Papazyan, A.; Muegge, I. *J. Biol. Inorg. Chem.* **1997**, *2*, 143–152.
40. Stevens, S. M. Jr.; Dunbar, R. C.; Price, W. D.; Sena, M.; Watson, C. H.; Nichols, L. S.; Riveros, J. M.; Richardson, D. E.; Eyler, J. R. *J. Phys. Chem. A* **2002**, *106*, 9686–9694.
41. Peschke, M.; Blades, A. T.; Kebarle, P. *J. Am. Chem. Soc.* **2000**, *122*, 10440–10449.
42. Peschke, M.; Blades, A. T.; Kebarle, P. *J. Phys. Chem. A* **1998**, *102*, 9978–9985.
43. Stace, A. J. *J. Phys. Chem. A* **2002**, *106*, 7993–8005.
44. Markham, G. D.; Glusker, J. P.; Bock, C. W. *J. Phys. Chem. B* **2002**, *106*, 5118–5134.
45. Vitale, G.; Valina, A. B.; Huang, H.; Amunugama, R.; Rodgers, M. T. *J. Phys. Chem. A* **2002**, *105*, 11351–11364.
46. Peschke, M.; Blades, A. T.; Kebarle, P. *J. Am. Chem. Soc.* **2000**, *122*, 10440–10449.
47. Rodriguez-Cruz, S. E.; Jockusch, R. A.; Williams, E. R. *J. Am. Chem. Soc.* **1999**, *121*, 8898–8906.
48. Rodriguez-Cruz, S. E.; Klassen, J. S.; Williams, E. R. *J. Am. Soc. Mass Spectrom.* **1999**, *10*, 958–968.
49. Raymond, K. S.; Grafton, A. K.; Wheeler, R. A. *J. Phys. Chem. B* **1997**, *101*, 623–631.
50. Wright, J. D.; Reynolds, C. A. *Int. J. Quantum Chem.* **1996**, *59*, 135–145.
51. Reynolds, C. A. *Int. J. Quantum Chem.* **1995**, *56*, 677–687.
52. Wolfe, J. J.; Wright, J. D.; Reynolds, C. A.; Saunders, A. C. G. *Anti-Cancer Drug Design* **1994**, *9*, 85–102.
53. Wheeler, R. A. *J. Am. Chem. Soc.* **1994**, *116*, 11048–11051.
54. Winger, P.; Weber, E. J.; Cramer, C. J.; Truhlar, D. G. *Phys. Chem. Chem. Phys.* **2000**, *2*, 1871–1871.
55. Winger, P.; Weber, E. J.; Cramer, C. J.; Truhlar, D. G. *Phys. Chem. Chem. Phys.* **2000**, *2*, 1231–1239.
56. Reynolds, C. A. *Int. J. Quantum Chem.* **1995**, *56*, 677–687.
57. Lister, S. G.; Reynolds, C. A.; Richards, W. G. *Int. J. Quantum Chem.* **1992**, *41*, 293–310.
58. Reynolds, C. A. *J. Mol. Graphics* **1989**, *7*, 174–175.
59. Reynolds, C. A.; King, P. M.; Richards, W. G. *J. Chem. Soc., Chem. Commun.* **1988**, 1434–1436.
60. Li, J.; Fisher, C. L.; Chen, J. L.; Bashford, D.; Noodleman, L. *Inorg. Chem.* **1996**, *35*, 4694–4702.
61. Chen, J. L.; Noodleman, L.; Case, D. A.; Bashford, D. *J. Phys. Chem.* **1994**, *98*, 11059–11068.
62. Connolly, M. L. *J. Am. Chem. Soc.* **1985**, *107*, 1118–1124.
63. Connolly, M. L. *Science* **1983**, *221*, 709–713.
64. Wu, J. H.; Reynolds, C. A. *Anti-Cancer Drug Design* **1996**, *11*, 415–420.
65. Wu, J. H.; Reynolds, C. A. *J. Am. Chem. Soc.* **1996**, *118*, 10545–10550.
66. Wu, J. H.; Winn, P. J.; Ferenczy, G. G.; Reynolds, C. A. *Int. J. Quantum Chem.* **1999**, *73*, 229–236.
67. Jeancharles, A.; Nicholls, A.; Sharp, K.; Honig, B.; Tempczyk, A.; Hendrickson, T. F.; Still, W. C. *J. Am. Chem. Soc.* **1991**, *113*, 1454–1455.
68. Baik, M. H.; Ziegler, T.; Schauer, C. K. *J. Am. Chem. Soc.* **2000**, *122*, 9143–9154.
69. Holm, R. H.; Kennepohl, P.; Solomon, E. I. *Chem. Rev.* **1996**, *96*, 2239–2314.
70. Glaser, T.; Hedman, B.; Hodgson, K. O.; Solomon, E. I. *Acc. Chem. Res.* **2000**, *33*, 859–868.

71. Solomon, E. I.; Randall, D. W.; Glaser, T. *Coord. Chem. Rev.* **2000**, *200*, 595–632.
72. Solomon, E. I.; LaCroix, L. B.; Randall, D. W. *Pure Appl. Chem.* **1998**, *70*, 799–808.
73. Solomon, E. I.; Lowery, M. D.; Guckert, J. A.; LaCroix, L. B. *Electron Transfer Reactions* **1997**, *253*, 317–330.
74. Svensson, B.; Jonsson, B. *J. Computat. Chem.* **1995**, *16*, 370–377.
75. Gunner, M. R.; Alexov, E.; Torres, E.; Lipovaca, S. *J. Biol. Inorg. Chem.* **1997**, *2*, 126–134.
76. NaraySzabo, G. *J. Biol. Inorg. Chem.* **1997**, *2*, 135–138.
77. Muegge, I.; Qi, P. X.; Wand, A. J.; Chu, Z. T.; Warshel, A. *J. Phys. Chem. B* **1997**, *101*, 825–836.
78. Churg, A. K.; Warshel, A. *Biochemistry* **1986**, *25*, 1675–1681.
79. Swartz, P. D.; Beck, B. W.; Ichiye, T. *Biophys. J.* **1996**, *71*, 2958–2969.
80. George, S. D.; Metz, M.; Szilagyi, R. K.; Wang, H. X.; Cramer, S. P.; Lu, Y.; Tolman, W. B.; Hedman, B.; Hodgson, K. O.; Solomon, E. I. *J. Am. Chem. Soc.* **2002**, *123*, 5757–5767.
81. Olsson, M. H. M.; Ryde, U. *J. Biol. Inorg. Chem.* **1999**, *4*, 654–663.
82. Olsson, M. H. M.; Ryde, U.; Roos, B. *J. Inorg. Biochem.* **1999**, *74*, 254.
83. Ryde, U.; Olsson, M. H. M. *Int. J. Quantum Chem.* **2002**, *81*, 335–347.
84. Ryde, U.; Olsson, M. H. M.; Roos, B. O.; De Kerpel, J. O. A.; Pierloot, K. *J. Biol. Inorg. Chem.* **2000**, *5*, 565–574.
85. Olsson, M. H. M.; Ryde, U. *J. Am. Chem. Soc.* **2002**, *123*, 7866–7876.
86. Segall, M. D.; Payne, M. C.; Ellis, S. W.; Tucker, G. T.; Eddershaw, P. J. *Xenobiotica* **1999**, *29*, 561–571.
87. Fisher, C. L.; Chen, J. L.; Li, J.; Bashford, D.; Noodleman, L. *J. Phys. Chem.* **1996**, *100*, 13498–13505.
88. Han, W. G.; Lovell, T.; Noodleman, L. *Inorg. Chem.* **2002**, *41*, 205–218.
89. Li, J.; Fisher, C. L.; Konecny, R.; Bashford, D.; Noodleman, L. *Inorg. Chem.* **1999**, *38*, 929–939.
90. Li, J.; Fisher, C. L.; Konecny, R.; Lovell, T.; Bashford, D.; Noodleman, L. *J. Inorg. Biochem.* **1999**, *74*, 212.
91. Konecny, R.; Li, J.; Fisher, C. L.; Dillet, V.; Bashford, D.; Noodleman, L. *Inorg. Chem.* **1999**, *38*, 940–950.
92. Mouesca, J. M.; Chen, J. L.; Noodleman, L.; Bashford, D.; Case, D. A. *J. Am. Chem. Soc.* **1994**, *116*, 11898–11914.
93. Noodleman, L.; Case, D. A.; Mouesca, J. M.; Lamotte, B. *J. Biol. Inorg. Chem.* **1996**, *1*, 177–182.
94. Li, J.; Nelson, M. R.; Peng, C. Y.; Bashford, D.; Noodleman, L. *J. Phys. Chem. A* **1998**, *102*, 6311–6324.
95. Sigfridsson, E.; Olsson, M. H. M.; Ryde, U. *Inorg. Chem.* **2001**, *40*, 2509–2519.
96. Datta, S. N.; Nehra, V.; Jha, A. *J. Phys. Chem. B* **1999**, *103*, 8768–8772.
97. Beck, B. W.; Koerner, J. B.; Ichiye, T. *J. Phys. Chem. B* **1999**, *103*, 8006–8015.
98. Datta, S. N.; Prabhakar, B. G. S.; Nehra, V. *J. Phys. Chem. B* **1999**, *103*, 2291–2296.
99. Crystal, J.; Friesner, R. A. *J. Phys. Chem. A* **2000**, *104*, 2362–2366.
100. Datta, S. N.; Parandekar, P. V.; Lochan, R. C. *J. Phys. Chem. B* **2001**, *105*, 1442–1451.
101. Kuramochi, H.; Noodleman, L.; Case, D. A. *J. Am. Chem. Soc.* **1997**, *119*, 11442–11451.

Comprehensive Coordination Chemistry II
ISBN (set): 0-08-0437486

Volume 2, (ISBN 0-08-0443249); pp 633–642

2.50 Comparison of DFT, AOM, and Ligand Field Approaches

R. J. DEETH
University of Warwick, Coventry, UK

2.50.1 INTRODUCTION 643
2.50.2 THE ARRIVAL OF DENSITY FUNCTIONAL THEORY 644
2.50.3 LFT vs. DFT 645
2.50.3.1 Metal-amines and π-Bonding 645
2.50.3.2 Spherical versus Non-spherical Potentials 646
2.50.3.3 Planar $[MCl_4]^{2-}$ Complexes 646
2.50.3.4 Excited States 647
2.50.3.5 DFT and LFT Working Together 648
2.50.4 CONCLUSIONS 649
2.50.5 REFERENCES 649

2.50.1 INTRODUCTION

Coordination chemists are used to interpreting the bonding in complexes in terms of the energies of the *d*-orbitals.[1] Both crystal field theory (CFT) and its ligand field theory (LFT) extension explicitly focus only on the *d*-functions but inferences about the overall nature of the metal–ligand interactions can be drawn from an analysis of their energies. By construction, CFT can only access *d*-orbital energy differences. In octahedral complexes, for example, an increasing *d*-orbital splitting was associated with an increasingly strong M—L interaction. However, within the strictly electrostatic CFT picture, the octahedral splitting should theoretically be directly proportional to the ligand charge, *q*. Experimentally, this is not the case and fluoride complexes, which on electrostatic grounds should show large splittings, actually display smaller splittings than in complexes with neutral ligands.

The culprit responsible for this failure of the electrostatic model is covalency. Thus, the ionic crystal field model was modified to encompass a more covalent molecular orbital (MO) picture.[2] The *d*-orbital splitting was therefore interpreted as a competition between σ- and π-bonding effects with π-donor ligands tending to give small splittings while π-acceptors give large splittings. Hence, this new ligand field theory ascribed some sense of absolute energy to the *d*-functions. For example, the lack of suitable π-orbitals on ammonia implies the d_π orbitals (d_{xz}, d_{yz}, and d_{xy}) are essentially nonbonding and have the same energy as the parent atomic *d*-orbitals. In essence, the CFT barycenter is replaced by a MO barycenter as illustrated in Figure 1 for the case of a complex with σ-only ligands.

However, let us be clear about the material difference between CFT and LFT. The underlying mathematical theory is identical. The energy levels are constructed from multiplets derived from the relevant *d* (or *f*) configuration. (Note that LFT can equally be applied to the *f* elements and the statements made concerning *d*-block systems implicitly cover *f*-block systems as well.) The change is that in LFT, the *d*-level splittings are not computed from first principles. Instead, they

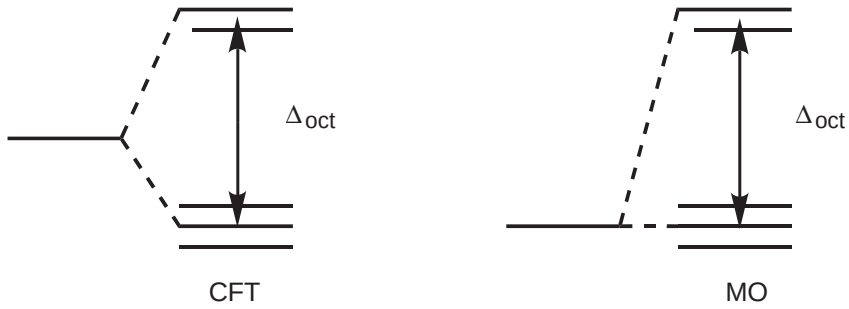

Figure 1 Illustration of CFT and MO barycenter energies for octahedral ML_6 where L is σ-bonding only.

are expressed in terms of parameters whose values are determined by fitting calculated values to their experimental equivalents (i.e., *d–d* spectra, magnetic susceptibilities, EPR *g*-values and metal hyperfine coupling constants).

Thus, $10Dq$ in CFT becomes Δ_{oct} in LFT. Moreover, the interelectron repulsion parameters are permitted to vary from their free-ion values (the Nephelauxetic effect); the orbital angular momentum operator required to compute magnetic properties is attenuated via a multiplicative constant—Steven's orbital reduction parameter, *k*—and some workers even advocate a separate reduction in the free-ion one-electron spin-orbit coupling parameters, ζ.[3,4] Thus, LFT is simply a parametric version of CFT.

Nevertheless, this need not prevent us from trying to interpret the changes in ligand field parameters in terms of MO concepts. For example, Steven's orbital reduction parameter is invariably less than unity and is often identified with the percentage of *d* character in the magnetic orbital which, in turn, is given by the square of the *d* coefficient in a Linear Combination of Atomic Orbitals (LCAO) representation. Hence, through usage and experience, coordination chemists have come to use both CFT and MO/LFT concepts freely to interpret the magnetic, spectroscopic, and geometric properties of metal complexes.

2.50.2 THE ARRIVAL OF DENSITY FUNCTIONAL THEORY

Since about 1990, the application of density functional theory (DFT) to chemical problems in general, and transition metal systems in particular, have exploded. The spark was the arrival in 1988 of analytical expressions for the DFT energy derivatives[5] which finally allowed DFT computer codes to perform automatic geometry optimizations.

Prior to this, it had already been established that even the simplest forms of DFT, based on the exchange-only Slater or Xα scheme,[6] could give good descriptions of the electronic structure of metal complexes and a number of contemporary applications confirmed this.[7–11] However, in combination with structure optimization, here at last was a quantum chemical method accurate enough for transition metal (TM) systems and yet still efficient enough to deliver results in a reasonable time. This was in stark contrast to the "competition" which was either based on the single-determinant Hartree–Fock approximation, which had been discredited as a viable theory for TM systems,[12] or on more sophisticated electron correlation methods (e.g., second order Møller–Plesset theory) which are relatively computationally expensive and thus, for the same computer time, treat much smaller systems that DFT.

DFT promised so much more than LFT and over the last decade or so, amazing advances have been made. On the one hand, LFT is restricted to just those energy levels dominated by *d* (or *f*) contributions. This limits its application to computing the "*d–d*" spectra, magnetic susceptibilities, and EPR parameters of essentially classical single-center Werner-type coordination complexes. DFT, on the other hand, not only treats "*d–d*" spectra[13,14] and EPR parameters[15] but also provides information on all the orbitals (not just the *d* set), can generate charge and spin density distributions, optimize both ground and transition state structures,[16,17] compute NMR properties of diamagnetic complexes,[18] and more. Moreover, DFT is not restricted to Werner complexes. Seemingly the only advantages left for LFT are:

(i) it is very much quicker to perform LFT calculations and
(ii) the accuracy of LFT transition energies, magnetic susceptibilities, and EPR parameters is usually higher than current DFT methods can achieve.

However, LFT is parametric so it is perhaps not surprising that LFT can deliver good agreement with experiment. The enduring legacy of LFT, apart from its pedagogic value, is that its concepts continue to provide a framework in which to interpret the physical properties of metal complexes in terms of the underlying bonding. It is only natural to explore whether DFT provides an equally viable framework.

2.50.3 LFT vs. DFT

Chapters 2.35 and 2.36 discuss the basis of LFT and suggest that the best way to parameterize the ligand field potential is via a ligand superposition scheme like the AOM. The AOM was originally introduced within the framework of semiempirical MO theory and the Wolfsberg–Helmholtz approximation.[19] Later, Gerloch, Woolley, and co-workers developed an alternative theoretical basis for LFT and the AOM which is based on the density functional theorem.[20] Both approaches reflect the angular momentum properties of the central *d*-orbitals and, given identical basis sets, molecular structures, and parameter values, generate identical results. There are some differences in the subsequent interpretation of the values of the parameters but these are not important here.

Recall from Chapter 2.35 that the ligand field model comprises three terms: one for the ligand field potential (H_{LF}); one for *d*–*d* interelectronic repulsion (H_{ER}); and one for spin-orbit coupling (H_{SO}). The most important feature of the AOM is that it separates each M–L interaction into separate σ and π contributions which, in principle, provides a direct, albeit qualitative, description of the bonding. Only H_{LF} contains any molecular symmetry information and this term thus determines the *d*-orbital splittings and hence the AOM e_λ parameter values. In contrast, H_{ER} and H_{SO} are spherically symmetric and reflect properties of the complex as a whole. These features have far reaching consequences when comparing the *d*-orbital energies from a ligand field analysis with the related orbitals from a density functional calculation.

2.50.3.1 Metal-amines and π-Bonding

In the AOM, it is normally assumed, and sometimes verified, that saturated amine ligands have no π-bonding capabilities, i.e., $e_\pi(\mathrm{N}) \equiv 0$.[21] Hence, for a simple metal hexaamine, $[\mathrm{M(NH_3)_6}]^{n+}$, the π-type "t_{2g}" orbitals are predicted to be degenerate and nonbonding (Equations (1a) and (1b)). Moreover, if the complex were subjected to a tetragonal distortion that maintained the effective D_{4h} symmetry, the three d_π functions would remain degenerate and nonbonding (Equations (2a)–(2d)):

$$O_h: \quad E(d_{z^2}) = E(d_{x^2-y^2}) = 3e_\sigma \tag{1a}$$

$$E(d_{xz}) = E(d_{yz}) = E(d_{xy}) = 4e_\pi \equiv 0 \tag{1b}$$

$$D_{4h}: \quad E(d_{x^2-y^2}) = 3e_\sigma(\mathrm{eq}) \tag{2a}$$

$$E(d_{z^2}) = e_\sigma(\mathrm{eq.}) + 2e_\sigma(\mathrm{ax}) \tag{2b}$$

$$E(d_{xz}) = E(d_{yz}) = 2e_\pi(\mathrm{eq}) + 2e_\pi(\mathrm{ax}) \equiv 0 \tag{2c}$$

$$E(d_{xy}) = 4e_\pi(\mathrm{eq}) \equiv 0 \tag{2d}$$

This result is already counter to the CFT prediction which, for a tetragonal elongation, predicts d_{xy} should rise while d_{xz} and d_{yz} should fall to compensate. This arises from the long-range interaction exerted by point charges and to the fact that point charges implicitly exert both σ and π effects. In the more sophisticated AOM, the "t_{2g}" degeneracy can only be raised through M—L bonding interactions, which are inherently short range and symmetry specific with regard to local σ and π bonding modes.

DFT calculations have been reported for the tetragonally elongated copper(II) diethylenetriamine complex, $[Cu(dien)_2]^{2+}$.[22] Significantly, the "d_{xy}" orbital lies several thousand wavenumbers below the d_{xz}/d_{yz} pair, a result which conflicts with both the AOM, which predicts degeneracy, and electrostatic CFT, which predicts d_{xy} should be above d_{xz}/d_{yz} rather than below. Moreover, if one takes the DFT *d*-orbital energies in an AOM analysis, e_π would not only be nonzero, but, assuming the magnitude of the axial e_π parameter is less than the magnitude of the equatorial e_π, the analysis based on Equations (2a)–(2d) would conclude that e_π is less than 0, i.e., that amines are π acceptors. Evidently, the DFT *d*-orbitals are not the same as the AOM *d*-orbitals.

Which model is correct? To answer this question we must also consider: How can we tell? The validity of a theoretical model is based on its ability to reproduce (and predict) experimentally observable quantities. An orbital is not observable *per se* and in essence is an artifact of the model. For $[Cu(dien)_2]^{2+}$, both the AOM and DFT reproduce the *d*–*d* transition energies and EPR *g*-values satisfactorily so they are both "correct." Why, then, are their orbitals different?

2.50.3.2 Spherical versus Non-spherical Potentials

Since orbitals are model dependent, different models will have different orbitals. The basic distinction between DFT *d*-orbitals and LFT *d*-orbitals arises from their respective treatments of interelectron repulsions. In LFT, *d*–*d* repulsion is treated within a spherical approximation. For d^1 and d^9 configurations, there is a single free-ion term and hence no need to consider *d*–*d* interelectron repulsion at all. In contrast, the Kohn–Sham orbitals in DFT are computed relative to the total molecular potential. For a tetragonal d^9 copper(II) complex, $d_{x^2-y^2}$ is singly occupied while the remaining *d*-functions are doubly occupied. Hence, to a first approximation, the "hole" in the equatorial plane results in less *d*–*d* repulsion in the plane than perpendicular to the plane with the result that the in-plane "d_{xy}" orbital falls relative to the out-of-plane d_{xz}/d_{yz} pair.

Yet, the DFT orbital splitting in the ground state does not translate into different "*d*–*d*" excitation energies. LFT predicts two "*d*–*d*" bands and when the "*d*–*d*" excitation energies are explicitly computed by DFT, via promoting electrons from occupied to the half-filled $d_{x^2-y^2}$ orbital and subtracting the energies of ground and excited states, only two unique excitation energies result.[22] Hence, both LFT and DFT provide a reasonable description of the experimentally observable data, but the single LFT *d*-orbital sequence, which applies to all the ligand field states, is different from the DFT ground state sequence.

In LFT, the mere fact of using atom-like *d*-functions to construct the many-electron multiplet states arising from the *d*-configuration implies that the potential around the metal is mainly atom like, i.e., essentially spherical. The LFT *d*-orbitals are defined relative to a notional average potential which affects all possible arrangements of the *d*-electrons. Thus, the LFT *d*-orbitals are implicitly designed to describe the ground and all the excited states simultaneously. In contrast, the DFT *d*-orbitals are defined relative to a particular state. Both DFT and LFT generally give the same ground state but this only requires that the configurations are the same, not that the detailed orbital sequences are identical. Although the DFT Kohn–Sham orbitals look like *d*-orbitals when plotted in three dimensions,[23] this does not imply they form the correct basis for a ligand field treatment.

2.50.3.3 Planar $[MCl_4]^{2-}$ Complexes

Consider, for example, planar tetrachlorometallate complexes. Metal chloride complexes provide a diverse source of experimental data against which to test theoretical models. Planar tetrachloro complexes like $[CuCl_4]^{2-}$ and $[PdCl_4]^{2-}$ have been well studied[24–28] and analyses of the "*d*–*d*" spectra[29] have established a *d*-orbital sequence of $d_{x^2-y^2} >> d_{xy} > d_{xz}/d_{yz} > d_{z^2}$. Assuming Cl is a "linear ligator" (i.e., a cylindrically symmetric π ligand), this sequence is easily accommodated

within the AOM. In particular, d_{xy} is predicted to lie above d_{xz}/d_{yz} since the energy of the former is $4e_\pi$, the latter $2e_\pi$, and $e_\pi > 0$ for a π-donor like chloride.

Early applications of DFT based on the exchange-only Xα models also gave good qualitative agreement with experiment and, for planar $[CuCl_4]^{2-}$, the same *d*-orbital sequence as that derived from ligand field and spectroscopic studies.[8] With hindsight, this agreement was fortuitous. Both the multiple scattering Xα (MSXα) and the discrete variational Xα (DVXα) methods employed spherical approximations when constructing the molecular potential. This tended to smooth the asymmetric *d*–*d* repulsion effects and made the DFT procedure more closely emulate LFT with the result that the DFT ground state orbital sequence matched that derived from spectroscopy.

Modern DFT no longer needs to approximate the molecular potential and calculations on $[PdCl_4]^{2-}$ [23,30] place d_{xy} below d_{xz} and d_{yz}. Note that both LFT and DFT predict the same ground state configuration, viz, $d_{x^2-y^2}{}^0 d_{z^2}{}^2 d_{xy}{}^2 d_{xz}{}^2 d_{yz}{}^2$, that both models place the $d_{x^2-y^2}$ orbital highest of the *d* set, and that the Kohn–Sham orbitals look as expected. However, the ground state DFT sequence is clearly not the same as that obtained from LFT with regard to the order of d_{xy} and d_{xz}/d_{yz}.

The low-spin d^8 complex $[PdCl_4]^{2-}$ is even more susceptible than $[Cu(dien)_2]^{2+}$ to the effects from nonspherical *d*–*d* repulsion since the $d_{x^2-y^2}$ orbital is completely empty. The lower in-plane *d*–*d* repulsion results in d_{xy} below d_{xz}/d_{yz} in apparent disagreement with the accepted *d*-orbital sequence. Again, if the DFT *d*-orbital energies are used directly in an AOM analysis, e_π would be negative implying a π-acceptor role for chloride. Of course, this conclusion is invalid since we cannot use DFT orbitals directly in a purely ligand field context. So, what is the nature of the Pd–Cl π interaction? The AOM predicts π donation based on an analysis of the *d*–*d* spectrum. The DFT charge distribution is also consistent with π donation in that the Cl^- π-orbitals are depleted in the complex relative to the uncoordinated ligand. Moreover, the DFT multiplet state energies agree with the experimental sequence of excited states[30] so that, judged by their ability to reproduce experimental data, both DFT and the AOM are equally good.

However, if one wished DFT to make more direct contact with LFT, the former must somehow try to capture the nature of the average spherical potential which defines the ligand field *d*-functions. Anthon and Schäffer[31] are attempting to bridge DFT and LFT in the context of using DFT to compute free-ion interelectron repulsion parameters. Special average-of-configuration states are used to define a fixed, spherical atomic potential that is then used to compute multiplet energies of the terms spanned by the configuration. The results are impressive and certainly better than previous estimates based on Hartree–Fock calculations. The goal is to deal with the full Nephelauxetic Effect nonempirically.

2.50.3.4 Excited States

The generality of DFT inevitably leads to compromises. This is particularly evident when computing excited state energies. Within LFT, it is easy to construct proper, single center determinantal descriptions of the *d*-based multiplet states and explicitly evaluate the configuration interactions between them. The only question is whether the spherical treatment of interelectronic repulsion and spin-orbit coupling is sufficiently accurate. In many instances, this appears to be the case.

In contrast, the construction of general, multicentered determinants is nontrivial[14] and DFT is still struggling to provide accurate excited state energies consistently. However, DFT has the considerable advantage of being able to compute charge transfer (CT) states which is beyond the scope of LFT. There are notable successes such as $[Cr(NH_3)_6]^{3+}$,[32,33] Cr^{3+} in fluoride lattices,[34] and for $[Ru(bipy)_3]^{2+}$ [35,36] where the CT state energies can be used to extract *d*–*d* excitation energies, but the performance of DFT is still a bit patchy. For example, in the tetrahedral manganese(VI), chromium(V), vanadium(IV), manganese(VII), chromium(VI), and vanadium(V) oxo anions, DFT sometimes places the metal 4*s* orbital anomalously low in energy which has a knock-on effect on the *d* excited states.[37]

An alternative to the construction of multiplet states is the use of time-dependent DFT (TDDFT, see Chapter 2.40). TDDFT not only offers the potential for computing accurate transition energies but also provides the transition moments so that the intensity of the transition can be assessed. For example, hexacarbonyl complexes of Cr, Mo, and W have been analyzed using relativistic TDDFT.[38] In contradiction of the original interpretation of the lowest

energy transitions being *d–d* bands, the TDDFT calculations assign the low energy features to charge transfer. This prompts a critical re-evaluation of the role of ligand field states in CO photodissociation.

2.50.3.5 DFT and LFT Working Together

The previous sections have focused largely on cases where DFT and LFT are apparently at odds and emphasized the differences between them. There are also many instances where the two models work together. After all, it would be good if our understanding of the bonding in a complex was independent of the model we happened to use to interpret the experimental data.

For example, consider the Nephelauxetic Effect. Analysis of the interelectron repulsion parameters derived from analyzing the *d–d* spectrum invariably leads to lower values than in the free ion. The interpretation is that, in the complex, the *d* electrons are, on average, further apart which is consistent with expanded *d*-functions in the complex and/or with *d* electron delocalization onto the ligands. Analysis of the electron density distribution from X-ray diffraction in *trans*-$[Ni(NH_3)_4(NO_2)_2]$ yields a *d*-orbital radius larger than that for free Ni^{2+}.[39] However, the unpaired electron density derived from polarized neutron diffraction (PND) data yields a *d*-orbital radius less than for free Ni^{2+} prompting Figgis to propose an "anti-Nephelauxetic effect." DFT calculations[39] support LFT in that the *d*-orbitals expand upon complex formation but also provide an explanation of the diffraction data.

For the formally d^8 Ni^{2+} center, there are five up-spin and three down-spin *d* electrons. Both sets are expanded relative to the free ion but the extra exchange interaction lowers and contracts the up-spin orbitals relative to down-spin. The X-ray diffraction experiment measures the sum of up- and down-spin densities while the PND experiments measure their difference. As shown qualitatively in Figure 2, the maximum for the sum density occurs at a slightly longer distance than the up-spin density curve, consistent with the experimental measure of a four percent increase in the *d*-function radius, while the maximum for the difference density occurs at a much shorter distance, consistent with the 8% contraction in the *d*-orbital radius used to analyze the PND data. Moreover, the small region of negative spin density lying along the Ni—L vectors is also explained by Figure 2. Thus, there is no anti-Nephelauxetic effect.

There are many other instances of the interplay between experiment, DFT, and LFT. Extensive work on the tetrachlorocuprate anion, $[CuCl_4]^{2-}$, has established that the composition of the singly occupied $d_{x^2-y^2}$ orbital is about 70% metal and 30% ligand.[40] However, DFT calculations suggest the inverse. Szilagyi *et al.*[28] have modified the DFT by including some Hartree–Fock exchange into the Becke/Perdew gradient corrected functional. By tuning the admixture, they make the description of the bonding more ionic which has the added benefit of improving the agreement with computed excited state energies.

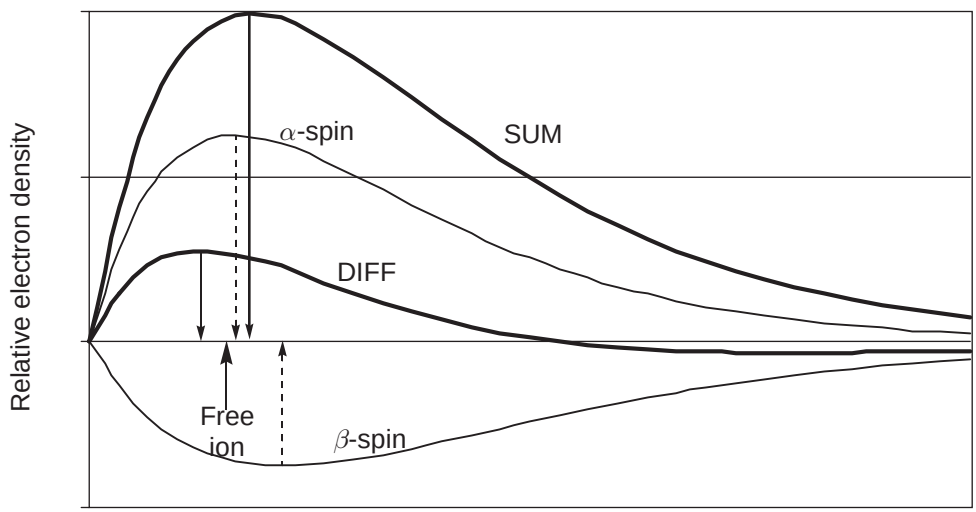

Figure 2 Schematic representation of radial density distributions in a high-spin d^8 complex.

DFT calculations on linear dihalides reveal unexpected groundstates. For example, LFT suggests that d_{z^2} should be the highest energy d-orbital for linear $CuCl_2$ while DFT yields a ^2E_g state.[41] This has prompted a re-evaluation of the ligand field description of this type of molecule and the recognition of the importance of a $d-s$ configuration interaction akin to that for planar ML_4 systems.[42,43]

2.50.4 CONCLUSIONS

DFT is an intrinsically one-electron approach and, as such, orbitals are a natural feature of the method. In contrast to HF theory, all the orbitals, both occupied and virtual, are defined with respect to the full molecular potential which confers greater physical meaning to both their energies and compositions. However, DFT orbitals and the d-orbitals of a LFT calculation are not the same and cannot be directly compared although they may share qualitatively similar features and, with care, common descriptions of the bonding in metal complexes can be developed.

The major difference is that LFT d-orbitals are defined relative to a notional spherical potential surrounding the metal and these d-orbitals can be used to construct not only the ground state but also all the excited states within the d manifold. In contrast, a DFT calculation will generally optimize its orbitals relative to a single state and will treat interelectron repulsion within the full molecular symmetry as opposed to the spherical approximation employed in LFT. Hence, the ground state DFT d-orbital energy sequence need not correspond to the LFT sequence. However, this does not imply that DFT cannot generate correct excited states. Rather, it requires separate calculations, either of Slater-type determinants or using time dependent theory.

For the moment, LFT can generally deliver better agreement with experiment, at least for the relatively limited set of properties accessible to it. In particular, the central field approximation inherent in LFT allows for a complete treatment of multiplet states and configuration interaction. While DFT has come a long way in a short time, computing accurate multiplet energies continues to present difficulties not least of which being that current functionals appear not to provide a uniform description of states with different spin multiplicities.[44] Magnetic properties such as EPR g-values and hyperfine coupling constants are also demanding for DFT since they require both a relativistic model and highly accurate descriptions near nuclei. Again, the implementation of spin-orbit coupling in LFT is relatively straightforward.

However, as the functionals improve, the accuracy of computed quantities will improve. Given the multitude of other important features which are available to DFT but not accessible to LFT, plus the fact the development of LFT has essentially stopped, it seems only a matter of time before DFT effectively supplants LFT as a computational procedure. Nevertheless, many concepts arising from LFT have stood the test of time and the link between LFT and DFT remains an area of active research.[31]

2.50.5 REFERENCES

1. Gerloch, M.; Woolley, R. G. *Prog. Inorg. Chem.* **1983**, *31*, 371–446.
2. Orgel, L. E. *An Introduction to Transition-Metal Chemistry: Ligand Field Theory*, 2nd edn., Methuen: London, 1966.
3. Gerloch, M. *Magnetism and Ligand Field Analysis*; Cambridge University Press: Cambridge, U.K, 1984.
4. Bridgeman, A. J.; Gerloch, M. *Prog. Inorg. Chem.* **1997**, *45*, 179–281.
5. Versluis, L.; Ziegler, T. *J. Chem. Phys.* **1988**, *88*, 322–328.
6. Slater, J. C. *The Self-consistent Field for Molecules and Solids*, Vol. 4, McGraw-Hill: New York, 1974.
7. Brenosa, A. G.; Moreno, M.; Aramburu, J. A. *J. Phys. Condes. Matter* **1991**, *3*, 7743–7750.
8. Deeth, R. J. *J. Chem. Soc., Dalton Trans.* **1990**, 355–363.
9. Deeth, R. J. *J. Chem. Soc., Dalton Trans.* **1991**, 1895–1900.
10. Deeth, R. J. *J. Chem. Soc., Dalton Trans.* **1991**, 1467–1477.
11. Armstrong, E. M.; Collison, D.; Deeth, R. J.; Garner, C. D. *J. Chem. Soc., Dalton Trans.* **1995**, 191–195.
12. Veillard, A. *Chem. Rev.* **1991**, *91*, 743–766.
13. Ziegler, T.; Rauk, A.; Baerends, E. J. *Theoret. Chim. Acta* **1977**, *43*, 261.
14. Daul, C. *J. Comput. Chem.* **1994**, *52*, 867.
15. Patchkovskii, S.; Ziegler, T. *J. Chem. Phys.* **1999**, *111*, 5730–5740.
16. Patchkovskii, S.; Ziegler, T. *J. Chem. Phys.* **2002**, *116*, 7806–7813.
17. Ziegler, T. *Can. J. Chem.* **1995**, *73*, 743–761.
18. Schreckenbach, G.; Wolff, S. K.; Ziegler, T. *J. Phys. Chem. A* **2000**, *104*, 8244–8255.
19. Schaeffer, C. E.; Jorgensen, C. K. *Mol. Phys.* **1965**, *9*, 401.
20. Woolley, R. G. *Mol. Phys.* **1981**, *42*, 703–720.

21. Figgis, B. N.; Hitchman, M. A. *Ligand Field Theory and Its Applications*; Wiley: New York, 2000.
22. Deeth, R. J. *J. Chem. Soc., Dalton Trans.* **2001**, 664–669.
23. Stowasser, R.; Hoffmann, R. *J. Am. Chem. Soc.* **1999**, *121*, 3414–3420.
24. Harrison, T. G.; Patterson, H. H.; Godfrey, J. J. *Inorg. Chem.* **1976**, *15*, 1291.
25. Hitchman, M. A.; Cassidy, P. J. *Inorg. Chem.* **1979**, *18*, 1745.
26. Pelletier, Y.; Reber, C. *Inorg. Chem.* **1997**, *37*, 721–728.
27. Lienke, A.; Klatt, G.; Robinson, D. J.; Koch, K. R.; Naidoo, K. J. *Inorg. Chem.* **2001**, *40*, 2352–2357.
28. Szilagyi, R. K.; Metz, M.; Solomon, E. I. *J. Phys. Chem. A* **2002**, *106*, 2994–3007.
29. Lever, A. B. P. *Inorganic Electronic Spectroscopy*, 2nd edn.; Elsevier: New York, 1984.
30. Baerends, E. J.; Deeth, R. J. *J. Chem. Soc., Faraday Trans.* **2003**, in press.
31. Anthon, C.; Schaffer, C. E. *Coord. Chem. Rev.* **2002**, *226*, 17–38.
32. Doclo, K.; De Corte, D.; Daul, C. *Inorg. Chem.* **1998**, *37*, 3842–3847.
33. Doclo, K.; De Corte, D.; Daul, C.; Gudel, H. U. *Inorg. Chem.* **1998**, *37*, 3842–3847.
34. Aramburu, J. A.; Moreno, M.; Doclo, K.; Daul, C.; Barriuso, M. T. *J. Chem. Phys.* **1999**, *110*, 1497–1507.
35. Buchs, M.; Daul, C. *Chimia* **1998**, *52*, 163–166.
36. Daul, C.; Baerends, E. J.; Vernooijs, P. *Inorg. Chem.* **1994**, *33*, 3538–3543.
37. Stuckl, A. C.; Daul, C. A.; Gudel, H. U. *J. Chem. Phys.* **1997**, *107*, 4606–4617.
38. Rosa, A.; Baerends, E. J.; van Gisbergen, S. J. A.; van Lenthe, E.; Groeneveld, J. A.; Snijders, J. G. *J. Am. Chem. Soc.* **1999**, *121*, 10356–10365.
39. Chandler, G. S.; Deeth, R. J.; Figgis, B. N.; Phillips, R. A. *J. Chem. Soc., Dalton Trans.* **1990**, 1417–1427.
40. Deeth, R. J.; Hitchman, M. A.; Lehmann, G.; Sachs, H. *Inorg. Chem.* **1984**, *23*, 1310–1320.
41. Deeth, R. J. *J. Chem. Soc., Dalton Trans.* **1993**, 1061–1064.
42. Bridgeman, A. J. *J. Chem. Soc., Dalton Trans.* **1997**, 4765–4771.
43. Bridgeman, A. J. *J. Chem. Soc., Dalton Trans.* **1996**, 2601–2607.
44. Dolg, M.; Liu, W.; Kalvoda, S. *Int. J. Quantum Chem.* **2000**, *76*, 359–370.

Comprehensive Coordination Chemistry II
ISBN (set): 0-08-0437486

Volume 2, (ISBN 0-08-0443249); pp 643–650

2.51
MO Description of Transition Metal Complexes by DFT and INDO/S

S. I. GORELSKY
Stanford University, CA, USA

2.51.1 KOHN–SHAM ORBITALS AND CONVENTIONAL MOLECULAR ORBITALS 651
2.51.2 METHODS TO DERIVE ATOMIC ORBITAL CONTRIBUTIONS TO MOLECULAR ORBITALS 652
2.51.2.1 Mulliken Population Analysis 654
2.51.2.2 Frontier Molecular Orbitals of $[Ru(terpy)_2]^{2+}$ 654
2.51.3 ORBITAL ENERGIES AND ELECTRONIC SPECTROSCOPY 656
2.51.4 CONCLUSIONS 656
2.51.5 REFERENCES 658

Molecular orbital (MO) models have played a major role in the understanding and interpretation of molecular electronic processes, including electronic spectroscopy, electron transfer reactions, ionization, and electron attachment. Orbital energies are critical quantities for many types of calculations. Frontier molecular orbitals (FMOs) are probably the most important MOs. FMOs are good indicators of the reactivity and photochemistry of chemical species.[1–14] Changes in their composition affect the properties of the electronic ground state and also the corresponding excited states, because these MOs are those that are involved in electronic transitions in the visible and UV regions. In transition metal chemistry, under the term *frontier orbitals*, we mean not only the HOMO and the LUMO, as is conventional in the literature, but all MOs which are close in energy to the HOMO and the LUMO. This is because, unlike organic molecules with well-separated electronic levels, transition metal complexes usually have several FMOs that are close in energy and, as a result, the two-orbital (HOMO, LUMO) description of such systems is not sufficient.

2.51.1 KOHN–SHAM ORBITALS AND CONVENTIONAL MOLECULAR ORBITALS

From the beginning of the utilization of density functional theory (DFT), the significance of Kohn–Sham (KS) orbitals has been de-emphasized[15] and they were regarded as only auxiliary mathematical constructs. Until recently, there was a widespread belief that the KS orbitals have no physical significance and should not be used for rationalization of experimental data in the same way as conventional MOs, and that their *only* connection to the observable properties is that the sum of the densities of the occupied KS orbitals is the exact electron density:

$$\rho_{exact}(\vec{r}) = \sum_i \eta_i^{\alpha} \left| \phi_i^{\alpha,KS}(\vec{r}) \right|^2 + \sum_i \eta_i^{\beta} \left| \phi_i^{\beta,KS}(\vec{r}) \right|^2 \quad (1)$$

where η_i^{α} and η_i^{β} are the occupation numbers ($0 \leq \eta_i \leq 1$) for α- and β-spin orbitals:

$$N = \sum_i (\eta_i^\alpha + \eta_i^\beta) \tag{2}$$

However, there is an increasing body of evidence that KS orbitals are much more useful and meaningful than they were held to be.

First, it has been shown for the $X\alpha$ method[16] and for DFT in general[17] that the variation of the total energy with respect to an orbital occupation is equal to the eigenvalue of that orbital, ε_i:

$$\varepsilon_i = \frac{\partial E}{\partial \eta_i} \tag{3}$$

Equation (3) is independent of the form of the exchange-correlation (XC) functional and implies that the KS orbital energies provide information about the electronegativity of the system.[16,18–22]

Secondly,

$$\varepsilon_{HOMO} = -IE_V \tag{4}$$

The property that the highest occupied KS orbital energy is equal to (minus) the first vertical ionization energy (IE_V) of the molecule[23–25] is directly related to the fact that the asymptotic behavior of the electron density is governed by the first ionization energy. A property such as Equation (4) is very desirable in any MO theory. Unfortunately Equation (4) holds only for the exact XC potential and many currently available XC potentials in DFT have deficiencies in their long-range behavior.[25–30] Approximate XC potentials which go too quickly to zero will underbind the highest-occupied KS orbital, and potentials which go too slowly to zero will overbind it. This problem, however, can be remedied by constructing more accurate XC potentials with the correct asymptotic behavior.[25,28,31–37]

In the Hartree–Fock (HF) theory, a meaning for the MO energies is provided by Koopmans' theorem.[38,39] According to this, the energies of the occupied MOs are equal to (minus) the corresponding *unrelaxed* (no change in the wave functions of the remaining electrons: "frozen orbital" approximation[39]) vertical ionization energies. Thus, Koopmans' theorem gives a way of calculating *approximate* vertical ionization energies. In the KS–DFT theory, there is no equivalent to Koopmans' theorem, which could relate occupied orbital energies to ionization energies except for the HOMO (Equation (4)). However, Baerends and co-workers have recently demonstrated that there is a very good agreement between the energies of the outer valence occupied KS orbitals and the corresponding *relaxed* vertical ionization energies.[40] The average difference (~0.1 eV) between (minus) the KS orbital energies and the experimental vertical ionization energies of the molecules CO, N_2, H_2O, and HF is approximately an order of magnitude smaller than for HF orbital energies. The theoretical analysis and numerical results allow the interpretation of $-\varepsilon_i$ of the occupied KS orbitals as approximate but accurate *relaxed* vertical ionization energies.

Thirdly, it has been demonstrated that shapes (Figure 1), nodal structures, momentum distributions, and symmetry properties of KS orbitals are similar to those calculated by the *ab initio*, semiempirical, and extended Hückel methods.[16,40–50]

Fourthly, there is theoretical and numerical evidence that some electronic transition energies are given accurately by differences of KS orbital energies. We will return to this point later in Section 2.51.3.

2.51.2 METHODS TO DERIVE ATOMIC ORBITAL CONTRIBUTIONS TO MOLECULAR ORBITALS

Electronic structure calculations yield the electronic energy and the wave function of a molecular system in a particular electronic state. The wave function itself is not very suitable for interpretation, since it is a function of the coordinates of all electrons. Yet we need simplified characteristics

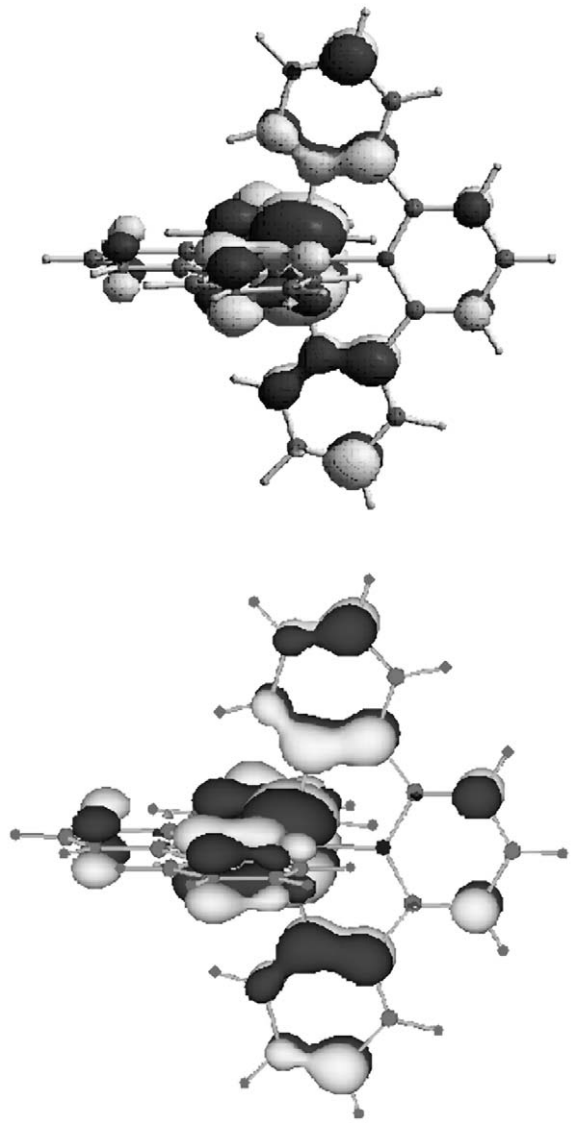

Figure 1 Isocontour surfaces (0.025 Å) of the HOMO (b_1 symmetry) of $[Ru(terpy)_2]^{2+}$. DFT(B3LYP/LanL2DZ) calculation (upper picture, Gaussian 98), INDO/S calculation (lower picture, HyperChem 5.11).[57]

of the wave function in order to gain insight into the electronic structure of molecules and to predict their chemical reactivities and other properties.

Much work has been done in the field of population analyses to assign a discrete charge to an atom in a molecule. Electron population analysis can be also applied to molecular systems to derive atomic orbital (AO) contributions to MOs.

Within the LCAO–MO formalism, the wave function for the i^{th} eigenstate of the molecule/ion can be written as

$$\phi_i^{\alpha} = \sum_{\mu} \boldsymbol{c}_{\mu i}^{\alpha} \chi_{\mu} \tag{5}$$

$$\phi_i^{\beta} = \sum_{\mu} \boldsymbol{c}_{\mu i}^{\beta} \chi_{\mu} \tag{6}$$

for an atom localized basis set $\{\chi_{\mu}\}$.[39]

If the MOs are obtained with zero differential overlap (ZDO) methods (see Chapter 2.38), then the overlap integrals, $S_{\mu\nu}$, between different AOs are neglected, and the contribution of the μ^{th} AO to the i^{th} MO is equal to the square of the corresponding LCAO coefficient, $(c_{\mu i}^{\alpha})^2$ for α spin and $(c_{\mu i}^{\beta})^2$ for β spin. As a result, the electron population of the atom A equals to

$$\sum_i [\eta_i^{\alpha} \sum_{\mu \in A} (c_{\mu i}^{\alpha})^2 + \eta_i^{\beta} \sum_{\mu \in A} (c_{\mu i}^{\beta})^2] \tag{7}$$

where i runs over all MOs. This is no longer the case if the overlap between AOs is not neglected. To analyze wave functions with non-zero AO overlap it is necessary to include the so-called overlap populations, $2c_{\mu i}^{\alpha} c_{\nu i}^{\alpha} S_{\mu\nu}$ and $2c_{\mu i}^{\beta} c_{\nu i}^{\beta} S_{\mu\nu}$, in calculations. Several ways have been proposed in the literature to deal with overlap populations.

2.51.2.1 Mulliken Population Analysis

The most popular and widely used procedure is the Mulliken population analysis (MPA).[51–55] In MPA, the overlap population $2c_{\mu i} c_{\nu i} S_{\mu\nu}$ ($\mu \in A$, $\nu \in B$) is split equally between atoms A and B, so the contribution of the μ^{th} AO of atom A to the i^{th} MO is equal to

$$\sum_{\nu} \boldsymbol{c}_{\mu i}^{\alpha} \boldsymbol{c}_{\nu i}^{\alpha} \boldsymbol{S}_{\mu\nu} (\alpha \text{ spin orbital}) \tag{8}$$

$$\sum_{\nu} \boldsymbol{c}_{\mu i}^{\beta} \boldsymbol{c}_{\nu i}^{\beta} \boldsymbol{S}_{\mu\nu} (\beta \text{ spin orbital}) \tag{9}$$

where the sum includes all AOs in the molecule. Two objections to MPA are frequently cited:[56]

1. Mulliken populations can have non-physical negative values or be in excess of two. The calculated AO contributions to MOs can exceed 100% or be negative.
2. Mulliken populations are sensitive to a basis set, particularly as the basis set is enlarged to get higher accuracy and includes polarization and diffuse functions. Two different basis sets could give identical properties (energy, electron density, etc.) but entirely different Mulliken populations.

The reason for these problems is the imbalance of overlap populations and the net atomic populations, and this imbalance is due primarily to the arbitrary equal distribution of the overlap population between atoms involved. In spite of these two problems, which have to be remembered when analyzing populations of orbitals and atoms, MPA is still frequently used for electron population analysis.

2.51.2.2 Frontier Molecular Orbitals of $[Ru(terpy)_2]^{2+}$

To compare FMOs from DFT and INDO/S, let's consider the $[Ru(terpy)_2]^{2+}$ complex (terpy = 2,2′;6′,2″-terpyridine, Figure 1) as an example. Table 1 shows irreducible representations, energies, and compositions (obtained using MPA) of the FMOs of this complex.[57,58] It can be seen that the FMO compositions derived from INDO/S calculations are very similar to those from DFT. Of course, different XC functionals have different accuracy and produce results of different quality. The local functional SVWN, with a well-known *overbinding tendency*,[25,59] produces more covalent structure and short Ru—N bonds (1.960 Å and 2.031 Å). The more complex BP86 functional gives more ionic character to the Ru–ligand interactions and accurate Ru—N bond distances (2.517 Å and 2.086 Å; X-ray:[60] 1.96–1.98 Å and 2.05–2.09 Å). The widely used hybrid B3LYP functional, which mixes a fraction of HF exchange with KS exchange, gives even higher ionic character to the Ru–ligand interactions and longer than experimental Ru—N bonds (2.011 Å and 2.110 Å). The INDO/S calculations using these DFT-optimized structures show the same trend: the structure optimized with the SVWN functional displays the greatest

Table 1 Irreducible representations, energies, and compositions[a] of the FMOs of $[Ru(terpy)_2]^{2+}$.[57] INDO/S calculations (results are shown in parentheses) were performed on the corresponding DFT optimized structures.

MO	Γ[b]	*SVWN*		*BP86*		*B3LYP*	
	(D_{2d})	*$-\varepsilon$(eV)*	*Ru(%)*	*$-\varepsilon$(eV)*	*Ru(%)*	*$-\varepsilon$(eV)*	*Ru(%)*
LUMO + 3	b_1	8.92 (6.02)	5 (5)	8.31 (6.05)	5 (4)	7.57 (6.01)	3 (4)
LUMO + 2	a_2	9.05 (6.19)	0 (0)	8.41 (6.18)	0 (0)	7.66 (6.12)	0 (0)
LUMO + 0,1	e	9.14 (6.35)	11 (8)	8.54 (6.37)	11 (7)	7.79 (6.31)	8 (6)
HOMO	b_1	11.24 (12.52)	62 (58)	10.58 (12.56)[c]	66 (62)	11.20 (12.63)[c]	70 (65)
HOMO-1,2	e	11.36 (12.54)	65 (64)	10.68 (12.52)[c]	68 (68)	11.31 (12.55)[c]	72 (71)
HOMO-3	a_2	12.44 (13.68)	0 (0)	11.76 (13.59)	0 (0)	12.36 (13.63)	0 (0)
HOMO-4	b_1	12.5 (13.82)	3 (6)	11.81 (13.71)	3 (6)	12.41 (13.74)	3 (6)

[a] AO contributions derived using MPA.[57] [b] Irreducible representations. [c] The order of these MOs is different in DFT and INDO/S calculations. HOMO and HOMO-1,2 are interchanged.

d_π(Ru)-π,π*(terpy) orbital mixing, and the structure obtained using the B3LYP functional shows the least amount of the d_π(Ru)-π,π*(terpy) mixing.

The agreement between DFT and INDO/S for FMO compositions holds for a large number of coordination compounds (Figure 2). This, however, cannot always be the case. First of all, due to significant differences between DFT and INDO/S, it can be expected that the further away we are from the HOMO and the LUMO the higher the differences between the MOs obtained from DFT calculations and those from INDO/S. Secondly, in order to obtain the agreement between DFT and INDO/S results, both methods should produce a correct description of the electronic structure of the particular molecular system. Since these computational methods do have their limitations, this may not be achievable for all systems under investigation. One such case involves the halide and pseudo-halide complexes of transition metals where DFT calculations with common XC functionals give a ground state M—X bonding description that is usually too covalent.[45,61,62] The problem appears to be more pronounced in complexes of late transition metals.

There is another difference in description between DFT and INDO/S. Unoccupied MO energies and HOMO–LUMO gaps differ very significantly in DFT and INDO/S. The HOMO–LUMO gaps

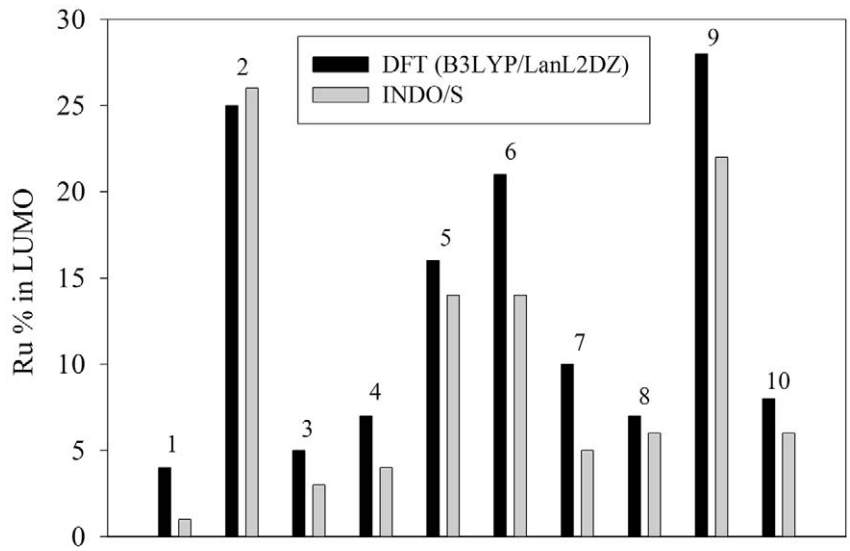

Figure 2 Ruthenium character of the LUMO of $[Ru(NH_3)_5py]^{2+}$ (1), $[Ru(NH_3)_5NO]^{3+}$ (2), $[Ru(NH_3)_4(LL)]^{2+}$ (LL = bpy (3), bpz (4), dioxolene (5), benzoquinonediimine (6)), $[Ru(terpy)_2]^{2+}$ (10) and ruthenium character of the LUMO + 1,2 of $[Ru(LL)_3]^{2+}$ (LL = bpy (7), bpz (8), benzoquinonediimine (9)), as derived from DFT (B3LYP/LanL2DZ) and INDO/S calculations using MPA.[57,58]

obtained from DFT calculations are always smaller than those calculated using *ab initio* or INDO/S methods. Let's take the $[Ru(terpy)_2]^{2+}$ complex as an example again. The HOMO–LUMO gap (Table 1) from the DFT calculations is 2.0–2.1 eV (SVWN and BP86), or 3.4 eV (B3LYP), reasonably close to the lowest energy MLCT band observed in the electronic spectrum of $[Ru(terpy)_2]^{2+}$ (2.62 eV[63,64]). On the other hand, INDO/S gives a much higher value of the HOMO–LUMO gap (~6.2 eV). The reason for such a discrepancy between DFT and INDO/S is explained below.

2.51.3 ORBITAL ENERGIES AND ELECTRONIC SPECTROSCOPY

The KS orbital energies can also be used for qualitative interpretation of the electronic spectra of atoms and molecules[29,65–67] and band gaps in solids.[68] In the HF or semiempirical ZDO methods, the unoccupied MOs are subject to the self-consistent field of all N electrons, whereas the occupied MOs are subject to the self-consistent field of the $(N-1)$ electrons (an electron in an occupied orbital does not interact with itself).[39] So, for unoccupied orbitals of the N-electron system, the MO energy ε_a corresponds to the interactions of an extra $(N+1)$th electron. For the excitation of an electron from the occupied MO ϕ_i to the unoccupied MO ϕ_a, an electron in ϕ_a has one less repulsion than it would have if this were electron affinity, namely with ϕ_i. As a result, the MO energy differences, $\varepsilon_a - \varepsilon_i$, obtained from HF or semiempirical INDO/S calculations are not estimates of transition energies, they have to be combined with appropriate J and K integrals (see Chapter 2.38).

In KS–DFT, the unoccupied orbitals are solutions in exactly the same potential as the occupied orbitals.[46] The unoccupied KS orbitals are therefore not up-shifted in the same way as are unoccupied MOs obtained from HF calculations and, thus, MO energy differences from DFT calculations can serve as the zero-order approximation to transition energies.[65] This has become evident from the development of time-dependent density functional theory (see Chapter 2.40). Levy has shown that the first excited state energy can be obtained, in principle, by a difference of KS orbital energies from two separate calculations: one for the ground state of the molecule (as usual), and one for a weighted ensemble state.[66] On the practical side, Savin *et al.* obtained the true XC potential for the He and Be atoms and found that orbital energy differences agreed with the average of singlet and triplet transition energies to within ~0.1 eV for excitations to Rydberg states.[65] This is not entirely surprising considering that Rydberg states converge to the ionization limit, which is given exactly by Equation (4). There are some less rigorous, but encouraging, results concerning low-energy transitions in extended systems aswell: Muscat *et al.* found a good empirical correlation between B3LYP HOMO–LUMO energy differences and the experimental band gaps in a wide variety of solids, with gaps varying between 1.0 eV and 9.0 eV.[68]

The semiempirical INDO/S CI method (see Chapter 2.38) has long established itself as a useful tool to predict electronic spectra of coordination compounds. On the other hand, TDDFT is a relatively new tool in coordination chemistry, and it is, of course, important that both INDO/S and TDDFT provide similar spectroscopic predictions and assignments of electronic transitions. Table 2 compares the calculated electronic spectra of $Cr(CO)_6$ and $Ni(CO)_4$. INDO/S[70] and TDDFT[71,72] reproduce the experimental spectra of these carbonyl complexes reasonably well (see also Figure 3) and display consistent transition assignments (at least for the dipole-allowed electronic transitions). Gorelsky and Lever studied the series $[Ru(LL)_n(bpy)_{3-n}]^{2+}$ and $[Ru(LL)(NH_3)_4]^{2+}$ (where LL is bpy = 2,2′-bipyridine, bpz = 2,2′-bipyrazine, bqdi = *o*-benzoquinonediimine) and demonstrated that both methods produce a correct description of the electronic structure and spectra of these complexes and usually give consistent assignments of electronic transitions.[42–45] Others also compared the performance of TDDFT and INDO/S using a test series of sulfur–organic compounds[74,75] and other organic chromophores.[75,76] The calculations demonstrated that both methods work reasonably well for $n \rightarrow \pi^*$ and $\pi \rightarrow \pi^*$ transitions. However, since these computational methods have their limitations, good agreement between INDO/S and TDDFT does not hold for all species. For example, the INDO/S assignment[70] for the electronic spectrum of $Ni(CO)_4$ is in some disagreement with the TDDFT assignment.[72]

2.51.4 CONCLUSIONS

KS–DFT gives (at least in principle) exact predictions for all ground state properties, so it is exact MO theory. Can it also be *perfect* in a sense that occupied MO energies are equal (with a negative sign) to vertical ionization energies and the differences between the energies of the occupied and

Table 2 Experimental and calculated (TDDFT and INDO/S) electronic spectra of $[Cr(CO)_6]$ and $[Ni(CO)_4]$.

Experiment[69,70]		*TDDFT (BP/ALDA)*[71,72]			*INDO/S CIS*[70]		
E[a]	f[b]	E[a]	f[b]	*Assignment*[c]	E[a]	f[b]	*Assignment*[c]
$[Cr(CO)_6]\ ^1A_{1g} \rightarrow\ ^1T_{1u}$ transitions							
4.4	0.25	4.19	0.03	$2t_{2g} \rightarrow 9t_{1u}$ (64%) $2t_{2g} \rightarrow 2t_{2u}$ (36%)	4.60	0.01	$2t_{2g} \rightarrow 9t_{1u}$ (59%) $2t_{2g} \rightarrow 2t_{2u}$ (41%)
5.5	2.3	5.76	1.52	$2t_{2g} \rightarrow 2t_{2u}$ (58%) $2t_{2g} \rightarrow 9t_{1u}$ (32%)	5.79	4.0	$2t_{2g} \rightarrow 2t_{2u}$ (56%) $2t_{2g} \rightarrow 9t_{1u}$ (36%)
$[Ni(CO)_4]\ ^1A_1 \rightarrow\ ^1T_2$ transitions							
4.5		4.70	0.006	$9t_2 \rightarrow 10t_2$ (56%) $9t_2 \rightarrow$ 3e (35%)	4.15	0.14	$9t_2 \rightarrow 10t_2$ (78%)
		4.82	0.099	$9t_2 \rightarrow$ 3e (49%) $9t_2 \rightarrow 10t_2$ (23%)	4.36	0.11	$9t_2 \rightarrow$ 3e (86%)
5.4		5.52	0.12	$9t_2 \rightarrow 2t_1$ (52%) 2e $\rightarrow 10t_2$ (19%)	5.36	0.45	$9t_2 \rightarrow 2t_1$ (56%) 2e $\rightarrow 2t_1$ (26%)
6.0	0.7[d]	6.74	1.0	2e $\rightarrow 2t_1$ (47%)	6.2	1.7	2e $\rightarrow 2t_1$ (70%)

[a] Transition energy (ev). [b] Oscillator strength. Note that INDO/S usually overestimates oscillator strengths of electronic transitions by a factor of ~2–3.[42] [c] Only the major parent excitations are reported.
[d] Estimated using $\varepsilon = 24{,}000\ mol^{-1}\ L\ cm^{-1}$ and $\Delta_{1/2} = 6{,}500\ cm^{-1}$.

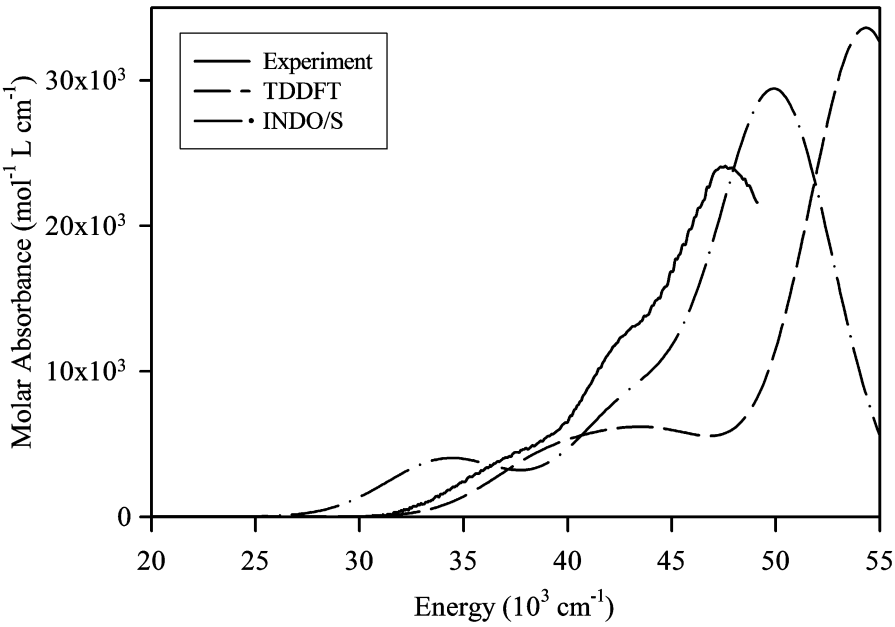

Figure 3 Experimental[70] (solid line) and calculated (INDO/S,[70] dash-dot line; TDDFT[72], dash line) spectrum of $Ni(CO)_4$. The calculated spectra were simulated using Gaussian bands with $\Delta_{1/2} = 6{,}500\,cm^{-1}$.[44,73] The oscillator strengths of electronic transitions from INDO/S calculations were reduced by a factor of 2.

unoccupied MOs approximate transition energies? This question in KS–DFT translates to another one: what meaning is there to the KS orbitals and their eigenvalues? The interpretation of KS orbitals has been a longstanding problem of DFT. Recent investigations of this problem have demonstrated that there are similarities as well as differences between the conventional HF MOs and the KS orbitals, however those differences do not preclude the use of the KS orbitals as a tool in qualitative MO considerations. The KS orbitals are, in fact, more *physical* than those of other MO theories because, after all, the KS orbitals are not only linked with a one-electron potential which includes all non-classical effects, they are also consistent with the exact ground state density (Equation (1).

The Kohn–Sham MO treatment, which is the basis for the TDDFT calculations, allows a MO interpretation of the ground state electronic structure and of the electronic spectrum. The use of KS orbitals affords a direct connection with many existing LCAO–MO treatments (based on semiempirical or HF orbitals).

KS-DFT with the exact XC functional is, in our opinion, the *perfect* MO treatment. However, the DFT calculations with the commonly used functionals still cannot be characterized as *perfect*. Of course, the search for the exact XC functional continues. Until this search is complete, DFT with approximate functionals and available semiempirical methods can serve as very useful research tools in computational transition-metal chemistry.

ACKNOWLEDGMENTS

The author would like to thank Drs. René Fournier and A. B. P. Lever for their input and suggestions.

2.51.5 REFERENCES

1. Fukui, K.; Yonezawa, T.; Shingu, H. *J. Chem. Phys.* **1952**, *20*, 722–725.
2. Fukui, K.; Yonezawa, T.; Nagata, C.; Shingu, H. *J. Chem. Phys.* **1954**, *22*, 1433–1442.
3. Fukui, K. *Theory of Orientation and Stereoselection* **1975**, Springer-Verlag: Berlin.
4. Fukui, K. *Science* **1982**, *218*, 747–754.
5. Woodward, R. B.; Hoffmann, R. *J. Am. Chem. Soc.* **1965**, *87*, 395–397.
6. Longuet-Higgins, H. C.; Abrahamson, E. W. *J. Am. Chem. Soc.* **1965**, *87*, 2045–2046.
7. Hoffmann, R.; Woodward, R. B. *J. Am. Chem. Soc.* **1965**, *87*, 2046–2048.

8. Hoffmann, R.; Woodward, R. B. *J. Am. Chem. Soc.* **1965**, *87*, 4388–4389.
9. Hoffmann, R.; Woodward, R. B. *J. Am. Chem. Soc.* **1965**, *87*, 4389–4390.
10. Klopman, G. *J. Am. Chem. Soc.* **1968**, *90*, 223–234.
11. Klopman, G., Ed., *Chemical Reactivity and Reaction Paths* **1974**, Wiley-Interscience: New York.
12. Pearson, R. G. *Symmetry Rules for Chemical Reactions* **1976**, Wiley: New York.
13. Salem, L. *J. Am. Chem. Soc.* **1968**, *90*, 543–552.
14. Salem, L. *J. Am. Chem. Soc.* **1968**, *90*, 553–566.
15. Parr, R. G.; Yang, W. *Density–Functional Theory of Atoms and Molecules* **1989**, Oxford University Press: New York.
16. Slater, J. C. *Quantum Theory of Molecules and Solids*, McGraw-Hill: New York **1974**; Vol. 4.
17. Janak, J. F. *Phys. Rev. B* **1978**, *18*, 7165–7168.
18. Bartolotti, L. J.; Flurchick, K. *Rev. Comput. Chem.* **1996**, *7*, 187–216.
19. Bartolotti, L. J. In *Structure and Bonding*; Sen, K. D., Jørgensen, C. K., Eds.; Springer-Verlag: Berlin 1987; Vol. 66.; pp 27–40.
20. Alonso, J. A.; Balbás, L. C. In *Structure and Bonding*; Sen, K. D., Jørgensen, C. K., Eds.; Springer-Verlag: Berlin 1987; Vol. 66.; pp 41–78.
21. Gázquez, J. L.; Vela, A.; Galván, M. In *Structure and Bonding*; Sen, K. D., Jørgensen, C. K. Eds.; Springer-Verlag: Berlin, 1987; Vol. 66.; pp 79–97.
22. Liu, G.-H.; Parr, R. G. *J. Am. Chem. Soc.* **1995**, *117*, 3179–3188.
23. Perdew, J. P.; Parr, R. G.; Levy, M.; Balduz, J. L., Jr. *Phys. Rev. Lett.* **1982**, *49*, 1691–1694.
24. Almbladh, C. O.; von Barth, U. *Phys. Rev. B* **1985**, *31*, 3231–3244.
25. Koch, W.; Holthausen, M. C. *A Chemist's Guide to Density Functional Theory* **2001**, 2nd ed.; Wiley-VCH: Weinheim.
26. Casida, M. E. In *Recent Developments and Applications of Modern Density Functional Theory*; Seminario, J. M., Ed., Elsevier: Amsterdam, **1995**, *4*391–439.
27. Casida, M. E.; Jamorski, C.; Casida, K. C.; Salahub, D. R. *J. Chem. Phys.* **1998**, *108*, 4439–4449.
28. Casida, M. E.; Casida, K. C.; Salahub, D. R. *Int. J. Quantum Chem.* **1998**, *70*, 933–941.
29. Casida, M. E.; Salahub, D. R. *J. Chem. Phys.* **2000**, *113*, 8918–8935.
30. Hamel, S.; Casida, M. E.; Salahub, D. R. *J. Chem. Phys.* **2002**, *116*, 8276–8291.
31. Van Leeuwen, R.; Baerends, E. J. *Phys. Rev. A* **1994**, *49*, 2421–2431.
32. Jemmer, P.; Knowles, P. J. *Phys. Rev. A* **1995**, *51*, 3571–3575.
33. Lembarki, A.; Rogemond, F.; Chermette, H. *Phys. Rev. A* **1995**, *52*, 3704–3710.
34. Santamaria, R. *Int. J. Quantum Chem.* **1997**, *61*, 891–898.
35. Kreibich, T.; Kurth, T.; Gross, E. K. U. *Adv. Quantum Chem.* **1999**, *33*, 31–48.
36. Tozer, D. J.; Handy, N. C. *J. Chem. Phys.* **1998**, *109*, 10180–10189.
37. Allen, M. J.; Tozer, D. J. *J. Chem. Phys.* **2000**, *113*, 5185–5195.
38. Koopmans, T. *Physica (Utrecht)* **1933**, *1*, 104.
39. Szabo, A.; Ostlund, N. S. *Modern Quantum Chemistry* **1996**, Dover Publications: Mineola NY.
40. Chong, D. P.; Gritsenko, O. V.; Baerends, E. J. *J. Chem. Phys.* **2002**, *116*, 1760–1772.
41. Stowasser, R.; Hoffmann, R. *J. Am. Chem. Soc.* **1999**, *121*, 3414–3420.
42. Gorelsky, S. I.; Lever, A. B. P. *J. Organomet. Chem.* **2001**, *635*, 187–196; **2002**, *659*, 202.
43. Gorelsky, S. I.; Lever, A. B. P.; Ebadi, M. *Coord. Chem. Rev.* **2002**, *230*, 97–105.
44. Gorelsky, S. I.; Lever, A. B. P. *Can. J. Anal. Sci. Spectrosc.*, **2003**, *48*, 93–105.
45. Gorelsky S. I. Ph.D. Dissertation, York University, 2001.
46. Baerends, E. J.; Gritsenko, O. V. *J. Phys. Chem. A* **1997**, *101*, 5383–5403.
47. Baerends, E. J. *Theor. Chem. Acc.* **2000**, *103*, 265–269.
48. Gritsenko, O. V.; Schipper, P. R. T.; Baerends, E. J. *J. Chem. Phys.* **1997**, *107*, 5007–5015.
49. Bickelhaupt, F. M.; Baerends, E. J. *Rev. Comput. Chem.* **2000**, *15*, 1–86.
50. Hamel, S.; Duffy, P.; Casida, M. E.; Salahub, D. R. *J. Electron Spectroscopy and Rel. Phenomena* **2002**, *123*, 345–363.
51. Mulliken, R. S. *J. Chem. Phys.* **1955**, *23*, 1833–1840.
52. Mulliken, R. S. *J. Chem. Phys.* **1955**, *23*, 1841–1846.
53. Mulliken, R. S. *J. Chem. Phys.* **1955**, *23*, 2338–2342.
54. Mulliken, R. S. *J. Chem. Phys.* **1955**, *23*, 2343–2346.
55. Mulliken, R. S. *J. Chem. Phys.* **1962**, *36*, 3428–3439.
56. Reed, A. E.; Weinstock, R. B.; Weinhold, F. *J. Chem. Phys.* **1985**, *83*, 735–746.
57. DFT calculations have been carried out using *Gaussian 98*, Revision A.7. INDO/S calculations were performed using *Hyperchem 5.11* and utilizing the Ru and N atomic parameters taken from Krogh-Jespersen, K.; Westbrook, J. D.; Potenza, J. A.; Schugar, H. J. *J. Am. Chem. Soc.* **1987**, *109*, 7025–7031.
58. Gorelsky, S. I.; *AOMix* program, http://www.obbligato.com/software/aomix/.
59. Kohn, W.; Becke, A. D.; Parr, R. G. *J. Phys. Chem.* **1996**, *100*, 12974–12980.
60. Pyo, S.; Perez-Cordero, E.; Bott, S. G.; Echegoyen, L. *Inorg. Chem.* **1999**, *38*, 3337–3343.
61. Turki, M.; Daniel, C.; Záliš, S.; Vlček, A., Jr.; van Slageren, J.; Stufkens, D. J. *J. Am. Chem. Soc.* **2001**, *123*, 11431–11440.
62. Szylagyi, R. K.; Metz, M.; Solomon, E. I. *J. Phys. Chem. A* **2002**, *106*, 2994–3007.
63. Lin, C.-T.; Böttcher, W.; Chou, M.; Creutz, C.; Sutin, N. *J. Am. Chem. Soc.* **1976**, *98*, 6536–6544.
64. Stone, M. L.; Crosby, G. A. *Chem. Phys. Lett.* **1981**, *79*, 169–173.
65. Savin, A.; Umrigar, C. J.; Gonze, X. *Chem. Phys. Lett.* **1998**, *288*, 391–395.
66. Levy, M. *Phys. Rev. A* **1995**, *52*, R4313–R4315.
67. Baerends, E. J.; Ricciardi, G.; Rosa, A.; van Gisbergen, S. J. A. *Coord. Chem. Rev.* **2002**, *230*, 5–27.
68. Muscat, J.; Wander, A.; Harrison, N. M. *Chem. Phys. Lett.* **2001**, *342*, 397–401.
69. Beach, N. A.; Gray, H. B. *J. Am. Chem. Soc.* **1968**, *90*, 5713–5721.
70. Kotzian, M.; Rösch, N.; Schröder, H.; Zerner, M. C. *J. Am. Chem. Soc.* **1989**, *111*, 7687–7696.
71. Rosa, A.; Baerends, E. J.; van Gisbergen, S. J. A.; van Lenthe, E.; Groeneveld, J. A.; Snijders, J. G. *J. Am. Chem. Soc.* **1999**, *121*, 10356–10365.

72. van Gisbergen, S. J. A.; Groeneveld, J. A.; Rosa, A.; Snijders, J. G.; Baerends, E. J. *J. Phys. Chem. A* **1999**, *103*, 6835–6844.
73. Gorelsky, S. I.; *SWizard* program, http://www.obbligato.com/software/swizard/.
74. Fabian, J. *Theor. Chem. Acc.* **2001**, *106*, 199–217.
75. Fabian, J.; Diaz, L. A.; Seifert, G.; Niehaus, T. *J. Mol. Struct. (Theochem)* **2002**, *594*, 41–53.
76. Kwasniewski, S. P.; Deleuze, M. S.; François, J. P.; *Int. J. Quantum Chem.* **2000**, *80*, 672–680.

Comprehensive Coordination Chemistry II
ISBN (set): 0-08-0437486

Volume 2, (ISBN 0-08-0443249); pp 651–660

2.52
AOMX: Angular Overlap Model Computation

H. ADAMSKY and T. SCHÖNHERR
Heinrich-Heine-Universität, Düsseldorf, Germany
and
M. ATANASOV
Bulgarian Academy of Sciences, Sofia, Bulgaria

2.52.1 INTRODUCTION 661
2.52.2 HAMILTONIAN, PARAMETERS, AND MATRICES 662
2.52.3 SYMMETRY CONSIDERATIONS 663
2.52.4 FEATURES OF AOMX 664
2.52.5 AOMX IN THE INTERNET 664
2.52.6 REFERENCES 664

2.52.1 INTRODUCTION

Since the 1980s, there has been a growing demand for a general ligand field program that is based on real d orbitals to help interpret highly resolved spectra of TM compounds in a straightforward manner. Increased spectral resolution at low temperatures together with sophisticated methods involving polarized light, time resolution, and magnetic fields have revealed electronic structures that could not be resolved previously. For the tedious work of assigning electronic states to absorption and emission spectra the angular overlap model (AOM) is preferred to crystal field theory because the AOM gives a more vivid view of chemical bonds in transition metal complexes and because it builds conceptual bridges to molecular orbital theory. An in-depth discussion of the AOM and its variants, as well as case studies of its applications to experimental data, can be found in Chapter 2.36.

The subject of this chapter is AOMX, a computer program that the authors decided to develop due to the lack of a general computational tool that allows for semiempirical calculations within the AOM parameter framework making extensive use of symmetry. The program was based on Hoggard's d^3 program (AOM1)[1] and was generalized to treat arbitrary d^n systems.[2] Further extensions have led to the present version, called AOMX.

This chapter is organized as follows: after defining the Hamiltonian and the parameterization scheme, we will explain how the symmetry of the eigenstates is exploited by AOMX, then some technical details are presented, and, finally, how to obtain and how to use the program.

2.52.2 HAMILTONIAN, PARAMETERS, AND MATRICES

AOMX computes ligand field states of d^n complexes using the common tetragonally quantized d_{xy}, d_{yz}, d_{zx}, $d_{x^2-y^2}$, d_{z^2} orbital basis and a Hamiltonian of the general form

$$\mathbf{H} = \mathbf{V}_{\mathrm{LF}} + \mathbf{V}_{\mathrm{ee}} + \mathbf{V}_{\mathrm{Trees}} + \mathbf{V}_{\mathrm{SO}} + \mathbf{V}_{\mathrm{mag}} \tag{1}$$

which is diagonalized using antisymmetrized product functions (Slater determinants). Group theoretical methods applied to the eigenfunctions of the system are utilized to compute the symmetry of the electronic states. The ligand field operator $\mathbf{V}_{\mathrm{LF}}$ is described by parameters e_λ, ($\lambda = \sigma, \pi_s, \pi_c, \delta_s, \delta_c$) (where the subscripts c (cosine) and s (sine) denote the components of the two-fold degenerate bonding types and become important in cases of anisotropic bonds) and the angular position of each ligand k as defined by its Eulerian angles Θ_k, Φ_k, Ψ_k, or Cartesian coordinates. In fact, AOMX always uses three Eulerian rotations as shown in Figure 1, which is the most general case. (Note that any radial dependence is separated off into the $\mathbf{V}_{\mathrm{LF}}$ parameters.) The corresponding 5×5 transformation matrix $\mathrm{F}_{\lambda i}(\Theta,\Phi,\Psi)$ was described in detail by Schäffer[3] and Schmidtke.[4] It decomposes each metal orbital ϕ_{Mi} into functions that are symmetry-adapted to one of the ligands k:

$$\begin{aligned} |\phi_{Mi}(x,y,z)\rangle &= \sum_\lambda |\phi_{Mi}(x''',y''',z''')\rangle\langle\,\phi_{Mi}(x''',y''',z''') \mid \phi_{Mi}(x,y,z)\rangle \\ &= \sum_\lambda |\phi_{Mi}(x''',y''',z''')\rangle \cdot \mathrm{F}_{\lambda i}(\Theta,\Phi,\Psi) \end{aligned} \tag{2}$$

With each ligand having an effective potential $\mathbf{V}^{\mathbf{eff}}_{L_k}$ and valence orbitals $\phi_{L_{k\lambda}}$, we can write the general AOM matrix element as a second-order perturbation term:

$$\begin{aligned} H_{ij}^{\mathrm{AOM}} &= \sum_\lambda \sum_{k=1}^{nL} \mathrm{F}_{\lambda i}(\Theta_k,\Phi_k,\Psi_k)\mathrm{F}_{\lambda j}(\Theta_k,\Phi_k,\Psi_k) \\ &\quad \times \left\{ \langle\phi_{M_\lambda}|\mathbf{V}^{\mathbf{eff}}_{L_k}|\phi_{M_\lambda}\rangle + \langle\phi_{M_\lambda}|\mathbf{V}^{\mathbf{eff}}_{L_k}|\phi_{L_{k\lambda}}\rangle\langle\phi_{L_{k\lambda}}|\mathbf{V}^{\mathbf{eff}}_{L_k}|\phi_{M_\lambda}\rangle/(\varepsilon_M - \varepsilon_{L_{k\lambda}}) \right\} \\ &= \sum_\lambda \sum_{k=1}^{nL} \mathrm{F}_{\lambda i}(\Theta_k,\Phi_k,\Psi_k)\mathrm{F}_{\lambda j}(\Theta_k,\Phi_k,\Psi_k) \cdot e_\lambda(k) \end{aligned} \tag{3}$$

Thus, the AOM matrix element is separated into a sum of angular geometry factors $\mathrm{F}_{\lambda i}$ and electronic parameters $e_\lambda(k)$ that contain all the rest, including ionic as well as covalent contributions. Note that we are dealing with independent local ligand potentials and that $\lambda = \sigma, \pi, \ldots$ corresponds to the well-known types of chemical bonds.

The AOMX program makes use of Equation (3) to compute the 5×5 matrix of the ligand field potential $\mathbf{V}_{\mathrm{LF}}$. Higher coordination spheres can easily be incorporated by adding more ligators to the system. Further corrections like phase coupling, misdirected valency (to be included in AOMX in 2004), and s–d mixing can be added, the latter being particularly relevant in square planar complexes. The electron repulsion $\mathbf{V}_{ee}$ is represented by Racah parameters A, B, C, and may optionally be corrected for anisotropic nephelauxetic effects by orbital reduction factors $\mu_i \leq 1$ leading to electron-repulsion integrals of the form $\mu_a\mu_b\mu_c\mu_d < \phi_a\phi_b|\mathrm{r}_{12}{}^{-1}|\phi_c\phi_d >$.[5] As a further two-electron correction, the Trees operator $\mathbf{V}_{\mathrm{Trees}} = \alpha \cdot \mathbf{L}^2$ (Trees parameter α) may

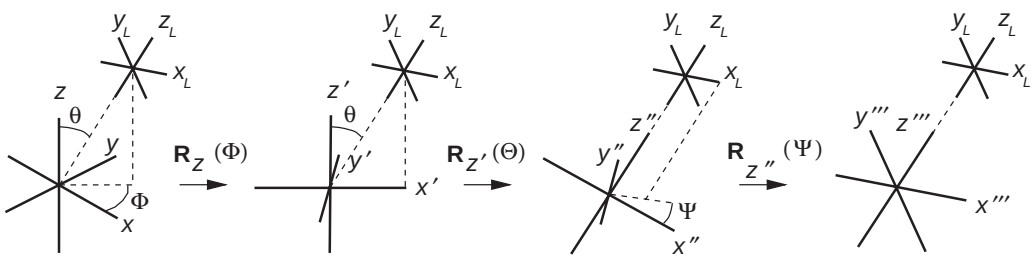

Figure 1 Rotation of the metal coordinate system by three Eulerian angles.

also be taken into account.[2,6] Matrix elements for including spin–orbit coupling are set up using the operator $\mathbf{V}_{SO} = \zeta\Sigma_i \mathbf{l}_i \cdot \mathbf{s}_i$ with the parameter ζ. Here, too, spatial anisotropy may be taken into account by defining the components of $\mathbf{l}$ as $k_x\mathbf{l}_x$, $k_y\mathbf{l}_y$ and $k_z\mathbf{l}_z$ with reduction factors $k_i < 1$.[7] Finally, the influence of an external magnetic field, described by the operator $\mathbf{V}_{mag} = \mu_B \cdot \mathbf{H}(\Theta_{mag}, \Phi_{mag}) \cdot \Sigma_i(\mathbf{l}_i + \mathbf{2s}_i)$, can be incorporated into the calculation, again with the option of anisotropic orbital momentum reduction.

Once the system is parameterized, the many-electron matrix is set up by successively applying the operators ofEquation (1) to simple anti-symmetrized product functions (Slater determinants). The size of the basis set is given by the number of possible distributions of n_d electrons over 10 spin orbitals, $n_D = \binom{10}{n_d}$, which is quite moderate: Taking advantage of the electron/hole equivalence (in hole configurations, the sign of matrix elements of one-electron operators will be inverted by the program), it can adopt values between 10 ($d^1 d^9$) and 252 (d^5). Complex Hermitian matrices of this size can be diagonalized very rapidly and without numerical problems using the conventional Householder algorithm, as implemented in the EISPACK package,[8] which is part of the AOMX source code.

2.52.3 SYMMETRY CONSIDERATIONS

As the basic functions are not symmetrized, the eigenvectors of the system do not exhibit any symmetry and would be useless as such. But it is evident that each of the eigenvectors must belong to an irreducible representation of the symmetry group of the underlying Hamiltonian. Except in the trivial case of no symmetry (C_1), AOMX automatically determines symmetries by applying group theoretical techniques as will be outlined here.

Symmetry information can be obtained if the characters of the state vector with respect to the symmetry operations of the group are found. For Ψ_i being the first of a g_i-fold set of degenerate states, this can be achieved by evaluating

$$\chi^{(\Psi_i)}(\mathbf{S}) = \sum_{k=1}^{i+g_i-1} \langle \Psi_k | \mathbf{S} | \Psi_k \rangle = \mathrm{Tr}(\mathbf{S}\{\Psi_i\}) \tag{4}$$

for each symmetry operator S and subsequent comparison of the results with the character table of the symmetry group of the complex compound. Special care has to be taken when rotating spin functions. In such cases the methods outlined in Wigner's textbook[9] must be applied. Thorough inspection of the symmetry properties of d^n systems (following Jørgensen's concept of holohedric symmetry (see Chapter 2.38, Section 2.38.3.1) shows that only a few representative symmetry operators need to be taken into account in order to identify the symmetry of a d^n state. Table 1 shows the relevant cases unambiguously.

Beyond symmetry, the eigenstate vectors also contain information about orbital occupations with respect to the one-electron basis functions ϕ_k, which can be very useful for chemists. AOMX computes orbital occupation numbers $q(\phi_m)$ in a state function Ψ_i from the diagonal elements of the one-electron density operator $\boldsymbol{\rho}_i$:

$$q(\phi_m) \equiv \langle \phi_m | \rho_i | \phi_m \rangle = \sum_{j=1}^{n_D} c_{ji}^* c_{ji} \sum_{k=1}^{n} \delta(j_k, m) \tag{5}$$

where n_D is the number of Slater determinants, n is the number of d electrons, and j_k denotes the orbital of the kth electron in the jth determinant of state i. In other words: AOMX does a

Table 1 Rotations needed to identify the irreps of d^n complexes.

	O	D_4	D_3	D_2	C_2	C_1
Ordinary group or unique reps of the double group	C_4^z, C_2^x	C_4^z, C_2^x	C_2^x	C_2^z, C_2^x	C_2^z	[a]
Double-valued reps of the double group	C_4^z	C_4^z	C_3^z	[a]	[a]	[a]

[a] distinction not required.

Mullikan-like population analysis, but without overlap densities because the orbital basis function are orthogonal to each other.

2.52.4 FEATURES OF AOMX

The program was designed with the aim in mind that it should be easy to use, allow for parameter fitting, and be fast and portable across systems. For this purpose, we developed a flexible input description language for defining the complex geometry, experimental state assignments, and parameter optimizations (using the Powell parallel subspace algorithm[10]) as well as multidimensional parameter scans. Parameters can also be constrained during optimizations or scans, and even alternative parameterization schemes (e.g., CF parameters) can be used as long as they can be related to the AOM parameter set. The output options include eigenvalues, wavefunctions, the symmetry of eigenstates, orbital occupation numbers, one-electron matrices of V_{LF}, V_{SO}, or V_{mag}, as well as interelectronic repulsion integrals.

The program is coded in standard Fortran 77 and is very fast; even multi-parameter fitting calculations are rapidly completed. Thanks to the widespread free GNU gcc/g77 compilers, it can be run on virtually any Unix/Linux system and also on Windows computers provided the GNU tools are installed on the machine.

2.52.5 AOMX IN THE INTERNET

AOMX is available in the Internet at the address http://www.aomx.de. This site will provide selected examples and an angular overlap model (AOM) parameter database, and will be further developed to a forum for scientific exchange about AOM applications to TM complexes.

2.52.6 REFERENCES

1. Hoggard, P. E. *Coord. Chem. Rev*. **1986**, *37a*, 85–120.
2. Adamsky, H. Thesis, University of Düsseldorf, 1995.
3. Schäffer, C. E. *Struct. Bonding* **1968**, *5*, 68–95.
4. Schmidtke, H.-H. *Z. Naturforsch*. **1964**, *19a*, 1502–1510.
5. Schmidtke, H.-H.; Adamsky, H.; Schönherr, T. *Bull. Chem. Soc. Jpn*. **1988**, *61*, 59–65.
6. Hoggard, P. E. *Z. Naturforsch*. **1982**, *37a*, 85–94.
7. Atanasov, M.; Schönherr, T. *Inorg. Chem*. **1990**, *29*, 4545–4552.
8. Smith, B. T.; Doyle, J. M.; Dongarra, J. J.; Ikebe, Y.; Klema, V. C.; Moler, C. B. *EISPACK Guide*; Springer-Verlag: Berlin, 1976.
9. Wigner, E. *Group Theory and its Applications to the Quantum Mechanics of Atomic Spectra*; Academic Press: New York, 1959.
10. Powell, M. J. D. *Comp. J*. **1964**, *7*, 155–162.

Comprehensive Coordination Chemistry II
ISBN (set): 0-08-0437486
Volume 2, (ISBN 0-08-0443249); pp 661–664

2.53
GAMESS and MACMOLPLT

M. W. SCHMIDT, B. M. BODE, and M. S. GORDON
Iowa State University, Ames, IA, USA

2.53 REFERENCES 666

The General Atomic and Molecular Electronic Structure System (GAMESS) is an *ab initio* quantum chemistry code that has been developed by the Gordon group since 1982. GAMESS is in use at well over 9,000 sites worldwide. These sites range from high schools to undergraduate colleges to research universities in the USA and worldwide to government laboratories to the private sector. Unlike nearly all such widely used codes, GAMESS is distributed at no cost to all users, simply by accessing www.msg.ameslab.gov and signing a license agreement.

An important feature of GAMESS is that an increasing number of its functionalities can be run on scalable computers, ranging from clusters of low-cost Linux computers to clusters of high-end workstations using advanced switching technology to massively parallel computers. The scalability of GAMESS is facilitated by the distributed data interface (DDI) functionality, developed by Graham Fletcher, which allows large data arrays to be distributed across all available nodes. Scalable features in GAMESS that make use of DDI include Hartree-Fock, MCSCF, density functional theory (DFT), closed shell second order perturbation theory (MP2) energies and gradients, multi-reference MP2 (MRMP2) energies, and RHF Hessians.

While GAMESS was originally developed as a research tool to provide computational understanding of such disparate areas as drug design, materials development, and condensed phase effects, in recent years attention has turned to the use of GAMESS for educational purposes. To this end, the full GAMESS code was migrated to both the Apple Macintosh and the PC. As a result, GAMESS is not only free, but it can be used effectively on low-cost, affordable hardware, allowing GAMESS to be run on computers ranging from individual PCs up through world class supercomputers at national centers. GAMESS is an especially user-friendly system on the Macintosh, since it is mouse driven and no knowledge of UNIX is required.

The utility of GAMESS for educational purposes has been dramatically increased by the development of the graphical interface MacMolPlt. MacMolPlt includes a simple molecule builder and input generator for GAMESS to prepare basic GAMESS input files. However, the real power of MacMolPlt is its ability to visualize the results of GAMESS calculations. MacMolPlt accepts output files from any version of GAMESS run on any platform. From the output files, MacMolPlt can illustrate structures including real time rotations, can animate molecular vibrations, minimum energy reaction paths, and dynamics trajectories, and can plot (in both two- and three-dimensions) molecular orbitals, localized orbitals, total electron densities, density differences, and electrostatic potential maps. Each of the surfaces is computed on the fly from the geometry, basis set, and orbital vectors at the request of the user and thus does not need to be pre-computed or stored. MacMolPlt includes the ability to produce output in a variety of formats including high-resolution images for full color printouts and QuickTime movies of any molecular animation. The combination of GAMESS and MacMolPlt have proved to be very useful in

classes ranging from freshman majors to physical chemistry laboratory to graduate computational chemistry. Both codes are continually being improved, both with regard to new features and ease of use, by the Gordon group. Future extensions will include the interface of MacMolPlt to other computational chemistry codes and the extension of the input generator to a large subset of GAMESS methods.

GAMESS has the capability to perform molecular orbital calculations at a wide variety of sophistication levels, ranging from semi-empirical and molecular mechanics calculations to the highest level of *ab initio* theory. *Ab initio* wavefunctions can be of the RHF, high-spin or low-spin ROHF, GVB, UHF, or MCSCF types. Analytic gradients are available for all wavefunctions, and analytic hessians are available for RHF, ROHF, and one-pair GVB wavefunctions. Numerical hessians can be calculated for all wavefunction types. Post-SCF correlation treatments include configuration interaction (CI), perturbation theory, and coupled clusters. Energies at second order in perturbation theory can be calculated for RHF, UHF, ROHF, and MCSCF wavefunctions. CI computations may follow all of these except UHF. A recent addition to GAMESS is the capability to perform a variety of coupled cluster calculations as developed by the Piecuch group at Michigan State University. DFT, a very popular alternative to traditional means for achieving some measure of electron correlation, has recently been added to GAMESS. A number of functionals have been implemented for RHF, UHF, and ROHF type Kohn-Sham calculations.

GAMESS can perform a wide range of quantum chemical calculations, including:

Optimization of molecular geometries in Cartesian or internal coordinates.
Determination of saddle points on potential energy surfaces.
Tracing intrinsic reaction paths for chemical reactions.
Vibrational analysis including infrared and Raman intensities.
Determination of *ab initio* classical trajectories without prior knowledge of the potential energy surface.
Calculation of properties, such as multipole moments, electrostatic potentials, electric fields and electric field gradients, polarizabilities and hyperpolarizabilities, electron and spin densities, population analyses, localized orbitals, and spin-orbit coupling.
The evaluation of the effects of solvation on chemical processes.
The analysis of reactions and dynamics occurring on surfaces.

The features for treating solvation and surface chemistry deserve special mention. Both methods fall into the general class of methods referred to as QM/MM (quantum mechanics interfaced with molecular mechanics). The surface chemistry approach, called surface integrated molecular orbital molecular mechanics or SIMOMM, is a traditional QM/MM method, in which the QM/MM boundary is implemented using "link atoms." Any QM method in GAMESS may be used as the embedded QM cluster, while the MM program TINKER is used for the MM part. The effective fragment potential (EFP) discrete solvation method is a very sophisticated approach, in which terms that account for Coulomb interactions, polarizability and exchange repulsion + charge transfer are added to the *ab initio* Hamiltonian. An interface that couples EFP with continuum methods is also available in GAMESS.

For more details about GAMESS and MacMolPlt, the reader is referred to the web page cited above and to the following references.[1–7]

ACKNOWLEDGMENTS

The development of GAMESS has been supported for more than 20 years by grants from the Air Force Office of Scientific Research, and more recently (for both GAMESS and MacMolPlt) by software development grants from the Department of Defense and the Department of Energy. Hardware grants from these agencies and from IBM have also aided the code developments.

2.53 REFERENCES

1. Schmidt, M. W.; Baldridge, K. K.; Boatz, J. A.; Elbert, S. T.; Gordon, M. S.; Jensen, J. H.; Koseki, S.; Matsunaga, N.; Nguyen, K. A.; Su, S.; Windus, T. L.; Dupuis, M.; Montgomery, J. A., Jr. *J. Comp. Chem.* **1993**, *14*, 1347.
2. Schmidt, M. W.; Gordon, M. S. *Annu. Rev. Phys. Chem.* **1998**, *49*, 233.
3. Shoemaker, J.; Burggraf, L. W.; Gordon, M. S. *J. Phys. Chem. A* **1999**, *103*, 3245.

4. Bode, B. M.; Gordon, M. S. *J. Mol. Graph.* **1999**, *16*, 133.
5. Fletcher, G. D.; Schmidt, M. W.; Gordon, M. S. *Adv. Chem. Phys.* **1999**, *110*, 267.
6. Schmidt, M. W.; Fletcher, G. D.; Bode, B. M.; Gordon, M. S. *Comput. Phys. Commun.* **2000**, *128*, 190.
7. Gordon, M. S.; Freitag, M. A.; Bandyopadhyay, P.; Kairys, V.; Jensen, J. H.; Stevens, W. J. *J. Phys. Chem.* **2001**, *105*, 293.

Comprehensive Coordination Chemistry II
ISBN (set): 0-08-0437486

Volume 2, (ISBN 0-08-0443249); pp 665–667

2.54
CAMMAG

A. J. BRIDGEMAN
University of Hull, Kingston upon Hull, UK
and
R. J. DEETH
University of Warwick, Coventry, UK

2.54.1 OVERVIEW 669
2.54.2 PARAMETRIZATION 670
2.54.2.1 Ligand-field Potential 670
2.54.2.2 Interelectron Repulsion and Spin–Orbit Coupling 670
2.54.2.3 Intensity Parameters 671
2.54.3 TRANSITION ENERGIES 671
2.54.4 MAGNETIC SUSCEPTIBILITIES AND *g*-VALUES 671
2.54.5 INTENSITY 671
2.54.5.1 Solution and Linearly Polarized Spectra 671
2.54.5.2 Circularly Polarized Spectra 672
2.54.6 CONCLUDING REMARKS 672
2.54.7 REFERENCES 672

2.54.1 OVERVIEW

CAMMAG is a program suite for the calculation of a wide variety of ligand-field properties. It was developed by Dr Malcolm Gerloch and co-workers over many years. The name of the program is derived from "CAMbridge MAGnetism" and reflects the early interests of the group particularly in single crystal, variable temperature magnetic anisotropies. Many of the theoretical developments of the ligand-field approach developed by the Cambridge group over the last three decades are implemented in the code. Various versions of the program are in use in laboratories around the world and this section describes the features of the most recent edition.[1] The theoretical background and examples of applications are discussed elsewhere[2–5] so only the capabilities are outlined here.

Ligand-field theory is concerned only with the low-lying electronic states of a *d*- or *f*-block metal complex which can be described by the rearrangements of electrons within the *d*- or *f*-shell. These states describe the magnetic properties (paramagnetism, *g*-values) and the "*d–d*" (or "*f–f*") electronic spectra (color, linear, and circular dichroism).

The ligand-field model implemented in CAMMAG is parametric. The user inputs appropriate ligand-field parameters which are used to calculate eigenvectors and eigenvalues for the desired ligand-field properties. These properties are then compared to experimentally determined values and the program provides various procedures—both manual and automated—by which the parameters may be varied until the experimental properties are reproduced as accurately as possible.

The program is divided into two segments: SETUP and RUN. In SETUP, everything is computed which is independent of the parameter values. The user selects a basis set which may

be defined as one of more terms or levels of the appropriate free ion. Basis sets may contain terms of one or more spin-multiplicities depending on the molecule to be studied and the accuracy required. With modern computing power, the full basis set is usually used in calculations, at least for *d*-block systems. The user also inputs the molecular geometry either in crystallographic or molecular coordinates. From this input, the program constructs a series of separate matrices to deal with the various terms in the ligand-field Hamiltonian.

In RUN, copies of these matrices are multiplied by a set of associated parameters and then summed. The total matrix is diagonalized and the ligand-field properties calculated from the resulting eigenvalues and eigenvectors.

2.54.2 PARAMETRIZATION

2.54.2.1 Ligand-field Potential

The ligand-field potential is parametrized directly using the *d*-orbital energies, or indirectly using "traditional" global parameters (Δ_{oct}, Δ_{tet}, Dq, Ds, and Dt, etc.) or local ("cellular ligand-field (CLF)") parameters (e_σ and e_π) for each ligand. The CLF parametrization (In its computational implementation, the CLF model is identical to the "angular overlap model" (AOM) and it is only in the interpretation of the underlying physics that the two approaches differ) is usually preferred, except for high symmetry molecules, as it provides the most transparent connection with the σ and π functionality of each distinct metal–ligand bond. For each ligand, the user defines values for e_σ, $e_{\pi\perp}$, and $e_{\pi||}$ representing, crudely, the σ-donor strength and the π-donor (or acceptor) strength of the ligand in two mutually perpendicular directions. These directions are defined in SETUP and are taken to reflect the expected functionality of the ligand. A ligand such as NH_3 is expected to be π-neutral and so $e_{\pi x} = e_{\pi y} = 0$ can be assumed. A ligand such as Cl^- is expected to be an isotropic π-donor so $e_{\pi x} = e_{\pi y}$. However, a ligand like pyridine is expected to π-bond to the metal only in the plane perpendicular ($\perp$) to the ring—$|e_{\pi\perp}| \neq 0$—but to be π-neutral parallel ($||$) to the plane of the ring—$|e_{\pi||}| = 0$. By appropriate choice of the local x- and y-axes, the number of parameters to be considered can therefore be significantly reduced.

Figure 1 represents a case where the metal–ligand bond path is not located along the metal–ligand vector. As discussed in Chapter 2.36, such "bent bonding" introduces a further parameter, $e_{\sigma\pi}$, to characterize the mixed σ and π component of the bonding. Whilst this extra level of parametrization is usually unnecessary for a treatment of transition energies, it is often a crucial component of an accurate modeling of rotatory strengths.

2.54.2.2 Interelectron Repulsion and Spin–Orbit Coupling

Interelectron repulsion integrals are parametrized via central-field Condon–Shortley parameters F_2 and F_4 (or the Racah equivalents B and C) for the *d*-block. For the *f*-block, the related E_1, E_2, and E_3 parameters are used together with an additional nine parameters to account for

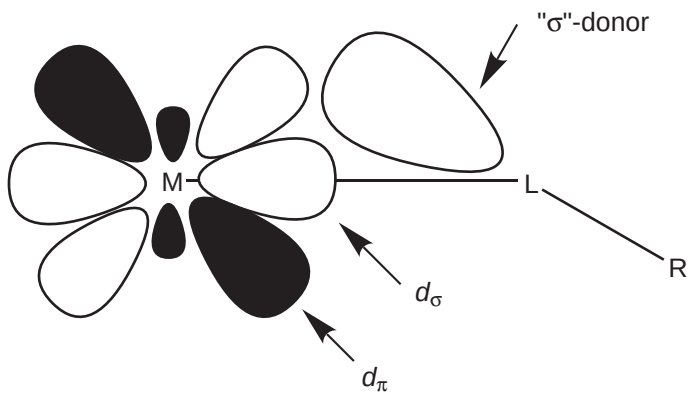

Figure 1 An example of bent bonding.

configuration interaction. Spin–orbit coupling is parametrized with the one-electron spin–orbit coupling constant, ζ. All of these parameters are spherical in that no recognition of the molecular shape is made and their magnitudes differ from their free-ion counterparts due to the nephelauxetic effect.

2.54.2.3 Intensity Parameters

The CLF intensity model (Chapter 7.11) parametrizes local transition moments using ${}^{L}t_{\lambda}$ parameters. For each M—L bond, parity mixing is deemed to arise from $\lambda = \sigma$, πx, and πy modes and from L = P and F (for *d*-block) and L = D and G (for *f*-block) sources arising from both metal- and ligand-based functions. For acentric complexes, the local transition moments are appropriately summed to yield global moments and polarizations. For vibronically sourced intensity, the local moments are multiplied by the ligand displacements for each vibrational mode and then summed. If these displacements are known, from a prior normal coordinate analysis, the contributions from different modes to the total static- and vibronic-sourced intensity is set and no extra parametrization is introduced. The model can then be used for both acentric, near-centric, and centric complexes and the relative contributions are decided computationally by the geometry and vibrational displacements. If the vibrational displacements are not known then the relative contributions from different modes and the relative static-to-vibronic intensities are parametrized.

The model calculates the relative intensity of transitions between the states built from a prior energy analysis. No simplification of the complex geometry is required and spin–orbit coupling and its effects are naturally included.

2.54.3 TRANSITION ENERGIES

The eigenvalues of the ligand-field Hamiltonian for the free-ion basis may be compared directly with experimental transition energies. The eigenvalues for the same ligand-field potential but for a d^1 or f^1 basis set yield the orbital energies. It is usual to adopt the actual crystallographic ligand positions and include spin–orbit coupling in an analysis as small distortions and spin–orbit mixing are often important in determining magnetic and spectroscopic properties. Assignments of spin–orbit levels in low-symmetry complexes can be made by projecting out the spin and the proportion of the irreducible representations of an ideal single group. Such assignments can be used together with selection rules to guide an analysis and to tie a least-squares procedure. The intensity model outlined below, however, allows a simultaneous modeling of energies and intensities making the use of such selection rules largely redundant.

2.54.4 MAGNETIC SUSCEPTIBILITIES AND *g*-VALUES

Calculation of single-center magnetic properties from the ligand-field eigenvectors requires input of Stevens' orbital reduction factor, *k*, and the temperature. CAMMAG provides the principal molecular and crystal susceptibilities and *g*-values (for odd-electron systems) and their orientations.

2.54.5 INTENSITY

2.54.5.1 Solution and Linearly Polarized Spectra

The intensity model provides the relative molecular and crystal electric dipole intensities of bands and their polarizations. When parametrized together with a prior normal coordinate analysis, acentric, near-centric, and centrosymmetric complexes can be treated on an equal footing and around 40 molecules with a variety of geometries have been studied. The absolute magnitude of the intensity parameters can be established via fitting to oscillator strengths. The variation of the intensity distribution with temperature is obtained through both the population of levels near the ground state and the temperature dependence of the vibrational displacements.

Magnetic dipole-derived intensity, which requires no parity mixing, is calculated in absolute units from the matrix elements of the magnetic moment operator and requires no additional parametrization. For *d–d* spectra, this source is generally unimportant. However, for *f–f* spectra, magnetic dipole-derived intensity must be included. As the electric dipole model only provides a relative intensity scale, a scaling parameter for the two sources must be introduced.

2.54.5.2 Circularly Polarized Spectra

The calculation of circular dichroism (CD) from solution or crystal spectra requires both electric-dipole and magnetic-dipole moments and these are naturally provided by an analysis of the energies and linear or unpolarized spectral intensities. CD is found to be an exacting test of the quality of the ligand-field eigenvectors and a simultaneous re-analysis of the ligand-field potential is often required. In particular, the correct modeling of rotatory strengths is only possible upon recognition of bent bonding effects.

2.54.6 CONCLUDING REMARKS

CAMMAG provides the means for a simultaneous modeling of much of the spectroscopic and magnetic properties of transition metal and *f*-block complexes. Whilst much of the work of Malcolm Gerloch and his co-workers centered on the development and implementation of the underlying theory and its testing through series of highly detailed analyses, CAMMAG is also useful as a tool *alongside* modern electronic methods. Full analyses using CAMMAG may require the availability of crystallographic coordinates, magnetic susceptibilities and orientations, linearly and circularly polarized spectra and vibrational frequencies. In the study of bioinorganic and gas- or solution-phase systems, such information may be lacking or incomplete. However, ligand-field methods still provide perhaps the only reliable technique for modeling transition energies and intensities, magnetic moments and *g*-values. The library of parameter values available provides the basis for the qualitative prediction of these properties and for their dependence on geometry. To encourage further development and use of the CLF model following Gerloch's retirement, CAMMAG is now freely available.[1]

2.54.7 REFERENCES

1. Dale, A. R.; Duer, M. J.; Fenton, N. D.; Gerloch, M.; Jones, M.; McMeeking, R. F. *CAMMAG5*, University of Cambridge, 2001. The program is available by contacting Dr. A. J. Bridgeman, University of Hull, UK, email a.j.bridgeman@hull.ac.uk.
2. Gerloch, M. *Magnetism and Ligand-Field Analysis*; Cambridge University Press: Cambridge, 1983.
3. Bridgeman, A. J.; Gerloch, M. *Prog. Inorg. Chem.* **1997**, *45*, 179–281.
4. Bridgeman, A. J.; Gerloch, M. *Coord. Chem. Rev.* **1997**, *165*, 315–446.
5. Jones, M. PhD thesis, University of Cambridge, Cambridge, 2001.

Comprehensive Coordination Chemistry II
ISBN (set): 0-08-0437486
Volume 2, (ISBN 0-08-0443249); pp 669–672

2.55 Ligfield

J. BENDIX
University of Copenhagen, Denmark

2.55.1 REFERENCES 675

Ligfield dates back to the late 1980s when it was developed as a program suite for the DOS operating system. About 30 different groups around the world have used the program. At the time of writing, a single executable, 32-bit version is being tested under Windows 95, Windows 98, and Windows 2000.

Currently Ligfield handles all p and d configurations as well as f^1–f^3 and complementary configurations. The program is built upon irreducible tensor methods in weak-field bases. Thus matrix representations of the operators entering the ligand-field Hamiltonian are initially generated in one of several possible weak-field bases. The techniques involved in setting up the matrices in fixed, symmetry-defined bases have been described in the literature.[1–3] However, Ligfield allows the user, by the technique of rediagonalizations,[4] to obtain matrix representations of any operator in any function basis, be it weak-field, strong-field, or intermediate-field bases.

The program philosophy is twofold. It aims at providing the nonspecialist with a user-friendly interface (Figure 1 shows the user interface for matrix generation) and easy access to the most common tasks. Simultaneously, the program is rich in more advanced facilities and provides the dedicated user with freedom in configuring the program and with access to many model properties that are not provided by other ligand-field programs.

To the category of common tasks belong the following: setting up ligand-field matrices using either the angular overlap model, purely symmetry defined, or user defined parametrizations; setting up matrices representing interelectronic repulsion (again with several choices of parametrization), spin-orbit coupling, and angular momenta; as well as diagonalizing sums of these matrices to obtain eigenvalues, eigenvectors, and symmetry-labels for the eigenfunctions. The program generates energy-level diagrams as a function of one free parameter (Tanabe–Sugano-type diagrams as in Figure 2) and allows the user to generate energy level diagrams as function of geometrical parameters (Walsh-type diagrams). The program also calculates magnetic susceptibilities and magnetizations as a function of temperature.

In addition there are some more advanced facilities: the possibility of manipulating individual elements of all matrices; the fitting of parameter values to observed energy differences; matrix algebra such as norms, overlaps, and rescaling; linear combination of matrices (useful for fixing parameter ratios); calculation of orbital populations and of the angular variation of the d- (or p- or f-) electron density for an arbitrary many-electron function; symmetry adaptation of function bases; and simulation of EPR spectra based on the ligand-field Hamiltonian rather than on spin-Hamiltonians.

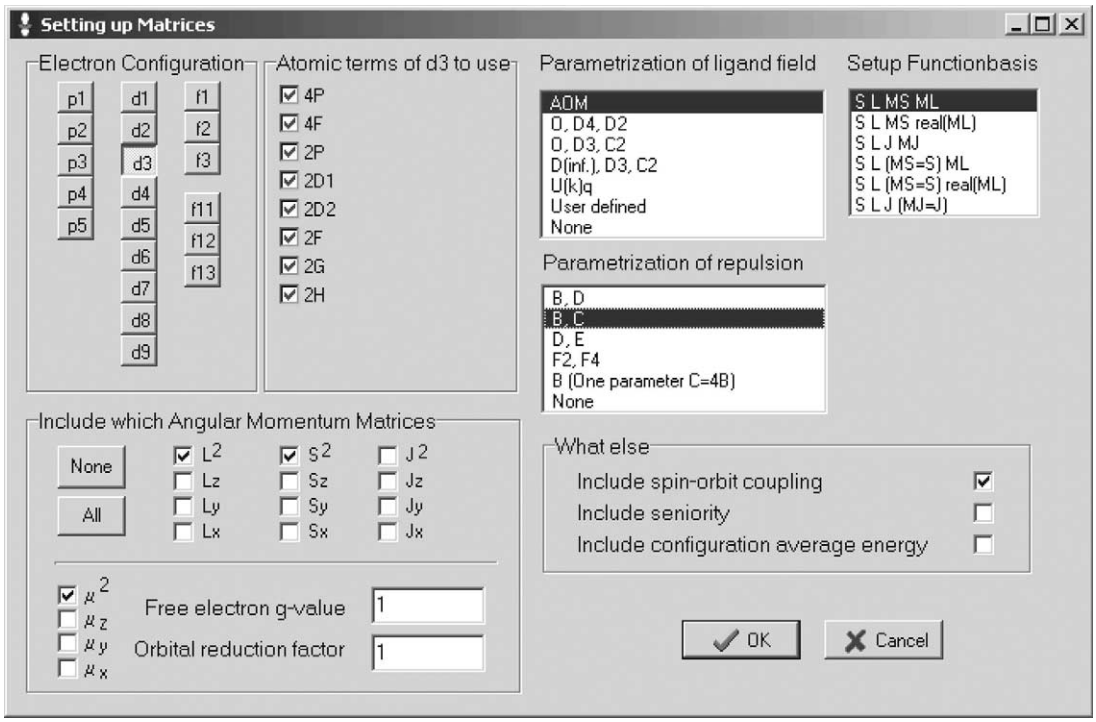

Figure 1 Example of the user interfaces.

All natural constants employed in the program can be edited and the user thus has full control over the units of the input and output. The program not only comes with built-in functions for displaying graphical output (energy level graphs, simulated EPR spectra, and electron densities), but also has translators that allow the output to be easily imported into Origin[5] (energy level diagrams) or POV-ray[6] (electron densities). The program also comes with a built-in text editor for convenient examination of results.

Although calculation of orbital populations and of the angular variation of electron densities were classified above as advanced facilities, these properties are very palpable and could prove a valuable aid for the coordination chemist to understand many-electron functions. The calculation of these properties relies on the insight that they can be described by general one-electron operators. Provided a means for constructing matrix representations of a complete set of one-electron operators in the many-electron basis in question is available, it is thus possible, although involved, to extract the above-mentioned properties. If the tensor operators $\mathbf{U}^k{}_q$ are taken as the full set ($k = 0 \ldots 2l$, $q = -k \ldots k$) including the odd k values, which are anti-Hermitian and therefore not normally needed in ligand-field contexts, they constitute a complete one-electron operator basis. It should thus be intuitively clear that the calculation of orbital populations and of electron densities follows the same lines as the generation of the ligand-field matrices.

In order to demonstrate the illustrative nature of electron densities, two examples are given in Figures 3a and 3b. The first of these depicts the ground state d-electron density distribution in an octahedral d^3 (or low-spin d^6) system. The maximal ligand-field stabilization for these configurations becomes directly visible in the way the electron density is directed away from ligators on the axes. The second figure shows a slightly more complicated example of the electronic ground state density for the all-horizontal D_{3d} configuration of $[Ti(H_2O)_6]^{3+}$. The consequences of the π-anisotropy of the Ti-water interaction are obvious. Also the fact that this conformation represents a situation with maximal super-hyperfine coupling of the electron spin to the hydrogen nuclei of the water ligands is easily appreciated.[7]

A reasonably detailed worked example is included in the printed manual for Ligfield. The program has been used in a number of publications from which more detail and inspiration can be obtained.[8–11] Copies of the program can be obtained free of charge, for academic use, from the author.

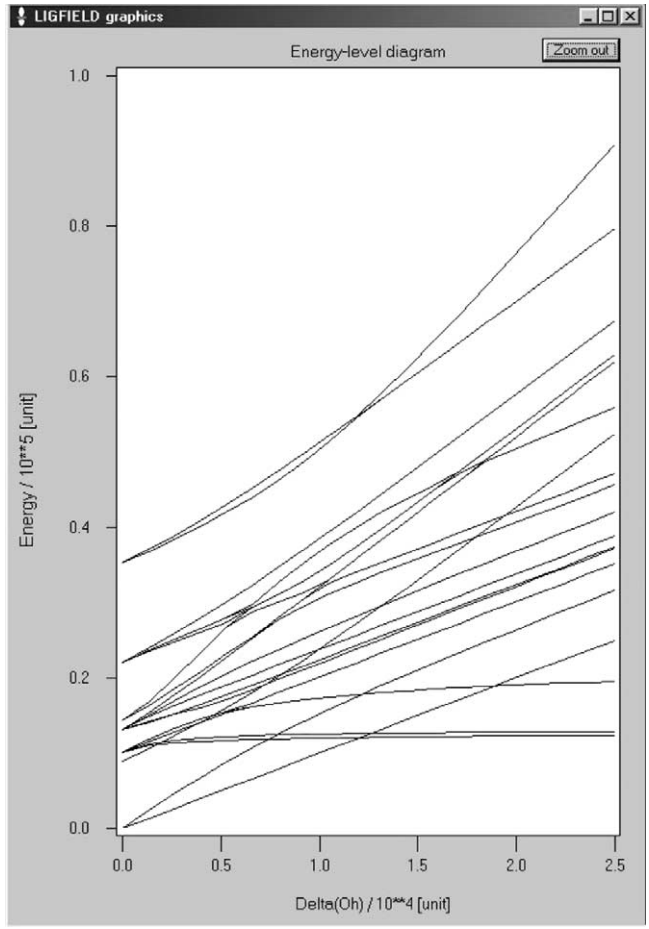

Figure 2 An energy level diagram for an octahedral d^3-system generated by Ligfield (3 s on 300 MHz Pentium II).

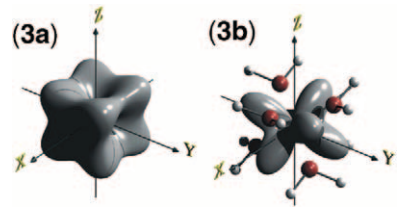

Figure 3 Angular variation of electron densities calculated with Ligfield and rendered in POV-ray 3.0. The *d*-electron densities (a) of the ground state of an octahedral d^3 (or d^6) system, and (b) of the ground state for the all-horizontal D_{3d} configuration of $[Ti(H_2O)_6]^{3+}$ with the ligating water molecules superimposed (*Z* is here the C_3-axis).

ACKNOWLEDGMENTS

The importance of Prof. C. E. Schäffer to the development of Ligfield cannot be overestimated.

2.55.1 REFERENCES

1. Nielson, C. W.; Koster, G. F. *Spectroscopic Coefficients for p^nd^{n}and f^n Configurations*; MIT Press: Cambridge, MA, 1963.
2. König, E.; Kremer, S. *Ligand Field Energy Diagrams*; Plenum: New York, 1977.
3. Gerloch, M. *Magnetism and Ligand-field Analysis*; Cambridge University Press: Cambridge, UK, 1983.
4. Brorson, M.; Jensen, G. S.; Schäffer, C. E. *J. Chem. Educ.* **1986**, *63(5)*, 387–91.
5. www.originlab.com.
6. www.povray.org.
7. Carver, G.; Bendix, J.; Tregenna-Piggott, P. L. W. manuscript in preparation.

8. Bendix, J.; Brorson, M.; Schäffer, C. E.; *Inorg. Chem.* **1993**, *32*, 2838–2849.
9. Meyer, K.; Bendix, J.; Metzler-Nolte, N.; Weyhermüller, T.; Wieghardt, K. *J. Am. Chem. Soc.* **1998**, *120*, 7260–7270.
10. Spichiger, D.; Carver, G.; Dobe, C.; Bendix, J.; Tregenna-Piggott, P. L. W.; Meier, R.; Zahn, G. *Chem. Phys. Lett.* **2001**, *337*, 391–397.
11. Wermuth, M.; Güdel, H. U. *J. Phys.: Condens. Matter* **2001**, *13*, 9583–9598.

Comprehensive Coordination Chemistry II
ISBN (set): 0-08-0437486

Volume 2, (ISBN 0-08-0443249); pp 673–676

2.56
ADF

S. J. A. VAN GISBERGEN
Scientific Computing and Modelling N.V., Amsterdam, The Netherlands
and
E. J. BAERENDS
Vrije Universiteit, Amsterdam, The Netherlands

2.56.1 INTRODUCTION 677
2.56.2 FUNCTIONALITY 677
2.56.2.1 Geometry Optimizations, Transition States, and Reaction Paths 677
2.56.2.2 Available Molecular Properties 678
2.56.2.3 Modeling Environmental Effects 678
2.56.3 CHEMICAL ANALYSIS OF RESULTS 678
2.56.4 ACCURACY 678
2.56.5 EFFICIENCY FOR CALCULATIONS ON LARGE MOLECULES 679
2.56.6 REFERENCES 679

2.56.1 INTRODUCTION

The Amsterdam Density Functional package (ADF)[1–3] is software for first-principles electronic structure calculations (quantum chemistry). ADF is often used in the research areas of catalysis, inorganic and heavy-element chemistry, biochemistry, and various types of spectroscopy. ADF is based on density functional theory (DFT) (see Chapter 2.39), which has dominated quantum chemistry applications since the early 1990s. DFT gives superior accuracy to Hartree–Fock theory and semi-empirical approaches, especially for transition-metal compounds. In contrast to conventional correlated post-Hartree–Fock methods, it enables accurate treatment of systems with several hundreds of atoms (or several thousands with QM/MM).[4,5]

2.56.2 FUNCTIONALITY

2.56.2.1 Geometry Optimizations, Transition States, and Reaction Paths

ADF enables geometry optimizations in Cartesian and internal coordinates.[6] An initial Hessian estimate speeds up the optimizations.[7] Various constraints can be imposed. Transition-state searches,[8] intrinsic reaction coordinates,[9] and linear transit calculations are available to further analyze the energy path from reactants, via the transition state, to the final products. Finite difference[10] and analytic second derivatives[11–13] yield IR frequencies and Hessians. These Hessians are helpful in finding and characterizing transition states.

2.56.2.2 Available Molecular Properties

A wide variety of molecular properties can be accurately obtained with ADF. The time-dependent DFT implementation[14] yields UV/Vis spectra (singlet and triplet excitation energies, as well as oscillator strengths), frequency-dependent (hyper)polarizabilities (nonlinear optics), Raman intensities, and van der Waals dispersion coefficients. Rotatory strengths and optical rotatory dispersion (optical properties of chiral molecules[15,16]), as well as frequency-dependent dielectric functions for periodic structures,[17] have been implemented as well. NMR chemical shifts[18,19] and spin–spin couplings,[20,21] ESR[22,23] (EPR)[24] *g*-tensors, magnetic[25] and electric[26] hyperfine tensors are available, as well as more standard properties like IR frequencies[10] and intensities, and multipole moments. Relativistic effects (ZORA[27] and spin–orbit coupling) can be included for most properties.

2.56.2.3 Modeling Environmental Effects

The conductor-like screening model (COSMO)[28] is available for molecules in a solvent. The QM/MM implementation[4] enables treatment of active sites in protein environments with many thousands of atoms.[5] Homogeneous electric fields and point charges can be specified. More advanced environment models are being implemented.

2.56.3 CHEMICAL ANALYSIS OF RESULTS

ADF contains several analysis options, offering the possibility of gaining detailed understanding of the chemical problem at hand. These methods underline the underlying philosophy that the Kohn–Sham orbitals in DFT can be used for a "quantitative MO theory."[29,30]

ADF analyzes its results in terms of user-specified subsystems from which the total system is built. The program specifies how the "fragment orbitals" (FOs) of the chemically meaningful subunits mix with FOs on other fragments to combine to the final molecular orbitals.

ADF calculates various chemically meaningful terms that add up to the bond energy, with an adaptation[29,31,32] of Morokuma's[33] bond-energy decomposition to the Kohn–Sham MO method. The individual terms are chemically intuitive quantities such as electrostatic energy, steric repulsion, Pauli repulsion, and orbital interactions. The latter are symmetry decomposed according to the Ziegler transition-state method.[31]

In addition to Mulliken charge analysis, ADF calculates several atomic charges that do not share the flaws of Mulliken (strong basis set dependence). These charge analysis methods ("Voronoy deformation density"[34] and "Hirshfeld"[35]) provide atomic charges that agree well with chemical intuition.

The full molecular symmetry, including many non-Abelian groups, is exploited. The proper symmetry labels to orbitals, excitations, vibrational modes are provided on output.

2.56.4 ACCURACY

ADF combines several technical features that ensure reliable and accurate calculations. Slater type orbitals (STOs) are used as basis functions. These resemble the true atomic orbitals more closely than the more common Gaussian type orbitals (GTOs). Therefore, fewer STOs than GTOs are needed for a certain level of accuracy. ADF has a database with thoroughly tested basis set files, ranging in quality from single-zeta to quadruple-zeta basis sets with various diffuse and polarization functions. They are available for all elements, including lanthanides and actinides. ADF uses the Te Velde–Baerends[36] numerical integration scheme, in which the grid is automatically adapted to the available basis functions and to the demanded number of significant digits.

Complex transition-metal compounds can be treated with the same stability as simpler systems containing only light atoms. The relativistic methods and basis sets[37,38] in ADF enable treatment of molecules with very heavy elements. The ADF approach removes the need for pseudopotential and effective core potential (ECP) approximations, even for lanthanides and actinides.

A variety of modern (meta-)GGA (generalized gradient approximation) exchange-correlation (xc) energy functionals, such as the van Voorhis–Scuseria functional,[39] are evaluated. For reliable property calculations, improved xc potentials with correct asymptotic behavior, such as SAOP[40] and GRAC,[41] have been developed.

2.56.5 EFFICIENCY FOR CALCULATIONS ON LARGE MOLECULES

For truly large system sizes (more than a few hundred atoms), a mix of quantum mechanics and molecular mechanics (QM/MM)[4,5] is often suitable. QM/MM calculations can be performed on much larger systems than pure QM calculations, because the approximate MM calculations are very fast. Various standard force fields (SYBYL, Amber, UFF) are available.

Most parts of ADF have been efficiently parallelized.[42] Because of the exponential spatial decay of the STO basis functions, linear scaling techniques reduce the computational complexity from $O(N_{at}^3)$ to $O(N_{at})$ for the most time-consuming parts of the calculation.[2,43] A density-fit procedure and the possibility of making a frozen core approximation[44] further reduce the cost of the calculations.

Finally we mention refs. 45, and 46, which contain some examples of ADF calculations in the area of coordination chemistry.

2.56.6 REFERENCES

1. te Velde, G.; Bickelhaupt, F. M.; Baerends, E. J.; van Gisbergen, S. J. A.; Guerra, C. F.; Snijders, J. G.; Ziegler, T. *J. Comput. Chem.* **2001**, *22*, 931–967.
2. Guerra, C. F.; Snijders, J. G.; te Velde, G.; Baerends, E. J. *Theor. Chem. Acc.* **1998**, *99*, 391–403.
3. Baerends, E. J.; Autschbach, J.; Bérces, A.; Bo, C.; Boerrigter, P. M.; Cavallo, L.; Chong, D. P.; Deng, L.; Dickson, R. M.; Ellis, D. E.; Fan, L.; Fischer, T. H.; Guerra, C. F.; van Gisbergen, S. J. A.; Groeneveld, J. A.; Gritsenko, O. V.; Grüning, M.; Harris, F. E.; van den Hoek, P.; Jacobsen, H.; van Kessel, G.; Kootstra, F.; van Lenthe, E.; Osinga, V. P.; S. Patchkovskii, S.; Philipsen, P. H. T.; Post, D.; Pye, C. C.; Ravenek, W.; Ros, P.; Schipper, P. R. T.; Schreckenbach, G.; Snijders, J. G.; Solà, M.; Swart, M.; Swerhone, D.; te Velde, G.; Vernooijs, P.; Versluis, L.; Visser, O.; van Wezenbeek, E.; Wiesenekker, G.; Wolff, S. K.; Woo, T. K.; Ziegler, T.; ADF2002.01, SCM, Theoretical Chemistry, Vrije Universiteit, Amsterdam; http://www.scm.com
4. Woo, T. K.; Cavallo, L.; Ziegler, T. *Theor. Chim. Acta* **1998**, *100*, 307.
5. Swart, M.; van de Bosch, M.; Berendsen, H. J. C.; Canters, G. W.; Snijders, J. G. unpublished.
6. Versluis, L.; Ziegler, T. *J. Chem. Phys.* **1988**, *322*, 88.
7. Fischer, T. H.; Almlöf, J. *J. Chem. Phys.* **1992**, *96*, 9005–9012.
8. Fan, L.; Ziegler, T. *J. Am. Chem. Soc.* **1992**, *114*, 10890.
9. Deng, L.; Ziegler, T. *J. Chem. Phys.* **1993**, *99*, 3823.
10. Fan, L.; Ziegler, T. *J. Phys. Chem.* **1992**, *96*, 6937–6940.
11. Bérces, A.; Dickson, R. M.; Fan, L.; Jakobsen, H.; Swerhone, D.; Ziegler, T. *Comp. Phys. Comm.* **1997**, *100*, 247.
12. Jacobsen, H.; Bérces, A.; Swerhorne, D. P.; Ziegler, T. *Comp. Phys. Comm.* **1997**, *100*, 263.
13. Wolff, S. K. unpublished.
14. van Gisbergen, S. J. A.; Snijders, J. G.; Baerends, E. J. *Comp. Phys. Comm.* **1999**, *118*, 119–138.
15. Autschbach, J.; Ziegler, T.; van Gisbergen, S. J. A.; Baerends, E. J. *J. Chem. Phys.* **2002**, *116*, 6930–6940.
16. Autschbach, J.; Patchkovskii, S.; Ziegler, T.; van Gisbergen, S. J. A.; Baerends, E. J. *J. Chem. Phys.* **2002**, *117*, 591–592.
17. Kootstra, F.; de Boeij, P. L.; Snijders, J. G. *J. Chem. Phys.* **2000**, *112*, 6517.
18. Schreckenbach, G.; Ziegler, T. *J. Phys. Chem.* **1995**, *99*, 606–611.
19. Wolff, S. K.; Ziegler, T.; van Lenthe, E.; Baerends, E. J. *J. Chem. Phys.* **1999**, *110*, 7689.
20. Autschbach, J.; Ziegler, T. *J. Chem. Phys.* **2000**, *113*, 936–947.
21. Autschbach, J.; Ziegler, T. *J. Chem. Phys.* **2000**, *113*, 9410.
22. van Lenthe, E.; van der Avoird, A.; Wormer, P. E. S. *J. Chem. Phys.* **1997**, *107*, 2488.
23. Schreckenbach, G.; Ziegler, T. *J. Phys. Chem.* **1997**, *A101*, 3388.
24. Patchkovskii, S.; Ziegler, T. *J. Phys. Chem.* **2001**, *A105*, 5490.
25. van Lenthe, E.; van der Avoird, A.; Wormer, P. E. S. *J. Chem. Phys.* **1998**, *108*, 4783–4796.
26. van Lenthe, E.; Baerends, E. J. *J. Chem. Phys.* **2000**, *112*, 8279–8292.
27. van Lenthe, E.; Baerends, E. J.; Snijders, J. G. *J. Chem. Phys.* **1993**, *99*, 4597.
28. Pye, C. C.; Ziegler, T. *Theor. Chim. Acta* **1999**, *101*, 396.
29. Bickelhaupt, F. M.; Baerends, E. J. *Rev. Comput. Chem.* **2000**, *15*, 1–86.
30. Baerends, E. J.; Gritsenko, O. V. *J. Phys. Chem.* **1997**, *101*, 5383–5403.
31. Ziegler, T.; Rauk, A. *Inorg. Chem.* **1979**, *18*, 1558.
32. Ziegler, T.; Rauk, A. *Inorg. Chem.* **1979**, *18*, 1755.
33. Morokuma, K. *J. Chem. Phys.* **1971**, *55*, 1236.
34. Bickelhaupt, F. M.; van Eikema Hommes, N. J. R.; Guerra, C. F.; Baerends, E. J. *Organometallics* **1996**, *15*, 2923.
35. Hirshfeld, F. L. *Theor. Chim. Acta* **1977**, *44*, 253.
36. te Velde, G.; Baerends, E. J. *J. Comput. Phys.* **1992**, *99*, 84–98.
37. van Lenthe, E.; Baerends, E. J., 2003, *J. Comput. Chem.*, accepted for publication.
38. Chong, D. P.; van Lenthe, E.; van Gisbergen, S. J. A.; Baerends, E. J. unpublished.
39. Voorhis, T. van; Scuseria, G. E. *J. Chem. Phys.* **1998**, *109*, 400.
40. Schipper, P. R. T.; Gritsenko, O. V.; van Gisbergen, S. J. A.; Baerends, E. J. *J. Chem. Phys.* **2000**, *112*, 1344–1352.
41. Grüning, M.; Gritsenko, O. V.; van Gisbergen, S. J. A.; Baerends, E. J. *J. Chem. Phys.* **2001**, *114*, 652–660.
42. Guerra, C. F.; Visser, O.; Snijders, J. G.; te Velde, G.; Baerends, E. J. *Methods and Techniques in Computational Chemistry*; Clementi, E.; Corongiu, G. Eds.; STEF: Cagliari, Italy, 1995: p 305.

43. van Gisbergen, S. J. A.; Guerra, C. F.; Baerends, E. J. *J. Comput. Chem.* **2000**, *21*, 1511–1523.
44. Baerends, E. J.; Ros, P. *Chem. Phys.* **1973**, *2*, 52.
45. Ziegler, T. *Can. J. Chem.* **1995**, *73*, 743.
46. Baerends, E. J.; Rosa, A. *Coord. Chem. Rev.* **1998**, *177*, 97–125.

Comprehensive Coordination Chemistry II
ISBN (set): 0-08-0437486

Volume 2, (ISBN 0-08-0443249); pp 677–680

2.57
DeMON

A. M. KÖSTER
CINVESTAV, Mexico City, Mexico
A. GOURSOT
Ecole Nationale Superiere de Chimie, Montpellier, France
and
D. R. SALAHUB
Steacie Institute for Molecular Sciences, Ottawa, ON, Canada

2.57.1 INTRODUCTION 681
2.57.2 METHODOLOGY 682
2.57.3 APPLICATIONS 683
2.57.4 REFERENCES 685

2.57.1 INTRODUCTION

The development of molecular density functional theory (DFT) methods has considerably simplified the calculation of transition metal clusters. This has also attracted the attention of coordination chemists to this technique. Here, we will describe the computational methodology implemented in the DFT program, deMon 2002.[1] This program results from the merging of the deMon-KS code from Montreal[2] and the ALLCHEM code from Hanover.[3] As a result the new code has the deMon functionalities such as the calculation of NMR shielding,[4] simulation of photoelectron[5] and IR and Raman spectra,[6] calculation of molecular polarizabilities and hyperpolarizabilities,[7] and other properties. The deMon functionality is coupled with the stable and efficient analytical[8] and numerical[9] integral evaluation and the improved self-consistent field (SCF) convergence[10] from ALLCHEM. The new program is well suited for the study of systems with several thousand basis functions. Different local, generalized gradient approximated (GGA) and meta-GGA functionals are available. Optimized effective potential and hybrid functionals are currently implemented and tested. Time dependent DFT is available over the post-deMon 2002 program DynaRho[11] which will be included into the main code soon.

Based on the previous implementation of the density functional tight-binding (DFTB) method[12] in ALLCHEM,[13] a hybrid DFT/DFTB method is currently under development. In the future this will be coupled to a molecular mechanics environment.

In the next section we describe the basic methodology of deMon 2002. In Section 2.57.3 we will present a few selected applications. To obtain more information about deMon 2002 or to get a demo version please contact: *Serguei.Patchkovskii@nrc.ca*.

2.57.2 METHODOLOGY

Here we describe briefly the solution of the Kohn–Sham orbital equation,[14]

$$\left(-\frac{1}{2}\nabla^2 + v(\mathbf{r}) + \int \frac{\rho(\mathbf{r}')}{|\mathbf{r}-\mathbf{r}'|}\mathrm{d}\mathbf{r}' + v_{\mathrm{xc}[\rho]}\right)\psi_i(\mathbf{r}) = \varepsilon_i\psi_i(\mathbf{r}) \tag{1}$$

using the linear combination of Gaussian-type orbitals (LCGTO) and the variational approximation of the Coulomb potential. For a more detailed review of this approach we refer to the work of Köster *et al.*[10] To avoid unnecessary complications in the presentation we restrict ourselves to the closed-shell case. In the LCGTO ansatz the Kohn–Sham orbitals are expanded into atomic orbitals:

$$\psi_i(\mathbf{r}) = \sum_{\mu} c_{\mu i}\mu(\mathbf{r}) \tag{2}$$

Here $\mu(r)$ represents an atomic orbital and $c_{\mu i}$ the corresponding molecular-orbital coefficient. With this expansion we find for the electronic density:

$$\rho(\mathbf{r}) = \sum_{\mu,\nu} P_{\mu\nu}\mu(\mathbf{r})\nu(\mathbf{r}) \tag{3}$$

$P_{\mu v}$ represents an element of the closed-shell density matrix defined as:

$$P_{\mu\nu} = 2\sum_{i}^{occ} c_{\mu i}c_{\nu i} \tag{4}$$

Using the LCGTO expansions for the Kohn–Sham orbitals (Equation (2)) and the electronic density (Equation (3)), the Kohn–Sham SCF energy expression[14] can be expressed as:

$$E_{\mathrm{SCF}} = \sum_{\mu,\nu} P_{\mu\nu}H_{\mu\nu} + \frac{1}{2}\sum_{\mu,\nu}\sum_{\sigma,\tau} P_{\mu\nu}P_{\sigma\tau}\langle\mu\nu||\sigma\tau\rangle + E_{\mathrm{xc}}[\rho] \tag{5}$$

The total energy is the sum of E_{SCF} and the nuclear repulsion energy, which can be calculated analytically. In Equation (5), $H_{\mu v}$ represents elements of the core Hamiltonian matrix. They are built from the kinetic and nuclear attraction energy of the electrons and describe the movement of an electron in the nuclear framework. The computation of this matrix has a formal quadratic scaling with the number of basis functions N of the system. The second term in Equation (5) represents the Coulomb repulsion energy of the electrons. In contrast to Hartree–Fock theory, the calculation of the Coulomb and exchange energies are separate in DFT. The Coulomb term introduces a formal N^4 scaling into the energy calculation. For the calculation of the exchange-correlation energy $E_{\mathrm{xc}}[\rho]$a numerical integration has to be performed. This integration scales formally as $N^2 \times G$, where G is the number of grid points necessary for the numerical integration. In deMon 2002 an adaptive grid is used for this integration.

From the above discussion it follows that the calculation of the Coulomb repulsion energy represents the most demanding computational task in Equation (5). The introduction of the variational approximation of the Coulomb potential reduces the formal scaling of this term to $N^2 \times M$. Here M is the number of auxiliary functions which is usually two to three times N. The variational approximation of the Coulomb potential is based on the minimization of the following self-interaction error:

$$\varepsilon_2 = \frac{1}{2}\iint \frac{[\rho(\mathbf{r}_1) - \tilde{\rho}(\mathbf{r}_1)]\cdot[\rho(\mathbf{r}_2) - \tilde{\rho}(\mathbf{r}_2)]}{|\mathbf{r}_1 - \mathbf{r}_2|}\mathrm{d}\mathbf{r}_1\mathrm{d}\mathbf{r}_2 \tag{6}$$

In deMon 2002 the approximate density $\tilde{\rho}(\mathbf{r})$ is expanded in primitive Hermite Gaussians $\overline{k}(\mathbf{r})$ which are centered at the atoms:

$$\tilde{\rho}(\mathbf{r}) = \sum_{k} x_k\overline{k}(\mathbf{r}) \tag{7}$$

With the LCGTO expansion for $\rho(r)$and $\tilde{\rho}(r)$we obtain the following approximate SCF energy $\tilde{E}_{\mathrm{SCF}}$:

$$\tilde{E}_{\mathrm{SCF}} = \sum_{\mu,\nu} P_{\mu\nu} H_{\mu\nu} + \sum_{k} x_k \sum_{\mu,\nu} P_{\mu\nu} \langle \mu\nu || k \rangle - \frac{1}{2} \sum_{k,l} x_k x_l \langle k || l \rangle + E_{\mathrm{xc}}[\rho] \tag{8}$$

The variation of this energy expression with respect to the molecular orbital coefficients, constraining the Kohn–Sham orbitals to be orthonormal,

$$\sum_{\mu,\nu} c_{\mu i} S_{\mu\nu} c_{\nu j} = \delta_{ij} \quad \forall\ i,j \tag{9}$$

yields:

$$\frac{\partial \tilde{E}_{\mathrm{SCF}}}{\partial c_{\mu i}} = \sum_{\nu} \left(H_{\mu\nu} + \sum_{k} x_k \langle \mu\nu || k \rangle + \langle \mu | \upsilon_{\mathrm{xc}} | \nu \rangle \right) c_{\nu i} - \sum_{\nu} \sum_{j} S_{\mu\nu} c_{\nu j} \varepsilon_{ji} \tag{10}$$

From Equation (10) we can derive the canonical LCGTO Kohn–Sham equations in matrix form,

$$\mathbf{Kc} = \mathbf{Sc}\varepsilon \tag{11}$$

with the elements of the Kohn–Sham matrix **K** defined as:

$$K_{\mu\nu} = H_{\mu\nu} + \sum_{k} x_k \langle \mu\nu || k \rangle + \langle \mu | \upsilon_{\mathrm{xc}} | \nu \rangle \tag{12}$$

In Equation (11), **S** represents the overlap matrix, **c** the molecular orbital coefficient matrix, and ε the Kohn–Sham orbital energies. The expansion coefficients x_k of the approximate density, necessary for the construction of the Kohn–Sham matrix, are calculated by the minimization of the self-interaction error ε_2:

$$\frac{\partial \varepsilon_2}{\partial x_m} = -\sum_{\mu,\nu} P_{\mu\upsilon} \langle \mu\nu || m \rangle + \sum_{k} x_k \langle k || m \rangle = 0 \quad \forall\ m \tag{13}$$

From Equations (12) and (13) it follows that only three-center electron repulsion integrals (ERIs) are necessary for the SCF and energy calculation in deMon 2002. Efficient integral recurrence relations for the ERIs can be derived due to the primitive Hermite Gaussian basis for the approximate density. Moreover, the asymptotic expansion of these integrals results in a linear scaling for the construction of the Kohn–Sham matrix. In Figure 1 the CPU time for the Kohn–Sham matrix construction is plotted against the basis set size for a series of alkanes. The DZVP basis set was used in these calculations. For the calculation of the exchange-correlation energy the local VWN functional was employed.

As can be seen from Figure 1 the construction of the Kohn–Sham matrix scales already for 1,500 basis functions subquadratically. Above 2,500 basis functions the scaling of the construction of the Kohn–Sham matrix becomes linear. The CPU times quoted in the figure refer to a 1.2 GHz AMD Athlon processor.

2.57.3 APPLICATIONS

Over the last decade deMon and ALLCHEM have been applied to various domains in chemistry. Here we present some selected applications. For a more detailed description of the application range of deMon please refer to the following review articles.[10,15–17]

Free and coordinated transition metal clusters can be calculated with deMon at reasonable computational cost. The simulation of vibrational resolved photoelectron spectra from these calculations has proven to be a powerful tool to determine the ground state structure of free[18] and coordinated transition metal clusters.[19] With the optimized ground state structures binding energies,[20] polarizabilities,[21] and other properties of free- and coordinated-transition metal clusters

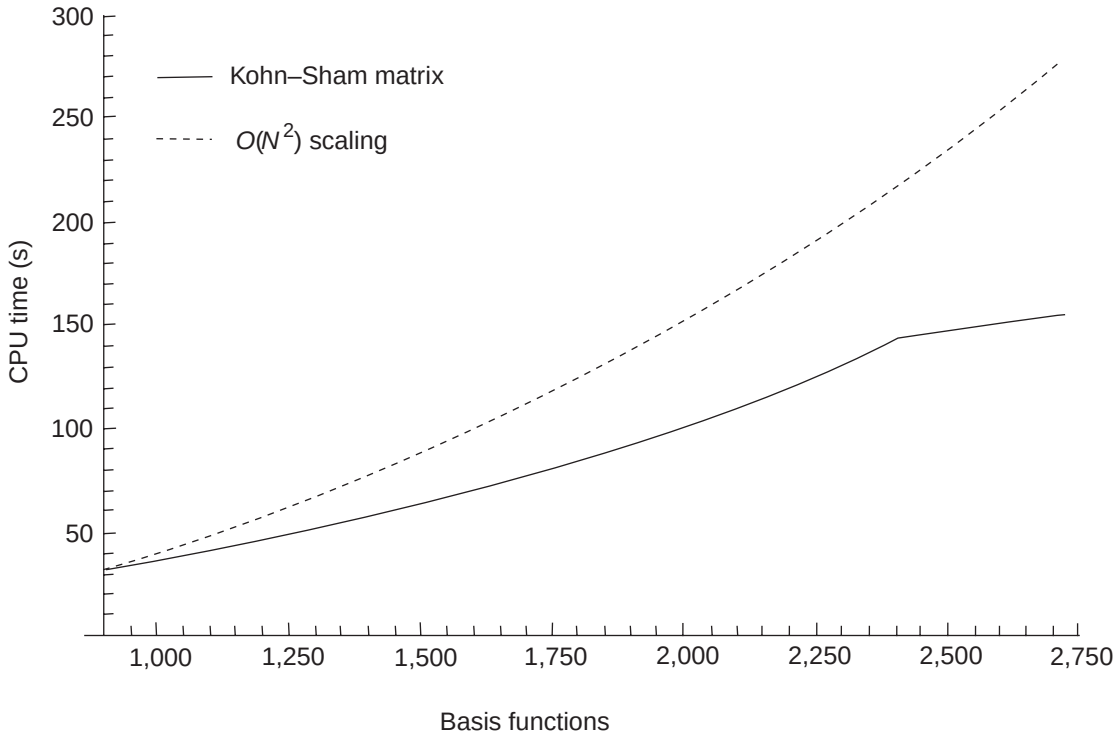

Figure 1 CPU time for the Kohn–Sham matrix construction plotted against the basis set size for a series of alkanes. The CPU times refer to a 1.2 GHz AMD Athlon processor.

can be calculated. This allows a critical evaluation of the used theoretical and experimental methods for the determination of molecular properties of such systems. The topological analysis of molecular fields, like the electrostatic potential, can be used to gain insight into the nature of the bonding in these compounds.[22] With the new deMon 2002 version these studies can be extended to more complex coordinated systems like 4-ferrocenyl-2′-methyl-4′-nitroazobenzene[23] (~2,000 basis functions) for which the molecular hyperpolarizability can be calculated within a few CPU hours on a personal computer.

Simulation of the NMR properties of zeolites has shown that our DFT-based predicting tools have reached enough accuracy to allow the assignment of the magic-angle spinning NMR signals to crystallographically distinct Si or Al sites. The NMR spectrum of a simple rigid structure like mazzite with only two crystallographic sites[24] as well as that of a flexible complex framework like zeolite-β[25] with nine NMR peaks within 11 ppm, have been described with an accuracy of 1–2 ppm and achieved with a moderate computational effort (model clusters of 30–40 atoms). The effects of geometrical factors (resulting in a linear dependence of the NMR shieldings with respect to average Si—O—Si angles) and those of electronic factors (presence of Al or B centers in the next coordination shell) have been analyzed, showing their strong inter-relationship. The study of B and Al containing zeolite models with H^+ and Na^+ counter-ions has allowed the rationalization of the dramatic consequence of exchanging Na^+ with H^+ in B substituted zeolites, in contrast to Al zeolites. Framework rupture yielding BO_3 units, as asserted by calculated and experimental ^{29}Si and ^{11}B NMR spectra, was observed.[26]

The investigation of transition metal ions (TMI) in zeolites is a much more challenging problem. Indeed, the location of the Al compensating cations, whatever their nature, is not known experimentally, since the Al positions are not known either. This lack of information is much more critical for TMI zeolites because different TMI sites are correlated with different coordinations between the metal ion and the zeolite oxygens, which indicates possible different reactivities. Theoretical predictions can thus help in the first step of the characterization of the solid by assigning the TMI sites and by comparing experimental and calculated properties. In addition, they also provide a fundamental understanding of the role of the zeolite framework in the catalytic reactivity.

The treatment of NO_x and N_2O gaseous emissions in zeolite-based catalysts has demonstrated that their high reactivity is related to the high dispersion of the TM ions or oxocations, justifying the study of zeolite models containing isolated TMIs. A comparative study of faujasites (FAU), Na-FAU, Cu^{I}-FAU, and Cu^{II}-FAU, has led to the conclusion that Cu^{II}-FAU has a very different electronic distribution compared to the two other systems.[27] Recent work, based on the comparison between calculated and experimental EPR hyperfine properties, confirm that, in this zeolite, a strong zeolite-to-metal charge transfer occurs, which can be described as a large delocalization of the electron density on the whole system.[28]

ACKNOWLEDGMENTS

The authors wish to thank Gabriel Merino and Beatriz Alcántara for assistance in the preparation of the manuscript.

2.57.4 REFERENCES

1. Köster, A. M.; Geudtner, G.; Goursot, A.; Heine, T.; Vela, A.; Salahub, D. R. 2002 deMon, NRC, Canada, webpage, http://www.sao.nrc.ca/sims/deMon/
2. Casida, M. E.; Daul, C.; Goursot, A.; Köster, A. M.; Pettersson, L. G. M.; Proynov, E.; St-Amant, A.; Salahub, D. R.; Duarte, H.; Godbout, N.; Guan, J.; Jamorski, C.; Leboeuf, M.; Malkin, V. G.; Malkina, O. L.; Sim, F.; Vela, A. deMon-KS Version 3.4, Montreal, Canada, 1996.
3. Köster, A. M.; Krack, M.; Leboeuf, M.; Zimmermann, B. ALLCHEM, Universität Hannover, Hanover, Germany, 1998.
4. Malkin, V. G.; Malkina, O. L.; Casida, M. E.; Salahub, D. R. *J. Am. Chem. Soc.* **1994**, *116*, 5898–5908.
5. Jamorski, C.; Casida, M. E.; Salahub, D. R. *J. Chem. Phys.* **1996**, *104*, 5134–5147.
6. Stirling, A. *J. Chem. Phys.* **1996**, *104*, 1254–1262.
7. Calaminici, P.; Jug, K.; Köster, A. M. *J. Chem. Phys.* **1998**, *109*, 7756–7763.
8. Köster, A. M. *J. Chem. Phys.* **1996**, *104*, 4114–4124.
9. Krack, M.; Köster, A. M. *J. Chem. Phys.* **1998**, *108*, 3226–3234.
10. Köster, A. M.; Calaminici, P.; Gómez, Z.; Reveles, U. *Density* Functional Theory Calculation of Transition Metal Clusters. In *Reviews of Modern Quantum Chemistry: A Celebration of the Contribution of Robert G. Parr*; Sen, K., Ed.; World Scientific Publishing Co: Singapore, 2002; pp 1439–1475.
11. Casida, M. Time Dependent Density Functional Response Theory for Molecules. In *Recent Advances in Density Functional Methods*, Chong, D. P., Ed.; World Scientific Publishing: Singapore, 1995; pp 155–192.
12. Seifert, G.; Porezag, D.; Frauenheim, T. *Int. J. Quantum Chem.* **1996**, *58*, 185–192.
13. Heine, T.; Fowler, P. W.; Rogers, K. M.; Seifert, G. *J. Chem. Soc., Perkin Trans.* **1999**, April, 707–711.
14. Parr, R. G.; Yang, W. *Density-Functional Theory of Atoms and Molecules*; Oxford University Press: New York, 1989.
15. Köster, A. M.; Leboeuf, M.; Salahub, D. R. Molecular Electrostatic Potentials from Density Functional Theory. In *Molecular Electrostatic Potentials, Concepts and Applications*; Murray, J. S.; Sen, K., Eds.; Elsevier: Amsterdam, 1996; pp 105–142.
16. Russo, N.; Abaskin, Y.; Calaminici, P.; Mineva, T.; Sicilia, E.; Toscano, M. Gausian Density Functional Method: An Alternative Tool for the Prediction of Physicochemical Properties. In *Recent Advances in Density Functional Methods*; Chong, D. P., Ed.; World Scientific Publishing: Singapore, 1995; Vol. 1, Chapter 9, pp 335–368.
17. Salahub, D. R.; Castro, M.; Fournier, R.; Calaminici, P.; Godbout, N.; Goursot, A.; Jamorski, C.; Kobayashi, H.; Martínez, A.; Pápai, I.; Proynov, E.; Russo, N.; Sirois, S.; Ushio, J.; Vela, A. Density Functional Description of Metal–Metal and Metal–Ligand Bonds. In *Theoretical and Computational Approaches to Interface Phenomena*; Sellers, H. L., Golab, J. T., Eds.; Plenum: New York, 1994; pp 187–218.
18. Calaminici, P.; Köster, A. M.; Carrington, T., Jr.; Roy, P. N.; Russo, N.; Salahub, D. R. *J. Chem. Phys.*, 4036–4044.
19. Yang, D. S.; Zgierski, M. Z.; Rayner, D. M.; Hackett, P. A.; Martínez, A.; Salahub, D. R.; Roy, P. N.; Carrington, T., Jr. *J. Chem. Phys.* **1995**, *103*, 5335–5342.
20. Jug, K.; Zimmermann, B.; Calaminici, P.; Köster, A. M. *J. Chem. Phys.* **2002**, *116*, 4497–4507.
21. Calaminici, P.; Köster, A. M.; Vela, A.; Jug, K. *J. Chem. Phys.* **2000**, *113*, 2199–2202.
22. Martínez, A.; Calaminici, P.; Köster, A. M.; Salahub, D. R. *J. Chem. Phys.* **2001**, *114*, 819–825.
23. Coe, B. J.; Foulon, J.-D.; Hamor, T. A.; Jones, C. J.; McCleverty, J. A. *Acta Cryst.* **1991**, *C47*, 2032–2035.
24. Valerio, G.; Goursot, A. *J. Phys. Chem.* **1999**, *103*, 51–58.
25. Valerio, G.; Goursot, A.; Vetrivel, R.; Malkin, V. G.; Malkina, O. L.; Salahub, D. R. *J. Am. Chem. Soc.* **1998**, *120*, 11426–11431.
26. Valerio, G.; Pevert, J.; Goursot, A.; di Renzo, F. *Phys. Chem. Chem. Phys.* **2000**, *2*, 1091–1094.
27. Berthomieu, D.; Krishnamurty, S.; Coq, B.; Delahay, G.; Goursot, A. *J. Phys. Chem.* **2001**, *105*, 1149–1156.
28. Berthomieu, D.; Ducere, J. M.; Goursot, A. *J. Phys. Chem.* B **2002,** *106*, 7483–7488.

Comprehensive Coordination Chemistry II
ISBN (set): 0-08-0437486
Volume 2, (ISBN 0-08-0443249); pp 681–685

2.58 Software for Computational Chemistry

S. I. GORELSKY
Stanford University, Stanford, CA, USA

2.58.1 REFERENCES 689

A listing of software for molecular modeling is presented in this chapter. Too many programs have been developed around the world for it to be possible to present here a complete list. Software packages for "pure" molecular mechanics (MM) and molecular dynamics (MD) calculations are not listed here. However, an interested person can locate omitted programs using review papers[1] and the indexes available on the Internet.[2–11] Extensive catalogs of programs are available from Quantum Chemistry Program Exchange (QCPE)[2] and Computational Chemistry List (CCL).[3] Many programs can be downloaded from CCL software archives.

Table 1 shows programs for *ab initio*, density functional, and semiempirical calculations. These programs differ in their properties, such as functionality, computational efficiency, user-friendliness, cost, user support, and computer platforms and operating systems on which they run. Some of these software packages have a graphical user interface (GUI). Others do not have a built-in GUI but, in many cases, there are pre- and post-processing programs (Table 2) that can help to prepare input files and to analyze output files. The corresponding websites contains detailed information about the software. Frequently, commercial software developers and vendors offer free trial versions of their programs.

A very helpful resource for *ab initio* and density functional calculations is the EMSL Gaussian Basis Set Order Form.[12]

Table 1 Software packages for *ab initio*, density functional and semiempirical calculations.

Program	*Universal Resource Location (URL)*[a]
"Hybrid" Packages[b]	
CADPAC 6	http://www-theor.ch.cam.ac.uk/software/cadpac.html
CRYSTAL 98	http://www.cse.clrc.ac.uk/cmg/CRYSTAL/
GAMESS	http://www.msg.ameslab.gov/GAMESS/; Chapter 2.53 http://classic.chem.msu.su/gran/gamess/index.html
Gaussian 03	http://www.gaussian.com/
GAMESS-UK	http://www.dl.ac.uk/CFS/cfs.html
Jaguar	http://www.schrodinger.com/Products/jaguar.html
HyperChem 7	http://www.hyper.com/
MOLPRO 2002	http://www.molpro.net/
NWChem	http://www.emsl.pnl.gov:2080/docs/nwchem/nwchem.html
PQS	http://www.pqs-chem.com/
Q-Chem	http://www.q-chem.com/
Qsite	http://www.schrodinger.com/Products/qsite.html
Spartan'02	http://www.wavefun.com/software/software.html
Titan	http://www.wavefun.com/software/titan/titan_main.html
TURBOMOLE	http://www.chemie.uni-karlsruhe.de:/TheoChem/turbomole/intro.en.html
Ab Initio Packages	
ACES II	http://www.qtp.ufl.edu/Aces2/
CASTEP[c]	http://www.accelrys.com/cerius2/castep.html
COLUMBUS	http://www.itc.univie.ac.at/~hans/Columbus/columbus.html
DALTON	http://www.kjemi.uio.no/software/dalton/dalton.html
HONDO 95	http://qcpe.chem.indiana.edu/
MOLCAS	http://www.teokem.lu.se/molcas/
Psi 3	http://zopyros.ccqc.uga.edu/
Density Functional Packages	
ACRES	http://cst-www.nrl.navy.mil/~singh/acres/info.html
ADF 2002	Chapter 2.56; http://www.scm.com/
AllChem	http://ws2.theochem.uni-hannover.de/AllChem/
DeFT	http://server.ccl.net/cca/software/SOURCES/FORTRAN/DeFT/index.shtml
DeMON	Chapter 2.57; http://www.demon-software.com/public_html/
DGauss[e]	http://www.cachesoftware.com/cache/dgauss/index.shtml
DMol[3] [c]	http://www.accelrys.com/cerius2/dmol3.html
DoD Planewave	http://cst-www.nrl.navy.mil/people/singh/planewave/v3.0/
WIEN2k	http://www.wien2k.at/
Semiempirical Packages	
AMPAC[d]	http://www.semichem.com/ampac.html
ArgusLab	http://www.planaria-software.com/
MOPAC 2002[e,f]	http://www.cachesoftware.com/mopac/index.shtml http://www.schrodinger.com/Products/mopac.html
MNDO97	http://www.mpi-muelheim.mpg.de/kofo/institut/arbeitsbereiche/thiel/themen/MNDO97.html
MSINDO	http://www.theochem.uni-hannover.de/software.html
PM3d	http://quark.unn.runnet.ru/TCG_SOFTWARE.htm
ZINDO[c,e]	http://www.qtp.ufl.edu/zindo.html

[a] All web links were current in November 2002. [b] Capable of *ab initio*, density functional, semiempirical and/or MM/MD calculations. [c] Included in *Cerius*[2] (http://www.accelrys.com/cerius2/index.html). [d] Available in the *SYBYL* Molecular Modelling environment (http://www.tripos.com/). [e] Available in *CAChe 5* (http://www.cachesoftware.com/cache/). [f] Earlier versions (*MOPAC 6*, *MOPAC 7*) are available from QCPE[2] and CCL.[3]

Table 2 Software for pre- and post-processing and data visualization.

Program	*Universal Resource Location (URL)*[a]
AIMPAC	http://www.chemistry.mcmaster.ca/aimpac/aimpac.html
AIM2000	http://www.aim2000.de/
Alchemy 2000	http://www.tripos.com/sciTech/inSilicoDisc/dataAnalysis/alchemy.html
ALP-Vibro	http://www.obbligato.com/software/alp-vibro/
AOMix	http://www.obbligato.com/software/aomix/
BABEL	http://smog.com/chem/babel/
Cerius^2	http://www.accelrys.com/cerius2/index.html
CheVi	http://www.simbiosys.ca/
Chem3D	http://www.camsoft.com/
DL Visualize	http://www.cse.clrc.ac.uk/cmg/DLV/
DS Viewer	http://www.accelrys.com/dstudio/ds_viewer/
Gabedit	http://hplasim2.univ-lyon1.fr/allouche/gabedit/
Garlic	http://pref.etfos.hr/garlic/
GaussView	http://www.gaussian.com/gvbroc.htm
Ghemical	http://bioinformatics.org/ghemical/
gOpenMol	http://www.csc.fi/gopenmol/
Insight^2	http://www.accelrys.com/insight/
KMovisto	http://mitglied.lycos.de/PageOfMH/index.html
Maestro	http://www.schrodinger.com/Products/maestro.html
MCM 95	http://hanicka.uochb.cas.cz/~bour/
Mol2Mol	http://www.compuchem.com/mol2mol.htm
MOLCAD	http://www.tripos.com/sciTech/inSilicoDisc/moleculeModeling/molcad.html
MOLDA	http://www.molda.org/
MOLDEN	http://www.caos.kun.nl/~schaft/molden/molden.html
MOLEKEL	http://www.cscs.ch/molekel/
MOLMOL	http://www.mol.biol.ethz.ch/wuthrich/software/molmol/
MOLVIEW	http://pro122lin.chemie.hu-berlin.de/Molview/
Orbdraw	http://www.serenasoft.com/orbdraw.html
PCMODEL	http://www.serenasoft.com/pcm8.html
PyMOL	http://pymol.sourceforge.net/
QMView	http://www.sdsc.edu/QMView/
RasMol	http://www.umass.edu/microbio/rasmol/
SWizard	http://www.obbligato.com/software/swizard/
Vibrate	http://www.serenasoft.com/vibrate.html
Viewmol	http://viewmol.sourceforge.net/
VMD	http://www.ks.uiuc.edu/Research/vmd/
XCrySDen	http://crystal.ijs.si/kokalj/xc/
Zoa	http://zoa.freeservers.com/

[a] All web links were current in November 2002.

2.58.1 REFERENCES

1. Boyd, D. B. In *Reviews in Computational Chemistry*. Lipkowitz, K. B.; Boyd, D. B., Eds.; VCH Publishers: New York, Volumes 1–7, 11. Appendix: Compendium of Software for Molecular Modeling.
2. http://qcpe.chem.indiana.edu/
3. http://www.ccl.net/chemistry/
4. http://www.chem.ac.ru/Chemistry/Soft/
5. http://www.qspr.pe.kr/
6. http://allserv.rug.ac.be/~tkuppens/chem/
7. http://www.chamotlabs.com/Freebies/Software.html
8. http://www.claessen.net/chemistry/soft_en.html
9. http://www.liv.ac.uk/ctichem/swrev.html
10. http://lacebark.ntu.edu.au/chem_ref.html
11. http://hackberry.chem.trinity.edu/ChemistrySoftware.html
12. http://www.emsl.pnl.gov:2080/forms/basisform.html

Comprehensive Coordination Chemistry II
ISBN (set): 0-08-0437486

Volume 2, (ISBN 0-08-0443249); pp 687–689

2.59 Spectroscopy and Electronic Structure of $[FeX_4]^{n-}$ (X = Cl, SR)

P. KENNEPOHL and E. I SOLOMON
Stanford University, Stanford, CA, USA

2.59.1 INTRODUCTION 691
2.59.2 ELECTRONIC STRUCTURE OF FERRIC SITES 692
2.59.2.1 Ligand Field Spectroscopy and Ground State Parameters 692
2.59.2.2 Charge Transfer Spectroscopy—Metal–ligand Bonding 695
2.59.2.3 X-ray Absorption Edges—Covalency of Fe 3*d* Orbitals 696
2.59.2.4 Variable Energy Valence Photoelectron Spectroscopy—Inverted Bonding Description 696
2.59.2.5 Density Functional Calculations—Electronic Structure Description of Ferric Complexes 697
2.59.3 ELECTRONIC STRUCTURE OF FERROUS SITES 698
2.59.3.1 Polarized Absorption and Variable Temperature, Variable Field Magnetic Circular Dichroism 698
2.59.3.2 Variable Energy Valence Photoelectron Spectroscopy 699
2.59.3.3 Density Functional Results 700
2.59.3.4 Summary 701
2.59.4 ELECTRONIC RELAXATION 702
2.59.5 ELECTRONIC STRUCTURE CONTRIBUTIONS TO ELECTRON TRANSFER 702
2.59.5.1 Reduction Potentials 702
2.59.5.2 Reorganization Energies 705
2.59.5.3 Electronic Coupling Matrix Element 705
2.59.6 SUMMARY 707
2.59.7 REFERENCES 708

2.59.1 INTRODUCTION

The importance of transition metal ions in biology has long been recognized, but their actual role in biological systems has only become the focus of intense study over the last few decades. The relatively recent birth of biological inorganic chemistry, or *bioinorganic chemistry*, followed the refinement of several biological and analytical methods that finally allowed isolation and investigation of biomolecules. Since then, the study of metallobiomolecules has expanded tremendously as a result of their fundamental importance to both biology and chemistry. In particular, the study of electron transfer (ET) sites in metalloproteins has not only provided significant insight into biological function, it has also proved exceedingly important in advancing our understanding of ET processes in general inorganic systems. Much of these detailed studies on metallobiomolecules have benefited from recent advances in protein crystallography. This has provided structural data at atomic resolution and allowed for detailed studies relating geometric and electronic structure to chemical reactivity and biological function.

Many FeS proteins are independent, single-function molecules whose primary role is *in vivo* transport of reducing/oxidizing equivalents (electrons/holes). The control of this electron flux is critical to proper biological activity. Although the specific biological mechanisms are not always well understood, long-range electron transport is essential for effective cellular regulation of electron flux. Four major types of FeS electron transport sites are known: mononuclear

[Fe(S Cys)$_4$], binuclear [Fe_2S_2(S Cys)$_4$], cubane-type [Fe_4S_4(S Cys)$_4$], and the related cuboidal [Fe_3S_4] sites. Rubredoxins (Rds) contain a mononuclear site that cycles between the high-spin ferrous (Fe^{II}, $3d^6$) and ferric (Fe^{III}, $3d^5$) oxidation states. Proteins containing multinuclear sites are also limited to these formal oxidation states and are collectively known as ferredoxins (Fds). The so-called *high-potential iron proteins* (HiPIP) are a subfamily of the cubane-type Fds that differ in the nature of their biologically accessible redox states. Modifications of these fundamental structural motifs are observed in several ET sites within multifunctional proteins and enzyme complexes. This review focuses on the simplest of the FeS active sites, the mononuclear four-coordinate site in Rd. Elucidation of the fundamental electronic structure characteristics of [FeX_4] redox couples has long been a focus of our research. These studies have evaluated the electronic factors that affect the thermodynamics and kinetics of ET.

The factors that affect ET reactivity are well defined within the context of the Marcus-Hush kinetic theory of ET; where the rate constant for ET is given as the product of three general terms: $k_{et} = \nu_{eff} \cdot \kappa_{el} \cdot T_{act}$. The component terms are defined as follows: ν_{eff} is the collisional frequency term (for bimolecular ET processes), κ_{el} is the electron transmission coefficient, and T_{act} is the activation term. The first term is essentially a statistical term that described how often an effective bimolecular collision might occur, whereas the second defines the ratio of those collisions that can lead to ET. The final term describes the energy distribution relative to the specific activation requirements for the system. Electronic structure considerations of ET reactivity are expressed in the last two of these terms. The activation term depends both on the reduction potentials (E^0) of the donor and acceptor sites, and on the (geometric) reorganization energy (λ_i) for optimal ET. (The total reorganization energy is composed of inner-sphere and outer-sphere components. The outer-sphere term relates to the response of the medium to the ET process and depends upon the choice of medium. We consider only the inner-sphere term, which directly relates to changes in the geometric structure of the redox site itself.) κ_{el} depends on both λ_i and H_{DA}, the electronic coupling matrix element that connects the donor and acceptor sites. From this brief summary, we see that correlation of electronic structure to the redox properties of a site requires inquiry into the redox potential of the site, its geometric change on redox, and the possible coupling pathways for ET to a particular redox partner. Thus, determining the factors that control E^0, λ_i, and H_{DA} are of critical importance in defining the ET reactivity of redox-active transition metal sites.

This review addresses these issues from the perspective of the *electronic structures* of the [FeX_4] ($X = Cl^-$, SR^-) redox couples and their influence on ET parameters. These sites are probed using a combination of spectroscopic methods and theoretical results from density functional (DFT) calculations. The available experimental data for the ferric complexes are presented in Section 2.59.2, providing a detailed description of the active site electronic structure when combined with results from DFT calculations. In Section 2.59.3, a similar analysis is performed on the ferrous complexes with focus on the differences and similarities between the reduced and oxidized sites and between the chloride and thiolate redox couples. Section 2.59.4 provides a mechanism to quantitatively evaluate the changes in the electronic structure of a site on redox, this is *electronic relaxation*. The information presented in Sections 2.59.2–2.59.4 is used in Section 2.59.5 to evaluate the influence of electronic structure on λ_i, H_{DA}, and E^0.

2.59.2 ELECTRONIC STRUCTURE OF FERRIC SITES

2.59.2.1 Ligand Field Spectroscopy and Ground State Parameters

The polarized single-crystal ligand field (LF) absorption spectrum for [PPh_4][$FeCl_4$][1,2] is given in Figure 1a; complex is near tetrahedral but has rigorous D_{2d} symmetry. These data, in conjunction with single-crystal MCD and transverse Zeeman polarized spectroscopies allowed assignment of the spin-forbidden $^4\Gamma \leftarrow {}^6A_1$ transitions in D_{2d} symmetry. From these data, the one-electron $3d$ orbital splitting pattern is derived[2] (Figure 2a) based upon Tanabe-Sugano matrices (to obtain $10Dq$, B, and C) and splitting of the low-energy $^4T_1$ and $^4T_2$ states (μ, δ); quantitative results are given in Table 1. The cubic LF splitting is large ($10Dq = 6{,}550\ cm^{-1}$) relative to the axial splittings (μ and δ). The LF analysis also reveals highly reduced Racah parameters, which reflect a very small electron repulsion in $[FeCl_4]^{1-}$ ($\beta = \beta_{complex}/B_{free\ ion} \approx 0.40$); this suggests high covalency in the Fe $3d$-orbitals.[2] Low-temperature Q-band EPR spectroscopy provide ground state information,

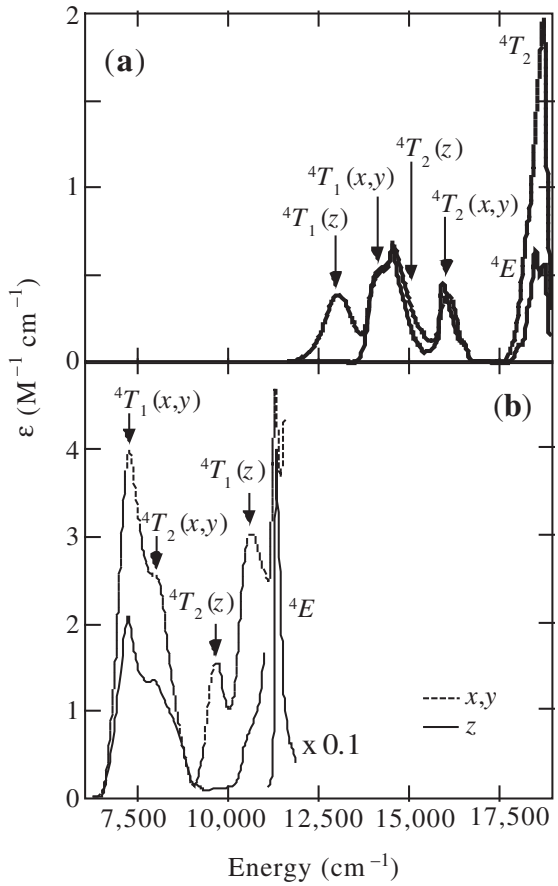

Figure 1 LF spectra for (a) $[FeCl_4]^{1-}$ and (b) $[Fe(SR)_4]^{1-}$ where R = 2,3,5,6,-(Me)C_6H. The assignments are based upon polarized single-crystal absorption, transverse Zeeman, and MCD spectroscopies.[1,2,5]

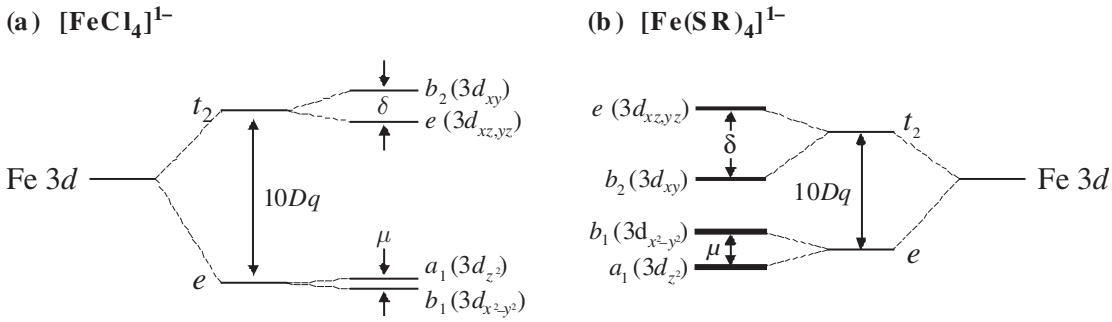

Figure 2 Fe 3*d* orbital splitting diagrams for (a) $[FeCl_4]^{1-}$ and (b) $[Fe(SR)_4]^{1-}$ as derived from LF analysis of the data in Figure 1.[5]

i.e., the molecular *g*-values and zero-field splitting (ZFS) for the axially distorted $[FeCl_4]^{1-}$ complex (see Table 1).[2]

The largest contribution to ZFS of the $^6A_1$ ground state is second-order spin-orbit coupling to low-symmetry split excited states. Griffith[3] developed a model (Equation (1a)) that correlates the energy splitting of the lowest energy $^4T_1$ excited state components in Figure 1a with *D*, the axial ZFS of the $^6A_1$ in high-spin d^5 systems. In Equation (1a), $\zeta_{Fe^{III}}$ is the atomic spin-orbit coupling for Fe^{III} and E_z and $E_{x,y}$ are the energies of the $^4T_1(z)$ and $^4T_1(x, y)$ excited states, respectively (from Figure 1a):

Table 1 Compilation of LF and Fe 3*d* orbital splitting parameters for the $[FeCl_4]^{2-,1-}$ and $[Fe(SR)_4]^{2-,1-}$ redox couples. All values are in cm^{-1} except for β and g values, which have no units.

	LF splittings			*Racah parameters*					
Species	$10Dq$	$X\mu$	δ	B	C	β	D	g_z	$g_{x,y}$
$[FeCl_4]^{1-}$	−6,550	−172	−1,331	444	2,728	0.40	−0.04	2.014,8	2.012,5
$[FeCl_4]^{2-}$	−4,100	−23	<10	830	3,430	0.87			
$[Fe(SR)_4]^{1-}$	−4,500	+1,250	+2,700	22	2,222	0.02	+2.4	2.015,9	2.021
$[Fe(SR)_4]^{2-}$	−3,500	−1,400	+700	620	2,800	0.65	−8.7	8.24	

$$D = \frac{\left(\zeta_{Fe^{III}}\right)^2}{5}\left(\frac{1}{E_z} - \frac{1}{E_{x,y}}\right) \tag{1a}$$

$$D = \frac{\left(\zeta_{Fe^{III}}\right)^2}{5}\left(\frac{k_z^2}{E_z} - \frac{k_{x,y}^2}{E_{x,y}}\right) \tag{1b}$$

Rather unexpectedly, Equation (1a) fails to predict the correct magnitude and *sign* of D for $[FeCl_4]^{1-}$ ($D_{calc} = +0.24\ cm^{-1}$ vs. $D_{exp} = -0.04\ cm^{-1}$). It was determined that the failure results from *anisotropic covalency*, i.e., the covalency of the axially split $3d_{xy}$ and $3d_{xz,xy}$ orbitals differ. The greater covalency of the $3d_{xy}$ orbital in the flattened T_d structure decreases the spin-orbit coupling to the $^4T_1(z)$ component relative to the coupling to the $^4T_1(x,y)$: in Equation (1b), $k_z^2 < k_{x,y}^2$ where k_z^2 and $k_{x,y}^2$ relate to the metal character in the $3d_{xy}$ and $3d_{xz,xy}$ orbitals, respectively. As a result, the axial ZFS is small and negative.[1] The importance of anisotropic covalency has been confirmed in a more recent treatment of the full D tensor, which explicitly includes ZFS contributions from all excited states (not just the lowest energy quartet components) using *ab initio* methods.[4]

There is a dramatic difference between the LF spectra for $[FeCl_4]^{1-}$and $[Fe(SR)_4]^{1-}$ (R = 2,3,5,6-(Me)C_6H)), as observed from Figure 1.[5] The spin-forbidden $^4\Gamma \leftarrow {}^6A_1$ transitions are lower in energy for the tetrathiolate by nearly 8,000 cm^{-1}; this shift is much larger than would generally be expected from LF arguments. As with the tetrachloride, assignment of these transitions provides experimental LF parameters (Table 1) and a 3*d* orbital splitting pattern (Figure 2b).[5] ZFS in $[Fe(SR)_4]^{1-}$ also requires the inclusion of anisotropic covalency to properly account for the sign and magnitude of D. In this case, however, D is much larger and positive, reflecting that the $3d_{xz,xy}$ orbitals are more covalent than the $3d_{xy}$ such that $k_z^2 > k_{x,y}^2$ in Equation (1b). The spectroscopically derived axial orbital splitting is much larger in the thiolate and different from the chloride, as evidenced by the sign and magnitude of μ and δ (see Table 1). The larger axial distortion and higher $3d_{xz,yz}$ orbital covalency results from the nature of the ligand orbitals involved in bonding with the metal ion (Figure 3). For the chloride, interactions occur through a σ-donor Cl 3*p* orbital as well as two π-donor Cl 3*p* orbitals. For thiolate ligands, one of the S 3*p* orbitals is involved in a σ-bond with C (SC_σ in Figure 3b) thus modifying its spatial distribution and energetics relative to the other two S 3*p* orbitals, which are π and σ relative to the metal. Most importantly, the SC_σ interaction redirects the S $3p\sigma-$orbital depending on the FeSC angle, which is >90°. The σ-type S 3*p* orbital thus forms a pseudo-σ bond with the iron. This pseudo-σ interaction dominates the axial splitting and anisotropic covalency of the Fe 3*d* orbitals in Figure 2b and results in a largely different orbital

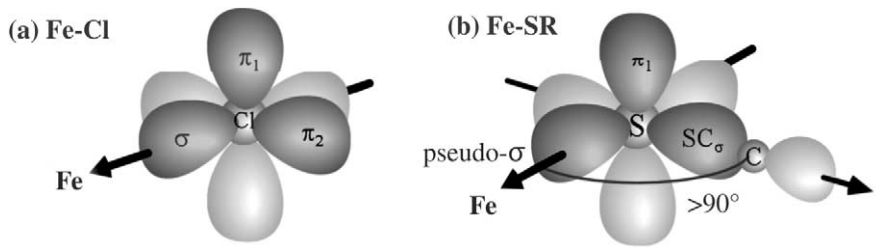

Figure 3 Important ligand fragment MOs for (a) chloride and (b) thiolate ligands involved in bonding with a transition metal. The many-atom thiolate orbitals are dominated by the strong SC σ-bond whereas the chloride 3*p* atomic orbitals interact solely with the metal 3*d* orbitals.

ordering than that observed for the chloride. Further, the splitting pattern and orbital covalencies, and hence the ZFS tensor in the tetrathiolate are highly dependent on the orientation of the αC in the thiolate ligand (i.e., the FeSC angle as well as the dihedral angle between the FeSC and SFeS planes) as this significantly affects the orientation of the pseudo-σ bond with the iron.

Both $[FeCl_4]^{1-}$and $[Fe(SR)_4]^{1-}$exhibit very small β values indicating significant ligand character in the spin-forbidden LF transitions. In fact, the values of β are so small (<0.50) that they suggest that these "LF transitions" are actually best described as ligand-to-metal charge transfer (LMCT) transitions. This assignment provides a clear explanation for the large shift observed in the LF spectra between the tetrachloride and tetrathiolate complexes in Figure 1 and is demonstrated by variable-photon energy photoelectron spectroscopy (VEPES) data (*vide infra*).

2.59.2.2 Charge Transfer Spectroscopy—Metal–ligand Bonding

The charge transfer spectrum for $[FeCl_4]^{1-}$ (Figure 4a) had previously been assigned under the assumption that transitions in the near-UV correspond exclusively to Fe $3d_\pi \leftarrow$ L $3p_\pi$ or π-type LMCT transitions. From valence photoelectron spectroscopy (PES) and DFT calculations (*vide infra*), however, it is clear that the complete CT manifold must occur within or near the experimentally accessible CT region (<40,000 cm^{-1}). The spectrum has, therefore, been reassigned as given in Figure 4a. This new assignment of the spectrum includes contributions from both π- and σ-LMCT transitions. The polarized single-crystal CT spectrum for $[Fe(SR)_4]^{1-}$ (R = 2-(Ph)C_6H_4) has also been obtained and assigned, as shown in Figure 4b.[6] The CT spectrum of $[Fe(SR)_4]^{1-}$ is red-shifted by ~8,000 cm^{-1} relative to $[FeCl_4]^{1-}$, as also observed in the LF spectra (*vide supra*). Contrary to the LF region (Figure 1), however, this behavior is expected for CT spectra based on the lower valence state ionization energy (VSIE) of the thiolate relative to Cl ligands. An important feature in the CT spectrum of the tetrathiolate that is not observed in the tetrachloride is the presence of a weak, low-energy CT transition at ~13,000 cm^{-1}, which corresponds to a very weak π-LMCT transition.

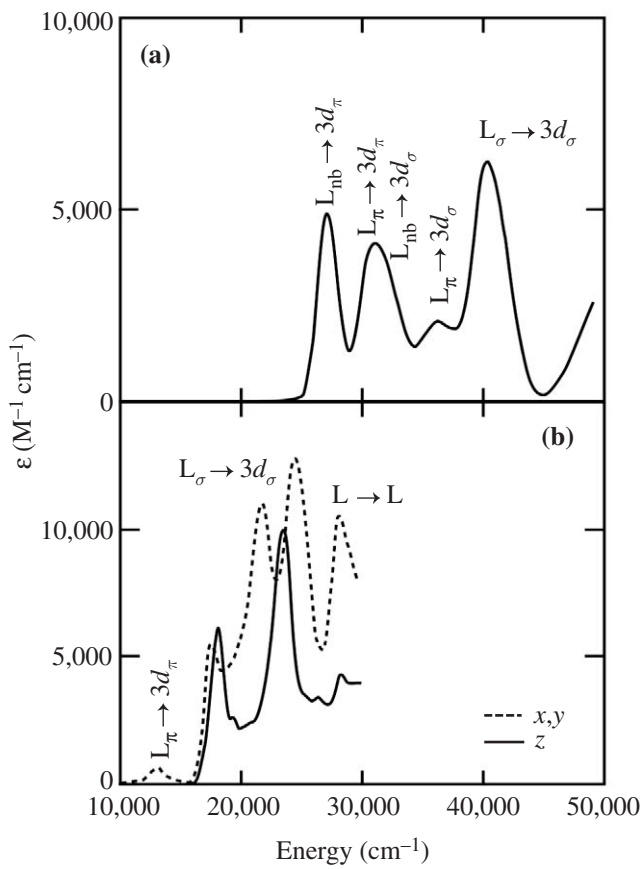

Figure 4 CT spectrum of (a) $[FeCl_4]^{1-}$[12] and (b) $[Fe(SR)_4]^{1-}$[6]. The assignment for the former differs from that given in the literature (see text).

(This had originally been assigned as the spin-forbidden "LF" transitions which are now understood to be at ~8,000 cm^{-1} lower energy due to their CT character.) Further, the total intensity of π-LMCT transitions for the thiolate is much lower than in the chloride, indicating that π interactions are much less important to bonding in the tetrathiolate.

2.59.2.3 X-ray Absorption Edges—Covalency of Fe 3*d* Orbitals

Ligand X-ray absorption spectroscopy (XAS) edges provide a direct probe of the ligand character in the empty 3*d* orbitals in a transition metal complex, thus giving an experimental method for determining the covalency of metal–ligand bonds. The chlorine and sulfur K-edge XAS edges for $[FeCl_4]^{1-}$ and $[Fe(SR)_4]^{1-}$ (R = Ph) have been obtained; the intensity of their pre-edges is directly related to the amount of L 3*p* character in the Fe 3*d* orbitals (see Shadle *et al.*[7] and Williams *et al.*[8] for details). There is significant ligand character in both species, although the S 3*p* character in the tetrathiolate complex (~30% per empty Fe 3*d* orbital) is greater than the Cl 3*p* character in the tetrachloride complex (~17% per orbital). These results demonstrate that the tetrathiolate complex is more covalent than the tetrachloride.

2.59.2.4 Variable Energy Valence Photoelectron Spectroscopy—Inverted Bonding Description

PES directly probes the molecular orbital (MO) structure of a molecular complex in the valence region. High-resolution data of molecular species are normally only obtained in the gas phase, but under certain circumstances such data can be obtained in the solid state. High-resolution VEPES single-crystal data were obtained for $[FeCl_4]^{1-}$ as shown in Figure 5. From the changes in the intensities of the VEPES ionization bands, the nature of the initial state MOs can be quantita-

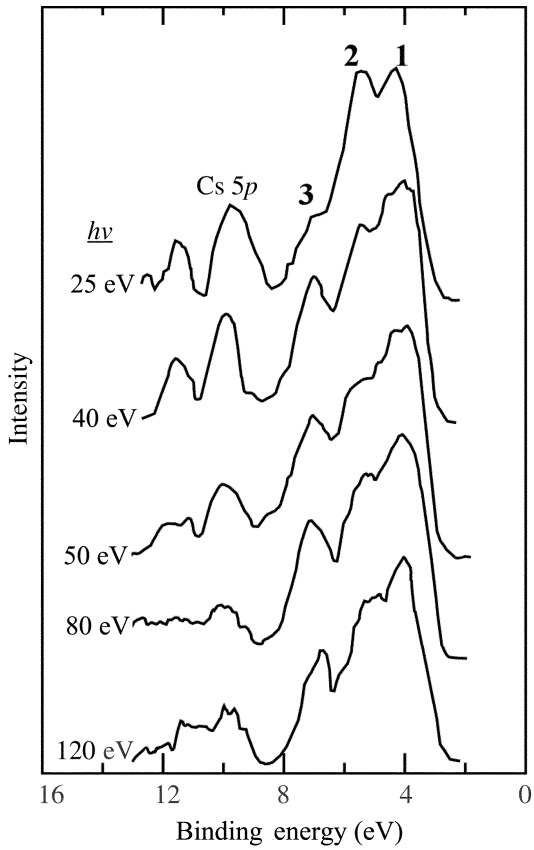

Figure 5 Single-crystal variable photon energy PES data for $[FeCl_4]^{1-}$ ($CsFeCl_4$).[9] Satellite peaks for this complex occur in the same energy region as the counterion Cs 5*p* peak. Complementary data from $RbFeCl_4$ (not shown) are clean in that energy region and have allowed detailed analysis of the satellite peaks in $[FeCl_4]^{1-}$.

tively determined. The low-binding energy peaks (regions 1–2) decrease in intensity with photon energy; this is consistent with ionization of MOs containing predominantly ligand character. Conversely, region 3 displays an intensity maximum at $h\nu \sim 45$ eV (observable in Figure 5 and increased intensity of 3 at $h\nu = 40$ eV relative to $h\nu = 25$ eV), corresponding with strong Fe 3*d* character in these deeper-lying MOs. Resonance profiles of specific peaks over the Fe 3*p* ionization threshold (~52 eV) probe the metal character and its energy distribution over the *final (ionized) states* in the PES experiment. Profiles for $[FeCl_4]^{1-}$ (see Butcher *et al.*[9] for details) indicate that region 3 is resonance enhanced, i.e., Fe 3*d* character remains in the same energy region in both the initial and final states. Since the Fe 3*d* character occurs in the same region in both the initial and final states, the electronic structure of the Fe^{IV} final state must be quite similar to the Fe^{III} initial state. It has also been found that there is little off-resonance shake-up satellite intensity,[9] which further indicates that the electronic structure does not change significantly on ionization (*vide infra*). (The satellite peaks are at about the same energy as the counter-ion Cs 3*p* peak in Figure 5 making it difficult to evaluate their intensity from these data. However, complementary data for $RbFeCl_4$ are clean in this area and clearly demonstrate the weak intensity of the off-resonance satellites in $[FeCl_4]^{1-}$.) Overall, the VEPES data provide a rather unusual electronic structure description for $[FeCl_4]^{1-}$: the highest energy MOs (region 1) have mostly ligand character, whereas the Fe 3*d* character is at much deeper binding energy (region 3). This is opposite from the normal behavior of transition metal complexes where the metal 3*d* orbitals are above the ligand valence orbitals. This "inverted" bonding scheme can be understood from DFT calculations.

2.59.2.5 Density Functional Calculations—Electronic Structure Description of Ferric Complexes

DFT calculations (using the VWN-BP86 functional) have been used to assist in the interpretation of the spectroscopic data that are available for $[FeCl_4]^{1-}$ and $[Fe(SR)_4]^{1-}$. Our results are generally in good agreement with other theoretical calculations on these systems. It has become customary in recent years to use hybrid functionals (e.g., B3LYP) to investigate transition metal systems; however, our investigations indicate that the BP86 pure DFT provides a more reasonable description of the electronic and geometric structure of high-spin iron systems. Spin-restricted DFT calculations on $[FeCl_4]^{1-}$ result in a typical transition metal MO scheme (Figure 6a) but are in poor agreement with spectroscopic data (*vide supra*). Removing the spin restriction (Figure 6b) allows the majority and minority spin orbitals in the $S = 5/2$ system to differ spatially and energetically, allowing for spin polarization of the Fe 3*d* manifold. These results are in much better agreement with experiments. Spin polarization splits the Fe 3*d* manifold into a filled $3d_\alpha$ and an empty $3d_\beta$ manifold that behave very differently. The five $3d_\alpha$ orbitals are so stabilized in energy that they drop below the Cl $3p_\alpha$ orbitals creating the inverted bonding scheme that was observed in the VEPES data in Figure 5. Conversely, the $3d_\beta$ orbitals remain above the Cl $3p_\beta$ orbitals. DFT results for $[Fe(SCH_3)_4]^{1-}$ are qualitatively very similar to those from $[FeCl_4]^{1-}$, although the high energy of the S 3*p* orbitals (relative to the Cl 3*p*) increases the covalency of the metal–ligand bonds, which are dominated by the interactions in the set of minority-spin β orbitals.

The $3d_\beta$ orbital splitting pattern for $[FeCl_4]^{1-}$ obtained from DFT (Figure 6, right) is quite similar to that observed from analysis of the low frequency (LF) and CT spectra (see Figure 2a). However, the DFT results overestimate the importance of π-contributions, affecting the magnitude of the splitting of the $3d_{z^2}$ and $3d_{x^2-y^2}$ orbitals (μ). DFT results for $[Fe(SCH_3)_4]^{1-}$ (not shown) are also in good agreement with the experimentally derived energy splitting, although the results are highly sensitive to the orientation and identity of the thiolate ligands. In any case, the bonding is dominated by the pseudo-σS 3*p* orbital (see Figure 3) with only minor contributions from π-interactions from the other S 3*p* orbital and the SC σ-bond.

A major result from the spin-unrestricted DFT calculations is the dramatic difference between the α- and β-spin orbital structures, which help explain the VEPES data and the CT nature of the spin-forbidden $^4\Gamma \leftarrow {}^6A_1$ LF transitions. The deep binding energy Fe 3*d* character in the valence PES data are the inverted $3d_\alpha$ orbitals. Also, we see that the spin-forbidden LF transitions are LMCT transitions between the highest occupied α-MOs (L 3*p*) and the lowest-unoccupied β-MOs (Fe 3*d*). However, the inverted bonding scheme does not exhibit itself in the spin-allowed CT spectra and in the nature of the ligand–metal bonding, both of which depend predominantly on the β-spin manifold. Therefore, it is of importance to note that although the inverted bonding scheme dominates much of the spectroscopy of $[FeCl_4]^{1-}$ and $[Fe(SR)_4]^{1-}$, it does not play a significant role in defining the bonding within the complex. The bonding is dominated by high

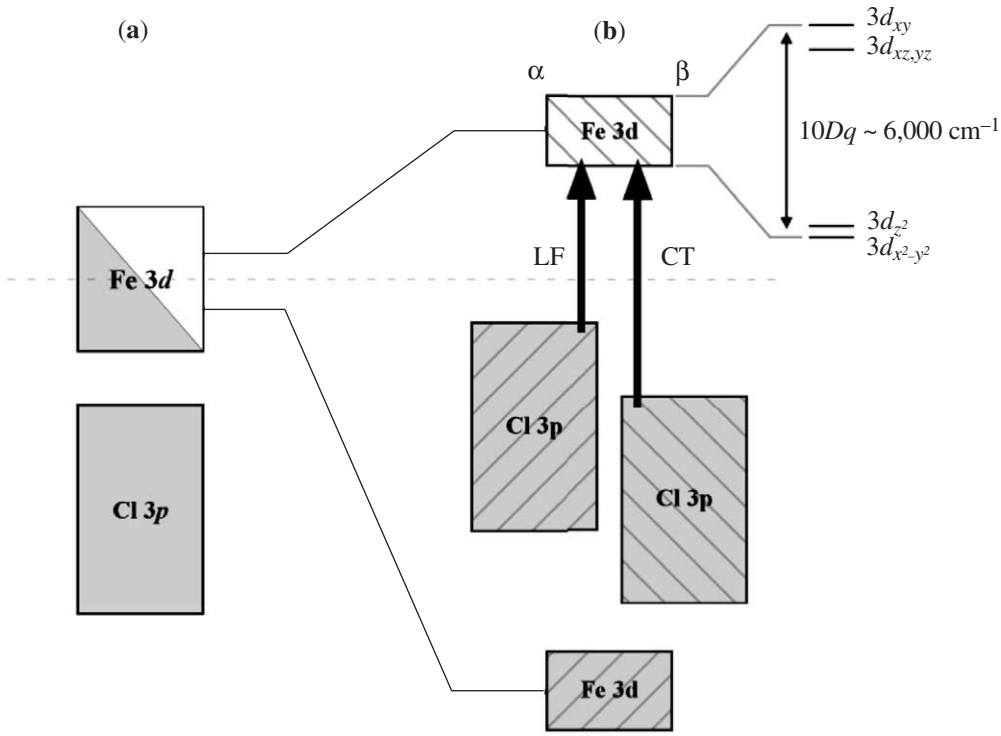

Figure 6 Qualitative (a) spin-restricted and (b) spin-unrestricted gas phase DFT results for $[FeCl_4]^{1-}$ from ADF[13–15] using the VWN-BP86[16–19] functional. The majority α-spin and minority β-spin orbital blocks are shaded differently.

covalency due to the low energy of the $3d_\beta$ manifold relative to the ligand valence orbitals, which are higher in energy in the thiolate complex.

2.59.3 ELECTRONIC STRUCTURE OF FERROUS SITES

2.59.3.1 Polarized Absorption and Variable Temperature, Variable Field Magnetic Circular Dichroism

The polarized single-crystal absorption data for $[Fe(SR)_4]^{2-}$ (R = 2-(Ph)C_6H_4) and for $[FeCl_4]^{2-}$ are given in Figure 7. In contrast to the ferric data, the spin-forbidden LF transitions for the chloride and thiolate complexes are not that different; the $[Fe(SR)_4]^{2-}$ transitions are lower than those for $[FeCl_4]^{2-}$ by only $\sim$2,500 cm^{-1}. Assignment of the visible $^3\Gamma \leftarrow {}^5T_2$ transitions allowed us to derive an orbital energy diagram for each of the complexes, as given in Figure 8. The LF parameters for each of the species are given in Table 1. Relative to the ferric species, the tetrachloride has a much smaller crystal field splitting ($10Dq$) and an electron repulsion parameter ($\beta = 0.87$) that indicates that the ferrous complex is far more ionic. The same observations hold for the tetrathiolate but in addition, there is a dramatic difference in the axial splitting as evidenced by the sign of μ (see Table 1), which results in the $3d_{z^2}$ being lowest in energy in the ferrous complex. This change in the lowest energy $3d_\beta$ orbital is due to the structural differences between the ferrous and ferric tetrathiolate models. The effect confirms the strong effect of the C_α-S thiolate orientation on the ground state of the tetrathiolate system. Determining ground state parameters for high-spin ferrous complexes is more difficult since they are integer spin nonKramers ions, which makes EPR studies more complex. However, the $^5T_2$ ground state parameters can be probed using excited state techniques, specifically using the magnetic field saturation and temperature-dependence behaviors of magnetic circular dichroism spectroscopic data (variable temperature, variable field MCD). This analysis was performed on the tetrathiolate model and the results are given in Table 1. Notably, a LF model does allow proper calculation of

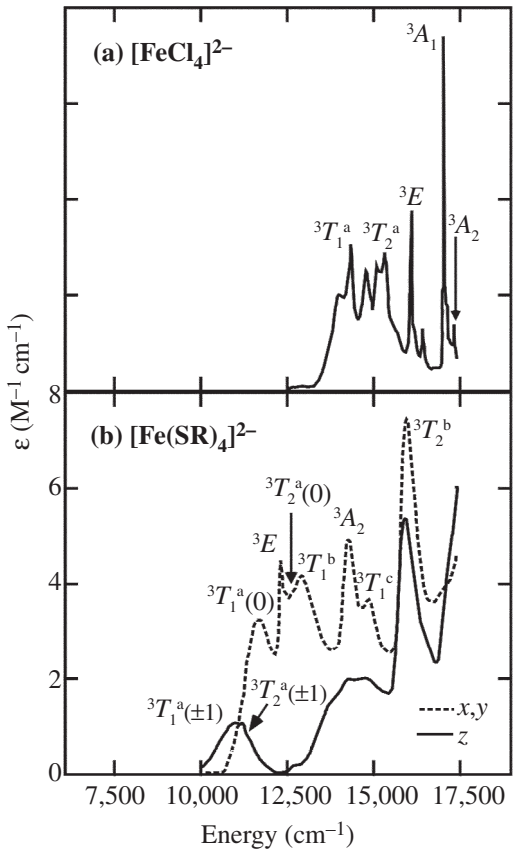

Figure 7 LF spectra for (a) $[FeCl_4]^{2-}$ [20] and (b) $[Fe(SR)_4]^{2-}$ [6] where R = 2-(Ph)C_6H_4.

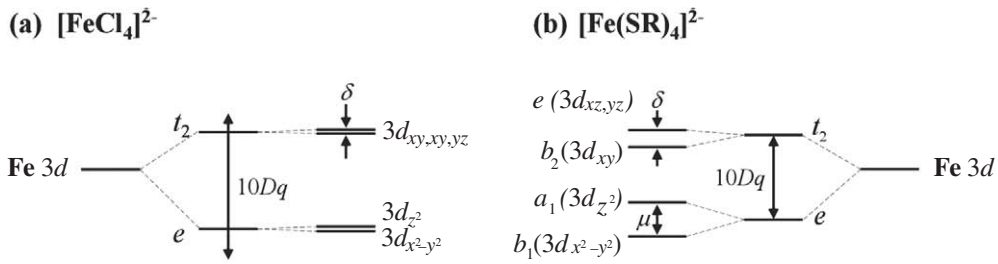

Figure 8 Fe 3*d* orbital splitting diagrams for (a) $[FeCl_4]^{2-}$ and (b) $[Fe(SR)_4]^{2-}$ as derived from LF analysis of the data in Figure 7.[6]

D – suggesting that differential orbital covalency is not important in the ferrous complex in sharp contrast to that observed in the ferric species (*vide supra*).

2.59.3.2 Variable Energy Valence Photoelectron Spectroscopy

Valence PES data for $[FeCl_4]^{2-}$ have been used to probe the MO structure of the ferrous site (Figure 9). The general shape of the photoelectron spectrum is quite similar to that for the ferric species except for a new peak on the low binding-energy side (labeled redox-active molecular orbital (RAMO)). That peak corresponds with the extra electron in the ferrous species, the lone electron in the $3d_\beta$ manifold. Although the overall shapes of the spectra are similar, the variable photon energy behavior is quite different in the ferrous relative to the ferric site. In the ferrous

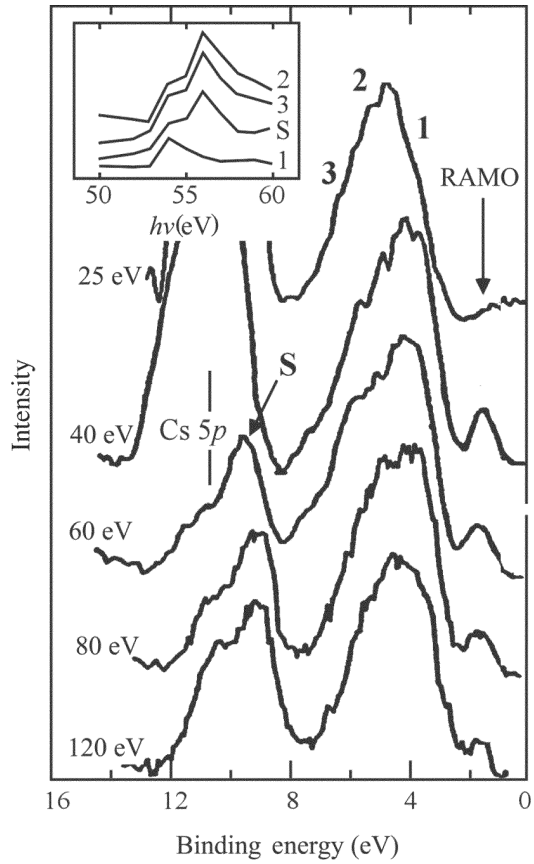

Figure 9 Single-crystal variable photon energy PES data for $[FeCl_4]^{2-}$ (Cs_3FeCl_5).[21] Note that the Cs 5*p* counterion peak has a very high cross-section at low photon energies. The resonance profiles for each of the labeled regions (1, 2, 3, and S) are given in the inset for Rb_3FeCl_5, for which the counterion peak does not interfere with the satellite peak (S).

complex, the lowest binding energy peaks (RAMO and 1 in Figure 9) have greatest intensity at ~45 eV indicating that they contain dominantly Fe 3*d* character. By contrast, the deeper binding energy peaks (2,3 in Figure 9) decrease in intensity with photon energy, which indicates that they are mostly ligand in character. This pattern indicates a normal bonding scheme, with the metal 3*d* character at higher energy than the ligand 3*p* orbitals. However, Fe 3*p* resonance enhancement profiles (see Figure 9, inset) indicate that the deeper binding energy regions (2 and 3 in Figure 9) gain metal 3*d* character in the final (i.e., oxidized) state. This indicates that Fe 3*d* character shifts to deeper binding energy in the Fe^{III} final state; notably, the Fe character shifts down to the same energy region that contains Fe 3*d* character in the initial state of $[FeCl_4]^{1-}$ (region 3 in both Figures 5 and 9). This correspondence between the final ionized state of the Fe^{II} complex and the initial state of the Fe^{III} species clearly indicates that the electronic structure changes from a normal bonding scheme in the ferrous state to an inverted bonding scheme in the ferric state. Additionally, the off-resonance shake-up satellite ("S" in Figure 9) is quite intense in the ferrous species. Since the satellite corresponds to a process where an electron is ionized and a second electron is excited from a ligand orbital to the metal 3*d* manifold (a CT process), it is formally a forbidden two-electron process that can only gain intensity through changes in the ferrous wave function on ionization. This is consistent with the idea that a substantial change in the electronic structure occurs on oxidation.

2.59.3.3 Density Functional Results

DFT calculations (VWN-BP86) were performed on $[FeCl_4]^{2-}$ and the results correlate very well with the experimental data. In this case, differences between spin-restricted and spin-unrestricted results are not as dramatic as in the ferric species (see Figure 10). The effect of spin polarization for high-spin Fe^{II} is still large but not sufficient to cause inversion of the ordering in the majority

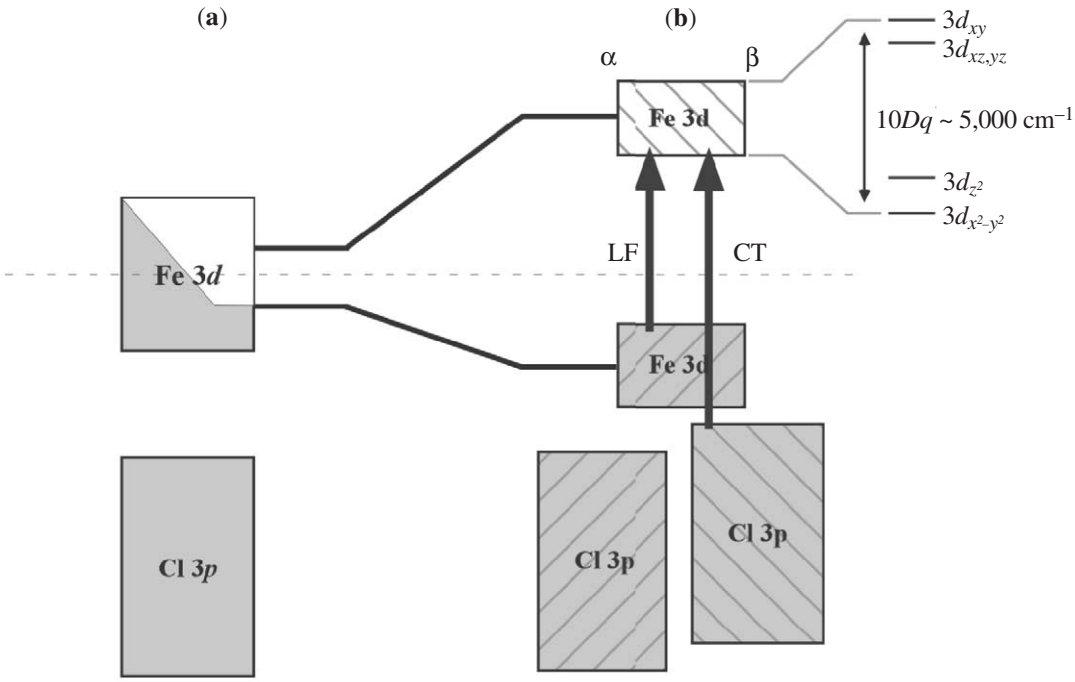

Figure 10 Qualitative (a) spin-restricted and (b) spin-unrestricted gas phase DFT results for $[FeCl_4]^{2-}$ from ADF[13–15] using the VWN-BP86[16–19] functional. The majority α-spin and minority β-spin orbital blocks are shaded differently.

spin orbitals. Both the $3d_\alpha$ and $3d_\beta$ MOs remain above the Cl $3p$ leading to a normal electronic structure for the ferrous complex. The results for $[Fe(SCH_3)_4]^{2-}$ are qualitatively similar to those for $[FeCl_4]^{2-}$ although the metal–ligand covalency is greater in the tetrathiolate as was the case for the ferric species. Additionally, the overall covalency of the ferrous species is lower than that of related ferric species due to the deeper binding energy of the Fe $3d$ manifold in the ferric species. This conclusion has been confirmed by a large change in the Cl $3p$ character in the empty $3d$ orbitals observed by Cl K-edge XAS (the Cl $3p$ character decreases from 17% to 9%, see Shadle *et al.*[7] for details).

2.59.3.4 Summary

The combination of spectroscopic and theoretical methods have provided a detailed description of the electronic structure of the $[FeCl_4]^{2-,1-}$ and $[Fe(SR)_4]^{2-,1-}$ redox couples. Of primary interest are the dramatic changes in electronic structure that occur on oxidation. Most notably, increased spin polarization causes inversion in the filled majority spin α-MOs. The largest effects of inversion in the α-MOs are observed in the LF transitions, which become mostly LMCT transitions in the ferric complexes and in the VEPES where the deepest binding energy peak (region 3 in Figure 5) has dominantly Fe $3d$ character. This inversion does not significantly affect the metal–ligand bonding since the Fe $3d_\alpha$ and L $3p_\alpha$ are filled. The unoccupied Fe $3d_\beta$ manifold, including the RAMO that contains the extra electron in the ferrous species, is also strongly affected by oxidation. The Fe $3d_\beta$ manifold is lowered in the oxidized form, which causes increased covalent mixing between the empty Fe $3d_\beta$ and the filled L $3p_\beta$, affecting the strength of the metal–ligand bonding in the ferric complexes. All of these changes in the electronic structure reflect a change in the molecular wave function on oxidation; this change is termed *electronic relaxation* and it is clearly of great importance in the $[FeCl_4]^{2-,1-}$ and $[Fe(SR)_4]^{2-,1-}$ redox couples. Note that the covalency and its change on oxidation is larger for the thiolate complex due to the lower ionization energy of the sulfur ligand valence orbitals.

The above results show that electronic relaxation is important in the ionization of ferrous complexes and can affect redox processes. For this reason, one-electron models used to investigate redox properties of these transition metal sites are incomplete. It thus becomes imperative to clearly define and quantify electronic relaxation in these redox couples in order to properly address ET reactivity in these sites.

2.59.4 ELECTRONIC RELAXATION

Electronic relaxation can be defined by decomposing the ionization process as given in Scheme 1; the change in the molecular wave function ($\Delta\Psi_{rlx}$) is considered as a response to a "frozen orbital" ionization. In the frozen orbital limit, the nature of the ionized electron is described by the RAMO, i.e., the orbital from which the electron was removed. Therefore, for $Fe^{II} \rightarrow Fe^{III*}$, the effective charge on the metal (Z_{eff}^{Fe}) changes by $\Delta q_{ion} = Z_{eff}^{Fe^{III*}} - Z_{eff}^{Fe^{II}}$, which corresponds to the amount of metal character (α^2) in the RAMO. If electronic relaxation is allowed to occur, ψ changes to stabilize the hole and causes Z_{eff}^{Fe} to change by $\Delta q_{rlx} = Z_{eff}^{Fe^{III}} - Z_{eff}^{Fe^{III*}}$ ($Fe^{III*} \rightarrow Fe^{III}$ in Scheme 1). Altogether, the ionization process causes a total change in charge (Δq_{redox}) that is the sum of the initial Δq_{ion} and the Δq_{rlx} due to electronic relaxation.

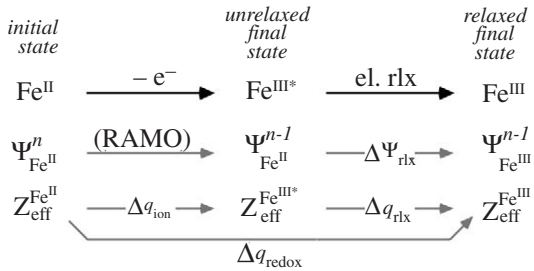

Scheme 1

As discussed above, the presence of satellite peaks in PES data result from changes in the wave function, thus allowing intensity to distribute into formally forbidden two-electron transitions. The relative intensity of such satellite peaks (as in Figure 9 for $[FeCl_4]^{2-}$) is, therefore, a direct experimental probe of the magnitude of electronic relaxation. However, an appropriate model is necessary to evaluate the experimental data and quantitatively determine Δq_{rlx} and a valence bond configuration interaction (VBCI) model has been developed specifically for this purpose. The basic model is given in Figure 11 and is developed in Kennepohl and Solomon[10] (the fundamental concepts involved in VBCI are also given in Chapter 1.88). The VBCI model as shown is effective for core ionizations (e.g., Fe 2*p*) and the model must be expanded to include atomic multiplets in order to properly evaluate valence ionization processes for many-electron metal ions. The most important result from application of this atomic multiplet-VBCI model to valence PES data of both $[FeCl_4]^{2-}$ and $[Fe(SR)_4]^{2-}$ is that Δq_{rlx} is extremely large in both systems although greater for the tetrathiolate species ($-0.70\,e^-$ and $-0.75\,e^-$, respectively). The effect of electronic relaxation in these species is to dramatically decrease the effective nuclear charge on the metal ($Z_{eff}^{Fe^{III*}}$ in Scheme 1), thus stabilizing the oxidized state.[10]

The origin of this large Δq_{rlx} for both ferrous species was evaluated by DFT calculations. The effect of electronic relaxation is readily observed by comparing the redox densities ($\Delta\rho_{redox} = \rho_{Fe^{II}} - \rho_{Fe^{III}}$) for $[Fe(SR)_4]^{2-}$ both with and without electronic relaxation (Figure 12). In the absence of relaxation, the ionization process is directly related to the RAMO, i.e., the orbital from which the electron is removed. The redox process is, therefore, primarily metal-based since, in this case, the RAMO has mostly $3d_{x^2-y^2}$ character. When relaxation is allowed to occur, the changes on the ligand are far greater, reflecting LMCT to stabilize the oxidized metal site. This added LMCT in the oxidized site is achieved due to the increased covalency of the metal–ligand bond (*vide supra*) in the oxidized state. This increase in covalency occurs primarily in the passive orbitals, i.e., those orbitals not directly involved in the ionization process.[10]

2.59.5 ELECTRONIC STRUCTURE CONTRIBUTIONS TO ELECTRON TRANSFER

2.59.5.1 Reduction Potentials

Reduction potentials (E^0) are highly variable in $[FeX_4]$ redox couples. In particular, the redox potentials of $[FeCl_4]^{2-,1-}$ and $[Fe(SCH_2CH_3)_4]^{2-,1-}$ differ by almost 1 V in acetonitrile (E^0 are -0.08 V and -1.0 V, respectively). (The vertical ionization energy also excludes energetic effects from geometric distortions upon redox that are important for adiabatic ET. The difference in adiabatic corrections for both species has been calculated at $\sim$0.2 eV, stabilizing the tetrachloride

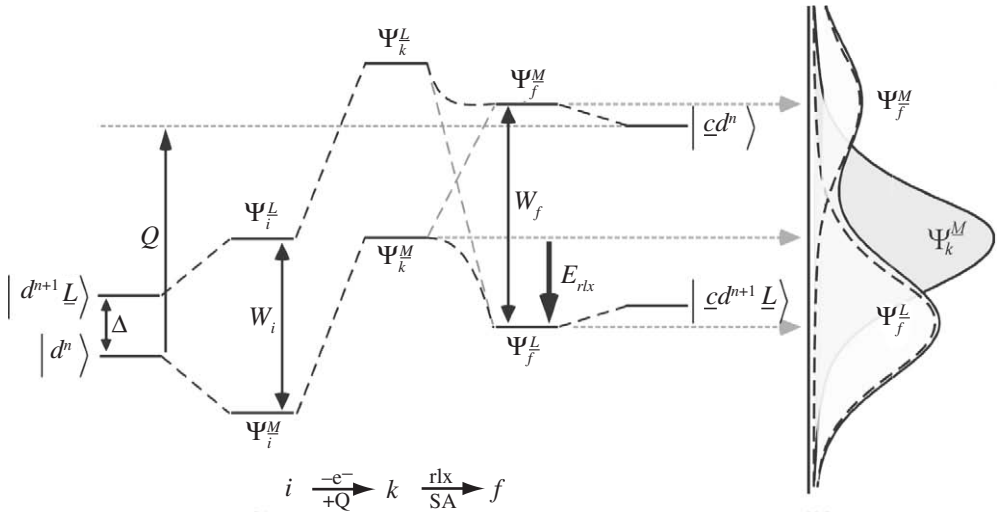

Figure 11 VBCI model developed to define electronic relaxation, i.e., the difference between the unrelaxed final state (Koopmans state) and the true relaxed final state.[10] The left side of the diagram represents the initial state configuration interaction between the $|d^n\rangle$ ground configuration and the $|d^{n+1}\underline{L}\rangle$ charge transfer configuration; these valence bond (VB) states are separated by Δ. The two VB wave functions mix (based upon the mixing parameter, T) to yield the CI-mixed $\Psi_i^{\underline{M}}$ and $\Psi_i^{\underline{L}}$ states, split by $W_i = \sqrt{\Delta^2 + 4T^2}$. To create the final state wave functions, the metal-based VB configuration ($|\underline{c}d^n\rangle$) is destabilized relative to the CT configuration ($|\underline{c}d^{n+1}\underline{L}\rangle$) by an amount Q, the magnitude of the $2p$–$3d$ hole interaction. These final state VB states also mix through T to give the correct final state wave functions ($\Psi_f^{\underline{M}}$ and $\Psi_f^{\underline{L}}$) split by $W_f = \sqrt{(\Delta - Q)^2 + 4T^2}$. The unrelaxed final state ($\Psi_k^{\underline{M}}$ and $\Psi_k^{\underline{L}}$) is defined by distributing the effect of Q to each of the CI-mixed wave functions based on the amount of $|d^n\rangle$ in the original ground state wave functions. The expected intensities of the PES transitions are shown on the far right. Without relaxation, a single peak is expected, corresponding with the energy of the $\Psi_k^{\underline{M}}$ state. Inclusion of relaxation redistributes the intensity over the $\Psi_f^{\underline{M}}$ and $\Psi_f^{\underline{L}}$ wave functions based on the sudden approximation.

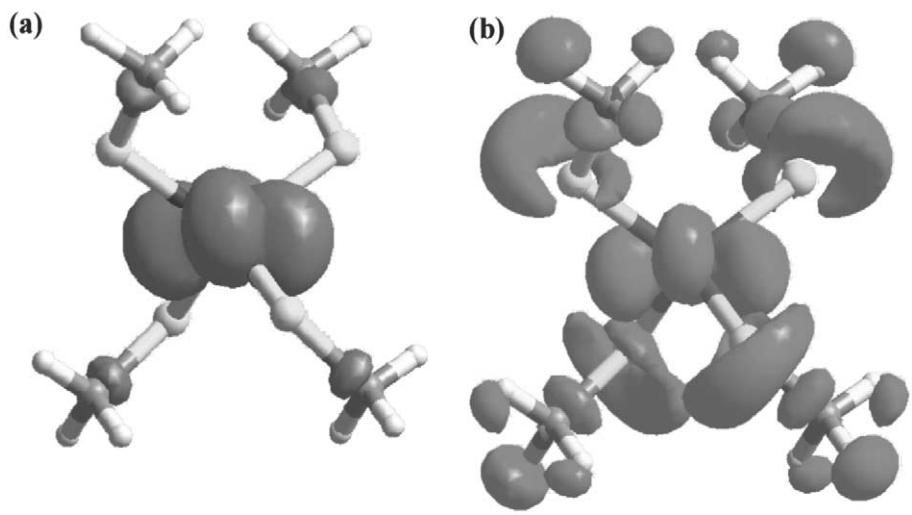

Figure 12 Redox densities for $[Fe(SCH_3)_4]^{2-,1-}$ (a) excluding and (b) including the effect of electronic relaxation.

relative to the tetrathiolate since the former exhibits more pronounced geometric changes upon redox.) The redox potentials of transition metal complexes are considered from the perspective of oxidation of the reduced (ferrous) species (not including solvent effects). Within this context, contributions can be divided into three intrinsic factors: (i) the effect of the LF on the RAMO, (ii) the energy of the $3d$ manifold given by the effective nuclear charge of the metal ion within the ligand environment, and (iii) the changes in the electronic and geometric structure on oxidation (i.e., electronic and geometric relaxation, where the latter corresponds to a reorganization energy).

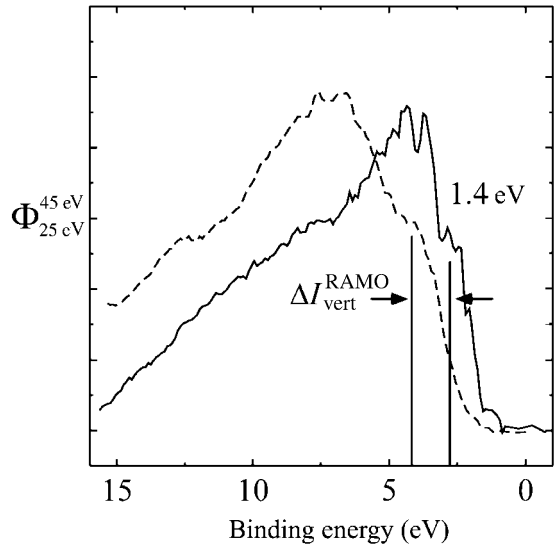

Figure 13 Valence ionization data for $[FeCl_4]^{2-}$ and $[Fe(SR)_4]^{2-}$ presented as $\Phi^{45\,eV}_{25\,eV}$ spectra (see Kennepohl and Solomon[10] for details). The spectra are referenced to the common tetraethyl ammonium counterion core ionization peaks.

The large difference in E^0 between the two redox couples is also observed as a large shift in the vertical ionization energies (I_{vert}) of the RAMO in each species, which indicate the tetrathiolate is ~1.4 eV easier to oxidize than the tetrachloride (see Figure 13). The experimental ΔI_{vert} demonstrates that there is a large difference in the *intrinsic* ionization potentials of the two species as contributions from the environment are not included.

LF effects are evaluated by comparison of the LF splitting diagrams for the ferrous species (Figure 8). In these diagrams, the RAMO corresponds the lowest energy 3*d* orbital. Direct comparison of the RAMO energy (relative to the baricenter of the 3*d* manifold) indicates that there is very little difference between the two systems; although $10Dq$ is greater for $[FeCl_4]^{2-}$, the axial splitting in $[Fe(SR)_4]^{2-}$ is larger and results in similar overall energies for the RAMO. From this, the LF effect is negligible and is not expected to play a significant role in defining the reduction potential of the redox couples.

The energy of the Fe 3*d* manifold is evaluated by theoretical correlation with experimental core binding energies. X-ray photoelectron spectroscopic (XPS) data for the Fe $2p_{3/2}$ core ionization allow us to determine the relaxation-correction core binding energy for each species (see Kennepohl and Solomon[10] for details). The Fe $2p_{3/2}$ binding energy for $[FeCl_4]^{2-}$ is nearly 1.4 eV greater than that for $[Fe(SR)_4]^{2-}$ indicating that the effective charge on the metal (Z^{Fe}_{eff}) is much greater in the tetrachloride. From this, we can estimate that the valence Fe 3*d* binding energies differ by ~1.2 eV (note that the core to valence shifts are ~0.9). Valence ionization is thus inherently easier for the tetrathiolate due to its lower Z^{Fe}_{eff}; this is a direct result of the greater covalency in the tetrathiolate complex relative to the tetrachloride. This effect clearly represents the dominant contribution to the 1.4 eV difference in I_{vert} between the two redox couples.

The effect of electronic relaxation is evaluated using the VBCI model discussed in Kennepohl and Solomon[10]. From this model, the energy stabilization due to electronic relaxation (E_{rlx}) can be calculated directly for either core or valence ionization (see Figure 11). In the valence region, it is found that $E_{rlx} \sim 0.4$ eV for $[FeCl_4]^{2-}$ and ~0.6 eV for $[Fe(SR)_4]^{2-}$. The influence of relaxation on the absolute ionization energies (and reduction potentials) is, therefore, very large, although the relative influence on ΔI_{vert} between the tetrathiolate and the tetrachloride is $\Delta E_{rlx} \sim 0.2$ eV.

Altogether, the greatest contribution to ΔI_{vert} between $[FeCl_4]^{2-,1-}$ and $[Fe(SR)_4]^{2-,1-}$ is the effective charge on the metal ion, which is much greater in the tetrachloride due to its lower metal–ligand covalency. Electronic relaxation also plays a significant role in ΔI_{vert}; the experimental data clearly demonstrate the overall importance of relaxation in ionization energies and reduction potentials. Lastly, LF splitting is negligible in these systems, even though LF effects are commonly regarded as influential in defining reduction potentials.

2.59.5.2 Reorganization Energies

The inner-sphere reorganization energy (λ_i) is determined by the intrinsic geometry change that occurs on redox; the metal–ligand bond distance change (Δr_{redox}) is usually the vibrational mode of greatest importance. From crystallographic data, $[FeCl_4]^{2-,1-}$ has a much larger geometric change on redox ($\Delta r_{redox} = 0.11$ Å) than $[Fe(SR)_4]^{2-,1-}$ ($\Delta r_{redox} = 0.05$ Å). This correlates with the experimental core Fe $2p_{3/2}$ binding energy shift between the reduced and oxidized species ($\Delta E^{redox}_{Fe\,2p_{3/2}}$), which is much larger for the tetrachloride (2.4 eV) than for the tetrathiolate (0.3 eV) indicating that Δq_{redox} is much larger in the former (see Kennepohl and Solomon[11] for details). This result is also observed in DFT results, which correlate well with the experimental results. The calculated Δq_{redox} for $[FeCl_4]^{2-,1-}$ is ~0.2 e^-, whereas that for $[Fe(SR)_4]^{2-,1-}$ is only 0.1 e^-. From this, it is concluded that Δr_{redox} (and by extension, λ_i) directly correlate with Δq_{redox} for a particular redox couple. This demonstrates that changes in the electrostatic attraction between the metal and the ligands dominate the changes observed in the bond distances on redox. Table 2 provides a breakdown of contributions to Δq_{redox}; the greater covalency of the tetrathiolate, as well as its greater electronic relaxation both contribute to its lower Δq_{redox} relative to the tetrachloride.

The origin of the small Δq_{redox} (and thus Δr_{redox}) for both species was investigated in detail by generating DFT-calculated potential energy surfaces for each of the species (Figure 14). Importantly, the Δr_{redox} calculated using the BP86 functional are in good agreement with those observed experimentally. (The calculated gas phase bond distances are larger than the experimental crystallographic bond distances, which is unsurprising due to the anionic nature of the complexes. The effect is less for the tetrathiolate since the negative is better distributed over the larger complex.) A potential energy surface is also generated for the unrelaxed oxidized species, thus allowing evaluation of the effect of electronic relaxation (see Fe^{III*} in Figure 14). Of great importance is that the Δr_{redox} without electronic relaxation are predicted to be 0.20 Å and 0.17 Å for $[FeCl_4]^{2-,1-}$ and $[Fe(SR)_4]^{2-,1-}$, respectively. The effect of electronic relaxation is, therefore, extremely important in both cases. The same effect is observed when λ_i is calculated from the surfaces; electronic relaxation decreases λ_i^{ese} from 1.7 eV to 0.8 eV for $[FeCl_4]^{2-,1-}$ and from 0.9 eV to 0.1 eV for $[Fe(SR)_4]^{2-,1-}$. (The calculated values for the inner-sphere reorganization energy are in good agreement with values obtained from the experimental structures (0.7 eV and 0.3 eV for the tetrachloride and the tetrathiolate, respectively.) Clearly, electronic relaxation has a dramatic effect on the inner-sphere reorganization energy in both redox couples, lowering λ_i^{ese} by almost 1 V in each case. For the tetrathiolate redox couple, the final effect is that both Δr_{redox} and λ_i^{ese} are inherently very small, allowing for facile ET.

2.59.5.3 Electronic Coupling Matrix Element

From Marcus-Hush theory, the electronic coupling matrix element (H_{DA}) is critically important in defining the rate of ET. For Rd, a structural model of the active site was constructed to include the surrounding protein fold and H-bonding interactions that directly influence the iron tetrathiolate active site in order to properly describe the electronic structure of the active site within the protein. (As shown previously, the electronic structure of these systems is highly dependent on the orientation of the thiolate.) From full DFT calculations on this structural model, the RAMO (Figure 15) is mostly Fe $3d_{z^2}$ in character (85%) with contributions from the S pseudo-σ and the SC_σ ligand orbitals. Note that the $3d_{x^2-y^2}$ RAMO obtained for the $[Fe(SCH_3)_4]^{2-,1-}$ model (and seen in Figure 12) differs from that calculated for Rd due to differences in the orientation of the αC in the thiolate ligands between the model and the protein active site. The $3d_{z^2}$ Rd RAMO is poorly oriented with respect to the protein surface such that direct overlap of the Fe $3d_{z^2}$ for electron self-exchange (ese) is not possible. Superexchange through to the cysteinate ligands is, therefore, required to allow for ese. The formalism developed by Newton (modified from McConnell) was used to determine H^0_{DA}, the matrix element for direct interaction of two Rd

Table 2 Charge decomposition of ionization process for $[FeCl_4]^{2-}$ and $[Fe(SR)_4]^{2-}$.[10,22]

Species	Δq_{ion}	Δq_{rlx}	Δq_{redox}
$[FeCl_4]^{2-,1-}$	+0.90	−0.70	+0.20
$[Fe(SR)_4]^{2-,1-}$	+0.85	−0.75	+0.10

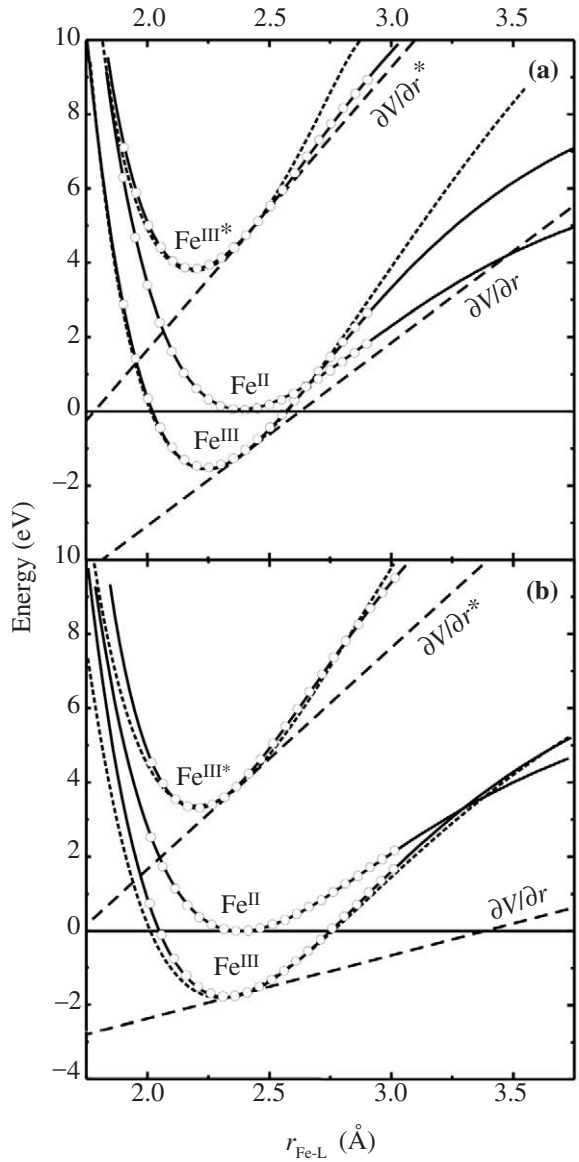

Figure 14 DFT-calculated potential energy surfaces for (a) $[FeCl_4]^{2-,1-}$ and (b) $[Fe(SCH_3)_4]^{2-,1-}$ for the reduced (Fe^{II}), unrelaxed oxidized (Fe^{III*}), and relaxed oxidized (Fe^{III}) sites. The solid lines are Morse potential fits to the calculated points at several Fe—L bond distances.

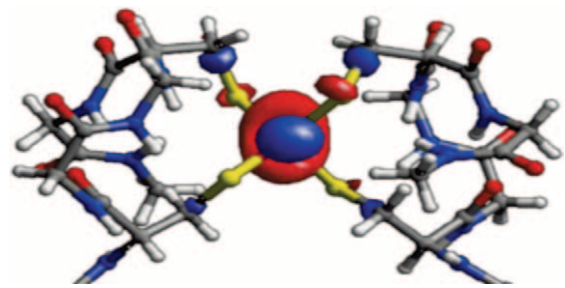

Figure 15 RAMO calculated for Rds from a truncated computational model from ADF using the VWN-BP86 functional.[11]

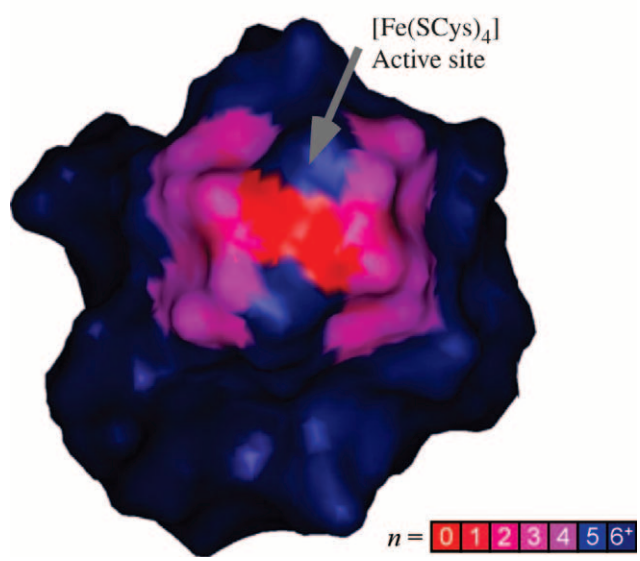

Figure 16 Surface electronic coupling map for Rds.[11]

active sites. H_{DA}^{0} is calculated to be $\sim$250 cm^{-1} assuming a purely one-electron process. Electronic relaxation on redox decreases H_{DA}^{0} to $\sim$200 cm^{-1}, indicating that relaxation is not as influential for H_{DA}^{0} as it is for λ_i^{ese} and E^0 (*vide supra*). This large coupling term results in an electron transmission that is $\sim$0.5, suggesting that direct S–S overlap of the thiolates of two Rd sites would result in near-adiabatic ese in Rd.

Application of the Beratan-Onuchic model for coupling over protein structures allows the creation of a surface map that indicates regions of the protein that have similar ese properties. The map is simplified such that each region (R_n) consists of areas on the surface that are n effective σ-bonds away from the active site, resulting in Figure 16. Regions R_0-R_3 correspond to the active site itself, as well as the β-methylenes on the two surface-exposed cysteinate ligands. Within these regions, electronic coupling for self-exchange is reasonable ($>10\,cm^{-1}$) but the overall surface area is small (<4%). Region R_4 ($H_{AD} \sim 4\,cm^{-1}$) is distinguished by a large surface area ($\sim$7%) and is dominated by solvent-exposed amide oxygens that are connected to the active site through H-bonds to the cysteinate sulfurs (O=C–NH$\cdots$S). Electron self-exchange between regions at five effective σ-bonds and beyond (R_{5+}) correspond to very small coupling ($<1\,cm^{-1}$) and should contribute little to the overall rate constant.

Using the Marcus-Hush equation for ET, and defining the overall rate as the integral over all possible $R_n \rightarrow R_m$ pathways (as defined above), a rate constant for ese of Rd is calculated at infinite ionic strength yielding $k_{exe}^{\infty} = 1.7 \times 10^6\ M^{-1}\ s^{-1}$, in fortuitous agreement with experimental results ($k_{exe}^{\infty} \sim 2 \times 10^6\ M^{-1}\ s^{-1}$). Of greater importance, however, is the relative effectiveness of the different pathways to the overall rate constant. As expected from the H_{DA} analysis above, regions R_0-R_4 (corresponding to $\sim$10% of the total surface area) are responsible for $\sim$90% of the rate constant. As a result, ET in Rd is highly localized to areas very near the active site and is limited to specific pathways shown in Figure 17: (A) through the β-methylenes of the surface-exposed cysteinate ligands and (B) through H-bonds to the surface-exposed (B_1) and buried (B_2) cysteinate sulfurs to the surface-exposed backbone amide oxygens.

2.59.6 SUMMARY

Our studies on the electronic structure of $[FeX_4]$ redox couples have led to important insights into the ET properties of such complexes, as well as those of Rds. These sites are dominated by changes in the electronic structure upon oxidation—termed electronic relaxation. This electronic relaxation has a dramatic effect on the ET thermodynamics (E^0) and the inner-sphere reorganization energy (λ_i^{ese}), which are essential to fast ET kinetics. The metal–ligand covalency of the sites is also critical in determining E^0, λ_i^{ese}, and H_{DA}. In Rd, ET is highly localized due to the small ligand

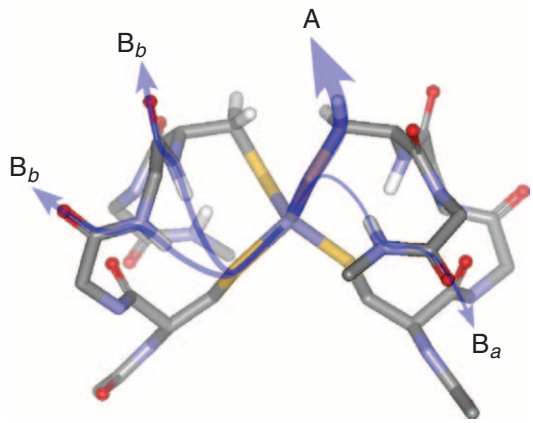

Figure 17 Dominant ET pathways calculated for the ese in Rds.[11]

contribution to the RAMO, thus limiting the range of electronic coupling through the protein matrix—although H-bonding to the active site extends it slightly. Detailed spectroscopic studies have provided significant insight into the electronic structure factors that affect the ET reactivity of redox-active iron sites of importance in biological systems.

ACKNOWLEDGMENTS

E.I.S. wishes to thank his past students and collaborators as indicated in the references cited herein for their outstanding contributions to this field. P.K. acknowledges NSERC (Canada) for graduate funding. This research is funded by NSF Grant CHE-9980549. Synchrotron data were obtained at the Stanford Synchrotron Radiation Laboratory (SSRL). SSRL is funded by the Department of Energy, Office of Basic Energy Sciences. The SSRL Biotechnology program is funded by the National Institutes of Health, National Center for Research Resources, Biomedical Technology Program, and the Department of Energy, Office of Biological and Environmental Research.

2.59.7 REFERENCES

1. Deaton, J. C.; Gebhard, M. S.; Koch, S. A.; Millar, M.; Solomon, E. I. *J. Am. Chem. Soc.* **1988**, *110*, 6241–6243.
2. Deaton, J. C.; Gebhard, M. S.; Solomon, E. I. *Inorg. Chem.* **1989**, *28*, 877–889.
3. Griffith, J. S. *The Theory of Transition-metal Ions*; Cambridge University Press, Cambridge, UK, 1964.
4. Neese, F.; Solomon, E. I. *Inorg. Chem.* **1998**, *37*, 6568.
5. Gebhard, M. S.; Deaton, J. C.; Koch, S. A.; Millar, M.; Solomon, E. I. *J. Am. Chem. Soc.* **1990**, *112*, 2217–2231.
6. Gebhard, M. S.; Koch, S. A.; Millar, M.; Devlin, F. J.; Stephens, P. J.; Solomon, E. I. *J. Am. Chem. Soc.* **1991**, *113*, 1640–1649.
7. Shadle, S. E.; Hedman, B.; Hodgson, K. O.; Solomon, E. I. *J. Am. Chem. Soc.* **1995**, *117*, 2259–2272.
8. Williams, K. R.; Hedman, B.; Hodgson, K. O.; Solomon, E. I. *Inorg. Chim. Acta* **1997**, *263*, 315–321.
9. Butcher, K. D.; Didziulis, S. V.; Briat, B.; Solomon, E. I. *J. Am. Chem. Soc.* **1990**, *112*, 2231–2242.
10. Kennepohl, P.; Solomon, E. I. *Inorg. Chem.* **2003**, *42*, 679–688.
11. Kennepohl, P.; Solomon, E. I. *Inorg. Chem.* **2003**, *42*, 689–695.
12. Robin, M. B.; Day, P. *Adv. Inorg. Chem. Radiochem.* **1967**, *10*, 247.
13. Te Velde, G.; Baerends, E. J. *J. Comput. Phys.* **1992**, *99*, 84–98.
14. Baerends, E. J.; Ellis, D. E.; Ros, P. *Chem. Phys.* **1973**, *2*, 41–51.
15. Guerra, C. F.; Snijders, J. G.; Te Velde, G.; Baerends, E. J. *Theor. Chem. Acc.* **1998**, *99*, 391–403.
16. Vosko, S. H.; Wilk, L.; Nusair, M. *Can. J. Phys.* **1980**, *58*, 1200–1211.
17. Becke, A. D. *Phys. Rev. A* **1988**, *38*, 3098–3100.
18. Perdew, J. P. *Phys. Rev. B* **1986**, *33*, 8822.
19. Perdew, J. P.; Burke, K.; Ernzerhof, M. *ACS Symp. Ser.* **1996**, *629*, 453–462.
20. Briat, B.; Canit, J. C. *Mol. Phys.* **1983**, *48*, 33–61.
21. Butcher, K. D.; Didziulis, S. V.; Briat, B.; Solomon, E. I. *Inorg. Chem.* **1990**, *29*, 1626–1637.
22. Kennepohl, P.; Solomon, E. I. *Inorg. Chem.* **2003**, *42*, 696–708.

Comprehensive Coordination Chemistry II
ISBN (set): 0-08-0437486

Volume 2, (ISBN 0-08-0443249); pp 691–708

2.60
Mixed Valence Dinuclear Species

J. T. HUPP
Northwestern University, Evanston IL, USA

2.60.1 INTRODUCTION 709
2.60.2 EARLY EXPERIMENTS: APPARENT EVIDENCE FOR VALENCE LOCALIZATION 711
2.60.3 EVIDENCE FOR VALENCE DELOCALIZATION 711
2.60.4 BORDERLINE BEHAVIOR 711
2.60.5 DELOCALIZATION MECHANISM 712
2.60.5.1 Theory 712
2.60.5.2 Experiment 714
2.60.6 DETAILED ELECTRONIC STRUCTURE 715
2.60.7 ANOTHER PERSPECTIVE 715
2.60.8 REFERENCES 716

2.60.1 INTRODUCTION

The Creutz–Taube ion, $(NH_3)_5Ru(\mu\text{-pyrazine})Ru(NH_3)_5^{5+}$, was one of the earliest intentionally prepared molecular mixed-valence complexes.[1,2] Initially formulated as Ru^{II}-bridge-Ru^{III}, it was intended by its designers to provide an example of the direct experimental assessment of the reorganization energy for an intramolecular electron transfer reaction—in this case:

$$Ru^{II}-bridge-Ru^{III} \longrightarrow Ru^{III}-bridge-Ru^{II} \quad (1)$$

Briefly, the idea was to use Hush's theory relating optical intervalence transfer (Equation (2)) to thermal electron transfer (Equation (1)).[3] As summarized in Figure 1 for a symmetrical system

$$Ru^{II}-bridge-Ru^{III} \xrightarrow{h\nu} Ru^{III}-bridge-Ru^{II} \quad (2)$$

an electronic absorption is expected at an optical energy equaling the total reorganization energy, and also equaling four times the activation free energy for nonadiabatic electron transfer. Hush had previously shown that the theory could be applied to mixed-valent mineral compounds, with optical intervalence transitions accounting in many cases for the colors of the minerals.[4] Before Creutz and Taube's report, however, the theory hadn't been applied to well-defined symmetrical molecular systems in solution environments.

As shown in Figure 2, the Creutz–Taube (CT) ion yields the intervalence absorption band promised by Hush theory.[1,2] Furthermore, the band appears at an energy that seems reasonable as an electron-transfer reorganization energy. In other respects, however, the observations are inconsistent with the Hush model. Most notably, the band is non-gaussian and is much narrower than expected from the model (which relates the width to the reorganization energy). Furthermore, it is relatively insensitive to solvent composition, with a residual sensitivity that differs from what is expected from solvent contributions to the reorganization energy. The observations were considered particularly striking in view of the closely related compound, $(NH_3)_5Ru(\mu\text{-}4,$

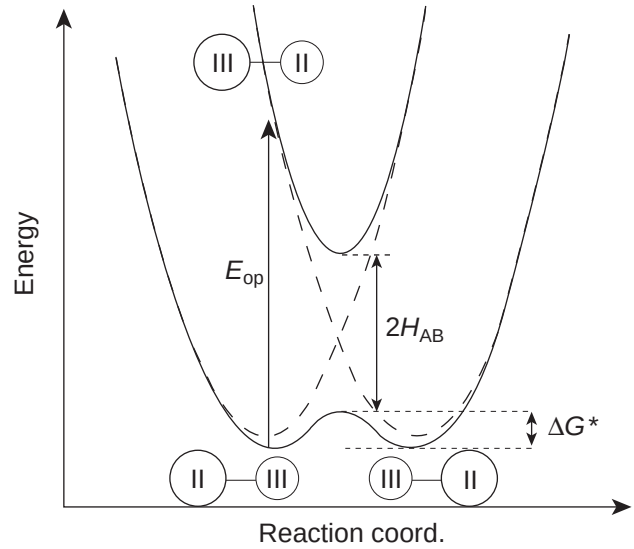

Figure 1 Hush diagram for intervalence transfer within a class II mixed-valence ion. The dotted lines correspond to diabatic potential energy surfaces. The solid lines are adiabatic potential energy surfaces. Electron transfer can occur either optically (vertical transition with energy, E_{op}, equaling λ) or thermally by moving along the lower adiabatic surface. In the diabatic limit, the barrier height for thermal electron transfer is $\lambda/4$.

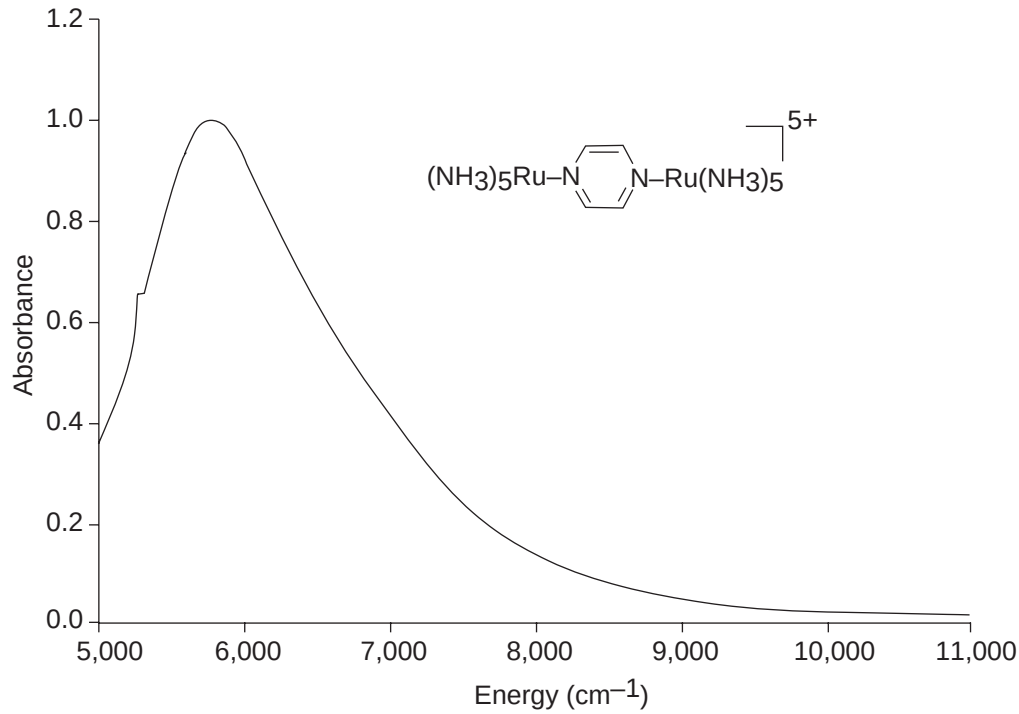

Figure 2 Electronic absorption spectrum of the Creutz–Taube ion in the intervalence region, in nitromethane as solvent.

4′-bipyridine)$Ru(NH_3)_5^{5+}$.[5] In contrast to the CT ion, this compound displays a broad gaussian intervalence band that varies in energy according to the optical and static dielectric properties of the solvent, as expected from Marcus–Hush theory.[3,6]

The disparate observations suggested an alternative formulation of the CT ion as a valence-delocalized compound, i.e., $Ru^{II1/2}$-bridge-$Ru^{II1/2}$, where the delocalization is an intrinsic electronic

property, not a dynamical timescale or hopping-rate related effect.[7] The question of localization versus delocalization turned out to be something of a challenge to answer. A large number of ingenious analyses were applied in the years following the initial report in 1969 of the ion's synthesis. Something of a consensus (in favor of delocalization) was finally reached around 1984.[8] At about the same time, theorists began to consider and debate competing ideas concerning the *mechanism* of delocalization.[9–12] Definitive experimental evidence in support of one of the mechanisms was finally obtained in 1994.[13]

2.60.2 EARLY EXPERIMENTS: APPARENT EVIDENCE FOR VALENCE LOCALIZATION

Several early experiments purporting to show valence localization were subsequently found to be artifactual (due to photo decomposition, contamination, and other problems). Others reported sound observations, but their interpretation proved to be more subtle than initially appreciated. For example, XPS measurements of the CT ion yielded two Ru peaks, seemingly indicating that atoms in two distinct oxidation states are present.[14] Hush and co-workers showed, however, that the high polarizability of the CT ion could lead to a splitting of the photoionized valence state of the delocalized complex and, therefore, two XPS peaks.[7,15]

2.60.3 EVIDENCE FOR VALENCE DELOCALIZATION

In 1984 six research groups pooled their expertise to study the CT ion.[8] Based on several experimental observations, including the following, they concluded that the ground-state complex exists in delocalized form: (i) X-ray crystallographic studies yielded identical metal–ligand bond lengths for the two metal centers. In contrast, $(NH_3)_5Ru^{II}$(pyrazine-$CH_3)^{3+}$ and $(NH_3)_5Ru^{III}$(pyrazine-$CH_3)^{4+}$ display Ru—N(pyrazine) bond lengths that differ by 0.13 Å.[16] (ii) ^{99}Ru Mössbauer measurements showed one quadrupole-split doublet peak, instead of the pair of peaks expected from a superposition Ru^{II} and Ru^{III} spectra. These results are consistent either with intrinsic delocalization or with detrapping (i.e., electron exchange within an intrinsically localized state, but on a time scale that is fast compared with the time scale sampled by the probe measurement). (iii) Polarized single-crystal ESR measurements that were not inconsistent with delocalization. (iv) Spectroelectrochemical measurements in the IR region showing a single NH_3 bend, rather than the pair expected from the simultaneous presence of Ru^{II} and Ru^{III} centers.[17] Similar observations have been reported by Beattie and co-workers for other regions of the IR spectrum.[7] Again, however, detrapping on the IR timescale could provide an alternative explanation. (Several examples of detrapping on the IR timescale have been reported by Meyer and co-workers,[18] as well as Kubiak and co-workers.[19]) More telling is the near absence of IR intensity for an asymmetric stretch of the pyrazine bridge. This band is readily observed in a valence-localized analog of the CT ion, $(bpy)_2ClRu(\mu$-pyrazine)$RuCl(bpy)_2^{3+}$.[20]

The conclusions of the six groups were reinforced in an interesting way by Curtis and co-workers who examined a series of CT-ion derivatives (*trans*-(ligand)$(NH_3)_4Ru(\mu$-pyrazine)$Ru(NH_3)_5^{5+}$ species) electrochemically.[21] They found that ligand-induced changes in formal potential at one ruthenium center induced a nearly identical shift in formal potential at the second ruthenium center where no change in coordination environment had been introduced. They concluded that electrons were added and removed from a fully delocalized orbital spanning both metal centers.

Electronic Stark effect studies by Oh and co-workers revealed that intervalence absorption by the CT ion is accompanied by essentially zero change in dipole moment and, therefore, zero metal-to-metal charge transfer.[22,23] The observations are consistent with a description of the complex as fully delocalized in both the ground state and intervalence excited state. At the same time, the researchers found that intervalence excitation of $(NH_3)_5Ru(\mu$-4,4′-bipyridine)$Ru(NH_3)_5^{5+}$ is accompanied by a large change in dipole moment and, therefore, substantial transfer of charge between metal centers, consistent with a valence-localized description.

2.60.4 BORDERLINE BEHAVIOR

In a conventional two-state electronic description, complete valence delocalization occurs when twice the electronic coupling energy (H_{ab}) exceeds the total trapping energy (i.e., the reorganization

energy plus any redox asymmetry). While the experiments described above indicate that the CT ion is fully valence delocalized, additional experiments suggest that the delocalization energy is only marginally greater than the trapping energy. The evidence comes chiefly from experiments in which the symmetry of the system is reduced, thereby increasing the trapping energy. For example, the *trans*-(ligand)$(NH_3)_4Ru(\mu$-pyrazine$)Ru(NH_3)_5^{5+}$ species studied by Curtis and co-workers display broader and more nearly gaussian intervalence absorption line shapes, implying less strong delocalization.[21] Furthermore, the breadth of the intervalence band scales essentially linearly with the magnitude of the introduced redox asymmetry—although in none of the cases examined by these authors does the width reach that expected from Hush's theory for a valence-localized assembly.[4]

A similar but more subtle perturbation has been described by Dong and co-workers.[24] Briefly, they observed that ammine-based hydrogen bonding effects could be exploited to achieve stepwise encapsulation of the two available $(NH_3)_5Ru$ sites with large crown ethers. When only one site is encapsulated, the intervalence absorption band is broadened and blue shifted, and acquires a more symmetrical shape. When both are encapsulated, the original line shape is largely restored. From electrochemical studies of monometallic analogs, the redox asymmetry introduced by encapsulating only one of the two available sites can be as large as ca. 0.3 eV. The corresponding spectral effects can be interpreted as manifestations of a polarization effect that, in the extreme, would correspond to valence localization, as shown schematically in Equation (3). Double encapsulation eliminates the redox asymmetry.

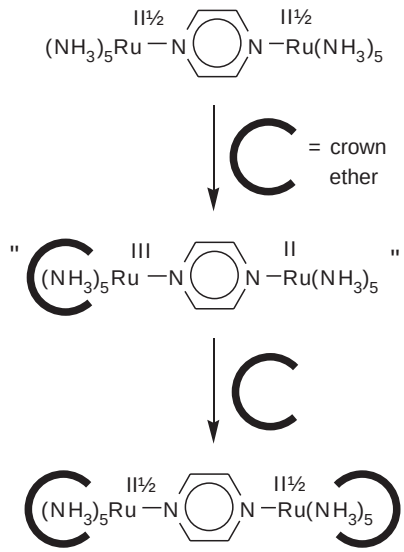

(3)

Resonance Raman spectroscopy studies show that both kinds of perturbations introduce substantial vibrational complexity; many more modes are coupled to the intervalence transition when the symmetry is reduced and the system is pushed in the direction of valence localization.[25]

2.60.5 DELOCALIZATION MECHANISM

2.60.5.1 Theory

According to Marcus–Hush theory[3,4,6] and similar two-state treatments, valence delocalization within symmetrical mixed-valence systems occurs when $2H_{ab}$ exceeds the reorganization energy, λ. Notably, the role played by the bridging ligand is to facilitate orbital mixing and initial-state/final-state coupling in an indirect or super-exchange sense, i.e., by providing virtual intermediate states featuring ligand-localized electrons or holes.[26] In the super-exchange treatment, the lower lying the virtual state, the greater the magnitude of the electronic coupling. For pyrazine-bridged ruthenium complexes, π^* virtual states (electron transfer) are expected to be more important than

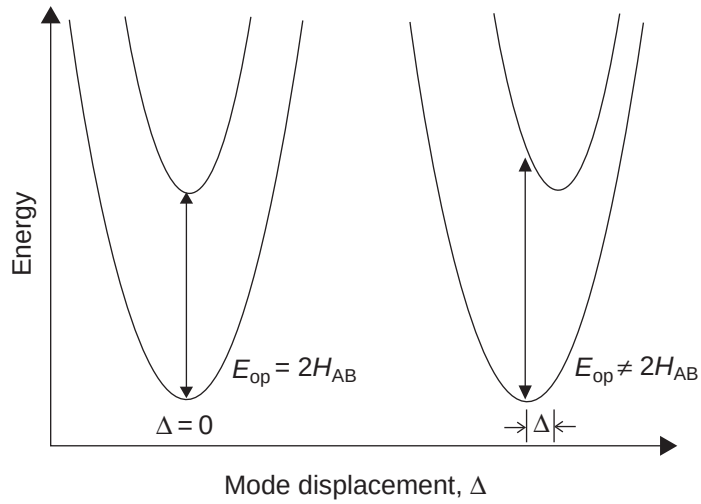

Figure 3 Potential energy surfaces for class III mixed-valence ions according to the two-state (left-hand side) and three-state (right-hand side) descriptions. In the two-state case, but not the three-state case, the energy of the delocalized "intervalence" transition equals $2H_{ab}$. Only in the three-state case are nonzero normal-mode displacements (Δ) encountered.

π virtual states (hole transfer), reflecting the closer energetic proximity of the former to the $d\pi$(Ru) donor and acceptor orbitals.

Piepho, Krausz, and Schatz (PKS) developed a two-state model that recognizes that, in the strong coupling limit, vibrational and electronic excitation may not be entirely separable processes.[9]

In two-state treatments (including Marcus–Hush–Mulliken and PKS), when H_{ab} is great enough to induce delocalization, the familiar isoenergetic initial and final electronic states (left- and right-hand diabatic states in Figure 1) are replaced with single-welled lower and upper states (nominal one-electron bonding and antibonding states). The energy difference between the states at the well minima is $2H_{ab}$. More generally, the energy difference equals $(\lambda(\Delta q)^2 + 4H_{ab}{}^2)^{1/2}$, where Δq is the amount of charge transferred upon intervalence excitation (zero in the case of a symmetrical class III system).[27] As shown in Figure 3 (left-hand panel), for a two-state delocalized system no mode displacement occurs upon intervalence excitation. Under these conditions, the only source of breadth for the absorption band, beyond inhomogeneous broadening, is a change in normal-mode frequency or force constant, manifest in the figure as a different degree of curvature for the upper versus lower surface. Importantly, the modes defining these surfaces are exclusively non-totally symmetric modes. From symmetry considerations, totally symmetric modes can't couple to an intervalence transition in a two-state description.

Two-state models—and the PKS model in particular—do a reasonable job of describing the intervalence absorption spectrum of the CT ion, but fail to capture the spectrum's solvent dependence. A model that does better, as described below, is a three-site/three-state model developed by Ondrechen and co-workers.[10,11] Briefly, rather than viewing bridging ligand orbitals as electronic participants only in a virtual or super-exchange sense, the model incorporates them explicitly in a real sense. In its simplest form, the model combines a $d\pi_{xz}$ orbital from each ruthenium atom (z defines the metal–bridge–metal axis) with a pyrazine π^* orbital to create three new orbitals that are formally bonding, nonbonding, and antibonding with respect to the ligand and two metal centers; see Figure 4. Of the three electrons available from the parent Ru orbitals, two occupy the bonding orbital and one half-occupies the nonbonding orbital. The intervalence transition corresponds to promotion of an electron from the three-center (metal–ligand–metal) bonding orbital to the two-center (metal–metal) nonbonding orbital. Thus, the transition has significant ligand-to-metal charge transfer (LMCT) character. Because the charge is symmetrically redistributed to both metal centers, however, there is no change in dipole moment—consistent with Stark measurements. Instead, the ion experiences a change in quadrupole moment.

Further work by Piepho (computational studies) indicates that in addition to a pyrazine π^* orbital, pyrazine π orbitals also likely participate[12]—a point also emphasized by Chou and Creutz.[28] In contrast to two-state models, both the Piepho and Ondrechen models permit

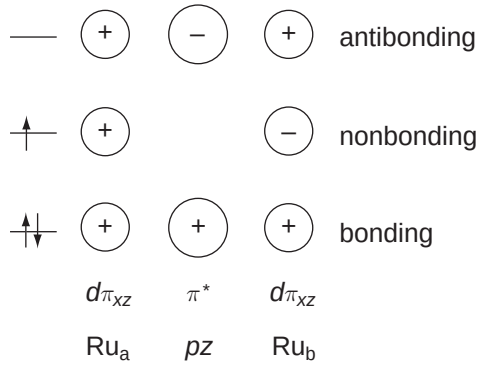

Figure 4 Qualitative three-state orbital diagram for the Creutz–Taube ion. The combination of two $d\pi_{xz}$(Ru) orbitals and one π^*(pyrazine) orbital yields three-center bonding and antibonding molecular orbitals, and a two-center nonbonding orbital. In this model, the intervalence transition at ca. 5,800 cm^{-1} corresponds to promotion of an electron from the bonding orbital to the nonbonding orbital.

coupling of totally symmetric vibrational modes to the intervalence transition, but preclude coupling of non-totally symmetric modes. As shown schematically in Figure 3 (right-hand panel), intervalence excitation, in the context of a three-site/three-state model, entails displacement of normal modes.

2.60.5.2 Experiment

Among the experimental observations seemingly favoring a three-site/three-state delocalization mechanism over a two-site mechanism is the solvent dependence of the intervalence band energy. The two-state model predicts a dependence upon solvent dielectric properties if the system is localized, but no variation with solvent if the system is delocalized. Instead the energy is invariant and is equal to $2H_{ab}$. In contrast, experimental measurements show that the band energy is very weakly solvent dependent. Furthermore, the residual solvent dependence does not correlate with dielectric properties. Instead, a correlation exists with the potential for the $CT^{5+/4+}$ redox couple. Ammine complexes typically exhibit strongly solvent-dependent redox potentials. The origin of the solvent dependence is in hydrogen bonding between ammine protons and solvent molecules, where changing the oxidation state of the metal center substantially affects the H-bonding capability of the ammines.

What about the three-state model? As Creutz and Chou have pointed out, here the salient feature is the energy gap between the $d\pi$(Ru) and π^*(pyrazine) orbitals used to generate the three-center bonding and two-center nonbonding orbitals of the delocalized mixed-valence ion.[28] By taking advantage of ammine-ligand/solvent H-bonding interactions, they were able to show in a series of electrochemical experiments that solvent variations could alter the energy of the $d\pi$(Ru) orbital while leaving the pyrazine π^* orbital energy largely unperturbed. Strongly Lewis basic solvents (strong hydrogen-bond acceptors) were found to provide the greatest degree of $d\pi$(Ru) orbital energy lowering. Accompanying the electrochemical effects are red shifts in the intervalence spectrum. Creutz and Chou concluded that the direction of the shift is consistent with a three-site delocalization mechanism involving a π^* orbital of the bridging ligand. Briefly, both the bonding and nonbonding molecular orbitals should be lowered in energy by ammine/solvent H-bonding. The effect should be greater, however, for the purely metal-derived nonbonding molecular orbital, than for the three-center (metal–bridge–metal) molecular orbital.

Similar effects have been observed based on double crown-ether encapsulation of the CT ion and a symmetrically substituted derivative, and similar conclusions have been reached concerning the applicability of a three-site delocalization mechanism.[29] In both the solvent and crown-encapsulation studies, however, the intervalence energy shifts are only about half as large as expected based on a simple $d\pi$(Ru)$-\pi^*$(pyrazine)$-d\pi$(Ru) delocalization scheme. The additional involvement of pyrazine π orbitals could account for the smaller than expected environmental effects.

Raman scattering spectra, recorded in resonance with the intervalence transition, have been reported.[13,30] They reveal strong coupling of the transition to a totally symmetric vibration of the bridge, ν_{6a}; see below. This rules out a two-state delocalization scheme, but is consistent with a

three-state scheme entailing light-induced transfer of charge symmetrically from the bridge to both metal centers. Additionally, the measurements show that only one Ru–N(pyrazine) vibration, a symmetrical Ru–pyrazine–Ru stretch (Equation (4)), is coupled to the transition.[30] Given the oxidation-state sensitivity of the metal-ligand vibrations, two would be expected if the ion existed in valence-localized form.

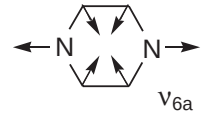

(4)

2.60.6 DETAILED ELECTRONIC STRUCTURE

In addition to the intense intervalence band found at ca. 5,800 cm^{-1}, the CT ion displays weaker electronic absorption bands at 2,200 cm^{-1} and possibly 3,500 cm^{-1}.[31] (Like the high-energy band, the band at 2,200 cm^{-1} is narrow: the full-width at half-height is ~1,400 cm^{-1}.) The existence of one or two low-energy electronic bands points to the involvement of $d\pi_{xy}$(Ru) and $d\pi_{yz}$(Ru) orbitals; see Figure 5. In contrast to $d\pi_{xz}$ orbitals, these are essentially unmixed and largely orthogonal to the bridging ligand's π and π^* orbitals. They can be viewed, therefore, as nonbonding orbitals that are localized on a single metal atom. Given this description, the low-energy intervalence transitions correspond to d–d transitions of an unusual kind: An electron is promoted from a localized $d\pi_{xy}$ or $d\pi_{yz}$ orbital to a delocalized $d\pi_{xz}$-derived orbital.[12] Thus, there is a net change in dipole moment and net (partial) metal-to-metal charge transfer; in the intervalence excited state, the hole created in the $d\pi_{xy}$ or $d\pi_{yz}$ orbital is confined to a single metal center. Because localized $d\pi_{xy}$ and $d\pi_{yz}$ orbitals exist on both metal centers, the low-energy intervalence transitions are doubly degenerate.

That the transitions are observed at all is likely a consequence of spin–orbit coupling and the resulting slight relaxation of orthogonality between the filled and half-filled $d\pi$(Ru) orbitals. Indeed, when replacing ruthenium with osmium, having a much larger spin–orbit coupling coefficient, an extremely rich near- and mid-infrared absorption spectrum is observed, featuring several intense electronic transitions.[32]

2.60.7 ANOTHER PERSPECTIVE

Another view is that the CT ion exists in valence-localized form in the ground state but may be delocalized in one or more of the intervalence excited states. The available Stark data would appear to be incompatible with the proposed localized ground state to delocalized intervalence excited state transition, since the transition would require partial charge transfer and a significant

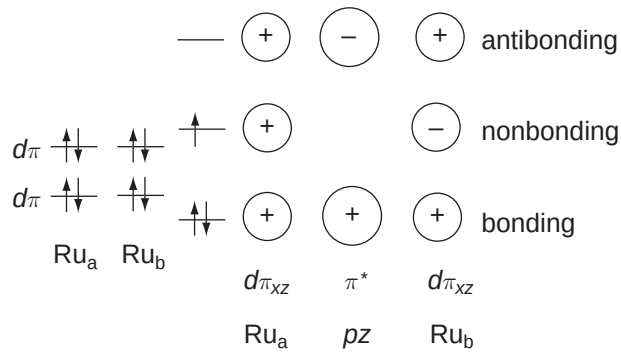

Figure 5 Qualitative orbital diagram for the Creutz–Taube ion with inclusion of localized $d\pi$ orbitals (two per metal center) The two low-energy intervalence transitions are ascribed to forbidden transitions involving promotion of an electron from a $d\pi_{xy}$ or $d\pi_{yz}$ orbital, confined to a single Ru, to the delocalized two-center nonbonding orbital.

ground-state/excited-state dipole moment difference. Demadis *et al*. have outlined how spin–orbit coupling, together with ligand-field asymmetry, could give rise to three intervalence bands, given a valence-localized ground state. Overlapping bands are identified at ~4,500, 6,300, and 7,300 cm^{-1}. The weak bands found at ~2,200 and ~3,500 cm^{-1} are assigned as Ru^{III}-localized $d-d$ transitions. The Demadis *et al*. description also accounts for the borderline behavior noted above. For example, residual IR intensity for an asymmetric pyrazine stretch can be explained by assuming weak localization. In the delocalized description, the residual intensity reflects environmental polarization of the ground electronic state (for example, by ion pairing), but the polarization is assumed to be too little to create a barrier on the ground potential energy surface. A summary description of the "orthodox" view would be that the CT ion is delocalized—but just barely, while a summary description of the alternative view would be that the CT is localized—but just barely.[18]

2.60.8 REFERENCES

1. Creutz, C.; Taube, H. *J. Am. Chem. Soc.* **1969**, *91*, 3988–3989.
2. Creutz, C.; Taube, H. *J. Am. Chem. Soc.* **1973**, *95*, 1086–1094.
3. Hush, N. S. *Trans. Faraday Soc.* **1961**, *57*, 557.
4. Hush, N. S. *Prog. Inorg. Chem.* **1967**, *8*, 391.
5. Tom, G. M.; Creutz, C.; Taube, H. *J. Am. Chem. Soc.* **1074**, *96*, 7827–7829.
6. Marcus, R. A. *J. Chem. Phys.* **1965**, *43*, 679.
7. Beattie, J. K.; Hush, N. S.; Taylor, P. R. *Inorg. Chem.* **1976**, *15*, 992–993.
8. Furholz, U.; Burgi, H. B.; Wagner, F. E.; Stebler, A.; Ammeter, J. H.; Krausz, E.; Clark, R. F. H.; Stead, M. J.; Ludi, A. *J. Am. Chem. Soc.* **1984**, *106*, 121–1239.
9. Piepho, S. B.; Krausz, E. R.; Schatz, P. N. *J. Am. Chem. Soc.* **1978**, *100*, 2996–3005.
10. Ondrechen, M. J.; Ellis, D. E.; Ratner, M. A. *Chem. Phys. Lett.* **1984**, *109*, 50–55.
11. Ondrechan, M. J.; Ko, J.; Zhang, L. T. *J. Am. Chem. Soc.* **1987**, *109,* 1666–1671, 1672–1676.
12. Piepho, S. B. *J. Am. Chem. Soc.* **1990**, *112*, 4197–4206.
13. Petrov, V.; Hupp, J. T.; Mottley, C. S.; Mann, L. C. *J. Am. Chem. Soc.* **1994**, *116*, 2171–2172.
14. Citrin, P. H. *J. Am. Chem. Soc.* **1973**, *95*, 6472–6473.
15. Hush, N. S. *Chem. Phys.* **1975**, *10*, 361–366.
16. Wishart, J.; Bino, A.; Taube, H. *Inorg. Chem.* **1986**, *25*, 3318–3222.
17. Best, S. P.; Clark, R. J. H.; McQueen, R. C. S.; Joss, S. *J. Am. Chem. Soc.* **1989**, *111*, 548–550.
18. Demadis, K. D.; Hartshorn, C. M.; Meyer, T. J. *Chem. Rev.* **2001**, *101*, 2655–2685, and references therein.
19. Ito, T.; Yamaguchi, T.; Kubiak, C. P. *Macromol. Symp.* **2000**, *156*, 269–275, and references therein.
20. Callahan, R. W.; Meyer, T. J. *Chem. Phys. Lett.* **1976**, *39*, 82–84.
21. Delarosa, R.; Chang, P. J.; Salaymeh, F.; Curtis, J. C. *Inorg. Chem.* **1985**, *24*, 4229–4231.
22. Oh, D. H.; Boxer, S. G. *J. Am. Chem. Soc.* **1990**, *112*, 8161–8162.
23. Oh, D. H.; Sano, M.; Boxer, S. *J. Am. Chem. Soc.* **1991**, *113*, 6880–6890.
24. Dong, Y. H.; Hupp, J. T.; Yoon, D. I. *J. Am. Chem. Soc.* **1993**, *115*, 4379–4380.
25. Petrov, V.; Williams, R. D.; Hupp, J. T. *Proceedings Of The XVth International Conference Of Raman Spectroscopy*, Asher, S. A., Stein, P., Eds.; John Wiley and Sons, New York, 1996; pp 768–771.
26. See, for example: Richardson, D. E.; Taube, H. *J. Am. Chem. Soc.* **1983**, *105*, 40–51.
27. Brunschwig, B. S.; Sutin, N. *Coord. Chem. Rev.* **1999**, *187*, 233–254.
28. Creutz, C.; Chou, M. H. *Inorg. Chem.* **1987**, *26*, 2995–3000.
29. Hupp, J. T.; Dong, Y. H. *Inorg. Chem.* **1994**, *33*, 4421–4424.
30. Lu, H.; Petrov, V.; Hupp, J. T. *Chem. Phys. Lett.* **1995**, *235*, 521–527.
31. Krausz, E. R.; Mau, A. W. H. *Inorg. Chem.* **1986**, *25*, 1484–1488.
32. Magnuson, R. H.; Lay, P. A.; Taube, H. *J. Am. Chem. Soc.* **1983**, *105*, 2507–2509.

Comprehensive Coordination Chemistry II
ISBN (set): 0-08-0437486
Volume 2, (ISBN 0-08-0443249); pp 709–716

2.61
Mixed Valence Clusters

B. K. BREEDLOVE, T. YAMAGUCHI, and T. ITO
Tohoku University, Sendai, Japan
and
C. H. LONDERGAN and C. P. KUBIAK
University of California, San Diego, CA, USA

2.61.1 INTRODUCTION 717
2.61.2 SYNTHESIS OF DIMERS OF TRIRUTHENIUM CLUSTERS 718
2.61.3 ELECTROCHEMISTRY 718
2.61.4 ELECTRONIC SPECTRA OF THE −1 MIXED VALENCE STATES 721
2.61.5 INFRARED SPECTROELECTROCHEMISTRY 722
2.61.5.1 Design of Spectroelectrochemical Cell 722
2.61.5.1.1 ν(CO) Band coalescence in the −1 mixed valence state 723
2.61.5.1.2 Evaluation of electron transfer rates from spectral lineshape analysis 725
2.61.6 SOLVENT DYNAMICS 727
2.61.7 CONCLUSIONS 729
2.61.8 REFERENCES 729

2.61.1 INTRODUCTION

Single-electron transfers are the simplest chemical reactions and are fundamentally important in biology (photosynthesis and respiration) and technology (photography, electrophotography, and solar energy conversion). Coordination chemistry has played a key role in developing and refining our understanding of electron transfer. The synthesis of model systems has advanced the understanding of the electronic structures and reactivity of the active sites of metalloproteins.[1] Sensitization of nanocrystalline TiO_2 electrodes with ruthenium and osmium polypyridyl complexes provides a basis for efficient solar energy conversion in regenerative photoelectrochemical cells.[2] Mixed valence complexes like the Creutz-Taube ion[3,4] have provided much of the experimental data essential to the advancement of modern theories of electron transfer.[5–8] This case study reports a conjoined effort between programs in synthetic coordination chemistry and infrared spectroelectrochemistry on mixed valence clusters.[9–11] The synthetic studies have produced a series of bridged triruthenium clusters of the type $[\{Ru_3(\mu_3\text{-}O)(CH_3COO)_6(CO)(L)\}_2(\mu\text{-BL})]$ (where L (ligand) = 1-azabicyclo-[2.2.2]octane (abco), dimethylaminopyridine (dmap), pyridine (py), cyanopyridine (cpy), etc.; BL (μ bridging ligand) = pyrazine (pz), bipyridine (bpy), 1,4-diazabicyclo[2,2,2]octane (dabco), etc.). The synthetic adjustment of the ancillary pyridyl and bridging ligands affords an unusual degree of control of the electrochemical and spectroscopic properties of these coordination clusters. Infrared spectroelectrochemical studies involving the mixed valence states between bridged cluster cores have led to the observation of dynamical effects due to rapid intramolecular electron transfer on infrared vibrational lineshape. This chapter traces the development of infrared spectroelectrochemistry (IRSEC) as a new tool for the study of rapid intramolecular electron transfer within mixed valence clusters. This study

shows how the coordinated interplay between synthesis and spectroscopy was used to improve our understanding of the scope and limitations of IRSEC methods for determining rate constants of intramolecular electron transfer reactions. As well, we show how the IRSEC method provides a steady state spectral probe for the observation of solvent dynamical control of electron transfer rates in mixed valence complexes.

2.61.2 SYNTHESIS OF DIMERS OF TRIRUTHENIUM CLUSTERS

The first μ_3-oxo ruthenium trimers were synthesized by Wilkinson and Spencer.[12,13] A strategy proposed by Balzani and co-workers,[14] "complex as metal, complex as ligand," was used to synthesize several different Ru_3 dimer complexes with the general formula $[\{Ru_3(\mu_3\text{-O})(CH_3COO)_6(CO)(L)\}_2(\mu\text{-BL})]$ (L = abco, dmap, cpy, etc.; BL = pz, bpy, dabco, etc.). As a synthetic precursor, $[Ru_3(\mu_3\text{-O})(CH_3COO)_6(CO)(L)(S)]$ (S (solvent molecule) = H_2O or ethanol) is quite versatile because it has a labile solvent molecule and can be synthesized with essentially any L.[15] In the strategy of Balzani and co-workers, this cluster behaves as the "complex" with a labile solvent ligand. When the labile solvent molecule S is substituted with a desired bridging ligand coordinated in an η^1-fashion, that cluster can be used as the "ligand". By combining the "complex" and "ligand" clusters, the cluster dimers, $[\{Ru_3(\mu_3\text{-O})(CH_3COO)_6(CO)(L)\}_2(\mu\text{-BL})]$, are produced.

The bridging ligands and terminal ligands employed in these studies are summarized in Figure 1. While bridging ligands such as dabco have been used in these studies, pyrazine and bipyridine have been used the most extensively for studying the mixed valence states of the cluster dimers. It is possible to synthesize cluster dimers with diisocyanide bridging ligands, but there are complications in their infrared spectra due to Fermi resonances.[16]

2.61.3 ELECTROCHEMISTRY

Table 1 summarizes the electrochemical data for the cluster dimers in this study. All of the dimers show three or four reversible redox processes, which are characterized by half-wave potentials for the different redox processes, $E_{1/2}$(ox/red). Apparent two-electron oxidation waves are observed for all of the complexes at approximately $E_{1/2}(+2/0) = +0.50$ and $E_{1/2}(+4/+2) = +1.3$ V vs. sodium saturated calomel electrode, correspond formally to $Ru_3^{III,III,II}$—BL—$Ru_3^{III,III,II}$/$Ru_3^{III,III,III}$—BL—$Ru_3^{III,III,III}$ and $Ru_3^{III,III,III}$–BL—$Ru_3^{III,III,III}$/$Ru_3^{III,III,IV}$—BL—$Ru_3^{III,III,IV}$. Each of the complexes with an aromatic bridging ligand, BL, displays two single electron reduction waves that correspond formally to $Ru_3^{III,III,II}$—BL—$Ru_3^{III,III,II}$/$Ru_3^{III,III,II}$–BL—$Ru_3^{III,II,II}$ (0/–1) and then $Ru_3^{III,III,II}$–BL—$Ru_3^{III,II,II}$/$Ru_3^{III,II,II}$–BL—$Ru_3^{III,II,II}$ (–1/–2). Toma and co-workers[17] reported that as the pK_a of the terminal ligand increases, the reductive $E_{1/2}$ values of a series Ru_3 monomers, $[Ru_3(\mu_3\text{-O})(CH_3COO)_6(L)_3]^{n+}$, shift toward more negative potentials. In the case of the Ru_3 dimers, the shifts in the average potential between $E_{1/2}$(0/–1) and $E_{1/2}$(–1/–2) toward more negative potentials follow a similar trend: abco (pK_a = 11.15) > dmap (pK_a = 9.71) > py (pK_a = 5.17) > cpy (pK_a = 1.7).

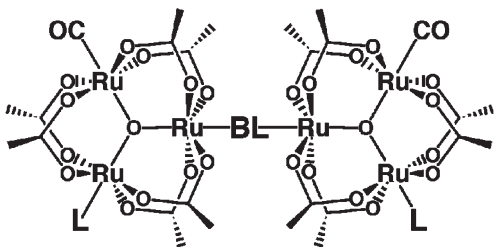

BL \ L	(abco)	(dmap)	(py)	(cpy)
(pz)	(1a)	(1b)	(1c)	(1d)
(bpy)	—	(2b)	(2c)	(2d)
(dap)	—	(3b)	—	—
(dabco)	—	(4b)	(4c)	(4d)

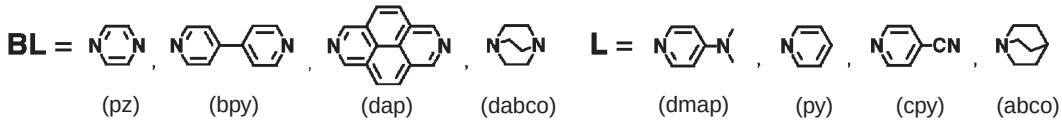

Figure 1 Structure of $[\{Ru_3(\mu_3\text{-O})(\mu\text{-}CH_3CO_2)_6(CO)(L)\}_2(\mu\text{-BL})]$ and numbering of the compounds.

Table 1 Electrochemical data for $[\{Ru_3(\mu_3\text{-}O)(\mu\text{-}CH_3CO_2)_6(CO)(L)\}_2(\mu\text{-}BL)]$.

Structure	$E_{1/2}(0/-1)$[a] (V)	$E_{1/2}(-1/-2)$[a] (V)	ΔE(mV)	K_c
(1a)	−0.89	1.33	440	2.7×10^7
(1b)	−0.81	1.19	380	2.7×10^6
(1c)	−0.68	0.93	250	1.7×10^4
(1d)	−0.84	1.31	470	9.2×10^7
(2b)	−1.11	1.23	120	1.1×10^2
(2c)	−1.03	1.11	80	2.3×10^1
(2d)	−0.91(2e)		~0	<10
(3b)	−1.08	1.20	120	1.1×10^2
(4b)	−1.25	1.31	60	3×10^1
(4c)	−1.12	1.17	50	7×10^0
(4d)	−0.94(2e)		~0	<10

[a] Cyclic voltammograms recorded in 0.1 M tetra-n-butylammonium hexafluorophosphate in dichloromethane, V versus saturated sodium chloride calomel electrode (SSCE).

More importantly, however, the splitting, ΔE, between the $(0/-1)$ and $(-1/-2)$ processes of (**1a**)–(**2d**) increases strongly with the pK_a of the ancillary ligand, as shown in Figure 2. The thermodynamic stability of the $Ru_3^{III,III,II}$—BL—$Ru_3^{III,II,II}$ oxidation state is reflected by the thermodynamic comproportionation constant, K_c. Thus, as the adjustable pyridyl ligand in the series (**1a**)–(**1d**) is changed from abco (**1a**) to dmap (**1b**), to an unsubstituted pyridine (**1c**) and then to an electron withdrawing cpy (**1d**), the values of ΔE and K_c decrease considerably. The

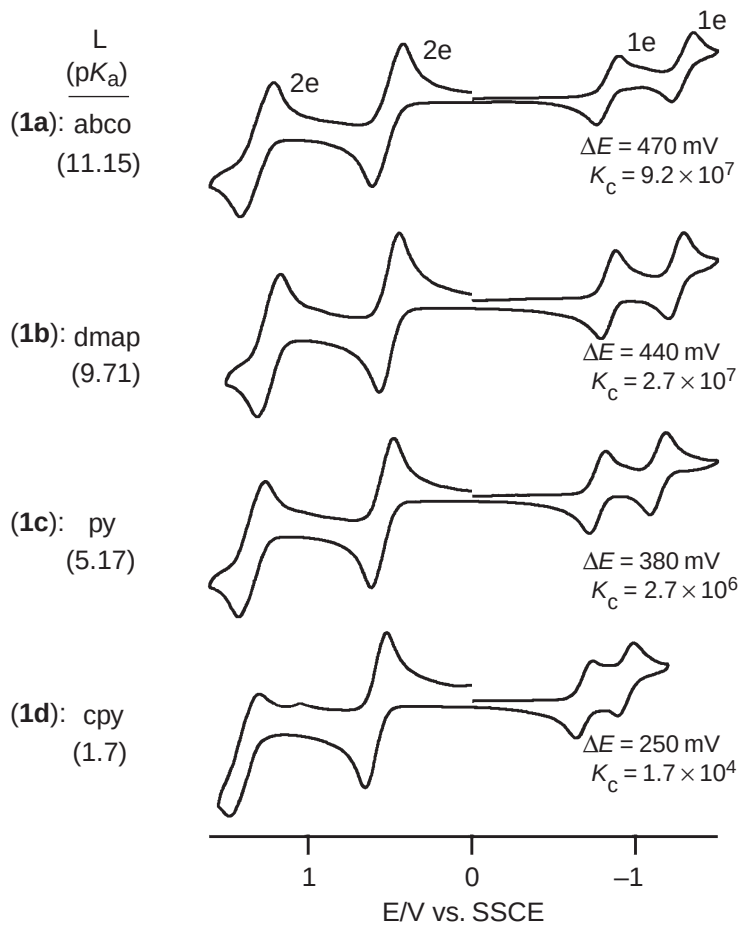

Figure 2 Cyclic voltammograms, ΔE, and K_c of $[\{Ru_3(\mu_3\text{-}O)(\mu\text{-}CH_3CO_2)_6(CO)(L)\}_2(\mu\text{-pz})]$ (L = abco (**1a**), dmap (**1b**), py (**1c**), cpy (**1d**)).

same trend is observed for the cluster dimers bridged by bpy (Table 1). Meyer and co-workers[18] reported analogous redox wave splitting for the noncarbonyl dimer $[\{Ru_3(\mu_3\text{-}O)(CH_3COO)_6(py)_2\}_2(\mu\text{-pz})]^{n+}$: ΔE = ca. 100 mV between the (+2/+1) and (+1/0) processes; ΔE = 270 mV between the (0/−1) and (−1/−2) processes. The carbonyl cluster dimers considered here have much larger ΔE values between the (0/−1) and (−1/−2) CV waves but no observable splitting between the (+2/+1) and (+1/0) waves.

The bridging ligand π-electron system mediates electronic coupling between the two Ru_3 centers, Figure 3 and the overlap between the Ru_3 cluster $d\pi$-electron system and the bridging ligand π^* system appears to be very favorable. A complex relationship exists between ΔE and electronic coupling (H_{AB}), but it is generally accepted that in symmetric mixed valence complexes, ΔE is roughly proportional to the coupling.[19] Although the trend in cyclic voltammetry data for compounds (**2b**–**d**) with bpy as the bridging ligand (Figure 3) is similar to that for compounds (**1b**–**d**) (Table 1), the values of K_c for (**2b**–**d**) are many orders of magnitude less than the values for the pz bridged complexes, (**1b**–**d**).

In general, electronic coupling falls off exponentially with increasing distance between electronically interacting centers as long as a similar medium between the centers remains.[20] The center to center separation between Ru_3O units in the crystal structure of (**1a**) is 10.9 Å,[11] and it is estimated at ca. 15.3 Å in bpy bridged dimers ((**2**) in Figure 1). The longer separation between Ru_3 centers in (**2b**–**d**) decreases the intercluster electronic coupling, thereby decreasing ΔE values. When a bridging ligand that has no π-electron system, dabco (**4**), is used, no splitting in the reduction waves is observed ($\Delta E \sim 0$). The cluster-to-cluster distance in (**1b**) is similar to that of (**4b**), but the electronic coupling between clusters has been completely extinguished in (**4b**) due to the nonconjugated nature of the bridge. In addition to the distance effect on electronic coupling

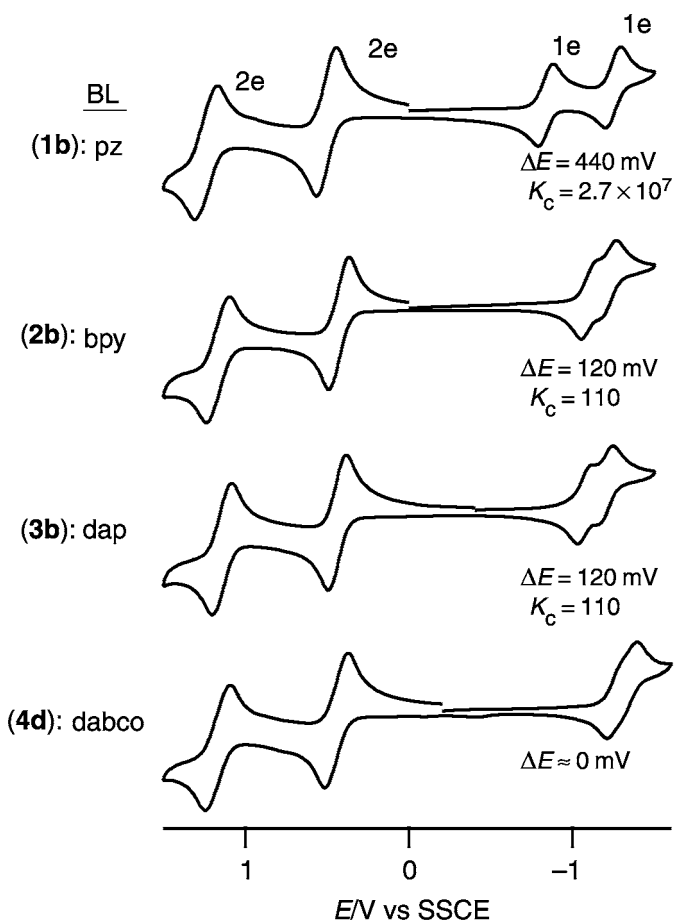

Figure 3 Cyclic voltammograms, ΔE, and K_c of $[\{Ru_3(\mu_3\text{-}O)(\mu\text{-}CH_3CO_2)_6(CO)(dmap)\}_2(\mu\text{-BL})]$ (BL = pz (**1b**), bpy (**2b**), dap (**3b**), dabco (**4b**)).

seen above, the π-conjugated or unconjugated nature of the bridging ligand is of great importance in these clusters.

Remote ligand control of electronic coupling in mixed valence complexes is not unusual.[21–23] However, to our knowledge the wide variation seen in (**1**)–(**2**) has not been reported previously in a single system. In the present case, it appears that two conditions are simultaneously met:

(i) very favorable overlap between the Ru_3 cluster $d\pi$-electron system and the bridging pz or bpy π^* system, and
(ii) the ability to raise or lower Ru_3 cluster $d\pi$-electron levels engaging the pz or bpy π^* system by changing the pK_a of the ancillary pyridyl ligand.

The relevant Ru d level then is closer to the pz π^* level in (**1a**$^-$) than it is in (**1d**$^-$); and closer to the bpy π^* level in (**2b**$^-$) than it is in (**2d**$^-$). Experimental evidence supports these descriptions of the metal–ligand electronic structure. The necessity of a conjugated bridge to enable electronic coupling between clusters is evident in the complete lack of coupling in (**4b**), (**4c**), and (**4d**). The control of the cluster $d\pi$ levels by the ancillary pyridyl ligand is shown by the fact that the average of the reduction potentials $E_{1/2}(0/-1)$ and $E_{1/2}(-1/-2)$ becomes more positive in the series from (**1b**) to (**1d**) and from (**2b**) to (**2d**) (Table 1). The favorable—yet tunable—interaction of the clusters with the bridging ligand π^* level is evident in that the metal to ligand charge transfer (MLCT) electronic absorption bands for the Ru-*d* to pz π^* transition appear at increasing energies in the series (**1a–d**) (481 nm in (**1a**), 482 nm in (**1b**), 475 nm (overlapped) in (**1c**), and 450 nm (overlapped) in (**1d**)).

2.61.4 ELECTRONIC SPECTRA OF THE −1 MIXED VALENCE STATES

In order to assess further the extent of electronic interaction between the two coupled Ru_3 units in the −1 mixed valence states, intervalence charge transfer (IVCT) spectra have been analyzed, and the results for the IT band shape analysis are summarized in Table 2. On going from (**1a**) to (**1d**), that is from more to less strongly interacting systems, the IVCT band positions shift from higher to lower energy. Concomitantly, the band intensities decrease and the bands broaden significantly as reflected in the band half-widths ($\Delta\tilde{\nu}_{1/2}$). This broadening is consistent with theoretical predictions for IVCT bandshape in strongly coupled systems.[8] These band shape analyses are undertaken with the understanding that there has been much discussion of the problems confronting Hush analysis of IVCT bands in the strongly coupled limit.[24,25]

The electronic coupling H_{AB}, derived from the optical spectra of the singly reduced (−1) charge transfer states, is given by Equation (1).[8]

$$H_{AB} = 2.05 \times 10^{-2} (\tilde{\nu}_{1/2} \nu_{max} \varepsilon_{max} \Delta\tilde{\nu}_{1/2})^{1/2} / r \quad (1)$$

Optical estimates of H_{AB} in these systems[10] range by nearly a factor of two from 2,490 cm^{-1} (**1a**$^-$) to 1,310 cm^{-1} (**1d**$^-$). In the Robin–Day classification of intervalence charge transfer complexes,[26] (**1d**$^-$) can be considered to be a largely charge localized Class II complex, based on $\Delta\tilde{\nu}_{1/2}$. According to a Hush analysis of intervalence charge transfer bands,[8] the expected half widths of the intervalence charge transfer (IVCT) bands are $\Delta\tilde{\nu}_{1/2}$(calc.) = 5,370 cm^{-1} for (**1a**$^-$), 5,290 cm^{-1} for (**1b**$^-$), 5,220 cm^{-1} for **1c**$^-$, and 4,990 cm^{-1} for (**1d**$^-$). Comparison of these values with the experimentally observed data in Table 2 indicates that (**1a**$^-$)–(**1c**$^-$) go beyond Robin–Day criteria[26] for Class II behavior and approach Class III (delocalized), whereas (**1d**$^-$) conforms

Table 2 Summary of electronic spectral data for the ICT bands of the mixed valence (−1) state of (**1a–d**).[a]

Structure	$\tilde{\nu}_{max}$ (cm^{-1})	ε_{max} (M^{-1} cm^{-1})	$\Delta\tilde{\nu}_{1/2}$ (cm^{-1})	H_{AB} (cm^{-1})
(1a)	12,300	14,400	4,100	2,490
(1b)	12,100	12,200	3,760	2,180
(1c)	11,800	10,700	3,930	2,060
(1d)	10,800	6,610	5,220	1,310

[a] Data at −10 °C.

more strictly to Hush Class II-type behavior. Hush analysis is thus not quite adequate for compounds (**1a**$^-$)–(**1c**$^-$), and they appear to be at the threshold of Class III.

We have been unable to observe the IVCT bands for (**2b**$^-$)–(**2d**$^-$) due to the experimental difficulties of working within small ΔE windows and the broad, weak bands expected in the less strongly coupled systems.

2.61.5 INFRARED SPECTROELECTROCHEMISTRY

A variety of spectroscopic techniques including Raman, luminescence, NMR, EPR, mass spectrometry, and circular dichroism, have been used to monitor the nature and redox behavior of electrogenerated or adsorbed species.[27] The simplicity and richness of the structural information obtained from infrared spectroelectrochemistry have contributed to its widespread use. Because the pz bridged dimers have relatively stable −1 mixed valence states and contain a good spectroscopic chromophore, i.e., CO, the nature and rate of charge transfer have been investigated further by infrared spectroelectrochemistry.

2.61.5.1 Design of Spectroelectrochemical Cell

The cell design[28,29] used in these studies is a modification of a cell reported by Mann and co-workers.[30,31] A disassembled view of the cell is shown in Figure 4(a) and a side view of the cell head is shown in Figure 4(b). The temperature of the cell is controlled by circulating high viscosity oil through the hollow brass heat exchanger that surrounds the three-electrode cell area. The electrode geometry is illustrated in Figure 4(c). Polished Pt or Au foil, 4.5 mm in diameter is soldered on a brass post and serves as the working electrode. A circular 0.5 mm Ag wire, 0.5 mm outside the perimeter of the working electrode, serves as a pseudo-reference electrode. The circular electrode geometry with the reference and counter electrodes configured concentrically around and near the working electrode is favored because it minimizes iR drop across the working electrode, inherent to thin layer electrochemical cells. By ensuring that the working electrode to counter electrode distance is the same everywhere in the cell, one can also achieve uniform current densities and potentials on the working electrode surface.

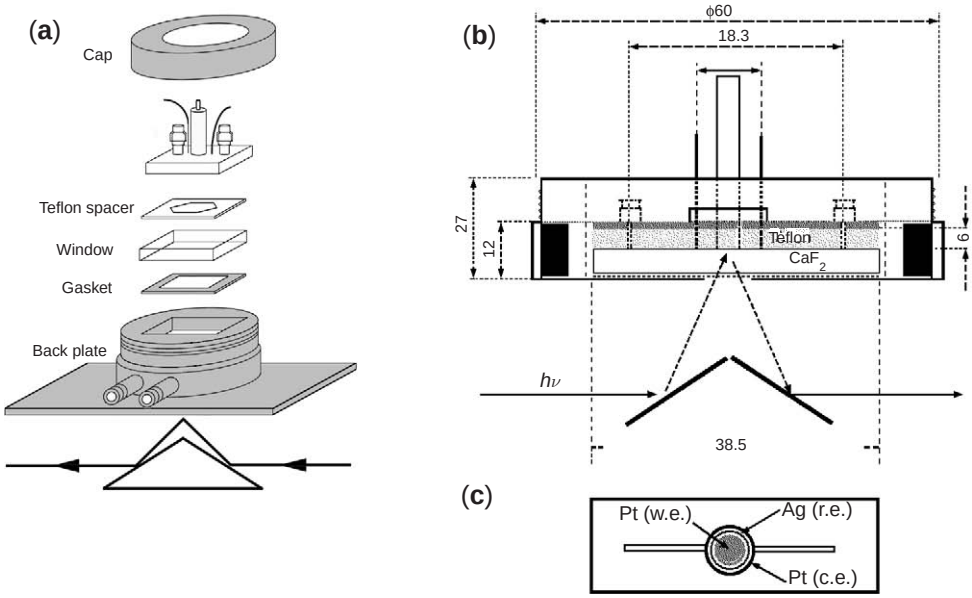

Figure 4 Spectroelectrochemistry (SEC) cell: (a) Dissassembled view of the cell; (b) Side view of the electrode head; (c) Electrode configuration (w.e. = working electrode, c.e. = counter electrode, r.e. = reference electrode).

2.61.5.1.1 ν(CO) Band coalescence in the −1 mixed valence state

The vibrational spectra of the complexes (**1a–d**), (**2b–d**) have been measured using reflectance IR spectroelectrochemistry (IRSEC). The IR spectra of (**1a–d**) in the neutral, −1 mixed valence, and −2 states are shown in Figure 5. From these spectra, it is clear that electronic coupling has a direct effect on the IR lineshape. In the isolated (0) state, (**1a**) (L = abco) exhibits a single ν(CO) band at 1,938 cm^{-1} (Figure 5(top)). The normal modes associated with C—O stretching of the carbon monoxide ligands on each $Ru_3^{III,III,II}$ unit have identical frequencies due to their identical local environments and large spatial separation. The doubly reduced species also gives rise to a single ν(CO) band, but at 1,890 cm^{-1} reflecting identical redox states at each $Ru_3^{III,II,II}$ cluster. Complexes (**1b–d**) also show only one ν(CO) band in the neutral state and −2 state. In view of these results, it is reasonable to expect that the −1 state of (**1a**) would show two ν(CO) bands, one characteristic of a $Ru_3^{III,III,II}$ environment and the other characteristic of $Ru_3^{III,II,II}$. However for the −1 mixed valence state of (**1a**), two ν(CO) bands are not observed. Rather, a broad absorption band centered at the average energy of the bands observed for the isolated (0) and doubly reduced (−2) states of (**1a**) is seen (Figure 5(top)). The degree of "coalescence" of the ν(CO) IR spectral bands depends on the degree of electronic coupling between the pyrazine-linked Ru_3 clusters (Figure 5), as H_{AB} decreases from 2,490 cm^{-1} (optical value) for (**1a**$^-$) to 1,310 cm^{-1} for (**1d**$^-$). Cluster (**1b**$^-$), with a slightly lower value (H_{AB} = 2,180 cm^{-1}) than (**1a**$^-$), shows a similar, but slightly broader, lineshape. Two distinct ν(CO) bands at 1,931 cm^{-1} and 1,904 cm^{-1} become partially resolved for (**1d**$^-$) with the smallest H_{AB} of the pz bridged dimers. Cluster (**1c**$^-$) with an intermediate value H_{AB} value of 2,060 cm^{-1} shows an intermediate degree of spectral "coalescence".

The bpy bridged compounds, (**2b–d**), also show only one sharp ν(CO) band in the IR in the neutral and −2 states. Figure 6 shows a comparison of the IR spectra of pz bridged (**1b**) and bpy bridged (**2b**) in the 0, −1 and −2 states. It is clear that the IR spectra of the neutral and −2 states of the dimers (**1b–d**) and (**2b–d**) are similar, but in the −1 mixed valence state, the spectra are very different. The spectrum of (**2b**$^-$) has two well-resolved and well-separated ν(CO) bands, perturbed only slightly relative to the spectra of the neutral and −2 states. Compound (**2c**$^-$) shows a similar spectrum to that of (**2b**$^-$).[10] Careful analysis of the spectrum for (**2b**$^-$) suggests that a small amount of broadening may be occurring. A spectrum of the −1 state of (**2d**) could not be obtained due to a <50 mV separation between the (0/−1) and (−1/−2) CV waves. In clusters (**2b–d**), the electronic coupling is small as observed in the cyclic voltammetry (*vide supra*), and overall, the singly reduced state of each can be viewed as a valence trapped or localized compound and classified as Class II (weakly coupled) in the Robin–Day scheme.[26]

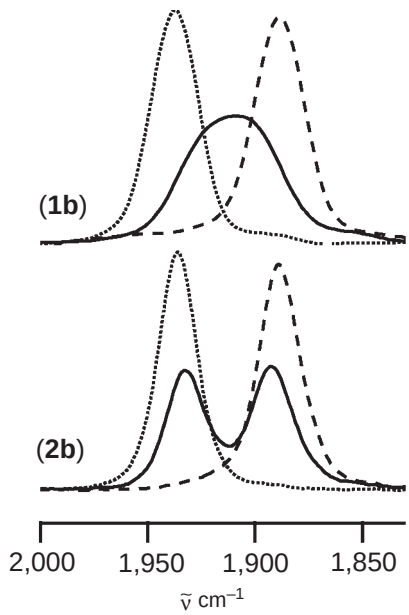

Figure 5 IR spectra in the ν(CO) region for $[\{Ru_3(\mu_3\text{-}O)(\mu\text{-}CH_3CO_2)_6(CO)(dmap)\}_2(\mu\text{-}BL)]^n$ (n = 0 (. . .), −1 (——), −2 (- - -)) for BL = pz (**1b**), bpy (**2b**).

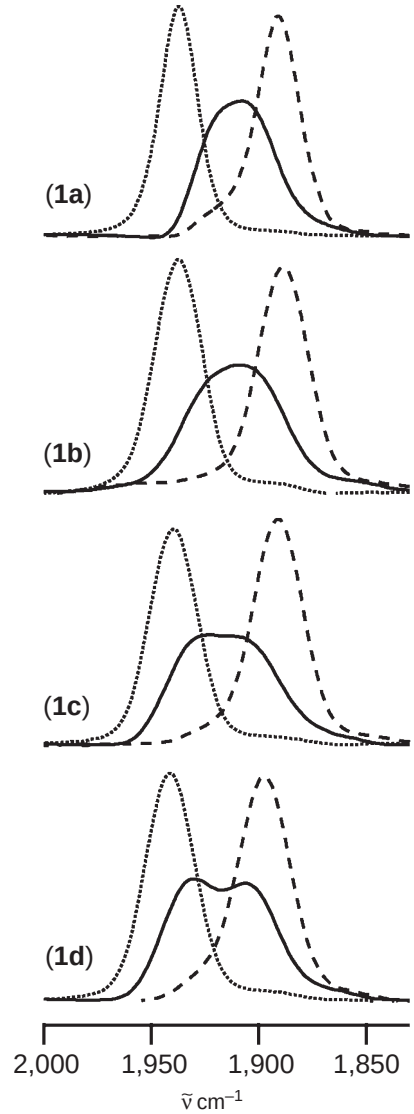

Figure 6 IR spectra in the ν(CO) region for $[\{Ru_3(\mu_3\text{-}O)(\mu\text{-}CH_3CO_2)_6(CO)(L)\}_2(\mu\text{-pz})]^n$ ($n = 0$ (. . .), -1 (——), -2 (- - -)) for L = abco (**1a**), dmap (**1b**), py (**1c**), cpy (**1d**).

The main point of comparison of the ν(CO) IR spectral region for the -1 mixed valence state of the pz bridged cluster, (**1b**), and the bpy bridged cluster, (**2b**), is to show the differences in IR spectral characteristics that arise from electronic interactions. The mixed valence states of (**1a**–**d**) show clear evidence of the strong electronic coupling seen also in the cyclic voltammogram and optical spectra. The longer bpy bridge in (**2b**–**d**) attenuates the electronic coupling such that the mixed valence state in (**2d**) is no longer defined. In simpler terms, the strongly interacting Ru_3 centers in the -1 states of (**1a**–**d**) have extensively "mixed" IR spectral features, which are quite different from the neutral and -2 state spectra. The weakly coupled systems (**2b**) and (**2c**) show essentially independent ν(CO) IR spectral features in the -1 state, quite similar to those observed in the neutral and -2 states. It is striking that the "mixing" of the IR spectral lineshape of the ν(CO) bands is directly related to the electronic coupling.

A fundamental question is whether the observed phenomenon of IR spectral coalescence arises from dynamics (as it does in NMR), or from differing degrees of static delocalization. It is conceivable, for example, that the coalesced IR spectra of the -1 states of (**1a**–**d**) (Figure 5) result not from dynamic exchange, but from a static delocalized electronic structure, or from an electronic structure that places most of the charge on the pz ring, such that the two CO ligands are equivalent. However, the experimental evidence, mentioned previously, suggests that this is not the case. When the mixed valence center separation is increased, as it is when the longer bpy ligand is used, almost no coalescence occurs.

As well, it was shown before that the amount of coupling, or coalescence, is controlled by the pK_a of the terminal ligand implying that the charge is on the cluster units.

2.61.5.1.2 *Evaluation of electron transfer rates from spectral lineshape analysis*

In NMR spectroscopy, a dynamic process occurring on the millisecond time scale can produce spectral broadening and coalescence. In order to observe any line broadening in the IR spectrum due to a dynamic process, the process must occur on a time scale shorter than 10 picoseconds (rate constant of $10^{11}\,s^{-1}$). Bloch equation type line shape analysis was used by both Grevels and Turner to study the IR band broadening in $Fe(CO)_3$(NBD) (NBD = norbornadiene).[32–34] Cannon and co-workers[35] estimated the rate of electron transfer in the mixed valence $[Fe^{III}{}_2Fe^{II}O(OOCMe)_6(py)_3]$ complex from $\nu_{as}(Fe_3O)$. The work by Cannon and co-workers is the only study to relate IR lineshape broadening to fast electron transfer. In our studies, a Bloch type analysis developed by McClung and co-workers[33] has been used to estimate rates of electron transfer. Figure 7 shows the simulated spectral lineshapes as a function of the electron transfer rate constant (k_e) and a comparison to the observed spectra of (**1a**$^-$)–(**1d**$^-$). The rates of electron transfer estimated by this type of simulation for (**1a**$^-$), (**1b**$^-$), (**1c**$^-$), and (**1d**$^-$) are $10 \pm 3 \times 10^{11}$, $9 \pm 3 \times 10^{11}$, $5 \pm 3 \times 10^{11}$, and $\sim 1 \times 10^{11}\,s^{-1}$, respectively. For (**1a**$^-$) and (**1b**$^-$) using this rate constant, the activation energy for electron transfer (ΔG^*) is estimated to be $350\,cm^{-1}$. This compares with the $\sim 12{,}100\,cm^{-1}$ reorganizational energy (ν_{max}, Table 2) between the ground state and excited state potential energy surfaces (Figure 8) and suggests that (**1a**$^-$) indeed can approach intra-well exchange behavior with a two potential well ground state potential energy surface characterized by a "bump" of less than $2kT$ between the respective wells. The spectral lineshape simulation for (**1d**$^-$) (Figure 7) gives $k_e = \sim 1 \times 10^{11}\,s^{-1}$, which is clearly less than the rate constants estimated for (**1a**$^-$)–(**1c**$^-$). Spectra simulated as a function of k_e for (**1d**$^-$) also show that k_e is very close to the lower limit that can be determined reliably by this approach. For example, Figure 7 also shows that at $k_e = 10^{11}\,s^{-1}$, two distinct spectral features are completely resolved, and this would be considered "slow exchange" on the IR time scale.

Are the rate constants estimated from the Bloch type treatment consistent with expectations based on theory? The −1 mixed valence state of complex (**1d**) is a Robin–Day class II complex, and thus its electron transfer rate constant can be independently estimated from Marcus theory. The semiclassical expression for the rate constant for intramolecular electron transfer, k_e, in a symmetric mixed valence complex with no net free energy change is given by

$$k_e = \kappa \nu_n \exp[-(\Delta G_\lambda * - H_{AB} + H_{AB}{}^2/4\Delta G_\lambda *)/RT] \quad (2)$$

where κ is the adiabaticity factor (unity for adiabatic reactions), ν_n is the nuclear frequency factor which can include both the solvent dielectric response frequency and bond length/bond angle reorganizations required by charge transfer between the localized valence states, $\Delta G_\lambda{}^*$ is the

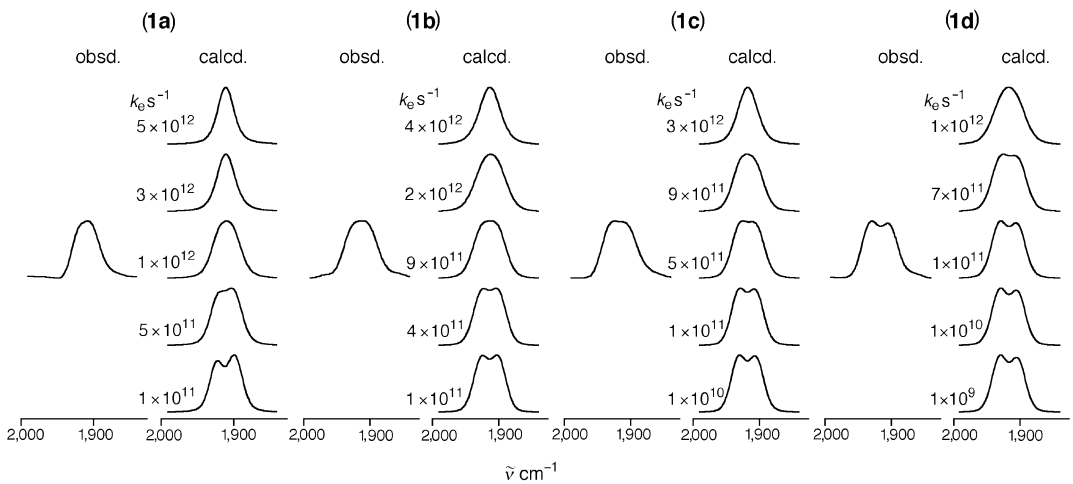

Figure 7 Comparison of observed to simulated infrared spectra in the ν(CO) region for (**1a**$^-$)–(**1d**$^-$) as a function of the intramolecular electron transfer rate constant, k_e.

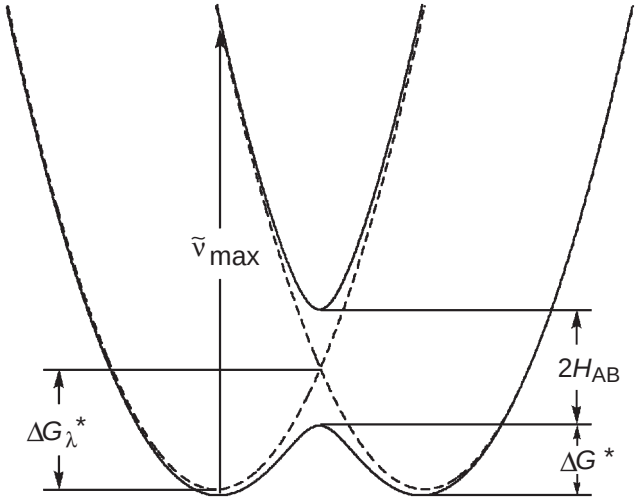

Figure 8 Potential energy diagram for a class II mixed valence complex.

reorganizational energy barrier, and H_{AB} is the electronic coupling between the metal centers.[36] By making certain assumptions (κ) = 1, $\nu_n = 5 \times 10^{12}\,s^{-1}$, $\Delta G_\lambda^* = \tilde{\nu}_{max}/4$), an exchange rate constant of $k_e = 1 \times 10^9\,s^{-1}$ at 263 K for (**1d**$^-$) is estimated using Equation (2) and data from the IVCT spectrum (Table 2). This is smaller by two orders of magnitude than the rate constant estimated from the IR lineshape simulation. We believe that the rate constants estimated by IR band shape analysis are more reliable than those estimates based on IVCT band analysis. The underestimation of k_e based on the IVCT band data and Equations (1) and (2) may arise from two factors:

(i) The value of r used in Equation (1) for the calculation of H_{AB} for (**1d**$^-$) might be significantly shorter than assumed (10.02 Å).[10] A shorter r value would give a larger H_{AB} and hence a larger k_e.
(ii) The electronic structure of (**1d**$^-$) may lie beyond the region where Equation (2) is applicable. An independent means of distinguishing electronically localized vs. delocalized systems is based on the IR spectra of the bridging pyrazine modes.

It has been often argued that in a mixed valence state of a pyrazine bridged dimer the appearance of a symmetric ν(pz) band at 1,580–1,590 cm^{-1} provides evidence for valence localization (class II), while a fully delocalized class III system does not show the ν_{symm}(pz) band.[37–40] In the present case, it was not possible to discuss the degree of delocalization based on the intensity of the ν_{symm}(pz) band, because the acetate ligand $\nu(COO)_{asym}$ bands obscure the ν_{symm}(pz) band. Meyer and co-workers pointed out the difficulty in the discrimination between localization and delocalization from the presence or the absence of ν_{symm}(pz).[24,39]

One way to view the possible physical limits on the exchange rate constants is to consider the slowest motions that render the two CO oscillators equivalent. In the –1 mixed valence state, the symmetric charge transfer complexes could be viewed as having two different ground state equilibrium C—O bond distances in the localized limit, resulting from π-backbonding effects of different cluster redox states. In the delocalized limit, there is one equilibrium C—O bond distance for both CO ligands, and one ν(CO) band. As the C—O bond distances adjust to charge transfer from one side of the mixed valence complex to the other, it is clear that the fastest time that the adjustments can be made is on the order of a few periods of vibration of the relevant mode. For the ν(CO) modes this would correspond to a rate constant of $5 \times 10^{13}\,s^{-1}$. However, the electron transfer rate will be determined by the slowest modes on the reaction coordinate,[7] and here it is likely that the frequencies which come into play would be in the 100–500 cm^{-1} range, corresponding to rates on the order of $1 \times 10^{13}\,s^{-1}$. The maximum rate constants to be expected from this simple argument are about an order of magnitude higher than those estimated from the Bloch type analysis of the IR lineshapes for the pz bridged dimers (**1a**$^-$)–(**1d**$^-$) but the lineshape simulations show that while coalescence appears to be occurring for (**1a**$^-$) and (**1b**$^-$) and nearly occurring for (**1c**$^-$) and (**1d**$^-$), these systems are by no means in a fast exchange regime. Thus, the Bloch type analysis does predict rate constants that at least are consistent with other simple physical considerations.

In contrast to ($\mathbf{1a}^-$)–($\mathbf{1d}^-$), it is difficult to determine the intramolecular electron transfer rates of ($\mathbf{2b}^-$) and ($\mathbf{2c}^-$) as they are below the lower limits of evaluation for this method. However, it is useful to consider the idea of "exchange intensity" introduced by Turner and co-workers[34] for such a system. "Exchange intensity" is a buildup of intensity in the middle of two exchanging spectral components in excess of what is expected for the simple superposition of two bands; this is a normal consequence of dynamic exchange processes when Bloch equations apply. The IR spectra of ($\mathbf{2b}^-$) and ($\mathbf{2c}^-$), in which the cluster units are weakly coupled, show relatively little intensity between the high and low energy features. Nonetheless, the rates of intramolecular electron transfer in the bpy bridged systems, ($\mathbf{2b}^-$) and ($\mathbf{2c}^-$) are expected to be rapid, although they are clearly not rapid enough to be observed in vibrational spectra. A comparison of the IR spectrum of ($\mathbf{2b}^-$), which is expected to be the fastest of the bpy bridged systems, with simulated spectra using rate constants, k_e in the range from $1 \times 10^2\,s^{-1}$ to $5 \times 10^{11}\,s^{-1}$,[10] shows that ($\mathbf{2b}^-$) could have a k_e of the order of $1 \times 10^{10}\,s^{-1}$ and still have a basically non-overlapped IR spectrum. As well, it shows that the IR method may become less reliable for $k_e < 10^{11}\,s^{-1}$.

2.61.6 SOLVENT DYNAMICS

The IR spectra of the complexes (**1b**–**d**) in their –1 mixed valence states in different organic solvents show that the extent of coalescence and the calculated electron transfer rates are highly solvent dependent.[41] Figure 9 shows examples of ν(CO) IR lineshapes of ($\mathbf{1c}^-$) in THF, methylene chloride, and acetonitrile. The differences are striking. The rate constants for electron transfer in ($\mathbf{1b}^-$), ($\mathbf{1c}^-$), ($\mathbf{1d}^-$), and ($\mathbf{1d'}^-$) (L = 3-cpy) have been measured in seven solvents. The results are summarized in Table 3. The electron transfer rate constants bear no relationship to static dielectric constants of the solvents studied. However, these data show a strong correlation with characteristic solvent relaxation times measured by Maroncelli and co-workers[42] in time-resolved fluorescence experiments on Coumarin 153, Figure 10. The best comparison is between the data for ($\mathbf{1b}^-$)–($\mathbf{1d'}^-$) and the solvent relaxation time parameter t_{1e}. The time, t_{1e}, is that required for a time-dependent spectral response, $S(t)$, to achieve 1/e of its original value and is considered to represent an overall time scale for the decay of the solvent response. It appears that the IR spectra of these mixed-valence complexes are a steady state spectral probe of ultrafast dynamic solvent relaxation processes which are otherwise only accessible using laser-pumped ultrafast time-resolved measurements.

The comparison between electron transfer rates in ($\mathbf{1b}^-$)–($\mathbf{1d'}^-$) and ultrafast emission red-shift data on dyes is remarkable given the differences in both spectroscopic chromophore and experi-

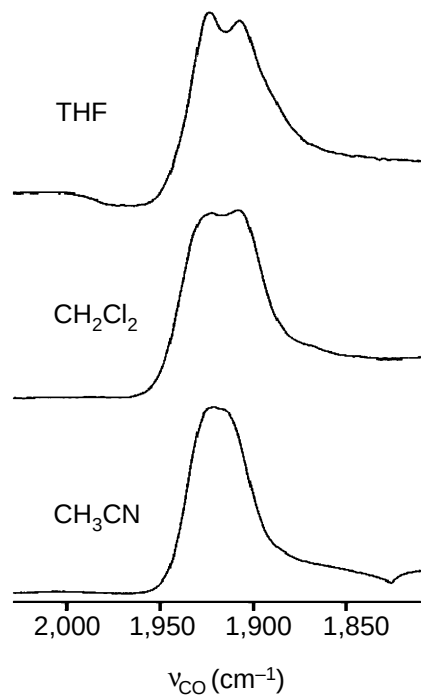

Figure 9 Solvent-dependence of lineshape coalescence of ($\mathbf{1c}^-$).

Table 3 Exchange times of the pz bridged clusters (**1**) in different solvents vs. solvent inertial relation times.

Solvent	(**1b**) (k_e^{-1}) (ps)	(**1c**) (k_e^{-1}) (ps)	(**1d′**) (k_e^{-1}) (ps)	(**1d**) (k_e^{-1}) (ps)	t_{1e} (ps)	$\langle\tau\rangle$ (ps)	ε_0
CH_3CN	0.035(5)	0.38(5)	0.72(10)	0.91(12)	0.15	0.26	35.94
CH_2Cl_2	0.50(5)	0.57(5)	0.72(12)	0.91(11)	0.38	0.56	8.93
DMF	0.67(12)	0.77(15)	0.91(10)	1.0(2)	0.67	0.92	36.71
THF	0.83(15)	0.95(15)	1.0(1)	1.0(1)	0.7	0.94	7.58
DMSO	0.77(10)	0.87(14)	–	1.1(1)	0.9	1.79	46.45
$CHCl_3$	1.5(2)	1.8(2)	1.9(1)	2.0(1)	2.3	2.8	4.81
HMPA	1.5(2)	2.2(2)	2.5(2)	3.3(3)	5.9	9.9	29.30

mental conditions. Since (**1b**$^-$)–(**1d′**$^-$) are strongly coupled mixed-valence compounds, the charge transferred may not be a full electron (alternatively, the effective electron transfer distance r may be short as discussed in Section 2.61.5.1.2 above), while in Coumarin 153 excitation results in transfer of virtually an entire electronic charge. Our IRSEC experiments are performed in the presence of supporting electrolyte under electrochemical conditions, and the IR chromophore is a ground state monoanion, not a charge separated excited state. Given these experimental differences, some discrepancies in overall solvent relaxation times due to potential ion-pairing and electrolyte-induced dielectric effects are expected. Although there is a virtually linear dependence of the electron transfer lifetimes (k_e^{-1}) on t_{1e}, the intercept of the linear relationship is not zero and the relative donor strength of the ancillary pyridine ligand (L = dmap, py, 3-cpy, and 4-cpy) clearly affects the rate. Although there is a large degree of solvent control of the electron transfer rate, solvent reorganization is not the only rate-determining factor (although it is clearly the most important in (**1b**$^-$)–(**1d′**$^-$)). Indeed, for the complex with the slowest electron transfer rates (**1d**$^-$), the rate does not appear to be solvent-dependent in the solvents with the shortest relaxation times. This may be an indication of a transition from solvent control to inner-sphere control of electron transfer rate.

The clear dependence of spectral coalescence on solvent dynamics implies that the origin of the coalescence is itself dynamic. In a semiclassical electron transfer theoretical framework (Equation (2)), this could be explained in terms of electron transfers with essentially zero activation energy. The rates would then converge to the nuclear frequency factor, ν_n, which in this case would appear to be dominated by solvent dipolar relaxation frequencies. In more recent solvent dynamical models, the observed effects could be considered to result from "solvent friction" limiting the rate of exploration of the electron transfer reaction coordinate.

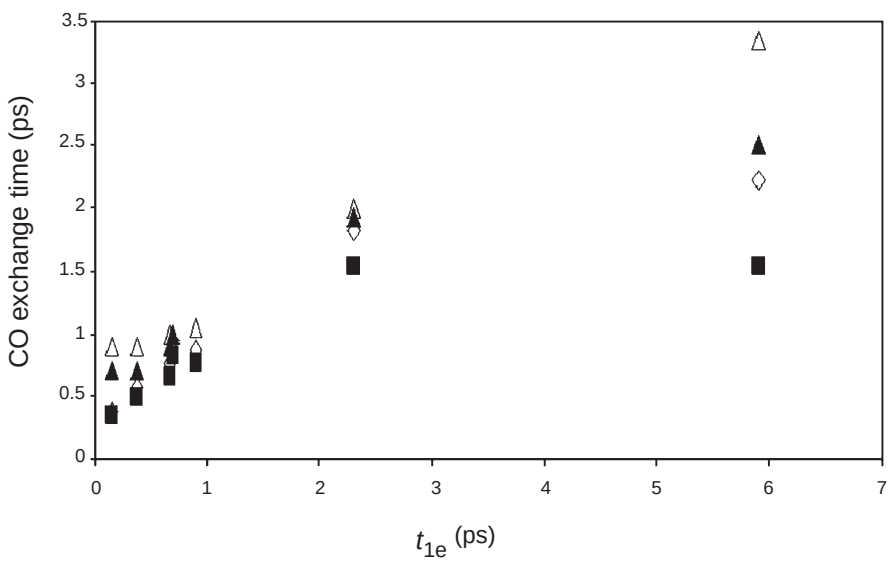

Figure 10 Exchange time (k_e^{-1}) from the IR lineshape coalescence simulation versus solvent inertial relaxation time (t_{1e}). ■ = data for (**1b**$^-$), ◊ = data for (**1c**$^-$), △ = data for (**1d**$^-$), ▲ = data for (**1d′**$^{-1}$).

2.61.7 CONCLUSIONS

IRSEC has been shown to be a convenient technique for studying electron transfer in mixed valence cluster dimers. Using infrared spectroelectrochemistry, it was possible to observe the mixed valence state of bridged triruthenium clusters, and the effects of the bridging ligand and terminal ligand pK_a on electronic coupling and rate of electron exchange were shown directly through changes in the IR bandshape, i.e., coalescence. We are currently expanding our studies to asymmetric bridged triruthenium clusters, where the terminal ligand on each cluster unit is different. Also, we are examining the applicability of this method for studying electron transfer in other mixed valence systems, such as simple dimers and more complex mixed metal clusters.

2.61.8 REFERENCES

1. Solomon, E. I.; Randall, D. W.; Glaser, T. *Coord. Chem. Rev.* **2000**, *200*, 595–632.
2. Bach, U.; Lupo, D.; Comte, P.; Moser, J. E.; Weissortel, F.; Salbeck, J.; Spreitzer, H.; Gratzel, M. *Nature* **1998**, *395*, 583–585.
3. Creutz, C.; Taube, H. *J. Am. Chem. Soc.* **1969**, *91*, 3988–3989.
4. Creutz, C. *Prog. Inorg. Chem.* **1983**, *30*, 1–73.
5. Jortner, J. *J. Chem. Phys.* **1976**, *64*, 4860–4867.
6. Jortner, J.; Bixon, M. (Eds) Electron Transfer—From Isolated Molecules to Biomolecules, In *Advances in Chemical Physics*; Wiley: New York, 1999; Vol. 106/107.
7. Piepho, S. B.; Krausz, E. R.; Schatz, P. N. *J. Am. Chem. Soc.* **1978**, *100*, 2996–3005.
8. Hush, N. S. *Prog. Inorg. Chem.* **1967**, *8*, 391–444.
9. Ito, T.; Hamaguchi, T.; Nagino, H.; Yamaguchi, T.; Washington, J.; Kubiak, C. P. *Science* **1997**, *277*, 660–663.
10. Ito, T.; Hamaguchi, T.; Nagino, H.; Yamaguchi, T.; Zavarine, I. S.; Richmond, T.; Washington, J.; Kubiak, C. P. *J. Am. Chem. Soc.* **1999**, *121*, 4625–4632.
11. Yamaguchi, T.; Imai, N.; Ito, T.; Kubiak, C. P. *Bull. Chem. Soc. Jpn.* **2000**, *73*.
12. Spencer, A.; Wilkinson, G. *J. Chem. Soc., Dalton Trans.* **1972**, 1570–1577.
13. Spencer, A.; Wilkinson, G. *J. Chem. Soc., Dalton Trans.* **1974**, 786–792.
14. Campagna, S.; Denti, G.; Serroni, S.; Ciano, M.; Juris, A.; Balzani, V. *Inorg. Chem.* **1992**, *31*, 2982–2984.
15. Kido, H.; Nagino, H.; Ito, T. *Chem. Lett.* **1996**, 745–746.
16. Ota, K.; Sasaki, H.; Matsui, T.; Hamaguchi, T.; Ito, T.; Kido, H.; Kubiak, C. P. *Inorg. Chem.* **1999**, *38*, 4070–4078.
17. Toma, H. E.; Da Cunha, C. J.; Cipriano, C. *Inorg. Chim. Acta* **1988**, *154*, 63–66.
18. Baumann, J. A.; Salmon, D. J.; Wilson, S. T.; Meyer, T. J. *Inorg. Chem.* **1979**, *18*, 2472–2479.
19. Evans, C. E. B.; Naklicki, M. L.; Rezvani, A. R.; White, C. A.; Kondratiev, V. V.; Crutchley, R. J. *J. Am. Chem. Soc.* **1998**, *120*, 13096–13103.
20. McConnell, H. M. *J. Phys. Chem.* **1961**, *35*, 508–515.
21. de la Rosa, R.; Chang, P. J.; Salaymeh, F.; Curtis, J. C. *Inorg. Chem.* **1985**, *24*, 4229–4231.
22. Lacoste, M.; Rabaa, H.; Astruc, D.; Ardoin, N.; Varret, F.; Saillard, J.-Y.; LeBeuze, A. *J. Am. Chem. Soc.* **1990**, *112*, 9548–9557.
23. Dong, Y. H.; Hupp, J. T. *Inorg. Chem.* **1992**, *31*, 3170–3172.
24. Demadis, K. D.; Hartshorn, C. M.; Meyer, T. J. *Chem. Rev.* **2001**, *101*, 2655–2686.
25. Nelson, S. F. *Chem. Eur. J.* **2000**, *6*, 581–588.
26. Robin, M. B.; Day, P. *Adv. Inorg. Chem. Radiochem.* **1967**, *10*, 247–422.
27. Niu, J. J.; Dong, S. J. *Rev. Anal. Chem.* **1996**, *15*, 1–171.
28. Wittrig, R. E.; Kubiak, C. P. *J. Electroanal. Chem.* **1995**, *393*, 75–86.
29. Zavarine, I. S.; Kubiak, C. P. *J. Electroanal. Chem.* **2001**, *2001*, 106–109.
30. Hill, M. G.; Bullock, J. P.; Wilson, T.; Bacon, P.; Blaine, C. A.; Mann, K. R. *Inorg. Chim. Acta* **1994**, *226*, 61–68.
31. Bullock, J. P. Ph. D. Thesis, Department of Chemistry; University of Minnesota: Minneapolis, MN; 1990.
32. Grevels, F.-W.; Jacke, J.; Klotzbucher, W. E.; Kruger, C.; Seevogel, K.; Tsay, Y. H. *Angew. Chem., Int. Ed. Engl.* **1987**, *26*, 885–887.
33. Grevels, F.-W.; Kerpen, K.; Klotzbucher, W. E.; McClung, R. E. D.; Russell, G.; Viotte, M.; Schaffner, K. *J. Am. Chem. Soc.* **1998**, *120*, 10423–10433.
34. Turner, J. J.; Gordon, C. M.; Howdle, S. M. *J. Phys. Chem.* **1995**, *99*, 17532–17538.
35. Wu, R. W.; Koske, S. K. A.; White, R. P.; Anson, C. E.; Jayasooriya, U. A.; Cannon, R. D. *J. Chem. Soc., Chem. Commun.* **1994**, 1657–1658.
36. Sutin, N. S. *Prog. Inorg. Chem.* **1983**, *30*, 441–498.
37. Callahan, R. W.; Keene, F. R.; Meyer, T. J.; Salmon, D. J. *J. Am. Chem. Soc.* **1977**, 1064–1073.
38. Baumann, J. A.; Salmon, D. J.; Wilson, S. T.; Meyer, T. J.; Hatfield, W. E. *Inorg. Chem.* **1978**, *17*, 3342–3350.
39. Demadis, K. D.; Neyhart, G. A.; Kober, E. M.; Meyer, T. J. *J. Am. Chem. Soc.* **1998**, *120*, 7121–7122.
40. Hornung, F. M.; Baumann, F.; Kaim, W.; Olabe, J. A.; Slep, L. D.; Fiedler, J. *Inorg. Chem.* **1998**, *37*, 311–316.
41. Londergan, C. H.; Salsman, J. C.; Ronco, S.; Dolkas, L. M.; Kubiak, C. P. *J. Am. Chem. Soc.* **2002**, *124*, 6236–6237.
42. Horng, M. L.; Gardecki, J. A.; Papazyan, A.; Maroncelli, M. *J. Phys. Chem.* **1995**, 17311–17337.

Comprehensive Coordination Chemistry II
ISBN (set): 0-08-0437486
Volume 2, (ISBN 0-08-0443249); pp 717–729

2.62 Non-biological Photochemistry Multiemission

A. J. LEES and S.-S. SUN
State University of New York at Binghamton, NY, USA

2.62.1 INTRODUCTION 731
2.62.2 EXCITED-STATE PROPERTIES OF DIIMINE RHENIUM(I) TRICARBONYL COMPLEXES: INTERRELATIONSHIPS BETWEEN MLCT, LLCT, AND IL EXCITED STATES 732
2.62.2.1 Complexes with Lowest MLCT Excited States 732
2.62.2.2 Complexes with Lowest LLCT Excited States 734
2.62.2.3 Complexes with Lowest IL Excited States 737
2.62.3 CONCLUDING REMARKS 739
2.62.4 REFERENCES 741

2.62.1 INTRODUCTION

Since the first systematic studies of the photophysical and photochemical properties of *fac*-$RRe^{I}(CO)_3(LL)$ complexes (where LL is a bidentate α-diimine ligand or two monodentate pyridyl ligands, and R is a halogen, an alkyl group, or a pyridyl ligand) in the mid-1970s by Wrighton and co-workers,[1–3] polypyridyl complexes of Re^{I} have played an important role in contributing to an understanding of the photophysical and light-induced electron-transfer (ET) and electronic energy-transfer (E_NT) processes. A number of investigations have appeared in the literature, based on complexes incorporating the $Re^{I}(CO)_3$(bpy) chromophore (bpy = 2,2′-bipyridine or its derivatives). These have elegantly demonstrated medium effects,[4,5] fundamental photophysical properties of metal-to-ligand charge transfer (MLCT) excited states,[6,7] and physical and/or chemical processes facilitated by covalently linked chromophore-quencher systems.[8,9]

These Re(I)-based compounds offer several advantages for elucidating the various excited-state properties of organometallic complexes. From a synthetic point of view, the incorporation of other ligands to the *fac*-$Re^{I}(CO)_3$(diimine) moiety is relatively easy, as is modification of the diimine ligands themselves.[10] Indeed, systematic tuning of the electronic properties of these complexes can be achieved by varying the substituents on the diimine ligand.[11] Altering the excited-state properties provides insight into the role of the acceptor diimine ligand in determining spectroscopic and photophysical characteristics. Moreover, the lifetimes of the lowest excited states of these *fac*-$Re^{I}(CO)_3$(diimine)-based complexes are usually sufficiently long enough to permit energy- or electron-transfer processes to nearby components when suitable energetic and electronic conditions are satisfied.[8]

In general, the excited-state properties of diimine rhenium(I) tricarbonyl complexes primarily occur through the lowest triplet excited states, due to rapid vibrational relaxation and intersystem crossing from the upper vibrational energy levels.[1,3] Thus, the nature of the lowest-energy π-acceptor ligands (either the diimine ligands or bridging ligands) plays a decisive role in determining the ultimate photophysical and/or photochemical properties. Various excited states

are generated, depending on the relative energy levels of the metal and ligand orbitals, as well as the extent of interaction between them. Many mononuclear diimine rhenium(I) tricarbonyl complexes are highly emissive ($\Phi_{em} = 0.001–0.1$) and feature relatively long emission lifetimes (10 ns to 1 μs) in solution, due to the existence of lowest energy triplet-centered MLCT excited states.[3,12] In these cases, the decay of the lowest-lying MLCT-emitting states is often primarily determined by an energy gap law effect.[13] Another prominent feature of these complexes is the large hypsochromic shift of their emission maxima on going from a fluid environment to a rigid medium. This so-called "luminescence rigidochromism" is related to changes in the solvation about the complex. Here, the long-lived triplet MLCT excited state is apparently raised in energy compared to the ground-state molecule, due to the restricted ability of the solvent molecules to reorient and stabilize the excited-state dipole moment.[2,4,6]

Clearly, there is an enormous richness in the photophysical and photochemical behavior of the excited states present in diimine rhenium(I) tricarbonyl complexes. Indeed, this plethora of molecular photophysical characteristics has led to a wide range of interesting and important applications, including their use as catalysts,[14–18] sensors,[19–23] probes for photo-polymerization,[4,24–27] photocleavage of DNA,[28–30] nonlinear optical materials,[31–33] and optical switches.[34–44] As noted above, the photophysical and photochemical properties of these rhenium(I) complexes are highly dependent on the nature of the lowest-lying excited states and are influenced greatly by the electronic properties of the diimine and ancillary ligands. This case study focuses on the photophysics in these systems and the way in which these excited states interrelate to one another in the energy degradation mechanisms and in the overall photochemistry. We will also describe how participating energy- and electron-transfer processes affect the excited-state properties of these molecules. Additionally, it will be shown how a range of physical techniques e.g., UV–vis, luminescence and resonance Raman spectroscopy, and associated time-resolved methods have been employed to characterize the photophysical behavior in such systems.

2.62.2 EXCITED-STATE PROPERTIES OF DIIMINE RHENIUM(I) TRICARBONYL COMPLEXES: INTERRELATIONSHIPS BETWEEN MLCT, LLCT, AND IL EXCITED STATES

In this section, some of the characteristics of different excited states, including their associated photophysical properties, will be discussed. Several possible transitions can occur in diimine rhenium(I) tricarbonyl complexes, including ligand field (LF), MLCT, ligand-to-ligand charge transfer (LLCT), σ-bond-to-ligand charge transfer (σ–π^*), and intraligand (IL) excited states. Due to the strong ligand field effect exerted from the third-row transition metal, the LF transitions are usually located at higher energies compared to other common transitions. Consequently, we will not concentrate in detail on the photophysical role of LF transitions in this case study. Also not discussed here in detail are σ–π^* transitions, because these give rise primarily to dissociation and not emission.

2.62.2.1 Complexes with Lowest MLCT Excited States

In general, diimine Re^I tricarbonyl complexes with lowest MLCT states feature fairly intense absorption bands in the near-UV to visible spectral region. These bands show negative solvatochromism (see Chapter 2.27), as revealed by band shifts to lower energy in less polar solvents.[1,3,6] The direction of the solvent dependence is associated with a reduced (and reversed) molecular dipole in their MLCT excited states. Emissions from these complexes are typically broad and structureless, and they also often exhibit a rigidochromic effect.[3,4,6] Tables 1 and 2 summarize the luminescence characteristics and environmental effects on absorption and emission maxima for $ClRe(CO)_3L$ complexes.[2] Both emission quantum yields and lifetimes are significantly increased when the solution is cooled to 77 K, implying that the radiative decay pathways are favored in the more rigid environment; the emission lifetimes are typically governed by the energy gap law.[11,13,45,46] Table 3 and Figure 1 summarize the excited-state decay parameters for the MLCT excited states of *fac*-$[LRe(CO)_3(bpy)](PF_6)$ complexes and their resulting energy gap plot, respectively. These complexes also usually exhibit substantial photostability under visible light irradiation and, due

Table 1 Luminescence characteristics for various $ClRe(CO)_3L$ complexes.[a,b]

	Emission max (10^{-3} cm^{-1})		*Lifetime* (μs)			
L	*298* K	*77* K	*298* K	*77* K	$\Phi_e(\pm 15\%)$[c] *at 298* K	$\Phi_e(\pm 15\%)$ *at 77* K
phen	17.33	18.94	0.3	9.6	0.036	0.33
bpy		18.87	0.6	3.8		
5-Me-phen	17.01	18.83	≤0.65	5.0	0.030	0.33
4,7-Ph_2-phen	17.24	18.18	0.4	11.25		
5-Cl-phen	17.12	18.69	≤0.65	6.25		
5-Br-phen	17.12	18.69	≤0.65	7.6	0.020	0.20
5-NO_2-phen	[d]	18.28		11.8		0.033
phen-5,6-dione	[d]	18.45		2.5		
biquin[e]	[d]	14.58				

[a] Data taken from ref. 2. [b] Measurements in EPA at 77 K or CH_2Cl_2 at 298 K. [c] Quantum yields determined in benzene at 298 K. [d] Luminescence was not detectable from these complexes in solution at 298 K. [e] biquin = 2,2′-biquinoline.

Table 2 Environmental effects on absorption and emission maxima of several $ClRe(CO)_3L$ complexes.[a]

L	*Environment* (*T*, K)	*First absorption max* (10^{-3} cm^{-1})	*Emission max* (10^{-3} cm^{-1}) (τ, μs)
phen	CH_2Cl_2(298)	26.53	17.33 (0.3)
	polyester resin(298)		18.52 (3.67)
	EPA(77)		18.94 (9.6)
5-Me-phen	benzene(298)	25.65	17.00 (≤0.65)
	CH_2Cl_2(298)	26.32	17.01
	CH_3OH(298)	27.05	17.00
	pure solid(298)		18.42
	polyester resin(298)		18.48 (3.5)
	EPA(77)		18.83 (5.0)
5-Br-phen	benzene(298)	25.32	17.15 (≤0.65)
	CH_2Cl_2(298)	25.84	17.12
	CH_3OH(298)	26.88	17.04
	pure solid(298)		17.83
	polyester resin(298)		18.32 (2.2)
	EPA(77)		18.69 (7.6)
5-Cl-phen	CH_2Cl_2(298)	25.91	17.12
	pure solid(298)		17.99
	EPA(77)		18.69 (6.25)

[a] Data taken from ref. 2.

Table 3 Excited-state decay parameters for the MLCT excited states of *fac*-$[LRe(CO)_3(bpy)](PF_6)$ complexes in deoxygenated methylene chloride at 296 K.[a]

L	E_{em} (10^{-3} cm^{-1})	Φ_e	τ (ns)	k_r (s^{-1})	k_{nr} (s^{-1})
Cl^-	16.08	0.005	51	9.79×10^4	1.95×10^7
4-(*N*,*N*-dimethylamino)pyridine	16.39	0.017	95	1.78×10^5	1.03×10^7
4-aminopyridine	16.75	0.052	129	4.06×10^5	7.34×10^6
N-methylimidazole	16.98	0.058	161	3.59×10^5	5.85×10^6
4-ethylpyridine	17.64	0.18	604	2.96×10^5	1.36×10^6
pyridine	17.92	0.16	669	2.36×10^5	1.26×10^6
$P(CH_3)_3$	18.38	0.27	1,169	2.32×10^5	6.23×10^5
CH_3CN	18.66	0.41	1,201	3.43×10^5	4.90×10^5

[a] Data taken from ref. 13.

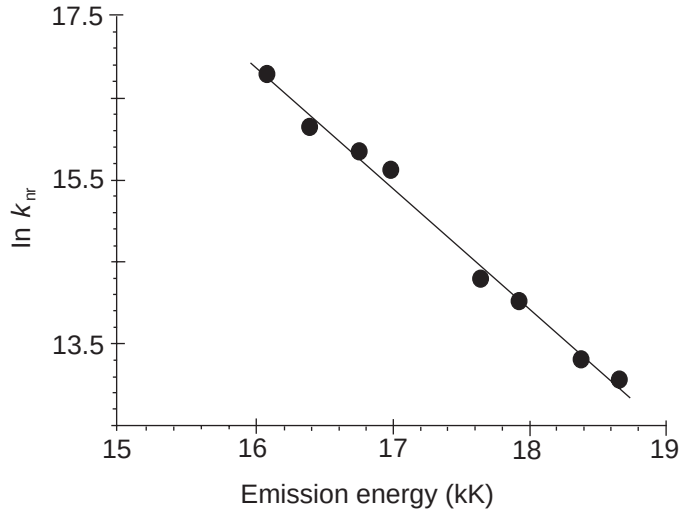

Figure 1 Plot of ln k_{nr} vs. E_{em} for the MLCT excited states of a series of *fac*-$LRe(CO)_3(bpy)$ complexes in CH_2Cl_2 at 296 K (see Table 3 for complexes). Adapted from ref. 13.

to their relatively long-lived triplet characteristics, the emission lifetimes are easily quenched by bimolecular electron- and/or energy-transfer processes in solution.[3,47]

The electronic structures of MLCT excited molecules of diimine Re^I tricarbonyl complexes can be viewed as a charge-separated species, $[LRe^{II}(CO)_3(diimine^{\bullet-})]^*$. With an essentially oxidized metal center and reduced diimine ligand, several spectroscopic techniques can be employed to detect the electronic and structural parameters of the excited states. The MLCT excited state experiences a decrease in the extent of Re–CO π-back bonding, and this effect can be easily monitored by time-resolved IR spectroscopy and time-resolved resonance Raman spectroscopy.[48,49] Thus, the nanosecond time-resolved IR spectrum of $ClRe(CO)_3(bpy)$ shows an average shift to higher energy by 55 cm^{-1} in the three υ(CO) bands and the transient infrared spectrum of $[(4\text{-Me-py})Re(phen)(CO)_3)]^+$ shows an average shift to higher energy by 46 cm^{-1} in the three υ(CO) bands.[50,51] Indeed, time-resolved IR spectroscopy has been able to differentiate the lowest excited state between MLCT or IL levels in $ClRe(bpy)(CO)_3$ containing phenyleneethynylene oligomers.[52] Transient resonance Raman spectroscopy also provides evidence, based on the resonance enhancement of the υ(CO) Raman peaks, for identifying the lowest excited states and possible excited-state intermediates.[53,54] In such cases, intense excited-state Raman lines have been observed that are associated with the radical anion of the diimine ligand.

2.62.2.2 Complexes with Lowest LLCT Excited States

In coordination complexes with both reducing- and oxidizing-type ligands, excited states can arise that are the result of charge transfer from one ligand to another. Several rhenium tricarbonyl-based chromophore-quencher complexes are known to have lowest excited states featuring LLCT character.[10,55] Owing to the very weak electronic interaction between the donor and the acceptor components, the extinction coefficients for such LLCT bands are usually very low. For example, the extinction coefficient of the LLCT band for complex $[(py\text{-}PTZ)Re^I(CO)_3(bpy)]^+$ is only 2.4 $M^{-1}cm^{-1}$.[56] Nevertheless, the LLCT state can be indirectly populated by MLCT excitation followed by an intramolecular electron-transfer process. A representative case is the chromophore-quencher complex, $[(py\text{-}PTZ)Re^I(CO)_3(bpy)]^+$. Optical excitation into the $d\pi$(Re) to π^* (bpy) MLCT transition generates the excited-state species, $[(py\text{-}PTZ)Re^{II}(CO)_3(bpy^{\bullet-})]^+$.[57] Thereafter, rapid electron transfer from py-PTZ to Re^{II} takes place, with a determined rate constant higher than $4.8 \times 10^9\ s^{-1}$. The species subsequently formed is $[(py\text{-}PTZ^{\bullet+})Re^I(CO)_3(bpy^{\bullet-})]^+$, which can be considered as a py-PTZ to bpy charge transfer (LLCT) excited state. Direct evidence for the formation of this charge-separated species has been provided from time-resolved resonance Raman and UV–vis spectroscopies, revealing that the complex has both the characteristics of the reduced $bpy^{\bullet-}$ and oxidized $PTZ^{\bullet+}$ moieties.[55,58,59] The LLCT excited state decays to the ground

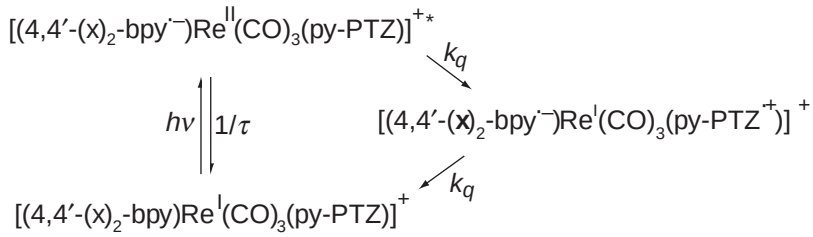

Scheme 1
(reproduced by permission of the American Chemical Society from *J. Phys. Chem.* **1991**, *95*, 5850–5858.)

state via back electron transfer from $bpy^{\bullet -}$ to $PTZ^{\bullet +}$ with a rate constant of $1.1 \times 10^7\ s^{-1}$.[58] Typically, the nonradiative decay parameters of the LLCT excited states in such complexes with analogous bpy derivatives follows the energy gap law. Scheme 1 summarizes the electron-transfer processes taking place in this system.[58]

Due to the generally nonemissive nature of LLCT states, their excited-state properties can be studied only by transient spectroscopy, or indirectly analyzed by their effect on the MLCT excited-state lifetimes of the emissive chromophores. However, if the electron-donor ligand is not stable toward oxidation, then subsequent photochemical reactions may occur. These irreversible photochemical reactions can, thus, be monitored to quantitatively determine the photophysical parameters of LLCT states.[60–65] Scheme 2 depicts the excited-state processes of a typical example, involving the rhenium chromophore coordinated to a 1,2-diamine donor ligand.[62] Initial excitation into the MLCT excited state is followed by rapid forward electron transfer from the 1,2-diamine donor ligand with a rate constant of $9.9 \times 10^6\ s^{-1}$. The subsequently formed 1,2-diamine radical cation is unstable and undergoes rapid C—C bond fragmentation to form an α-amino radical and an iminium ion.[66,67] The calculated lower limits for the rate constants of back electron transfer and bond fragmentation are 1.5×10^8 and $1.0 \times 10^8\ s^{-1}$, respectively.

Another important type of LLCT state arising in diimine rhenium(I) tricarbonyl complexes is found in $IRe^I(CO)_3$(diimine) complexes. When I replaces Cl or Br, the lowest excited states changes from being MLCT in nature to that of XLCT (halide-to-ligand charge transfer) in character.[68] Figure 2 clearly shows that the lowest energy band of the transient absorption

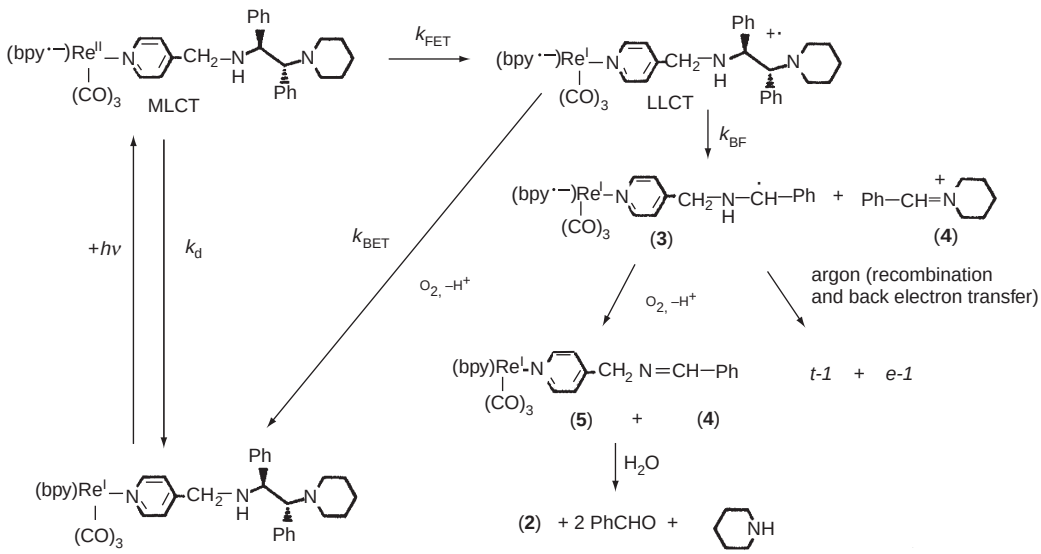

Scheme 2
(reproduced by permission of the American Chemical Society from *J. Phys. Chem.* **1995**, *99*, 1961–1968.)

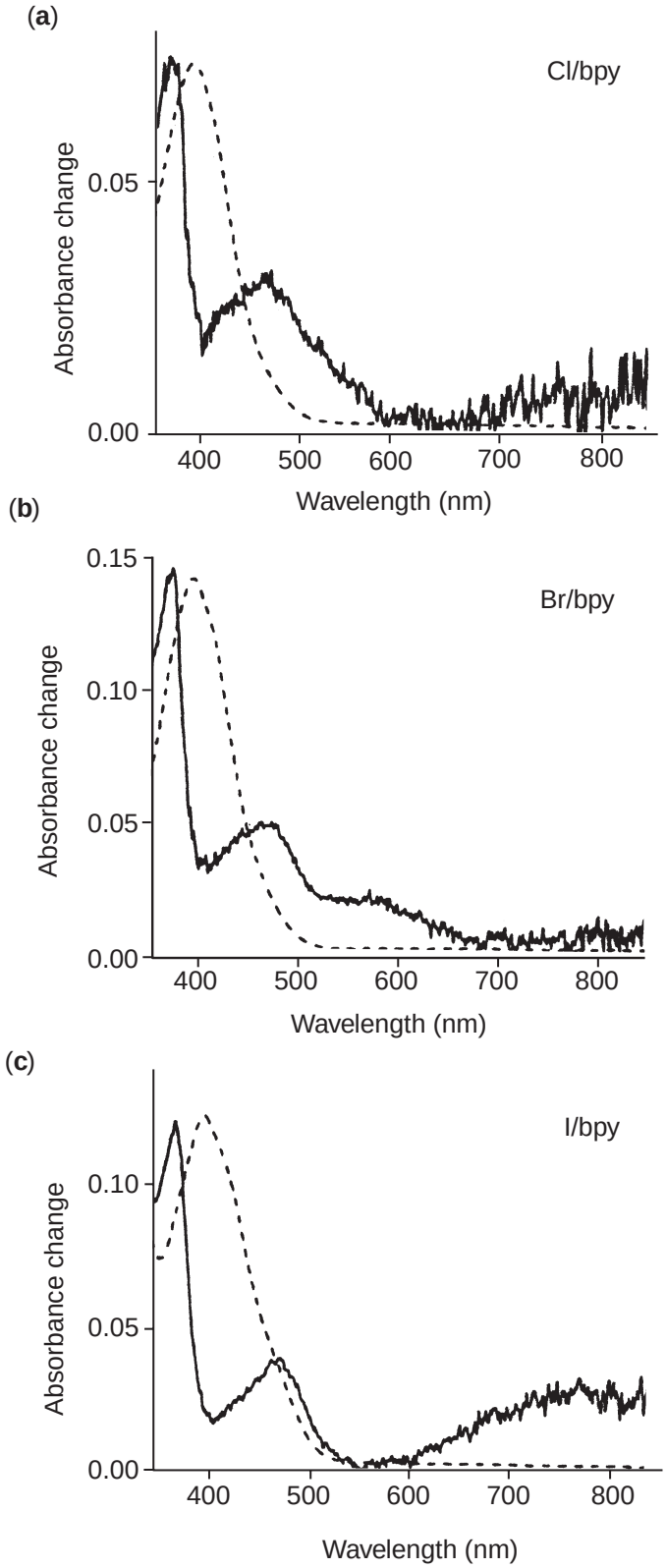

Figure 2 Ground state (– – – –) and transient absorption (———) spectra of $XRe(CO)_3(bpy)$ in THF measured 10 ns after laser excitation at 460 nm. X = (a) Cl; (b) Br; (c) I. (reproduced by permission of the American Chemical Society from ref. 69.).

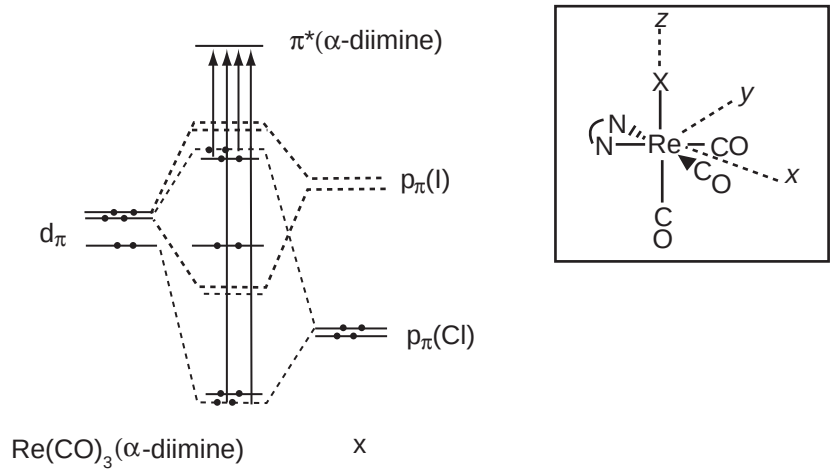

Scheme 3

spectrum is red shifted on progressing from Cl^- to I^-.[69] For the case of $IRe^I(CO)_3$(bpy), a broad but distinct low-energy band appears around 780 nm. In contrast to the above-mentioned LLCT (L to diimine) transitions, which are weak due to the very small electronic coupling between the donor and acceptor, the halide p_y and π^* (diimine) orbitals are now directly coupled by either sharing the metal d_{yz} orbital or by through-space p_y-π^* interactions (see Scheme 3). Thus, XLCT transitions exhibit comparable or slightly weaker intensities compared to MLCT transitions, as shown in Figure 3.[69]

2.62.2.3 Complexes with Lowest IL Excited States

Lowest IL states usually occur in complexes containing extended conjugation of the ligands, where the electron is excited predominantly from the ligand-based n- or π-orbitals. Typical characteristics of IL emissions are structured profiles and longer emission lifetimes compared to MLCT transitions.[70–78] The emission lifetimes are sometimes greatly influenced by temperature or medium effects, though, due to the presence of close-lying MLCT states.[79]

An early report by Wrighton and co-workers revealed that complex $ClRe(CO)_3$(3-benzoylpyridine)$_2$ exhibits typical ^{3}MLCT emission in room-temperature benzene solution. However, in a 77 K EPA glass, the rigidochromic effect shifts the ^{3}MLCT state to higher energy and, thus, multiple emissions from both ^{3}MLCT and ^{3}IL (n-π^*) excited states can be observed (see Figure 4). Here, the ^{3}MLCT and ^{3}n-π^* states are clearly not thermally equilibrated in this glassy environment at low temperature.[71]

Many $LRe(CO)_3$(X-phen) complexes, where L is a Lewis base and X-phen is phenanthroline or its derivatives, exhibit overlapping emissions from both ^{3}MLCT and ^{3}IL (π–π^*) excited states at room temperature. By varying L, X-phen, and temperature, the emitting states can be tuned from ^{3}MLCT to $^3\pi$–π^* in nature. Figure 5 compares the emission spectra of a series of (py)$Re(CO)_3$(X-phen) complexes at 298 K and 77 K. More structured emissions were observed at 77 K, as well as in complexes with higher ^{3}MLCT excited states.[72] The excited-state decays are also more complicated at low temperature and feature bi- or multi-exponential kinetics.[73]

An intriguing example reported by Meyer and co-workers has revealed that the observed ^{3}MLCT emission in a system with close-lying ^{3}MLCT and ^{3}IL states does not necessarily prove that the lowest excited state is ^{3}MLCT in character. In the case of $ClRe(CO)_3$(dppz) (dppz is dipyrido[3,2-*a*:2′,3′-*c*]phenazine), the lowest excited state was determined to be the $^3\pi$–π^* excited state by time-resolved resonance Raman spectroscopy, although the emission apparently originates from the ^{3}MLCT excited state. Replacing Cl by PPh_3 yields emission originating from the $^3\pi$–π^* state, which is also confirmed by time-resolved resonance Raman spectroscopy.[80]

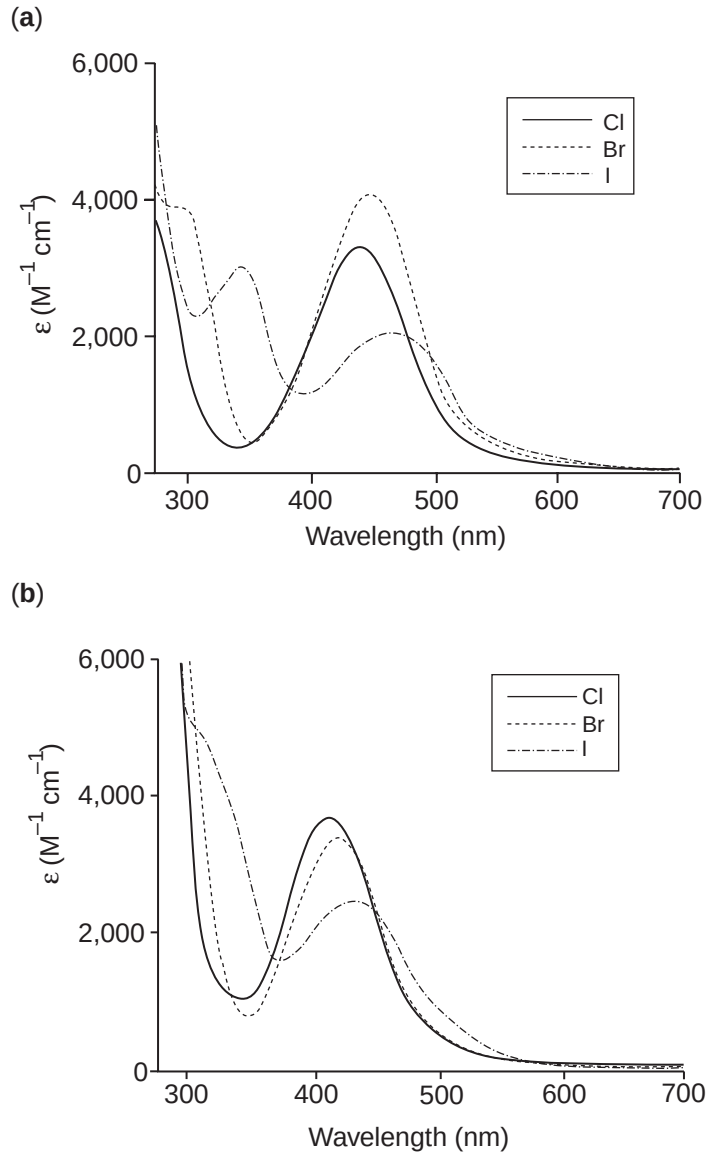

Figure 3 Electronic absorption spectra of (a) $XRe(CO)_3$(iPr-DAB); and (b) $XRe(CO)_3$(iPr-PyCa) (X = Cl, Br, I) in THF at 293 K. Adapted from ref. 69.

Complexes incorporating a ligand with a lowest non-emissive ^{3}IL excited state that is energetically tunable by light-induced structural change (such as in stilbene or azobenzene derivatives) have potential applications as light-switching materials. When the olefin or azo groups are in *trans*-conformations, the complexes are weakly or non-emissive due to the presence of lowest non-emissive $^3\pi$–π^* or ^{3}n–π^* excited states. Excitation into their ^{3}MLCT excited state sensitizes the $^3\pi$–π^* or ^{3}n–π^* excited states and results in *trans-cis* isomerization of the ligand. The $^3\pi$–π^* or ^{3}n–π^* excited states in the *cis*-conformer are shifted to a higher energy position compared to the emissive ^{3}MLCT state and, consequently, strong emission is observed.

Several reports have taken advantage of this unique property to design a variety of photoswitching systems in recent years.[34–36,38,39,42–44] Moore and co-workers reported one particularly interesting example.[36] The complexes in their study are *fac*-$Re(CO)_3$(bpy) chromophores linked by a styryl pyridine that attaches an amine or an azacrown ether group (see Scheme 4 for structures). The absorption spectra of these complexes feature an intense intraligand charge-transfer (ILCT) band, which can be removed by protonation of the amine or azacrown

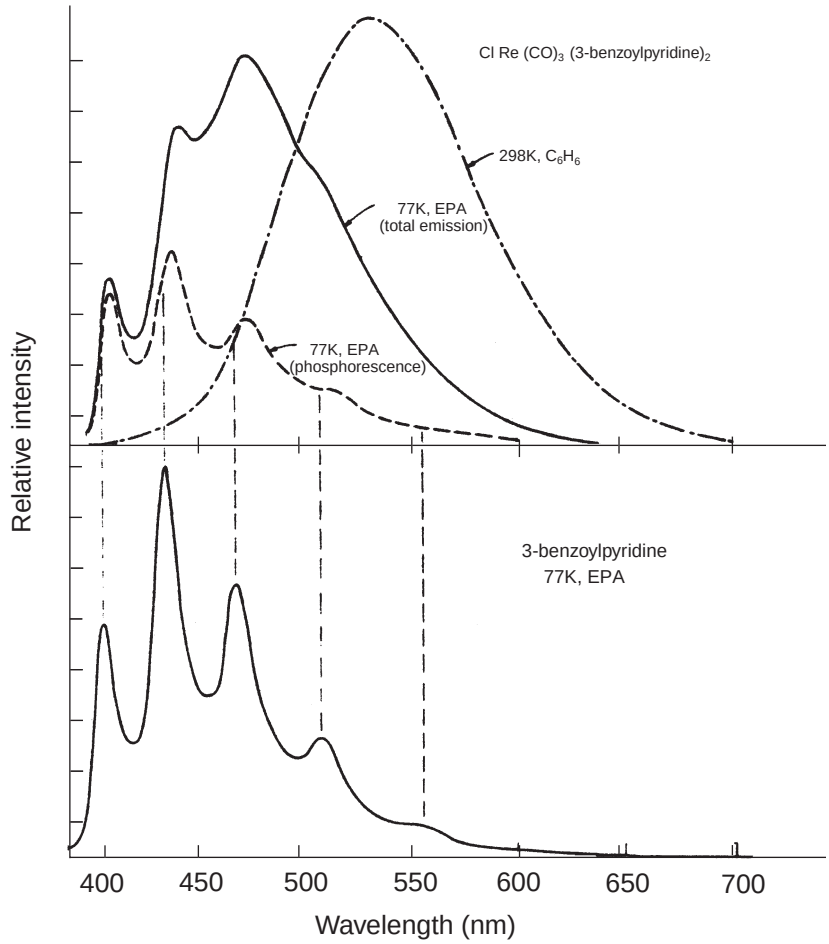

Figure 4 Emission spectra of $ClRe(CO)_3$(3-benzoylpyridine) and the free ligand following excitation at 330 nm (not shown at same sensitivity). Adapted from ref. 71.

ether (see Figure 6). Both the amine and azacrown complexes are only weakly emissive at room temperature. Prolonged irradiation of the complexes into either the ILCT or MLCT states results in no change of the absorption spectrum, indicative of negligible photochemistry. However, under the same experimental conditions with the protonated complexes, the absorption spectra changed profoundly, and this is consistent with efficient *trans-cis* photoisomerization at the olefin bond. Notably, the emission in these protonated species is also enhanced during the irradiation, reflecting the higher energy position of the $^3\pi$–π^* states compared to the ^{3}MLCT states in the *cis*-styryl pyridine complexes (see Figure 7).

2.62.3 CONCLUDING REMARKS

This case study deals with different photophysical properties of a variety of diimine rhenium(I) tricarbonyl complexes. The exceptionally diverse photophysical behavior of these complexes is largely dependent on the nature of their lowest excited states. Varying the substituents on either the diimine ligands or ancillary ligands can easily change the relative order of these excited states and provides a way to tune the excited-state characteristics. A range of important applications is now becoming apparent, based on the richness of the photophysical and photochemical properties of diimine rhenium(I) tricarbonyl complexes.

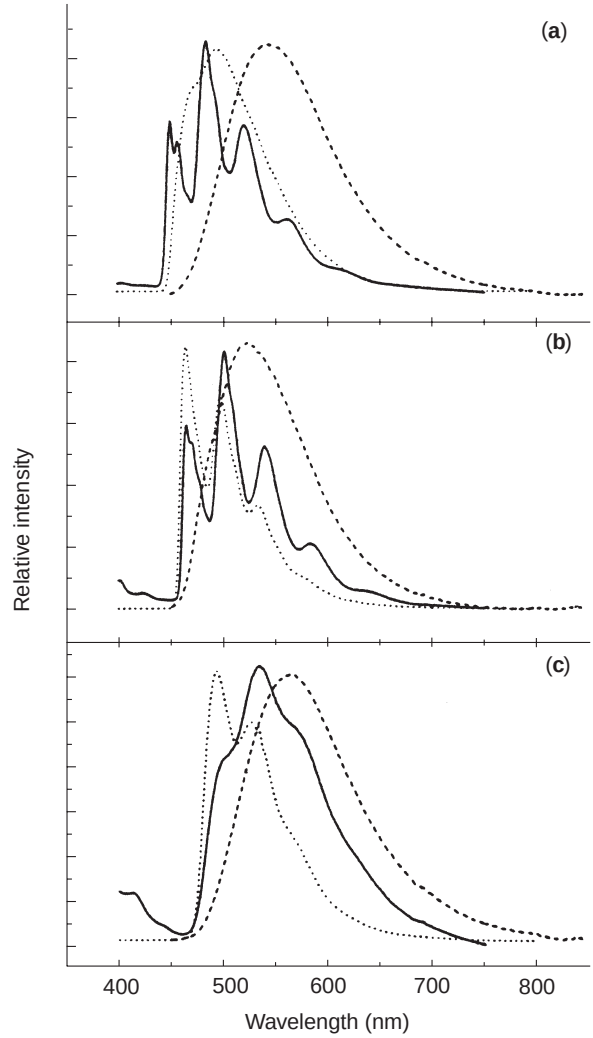

Figure 5 Emission spectra recorded in ethanol–methanol (4:1): (- - - - -) (py)$Re(CO)_3L^+$ at 298 K, (·····) (py)$Re(CO)_3L^+$ at 77 K, and (———) free ligand at 77 K. Excitation wavelength was 355 nm (complexes) or 320 nm (ligands); L = (a) 2,9-Me_2phen; (b) 3,4,7,8-Me_4phen; (c) 5-Phphen. Adapted from ref. 72.

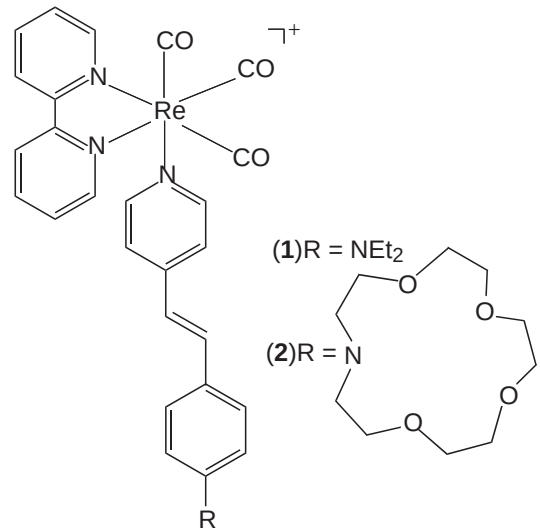

Scheme 4

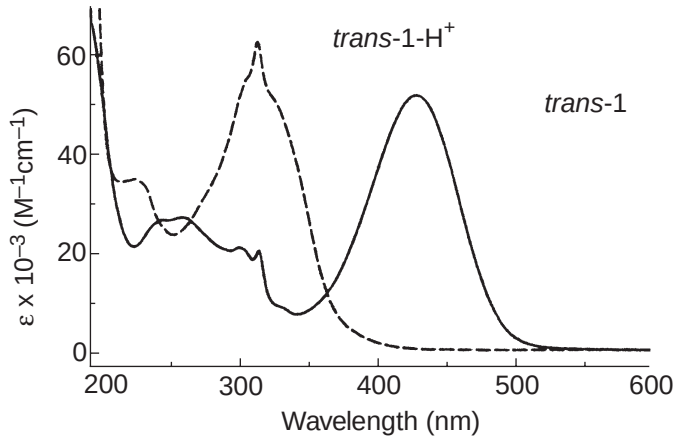

Figure 6 Electronic absorption spectra of *trans*-(**1**) in CH_3CN and on addition of excess HCl (see Scheme 4 for structure). Adapted from ref. 36.

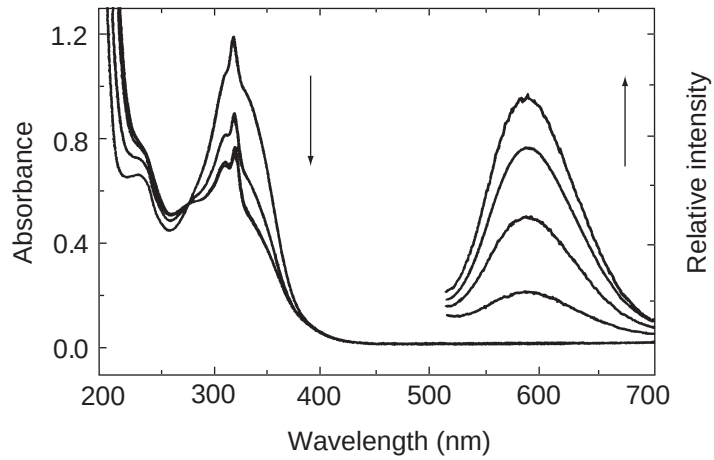

Figure 7 Electronic absorption spectra of *trans*-(**1**) in CH_3CN with excess HCl added after irradiation at 406.7 nm for 0, 30, 120, and 180 min, along with corresponding emission spectra obtained on excitation at 380 nm (no distinct emission features were observed at wavelengths lower than 500 nm). Adapted from ref. 36.

2.62.4 REFERENCES

1. Geoffroy, G. L.; Wrighton, M. S. *Organometallic Photochemistry*; Academic Press: New York, 1979.
2. Wrighton, M.; Morse, D. L. *J. Am. Chem. Soc.* **1974**, *96*, 998–1003.
3. Lees, A. J. *Chem. Rev.* **1987**, *87*, 711–743.
4. Lees, A. J. *Comments Inorg. Chem.* **1995**, *17*, 319–346.
5. Chen, P.; Meyer, T. J. *Chem. Rev.* **1998**, *98*, 1439–1477.
6. Stufkens, D. J. *Comments Inorg. Chem.* **1992**, *13*, 359–385.
7. Vogler, A.; Kunkely, H. *Coord. Chem. Rev.* **2000**, *200–202*, 991–1008.
8. Balzani, V.; Juris, A.; Venturi, M.; Campagna, S.; Serroni, S. *Chem. Rev.* **1996**, *96*, 759–833.
9. Schanze, K. S.; Walters, K. A. Photoinduced Electron Transfer in Metal–Organic Dyads. In *Organic and Inorganic Photochemistry*; Ramamurthy, V., Schanze, K. S., Eds.; Molecular and Supramolecular Photochemistry Series, Vol. 2; Marcel Dekker: New York, 2000; Chap. 3, pp 75–127.
10. Schanze, K. S.; MacQueen, D. B.; Perkins, T. A.; Cabana, L. A. *Coord. Chem. Rev.* **1993**, *122*, 63–89.
11. Worl, L. A.; Duesing, R.; Chen, P.; Della Ciana, L.; Meyer, T. J. *J. Chem. Soc., Dalton Trans.* **1991**, 849–858.
12. Kalyanasundaram, K. *Photochemistry of Polypyridine and Porphyrin Complexes*; Academic Press: New York, 1992; Chap. 10, pp 321–329.
13. Caspar, J. V.; Meyer, T. J. *J. Phys. Chem.* **1983**, *87*, 952–957.
14. Koike, K.; Hori, H.; Ishizuka, M.; Westwell, J. R.; Takeuchi, K.; Ibusuki, T.; Enjouji, K.; Konno, H.; Sakamoto, K.; Ishitani, O. *Organometallics* **1997**, *16*, 5724–5729.
15. Johnson, F. P. A.; George, M. W.; Hartl, F.; Turner, J. J. *Organometallics* **1996**, *15*, 3374–3387.
16. Sullivan, B. P.; Meyer, T. J. *Organometallics* **1986**, *5*, 1500–1502.
17. Sullivan, B. P.; Meyer, T. J. *J. Chem. Soc., Chem. Commun.* **1984**, 1244–1246.
18. Hawecker, J.; Lehn, J.-M.; Ziessel, R. *J. Chem. Soc. Chem. Commun.* **1983**, 536–538.

19. Sun, S.-S.; Lees, A. J. *Chem. Commun.* **2000**, 1687–1688.
20. Mizuno, T.; Fukumatsu, T.; Takeuchi, M.; Shinkai, S. *J. Chem. Soc., Perkin Trans.* **2000**, *1*, 407–413.
21. Keefe, M. H.; Sloan, R. V.; Hupp, J. T.; Czaplewski, K. F.; Snurr, R. Q.; Stern, C. L. *Langmuir* **2000**, *16*, 3964–3970.
22. Bakir, M.; McKenzie, J. A. M. *J. Chem. Soc., Dalton Trans.* **1997**, 3571–3578.
23. Demas, J. N.; DeGraff, B. A. *Anal. Chem.* **1991**, *63*, A829–A837.
24. Lees, A. J. *Coord. Chem. Rev.* **1998**, *177*, 3–35.
25. Kotch, T. G.; Lees, A. J.; Fuerniss, S. J.; Papathomas, K. I.; Snyder, R. W. *Inorg. Chem.* **1993**, *32*, 2570–2575.
26. Kotch, T. G.; Lees, A. J.; Fuerniss, S. J.; Papathomas, K. I. *Chem. Mater.* **1992**, *4*, 675–683.
27. Lees, A. J. Luminescent Metal Complexes as Spectroscopic Probes of Monomer/Polymer Environments. In *Optical Sensors and Switches*; Ramamurthy, V., Schanze, K. S., Eds.; Molecular and Supramolecular Photochemistry Series, Vol. 7; Marcel Dekker: New York, 2001; Chap. 5, pp 209–255.
28. Yam, V. W.-W.; Lo, K. K.-W.; Cheung, K.-K.; Kong, R. Y.-C. *J. Chem. Soc., Dalton Trans.* **1997**, 2067–2072.
29. Stoeffler, H. D.; Thornton, N. B.; Temkin, S. L.; Schanze, K. S. *J. Am. Chem. Soc.* **1995**, *117*, 7119–7128.
30. Oriskovich, T. A.; White, P. S.; Thorp, H. H. *Inorg. Chem.* **1995**, *34*, 1629–1631.
31. Yam, V. W.-W.; Yang, Y.; Yang, H.-P.; Cheung, K.-K. *Organometallics* **1999**, *18*, 5252–5258.
32. Briel, O.; Sunkel, K.; Krossing, I.; Noth, H.; Schmalzlin, E.; Meerholz, K.; Brauchle, C.; Beck, W. *Eur. J. Inorg. Chem.* **1999**, 483–490.
33. Bourgault, M.; Baum, K.; Le Bozec, H.; Pucetti, G.; Ledoux, I.; Zyss, J. *New J. Chem.* **1998**, 517–522.
34. Sun, S.-S.; Robson, E.; Dunwoody, N.; Silva, A. S.; Brinn, I. M.; Lees, A. J. *Chem. Commun.* **2000**, 201–202.
35. Sun, S.-S.; Lees, A. J. *Organometallics* **2002**, *21*, 39–49.
36. Lewis, J. D.; Perutz, R. N.; Moore, J. N. *Chem. Commun.* **2000**, 1865–1866.
37. Fernandez-Acebes, A.; Lehn, J.-M. *Chem. Eur. J.* **1999**, *5*, 3285–3292.
38. Yam, V. W.-W.; Lau, V. C.-Y.; Wu, L.-X. *J. Chem. Soc., Dalton Trans.* **1998**, 1461–1468.
39. Yam, V. W.-W.; Lau, V. C.-Y.; Cheung, K.-K. *J. Chem. Soc., Chem. Commun.* **1995**, 259–261.
40. Beyeler, A.; Belser, P.; De Cola, L. *Angew. Chem. Int. Ed. Engl.* **1997**, *36*, 2779–2781.
41. Wrighton, M. S.; Morse, D. L.; Pdungsap, L. *J. Am. Chem. Soc.* **1975**, *97*, 2073–2079.
42. Itokazu, M. K.; Polo, A. S.; de Faria, D. L. A.; Bignozzi, C. A.; Murakami Iha, N. Y. *Inorg. Chim. Acta* **2001**, *313*, 149–155.
43. Argazzi, R.; Bertolasi, E.; Chiorboli, C.; Bignozzi, C. A.; Itokazu, M. K.; Murakami Iha, N. Y. *Inorg. Chem.* **2001**, *40*, 6885–6891.
44. Schanze, K. S.; Lucia, L. A.; Cooper, M.; Walters, K. A.; Ji, H.-F.; Sabina, O. *J. Phys. Chem. A* **1998**, *102*, 5577–5584.
45. Baiano, J. A.; Kessler, R. J.; Lumpkin, R. S.; Munley, M. J.; Murphy, W. R., Jr. *J. Phys. Chem.* **1995**, *99*, 17680–17690.
46. Hino, J. K.; Della Ciana, L.; Dressick, W. J.; Sullivan, B. P. *Inorg. Chem.* **1992**, *31*, 1072–1080.
47. Kalyanasundaram, K. *J. Chem. Soc., Faraday Trans. 2* **1986**, *82*, 2401–2415.
48. Schoonover, J. R.; Bignozzi, C. A.; Meyer, T. J. *Coord. Chem. Rev.* **1997**, *165*, 239–266.
49. Schoonover, J. R.; Strouse, G. F. *Chem. Rev.* **1998**, *98*, 1335–1355.
50. George, M. W.; Johnson, F. P. A.; Westwell, J. R.; Hodges, P. M.; Turner, J. J. *J. Chem. Soc., Dalton Trans.* **1993**, 2977–2979.
51. Schoonover, J. R.; Strouse, G. F.; Dyer, R. B.; Bates, W. D.; Chen, P.; Meyer, T. J. *Inorg. Chem.* **1996**, *35*, 273–274.
52. Walters, K. A.; Dattelbaum, D. M.; Ley, K. D.; Schoonover, J. R.; Meyer, T. J.; Schanze, K. S. *Chem. Commun.* **2001**, 1834–1835.
53. Chen, P.; Curry, M.; Meyer, T. J. *Inorg. Chem.* **1989**, *28*, 2271–2280.
54. Schoonover, J. R.; Chen, P.; Bates, W. D.; Dyer, R. B.; Meyer, T. J. *Inorg. Chem.* **1994**, *33*, 793–797.
55. Shaver, R. J.; Perkovic, M. W.; Rillema, D. P.; Woods, C. *Inorg. Chem.* **1995**, *34*, 5446–5454.
56. Katz, N. E.; Mecklenburg, S. L.; Graff, D. K.; Chen, P.; Meyer, T. J. *J. Phys. Chem.* **1994**, *98*, 8959–8961.
57. Chen, P.; Westmoreland, T. D.; Danielson, E.; Schanze, K. S.; Anthon, D.; Neveux, P. E., Jr.; Meyer, T. J. *Inorg. Chem.* **1987**, *26*, 1116–1126.
58. Chen, P.; Duesing, R.; Graff, D. K.; Meyer, T. J. *J. Phys. Chem.* **1991**, *95*, 5850–5858.
59. Schoonover, J. R.; Strouse, G. F.; Chen, P.; Bates, W. D.; Meyer, T. J. *Inorg. Chem.* **1993**, *32*, 2618–2619.
60. Wang, Y.; Schanze, K. *Chem. Phys.* **1993**, *176*, 305–319.
61. Wang, Y.; Hauser, B. T.; Rooney, M. M.; Burton, R. D.; Schanze, K. S. *J. Am. Chem. Soc.* **1993**, *115*, 5675–5683.
62. Wang, Y.; Lucia, L. A.; Schanze, K. S. *J. Phys. Chem.* **1995**, *99*, 1961–1968.
63. Lucia, L. A.; Wang, Y.; Nafisi, K.; Netzel, T. L.; Schanze, K. S. *J. Phys. Chem.* **1995**, *99*, 11801–11804.
64. Wang, Y.; Schanze, K. S. *J. Phys. Chem.* **1996**, *100*, 5408–5419.
65. Trammell, S.; Goodson, P. A.; Sullivan, B. P. *Inorg. Chem.* **1996**, *35*, 1421–1422.
66. Kellett, M. A.; Whitten, D. G. *J. Am. Chem. Soc.* **1989**, *111*, 2314–2316.
67. Leon, J. W.; Whitten, D. G. *J. Am. Chem. Soc.* **1993**, *115*, 8038–8043.
68. Stufkens, D. J.; Vlcek, A., Jr. *Coord. Chem. Rev.* **1998**, *177*, 127–179.
69. Rossenaar, B. D.; Stufkens, D. J.; Vlcek, A., Jr. *Inorg. Chem.* **1996**, *35*, 2902–2909.
70. Fredericks, S. M.; Luong, J. C.; Wrighton, M. S. *J. Am. Chem. Soc.* **1979**, *101*, 7415–7417.
71. Giordano, P. J.; Fredericks, S. M.; Wrighton, M. S.; Morse, D. L. *J. Am. Chem. Soc.* **1978**, *100*, 2257–2259.
72. Wallace, L.; Rillema, D. P. *Inorg. Chem.* **1993**, *32*, 3836–3843.
73. Wallace, L.; Jackman, D. C.; Rillema, D. P.; Merkert, J. W. *Inorg. Chem.* **1995**, *34*, 5210–5214.
74. Zipp, A. P.; Sacksteder, L.; Streich, J.; Cook, A.; Demas, J. N.; DeGraff, B. A. *Inorg. Chem.* **1993**, *32*, 5629–5632.
75. Leasure, R. M.; Sacksteder, L.; Nesselrodt, D.; Reitz, G. A.; Demas, J. N.; DeGraff, B. A. *Inorg. Chem.* **1991**, *30*, 3722–3728.
76. Del Guerzo, A. D.; Leroy, S.; Fages, F.; Schmehl, R. H. *Inorg. Chem.* **2002**, *41*, 359–366.
77. Juris, A.; Campagna, S.; Bidd, I.; Lehn, J.-M.; Ziessel, R. *Inorg. Chem.* **1988**, *27*, 4007–4011.
78. Ziessel, R.; Juris, A.; Venturi, M. *Inorg. Chem.* **1998**, *37*, 5061–5069.
79. Baba, A. I.; Shaw, J. R.; Simon, J. A.; Thummel, R. P.; Schmehl, R. H. *Coord. Chem. Rev.* **1998**, *171*, 43–59.
80. Schoonover, J. R.; Bates, W. D.; Meyer, T. J. *Inorg. Chem.* **1995**, *34*, 6421–6422.

Comprehensive Coordination Chemistry II
ISBN (set): 0-08-0437486

Volume 2, (ISBN 0-08-0443249); pp 731–742

2.63 Nitrosyl and Oxo Complexes of Molybdenum

J. A. McCLEVERTY and M. D. WARD
University of Bristol, UK

2.63.1 INTRODUCTION 743
2.63.2 MONONUCLEAR COMPLEXES 744
2.63.3 DINUCLEAR COMPLEXES 745
2.63.3.1 Electrochemical Behavior 745
2.63.3.2 Electronic Structure 747
2.63.4 SPECTROELECTROCHEMISTRY 749
2.63.4.1 Dinuclear Nitrosyl Dipyridyl Complexes 749
2.63.4.2 Dinuclear Oxo–Diphenolato Complexes 750
2.63.5 SPECTROSCOPIC STUDIES OF MIXED-VALENCE STATES 752
2.63.5.1 Use of IR and EPR Spectroscopy for Characterizing Mixed-valence Complexes 752
2.63.5.2 Delocalization in the Two Different Mixed-valence States of $[\{Mo(NO)Tp^*X\}_2(\mu\text{–pz})]^n$ (n=+1, −1) 753
2.63.5.3 Effects of Ligand Substitution Pattern on Mixed-valence States 754
2.63.6 MAGNETIC PROPERTIES OF DINUCLEAR MOLYBDENUM COMPLEXES 754
2.63.6.1 EPR Spectral Properties 754
2.63.6.2 Magnetic Susceptibility Studies of Nitrosyl and Oxo Complexes 755
2.63.7 CONCLUSION: CORRELATION BETWEEN MAGNETIC AND ELECTRONIC INTERACTIONS 756
2.63.8 REFERENCES 756

2.63.1 INTRODUCTION

In polynuclear complexes, an *electronic* interaction between redox-active metal fragments is manifested by a separation between metal-centered redox couples and the consequent formation of stable mixed-valence states. Such behavior is a function of the length, substitution pattern, and conformation of the bridging ligand, and arises when the odd electron or hole (depending on whether the mixed-valence state is generated by reduction or oxidation) is delocalized across the bridging ligand. *Magnetic exchange* interactions between metals in polynuclear complexes can also be dependent on the nature of the pathway linking the metal ions.[1,2] If the metal-based magnetic orbitals are sufficiently close to overlap directly, then the nature of the magnetic interaction depends on their relative symmetry,[3–6] and this has been exploited in the preparation of complexes with predictable magnetic properties.[1,2,7,8] If, however, the magnetic orbitals are too far apart to overlap directly, but require the participation of bridging ligand orbitals to mediate the interaction (a super-exchange process), then the properties of the bridging ligand become as important as they are in mediating electronic interactions. This principle has received relatively little systematic attention for metal complexes, in contrast to extensive work on organic poly-radicals in which the relationship between their magnetic properties, structure and topology has been extensively studied.[9–14]

Until recently magnetic and electronic interactions across bridging ligands in polynuclear compounds were treated quite separately, although both clearly depend on the nature of the ligand through which the interaction is transmitted. This partly reflects the fact that the complexes most often used to probe electronic interactions are based on diamagnetic fragments such as Ru^{II},[15–18] whereas studies on magnetic exchange interactions frequently involve first-row transition metals and lanthanide(III) ions in coordination environments where they do not show reversible redox interconversions.[1]

However, by development of the chemistry of the kinetically and thermodynamically stable dinuclear tris(3,5-dimethylpyrazolyl)borato molybdenum nitrosyl and oxo complexes, it has been possible to perform *combined* studies of electronic and magnetic interactions. The purpose of this case study is to illustrate how a wide variety of physical methods has been used in this area, and to show how, in these complexes, the electronic and magnetic interactions—despite being quite different phenomena—share the same relationship to the structure of the bridging ligand.

2.63.2 MONONUCLEAR COMPLEXES

The base from which the study of dinuclear species has been developed is the mononuclear species [Mo(E)(Tp*)XL] where E = NO[19] or O,[20] X = halide, and L is an anionic (phenolate, amide, halide, SR) or neutral pyridine (py) ligand. Generally, when E = NO, L is a pyridine derivative, and when E = O then L is a phenolate derivative (Figure 1). Other combinations have been prepared but these are the ones that have been most extensively studied.

The *formal* metal oxidation state in the nitrosyl complex [Mo(NO)(Tp*)Cl(py)] is I (assuming coordination by NO^+, low-spin d^5 configuration),[21,22] and in the oxo complex [Mo(O)(Tp*)-Cl(OPh)] it is V (d^1 configuration).[20,22] Both complexes are redox active. [Mo(NO)(Tp*)Cl(py)], a 17 valence-electron species, undergoes one-electron to the diamagnetic 18-electron monoanion formally containing Mo^0; and one-electron oxidation to the 16-electron Mo^{II}-containing monocation. Similarly, [Mo(O)(Tp*)Cl(OPh)] can be oxidized and reduced to the corresponding Mo^{VI} and Mo^{IV} species, respectively.

$$[Mo^0(NO)(Tp^*)Cl(py)]^- \rightleftharpoons [Mo^I(NO)(Tp^*)Cl(py)] \rightleftharpoons [Mo^{II}(NO)(Tp^*)Cl(py)]^+$$

$$[Mo^{IV}(O)(Tp^*)Cl(OPh)]^- \rightleftharpoons [Mo^V(O)(Tp^*)Cl(OPh)] \rightleftharpoons [Mo^{VI}(O)(Tp^*)Cl(OPh)]^+$$

Several factors combine to make these two metal complex units particularly useful for the combined study of electronic and magnetic interactions. First, they are relatively easily attached to a range of difunctionalized bridging ligands (bis-pyridines for the nitrosyl complexes; bis-phenolates for the oxo complexes) whose length, conformation, and topology can be varied extensively and systematically. Second, both fragments are redox active, permitting the study of electronic interactions between the metal centers by voltammetry and spectroelectrochemistry. Third, both are paramagnetic ($S = 1/2$) in their usual oxidation state, enabling the study of magnetic exchange interactions by EPR spectroscopy and susceptibility measurements; in each case (see later) the unpaired electron is in the metal d_{xy} orbital, which is correctly oriented to overlap with the π systems of aromatic bridging ligands. Finally, it is worth pointing out that the large difference in formal oxidation state (I and V) is offset by the strongly electron-withdrawing

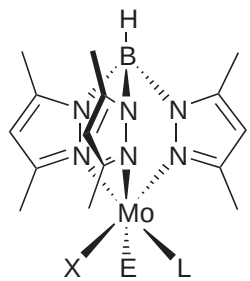

Figure 1 The core units [Mo(NO)(Tp*)X(py)] and [Mo(O)(Tp*)X(OPh)].

nature of the NO^+ ligand in the former case, and the O^{2-} ligand in the latter.[23] The electron density associated with each type of metal center is far more similar than the difference in oxidation states suggests, which partly accounts for the similarity in their redox properties.

2.63.3 DINUCLEAR COMPLEXES

Incorporation of these redox-active, paramagnetic mononuclear units into bridged dinuclear complexes is straightforward given the availability of a large number of 4,4′-dipyridyl and 4,4′-diphenolato ligands. The former link two molybdenum nitrosyl termini, e.g., [{Mo(NO)-Tp*Cl}$_2$(pyEpy)] (pyEpy = generic class of dipyridyl ligands with a spacer E) and the latter connect oxo-molybdenum groups, e.g., [{Mo(O)Tp*Cl}$_2$($OC_6H_4EC_6H_4O$)] (Figure 2). The molecular structure of the dipyridyl complex where E = $-(CH{=}CH)_4-$ (Figure 2) has been determined crystallographically.[24] The structural data reveal that the pyridine rings and the polyene chain are essentially coplanar, and that reasonably good overlap between the metal d_{xy} and pyridine π orbitals is possible. The crystal structures of numerous dinuclear oxo–Mo^V complexes with bis-phenolato bridging ligands have also been determined.[25,26]

2.63.3.1 Electrochemical Behavior

Both types of dinuclear complex are redox-active. Given that each mononuclear unit can undergo both reduction and oxidation, the dinuclear complexes are expected to undergo four redox processes linking the members of a five-membered electron transfer chain.[24,26–30] For the nitrosyl-based series, the oxidation states of the five members of the chain are

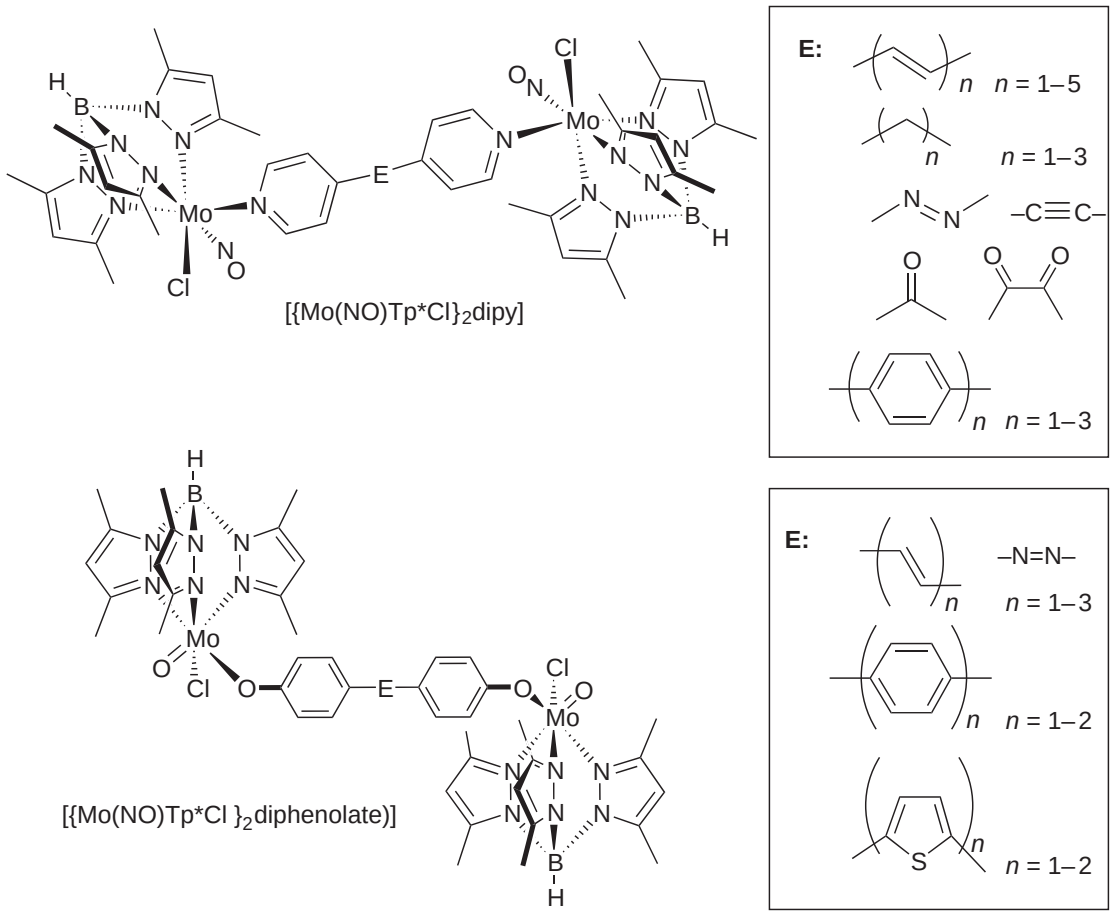

Figure 2 Dinuclear nitrosyl and oxo molybdenum complexes.

$$[Mo^0 - Mo^0]^{2-} \rightleftharpoons [Mo^0 - Mo^I]^- \rightleftharpoons [Mo^I - Mo^I] \rightleftharpoons [Mo^I - Mo^{II}]^+ \rightleftharpoons [Mo^{II} - Mo^{II}]^{2+}$$

and for the oxo-based series, the redox chain may be summarized as

$$[Mo^{IV} - Mo^{IV}]^{2-} \rightleftharpoons [Mo^{IV} - Mo^{V}]^- \rightleftharpoons [Mo^{V} - Mo^{V}] \rightleftharpoons [Mo^{V} - Mo^{VI}]^+ \rightleftharpoons [Mo^{VI} - Mo^{VI}]^{2+}$$

Despite this similarity between the two series, there is an important difference in their redox behavior. Within the $[\{Mo(NO)Tp^*Cl\}_2(dipy)]^z$ redox series ($z = -2$ to $+2$), there are two distinct and well-separated one-electron reduction processes [Mo^0/Mo^I couples, giving $z = -1$ and -2; see Figure 3a] in which the interaction between the metal centers, measured by the difference between the first and second formation potentials (ΔE_f), can be very large (e.g., 765 mV across 4,4′-bipyridine in CH_2Cl_2, corresponding to a comproportionation constant of ca. 10^{13}).[24] However, the two oxidations [Mo^I/Mo^{II} couples, giving $z = +1$ and $+2$] are essentially coincident, with their potentials so close that they cannot be separated by cyclic voltammetry, resulting in a single double-intensity wave corresponding to sequential transfer of two electrons at the same potential. For the $[\{Mo(O)Tp^*Cl\}_2(diphenolate)]^z$ redox series ($z = -2$ to $+2$, Figure 3b) the exact opposite occurs. The two reductions [Mo^{IV}/Mo^V couples, giving $z = -1$ and -2] are essentially coincident

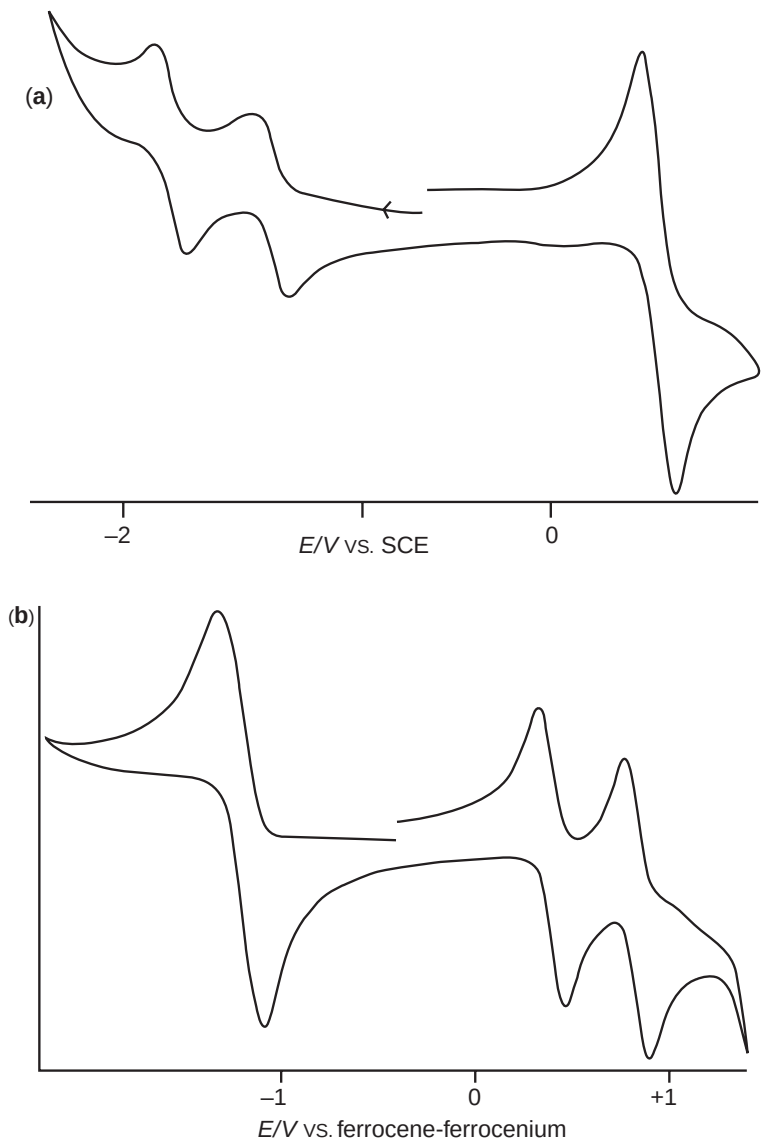

Figure 3 CVs of representative (a) $[\{Mo(NO)Tp^*Cl\}_2(dipy)]$ and (b) $[\{Mo(O)Tp^*Cl(diphenolate)]$ complexes, recorded in CH_2Cl_2 at room temperature using a Pt bead electrode and $[Bu_4N]PF_6]$ as supporting electrolyte, at a scan rate of 200 mV s^{-1}.

Table 1 Separation between first and second reduction or oxidation potentials, ΔE_f, and exchange coupling constants, J, as a function of bridging ligand.

Bridging ligand	ΔE_f[a]	J[c]	*Bridging ligand*	ΔE_f[b]	J[c]
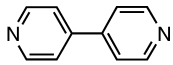	765	−33	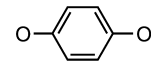	990	−80
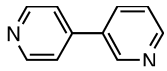	460	+0.8	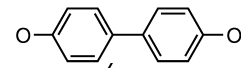	480	−13.2
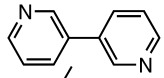	210	−1.5	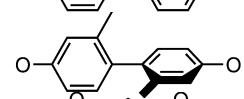	230	−2.8
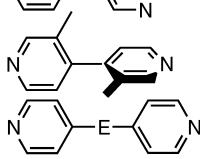	380	−3.5	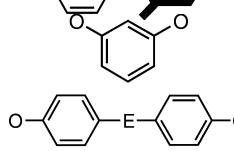	[d]	+9.8
E=HC=CH	582	−18	E=N=N	220	−12.8
E=(HC=CH)$_4$	110	−6.6	E=HC=CH	340	−3.6
			E=C≡C	350	−7.0
			E= 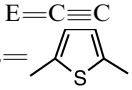	370	−12.8

[a] Separation between first and second reduction potentials, in mV; [b] separation between first and second oxidation potentials, in mV
[c] J determined using the exchange spin Hamiltonian in the form $H = -J(\mathbf{S_1S_2})$, in cm^{-1}; [d] irreversible wave; separation not detected.

and result in a single double-intensity wave, but the two oxidations [Mo^V/Mo^{VI} couples, giving $z = +1$ and $+2$] are well separated, the interactions again being substantial (990 mV across [1,4-$OC_6H_4O]^{2-}$ in CH_2Cl_2, leading to a comproportionation constant of ca. 10^{17}). The magnitudes of the separation between the Mo^0/Mo^I couples of the nitrosyl series, and between the Mo^V/Mo^{VI} couples of the oxo series, depend on the exact nature of the bridging group (see Table 1 for examples),[24,30] but all the members of each series show the same general behavior whose origin is discussed in the next section. The efficiency of the connecting group E of the bridging ligand (Figure 2) in facilitating delocalization across the complexes is thienyl > ethenyl > phenyl, the thienyl units being particularly effective in maintaining large separations between the potentials over long distances.[22,25,26,30,31]

Significantly, it is apparent that any ligand with a *meta*-substituted aromatic linker results in weaker electronic coupling (less delocalization in the mixed-valence state) than *para*-substituted analogs: the series 4,4′-, 3,4′-, and 3,3′-bipyridine is instructive in this respect.[32] This accords with the principle that delocalization is difficult across *meta*-phenylene spacers, a phenomenon which is familiar to undergraduate arrow-pushers attempting to rationalize the electronic effects of substituents on aromatic rings. We return to this point later.

2.63.3.2 Electronic Structure

To understand the electrochemical behavior, it is necessary to inspect the frontier orbitals in these nitrosyl and oxo species. First, the simple electronic structure of *mononuclear* [Mo(E)Tp*XL] species (E = NO or O) must be determined. The Mo–NO/O axis is defined as the z-axis and all other ligand donor atoms occupy the other coordinates, as shown in Figure 4.[33] In the nitrosyl complex, the NO ligand is a strong π acceptor and so the two empty NO π^* orbitals overlap with the d_{xz} and d_{yz} orbitals, thereby lowering them, but leaving the d_{xy} orbital unchanged. The configuration of the Mo^I centers is therefore $d_{xz}^2 d_{yz}^2 d_{xy}^1$. In the $\{Mo(O)Tp^*Cl\}^+$ fragment, the oxo ligand is a strong π donor, the filled oxygen p_x and p_y orbitals overlapping with the metal d_{xz} and d_{yz} orbitals, raising them but again leaving the d_{xy} orbital unchanged. The Mo^V electronic configuration is therefore $d_{xy}^1 d_{xz}^0 d_{yz}^0$. In both cases, the d_{xy} orbital (which contains the unpaired electron) is of the correct symmetry for d_π–p_π overlap with the donor atom of the phenolato or pyridine ligand.

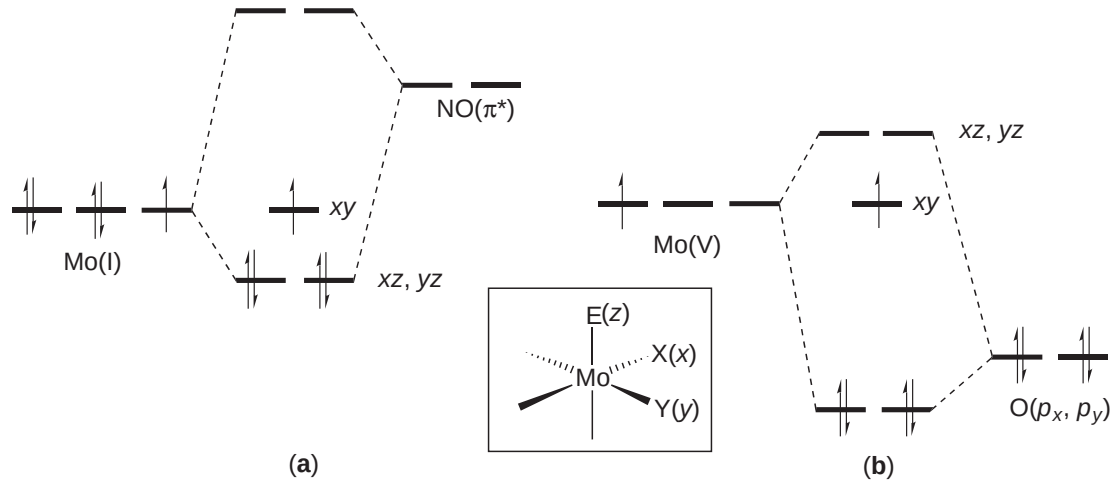

Figure 4 Ground-state electronic configurations for mononuclear complexes containing (a) {Mo(NO)Tp*Cl} bound to a pyridine ligand, and (b) $\{Mo(O)Tp^*Cl\}^+$ bound to an phenolate ligand.

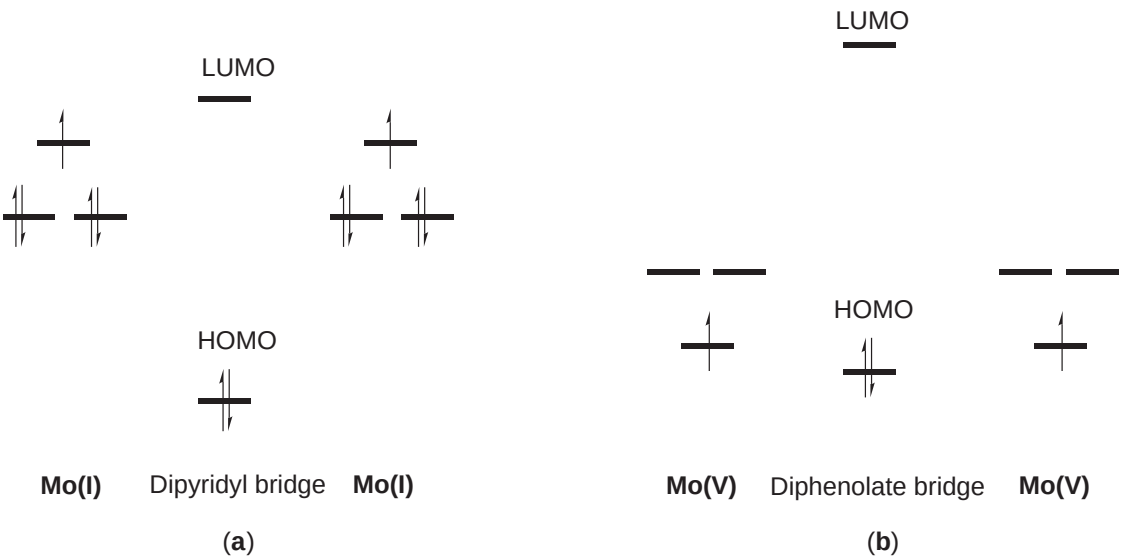

Figure 5 Qualitative MO scheme for (a) $[\{Mo(NO)Tp^*Cl\}_2(dipy)]$ and (b) $[Mo(O)Tp^*Cl\}_2(diphenolate)]$.

Using these frontier orbitals, a simple qualitative molecular orbital scheme can be constructed for the dinuclear species by including the HOMO and LUMO of the bridging ligand (Figure 5).[33] For the nitrosyl complexes, the relatively high-energy d_{xy} orbitals lie just below the low-lying π^* orbitals of the dipyridyl bridging ligand. When an electron is added to one of the d_{xy} orbitals [i.e., the first Mo^0/Mo^I couple], the resulting negative charge can delocalize effectively through the dipyridyl π^* orbital which is (i) close in energy to the d_{xy} orbital, (ii) overlapping with it, and (iii) empty, such that it can accommodate the extra electron. Thus, the reduced mixed-valence state $[Mo^0–(L)–Mo^I]^-$ is close in energy to the alternative canonical form $[Mo^I–(L^-)–Mo^I]^-$ in which the bridging ligand is reduced; this recognizes the well-documented ability of oligopyridine ligands to reduce easily.[34] The resultant delocalization of the extra electron across the bridging ligand in the mixed-valence state makes the second reduction more difficult and accounts for the large separation between the two Mo^0/Mo^I couples. In contrast, the cationic mixed-valence state (generated by removing a d_{xy} electron) cannot use the bridging ligand LUMO for delocalization of the positive hole, as this orbital is empty. To convert $[Mo^I–(L)–Mo^{II}]^+$ to the alternative canonical form $[Mo^I–(L^+)–Mo^I]^+$, which would be required for delocalization of the positive charge, requires participation of the ligand HOMO which is remote in energy from the metal d_{xy}

orbital. Accordingly, the oxidized mixed-valence state is not delocalized effectively, and the two Mo^{I}/Mo^{II} couples are metal-localized and at almost coincident potentials. In summary, it is clear from Figure 5a that the reductions of [{Mo(NO)Tp*Cl}$_2$(dipy)] are significantly bridging-ligand centered whereas the oxidations are almost completely metal-centered.

In the dinuclear oxo–Mo^{V} complexes with bis-phenolate bridges, the situation is exactly reversed (Figure 5b). The relatively low-energy d_{xy} orbitals lie just above the bridging ligand HOMO, which is relatively high in energy because of the double negative charge on this ligand. From Figure 5b it is clear that the additional positive hole in the oxidized mixed-valence state $[Mo^{V}–(L)–Mo^{VI}]^{+}$ can delocalize across the HOMO of the bridging ligand *via* the canonical form $[Mo^{V}–(L^{+})–Mo^{V}]^{+}$ in which the ligand is oxidized, such that the two Mo^{V}/Mo^{VI} couples are strongly separated. In contrast, the reduced mixed-valence state $[Mo^{IV}–(L)–Mo^{V}]^{-}$ cannot use the bridging ligand HOMO for delocalization of the negative charge because this orbital is already full. Delocalization *via* the canonical form $[Mo^{V}–(L–)–Mo^{V}]^{-}$ requires the participation of the bridging ligand LUMO, which is very high in energy. Accordingly, the Mo^{V}/Mo^{VI} couples are strongly interacting because they have a significant degree of ligand-centered character and are spatially close, whereas the Mo^{IV}/Mo^{V} couples are almost completely metal-centered and have near-coincident formation potentials. That oxidation of the diphenolato ligand could play a significant role in the description of these oxidized complexes is consistent with the known propensity of *para*-substituted diphenols to be oxidized to quinones and has important consequences for the behavior of this class of complex, particularly their electrochromic properties.[35] The doubly oxidized species, for example, could be described as either [{Mo^{VI}}–{diphenolate^{2-}}–{Mo^{VI}}] or [{Mo^{V}}–{quinone}^{0}–{Mo^{V}}] depending on the extent of the contribution to the oxidation processes from the bridging ligand.

2.63.4 SPECTROELECTROCHEMISTRY

The simple electronic considerations outlined above show that the bridging ligands play a significant role in the electrochemistry of the dinuclear species described above. This raised the question as to what extent quinonoidal forms such as those shown in Figure 6 might be involved in the reduction of the Mo^{I}–nitrosyl and the oxidation of the Mo^{V}–oxo complexes, respectively. UV/Vis/NIR spectroelectrochemistry provided useful insights into this because the electronic transitions in the two extreme canonical forms are expected to be quite different.

2.63.4.1 Dinuclear Nitrosyl Dipyridyl Complexes

As described above, these complexes are oxidized in two near-simultaneous one-electron steps, but are reduced sequentially in two well-separated one-electron processes. As the mononuclear and dinuclear nitrosyl complexes are reduced to monoanions, strong bands in the NIR region evolved.[24,36] The behavior of mononuclear [Mo(NO)Tp*Cl(py)] on reduction in dichloromethane is illustrated in Figure 7a. Of the original metal-to-ligand charge-transfer (MLCT) bands, the one at highest energy almost doubles in intensity but, more dramatically, a strong new band appears at 804 nm. This is also a Mo[d(π)] $\rightarrow$ py(π^*) MLCT absorption,[36] occurring at lower energy because the energy of the metal-centered $d\pi$ orbitals increases on reduction bringing them closer to the ligand-centered acceptor LUMO orbitals, as discussed in Section 2.63.3.2. The electron-rich nature of the Mo^{0} center accounts for the intensity of the transition which will have a high transition dipole moment. More remarkable events occur on reduction of the dinuclear species such as [{Mo(NO)Tp*Cl}$_2${py(CH=CH)$_3$py}] (Figure 7b). Very strong charge transfer bands evolve, whose intensities and vibrational fine structure are characteristic of polyene chromophores (albeit at rather lower energies than would normally be expected) which indicate substantial participation of the bridging-ligand LUMO in the reductions of this (and related) complexes.[24]

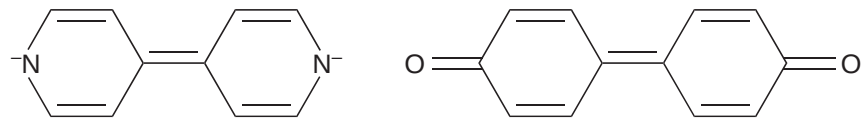

Figure 6 Quinonoidal forms of reduced 4,4-dipyridyl and oxidized 4,4′-diphenolate ligands.

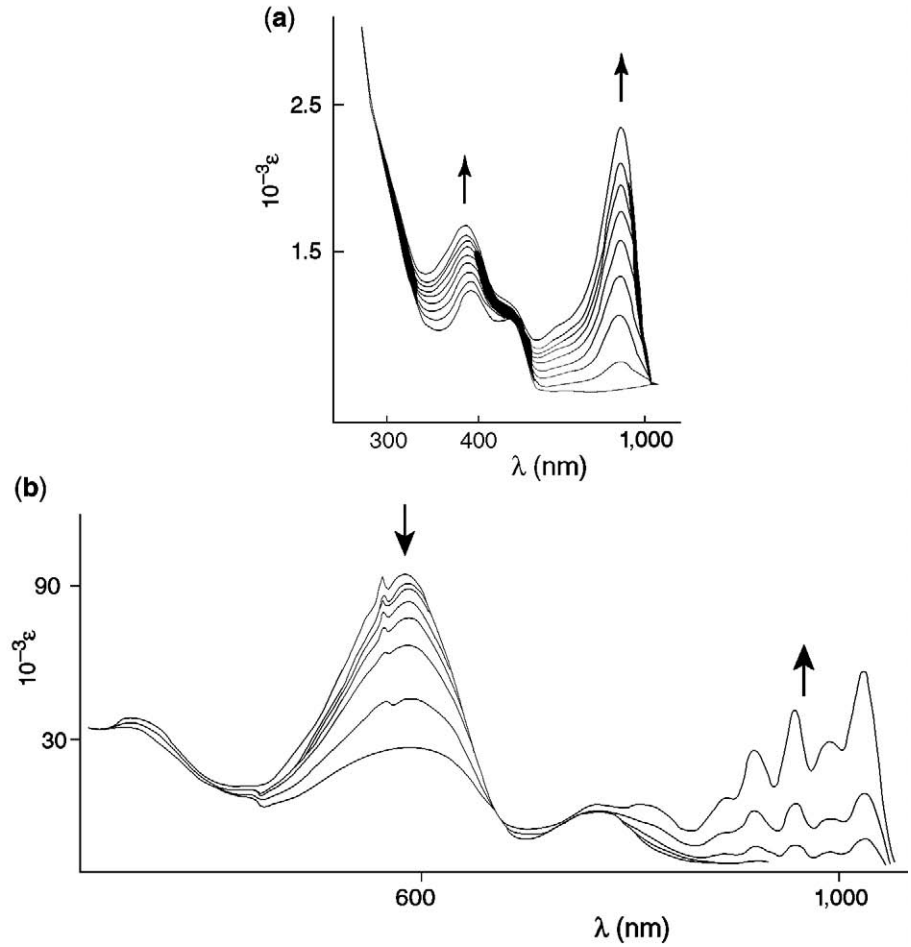

Figure 7 Spectroelectrochemistry of (a) [Mo(NO)Tp*Cl(py)] and (b) [{Mo(NO)Tp*Cl}$_2$ {py(CH=CH)$_3$py}] (ε in dm^3 mol^{-1} cm^{-1}), showing changes in electronic spectra on reduction to generate the corresponding monoanions, in CH_2Cl_2 (a) or DMF (b) at −20 °C using $[Bu_4N]PF_6$] as supporting electrolyte.

2.63.4.2 Dinuclear Oxo–Diphenolato Complexes

The complexes [{Mo(O)Tp*Cl}$_2$(diphenolate)] (Figure 2) may be oxidized sequentially to a mono- and a dication, and reduced, usually in two coincident one-electron steps, to a dianion. Spectroelectrochemical studies provided unexpected information about the nature of the oxidized species, however.[26,30] The lowest energy electronic transition in neutral mononuclear [Mo(O)Tp*Cl(OAr)] is a phenolate → Mo^{V} LMCT process, occurring in the region 500–700 nm (see Figure 8a, for a typical example). On oxidation, this evolves into two stronger peaks, one at ca. 550 nm, and the other close to the near-IR region, between 700 and 900 nm, both being assigned as phenolate → Mo^{VI} LMCT processes.

The dinuclear complexes with $\{O(C_6H_4)_nO\}^{2-}$ bridging ligands show similar behavior on oxidation, as shown in Figure 8b. On oxidation of the [Mo^{V}–Mo^{V}] form to [Mo^{V}–Mo^{VI}]$^{+}$ and then [Mo^{VI}–Mo^{VI}]$^{2+}$, an intense near-IR transition develops which was assigned on the basis of ZINDO ROHF calculations as a phenolate → Mo^{VI} LMCT transition originating from the bridging ligand, following metal-centered oxidation.[26] This is consistent with the simple orbital diagram in Figure 5b.[26,28,30] That the first two oxidations are predominantly metal-centered is to be expected, although it would only require a small change in the relative energies of ligand frontier orbitals following the first oxidation to change this picture for subsequent oxidations (see below). It is also clear that the spectra of [{Mo(O)Tp*Cl}$_2$-{O(C$_6$H$_4$)$_n$O}]$^{2+}$ are quite different from those of the related polyphenylene quinones (which would arise if the oxidations were wholly ligand-centered), whose $\pi \rightarrow \pi^*$ transitions would be much higher in energy.

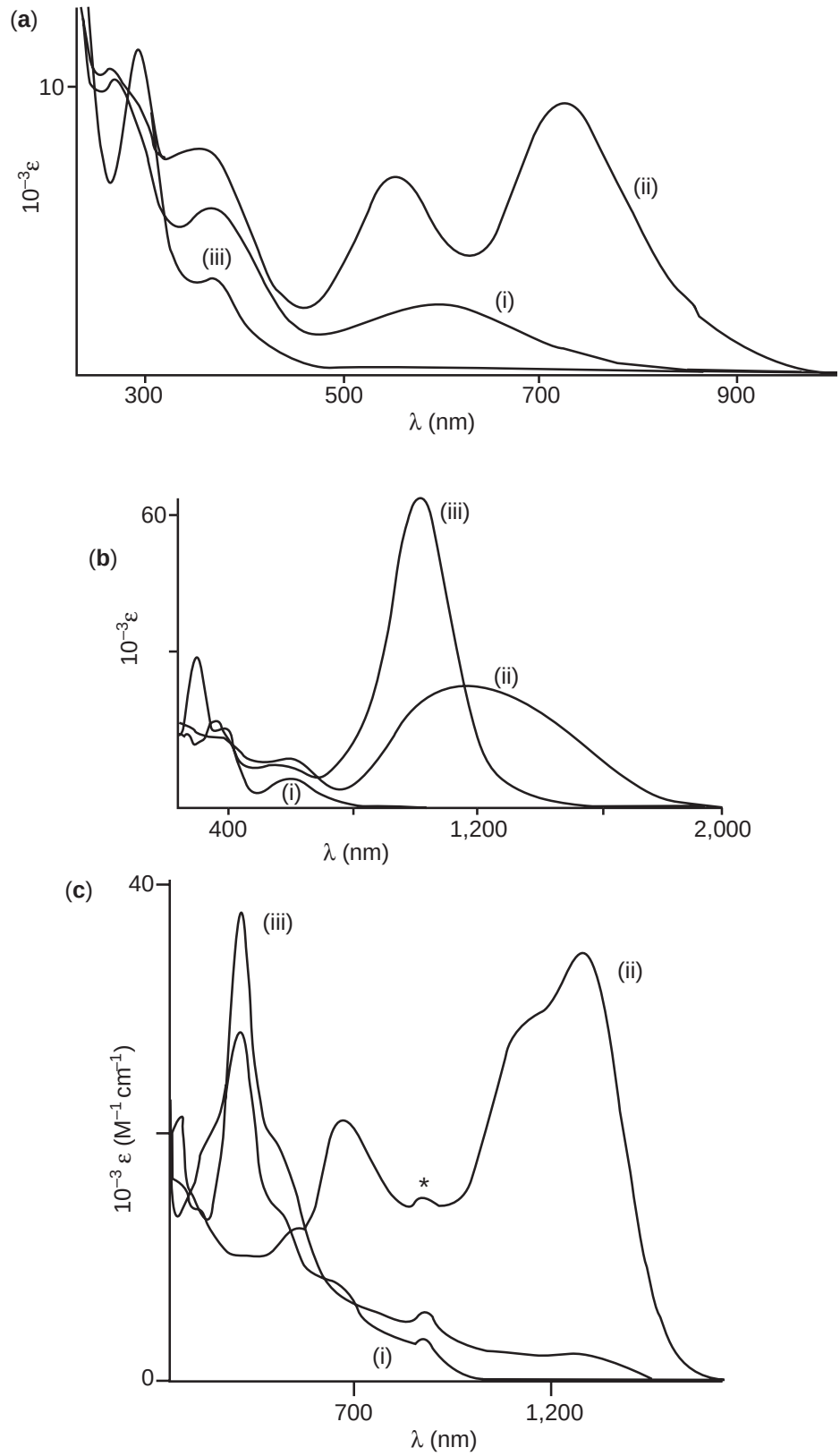

Figure 8 Electronic spectra in CH_2Cl_2 of (a) $[Mo(O)Tp^*Cl(OC_6H_4OMe\text{–}p)]^{n+}$ ($n = 0$, 1); (b) $[\{Mo(O)Tp^*Cl\}_2\{O(C_6H_4)_3O\}]^{n+}$ ($n = 0$, 1, 2); and (c) $[\{Mo(O)Tp^*Cl\}_2(OC_6H_4N{=}NC_6H_4O]^{n+}$ ($n = 0$, 1, 2) (ε in $dm^3\ mol^{-1}\ cm^{-1}$) (i) neutral species, (ii) monocation, (iii) dication.

The spectroelectrochemical behavior of [{Mo(O)Tp*Cl}$_2$($OC_6H_4N{=}NC_6H_4O$)] (Figure 8c) is, however, quite different.[30] The spectrum of the mono-oxidized form [Mo^V–Mo^{VI}]$^+$ exhibits an absorption maximum at $\lambda_{max} = 1{,}268$ nm, strongly characteristic of a phenolato → Mo^{VI} LMCT process following metal-centered oxidation. However, following the second oxidation this NIR absorption is replaced by a quite different absorption at $\lambda_{max} = 409$ nm, characteristic of the $\pi \rightarrow \pi^*$ transition of a bridging quinone. According to these spectra the sequence of events during the oxidations is [Mo^V–(diphenolate^{2-})–Mo^V] → [Mo^V–(diphenolate^{2-})–Mo^{VI}]$^+$ → [Mo^V–(quinone)–Mo^V]. ZINDO calculations on this and closely related species are broadly consistent with this view, and a variety of other bis-phenolate bridging ligands show similar behavior.[30]

So, the oxidative behavior of [{Mo(O)Tp*Cl}$_2${$O(C_6H_4)_nO$}] is significantly different from that of [{Mo(O)Tp*Cl}$_2$($OC_6H_4N{=}NC_6H_4O$)] as a result of an internal charge redistribution associated with the second oxidation; one-electron oxidation of [Mo^{VI}–(diphenolate^{2-})–Mo^V]$^+$ affords [Mo^{VI}–(diphenolate^{2-})–Mo^{VI}]$^{2+}$ with the former, but [Mo^V–(quinone)–Mo^V]$^{2+}$ with the latter. Such internal charge redistribution is well known, occurring in dithiolene, catecholato, bipyridyl, and nitrosyl complexes. This behavior is sometimes referred to as "non-innocence" and occurs in complexes in which the metal *and* at least one ligand is capable of redox behavior, and when significant mixing of metal-based and ligand-based frontier orbitals, which are very close in energy, is possible.[37] The presence of ligand participation in the oxidation processes agrees with the large separation between the potentials of the two "Mo^V/Mo^{VI}" couples, as outlined above.

2.63.5 SPECTROSCOPIC STUDIES OF MIXED-VALENCE STATES

A combination of electrochemistry, and EPR and IR spectroscopy proved ideal for examining mixed-valence states in several of the dinuclear complexes. Two issues are highlighted here: (i) the different properties of the two mixed-valence states (one generated by oxidation, one by reduction) for the complex [{Mo(NO)Tp*Br}$_2$(μ–pz)] (pz = pyrazine),[38] and (ii) the effect of ligand substitution pattern (*o*, *m*, or *p*-diamidobenzene) in the series of complexes [{Mo^{II}(NO)Tp*X}$_2$ {μ–$C_6H_4(NH)_2$}].[39]

2.63.5.1 Use of IR and EPR Spectroscopy for Characterizing Mixed-valence Complexes

Before the above-mentioned cases are discussed it will be helpful to explain what the IR and EPR spectra of the mixed-valence complexes could show. For IR, the strong nitrosyl stretching vibration in the 1,600–1,700 cm^{-1} region provides a convenient probe of the electron density at the metal center, since it is susceptible to the effects of back-bonding in the same way as carbonyl ligands. A mixed-valence state such as Mo^I/Mo^0 or Mo^{II}/Mo^I that is localized on the IR timescale (ca. 10^{-13} s) will show two distinct NO stretching vibrations, assignable to the inequivalent metal termini; a mixed-valence state that is delocalized on the IR timescale will show a single NO stretching vibration at an intermediate, averaged position.

The EPR spectra of molybdenum complexes frequently provide useful information from the pattern of hyperfine coupling, arising from those Mo nuclei with I (nuclear spin) >0. While ca. 75% of the isotopes of molybdenum have $I = 0$, the remaining 25% have $I = 5/2$ and give coupling constants similar to one another as they have almost the same nuclear magnetic moments. The EPR spectrum of a mononuclear molybdenum complex having one unpaired electron therefore consists of a singlet (75% of the total intensity) superimposed on a sextet (25% of the total intensity) at the same g value. For the oxo–Mo^V and nitrosyl–Mo^I complexes discussed here, the hyperfine coupling constant A_{Mo} is ca. 5.0 mT.[33] A mixed-valence complex in which the unpaired electron is localized on the EPR timescale (ca. 10^{-9} s) will therefore give an EPR spectrum identical to that of simple mononuclear complexes. However, if the unpaired electron is delocalized between both metal centers on the EPR timescale, the spectrum is more complicated due to coupling of the spin to both Mo nuclei with all their different nuclear spin combinations. It will consist of a singlet ($I = 0$, $I = 0$ nuclear spin combination, 56% probability), a 1:1:1:1:1:1 sextet ($I = 5/2$, $I = 0$, 38%) and a 1:2:3:4:5:6:5:4:3:2:1 undecet ($I = 5/2$, $I = 5/2$, 6%) superimposed on each other, with the hyperfine coupling constant halved to ca. 2.5 mT. Examples of the two types of spectrum are shown in Figure 9; although not all the components are completely resolved, especially in the delocalized case where the coupling constant is halved, the two types of spectrum are clearly distinguishable.

2.63.5.2 Delocalization in the Two Different Mixed-valence States of $[\{Mo(NO)Tp^*X\}_2(\mu\text{–pz})]^n$ ($n = +1, -1$)

$[\{Mo(NO)Tp^*Br\}_2(\mu\text{–pz})]^n$ is a five-membered redox chain, with four redox processes [formally, two Mo^0/Mo^I couples and two Mo^I/Mo^{II} couples] giving species with $n = -2, -1, 0, +1, +2$. For the reasons outlined above, the separation between the two Mo^0/Mo^I couples (1,440 mV) is much larger than the separation between the two Mo^I/Mo^{II} couples (110 mV).[38] Although the comproportionation constant for the cationic mixed-valence state is quite small it is still large enough to permit this species to be formed, and both the cationic and anionic mixed-valence states ($n = -1, +1$) could be generated chemically by one-electron reduction or oxidation of the starting complex.

The EPR spectrum of $[\{Mo(NO)Tp^*Br\}_2(\mu\text{–pz})]^-$ gives a "delocalized" EPR spectrum (cf. Figure 9b), indicating delocalization of the unpaired electron over the pyrazine bridge on the EPR time scale (i.e., an exchange rate for delocalization of $>10^9\,s^{-1}$). Further, the IR spectrum showed a single NO stretching vibration at 1,585 cm^{-1} (cf. 1,626 cm^{-1} for neutral $[\{Mo(NO)Tp^*Br\}_2(\mu\text{–pz})]$); the shift of this vibration to lower energy arises from greater back-bonding from the more electron-rich metal centers. The presence of a single stretching vibration means that the electron exchange is fast even on the IR timescale (exchange rate $>10^{13}\,s^{-1}$). In contrast, the EPR spectrum of the oxidized mixed-valence state $[\{Mo(NO)Tp^*Br\}_2(\mu\text{–pz})]^+$ showed a "localized" EPR spectrum (cf. Figure 9a), implying that any delocalization is occurring with an exchange rate of less than $10^9\,s^{-1}$. In agreement with this the IR spectrum of $[\{Mo(NO)Tp^*X\}_2(pz)]^+$ showed two distinct NO stretching bands at 1,717 and 1,608 cm^{-1}, assignable to localized Mo^{II} and Mo^I fragments.

The behavior of this complex is entirely consistent with the MO picture in Figure 5a, which predicts that substantial delocalization will occur across the bridging ligand in the reduced mixed-valence state but not in the oxidized mixed-valence state. The combined use of IR and EPR spectroscopy to study these complexes was particularly helpful as it provided information on time scales. In contrast, UV/Vis/NIR spectroscopy was not so helpful in these cases as the expected IVCT transitions were obscured by other strong charge-transfer bands.

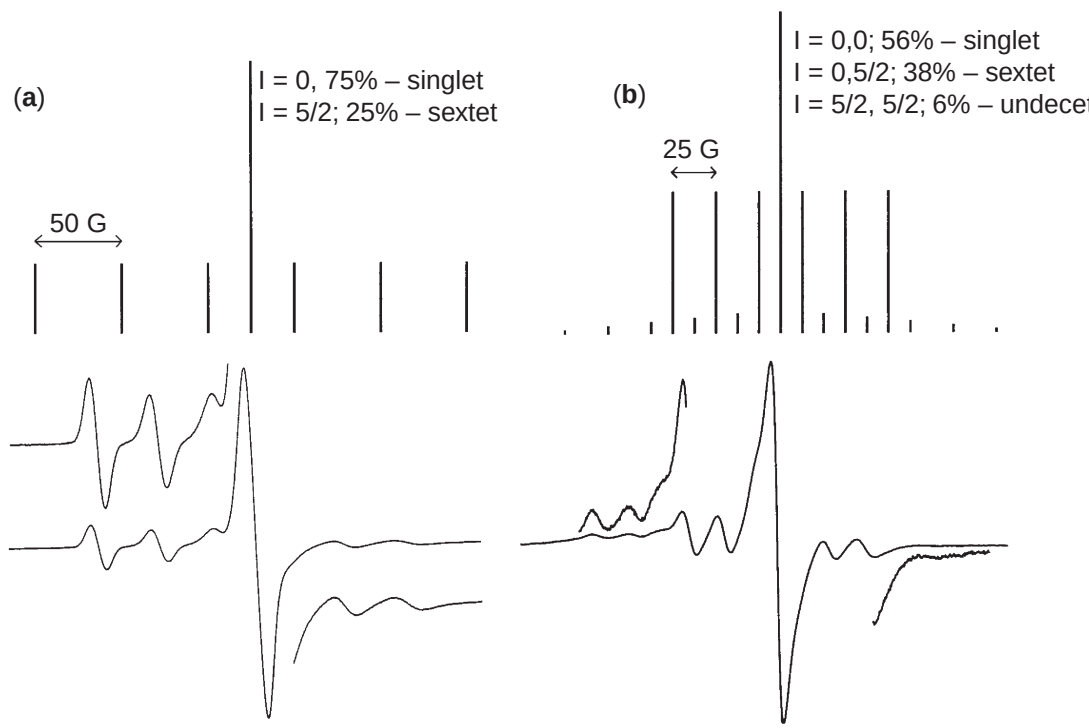

Figure 9 Typical EPR spectra of (a) a mononuclear Mo complex with one unpaired electron, showing hyperfine coupling to one metal centre; (b) a dinuclear mixed-valence complex in which the single unpaired electron is coupled equally to both Mo nuclei due to delocalization; recorded at 300 K in CH_2Cl_2 solution.

2.63.5.3 Effects of Ligand Substitution Pattern on Mixed-valence States

In the three complexes [{Mo^{II}(NO)Tp*X}$_2$(μ–$C_6H_4(NH)_2$)], two nitrosyl-Mo^{II} centers are linked by *o*-, *m*-, or *p*-diamidobenzene as bridging ligand.[39] The Mo^{II} centers (formally 16 valence-electron) have the low-spin d^4 configuration $d_{xz}^2 d_{yz}^2 d_{xy}^0$ and are accordingly diamagnetic; they undergo reversible reduction to Mo^{I} at negative potentials, with the dinuclear complexes each showing two well-separated Mo^{I}/Mo^{II} couples. The redox potentials of the three complexes are in Table 2; it will be apparent that the redox splitting is less across the *meta*-substituted bridge than across the other two, as mentioned earlier. Nevertheless the splittings are sufficiently large in each case for the anionic Mo^{II}/Mo^{I} mixed-valence state to be generated by chemical reduction using cobaltocene, which is a strong enough reductant to effect the first reduction but not the second.

The complexes with *o*- and *p*-$[C_6H_4(NH)_2]^{2-}$ as bridging ligands both gave a "delocalized" EPR spectrum (Figure 9b) in solution at room temperature, but showed two distinct NO stretching frequencies characteristic of distinct Mo^{I} and Mo^{II} centers in their IR spectra. From the different information provided by the two techniques we can bracket the timescale for electron delocalization; the unpaired electron must be exchanging at a rate faster than $10^9\,s^{-1}$ (hence, delocalized by EPR spectroscopy) but less than $10^{13}\,s^{-1}$ (hence, localized by IR spectroscopy). In contrast, the complex with the *meta*-substituted bridging ligand gave a "localized" EPR spectrum (Figure 9a) (and is also necessarily localized according to its IR spectrum). Thus, the poorer delocalization across the *meta*-substituted bridging ligand—which is apparent from the separations between successive Mo^{I}/Mo^{II} couples in the cyclic voltammograms—results in a decrease in the electron exchange rate such that it is now slow on the EPR timescale. Again, in these complexes it was not possible to study the IVCT transitions by electronic spectroscopy because they were obscured by much more intense low-energy charge-transfer transitions.

2.63.6 MAGNETIC PROPERTIES OF DINUCLEAR MOLYBDENUM COMPLEXES

2.63.6.1 EPR Spectral Properties

The occurrence of magnetic exchange between the two unpaired spins in the dinuclear nitrosyl–Mo^{I} complexes was initially apparent from their EPR spectra which, with a wide variety of dipyridyl bridging ligands, looked like that in Figure 9b arising from hyperfine coupling to two Mo centers.[24,27,33] In a mixed-valence complex this denotes delocalization of the single unpaired electron, but in an *isovalent* complex with *two* unpaired electrons it arises because of a magnetic exchange interaction between the electron spins localized on individual metal centers, such that $|J| \gg A_{Mo}$, where J is the energy of the exchange interaction and A_{Mo} is the energy of the electron–nuclear hyperfine interactions (ca. $0.01\,cm^{-1}$ in these complexes).[40,41] An "exchange-coupled" spectrum of this sort will arise as long as the magnitude of the exchange interaction, irrespective of its sign, is above this extremely small lower limit. Such exchange-coupled spectra are well-

Table 2 Seperation between first and second reduction potentials, ΔE_f, obtained from the isomers of [Mo(NO)Tp*Cl$_2$(μ–$C_6H_4(NH)_2$)].

Complex	ΔE_f (mV)
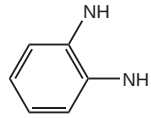	778
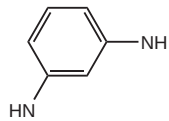	371
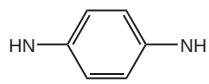	917

documented in nitroxide di-radicals, where coupling of both electrons to both nitrogen nuclear spins occurs, even across saturated spacers where there is no possibility of physical delocalization of the electrons.[40,41] Similar spectra were obtained for the dinuclear oxo–Mo^{V} complexes containing bis-phenolate bridging ligands, for the same reason.[28] Accordingly, the exchange coupling constants for several members of both series of dinuclear complexes were determined from variable-temperature susceptibility measurements.[30,32,42,43]

2.63.6.2 Magnetic Susceptibility Studies of Nitrosyl and Oxo Complexes

Some data resulting from the magnetic measurements are collected in Table 1; a negative sign for J indicates antiferromagnetic coupling and a positive sign indicates ferromagnetic coupling.

The results obtained from the dipyridyl-bridged NO–Mo^{I} complexes show that there is an alternation in the sign of J as the bridging ligand substitution pattern changes from 4,4′ through 4,3′ to 3,3′, for both the bipyridyl and bis(pyridyl)ethene ligand series;[32] i.e., the sign of the exchange interaction alternates between antiferromagnetic and ferromagnetic as the number of atoms in the pathway between the interacting spins alternates between even and odd. This is only consistent with a spin-polarization mechanism for propagation of the exchange interaction, as shown in Figure 10. In this model, the unpaired electron on one Mo atom results in a small induced spin in the opposite sense of the electron cloud on the adjacent atom; the effect is propagated through the bridging ligand, with the induced spins alternating, and this ultimately controls the direction of spin of the unpaired electron on the second metal center. A necessary consequence of this is that *para*-substituted bridging ligands (with an even number of atoms in the bridging pathway) give antiferromagnetic coupling as long as spin-polarization is the dominant exchange mechanism, whereas *meta*-substituted bridging ligands (with an odd number of atoms in the bridging pathway, whichever route is taken across the bridging ligand) give ferromagnetic coupling. Exactly similar behavior is seen for the oxo–Mo^{V} complexes, where the complex containing the dianion of 1,4-dihydroxybenzene as bridging ligand is antiferromagnetically coupled, but the 1,3-isomer is ferromagnetically coupled (Figure 10).[42] The principle extends to trinuclear complexes; for example, in $[\{Mo(O)Tp^{*}Cl\}_3(\mu^3\text{–}1,3,5\text{-}C_6H_3O_3)]$ each oxo–Mo^{V} unit shares a *meta*-substituted relationship with the other two due to the structure of the bridging ligand (the trianion of 1,3,5-trihydroxybenzene). This complex accordingly has an $S = 3/2$ ground state with all three electrons ferromagnetically coupled.[42]

A note of caution is, however, appropriate. When metal centers are close together, the angular relationship between the magnetic orbitals can be significant. This means that exchange coupling may be influenced not only by the topology of the bridging ligand but also by the relative

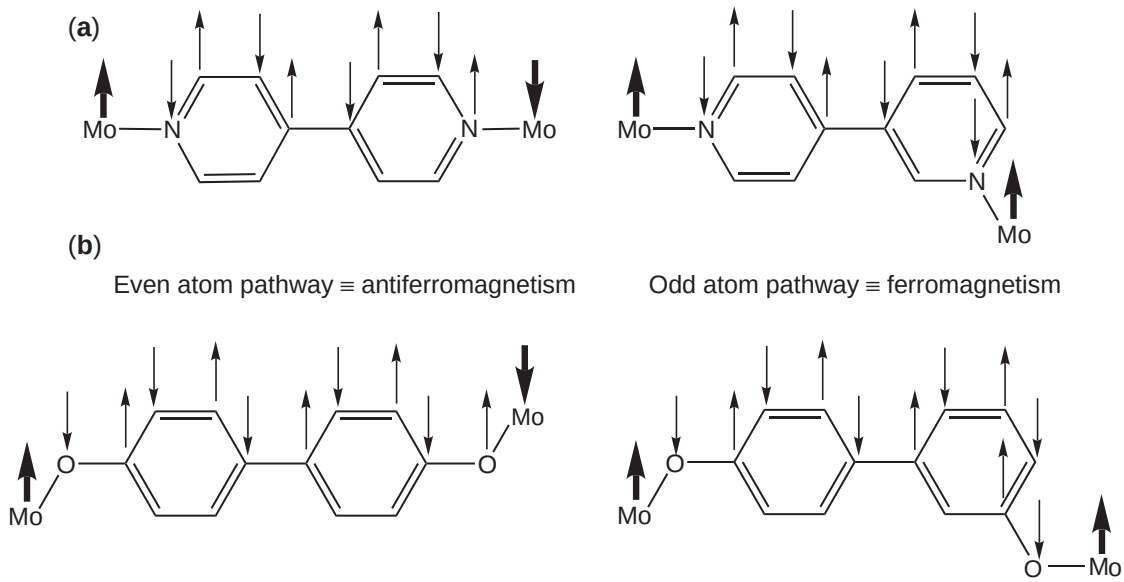

Figure 10 The spin-polarisation mechanism over (a) 4,4′- and 3,4′-dipyridyl bridging ligands; and (b) 4,4′- and 4,3′-$[OC_6H_4C_6H_4O]^{2-}$ bridging ligands.

orientation of the two {Mo(E)Tp*X} (E = NO or O, X = halide) moieties with respect to the bridging ligand.[44] Thus, spin polarization may not be the dominant mechanism determining spin–spin coupling, although in all the cases we studied, it provided a reliable prediction of the sign of J.

The results in Table 1 also show that J is dependent on the conformation of the bridging ligand.[42] Comparing the data obtained from the 4,4′-dipyridyl-bridged complex, where there is a twist of ca. 26° between the two pyridine rings) with that from the 3,3′-dimethyl-4,4′-dipyridyl analog (where the twist is 90°) it is clear that the magnitude of J decreases by about 90% as the two halves of the bridging ligand become orthogonal. Conversely, when the bridging ligand is constrained to be planar (3,8-phenanthroline) the value of J increases to $-36\,cm^{-1}$. Comparison of the dinuclear oxo–Mo^{V} complexes based on 4,4′-biphenol ($J = -13\,cm^{-1}$) and 2,2′-dimethyl-4,4′-biphenol ($J = -2.8\,cm^{-1}$) gives a similar result. This is further evidence, if any is needed, that the spin-polarization mechanism is propagated via the delocalized π system of the bridging ligand.

2.63.7 CONCLUSION: CORRELATION BETWEEN MAGNETIC AND ELECTRONIC INTERACTIONS

The previous sections have shown how (i) the strength of the electronic interaction between the metal centers is dependent on the structure of the bridging ligand, with *para*-substituted bridging ligands giving more effective electronic delocalization than *meta*-substituted ones; and (ii) the sign of the magnetic interaction is also dependent on the structure of the bridging ligand, with *para*-substituted bridging ligands giving antiferro-magnetic coupling and *meta*-substituted ones giving ferromagnetic coupling. Thus the two types of interaction are correlated with one another even though they have different mechanisms and energies. The electronic interaction is related to delocalization of an unpaired electron or hole in a *mixed-valence* state; although we have not calculated coupling constants V_{ab} for our complexes as the IVCT transitions are usually obscured, values of V_{ab} in strongly interacting complexes are typically hundreds or thousands of cm^{-1}.[15–18] In contrast, the magnetic interaction (in an *isovalent* state) is based on the ability of an unpaired electron to polarize the adjacent electron cloud and, as we have seen, typically has a magnitude of a few cm^{-1} in the same complexes. Nevertheless, the two phenomena are correlated because those structural properties of the bridging ligand responsible for effective delocalization are also responsible for antiferromagnetic coupling; conversely, those structural properties that inhibit delocalization are also responsible for ferromagnetic coupling. These considerations have been extended successfully to more topologically complex bridging ligands such as the various isomers of dihydroxynaphthalene.[45]

2.63.8 REFERENCES

1. Kahn, O. *Molecular Magnetism*, VCH Publishers: New York 1993.
2. Bushby, R. J.; Paillaud, J.-L.; Molecular Magnets, in Petty, M. C.; Bryce, M. R.; Bloor, D., Eds.; *Introduction to Molecular Electronics*, Edward Arnold: London, 1995, pp 72–91.
3. Goodenough, J. B. *Phys. Rev.* **1955**, *100*, 564–573.
4. Goodenough, J. B. *J. Phys. Chem. Solids* **1958**, *6*, 287–297.
5. Kanamori, J. *J. Phys. Chem. Solids* **1959**, *10*, 87–98.
6. Ginsberg, A. P. *Inorg. Chim. Acta Rev.* **1971**, *5*, 45–68.
7. Kahn, O. *Struct. Bonding* **1987**, *68*, 89–167.
8. Gordon-Wylie, S. W.; Bominaar, E. L.; Collins, T. J.; Workman, J. M.; Claus, B. L.; Patterson, R. E.; Williams, S. A.; Conklin, B. J.; Yee, G. T.; Weintraub, S. T. *Chem. Eur. J.* **1995**, *1*, 528–537.
9. Miller, J. S.; Epstein, A. J. *Angew. Chem., Int. Ed. Engl.* **1994**, *33*, 385–415.
10. Iwamura, H. *Pure Appl. Chem.* **1993**, *65*, 57–64.
11. Rajca, S. *Chem. Rev.* **1994**, *94*, 871–893.
12. Rajca, S.; Rajca, A. *J. Am. Chem. Soc.* **1995**, *117*, 9172–9179.
13. Yoshizawa, K.; Hoffman, R. *Chem. Eur. J.* **1995**, *1*, 403–413.
14. Iwamura, H.; Koga, N. *Acc. Chem. Res.* **1993**, *26*, 346–351.
15. Ward, M. D. *Chem. Soc. Rev.* **1995**, *24*, 121.
16. Reimers, J. R.; Hush, N. S. *Inorg. Chem.* **1990**, *29*, 3686.
17. Ribou, A.-C.; Launay, J.-P.; Sachtleben, M. L.; Li, H.; Spangler, C. W. *Inorg. Chem.* **1996**, *35*, 3735.
18. Demadis, K. D.; Hartshorn, C. M.; Meyer, T. J. *Chem. Rev.* **2001**, *101*, 2655–2685.
19. McCleverty, J. A.; Seddon, D.; Bailey, N. A.; Walker, N. W. *J. Chem. Soc., Dalton Trans.* **1976**, 898–908.
20. Chang, C. S. J.; Enemark, J. H. *Inorg. Chem.* **1991**, *30*, 683–688.
21. Enemark, J. H.; Feltham, R. D. *Coord. Chem. Rev.* **1974**, *13*, 339–406.
22. McCleverty, J. A.; Ward, M. D.; Jones, C. J. *Comments Inorg. Chem.* **2001**, *22*, 293–326.
23. Westcott, B. L.; Enemark, J. H. *Inorg. Chem.* **1997**, *36*, 5404–5405.

24. McWhinnie, S. L. W.; Thomas, J. A.; Hamor, T. A.; Jones, C. J.; McCleverty, J. A.; D. Collison, Mabbs, F. E.; Harding, C. J.; Yellowlees, L. J.; Hutchings, M. G. *Inorg. Chem.* **1996**, *35*, 760–774.
25. Ung, V. Â.; Bardwell, D. A.; Jeffery, J. C.; Maher, J. P.; McCleverty, J. A.; Ward, M. D.; Williamson, A. *Inorg. Chem.* **1996**, *35*, 5290–5299.
26. Harden, N. C.; Humphrey, E. R.; Jeffery, J. C.; Lee, S.-M.; Marcaccio, M.; McCleverty, J. A.; Rees, L. H.; Ward, M. D. *J. Chem. Soc., Dalton Trans.* **1999**, 2417–2426.
27. Das, A.; Maher, J. P.; McCleverty, J. A.; Navas Badiola, J. A.; Ward, M. D. *J. Chem. Soc., Dalton Trans.* **1993**, 681–686.
28. Ung, V. Â.; Bardwell, D. A.; Jeffery, J. C.; Maher, J. P.; McCleverty, J. A.; Ward, M. D.; Williamson, A. *Inorg. Chem.* **1996**, *35*, 5290–5299.
29. McDonagh, A. M.; Ward, M. D.; McCleverty, J. A. *New J. Chem.* **2001**, *25*, 1236–1243.
30. Bayly, S. R.; Humphrey, E. R.; de Chair, H.; Paredes, C. G.; Bell, Z. R.; Jeffery, J. C.; McCleverty, J. A.; Ward, M. D.; Totti, F.; Gatteschi, D.; Courric, S.; Steele, B. R.; Screttas, C. G. *J. Chem. Soc., Dalton Trans.* **2001**, 1401–1414.
31. Hock, J.; Cargill Thompson, A. M. W.; McCleverty, J. A.; Ward, M. D. *J. Chem. Soc., Dalton Trans.* **1996**, 4257–4263.
32. Cargill Thompson, A. M. W.; Gatteschi, D.; McCleverty, J. A.; Navas Badiola, J. A.; Rentschler, E.; Ward, M. D. *Inorg. Chem.* **1996**, *35*, 2701–2703.
33. McCleverty, J. A.; Ward, M. D. *Acc. Chem. Res.* **1998**, *31*, 842–851.
34. Kemp, W. In *Organic Spectroscopy*; Macmillan: London, 1979; p 154.
35. McDonagh, A. M.; Bayly, S. R.; Riley, D. J.; Ward, M. D.; McCleverty, J. A.; Cowin, M. A.; Morgan, C. N.; Varrazza, R.; Penty, R. V.; White, I. H. *Chem. Mater.* **2000**, *123*, 2523–2524.
36. Kowallick, R.; Jones, A. N.; Reeves, Z. R.; Jeffery, J. C.; McCleverty, J. A.; Ward, M. D. *New J.Chem.* **1999**, *23*, 915–921.
37. Ward, M. D.; McCleverty, J. A. *J. Chem. Soc., Dalton Trans.* **2002**, 275–288, and references therein.
38. Wlodarczyk, A.; Doyle, G. A.; Maher, J. P.; McCleverty, J. A.; Ward, M. D.; Thomas, J. A.; Jones, J. C. *J. Chem. Soc., Chem. Commun.* **1997**, 769–770.
39. Wlodarczyk, A.; Maher, J. P.; McCleverty, J. A.; Ward, M. D. *J. Chem. Soc., Dalton Trans.* **1997**, 3287–3298.
40. Reitz, D. C.; Weissman, S. I. *J. Chem. Phys.* **1960**, *33*, 700.
41. Brière, R.; Dupeyre, R.-M.; Lemaire, H.; Morat, C.; Raassat, A.; Rey, P. *Bull. Soc. Chim. Fr.* **1965**, *34*, 4828.
42. Ung, V. Â.; Cargill Thompson, A. M. W.; Bardwell, D. A.; Gatteschi, D.; .Jeffery, J. C.; McCleverty, J. A.; Totti, F.; Ward, M. D. *Inorg. Chem.* **1997**, *36*, 3447–3454.
43. Ung, V. Â.; Couchman, S.; Jeffery, J. C.; McCleverty, J. A.; Ward, M. D.; Totti, F.; Gatteschi, D. *Inorg. Chem.* **1999**, *38*, 365–369.
44. Bencini, A.; Gatteschi, D.; Totti, F.; Sanz, D. N.; McCleverty, J. A.; Ward, M. D. *J. Phys. Chem. A* **1998**, *102*, 10545–10551.
45. Bayly, S.; McCleverty, J. A.; Ward, M. D.; Gatteschi, D.; Totti, F. *Inorg. Chem.* **2000**, *39*, 1288–1293.

Comprehensive Coordination Chemistry II
ISBN (set): 0-08-0437486

Volume 2, (ISBN 0-08-0443249); pp 743–757

2.64
Structure of Oxo Metallic Clusters

R. J. ERRINGTON
University of Newcastle-upon-Tyne, UK

2.64.1 INTRODUCTION 759
2.64.2 A HYDROLYTIC STRATEGY FOR NONAQUEOUS HEXAMETALATE SYNTHESIS 759
2.64.3 NONAQUEOUS POLYOXOMETALATE REACTIVITY 763
2.64.3.1 Alkoxide Exchange 763
2.64.3.2 Aryloxide and Other Derivatives 765
2.64.3.3 Hydrolysis 765
2.64.3.4 Oxo Metathesis 765
2.64.3.5 Base Degradation 766
2.64.3.6 Polyoxometalates as Nucleophiles 767
2.64.4 CHARACTERIZATION 769
2.64.4.1 Hexametalates 769
2.64.4.2 Derivatives Based on the Keggin Structure 771
2.64.5 CONCLUSIONS 772
2.64.6 REFERENCES 772

2.64.1 INTRODUCTION

The field of polyoxometalate chemistry continues to expand and diversify, and whilst the majority of chemistry in this area is still carried out in aqueous media, interest in nonaqueous and solid state systems and in the incorporation of polyoxometalates at interfaces (liquid–liquid, liquid–air and solid–air) is growing rapidly.[1–3] The complex, pH-dependent equilibria associated with aqueous polyoxometalate chemistry have been studied in detail and several families of structures and related derivatives are now well established. Speciation in nonaqueous solutions is often markedly different, and in organic solvents the choice of reagents for reactivity studies need not be restricted by hydrolytic sensitivity. Tetraalkylammonium cations impart organic solubility to these molecular metal oxides, and nonaqueous studies generally involve $Bu^n_4N^+$ salts in polar solvents such as MeCN (acetonitrile). The rational syntheses of a series of hexametalates presented in Section 2.64.2 serve to illustrate various nonaqueous aggregation strategies that use moisture-sensitive precursors, whilst reactions that enable the systematic manipulation of structure and surface functionality are discussed in Section 2.64.3. Techniques for studying the structural and electronic properties of polyoxometalates are highlighted in Section 2.64.4 with reference to selected examples from the previous sections.

2.64.2 A HYDROLYTIC STRATEGY FOR NONAQUEOUS HEXAMETALATE SYNTHESIS

In the synthesis of a general polyoxometalate $[X_xM_yO_z]^{n-}$, where X is a heteroelement, starting materials are selected so as to provide the various constituent parts, i.e., the metal oxide, the anionic charge, and (for heteropolyanions) the heteroelement oxide. In recent years,

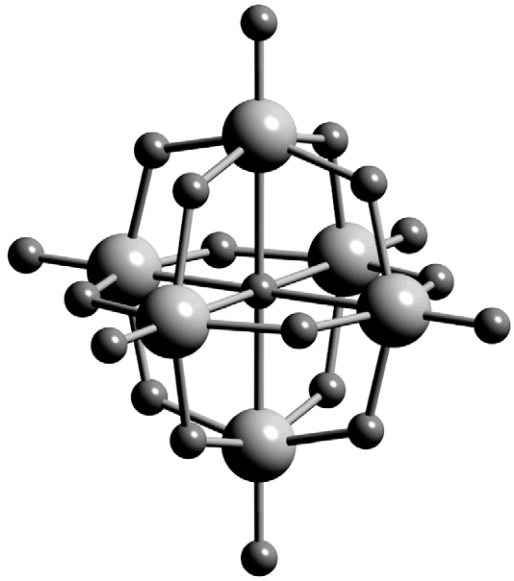

Figure 1 Structure of $[W_6O_{19}]^{2-}$.

a nonaqueous strategy has evolved that provides access to a range of hexametalates $[LM'M_5O_{18}]^{n-}$ using metal alkoxides as the metal oxide source and tetraalkylammonium salts of oxometalates, e.g., $(Bu^n_4N)_2[WO_4]$, $(Bu^n_4N)_2[MoO_4]$, $(Bu^n_4N)_2[Mo_2O_7]$, and $(Bu^n_4N)_4[Mo_8O_{26}]$ as sources of anionic charge.[4–6] In these reactions, the starting alkoxides are hydrolyzed to produce polynuclear oxide frameworks in a process which is related to the production of oxide materials by the sol–gel method (see Chapter 1.40). Retrosynthetic analysis (or deconstruction) is a useful aid in the design of synthetic routes to polyoxoanions, as illustrated in the following examples of rational hexametalate assembly. The contribution from the anionic component is first separated and then suitable precursors for the metal oxide and heteroelement fragments can be identified:

$$5WO(OMe)_4 + [WO_4]^{2-} + 10H_2O \rightarrow [W_6O_{19}]^{2-} + 20MeOH \quad (1)$$

The retrosynthetic analysis for the parent hexatungstate $(Bu^n_4N)_2[W_6O_{19}]$ (Figure 1) is shown in Scheme (1) (boxed items are starting materials). The yield from the associated hydrolysis reaction (see Equation (1)) is essentially quantitative, emphasizing the stability of this hexanuclear framework in organic media. Surface alkoxides have been incorporated to introduce reactive sites into the otherwise inert tungsten oxide shell, and Scheme (2) shows the retrosynthetic analysis which led to the synthesis of $(Bu^n_4N)_3[(MeO)TiW_5O_{18}]$ (Figure 2) by hydrolysis of a mixture of tungsten and titanium alkoxides in the presence of $[WO_4]^{2-}$ (see Equation (2)).

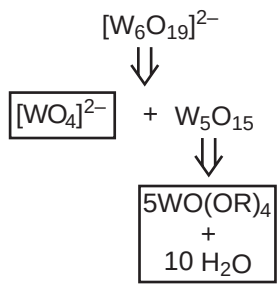

Scheme 1

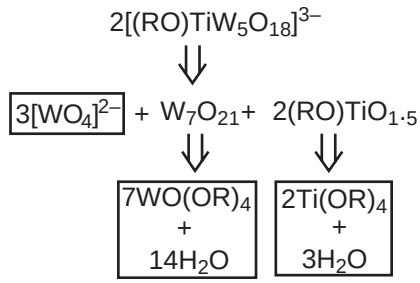

Scheme 2

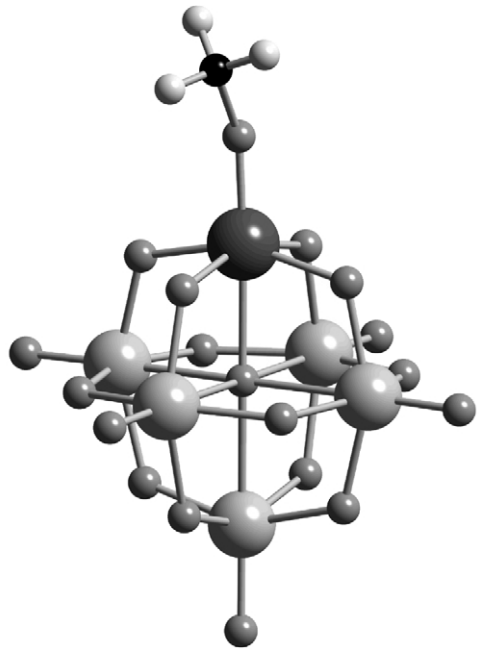

Figure 2 Structure of $[(MeO)TiW_5O_{18}]^{3-}$.

$$7WO(OMe)_4 + 2Ti(OMe)_4 + 3[WO_4]^{2-} + 17H_2O \rightarrow 2[(MeO)TiW_5O_{18}]^{3-} + 34MeOH \quad (2)$$

$(Bu^n{}_4N)_6[\{(MeO)ZrW_5O_{18}\}_2]$ (Figure 3) has been prepared in a similar fashion from $[\{Zr(OR)_4(ROH)\}_2]$ ($R = Pr^n$, Bu^n), with addition of an excess of methanol subsequent to hydrolysis to ensure exchange of any residual alkoxide groups from the zirconium alkoxide starting material (see Equation (3), $R' =$ mixed Me/R). This hydrolytic approach has been modified to provide access to the chloro derivative $[ClTiW_5O_{18}]^{3-}$[7] from the "virtual" nucleophilic oxometalate $[W_5O_{18}]^{6-}$ (see Scheme (3)). Volatiles were removed after the initial hydrolysis step (see Equation (4)), and the residual solid was dissolved in MeCN before addition of a solution of $[TiCl_4(MeCN)_2]$ (see Equation (5)).[8] The group 5 derivatives $[VW_5O_{19}]^{3-}$ and $[(MeO)NbW_5O_{18}]^{2-}$ have also been prepared from $[VO(OMe)_3]$ and $[Nb(OMe)_5]$ respectively (see Equations (6) and (7)). Following the retrosynthetic analysis shown in Scheme (4), the molybdotitanate $[(Pr^iO)TiMo_5O_{18}]^{3-}$ (Figure 4) has been synthesized by hydrolysis of $Ti(OPr^i)_4$ in the presence of oxomolybdates $[Mo_2O_7]^{2-}$ and $[Mo_8O_{26}]^{4-}$ (see Equation (8)):[8]

$$7WO(OMe)_4 + [\{Zr(OR)_4(ROH)\}_2] + 3[WO_4]^{2-} + 17H_2O \rightarrow [\{(R'O)ZrW_5O_{18}\}_2]^{6-} + 36R'OH \quad (3)$$

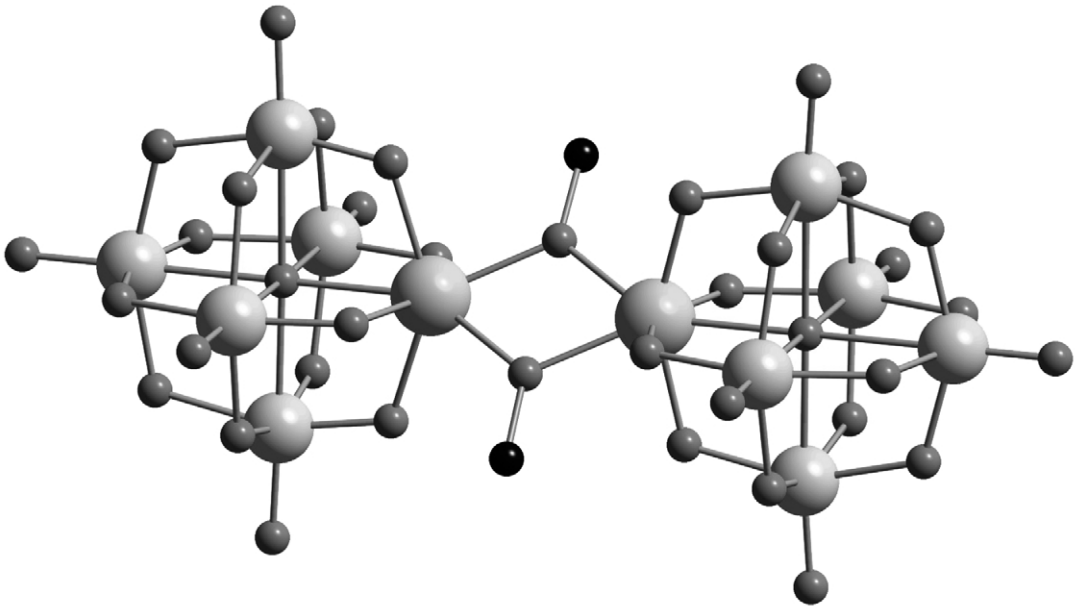

Figure 3 Structure of $[\{\mu\text{-MeO})ZrW_5O_{18}\}_2]^{6-}$.

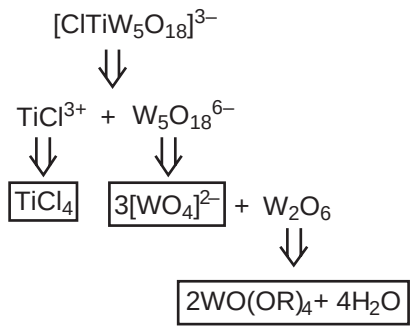

Scheme 3

$$2WO(OR)_4 + 3[WO_4]^{2-} + 4H_2O \rightarrow \text{“}[W_5O_{18}]^{6-}\text{”} + 8ROH \quad (4)$$

$$\text{“}[W_5O_{18}]^{6-}\text{”} + [TiCl_4(MeCN)_2] \rightarrow [ClTiW_5O_{18}]^{3-} + 3Cl^- + 2MeCN \quad (5)$$

$$7WO(OMe)_4 + 2VO(OMe)_3 + 3[WO_4]^{2-} + 17H_2O \rightarrow [VW_5O_{19}]^{3-} + 34MeOH \quad (6)$$

$$4WO(OMe)_4 + Nb(OMe)_5 + [WO_4]^{2-} + 10H_2O \rightarrow [(MeO)NbW_5O_{18}]^{2-} + 20MeOH \quad (7)$$

$$2Ti(OPr^i)_4 + [Mo_2O_7]^{2-} + [Mo_8O_{26}]^{4-} + 3H_2O \rightarrow 2[(Pr^iO)TiMo_5O_{18}]^{3-} + 6Pr^iOH \quad (8)$$

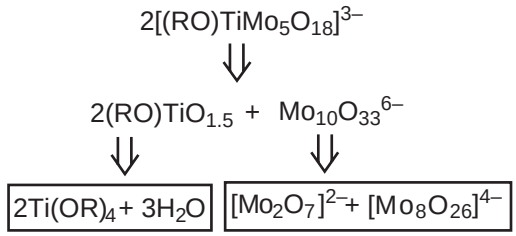

Scheme 4

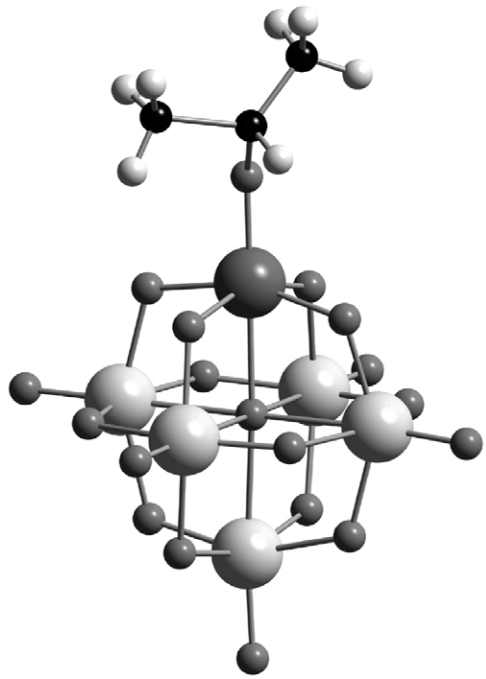

Figure 4 Structure of $[(Pr^{i}O)TiMo_5O_{18}]^{3-}$.

These reactions provide considerable scope for the rational manipulation of heteronuclear hexametalates, although little is known about the hydrolytic aggregation processes involved, except that the 1:1 reaction between $[WO_4]^{2-}$ and $[WO(OMe)_4]$ proceeds via rapid ligand redistribution to give the structurally dynamic dinuclear species $[W_2O_5(OMe)_4]^{2-}$.[9] As a result of these exchange processes, stoichiometric hydrolysis with ^{17}O-enriched water produces polyoxometalates with ^{17}O-enriched oxo sites, and reactions are readily monitored by ^{17}O NMR spectroscopy. In addition, these reactions provide an efficient means of producing ^{17}O-enriched samples for subsequent reactivity studies (see Section 2.64.4).

2.64.3 NONAQUEOUS POLYOXOMETALATE REACTIVITY

Access to a family of alkoxohexametalates has provided an opportunity for systematic studies of their reactivity towards HX substrates. Recent examples of these and other systematic nonaqueous studies are given below.

2.64.3.1 Alkoxide Exchange

NMR studies of alcoholysis reactions show the metal alkoxide sites in $[(RO)M'M_5O_{18}]^{3-}$ to be comparatively inert. Alkoxide peaks in ^{1}H NMR spectra show no broadening due to exchange up

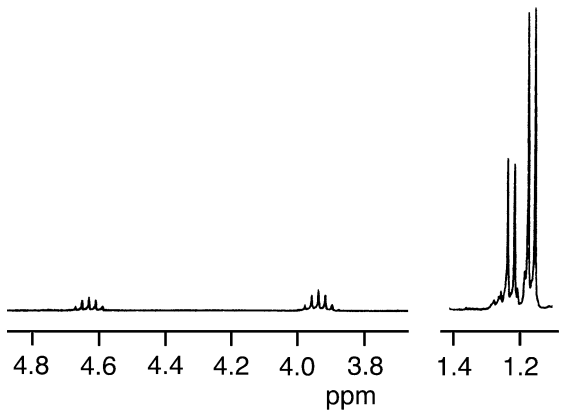

Figure 5 ^{1}H NMR spectrum of a mixture of $(Bu^{n}{}_{4}N)_{3}[(Pr^{i}O)TiMo_{5}O_{18}]$ and $Pr^{i}OH$ in $CD_{3}CN$ at 343 K.

to 70 °C (Figure 5), but off-diagonal peaks in ^{1}H EXSY (Exchange Spectroscopy) NMR experiments enable the rates for MeOH exchange with $[(MeO)TiW_{5}O_{18}]^{3-}$ and $[\{(MeO)ZrW_{5}O_{18}\}_{2}]^{6-}$ (Figure 6) to be estimated as $\sim 0.03\,s^{-1}$ and $\sim 1\text{–}10\,s^{-1}$ respectively at 75 °C.[8,10] Hence, the reaction between $[(Pr^{i}O)TiMo_{5}O_{18}]^{3-}$ and MeOH requires prolonged heating to go to completion.

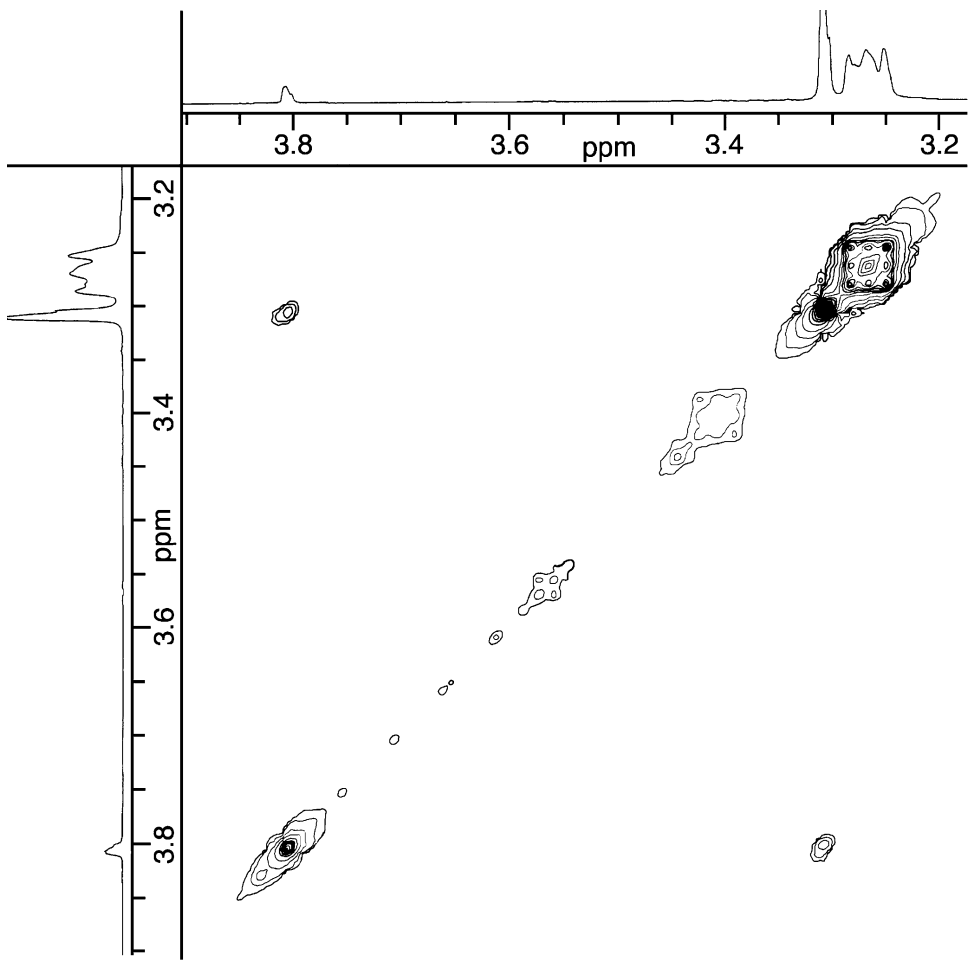

Figure 6 ^{1}H EXSY NMR spectrum of a mixture of $(Bu^{n}{}_{4}N)_{6}[\{\mu\text{-}MeO)ZrW_{5}O_{18}\}_{2}]$ and MeOH in $CD_{3}CN$ at 343 K.

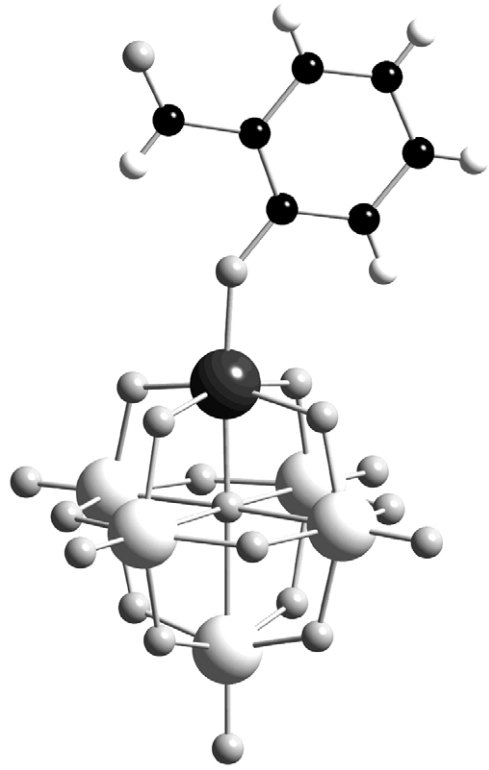

Figure 7 Structure of $[\{2\text{-}(CHO)C_6H_4O\}TiMo_5O_{18}]^{3-}$.

2.64.3.2 Aryloxide and Other Derivatives

Reactions involving protic reagents HX (e.g., X = OAr, $OC_6H_4(CHO)$-2, acetylacetonate (ACAC), O_2CR) proceed with heating to give $[XM'M_5O_{18}]^{n-}$ species. The salicylaldehyde derivative $[\{2\text{-}(OCH)C_6H_4O\}TiMo_5O_{18}]^{3-}$ (Figure 7) and aryloxides $[(ArO)M'W_5O_{18}]^{3-}$ (M′ = Ti, Zr) are monomeric with a six-coordinate heterometal and terminal aryloxide ligands, whereas $[(ACAC)ZrW_5O_{18}]^{3-}$ (Figure 8) and $[(CH_3CO_2)ZrW_5O_{18}]^{3-}$ (Figure 9) contain seven-coordinate Zr.[8,10]

2.64.3.3 Hydrolysis

In stoichiometric hydrolysis reactions, the titanium species $[(MeO)TiW_5O_{18}]^{3-}$ and $[(Pr^iO)TiMo_5O_{18}]^{3-}$ require prolonged heating to produce the oxo-bridged $[(\mu\text{-}O)\{TiW_5O_{18}\}_2]^{6-}$ (Figure 10) and $[(\mu\text{-}O)\{TiMo_5O_{18}\}_2]^{6-}$ respectively, whereas the niobium tungstate $[(MeO)NbW_5O_{18}]^{2-}$ is more readily hydrolyzed to give $[(\mu\text{-}O)\{NbW_5O_{18}\}_2]^{4-}$ (Figure 11). The difference in reactivities is likely to be due to the lower charge on the tungstoniobate.[4,8,10] The oxo-bridged niobate is eclipsed with a linear Nb—O—Nb linkage, whilst the titanate structures are slightly twisted with Ti—O—Ti angles of ~173°.

2.64.3.4 Oxo Metathesis

The hexamolybdate $[Mo_6O_{19}]^{2-}$ reacts with $Ph_3P{=}NAr$,[11] RNCO,[12,13] ArNCO,[13] or $ArNH_2$[14,15] in organic solvents to give organoimido derivatives $[Mo_6(NR)_xO_{19-x}]^{2-}$, and structures of $[(Bu^tN)\text{-}Mo_6O_{18}]^{2-}$[12] and $[(4\text{-}H_2NC_6H_4N)_2\text{-}Mo_6O_{17}]^{2-}$[14] are shown in Figures 12 and 13 respectively. These reactions generally require elevated temperatures, although it has been reported that stoichiometric amounts of *N,N*-dicyclohexylcarbodiimide accelerate reactions involving 2,6-dialkyl aromatic amines.[15]

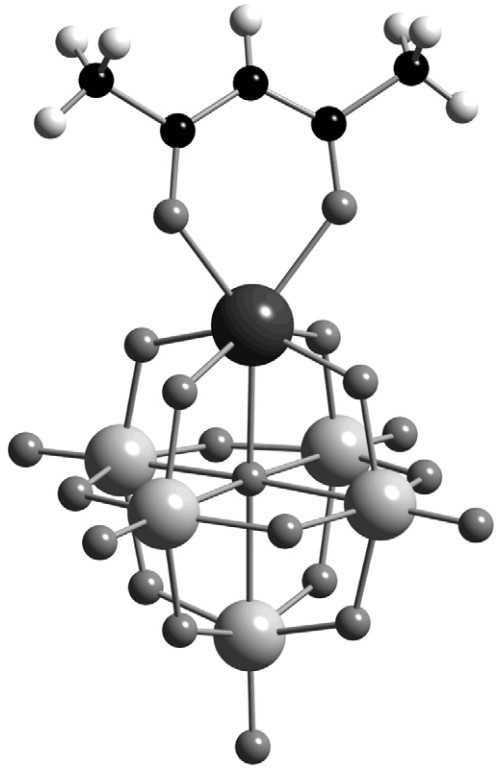

Figure 8 Structure of $[(acac)ZrW_5O_{18}]^{3-}$.

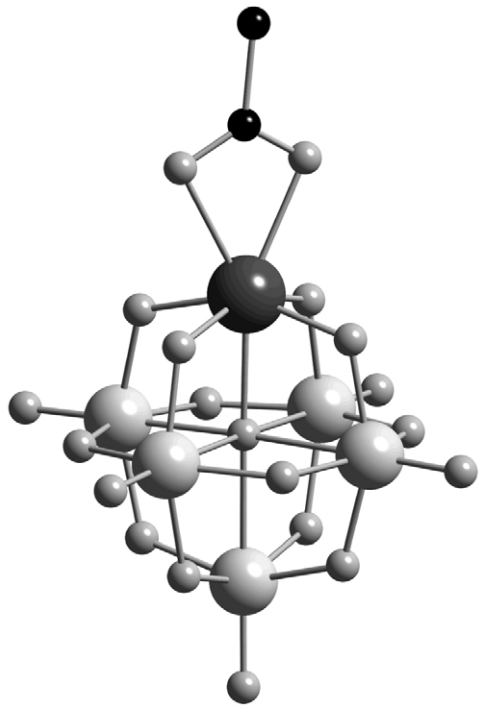

Figure 9 Structure of $[(CH_3CO_2)ZrW_5O_{18}]^{3-}$.

2.64.3.5 Base Degradation

Lacunary polyoxometalates feature extensively in systematic functionalization strategies, and it is possible to generate these nucleophilic species by base degradation in nonaqueous solvents. For

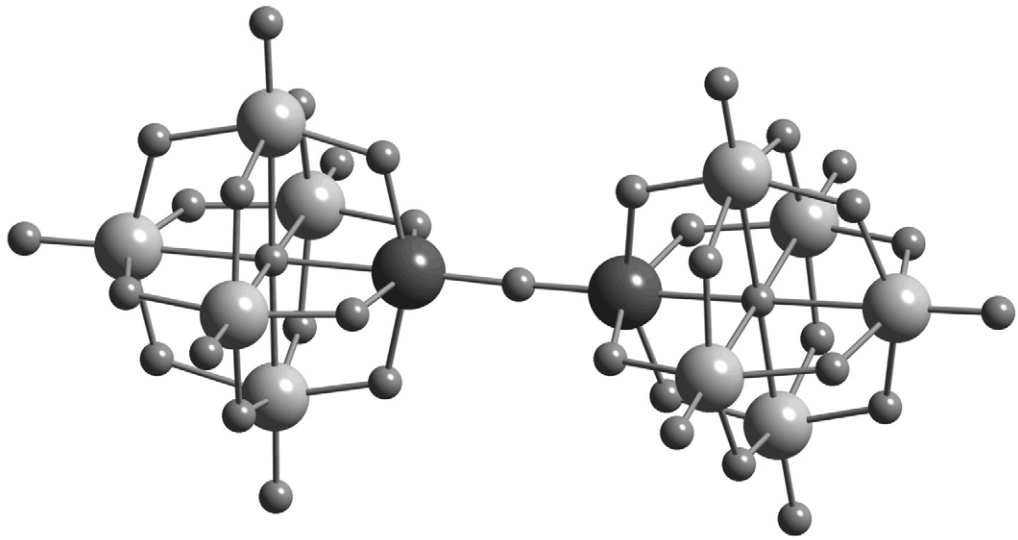

Figure 10 Structure of $[(\mu\text{-O})\{TiW_5O_{18}\}_2]^{6-}$.

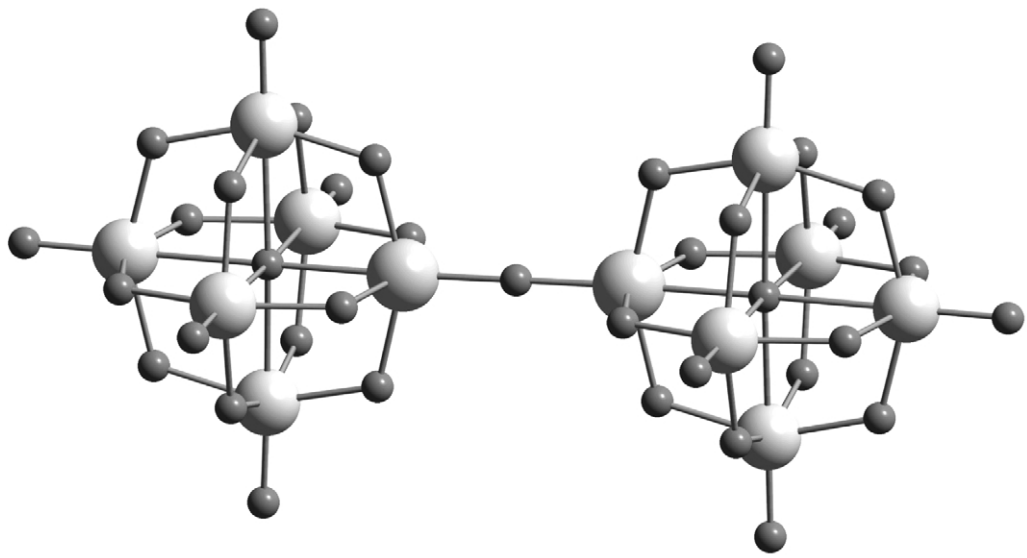

Figure 11 Structure of $[(\mu\text{-O})\{NbW_5O_{18}\}_2]^{4-}$.

example, treatment of a suspension of $Na_3[PW_{12}O_{40}]\cdot xH_2O$ in MeCN with $[Bu^n{}_4N][OH]$ results in excision of $[WO_4]^{2-}$ and formation of $[Bu^n{}_4N]_6[NaPW_{11}O_{39}]$ (Equation (9)) in which one of the framework $[W{=}O]^{4+}$ sites has been replaced by Na^+ (which in the crystal structure is disordered over nine of the 12 sites):[16]

$$Na_3[PW_{12}O_{40}] + 6[Bu^n{}_4N][OH] \rightarrow [Bu^n{}_4N]_6[NaPW_{11}O_{39}] + Na_2WO_4 + 3H_2O \quad (9)$$

2.64.3.6 Polyoxometalates as Nucleophiles

Polyoxometalates with higher surface charge densities interact with a range of Lewis acidic main-group and transition-metal species. Hence, *cis*-$[Nb_2W_4O_{19}]^{4-}$ reacts with $[\{(\eta^5\text{-}C_5Me_5)RhCl_2\}_2]$ or $[(\eta^5\text{-}C_5Me_5)Rh(MeCN)_3]^{2+}$ to give $[(\eta^5\text{-}C_5Me_5)Rh\text{-}(Nb_2W_4O_{19})]^{2-}$[17] and with $[(CO)_3M(MeCN)_3]^+$ (M = Mn, Re) to give $[(CO)_3M(Nb_2W_4O_{19})]^{3-}$.[18,19] Silyl halides $RSiCl_3$ react with $[NaPW_{11}O_{39}]^{6-}$ in CH_2Cl_2 or MeCN to give siloxane derivatives $[PW_{11}O_{39}(R_2Si_2O)]^{3-}$

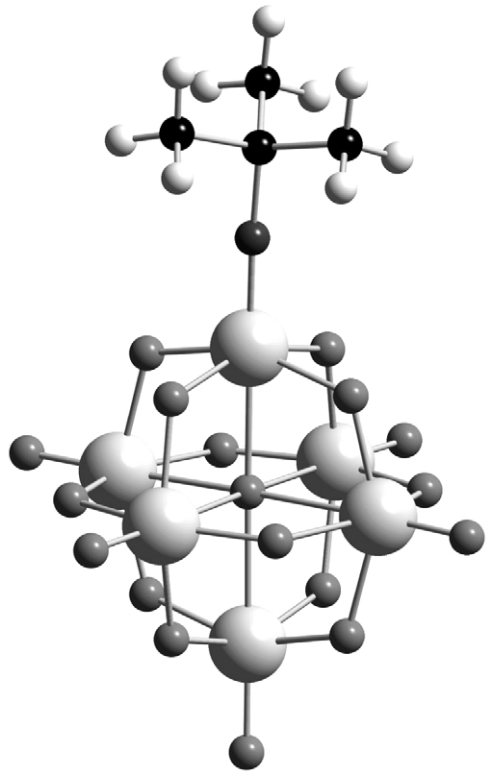

Figure 12 Structure of $[(Bu^tN)Mo_6O_{18}]^{2-}$.

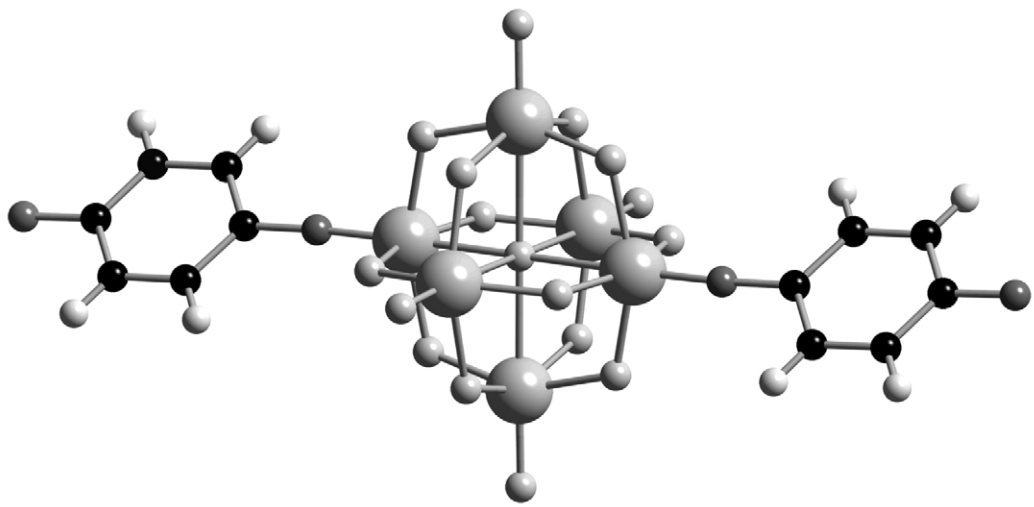

Figure 13 Structure of $[(4\text{-}H_2NC_6H_4N)_2Mo_6O_{17}]^{2-}$.

(Figure 14).[16] In reactions between the lacunary Keggin species $[NaPW_{11}O_{39}]^{6-}$ and $[PW_9O_{34}]^{9-}$ and $C_2O_2Br_2$ or $SOBr_2$ the Lewis acidic main group element is not retained, and elimination of oxide species leads instead to the formation of $[PW_9O_{28}Br_6]^{3-}$ (Figure 15), providing the first examples of direct polyoxometalate halogenation.[20]

Another method of increasing the basicity of a polyoxometalate and thereby enhancing interactions with Lewis acids is to increase its charge by reduction. Hence, when the six-electron reduction of $(Bu^n{}_4N)_3[PMo_{12}O_{40}]$ in MeCN is carried out in the presence of $[VOCl_3(DME)]$ (Equation (10)) the bi-capped, six-electron reduced species $[PMo_{12}O_{40}(VO)_2]^{3-}$ is produced

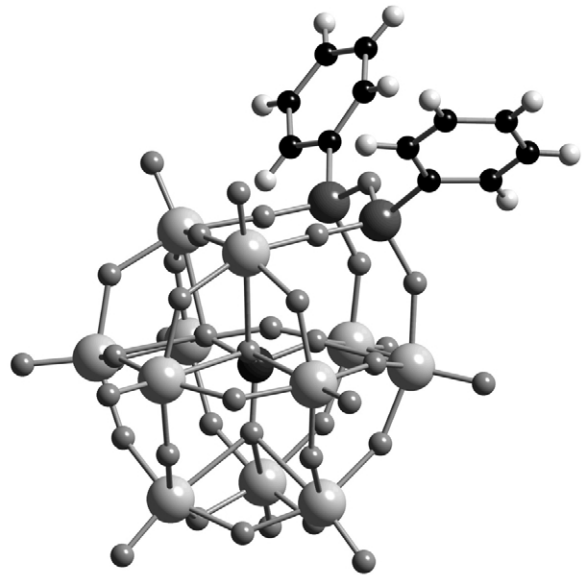

Figure 14 Structure of $[PW_{11}O_{39}(Ph_2Si_2O)]^{3-}$.

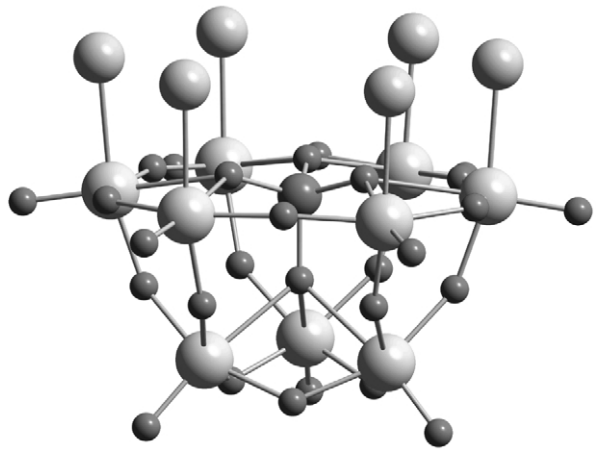

Figure 15 Structure of $[PW_9O_{28}Br_6]^{3-}$.

(Figure 16).[21] The potential of this nonaqueous approach to rational reductive aggregation has yet to be fully explored:

$$[PMo_{12}O_{40}]^{3-} + 6e^- + 2[VOCl_3(DME)] \rightarrow [PMo_{12}O_{40}(VO)_2]^{3-} + 6Cl^- + 2DME \qquad (10)$$

2.64.4 CHARACTERIZATION

X-ray crystallography has underpinned the expansion in polyoxometalate chemistry and the structures shown in Figures 1–16 serve to emphasize its importance. In this section, various complementary techniques are illustrated with reference to some of the polyoxometalates highlighted above.

2.64.4.1 Hexametalates

Surface organic groups are routinely studied by ^1H and ^{13}C NMR spectroscopy when the relevant peaks are not obscured by those of organic cations. In nonaqueous solutions, the nature of the

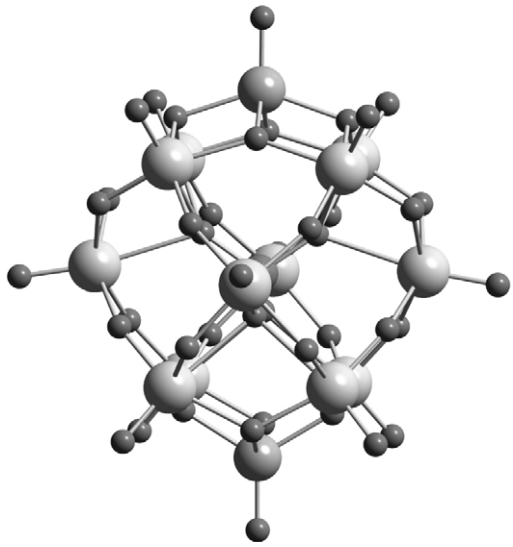

Figure 16 Structure of $[PMo_{12}O_{40}(VO)_2]^{3-}$.

oxide framework is readily investigated by ^{17}O NMR (particularly when samples are enriched in ^{17}O) because of the wide chemical shift range for oxygens with different connectivities.[22] The ^{17}O NMR spectrum for $[(MeO)TiW_5O_{18}]^{3-}$ demonstrates the characteristic pattern for $[LM'M_5O_{18}]^{n-}$ species, with two terminal W=O peaks (in a ratio of 4:1), one M′—O—M peak, two M—O—M peaks and a central μ_6-O peak (Figure 17).[4] Tungsten-183 NMR provides additional direct structural information for tungstates, provided sufficiently concentrated solutions can be obtained (greater than ~1 M in W). In ^{183}W NMR spectra of $[(MeO)TiW_5O_{18}]^{3-}$ and its derivatives, the unique axial W appears 15–25 ppm downfield of $[W_6O_{19}]^{2-}$ ($\delta_W = 47.8$), while the equatorial W peak is shifted a similar amount upfield.[4,10] Electronic effects are also reflected in IR spectra of $[LM'W_5O_{18}]^{3-}$ (M = Ti, Zr) where, due to the higher anion charge, the main bands due to ν(WO) for terminal W=O and bridging W—O—W are shifted 20–30 cm^{-1} to lower wavenumbers from those in the IR spectrum of $[W_6O_{19}]^{2-}$ at 976 cm^{-1} and 814 cm^{-1} respectively (Figure 18).

Polyoxometalate speciation in nonaqueous solvents has been investigated by electrospray ionization mass spectrometry (ESMS).[23] This low energy ionization method minimizes fragmentation, e.g., $(Bu^n_4N)_2[Mo_6O_{19}]$ gives ion clusters with m/z values centered at 440 and 1,123 due to $[Mo_6O_{19}]^{2-}$ and $\{(Bu^n_4N)[Mo_6O_{19}]\}^-$ respectively.

Electronic effects in the series of organoimido-substituted hexamolybdates $[Mo_6(NR)_xO_{19-x}]^{2-}$ have been probed by a combination of X-ray crystallography, visible spectroscopy, NMR

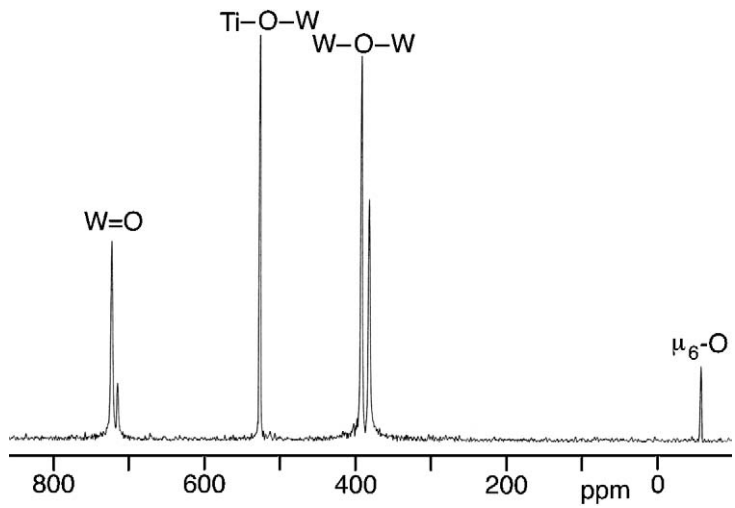

Figure 17 ^{17}O NMR spectrum of $(Bu^n_4N)_3[(MeO)TiW_5O_{18}]$.

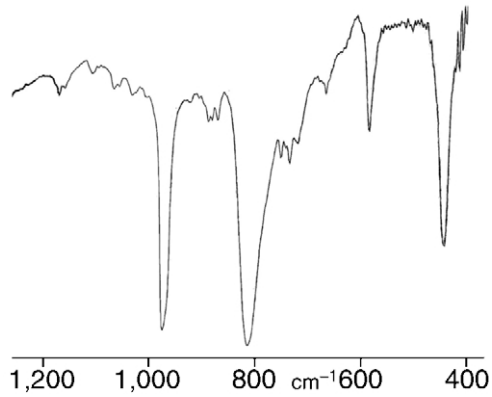

Figure 18 IR spectrum of $(Bu^n_4N)_2[W_6O_{19}]$.

spectroscopy (^{95}Mo, ^{17}O, and ^{14}N), and cyclic voltammetry.[13] Trends in bond lengths, λ_{max}, δ_{Mo}, δ_O, δ_N, and $E_{1/2}$ values are consistent with greater π-donation from NR than from O and suggest a redistribution of increasing electron density onto terminal M=O in polysubstituted arylimido species. These effects are also apparent in IR spectra of organoimido derivatives, where the two main ν(MoO) bands appear at lower wavenumbers than those in the IR spectrum of $[Mo_6O_{19}]^{2-}$. An analysis of structure and bonding in $[M_6O_{19}]^{n-}$ (M = Nb, Ta, Mo, W) using density-functional methods also indicated an increase in electron density at terminal oxygens upon reduction.[24]

2.64.4.2 Derivatives Based on the Keggin Structure

Tungsten-183 NMR is used extensively to elucidate structures derived from the Keggin $[EW_{12}O_{40}]$ structure. For example, the 2:2:2:1:2:2 pattern in the ^{183}W NMR spectrum of $(Bu^n_4N)_6[NaPW_{11}O_{39}]$ (Figure 19) is characteristic of a α-EW_{11} structure with C_s symmetry.[16] When $^2J_{WW}$ couplings are resolved, detailed analysis of connectivities in this type of structure are possible using 2D COSY (Correlation Spectroscopy) and INADEQUATE (Incredible Natural Abundance Double Quantum Experiment) NMR techniques (larger J_{WW} values are generally associated with larger W—O—W bond angles).[25,26] The peak for the six brominated tungstens in $[PW_9O_{28}Br_6]^{3-}$ ($\delta_W = 189$) is shifted significantly downfield from that for the other three tungstens ($\delta_W = -123$) and $^2J_{WW} = 25$ Hz, consistent with the W—O—W angles of ~148°. By comparison, in $[(MeO)TiW_5O_{18}]^{3-}$ Wax—O—W_{eq} = ~118° and $^2J_{WW} = 6$ Hz.

Little or no fragmentation is apparent in the ESMS analysis of nonaqueous solutions of Keggin derivatives. The main peaks in the spectrum of an acetonitrile solution of $(Bu^n_4N)_3[PW_{11}O_{39}(Si_2Ph_2O)]$ (Figure 20) are due to $[PW_{11}O_{39}(Si_2Ph_2O)]^{3-}$, $\{H[PW_{11}O_{39}(Si_2Ph_2O)]\}^{2-}$, and $\{(Bu^n_4N)[PW_{11}O_{39}(Si_2Ph_2O)]\}^{2-}$ at m/z values of 968, 1,452, and 1,573 respectively. Fast-atom

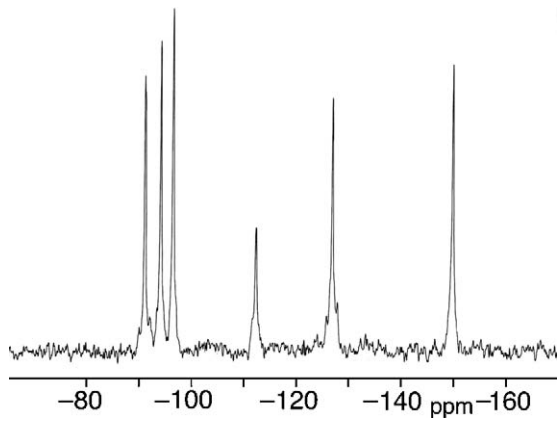

Figure 19 ^{183}W NMR spectrum of $(Bu^n_4N)_6[NaPW_{11}O_{39}]$.

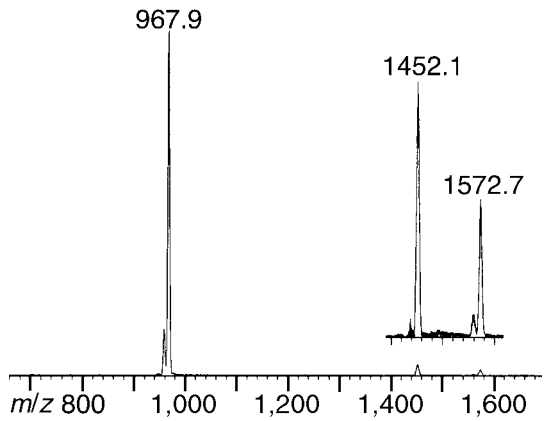

Figure 20 Negative-ion ESMS of a solution of $(Bu^n{}_4N)_3[PW_{11}O_{39}(Si_2Ph_2O)]$ in MeCN.

bombardment mass spectrometry is less convenient because of the poor solubility of the polyoxometalates in the matrix materials and fragmentation is more extensive.[27]

DFT methods have been used to investigate the redox properties of reduced $[PMo_{12}O_{40}(VO)_2]^{n-}$ polyoxoanions (Figure 16). Computed relative stabilities revealed minimal energies for $n = 2$ and 3, corresponding to 5- or 6-electron reduced species, although more highly reduced states are stabilized by cations that may interact with the anion surface.[28]

Finally, analytical ultracentrifugation (AUC) is useful for the characterization of much larger polyoxometalate assemblies in solution. Organic soluble colloidal particles formed by interactions between $[H_3Mo_{57}V_6(NO)_6O_{183}(H_2O)_{18}]^{21-}$ and amphiphilic tetraalkylammonium cations have been shown to have molar masses between 25,460 g mol^{-1} and 71,850 g mol^{-1} and diameters between 4 nm and 6 nm in various solvents.[29]

2.64.5 CONCLUSIONS

Rational synthetic methodologies are emerging from nonaqueous studies of polyoxometalate chemistry in which solution speciation, structure, and reactivity can be probed with a variety of techniques. Systematic manipulation of structure and composition is possible, and provides the experimental basis for a detailed understanding of electronic properties through computational methods. The ability to incorporate reactive surface functionality into polyoxometalates creates new opportunities for catalytic studies and for the synthesis of giant oxide structures and supramolecular assemblies with interesting electronic, magnetic, and photonic properties.

2.64.6 REFERENCES

1. Pope, M. T.; Müller, A., Eds., *Polyoxometalates: From platonic solids to anti-retroviral activity* **1994**, Kluwer: Dordrecht, The Netherlands.
2. Pope, M. T.; Müller, A., Eds., *Polyoxometalate chemistry: From topology via self-assembly to applications* **2001**, Kluwer: Dordrecht, The Netherlands.
3. Hill, C. L.; Müller, A., Eds., *Chem. Rev.* **1998**, *98*, 1–389 (an issue dedicated to polyoxometalate chemistry).
4. Clegg, W.; Elsegood, M. R. J.; Errington, R. J.; Havelock, J. *J. Chem. Soc., Dalton Trans.* **1996**, 681–690.
5. Errington, R. J. Rational Approaches to Polyoxometalate Synthesis, In *Polyoxometalate chemistry: From topology via self-assembly to applications*; Pope, M. T.; Müller, A., Eds.; Kluwer: Dordrecht, The Netherlands, 2001; pp 7–22.
6. Errington, R. J. General Strategies for Non-Aqueous Polyoxometalate Synthesis, In *Polyoxometalate Molecular Science*, Borras, J. J.; Coronado, E.; Müller, A.; Pope, M. T., Eds.; Kluwer: Dordrecht, The Netherlands, 2003; pp 55–77.
7. Day, V. W.; Earley, C. W.; Klemperer, W. G.; Maltbie, D. J. *J. Am. Chem. Soc.* **1985**, *107*, 8621–8262.
8. Errington, R. J.; Murphy C. J., unpublished results.
9. Clegg, W.; Errington, R. J.; Fraser, K. A.; Richards, D. G. *J. Chem. Soc. Chem. Comm.* **1993**, 1105–1107.
10. Errington, R. J.; Petkar, S. S., unpublished results.
11. Du, Y. H.; Rheingold, A. L.; Maatta, E. A. *J. Am. Chem. Soc.* **1992**, *114*, 345–346.
12. Errington, R. J.; Lax, C.; Richards, D. G.; Clegg, W.; Fraser, K. A. New Aspects of Non-Aqueous Polyoxometalate Chemistry, In *Polyoxometalates: From platonic solids to anti-retroviral activity*; Pope, M. T.; Müller, A., Eds.; Kluwer: Dordrecht, The Netherlands, 1994; pp 105–114.

13. Strong, J. B.; Yap, G. P. A.; Ostrander, R.; Liable-Sands, L.; Rheingold, A. L.; Thouvenot, R.; Gouzerh, P.; Maatta, E. A. *J. Am. Chem. Soc.* **2000**, *122*, 639–649.
14. Clegg, W.; Errington, R. J.; Holmes, S. A.; Schäfer, A. *Chem. Comm.* **1995**, 455–456.
15. Wei, Y.; Xu, B.; Barnes, C. L.; Peng, Z. *J. Am. Chem. Soc.* **2001**, *123*, 4083–4084.
16. Wingad, R. L., Ph.D. Thesis, University of Newcastle-upon-Tyne, 1999.
17. Besecker, C. J.; Day, V. W.; Klemperer, W. G.; Thompson, M. R. *J. Am. Chem. Soc.* **1984**, *106*, 4125–4136.
18. Besecker, C. J.; Klemperer, W. G. *J. Am. Chem. Soc.* **1980**, *102*, 7598–7600.
19. Besecker, C. J.; Day, V. W.; Klemperer, W. G.; Thompson, M. R. *Inorg. Chem.* **1985**, *24*, 44–50.
20. Errington, R. J.; Wingad, R. L.; Clegg, W.; Elsegood, M. R. *J. Angew. Chem. Int. Ed. Eng.* **2000**, *39*, 3884–3886.
21. Bakri, R., Ph.D. Thesis, University of Newcastle-upon-Tyne, 1998.
22. Filowitz, M.; Ho, R. K. C.; Klemperer, W. G.; Shum, W. *Inorg. Chem.* **1979**, *18*, 93–103.
23. Lau, T.-C.; Wang, J.; Guevremont, R.; Siu, K. W. *Chem. Comm.* **1995**, 877–878.
24. Bridgeman, A. J.; Cavigliasso, G. *Inorg. Chem.* **2002**, *41*, 1761–1770.
25. Brevard, C.; Schimpf, R.; Tourné, G.; Tourné, C. M. *J. Am. Chem. Soc.* **1983**, *105*, 7059–7063.
26. Domaille, P. J. *J. Am. Chem. Soc.* **1984**, *106*, 7677–7687.
27. Finke, R. G.; Droege, M. W.; Cook, J. C.; Suslick, K. S. *J. Am. Chem. Soc.* **1984**, *106*, 5750–5751.
28. Maestre, J. M.; Poblet, J. M.; Bo, C.; Casan-Pastor, N.; Gomez-Romero, P. *Inorg. Chem.* **1998**, *37*, 3444–3446.
29. Kurth, D. G.; Lehmann, P.; Volkmer, D.; Colfen, H.; Koop, M. J.; Müller, A.; Du Chesne, A. *Chem. Eur. J.* **2000**, *6*, 385–393.

Comprehensive Coordination Chemistry II
ISBN (set): 0-08-0437486

Volume 2, (ISBN 0-08-0443249); pp 759–773

2.65
Centred Zirconium Clusters

T. HUGHBANKS
Texas A & M University, College Station, TX, USA

2.65.1 INTRODUCTION 775
2.65.2 ELECTRONIC SPECTROSCOPY 775
2.65.2.1 UV–visible Spectra 775
2.65.2.2 Other Electronic Spectra 777
2.65.3 CYCLIC VOLTAMMETRY TO PROBE FRONTIER ORBITALS 777
2.65.3.1 General Redox Behavior 777
2.65.3.2 Cyclic Voltammetric Results and Electronic Structure 777
2.65.4 NMR AS A PROBE OF CAGE-INTERSTITIAL BONDING 780
2.65.4.1 General NMR Properties of Interstitial Atoms in Zr_6 Clusters 780
2.65.4.2 Interpreting Interstitial-atom Chemical Shifts 780
2.65.5 ^{57}FE MÖSSBAUER ISOMER SHIFTS 781
2.65.5.1 Mössbauer Isomer Shifts and *s*-Electron Density 781
2.65.5.2 Mössbauer Isomer Shifts in Fe-centered Zirconium Clusters 781
2.65.6 REFERENCES 782

2.65.1 INTRODUCTION

When a polynuclear metal cluster serves as host to an interstitial atom, it provides a unique chemical environment, the nature of which has only recently come into focus. Conversely, the ways in which interstitial atoms influence the properties and chemistry of the rest of the cluster have not been the subject of systematic investigations.

In the 1980s, reports from Corbett's and Simon's laboratories presented a then-new chemistry based on interstitially stabilized clusters of zirconium and the rare-earth elements.[1–13] Coincident with those discoveries, molecular orbital schemes were offered to aid in understanding the electronic factors that exert influence on the stability of these cluster-based compounds. Nevertheless, direct physical measurements that supported the schemes were relatively scarce, and were almost entirely restricted to magnetic susceptibilities.[14–21]

A survey of some of the now considerable physical evidence in support of bonding schemes offered for interstitial stabilization of clusters is presented here. This evidence derives from optical, NMR, and Mössbauer spectroscopy, and measurements of magnetic and electrochemical properties. The gathering of much of this evidence has been made possible by successful efforts to excise centered hexazirconium clusters from solid state precursors and to study them as discrete complexes, $[(Zr_6Z)X_{12}L_6]^{n-}$ (Figure 1), both in solution and as discrete species in salts.

2.65.2 ELECTRONIC SPECTROSCOPY

2.65.2.1 UV–visible Spectra

Electronic spectra can potentially provide a wealth of information concerning the nature of bonding in a cluster, and such spectra have figured prominently in investigations of cluster

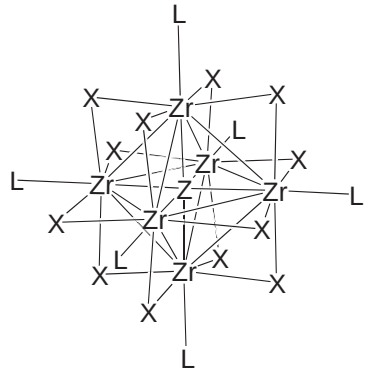

Figure 1 Structure of Z-centered hexazirconium clusters, $(Zr_6Z)X_{12}L_6$.

electronic structure (see also Chapter 2.22). The largest body of spectral investigations have been concerned with dinuclear complexes,[22] but some spectroscopic investigations of hexanuclear clusters have also been reported.[23–27] In many instances, LMCT transitions obscure most of the excitations involving the manifold of metal–metal bonded orbitals. The study of optical spectra in larger clusters can also be hampered by *too much* information since spectra can contain many overlapping and unresolved transitions.

Centered hexazirconium clusters exhibit rich electronic absorption spectra that have been only partially interpreted; one example is discussed here.[28] The spectra of $[(Zr_6Z)X_{12}L_6]^{n-}$ clusters exhibit a very large energy "window" over which LMCT transitions are absent. This window can be as large as $\sim$40,000 cm^{-1} and is a consequence of the large gap between ligand-based orbitals and the high-lying 4*d* orbitals of zirconium. Thus, for example, all the transitions seen in solution (MeCN) spectrum (Figure 2) for the $[(Zr_6FeCl_{12})Cl_6]^{4-}$ ion have slightly red-shifted counterparts in solutions of the bromide supported analog, $[(Zr_6FeBr_{12})Br_6]^{4-}$, and no major spectral changes that would be expected for LMCT transitions are observed. As indicated by the labeling, at least seven bands are observable in this spectrum. The octahedral symmetry of the cluster complex allows one to apply constraints imposed by selection rules and to assign and interpret this spectrum in terms of one-electron, orbital-to-orbital transitions—though extensive configuration interaction among the dipole-allowed T_{1u} excited states seems likely. Kohn–Sham eigenvalues from the DFT (BLYP) level calculations are useful in an assignment of the three lowest energy transitions: allowed t_{1u}(HOMO) $\rightarrow t_{2g}$ and t_{1g} orbital excitations (see Figure 6). Transitions **1** and **2** involve orbital excitations from the Zr-localized HOMO to two t_{2g}* orbitals with Zr—Fe antibonding character. The partial charge-transfer that occurs in these transitions is probably responsible for their relatively strong intensity; a weaker transition, **3**, is assigned as a

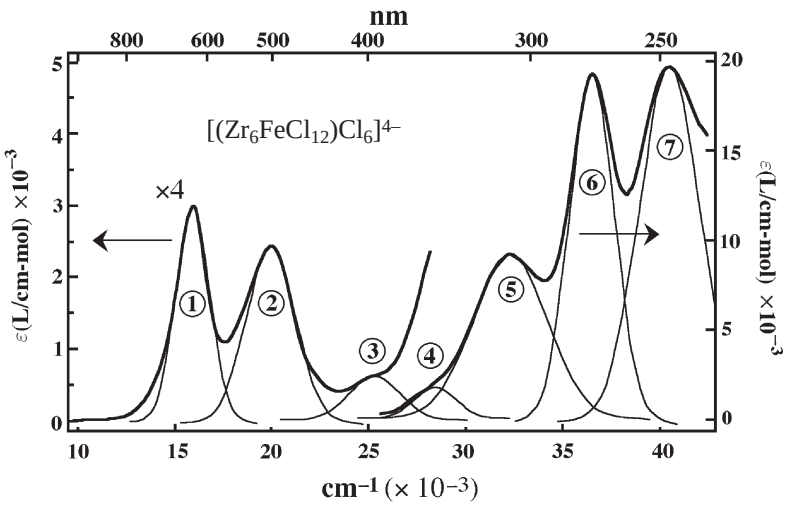

Figure 2 UV–visible spectrum of $[(Zr_6Fe)Cl_{18}]^{4-}$ in MeCN.

Zr—Zr(bonding) → Zr—Zr(antibonding) excitation. Higher energy transitions are more difficult to assign because there are several plausible candidates in the same energy range.

2.65.2.2 Other Electronic Spectra

Because of the wide spectral window offered by hexazirconium clusters, such systems offer an unequaled opportunity to test theoretical understanding of excited states in metal–metal bonded systems (See Chapter 2.22). Consequently, more complete experimental investigations are needed to characterize the nature of the excited states in $[(Zr_6FeCl_{12})Cl_6]^{4-}$ and related systems. For example, magnetic circular dichroism spectroscopy has the potential to reveal much about the nature of metal–metal bonding in hexanuclear clusters (see Chapter 2.25). However, this technique has been used in only one instance in the study of $[(Nb,Ta)_6X_{12}]^{n+}$ clusters,[29] and that study led its authors to propose a bonding scheme in contradiction to all previously proposed bonding schemes and in contradiction to the scheme presented here. Modern theory should help in spectral interpretation (e.g., evaluating terms that determine the signs of Faraday terms in the MCD spectra). Photoelectron spectroscopy has been applied to hexanuclear systems only in the solid state and the resolution of those measurements is too low to serve as more than a qualitative probe of metal–metal bonding;[30,31] the acquisition of gas-phase spectra is, of course, dependent on whether any hexanuclear zirconium cluster derivatives with sufficient volatility can be found.

2.65.3 CYCLIC VOLTAMMETRY TO PROBE FRONTIER ORBITALS

2.65.3.1 General Redox Behavior

One of the most surprising aspects of the chemistry of centered hexazirconium clusters is their redox behavior. Because the lower oxidation states of zirconium are generally inaccessible via solution-phase synthesis, it had been generally expected that the clusters would behave as very strong reducing agents when excised from the solid state.[32–35] As it turns out, the reactivity of these clusters is not so simply described. If care is taken to confine their reactivity to simple electron transfer, most of these clusters are not particularly strong reducing agents and will not reduce protons in acidic aqueous solution. Cyclic voltammetry (see Chapter 2.15) was important in clarifying the nature of hexazirconium cluster reactivity and, as an added benefit, reveals much about the systematics of cluster electronic structure.[36–40]

2.65.3.2 Cyclic Voltammetric Results and Electronic Structure

Redox potentials of $[(Zr_6Z)X_{12}]L_6$ clusters involve cluster frontier orbitals (HOMOs and LUMOs). The bonding schemes shown in Figures 3 and 6 predict that the frontier orbitals of interstitially stabilized clusters may have no interstitial atom character, i.e., they are of the wrong symmetry to include contributions from the interstitial atom valence orbitals. The reason for this general property is simple: when cage orbitals strongly interact with an interstitial atom, Zr_6—Z bonding orbitals are stabilized and their antibonding counterparts are destabilized. Cage orbitals that are of the wrong symmetry to interact remain in the intervening energy range and form the frontier orbitals. The bonding schemes also predict a HOMO–LUMO gap that is sensible in view of the usual observed numbers of cluster bonding electrons (CBEs) in both main-group- and transition-metal-centered clusters (14 and 18 CBEs, respectively).

The comparative redox behavior of $[(Zr_6Z)Cl_{18}]^{n-}$ clusters provides excellent support for the qualitative scheme just described. Figure 4 shows cyclic voltammograms for these species in the presence of excess chloride in MeCN. Consider first the Be-centered species, $(Zr_6BeCl_{18})^{3-,4-,5-}$ (11, 12, and 13 CBEs). All exhibit good stability in MeCN on the time scale of CV scans; three consecutive redox waves are clearly observed at −1.45 V, −1.04 V, and −0.56 V, which respectively correspond to $(Zr_6BeCl_{18})^{5-/6-}$, $(Zr_6BeCl_{18})^{4-/5-}$, and $(Zr_6BeCl_{18})^{3-/4-}$ redox couples. The presence of three waves and their nearly equal spacing is indicative of the degeneracy of the cluster HOMO. The spacing ($\Delta E_{1/2}$), are characteristically ~0.4–0.55 V when they correspond to successive redox couples involving the same or degenerate orbitals. Shifts of this magnitude were also observed in electrochemical studies in basic $AlCl_3$/ImCl ionic liquids[36] and aqueous

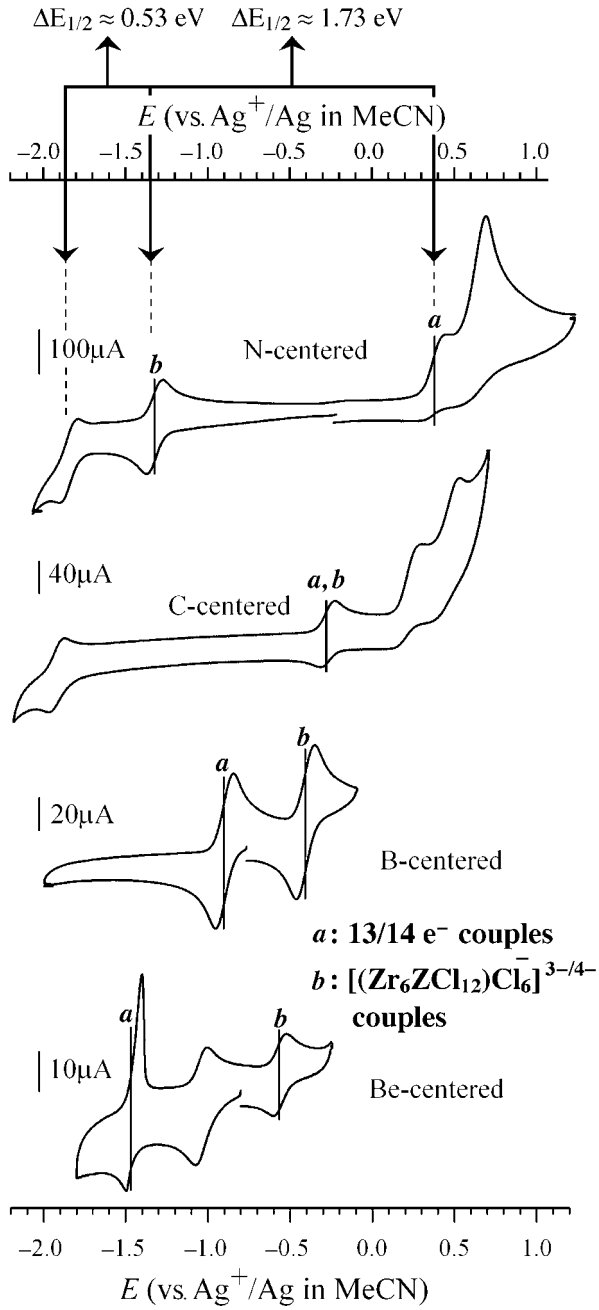

Figure 3 Cyclic voltammograms for $[(Zr_6Z)Cl_{18}]^{4-}$, Z = Be, B, C, N: (a) waves for oxidation of the 14 e^- species, (b) waves for the $[(Zr_6Z)Cl_{18}]^{3-/4-}$ couples.

solution.[38] In cases where both cluster oxidation and reduction can be observed, this characteristic allows an estimation of the HOMO–LUMO gap, as illustrated at the top of Figure 3 for the N-centered cluster. The oxidation wave (the $(Zr_6NCl_{18})^{2-/3-}$, 13/14 CBE, couple) and the reduction wave (the $(Zr_6NCl_{18})^{3-/4-}$, 14/15 CBE, couple) are separated by 1.73 V. However, a second reduction wave (the $(Zr_6NCl_{18})^{4-/5-}$, 15/16 CBE, couple) lies some 0.53 V further negative than the first reduction wave. Since this second reduction presumably corresponds to placing a second electron in the cluster LUMO, the 0.53 V gap is just the result of electron–electron repulsion. Since $\Delta E_{1/2}$ values of this magnitude are characteristic, we can estimate the cluster HOMO–LUMO gap to be about 1.2 eV (= 1.73 − 0.53 eV). A similar gap is deduced for the C-centered cluster, as is evident from the close similarities in the spacing of waves in the voltammograms for

these two clusters. The same chain of reasoning was applied to the analysis of data for $(Zr_6FeCl_{18})^{4-}$ obtained in Cl^--rich ionic liquids and a gap of ~1.45 eV or greater was estimated.[36] These HOMO–LUMO gap estimates agree well with thresholds for absorption in optical spectra; Be-, B-, and C-centered chloride clusters all exhibit HOMO–LUMO transitions at the appropriate wavelengths in the near-IR region, while the lowest energy transition for Fe- and Mn-centered clusters are in the visible region.[28]

Not surprisingly, cluster charge is the most important determinant of reduction potential in MeCN. Reduction potentials ($E_{1/2}$'s) of species with the same charge change modestly on moving through the series Be → B → C, despite the different CBE counts and interstitial atoms. $E_{1/2}$ for the $(Zr_6ZCl_{18})^{3-/4-}$ redox couples (marked "b" in Figure 4) increases from −0.56 V, to −0.41 V, and to −0.29 V as Z changes from Be to B to C. These shifts of 0.15 V can be attributed to the increase in interstitial (Z) electronegativity on moving through this series. As the Zr—Z bonds become more polarized towards the Z atom, the positive charge on the Zr_6 cage increases and the oxidation moves to more positive potential. Of course, in the N-centered case, the $(Zr_6NCl_{18})^{3-/4-}$ redox couple does not lie at ca. −0.14 V, but it is instead observed at a much more *negative* value ($E_{1/2} = -1.35$ V), since the oxidation of the $(Zr_6NCl_{18})^{4-}$ ion involves electron loss from the a_{2u} orbital that lies ~1.2 eV above a filled t_{2g} set.

To summarize, the redox behavior of $[(Zr_6Z)X_{12}]$-based clusters can be systematically understood because electron transfers involve cluster frontier orbitals that are by nature *nonbonding* with respect to Zr_6—Z interactions. Zr_6—Z bonding electrons lie in more deeply occupied orbitals and their (unoccupied) antibonding counterparts lie well above the LUMO. As a consequence of these features, the oxidation and reduction potentials of clusters bearing identical terminal ligands (e.g., H_2O or X^-), are determined mostly by the cluster's charge with the electronegativity of the interstitial atom (Z) and the supporting halides (X) having secondary roles.[36,37,40]

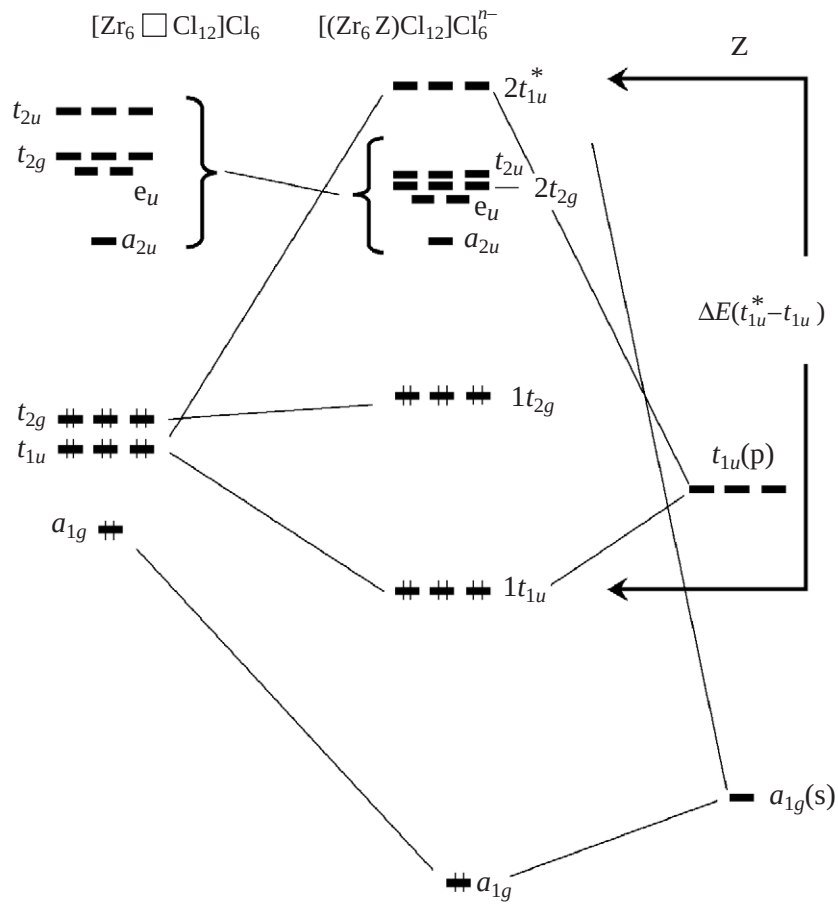

Figure 4 Molecular orbitals for $[(Zr_6Z)Cl_{18}]^{4-}$, derived from an empty cluster, $[(Zr_6\square)Cl_{18}]$, and an main-group atom, Z. The energy gap between the bonding t_{1u} and the antibonding t_{1u}^* orbitals is indicated.

2.65.4 NMR AS A PROBE OF CAGE-INTERSTITIAL BONDING

2.65.4.1 General NMR Properties of Interstitial Atoms in Zr_6 Clusters

Because of the near-octahedral symmetry about the Z-atom in $[(Zr_6Z)X_{12}]$ clusters, the electric field gradient at the nucleus is small enough that line broadening is dramatically curtailed for quadrupolar nuclei (see Chapter 2.1). Fortunately, this remains true even when the distribution of ligands (L) on the cluster exterior is asymmetric. The Z-atom's nucleus is still sensitive enough to the presence of ligands on the exterior of the cluster to be a useful probe of their presence via changes in chemical shift and, sometimes, spin–spin coupling. Thus, Z-centered hexanuclear zirconium clusters exhibit NMR spectra with high resolution, good sensitivity, chemical shift ranges with useful breadth, and interpretive simplicity. These molecules also offer invaluable potential for studying trends in NMR properties since no other series of molecules offers such a variety of nuclei within a single chemical environment.

2.65.4.2 Interpreting Interstitial-atom Chemical Shifts

The distinctive NMR properties of ^{13}C-, ^{11}B-, and ^{15}N-interstitial atoms has been a subject of interest to investigators of polynuclear metal clusters for many years.[41–57] However, it was not until Fehlner and co-workers put forward a semiquantitative framework to account for the extreme deshielding observed for interstitial nuclei that a coherent understanding of these NMR properties emerged.[51,58] Fehlner's approach was based on Ramsey's expression for the paramagnetic contribution to chemical shifts that emerges from perturbation theory.[59,60] In essence, paramagnetic contributions arise from second-order mixing of paramagnetic excited states into the diamagnetic ground state by the applied magnetic field. Kaupp used DFT to explicitly calculate chemical shifts for some ^{13}C-centered clusters and demonstrated the qualitative correctness of Fehlner's approach.[61] This work also clearly demonstrated that explanations of interstitial atom chemical shifts in terms of interstitial radius vs. cage size match (or mismatch)[49,50] or interstitial atom orbital-hybridization assignments[48,56] are essentially fallacious.

Fehlner and co-workers identified three factors that are qualitatively important in understanding trends in paramagnetic contributions to the chemical shift for main-group interstitial atoms:[51,58] (i) the effective interstitial atom *p*-orbital radii, via the $\langle 1/r^3 \rangle$ dependence in Ramsey's expression; (ii) the magnitude of the interstitial *p*-orbital contributions to the molecular orbitals involved in the ground to excited state excitations and orbital symmetries—which defines the *significant* excited states; and (iii) energy gaps between the ground and significant excited states, via the $(1/\Delta E)$ dependence of excited state mixing coefficients in second-order perturbation theory. Centered hexazirconium clusters offer an especially attractive opportunity to test the utility of these criteria and to use the criteria to extract valuable insight into the nature of chemical bonding between the Zr_6 cage and the centering atom (Z), and we will turn to such matters below.

One interesting trend concerns the relative chemical shift magnitudes for $[(Zr_6Z)X_{12}]$ clusters on moving through the $Z = Be \rightarrow N$ series: 77 ppm (^{9}Be), ~180–215 ppm (^{11}B), 460–532 ppm (^{13}C), 246–271 ppm (^{15}N).[38,40,62–64] Because these are all given relative to different standards and the comparisons are necessarily qualitative, it should be noted that for all these nuclei, chemical standards are rather highly shielded and have small paramagnetic shift contributions, while Z-centered clusters are in every case at the extreme deshielded end of the known chemical shift ranges precisely because of the large paramagnetic shift contributions. The increase in $\langle 1/r^3 \rangle$ as the 2*p*-orbital radii decrease across this series is responsible for most of the increase in paramagnetic shifts on moving from ^{9}Be to ^{13}C, but the smaller shifts for ^{15}N-atoms in Zr_6 cages are due to much greater polarity and somewhat poorer overlap in Zr—N bonding than occurs in clusters centered by the three less electronegative atoms.

A remarkable correlation between chemical shifts and Zr—Z bond strengths emerges by applying a simple (nonrigorous) analysis to results obtained with density functional calculations (see Chapter 2.39). The molecular orbital diagram in Figure 4 shows the essential excitation energy, $\Delta E(t_{1u}^* - t_{1u})$, that is the focus of this analysis. The application of group theory reveals that an applied magnetic field mixes only excited states of T_{1g} symmetry into the ground state for an octahedral molecule.[62,65] Of such T_{1g} states, the excitation involving the bonding–antibonding gap in the MO diagram should be most important, because both the ground and excited ends of that excitation involve significant Z-atom *p* character (criterion (b)). In Figure 5 we show plots of

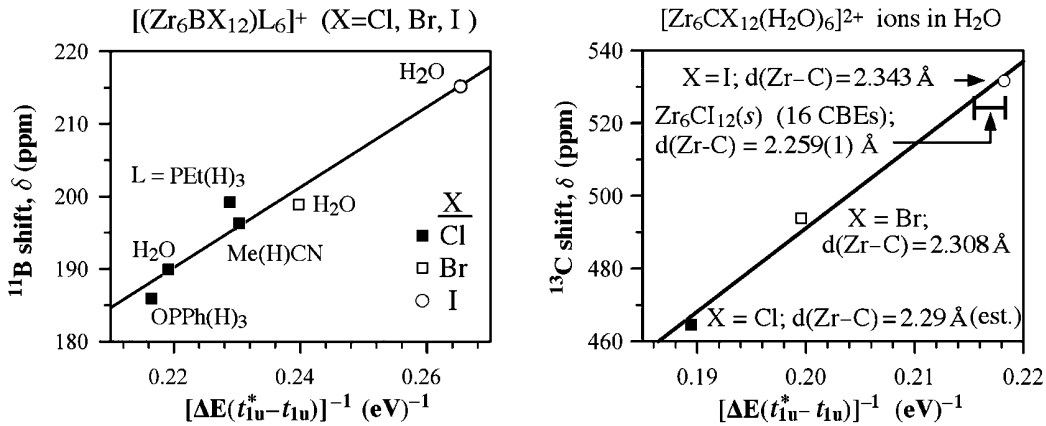

Figure 5 Correlation of chemical shifts for ^{11}B- and ^{13}C-centered clusters with the reciprocal of the t^*_{1u}– t_{1u} energy gap, $[\Delta E(t^*_{1u}– t_{1u})]^{-1}$.

chemical shifts vs. $[\Delta E(t^*_{1u}– t_{1u})]^{-1}$ for the several boron and carbon-containing clusters. The excitation energies are not rigorously calculated, we used a simple expedient of taking the difference of the Kohn–Sham orbital energies. It is nevertheless interesting that this bonding–antibonding energy gap, a qualitative measure of the strength of Zr_6—Z bonding strength, is inversely related to the chemical shift. It is notable that the chemical shift does not necessarily correlate with Zr—Z bond length variations, as can be seen in the examples included in Figure 5 (at right).

The correlations illustrated in Figure 5 recall a long-ago-established inverse correlation between ^{59}Co chemical shifts and ligand field strength in low-spin Co^{III} complexes.[66–73] More specifically, the reciprocal of the A_{1g}(ground state)–T_{1g}(excited state) energy gap is proportional to the downfield ^{59}Co chemical shift in low-spin Co^{III} complexes. Interestingly, the extreme *relative* deshielding observed for interstitial ^{9}Be, ^{11}B, ^{13}C, ^{15}N, and ^{155}Mn (compared to other molecules with these nuclei), does not extend to ^{59}Co shifts; the ^{59}Co resonance for $Zr_6CoCl_{15}(s)$ (4,047 ppm) is quite ordinary in the context of the large known ^{59}Co chemical shift range (~−3,900 ppm to +15,100 ppm). This is perhaps an indication that 3*d* orbital splittings engendered by Zr—Co bonding is comparable to an average low-spin Co^{III} complex.

2.65.5 ^{57}FE MÖSSBAUER ISOMER SHIFTS

2.65.5.1 Mössbauer Isomer Shifts and *s*-Electron Density

When drawing correlations within a series of related compounds, ^{57}Fe Mössbauer isomer shifts can be a useful indication of oxidation state (see Chapter 2.20).[74–77] Of course, the isomer shift is more directly a measure of the "chemical shift" in the electron density at the ^{57}Fe nucleus in the sample vs. the source. This means that an isomer shift is an indicator of the *s* electron density at the same nucleus, and in practice, the 4*s* and 3*s* densities are those most sensitive to changes in the nucleus' chemical environment. The chain of reasoning that connects the oxidation state to *s* electron density changes goes roughly as follows: As the Fe oxidation state increases, the number of 3*d* electrons decreases, which in turn decreases the shielding of both the 4*s* and 3*s* electrons.[74–76,78] The (always doubly occupied) 3*s* core-orbital becomes more contracted, and the 4*s* orbital also becomes less diffuse and drops in energy—which increases its contribution to the occupied, bonding (primarily ligand-based) molecular orbital(s) in the valence region. Thus, both the 4*s* and 3*s* contribution to the electron density at the nucleus increase. In ^{57}Fe Mössbauer spectra, this translates into a trend of increasingly negative isomer shifts with increasing oxidation state.

2.65.5.2 Mössbauer Isomer Shifts in Fe-centered Zirconium Clusters

Mössbauer measurements on Fe-centered zirconium clusters dramatically illustrate the limitations of the oxidation state/isomer shift correlation just discussed.[79] Indeed, the ^{57}Fe isomer shifts

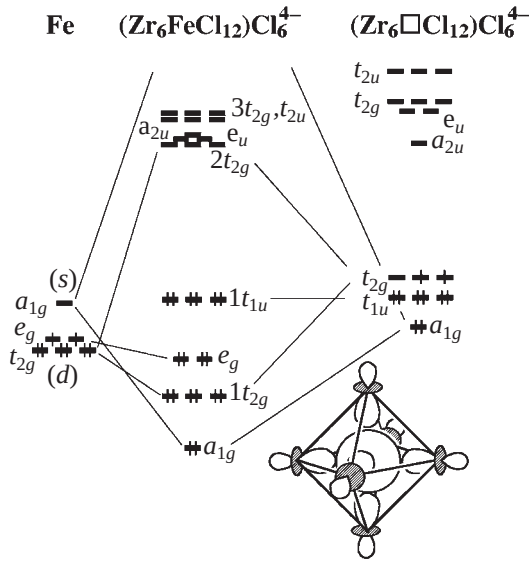

Figure 6 Molecular orbitals for $[(Zr_6Fe)Cl_{18}]^{4-}$, derived from an empty cluster, $[(Zr_6)Cl_{18}]$, and an Fe atom. The large Fe 4*s* contribution to the bonding a_{1g} orbital is illustrated.

measured on these clusters are the most negative ever recorded ($\delta = -0.95\,mm\,s^{-1}$ for Zr_6FeCl_{14} and KZr_6FeCl_{15})—and in no reasonable description would we assign a high iron oxidation state to these molecules! It is not clear that *any* oxidation state assignment for iron in a $[(Zr_6Fe)X_{12}]$ cluster has much intrinsic meaning, but it does seem clear that when surrounded by a cage of electropositive zirconium, iron will most likely be *negatively* charged. How are we to account for this anomalous behavior and what does it tell us about chemical bonding in this unique environment?

A schematic MO diagram illustrating the interaction of the Fe 3*d* and 4*s* orbitals with the surrounding $[(Zr_6Fe)X_{12}]$ cage orbitals is shown in Figure 6. The relative energetic placement of 3*d* vs. cage MOs is not of quantitative significance, but the net calculated (DFT, BLYP) populations of the 3*d* and 4*s* orbitals suggests that this diagram is qualitatively reasonable in that respect. The calculated Mulliken populations of these AOs ($3d^{6.92}4s^{0.92}$) provide some insight into very negative isomer shifts observed; the 4*s* population is much higher than calculated by the same method for reference molecules like $Fe(CO)_5$ ($3d^{6.96}4s^{0.23}$; $\delta = -0.09\,mm\,s^{-1}$) or $FeCp_2$ ($3d^{7.02}4s^{0.48}$; $\delta = 0.45\,mm\,s^{-1}$), while the 3*d* populations are quite comparable. The electropositive nature of the Zr_6 cage is ultimately responsible for this large 4*s* orbital population. The Zr_6—Fe bonding a_{1g} orbital (depicted) is more Fe-localized than would be an analogous bonding totally symmetric orbital in an inorganic or organometallic complex, in which such an orbital is dominated by a linear combination of ligand-localized donor orbitals.

Finally, it should be noted that the Zr—Fe bonding is quite strong in these clusters, as is indicated by comparing the observed short Zr—Fe distances (ca. 2.43 Å in Zr_6Cl_{12}-based clusters) with the sum of the single-bond radii of the elements (2.64 Å). Consequently, the Fe 3*d* orbitals in the cluster mix extensively with the surrounding Zr_6 cage orbitals and an enhanced nephelauxetic effect may be responsible for reducing the shielding effect that the 3*d* electron density provides to the 3*s* and 4*s* electrons.

2.65.6 REFERENCES

1. Ziebarth, R. P.; Corbett, J. D. *J. Am. Chem. Soc.* **1985**, *107*, 4571–4573.
2. Smith, J. D.; Corbett, J. D. *J. Am. Chem. Soc.* **1985**, *107*, 5704–5711.
3. Corbett, J. D.; McCarley, R. E. In *Crystal Chemistry and Properties of Materials with Quasi-one-dimensional Structures*; Rouxel, J., Ed.; Reidel: New York, 1986, pp 179–204.
4. Corbett, J. D. *Inorg. Chem.* **2000**, *39*, 5178–5198.
5. Ziebarth, R. P.; Corbett, J. D. *Acc. Chem. Res.* **1989**, *22*, 256–262.
6. Corbett, J. D. *Pure Appl. Chem.* **1992**, *64*, 1395–1408.
7. Corbett, J. D. *J. Chem. Soc., Dalton Trans.* **1996**, 575–587.
8. Simon, A. *Angew. Chem. Intl. Ed. Engl.* **1981**, *20*, 1–22.
9. Simon, A. *J. Solid State Chem.* **1985**, *57*, 2–16.

10. Simon, A.; Mattausch, H.; Miller, G. J.; Bauhofer, W.; Kremer, R. K. In *Handbook on the Physics and Chemistry of Rare Earths*; Gschneidner, K., Eyring, L., Eds.; Elsevier Science Publishers: Amsterdam, 1991; Vol. 15, pp 191–285.
11. Simon, A. In *Solid State Chemistry: Compounds*; Cheetham, A. K., Day, P., Eds.; Oxford University Press: Oxford, U.K., 1992; Vol. 2, pp 112–165.
12. Simon, A. *Pure Appl. Chem.* **1995**, *67*, 311–312.
13. Simon, A. In *Clusters and Colloids*; Schmid, G., Ed.; V C H Verlagsgesellschaft: Weinheim, Germany, 1994, pp 373–458.
14. Dudis, D. S.; Corbett, J. D. *Inorg. Chem.* **1987**, *26*, 1933–1940.
15. Hughbanks, T.; Rosenthal, G.; Corbett, J. D. *J. Am. Chem. Soc.* **1988**, *110*, 1511–1516.
16. Payne, M. W.; Dorhout, P. K.; Kim, S.-J.; Hughbanks, T. R.; Corbett, J. D. *Inorg. Chem.* **1992**, *31*, 1389.
17. Lulei, M.; Corbett, J. D. *Z. Anorg. Allg. Chem.* **1996**, *622*, 1677–1684.
18. Uma, S.; Martin, J. D.; Corbett, J. D. *Inorg. Chem.* **1999**, *38*, 3825–3830.
19. Simon, A.; Schnering, H. G. v.; Wohrle, H.; Schäfer, H. *Z. Anorg. Allg. Chem.* **1965**, *339*, 155–170.
20. Böttcher, F.; Simon, A.; Kremer, R.; Buchkremer-Hermanns, H.; Cockroft, J. *Z. Anorg. Allg. Chem.* **1991**, *598/599*, 25.
21. Bauhofer, W.; Cockcroft, J. K.; Kremer, R. K.; Mattausch, H.; Schwarz, C.; Simon, A. *J. Phys., Colloq.* **1988**, C8893/C898–894.
22. Cotton, F. A.; Walton, R. A. *Multiple Bonds Between Metal Atoms*, 2nd ed.; Oxford University Press: New York, 1993.
23. Spreckelmeyer, V. B. *Z. Anorg. Allg. Chem.* **1969**, *365*, 225–242.
24. Fleming, P. B.; McCarley, R. E. *Inorg. Chem.* **1970**, *9*, 1347–1354.
25. Barnard, P. A.; Sun, I.-W.; Hussey, C. L. *Inorg. Chem.* **1990**, *29*, 3670–3674.
26. Robinson, L. M.; Bain, R. L.; Shriver, D. F.; Ellis, D. E. *Inorg. Chem.* **1995**, *34*, 5588–5596.
27. Hussey, C.; Quigley, R.; Seddon, K. *Inorg. Chem.* **1995**, *34*, 370–377.
28. Bond, M. R.; Hughbanks, T. *Inorg. Chem.* **1992**, *31*, 5015–5021.
29. Robbins, D. J.; Thomson, A. J. *J. Chem. Soc., Dalton Trans.* **1972**, 2350–2364.
30. Hamer, A. D.; Walton, R. A. *Inorg. Chem.* **1974**, *13*, 1446–1451.
31. Best, S. A.; Walton, R. A. *Inorg. Chem.* **1979**, *18*, 484–488.
32. Fay, R. C. In *Main Group & Early Transition Elements*; Pergamon: Oxford, 1987; Vol. 3, pp 363–451.
33. Soloveichik, G. L. In *Encyclopedia of Inorganic Chemistry*; King, R. B., Ed.; John Wiley: Chichester, 1994, Vol. 8, pp 4475–4506.
34. Rogel, F.; Corbett, J. D. *J. Am. Chem. Soc.* **1990**, *112*, 8198–8200.
35. Chen, L.; Cotton, F. A.; Klooster, W. T.; Koetzle, T. F. *J. Am. Chem. Soc.* **1997**, *119*, 12175–12183.
36. Sun, D.; Hughbanks, T. *Inorg. Chem.* **1999**, *38*, 992–997.
37. Xie, X.; Hughbanks, T. *Solid State Science* **1999**, *1*, 463–472.
38. Xie, X.; Hughbanks, T. *Inorg. Chem.* **2000**, *39*, 555–561.
39. Xie, X.; Jones, J. N.; Hughbanks, T. *Inorg. Chem.* **2001**, *40*, 522–527.
40. Xie, X.; Hughbanks, T. *Inorg. Chem.* **2002**, *41*, 1824–1830.
41. Bradley, J. S. *Adv. Organomet. Chem.* **1983**, *22*, 1–58.
42. Blohm, M. L.; Gladfelter, W. L. *Organometallics* **1985**, *4*, 45–52.
43. Hriljac, J. A.; Swepston, P. N.; Shriver, D. F. *Organometallics* **1985**, *4*, 158–166.
44. Fry, C. G.; Smith, J. D.; Gerstein, B. C.; Corbett, J. D. *Inorg. Chem.* **1986**, *25*, 117–118.
45. Bordoni, S.; Heaton, B. T.; Seregni, C.; Strona, L.; Goodfellow, R. J.; Hursthouse, M. B.; Thornton-Pett, M.; Martinengo, S. *J. Chem. Soc. Dalton Trans.* **1988**, 2103–2108.
46. Rath, N. P.; Fehlner, T. P. *J. Am. Chem. Soc.* **1988**, *110*, 5345–5349.
47. Hong, F.-E.; Coffy, T. J.; McCarthy, D. A.; Shore, S. G. *Inorg. Chem.* **1989**, *28*, 3284.
48. Bailey, P. J.; Duer, M. J.; Johnson, B. F. G.; Lewis, J.; Conole, G.; McPartlin, M.; Powell, H. R.; Anson, C. E. *J. Organomet. Chem.* **1990**, *383*, 441–461.
49. Mason, J. *J. Am. Chem. Soc.* **1991**, *113*, 24–26.
50. Mason, J. *J. Am. Chem. Soc.* **1991**, *113*, 6056–6062.
51. Khattar, R.; Fehlner, T. P.; Czech, P. T. *New J. Chem.* **1991**, *15*, 705–711.
52. Beringhelli, T.; D'Alfonso, G.; Molinari, H.; Sironi, A. *J. Chem. Soc. Dalton Trans.* **1992**, 689–695.
53. Housecroft, C. E.; Matthews, D. M.; Waller, A.; Edwards, A. J.; Rheingold, A. L. *J. Chem. Soc., Dalton Trans.* **1993**, 3059–3070.
54. Tian, Y.; Hughbanks, T. *Inorg. Chem.* **1995**, *34*, 6250–6254.
55. Tian, Y. Ph.D. Thesis, Texas A&M University, 1995.
56. Heaton, B. T.; Iggo, J. A.; Longoni, G.; Mulley, S. *J. Chem. Soc., Dalton Trans.* **1995**, 1985–1989.
57. Pergola, R. D.; Cinquantini, A.; Diana, E.; Garlaschelli, L.; Laschi, F.; Luzzini, P.; Manassero, M.; Repossi, A.; Sansoni, M.; Stanghellini, P. L.; Zannello, P. *Inorg. Chem.* **1997**, *36*, 3761–3671.
58. Fehlner, T. P.; Czech, P. T.; Fenske, R. F. *Inorg. Chem.* **1990**, *29*, 3103–3109.
59. Ramsey, N. F. *Phys. Rev.* **1950**, *78*, 699–703.
60. Mason, J. *Multinuclear NMR* **1987**, Plenum: New York.
61. Kaupp, M. *Chem. Commun.* **1996**, 1141–1142.
62. Harris, J. D.; Hughbanks, T. *J. Am. Chem. Soc.* **1997**, *119*, 9449–9459.
63. Xie, X.; Reibenspies, J. H.; Hughbanks, T. *J. Am. Chem. Soc.* **1998**, *120*, 11391–11400.
64. Sun, D.; Hughbanks, T. *Inorg. Chem.* **2000**, *39*, 1964–1968.
65. Griffith, J. S.; Orgel, L. E. *Trans. Faraday Soc.* **1957**, *53*, 601–606.
66. Lucken, E. A. C.; Noack, K.; Williams, D. F. *J. Chem. Soc. (A)* **1967**, 148–154.
67. Mooberry, E. S.; Sheline, R. K. *J. Chem. Phys.* **1972**, *56*, 1852–1855.
68. Yamasaki, A.; Yajima, F.; Fujiwara, S. *Inorg. Chim. Acta* **1968**, *2*, 39–42.
69. Juranic, N. *Inorg. Chem.* **1983**, *22*, 521–525.
70. Dharmatti, S. S.; Kanekar, C. R. *J. Chem. Phys.* **1959**, *31*, 1436–1437.
71. Doddrell, D. M.; Bendall, M. R.; Healy, P. C.; Smith, G.; Kennard, C. H. L.; Raston, C. L.; White, A. H. *Aust. J. Chem.* **1979**, *32*, 1219–1230.

72. Weiss, R.; Verkade, J. G. *Inorg. Chem.* **1979**, *18*, 529–530.
73. Navon, G. *J. Phys. Chem.* **1981**, *85*, 3547–3549.
74. Shenoy, G. K. *Mössbauer Spectroscopy Applied to Inorganic Chemistry*; Long, G. J., Ed.; Plenum Press: New York, 1984, Vol. 1, pp 57–76.
75. Guenzburger, D.; Esquivel, D. M. S.; Danon, J. *Phys. Rev. B: Condens. Matter* **1978**, *18*, 4561–4569.
76. Dunlap, B. D.; Kalvius, G. M. In *Mössbauer Isomer Shifts*; Shenoy, G. K., Wagner, F. E., Eds.; North-Holland: Amsterdam, 1978, pp 15–48.
77. Russo, U.; Long, G. J. In *Mössbauer Spectroscopy Applied to Inorganic Chemistry*; Long, G. J., Grandjean, F., Eds.; Plenum Press: New York, 1989, Vol. 3, pp 289–329.
78. Walker, L. R.; Wertheim, G. K.; Jaccarino, V. *Phys. Rev. Lett.* **1961**, *6*, 98–101.
79. Long, G. L.; Hautot, D.; Mohan, A.; Hughbanks, T.; Xie, X.; Grandjean, F. *J. Am. Chem. Soc.* **1998**, *120*, 12163–12164.

Comprehensive Coordination Chemistry II
ISBN (set): 0-08-0437486

Volume 2, (ISBN 0-08-0443249); pp 775–784

2.66 Case Study of the Dicyanamidebenzene System

R. J. CRUTCHLEY
Carleton University, Ottawa, ON, Canada

2.66.1 INTRODUCTION 785
2.66.2 CRYSTALLOGRAPHY 786
2.66.3 THEORY 787
2.66.4 ANTIFERROMAGNETIC SUPEREXCHANGE 788
2.66.4.1 SQUID Magnetometer Studies 788
2.66.4.2 Paramagnetic ^{1}H NMR Spectroscopy 789
2.66.5 SOLVENT-DEPENDENT METAL–METAL COUPLING IN MIXED-VALENCE COMPLEXES 790
2.66.5.1 Comproportionation Equilibrium 790
2.66.5.2 Spectroelectrochemistry 792
2.66.5.2.1 UV–vis NIR Studies 792
2.66.5.2.2 Infrared Studies 793
2.66.6 REFERENCES 795

2.66.1 INTRODUCTION

In 1983 Creutz published a review,[1] showing that the vast majority of mixed-valence complexes were those incorporating a π-acceptor bridging ligand. The dominant superexchange pathway for metal–metal coupling was therefore one in which the donor wavefunction mixes with the unfilled orbitals of the bridging ligand, thereby extending itself onto the bridging ligand and effectively reducing the separation between donor and acceptor wavefunctions. This mechanism of superexchange is referred to as resonance or electron-transfer superexchange, and the studies that arose from these mixed-valence complexes investigated the properties derived from this mechanism. There is, however, an alternative mechanism for superexchange, in which the acceptor wavefunction mixes with the filled orbitals of the bridging ligand, thereby extending the acceptor wavefunction over the bridge. This mechanism of superexchange in mixed-valence complexes is referred to as hole-transfer superexchange. The challenge of studying hole-transfer superexchange resulted in the syntheses and study of the properties of dinuclear ruthenium complexes of dicyanamidobenzene ligands.

The bridging ligand, 1,4-dicyanamidebenzene dianion (**1**), is an extremely efficient mediator of metal–metal coupling between ruthenium ions, despite the separation between metal ions of over 13 Å. As will be shown, this is due to an energetically favorable match between the π HOMO of (**1**) and the $d\pi$-orbitals of the ruthenium ions. By varying the nature of the substituents on (**1**), it is possible to vary the energy of the HOMO and observe its effect on superexchange. Four derivatives of (**1**) have been characterized: 2,3,5,6-tetrachloro-1,4-dicyanamidebenzene dianion (**2**); 2,5-dichloro-1,4-dicyanamidebenzene dianion (**3**); 2,5-dimethyl-1,4-dicyanamidebenzene dianion (**4**);[2] and, finally, 2,3,5,6-tetramethyl-1,4-dicyanamidebenzene dianion (**5**).[3]

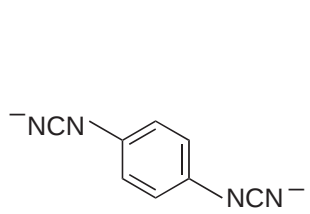

(1)

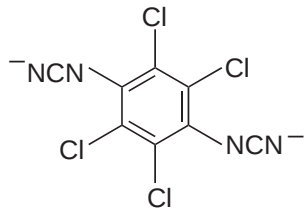

(2)

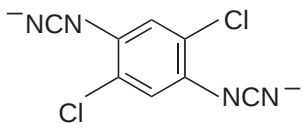

(3)

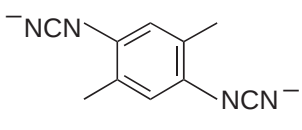

(4)

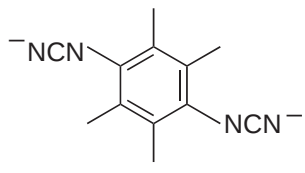

(5)

Varying the nature of the auxiliary ligands about the metal ion can also be used to change the energy of ruthenium $d\pi$-orbitals. For this reason, the following families of ruthenium dinuclear complexes were synthesized: $[\{Ru(NH_3)_5\}_2(\mu\text{-L})]^{4+}$, where L = (**1**), (**2**), (**3**), (**4**), and (**5**);[2–4] *trans,trans*-$[\{Ru(NH_3)_4(py)\}_2(\mu\text{-L})]^{4+}$, where py = pyridine and L = (**1**), (**2**), (**3**), and (**4**);[5] *mer,mer*-$[\{Ru(NH_3)_3\text{–}(bpy)\}_2(\mu\text{-L})]^{4+}$, where bpy = 2,2′-bipyridine and L = (**1**), (**3**), and (**4**);[6] and, finally, $[\{Ru(trpy)(bpy)\}_2(\mu\text{-}1)]^{2+}$.[7]

The ammine complexes are also subject to a donor–acceptor interaction between solvent lone-pair electrons and the hydrogen atoms of the ammine ligands (Scheme 1). This interaction has the effect of making the ammine ligand more amide-like in its bonding, transferring π-electron density to the partially filled $d\pi$-orbital of Ru^{III}, and thereby raising the energy of the Ru^{III} $d\pi$-orbitals and weakening the Ru^{III}–cyanamide π-bond.

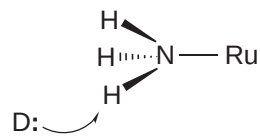

Scheme 1

Thus, by varying the bridging ligand, the auxiliary ligands, and the solvent, the extent of hole-transfer superexchange between ruthenium ions bridged by 1,4-dicyanamidebenzene dianion ligands can be purposefully varied and related to changes in the electronic properties of complexes. These properties were studied by a range of physical techniques: temperature-dependent, solid-state magnetic susceptibility measurements; proton nuclear magnetic resonance spectroscopy; cyclic voltammetry; and finally spectroelectrochemistry, in both the UV–vis NIR and IR ranges. Structure–function relationships require crystallography in combination with theory, and these are discussed first.

2.66.2 CRYSTALLOGRAPHY

Crystal structures of the tetraphenylarsonium salts of (**1**), (**2**), (**3**), and (**4**) all showed that the anionic cyanamide groups were in an *anti* conformation and approximately planar to the phenyl ring.[8] For (**5**), steric repulsion forced the cyanamide groups out of plane, but still in an *anti* conformation.[3] This preference for a planar geometry was rationalized by a π interaction between the cyanamide π-bonds and those of the phenyl ring. Crystal structures of the Ru^{III} dinuclear complexes, $[\{Ru(NH_3)_5\}_2(\mu\text{-}1)]^{4+}$,[2] *trans,trans*-$[\{Ru(NH_3)_4(py)\}_2(\mu\text{-}1)]^{4+}$, where py = pyridine,[5] and *mer,mer*-$[\{Ru(NH_3)_3(bpy)\}_2(\mu\text{-}1)]^{4+}$, where bpy is 2,2′-bipyridine,[6] all showed retention of the planar geometry of (**1**) and coordination of the cyano-nitrogen to Ru^{III}. Coordination of the amido nitrogen of the cyanamide group has not been observed crystallographically and this is probably due to

steric hindrance. The *anti* configuration of cyanamide groups, while observed in the crystal structures of $[\{Ru(NH_3)_5\}_2(\mu\text{-}1)]^{4+}$ and $-[\{Ru(NH_3)_3(bpy)\}_2(\mu\text{-}1)]^{4+}$, is not a constant. The crystal structure of *trans, trans*-$[\{Ru(NH_3)_4(py)\}_2(\mu\text{-}1)]^{4+}$ showed a planar (**1**) with cyanamide groups adopting a *syn* conformation.[5] This implies that in solution the cyanamide groups may rotate about the phenyl ring. The barrier for this rotation is likely to be small for the free ligand but, for a dinuclear complex, resonance exchange between the metals should make a significant contribution to the rotation barrier. In addition, the crystal structure of $[\{Ru(NH_3)_5\}_2(\mu\text{-}1)]^{4+}$ showed two Ru^{III}–cyanamide conformations, the commonly observed linear coordination mode (Ru^{III}—NCN bond angle of 175.1°), and a bent coordination mode (Ru^{III}—NCN bond angle of 149.8°).[2]

2.66.3 THEORY

Because of the difficulty of performing calculations on large transition-metal complexes, early calculations focused on the more tractable dicyanamidobenzene dianion ligands, which were assumed to possess an ideal planar geometry. Extended Hückel theory showed that a nonbonding π-highest occupied molecular orbital (HOMO) spanned the entire molecule, and thereby provided a superexchange pathway between metal ion $d\pi$-orbitals.[2] In addition, the lowest unoccupied molecular orbital (LUMO) was essentially localized in the phenyl ring and was thus unsuited to function as a superexchange pathway. These results were later confirmed by *ab initio* calculations and are shown in Figure 1. Whether the cyanamide groups adopt a *syn* or *anti* conformation, there is little change in the appearance of the HOMO or LUMO, although it is expected that the *anti* conformation will be more stable due to the increased separation of negative cyanamide groups.

As mentioned in Section 2.66.2, (**5**) is a nonplanar 1,4-dicyanamidebenzene ligand with the cyanamide groups partially decoupled from the phenyl ring π-system. In contrast to the planar dicyanamidebenzene ligands, extended Hückel calculations show that its π-HOMO is largely localized on the phenyl ring[3] and this is expected to attenuate metal–metal coupling in complexes incorporating this bridging ligand.

Only semi-empirical methods to evaluate optimized geometry have been applied to the dinuclear Ru^{III} complexes at this time (2002). Good agreement was found between these gas-phase calculations and the crystal structure of the cation $[\{(Ru(NH_3)_3(bpy)\}_2(\mu\text{-}1)]^{4+}$.[9]

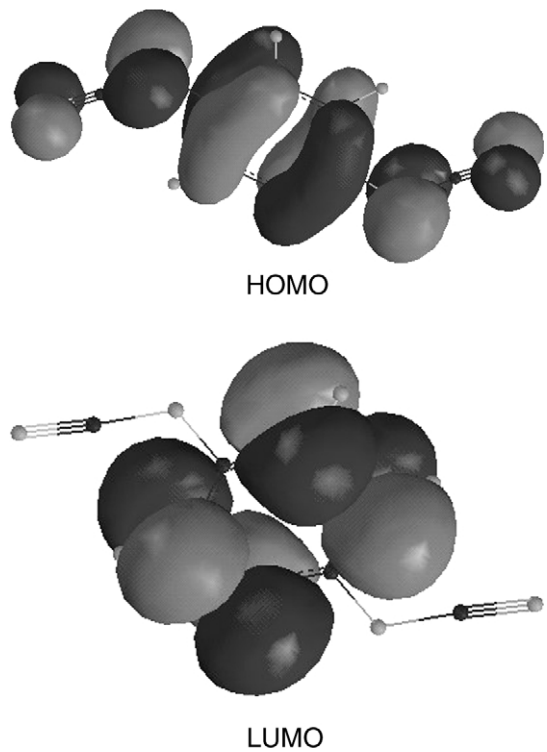

Figure 1 Calculated geometries for the highest occupied molecular orbital (HOMO) and the lowest unoccupied molecular orbital (LUMO) of 1,4-dicyanamidebenzene dianion.

2.66.4 ANTIFERROMAGNETIC SUPEREXCHANGE

2.66.4.1 SQUID Magnetometer Studies

If two metal ions with spin $S = 1/2$ are antiferromagnetically coupled, a singlet ground state and an excited triplet state are created with a separation of energy equal to $-2J$, where J is the exchange coupling constant. For Ru^{III} ions bridged by 1,4-dicyanamidobenzene, antiferromagnetic exchange occurs via the superexchange mechanism, and the electronic consequence of this interaction can be observed spectroscopically through the Ru^{III}–cyanamide LMCT transition (Scheme 2).

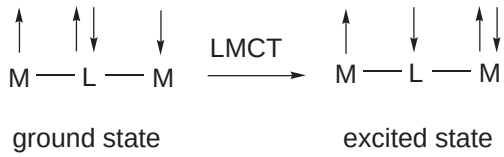

Scheme 2

In the LMCT excited state the unpaired electrons can couple, but can do so only if their spins are opposite. The mixing of the LMCT excited state with the ground state therefore stabilizes a ground state in which the electrons are antiparallel.

Solid-state, temperature-dependent magnetic susceptibility experiments were performed on the dinuclear ruthenium complexes using a SQUID magnetometer.[2] A representative study is shown in Figure 2 of the data derived for the tosylate salt of $[\{Ru(NH_3)_5\}_2(\mu\text{-}1)]^{4+}$. The broad minimum that is seen in Figure 2 is characteristic of intramolecular antiferromagnetic exchange and results from the favorable energy and symmetry match of the Ru^{III} $d\pi$-orbitals and the π HOMO of the bridging ligand. The background temperature-dependent paramagnetic susceptibility data for the complexes were fitted assuming isotropically coupled spins, and by using the modified Bleaney-Bowers expression,[10]

$$\chi_M = \frac{C}{(T-\theta)} + \left(\frac{2Ng^2\beta^2}{3kT}\right)\left[1 + \frac{1}{3}\exp\left(\frac{-2J}{kT}\right)\right]^{-1} + \chi_0 \qquad (1)$$

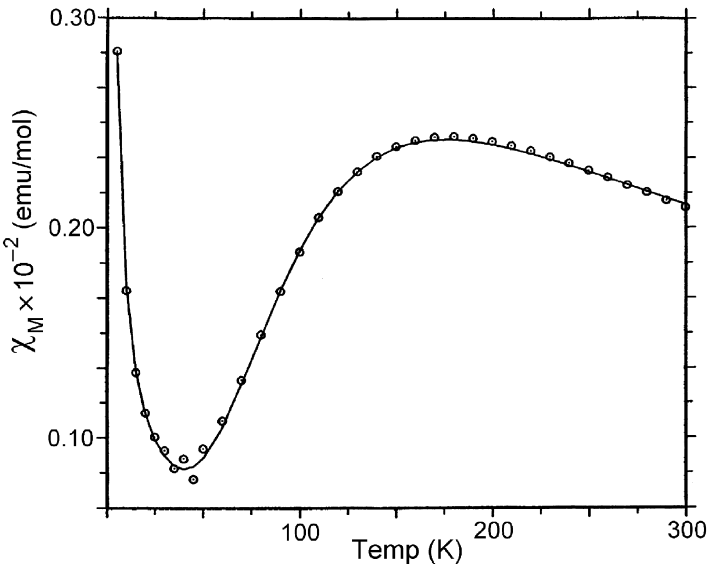

Figure 2 Experimental (⊙) and modeled (—) temperature dependences for the molar magnetic susceptibility of $[\{Ru(NH_3)_5\}_2(\mu\text{-}1)][\text{tosylate}]_4$ (reproduced with permission from ref. 2; © 1992, American Chemical Society).

Table 1 Best-fit parameters for magnetic susceptibility of $[\{Ru(NH_3)_5\}_2(\mu\text{-L})]^{4+}$ complexes using Equation (1) and LMCT band energy.

L	g (cm^{-1})	$-J$	$LMCT$ (cm^{-1})
(**1**)$[ClO_4]_4$		≥400	11,560
(**1**)[tosylate]$_4$	1.95	100	11,560
(**4**)$[ClO_4]_4$		≥400	9,560
(**5**)$[ClO_4]_4$	1.76	110	12,580
(**3**)$[Cl]_4$	1.69	95.9	12,450
(**2**)$[Cl]_4$	1.96	61.9	14,020

where g is the powder average g value, $C/(T-\theta)$ is a Curie-Weiss term that corrects for any paramagnetic impurity at low temperatures, and χ_0 is a correction for any temperature-dependent paramagnetism. The resulting exchange constants of the complexes have been compiled in Table 1, together with the energy of the complexes lowest-energy LMCT band, a qualitative measure of the energy gap between the bridging ligand's HOMO and the partially filled $d\pi$-orbital of Ru^{III}. The exchange constants in Table 1 are all antiferromagnetic, with the magnitude of $-J$ approximately increasing with decreasing LMCT energy. The complexes *trans,trans*-$[\{Ru(NH_3)_4(py)\}_2(\mu\text{-L})]^{4+}$, where L = (**1**), (**2**), (**3**), and (**4**), and *mer,mer*-$[\{Ru(NH_3)_3(bpy)\}_2(\mu\text{-L})]^{4+}$, where L = (**1**), (**3**), and (**4**), are diamagnetic in the solid state, which indicates that $-J \geq 400\,cm^{-1}$.[9] The dependence of antiferromagnetic exchange on LMCT energy is given a more quantitative understanding by examining the valence-bond theory approach to antiferromagnetic exchange of Tuczek and Solomon.[11] Their final expression for antiferromagnetic exchange was:

$$-J = \frac{h_{d\pi}^4}{\Delta^2}\left(\frac{1}{U} + \frac{2}{E_{DCT}}\right) \tag{2}$$

where the transfer integral (or metal–ligand coupling element), $h_{d\pi}$, is the resonance exchange integral associated with a one-electron charge transfer between the bridging ligand and the metal, Δ is the energy difference between the ground state and the LMCT excited state, U is the metal-to-metal charge transfer MMCT transition energy, and E_{DCT} is the difference in energy between the ground and double charge transfer states.

In Table 1, the perchlorate salt of $[\{Ru(NH_3)_5\}_2(\mu\text{-}1)]^{4+}$ possesses a considerably larger antiferromagnetic exchange constant compared to the analogous tosylate salt. It seems probable that this arises because of a difference in the crystal structures. Indeed, as shown below, outer-sphere perturbations can significantly reduce antiferromagnetic exchange in these complexes.

2.66.4.2 Paramagnetic ^{1}H NMR Spectroscopy

The ammine dinuclear ruthenium(III) complexes show a remarkable dependence of antiferromagnetic exchange upon the nature of the outer coordination.[12] This is illustrated by Figure 3, which shows the solvent dependence of the lowest-energy LMCT band of $[\{Ru(NH_3)_5\}_2(\mu\text{-}1)]^{4+}$. The rapid decrease in LMCT band oscillator strength with solvent results from the decoupling of Ru^{III} from the cyanamide group, because of the outer-sphere donor–acceptor interaction between the solvent's nonbonding electron pairs and the protons of the ammine ligands (Section 2.66.1). If the Ru^{III} ions are decoupled from the cyanamide groups, it follows that the Ru^{III} ions are decoupled from the superexchange pathway and that antiferromagnetic exchange will be weakened. This is theoretically supported by Equation (2) and the metal–ligand coupling element, $h_{d\pi}$, which can be determined from experimental charge-transfer band properties by using the expression from Mulliken and Hush,[13]

$$h_{d\pi} = \frac{3.03 \times 10^2}{r}(\nu_{max} f)^{1/2} \tag{3}$$

where ν_{max} is the charge transfer band maximum in cm^{-1}, f is the oscillator strength of a single metal–ligand chromophore, and r is the transition moment length, which is usually taken to be the separation between donor and acceptor in Å. Thus, complexes that are diamagnetic in the solid state may exhibit significant paramagnetism in strongly donating solvents, as shown by their contact- and pseudocontact-shifted ^{1}H NMR spectra.

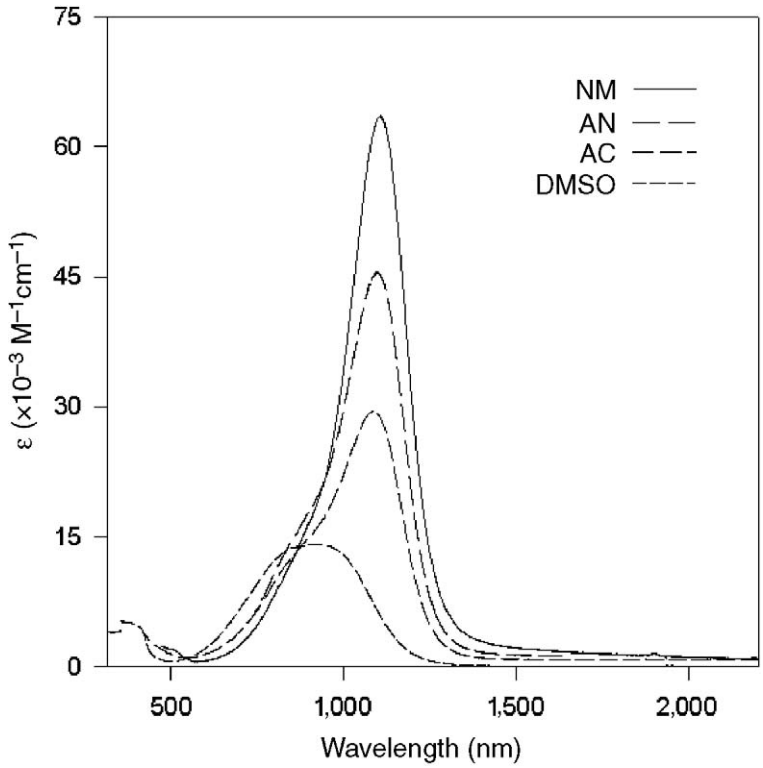

Figure 3 Solvent dependence of the LMCT band of $[\{Ru(NH_3)_5\}_2(\mu\text{-}1)]^{4+}$ in nitromethane (NM), acetonitrile (AN), acetone (AC), and DMSO (reproduced with permission from ref. 4; © 1998, American Chemical Society).

The solution magnetic susceptibilities of the pentaammineruthenium dinuclear complexes were calculated from NMR chemical shifts by using the Evans method.[12,14] Antiferromagnetic exchange constants were estimated from these room-temperature, molar, magnetic susceptibility data and correlated to calculated values by using Equations (2) and (3).[12] The correlation was quite good for data derived from aprotic solvents, but the difference between aprotic and protic data suggests that there are two pathways for antiferromagnetic superexchange. This is discussed in greater detail in Chapter 2.45.

2.66.5 SOLVENT-DEPENDENT METAL–METAL COUPLING IN MIXED-VALENCE COMPLEXES

2.66.5.1 Comproportionation Equilibrium

The stability of a mixed-valence complex is measured by the free energy of comproportionation, ΔG_c, according to the comproportionation equilibrium:

$$[Ru^{II}\text{-}Ru^{II}] + [Ru^{III}\text{-}Ru^{III}] \overset{K_c}{\longleftrightarrow} 2[Ru^{III}\text{-}Ru^{II}] \tag{4}$$

which also defines the comproportionation constant, K_c. ΔG_c may be determined electrochemically by using cyclic voltammetry, where the difference between metal-centered redox couple potentials, $\Delta E = E^{\circ}_{M2} - E^{\circ}_{M1}$:

$$[Ru^{II}\text{-}Ru^{II}] \overset{E^{\circ}_{M1}}{\longleftrightarrow} + [Ru^{III}\text{-}Ru^{II}] \overset{E^{\circ}_{M2}}{\longleftrightarrow} [Ru^{III}\text{-}Ru^{III}] \tag{5}$$

can be related to the free energy of comproportionation via the Nernst equation. The magnitude of K_c is determined by the sum of all energetic factors relating to the stability of the reactant and product complexes. For the dinuclear ruthenium complexes incorporating the 1,4-dicyanamidobenzene bridging ligand, five distinct factors contribute to the magnitude of ΔG_c:

$$\Delta G_c = \Delta G_s + \Delta G_e + \Delta G_i + \Delta G_r + \Delta G_{ex} \tag{6}$$

where ΔG_s reflects the statistical distribution of the comproportionation equilibrium; ΔG_e accounts for the electrostatic repulsion of the two like-charged metal centers; ΔG_i is an inductive factor dealing with competitive coordination of the bridging ligand by the metal ions; ΔG_r is the free energy of resonance exchange, the only component of ΔG_c which represents "actual" metal–metal coupling; and finally, ΔG_{ex} is the free energy of antiferromagnetic exchange. Unlike the other four terms, which all favor the mixed-valence product of Equation (4), ΔG_{ex} measures a stabilizing influence upon a reactant complex, and thus is of opposite sign to the remaining terms of Equation (6). It is not appropriate to relate the magnitude of the comproportionation constant to the extent of metal–metal coupling for weakly coupled mixed-valence complexes, because of the relatively important contribution of the other terms in Equation (6). However, for strongly coupled systems, the resonance term ΔG_r makes the dominant contribution to ΔG_c, and the other terms are of minor importance. Finally, the free energy of comproportionation results from the formation of two mixed-valence complexes (Equation (4)). To be congruent with theory, we must consider the free energy of comproportionation per mixed-valence complex, or $\Delta G_c' = 0.5\Delta G_c$. By analogy, we define the free energy of resonance exchange per mixed-valence complex as $\Delta G_r' = 0.5\Delta G_r$.

In Section 2.66.4.2, the effect of solvent on the LMCT bands of $[\{Ru(NH_3)_5\}_2(\mu\text{-}1)]^{4+}$ (Figure 3) clearly indicated a change in the electronic structure of the complex and, as a result, the extent of antiferromagnetic exchange was dramatically perturbed. It should not be surprising that the degree of metal–metal coupling in the mixed-valence complexes, and hence their comproportionation constants, should also show a considerable solvent dependence. Figure 4 shows the cyclic voltammograms of the $Ru^{III/II}$ couples of $[\{Ru(NH_3)_5\}_2(\mu\text{-}1)]^{4+}$ in water (a) and acetone (b). In water, the $Ru^{III/II}$ couples are nearly superimposed on each other, indicating that the extent of metal–metal coupling (ΔG_r) is very weak. However in acetone, the $Ru^{III/II}$ couples have become completely separated, indicating that the extent of metal–metal coupling has dramatically increased. In aprotic solvents, the magnitude of the comproportionation constant decreases with increasing solvent donor properties, and is due to the donor–acceptor interaction between solvent and ammine protons (Section 2.66.1). In water, protonation of the cyanamide groups provides another mechanism by which metal–metal coupling can be disrupted. The solvent-dependent cyclic voltammetry of all the ammine complexes has been performed and the data compiled.[4,15]

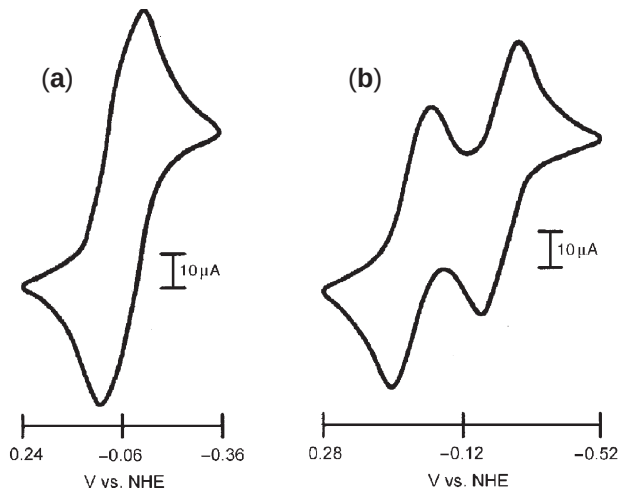

Figure 4 Cyclic voltammograms of the $Ru^{III/II}$ couples of $[\{Ru(NH_3)_5\}_2(\mu\text{-}1)]^{4+}$ in (a) water and (b) acetone.

In order to extract the value of ΔG_r from the free energy of comproportionation, the free energy terms ΔG_s, ΔG_e, ΔG_i, and ΔG_{ex} must be evaluated. The antiferromagnetic exchange term ΔG_{ex} may be estimated from room-temperature magnetic moments, as discussed in Chapter 2.45. Comprehensive estimates of ΔG_{ex} (or one-half the separation between singlet ground and triplet excited states) are available for the pentaammine complexes, and to a lesser extent for the tetraammine complexes.[4] The nonexchange contributions to ΔG_c, i.e., $\Delta G_{ne} = \Delta G_s + \Delta G_e + \Delta G_i$, were estimated from the ΔG_c of the most weakly coupled mixed-valence complex and corrected for the change in ΔG_e with solvent.[4]

Because both free energy values for antiferromagnetic exchange and nonexchange contributions to ΔG_c can be determined, it is now possible to extract an experimental value for the free energy of resonance exchange in the mixed-valence complexes. Theory, together with electronic absorption data, provides a route to ΔG_r that can be used for comparison, and that is the subject of the next section.

2.66.5.2 Spectroelectrochemistry

2.66.5.2.1 UV–vis NIR Studies

A mixed-valence complex will fall into one of three categories, as proposed by Robin and Day,[16] depending upon the degree of coupling between the metal centers. Completely valence-trapped complexes (no coupling between the metal centers) are termed Class I, while complexes in which the valence electrons are fully delocalized (very strong coupling between the metal centers) are termed Class III. All complexes whose behavior falls between these extremes constitute Class II.

For symmetric Class II mixed-valence complexes, the relationship between $\Delta G_r'$ and the metal–metal coupling element is given by:[17]

$$\Delta G_r' = H_{MM}^2 / E_{IT} \tag{7}$$

where, E_{IT} and H_{MM} are the intervalence band energy and metal–metal coupling element, respectively. The derivation of the general equation for the effective (i.e., indirect) coupling of the metal centers is discussed in detail in Chapter 2.44. Its general form is:[4,13]

$$H_{MM'} = \frac{H_{ML} H_{M'L}}{2\Delta E_{ML}^{eff}} + \frac{H_{LM} H_{LM'}}{\Delta E_{LM}^{eff}} \tag{8}$$

The coupling element $H_{MM'}$ of Equation (8) is the effective metal–metal coupling, while the coupling elements in the two terms on the right of Equation (8) are associated with metal–ligand interactions of the electron-transfer and hole-transfer pathways, respectively. The denominators are reduced energy gaps between metal and ligand orbitals. For the complexes of this study, only the hole-transfer pathway, and thus the second term of Equation (8), need be considered: and given the approximation $H_{LM} = H_{LM'}$, Equation (8) simplifies to:

$$H_{MM'} = \frac{H_{LM}^2}{\Delta E_{LM}^{eff}} \tag{9}$$

H_{LM} values were evaluated using Equation (3) and the electronic absorbance data of the low-energy LMCT band of the polyaammineruthenium dinuclear complexes, assuming a value of $r = 6.5$ Å, which is the distance between Ru^{III} and the center of the 1,4-dicyanamidobenzene bridging ligand. The experimental LMCT oscillator strength should be divided by a factor of two in order to compensate for the absorption of two Ru^{III}-cyanamide chromophores. The reduced energy gap for the hole-transfer case is given by:[13]

$$\Delta E_{LM}^{eff} = \left[0.5 \left(\frac{1}{E_{LMCT}} + \frac{1}{E_{LMCT} - E_{IT}} \right) \right]^{-1} \tag{10}$$

where E_{LMCT} is the energy of the LMCT band at λ_{max}.

The electronic absorption data for the polyaammineruthenium dinuclear complexes were obtained by spectroelectrochemical studies, using an optically transparent, thin-layer electrochemical (OTTLE) cell.[15,18] It is important that the effect of electrochemical titration on the

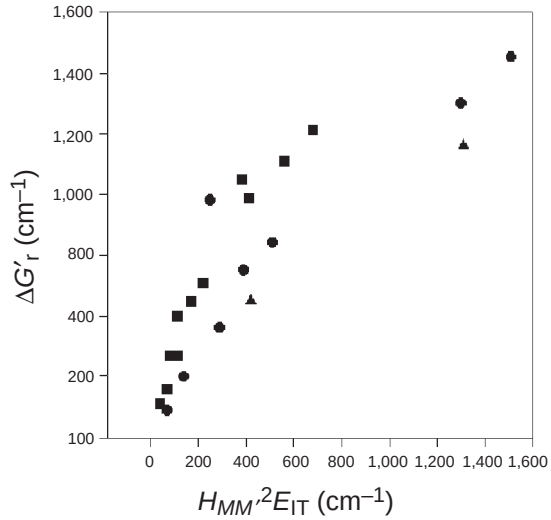

Figure 5 Plot of $\Delta G_r'$ vs. $H_{MM'}^2/E_{IT}$ for the pentaammine (■), tetraammine (●) and triammine (▲) complexes (reproduced with permission from ref. 4; © 1998, American Chemical Society).

absorption spectrum of the complex be consistent with the stepwise, reversible reduction of the complex. Specifically, isosbestic points must be maintained during a single redox process and, upon reversing the applied potential, the original spectrum is obtained. The electronic absorption data required to calculate theoretical values of $H_{MM'}$ and hence, by using Equation (7), theoretical values of $\Delta G_r'$, have been published, but the final result for all the polyammineruthenium dinuclear complexes is shown in Figure 5.

The success of Equation (9) in predicting metal–metal coupling for the complexes of this study is shown by the good correlation between $H_{MM'}^2/E_{IT}$ and $\Delta G_r'$ for the pentaammine, tetraammine, and triammine complexes in Figure 5. In addition, these results strongly support the realization that metal–ligand and metal–metal coupling elements are related to charge-transfer band oscillator strengths. The curvature in the data may be real, since it may result from the breakdown in Equation (7) as strong coupling or Class III mixed-valence properties are obtained. The examination of the Class II/Class III boundary is the subject of the IR spectroelectrochemical studies discussed below.

2.66.5.2.2 Infrared Studies

It would be of some theoretical and practical importance to know the magnitude of resonance exchange energy required to achieve a delocalized state in a mixed-valence complex. In this regard, infrared spectroscopy has been recognized as a powerful means of examining electron transfer in mixed-valence complexes, as its time scale (10^{-13} s) gives an almost instantaneous view of the state of a fluxional molecule.[19]

For the dinuclear ruthenium complexes incorporating 1,4-dicyanamidobenzene ligands, the cyanamide stretch ν(NCN) provides an excellent marker, as it absorbs strongly and normally appears between 2,100 cm^{-1} and 2,200 cm^{-1}, a region that is free of most solvent interference. It has been shown that reduction of the mononuclear complex, *mer*-$[Ru(NH_3)_3(bpy)$-(2,3-dichlorophenylcyanamide)$]^{2+}$, results in a shift of ν(NCN) from 2,120 cm^{-1} to 2,180 cm^{-1} for cyanamide bound to Ru^{III} and Ru^{II} respectively.[19] This shift to higher energies is unexpected, but it can be explained by the polarization of the cyanamide group as shown in Scheme 3.

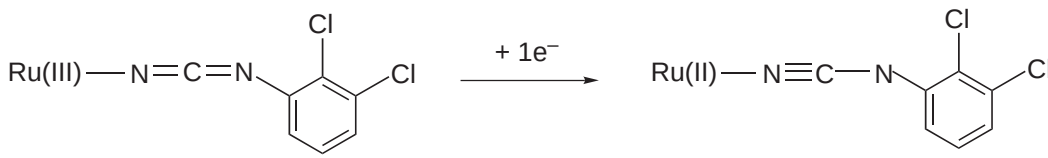

Scheme 3

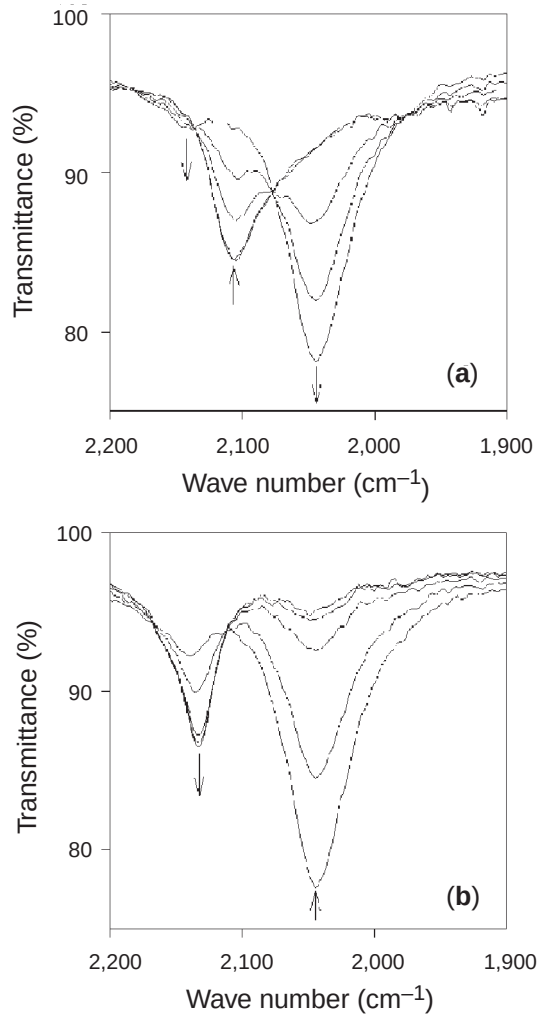

Figure 6 (a) IR spectra showing the reduction of the [III,III] complex, $[\{Ru(NH_3)_5\}_2(\mu\text{-}Me_2dicyd)][PF_6]_4$ to the [III,II] complex; (b) IR spectra showing the reduction of the mixed-valence complex to the [II,II] complex, in DMSO solution (reproduced with permission from ref. 19; © 2001, American Chemical Society).

The presence of both these resonance forms is seen in the IR spectroelectrochemical reduction of $[\{Ru(NH_3)_5\}_2(\mu\text{-}4)]^{4+}$ in DMSO (Figure 6). In Figure 6a, the reduction of [III,III] to [III,II] results in the loss of the single ν(NCN) band at 2,110 cm^{-1} and the growth of two new ν(NCN) bands at 2,040 cm^{-1} and 2,150 cm^{-1} that are assigned to cyanamide groups bound to Ru^{III} and Ru^{II}, respectively. Complete reduction to [II,II] (Figure 6b) gives only a single band at 2,140 cm^{-1}. These results are entirely consistent with Class II behavior in which there are identifiable Ru^{III} and Ru^{II} ions in the mixed-valence state.

Figure 7 shows the IR spectroelectrochemical reduction of *trans,trans*-$[\{Ru(NH_3)_4(pyridine)\}_2(\mu\text{-}3)]^{4+}$ in DMSO. Upon reduction of [III,III] to [III,II] in Figure 7a, the single ν(NCN) band at 2,090 cm^{-1} simply reduces intensity. Further reduction to the [II,II] complex (Figure 7b) results in the appearance of a new band at 2,140 cm^{-1}. These results are consistent with Class III behavior in the mixed-valence state in which the metal ions are indistinguishable. As can be seen in Figure 6a, the average energy of the ν(NCN) bands in the [III,II] complex is approximately the same as that of the single ν(NCN) band of the [III,III] complex. In Figure 7a, it is therefore coincidence that the ν(NCN) energy of the Class III mixed-valence complex is the same as that of the [III,III] complex.

By examining a number of complexes that spanned the range of Class II to Class III behavior, it was possible to show that the properties of the complex, *trans,trans*-$[\{Ru(NH_3)_4(py)\}_2(\mu\text{-}3)]^{3+}$ in acetonitrile can be regarded as benchmarks for delocalization for polyammineruthenium dinuclear complexes incorporating 1,4-dicyanamidobenzene bridging

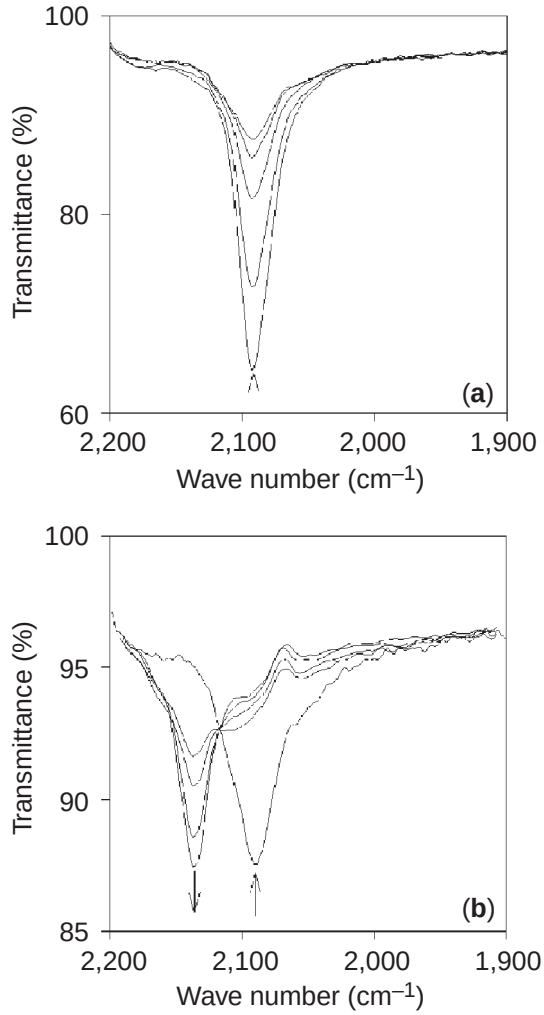

Figure 7 (a) IR spectra showing the reduction of the [III,III] complex, *trans,trans*-[{$Ru(NH_3)_4$-(py)}$_2$(μ-Me_2dicyd)][PF_6]$_4$ to the [II1/2,II1/2] complex; (b) IR spectra showing the reduction of the mixed-valence complex to the [II,II] complex, in acetonitrile solution (reproduced with permission from ref. 19; © 2001, American Chemical Society).

ligands.[19] It was shown that this complex obeys the general condition for delocalization in symmetric mixed-valence complexes, $2H = \lambda$, and possesses an experimental free energy of resonance exchange $\Delta G_r' = 1{,}250\,\mathrm{cm}^{-1}$ and resonance exchange integral $H = 3{,}740\,\mathrm{cm}^{-1}$.

2.66.6 REFERENCES

1. Creutz, C. *Prog. Inorg. Chem.* **1983**, *30*, 1–73.
2. Aquino, M. A. S.; Lee, F. L.; Gabe, E. J.; Bensimon, C.; Greedan, J. E.; Crutchley, R. J. *J. Am. Chem. Soc.* **1992**, *114*, 5130–5140.
3. Aquino, M. A. S.; Lee, F. L.; Gabe, E. J.; Greedan, J. E.; Crutchley, R. J. *Inorg. Chem.* **1991**, *30*, 3234–3236.
4. Evans, C. E. B.; Naklicki, M. L.; Rezvani, A. R.; White, C. A.; Kondratiev, V. V.; Crutchley, R. J. *J. Am. Chem. Soc.* **1998**, *120*, 13096–13103.
5. Rezvani, A. R.; Bensimon, C.; Cromp, B.; Reber, C.; Greedan, J. E.; Kondratiev, V.; Crutchley, R. J. *Inorg. Chem.* **1997**, *36*, 3322–3229.
6. Evans, C. E. B.; Yap, G. P. A.; Crutchley, R. J. *Inorg. Chem.* **1998**, *37*, 6161–6167.
7. Rezvani, A. R.; Evans, C. E. B.; Crutchley, R. J. *Inorg. Chem.* **1995**, *34*, 4600–4604.
8. Aquino, M. A. S.; Crutchley, R. J.; Lee, F. L.; Gabe, E. J.; Bensimon, C. *Acta Cryst.* **1993**, *C49*, 1543–1547.
9. Crutchley R. J. Unpublished results.
10. Carlin, R. L. *Magnetochemstry*; Springer-Verlag: Berlin, 1986.
11. Tuczek, F.; Solomon, E. I. *Inorg. Chem.* **1993**, *32*, 2850–2862.

12. Naklicki, M. L.; White, C. A.; Plante, L. L.; Evans, C. E. B.; Crutchley, R. J. *Inorg. Chem.* **1998**, *37*, 1880–1885.
13. Creutz, C.; Newton, M. D.; Sutin, N. *J. Photochem. Photobiol. A: Chem.* **1994**, *82*, 47–59.
14. Evans, D. F. *J. Chem. Soc.* **1959**, 2003–2005.
15. Evans, C. E. B. Ph.D. Thesis, Carleton University, Ottawa, Canada, 1998.
16. Robin, M. B.; Day, P. *Adv. Inorg. Chem. Radiochem.* **1967**, *10*, 247–422.
17. Richardson, D. E.; Taube, H. *Coord. Chem. Rev.* **1984**, *60*, 107–129.
18. Krejcik, M.; Danek, M.; Hartl, F. *J. Electronanal. Chem.* **1991**, *317*, 179–187.
19. DeRosa, M. C.; White, C. A.; Evans, C. E. B.; Crutchley, R. J. *J. Am. Chem. Soc.* **2001**, *123*, 1396–1402.

Comprehensive Coordination Chemistry II
ISBN (set): 0-08-0437486

Volume 2, (ISBN 0-08-0443249); pp 785–796

2.67
Appendix to Volume 2

JON A. McCLEVERTY
University of Bristol, Bristol, UK
and
THOMAS J. MEYER
Los Alamos National University, Los Alamos, New Mexico, USA

This appendix provides access to original chapters from Comprehensive Coordination Chemistry (published in 1987) that are relevant to this volume of Comprehensive Coordination Chemistry II (CCC2) but that are not cited by a specific chapter in CCC2.

For further details please see the end of the Preface under the General Information tab.

PDF 1. Chapter 10 Applications in Analysis